Broadband Dielectric Spectroscopy

F. Kremer · A. Schönhals (Eds.)

Broadband Dielectric Spectroscopy

With 393 Figures and 22 Tables

Springer

PROFESSOR DR. FRIEDRICH KREMER
University of Leipzig
Faculty of Physics and Geosciences
Linnéstraße 5
04103 Leipzig, Germany
e-mail: kremer@physik.uni-leipzig.de

PRIV.-DOZ. DR. ANDREAS SCHÖNHALS
Federal Institute for Materials
Research and Testing
Unter den Eichen 87
12205 Berlin, Germany
e-mail: andreas.schoenhals@bam.de

Foreword

The interaction of electromagnetic (EM) radiation with molecular systems gives rise to quantized transitions between the electronic, vibrational and rotational molecular energy states which may be observed by UV/visible and infra-red absorption spectroscopies at frequencies above about 1 THz (10^{12} Hz). These quantum spectroscopies for molecules in the gaseous, liquid and solid states form a large part of physical chemistry and chemical physics. However, if one asks a fellow scientist "what happens when EM radiation in the range 10^{-6} to 10^{12} Hz is applied to those systems" the answer is usually tentative and incomplete, which shows that a majority of scientists are unfamiliar with the dielectric dispersion and absorption phenomena that occur in this vast frequency range due to (i) dipole relaxation arising from the reorientational motions of molecular dipoles and (ii) electrical conduction arising from the translational motions of electric charges (ions, electrons). This is the domain of *Broadband Dielectric Spectroscopy* (BDS).

At frequencies below about 10^8 Hz a dielectric sample is regarded as a complex electrical impedance $Z^*(\omega)$, expressed in terms of the resistance $R(\omega)$ and capacitance $C(\omega)$, which are frequency-dependent *extensive* properties (here $\omega = 2\pi f$/Hz where f is the measuring frequency). The *intensive* complex dielectric quantities of dielectric permittivity $\varepsilon^*(\omega)$, electrical modulus $M^*(\omega)$, electrical conductivity $\sigma^*(\omega)$ and resistivity $\rho^*(\omega)$ are immediately derivable from $Z^*(\omega)$. Researchers traditionally use these different quantities to express BDS data for materials, which is a source of confusion when assessing the dielectric/electrical properties of a given material reported in the literature. Dipole relaxation behaviour is normally represented in terms of ε^* and electric conduction behaviour in terms of σ^*, Z^*, M^* or ρ^*.

Starting in the late nineteenth century, dielectric measurement techniques were developed for materials such as molecular liquids and solids and moderately-conducting materials such as electrolytes and semiconductors. Transient current methods were used for very low frequencies ($f < 1$ Hz) and a.c. bridges for power, audio, UHF and VHF frequencies (1 to 10^7 Hz). In the 1940s distributed circuit methods were introduced for microwave frequencies (10^8 to 10^{11} Hz) and in the 1970s novel spectroscopic methods were developed for far infrared frequencies (3×10^{11} to 3×10^{12} Hz). In the main, measurements were made point-by-point at each frequency in the range of interest, which was difficult, and time-consuming. This held back the use of dielectric spectroscopy as an investigative physical technique at times when rapid advances were being made in the related techniques of NMR, quasi-elastic light scattering and photon-correlation spectroscopy. Nevertheless extensive dielectric data for a host of organic and inor-

ganic materials were obtained prior to the early 1980s using these methods. Subsequently modern commercial impedance measuring devices for low frequencies and commercial network analysers, time-domain reflectometers and laser spectroscopies for high frequencies became available and were developed for broadband dielectric studies of materials. Automatic measurement and processing methods, made possible by on-line computers used in combination with the new instruments, transformed dielectric measurements of materials. Now it is possible to obtain accurate dielectric data quickly and efficiently over the entire frequency range 10^{-6} to 10^{12} Hz and means that BDS has now taken its rightful place alongside other modern investigative techniques for studying the structure and molecular dynamics of materials.

Debye (1927) established that *dielectric relaxation*, which is the dispersion of the real permittivity (ε') and the occurrence of dielectric absorption (ε'') in the *f*-domain for dipolar liquids and solids, was due to the reorientational motions of the molecular dipoles. Many dielectric studies followed, especially those by Smyth (Princeton) and Cole (Brown) that were started in the 1930s. Early areas of study included dipolar liquids (e.g. chlorobenzene, polar solutes in non-polar solvents), rotator-phase crystals (e.g. cyclohexanol, the polymorphs of ice), non-polar polymers (e.g. polyethylene, polypropylene), polar polymers (e.g. polyacrylates, nylons, polyamides). Knowledge of the low frequency permittivity allowed molecular dipole moments to be determined, which was useful for the elucidation of molecular structures prior to the use of modern spectroscopic techniques. The dielectric loss spectra characterized the reorientational dynamics of molecules in the different materials. Also dielectric studies were made for inorganic solids that have ferroelectric properties (e.g. barium titanate) or are semi-conducting (e.g. doped silicon, organic photoconductors and semi-conductors) which have important applications in solid state devices. In parallel, extensive BDS data were obtained for electrolytes, polyelectrolytes, organic and inorganic semi-conductors, giving information on electrical conductivity and hence the mobilities of the effective charge carriers. More recently many BDS studies have been made for novel polymers, glass-forming liquids, liquid crystals (e.g. alkylcyanobiphenyls), polymeric liquid crystals (e.g. polysiloxanes with mesogenic side chains), ferroelectric organic materials (e.g. chiral alkylcyanobiphenyls and their polymeric derivatives), electrolytes (e.g. KCl/H_2O), molten salts (e.g. $Ca-K/NO_3$) and polyelectrolytes (e.g. polyethylene oxide/salt solutions). Such researches were often motivated by the applications of these materials in devices for modern technology. For example (i) the dielectric anisotropy of the liquid crystal is the source of the optical switching process in liquid crystal displays while (ii) new thin-film solid-state electrolytes are sought for battery applications.

As the data-base for the broadband dielectric behaviour of different materials increased, phenomenological and molecular theories for dipole relaxation and charge conduction were developed. The molecular theories required the deduction of $\varepsilon^*(\omega)$ or $\sigma^*(\omega)$ from the field-induced perturbation of the field-free reorientational and translational motions of molecular species. Such theories become extremely difficult for complex motions, e.g. as for multi-site motions of dipoles or ions in crystals or structured liquids. The situation changed completely when Kubo (1957), using linear response theory and time-dependent sta-

tistical mechanics, showed that $\sigma^*(\omega)$ was related, via Fourier transformation, to the field-free mean-squared displacement of charges with time $\langle \Delta R^2(t) \rangle$ or to their velocity correlation function $\langle \mathbf{v}(0)\mathbf{v}(t) \rangle$. For dielectric relaxation Glarum (1961) and Cole (1965) related $\varepsilon^*(\omega)$, via Fourier transformation, to the field-free dipole moment correlation function $\langle \boldsymbol{\mu}(0)\boldsymbol{\mu}(t) \rangle$ with time. Thus Fourier inversion of $\sigma^*(\omega)$ or $\varepsilon^*(\omega)$ gave direct determinations of these t-dependent molecular properties, which could in turn be fitted by chosen models for motions of molecules or charges. Research texts dealing with dielectric data (mainly for molecular liquids and solids) were published by Smyth (1955), Fröhlich (1958), Hill, Vaughan, Price and Davies (1969) and Böttcher and Bordewijk (1978) and for polymers by McCrum, Read and Williams (1967) and Runt and Fitzgerald (eds) (1997). Obviously the wide range of materials studied in different frequency bands for their dipole relaxation and conduction behaviour, the differing backgrounds of the researchers (physicists, chemists, materials scientists, electrical engineers, chemical engineers, theorists) and the publication of the researches in different journals of physics, physical chemistry/chemical physics, electrical engineering, polymer science and materials science made it increasingly difficult for scientists to monitor overall activities in dielectric spectroscopy. A great help to this effect have been the *International Discussion Meetings on Relaxations in Complex Systems* organized by K. L. Ngai and his associates held in Crete (1990), Alicante (1993) and Vigo (1997), published as special issues of J Non-Crystalline Solids, and that held in Crete (2001) where researchers in different areas of dielectrics science have been brought together along with a host of researchers that use related relaxation, scattering and spectroscopic techniques for the study of the dynamics of materials.

The stage has been reached where the foundations of broadband dielectric spectroscopy are well-established in terms of the large body of literature for the dielectric behaviour of dipolar materials and moderately-conducting electrolyte systems, phenomenological and molecular theories that relate $\varepsilon^*(\omega)$ and $\sigma^*(\omega)$ to empirical relaxation functions and to time-dependent molecular properties that give information on the reorientational and translational motions of molecules and charges in molecular liquids and solids. In this book the editors Friedrich Kremer and Andreas Schönhals have built on these foundations, through their own contributions and those of other leading scientists, taking the subject forward into those areas where BDS is making vital and new contributions to our understanding of the dynamics of complex systems. After a summary of the essentials of modern experimental techniques and dielectric theories (Chaps. 1–3) experimental data are shown over the entire frequency range for glasses, supercooled liquids, amorphous polymers (Chaps. 4, 5, 7), (polymeric) liquid crystals (Chap. 10) and semi-conducting disordered materials (Chap. 12) where multiple dipole relaxations are observed and are analysed in terms of particular motional processes. BDS provides a powerful method for studying the dynamics of molecules in confined spaces down to the mesoscopic and molecular levels (Chap. 6). Since the capacitance of a dielectric sample is inversely proportional to its thickness, BDS is highly suitable for studies of ultra-thin films, in contrast to NMR, light scattering and other spectroscopic techniques. The effects of film thickness on molecular dynamics in ultra-thin poly-

mer films are clearly demonstrated (Chap. 11) and provide severe tests of results for glass-forming materials obtained from other physical techniques. In-homogeneous media (Chap. 13) give rise to interfacial polarization in addition to dipole relaxation and charge-conduction and this is particularly important in multi-phase liquids and polymers, emulsions and biological systems. The component structures of relaxation processes and the questions of dynamic heterogeneity in organic materials are further elucidated by the new, sophisticated techniques of pulsed and non-resonant dielectric hole-burning (Chap. 14). BDS studies provide evidence for the structure and molecular dynamics in all these systems, evidence is obtained on the molecular dynamics which complements that obtained using the related techniques of solvation dynamics (Chap. 15), dynamical mechanical spectroscopy (Chap. 16), multi-dimensional multi-nuclear NMR (Chap. 17) and neutron scattering (Chap. 18). While dielectric relaxation behaviour is usually studied over wide ranges of frequency and sample temperature, the relaxation strength, relaxation time and its distribution are all affected significantly by applied pressure. This 'forgotten variable' (G. Floudas, Chap. 8) can be used to separate overlapping relaxations or induce crystallization – which transforms the relaxation behaviour in crystallizable polymers. Modern techniques allow broadband dielectric measurements to be made in real time for polymerizing systems where a liquid mixture transforms to a glass or an elastomer during reaction (Chap. 9). These studies monitor changes in molecular dynamics during the polymerization reaction and demonstrate the role of diffusion-control on reaction rate when a glass is formed.

Thus the editors and contributors show in this remarkable book that modern BDS techniques, as applied to a wide range of amorphous, crystalline and liquid crystalline systems, can give new and vital information on the reorientational and translational motions of dipolar molecules or electric charges and how the characteristics of these motions vary with temperature and pressure and with the physical condition of the material (bulk or thin film, confined geometries, macroscopic orientation (e.g. for liquid crystals)). They show how the wide frequency range of BDS may be utilised to obtain a detailed knowledge of individual motional processes whose time-scale may be in a range from picoseconds to kiloseconds and show further how this information complements that obtained for the same materials using related relaxation, scattering and spectroscopic techniques. A new researcher, or one from a related field of study, will find this 'state-of-the-art' account of broadband dielectric spectroscopy to be invaluable since inter alia it provides clear examples of the power of the technique to elucidate the dynamics of condensed systems, many of which have applied interest. Most important of all, the information provided by the BDS researches described here will stimulate new lines of research, not only into the applications of modern dielectric techniques to new materials and to time-varying systems but also to the development of further novel techniques that will test and extend the conclusions reached presently from BDS, NMR, mechanical relaxation, light scattering, neutron scattering, optical relaxation and related techniques concerning the detailed nature of molecular dynamics in organic and inorganic materials.

Swansea, UK, July 2002   *Prof. Dr. Graham Williams*

Preface

The interaction of electromagnetic waves with matter in the frequency regime between 10^{-6} and 10^{12} Hz is the domain of broadband dielectric spectroscopy. In this extraordinarily extended dynamic range, molecular and collective dipolar fluctuations, charge transport and polarization effects at inner and outer boundaries take place, and determine the dielectric properties of the material under study. Hence broadband dielectric spectroscopy enables us to gain a wealth of information on the dynamics of bound (dipoles) and mobile charge carriers depending on the details of the molecular system. In recent years novel dielectric instrumentation has been developed which allows for automatic measurements in nearly the entire range from ultra low frequencies up to the Far Infra Red.

It is intended that this book be more than a monograph at the leading edge of research. Therefore in three introductory chapters written in the style of a textbook, broadband dielectric spectroscopy is described in its theoretical foundation, its experimental techniques, and in the way dielectric spectra have to be analyzed. In the chapters 4–13, examples are described where the dielectric method has made important contributions to modern scientific topics. This is, of course, far from being a comprehensive overview and corresponds to the research interests of the editors. In chapters 14 and 15, two novel experimental techniques are introduced which are closely related to dielectric spectroscopy. Special attention is given in chapters 16–18 to the comparison between dielectric and other spectroscopic techniques such as mechanical, NMR, and neutron scattering.

The editors would like to thank all the contributors to this volume for their efficient collaboration. Many chapters of the book were read by G. Williams who made numerous suggestions from which the book benefited a great deal. The patient help of Mrs. I. Grünwald in typing some of the manuscripts and managing the correspondence is thankfully acknowledged. The editors would also like to thank Dr. M. Hertel and Springer Verlag for the competent cooperation.

July 2002

F. Kremer
A. Schönhals

Contributors

A. Arbe
Unidad de Física de Materiales (CSIC-UPV/EHU), Apartado 1072,
20080 San Sebastian, Spain
e-mail: waparmea@sc.ehu.es

R. Böhmer
Experimental Physics III, University of Dortmund, 44221 Dortmund, Germany
e-mail: Roland.Bohmer@Uni-Dortmund.de

J. Colmenero
Departamento de Física de Materiales, Universidad del País Vasco,
and Donostia International Physics Center, Apartado 1072,
20080 San Sebastian, Spain
e-mail: wapcolej@sc.ehu.es

G. Diezemann
Institute for Physical Chemistry, Johannes Gutenberg-University,
55099 Mainz, Welderweg 11, Germany
e-mail: diezeman@mail.uni-mainz.de

G. Floudas
University of Ioannina, Department of Physics, P.O. Box 1186,
451 10 Ioannina, Greece
e-mail: gfloudas@cc.uoi.gr

K. Fukao
Kyoto Institute of Technology, Department of Polymer Science and
Engineering, Matsugasaki, Sakyo-ku, Kyoto 606-8585, Japan
e-mail: fukao@ipc.kit.ac.jp

L. Hartmann
University of Leipzig, Faculty for Physics und Geosciences, Linnéstr. 5
04103 Leipzig, Germany
e-mail: lhartmann@physik.uni-leipzig.de

A. Huwe
Opto Speed Deutschland GmbH, Am Kavalleriesand 3, 64295 Darmstadt

F. Kremer
University of Leipzig, Faculty for Physics und Geosciences, Linnéstr. 5
04103 Leipzig, Germany
e-mail: kremer@physik.uni-leipzig.de

A. Loidl
University of Augsburg, Chair of Experimental Physics V, Universitätsstrasse 2,
86135 Augsburg, Germany
e-mail: alois.loidl@physik.uni-augsburg.de

P. Lunkenheimer
University of Augsburg, Chair of Experimental Physics V, Universitätsstrasse 2,
86135 Augsburg, Germany
e-mail: peter.lunkenheimer@physik.uni-augsburg.de

J. Mijovic
Department of Chemical Engineering and Chemistry, and The Herman F. Mark
Polymer Research Institute, Polytechnic University, Six MetroTech Center,
Brooklyn, NY 11201 USA
e-mail: jmijovic@poly.edu

T. Pakula
Max-Planck-Institute for Polymer Research, Postfach 3148, 55021 Mainz,
Germany
e-mail: pakula@mpip-mainz.mpg.de

R. Richert
Department of Chemistry and Biochemistry, Arizona State University, Tempe,
AZ 85287-1604, USA
e-mail: ranko@asu.edu

D. Richter
Institute of Solid State Research, Research Centre Jülich, 52425 Jülich, Germany
e-mail: D.Richter@fz-juelich.de

S. A. Różański
Higher Vocational State School in Pila, ul. zeromskiego 14, 64-920 Pila, Poland
e-mail: srozansk@szkoly.edu.pl

A. Schönhals
Federal Institute for Materials Research and Testing, Fachgruppe VI.3,
Unter den Eichen 87, 12205 Berlin, Germany
e-mail: andreas.schoenhals@bam.de

P. A. M. Steeman
DSM Research, P.O. Box 18, 6160MD Geleen, The Netherlands
e-mail: paul.steeman@dsm.com

J. van Turnhout
Delft University of Technology, Dept. of Polymer Material & Engineering,
Julianalaan 136, 2628BL, Delft, The Netherlands
e-mail: j.vanturnhout@tnw.tudelft.nl

Contents

**8   Effect of Pressure on the Dielectric Spectra
          of Polymeric Systems** 295
          G. Floudas

9   Dielectric Spectroscopy of Reactive Network-Forming Polymers 349
          J. Mijovic

1 Theory of Dielectric Relaxation

A. Schönhals · F. Kremer

1.1
Introduction

The interaction of electromagnetic fields with matter is described by Maxwell's equations (Eqs. 1.1–1.4)

$$\text{rot } \boldsymbol{E} = -\frac{\partial}{\partial t} \boldsymbol{B} \tag{1.1}$$

$$\text{rot } \boldsymbol{H} = \boldsymbol{j} + \frac{\partial}{\partial t} \boldsymbol{D} \tag{1.2}$$

$$\tag{1.3}$$

$$\text{div } \boldsymbol{D} = \rho_e$$

and

$$\text{div } \boldsymbol{B} = 0 \tag{1.4}$$

In this set of equations $\boldsymbol{E}$ and $\boldsymbol{H}$ describe the electric and magnetic field, $\boldsymbol{D}$ the dielectric displacement, $\boldsymbol{B}$ the magnetic induction, $\boldsymbol{j}$ the current density and ρ_e the density of charges [1]. For small electric field strengths $\boldsymbol{D}$ can be expressed by

$$\boldsymbol{D} = \varepsilon^* \varepsilon_0 \boldsymbol{E} \tag{1.5}$$

where ε_0 is the dielectric permittivity of vacuum ($\varepsilon_0 = 8.854 \times 10^{-12}$ As V^{-1} m^{-1}). ε^* is the complex dielectric function or dielectric permittivity [2]. According to Maxwell's equations (Eqs. 1.1–1.4) ε^* is time (or frequency) dependent if time dependent processes take place within the sample. There can be different reasons for this. Resonance phenomena are due to atomic or molecular vibrations and can be analysed by optical spectroscopy. The discussion of these processes

---

[1] Units: E – [Vm^{-1}]; H – [Am^{-1}]; B – [Vs m^{-2}]; D – [As m^{-2}]; j – [A m^{-2}].

[2] According to Eq. (1.5) also a linear relationship between the magnetic field H and the magnetic induction $\boldsymbol{B}$ can be defined as $\boldsymbol{B} = \mu^* \mu_0 \boldsymbol{H}$ where $\mu^* = \mu' - i\,\mu''$ is the complex magnetic permittivity. μ' and μ'' denote the corresponding real and loss part. μ_0 is the magnetic permittivity of vacuum ($\mu_0 = 1.256637 \times 10^{-6}$ Vs A^{-1} m^{-1}). μ_0 and ε_0 are related by $\varepsilon_0\,\mu_0 = \dfrac{1}{c^2}$ where c is the velocity of light in vacuum.

is out of the scope of this book. Relaxation phenomena are related to molecular fluctuations of dipoles due to molecules or parts of them in a potential landscape. Moreover, drift motion of mobile charge carriers (electrons, ions or charged defects) causes conductive contributions to the dielectric response. In general, time dependent processes within a material lead to a difference of the time dependencies of the outer electrical field $E(t)$ and the resulting dielectric displacement $D(t)$. For a periodic electrical field[3] $E(t) = E_0 \exp(-i\omega t)$ (ω is the radial frequency[4], $i = \sqrt{-1}$) the complex dielectric function ε^* is defined by

$$\varepsilon^*(\omega) = \varepsilon'(\omega) - i\varepsilon''(\omega) \tag{1.6}$$

where $\varepsilon'(\omega)$ is the real part and $\varepsilon''(\omega)$ the imaginary part of the complex dielectric function. In the stationary case which will only be considered during the course of this chapter the difference of the time dependencies of $E(t)$ and and $D(t)$ is a phase shift. Due to Maxwell's equations the complex dielectric function is related to the complex index of refraction by

$$\varepsilon^* = (n^*)^2 \tag{1.7}$$

with $n^*(\omega) = n'(\omega) + in''(\omega)$. In this sense dielectric (relaxation) spectroscopy can be regarded as continuation of optical spectroscopy to lower frequencies. The corresponding function to $\varepsilon^*(\omega)$ in the time domain is the time dependent dielectric function $\varepsilon(t)$ where the relationship between $\varepsilon^*(\omega)$ and $\varepsilon(t)$ is discussed during the course of this chapter.

Because D and E are vectors $\varepsilon^*(\omega)$ (or $\varepsilon(t)$) is in general a tensor. This becomes important for anisotropic systems like liquid crystalline [5] or crystalline materials. For sake of simplicity the tensorial character of the dielectric properties is neglected in the further discussion of this chapter.

The polarization P describes the dielectric displacement which originates from the response of a material to an external field only. Hence it is defined as

$$P = D - D_0 = (\varepsilon^* - 1)\,\varepsilon_0 E = \chi^* \varepsilon_0 E \quad \text{with} \quad \chi^* = (\varepsilon^* - 1) \tag{1.8a}$$

where χ^* is the dielectric susceptibility of the material under the influence of an outer electric field. For higher field strengths ($> 10^6$ V m^{-1})[5] non-linear effects may take place which can be described by

$$P = \varepsilon_0 \chi^* E + \beta_1 E^2 E \ldots \quad \text{in general} \quad P = \varepsilon_0 \chi^* E + \sum_{\substack{i=1\ldots \\ \text{odd}}} \beta_i E^{i+1} E \tag{1.8b}$$

---

[3] This is not an essential assumption because every time dependence can be represented by a periodical one applying Fourier analysis.

[4] ω denotes the radial frequency with the unit [rad s^{-1}]. The relation to the technical frequency ν is $\nu = \omega/2\pi$. The unit of ν is [Hz].

[5] Clearly the actual value of the electric field strength at which the dielectric behaviour becomes non-linear depends on the system under investigation. On the one hand for poly(tetra fluoro ethylene) (Teflon) a value $> 5 \times 10^6$ V m^{-1} is observed. On the other the dielectric behaviour of ferroelectric liquid crystals shows non-linear effects for field strengths of 10^3 V m^{-1}.

The coefficients β_i are called hyperpolarizabilities. It should be further noted that only odd powers contribute to that series development for thermodynamic and symmetry reasons (note $P(E) = -P(-E)$). In the course of this chapter only considerations which are based on the linear approximation (Eqs. 1.5 and 1.8a) will be discussed.

Similar to Eq. (1.5) Ohms law

$$j = \sigma^* E \tag{1.9}$$

gives the relationship between the electric field and the current density j where $\sigma^*(\omega) = \sigma'(\omega) + i\sigma''(\omega)$ is the complex electric conductivity. σ' and σ'' are the corresponding real and imaginary parts. Because the current density and the time derivative of the dielectric displacement are equivalent quantities according to Eqs. (1.2) and (1.5) it holds

$$\sigma^* = i\omega\varepsilon_0\varepsilon^* \tag{1.10}$$

This chapter is organized as follows. In the first part the essential points of electrostatics are reviewed. That means the dielectric properties are discussed at an infinite time after an application of an outer electric field. In the second part the theory of time dependent dielectric processes is developed in the frame of the linear response scheme.

1.2
Electrostatics

In general a macroscopic polarization P can be related to microscopic dipole moments p_i[6] of the molecules or particles within a volume V by

$$P = \frac{1}{V}\sum p_i \tag{1.11a}$$

where i counts all dipole moments in the system[7]. Molecules (or particles) have a dipole moment if the electric centres of gravity of positive and negative charges do not match. The simplest case is given by a positive charge $+q$ and a negative one $-q$ being separated by a distance d with the dipole moment $p = qd$. For any distribution of charges $\rho_e(r)$ the dipole moment can be expressed by $p = \int_V r\rho_e(r)\, d^3r$.

The microscopic dipole moments can have a permanent or an induced character. The latter is caused by the local electrical field E_{Loc} which distorts a neutral distribution of charges. In the linear case $p = \alpha E_{Loc}$ holds where the polarizability[8] α is a measure for the mobility of negative and positive charges. One

---

[6] During the course of this chapter dipole moments will in general be labelled by p. For permanent dipole moments the notation μ is used.

[7] The SI unit of the dipole moment is As m. But very often also the unit Debye (D) is used where $1\,D = 3.336 \times 10^{-30}$ As m.

[8] Similar to ε^* α is also a tensor which is neglected for sake of simplicity.

example of induced polarization is the electronic polarization where the negative electron cloud of an atom (molecule) is shifted with respect to the positive nucleus. Electronic polarization takes place on a time scale of 10^{-12} s because of the low mass of the electron. Atomic polarization can take place at a slightly longer time scale. These effects can be summarized by an induced polarization P_∞. Another example of charge separation which is based on a completely different mechanism is the electrode [6] and the Maxwell/Wagner-Polarization [7].

Many molecules have a permanent dipole moment $\boldsymbol{\mu}$ which can be oriented by an electrical field. Hence for a system containing only one kind of dipoles Eq. (1.11a) becomes

$$P = \frac{1}{V}\sum \boldsymbol{\mu}_i + P_\infty = \frac{N}{V}\langle \boldsymbol{\mu}\rangle + P_\infty \tag{1.11b}$$

where N denotes the whole number of dipoles in the system and $\langle\boldsymbol{\mu}\rangle$ the mean dipole moment. If the system contains different kinds of dipoles one has to sum up over all kinds. This is neglected for the sake of simplicity in further considerations.

In general the mean value of the dipole moment is determined by different factors. Assuming that inertia effects contribute only to P_∞ the main factors are the interaction of dipoles and the strength of the electric field at the location of the dipole. Assuming in the simplest approach first that the dipoles do not interact with each other and second that the electric field E_{Loc} at the location of the dipole is equal to the outer electrical field the mean value of the dipole moment is given only by the counterbalance of the thermal energy and the interaction energy W of a dipole with the electric field given by $W = -\boldsymbol{\mu}\cdot E$. According to Boltzmann statistics one gets [4, 8]

$$\langle\boldsymbol{\mu}\rangle = \frac{\displaystyle\int_{4\pi} \boldsymbol{\mu}\exp\left(\frac{\boldsymbol{\mu}\cdot E}{k_B T}\right)\mathrm{d}\Omega}{\displaystyle\int_{4\pi}\exp\left(\frac{\boldsymbol{\mu}\cdot E}{k_B T}\right)\mathrm{d}\Omega} \tag{1.12a}$$

where T is temperature, k_B Boltzmann constant and $\mathrm{d}\Omega$ the differential space angle. The factor $\exp\left(\dfrac{\boldsymbol{\mu}\cdot E}{k_B T}\right)\mathrm{d}\Omega$ gives the probability that the dipole moment vector has an orientation between Ω and $\Omega + \mathrm{d}\Omega$. Only the dipole moment component which is parallel to the direction of the outer electric field contributes to the polarization. Therefore the interaction energy is given by $W = -\mu E\cos\theta$ where θ is the angle between the orientation of the dipole moment and the electrical field (see inset Fig. 1.1). So Eq. (1.12a) simplifies to

$$\langle\mu\rangle = \frac{\displaystyle\int_0^\pi \mu\cos\theta\exp\left(\frac{\mu E\cos\theta}{k_B T}\right)\frac{1}{2}\sin\theta\,\mathrm{d}\theta}{\displaystyle\int_0^\pi\exp\left(\frac{\mu E\cos\theta}{k_B T}\right)\frac{1}{2}\sin\theta\,\mathrm{d}\theta} \tag{1.12b}$$
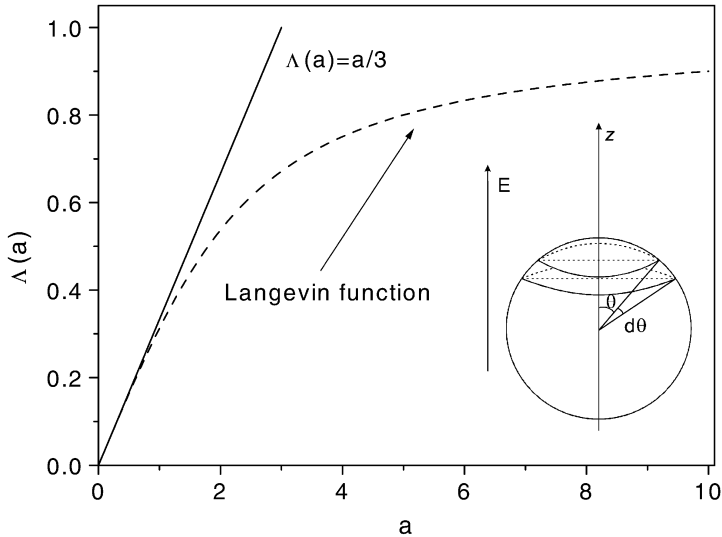
Fig. 1.1. Dependence of the Langevin function $\Lambda(a)$ vs a (*dashed line*) together with the linear approximation (*solid line*). The *inset* shows the geometrical scheme (spherical coordinate system) for derivation of Eq. (1.13)

The term $^1/_2 \sin \theta$ corresponds to components of the space angle in θ direction. With $x = (\mu E \cos \theta)/(k_B T)$ and $a = (\mu E)/(k_B T)$ Eq. (1.12b) can be rewritten as

$$\langle \cos\theta \rangle = \frac{1}{a} \frac{\int_{-a}^{a} x \exp(x)\, dx}{\int_{-a}^{a} \exp(x)\, dx} = \frac{\exp(a) + \exp(-a)}{\exp(a) - \exp(-a)} - \frac{1}{a} = \Lambda(a) \tag{1.13}$$

where $\Lambda(a)$ is the Langevin function. The dependence of Λ on a is given in Fig. 1.1. For small values of interaction energy of a dipole with the electric field (field strengths $|E| \leq 10^6$ Vm^{-1})[9] compared to the thermal energy $\Lambda(a) \approx a/3$ holds. Therefore Eq. (1.12) reduces to

$$\langle \boldsymbol{\mu} \rangle = \frac{\mu^2}{3k_B T} \boldsymbol{E} \tag{1.14a}$$

Inserting Eq. (1.14a) into Eq. (1.11b) yields

$$\boldsymbol{P} = \frac{\mu^2}{3k_B T} \frac{N}{V} \boldsymbol{E} \tag{1.14b}$$

---

[9] It can be shown that this linear approximation is valid for $a = \dfrac{\mu E}{k_B T} < 0.1$ or $E < \dfrac{0.1\, k_B T}{\mu}$. For higher field strengths more terms of the series development

$$\Lambda(a) = \frac{1}{3}a - \frac{1}{45}a^3 + \frac{2}{945}a^5 \dots$$

have to be used.

and with the aid of Eq. (1.8a) the contribution of the orientational polarization to the dielectric function can be calculated as

$$\varepsilon_S - \varepsilon_\infty = \frac{1}{3\varepsilon_0} \frac{\mu^2}{k_B T} \frac{N}{V} \tag{1.15}$$

where $\varepsilon_S = \lim\limits_{\omega \to 0} \varepsilon'(\omega)$. $\varepsilon_\infty = \lim\limits_{\omega \to \infty} \varepsilon'(\omega)$ covers all contributions to the dielectric function which are due to electronic and atomic polarization P_∞ in the optical frequency range.

Equation (1.15) enables one to estimate the mean molecular dipole moment of $\langle \mu^2 \rangle^{1/2}$ from dielectric spectra. However, one has to keep in mind that two main assumptions were made to derive Eq. (1.15): (i) the dipoles should not interact with each other which is true only for very diluted systems and (ii) local field effects (shielding of the outer electric field, see below) are negligible. In the following considerations effects which are due to a shielding of the outer electrical field will be discussed first. After that some methods to model the interaction between different dipoles are described.

Shielding effects which are also known as local field effects (or internal reaction fields) are due to the fact that a molecule with a permanent dipole is surrounded by other particles. So the field of that permanent dipole polarizes its environment proportional to the polarizability α. Moreover, if the surrounding particles also have permanent dipole moments their orientation will be influenced too. A calculation of the interplay of these two effects is in principle possible by means of statistical mechanics but in practice it is difficult to take into account both the interaction of molecules and the microscopic structure. The first approach to treat this problem was published by Lorentz [9]. A cavity was considered in an infinitely extended media and the polarization P of that cavity was calculated (see Fig. 1.2a). It was assumed that the local electrical field E_{Loc} is proportional to the polarization of the cavity $E_{Loc} = E + a_{Lor}(P/\varepsilon_0)$ and that the surrounding media can be described by the static dielectric permittivity ε_S. For a sphere[10] (so called Lorentz sphere) the coefficient a_{Lor} is equal to 1/3. The relation between the dielectric function and the polarizability α was derived by Mossotti [11] and Clausius [10]. For apolar molecules the polarization induced by the total electrical (outer

---

[10] According to Lorentz the internal field in homogeneously polarized matter can be calculated as the field in a virtual sphere where the outer electrical field induces apparent charges on the surface of this virtual sphere. The electric field due to these charges is calculated by dividing the surface of the sphere in infinitesimally small bands perpendicular to the outer field. The apparent surface charge density on these bands is given by $-P \cos \theta$ and the corresponding surface element by $1/2\ r^2 \sin\theta\ d\theta$. θ is the angle between the direction of the outer and the induced field. The charge on each band can be calculated to $dQ = -1/2\ r^2 P \sin\theta \cos\theta\ d\theta$. The field contribution dE_{Sphere} in the direction of the outer electric field is given by $dE_{Sphere} = \dfrac{\cos\theta}{\varepsilon_0} \dfrac{dQ}{r^2}$. Therefore the field due to the sphere is

$$E_{Sphere} = \frac{P}{2\varepsilon_0} \int\limits_0^\pi \sin\theta \cos^2\theta\ d\theta = \frac{1}{3} \frac{P}{\varepsilon_0}$$

The local electrical field is given by $E_{Loc} = E + E_{Sphere} = \dfrac{\varepsilon_S + 2}{3} E$.

Fig. 1.2. Schematic illustrations for the derivation of: **a** the Clausius/Mossotti equation; **b** the Onsager formula; **c** the Kirkwood/Fröhlich correlation factor

$$E_{Loc} = E + \tfrac{1}{3}P/\varepsilon_0$$

(a)

$$m = \mu + \alpha E_{Loc}$$

(b)

(c) $\tilde{N}$ interacting dipoles having an effective dipole moment μ
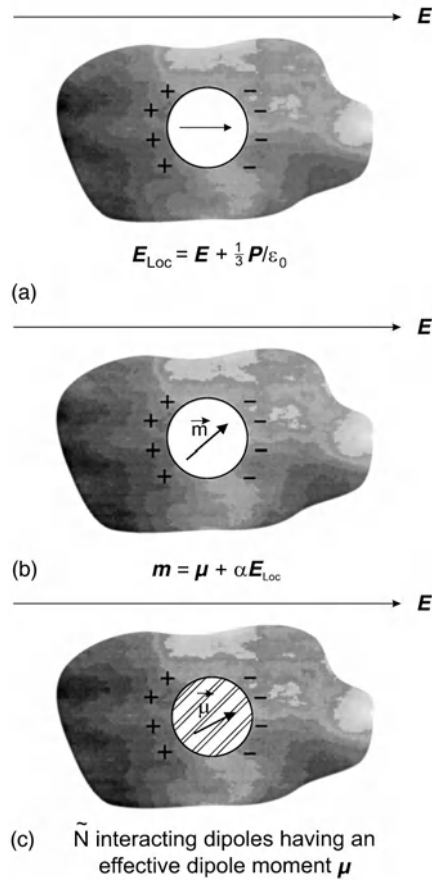
field and Lorentz-) field is given by $P = \dfrac{N}{V}\alpha E = \dfrac{N}{V}\dfrac{\varepsilon_S + 2}{3}E$. For the static case Eq. (1.8a) gives $P = \varepsilon_0(\varepsilon_S - 1)E$. The combination of both equations gives [4]

$$\frac{\varepsilon_S - 1}{\varepsilon_S + 2}\frac{M}{\rho} = \frac{1}{3}\frac{N_A}{\varepsilon_0}\alpha \qquad (1.16a)$$

where the volume density of dipoles $\dfrac{N}{V}$ is expressed by $\dfrac{\rho}{M}N_A$. M is the molar mass of the molecule and ρ is the density of the system. N_A denotes the Avogadro number. For polar molecules the effect of orientation polarization has to be included and with Eq. (1.14b) one finds

$$\frac{\varepsilon_S - 1}{\varepsilon_S + 2}\frac{M}{\rho} = \frac{1}{3}\frac{N_A}{\varepsilon_0}\left(\alpha + \frac{\mu^2}{3k_BT}\right) \qquad (1.16b)$$

which is also known as the Debye-formula.

Table 1.1. Comparison of dipole moments measured in the gas phase μ_{Gas} and estimated from the dielectric properties of a liquid using the Onsager formula μ_{Onsag} (Eq. 1.17). In addition the Onsager factor is given. The data are taken from [4]

Compound	T [K]	ε_S	ε_∞	$\varepsilon_S - \varepsilon_\infty$	μ_{Onsag} [D]	μ_{Gas} [D]	F
Chloroform	239	4.77	2.20	2.57	1.18	1.01	2.39
Bromoform	293	4.39	2.70	1.69	0.92	0.99	2.81
Chloromethane	253	12.6	1.97	10.6	1.74	1.87	2.43
Bromomethane	273	9.82	2.17	7.65	1.55	1.81	2.76
Bromoethane	293	9.39	2.13	7.26	1.84	2.03	2.55
Dichloromethane	288	9.28	2.13	7.15	1.68	1.60	2.55
Dibromomethane	288	7.41	2.49	4.92	1.37	1.43	2.87
Nitromethane	303	35.9	1.99	33.9	3.44	3.46	2.58
Cyanomethane	293	27.2	1.96	25.2	3.36	4.02	2.52
Chlorobenzene	293	5.64	2.43	3.27	1.40	1.69	2.69
Ethoxymethane	293	4.37	1.92	2.45	1.40	1.15	2.10
2,2-Dichloropropane	293	11.37	2.10	9.27	2.45	2.27	2.56
Cyanobenzene	288	26.0	2.44	23.5	3.48	4.18	3.13
Nitrobenzene	293	34.89	2.52	32.3	4.06	4.22	3.28
Propanone	298	20.7	1.93	18.7	3.03	2.88	2.45
Trimethylamine	273	2.57	1.95	0.62	0.66	0.61	1.88

The most general extension of the Debye-formula for polar molecules was given by Onsager by the theory of the reaction field [12] which considers the enhancement of the permanent dipole moment of a molecule $\boldsymbol{\mu}$ by the polarization of the environment [11] (reaction field) (Fig. 1.2b). For a spherical cavity the reaction field is parallel to the permanent dipole moment and for the resulting dipole moment of the molecule $\boldsymbol{m} = \boldsymbol{\mu} + \alpha \boldsymbol{E}_{Loc}$ holds. The detailed calculation [4, 12] gives

$$\varepsilon_S - \varepsilon_\infty = \frac{1}{3\varepsilon_0} F \frac{\mu^2}{k_B T} \frac{N}{V} \tag{1.17a}$$

with

$$F = \frac{\varepsilon_S (\varepsilon_\infty + 2)^2}{3(2\varepsilon_S + \varepsilon_\infty)} \tag{1.17b}$$

Equation (1.17) can be used to estimate dipole moments for non-associating organic liquids. For an overview see Table 1.1 where for a number of molecules the dipole moment calculated using Eq. (1.17) was compared with that measured in the gas phase. The values were taken from [4]. In many cases a reasonable agreement was found. Moreover Table 1.1 gives the F-value which corresponds to the error which is made neglecting the reaction field. In most cases $F \approx 1.9 - 3.3$ was found for a variation of $\varepsilon_S - \varepsilon_\infty$ from 0.6 to 34. This means that the Onsager factor

---

[11] The field strength of the reaction field can be in the order of $10^5 \, V \, m^{-1}$ [4].

Table 1.2. Comparison of dipole moments measured in the gas phase μ_{Gas} and estimated from the dielectric properties of the liquid using the Onsager formula μ_{Onsag} (Eq. 1.17) for associating compounds. In addition the Kirkwood/Fröhlich factor is given. The data are taken from [4]

Compound	$T\,[K]$	$\mu_{\text{Onsag}}\,[D]$	$\mu_{\text{Gas}}\,[D]$	g
Hydrogen cyanide	293	5.66	2.98	1.899
Methanol	293	2.95	1.70	4.650
Formamide	293	4.91	3.73	1.310
Propionic acid	293	0.87	1.75	0.497
Heptanol-1	293	2.90	1.66	1.746
3-Ethylpentanol-3	297	1.08	1.61	0.670

F is an unspecific correction. A more refined discussion of the whole problem can be found in [4].

For polar associating liquids Eq. (1.17) fails. Table 1.2 compares the dipole moments for associating liquids estimated from the Onsager equation with that measured in the gas phase. The reasons for the failure are static orientation correlations between molecules which are not considered in the derivation of the Onsager equation. Such specific interactions between molecules can be caused for instance by hydrogen bonding, steric interactions etc. and can lead to associations of molecules. Dielectric spectroscopy on such liquids measures the effective dipole moment of such assemblies which can be greater or smaller compared to the dipole moment of the single molecule depending on the molecular structure.

In the frame of statistical mechanics [4, 13] the contribution of the orientation polarization to the dielectric function is given by

$$\varepsilon_S - \varepsilon_\infty = \frac{1}{3k_B T \varepsilon_0} \frac{\langle P(0) P(0) \rangle}{V} = \frac{1}{3k_B T \varepsilon_0} \frac{\left\langle \sum_i \boldsymbol{\mu}_i(0) \sum_j \boldsymbol{\mu}_j(0) \right\rangle}{V} \tag{1.18}$$

where $\langle P(0) P(0) \rangle$ is the static correlation function of polarization (dipole) fluctuations. The symbol (0) refers to an arbitrary time, for instance $t = 0$. In further consideration it is dropped for brevity. The averaging denoted by the brackets has to be done over the whole system considering all interactions. From a practical point of view this seems to be difficult to do. Therefore Kirkwood [14–16] and Fröhlich [17] introduced the correlation factor g to model the interaction between dipoles with respect to the ideal case of non-interacting dipoles. In general the Kirkwood/Fröhlich correlation factor is defined by

$$g = \frac{\left\langle \sum_i \boldsymbol{\mu}_i \sum_j \boldsymbol{\mu}_j \right\rangle}{N \mu^2} = 1 + \frac{\left\langle \sum_i \sum_{i<j} \boldsymbol{\mu}_i \boldsymbol{\mu}_j \right\rangle}{N \mu^2} = \frac{\mu_{\text{Interact.}}^2}{\mu^2} \tag{1.19}$$

where μ^2 is the mean square dipole moment for non-interacting isolated dipoles which can be measured, for instance, in the gas phase or for diluted solutions. The g-factor can be smaller or greater than 1 depending on the case if the mole-

cules have the tendency to orient anti-parallel or parallel. So the experimental determination of g enables one to estimate the orientation of the molecules with respect to each other.

Equation (1.19) is a formal definition of the Kirkwood/Fröhlich correlation factor. For a practical calculation of g Eq. (1.19) has the same difficulties as Eq. (1.18). To simplify this problem Kirkwood/Fröhlich considered a region containing $\tilde{N}$ molecules (see Fig. 1.2c) [4, 17]. These $\tilde{N}$ molecules were treated explicitly. The remaining $N - \tilde{N}$ molecules were considered like in the Onsager approach as an infinite continuum where the dielectric behaviour is characterized by ε_S. With these assumptions one gets

$$\varepsilon_S - \varepsilon_\infty = \frac{1}{3\varepsilon_0} F g \frac{\mu^2}{k_B T} \frac{N}{V} \tag{1.20a}$$

with

$$g = 1 + \frac{\left\langle \sum\limits_{i=1}^{\tilde{N}} \sum\limits_{i<j} \boldsymbol{\mu}_i \, \boldsymbol{\mu}_j \right\rangle}{\tilde{N} \mu^2} \tag{1.20b}$$

The accuracy of this method can be made as high as necessary by making $\tilde{N}$ as large as needed. A first approach to calculate g is to consider only the nearest neighbours of a selected test dipole. For that case g can be approximated by

$$g = 1 + z \langle \cos \psi \rangle \tag{1.21}$$

where z is the coordination number and ψ is the angle between the test dipole and a neighbour [4]. Table 1.2 gives some values for g for different liquids. It shows also the large effect that orientation correlations expressed by g can have on ε_S.

For an isolated polymeric chain the calculation of g is much more complicated than for low molecular weight molecules because 10^4 to 10^6 carbon atoms are covalently bound for that case. However, theoretical considerations are possible in the frame of the *R*otational *I*someric *S*tate (RIS-) model [18]. In the case of rod-like polymers orientation correlations can lead to giant dipole moments for the whole chain. A detailed discussion about that problem concerning different chain structures can be found in [19]. A discussion is also given in Chap. 7.

1.3
Dielectric Relaxation (Dielectric Retardation)

1.3.1
Linear Response Theory and Fluctuation Dissipation Theorem

The dielectric relaxation theory for small electric field strengths is a special case of linear response theory [13] (see Appendix 1.1). In the following we will only focus on the isotropic system. Within this approach the time dependent response $y(t)$ of a system, this means the response of the system following a dis-

turbance $x(t)$, can be described by a linear equation. In dielectrics the distur-
bance is the time dependent external electrical field $x(t) = E(t)$ and the response
of the system is the polarization $y(t) = P(t)$. In that case linear response theory
gives [20]

$$P(t) = P_\infty + \varepsilon_0 \int_{-\infty}^{t} \varepsilon(t-t') \frac{dE(t')}{dt'} dt' \tag{1.22}$$

where $\varepsilon(t)$ is the time dependent dielectric function and P_∞ covers all contribu-
tions arising from induced polarization. Equation (1.22) is based only on linear-
ity (the response of the system on two disturbances is the sum of the two single
reactions) and causality (only disturbances in the past contribute to the re-
sponse at the time t). $\varepsilon(t)$ can be measured directly as the time dependent re-
sponse caused by a step-like change of the outer electrical field ($dE(t)/dt = E_0$
$\delta(t)$; $\varepsilon(t) = (P(t) - P_\infty)/E_0 \varepsilon_0$). The relationships between the time dependence of
the electric field, the polarization and the time dependent relaxation function is
sketched in Fig. 1.3 for a step-like change of the electric field.

Because the polarization is an intensive thermodynamic quantity $\varepsilon(t)$ is a
generalized compliance. This statement is important because if different exper-
imental methods are compared a generalized compliance (modulus) should
be compared with a compliance (modulus). For a comparison of dielectric
relaxation with other relaxational methods (like mechanical one etc.) see
Appendix 1.1.

If a stationary periodic disturbance $E(t)(\omega) = E_0 \exp(-i\omega t)$ is applied to the
system where ω is the angular frequency, Eq. (1.22) is transformed to

$$P(t)(\omega) = \varepsilon_0(\varepsilon^*(\omega) - 1)E(t)(\omega) \quad \text{with} \quad \varepsilon^*(\omega) = \varepsilon'(\omega) - i\varepsilon''(\omega) \tag{1.23}$$

where $\varepsilon^*(\omega)$ is the complex dielectric function. $\varepsilon'(\omega)$ is proportional to the en-
ergy stored reversibly in the system per period and the imaginary part $\varepsilon''(\omega)$ is
proportional to the energy which is dissipated per period. The relationship of
$\varepsilon^*(\omega)$ to the time dependent dielectric function $\varepsilon(t)$ is given by

$$\varepsilon^*(\omega) = \varepsilon'(\omega) - i\varepsilon''(\omega) = \varepsilon_\infty - \int_{0}^{\infty} \frac{d\varepsilon(t)}{dt} \exp(-i\omega t)\, dt \tag{1.24}$$

Equation (1.24) is a one-sided Fourier or full imaginary Laplace transformation
[20]. Some further relationships between the time and frequency domain are
given in Fig. 1.4.

Like for all one-sided Fourier transformations of a causal function the real
and the imaginary part of $\varepsilon^*(\omega)$ are related to each other by the Kramers/Kronig
relations [13, 20] (for a derivation of Eq. (1.25) see Appendix 1.2):

$$\varepsilon'(\omega) - \varepsilon_\infty = H[\varepsilon''(\omega)] = \frac{1}{\pi} \oint \frac{\varepsilon''(\xi)}{\xi - \omega}\, d\xi$$

and
$$\tag{1.25}$$

$$\varepsilon''(\omega) = -H[\varepsilon'(\omega) - \varepsilon_\infty]$$
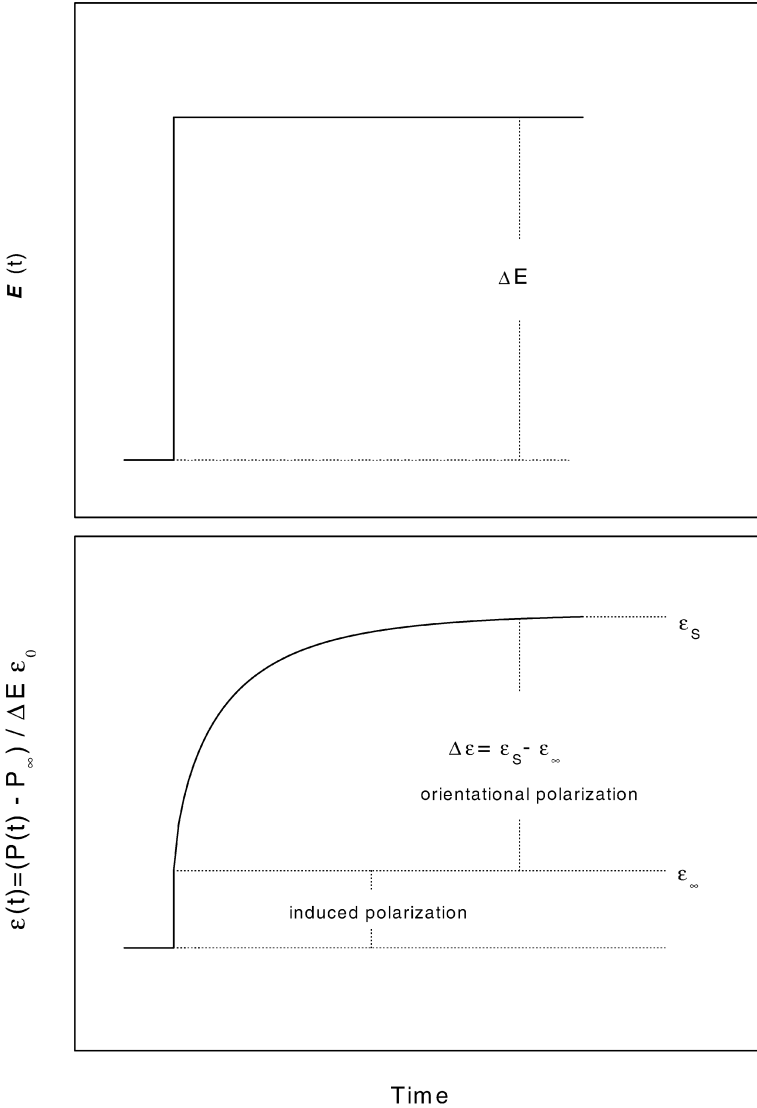
Fig. 1.3. Schematic relationships between the time dependence of the electric field ΔE (*small solid line*), the polarization P and the time dependent relaxation function $\varepsilon(t)$ (*heavy solid line*). The vector sign is omitted for sake of simplicity in the figure. The symbols denote the norm of the corresponding vectors

Complex Dielectric Function

$\varepsilon*(\omega)$

Time Dependent Dielectric Function

$\varepsilon(t)$

$$\frac{d\varepsilon(t)}{dt} = \frac{1}{2\pi}\int_0^\infty (\varepsilon*(\omega)-\varepsilon_\infty)\exp(i\omega t)\,d\omega$$

$$\varepsilon*(\omega) = \varepsilon_\infty - \int_0^\infty \frac{d\varepsilon(t)}{dt}\exp(-i\omega t)\,dt$$

$$L(\ln\tau) = -\frac{1}{\pi\Delta\varepsilon}\lim_{\rho\to\infty}\mathrm{Im}\,\varepsilon*(-\tau^{-1}+i\rho)$$

$$\varepsilon*(\omega)-\varepsilon_\infty = \Delta\varepsilon\int_{-\infty}^\infty \frac{L(\tau)}{1+i\omega\tau}\,d\ln\tau$$

$$L(\tau) = \frac{1}{\Delta\varepsilon}\lim_{k\to\infty}\frac{(-1)^{k+1}}{(k-1)!}\frac{(k\tau)^k}{\tau}\left[\frac{d^k\varepsilon(t)}{dt^k}\right]_{t=k\tau}$$

$$\frac{d\varepsilon(t)}{dt} = -\Delta\varepsilon\int_{-\infty}^\infty \tau^{-1}L(\tau)\exp\left(-\frac{t}{\tau}\right)d\ln\tau$$

$L(\tau)$

Dielectric Relaxation Time Distribution
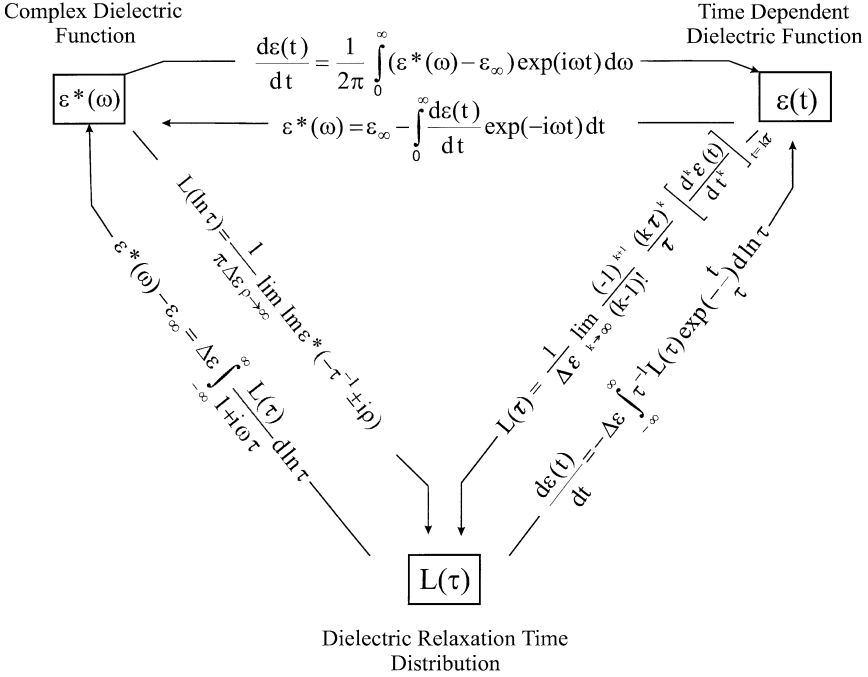
Fig. 1.4. Transformation relationships of linear dielectric response theory

The functional $H[\ ]$ denotes the Hilbert transformation. From an experimental point of view Eq. (1.25) means that both $\varepsilon'(\omega)$ and $\varepsilon''(\omega)$ carry the same information. Some numerical programs to solve Eq. (1.24) are for instance published in [21]. However, because of the limited frequency range and conductivity contributions including Maxwell/Wagner or electrode polarization the practical applicability of the Kramers/Kronig transformations is limited for dielectric experiments. The well known relationship that the dielectric strength $\Delta\varepsilon$ can be obtained by integrating the imaginary part

$$\varepsilon_S - \varepsilon_\infty = \Delta\varepsilon = \frac{2}{\pi}\int_0^\infty \varepsilon''(\omega)\,d\ln\omega \tag{1.26}$$

is obtained directly from Eq. (1.25) for $\omega = 0$ (for details see [17, 20] or Appendix 1.2).

As already pointed out the time dependent dielectric function $\varepsilon(t)$ or the complex dielectric function $\varepsilon^*(\omega)$ are generalized compliances. The related modulus is called electric modulus $M(t)$ in the time domain and complex electric modulus $M^*(\omega) = M'(\omega) + iM''(\omega)$ in the frequency domain where M' and M'' denote corresponding real and imaginary parts. The relationship between the compliance and the modulus is given by

$$\int_{-\infty}^\infty M(t-\tau)\,\varepsilon(\tau)\,d\tau = -\delta(t) \tag{1.27}$$

where $\delta(t)$ is the Dirac function. In the frequency domain

$$M^*(\omega)\,\varepsilon^*(\omega) = 1$$

with $\quad M'(\omega) = \dfrac{\varepsilon'(\omega)}{\varepsilon'^{2}(\omega) + \varepsilon''^{2}(\omega)} \quad$ and $\quad M''(\omega) = \dfrac{\varepsilon''(\omega)}{\varepsilon'^{2}(\omega) + \varepsilon''^{2}(\omega)}$ \hfill (1.28)

holds (see [20] or Appendix 1.2).

Thermodynamic quantities which characterize a macroscopic sample are average values. However, because of the stochastic thermal movement of the molecules (or particles) these quantities fluctuate around their mean values [13]. This general statement is of course also true for the polarization of a material[12]. According to Appendix 1.3 for the stationary state the auto correlation function of the polarization fluctuation $\Phi(\tau)$ is given by

$$\Phi(\tau) = \frac{\langle \Delta P(\tau)\Delta P(0)\rangle}{\langle \Delta P^2\rangle} \tag{1.29}$$

where τ denotes the time variable. It is obvious that $\Phi(0) = 1$ and $\Phi(\tau \to \infty) = 0$ hold. Inserting Eq. (1.11b) one gets for $\Phi(\tau)$ [20–23]

$$\Phi(\tau) = \frac{\sum\limits_i \langle \boldsymbol{\mu}_i(0)\boldsymbol{\mu}_i(\tau)\rangle + 2\sum\limits_i\sum\limits_{i<j}\langle\boldsymbol{\mu}_i(0)\boldsymbol{\mu}_j(\tau)\rangle}{\left\langle\left(\sum\limits_i\boldsymbol{\mu}_i\right)^2\right\rangle} \tag{1.30}$$

Equation (1.30) is the time dependent generalization of Eq. (1.18). The first part in Eq. (1.30) is the dipole-dipole auto-correlation function while the second part describes cross-correlations. It was argued that the cross-correlation terms can have a considerable magnitude and that their sign can be negative or positive [22, 23]. Also, the analysis of experimental data for the dynamic glass transition (α-relaxation) indicates that cross-correlations might be important. For instance the temperature dependence of the dielectric relaxation strength of the dynamic glass transition shows for a broad variety of materials a much stronger temperature dependence than predicted by the Onsager/Kirkwood/Fröhlich theory (Eq. 1.20) [24, 25] (see also Chap. 4). That can be regarded as a hint that cross-correlation terms can be important for complex (cooperative relaxation) processes. It should be noted that cross-correlation terms not only include static correlations – which can be described in principle by the Kirkwood/Fröhlich correlation factor – but also dynamic correlations. Clearly the cross-correlations will decay with increasing distance between dipoles i and j. It was further argued

---

[12] Normally the magnitude of the fluctuations are small and proportional to $N^{-1/2}$ where N is the number of particles in the system. In the case of phase transitions of second order the extent of the fluctuations can reach macroscopic dimensions.

by Williams and coworkers [26] that the time dependence of the cross-correlations may be equal to the time dependence of the auto-correlation function of a selected test dipole.

The inverse Fourier transformation of the correlation function $\Phi(\tau)$

$$(\Delta P^2)_\omega = \frac{\langle \Delta P^2 \rangle}{2\pi} \int\limits_{-\infty}^{\infty} \Phi(\tau) \exp(i\omega\tau)\, d\tau \qquad (1.31)$$

is called spectral density $(\Delta P^2)_\omega$ and is a measure for the frequency distribution of the fluctuation ΔP. If the correlation function can be characterized by a correlation time τ_C (e.g. $\Phi(\tau) = \Phi(\tau/\tau_C)$) for the spectral density $(\Delta P^2)_\omega > 0$ holds for a frequency interval around $1/\tau_C$. In probability theory the spectral density is also called power spectrum [27]. Historically this name originates from the statistical investigation of voltage fluctuations within an insulator. For a further discussion of that quantity see Appendix 1.3.

Another representation to express the characteristic frequencies or times which contribute to the dielectric response is the relaxation time distribution $L(\tau)$. For the complex dielectric function

$$\varepsilon^*(\omega) - \varepsilon_\infty = \Delta\varepsilon \int\limits_{-\infty}^{\infty} \frac{L(\tau)}{1 + i\omega\tau}\, d\ln\tau \quad \text{with} \quad \int\limits_{-\infty}^{\infty} L(\tau)\, d\ln\tau = 1 \qquad (1.32)$$

holds. A more complete set of equations is given in Fig. 1.3. Equation (1.32) measures the frequency distribution within the dielectric response by Debye functions [13]. From a mathematical point of view Eq. (1.32) represents a Stiltje-transformation.

The Fluctuation Dissipation Theorem (FDT) of Callen and Welton [13, 28, 29] relates the response of a system onto an outer disturbance to the spontaneous fluctuations within the system. For classical systems (no quantum effects)

$$(\Delta P^2)_\omega = \frac{1}{k_B T} \frac{\varepsilon''(\omega) - 1}{\pi\omega}$$

and

$$\Phi(\tau) = -\frac{1}{k_B T} \frac{\varepsilon(\tau) - 1}{\Delta\varepsilon}$$

$$(1.33)$$

holds. The macroscopic response is related to the microscopic fluctuations by these equations. Equation (1.33) means that for a small (linear) disturbance a system reacts only in the way it fluctuates.

1.3.2
Theoretical Considerations (Models)

From a microscopic point of view the correlation function can be calculated by means of irreversible statistical mechanics [30]. In principle the polarization

---

[13] See Sect. 1.3.2 for more details.

$P = P(q, p)$ is a function of all coordinates q and impulses p. The energy of the system is described [30] by the Hamiltonian

$$H = H_0 + H_1(t) \quad \text{with} \quad H_1(t) = -P(q, p)E(t) \tag{1.34}$$

H_0 is the equilibrium energy of the system and H_1 represents the energy of small fluctuations. The correlation function of the polarization fluctuation is given by

$$\langle P(0)P(\tau) \rangle = \int \mathrm{d}p \int \mathrm{d}q \, P(p, q) f(p, q)$$

with   (1.35)

$$f(p, q) = Q^{-1} \exp\left[-\frac{H(p, q)}{k_B T} \right]$$

where Q is the partition function of the system [13, 30].

The evaluation of Eq. (1.35) is difficult because only in rare cases the polarization is known as a function of all coordinates and impulses. So usually models have to be used to describe dielectric relaxation phenomena and to extract information from them.

Equation (1.35) is a general relationship of statistical physics. However, taking into consideration that dielectric spectroscopy measures reorientation properties of dipoles which are bound to molecules one can introduce in the sense of Eq. (1.12) spherical coordinates instead of Cartesian. Therefore, for a reference dipole Eq. (1.35) can be rewritten [32] as (see inset of Fig. 1.1)

$$\Phi(t) = \frac{\langle \boldsymbol{\mu}(t) \cdot \boldsymbol{\mu}(0) \rangle}{\langle \mu^2 \rangle} = \int_{\Omega} \int_{\Omega_0} f(\Omega, t/\Omega_0, 0) f(\Omega_0) \cos\theta \, \mathrm{d}\Omega \, \mathrm{d}\Omega_0 \tag{1.36}$$

where $f(\Omega_0)$ [14] is the initial distribution of dipoles and $f(\Omega, t/\Omega_0, 0)$ is the conditional probability of obtaining the dipole vector at Ω at the time t given it had the orientation Ω_0 at $t = 0$. $\cos\theta$ denotes the projection of the dipole vector $\boldsymbol{\mu}(\Omega)$ having an orientation Ω at the time t on the vector $\boldsymbol{\mu}(\Omega_0)$ having an orientation at Ω_0 at $t = 0$.

Mori, Zwanzig and coworkers (see [31] for details) have shown that every[15] time correlation function can be expressed by a memory function $K(t)$. This fact was emphasized by Williams recently [32, 33]. There are several ways to express $\Phi(t)$ by $K(t)$. One possibility is to express the Fourier transformation $\Phi^*(\omega)$ of $\Phi(t)$ by a continuous fraction[16] of the Fourier transformations $K_n^*(\omega)$ of the n-th memory function $K_n(t)$. This continuous fraction can be truncated at some level $m < n$. Another way for the representation of $\Phi(t)$ has been given by Berne

---

[14] Note that $f(\Omega_0)$ is a constant for an isotropic liquid material.

[15] That statement is very general and can be applied to any relaxation or transport process.

[16]
$$\Phi^*(\omega) = \cfrac{K_0^*(0)}{i\omega + \cfrac{K_1(0)}{i\omega + \cfrac{K_2^*(0)}{i\omega + K_3^*(0) \ldots}}}$$

[31]. $\Phi(t)$ was expressed by a coupled set of Voltera integral equations involving the memory functions $K_n(t)$ which corresponds of course to the continuous fraction representation. It was emphasized by Douglas and Hubbard [34] that the correlation function of an observable property can be described by [31]

$$\frac{d\Phi(t)}{dt} = -\int_0^t K(t-\tau)\Phi(\tau)\,d\tau \tag{1.37}$$

If $K(t)$ can be calculated by a molecular model or if $K(t)$ can be expressed by an empirical function the correlation function and also the observable quantities like the dielectric function can be calculated. In the frame of the linear response theory the memory function can be related to the correlation function of the fluctuation of the projected forces [30].

1.3.2.1
Debye Relaxation

Neglecting inertia effects the most simple ansatz to calculate the time dependence of dielectric behaviour is the assumption that the change of the polarization is proportional to its actual value (first order differential equation.) [8, 17, 20]

$$\frac{dP(t)}{dt} = -\frac{1}{\tau_D}P(t) \tag{1.38}$$

where τ_D is a characteristic relaxation time. Equation (1.38) leads to an exponential decay for the correlation function $\Phi(\tau)$

$$\Phi(\tau) = \exp\left[-\frac{t}{\tau_D}\right] \tag{1.39}$$

For the complex dielectric function $\varepsilon^*(\omega)$

$$\varepsilon^*(\omega) = \varepsilon_\infty + \frac{\Delta\varepsilon}{1+i\omega\tau_D} \tag{1.40}$$

is obtained [17].

Equation (1.39) does not fulfil the mathematical conditions which are necessary for a correlation function for $t \to 0$. So for short times $\Phi(\tau)$ have to be replaced by another functional relationship like a Gaussian one.

The phenomenological Eq. (1.39) can be justified by different molecular models. The first is a simple double potential model with stable states 1 and 2. The states have the populations n_1 and n_2. Thermal fluctuations lead to transitions from 1 to 2 with the rate Γ_{12} and from 2 to 1 with the rate Γ_{21} (see Fig. 1.5a).

---

[17] For more details see Chap. 3.

Fig. 1.5. a Model of a double minimum potential. An outer electrical field disturbs the symmetrical potential by $\Delta U = -\boldsymbol{\mu} E \neq 0$. **b** Model of an asymmetric four minima potential for a dipole [40]
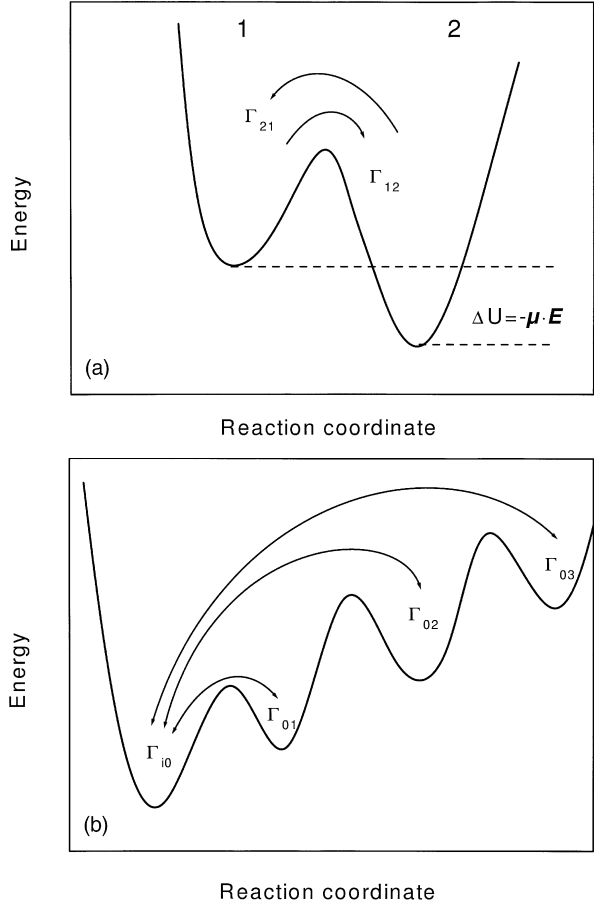
A symmetrical potential ($\Gamma_{12} = \Gamma_{21} = \Gamma$, $n_1 = n_2 = 1/2$) is disturbed by an outer electrical field of $\Delta U = -\boldsymbol{\mu} E \neq 0$ which leads to $\Gamma_{12} \neq \Gamma_{21}$ and $n_1 \neq n_2$:

$$n_2 = n_1 \exp\left[-\frac{2\Delta U}{k_B T}\right] \tag{1.41}$$

The polarization of the system can be calculated to $P = \boldsymbol{\mu}(n_1 - n_2)$. After switching off the electrical field ($\Delta U = 0$) at the time $t = 0$ the populations change according to $dn_1/dt = -n_1\Gamma + n_2\Gamma$. For the polarization

$$\frac{dP}{dt} = \boldsymbol{\mu}\left[\frac{dn_1}{dt} - \frac{dn_2}{dt}\right] = -2\boldsymbol{\mu}\,\Gamma[n_1 - n_2] = -2\Gamma P(t) \tag{1.42}$$

is obtained. Equation (1.42) corresponds to Eq. (1.39) with $\tau_D = 1/2\,\Gamma$.

The Debye relaxation can be also derived in the frame of the rotational diffusion model. Within this model the motion of a rigid isolated fluctuating dipole

(rotator) is regarded in viscous media under the influence of a stochastic force. For the sake of simplicity the outer electrical field $E(t)$ should have the direction of the z-axis. The dynamical behaviour of the rotator is given by its radius and the rotational diffusion coefficient D_{Rot}. The distribution function of the orientations $f(r,t)$ can be described by a Focker/Planck equation [30]

$$\frac{\partial f(r,t)}{\partial t} = D_{\text{Rot}} \Delta \left[f(r,t) - \frac{\boldsymbol{\mu} \, \boldsymbol{E}(t)}{k_B T} f(r,t) \right] \tag{1.43}$$

where Δ means the second differential with regard to space coordinates. The transition to spherical coordinates and taking into consideration that the problem is symmetric with regard to x and y leads to (see inset Fig. 1.1)

$$\frac{\partial f}{\partial t} = D_{\text{Rot}} \left(\frac{1}{\sin \theta} \frac{\partial}{\partial \theta} \left(\sin\theta \left(\frac{\partial f}{\partial \theta} + \frac{\boldsymbol{\mu} \, \boldsymbol{E}(t) \sin\theta}{k_B T} f \right) \right) + \frac{1}{\sin^2 \theta} \frac{\partial^2 f}{\partial \phi^2} \right) \tag{1.44}$$

Because of the assumed symmetry of the rotator with regard to its long axis, Eq. (1.44) can be solved by development into Legendre polynomials $P_m(\cos(\theta))$ [35] (see also Eq. (1.13), m counts the order of the polynomials) and the correlation function can be expressed by (see for instance [31, 32])

$$\langle P_m(\cos\theta(t)) \, P_m(\cos\theta(t)) \rangle = \exp(-m(m+1)D_{\text{Rot}} \, t) \tag{1.45}$$

Only the component of the dipole moment which is parallel to the outer electrical field contributes and hence only the first polynomial ($m = 1$) $P_1(\cos(\theta)) = \cos(\theta)$ has to be considered. That means for the dielectric relaxation the model of rotational diffusion leads to an exponential correlation function with $\tau_D = 1/(2 D_{\text{Rot}})$. For other experiments like Kerr effect measurements [37], Raman and light scattering [38] or NMR spectroscopy [39] the measured quantity is proportional to $P_2(\cos(\theta))$. That must be considered in a comparison of different experimental methods.

In the frame of the memory function formalism (compare Eq. (1.37)) the Debye relaxation is obtained by

$$K(t-\tau) = \frac{\delta(t-\tau)}{\tau_D} \tag{1.46}$$

Equation (1.46) implies that the molecular events leading to a Debye-like relaxation are not correlated neither in time nor in space.

1.3.2.2
Models for Non-Debye Relaxation

Only in rare cases a Debye-like relaxation behaviour according to Eqs. (1.39) and (1.40) is observed. Usually the measured dielectric functions are much broader than predicted by the Debye function. Moreover, in many cases the dielectric function is asymmetric. That means that the short time (high frequency) be-

haviour is more pronounced than the long time (low frequency) one. This is called non-Debye or sometimes non-ideal dielectric relaxation behaviour.

Formally such a non-Debye relaxation behaviour can be expressed in every case by a superposition of Debye-functions with different relaxation times (see Eq. 1.32). It should be pointed out that a formal separation of non-Debye relaxation behaviour into different Debye-like relaxation processes does not justify a molecular interpretation according to independent Debye-like relaxation processes[18]. Such an interpretation might be true for special types of molecular motions (like local molecular motions). In these cases one can argue that the dielectric spectra result from a distribution of different environments which modifies the activation energy. However, such an interpretation fails for cooperative processes.

A simple case to obtain a relaxation time spectrum is an extension of the double minimum potential model (see Fig. 1.5a) to an asymmetric four minima potential (see Fig. 1.5b) [40]. Such a four minima potential model can be regarded as a simple realization of a more complicated energy landscape.

The definition of the used quantities like the transition rates Γ_{0i} or the populations of the states n_i can be taken from Fig. 1.5b. The probability w_i that the system is in the state i is given by

$$w_i = \frac{\exp\left(-\dfrac{U_i}{k_B T}\right)}{\displaystyle\sum_{i=k}^{3}\exp\left(-\dfrac{U_k}{k_B T}\right)} \quad i = 0, 1, 2, 3 \tag{1.47}$$

Denoting with $\boldsymbol{\mu}_{i0} = \boldsymbol{\mu}_i - \boldsymbol{\mu}_0$ the change of the dipole moment the probability w_i that the system is in the state i with an applied field is given by

$$w_{iE} = \frac{\exp\left(-\left[\dfrac{U_i - \boldsymbol{\mu}_{i0}\boldsymbol{E}}{k_B T}\right]\right)}{\displaystyle\sum_{i=k}^{3}\exp\left(-\left[\dfrac{U_k - \boldsymbol{\mu}_{k0}\boldsymbol{E}}{k_B T}\right]\right)} = w_i \frac{1 + \dfrac{\boldsymbol{\mu}_{i0}\boldsymbol{E}}{k_B T}}{1 + \displaystyle\sum_{k=0}^{3} w_k \dfrac{\boldsymbol{\mu}_{k0}\boldsymbol{E}}{k_B T}} \tag{1.48}$$

where $\boldsymbol{\mu}_{i0}\boldsymbol{E}/k_B T \ll 1$ was used. In analogy to Eq. (1.42) for the dynamics of the system the following system of differential equations can be given (see Fig. 1.5b):

$$\begin{aligned}
&dn_0/dt + n_0(\Gamma_{01} + \Gamma_{02} + \Gamma_{03}) - n_1\Gamma_{10} - n_2\Gamma_{20} - n_3\Gamma_{30} = 0 \\
&-n_0\Gamma_{0j} + dn_j/dt + n_j\Gamma_{j0} = 0 \quad j = 1, 2, 3
\end{aligned} \tag{1.49}$$

where Γ_{i0} and Γ_{0i} denote the transition rates according to

$$\Gamma_{i,0} = \Gamma_{i,\infty}\exp\left(-\frac{\Delta U_i}{k_B T}\right), \ \Gamma_{0,i} = \Gamma_{i,\infty}\exp\left(-\frac{\Delta U_i + U_i}{k_B T}\right) \tag{1.50}$$

---

[18] It should be noted that within linear response it is not possible to decide if a relaxation process is homogenously or inhomogenously broadened. This is possible using non-linear methods like for instance dielectric hole-burning spectroscopy (see Chap. 14).

$\Gamma_{i,\infty}$ are the transition rates in equilibrium. The solution of Eq. (1.49) with the ansatz $n_j = N_j \exp(-\lambda_j/t)$ leads to an algebraic equation for the four relaxation rates λ_j. One relaxation rate is identical zero. Therefore the asymmetric four minima potential model leads to a relaxation time spectrum with three different relaxation rates or times where the time dependence of the populations (which are directly related to the change in polarization) are given by

$$n_j(t) = n_{j,\infty} + \sum_{i=1}^{3} N_{i,j} \exp(-\lambda_i t) \quad j = 1, 2, 3 \tag{1.51}$$

The values N_{ij} can be calculated from the initial conditions and from the population of the different states in equilibrium (see Eq. 1.48). Some further consideration of two- and multiple site models can be found in [41] which have been developed using group theory. It should be noted that by this method field-free time-correlation functions can also be derived [42].

In many cases the non-Debye relaxation behaviour in the time domain is empirically described by the Kohlrausch/Williams/Watts-function [43, 44] (KWW-function) which reads

$$\Phi(\tau) = \exp\left[-\left(\frac{t}{\tau_{\mathrm{KWW}}} \right)^{\beta_{\mathrm{KWW}}} \right] \tag{1.52}$$

The stretching parameter β_{KWW} ($0 < \beta_{\mathrm{KWW}} \leq 1$) leads to an asymmetric broadening of $\Phi(\tau)$ at short times (high frequencies) compared with the exponential decay ($\beta_{\mathrm{KWW}} = 1$). τ_{KWW} is the related relaxation time. The corresponding memory function for a correlation function according to the KWW-function can be estimated to be [32, 34]

$$K(t, \tau) = \delta(t - \tau)\,\Omega(\tau) \quad \text{with} \quad \Omega(\tau) \sim \tau^{\beta_{\mathrm{KWW}} - 1} \tag{1.53}$$

There are many models in the literature to understand or to derive Eq. (1.52) from a molecular point of view. One of the first models was developed by Glarum and is called Defect-Diffusion-Model [45]. It starts from the consideration that a selected dipole can reorient if a so-called defect reaches it. From a molecular point of view such a defect can be regarded as a decrease of the local density close to the dipole (increase of free volume; for the free volume model see for instance [46]). For the correlation function $\Phi(t)$

$$\Phi(t) = \exp\left(-\frac{t}{\tau_{\mathrm{D}}} \right)[1 - \psi(t)] \tag{1.54}$$

was proposed where $\psi(t)$ is the probability that a defect reaches the dipole. It was furthermore assumed that the defect diffuses through the sample. Therefore a one-dimensional diffusion equation [19] for the movement and an equipartition of defects was assumed. The solution of these equations leads to a KWW-type

---

[19] The model was also extended to the three-dimensional case. For the correlation function a dependency close to the Debye function was obtained [47].

correlation function with $\beta_{KWW} \approx 0.5$. To explain also other values of β_{KWW} the Defect Diffusion model was extended including a waiting time distribution for the diffusion of defects [48–50]. This idea was developed mainly by Bendler, Shlesinger and Montroll. To recover a KWW-type correlation function the waiting time distribution must have a functional form proportional to

$$\sim t^{\beta_{KWW}-1}/\Gamma(\beta_{KWW}) \tag{1.55}$$

where $\Gamma(\ )$ is the Gamma function. From a mathematical point of view this is a Levy distribution [50]. Zwanzig showed that the incorporation of a waiting time distribution corresponds to a change from classical random walks (ordinary diffusion) to continuous time random walks [51].

Another way to look at the physical basis of the KWW-function was introduced by Ngai [52–54] (coupling scheme). (For a further discussion of the coupling scheme see also [55–57].) It was assumed that the primary relaxation mechanism of the molecules (primary species) is due to a coupling among the molecules. This will lead to a time dependent relaxation rate according to

$$\frac{d\Phi}{dt} = -\frac{1}{\tau_0} f(t)\,\Phi(t) \tag{1.56}$$

where τ_0 is a time constant (primitive relaxation time) and $f(t)$ is a (reduced) time dependent relaxation rate. The former characterizes the interaction of the primary species with a heat bath. At a time τ_c the coupling of the primary species leads to a change of the dynamics and the relaxation rate slows down. So roughly speaking τ_c measures the complexity of the system. The theoretical basis of a time dependent relaxation rate is provided by the classical Liouville dynamics [58] supplemented by an extension of the Dirac constraint theory with time dependent constrains [59, 60]. In the coupling scheme for the time dependent relaxation rate f(t)

$$f(t) = \begin{cases} 1 & \text{for} & \tau_c^{-1}t < 1 \\ (\tau_c^{-1}t)^{-n_c} & \text{for} & \tau_c^{-1}t > 1 \ \text{ and } \ 0 < n_c < 1 \end{cases} \tag{1.57}$$

was assumed empirically. The parameter n_c characterizes the strength of the coupling between the primary species. With Eq. (1.57) Eq. (1.56) gives a KWW-type correlation function with $\beta_{KWW} = 1 - n_c$ and

$$\tau^* = \tau_{KWW} = [\tau_c^{-n_c}\tau_0]^{\left(\frac{1}{1-n_c}\right)} \tag{1.58}$$

where τ^* is an effective relaxation time of the system. Very recently the coupling scheme was further supported by the theory which considered the dynamical behaviour of interacting arrays of coupled non-linear oscillators [61].

In the frequency domain the data are often described by the empirical function of Havriliak and Negami [62] which reads

$$\varepsilon^*_{HN}(\omega) = \varepsilon_\infty + \frac{\Delta\varepsilon}{(1 + (i\omega\tau_{HN})^\beta)^\gamma} \tag{1.59}$$

The fractional shape parameters β and γ $(0 < \beta; \beta\gamma \leq 1)$ describe symmetric and asymmetric broadening of the complex dielectric function[20]. Moreover β and γ are related to the limiting behaviour of the complex dielectric function at low and high frequencies:

$$\varepsilon_0 - \varepsilon'(\omega) \sim \omega^m; \varepsilon'' \sim \omega^m \quad \text{for} \quad \omega \ll 1/\tau_{HN} \text{ with } m = \beta \tag{1.60}$$

$$\varepsilon'(\omega) - \varepsilon_\infty \sim \omega^{-n}; \varepsilon'' \sim \omega^{-n} \quad \text{for} \quad \omega \gg 1/\tau_{HN} \text{ with } n = \beta\gamma \tag{1.61}$$

That behaviour was called universal dielectric response by Jonscher [63]. Douglas and Hubbard [34] have shown that the memory function $K(t)$ which leads to a relaxation behaviour according to the HN-function can be approximated by

$$K(t, \tau, \gamma, \beta) = \frac{\Omega_0 (t-\tau)^{\gamma-2} \tau^{-\beta}}{\Gamma(\gamma-1)} \tag{1.62}$$

There is only one molecular model which predicts a correlation function with two shape parameters – the Cluster-Model of Dissado and Hill [64]. The model starts from the consideration that the structure of a material is inhomogeneous in general. From a very general point of view disorder means that the structure of a material can be reorganized into different levels which correspond to length scales ranging from the microscopic to the macroscopic. The structure on each level will be localized over its scale and will be further the element – in a kind of coarse grained model – of structure with the next larger size. In the Dissado/Hill-model the material is described on a molecular scale by clusters. In the case of an ordered (crystalline) solid a cluster can be defined as a distortion. In the alternative case of a liquid the clusters are assumed to be partly associated molecules [64]. In the spirit of such a model the clusters are not static but dynamic. That means the cluster will be built up, exist for a certain time and will be annihilated. Consequently, two kinds of molecular motions are possible: inter-cluster and intra-cluster motions. The latter corresponds to the appearing and the disappearing of clusters. Dissado and Hill could show that in the frame of such a model the correlation of the inter-cluster motion should have the functional form

$$\sim \exp(-\gamma_c t)(\zeta t)^{-n} \tag{1.63}$$

where γ_C is a rate for localized fluctuations (coupling to a heat bath) and ζ^{-1} corresponds to the lifetime of the clusters. The parameter n $(0 < n \leq 1)$ defines the order within the cluster: $n = 0$ completely disordered and $n = 1$ perfect three-dimensional crystalline material.

It was argued further that the probability of the disappearance of a cluster at the time t_1 can be written as $\sim t_1^{-m}$ where m $(0 < m \leq 1)$ is a parameter which defines the order of the array of clusters. For consistency reasons the probability to build a cluster must have the form $\sim (t-t_1)^m$ for $t > t_1$. Therefore the probability

---

[20] For a more detailed discussion see Chap. 3.

to change the array of clusters completely can be written as $(t - t_1)^m \, t_1^{-m}$ and the correlation function of the whole process can be expressed as

$$\phi(t) = \frac{\int\limits_0^t \exp[-\gamma_c(t-t_1)] \, [\zeta(t-t_1)]^{-n} (t-t_1)^m \, t_1^{-m} \, dt_1}{\int\limits_0^t (t-t_1)^m \, t_1^{-m} \, dt_1} \tag{1.64}$$

Equation (1.64) can be integrated which leads to

$$\phi(t) = \frac{\Gamma(1+m-n)}{\Gamma(2-n)\,\Gamma(1+m)} \, \gamma_c \, A_c \, \exp(-\gamma_c t)(\gamma_c t)^{-n} \, {}_1F_1(1-m, 2-n, \gamma_c t) \tag{1.65}$$

where ${}_1F_1(\;)$ is the confluent hypergeometric function [35].

Appendix 1.1
Linear Response Theory

An outer disturbance $x(t)$ may act on a system and may cause the response $y(t)$. Assuming linearity (the response of the system on two disturbances is equal to the sum of the two single reaction) and causality (only disturbances in the past contribute to a response at the time t) the response $y(t)$ can be described by following linear material equation:

$$y(t) = y_\infty + \int\limits_{-\infty}^t \tilde{J}(t-t') \, \frac{dx(t')}{dt'} \, dt' \tag{A1.1}$$

$\tilde{J}(\tau)$ is the so-called memory or material function which can be measured as the time dependent response to a step-like disturbance (δ denotes the Dirac function):

$$\frac{dx(t)}{dt} = x_0 \, \delta(t) \;\Rightarrow\; \tilde{J}(t) = \frac{y(t) - y_\infty}{x_0} \tag{A1.2}$$

y_∞ is the response which is not due to relaxation processes (response for very short times, fully elastic response). Partial integration leads to a further representation of Eq. (A1.1) which is often used in the literature:

$$y(t) = y_S + \int\limits_0^\infty \frac{\tilde{J}(t')}{dt'} \, x(t-t') \, dt' \tag{A1.3}$$

where y_S is the static response for long times.

Because Eqs. (A1.1) and (A1.3) are linear they can be inverted:

$$x(t) = x_\infty + \int_{-\infty}^{t} \tilde{G}(t-t') \frac{dy(t')}{dt'} dt'$$

or

$$x(t) = x_S + \int_{0}^{\infty} \frac{\tilde{G}(t')}{dt'} y(t-t') \, dt'$$

(A1.4)

$x(t)$ and $y(t)$ form a pair of conjugated variables. In the frame of linear response theory $y(t)$ is regarded as an extensive quantity (proportional to the volume of the system); in that case $\tilde{J}(\tau)$ is called a generalized compliance and the time dependent process is called retardation. If $y(t)$ is an intensive quantity (independent of the volume) according to Eqs. (A1.1) and (A1.4) $x(t)$ must be an extensive quantity (proportional to the volume of the system). The corresponding material function $\tilde{G}(\tau)$ is a generalized modulus. The time dependent process is defined as relaxation. Because Eq. (A1.4) is the inverse of Eq. (A1.1) $\tilde{J}(\tau)$ and $\tilde{G}(\tau)$ are related to each other by

$$\int_{-\infty}^{-\infty} \tilde{J}(t-t')\tilde{G}(t')dt' = \delta(t)$$

(A1.5)

In the following for the time dependence of $x(t)$ a periodic disturbance $x(t) = x_0 \exp(-i\omega t)$ will be assumed where ω is the (radial) frequency. In the stationary case one finds

$$J^*(\omega) = J'(\omega) - iJ''(\omega) = J_\infty - \int_{0}^{\infty} \frac{d\tilde{J}(\tau)}{d\tau} \exp(-i\omega t) \, d\tau$$

(A1.6)

where $\tilde{J}^*(\omega)$ is the generalized complex susceptibility. Again partial integration leads to

$$J^*(\omega) = J'(\omega) - iJ''(\omega) = J_S - i\omega \int_{0}^{\infty} \tilde{J}(\tau) \exp(-i\omega t) \, d\tau$$

(A1.7)

The corresponding equations for the modulus are

$$G^*(\omega) = G'(\omega) - iG''(\omega) = G_\infty - \int_{0}^{\infty} \frac{d\tilde{G}(\tau)}{d\tau} \exp(-i\omega t) \, d\tau$$

or

$$G^*(\omega) = G'(\omega) - iG''(\omega) = G_S - i\omega \int_{0}^{\infty} \tilde{G}(\tau) \exp(-i\omega t) \, d\tau$$

(A1.8)

The indices S and ∞ denote the corresponding values for $\omega \to 0$ and $\omega \to \infty$ respectively.

As a consequence of Eq. (A1.5) the simple relation

$$G^*(\omega) \, J^*(\omega) = 1$$

(A1.9)

Table A1.1. Comparison of different experimental methods in the frame of the linear response theory

Type of Experiment	Disturbance[a] $x(t)$	Response[a] $y(t)$	Compliance $\tilde{J}(\tau)$ or $J^*(\omega)$	Modulus $\tilde{G}(\tau)$ or $G^*(\omega)$
Dielectric	Electric field E	Polarization P	dielectric susceptibility $\chi^*(\omega) = (\varepsilon^*(\omega)-1)$	Electric modulus
Mechanical shear	Shear tension σ	Shear angel	Shear compliance $J(t)$	Shear modulus $G(t)$
Isotropic compression	Pressure p	Volume V	Volume compliance $B(t)\,V$	Compression modulus $K(t)$
Magnetic	Magnetic field H	Magnetization M	Magnetic susceptibility $\mu^*(\omega)-1$	–
Temperature change	Temperature T	Entropy S	Entropy compliance $J_S(t)$	Temperature modulus $G_T(t)$

[a] Depending on the definition of the different quantities in some case a multiplication with the volume is necessary to meet the definition of extensive and intensive quantities.

holds between the generalized compliance and the generalized modulus in the frequency domain.

The different experimental methods in the frame of the linear response theory are compared in Table A1.1.

Appendix 1.2
Derivation of the Kramers/Kronig-Relationships

To derive the Kramers/Kronig relationships, methods of complex function theory have to be employed. Cauchy's integral theorem states that the integral of $f(\xi)$ (ξ- is a complex quantity) along a closed contour C inside a simple connected region is zero, i.e.

$$\oint_C f(\xi)\,\mathrm{d}\xi = 0 \tag{A2.1}$$

The only requirement for Eq. (A2.1) is that $f(\xi)$ is analytic inside the region surrounded by C [65]. With the aid of Cauchy's integral theorem the following formula can be obtained expressing the value of a function $f(\omega)$ in a point $\xi = \omega$ in terms of values of the function on a closed contour surrounding the point ω

$$f(\omega) = \frac{1}{2\pi i}\oint_C \frac{f(\xi)}{\xi-\omega}\,\mathrm{d}\xi \tag{A2.2}$$

Fig. A2.1. Integration path C for the derivation of the Kramers/Kronig relationships: **a** without a singularly at $\xi = 0$; **b** with a singularity at $\xi = 0$ according to $f(\xi) = iA/\xi$
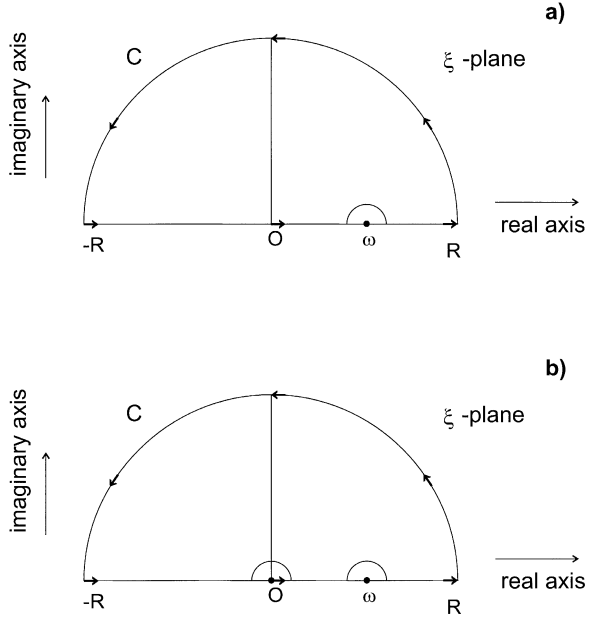
The Chauchy integral formula is valid for functions which are analytic in the region enclosed by C and on C itself.

To derive the Kramers/Kronig relationships $f(\xi) = \varepsilon^*(\xi) - \varepsilon_\infty$ is considered with an integration path, formed by the closed contour of the real axis (avoiding ω) and the semicircle in the upper complex half plane (see Fig. A2.1). According to Eq. (A2.2) one gets

$$\varepsilon^*(\omega) - \varepsilon_\infty = \frac{1}{2\pi i} \left[\int_{-R}^{R} \frac{\varepsilon^*(\xi) - \varepsilon_\infty}{\xi - \omega} \, d\xi + \int_{\substack{\text{semi-}\\\text{circle}}} \frac{\varepsilon^*(\xi) - \varepsilon_\infty}{\xi - \omega} \, d\xi \right] \tag{A2.3}$$

Because $\varepsilon^*(\xi) - \varepsilon_\infty$ goes to zero for $R \to \infty$ the function $(\varepsilon^*(\xi) - \varepsilon_\infty)/(\xi - \omega)$ approaches zero stronger than $1/\xi$ for $R \to \infty$. So the second integral vanishes for $R \to \infty$ and Eq. (A2.3) becomes

$$\varepsilon^*(\omega) - \varepsilon_\infty = \frac{1}{2\pi i} \int_{-\infty}^{\infty} \frac{\varepsilon^*(\xi) - \varepsilon_\infty}{\xi - \omega} \, d\xi \tag{A2.4}$$

The integral in Eq. (A2.4) means the Chauchy principal value of the integral

$\int_{a}^{b} f(x) \, dx = \lim_{r \to 0} \left[\int_{a}^{x_0 - r} f(x) \, dx + \int_{x_0 + r}^{b} f(x) \, dx \right]$. Note that the integration variable ξ

in Eq. (A2.4) is a real quantity. The separation into the real and imaginary part gives the Kramers/Kronig relations (see Eq. 1.25):

$$\varepsilon'(\omega) - \varepsilon_\infty = \frac{1}{\pi} \oint \frac{\varepsilon''(\xi)}{\xi - \omega} \, d\xi$$

and

$$\varepsilon''(\omega) = -\frac{1}{\pi} \oint \frac{\varepsilon'(\xi) - \varepsilon_\infty}{\xi - \omega} \, d\xi$$

(A2.5)

From the definition of the complex dielectric function (Eq. 1.24) the relation

$$\varepsilon^*(-\omega) = \varepsilon^*(\omega)$$

(A2.6)

follows where $\hat{\varepsilon}^*(\omega)$ is the complex conjugated function of $\varepsilon^*(\omega)$. Separation into the real and imaginary part yields

$$\varepsilon'(-\omega) = \varepsilon'(\omega) \quad \text{and} \quad \varepsilon''(-\omega) = -\varepsilon''(\omega)$$

(A2.7)

With Eq. (A2.7), Eq. (A2.5) can be written as

$$\varepsilon'(\omega) - \varepsilon_\infty = \frac{1}{\pi} \oint \frac{\varepsilon''(\xi)}{\xi - \omega} \, d\xi = \frac{1}{\pi} \int_0^\infty \frac{\varepsilon''(\xi)}{\xi - \omega} \, d\xi + \frac{1}{\pi} \int_0^\infty \frac{\varepsilon''(\xi)}{\xi + \omega} \, d\xi$$

(A2.8)

which leads to

$$\varepsilon'(\omega) - \varepsilon_\infty = \frac{2}{\pi} \int_0^\infty \frac{\xi \varepsilon''(\xi)}{\xi^2 - \omega^2} \, d\xi$$

(A2.9)

Recalling that $\varepsilon_S = \varepsilon'(0)$ one finds for $\omega \to 0$

$$\varepsilon_S - \varepsilon_\infty = \Delta\varepsilon = \frac{2}{\pi} \int_0^\infty \varepsilon''(\xi) \frac{d\xi}{\xi} = \frac{2}{\pi} \int_0^\infty \varepsilon''(\xi) d\ln\xi$$

(A2.10)

If the function $f(\xi)$ has a singularity with $f(\xi) = iA/\xi$ at $\xi = 0$ then the surrounding of that singularity by a semi circle (Fig. A2.1b) gives the additional real contribution $- A/\omega$ which has to be added to Eq. (A2.4) yielding

$$\varepsilon''(\omega) = -\frac{1}{\pi} \oint \frac{\varepsilon'(\xi) - \varepsilon_\infty}{\xi - \omega} \, d\xi + \frac{A}{\omega}$$

(A2.11)

Therefore, one has to conclude that a conductivity term proportional to A/ω in the imaginary part of the complex dielectric function has no contribution in the real part.

Appendix 1.3
Fluctuation Dissipation Theorem

Thermodynamic quantities which characterize a macroscopic sample are average values. Because of the stochastic motions of the molecules (or particles) these quantities fluctuate around their mean value [13]. An example for that is Brownian Motion. Let $x(t)$ be a quantity of a well defined subsystem[21] of a sample with a macroscopic significance and $\langle x \rangle$ its average value. For instance, x can be the volume, the energy or also the polarization of the subsystem. $\Delta x(t) = x(t) - \langle x \rangle$ defines the stochastic process of the fluctuations of $x(t)$. For a stationary process the average value $\langle \Delta x(t) \rangle$ vanishes but the mean quadratic fluctuation $\langle \Delta x(t)^2 \rangle = \langle \Delta x^2 \rangle$ is different from zero. The correlation function is defined as average of the product of two values Δx separated by a time τ

$$\Psi(\tau) = \langle \Delta x(t) \Delta x(t + \tau) \rangle \tag{A3.1}$$

The correlation function describes the dependence of $\Delta x(t + \tau)$ on $\Delta x(t)$. In the stationary state the time t does not play a role:

$$\Psi(\tau) = \langle \Delta x(0) \Delta x(\tau) \rangle \tag{A3.2}$$

with $\Psi(-\tau) = \Psi(\tau)$. That means Ψ is a symmetrical function with regard to τ. For $\tau \to \infty$ $\Psi = 0$ holds. The relationship of the correlation function to $\langle \Delta x^2 \rangle$ is given by $\langle \Delta x^2 \rangle = \Psi(0)$. Therefore often the normalized correlation function

$$\Phi(\tau) = \frac{\langle \Delta x(0) \Delta x(\tau) \rangle}{\langle \Delta x^2 \rangle} \tag{A3.3}$$

is considered. The inverse Fourier transformation of the correlation function $\Psi(\tau)$

$$(\Delta x^2)_\omega = \frac{1}{2\pi} \int_{-\infty}^{\infty} \Psi(\tau) \exp(i\omega\tau) \, d\tau \tag{A3.4}$$

is called spectral density $(\Delta x^2)_\omega$ and is a measure for the frequency distribution of the fluctuation Δx. (In the theories of stochastic processes $(\Delta x^2)_\omega$ is often called power spectrum [27]. Historically this name stems from the statistical treatment of the voltage fluctuations in an insulator.) The relationship to the mean square fluctuation is given by

$$\langle \Delta x^2 \rangle = \Psi(0) = \int_{-\infty}^{\infty} (\Delta x^2)_\omega \, d\omega > 0 \tag{A3.5}$$

and it holds $(\Delta x^2)_\omega = (\Delta x^2)_{-\omega}$

---

[21] According to [13] a subsystem is defined as a small but macroscopic part of the sample having all its natural interaction with the surrounding.

The Fluctuation Dissipation Theorem (FDT) of Callen and Welton [28] relates the response of a system to an outer disturbance to the spontaneous fluctuations of the system. For classical systems (no quantum effects)

$$(\Delta x^2)_\omega = \frac{1}{k_B T} \frac{\tilde{J}''(\omega)}{\pi \omega}$$

and   (A3.6)

$$\Psi(\tau) = -\frac{1}{k_B T} \tilde{J}(\tau)$$

hold, relating the macroscopic response to the internal fluctuations of a subsystem. Equation (A3.6) means that – within the linear response – a system reacts and fluctuates based on the same microscopic mechanism.

List of Abbreviations and Symbols

a	Reduced electrical interaction energy
B	Volume compliance
$\mathbf{B}$	Magnetic induction
d	Distance
$\mathbf{D}$	Dielectric displacement
$\mathbf{E}$	Electric field
F	Onsager factor
$_1F_1$	Confluent hypergeometric function of the order l,l
g	Kirkwood/Fröhlich correlation factor
G_T	Temperature modulus
G^*	Shear modulus
$\tilde{G}$	Generalized modulus
H	Hamiltonian
$H[]$	Hilbert transformation
$\mathbf{H}$	Magnetic field
$\mathbf{j}$	Current density
J^*	Shear compliance
$\tilde{J}$	Generalized compliance
J_S	Entropy compliance
k_B	Boltzmann constant ($k = 1.381 \times 10^{-23}$ J K^{-1})
K	Memory function
L	Relaxation time distribution
$\mathbf{m}$	Effective dipole moment
m, n	Low and high frequency slope of the HN-function
M	Molar mass of a particle
$M^*; M', M''$	Complex electrical modulus; real and imaginary part of the electrical modulus
n_c	Coupling parameter
$n^*; n', n''$	Complex index of refraction; real and imaginary part of the complex index of refraction

N_A	Avogadro number ($N_A = 6.022 \times 10^{23}$ mol^{-1})
$\boldsymbol{p}$	Microscopic dipole moment
$\boldsymbol{P}$	Polarization
q	Charge
Q	Partition function of a system
S	Entropy
t	Time
T	Temperature
U, U_i	Potential energy
V	Volume
w	Transition probabilities
α	Polarizability
β_{KWW}	Stretching parameter of the KWW-function
$\beta; \gamma$	Fractional shape parameters of the HN-function
β_i	Hyperpolarizabilities
$\varepsilon^*; \varepsilon', \varepsilon''$	Complex dielectric function, real and imaginary part of the complex dielectric function
ε_0	Dielectric permittivity of vacuum ($\varepsilon_0 = 8.854 \times 10^{-12}$ As V^{-1} m^{-1})
$\varepsilon_S; \varepsilon_\infty$	$\varepsilon_S = \lim\limits_{\omega \to 0} \varepsilon'(\omega); \varepsilon_\infty = \lim\limits_{\omega \to \infty} \varepsilon'(\omega)$
$\Delta\varepsilon = \varepsilon_S - \varepsilon_\infty$	Dielectric strength, dielectric intensity
Γ	Molecular transition rate
$\Gamma()$	Gamma function
δ	Dirac-(delta-) function
θ	Angle between the dipole moment and the electric field
$\Lambda()$	Langevin function
$\boldsymbol{\mu}$	Permanent dipole moment
v, ω	Frequency, radial frequency
ρ_e	Density of charges
$\sigma^*; \sigma', \sigma''$	Complex conductivity, real and imaginary part of the complex conductivity
τ	Relaxation time
$\tau_D, \tau_{HN}, \tau_{KWW}$	Relaxation time of the Debye-, HN- and KWW-function
Φ	Correlation function of the polarization fluctuation
χ^*	Dielectric susceptibility
$\Omega; (\theta \text{ and } \phi)$	Space angle
FDT	Fluctuation Dissipation Theorem
HN	Havriliak/Negami
KWW	Kohlrausch/Williams/Watts

References

1. Maxwell JC (1865) Phil Trans 155:459
2. Maxwell JC (1868) Phil Trans 158:643
3. Landau LD, Lifschitz EM (1977) Textbook of theoretical physics, vol. II. Classical field theory. Akademie-Verlag, Berlin
4. Böttcher CJF (1973) Theory of electric polarization, vol. I. Dielectrics in static fields. Elsevier Amsterdam, Oxford, New York
5. de Gennes PG (1974) The physics of liquid crystals. Clarendon Press, Oxford
6. Sillars RW (1937) J Inst Elect Eng 80:378
7. Wagner RW (1914) Arch Elektrotech 2:371
8. Debye P (1929) Polar molecules. Chemical catalog, reprinted by Dover
9. Lorentz HA (1879) Ann Phys 9:641
10. Clausius R (1879) Die mechanische Wärmelehre, Vol. II. Braunschweig
11. Mossotti PF (1847) Bibl Univ Modena 6:193
12. Onsager L (1938) J Am Chem Soc 58:1486
13. Landau LD, Lifschitz EM (1979) Textbook of theoretical physics, vol. V. Statistical physics. Akademie-Verlag, Berlin
14. Kirkwood JG (1939) J Chem Phys 58:911
15. Kirkwood JG (1940) Ann NY Acad Sci 40:315
16. Kirkwood JG (1946) Trans Faraday Soc 42A:7
17. Fröhlich H (1958) Theory of dielectrics. Oxford University Press, London
18. Flory JP (1989) Statistical mechanics of chain molecules. Hanser Verlag, München
19. Riande E, Saiz E (1992) Dipole moments and birefringence of polymers. Prentice Hall, Englewood Cliffs, New Jersey
20. Böttcher CJF, Bordewijk P (1978) Theory of electric polarization, vol. II. Dielectrics in time-dependent fields. Elsevier Amsterdam, Oxford, New York
21. Steeman PAM, van Turnhout J (1997) Colloid Polym Sci 275:106
22. Williams G (1979) Adv Polym Sci 33:60
23. Cook M, Watts DC, Williams G (1970) Trans Faraday Soc 66:2503
24. Schönhals A, Kremer F, Hofmann A, Fischer EW, Schlosser E (1993) Phys Rev Lett 70:3459
25. Schönhals A (1997) Dielectric properties of amorphous polymers. In: Runt JP, Fitzgerald JJ (eds) Dielectric spectroscopy of polymeric materials. ACS Books, Washington DC, p 81
26. Williams G, Cook M, Hains PJ (1972) J Chem Soc, Faraday Trans II 68:1045
27. Gnedenko BW (1957) Textbook of probability mathematics. Akademie Verlag, Berlin
28. Callen HB, Welton TA (1951) Phys Rev 83:34
29. Kubo R (1957) Phys Soc Japan 12:570
30. Kubo R, Toda M, Hashitsume N (1985) Statistical physics II. Springer, Berlin Heidelberg New York
31. Berne BJ (1971) In: Eyring H, Henderson D, Jost W (eds) Physical chemistry, an advanced treatise, vol. VIII B. The liquid state. Academic Press, New York
32. Williams G (1995) Dielectric relaxation spectroscopy of amorphous polymer systems: the modern approaches. In: Riande E (ed) Keynote lectures in selected topics of polymer sciences, Madrid, p 1
33. Williams G, Fournier J (1996) J Chem Phys 184:5690
34. Douglas JF, Hubbard JB (1991) Macromolecules 24:3163
35. Abramowitz M, Stegun IA (1965) Handbook of mathematical functions. Dover Press, New York
36. Williams G (1978) Chem Soc Rev 7:22
37. Rosato V, Williams G (1981) J Chem Soc Faraday Trans 77:1767
38. Berne BJ, Pecora R (1976) Dynamic light scattering. Wiley, New York
39. Connor TM (1964) Trans Faraday Soc 60:1574
40. Genzel L, Kremer F, Poslitsch A, Bechthold G (1983) Biopolymers 22:1715
41. Cook M, Williams G (1971) Trans Faraday Soc 67:990
42. Williams G (1972) Chem Rev 72:55

43. Williams G, Watts DC (1970) Trans Faraday Soc 66:80
44. Kohlrausch R (1847) Ann Phys 12:393
45. Glarum SH (1960) J Chem Phys 33:639
46. Cohen MH, Turnbull D (1959) J Chem Phys 31:1164; Doolittle AK (1951) J Appl Phys 22:1471
47. Hunt BJ, Powles JG (1961) Proc Phys Soc 88:513
48. Montroll E, Bendler JT (1984) J Stat Phys 34:129
49. Shlesinger MF, Montroll E (1984) Proc Natl Acad Sci USA 81:1280
50. Montroll EW, Lebowitz JL (1979) Studies in statistical mechanics. North Holland Publishing Company, Amsterdam
51. Zwanzig, R (1983) J Stat Phys 30:255
52. Ngai KL (1979) Comments Solid State Phys 9:127
53. Ngai KL (1980) Comments Solid State Phys 9:141
54. Rajagopal AK, Ngai KL, Rendell RW, Teitler S (1983) J Stat Phys 30:285
55. Relaxation Complex Systems I (1991) Kreta
56. Relaxation Complex Systems II (1994) Alicante
57. Relaxation Complex Systems III (1997) Vigo
58. Sundrahan ECG, Mukundan N (1986) Classical dynamics: a modern perspective. Academic Press, New York
59. Dirac APM (1964) Lectures on quantum mechanics. Yeshiva University, New York
60. Sahoo D, Venkataraman G (1975) Pramana 185:20
61. Ngai KL, Tsang KY (1999) Phys Rev E 60:4511
62. Havriliak S, Negami S (1966) J Polym Sci C14:99
63. Jonscher A (1983) Dielectric relaxation in solids. Chelsea Dielectrics Press, London
64. Dissado LA, Hill RM (1983) Proc R Soc London 390:131
65. Smirnow WI (1967) Textbook of higher mathematics III/2. Deutscher Verlag der Wissenschaften, Berlin

2 Broadband Dielectric Measurement Techniques (10⁻⁶ Hz to 10¹² Hz)

F. Kremer · A. Schönhals

2.1
Introduction

The complex dielectric[1] function $\varepsilon^*(\omega) = \varepsilon'(\omega) - i\varepsilon''(\omega)$ can be measured in the extraordinary broad frequency regime [1–13] from 10^{-6} Hz up to 10^{12} Hz (in wavelength 3×10^{16} cm – 0.03 cm). To span this dynamic range different measurement systems based on different measurement principles have to be combined (Fig. 2.1). From 10^{-6} to 10^7 Hz lumped circuit methods are used in which the sample is treated as a parallel or serial circuit of an ideal capacitor and an ohmic resistor. Effects of the spatial extent of the sample on the electric field distribution are neglected. With increasing frequency the geometrical dimensions of the sample capacitor become more and more important limiting this approach to about 10 MHz. In addition parasitic impedances caused by cables, connectors, etc. become important at frequencies >100 kHz.

Using distributed circuit methods (10^7 Hz – 10^{11} Hz) the complex dielectric function is deduced by measuring the complex propagation factor (in reflection or transmission). Both, waveguide as well as cavity techniques can be applied.

In the dynamic range between 10^{-6} Hz and 10^{10} Hz the complex dielectric function $\varepsilon^*(\omega)$ can also be deduced from a measurement of the time dependent dielectric function $\varepsilon(t)$. The latter is related to $\varepsilon^*(\omega)$ via a Fourier transformation

$$\varepsilon^*(\omega) - \varepsilon_\infty = \int\limits_{-\infty}^{+\infty} \dot{\varepsilon}(t)\, e^{-i\,\omega t}\mathrm{d}t \tag{2.1}$$

with $\varepsilon_\infty = \varepsilon'$ ($v \approx 10^{11}$ Hz). For frequencies between 10^{10} Hz – 10^{12} Hz (in wave numbers $\bar{\lambda} = \lambda^{-1} = 0.3$ cm^{-1} – 30 cm^{-1}, λ: wavelength in vacuum) quasioptical set-ups as polarizing Mach-Zehnder interferometers or oversized cavity resonators are employed. The latter has the advantage that it is suitable for very low loss materials and for measurements at low temperatures. The main experimental difficulty in this frequency range arises from the large coherence length of

---

[1] Dielectric data are also often presented in terms of the complex conductivity $\sigma^* = i\omega\varepsilon_0\varepsilon^*$ or the complex electrical modulus $M^* = 1/\varepsilon^*$. For dipolar relaxation processes ε^* is usually used while for systems with mainly conductive processes σ^* or M^* prevails.
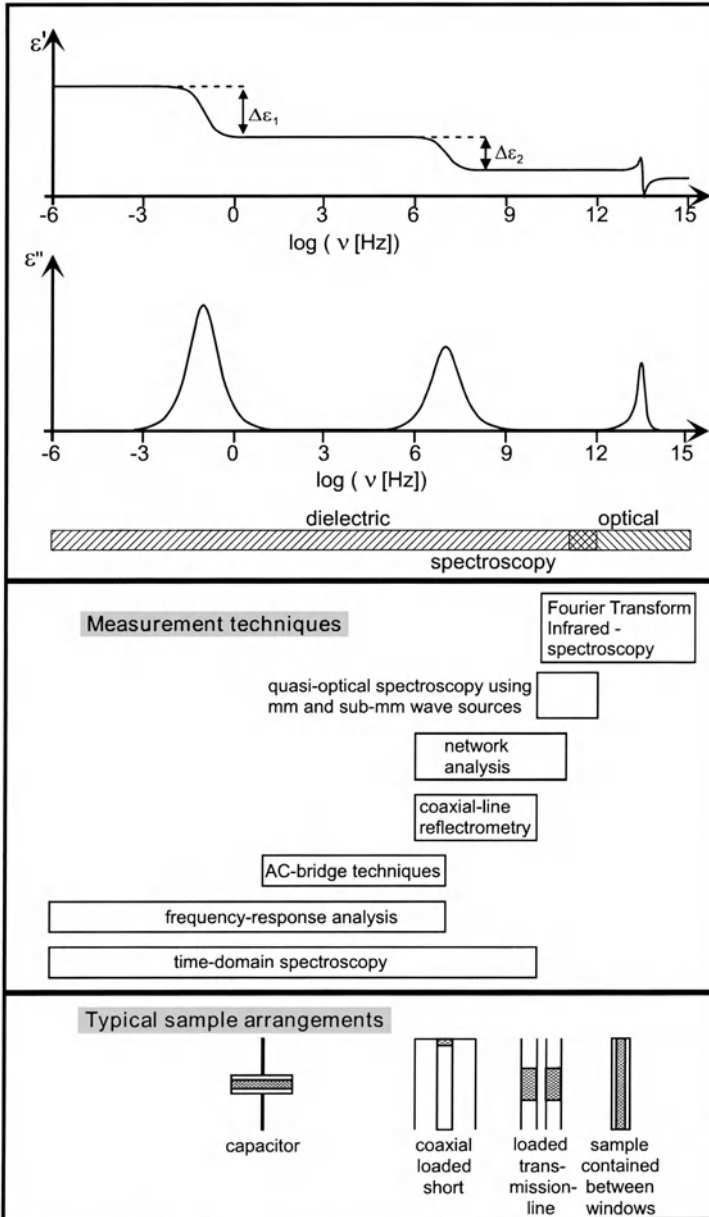
Fig. 2.1. Survey of measurement techniques used in the frequency range from 10^{-6} Hz – 10^{15} Hz

the mm- and sub-mm-wave sources (backward wave oscillators, klystrons, gun-oscillators, etc.) resulting in multiple standing wave patterns. Above 10^{11} Hz Fourier-Transform spectrometers are used. Due to the throughput and the multiplex advantages they are superior to arrangements using monochromators. More specialized dielectric techniques are discussed in Chaps. 14–16.

2.2
Measurements in the Frequency Domain from 10^{-6} Hz to 10^{11} Hz

For a capacitor C^* filled with a material under study the complex dielectric function is defined as

$$\varepsilon^*(\omega) = \varepsilon'(\omega) - i\,\varepsilon''(\omega) = \frac{C^*(\omega)}{C_0} \tag{2.2}$$

where C_0 is the vacuum capacitance of the arrangement. ω is the angular frequency with $\omega = 2\pi\nu = 2\pi T^{-1}$ with T as time for one period. $\varepsilon'(\omega)$ and $\varepsilon''(\omega)$ describe the real and imaginary part of the complex dielectric function. Using a sinusoidal electric field $E^*(\omega) = E_0 \exp(i\omega t)$ with the angular frequency ω and at field strengths within linear response (for most materials $E_0 \leq 10^6$ V cm^{-1}) the dielectric function can be derived by measuring the complex impedance $Z^*(\omega)$ of the sample

$$\varepsilon^*(\omega) = \frac{J^*(\omega)}{i\omega\varepsilon_0 E^*(\omega)} = \frac{1}{i\omega Z^*(\omega)C_0} \tag{2.3}$$

where $J^*(\omega)$ is the complex current density and ε_0 the permittivity of free space. To cover the frequency domain from 10^{-6} Hz up to 10^{11} Hz four different systems based on different measurement techniques are employed [14]: Fourier correlation analysis in combination with dielectric converters (10^{-6} Hz – 10^7 Hz) [15–17], impedance analysis (10^1 Hz – 10^7 Hz), RF-reflectometry (10^6 Hz – 10^9 Hz) [18, 19] and network analysis (10^7 Hz – 10^{11} Hz) [20, 21].

2.2.1
Fourier Correlation Analysis

The basic principle is shown in Fig. 2.2. Typically a sine wave voltage $U_1(t)$ with frequency $\omega/2\pi$ is applied to the sample by a generator, covering the frequency range from 10^{-6} Hz to 10^7 Hz[2]. The resistor R converts the sample current $I_S(t)$ into a voltage $U_2(t)$. $U_1(t)$ and $U_2(t)$ are analyzed with respect to the amplitudes and phases of their harmonic Fourier base waves $U_1^*(\omega)$ and $U_2^*(\omega)$ by two phase sensitive sine wave correlators. The complex sample impedance Z_S^* is calculated

---

[2] Fourier correlation analysis for frequencies $< 10^{-2}$ Hz becomes extremely time consuming. In this case measurements in the time domain are advantageous.

Fig. 2.2. Scheme of a Fourier correlation analyzer. Taken from [10] with permission
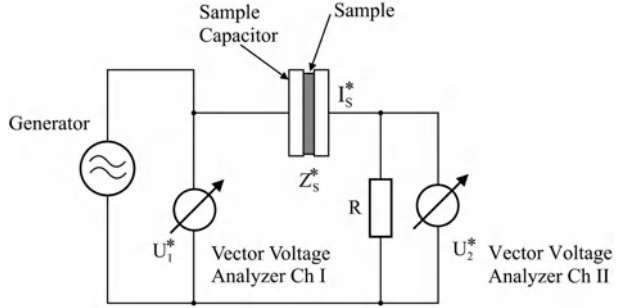
from the measured data by

$$Z_S^*(\omega) = \frac{U_S^*(\omega)}{I_S^*(\omega)} = R\left(\frac{U_1^*(\omega)}{U_2^*(\omega)} - 1\right) \tag{2.4}$$

where $U_S^*(\omega)$ and $I_S^*(\omega)$ are the sample voltage and current. The response of the correlator to the signal $U_i(t)$ are the two components

$$U_j'(\omega) = \frac{1}{NT}\int_0^{NT} U_j(t)\ \sin(\omega t)\,\mathrm{d}t \tag{2.5a}$$

and

$$U_j''(\omega) = \frac{1}{NT}\int_0^{NT} U_j(t)\ \cos(\omega t)\,\mathrm{d}t \tag{2.5b}$$

with $j = 1,2$. U_j' is the in phase component and U_j'' the orthogonal (90° shifted or quadrature) component of the harmonic base wave. N is the number of periods with duration $T = 2\pi/\omega$ measured by the correlator[3].

For technical implementation of Fourier correlation analysis one has to realize Eq. (2.5a/b). This is done in conventional systems by analog components. From the main oscillator, the reference sin and cos signals are created by a 90°

---

[3] For readers having no experience in Fourier analysis, the following may be helpful in order to understand the correlator operation. If $U_i(t)$ is a sine wave with amplitude U_0 and phase angle ϕ

$$U_i(t) = U_0 \sin(\omega t + \phi) \tag{2.5c}$$

for the product holds

$$U_j(t)\sin(\omega t) = U_0 \sin(\omega t + \phi)\sin(\omega t) = \frac{U_0}{2}(\cos(\phi) - \cos(2\omega + \phi)) \tag{2.5d}$$

As the integration in Eqs. (2.5a/b) is applied over a number of periods T, the second term in Eq. (2.5d) averages to zero. Therefore, the integral (Eq. 2.5a) becomes $U_i'(\omega) = U_0\cos(\phi)/2$. With the same arguments, $U_i''(\omega) = U_0\sin(\phi)/2$. If $U_i(t)$ is a signal of arbitrary type like, e.g., a sine wave superimposed with noise, it can be transformed into its Fourier representation consisting of a number of sine waves. For each frequency component both terms of

phase shifter, multiplied with the test signal and finally integrated. Modern systems digitize the test signal and approximate numerically Eqs. (2.5a/b) by a signal processor avoiding by that the drift and the non-linearity of analogue components. Fourier correlation analyzers are commercially available as frequency response analyzers or lock-in amplifiers from Agilent Technologies, EG & G, Novocontrol, Solartron and Stanford Research Systems.

2.2.2
Dielectric Converters in Combination with Fourier Correlation Analysis

For measurements, the setup from Fig. 2.2 with the resistor R suffers from several limitations and therefore a dielectric converter is usually used for conversion of the sample current to $U_2(t)$ [15–17]. The Fourier correlation analysis is done either by an additional frequency response analyzer or lock-in amplifier. The dielectric converter uses a broadband electrometer amplifier with variable gain (Fig. 2.3) in order to match the huge impedance range required for dielectric measurements which typically covers about 13 orders of magnitude over the frequency range from 1 mHz to 10 MHz.

If $Z_X^*(\omega)$ is a variable impedance which can be changed in resistance and capacitance, the sample impedance $Z_S^*(\omega)$ of a direct measurement is given by

$$Z_S^*(\omega) = \frac{U_{1S}^*(\omega)}{I_S^*(\omega)} = -\frac{U_{1S}^*(\omega)}{U_{2S}^*(\omega)} Z_X^*(\omega) \tag{2.6}$$

The accuracy of the measurement according to Eq. (2.6) is limited due to amplitude and phase errors in the current to voltage converter and the correlators.

Further improvement results from a comparison of the sample capacitor with a variable converter internal reference capacitor with impedance $Z_R^*(\omega)$. If a reference measurement under the same conditions (especially for the current-to-voltage converter) is made

$$Z_R^*(\omega) = \frac{U_{1R}^*(\omega)}{I_R^*(\omega)} = -\frac{U_{1R}^*(\omega)}{U_{2R}^*(\omega)} Z_X^*(\omega) \tag{2.7}$$

(continued Footnote 3)

Eq. (2.5d) are frequency dependent and will average out to zero if the integration is performed over many periods. The only frequency component which does not average out is the one at the correlator frequency $\omega/2\pi$. Therefore, the correlator phase-sensitively detects the base Fourier component contained in any input signal. All other contributions are averaged out. The quality of suppression increases with averaging time determined by the number N of integration periods. Therefore, this technique generally is used in precision instrumentation like lock-in amplifiers for noise suppression or if small signals have to be measured, e.g., measuring a signal in the nV range superimposed by a 1000 times higher noise signal is possible. These properties are the basis for the many advantages sine wave correlation systems offer with respect to non-correlated analysis systems like, e.g., time domain techniques or bridges where any noise or non-linear response usually strongly contributes to the measured signal. As a further advantage of sine wave correlation systems, higher harmonic signal components may readily evaluated by increasing the number N in Eqs. (2.5a/b).
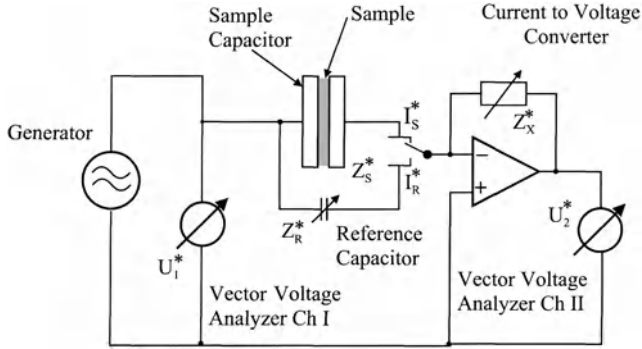
Fig. 2.3. Scheme of a dielectric converter in the low-frequency range with electrometer amplifier and variable reference capacitor

Combining Eqs. (2.6) and (2.7) yields

$$Z_S^*(\omega) = \frac{U_{1S}^*(\omega)}{U_{2S}^*(\omega)} \cdot \frac{U_{2R}^*(\omega)}{U_{1R}^*(\omega)} \cdot Z_R^*(\omega) \tag{2.8}$$

which is independent of linear amplitude or phase errors of the correlators, as they enter both in the sample and reference measurement and therefore are canceled out. This works in practice only if the sample impedance and reference impedance are nearly in the same range. In this case the accuracy is limited only by the correlator resolution. Therefore, the reference capacity for some dielectric converters can be adjusted, e.g., in 64 steps between 25 pF and 2 nF [16, 17].

For frequencies <100 kHz (Fig. 2.3) a low current operational amplifier can be used. Such amplifiers are available for extreme low input currents down to some fA. On the other hand, these amplifiers are limited to low frequencies. Therefore, some dielectric converters [16] use for frequencies between 10^5 Hz and 10^7 Hz a different technique of current to voltage conversion (Fig. 2.4). The a.c. voltage of the generator drives a buffer amplifier which decouples the sample. In contrast to Fig. 2.3 the active current-to-voltage converter is replaced by a passive variable impedance Z_X^*. For ideal components and neglecting inductive effects one finds

$$Z_S^*(\omega) = Z_X^* \left(\frac{U_{1S}^*(\omega)}{U_{2S}^*(\omega)} - 1 \right) \tag{2.9}$$

With this equation the reference technique can be applied in a similar manner as above.

Dielectric converters enable one to measure highly accurate results for capacitive samples with not too high losses and only low d.c. conductivity. For high d.c. conductivity or high dielectric losses, the sample impedance is mainly resistive and often not in the range of the reference capacitors. For such kinds of samples, impedance analysis as discussed below often yields better results.
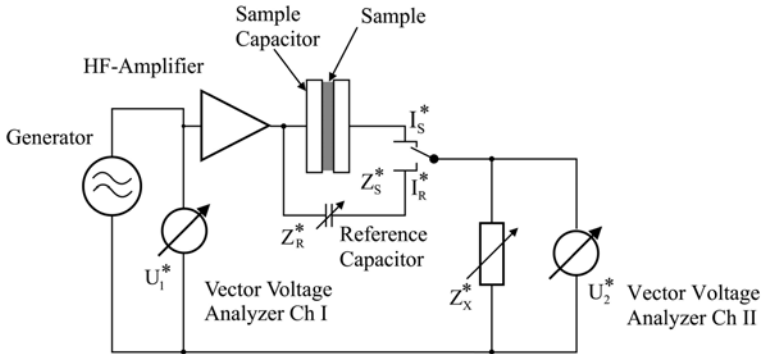
Fig. 2.4. Scheme of a dielectric converter in the high-frequency range with variable impedance and variable reference capacitors

Using state of the art equipment, an accuracy in $\tan\delta = \dfrac{\varepsilon''}{\varepsilon'}$ better than 10^{-4} can be achieved over a broad frequency range. The limits for high impedance and low capacitance are around 10^{14} Ω and 1 pF. Low impedances down to about 100 Ω may be measured too, but only with reduced accuracy due to the limitations of the reference technique.

Dielectric converters in combination with frequency response analyzers (FRAs) or lock-in amplifiers are commercially available from, e.g. Novocontrol and Solartron.

Similar systems with electrometer amplifiers but without reference technique are commercially available from, e.g. Micromet, Rheometrics, Seiko, and TA Instruments.

2.2.3
Impedance Analysis

Two kind of techniques have to be distinguished. The first is the I-V method referring to the direct phase sensitive measurement of the sample current and voltage. It is similar to the dielectric converter techniques described above. Instead of an electrometer amplifier, a broadband current to voltage converter is used without reference technique.

An alternative technique is the a.c. impedance bridge shown in Fig. 2.5 which consists of the sample capacitance $Z_S^*(\omega)$ and the adjustable compensation impedance $Z_C^*(\omega)$. On the left hand side of the bridge, the generator drives the sample with the fixed and known a.c. voltage $U_S^*(\omega)$ which causes the current $I_S^*(\omega)$ to flow into P_I. On the right hand side of the bridge, the variable amplitude-phase generator (VAPG) feeds the current $I_C^*(\omega)$ through the compensation impedance $Z_C^*(\omega)$ into P_I. The bridge will be balanced, if $I_S^*(\omega)$ equals $-I_C^*(\omega)$ which corresponds to $I_0 = 0$. Any deviation is detected by the zero voltage detector which changes the amplitude and phase of the variable amplitude phase generator

Fig. 2.5. Scheme of an impedance bridge
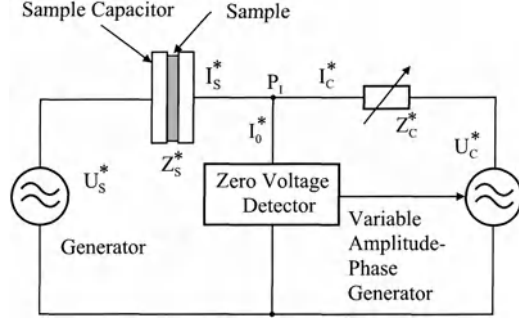
(VAPG) as long as $I_0 \neq 0$. In the balanced state, the sample impedance is calculated as

$$Z_S^*(\omega) = \frac{U_S^*(\omega)}{I_S^*(\omega)} = -\frac{U_S^*(\omega)}{U_C^*(\omega)} Z_C^*(\omega) \tag{2.10}$$

Impedance bridges or analyzers which are not specially designed for dielectric measurements typically work from 10 Hz to 10 MHz. For dielectric samples, they suffer from the inverse problem of the dielectric converter systems as optimized for low (typically 10 mΩ) to medium impedance with a limit of about 100 MΩ. This limit is reached for typical dielectric samples (100 pF, $\tan\delta = 0.01$) at about 1 kHz. The typical accuracy in $\tan\delta$ is $< 10^{-3}$. Here, a.c.-impedance analyzers or bridges offer a suitable and inexpensive solution for applications which do not require a large frequency and a high impedance range. Due to the fact that the measurement time is lower compared with systems using reference techniques, a.c.-impedance bridges are particularly suited for measurements on materials with time-dependent dielectric properties (monitoring of chemical reactions, characterization of phase transitions, etc.). Impedance analyzers or bridges are commercially available from several manufactures like, e.g., Agilent Technologies, Novocontrol, Solartron, QuadTech, and Wayne Kerr.

2.2.4
Integrated Dielectric Analyzers

Systems combining the advantages of Fourier correlation analysis, with dielectric converters and impedance analysis, are the latest progress in dielectric instrumentation [17]. These incorporate in one device a direct digital synthesizer generator, two digital precision sine wave correlators, a state of the art dielectric converter, and a direct I–V current to voltage converter for the low impedance range. For typical dielectric capacitive samples, the dielectric converter is used as a precision front end. In this mode broadband phase and $\tan\delta$ accuracy $< 3\times10^{-5}$ is available. If the sample impedance is out of the dielectric converter reference capacitor range, the front end is switched automatically to the I–V converter.

   With this concept an overall impedance range from 0.01 Ω to 10^{14} Ω is covered with one single device. The wide impedance range results in a wide capacity range as well. Ultralow capacities can be measured with high precision to a limit of 1 fF (10^{-15} F). High resolution dielectric analyzers are commercially available from Novocontrol.

2.2.5
Samples and Sample Cells for Frequencies <10 MHz

Typical samples have a thickness of ≈ 50 µm and diameter of 10 mm resulting in a capacitance of 69.5 pF for a value of $\varepsilon' = 5$. It is essential to measure the sample temperature in the immediate sample neighborhood and to keep the sample temperature as constant as possible. As sample geometry a parallel plate capacitor arrangement is commonly used.

   For the techniques discussed so far, a sample cell is required which is connected by BNC cables to the impedance plugs of the measurement system. Due to the parasitic inductance of the lines and connectors the high frequency limit is reached at about 1 MHz. At the lower frequency range end, very small currents down to fA have to be measured. In this region, the measurement may be obscured by noise pick up and piezoelectric charges in the cables due to mechanical stress. Therefore a sophisticated cell and cable design optimized for both high frequency performance and best insulation over the entire frequency and temperature range is required.

   As an alternative, active sample cells may be used where the electrometer amplifier and the reference capacitors are integrated in the sample cell head avoiding BNC cables in the sample impedance circuit [16, 17]. For such systems, the active cell can be considered as an analyzer system and the accuracy and range specifications apply in parallel. This is in contrast to systems with BNC cables and passive sample cells which are usually specified at the analyzer BNC input plugs neglecting cable and cell effects.

2.2.6
RF Reflectometry

Coaxial line reflectometry [14, 18, 19] can be employed at frequencies from 1 MHz to 10 GHz. In contrast to the low frequency techniques already described, above 1 MHz the measurement cables significantly contribute to the sample impedance. Above approximately 30 MHz standing waves arise in the line and a direct measurement of the sample impedance completely fails. This can be avoided by application of microwave techniques taking the measurement line as the main part of the measured impedance into account. Therefore, precision lines and sample cells with defined propagation constants are required. A schematic of the measurement technique is shown in Fig. 2.6. The sample capacitor is used as the termination of a precision coaxial line.

   The complex reflection factor $r^*(l)$ of the line (length l) depending on the sample impedance is measured with a microwave reflectometer. For this pur-
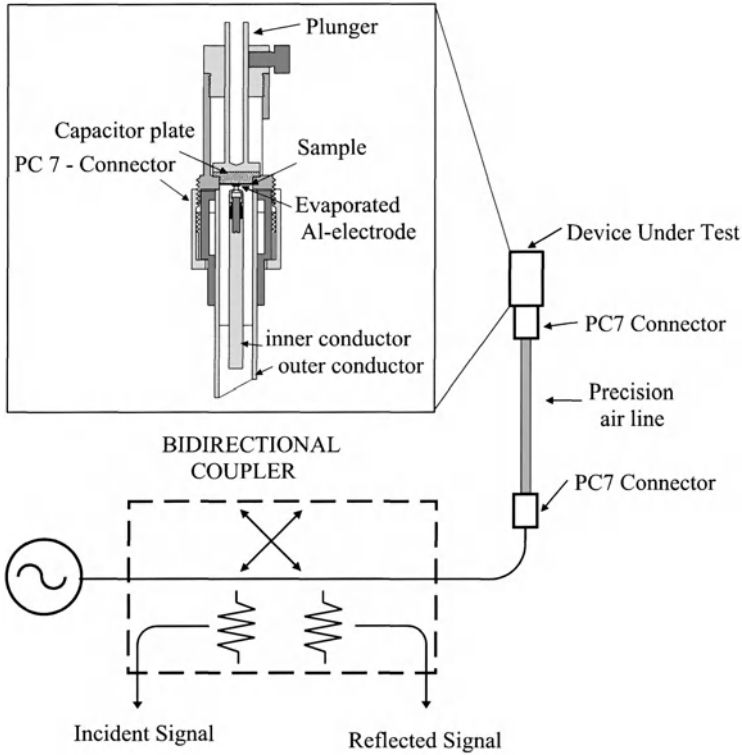
Fig. 2.6. Scheme of the coaxial line reflectometer with sample head

pose, the incoming and reflected waves are separated with two directional couplers and are measured in amplitude and phase. $r^*(x)$ is defined as the ratio of the voltages (or electrical fields) of the reflected and the incoming wave of the line. It depends on the location of the measurement along the line

$$r^*(x) = \frac{U^*_{\text{refl}}(x)}{U^*_{\text{inc}}(x)} \tag{2.11}$$

For an ideal line, $r^*(l)$ which is measured by the reflectometer is related to the reflection factor $r^*(0)$ at the beginning ($l = 0$) of the line by

$$r^*(l) = r^*(0)\exp[2l(\alpha + i\beta)] \tag{2.12}$$

where α is the attenuation coefficient $\left(\alpha = \dfrac{2\pi n''}{\lambda}\right)$ and β the phase (or propagation) coefficient $\left(\beta = \dfrac{2\pi n'}{\lambda}\right)$. From Eq. (2.11) the sample impedance is calculated as

$$Z^*_S(\omega) = Z_0 \frac{1 + r^*(l)}{1 - r^*(l)} \tag{2.13}$$

where Z_0 is the wave resistance of the line. As can be seen from Eq. (2.13), the measurement range is limited to sample impedances Z_S^* being in the region of Z_0.

In practice, the lines are not ideal and sophisticated calibration procedures have to be applied and low loss precision lines matching the output resistance of the reflectometer are required. The line parameters α, β must be homogeneous over the whole line and also independent of temperature, as the calibration generally can only be carried out at room temperature. The same criteria mentioned for the line apply to the sample cell. Therefore, an additional calibration which eliminates the influence of internal impedances in the sample cell is necessary. In order to keep the waveguide as short as possible, the cryostat with the sample has to be closely mounted at the frontend of the analyzer. Coaxial line reflectometers cover the frequency range between 1 MHz and ~3 GHz. Based on Agilent RF-impedance analyzers an accuracy in $\tan \delta < 10^{-2}$ can be realized (HP 4291 B: 1 MHz–1.8 GHz, HP 4991 A: 1 MHz–3 GHz). Sample cells, precision extension line, and dedicated cryostats are commercially available.

2.2.7
Network Analysis

At frequencies above 1 GHz network analysis [20, 21] can be used (Fig. 2.7) in which not only the reflected wave but also the wave transmitted through a sample is analyzed in terms of phase and amplitude. This allows the frequency range to be extended up to 100 GHz. However, with increasing frequency and hence decreasing dimensions of coaxial lines or waveguides, the calibration procedure becomes cumbersome. With network analyzers based on the Agilent 8510 an accuracy in $\tan \delta < 10^{-2}$ is possible.

Fig. 2.7. Scheme of the vectorial network analyzer with transmission cell
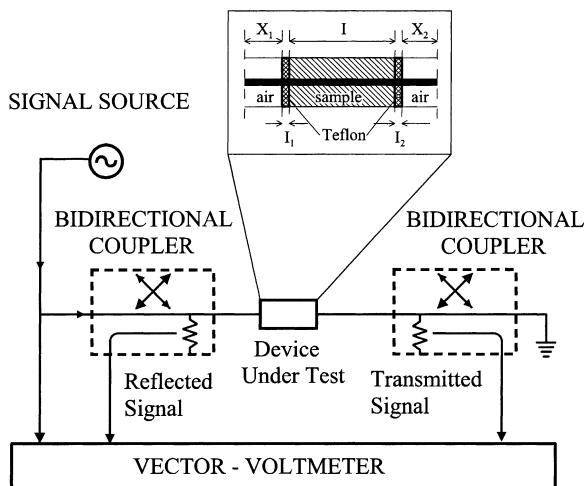
2.2.8
Impedance and Frequency Ranges Overview

It is convenient to represent the sample impedance as a capacitor C_s related to ε' in parallel circuit with a resistor R_s related to ε'' and the material d.c. conductivity σ_{dc}.

The serial impedance of the sample capacitor is

$$Z_s^* = \frac{U_s}{I_s' + i\,I_s''} = \frac{1}{iC_0 \left(\omega \varepsilon^* - i\dfrac{\sigma_{\mathrm{dc}}}{\varepsilon_0} \right)} \tag{2.14}$$

The parallel impedance Z_p^* is defined with respect to each sample current component I' and I'' as

$$Z_p^* = \frac{U_s}{I_s'} + i\frac{U_s}{I_s''} \tag{2.15}$$

Combination with Eq. (2.14) yields

$$Z_p' = \frac{1}{\left(\omega \varepsilon'' + \dfrac{\sigma_{\mathrm{dc}}}{\varepsilon_0} \right) C_0} \quad \text{and} \quad Z_p'' = \frac{1}{\omega \varepsilon' C_0} \tag{2.16}$$

The dark shaded area in Fig. 2.8 shows Z_p' and Z_p'' for a typical dielectric sample with capacity C_s around 100 pF, loss factor $\tan\delta$ in the range from 10^{-4} to 1 and $\sigma_{\mathrm{dc}} = 0$. Both Z_p' and Z_p'' show the typical $1/\omega$ increase with decreasing frequency for capacitive samples. Due to the broad frequency regime, the impedance range becomes extraordinary large. For high losses with e.g. $\tan\delta = 1$, the real and imaginary parts of Z_p^* become equal. With decreasing ε'' and $\tan\delta$, Z_p' increases linearly shifting for constant $\tan\delta$ and C_s to higher impedances.

For comparison, the typical impedance ranges of the several analysis techniques are shown, too. The outer border lines of each range correspond to 10% accuracy for each Z_p component which may be seen as a reasonable limit for the usable range. For impedance points within this range, accuracy linearly increases from 10% with the logarithmic distance to the border line until the systems base accuracy is reached. For example, if the impedance point is located within the range two orders of magnitude apart from a border line, the accuracy would be 0.1%. The total impedance limit (100% error) would be reached for impedance points one order of magnitude outside the marked areas.

As can be seen from Fig. 2.8, the capacitive component Z_p'' related to ε' is generally lower in impedance (for $\tan\delta < 1$) and therefore it can be measured with all techniques within their frequency range. At the high frequency end, the RF reflection and network analyzers suffer from too low sample impedances. Therefore, one usually reduces the sample capacity by increasing the sample thickness or decreasing its diameter. Typical values are within 1 pF – 10 pF for
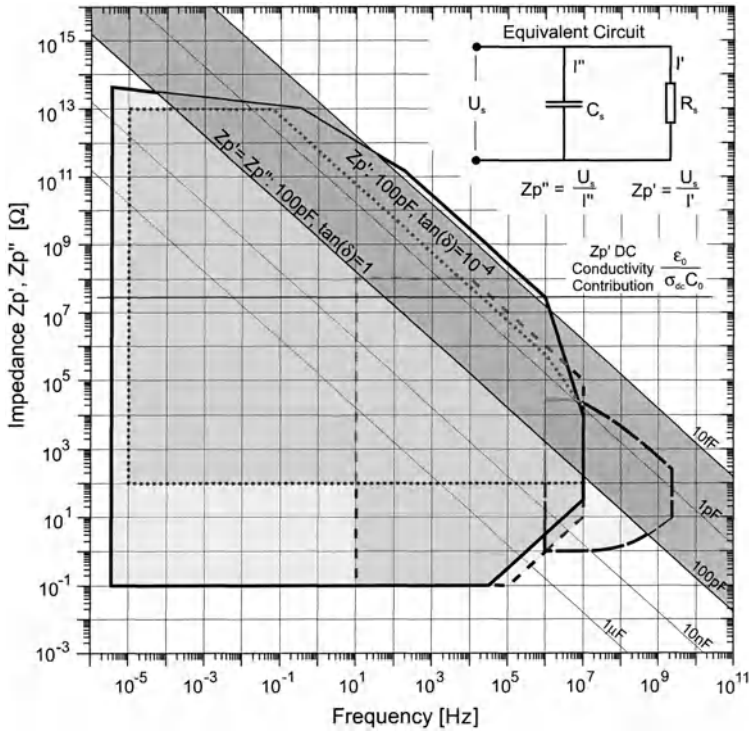
Fig. 2.8. Ranges (10 % accuracy) of complex impedance [Z_p' Z_p''] and frequency for a dielectric sample (100 pF, $\tan\delta$ from 10^{-4} to 1) represented by a parallel circuit of a capacitor and resistor (inlet). Different measurement systems are compared: --- Impedance analyzer, •••• Dielectric converter with Fourier correlation analyzer, —— Dielectric analyzer, — •• — RF reflectometer and network analyzer

optimized performance at the high frequency end. This is only possible at the further cost of decreased accuracy at the RF low frequency range end (1 MHz).

For the Z_p' component related to ε'', the situation becomes more critical with decreasing losses. For $\tan\delta = 10^{-2}$, the 10 % borderline applies for all systems at frequencies >10 MHz, meaning that low loss dielectrics cannot be measured at high frequencies with the broadband techniques presently available. The general impedance analyzers reach their Z_p' 10 % limit below about 1 kHz. With further decreasing losses <10^{-3}, the dielectric converters reach their 10 % border line as well. Lower loss samples down to 10^{-4} can be measured with the dielectric analyzer from about 10 Hz – 100 kHz.

The d.c. conductivity contributes, according to Eq. (2.16), a frequency independent part $\dfrac{\varepsilon_0}{\sigma_{dc} C_0}$ to Z_p' which is drawn as a horizontal line in Fig. 2.8. This line confines the dielectric contribution $\dfrac{1}{\omega \varepsilon'' C_0}$ to Z_p' at high impedance. As Z_p'' increases to low frequencies with $1/\omega$, there is always a turn over frequency

$$\omega_t = \frac{\sigma_{dc}}{\varepsilon_0 \, |\varepsilon^*|}$$ where the sample impedance changes from capacitive to resistive characteristics. Depending on the material, σ_{dc} and with this ω_t may vary over many orders of magnitude especially if measured at different temperatures. For high d.c. conductivity, Z_p' may become small at low frequencies. This causes problems for systems based on dielectric converters, as their reference capacitor technique usually fails in this range. It is then more convenient to use the general impedance techniques or the dielectric analyzer which offer high accuracy over the entire impedance range both for low loss and high conductive samples.

2.3
Measurement Systems in the Time Domain from 10^{-6} Hz to 10^{10} Hz

In the dynamic range from 10^{-6} Hz to 10^{10} Hz the complex dielectric function can also be determined by measuring the time dependence of the (d.c.)-polarization current of a (loaded) sample capacitor [22–26]. The experimental approach is simple and because of the multiplex advantage less time consuming than measurements in the frequency domain. However, this is possible only on the expense of a reduced accuracy. In analogy to Eq. (2.1)

$$\varepsilon(t) = \frac{C(t)}{C_0} \quad \text{and} \quad \frac{d\varepsilon(t)}{dt} = \frac{I(t)}{C_0 \, U_{Pol}} \tag{2.17}$$

hold where $I(t)$ is the polarization current and U_{Pol} the polarizing voltage. C_0 is the capacitance of the empty capacitor. According to Eq. (2.13) the time dependent dielectric function is determined from a measurement of the time dependence of the (d.c.)-polarization current $I(t)$. (Depolarization experiments are often more convenient because they are not disturbed by a d.c.-conductivity contribution. The driving external electric field is zero.) A typical experimental

Fig. 2.9. Scheme of the time-domain set-up for frequencies up to 100 Hz with mechanical switches and up to 10^4 Hz with electronic switches [22]
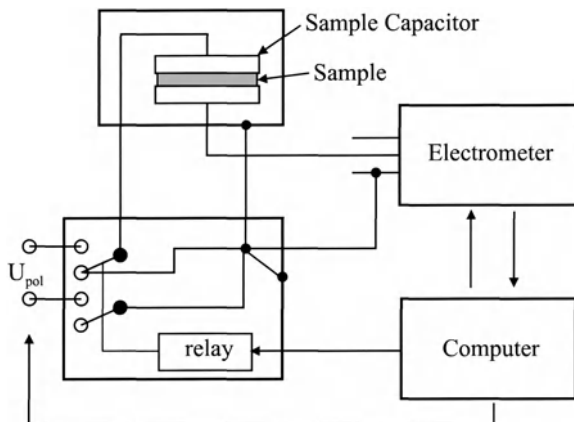
set-up for a low frequency (≤ 10 kHz) time domain spectrometer is shown in Fig. 2.9. In order to achieve a high resolution in $\tan \delta \leq 10^{-3}$ three requirements must be fulfilled: (i) a sensitive electrometer covering a wide dynamic range from 10^{-3} A to 10^{-15} A (Keithley 617 or Keithley 6517), (ii) low noise triaxial cables with an insulation resistance of $\geq 10^{15}$ Ω, and (iii) earth loops caused by different ground sites must be avoided.

An example of a time domain measurement is presented in Fig. 2.10a/b for the glass transition range of poly(propylene glycol) [27]. To obtain the complex dielectric function in the frequency domain a Fourier transform would be necessary. As a rough estimation of $\varepsilon^*(\omega)$ the function $\pi/2t\, d\varepsilon/dt$ can be used, which is called the Hamon-transformation [23]. This representation of the time domain measurements shows maxima for relaxation processes similar as for the loss part of the complex dielectric function ε''. An example is given for poly(propylene glycol) in Fig. 2.10b. With the relation $\omega = 0.2\pi\, t^{-1}$ the Hamon-transformation can be directly compared with ε'' with respect to the maximum position and high frequency behavior of a relaxation process. At the low frequency side of a relaxation process these two functions behave differently. An

Fig. 2.10.
a Depolarization current vs time at different temperatures as indicated. **b** Data after a Hamon transformation. Sample: poly(propylene glycol)
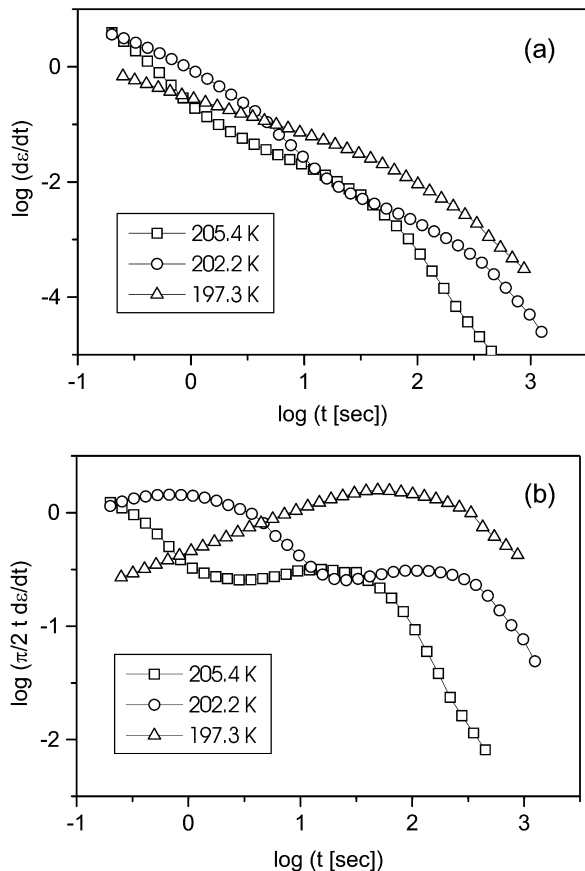
exact transformation of time domain data into the frequency domain requires a Fourier transform which can be done numerically (see for instance [28, 29]). Some approximative methods are discussed in [30, 31].

An alternative approach to the dielectric polarization as a function of time is based on the recent development of electrical modulus $M(t)$ measurements. Under the condition of a constant charge (instead of the usual constant field case), the voltage across the capacitor is proportional to the polarization and to the modulus $M(t)$, with $M^*(\omega) = 1/\varepsilon^*(\omega)$. The experimental setup creates a step function in the dielectric displacement $D(t)$, while the voltage $U(t) \sim M(t)$ across the capacitor is measured [24a]. In order to assure a constant D for $t \geq 0$ the setup should not allow any external current flow within the circuit, i.e., a high input resistance of the voltmeter is essential. The step function in $D(t)$ at $t = 0$ is realized by connecting a voltage source with $U = U_0$ to the discharged capacitor for a short period of time. Figure 2.11 displays a schematic diagram of such a setup which employs the guarding technique in order to minimize cable capacitance effects. With a Keithley 6517 electrometer serving as voltmeter with guarded input ($R_{in} \geq 200$ TΩ, $C_{in} \approx 2$ pF, $I_{bias} \leq 2$ fA) and as voltage source, the polarization can be measured for times 10^{-3} s to 10^6 s.

The modulus technique is advantageous in several ways. For dielectric relaxation measurements at long times one can exploit the fact that $M(t)$ decays faster than $\varepsilon(t)$ under identical conditions. The time scale relation for KWW type responses is given by

$$\tau_M = \left(\frac{\varepsilon_\infty}{\varepsilon_s}\right)^{\frac{1}{\beta_\varepsilon}} \tau_\varepsilon = \left(\frac{M_s}{M_\infty}\right)^{\frac{1}{\beta_M}} \tau_\varepsilon, \ \beta_M \approx 0.8 \, \beta_\varepsilon \tag{2.18}$$

where $M_s = \varepsilon_s^{-1}$ and $M_\infty = \varepsilon_\infty^{-1}$ denote the electric modulus in the limits $t \to \infty$ and $t \to 0$, respectively [24b]. For the example of a polymer system shown in Fig. 2.12, this feature allowed access of an average time scale for dipole fluctuations $\log(\tau[s])$ = 7.53 (1.1 years). For ionic conductors, even severe cases of electrode polarization give rise to only small effects in the $M(t)$ signal [24c]. Furthermore, the technique has allowed dielectric hole-burning measurements to be applied to vitreous ionic conductors (see Chap. 14 on non-resonant dielectric hole burning spectroscopy).

Dielectric measurements in the time domain can be extended to high frequencies covering the range from 10^5 Hz to 2×10^{10} Hz [26]. As in the reflec-

Fig. 2.11. Schematic diagram for measuring the dielectric modulus $M(t)$ in the time domain
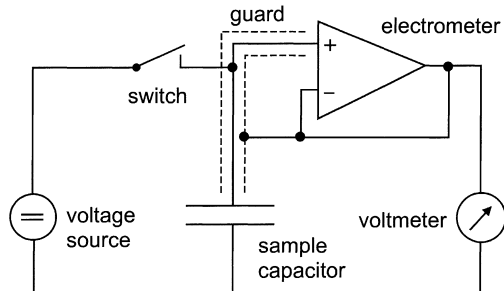
Fig. 2.12. Experimental results for the dielectric modulus $M(t)$ for poly(vinyl acetate) at temperatures from 291 K to 323 K in steps of 2 K. The contributions above and below the plateau at ≈ 0.5 reflect the α-process and d.c.-conductivity, respectively
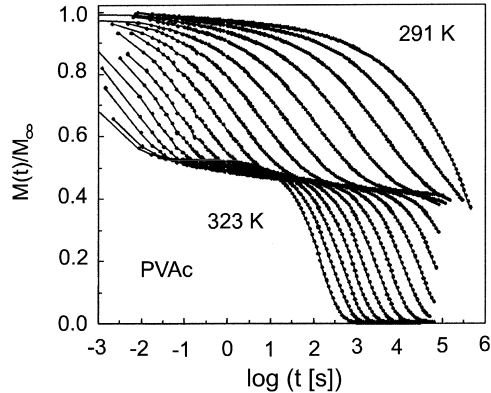
tometer approach (see below) the sample is located at the end of a coaxial transmission line. A rectangular step voltage is sent to the sample cell and the reflected pulse is measured by use of a fast digital oscilloscope. Hence the accessible frequency range is determined by the width and rise time of the incident pulse. The resolution of these spectrometers is smaller than that of the equipment which is based on network analyzers in the frequency domain.

2.4
Quasioptical Set-Ups in the Frequency Range from 10^{10} Hz to 10^{12} Hz

In the frequency regime between 10^{10} Hz and 10^{12} Hz (mm- and sub-mm-waves) on the low frequency side ($< \sim 100$ GHz) coaxial and waveguide techniques are used and above 300 GHz ($\bar{\lambda} = 10$ cm^{-1}) Fourier-Transform spectroscopy is employed. The intermediate range is bridged by "quasioptical"-methods [32–35] using unguided monochromatic electromagnetic waves propagating through "free space". As radiation sources typically backward-waveoscillators (BWO) are applied because of their tunability in frequency (in contrast to gunoscillators or clystrons which are narrow banded). The scheme of a quasioptical mm- and sub-mm-wave spectrometer based on a polarizing double beam Mach-Zehnder interferometer is shown in Fig. 2.13. The radiation of the BWO is emitted by a horn-antenna and focused by Teflon lenses. For measurements of the transmission $T(\omega)$ one arm of the interferometer is blocked. A set of two lenses is used to focus the radiation at the position of the sample in the cryostat or oven. The radiation is detected by a Golay cell or a (pumped) Helium InSb-bolometer. To reduce the noise level a chopper in the beam path and phase sensitive detection is applied. Two consecutive frequency sweeps with and without the sample at each temperature are made leading to a precise determination of the transmission coefficient T. Values as low as $T = 10^{-7}$ can be detected.

To record the phase shift $\varphi(\omega)$ the instrument works in the interferometer mode. For that the beam is split using a 45° wire-grid. In the second arm of the spectrometer a similar set of lenses is mounted in order to make the optical path
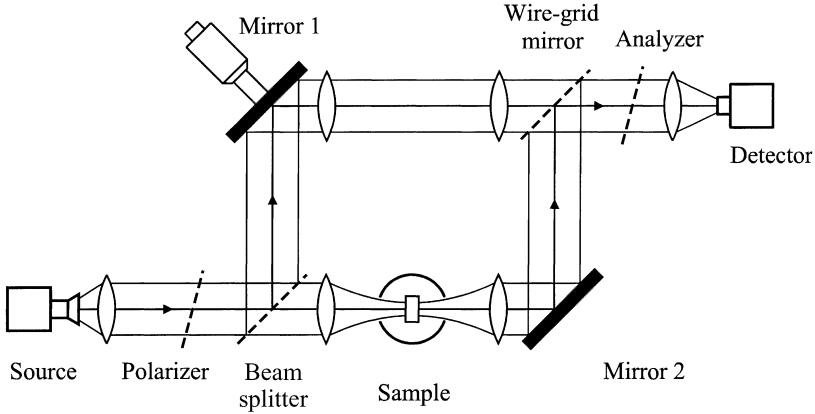
Fig. 2.13. Scheme of the polarizing quasioptical Mach-Zehnder interferometer for the mm- and sub-mm-wave regime

length identical to that of the first arm (without sample). After combination of the two beams by another 45°-wire-grid the radiation is detected. Using the movable mirror in the reference arm the phase shift $\varphi(\omega)$ of the sample is measured. For an isotropic sample layer the complex transmission coefficient $t^* = \sqrt{T(v)}\exp{(i(v))}$ is determined by the following well known relationships [32, 33]

$$T = E\frac{(1-R)^2 + 4R\sin^2\psi}{(1-RE)^2 + 4RE\sin^2(N+\psi)}$$

$$\varphi = N + \arctan\frac{ER\sin 2(N+\psi)}{1 - ER\cos 2(N+\psi)} + \arctan\frac{b}{a^2+b^2+a} - \arctan\frac{b}{a+1}$$

$$E = \exp\left(-\frac{4\pi n''d}{\lambda}\right), \qquad N = \frac{4\pi n'd}{\lambda}$$

$$R = \frac{(a-1)^2+b^2}{(a+1)^2+b^2}, \qquad \psi = \arctan\frac{2b}{a^2+b^2-1}$$

$$n' + in'' = \sqrt{\varepsilon^*\mu^*}, \qquad a+ib = \sqrt{\frac{\mu^*}{\varepsilon^*}}$$

(2.19)

where λ is the wavelength of the radiation, d the sample thickness, and ε^* and μ^* the complex dielectric permittivity and magnetic permeability of the substance, respectively.

A principal difficulty for measurements in the mm- and sub-mm-wave frequency range using monochromatic sources results from the high coherence length of the radiation. This gives rise to multiple interference patterns which may spoil the experimental accuracy. Phase-shakers can be used to circumvent

this problem [32]. For the above described Mach-Zehnder set-up the minimum detectable value for ε'' is limited by the maximum thickness of the sample only. A typical minimal value for the measurement of $\tan \delta$ is 10^{-2}.

An alternative experimental approach in the mm- and sub-mm-wave regime are oversized cavities [36, 37] with typical dimensions being much larger than the wavelength: using high reflectivity walls and "mode stirrers" an isotropic and homogeneous field is generated on a time-averaged basis. The usefulness of the device arises from several advantages. For absorption measurements of gaseous samples the oversized cavity serves as a long-path absorption cell, thus providing a manifold increase in sensitivity compared to a single-path set-up. The photon-storing capability of the device can also be used for measuring the resistivity of metals. In this case the walls of the oversized cavity are partly composed of the materials under study. For inhomogeneous samples, the main advantage arises from the fact that such measurements are only sensitive to the absorption loss in the specimen and not to scattering and reflection losses. Thus, specimen preparation in a plane-parallel form is not necessary, as it is for quasi-optical methods. It therefore allows for the quantitative study of a substantial body of materials, including powders, thin films, and composites. This applies to the whole mm- and sub-mm-wave spectrum. For low temperature absorption
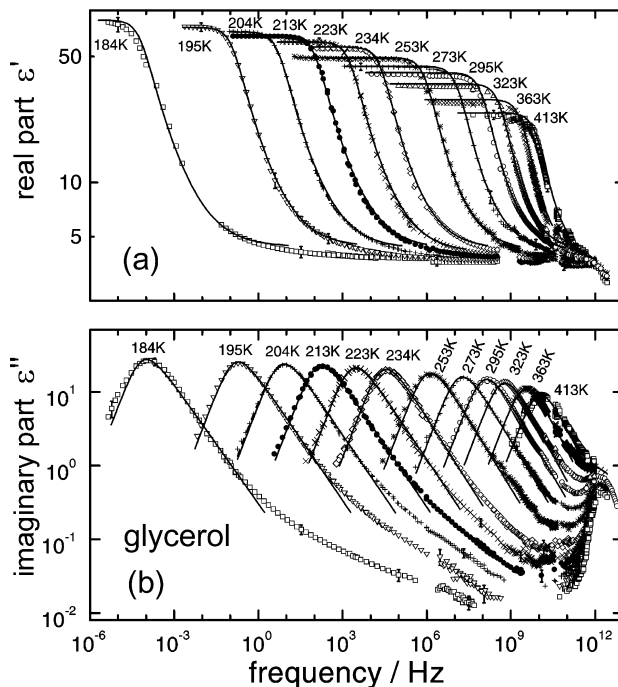
Fig. 2.14. Dielectric spectra: **a** real part ε'; **b** imaginary part ε'' for glycerol as measured in the entire frequency regime from 10^{-6} Hz to 10^{12} Hz. The dynamic glass transition is seen over many decades in frequency with varying temperature. In addition in ε'' the excess wing and the boson peak show up (see Chap. 5) [38]

measurements the device can be used with a cryostat such that the total sample chamber inside the oversized cavity is composed of fused silica which is nearly transparent in this spectral range. By that serious problems can be circumvented by heat conduction in waveguide systems or by standing waves between the windows of the cryostat in quasioptical systems. The main disadvantage of oversized cavities is the loss of phase information. Thus only indirect measurements of the real part ε' of the complex dielectric function are possible. Details are discussed in [37].

For frequencies above 10^{12} Hz Fourier-Transform spectrometers are employed which are also available for the far infrared (e.g., Bruker 113v and 66v/s). If only the transmission and the reflection spectra are measured the complex permittivity can be determined by a Kramers-Kronig transformation. Using dispersive Fourier-Transform spectroscopy the complex dielectric function is measured directly [33, 34].

The complex dielectric spectrum of the glass-forming liquid glycerol as measured from 10^{-6} Hz to 10^{13} Hz is shown in Fig. 2.14. It is nicely demonstrated how well the different measurement systems can be combined.

2.5
Conclusions

With modern equipment it is possible to cover the entire regime from 10^{-6} Hz to 10^{12} Hz without any gap. For that different measurement systems based on different physical principles have to be combined: Fourier correlation analyzers (10^{-6} Hz to 10^{7} Hz), impedance analyzers (10 Hz to 10^{6} Hz), coaxial line reflectometers (10^{6} Hz to 10^{9} Hz), network analyzers (10^{7} Hz to 10^{10} Hz), quasi-optical interferometers (10^{10} Hz to 10^{12} Hz), and Fourier spectrometers (10^{11} Hz to IR). In the time domain measurement systems between 10^{-6} Hz and 10^{10} Hz can be employed but with reduced accuracy.

List of Abbreviations and Symbols

c	Speed of light
C_0	Vacuum capacitance
$E^*(\omega)$	Complex sinusoidal electric field strength
$J^*(\omega)$	Complex sinusoidal current density
$M^*(\omega) = M'(\omega) + iM''(\omega)$	Complex electrical modulus
$n^*(\omega) = n'(\omega) - in''(\omega)$	Complex index of refraction
R	Resistor
$r^*(x)$	Complex reflection at position x
$t^*(x)$	Complex transmission at position x
$U^*(\omega)$	Complex voltage
$Z^*(\omega)$	Complex impedance
α	Damping constant
β	Propagation constant
$\beta_\varepsilon, \beta_M$	KWW stretching parameter for the dielectric perimittivity and for the electric modulus
$\tan\delta = \dfrac{\varepsilon''}{\varepsilon'}$	Tangents of the phase angle between $\varepsilon'(\omega)$ and $\varepsilon''(\omega)$
$\varepsilon(t)$	Time dependent dielectric function
ε_0	Permittivity of free space ($\varepsilon_0 = 8.854 \times 10^{-12}$ As V^{-1} m^{-1})
$\varepsilon^*(\omega) = \varepsilon'(\omega) - i\varepsilon''(\omega)$	Complex dielectric permittivity or function[4]
$\mu^*(\omega) = \mu'(\omega) - i\mu''(\omega)$	Complex magnetic permeability
λ	Wavelength in vacuum
$\bar{\lambda}$	Wavenumber
ν	Frequency
σ_{dc}	Direct current conductivity
$\sigma^*(\omega) = \sigma'(\omega) + i\sigma''(\omega)$	Complex conductivity
τ_ε, τ_M	Relaxation time of the KWW-function for the dielectric perimittivity and for the electric modulus
$\varphi(\omega)$	Phase shift
ω	Angular frequency

---

[4] The complex index of refraction and the complex dielectric permittivity are related by Maxwell's relation $\varepsilon^* = (n^*)^2$

$$n' = \left(\frac{\varepsilon'}{2}\right)^{\frac{1}{2}}\left\{\left[1+\left(\frac{\varepsilon''}{\varepsilon'}\right)^2\right]^{\frac{1}{2}}+1\right\}^{\frac{1}{2}}$$

$$n'' = \left(\frac{\varepsilon'}{2}\right)^{\frac{1}{2}}\left\{\left[1+\left(\frac{\varepsilon''}{\varepsilon'}\right)^2\right]^{\frac{1}{2}}-1\right\}^{\frac{1}{2}}$$

$$\varepsilon' = n'^2 - n''^2$$

$$\varepsilon'' = 2n'n''$$

a.c.	Alternating current
d.c.	Direct current
BWO	Backward-wave oscillator
FRA	Frequency response analyzer
KWW	Kohlrauch/Williams/Watts
RF	Radio frequency
TDR	Time domain reflectometer
VAPG	Variable amplitude-phase generator

References

1. (a) Field RF, von Hippel AR(eds) (1954) Dielectric materials and applications. MIT Press & Wiley, New York; (b) von Hippel AR (ed) (1954) Dielectric materials and waves. MIT Press & Wiley, New York; (c) Westphal WB, von Hippel AR (eds) (1954) Dielectric materials and applications. MIT Press & Wiley, New York
2. McCrum NG, Read BE, Williams G (1967) Anelastic and dielectric effects in polymeric solids. Wiley, New York: reprinted 1991 by Dover, New York
3. Hill NE, Vaughan W, Price AH, Davis M (1969) Dielectric properties and molecular behaviour. Van Nostrand, London
4. Vaughan W, Smyth CP, Powles JG (1972) In: Weissberger A, Rossiter BW (eds) Physical methods of chemistry. Wiley-Interscience, New York
5. Blythe AR (1979) Electrical properties of polymers. Cambridge University Press
6. Boyd RH (1980) In: Fava RA (ed) Methods of experimental physics, vol 16, part C. Academic Press, Orlando FL
7. Pochan JM, Fitzgerald JJ, Williams G (1993) In: Rossiter BW, Baetzold RC (eds) Determination of electronic and optical properties. Wiley, New York
8. Craig DQM (1995) Analysis of pharmaceutical systems. Taylor & Francis, London
9. Gordy W, Smith WV, Trambarulo RF (1953) Microwave spectroscopy. Wiley, New York
10. Kremer F, Arndt M (1997) Fundamentals and applications. In: Runt JP, Fitzgerald JJ (eds) Dielectric spectroscopy of polymeric materials. American Chemical Society, Washington DC
11. Afsar MN, Button KJ (1981) Infrared and millimeter waves, vol 2, p 1029
12. Chamberlain J, Chantry GW (1973) High frequency dielectric measurement. IPC Science and Technology Press, Guildford
13. Birch JR, Parker TJ (1979) Dispersive Fourier transform spectrometry. In: Button KJ (ed) Infrared and millimeter waves. Academic Press, New York, p 137
14. Kremer F, Boese D, Maier G, Fischer EW (1989) Prog Colloid Polym Sci 80:129
15. Pugh J, Ryan T (1979) IEE Conference on Dielectric Materials, Measurements and Applications 177:404
16. Schaumburg G (1994) Dielectric Newsletter of Novocontrol, issue March 1994
17. Schaumburg G (1999) Dielectric Newsletter of Novocontrol, issue May 1999
18. Böhmer R, Maglione M, Lunkenheimer P, Loidl A (1989) J Appl Phys 65:901
19. Jiang GQ, Wong WH, Raskovida EY, Clark WG, Hines WA, Sanny J (1993) Rev Sci Instrum 64:1614
20. Collin RE (1966) Foundations for microwave engineering, 2nd edn. McGraw-Hill, New York
21. Hewlett Packard (1985) Measuring the dielectric constant of solids with the HP8510 network analyser. Hewlett Packard Product Note 8510–3
22. Mopsik FI (1984) Rev Sci Instrum 55:79
23. Hamon BV (1952) Proc Inst Electr Eng 99:27
24. (a) Wagner H, Richert R (1997) Polymer 38:255; (b) Richert R (2000) Physica A 287:26; (c) Wagner H, Richert R (1999) J Appl Phys 85:1750
25. Feldman Y (1995) Dielectric Newsletter of Novocontrol, issue March 1995

26. (a) Cole RH (1975) J Phys Chem 79:1459; (b) Cole RH (1975) J Phys Chem 79:1469; (c) Clarkson TS, Crossley J,Tuxworth RW, Williams G (1977) Adv Mol Relaxation Processes 10:173
27. Schönhals A (1996) Habilitation thesis. Technische Universität, Berlin
28. William G (1963) Polymer 4:27
29. Johnson E, Anderson EW, Furukawa T (1981) Ann Rep Conf Electr Insul Dielectr, p 258
30. Brather A (1979) Colloid Polym Sci 257:725
31. Simon GP, Williams G (1993) Polymer 34:2038
32. Volkov AA, Goncharov YG, Kozlov GV, Lebedev SP, Prokhorov AM (1985) Infrared Phys 25:369
33. Volkov AA, Kozlov GV, Prokhorov AM (1989) Infrared Phys 29:747
34. Genzel L, Poglitsch A, Hässler S (1986) Infrared Millimeter Waves 6:741
35. Schneider U, Lunkenheimer P, Pimenov A, Brand R, Loidl A (2001) Ferroelectrics 249:89
36. Gebbie HA, Bohlander RA (1972) Appl Opt 11:723
37. Kremer F, Poglitsch A, Böhme D, Genzel L (1984) Infrared Millimeter Waves 11:141
38. Lunkenheimer P, Schneider U, Brand R, Loidl A (2000) Contemp Phys 41:15

3 Analysis of Dielectric Spectra

A. Schönhals · F. Kremer

3.1
Introduction

The complex dielectric function $\varepsilon^*(\omega)$ in its dependence on angular frequency $\omega = 2\pi\nu$ (ν-frequency of the outer electrical field) and temperature originates from different processes: (i) microscopic fluctuations of molecular dipoles [1] (rotational diffusion[1]), (ii) the propagation of mobile charge carriers (translational diffusion of electrons, holes or ions), and (iii) the separation of charges at interfaces which gives rise to an additional polarization. The latter can take place at inner dielectric boundary layers (Maxwell/Wagner/Sillars-polarization [2, 3]) on a mesoscopic scale and/or at the external electrodes contacting the sample (electrode polarization) on a macroscopic scale. Its contribution to the dielectric loss can be orders of magnitude larger than the dielectric response due to molecular fluctuations.

Each of the above mentioned processes has specific features in the frequency and temperature dependence of the real and imaginary part of the complex dielectric function. It is the objective of this chapter to discuss the methods to analyze, to separate, and to quantify their different contributions to the dielectric spectra.

Relaxation processes are characterized by a peak in the imaginary part ε'' and a step-like decrease of the real part ε' of the complex dielectric function $\varepsilon^*(\omega) = \varepsilon'(\omega) - i\varepsilon''(\omega)$ ($i = \sqrt{-1}$) with increasing frequency. In contrast, conduction phenomena show an increase of the imaginary part of the dielectric function with decreasing frequency. For pure ohmic conduction the real part of $\varepsilon^*(\omega)$ is independent of frequency while for non-ohmic conduction or polarization effects (at inner boundaries or external electrodes) the real part of $\varepsilon^*(\omega)$ increases with decreasing frequency. A schematic representation of the frequency dependence of $\varepsilon^*(\omega)$ is given in Fig. 3.1.

Alternative representations of the dielectric properties of a material are the complex conductivity $\sigma^*(\omega)$ or the complex electric modulus $M^*(\omega)$ (see Chap. 1). They emphasize different aspects of polarization and charge transport in a material as discussed below.

---

[1] In special cases like the normal mode relaxation (see Chap. 7) the translational diffusion can be deduced from dielectric measurements.

Fig. 3.1. Scheme of the real ε' (*solid line*) and the imaginary ε'' (*dashed line*) part of the complex dielectric function for a relaxation process and an **a** ohmic or **b** non-ohmic conductivity. In the latter case electrode polarisation is observed
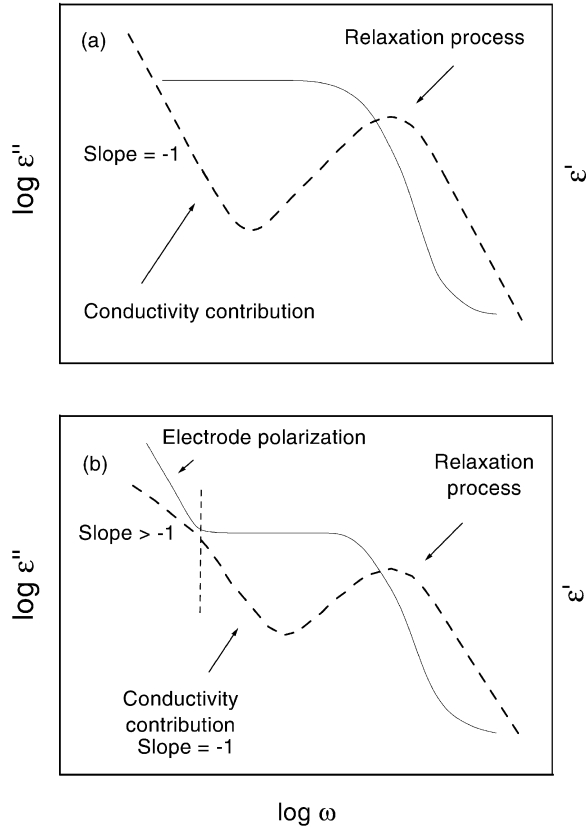
3.2
Dipolar Fluctuations

One of the most important applications of dielectric spectroscopy is the investigation of relaxation processes which are due to rotational fluctuations of molecular dipoles. As they are related to characteristic parts of a molecule (functional groups etc.) or to the molecule as a whole, information about the dynamics of a molecular ensemble can be obtained by analyzing the dielectric function. If the frequency $v = \omega/2\pi$ of the applied outer electric field corresponds to reorientation times τ of molecular dipoles the complex dielectric function shows a characteristic pattern. With increasing ω the real part $\varepsilon'(\omega)$ decreases step-like whereas the imaginary part $\varepsilon''(\omega)$ exhibits a maximum (Fig. 3.2). The essential quantities which characterize a dielectric relaxation process can be extracted from that behavior. The frequency of maximal loss v_p is related to a characteristic relaxation rate $\omega_p = 2\pi v_p$ or relaxation time $\tau_p = 1/\omega_p$ of the fluctuating dipoles. From the shape of the loss peak the distribution of relaxation times can be deduced. The dielectric strength $\Delta\varepsilon$ of a relaxation process can be determined
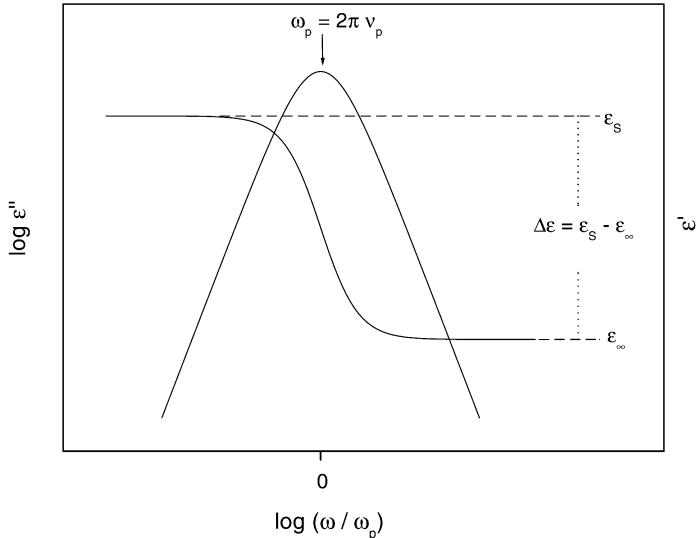
Fig. 3.2. Real ε' and imaginary part ε'' of the complex dielectric function vs normalized frequency for a Debye relaxation process

either from the area under the loss peak $\varepsilon''(\omega)$ or from the step in $\varepsilon'(\omega)$. Since $\varepsilon'(\omega)$ and $\varepsilon''(\omega)$ are interrelated by the Kramers/Kronig-relations [1], both contain the same information.

3.2.1
Analysis of Dielectric Spectra – Model Functions

Dielectric relaxation processes are usually analyzed using model functions. Starting from the theoretically well founded Debye function (see Chap. 1) several formulas for both the frequency and the time domain have been suggested to describe the experimentally observed spectra. The most important of these approaches are discussed below.

The Debye function for the frequency dependence of $\varepsilon^*(\omega)$ is given by

$$\varepsilon^*(\omega) = \varepsilon_\infty + \frac{\Delta\varepsilon}{1 + i\omega\tau_D} \tag{3.1}$$

where $\Delta\varepsilon = \varepsilon_S - \varepsilon_\infty$ is the dielectric relaxation strength or intensity with $\varepsilon_S = \lim\limits_{\omega\tau \ll 1} \varepsilon'(\omega)$ and $\varepsilon_\infty = \lim\limits_{\omega\tau \gg 1} \varepsilon'(\omega)$. The Debye relaxation time τ_D is related to the position of maximal loss by $\omega_p = 2\pi\nu_p = 1/\tau_D$ (see Fig. 3.2). The separation of $\varepsilon^*(\omega)$ in the real and the imaginary part is given in Table 3.1. The loss peak is symmetric with a half width ω_D of 1.14 decades.

In most cases the half width of measured loss peaks is much broader than predicted by Eq. (3.1) (up to six decades) and in addition their shapes are asym-

Table 3.1. Compilation of different model functions for the frequency domain

Model function	Dielectric function	Real part	Imaginary part	Relaxation Time Distribution
	$\dfrac{\varepsilon^*(\omega)-\varepsilon_\infty}{\Delta\varepsilon}$	$\dfrac{\varepsilon'(\omega)-\varepsilon_\infty}{\Delta\varepsilon}$	$\dfrac{\varepsilon''(\omega)}{\Delta\varepsilon}$	$L(\tau)$
Debye	$\dfrac{1}{1+i\omega\tau_D}$	$\dfrac{1}{1+(\omega\tau_D)^2}$	$\dfrac{\omega\tau_D}{1+(\omega\tau_D)^2}$	$\delta(\tau_D)$
Cole/Cole	$\dfrac{1}{1+(i\omega\tau_{CC})^\beta}$ $0<\beta\leq 1$	$(1+\omega\tau_{CC})^\beta\cos(\beta\pi/2)\,r^{-1}(\omega)$ $r(\omega)=1+2(\omega\tau_{CC})^\beta\cos(\beta\pi/2)+(\omega\tau_{CC})^{2\beta}$	$(\omega\tau_{CC})^\beta\sin(\beta\pi/2)\,r^{-1}(\omega)$	$\dfrac{1}{2\pi}\dfrac{\sin\beta\pi}{\cosh(\ln\tau/\tau_{CC})+\sin\beta\pi}$
Cole/Davidson	$\dfrac{1}{(1+i\omega\tau_{CD})^\gamma}$ $0<\gamma\leq 1$	$\cos(\Phi)^\gamma\,\cos\gamma\Phi$ $\tan\Phi=\omega\tau_{CD}$	$\cos(\Phi)^\gamma\,\sin\gamma\Phi$ $\tan\Phi=\omega\tau_{CD}$	$\dfrac{\sin\gamma\pi}{\pi}\left[\dfrac{\tau}{\tau_{CD}-\tau}\right]^\gamma$ for $\tau\leq\tau_{CD}$; 0 for $\tau>\tau_{CD}$
Havriliak/Negami	$\dfrac{1}{(1+(i\omega\tau_{HN})^\beta)^\gamma}$ $0<\beta\leq 1$ $0<\beta\gamma\leq 1$	$r(\omega)\cos[\gamma\psi(\omega)]$ $r(\omega)=\left[1+2(\omega\tau_{HN})^\beta\cos\left(\dfrac{\beta\pi}{2}\right)+(\omega\tau_{HN})^{2\beta}\right]^{-\gamma/2}$ $\psi(\omega)=\arctan\left[\dfrac{\sin(\beta\pi/2)}{(\omega\tau_{HN})^{-\beta}+\cos(\beta\pi/2)}\right]$	$r(\omega)\sin[\gamma\psi(\omega)]$	$\dfrac{1}{\pi}y^{\beta\gamma}(\sin(\gamma\Theta(y))\Omega(y)$ $y=\tau/\tau_{HN}$ $\Omega(y)=[1+2y^\beta\cos(\pi\beta)+y^{2\beta}]^{-\gamma/2}$ $\Theta(y)=\arctan\left[\dfrac{\sin(\pi\beta)}{y^\beta+\cos(\pi\beta)}\right]$

metric with a high frequency tail. This is called non-Debye (or non ideal) relaxation behavior. In the literature several empirical model functions – mostly generalizations of the Debye function – have been developed and tested which are able to describe broadened and/or asymmetric loss peaks. A compilation of the most important formulas gives Table 3.1.

A broadening of the dielectric function can be described by the Cole/Cole-function [4]

$$\varepsilon_{CC}^{*}(\omega) = \varepsilon_{\infty} + \frac{\Delta\varepsilon}{1+(i\omega\tau_{CC})^{\beta}} \tag{3.2}$$

where $0 < \beta \leq 1$ leads to a symmetrical broadening for the relaxation function compared to Eq. (3.1). For $\beta = 1$ the Debye-function is obtained. The Cole/Cole-relaxation time τ_{CC} gives the position of maximal loss by $\omega_p = 2\pi\nu_p = 1/\tau_{CC}$.

Many experimental results, especially on liquids or low molecular glass-forming materials, show that the complex dielectric function can have also an asymmetric broadening which can be described by the Fuoss/Kirkwood- [5] or by the Cole/Davidson function [6, 7] which reads

$$\varepsilon_{CD}^{*}(\omega) = \varepsilon_{\infty} + \frac{\Delta\varepsilon}{(1+i\omega\tau_{CD})^{\gamma}} \tag{3.3}$$

The parameter γ $(0 < \gamma \leq 1)$ describes an asymmetric broadening of the relaxation function for frequencies $\omega > 1/\tau_{CD}$ where τ_{CD} is the Cole/Davidson-relaxation time. For $\gamma = 1$ the Debye-function is recovered again. It should be noted that for an asymmetric model function like the Cole/Davidson-function the characteristic relaxation time of the model function does not coincide with the relaxation time which is related to the position of maximal loss. The relationship of both quantities depends on the shape parameters. For the Cole/Davidson-equation (Eq. 3.3) one obtains [8]

$$\omega_p = \frac{1}{\tau_{DC}}\tan\left[\frac{\pi}{2\gamma+2}\right] \tag{3.4}$$

A more general model function was introduced by Havriliak and Negami [9, 10] (HN-function) (Eq. 3.5) which is in fact a combination of the Cole/Cole- and the Cole/Davidson-function:

$$\varepsilon_{HN}^{*}(\omega) = \varepsilon_{\infty} + \frac{\Delta\varepsilon}{(1+(i\omega\tau_{HN})^{\beta})^{\gamma}} \tag{3.5}$$

Real and imaginary part for the HN-function are given in Table 3.1. For the fractional shapeparameters β and γ which describe the symmetric and asymmetric broadening of the complex dielectric function $0 < \beta, \beta\gamma \leq 1$ holds. Figure 3.3 gives some examples of the HN-function for selected shape parameters.

The parameters β and γ are related to the limiting behavior of the complex dielectric function at low and high frequencies:

$$\varepsilon_S - \varepsilon'(\omega) \sim \omega^m; \ \varepsilon'' \sim \omega^m \ \text{ for } \ \omega \ll 1/\tau_{HN} \ \text{ with } \ m = \beta \tag{3.6}$$
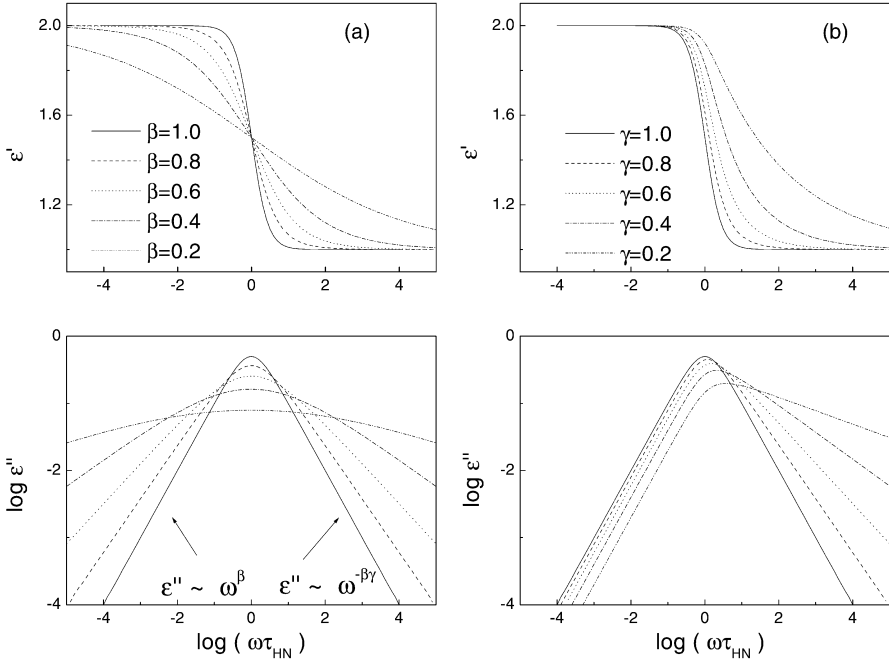
Fig. 3.3. Complex dielectric permittivity for the Havriliak/Negami-function with fixed: **a** $\gamma = 1$; **b** $\beta = 1$ ($\tau_{HN} = 1$ s, $\Delta\varepsilon = 1$, $\varepsilon_\infty = 1$)

$$\varepsilon'(\omega) - \varepsilon_\infty \sim \omega^{-n}; \; \varepsilon'' \sim \omega^{-n} \quad \text{for} \quad \omega \gg 1/\tau_{HN} \quad \text{with} \quad n = \beta\gamma \quad (3.7)$$

In other words, the shape parameters m and n, introduced by Jonscher [11], are the slopes of $\log \varepsilon''$ vs $\log \omega$ at low and high frequencies with regard to the position of maximal loss.

The position of maximal loss depends on the parameters β and γ according to [8, 12]

$$\omega_p = \frac{1}{\tau_{HN}} \left[\sin\frac{\beta\pi}{2+2\gamma} \right]^{1/\beta} \left[\sin\frac{\beta\gamma\pi}{2+2\gamma} \right]^{-1/\beta} \quad (3.8)$$

Figure 3.4 gives the dielectric loss of poly(chloro styrene) for the α-relaxation (dynamic glass transition) at a temperature of 428.6 K. The Cole/Davidson-, the Cole/Cole- and the HN-function are fitted to the data. Only the HN-function is able to describe the data in the whole frequency range. This means that for a complete description of an isolated relaxation region at least a set of *four* parameters is needed.

It has been known for a long time that at least for the dielectric α-relaxation the loss data are described only incompletely for frequencies $\nu > 10^3 \nu_p$ by any of the model functions mentioned above [6, 7, 13–15]. This is demonstrated in
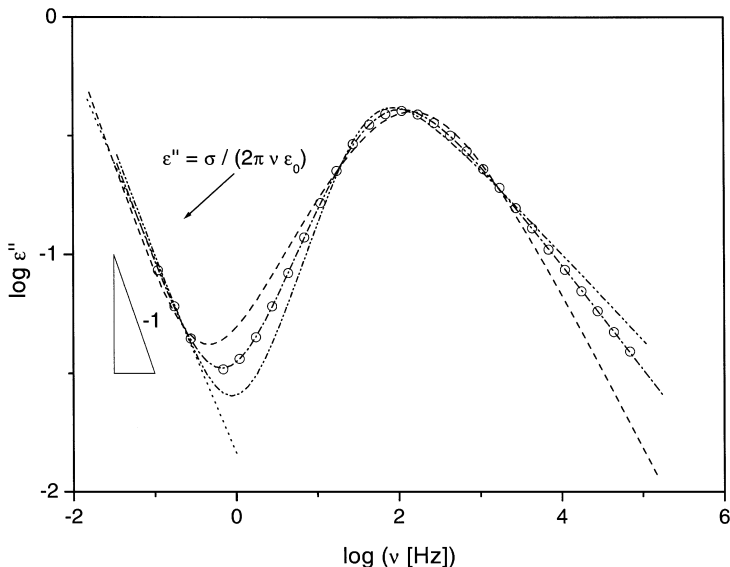
Fig. 3.4. Imaginary part ε'' ($\bigcirc$) vs frequency for poly(chloro styrene) at $T = 428.6$ K. The data are described by a superposition of a conductivity contribution (*dotted line*) and different model functions to relaxation processes: *dashed-dotted-dashed* Havriliak/Negami-, *dashed-dotted-dotted-dashed* Cole/Davidson-, and *dashed* Cole/Cole-function. The error of the measurement is smaller than the size of the symbols

Fig. 3.5 where the dielectric loss for glycerol is plotted vs frequency over nine decades in frequency.

Nagel and coworkers suggested a scaling function to model this behavior [14]. But this function lacks any theoretical foundation and is valid only for the special case $m = 1$ [15]. A possible theoretical explanation of this high frequency wing was suggested by Chamberlin and Kingsbury based on the concept of dynamical heterogeneity [16].

Figure 3.5 shows that the major contribution of the relaxation function is well described by a single HN-formula (more than five decades in frequency). Only the wing at high frequencies cannot be covered by the fit. For a more detailed discussion see Chaps. 4 and 5.

Within the framework of linear response theory the dielectric behavior in the frequency domain is related to that in the time domain by a Fourier transform (see Chap. 1 or [1]). Hence the analogous formula to Eq. (3.1) is in the time domain a simple exponential decay. This means that the time dependent dielectric function $\varepsilon(t)$ is given by

$$\varepsilon(t) - \varepsilon_\infty = \Delta\varepsilon \left[1 - \exp\left(-\frac{t}{\tau_D}\right) \right] \text{ or } \frac{d\varepsilon(t)}{dt} = \frac{\Delta\varepsilon}{\tau_D} \exp\left(-\frac{t}{\tau_D}\right) \tag{3.9}$$

Often a non-Debye relaxation behavior in the time domain can be described by the empirical Kohlrausch/Williams/Watts (KWW) function [17, 18] which reads
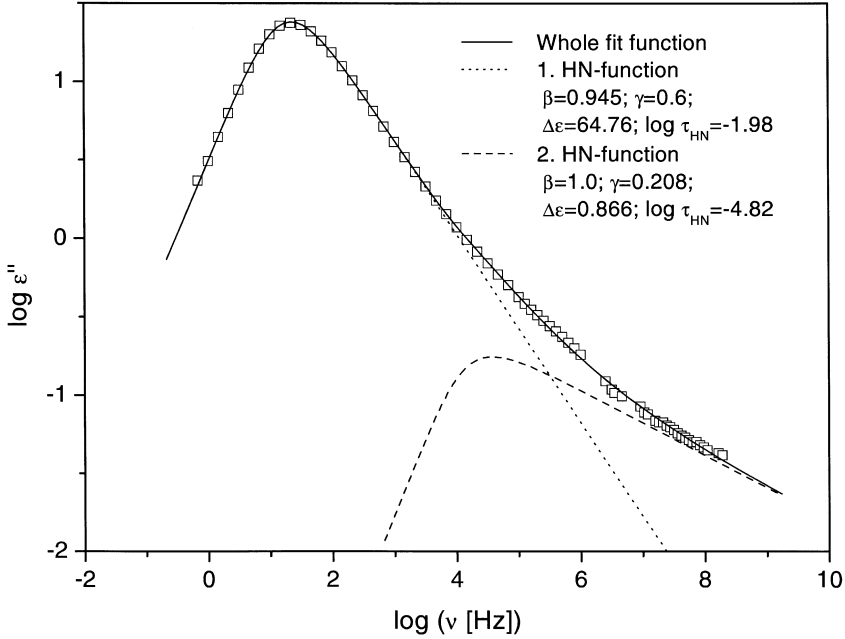
Fig. 3.5. High frequency deviation of the α-relaxation of glycerol compared to the HN-function at $T = 208.3$ K. This high frequency wing is described by a second HN-function. A comparison of the estimated relaxation strengths for both functions shows that the contribution of the high frequency wing is small

$$\varepsilon(t) - \varepsilon_\infty = \Delta\varepsilon \left[1 - \exp\left(\left(-\frac{t}{\tau_{\mathrm{KWW}}} \right)^{\beta_{\mathrm{KWW}}} \right) \right] \tag{3.10a}$$

or

$$\frac{d\varepsilon(t)}{dt} = \Delta\varepsilon \left(\frac{t}{\tau_{\mathrm{KWW}}} \right)^{\beta_{\mathrm{KWW}}-1} \frac{\beta_{\mathrm{KWW}}}{\tau_{\mathrm{KWW}}} \exp\left(-\left(\frac{t}{\tau_{KWW}} \right)^{\beta_{\mathrm{KWW}}} \right) \tag{3.10b}$$

The stretched exponential parameter β_{KWW} leads to an asymmetric broadening of $\varepsilon(t)$ at short times (high frequencies) compared to an exponential decay ($\beta_{\mathrm{KWW}} = 1$). τ_{KWW} is the corresponding relaxation time. Several models to interpret the KWW-function from a molecular point of view are discussed in Chap. 1.

In the time domain an expression analogous to Eq. (3.5) does not exist. However, according to linear response theory the following relationship holds:

$$\frac{d\varepsilon_{\mathrm{HN}}(t)}{dt} = \dot{\varepsilon}_{\mathrm{HN}}(t) = \frac{1}{\pi} \int_0^\infty \frac{\Delta\varepsilon}{(1 + (i\omega\tau_{\mathrm{HN}})^\beta)^\gamma} \exp(i\omega t)d\omega \tag{3.11}$$

Equation (3.11) represents a model function with four parameters in the time domain. It cannot be solved analytically but a fast numerical algorithm is

available [19]. For long and short times compared to τ_{HN} one finds

$$t \frac{d\varepsilon}{dt} \sim t^{-m} \quad \text{for} \quad t \gg \tau_{HN} \quad \text{with} \quad m = \beta \tag{3.12}$$

$$t \frac{d\varepsilon}{dt} \sim t^{+n} \quad \text{for} \quad t \ll \tau_{HN} \quad \text{with} \quad n = \beta\gamma \tag{3.13}$$

Equations (3.12) and (3.13) correspond to Eqs. (3.6) and (3.7) in the frequency domain. The representation $t\, d\varepsilon/dt$ of the time-dependent dielectric function is chosen according to the Hamon method [20]. It should be noted that Eq. (3.5) can be expanded in a Taylor-series which can be Fourier transformed step by step. Thus a series representation for $\varepsilon(t)$ [21] or $d\varepsilon/dt$ [1, 19] is obtained. For $\varepsilon(t)$ one gets the Riesz function [21]

$$\varepsilon_{HN}(t) = \frac{1}{\tau_{HN}} \sum_{j=0}^{\infty} \frac{(-1)^j}{j!} \frac{\Gamma(\gamma+j)}{\Gamma(\gamma)} \frac{(t/\tau_{HN})^{\beta(\gamma+j)-1}}{\Gamma(\beta(\gamma+j))} \tag{3.14}$$

but the convergence of this series is insufficient at least for broadened dielectric spectra.

As pointed out already the dielectric properties measured in frequency and time domain are related to each other by a Fourier transform:

$$\varepsilon^*(\omega) - \varepsilon_\infty = \int_{-\infty}^{+\infty} \dot{\varepsilon}(t)\, e^{-i\omega t}\, dt \tag{3.15}$$

Therefore several attempts have been made to derive simple mathematical expressions to interrelate the dielectric behavior in the frequency and in the time domain and/or to compare the results.

The most common approximation for Eq. (3.15) is the Hamon transform [20]. A plot of $\pi/2t\, d\varepsilon/dt$ vs $\omega = 0.2\pi/t$ displays a chart which corresponds to the imaginary part of the complex dielectric function $\varepsilon''(\omega)$. Both quantities have the same position of maximal loss and the dependence on the high frequency side ($\omega > \omega_p$) can be directly compared as well. On the low frequency side both functions have a different dependence on ω. More refined transformation formulas were developed by Brather [22]. The accuracy of these relationships has been discussed by Simon and Williams [23].

Patterson and Lindsay [24] derived a relationship between the Cole/Davidson function and KWW formula which both have one shape parameter only. This work was extended by Colmenero et al. [25]. They interrelated the HN- and the KWW function leading to the following approximations:

$$\log \frac{\tau_{HN}}{\tau_{KWW}} \approx 2.6\,(1 - \beta_{KWW})^{0.5} \exp(-3\beta_{KWW})$$

$$\beta\gamma \approx \beta_{KWW}^{1.23} \tag{3.16}$$

For the limits of these formulas see [25]. It is important to note that the HN-function has two shape parameters while the KWW formula has only one. Hence
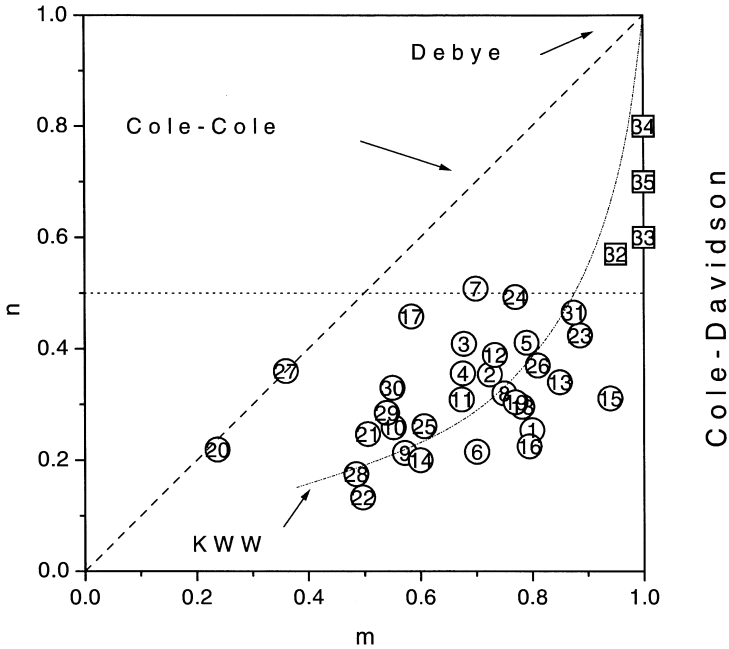
Fig. 3.6. Shape parameters n and m for the dielectric α-relaxation for different polymeric ($\bigcirc$) and low molecular weight systems ($\square$). Data see Appendix 3.1. (Redrawn from [27] with permission of American Chemical Society)

during the transformation from the frequency to the time domain information is lost. This was also discussed in a recent publication by Snyder and Mopsik [26]. It is also evident from Fig. 3.6 where shape parameters m and n for the dielectric α-relaxation of a representative number of low molecular weight and polymeric materials are plotted [27]. In addition the theoretical relationships between m and n according to the Cole/Davidson-, the Cole/Cole- and the Kohlrausch/Williams/Watts function are included. A more complete compilation of data has been published by Jonscher [11] and Havriliak and Havriliak [21] in a similar representation. Figure 3.6 proves that in general no correlation between the shape parameters exists. Hence it has to be concluded that two shape parameters are necessary to describe a dielectric relaxation process.

To analyze the results of dielectric measurements the model functions were fitted to the dielectric data. As it was already pointed out in the frequency domain the most general model function is the HN-formula. Each parameter of the HN-function can be estimated by

$$\sum_i w_i \, [\varepsilon_i^* - \varepsilon_{HN}^*(\omega_i)]^2 \;\rightarrow\; \min \tag{3.17}$$

where w_i is a weighting factor which can be used to take into consideration the different accuracy of data measured with different equipment while i counts the

experimental points. The fitting procedure can be carried out by using ε''- or ε' data or by taking both into account. However, the practical experience shows that the different approaches lead to nearly identical results so that in the most cases only the ε'' data are used.

Rarely isolated relaxation regions are observed. Usually different relaxation processes and often also a conductivity contribution add up. If the latter is of pure electronic origin it has no contribution to ε' while $\varepsilon'' = \dfrac{\sigma_0}{\varepsilon_0 \omega}$ where σ_0 is the d.c.-conductivity of the sample and ε_0 is the dielectric permittivity of vacuum ($\varepsilon_0 = 8.854 \times 10^{-12}$ As V^{-1} m^{-1}). In practice often $\varepsilon'' \sim \omega^{-s}$ with $s < 1$ is observed. This is the case for ionic charge carriers which cause electrode- or Maxwell-Wagner-polarization effects, as discussed below. Hence as dielectric function[2]

$$\varepsilon^*(\omega) = -i a \left(\frac{\sigma_0}{\varepsilon_0 \, \omega^S} \right) + \varepsilon_{HN}^*(\omega) \tag{3.18}$$

can be fitted to the data. The factor a having the dimensionality (Hz)$^{-1}$ (rad Hz)^s.

If several relaxation regions are observed in the available frequency window the HN-function can be used to describe and moreover to separate the different processes. Provided that the different relaxation regions are independent and hence the contribution of each process to the complex dielectric function is additive

$$\sum_i w_i \left[\varepsilon_i^* - \sum_k \varepsilon_{HN,k}^*(\omega_i) \right]^2 \rightarrow \min \tag{3.19}$$

holds, where k counts for the different relaxation regions. An example for the application of Eq. (3.19) is presented in Fig. 3.7 where two HN-functions and a conductivity term are fitted to dielectric loss data of poly(cis-1,4 isoprene) in order to separate the contributions of segmental and chain dynamics.

The discussed method to evaluate measurements in the frequency domain can be transformed to the time domain. According to Eq. (3.16) one gets

$$\sum_j w_j \left[t_j \dot{\varepsilon}_j - \sum_k t_j \, \dot{\varepsilon}_{HN}(t_j) \right] \rightarrow \min \tag{3.20}$$

where $\dot{\varepsilon}_{HN}(t)$ can be calculated by Eq. (3.11). The outlined approach can be easily extended to analyze measurements which are carried out partly in time and partly in frequency domain. By minimizing

$$\sum_i w_i \left[\varepsilon_i^* - \sum_k \varepsilon_{HN,k}^*(\omega_i) \right]^2 + \sum_j w_j \left[t_j \dot{\varepsilon}_j - \sum_k t_j \dot{\varepsilon}_{HN,k}(t_j) \right]^2 \rightarrow \min \tag{3.21}$$

---

[2] Equation (3.18) describes only the contribution to ε'' and not to ε' (see Sect. 3.4).
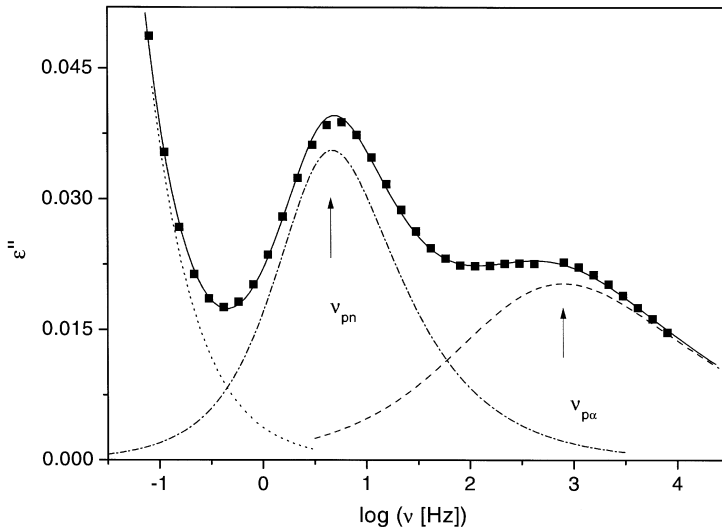
Fig. 3.7. Fit of two HN-functions to separate the α-relaxation (segmental relaxation) and the chain dynamics (Rouse modes) for poly(*cis*-1,4 isoprene) with a molecular weight of $M_w = 1400$ g mol^{-1} at $T = 216$ K [28]. The *solid line* is the sum of the segmental mode (*dashed line*), the normal mode (*dashed-dotted line*) and a conductivity contribution (*dotted line*). The experimental error is smaller than the size of the symbols. For a detailed discussion see Chap. 7. (Redrawn from [28] with permission)

with the same parameter set a consistent evaluation of frequency and time domain measurements is possible where in both the same model function is used. Hence there is no need to use the KWW-functions in the time domain and the HN-function in the frequency domain as sometimes proposed (e.g. [25]). Figure 3.8 demonstrates the application of Eq. (3.20) for the analysis of time domain measurements and also the use of Eq. (3.21) for a joint evaluation in the time and frequency domain [29].

In general all parameters of a relaxation process are temperature dependent. The most significant temperature dependencies are due to the relaxation time and the dielectric relaxation strength. Usually the isothermally measured dielectric spectra are evaluated to extract the temperature dependence of all parameters. However, there are also methods published in the literature where a set of isochronal data measured at different temperatures is analyzed [21, 30–32]. Due to the temperature dependence of the relaxation parameters functional relationships have to be assumed. Furthermore this method cannot be applied for the analysis of the dielectric response of materials which show phase transitions or phase separation etc. where the dielectric behavior may change discontinuously.

It has been discussed in Chap. 1 that in the frame of thermodynamic considerations the complex dielectric function is a generalized compliance. According to linear response theory the dielectric data can be also described by the corre-
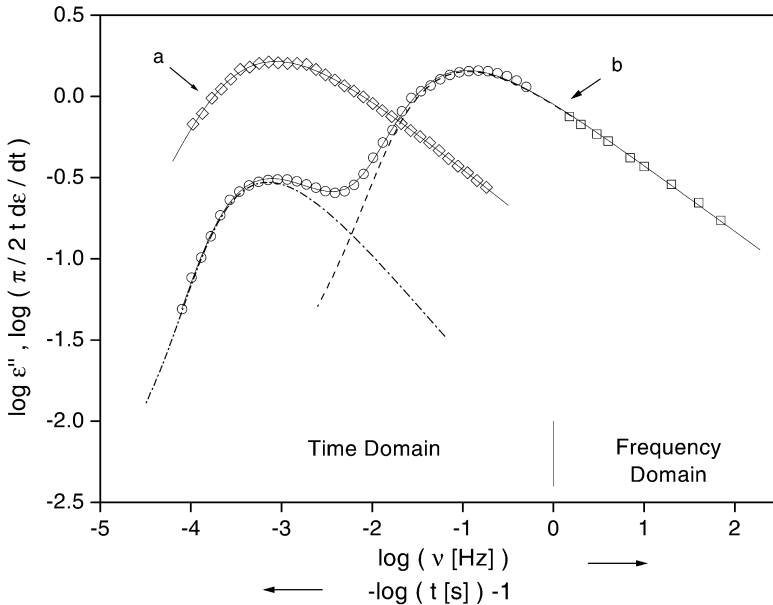
Fig. 3.8. Examples for the evaluation of time domain measurements for poly(propylene glycol) $M_W = 4000$ g mol^{-1} (a) Evaluation of an isolated relaxation region in the time domain; (b) Evaluation of a measurement which was carried out partly in the time and partly in the frequency domain. Two HN-functions were fitted to the whole spectrum [29]. The *solid line* is the sum of the segmental mode (*dashed line*) and the normal mode (*dashed-dotted line*). The experimental error is smaller than the size of the symbols

sponding complex electric modulus $M^*(\omega)$ where

$$M^*(\omega) \cdot \varepsilon^*(\omega) = 1 \quad \text{with} \quad M^*(\omega) = M'(\omega) + i M''(\omega) \tag{3.22}$$

holds (see Chap. 1). A method to measure the dielectric modulus directly is discussed in Chap. 2.

If $\varepsilon^*(\omega)$ is described by the Debye-function for the corresponding modulus[3]

$$M^*(\omega) - M_\infty = \frac{\Delta M}{1 + i \omega \tau_{\text{D--M}}} \tag{3.23}$$

is obtained with $\Delta M = M_S - M_\infty$, $M_S = 1/\varepsilon_S$ and $M_\infty = 1/\varepsilon_\infty$. This means that if the compliance is Debye-like, the frequency dependence of the modulus also follows the Debye function. For the electric relaxation time $\tau_{\text{D--M}} = (\varepsilon_\infty/\varepsilon_S) \tau_D$ is calculated and because $\varepsilon_\infty < \varepsilon_S$ is valid $\tau_{\text{D--M}} < \tau_D$ holds. Therefore, a relaxation process appears in the modulus representation at a higher frequency than for the corre-

---

[3] Note that the sign of ΔM is negative in that notation.

sponding compliance expressed by $\varepsilon^*(\omega)$. This means that in the modulus formulation the high frequencies have greater weight. The differences in the relaxation times obtained for a modulus or a compliance must be considered comparing the results complementary experimental methods like dielectric or mechanical spectroscopy (see Chap. 17).

If $\varepsilon(t)$ as compliance is modeled by the KWW-function (Eq. 3.10) $\tau_{\text{KWW-M}} = \left(\dfrac{\varepsilon_\infty}{\varepsilon_S}\right)^{\beta_{\text{KWW}}} \tau_{\text{KWW}}$ holds approximately for $1 \leq \varepsilon_S/\varepsilon_\infty \leq 11$ and $0.3 \leq \beta_{\text{KWW}} \leq 1$ [33]. For the stretching parameters $\beta_{\text{KWW-M}} = 0.8\,\beta_{\text{KWW}}$ is obtained [33]. In general the model functions discussed in this paragraph can also be applied in the modulus formulation taken into consideration the inverse sign of the relaxation increment. For the HN-formula (Eq. 3.5) as compliance the corresponding modulus $M_{\text{HN}}^*(\omega)$ cannot be calculated exactly but in a good approximation a proper model function is given by

$$M_{\text{HN}}^*(\omega) = M_\infty + \frac{\Delta M}{(1 + (-i\,(\omega\,\tau_{\text{HN-M}})^{-1})^\beta)^\gamma} \tag{3.24}$$

where mainly the frequency is changed to its reciprocal value [32].

3.2.2
Analysis of Dielectric Spectra – Model Free

Cole and Cole [4] suggest plotting dielectric spectra as $\varepsilon''(\omega)$ vs $\varepsilon'(\omega)$ (Cole/Cole plot, Argand plot). In such a representation for a Debye-function (Eq. 3.1, Fig. 3.9a) the data points lie on a semicircle which intersects the ε' axis at ε_∞ and $\varepsilon_\infty + \Delta\varepsilon$. This statement is also valid if the data cannot be described by a single relaxation time. Figure 3.9b displays the Cole/Cole-plot for the Cole/Cole-function. A circular arc which cuts the ε' axis under the angle of $^1/_2\,\pi\beta$ on both sides is obtained. It indicates a symmetric relaxation function and in addition to ε_∞ and $\Delta\varepsilon$ the shape parameter β (symmetrical broadening) can also be estimated. Using Cole/Cole-plots it can be easily decided whether the data have to be described by a symmetric or by an asymmetric distribution of relaxation times. This becomes evident from Fig. 3.9c where a Cole/Cole-representation for the HN-functions is shown. The angle of the intersection with the ε' axis is $^1/_2\,\pi\beta\gamma$ at the high frequency side and $^1/_2\,\pi\beta$ at low frequencies.

In addition to the characterization of an isolated relaxation process the Cole/Cole plot can also be used to separate overlapping relaxation regions as demonstrated in Fig. 3.10, where the Cole-Cole plot for poly(propylene glycol) is shown. The chart displays clearly a double arc which indicates two overlaying relaxation processes. For each process the dielectric strength and the shape parameters can be extracted.

Broadened relaxation processes can be formally described by a superposition of Debye-functions with different relaxation times [1]

$$\varepsilon^*(\omega) = \varepsilon_\infty + \Delta\varepsilon \int \frac{L(\tau)}{1 + i\omega\tau}\ \mathrm{d}\ln\tau \tag{3.25}$$

Fig. 3.9. Cole-Cole plots for different model functions with $\Delta\varepsilon = 1$, $\varepsilon_\infty = 1$ and $\tau = 1$ s: **a** Debye-function; **b** Cole/Cole-function with $\beta = 0.5$; **c** HN-function with $\beta = 0.7$ and $\gamma = 0.6$
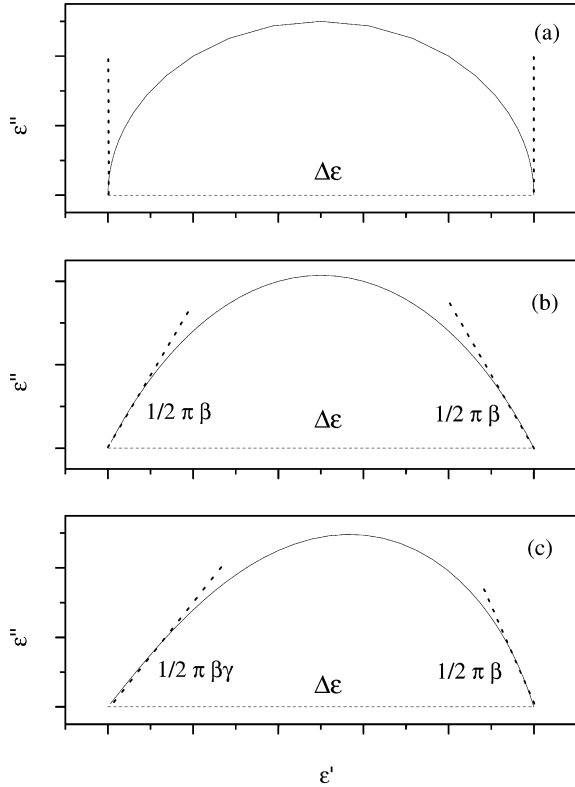
where the relaxation time distribution $L(\tau)$ fulfills the normalizing condition

$$\int L(\tau)\, d\ln\tau = 1 \tag{3.26}$$

For the time domain

$$\varepsilon(t) - \varepsilon_\infty = \Delta\varepsilon \int L(\tau)\left[1 - \exp\left(-\frac{t}{\tau}\right)\right] d\ln\tau \tag{3.27}$$

holds.

It cannot be concluded from Eqs. (3.22) or (3.24) that the molecular origin of a non-Debye behavior is a relaxation of several independent relaxators (heterogeneous relaxation) which behave Debye-like. In some cases such an interpretation may be correct like in the case of local relaxation processes. However, in other cases such a conclusion is questionable because the non-exponential character of the relaxation process might be a feature of the molecular process itself (homogeneous relaxation). A discrimination between these two interpretation schemes is not possible in the framework of linear relaxation theory. A possibility to discriminate experimentally between these interpretations are dielectric hole burning experiments (see Chap. 14). The relaxation time spectra discussed for the model functions are given in Table 3.1.

Fig. 3.10. a Real part ε' (*open circles*) and imaginary part ε'' (*open squares*) of poly(propylene glycol) at $T = 213.7$ K. **b** Cole-Cole representation of the data in a. The experimental error is smaller than the size of the symbols
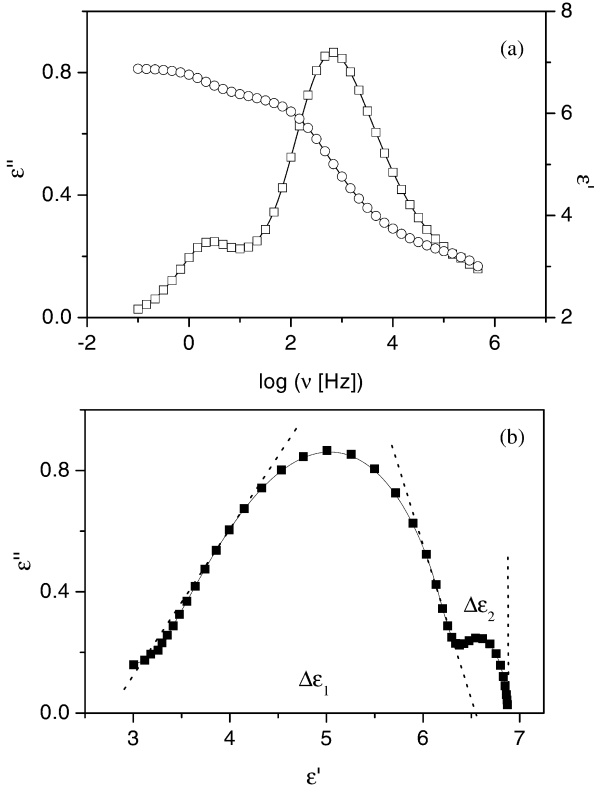
In most cases the relaxational dynamics is characterized by the frequency of maximal loss $\omega_p = 2\pi\,\nu_p$ or the relaxation time $\tau_p = 1/\omega_p$. This key feature of the molecular dynamics can be extracted from the experimental data model free. With the aid of the relaxation time distribution $L(\tau)$ and the discussed model functions different mean values of the relaxation time can be defined. The simplest cases is the mean value $\langle\tau\rangle$

$$\langle\tau\rangle = \int_{\text{Peak}} \tau\,L(\tau)\,\mathrm{d}\tau \tag{3.28}$$

For the Debye-function the linear mean value $\langle\tau\rangle$ is equal to τ_D because the relaxation time spectrum $L(\tau)$ is the Dirac- (delta) function. Applying Eq. (3.28) to the spectrum of the KWW-function a mean value $\langle\tau\rangle_{\text{KWW}}$ can be calculated to

$$\langle\tau\rangle_{\text{KWW}} = \frac{\tau_{\text{KWW}}}{\beta_{\text{KWW}}}\,\Gamma(\beta_{\text{KWW}}^{-1}) \tag{3.29}$$

where $\Gamma(x)$ is the Gamma function. Moreover, for the Cole/Davidson-function the mean value can be calculated numerically according to Eq. (3.28). However, one has to state that the mean value $\langle\tau\rangle$ does not exist for the Cole/Cole-function
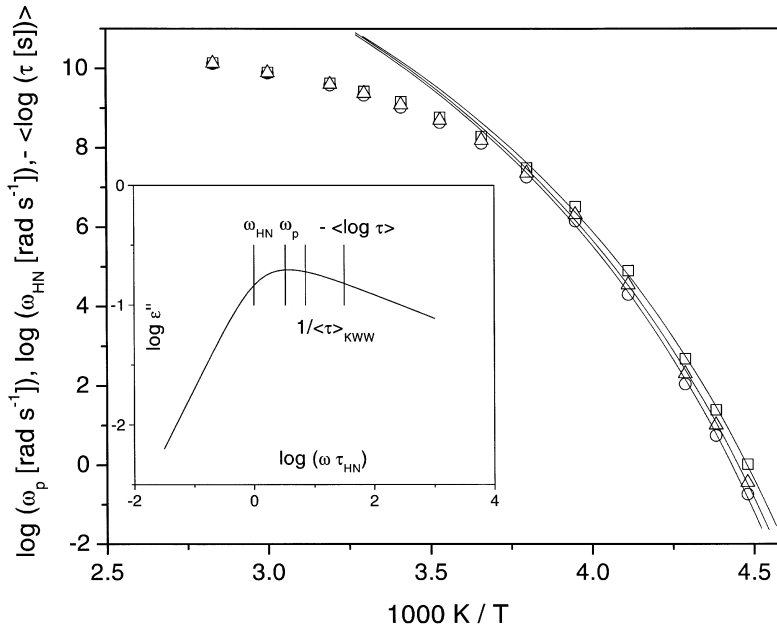
Fig. 3.11. Comparison of the temperature dependence of ω_p ($\square$), $\omega_{HN} = 1/\tau_{HN}$ ($\triangle$) and $-\langle\log\tau\rangle$ ($\bigcirc$) for the glass-forming liquid salol. The data were taken from [34]. The error of the data is smaller than the size of the symbols. The lines are fits of the Vogel/Fulcher/Tamann equation to the data (see [34] for details). The *inset* compares ω_p, $\omega_{HN} = 1/\tau_{HN}$, $1/\langle\tau\rangle_{KWW}$, and $-\langle\log\tau\rangle$ calculated for the HN-function with $\beta = 1$ and $\gamma = 0.2$

and also for the HN-function. Therefore a logarithmic mean value of the relaxation time can be defined according to

$$\langle\log\tau\rangle = \frac{\int\limits_{Peak} \log\tau\, L(\tau)\, \mathrm{d}\log\tau}{\int\limits_{Peak} L(\tau)\, \mathrm{d}\log\tau} \qquad (3.30)$$

A detailed discussion of the different mean values can be found in [34]. In general the mean values differ from the position of maximal loss ω_p. The degree of that deviation depends on the shape of the dielectric function. In the inset of Fig. 3.11 the different mean values are compared for the HN-function with $\beta = 1$ and $\gamma = 0.2$. $\log(\omega_{HN})$ differs from $-\langle\log\tau\rangle$ by more than two decades. Figure 3.11 shows the temperature dependence of ω_p, $\omega_{HN} = 1/\tau_{HN}$ and $-\langle\log\tau\rangle$ for the glass-forming liquid salol. With increasing temperature the loss peak becomes smaller and the different mean values coincide together.

To estimate the relaxation time spectra from the experimental data requires inversion of Eqs. (3.25) or (3.27). From a mathematical point of view this is a so-called ill-conditioned problem because Eq. (3.25) is essential a Fredholm integral equation of the first order. A software package to solve that problem is provided by Provencher [35] (CONTIN). Recently the Tikhonov regularization al-

gorithm has been used to calculate the relaxation time spectra from the measured data. This method takes the curvature of $L(\tau)$ into account by an additional term $\lambda L''(\tau)$ [36, 37]. λ is the regularization parameter and $L''(\tau)$ describes the second derivative of the relaxation time distribution function. If λ is too small, unphysical oscillations in $L(\tau)$ occur, but if it is too large the shape of $L(\tau)$ will be over-smoothed resulting in a loss of information. The self-consistency method of Honerkamp and Weese [38, 39] provides a reliable value for the regularization parameter λ. Schäfer et al. [40–42] developed a program using the above mentioned methods to calculate the relaxation time distribution function $L(\tau)$ for equidistant values of $\log \tau$ from dielectric spectra after subtraction of a possible conductivity contribution.

In Fig. 3.12 the Havriliak/Negami analysis and the Tikhonov algorithm are compared with respect to their ability to resolve the two relaxation processes of a bimodal spectrum. Therefore dielectric data were simulated, based on two neighboring processes, consisting of 70 points in the frequency range from 10^{-1} to 10^6 Hz (ten data points per decade). For simplicity the spectrum does not contain a conductivity contribution. The first process has a relaxation strength of $\Delta\varepsilon_1 = 1/3$ and a mean relaxation time $\log(\tau_{HN1}/s) = -4$. The second process has a longer relaxation time ($\log(\tau_{HN2}/s) = -3.6$) and a relaxation strength $\Delta\varepsilon_2 = 2/3$ so that the weaker process might disappear in the wing of this stronger process. Gaussian random numbers with a standard deviation of 10^{-4} were added to simulate experimental noise. Figure 3.12 shows the deconvolution of the data and the resulting relaxation time distribution functions.

As expected the fit using *one* Havriliak/Negami function is not satisfactory compared to the one based on two relaxation processes (compare inset Fig. 3.12 and σ_{sit}). The best fit is obtained from the Tikhonov algorithm but without detecting the bimodal nature of the original data. Analyzing experimental data by using the two numerical methods (Fig. 3.13) works equally well for both techniques and delivers similar results for the relaxation time distribution functions. On the long time side of $L(\tau)$ the Tikhonov algorithm can be easily disturbed by artifacts due to electrode polarization and the conductivity contribution.

In summary the Tikhonov algorithm has the advantage that it permits the determination of the relaxation time distribution functions from the measured dielectric data without any model assumptions. However, it does not deliver additional information in comparison to the conventional Havriliak/Negami-fits. Concerning the power to discriminate between neighboring relaxation processes it does not provide any advantage or an enhanced resolution.

In order to ease the analysis of dielectric spectra which are composed of closely adjacent relaxation processes van Turnhout and Wübbenhorst [43] suggest one analyzes the frequency dependence of the derivative $\partial\varepsilon'/\partial\log\omega$. For a Debye-process

$$\frac{\partial\varepsilon'}{\partial\log\omega} = -\varepsilon''^2 \tag{3.31}$$

is derived. The following features hold: (i) A relaxation peak in ε'' gives a minimum in $\partial\varepsilon'/\partial\log\omega$. (ii) Because of the squared ε'' in Eq. (3.31) the minimum is narrower than the peak in ε''. Therefore, strongly overlapping relaxation peaks
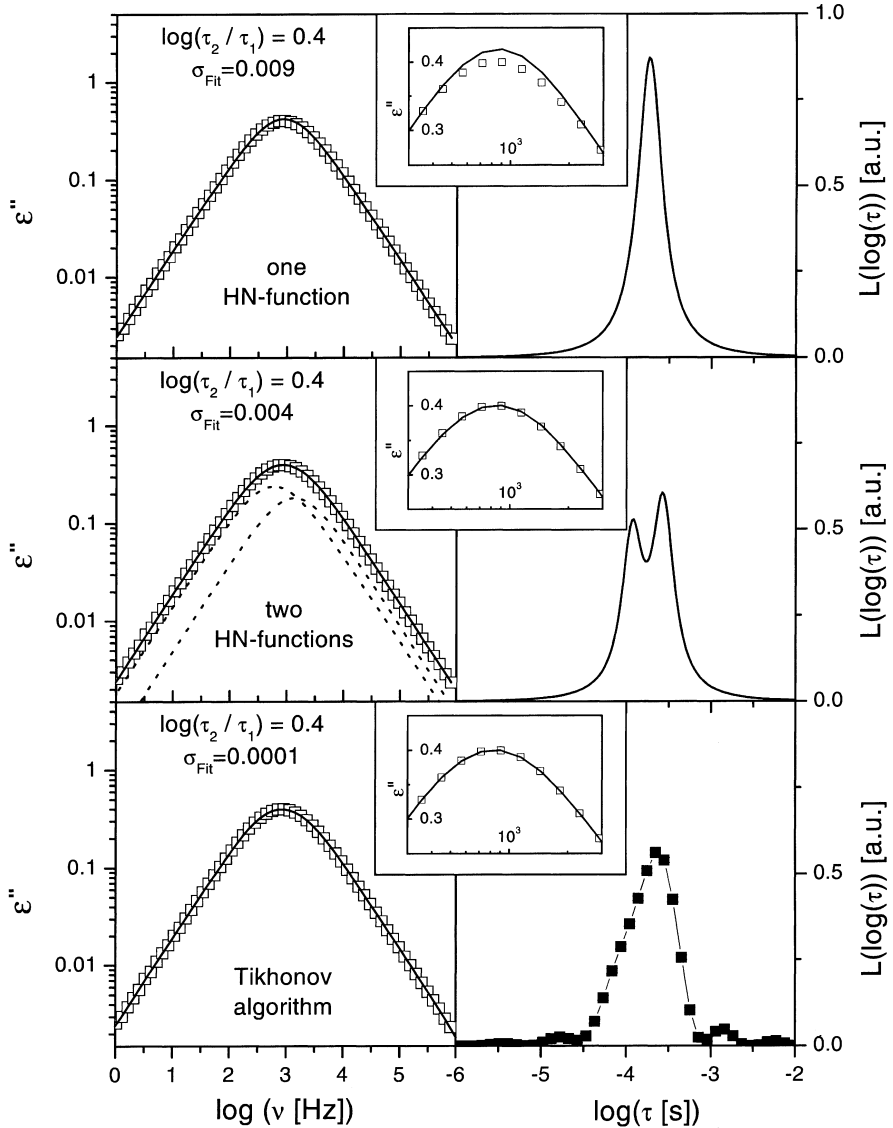
Fig. 3.12. Deconvolution of a model spectrum consisting of two relaxation processes whose difference in relaxation times is 0.4 decades. Details are explained in the text. The spectra (*open squares*) are fitted with one HN-function (*top*), two HN-functions (*center*), and with the Tikhonov algorithm (*bottom*). On the *left side* are the spectra and on the *right side* there are the relaxation time distribution functions. σ_{sit} denotes the standard deviation of the fits. As a guide to the eye the points of the relaxation time distribution for the Tikhonov algorithm are connected by lines. The quality of the fits is indicated by the standard deviation σ_{sit} and can moreover directly deduced from the *insets*
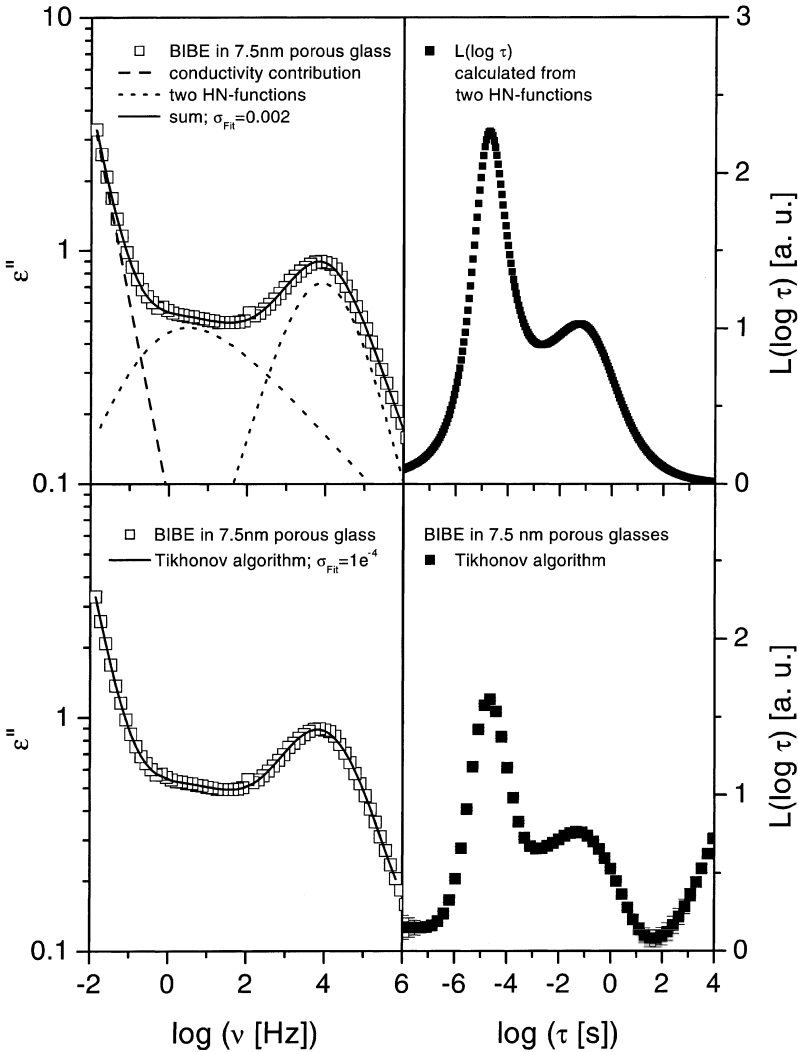
Fig. 3.13. Dielectric spectrum of Benzoin isobutylether (BIBE) in a porous glass with 7.5 nm pore diameter at 250 K (*left side*). *Top*: the data analysis is shown using two HN-functions (*dotted curve*) and a conductivity contribution (*dashed line*). The *solid curve* is the resulting sum. *Bottom*: the spectra are analyzed using the Tikhonov algorithm. On the *right side* the relaxation time distribution functions are shown

are better resolved; this is supported by the fact that the discussed derivative can be regarded as the simplest approximation of the relaxation time spectrum [1]. (iii) Conductivity contributions according to $\varepsilon'' \sim 1/\omega$ do not play any role because for such a dependence the real part ε' is independent of frequency. Therefore electrode polarization and Maxwell/Wagner effects can be analyzed in more detail [43].
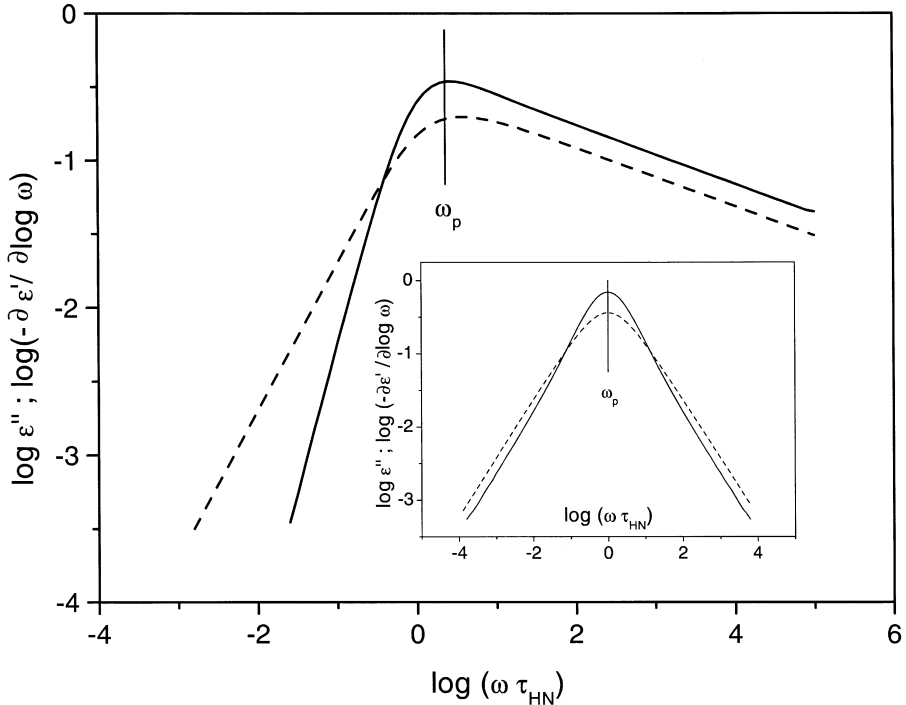
Fig. 3.14. Comparison of $\varepsilon''(\omega)$ (*dashed line*) and $\partial\varepsilon'/\partial\log\omega$ (*solid line*) calculated according to the HN-function with $\beta = 1$ and $\gamma = 0.2$. This *inset* shows the chart for $\beta = 0.8$ and $\gamma = 1$. For all calculations $\Delta\varepsilon = 1$ and $\tau_{HN} = 1$ is assumed

A theoretical comparison of the position of maximum loss ω_p and the frequency of the minimum of $\partial\varepsilon'/\partial\log\omega$ is presented in [43] for HN-functions with $\gamma = 1$ (symmetrical relaxation function). For the HN-function

$$\frac{\partial\varepsilon'_{HN}}{\partial\log\omega} = -\frac{\beta\gamma\,\Delta\varepsilon(\omega\tau_{HN})^{\beta}\cos(\beta\pi/2 - (1+\gamma)\Psi(\omega))}{[1 + 2(\omega\tau_{HN})^{\beta}\cos(\beta\pi/2) + (\omega\tau_{HN})^{2\beta}]^{\frac{1+\gamma}{2}}} \tag{3.32}$$

holds. Concerning the definition of $\Psi(\omega)$ see Table 3.1. Figure 3.14 compares ε'' and the derivative $\partial\varepsilon'/\partial\log\omega$ for the HN-function with two different sets of parameters (symmetric and asymmetric broadening). This figure shows that the maximum positions for both quantities occur exactly at the same frequency position. Moreover it also becomes obvious that the half-width of the derivative is always smaller than the half-width of the loss peak.

The power of the proposed approach is demonstrated in Fig. 3.15 where the imaginary part $\varepsilon''(\nu)$ of a liquid crystalline side group polymethacrylate with mesogenic groups for different measuring temperatures is shown (for more details see [44]). Only for the highest temperature two relaxation peaks are de-

Fig. 3.15. Dielectric spectra for a liquid crystalline side group polymer (the chemical structure is given in the inset): **a** log ε'' vs logν for different temperatures: (□): 393.8 K, (○): 373.8 K, (△): 359.1 K; the different relaxation processes are indicated; **b** representation of the data shown in **a** as $\partial\varepsilon'/\partial\log\nu$ vs log ν
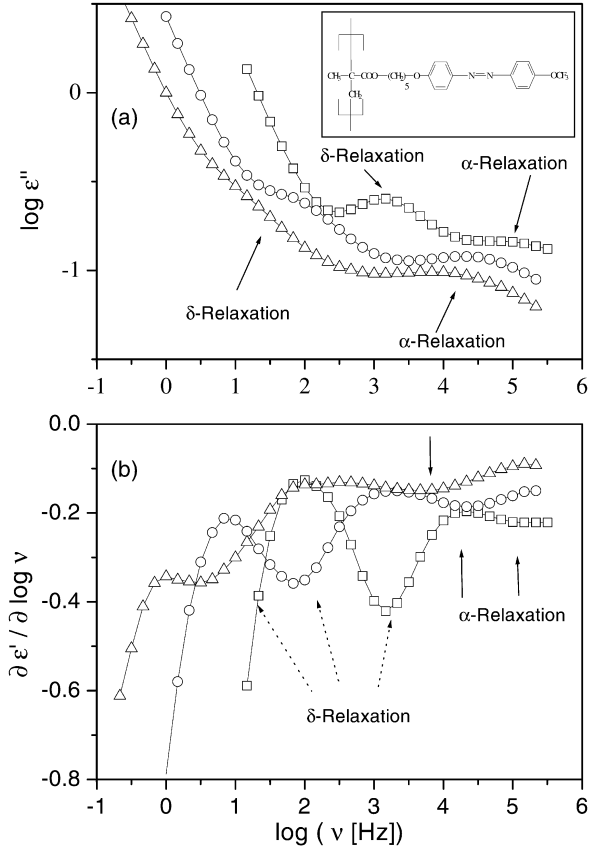
tectable. The relaxation peak at the higher frequency is assigned to the α-relaxation which corresponds to micro-Brownian motion of the polymer backbone segments (dynamic glass transition). The peak at lower frequencies is called δ-relaxation which is due to rotational fluctuations of the mesogenic units around its short axis. At lower temperatures it appears as a weak shoulder overlapped by a conductivity contribution. At the lowest temperature ($T = 359.1$ K) the α-relaxation peak is broadened and therefore it is difficult to extract the relaxation rate for this process. Figure 3.15b gives the derivative $\partial\varepsilon'/\partial\log\nu$ for the same temperatures displaying a well defined minimum for the δ-process. Furthermore the relaxation rate for the α-process can be identified unambiguously.

To extend this approach analogously to Eq. (3.17)

$$\sum_i w_i \left[\left(\frac{\partial\varepsilon'}{\partial\log\omega} \right)_i - \sum_k \frac{\partial\varepsilon'_{HN,k}(\omega_i)}{\partial\log\omega} \right]^2 \rightarrow \min \qquad (3.33)$$

can be minimized. Such an approach allows one to estimate the dielectric relaxation strength and the shape of a relaxation region in addition to the relaxation

rate. Some further examples for the application of this method can be found in [45].

3.3
Fluctuations of Mobile Charge Carriers

According to Maxwell's equations the current density $j = \sigma^* E$ and the time derivative of the dielectric displacement $\dfrac{dD}{dt} = i\omega\varepsilon^*\varepsilon_0 E$ are equivalent where $\sigma^*(\omega)$ is the complex conductivity (see Chap. 1). Hence for sinusoidal electrical fields $E(\omega) = E_0 e^{i\omega t}$ and $\varepsilon^*(\omega)$ and $\sigma^*(\omega)$ are related to each other by

$$\sigma^*(\omega) = \sigma'(\omega) + i\sigma''(\omega) = i\omega\varepsilon_0\,\varepsilon^*(\omega) \tag{3.34a}$$

The real and imaginary part of $\sigma^*(\omega)$ is given by

$$\sigma'(\omega) = \omega\varepsilon_0\,\varepsilon''(\omega); \qquad \sigma''(\omega) = \omega\varepsilon_0\,\varepsilon'(\omega) \tag{3.34b}$$

For pure electronic conduction no contribution arises to ε' while $\varepsilon''(\omega) = \dfrac{\sigma_0}{\varepsilon_0\,\omega}$ increases linearly with decreasing frequency. σ_0 is the (electronic) d.c.-conductivity. Hence in the conductivity representation (see Eq. 3.34) for electronic conduction the real part $\sigma'(\omega)$ is constant (σ_0) and the imaginary part σ'' increases linearly with frequency.

   According to Eq. (3.22) the dielectric properties for a electronic conduction can also be expressed in the modulus representation. For its imaginary part

$$M''(\omega) = M_\infty \frac{\omega\tau_{\text{Cond}}}{1 + (\omega\tau_{\text{Cond}})^2} \tag{3.35}$$

is obtained. Equation (3.35) is similar to the imaginary part of $M^*(\omega)$ for a Debye-like relaxation process and peaks at $\omega_M\tau_{\text{Cond}} = 1$ with $\tau_{\text{Cond}} = \varepsilon_0\varepsilon_\infty/\sigma_0$. Therefore from the position of maximum loss ω_M the d.c.-conductivity can be estimated. The corresponding real part of the modulus increases from zero to $M_\infty = 1/\varepsilon_\infty$. In addition to complex conductivity the electric modulus representation is also applied frequently for the analysis of the data obtained for conducting systems. Figure 3.16 shows a theoretical example for two values of conductivity. Deviations from Eq. (3.35) can be described by model function as described in Sect. 3.2.1 like the Cole/Davidson- (Eq. 3.3) or the Fourier-transformed KWW-function (Eq. 3.10). The d.c.-conductivity σ_0 can be estimated by

$$\sigma_0 = \frac{\varepsilon_0\,\varepsilon_\infty}{\langle\tau\rangle} \tag{3.36}$$

where $\langle\tau\rangle$ is a mean (characteristic) relaxation time for conductivity which can be defined in accordance with Eq. (3.28). It was argued that ε_∞ varies only weakly from system to system (typical values are in the range from 2 to 20) and σ_0 and its temperature dependence should be mainly due to that of $\langle\tau\rangle$.
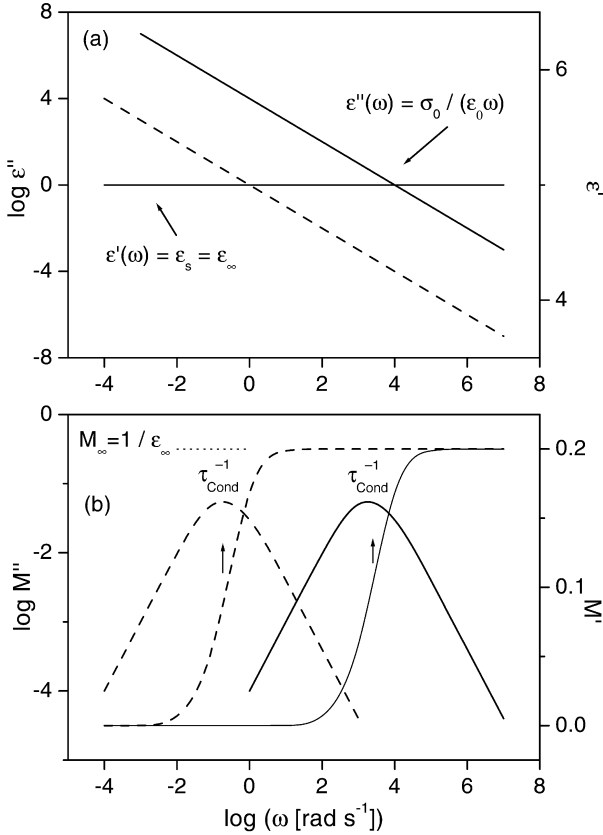
Fig. 3.16. **a** Theoretical example for a complex dielectric function with a pure ohmic contribution: $\sigma_0/\varepsilon_0 = 1$ (*dashed line*), $\sigma_0/\varepsilon_0 = 10^4$ (*solid line*), $\varepsilon' = 5$. **b** Real part M' and imaginary part M'' of the complex electric modulus according to the complex dielectric function given in a): $\sigma_0/\varepsilon_0 = 1$ (*dashed line*), $\sigma_0/\varepsilon_0 = 10^4$ (*solid line*)

In disordered systems the charge transport takes place due to hopping conduction [46]. Moreover the motion of a charge in these systems is accompanied by an electrical relaxation: an ionic or electronic (in case of a polaron) charge is surrounded by negative or positive counter charges. A hop of a charge carrier to a new site can only lead to a successful charge transport if the polarization cloud follows. Otherwise the charge carrier will jump back with a high probability. This mutual movement of the charge carrier and the surrounding polarization cloud requires an electrical relaxation time τ_σ. If the frequency of the outer electrical field is higher than $1/\tau_\sigma$ its effect on the charge transport averages out. For frequencies lower than $1/\tau_\sigma$ the relaxation of the polarization cloud is in phase with the outer electrical field. For that case the field supports the propagation of the charges. Hence this electrical relaxation gives rise to a contribution in the complex dielectric function which increases with decreasing frequency. This is

Fig. 3.17. Complex dielectric function of a zwitterionic polymer poly{3-[N-(ω-methacrylogloxyalkyl)-N,N-dimethyl ammonio] propane sulfonate} doped with 100 mol% NaI at the indicated temperatures. The lines are fits of Eq. (3.39) to the data. The fit parameters are given in table 3.2 of the Appendix. The dashed line indicates the contribution due to electrode polarization
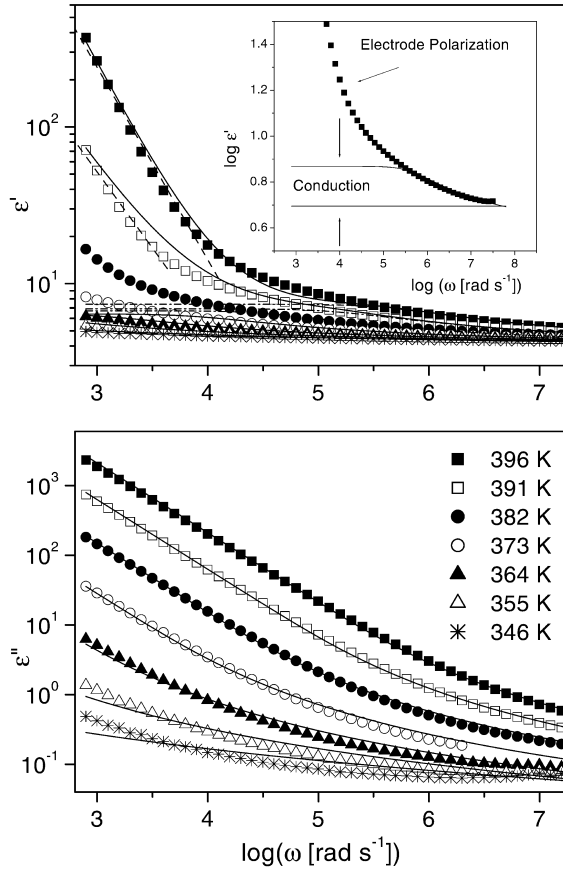
the essence of the Debye/Hückel/Falkenhagen theory [47–49]. It explains the experimental observation that for electrolytes the real part ε' increases with decreasing frequency. (Additionally one has to expect electrode polarization effects in ionic conductors.) Within this phenomenological picture there is no need to treat the d.c.- and a.c.-conductivity in disordered systems as separate processes as sometimes discussed in the literature (see for instance [50–52]).

It is remarkable that the complex conductivity σ^* is similar in its frequency- and temperature (including also charge carrier concentration) dependence for a broad variety of quite different materials, e.g., ionic glasses, ion conducting polymers, electron conducting conjugated polymers, or electron conducting carbon black composites (see Chap. 12 and, for instance, [50–56]).

As example spectra of the zwitter-ionic polymer poly{3-[N-(ω-methacrylogloxyalkyl)-N,N-dimethyl ammonio]propane sulfonate} doped with 100 mol % NaI] presented in ε^* and σ^* are shown in Figs. 3.17 and 3.18 (for details see Chap. 12 and [57]). The imaginary part ε'' increases with decreasing frequency due to conduction (see Fig. 3.17). Also the real part increases due to electrical re-

Fig. 3.18. Complex conductivity for the data presented in Fig. 3.17. Lines are due to fits of Eq. (3.39) to the data. The fit parameters are given in table 3.2 of the Appendix
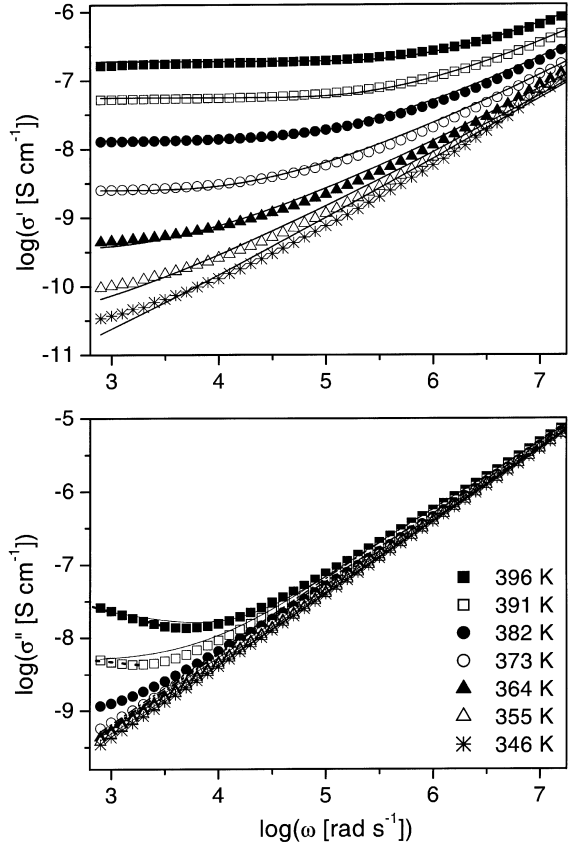
laxation phenomena (see Fig 3.17 and inset of Fig. 3.17). At lower frequencies ($\omega < 10^4$ rad s^{-1}) this relaxational contribution to ε' is superimposed by electrode polarization effects (see Sect. 3.4.2).

For the real part $\sigma'(\omega)$ on the low frequency side a plateau value is obtained which can be extrapolated to the d.c.-conductivity σ_0 for $\omega \to 0$ (see Fig 3.18). At a critical frequency $\omega_c = 2\pi\, v_c$ the dispersion of σ' sets in. The latter can be determined by smoothing the data and calculating numerically the maximum in $\partial^2\sigma'/\partial\omega^2$. The imaginary part of the complex conductivity decreases with decreasing frequency (see Fig. 3.18). The increase at low frequencies again indicates electrode polarization which will be discussed in Sect. 3.4.2.

According to Barton/Nakajima/Namikawa [58] (BNN-relationship)

$$\omega_c \sim \sigma_0 \tag{3.37}$$

holds. (For further details see Chap. 12.) For $\omega > \omega_c\, \sigma'$ increases strongly with frequency. This behavior is quite general and is found for a variety of semi-conducting systems as discussed in Chap. 12 (see also [58, 59]).

In addition to complex permittivity and conductivity Fig. 3.19 gives the complex modulus representation for the data present in Fig. 3.17. It is demonstrated

Fig. 3.19. Complex electric modulus for the data presented in Fig. 3.17. Lines are due to fits of Eq. (3.39) to the data. The fit parameters are given in Appendix 3.2. Taken from [57] with permission
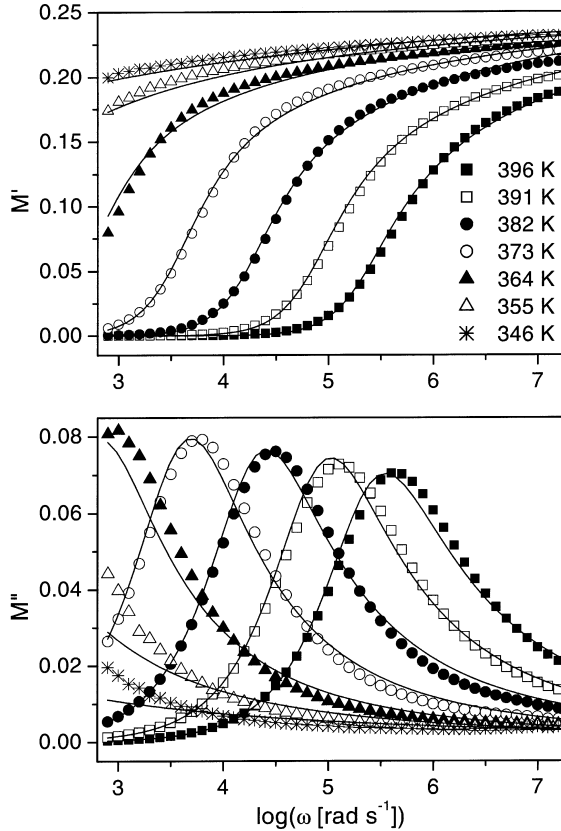
that the increase in ε'' with decreasing frequency is transformed into a peak in M''.

Model functions like KWW- or the Cole/Davidson-function transformed into the conductivity representation have been used to analyze the frequency dependence of the complex dielectric conductivity or modulus. A critical discussion of this procedure can be found in [50–52, 60] and Chap. 12. Neither the KWW- nor the Cole/Davidson function can describe the data in the whole frequency range [60]. Jonscher [61, 62] proposed the following equation (later modified [63])

$$\sigma'(\omega) = \sigma_0 + A\omega^s = \sigma_0[1 + (\omega\tau)^s] \tag{3.38}$$

for the frequency dependence of the real part of the complex conductivity. In Eq. (3.38) τ is a time constant for conductivity relaxation related to ω_c. For $\omega \gg 1/\tau$ Eq. (3.38) gives a power law characterized by s ($0 < s \leq 1$) while for $\omega \ll 1/\tau$ the d.c.-conductivity σ_0 is recovered. Equation (3.38) fits the data reasonable well especially for $\omega \gg 1/\tau$ [51, 58, 60] but it lacks any theoretical foundation.

The random free energy barrier model as developed by Dyre [64] which assumes that conduction takes place by hopping of charge carriers in a spatially

randomly varying energy landscape provides a basic to analyze conduction phe-nomena on a theoretical level. Within the Continuous-Time-Random Walk (CTRW) approximation [65] the following expression for the complex conduc-tivity $\sigma^*(\omega)$ is obtained [64]

$$\sigma^*(\omega) = \sigma_0 \left[\frac{i\omega\tau_e}{\ln(1 + i\omega\tau_e)} \right] \tag{3.39a}$$

where τ_e is the attempt frequency to overcome the largest barrier determining the d.c.-conductivity. Splitting into real and imaginary parts delivers

$$\sigma'(\omega) = \frac{\sigma_0\,\omega\tau_e\,\arctan(\omega\tau_e)}{\frac{1}{4}\,\ln^2(1+\omega^2\tau_e^2) + (\arctan\omega\tau_e)^2} \tag{3.39b}$$

$$\sigma''(\omega) = \frac{\sigma_0\omega\tau_e\,\ln(1+\omega^2\tau_e^2)}{\frac{1}{2}\,\ln^2(1+\omega^2\tau_e^2) + 2\,(\arctan\omega\tau_e)^2} \tag{3.39c}$$

Equation (3.39) is used to fit the data present in Figs. 3.17, 3.18, and 3.19 (the electrode polarizations were modeled within the fractal model; see Sect. 3.4.2, Eq. 3.48). The estimated parameters are given in Appendix 2. The spectra (both real and imaginary part) are well described in its frequency- and temperature dependence using only two adjustable parameters.
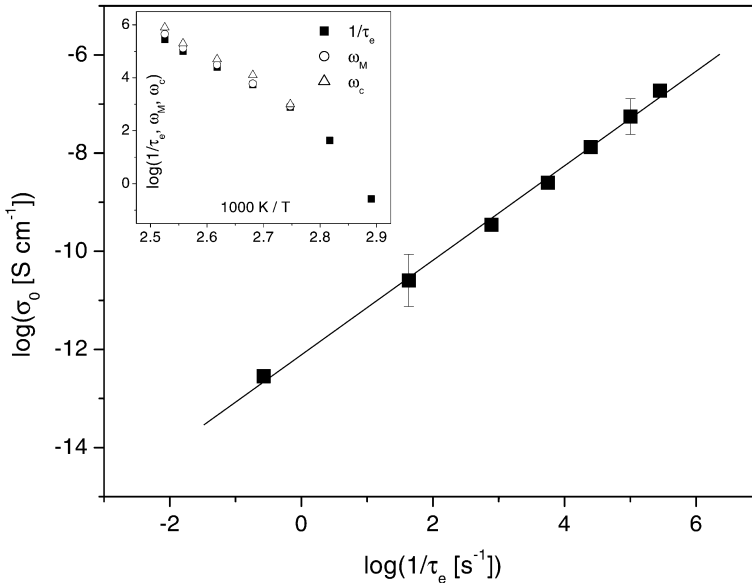
Fig. 3.20. Proof of the BNN-relationship: ■ – data for the zwitter-ionic system (see Fig. 3.16) The *line* is a linear regression to these data. The *inset* compares relaxation times (or frequen-cies) for conduction estimated with different methods. Taken from [57] with permission

From the fits according to Eq. (3.39) the d.c.-conductivity σ_0 and the electrical relaxation time τ_e are obtained. As shown in Fig. 3.20 the BNN-relation (see Eq. 3.37) is well fulfilled. It indicates that d.c.- and a.c.-conduction are based on the same mechanism of charge transport.

3.4
Separation of Charges

Charge carriers can be blocked at inner dielectric boundary layers (Maxwell/Wagner/Sillars polarization [2, 3]) on a mesoscopic scale or at the external electrodes contacting the sample (electrode polarization) on a macroscopic scale. In both cases this leads to a separation of charges which gives rise to an additional contribution to the polarization. The charges may be separated over a considerable distance. Therefore the contribution to the dielectric loss can be by orders of magnitude larger than the dielectric response due to molecular fluctuations.

3.4.1
Mesoscopic Scale: Maxwell/Wagner/Sillars Polarization

Maxwell/Wagner polarization processes have to be taken into consideration during the investigation of inhomogeneous materials like suspensions or colloids [66], biological materials [67], phase separated polymers, blends, crystalline or liquid crystalline polymers (see Chap. 13). They play also an important role in investigating the dielectric behavior of molecules in confining space (see Chap. 6). As an example of the influence of Maxwell/Wagner polarization Fig. 3.21 shows the real part of the complex dielectric function for a liquid crystalline side group polymer (see also Fig. 3.15). In the liquid crystalline state the material has a nanophase separated structure (smectic layers) which disappears above the phase transition. At the internal phase boundaries charges can be blocked which gives rise to a Maxwell/Wagner polarization. That causes a strong increase in ε' with decreasing frequency. Above the phase transition the phase boundaries disappear and therefore the charges cannot be blocked anymore and ε' is reduced compared to the liquid crystalline state. In the inset of Fig. 3.21 the dielectric loss is plotted vs frequency for the same temperatures as for ε'. Also the slope of the conductivity contribution is influenced by the Maxwell/Wagner process. In the isotropic state the conductivity is nearly ohmic while in the liquid crystalline state with a phase separated structure the frequency dependence of the conductivity is weaker.

The most simple model to describe an inhomogeneous structure is a double layer arrangement where each layer is characterized by its permittivity ε_i and by its relative conductivity σ_{ri}. That model is sketched in Fig. 3.22 together with the equivalent circuit. For the complex dielectric function one gets

$$\tilde{\varepsilon}^*(\omega) = \tilde{\varepsilon}_\infty + \frac{\Delta\tilde{\varepsilon}}{1 + i\,\omega\,\tau_{MW}} \tag{3.40a}$$
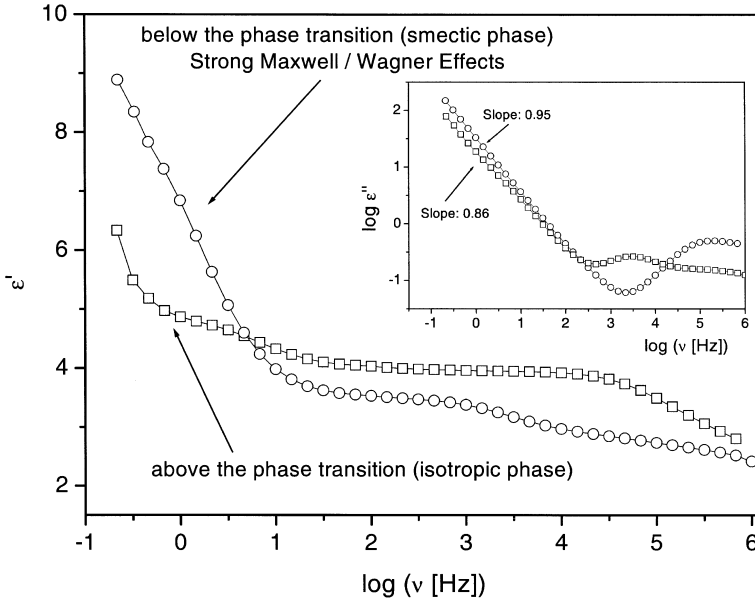
Fig. 3.21. ε' vs logarithm of frequency for the side group polymer given in Fig. 3.15: □ 408.8 K (isotropic state), ○ 398.85 K (smectic A phase). The *inset* shows the dielectric loss for the same temperatures
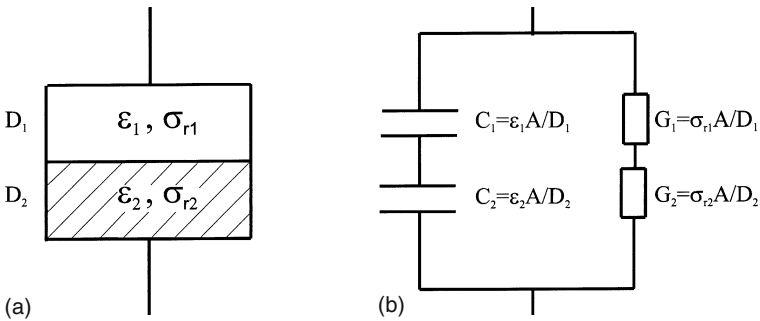
Fig. 3.22. a Two dielectric layers in series. ε_i and σ_{ri} are the corresponding dielectric permittivities and conductivities. **b** Equivalent circuit where A is the diameter of the electrodes and D_i is the spacing of the layers

Equation (3.40a) is similar to Eq. (3.1) but the parameters have a completely different meaning and physical foundation. For $D_1 = D_2$ it holds $\tilde{\varepsilon}_\infty = \varepsilon_1\varepsilon_2/(\varepsilon_1 + \varepsilon_2)$ and $\Delta\tilde{\varepsilon} = \dfrac{\varepsilon_2\sigma_{r1} + \varepsilon_1\sigma_{r2}}{(\sigma_{r1} + \sigma_{r1})^2(\varepsilon_1 + \varepsilon_2)}$. For the relaxation time τ_{MW} of the interfacial polarization

$$\tau_{MW} = \varepsilon_0 \frac{\varepsilon_1 + \varepsilon_2}{\sigma_{r1} + \sigma_{r2}} \tag{3.40b}$$

Fig. 3.23. a Spherical parti-
cle to derive Maxwell's
equations for a suspension.
b Model to derive the mix-
ture equations. The small
particles are the same as
sketched in a

(a)

(b)
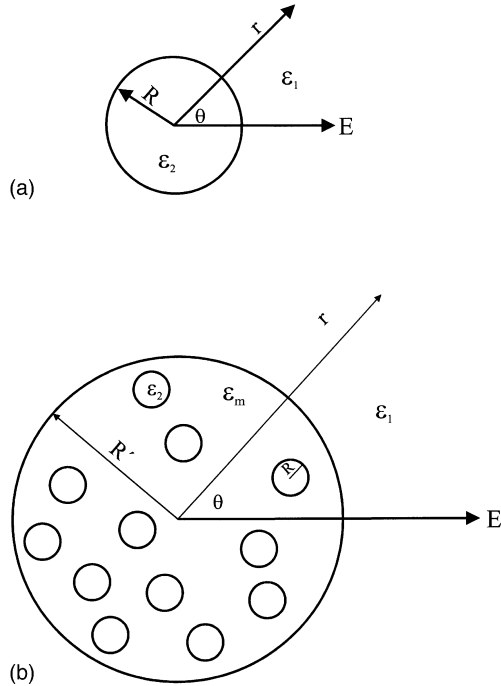
is obtained. The relaxation time scales inversely with the conductivity of the
system. That means that Maxwell/Wagner effects are more pronounced for
conductive materials. This quite simple example demonstrates that the dielec-
tric response of an inhomogeneous medium can be frequency dependent al-
though none of the individual components has frequency dependent dielectric
properties. The frequency dependence can be similar to an orientational polar-
ization.

A more molecular point of view to treat interfacial polarization phenomena
was developed by Maxwell [68] and generalized by Wagner [2] and Sillars [3]
later. Maxwell considered a spherical particle with a dielectric permittivity ε_2
and the radius R suspended in an infinitely extended medium characterized by
ε_1 (see Fig. 3.23a) [67]. The electric potentials caused by an electric field E out-
side and inside the sphere Ψ_1 and Ψ_2 can be calculated by solving of the corre-
sponding Laplace equations:

$$\nabla^2 \Psi_1 = 0 \qquad \nabla^2 \Psi_2 = 0 \tag{3.41}$$

where ∇^2 is the Laplace operator. The solution of Eq. (3.41) is straightforward us-
ing spherical coordinates. Taking further into consideration that the potentials
must be continuous at the boundary of the sphere, i.e.

$$\Psi_1 = \Psi_2 \text{ and } \varepsilon_1 \frac{\partial \Psi_1}{\partial r} = \varepsilon_2 \frac{\partial \Psi_2}{\partial r} \tag{3.42}$$

holds for $r = R$, one ends up with

$$\Psi_1 = -\left(\frac{\varepsilon_1 - \varepsilon_2}{2\varepsilon_1 + \varepsilon_2}\frac{R^3}{r^3} + 1\right) Er\cos\theta \quad \text{(outside)} \tag{3.43a}$$

$$\Psi_2 = -\left(\frac{\varepsilon_1 - \varepsilon_2}{2\varepsilon_1 + \varepsilon_2} + 1\right) Er\cos\theta \qquad \text{(inside)} \tag{3.43b}$$

To calculate the properties of a suspension in an effective medium approach N small spheres with a radius R discussed above are embedded in a large sphere with a radius R' (see Fig 3.23b). According to Eq. (3.43a) for the potential Ψ_P outside the large sphere

$$\Psi_P = -\left(\frac{\varepsilon_1 - \varepsilon_M}{2\varepsilon_1 + \varepsilon_M}\frac{R'^3}{r^3} + 1\right) Er\cos\theta \tag{3.44a}$$

holds where ε_M is the homogeneous permittivity of the large sphere considered as an effective medium. On the other hand Ψ_P can be also expressed as the sum[4] of the potentials due to the N small particles

$$\Psi_P = -\left(\frac{\varepsilon_1 - \varepsilon_2}{2\varepsilon_1 + \varepsilon_2}\frac{R^3}{r^3}N + 1\right) Er\cos\theta \tag{3.44b}$$

Clearly the potentials calculated by Eqs. (3.44a) and (3.44b) must be equal which leads to

$$\varepsilon_M = \varepsilon_1 \frac{(2\varepsilon_1 + \varepsilon_2) - 2\rho(\varepsilon_1 - \varepsilon_2)}{(2\varepsilon_1 + \varepsilon_2) + 2\rho(\varepsilon_1 - \varepsilon_2)} \tag{3.45a}$$

where $\rho = NR/R'$ is the volume fraction of the small particles. Only for small ρ ε_M increases linearly with the volume fraction according to

$$\varepsilon_M = \varepsilon_1 \left(1 + 3\rho\frac{(\varepsilon_1 - \varepsilon_2)}{2\varepsilon_1 + \varepsilon_2}\right) \tag{3.45b}$$

That approach was improved by Wagner [2] considering the permittivity as complex quantity. Later Sillars [3] generalized the treatment to particles with an ellipsoidal shape. The theory was further extended to high concentration of fillers [66] and to particles surrounded by a (conducting) layer. For a deeper discussion see Chap. 13.

Analyzing dielectric measurements in terms of Maxwell/Wagner processes one has to keep in mind that the shape of the particles and their properties must be known to obtain reliable results.

---

[4] It was assumed that the small particles do not interact with each other. That means that the concentration should be not too high.
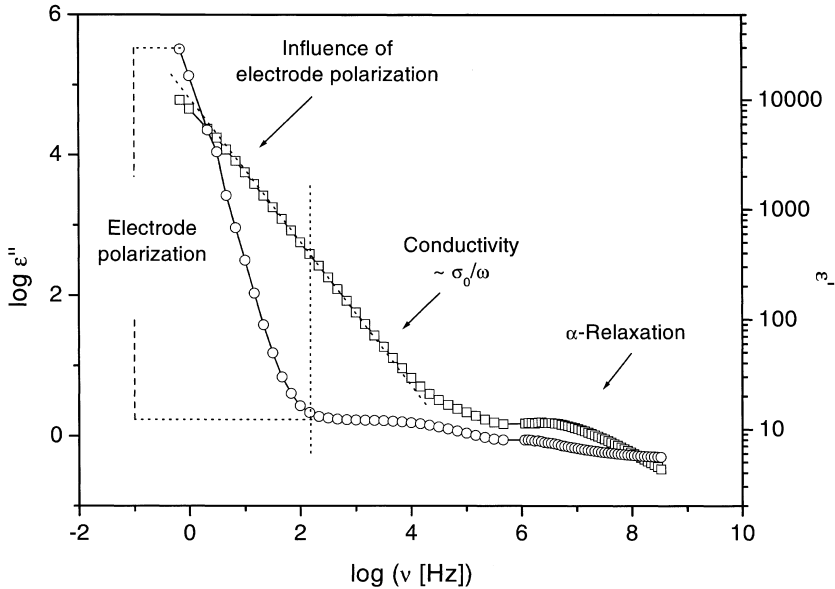
Fig. 3.24. Real part ε'(*open circles*) and imaginary part ε''(*open squares*) of complex dielectric function for poly(propylene glycol) with a molecular weight of 1000 g mol^{-1} complexed with 0.1 mol %LiClO$_4$ at $T = 259.1$ K. The strong increase of ε' at low frequencies is due to electrode polarization

3.4.2
Electrode Polarization

Electrode polarization[5] is an unwanted parasitic effect during a dielectric experiment because it can mask the dielectric response of the sample. It occurs mainly for moderately to highly conducting samples and influences the dielectric properties at low frequencies. Both the magnitude and the frequency position of electrode polarization depend on the conductivity of the sample and can result in extremely high values of the real and imaginary part of the complex dielectric function. In Fig. 3.24 the complex dielectric function is plotted for poly(propylene glycol) with a molecular weight of 1000 g mol^{-1} complexed with 0.1 mol% LiClO$_4$ in the frequency range from 10^{-1} Hz to 10^9 Hz. At low frequencies the real part increases strongly with decreasing frequencies up to very high values which cannot be explained by molecular relaxation processes. Such a behavior is a clear sign of electrode polarization.

The molecular origin of that effect is the (partial) blocking of charge carriers at the sample/electrode interface. This leads to a separation of positive and negative charges which gives rise to an additional polarization. The theoretical

---

[5] It should be noted that in contrast to molecular fluctuations and charge transport, electrode polarization is a macroscopic phenomenon.

treatment of electrode polarization goes back to Warburg [69] and Fricke [70], the latter having already predicted the frequency dependence of the complex dielectric function due to electrode polarization.

In the framework of a simple model the blocking of charges at the sample/electrode interface can be described by an electrical double layer with an effective spacing characterized by its Debye length L_D. This double layer causes a large capacitance in series to the investigated sample. The time dependence[6] of the electrode polarization is due to charging and discharging of that double layer. The model given in Fig. 3.22 can be used to estimate the effect of electrode polarization. From Eq. (3.40b) for the characteristic time constant of that process τ_{EP}

$$\tau_{EP} \approx \frac{\varepsilon_s \varepsilon_0}{\sigma_0} \frac{D}{2L_D} \tag{3.46}$$

can be estimated for $D \gg L_D$ where σ_0 is the d.c.-conductivity of the system. Equation (3.46) shows that the influence of electrode polarization on the measured complex dielectric function increases with increasing conductivity σ_0 because the effect is shifted to higher frequencies. On the other hand with increasing thickness D of the sample the process of electrode polarization shifts to lower frequencies. Therefore electrode polarization can be distinguished from the bulk behavior of a sample by studying the effects of changing the electrode materials and/or of the sample thickness on the frequency dependence of the dielectric function.

For a discussion of the dielectric properties of the sample alone the measurements have to be corrected for electrode polarization effects. That can be difficult because the capacitance C_{EP} and the impedance Z_{EP}^* due to electrode polarization can be extremely large especially for high conducting samples or materials in aqueous solution. Different techniques to correct for electrode polarization have been discussed by Schwan [71–74]. All of them are based on differences in the model description of the electrode polarization process (changing of the equivalent circuit) or the experimental estimation of its parameters and subtracting it from the raw data.

The first approach called substitution method is more or less related to measurement techniques. A sample with unknown dielectric properties is replaced by a known sample. The reference sample must be chosen in such a way that it mimics the ionic nature of the sample to investigate. In general that seems difficult to realize and can be used only for model systems. A deeper discussion about the reliability of this method can be found in [72, 74].

Because electrode polarization is sensitive to the sample thickness some correction for electrode polarization can be done by varying the thickness (or more general the geometric dimensions) of the sample. If $Z_i^* = Z_p^* + Z_{Si}^*$ denotes the impedance of a measurement i where Z_p^* and Z_{Si}^* are the impedances due to electrode polarization and due to the sample then the difference of two measurements

$$Z_1^* - Z_2^* = Z_{S1}^* - Z_{S2}^* \tag{3.47}$$

---

[6] One has to note that electrode polarization is not a relaxation process. Therefore the time constant of that process should not be called a relaxation time.

is independent of electrode polarization. That method is accurate if it is assumed that electrode polarization does not vary with the electrode distance which can be checked by investigating a series of samples with different thickness. In the case of $Z_p^* \gg Z_{Si}^*$ the subtraction procedure can lead to substantial errors.

The double layer model for electrode polarization discussed above leads to a Debye-like frequency dependence of this process (see Eq. 3.40a). Therefore in agreement with the ideas developed in Sect. 3.2.1 the frequency dependence of the electrode polarization can be described by a model function or by an apparent conductivity (see Eq. 3.18). Due to the fractal nature of the electrode surfaces [75] only in rare cases is a Debye-like frequency dependence for the electrode polarization found. Often fractal power laws for the frequency dependence for the complex dielectric function are observed (see for instance [70, 74]). Fractal power laws also follow from different theoretical treatments of electrode polarization [70, 75]. Therefore, to correct the measurements for electrode polarization one can assume

$$\varepsilon'_{EP}(\omega) - \varepsilon_s = A\omega^{-\lambda}; \qquad \varepsilon''_{EP}(\omega) \sim \omega^{-\lambda} \text{ for } \omega > 1/\tau_{EP} \qquad (3.48)$$

where λ $(0 < \lambda \le 1)$ is a parameter describing the fractal character of the underlying process and ε_s is the permittivity which is due to orientational polarization. Equation (3.48) can be included the fitting procedures in the same manner as discussed in Sect. 3.2.1 to separate the electrode polarization from dipolar relaxations. Applications of this equation are used in Chap. 12 analyzing the data for semiconducting polymer/salt systems.

3.5
Conclusion – How to Analyze Dielectric Spectra

The following rules may be of help in analyzing dielectric spectra:

1. Check whether the dielectric response of the sample under study is dominated by mobile or bound charge carriers, i.e., whether the conductivity contribution or molecular relaxation processes preponderates.
2. Samples which are characterized by molecular relaxation processes should be analyzed using generalized relaxation functions as outlined in Sect. 3.2.1. The main information which can be extracted is the relaxation time $\tau(T)$, the dielectric strength $\Delta\varepsilon(T)$, and the shape parameters $n(T)$, $m(T)$ of the relaxation time distribution function. Hence the relaxation process is characterized by four independent parameters. The relaxation time distribution function can be obtained as well by employing the (model-free) Thikonov regularization technique (see Sect. 3.2.2). Possible non-linearities have to be checked; this is especially important in case of collective fluctuations as they occur in (anti-)ferroelectric liquid crystalline systems.
3. In case of a dominating conductivity contribution the data may be represented in $\varepsilon^*(\omega)$, $\sigma^*(\omega)$, or $M^*(\omega)$. From fits based on a random free-energy barrier model as developed by Dyre the direct current (d.c.) conductivity σ_0

and the electrical relaxation time τ_e can be deduced. Ionic and electronic charge carriers have in principle a similar frequency and temperature dependence. Electrode polarization effects are only to be expected for materials with a high concentration of ionic charge carriers. The possibility of a non-linear response of the sample must be checked.

Appendix 3.1. Fit parameters

Table 3.1. Shape Parameter m and n for different monomers and polymers: Coordinates for Fig. 3.6

Nr.	Material	T[K]	m	n	Ref.
1	Poly(methylacrylate)	303.2	0.8	0.254	[76]
2	Poly(isobutyl methacrylate)	375.9	0.724	0.354	[77]
3	Poly(n-hexyl methacrylate)	305.8	0.678	0.409	[77]
4	Poly(n-butyl methacrylate)	332.1	0.676	0.356	[77]
5	Poly(nonyl methacrylate)	315.9	0.790	0.411	[77]
6	Poly(cyclohexyl methacrylate)	394.2	0.701	0.215	[77, 78]
7	Polyacetaldehyde	276.6	0.699	0.508	[79]
8	Polystyrene	>377.0	0.75	0.320	[80]
9	Poly(methyl methacrylate)	345.1	0.572	0.213	[81]
10	Oligo(methyl methacrylate)	283.2	0.552	0.259	[81]
11	Oligo(vinyl acetate)	275.9	0.674	0.309	[81]
12	Poly(p-chloro styrene)	412.2	0.733	0.389	[82]
13	Poly(o-chloro styrene)	>404	0.850	0.340	[80]
14	Poly(p-chloro styrene)	>366	0.600	0.200	[83]
15	Copolymer from phenyl methacrylate and acrylnitrile	418.1	0.940	0.311	[83]
16	Poly(bisphenol-A-carbonate)	437	0.795	0.225	[9]
17	Poly(vinyl formal)	403.1	0.584	0.458	[84]
18	Poly(vinyl acetal)	373.1	0.782	0.296	[84]
19	Poly(vinyl butyral)	358.1	0.770	0.304	[85]
20	Epoxy resin 1	373.1	0.237	0.219	[86]
21	Epoxy resin 2	291.1	0.506	0.247	[86]
22	Epoxy resin 3	328.1	0.497	0.133	[86]
23	Poly(vinyl octanate)	267.1	0.886	0.424	[87]
24	Poly(vinyl decanate)	270.9	0.770	0.493	[88]
25	Poly(bisphenol-A-isophthalate)	464.1	0.607	0.261	[9]
26	PET amorphous	350.8	0.810	0.370	[88]
27	PET crystalline, 29%	361.4	0.360	0.360	[88]
28	Polyurethane 1	264.9	0.485	0.175	[29]
29	Polyurethane 2	304.4	0.435	0.150	[29]

30	Polyurethane 3	341.3	0.540	0.285	[29]
31	Poly(vinyl acetate)	342	0.875	0.465	[89]
32	Glycerol	200	0.97	0.58	[15]
33	Propylene glycol	175	1	0.61	[15]
34	Salol	290	1	0.8	[90]
35	Propylene carbonate	175	1	0.7	[90]

Table 3.2. Parameter of the fits of the random free energy barrier model for conductivity [64] to the data of a zwitter-ionic polymethacrylates poly{3-[N-(ω-methacrylogloxyalkyl)-[N,[N-dimethyl ammonio]propane sulfonate} doped with 100 mol% NaI

T [K]	σ_0 [S cm^{-1}]	τ_e [s]	A [(rad s^{-1})$^\lambda$]	λ
396	1.9×10^{-7}	3.6×10^{-6}	2.4×10^6	1.32
391	5.6×10^{-8}	1×10^{-5}	7×10^4	1.03
382	1.3×10^{-8}	4×10^{-5}	6×10^2	0.55
373	1.3×10^{-8}	1.8×10^{-4}	–	–
364	4.4×10^{-10}	6.4×10^{-4}	–	–
355	6.8×10^{-11}	4.2×10^{-3}	–	–
346	8.6×10^{-12}	4×10^{-2}	–	–

List of Abbreviations and Symbols

a	Constant
D	Sample thickness
i	Imaginary unit $i = \sqrt{-1}$
L	Dielectric relaxation time distribution
L_D	Thickness of the Debye layer
m, n	Low and high frequency slope of the HN-function
M^*, M', M''	Complex electric modulus, real and imaginary part of the complex modulus
M_s, M_∞	$M_s = \lim_{\omega\tau \ll 1} M'(\omega) = 1/\varepsilon_S$; $M_\infty = \lim_{\omega\tau \gg 1} M'(\omega) = 1/\varepsilon_\infty$
s	Exponent characterizing the frequency dependence of the conductivity
t	Time
Z^*	Impedance
$\beta, \gamma, \beta_{KWW}$	Shape parameter of the Cole/Cole-, Cole/Davidson-, HN-and KWW-function
$\Gamma()$	Gamma function
$\varepsilon^*, \varepsilon', \varepsilon''$	Complex dielectric function or permittivity, real and imaginary part of the complex dielectric function
$\varepsilon_S, \varepsilon_\infty$	$\varepsilon_S = \lim_{\omega\tau \ll 1} \varepsilon'(\omega)$; $\varepsilon_\infty = \lim_{\omega\tau \gg 1} \varepsilon'(\omega)$

$\Delta\varepsilon = \varepsilon_S - \varepsilon_\infty$	Dielectric strength
ε_0	Dielectric permittivity of vacuum, $\varepsilon_0 = 8.854 \times 10^{-12}$ As V^{-1} m^{-1}
λ	Fractal parameter for electrode polarization; Regularization parameter
ν, ω	Frequency, radial frequency
ν_p, ω_p	Relaxation rate at maximal loss
$\sigma^*, \sigma', \sigma''$	Complex conductivity, real and imaginary part of the complex conductivity
σ_0	d.c.-conductivity
τ	Relaxation time
$\tau_D, \tau_{CC}, \tau_{CD}, \tau_{HN}, \tau_{KWW}$	Relaxation time of Debye-, Cole/Cole-, Cole/Davidson-, HN- and KWW-function
τ_e	Relaxation time for conductivity relaxation
τ_{MW}, τ_{EP}	Relaxation time for the Maxwell/Wagner process and for electrode polarization
a.c.	Alternating current
BNN	Barton/Nakajima/Namikawa
CC	Cole/Cole
CD	Cole/Davidson
d.c.	Direct current
HN	Havriliak/Negami
KWW	Kohlrausch/Williams/Watts

References

1. Böttcher CJF, Bordewijk P (1978) Theory of electric polarization, vol II. Dielectrics in time-dependent fields. Elsevier, Amsterdam Oxford New York
2. Wagner RW (1914) Arch Elektrotech 2:371
3. Sillars RW (1937) J Inst Elect Eng 80:378
4. Cole KS, Cole RH (1941) J Chem Phys 9:341
5. Fuoss RM, Kirkwood JG (1941) J Am Chem Soc 63:385
6. Davidson DW, Cole RH (1950) J Chem Phys 18:1417
7. Davidson DW, Cole RH (1951) J Chem Phys 19:1484
8. Diaz-Calleja R (2000) Macromolecules 33:8924
9. Havriliak, S, Negami S (1966) J Polym Sci C 16:99
10. Havriliak, S, Negami S (1967) Polymer 8:161
11. Jonscher AK (1983) Dielectric relaxation in solids. Chelsea Dielectrics Press, London
12. Boersema A, van Turnhout J, Wübbenhorst M (1998) Macromolecules 31:7453; Schröter K, Unger R, Reissig S, Garwe F, Kahle S, Beiner M, Donth E (1998) Macromolecules 31:8966
13. Yoshihara M, Work RN (1981) J Chem Phys 70:5872
14. Dixon KP, Wu L, Nagel SR, Williams BD, Carini J (1990) Phys Rev Lett 65:1108
15. Schönhals A, Kremer F, Schlosser E (1991) Phys Rev Lett 67:999
16. Chamberlin RV, Kingsbury DW (1994) J Non-Cryst Solids 172–174:318; Chamberlin RV (1999) Phys Rev Lett 82:2520
17. Kohlrausch R (1847) Ann Phys 12:393
18. Williams G, Watts DC (1970) J Chem Soc Faraday Trans II 68:1045
19. Schönhals A (1991) Acta Polymerica 42:149

20. Hamon VB (1952) Proc Instr Electr IV Monograph 2
21. Havriliak S, Havriliak SJ (1997) Dielectric and mechanical relaxation in materials. Hanser, München
22. Brather A (1979) Colloid Polym Sci 257:725
23. Simon GP, Williams G (1993) Polymer 34:3028
24. Lindsay CP, Patterson GD (1980) J Chem Phys 73:3348
25. Alavarez F, Alegria A, Colmenero J (1991) Phys Rev B 44:7306
26. Snyder CR, Mopsik FI (1999) Phys Rev B 60:984
27. Schönhals A (1997) In: Runt JP, Fitzgerald JJ (eds) Dielectric spectroscopy of polymeric materials. ACS-Books, Washington DC
28. Schönhals A (1993) Macromolecules 26:1309
29. Schlosser E, Schönhals A (1989) Colloid Polym Sci 267:133
30. Alig I, Stieber F, Wartewig S (1991) Polymer 32:2146
31. Roter G, Ishida H (1992) Macromolecules 25:2170
32. Schlosser E, Schönhals A, Carius HE, Goering H (1993) Macromolecules 26:6027
33. Wagner H, Richert R (1997) Polymer 38:255
34. Hofmann A (1993) Breitbandige dielektrische Spektroskopie zur Untersuchung von Relaxationsprozessen in glasbildenden Systemen, PhD Thesis, University Mainz
35. Provencher SW (1982) Comput Phys Commun 27:213
36. Tikhonov AN, Arsenin VY (1977) Solutions of ill-posed problems. Wiley, New York
37. Groetsch CW (1984) The theory of Tikhonov regularization for Fredholm equations of the first kind. Pitman, London
38. Honerkamp J, Weese J (1990) Cont Mech Thermodyn 2:17
39. Weese J (1992) Comput Phys Commun 69:99
40. Schäfer H, Bauch H (1995) Phys Lett A 199:33
41. Schäfer H, Stannarius R (1995) J Magn Reson B 106:14
42. Schäfer H, Sternin E, Stannarius R, Arndt M, Kremer F (1996) Phys Rev Lett 76:2177
43. van Turnhout J, Wübbenhorst M (2000) Dielectr Newsl, Issue November, NOVOCONTROL GmbH, Hundsangen
44. Schönhals A, Ruhmann R, Thiele T, Prescher D (1997) In: Jenekhe SA, Wynne, KJ (eds) Photonic and opto-electronic polymers. ACS Symposium Series
45. Wübbenhorst M, van Koten E, Jansen J, Mijs M, van Turnhout J (1997) Macromol Chem Rapid Comm 18:139
46. Boettger H, Bryksin VV (1985) Hopping conducting in solids. Akademie, Berlin
47. Debye P, Falkenhagen H (1928) Phys Z 29:121
48. Debye P, Falkenhagen H (1928) Phys Z 29:401
49. Debye P, Hückel E (1923) Phys Z 24:185
50. Hyde JM, Tomozawa M, Yoshiyagawa M (1987) Phys Chem Glasses 28:174
51. Nowick AS, Lim BS (1994) J Non Cryst Solids 172/174:1389
52. Macedo PB, Moynihan CT, Bose R (1972) Phys Chem Glasses 13:171
53. Meyer WH (1998) Adv Mater 10:439
54. Mertens IJA, Wübbenhorst M, Oosterbaan WD, Jenneskens LW, van Turnhout J (1999) Macromolecules 32:3314; Cleij TJ, Jenneskens LW, Wübbenhorst M, van Turnhout J (1999) Macromolecules 32:8663
55. Kremer F, Dominguez L, Meyer WH, Wegner G (1989) Polymer 30:2023
56. Sidebottom DL, Roling B, Funke K (2000) Phys Rev B 63:024301
57. Różański SA, Kremer F (1995) Macromol Chem Phys 196:877
58. Dyre JC, Schrøder TB (2000) Rev Mod Phys 72:873
59. Sidebottom DL (1999) Phys Rev Lett 82:3653
60. Moynihan CT (1994) J Non Cryst Solids 172/174:13
61. Jonscher AK (1977) Nature 267:673
62. Jonscher AK (1980) Phys Thin Films 11:205
63. Almond DP, Duncan GK, West AR (1983) Solid State Ionics 8:159
64. Dyre JC (1988) J Appl Phys 64:2456
65. Montroll E, Weiss GH (1965) J Math Phys 6:167

66. Hanai T (1968) In: Sherman P (ed) Emulsion science. Academic Press, New York
67. Takashima S (1989) Electrical properties of biopolymers and membranes. Adam Hilger, Bristol
68. Maxwell JC (1892) Treatise on electricity and magnetism. Clarendon, Oxford
69. Warburg E (1901) Ann Phys 6:125
70. Fricke H (1924) Phys Rev 24:575; Fricke H (1925) Phys Rev 26:678; Fricke H (1932) Philos Mag 14:310
71. Schwan HP (1951) Z Naturforsch 6b:121
72. Schwan HP (1966) Biophysik 201:181
73. Schwan HP (1968) Ann NY Acad Sci 148:191
74. Schwan HP, Onaral B (1985) Med Biol Eng Comput 23:28
75. Liu SH (1985) Phys Rev Lett 55:529
76. Ishida Y (1961) Kolloid-Z 174: 124
77. Ishida Y, Yamafuji K (1961) Kolloid-Z 177: 98
78. Strella S, Chinai SN (1958) J. Polym Sci 31:45
79. Ferry DJ, Strella S (1958) J Colloid Sci 13:45
80. Alexandrovish PS, Karasz FE, McKnight WJ (1980) Polymer 21:488
81. Ikada E, Sugimura T,Watanabe T (1975) Polymer 15:201
82. Schlosser E (1982) Polym Bull 8:461
83. Curtis A (1962) SPE Trans 2:82
84. Funt BL, Sutherland TH (1952) Can J Chem 30:940
85. Dittmer M (1969) PhD Thesis, Univ Leipzig
86. Schlosser E (1968) Plaste Kautsch 15:652
87. Bure JA (1962) PhD Thesis, Penn State Univ
88. Schlosser E, Schönhals A (1989) Colloid Polym Sci 267:963
89. Nozaki R, Mashimo S (1987) J Chem Phys 87:2271
90. Schönhals A, Kremer F, Hofmann A, Schlosser E, Fischer EW (1993) Phys Rev Lett 70:3459

4 The Scaling of the Dynamics of Glasses and Supercooled Liquids

F. Kremer · A. Schönhals

4.1
Introduction

Despite the fact that glasses are materials which have been available since the rise of mankind and despite the fact that they play an essential role in modern technology their physical understanding is still controversial and remains an unresolved problem of condensed matter physics [1, 2, 3a–d]. The most prominent features observed when a glass-forming liquid or polymer melt cools down is the rapid increase of the characteristic relaxation time and the strong non-Debye behaviour of the relaxation function. This has been observed by a manifold of different experimental methods including mechanical-dynamical spectroscopy [4], ultrasonic attenuation [5], light [6] and neutron scattering [7] (see Chap. 18), NMR spectroscopy [8] (see Chap. 17) and especially broadband dielectric spectroscopy [9–33].

In the high temperature limit the dielectric relaxation time has a typical value of about $\tau_\infty \cong 10^{-13}$ s, describing local orientational fluctuations. In this range the viscosity of the liquid has a value of about 10^{-2} to 10^{-1} poise. With decreasing temperature both the relaxation time and the viscosity increase strongly and can be approximated by the empirical Vogel-Fulcher-Tammann (VFT)-equation [34a–c][1]

$$\nu(T) = \frac{1}{2\pi\,\tau(T)} = \nu_\infty \exp\left[\frac{-DT_0}{T - T_0}\right] \tag{4.1}$$

where $\nu_\infty = (2\pi\,\tau_\infty)^{-1}$, D is a constant and T_0 denotes the Vogel temperature. (Sometimes T_0 is also called ideal glass transition temperature.) The degree of deviation from an Arrhenius-type temperature dependence provides a useful classification of glass forming systems [35]. Materials are called "fragile" if their $\nu(T)$ dependence deviates strongly from an Arrhenius-type behaviour and "strong" if $\nu(T)$ is close to the latter. As a quantitative measure of "fragility" the parameter D in Eq. (4.1) can be used [35]. At the calorimetric glass transition T_g $\nu(T_g)$ and the viscosity $\eta(T_g)$ have reached a typical value of ~10^{-2} Hz and ~10^{13} poise, respectively. In general, T_0 is found to be approximately 40 K below

---

[1] A more refined analysis based on the derivate with respect to temperature (see below) proves that the VFT-equation is a coarse-grained description only.

T_g. Thus, the change in the dynamics of the glass-forming processes spans more than 15 decades.

The divergence of Eq. (4.1) at $T = T_0$ is also supported by the so-called Kauzmann paradox occurring in the entropy determined by measurements of the specific heat [36–40]. If the entropy of the supercooled liquid is extrapolated to low temperatures, it seems to become identical to that of a crystal or even smaller at $T = T_0$. In some theories (like the Gibbs-DiMarzio model [41] for polymers) the Kauzmann paradox is resolved by a phase transition. However, the physical meaning of the divergence of $v(T)$ at $T = T_0$ remains unclear. Because of the universality of Eq. (4.1) T_0 should be regarded as a characteristic temperature for the dynamic glass transition.

The glassy dynamics is often discussed in a simplified picture. A molecule fluctuates in the cage of its neighbours. Its "rattling" motion is assigned to a fast secondary β-relaxation which takes place on a time scale of 10^{-10} s to 10^{-12} s following an Arrhenius-type temperature dependence

$$v(T) = v_\infty \exp\left(\frac{-E_A}{k_B T}\right) \tag{4.2}$$

where E_A is the activation energy, k_B the Boltzmann constant and v_∞ the relaxation rate in the high temperature limit. The reorientations of the molecules forming the cage corresponds to the dynamic glass transition or α-relaxation obeying a VFT-temperature dependence. This relaxation process must be – at least to some extent – cooperative; i.e. the fluctuations of the molecules forming the "cage" cannot be independent from each other. The extension of the size of such "cooperatively rearranging domains" [41, 42] is one of the central (and controversial) topics of glass research.

The relaxation function of the α-relaxation is usually broadened. Its high frequency side often exhibits two power laws. In the case of glycerol this was observed already by Davidson and Cole [43] and interpreted as caused by high frequency vibrations. It is nowadays established for a variety of glass-forming (low molecular weight and polymeric) materials [21, 33, 44–46]. Novel experiments [30, 50, 51] indicate that one should consider the high-frequency contribution ("wings") as a type of secondary relaxation (see also Chap. 5). On the other hand, Chamberlin [47–49] has shown that the scaling of the temperature dependence (VFT-dependence) of the α-relaxation as well as the existence of two power laws on the high frequency side can be quantitatively comprehended based on a mean field theory applied to small finite systems.

Many systems show additionally a slow secondary β-relaxation (with an Arrhenius-type temperature dependence). This process being observed for relaxation rates $\sim < 10^8$ Hz can often be assigned to intramolecular fluctuations. However, there are several examples like the low-molecular weight liquid ortho-terphenyl (OTP) [11, 12] or the main chain polymer poly(ethylene terephthalate) (PET) [33] where such an interpretation is not possible without ambiguity. Therefore, it was argued by Goldstein and Johari [11, 12] that the slow β-relaxation should be regarded as a precursor for the dynamic glass transition. The slow β-relaxation separates from the α-process in the frequency range from 10^7 to 10^8 Hz

($T \approx 1.2\ T_g$). There are several scenarios in the literature about the separation of the α- and β-relaxation (see also Chaps. 5 and 7). Light and neutron scattering experiments find in that temperature region characteristic anomalies of the Debye-Waller-factor. Furthermore a breakdown of the Stokes-Einstein equation which links rotational and translational diffusion is observed [54]. In the THz regime a further molecular process is observed, the "boson peak" [37] which has many similarities with the Poley absorption [52, 53]. Its molecular interpretation is controversial as well [55–59]. At ultra-slow relaxation rates (5–8 decades below the dynamic glass transition) fluctuations of clusters exist [60, 61].

In recent years growing evidence was found that the dynamics in supercooled liquids is spatially heterogeneous. When a liquid is cooled far below its melting point, the dynamics in some regions of the probe can be orders of magnitude faster than in adjacent regions only a few nanometers away. This is experimentally proven by several approaches such as multidimensional NMR [62], dielectric non-resonant spectral hole burning [63] (see Chap. 10), solvation dynamics [64] (see Chap. 15) and optical photobleaching [65]. The reader is referred to the reviews of Sillescu [66] and Ediger [67].

In summary, glassy materials show a subtle dynamics which is at present not well understood. Dielectric spectroscopy with its extraordinary frequency range (10^{-6} Hz to 10^{13} Hz) is an ideal tool to study this dynamics. State of the art results will be presented in this and the following chapter by Lunkenheimer and Loidl. The former will focus on the frequency range below 10^{10} Hz while the latter will discuss primarily novel results at higher frequencies. In detail in this chapter the following questions will be addressed: (i) what is the scaling of relaxation processes with temperature, (ii) is time-temperature superposition in general valid for (dielectric) relaxation processes, (iii) are there characteristic temperatures in the scaling of the dynamic glass transition, (iv) what is the molecular origin of the "high-frequency" wing which is observed in the dynamic glass transition of many (low molecular weight and polymeric) systems, (v) does the slow-β-relaxation obey the predictions of the mode-coupling theory as studied for the case of poly(ethylene terephthalate)?

4.2
Theories Describing the Scaling of the Dynamics in Glass-Forming Systems

The fluctuations of a molecular system being connected to a heat bath can be described in the simplest case by a double minimum potential. Assuming that the material specific potential barrier is temperature independent, the fluctuations are determined by the dynamic equilibrium between the (at least) two substates and for the relaxation rate ν an Arrhenius-type temperature dependence is obtained (Eq. 4.2). It is characteristic for secondary relaxation processes like the slow and the fast β-relaxation (Fig. 4.1b). In glass forming systems close to the calorimetric glass transition the situation is more complex. There are several different concepts and theories to understand the molecular dynamics based on thermodynamic and/or kinetic considerations. One example for the extension
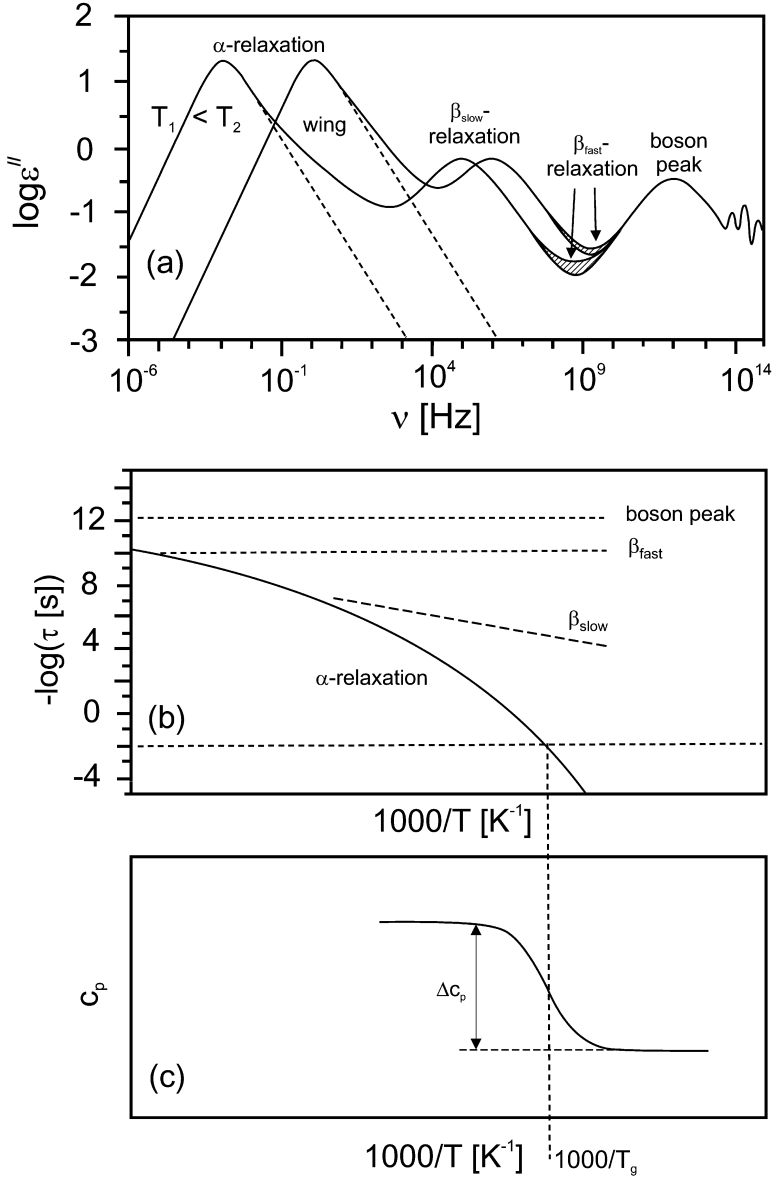
Fig. 4.1. Scheme of the dynamics taking place in glass-forming liquids: **a** imaginary part ε'' of the complex dielectric function vs frequency for two temperatures T_1 and T_2 – the dynamic glass transition ("α-relaxation"), the slow β-relaxation, the fast β-process and the boson peak are shown (not all of these four loss processes are necessarily present in a glass-forming system); **b** activation plot (relaxation rate vs inverse temperature) of the loss processes shown in **a**; **c** calorimetric determination of the glass transition temperature (specific heat at constant pressure) c_p vs inverse temperature for a certain cooling rate

of the simple double minimum potential to glass-forming systems is the energy landscape model discussed by Angell [68] or Stillinger [69, 70]. In this section the free volume theory, the concept of cooperativity and the mode-coupling theory (MCT) will be introduced briefly.

The empirical VFT-dependence (Eq. 4.1) can be justified by two theoretical approaches, the Adam-Gibbs model [42] and the free volume theory as developed by Doolittle [71] and Cohen [72, 73]. The latter is based on four assumption

1. To every molecule or segment of a polymer chain a local volume V can be attributed.
2. If V is larger than a critical value V_c the surplus can be considered as "free" $V_f = V - V_c$.
3. The mechanism of molecular transport is a jump over a distance corresponding to the size of the molecule V_M (~hard core volume). Such a process is possible only if the free volume $V_f \geq V^* \approx V_M$ where V^* is the minimal free volume required for a jump of a molecule (or segment) between to sites
4. The molecular rearrangement of free volume does not "cost" free energy.

Its statistics follows a Boltzmann distribution being normalised by the (constant) total free volume of the system. A molecule or a polymer segment changes its position via jumps only if the necessary free volume is provided. Hence for the jump rate $1/\tau$

$$\frac{1}{\tau} \sim \int_{V^*}^{\infty} \exp\left[-\frac{V_f}{\overline{V}_f}\right] dV_f \sim \exp\left[-\frac{V^*}{\overline{V}_f}\right] \tag{4.3}$$

is obtained where $\overline{V}_f$ is the averaged free volume. Assuming that the relative averaged free volume $\bar{f} = \overline{V}_f/V$ (V: total volume) depends linearly on temperature

$$\bar{f} = f_g + \alpha_f(T - T_g) \tag{4.4}$$

while $f^* = \dfrac{V^*}{V}$ is temperature independent results in a VFT-equation. α_f is the thermal expansion coefficient of the free volume and f_g the relative free volume at T_g. Comparison with Eq. (4.1) delivers

$$DT_0 = \frac{f^*}{\alpha_f} \qquad T_0 = T_g - \frac{f_g}{\alpha_f} \tag{4.5}$$

In the framework of the free volume concept T_0 is the temperature at which $\overline{V}_f$ vanishes. One has to note that in this simple model no characteristic length scale is involved. Furthermore all transport properties should have the same temperature dependence because the jump between holes is the only transport mechanism. Thus a decoupling of rotational and translational diffusion cannot be explained within this model. Cohen and Grest [73] extended this approach by considering solid- and liquid-like clusters in a percolation approach.

The approach of Adam and Gibbs [42] assumes the existence of "Cooperatively Rearranging Regions (CRR)" being defined as the smallest volume

which can change its configuration independent from neighbouring regions. Adam and Gibbs related the relaxation time to the numbers of particles (molecules for a low molecular liquid, segments for a polymer) $z(T)$ per CRR by

$$\frac{1}{\tau} \sim \exp\left[-\frac{z(T)\Delta E}{k_B T}\right] \tag{4.6}$$

where ΔE is a free energy barrier for one molecule. $z(T)$ can be expressed by the total configurational entropy $S_c(T)$ as $z(T) = S_c(T)/(N k_B \ln 2)$ where N is the total number of particles and $k_B \ln 2$ the minimum entropy of a CRR assuming a two-state model. Using thermodynamic considerations $S_c(T)$ can be linked to the change of the heat capacitance Δc_p at the glass transition by

$$S_c(T) = \int_{T_2}^{T} \frac{\Delta c_p}{T} \, \mathrm{d}T \tag{4.7}$$

With $T_2 = T_0$ and $\Delta c_p \approx C/T$ from Eqs. (4.6) and (4.7) the VFT-dependence follows. At T_0 the configurational entropy vanishes and the size of a CRR diverges as $z(T) \sim \dfrac{1}{C(T-T_0)}$. The Adam-Gibbs model does not provide information about the absolute size of a CRR at T_g.

In his fluctuation approach Donth [74, 75a,b] developed a formula which connects the height of the step in c_p and the temperature fluctuation δT of a CRR at T_g with the correlation length ξ as

$$\xi^3 \sim V_{\mathrm{CRR}} = \frac{k_B T_g^2 \Delta(1/c_p)}{\rho(\delta T)^2} \tag{4.8}$$

where ρ is the density and $\Delta(1/c_p)$ the step of the reciprocal specific heat (if $c_V \approx c_p$ is assumed). Experimentally δT can be extracted from the width of the glass transition [76, 77]. Recently, it became possible to extract δT directly form thermal heat spectroscopy measurements [78, 79]. A similar formula can be derived using energy fluctuations instead of entropy fluctuations [66].

Within the fluctuation approach for the temperature dependence of ξ

$$\xi(T) \sim \frac{1}{(T-T_0)^{\frac{2}{3}}} \tag{4.9}$$

is obtained. A similar equation was derived by Kirkpatrick and Tirumalai [80] using scaling arguments.

The mode-coupling theory (MCT) of the glass transition (for reviews see [81–84]) is an essentially hydrodynamic approach being based on a generalised non-linear oscillator equation

$$\frac{\mathrm{d}^2 \Phi_q(t)}{\mathrm{d}t^2} + \Omega^2 \Phi_q(t) + \zeta \frac{\mathrm{d}\Phi_q(t)}{\mathrm{d}t} + \Omega^2 \int_0^t m_q(t-\tau) \frac{\mathrm{d}\Phi_q(\tau)}{\mathrm{d}\tau} \, \mathrm{d}\tau = 0 \tag{4.10}$$

where the normalised density correlation function $\Phi(t)_q$ is defined as

$$\Phi_q(t) = \frac{\langle \Delta\rho_q(t)\Delta\rho_q(0) \rangle}{\langle \Delta\rho_q^2 \rangle} \tag{4.11}$$

where $\Delta\rho_q(t)$ are density fluctuations at a wavevector q, Ω is a microscopic oscillator frequency and ζ describes a frictional contribution. While the first three terms of Eq. (4.10) correspond to a damped harmonic oscillator the fourth term contains a memory function $m_q(t-\tau)$. The physical idea of this memory term can be visualised for a hard-sphere system which interacts only by elastic scattering. For low densities the collisions at two different points in space-time are independent from each other. Hence $m_q(t) \sim \delta(t)$ with $\delta(t)$ being the Dirac-function. With increasing density the collisions become correlated. This results in the "cage effect" mentioned above. At a short time scale a particle is enclosed in the transient cage of its neighbours. The correlated motions within the cage lead to a strong increase of the internal friction. On a longer time scale the cages are destroyed by diffusional rearrangements and hence the friction decreases. As a consequence the total frictional losses in the system become time dependent. This is considered by the integral term in Eq. (4.10)[2].

To solve Eq. (4.10) requires an ansatz for $m_q(t)$. As already shown by Leutheuser [81] and Bengtzelius et al. [82] a simple Taylor-expansion of m leads to a relaxational response of Φ_q having some similarity with the dynamic glass transition. Assuming $m_q(t) = v_1\Phi_q(t) + v_2\Phi_q^2(t)$ (F_{12}-model [83]) delivers a two-step decrease of the correlation function $\Phi_q(t)$. The faster contribution is interpreted in terms of a β-relaxation while the slower component is attributed to the dynamic glass transition (α-relaxation). Its relaxation time diverges at a critical temperature T_c where a phase transition from an ergodic ($T > T_c$) to a non-ergodic ($T < T_c$) state takes place. In detail this (idealised) version of MCT makes the following predictions:

1. For $T > T_c$ the relaxation time τ_α of the α-relaxation scales according to

$$\tau_\alpha \sim \eta \sim \left[\frac{T_c}{T - T_c}\right]^\gamma \tag{4.12}$$

   where γ is a constant.
2. The relaxation function of the α-relaxation can be described by

$$\Phi_q(t) \sim \exp\left[-\left(\frac{t}{\tau_\alpha}\right)^{\beta_{KWW}}\right] \tag{4.13}$$

---

[2] Concerning the interrelationship between time-correlation functions for molecular reorientation, their apparent memory function and the dielectric permittivity of the dynamic glass transition, see also [85].

with $0 < \beta_{KWW} \leq 1$, where Φ_0 is the amplitude of the α-relaxation. For $T > T_c$ the relaxation time distribution should be temperature independent, i.e. time-temperature-superposition should hold.

3. Above and close to the critical temperature T_c the minimum of the susceptibility ε''_{min}, ω_{min} between the α-relaxation and the β-relaxation should follow a power law

$$\varepsilon''_{min} \sim \left| \frac{T - T_c}{T_c} \right|^{\frac{1}{2}} \tag{4.14}$$

4. The scaling of the α- and β-relaxation follows a master function

$$\varepsilon''(\omega) = \frac{\varepsilon''_{min}}{a+b} \left[b \left(\frac{\omega}{\omega_{min}} \right)^a + a \left(\frac{\omega_{min}}{\omega} \right)^b \right] \tag{4.15}$$

with exponents a and b that are connected by

$$\frac{\Gamma^2(1+b)}{\Gamma(1+2b)} = \lambda = \frac{\Gamma^2(1-a)}{\Gamma(1-2a)} \tag{4.16}$$

where Γ is the Γ-function.

5. These exponents also determine the temperature dependence of the frequency of the minimum of the susceptibility and of the frequency of the maximum ω_{max} of the α-relaxation

$$\omega_{min} \sim \left| \frac{T - T_c}{T_c} \right|^{\frac{1}{2a}} \tag{4.17}$$

$$\omega_{max} \sim \left| \frac{T - T_c}{T_c} \right|^{\left(\frac{1}{2a} + \frac{1}{2b} \right)} \tag{4.18}$$

The dynamic glass transition spans an extraordinary wide time scale bridging microscopic (10^{-11} s) and ultraslow fluctuations (10^6 s). In order to analyse its temperature dependence in detail it is conclusive to calculate the derivative of the relaxation rate with respect to $1/T$. For the VFT-equation (Eq. 4.1), the Arrhenius dependence (Eq. 4.2) and the temperature dependence suggested by MCT (Eq. 4.11) for $T > T_c$, the following formulas hold:

– VFT:

$$\frac{d \log \nu}{d(1/T)} = - (DT_0) \left(1 - \frac{T_0}{T} \right)^{-2} \cdot \log e \tag{4.19}$$

– Arrhenius:

$$\frac{d \log \nu}{d(1/T)} = \frac{-E_A}{k_B} \cdot \log e \tag{4.20}$$
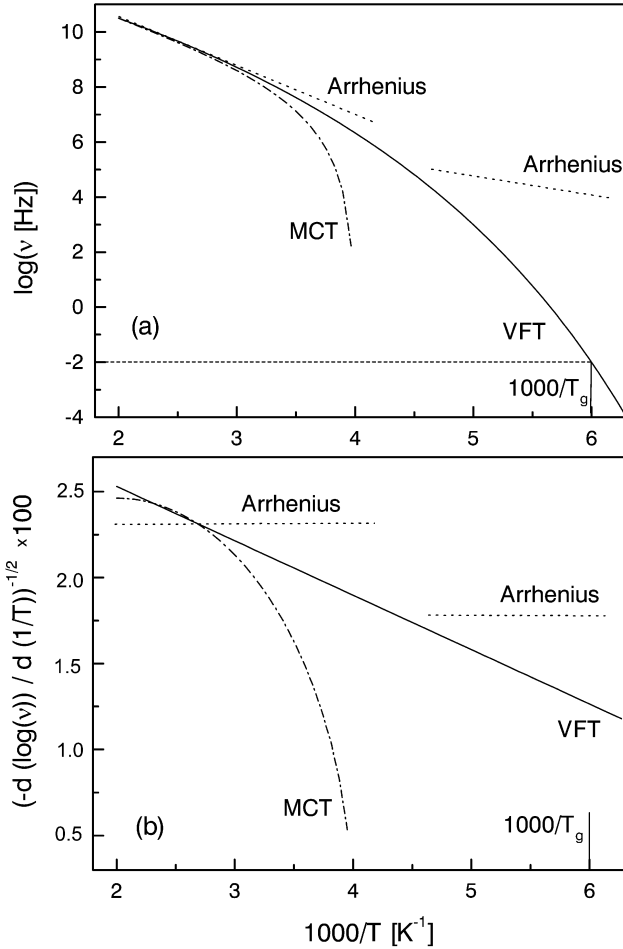
Fig. 4.2. a The scaling behaviour as predicted by the Arrhenius-equation (Eq. 4.2), the Vogel-Fulcher-Tammann equation (VFT) (Eq. 4.1) and the mode-coupling theory (MCT) (Eq. 4.12). The glass transition temperature T_g is indicated. **b** Differential quotient $(-\mathrm{d}(\log(\nu))/\mathrm{d}(1/T))^{-1/2} \times 100$ for the functionalities shown in a

– MCT:

$$\frac{\mathrm{d}\log\nu}{\mathrm{d}(1/T)} = \frac{\gamma \cdot \log e}{T_c/T^2 - 1/T} \tag{4.21}$$

Hence in a plot of $(-\mathrm{d}\log\nu/\mathrm{d}(1/T))^{-1/2}$ vs $1/T$ the VFT dependence shows up as a straight line. The derivative plots enable to analyse in detail the scaling with temperature (Fig. 4.2). This is especially true for the high temperature regime. With modern equipment (having a temperature stability of typically $\pm$ 0.02 K, see Chap. 2) it is possible to trace the evolution of the dielectric spectra in steps of

one degree or less. By that experimentally difference quotients $\Delta(-\log\nu)/\Delta(1/T)$ can be determined and compared with the analytical derivatives.

4.3
Temperature Dependence of the Dynamic Glass Transition

The dynamic glass transition is determined by intermolecular interactions. It shows up in different quantities as density fluctuations (as measured with (light) scattering techniques), dielectric relaxation or the viscosity. In the following several typical low molecular weight glass forming systems will be compared: ortho-terphenyl (OTP), salol, glycerol, propylene carbonate, propylene glycol and poly(propylene glycol). While orthoterphenyl and salol can be considered as van der Waals liquids, despite the fact that salol has H-bonds (binding primarily within a molecule), glycerol and propylene glycol are typical H-bond forming liquids. To compare directly the scaling behaviour of a low molecular glass-forming liquid with that of a polymer poly(propylene glycol) with a molecular weight of $4000\,\mathrm{g\,mol^{-1}}$ is chosen as well.

The dynamic glass transition in ortho-terphenyl (OTP) was measured by light scattering techniques, dielectric spectroscopy and the viscosimetry (Fig. 4.3a,b). All methods deliver within experimental accuracy a similar dependence in the entire temperature range (unfortunately OTP has weak dielectric relaxation processes, so that the spectra above 10^6 Hz cannot be measured with sufficient accuracy.). A weak Arrhenius-like secondary relaxation is observed as well. Its molecular assignment (if it exists) is not known. Analysing the temperature dependence in the derivative plots (Fig. 4.3b) proves that it is *not* possible to describe the experimental data adequately by use of *one* VFT-equation. On the other hand it would be not possible to replace the VFT-dependence by an Arrhenius function as one might expect from the raw data in Fig. 4.3a.

For salol as well it is found that density fluctuations, dielectric relaxation and viscosity scale with each other in the entire temperature range (Fig. 4.4a). The data at temperatures >300 K can be equally well described by the Arrhenius equation and the MCT-ansatz (Eq. 4.12). The derivative plot (Fig. 4.4b), however, proves that the Arrhenius-fits fails. As in OTP it is not possible to describe the temperature dependence with *one* VFT-fit in the entire temperature range.

For glycerol (Fig. 4.5a) the data at temperatures ≥ 270 K seems to follow equally well – a VFT-, an Arrhenius- or – a MCT-fit. However, from the derivative plot (Fig. 4.5b) one must conclude that neither an Arrhenius- nor an MCT-ansatz describe the temperature dependence correctly within the limits of experimental accuracy. Instead it is possible to fit the data in the entire temperature range by use of two VFT-equations (VFT$_1$ and VFT$_2$).

In propylene carbonate (Fig. 4.6a) the situation is similar to that in glycerol. Neither an Arrhenius- nor the MCT-ansatz are adequate fits (Fig. 4.6b). Two VFT dependencies are necessary to describe the data in its temperature dependence.
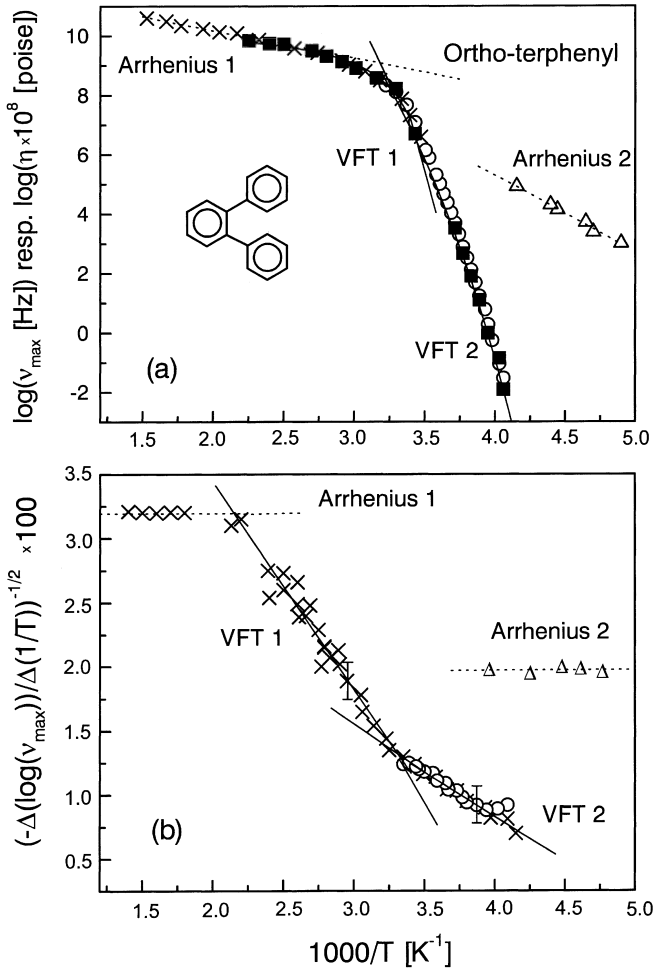
Fig. 4.3. a Activation plot ($\log \nu_{max}$ vs $1000\,T^{-1}$) for ortho-terphenyl (OTP) as obtained from Havriliak-Negami fits – dielectric α-relaxation [32b] (*open circles*); dielectric β-relaxation [11] (*open triangles*); the α-relaxation as measured with Photon-Correlation and Brillouin-Spectroscopy [32c] (*filled squares*) and the viscosity ($10^8 \times \eta$ [poise]) [32c] (*crosses*). The *error bars* are smaller than the size of the symbols if not indicated otherwise. *Solid line* (VFT1): VFT-fit with $\log \nu_\infty = 21.3$, $DT_0 = 1820$ K, $T_0 = 168$ K; *dashed line* (Arrhenius 1): Arrhenius fit with $\log \nu_\infty = 12.1$, $E_A/k_B = 980$ K; *solid line* (VFT2): VFT-fit with $\log \nu_\infty = 11.0$, $DT_0 = 225$ K, $T_0 = 242$ K; *dashed line* (Arrhenius 2): Arrhenius-fit with $\log \nu_\infty = 15.0$, $E_A/k_B = 2543$ K. **b** Difference quotient $(-\Delta(\log(\nu_{max}))/\Delta(1/T))^{-1/2}$ vs $1000/T$ for the dielectric and the viscosity data shown in **a**

Fig. 4.4. a Activation plot of salol. The dielectric α-relaxation [32b] (*open circles*), the α-relaxation measured with light scattering (Photon-Correlation-Spectroscopy and Brillouin-Scattering) [32c] (*open diamonds*) and the viscosity (multiplied by $10^{7.75} \cdot \eta$ [poise]) (*filled triangles*) (taken from [32c]. The *error bars* are smaller than the size of the symbols if not indicated otherwise. *Solid line* (VFT1): VFT-fit with (log $\nu_\infty = 24$, $DT_0 = 2070$ K, $T_0 = 141$ K; *dashed-dotted line*: MCT-fit with log $\nu_\infty = 10.1$, $\gamma = 1.72$, $T_c = 270$ K; *dashed-line*: Arrhenius-fit with log $\nu_\infty = 11.9$, $E_A/k_B = 928$ K. *Solid line* (VFT2): VFT-fit with log $\nu_\infty = 10.5$, $DT_0 = 225$ K, $T_0 = 224$ K. (For the fits the dielectric data were used only. **b** Difference quotient $(-\Delta(\log(\nu_{max}))/\Delta(1/T))^{-1/2}$ vs $1000/T$ for the dielectric data shown in **a**
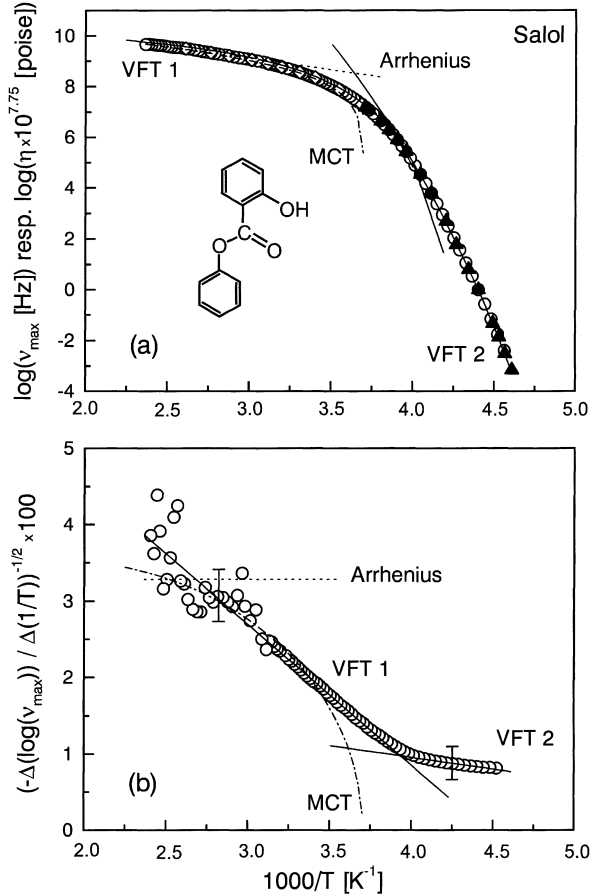
Figure 4.7 compares the temperature dependence of the relaxation rate of the α-relaxation of propylene glycol with its polymeric pendant poly(propylene glycol). For both materials the curved trace of the relaxation rate vs inverse temperature is observed. Due to the increased intramolecular interaction the relaxation rate for polymeric material is shifted to higher temperatures. The application of the described derivation technique shows that for both systems the temperature dependence of the relaxation rate of the α-relaxation can be described by a high and a low temperature VFT-equation. Hence with regard to the temperature dependence of the relaxation rate there is no essential difference between the low molecular weight and the polymeric glass-forming system.

A dielectric relaxation process is not only characterised by the relaxation rate but also by its dielectric strength and by the shape of the relaxation time distribution function. In the following the temperature dependence of these two quantities will be discussed for the α-relaxation.

Figure 4.8a shows $(T\Delta\varepsilon)^2$ vs temperature for propylene carbonate, propylene glycol, glycerol and for salol. According to the Onsager-Kirkwood-Fröhlich ap-

Fig. 4.5. a Activation plot for glycerol. Data taken from [32b]. The *error bars* are smaller than the size of the symbols if not indicated otherwise. *Dashed line*: Arrhenius fit with $\log \nu_\infty = 16.9$, $E_A/k_B = 2650$ K. *Dashed-dotted line*: MCT fit with $\log \nu_\infty = 10.4$, $\gamma = 5.5$, $T_c = 218.5$ K. *Solid line*: VFT-fits (VFT): $\log \nu_\infty = 13.7$, $DT_0 = 952.1$ K, $T_0 = 130.7$ K; (VFT$_1$): $\log \nu_\infty = 12.3$, $DT_0 = 532$ K, $T_0 = 170.2$ K; (VFT$_2$): $\log \nu_\infty = 14.3$, $DT_0 = 1065$ K, $T_0 = 126$ K. **b** Experimentally determined difference quotient $(-\Delta(\log(\nu_{max}))/\Delta(1/T))^{-1/2} \cdot 100$ vs $1000/T$. The lines describe the fits shown in **a**
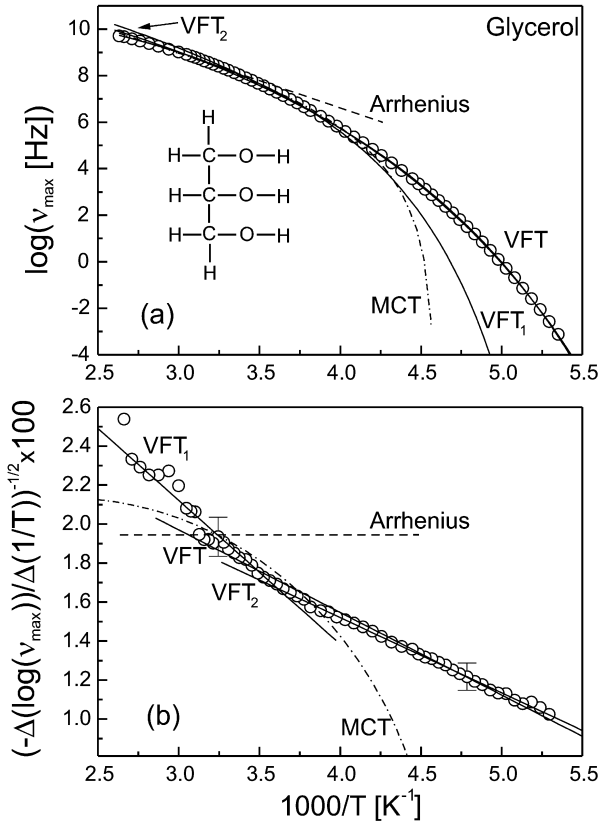
proach (see Chap. 1) that quantity should be independent of temperature. However, Fig. 4.8a shows that $(T\Delta\varepsilon)^2$ has a strong temperature dependency which can not be explained by the temperature dependence of the density. Moreover one finds that the temperature dependence of $\Delta\varepsilon$ changes in the temperature range where the transition from the low temperature VFT behaviour to a high temperature VFT- or to an Arrhenius-dependence is observed. The change in the temperature dependence of $(T\Delta\varepsilon)^2$ is more pronounced for the van der Waals liquids. If dipole fluctuations and density fluctuations are coupled one would expect a similar behaviour for the product $T\Delta\varepsilon$ as predicted for the Debye Waller factor. Figure 4.8a does *not* show the functional form expected from MCT [83, 84], i.e. $T\Delta\varepsilon \sim (T_c - T)^{1/2}$ for $T < T_c$ and $T \Delta\varepsilon \approx$ constant for $T > T_c$ [29].

The shape parameter β of the Cole-Davidson function shows a pronounced temperature dependence as shown for glycerol, propylene glycol and propylene carbonate (Fig. 4.8b). This holds for the vast majority of glass-forming (low molecular weight and polymeric) systems thus proving that time-temperature superposition is in general *not* fulfilled. Also the MCT-prediction of Eq. (4.12) is *not* valid. Hence the construction of so-called master-plots is a coarse-grained description of relaxation processes only.
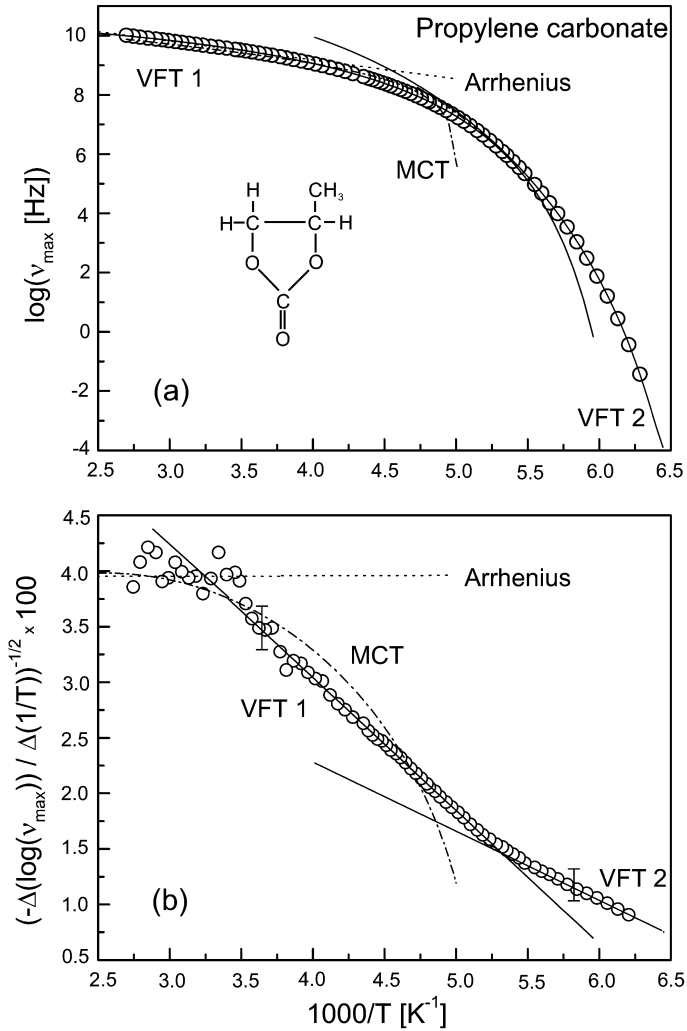
Fig. 4.6. a Activation plot for propylene carbonate. Data taken from [32b]. The *error bars* are smaller than the size of the symbols if not indicated otherwise. *Dashed line*: Arrhenius fit with $\log \nu_{\infty} = 11.7$, $E_A/k_B = 640$ K. *Solid line* (VFT$_1$): VFT fit with $\log \nu_{\infty} = 10.7$, $DT_0 = 163$ K, $T_0 = 153$ K. *Dashed dotted line*: MCT fit with $\log \nu_{\infty} = 10.1$, $\gamma = 1.7$, $T_c = 199$ K. *Solid line* (VFT$_2$): VFT fit with $\log \nu_{\infty} = 13.4$, $DT_0 = 416$ K, $T_0 = 131$ K. **b** Experimentally determined difference quotient $(-\Delta(\log(\nu_{max}))/\Delta(1/T))^{-1/2} \cdot 100$ vs $1000/T$. The lines describe the fits shown in **a**.
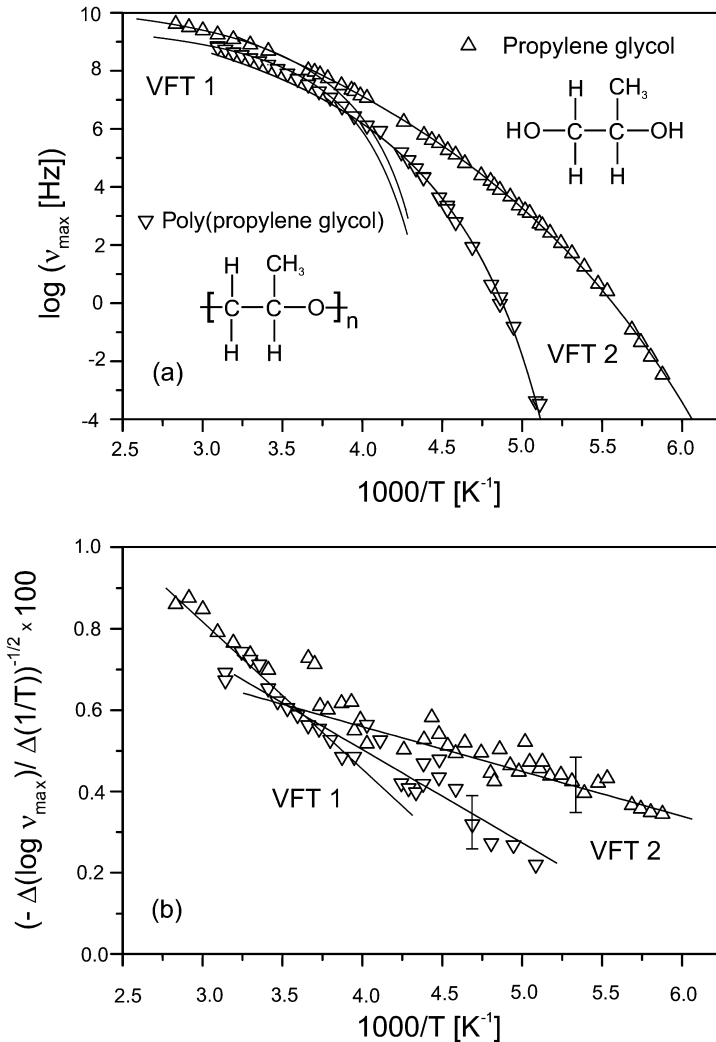
Fig. 4.7. a Activation plot for propylene glycol (*open triangles*) and the polymeric pendant poly(propylene glycol) (*inverted open triangles*).The *error bars* are smaller than the size of the *symbols* if not indicated otherwise. S*olid lines* (VFT$_2$): VFT-fits with $\log v_\infty = 13.7$, $DT_0 = 940$ K, $T_0 = 114.6$ K for propylene glycol and $\log v_\infty = 11.1$, $DT_0 = 401$ K, $T_0 = 169$ K for poly(propylene glycol)). *Solid lines* (VFT$_1$): VFT-fits for the upper temperature range with $\log v_\infty = 10.8$, $DT_0 = 176{,}4$ K; $T_0 = 211$ K for propylene glycol and $\log v_\infty = 10.4$, $DT_0 = 182$ K, $T_0 = 211$ K for polypropylene glycol. **b** Difference quotient $(-\Delta(\log(v_{max}))/\Delta(1/T))^{-1/2} \cdot 100$ vs $1000/T$. The lines describe the fits shown in **a**
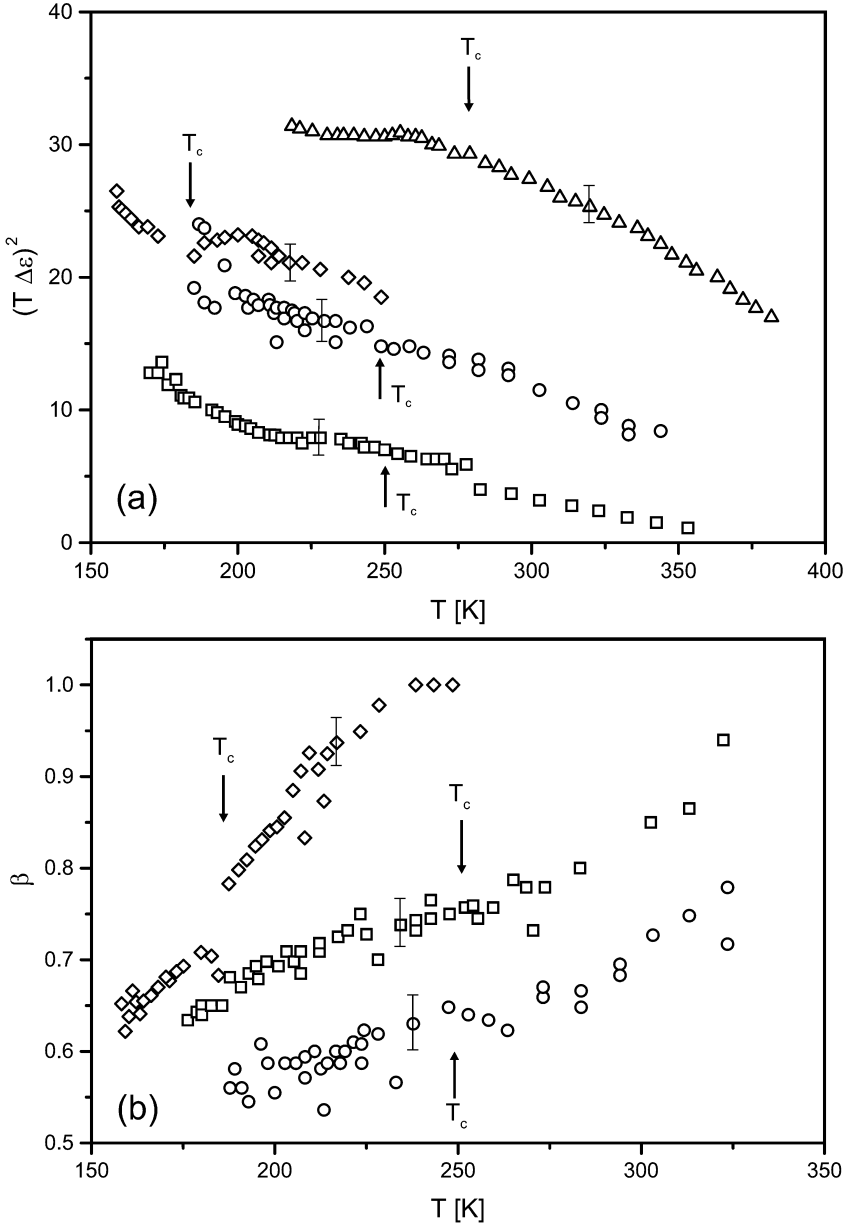
Fig. 4.8. a $(T \Delta \varepsilon)^2$ vs T; (*open circles*) glycerol, (*open squares*) propylene glycol, (*open diamonds*) propylene carbonate, (*open triangles*) salol (data taken from [15]). The *error bars* are smaller than the size of the *symbols* if not indicated otherwise. The critical temperatures T_c of the MCT are indicated for different materials. Taken from [29] with permission. **b** Shape parameter β for (*open circles*) glycerol, (*open squares*) propylene glycol and (*open diamonds*) propylene carbonate from the Cole-Davidson function $\varepsilon^*(\omega) = \varepsilon_\infty + \dfrac{\Delta \varepsilon}{(1 + (i \omega \tau))^\beta}$ vs T
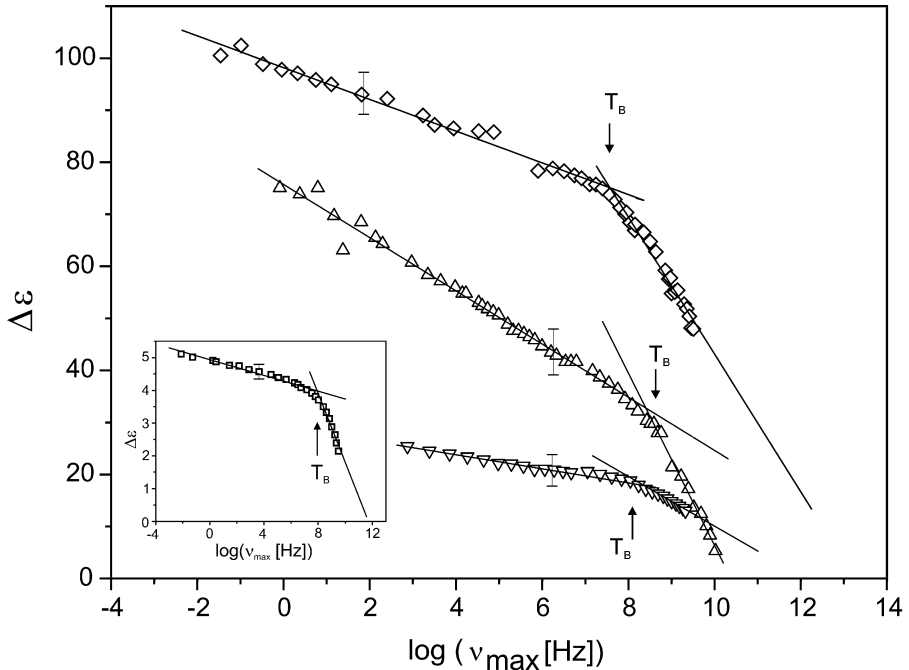
Fig. 4.9. $\Delta\varepsilon$ vs log ν_{max} for (*open triangles*) propylene glycol, (*inverted open triangles*) poly(propylene glycol) and (*open diamonds*) propylene carbonate and (*open squares*) salol (data taken from [15]). The *error bars* are smaller than the size of the *symbols* if not indicated otherwise. The *lines* are fits of linear equations to the different sets of the data. The crossover temperature T_B is indicated for both materials

The static quantity dielectric strength $\Delta\varepsilon$ and the dynamic variable mean relaxation rate ν_{max} reflect different properties of the same underlying motional process. Hence both should be correlated in their temperature dependence. In Fig. 4.9 $\Delta\varepsilon$ is plotted vs log ν_{max} for various glass formers. Two well separated regions are observed which can be approximated by a linear dependence of $\Delta\varepsilon$ vs log ν_{max}. The intersection of both defines – model-free – a crossover frequency ν_B between 10^7 and 10^8 Hz indicating a change in the dynamics of the α-relaxation. This takes place at a temperature T_B far above the glass transition temperature T_g. Similar crossover relaxation rates ν_B respective temperatures T_B are observed for a manifold of glass-forming systems of completely different molecular structure (low molecular weight and polymeric systems, van der Waals liquids but also hydrogen bonded systems) proving that it is a general feature of the dynamic glass transition [86]. The existence of a crossover temperature T_B can be well comprehended within the framework of cooperativity models of the dynamic glass transition. The dielectric strength $\Delta\varepsilon$ is determined by the dipole-dipole correlation function containing both self-correlation and cross-correlation (with neighbouring dipolar units) terms. If cooperative interactions become important, cross-correlations are no longer negligible. This is the case for $T < T_B$ where T_B marks the

onset of cooperativity. It is characterised by a length scale $\xi(T)$ defining the size of cooperatively rearranging domains. For $T > T_B$ the dynamic glass transition can be regarded as the fluctuation of nearly independent polar units. Hence extrapolating the high frequency dependence for $\Delta\varepsilon \to 0$ results in values of about 10^{13} Hz which is an upper limit for the relaxation rate (and usually obtained as prefactor of an Arrhenius- or VFT-equation). For $T < T_B$ such an extrapolation delivers unreasonable limit frequencies. This reflects the fact that the fluctuating unit is now the cooperatively rearranging region of size $\xi(T)$. It is evident that a quantitative description requires to model the intermolecular interactions.

4.4
Scaling of the Relaxation Time Distribution Function of the Dynamic Glass Transition

Generalised relaxation functions (like the Cole-Cole, the Cole-Davidson or the Havriliak-Negami function, see Chap. 3) being characterised by *one* slope on the high frequency side of the dielectric loss vs frequency are only at first glance an adequate description of the dynamic glass transition. A closer examination shows that strong deviations occur for frequencies ≥ 100 times the mean relaxation rate. They become pronounced with decreasing temperature. This is exemplified for glycerol in Fig. 4.10. Formally it is of course possible to treat the "high frequency wings" as an additional relaxation process (Fig. 4.11a). This results – in the case of glycerol – in a temperature dependence of the additional process which resembles the VFT-behaviour of the dynamic glass transition (Fig. 4.11b). Hence this process cannot be considered as a simple secondary relaxation with Arrhenius-type temperature dependence.

The dynamic glass transition is – according to the MCT [83, 84] – a two-step process with the Kohlrausch-Williams-Watts (KWW)-function

$$\Phi(t) \sim \exp\left[-(t / \tau_\alpha)^{\beta_{KWW}}\right], \ t \geq \tau_\alpha \tag{4.22}$$

Table 4.1. Fit parameters β_{KWW} and $b_{measured}$ as extracted from the slope of the high frequency wing of the α-relaxation. b_{MCT} is the value deduced using Eqs. (4.16) and (4.24) of MCT

T [K]	β_{KWW}	$b_{measured}$	b_{MCT}
193	0.56	0.23	0.62
203	0.59	0.29	0.66
208	0.60	0.27	0.66
213	0.59	0.33	0.65
218	0.60	0.32	0.66
223	0.60	0.37	0.66
228	0.60	0.38	0.66
233	0.61	0.43	0.66
243	0.65	0.34	0.71
253	0.63	0.38	0.69
263	0.66	0.39	0.72
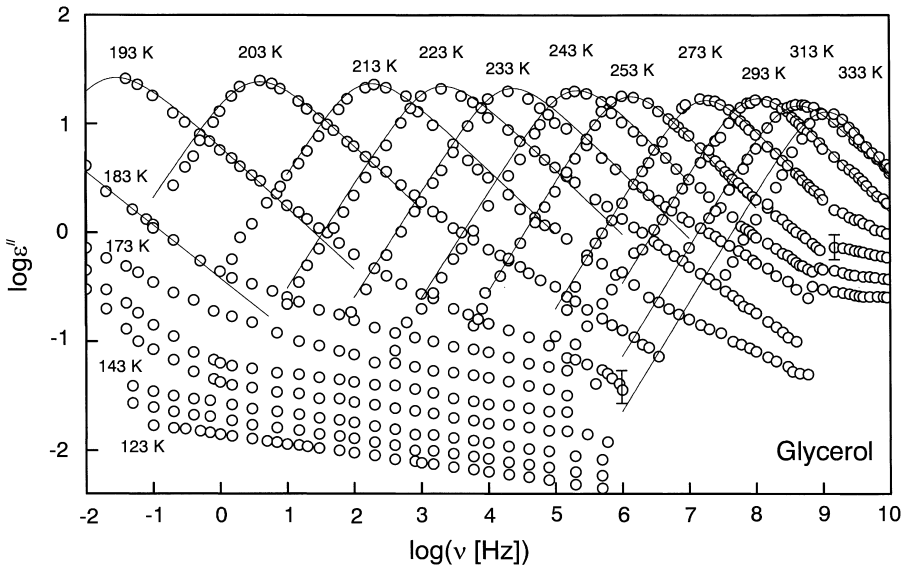
Fig. 4.10. Imaginary part ε'' of the dielectric function vs frequency at temperatures as indicated in K for glycerol. The solid lines are Havriliak-Negami fits. If not indicated otherwise *errors bars* are not larger then the size of the *symbols*

and a short time region with the von Schweidler law

$$\Phi(t) = -B \cdot (t/\tau_\alpha)^b, \ t \leq \tau_\alpha \tag{4.23}$$

where β_{KWW} and b are constants. Transformed in the frequency domain this approach results in a high frequency wing of the dynamic glass transition being characterised by two power laws having exponents β_{KWW} and b. Hence the constants β_{KWW} and b can be directly deduced from the slopes of the high frequency wing of the α-relaxation (Fig. 4.10, Table 4.1). According to MCT [83, 84] the stretched exponential and the exponent-parameter are linked

$$\beta_{KWW} = \frac{-\ln 2}{\ln(1-\lambda)} \tag{4.24}$$

Thus with the left-hand side of Eq. (4.16) the predictions of MCT for the relationship between β_{KWW} and b can be examined. Pronounced quantitative disagreement is found (Fig. 4.12b and Table 4.1). The MCT Eqs. (4.16) and (4.24) predict much larger values of b than observed experimentally.

While for glycerol the "high-frequency wing" is characterised by one slope (see as well Chap. 5) for salol indeed an additional process is observed. This results in a curved slope of the "wing" (Fig. 4.13). Unfortunately salol has a strong tendency to crystallise. It is therefore not a suitable candidate for measurements in the supercooled liquid regime. For polyalcohols it was shown that from glyc-
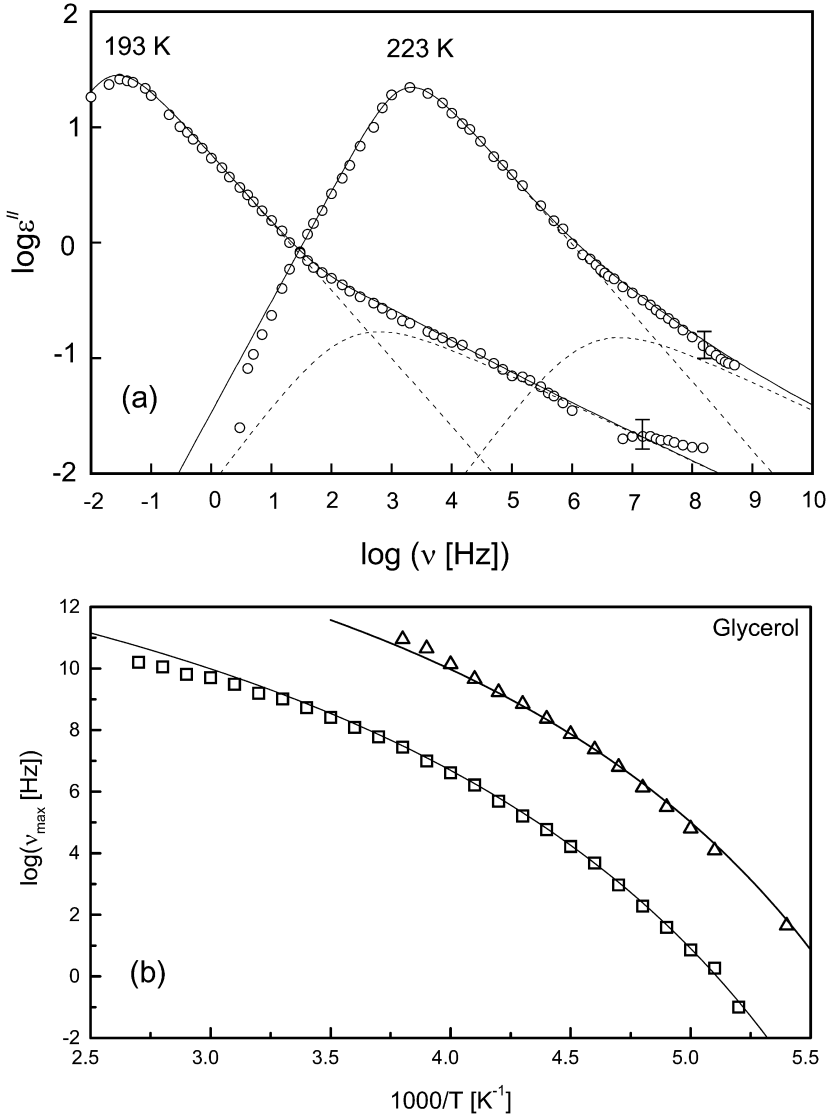
Fig. 4.11. **a** Formal description of the high frequency wing by the superposition of two HN-relaxation processes. The *error bars* are smaller than the size of the *symbols* if not indicated otherwise. The fit parameters for the measurement at 193 K are: first process: $\Delta\varepsilon = 76$, $\alpha = 0.91$, $\gamma = 0.62$, $\tau = 8.5$ s; second process: $\Delta\varepsilon = 0.8$, $\alpha = 0.8$, $\gamma = 0.3$, $\tau = 8.5 \times 10^{-4}$ s. At 223 K: First process: $\Delta\varepsilon = 59$, $\alpha = 0.96$, $\gamma = 0.62$, $\tau = 1.1 \times 10^{-4}$ s; second process: $\Delta\varepsilon = 0.45$, $\alpha = 0.8$, $\gamma = 0.3$, $\tau = 2.8 \times 10^{-8}$ s. **b** Relaxation time for the two relaxation processes (used in Fig. 4.11a to describe the data) vs inverse temperature. Taken from [33] with permission
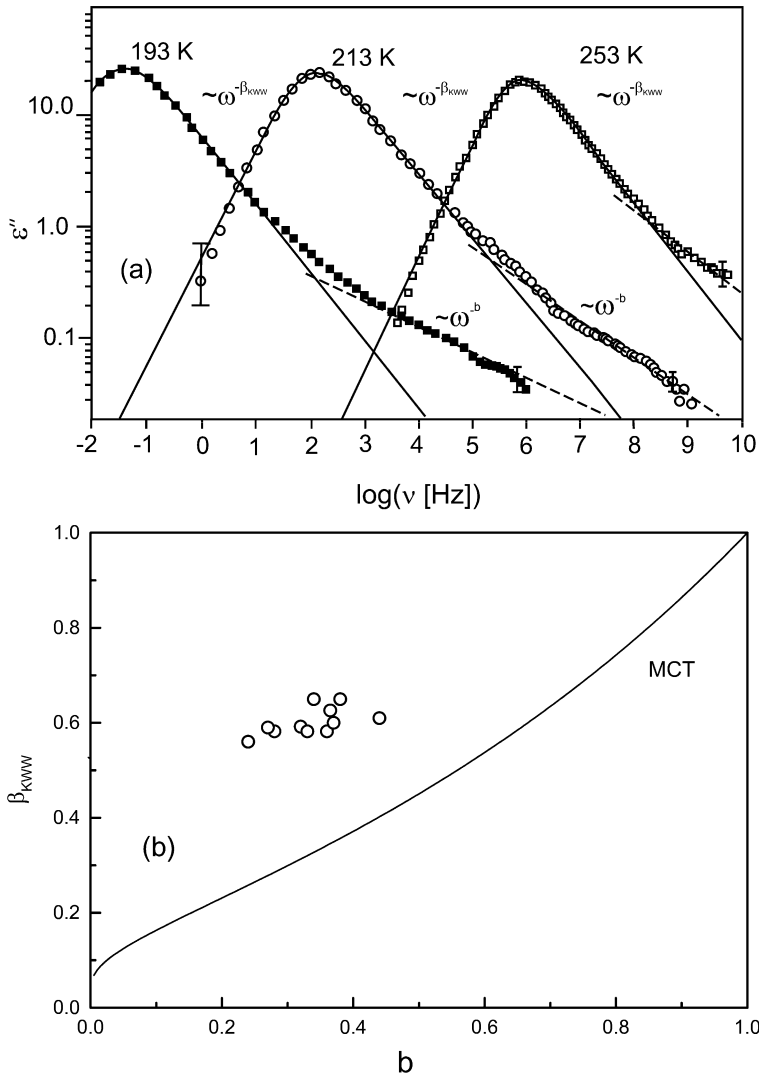
Fig. 4.12. a The high-frequency wing of the dynamic glass transition of glycerol as described by two power laws. Fit-parameters see Table 4.1. **b** The relationship between β_{KWW} and b as suggested by MCT according the Eqs. (4.5) and (4.13). The *open circles* are the experimental findings (see Table 4.1)

erol to threitol, xylitol and sorbitol the secondary relaxation changes gradually from a wing type scenario to a pronounced β-peak [51].

The observation of "high frequency wings" in dielectric relaxation processes caused Nagel and coworkers [44, 45] to suggest a special scaling: By plotting $w^{-1}\log[\varepsilon'' \nu_{max}/(\Delta \varepsilon \nu)]$ vs $w^{-1}(1+w^{-1})\log(\nu/\nu_{max})$ one can show that for a variety of materials the spectra collapse onto each other. w denotes the half-width of the loss peak, normalized to that of the Debye function. However, the question re-
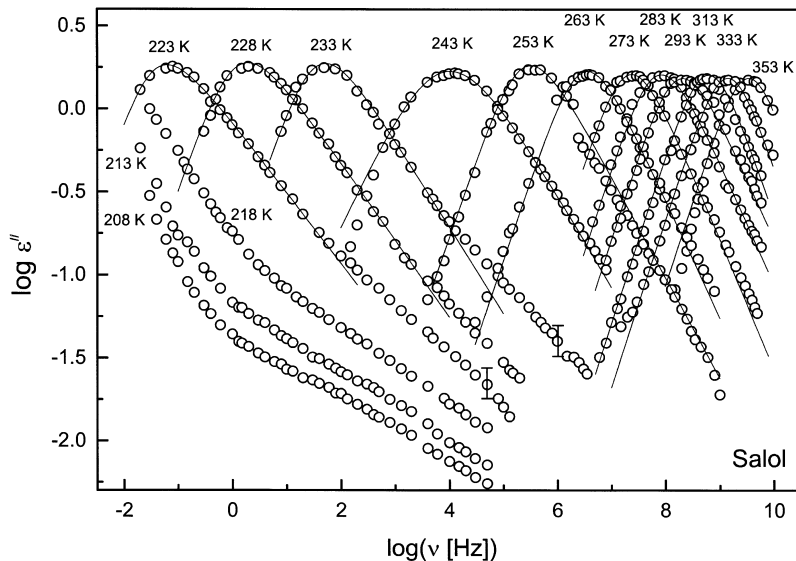
Fig. 4.13. Imaginary part ε'' vs frequency for salol at temperatures as indicated in K. The *solid line* is a fit according to the Havriliak-Negami equation. If not indicated otherwise *errors bars* are not larger then the size of the *symbols*

mains open, what the physical interpretation of the above quantities is (this point is even not raised by the authors)? Furthermore one can show that materials having on the low frequency side of the relaxation function a slope $m \neq 1$ do *not* follow the above-mentioned dependencies. Numerous examples of materials with $m \neq 1$ are known in the literature [87]. (A further discussion of the high frequency "wings" will be presented in Chap. 5.)

4.5
Scaling of the Dynamic Glass Transition and the Slow β-Relaxation in Poly(ethylene terephthalate) (PET)

Poly(ethylene terephthalate) (PET) is a main chain polymer having a dielectrically active α- and β-relaxation process. Their scaling has been used in an MCT analysis [88]. However, due to the fact that in these studies the dielectric data were limited to frequencies below 10^6 Hz, the β-relaxation could be observed to a reduced fraction only. In covering the frequency range from 10^{-2} to 10^9 Hz experimental data are acquired which enables one to analyse the β-relaxation fully. Due to the strong tendency of PET to crystallise, the measurements are restricted to temperatures below 367 K [33]. This means that the interesting regime where α- and β-relaxation merge is not accessible for PET in the pure amorphous state.

By use of two HN relaxation functions the data (Fig. 4.14) can be described within the limits of experimental accuracy (solid line in Fig. 4.14). From the fit a
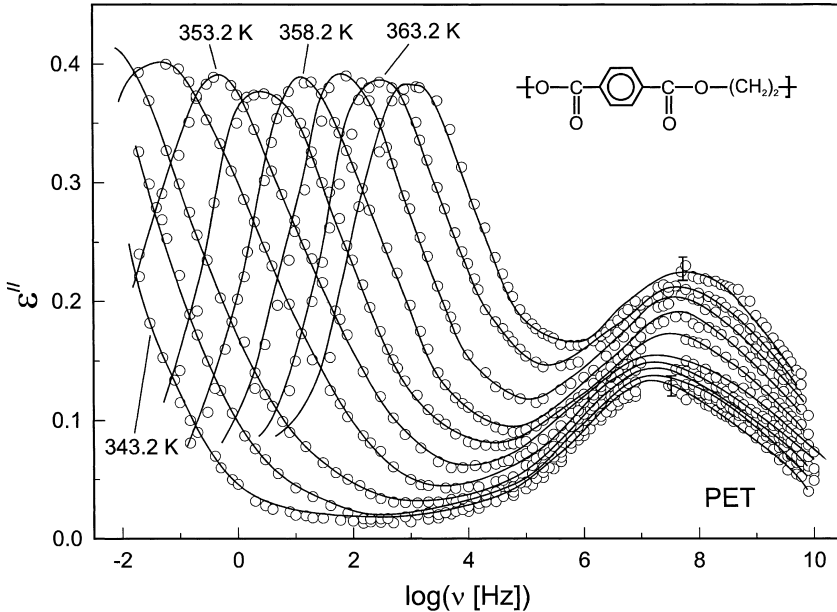
Fig. 4.14. Imaginary part ε'' vs frequency for amorphous poly(ethylene terephthalate) (PET) at temperatures as indicated in K (temperature steps: 2.5 K). The *solid line* is the fit using two superimposed Havriliak-Negami relaxation functions. If not indicated otherwise the *error bars* are not larger then the size of the *symbols*. Taken from [33] with permission

precise determination can be obtained for the maximum of the dynamic glass transition (α-relaxation) and the minimum between the α- and β-relaxation. The former follows a VFT-dependence, the latter has an Arrhenius-type thermal activation.

The critical temperature T_c of the MCT can be determined by the power laws of Eqs. (4.14) and (4.17). A plot of ε''_{min} or ω^{2a}_{min} vs T (Fig. 4.16) should give straight lines intersecting the abscissa at T_c. The solid lines show such a fitting procedure to the high temperature points (with $a = 0.44$), yielding a value of $T_c = 355 \pm 3$ K [33]. It must be noted that the measurement points lie on a continuously bending curve. Therefore the determination of T_c depends on the temperature range selected for the fit.

The power laws of Eqs. (4.14), (4.17) and (4.18) can be combined to extract the parameters a and b without explicitly knowing T_c (Fig. 4.17a,b). The proportionality of ε''_{min} to ν^{2a}_{min} is fulfilled, resulting in a value of $a = 0.44 \pm 0.09$.

The proportionality of ε''_{min} to ν_{max} is also fulfilled (Fig. 4.17b), resulting in a value for the slope of $s = 0.17 \pm 0.02$. With s and the parameter a (determined in Fig. 17a) a value for $b = (a \times s)/(a - s) = 0.30 \pm ^{0.11}_{0.08}$ is obtained. A fit of the minimum of the susceptibility between the α- and β-relaxation (Fig. 4.18) with Eq. (4.15) should give the parameters a and b as well. For the fit data at temperatures in the interval of 10 K above T_c are used. The frequency range taken is thus limited by the logarithmic medium value between the frequency of the mini-
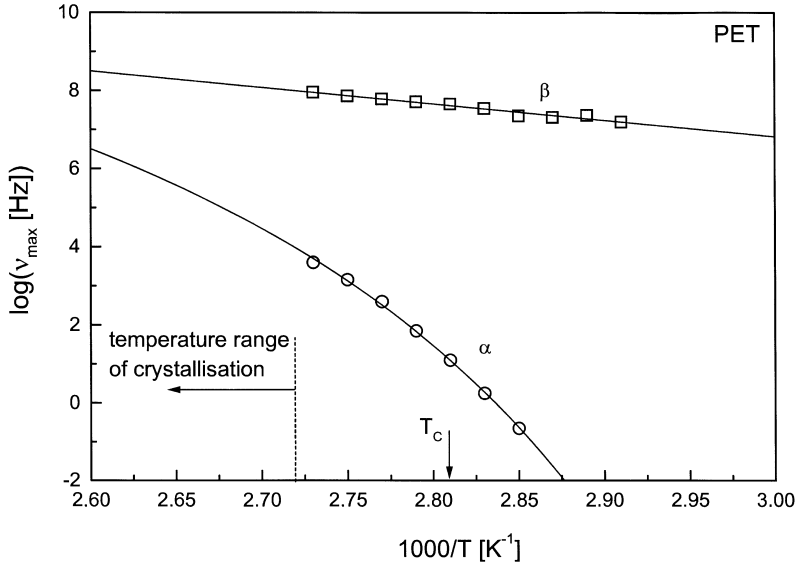
Fig. 4.15. Activation plot for amorphous PET. The *solid lines* correspond to a fits according to the VFT-equation (log $v_\infty = 17.5$, $DT_0 = 754.5$ K, $T_0 = 304$ K) and to the Arrhenius equation (log $v_\infty = 17.4$, $E_A = 66$ kJ mol^{-1}) respectively. Taken from [33] with permission
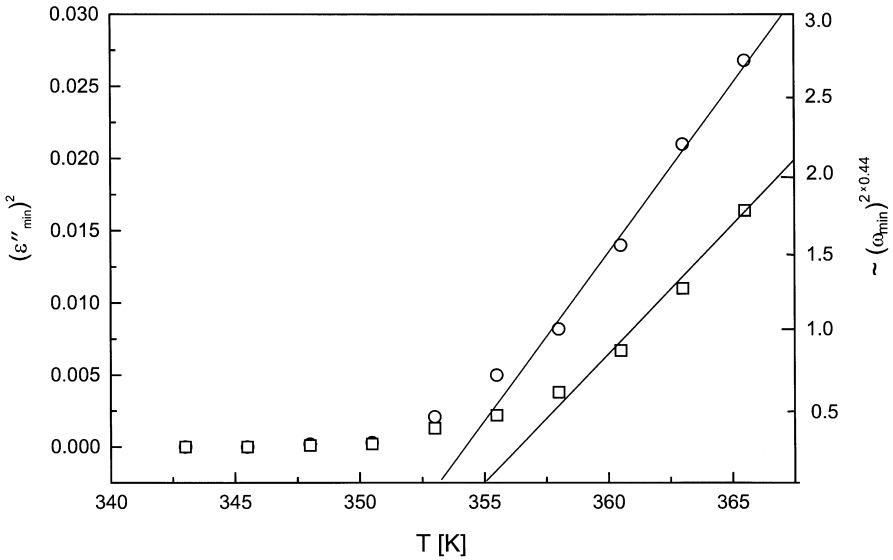
Fig. 4.16. Determination of the critical temperature T_c assumed by MCT according to Eq. (4.14) (*open circles*) and to Eq. (4.17) (*open squares*). The intersection of the *solid lines* gives a value for T_c. Taken from [33] with permission
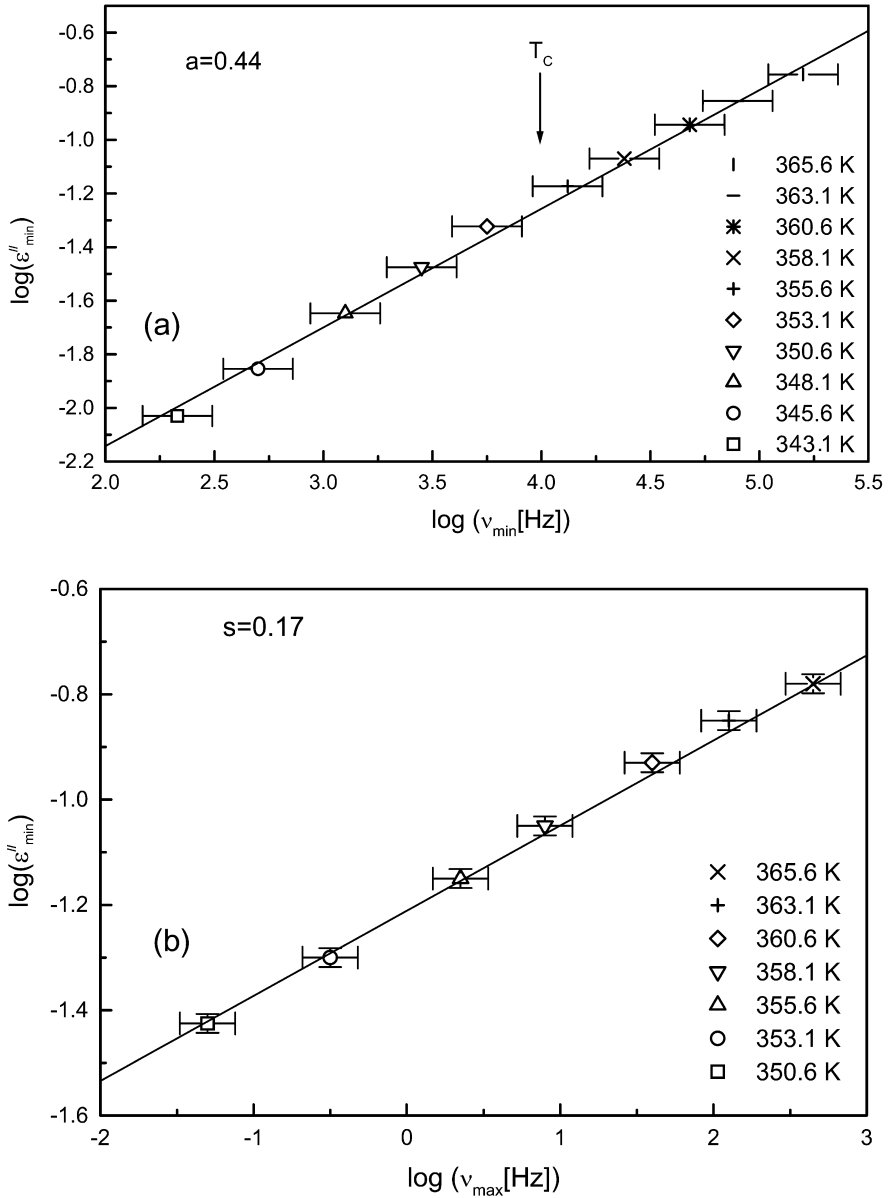
Fig. 4.17. **a** Determination of the exponent parameter a using the power law of Eqs. (4.14) and (4.17). **b** Determination of the exponent parameter $S_2 = \dfrac{a \cdot b}{a+b}$ using the power law of Eqs. (4.17) and (4.18). Taken from [33] with permission
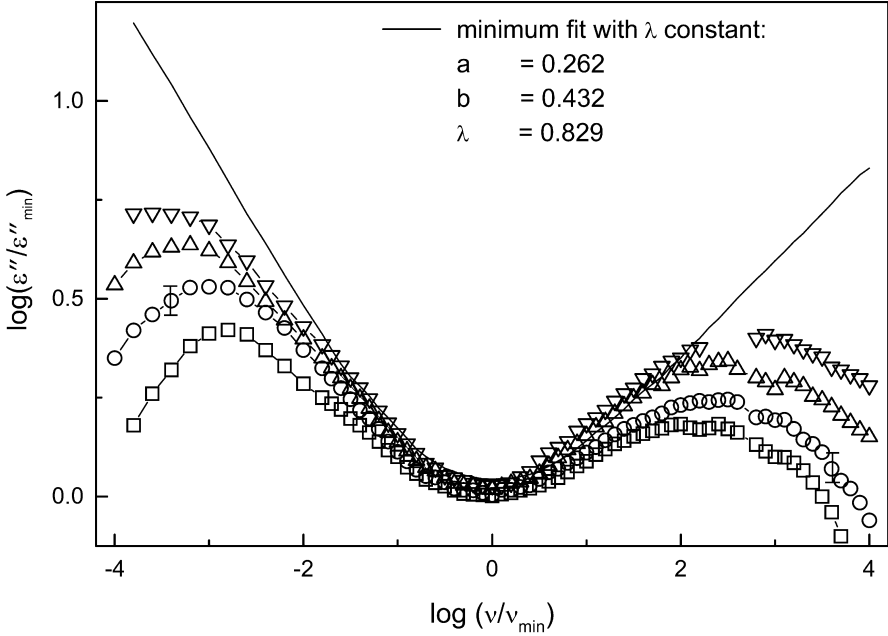
Fig. 4.18. Rescaled plot of the minimum between the α- and β-relaxation. The *solid line* shows a fit with Eq. (4.15) with λ-constraint of Eq. (4.16) to measurements at temperatures $T_c \leq T \leq T_c + 10$. Taken from [33] with permission

mum and the α-relaxation peak on the low and the frequency of the minimum and the β-relaxation peak on the high frequency side. This gives a value of $\lambda = 0.83$ with parameters $a = 0.26$ and $b = 0.43$. Comparing these parameters with the ones obtained by the power laws (Table 4.2) gives no agreement within experimental accuracy. Refining the memory Kernel $m_q(t)$ in Eq. (4.10) enables one to extend the MCT approach. This delivers in the "A_3-scenario" quantitative agreement between theory and experiment [89].

Table 4.2. Fit parameters a and b as deduced from Fig. 4.17a/b. λ_a and λ_b correspond to the right and left side of Eq. (4.16). The data in the second row ("minimum fit") are the result of a fit with Eq. (4.15) to the rescaled minimum between α- and β-relaxation (Fig. 4.17). Sample: amorphous PET

	a	b	λ_a	λ_b
Power laws	0.44 ± 0.09	$0.30 \pm {}^{0.11}_{0.08}$	0.32 ± 0.32	$0.91 \pm {}^{0.03}_{0.07}$
Minimum fit	0.26	0.43	0.83	

4.6
Conclusions

Broadband dielectric spectroscopy is a versatile tool to analyse details of the scaling of relaxation processes. Typically four dielectric loss processes are observed in supercooled liquids: the dynamic glass transition (α-relaxation), a slow secondary relaxation (β_{slow}), a fast secondary relaxation (β_{fast}) and at 10^{12} Hz the boson peak. Below 10^{10} Hz primarily the dynamic glass transition and the β_{slow} relaxation are present. In detail the following conclusions can be drawn:

1. For all analysed (low molecular weight and polymeric) systems the dynamic glass transition follows a Vogel-Fulcher-Tammann- – or Williams-Landel-Ferry – like temperature dependence. A more refined analysis based on derivative plots reveals further details proving that this is a *coarse grained* description of glassy dynamics only and that every molecular system has its own signature in the temperature dependence of the dynamics.
2. In all analysed (low molecular weight and polymeric) systems for the dynamic glass transition time temperature superposition is *not* fulfilled; it can be regarded as an approximation only.
3. For all analysed systems a change in the temperature dependence of the dynamic glass transition is observed at a relaxation rate of about 10^8 Hz. This may be interpreted in the framework of the mode-coupling theory as an indication of the development of nonergodicity at T_c but it can be explained as well as the onset of cooperativity at T_B. Hence the dynamic glass transition is characterised by *three* temperatures: (I) the temperature for which the high frequency limit v_∞ is reached, (II) the temperature T_B or T_c and (III) the Vogel temperature T_0.
4. The dynamic glass transition often shows an additional contribution ("wing") on the high frequency. It has presumably to be comprehended as a type of secondary relaxation [33, 50, 51]. An alternative explanation is based on dynamic heterogeneities in the supercooled liquid [47–49].
5. For the case of poly(ethylene terephthalate) (PET) a refined analysis of the scaling of the dynamic glass transition and the secondary (β_{slow}) relaxation proves that the predictions of the idealised mode-coupling theory (at least in the $F_{1,2}$ scenario) are *not* fulfilled. Instead it is suggested that the β_{slow} relaxation has to be interpreted as a molecular fluctuation.

List of Abbreviations and Symbols

A, a, b	Constants
D	Fragility parameter
E_A	Activation energy
$\bar{f}$	Averaged relative free volume
k_B	Boltzmann constant
$m_q(t)$	Memory function for wave vector q
p	Constant
S_c	Configurational entropy
T	Temperature
T_c	Critical temperature according to MCT
T_g	Glass transition temperature
T_0	Vogel temperature (ideal glass transition temperature)
V	Volume
V_c	Critical free volume
V_f	Free volume
$\bar{V}_f$	Averaged free volume
α_f	Thermal expansion coefficient for the free volume
β	Constant
β_{KWW}	Stretching parameter according to Kohlrausch-Williams-Watts (KWW)
γ	Constant
Δc_p	Specific heat at constant pressure
$\Delta\varepsilon$	Dielectric strength
$\varepsilon^*, \varepsilon', \varepsilon''$	Complex dielectric function, real and imaginary part
η	Viscosity
ν	Frequency
ν_c	Critical frequency
ν_{max}	Relaxation rate at maximum dielectric loss
ν_∞	Relaxation rate for $(T \to \infty)$
$\xi(T)$	Correlation length
ρ_q	Density fluctuation at wave vector q
τ_a	Relaxation time of α-relaxation
$\Phi_q(t)$	Density correlation function for wave vector q
Φ_0	Amplitude of the α-relaxation
ω	Angular frequency
CRR	Cooperatively Rearranging Regions
HN	Havriliak-Negami
KWW	Kohlrausch-Williams-Watts
MCT	Mode-coupling theory
OTP	Ortho-terphenyl
PET	Poly(ethylene terephthalate)
VFT	Volgel-Fulcher-Tammann

References

1. Anderson PW (1995) Science 267:1615
2. Wong J, Angell CA (1976) Glass: structure by spectroscopy. Marcel Dekker, New York
3. a. Ngai KL, Wright GB (eds) (1984) Proceedings of the Conference on Relaxation in Complex Systems. National Technical Information Service, Springfield 1981; b. Ngai KL (ed) (1991) Proceedings of the Conference on Relaxation in Complex Systems. Crete. J Non-Cryst Solids 131–133; c. Ngai KL, Riande E (eds) (1994) Proceedings of the Conference on Relaxation in Complex Systems, Alicante. J Non-Cryst Solids 172–174; d. Ngai KL, Riande E (eds) (1998) Proceedings of the Conference on Relaxation in Complex Systems, Vigo. J Non-Cryst Solids 235–237
4. Jeong YH (1987) Phys Rev A36:766
5. Jeon YH, Nagel SR, Bhattacharya S (1986) Phys Rev A 34:602
6. Demonlin C, Montrose CT, Ostrowsky N (1974) Phys Rev A9:1740
7. Mezei F, Knaak W, Farago B (1987) Phys Rev Lett 58:571
8. Schmidt-Rohr K, Spiess HW (1994) Multidimensional solid-state NMR and polymers. Academic Press, London
9. Williams G, Watts DC (1970) Trans Faraday Soc 66:80
10. Williams G, Watts DC, Dev SB, North AM (1971) Trans Faraday Soc 67:1323
11. Johari GP, Goldstein M (1970) J Chem Phys 53:2372
12. Johari GP (1976) In: Goldstein M, Simha R (eds) The glass transition and the nature of the glassy state. Ann New York Acad Sci 279:117
13. Johari GP, Pathmanathan (1986) J Chem Phys 85:6811
14. Dixon PK, Wu L, Nagel SR, Williams, BD, Carini JP (1990) Phys Rev Lett 65:1108
15. Dixon PK (1990) Phys Rev B 42:8179
16. Dixon PK, Menon N, Nagel SR (1994) Phys Rev E 50:1717
17. Menon N, O'Brian KP, Dixon PK, Wu L, Nagel SR Williams BD, Carini JP (1992) J Non-Cryst Solids 141:61
18. Menon N, Nagel SR (1993) Phys Rev Lett 71:1095
19. Menon N, Nagel SR (1995) Phys Rev Lett 74:1230
20. Lunkenheimer P, Gerhard G, Drexler F, Böhmer R, Loidl A (1995) Z Naturforsch 50a:1151
21. Lunkenheimer P, Pimenov A, Schiener B, Böhmer R, Loidl A (1996) Europhys Lett 33:611
22. Lunkenheimer P, Loidl A (1996) J Chem Phys 104:4324
23. Lunkenheimer P, Pimenov A, Dressel M, Goncharev YG, Böhmer R, Loidl A (1996) Phys Rev Lett 77:318
24. Lunkenheimer P, Pimenov A, Loidl A (1997) Phys Rev Lett 78:2995
25. Lunkenheimer P, Pimenov A, Dressel M, Schiener B, Schneider U, Loidl A (1997) Progr Theor Phys Suppl 126:123
26. Lunkenheimer P, Schneider U, Brand R, Loidl A (1999) In: Tokuyama M, Oppenheim I (eds) Slow dynamics in complex systems: 8th Tohwa University International Symposium. AIP, New York, AIP Conf Proc 469:433
27. Schönhals A, Kremer F, Schlosser E (1991) Phys Rev Lett 67:999
28. Schönhals A, Kremer F, Hofmann A, Fischer EW, Schlosser E (1993) Phys Rev Lett 70:3459
29. Schönhals A, Kremer F, Stickel F (1993) Phys Rev Lett 71:4096
30. Schönhals A, Kremer F, Schlosser E (1993) Prog Colloid Polym Sci 91:39
31. Schönhals A, Kremer F, Hofmann A, Fischer EW (1993) Physica A 201:263
32. a. Stickel F, Fischer EW, Schönhals A, Kremer F (1994) Phys Rev Lett 73:2936; b. Stickel F, Fischer EW, Richert R (1995) J Chem Phys 102:6521; c. Hansen C (1997) Dissertation, Universität Mainz
33. Hofmann A, Kremer F, Fischer EW, Schönhals A (1994) In: Richert R, Blumen A (eds) Disorder effects on relaxational processes. Springer, Berlin Heidelberg New York, chap 10, p 309
34. a. Vogel H (1921) Phys Z 22:645; b. Fulcher GS (1923) J Am Ceram Soc 8:339; c. Tammann G, Hesse W (1926) Z Anorg Allg Chem 156:245

35. Angell CA (1985) In: Ngai KL, Wright GB (eds) Relaxations in complex systems. NRL, Washington, DC, p 3
36. Kauzmann W (1942) Rev Mod Phys 14:12
37. Zallen R (1983) The physics of amorphous solids. Wiley, New York
38. Kauzmann W (1948) Chem Rev 43:219
39. Johari G (2000) J Chem Phys 112:7518
40. Johari G (2000) J Chem Phys 113:751
41. Gibbs JH, DiMarzio EA (1958) J Chem Phys 28:373
42. Adam G, Gibbs JH (1965) J Chem Phys 43:139
43. Davidson DW, Cole RH (1951) J Chem Phys 19:1484
44. Dixon PK, Wu L, Nagel SR, Williams BD, Carini JP (1990) Phys Rev Lett 65:1108
45. Leheny RL, Nagel SR (1997) Europhys Lett 39:447
46. Kudlik A, Benkhof S, Blochowicz T, Tschirwitz C, Rössler E (1999) J Mol Struct 479:201
47. Chamberlin RV, Schiener B, Böhmer R (1997) Mat Res Soc Symp Proc 455:117
48. Chamberlin RV (1999) Phys Rev Lett 82:2520
49. Chamberlin RV (2002) Phase Transitions (in press)
50. Schneider U, Brand R, Lunkenheimer P (2000) Phys Rev Lett 84:5560
51. Döß A, Paluch M, Sillescu H, Hinze G (2002) Phys Rev Lett 88:095,701
52. Poley JP (1955) J Appl Sci B4:337
53. Johari GP (2002) J Non-Cryst Solids (in press)
54. Fujara F, Geil B, Sillescu H, Fleischer G (1992) Z Phys B88:195
55. Karpov VG, Klinger MI, Ignatiev FN (1983) Sov Phys JETP 57:439
56. Buchenau U, Galperin YM, Gurevich VL, Parshin DA, Ramos MA, Schober HR (1992) Phys Rev B 46:2798
57. Elliot SR (1992) Europhys Lett 19:201
58. Malinovsky VK, Novikov VN, Sokolov AP (1987) J Non-Cryst Solids 90:485
59. Schirmacher W, Diezemann G, Ganter C (1998) Phys Rev Lett 81:136
60. Fischer EW (1993) Physica A 201:183
61. Patkowski A, Thurn-Albrecht T, Banachowicz E, Steffen W, Bösecke PT, Narayanan T, Fischer EW (2000) Phys Rev E 61:6909
62. Tracht U, Wilhelm M, Heuer A, Feng H, Schmidt-Rohr K, Spiess HW (1998) Phys Rev Lett 81:2727
63. Schiener B, Böhmer R, Loidl A, Chamberlin RV (1996) Science 274:752
64. Richert R (1997) J Phys Chem B101:6323
65. Cicerone MR, Ediger MD (1993) J Phys Chem 97:10,489
66. Sillescu H (1999) J Non-Cryst Solids 243:81
67. Ediger MD (2000) Annu Rev Phys Chem 51:99; Böhmer R (1998) Curr Opin Solid State Mat Sci 3:378
68. Angell CA (1997) Physica D 107:122
69. Stillinger FH (1995) Science 267:1935
70. Debenedetti PG, Stillinger FH (2000) Nature 410:259
71. Doolittle AK (1951) J Appl Phys 22:1471
72. Cohen MH, Turnbull D (1959) J Chem Phys 31:1164
73. Cohen MH, Grest GS (1979) Phys Rev B 20:1077
74. Donth EJ (1981) Glasübergang. Akademie Verlag, Berlin
75. a. Donth EJ (1992) Relaxation and thermodynamics in polymers, glass transition. Akademie Verlag, Berlin; b. Donth EJ (2001) The glass transition. Springer, Berlin Heidelberg New York
76. Donth E (1982) J Non-Cryst Solid 53:325
77. Schneider K, Schönhals A, Donth E (1981) Acta Polym 32:471
78. Donth E, Hempel E, Schick C (2000) J Phys:Cond Mat 12:L281
79. Donth E, Huth H, Beiner M (2001) J Phys:Cond Mat 13:L451
80. Kirkpatrick TR, Tirumalai D (1989) Phys Rev A 40:1045
81. Leutheuser E (1984) Phys Rev A 29:2765
82. Bengtzelius U, Götze W, Sjölander A (1984) J Phys C 17:5915

83. Götze W (1985) Z Phys B 60:195
84. Götze W, Sjögren L (1992) Rep Prog Phys 55:241
85. Williams G, Fournier J (1996) J Chem Phys 104:5690
86. Schönhals A (2001) Europhys Lett 56:815
87. Havriliak S Jr, Havriliak SJ (1997) Dielectric and mechanical relaxation in materials. Hauser Pubishers, Munich
88. Götze W, Sjögren L (1991) J Non-Cryst Solids 131:161
89. Elisson H, Mellander B-E, Sjögren L (1998) J Non-Cryst Solids 235/237:101

5 Glassy Dynamics Beyond the α-Relaxation

P. Lunkenheimer · A. Loidl

5.1
Introduction

Glassy materials have been used by man since prehistoric times [1, 2] and nowadays are ubiquitous in our daily live. There are of course the classical technical applications in, e.g. architecture (windows), for containers or for optical components. However, recently glassy materials have also gained increasing importance in quite different fields, e.g. communication technique (optical fibres) or medicine (bioactive implants). The modern definition of glass as a non-crystalline solid includes also the large group of the polymers and glass ceramics, but also more exotic materials as amorphous metals, which are believed to have a great technological future. Glasslike behaviour is also found in some crystalline materials, the so-called plastic crystals and orientational glasses, which at low temperatures are characterized by static disorder with respect to the *orientational* degrees of freedom of the translationally ordered molecules [3]. These materials are often considered as model systems for "conventional" glass formers and they are much simpler to treat in theoretical and simulation approaches to the glassy state.

Despite a long history of investigation of glassy materials and of the transition from the liquid to the glassy state, our physical understanding of this phenomenon is poor and commonly considered as one of the great unresolved problems of condensed matter physics [4–7]. However, during recent years significant theoretical and experimental advances have led to a renewed interest in the physics of glasses, giving rise to the hope that a breakthrough in the understanding of the glassy state may be within reach in the near future. Most of the recent experimental studies of this topic focus on the *dynamic* behaviour of glass formers and their high-temperature precursors, the supercooled liquids. Glassy dynamics exhibits some very intriguing phenomena whose explanation is a challenge for any theory of the glassy state and the glass transition. For example, going from the liquid to the glassy state, the α-relaxation time, characterizing the structural relaxation, changes continuously over many orders of magnitude (Chap. 4) and it is a major challenge to experimentalists to follow this huge change from the glass to the liquid state. Stimulated by various new theoretical and phenomenological approaches of glassy dynamics, in recent years the scientific interest has started to focus on the dynamic processes prevailing at timescales *shorter* than that of the α-relaxation, e.g. the excess wing or the fast

β-process (see below). Glassy dynamics, including those fast processes, are also of great technological importance. For example, so-called aging effects, i.e. time-dependent changes of the properties, can affect the long-time performance of polymer-based data-storage media. The abovementioned fast processes are of relevance in the development of low-loss and low-dielectric-constant materials for applications in high-frequency communication electronics.

Dielectric spectroscopy is one of the most commonly used techniques for the investigation of the dynamic response of glass-forming materials [e.g., 8–15]. An exceptionally broad frequency range is accessible with this method, which makes it an ideal tool to follow the α-relaxation dynamics during its many decade change from T_g, deep into the liquid state (Chap. 4). Moreover, all the additional contributions beyond the α-relaxation can be detected in broadband dielectric spectra of glass-forming materials. In dielectric loss spectra of many glass-forming materials, some decades above the α-peak frequency ν_p, an excess wing (also called "high-frequency wing") shows up as an excess contribution to the high-frequency flank of the α-peak [9, 12, 16–19]. Some intriguing scaling properties of α-peak and excess wing were found by Nagel and co-workers [9]. Despite some theoretical approaches describing the excess wing being proposed [20–22], up to now there is no commonly accepted explanation of its microscopic origin. In many glass-forming materials, besides the α-peak, further relaxation processes lead to additional peaks or shoulders in $\varepsilon''(\nu)$, usually located in the kHz–MHz region. They are termed β-relaxations (or γ, δ, … relaxations if there are more than one), sometimes with the addition "slow" to avoid confusion with the fast β-process of mode-coupling theory (see below). It was proposed that the occurrence of β-relaxations is an inherent property of the supercooled state [23, 24] but their microscopic origin is still a matter of controversy.

The interest in even higher frequencies in the GHz-THz region was mainly stimulated by the mode-coupling theory (MCT) of the glass transition [25–28], which is currently the most promising, but also most controversially discussed theoretical approach of the glass transition. MCT rationalises the glass transition in terms of a dynamic phase transition at a critical temperature T_c, significantly *above* T_g, in marked contrast to the "phase transition" at the Vogel-Fulcher temperature $T_{VF} < T_g$ suggested by the Vogel-Fulcher-Tammann (VFT) behaviour of the α-relaxation time (Chap. 4). In the relevant temperature region, the α-relaxation dynamics are rather fast ($\tau \approx 10^{-10}$ to 10^{-6} s). In addition, for the 10^{-12} to 10^{-9} s time window, MCT predicts an additional contribution, now commonly termed the fast β-process. In addition, various competing theories have appeared, e.g. the coupling model (CM) [29–31], the frustration-limited domain (FLD) theory [22, 32] and the model of dynamically correlated domains [20]. Fast processes are also predicted in the CM and in a recent extension of the dynamically correlated domain model using the Weiss mean-field theory [21] and they are also believed to play a role in the FLD theory [22]. In addition, in a recently proposed model fast processes are considered as the relaxation-like part of vibrational excitations [33]. The most prominent methods used up to now to investigate the region of the predicted fast processes are neutron and light scattering (see, e.g. [34–38]). Unfortunately, until recently, this region lay just at the high frequency edge (about 10 GHz) of the range available even in very well

equipped dielectric laboratories (but see, e.g. [14]). However, recent experimental advances [39–41] made it possible to obtain continuous dielectric spectra on glass-forming materials extending well into the relevant region [42–45] and the detection of fast processes in dielectric spectra of glass-forming materials is now well established [15, 46, 47].

From light and neutron scattering experiments it is well known that at some THz the so-called boson peak occurs in the scattering function of glass-forming materials, which is directly related to the imaginary part of the susceptibility χ''. The boson peak is also detectable by dielectric spectroscopy using infrared techniques [e.g. 46–55]. A variety of explanations of the boson peak have been proposed [e.g. 56–61]. While it seems likely that vibrational excitations are responsible for the boson peak, until now no consensus on a detailed microscopic explanation of this feature was achieved.

The topic of the present chapter will be the dynamic processes taking place at time scales significantly shorter than that of the α-process, including the excess wing, the slow β-process, the fast β-process and the boson peak. All these processes, which seem to be more or less universally present in glassy materials, have found considerable experimental and theoretical interest during recent years and it is commonly felt that the explanation of these phenomena is a prerequisite for the understanding of the glass transition. Some of the presented dielectric spectra cover a frequency range of nearly 19 decades. Only this extremely broad dynamic window available in dielectric spectroscopy allows for the investigation of this large variety of dynamic processes using one experimental probe only.

5.2
Dynamic Processes in Glass-Forming Materials

In this section an overview of the various dynamic features observed in dielectric spectra of glass-forming materials will be given. Figure 5.1 represents a schematic plot of broadband loss spectra demonstrating the most common contributions for two typical cases of glass-forming materials [15]. The α-process leads to a dominant loss peak at $v_p \approx v_\tau = 1/(2\pi \langle \tau_\alpha \rangle)$, with $\langle \tau_\alpha \rangle$ the average α-relaxation time. Figure 5.1 depicts the situation near T_g, with the α-peak situated at a rather low frequency. With increasing temperature it will rapidly shift to higher frequencies. As mentioned in the introduction, in addition to the α-relaxation, a variety of other features show up in broadband dielectric spectra of glasses and supercooled liquids as indicated in Fig. 5.1. It should be noted that the amplitudes of all these processes beyond the α-process are rather small compared to the dominating α-peak. Nevertheless they have attracted considerable interest in recent years and the understanding of their microscopic origin is considered as a prerequisite for a thorough understanding of the glass transition and glass state.

If mobile charge carriers are present, conductivity contributions lead to a divergence of $\varepsilon''(v)$ for low frequencies ($\varepsilon'' \sim \sigma'/v$, Chap. 1). Their amplitude can vary extremely for different glass formers and in some cases can completely suppress other features in the spectra. Because of this non-universal nature of conductivity contributions, they have been omitted in Fig. 5.1.
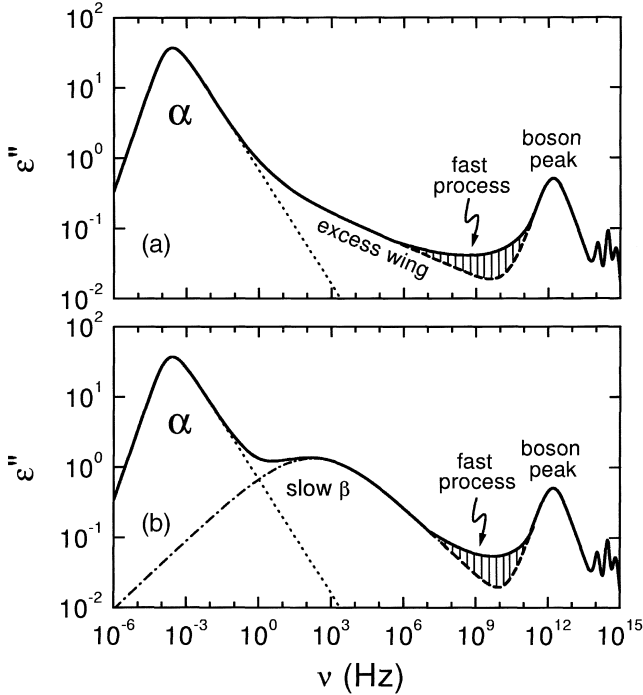
Fig. 5.1. Schematic view of the frequency dependent dielectric loss in glass-forming materials as observed in extremely broadband measurements [15]. Two typical cases are shown, namely the response of: **a** glass formers showing an excess wing; **b** glass formers with a well resolved β-relaxation peak. The possible contribution of an additional fast process in the minimum region preceding the boson peak is indicated by the *hatched area*

At frequencies some decades above ν_p the empirical functions used for the description of the α-peak (Chap. 3) fail and in many glass formers an "excess wing" shows up (Fig. 5.1a). It can be reasonably well described by a second power law, $\varepsilon'' \sim \nu^{-b}$ with $b < \beta$ [12, 17–19, 62], in addition to the power law $\nu^{-\beta}$, commonly found at $\nu > \nu_p$. This excess contribution was already noted in the early work of Davidson and Cole [16] and was found in a variety of glass-forming materials [9, 12, 17–19]. Some microscopic explanations for its occurrence have been proposed in [20–22]. A very interesting property of the excess wing was found by Nagel and co-workers [9]: by an appropriate scaling of the axes, it is possible to collapse the $\varepsilon''(\nu)$-curves, including the excess wing, for different temperatures and even for different materials onto one master curve. This finding led to the notion that the excess wing is part of the α-relaxation. The applicability of this so-called Nagel scaling has been controversially discussed during recent years [63–73]. Many efforts have been made to check for its validity in a variety of materials [e.g. 63, 64, 66, 68, 69, 74, 75]. Moreover, using low-temperature extrapolations based on these scaling properties, the approach of $b = 0$ for a temperature near T_{VF} was proposed [13]. It was argued that this constant loss

behaviour could imply a divergence of the static susceptibility, supporting speculations about a phase transition near T_{VF} [13].

In many glass-forming materials, a slow β-relaxation shows up as indicated in Fig. 5.1b. By considering the detailed molecular structure of a material, β-processes sometimes can be ascribed to an internal change of the molecular conformation, e.g. the movement of a molecular side group in a polymer. However, Johari and Goldstein [23, 24] demonstrated that secondary relaxation processes are a rather universal property of glass formers and also show up in relatively simple molecular glass formers, where intramolecular contributions seem unlikely. Also in polymers without rotatable side groups β-processes were found [10]. This led to the notion that these so-called Johari-Goldstein β-relaxations may be inherent to glass-forming materials in general [23, 24]. However, the microscopic processes behind this kind of β-relaxations are still controversially discussed (see, e.g. [19]). It is commonly assumed that the excess wing and the Johari-Goldstein β-relaxations are due to different processes [9, 19] and even the existence of two classes of glass-formers was suggested – "type A" without a β-process but showing an excess wing (corresponding to Fig. 5.1a) and "type B" with a β-process (Fig. 5.1b) [19]. While this classification will be used in the further course of the present chapter, to denote quickly systems with clear excess wing or β-relaxation, however, one has to state clearly that it may be somewhat oversimplifying: There are examples that do not fit into this scheme, e.g. in [19] the simultaneous occurrence of both features in one material was proposed and also Salol (Chap. 4) and ethanol (Sect. 5.4.2) are difficult to be clearly classified as Type A or B. In addition, it seems possible that excess wing and β-relaxation are due to the same microscopic process [12, 76–80]. From an experimental point of view, recently some strong hints have emerged that the excess wing is simply the high-frequency flank of a β-peak, hidden under the dominating α-peak [81].

At some THz a second loss peak shows up that can be identified with the so-called boson peak known from neutron and light scattering [35, 37]. The boson peak is a universal feature of glass-forming materials [46–55] and corresponds to the commonly found excess contribution in specific heat measurements at low temperatures [2, 82]. A variety of explanations of the boson peak has been proposed, e.g. in terms of the soft potential model [56, 57], phonon localization models [58, 59], or a model of coupled harmonic oscillators with a distribution of force constants [60]. The occurrence of the boson peak was also modelled within the MCT [61]. The term "boson peak" is originally defined for the scattering function S, which, by means of the fluctuation-dissipation theorem [83], is in good approximation connected to the imaginary part of the susceptibility via $\chi'' = \varepsilon'' \sim S\nu$. However, often the term "boson peak" is also used for the corresponding peak in $\chi''(\nu)$ and this notation will be followed in the present work. Its name originates from the temperature dependence of its intensity, observed in the scattering experiments, which can be explained assuming Bose-Einstein statistics. It should be noted that it has been known for many decades [84] that dipolar liquids show an infrared absorption-peak in the THz region, termed Poley absorption [85, 86]. It was interpreted in terms of librational motions of the dipoles [87, 88]. One has to be aware that the boson peak, defined in $S(\nu)$,

may correspond to a shoulder only in the absorption $\alpha(\nu)$, which is roughly proportional to $S\nu^2$. Nevertheless it seems likely that Poley absorption and the boson peak are due to the same microscopic process [53, 54].

Between the α-peak and the boson peak, obviously a minimum in $\chi''(\nu)$ must exist, as found in a variety of scattering experiments and recently also in extreme broadband dielectric experiments [e.g. 14, 42, 44, 45]. As mentioned in the Introduction, the interest in this region was mainly stimulated by the MCT [25–28], which predicts that a fast process (called *fast* β-relaxation, to distinguish it from the *slow* Johari-Goldstein β-relaxation) will lead to significant additional contributions in this minimum region. The experimental results indeed provide evidence for a fast process in this region, as the spectral response near the minimum cannot be explained assuming a simple superposition of α-peak (including excess wing) and boson peak. This is schematically indicated by the hatched area in Fig. 5.1a,b.

Finally, in the infrared region various resonance-like features can be expected, which are due to phonon-like modes and vibrational and rotational excitations of the molecules. These features are totally decoupled from the glass transition and not further considered in the present work.

5.3
Broadband Dielectric Spectra of Glass-Forming Materials

In the present section we will show dielectric spectra on a variety of materials that are typical members of different classes of glass formers and summarize the main experimental findings. Most of these results have been published previously [15, 42–47, 62, 66, 67, 69, 81, 89–94]. In the following sections the processes beyond the α-relaxation will be discussed in more detail.

Broadband dielectric spectra are provided for the molecular glass formers glycerol ($T_g \approx 185$ K), propylene carbonate (PC, $T_g \approx 159$ K), and ethanol ($T_g \approx 97$ K) and for the ionically conducting glass-former $[Ca(NO_3)_2]_{0.4}[KNO_3]_{0.6}$ (CKN, $T_g = 333$ K). These materials can easily be vitrified and have glass transition temperatures that lie in a convenient temperature region (150 K–350 K). They cover a rather wide range of fragilities in the "strong-fragile" classification scheme introduced by Angell [95]. Glycerol, PC and CKN are among the most thoroughly investigated glass formers. In addition, we will show spectra for the plastic crystal *ortho*-carborane, in which the plastic phase also can be supercooled. The molecules of o*rtho*-carborane and the investigated molecular glass formers have relatively large dipolar moments, which is a prerequisite for dielectric measurements. In CKN, the dielectric experiments directly couple to the ionic conductivity as elaborated in more detail below.

In Figs. 5.2 and 5.3, spectra of the real part of the dielectric function ε' and the dielectric loss ε'' of glass-forming glycerol and PC are shown for various temperatures. Both materials are low molecular-weight organic glass formers with relatively simple molecular structure, a group of materials that is often chosen for experimental investigations of glassy dynamics. While for PC intermolecular interactions are mainly due to the relatively weak van der Waals forces, the hy-
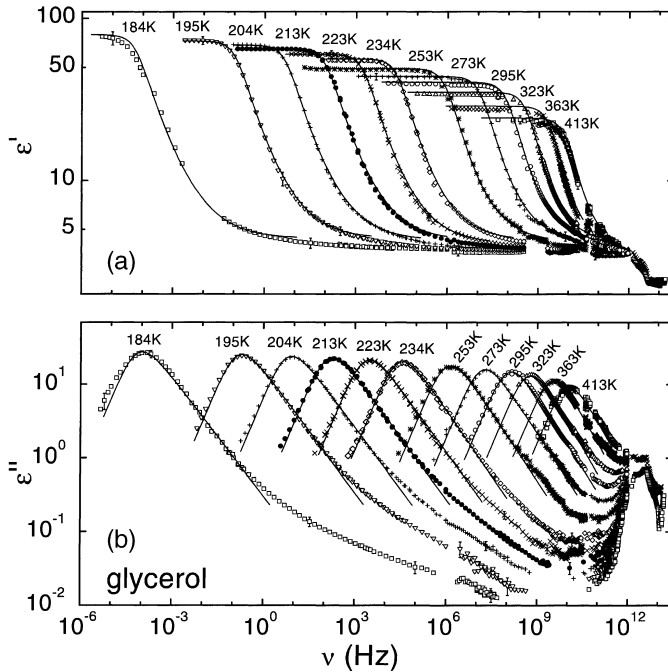
Fig. 5.2. Frequency dependence of the real **a** and the imaginary part **b** of the dielectric permittivity in glycerol at various temperatures [17, 42, 46, 94]. The *lines* are fits of the region near v_p with the CD function, performed simultaneously on ε' and ε''

drogen bonds in glycerol lead to the formation of a molecular network. PC is a rather fragile glass former (fragility parameter[1] $m = 104$ [96]); glycerol ($m = 53$ [96]) can be characterized as moderately strong. Despite these differences, the permittivity spectra of both materials look qualitatively similar: The spectra of $\varepsilon''(v)$ (Figs. 5.2b and 5.3b) follow the schematic behaviour of Fig. 5.1a, i.e. they are typical "type A" glass formers in the classification scheme of [19]. $\varepsilon''(v)$ exhibits asymmetrically shaped α-relaxation peaks. They are accompanied by relaxation steps in $\varepsilon'(v)$ as seen in Figs. 5.2a and 5.3a. Changing the temperature by about a factor of two, both features shift by 14 decades of frequency, which mirrors the dramatic slowing down of the structural α-dynamics during the transition from the low-viscosity liquid to the glass. The regime around v_p can be described by the Cole-Davidson (CD) function (Chap. 3), as shown by the lines in Figs. 5.2 and 5.3. A more detailed treatment of the α-relaxation dynamics revealed by these results can be found in [15, 47, 92].

At frequencies $v > v_p$, $\varepsilon''(v)$ follows a power law $\varepsilon'' \sim v^{-\beta}$. At higher frequencies deviations from this power law occur. At high temperatures ($T \geq 273$ K for glycerol, $T \geq 203$ K for PC), $\varepsilon''(v)$ shows a smooth transition into a minimum. At lower temperatures an excess wing develops showing up as a second power law,

---

[1] The fragility parameter is defined by $m = \mathrm{d}\log\tau/\mathrm{d}(T_g/T)$ at $T = T_g$ [96].
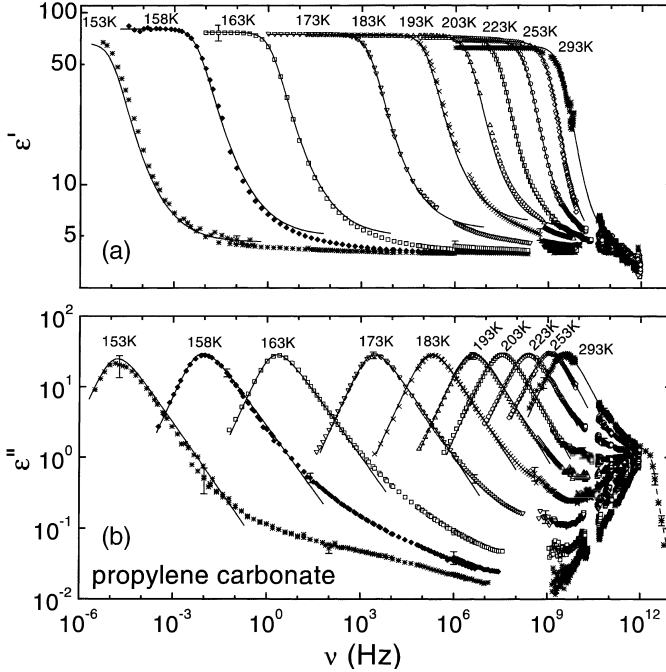
Fig. 5.3a,b. Frequency dependence of the real **a** and the imaginary part **b** of the dielectric permittivity in PC at various temperatures [45, 47]. The *solid lines* are fits of the region near ν_p with the CD function, performed simultaneously on ε' and ε''. The *dashed line* in the boson peak region is drawn to guide the eyes

ν^{-b} with $b < \beta$ before the minimum region is reached. The exponent b increases with increasing temperature and at high temperatures the excess wing seems to merge with the α-peak. The excess wing is accompanied by an additional decrease in $\varepsilon'(\nu)$. This can be inferred from the overestimation of the value of ε_∞ by the fits with the CD function in Figs. 5.2a and 5.3a. The excess wing will be discussed in detail in Sect. 5.4.

In the GHz-THz frequency region a minimum in $\varepsilon''(\nu)$ is observed for both materials. With decreasing temperature, its amplitude and frequency position decreases and it becomes significantly broader. In this region there is evidence for an additional contribution by a fast process as will be discussed in detail in Sect. 5.5.1. For glycerol, in the THz region a peak shows up. The peak frequency is temperature independent within the experimental error; its amplitude increases weakly with temperature. Corresponding to the peak in $\varepsilon''(\nu)$, $\varepsilon'(\nu)$ exhibits a step-like decrease near 1 THz (Figs. 5.2a and 5.3a). For 363 K no minimum and no peak but only a shoulder is detected, due to the close vicinity of α- and THz-peaks. The situation is similar in PC at 293 K. Despite that in PC the THz-region has been investigated at room temperature only, it can be anticipated that at lower temperatures the shoulder will develop into a peak too. In both materials this peak is located at the same frequency as that found in $\chi''(\nu)$ from light and neutron scattering experiments [97–99] (see Sect. 5.5.2) and
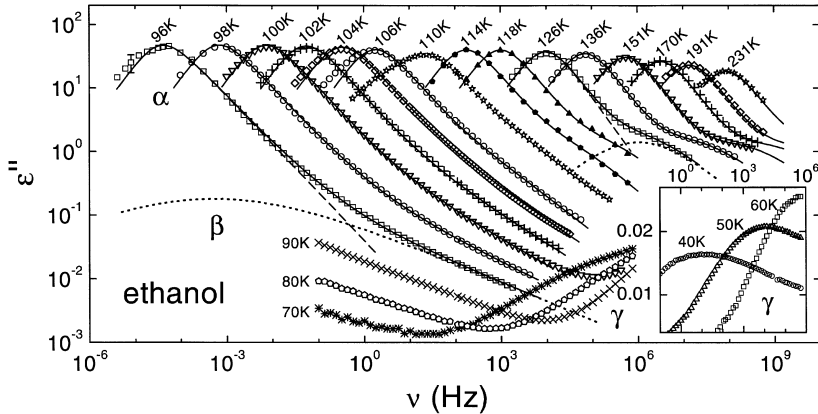
Fig. 5.4. Frequency dependent dielectric loss of glass-forming ethanol for various temperatures [93]. The *solid lines* are fits with the sum of a CD and a CC function, performed simultaneously for ε'' and ε' (not shown). For 96 K and 126 K, the *dashed lines* show the two constituents of the fits. The *inset* gives a separate view of the low-temperature results. (From [93]. Copyright (2000) by the American Physical Society)

thereby can be identified with the boson peak. It should be noted that the increase of $\varepsilon''(\nu)$ towards the boson peak is much steeper in glycerol than in PC. A more detailed discussion of the boson peak will be given in Sect. 5.5.3. In glycerol at frequencies around 10 THz some resonance-like features appear, which mark the onset of the regime of intramolecular excitations.

In Fig. 5.4, dielectric loss spectra of glass-forming ethanol are shown for various temperatures [93]. Ethanol ($m = 52$ [100]) belongs to the group of primary alcohols. In primary alcohols, due to the single hydroxyl group, no network can be formed and most likely in the liquid and glassy states the molecules form short chains with varying length [101, 102]. The recent scientific interest in glass-forming ethanol was stimulated by the fact that it can be prepared both in a structurally disordered glass and in an orientationally disordered, plastic crystalline state. Various experimental investigations of both states of ethanol [103–108] have enhanced our understanding of the importance of orientational degrees of freedom, also in structurally disordered supercooled liquids and glasses. In the context of the present work, glass-forming ethanol is of interest due to its interesting excess wing properties [93]. In Fig. 5.4 at temperatures 96 K $\leq T \leq$ 106 K the typical excess wing is observed and at first glance ethanol seems to be another example of a typical "type A" glass former [107, 108]. However, the high frequency measurements above 1 MHz reveal a shoulder in the excess wing region. This result strongly suggests that the excess wing in ethanol is in fact due to a β-relaxation process. This finding will be discussed further in Sect. 5.4.2. In addition, at low temperatures and frequencies above the excess wing region, $\varepsilon''(\nu)$ starts to rise again and finally, below 60 K, a second relaxation peak shifts into the frequency window [107, 108] (inset of Fig. 5.4). Overall one has three relaxation processes in glass-forming ethanol – the α-process, a β-process causing the excess wing and a low temperature γ-process.
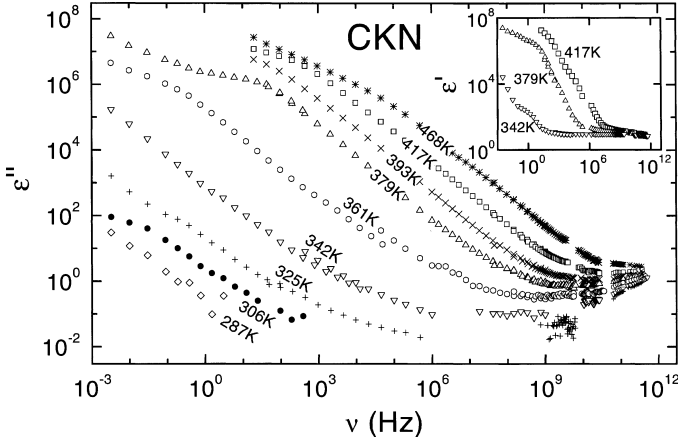
Fig. 5.5. Dielectric loss of CKN for various temperatures [43, 44, 92]. The inset shows $\varepsilon'(\nu)$ for three temperatures

However, it should be mentioned that in other primary alcohols three relaxation processes have been detected too [109–111] and that, e.g. in 1-propanol the dominating relaxation peak was assumed not to be connected with the structural α-relaxation (for a more detailed discussion see [93]). As measurements of supercooled ethanol in the submillimeter and infrared region have not been performed yet, no information about the minimum and boson peak is available for this material.

Figure 5.5 shows the dielectric loss spectra of glass-forming CKN for various temperatures. CKN ($T_g = 333$ K, $m = 94$) is a typical ionically conducting glass former. Its dielectric loss spectra are dominated by a huge increase towards low frequencies. This behaviour can be ascribed to conductivity contributions from ionic transport. If, e.g. a frequency-independent conductivity, $\sigma(\nu) = \sigma_{dc}$, is assumed, $\varepsilon'' \sim \sigma_{dc}/\nu$ is expected. At the lowest frequencies the high-temperature curves show a transition to a weaker frequency dependence. This is a common behaviour for ionic conductors and ascribed to electrode polarization effects ("blocking electrodes") [112, 113]. Electrode polarization also leads to very large values of ε' for low frequencies as seen in the inset of Fig. 5.5. There are various theoretical models of ionic conductivity that also make distinct predictions on its frequency dependence [e.g. 114–117]. In [118] conductivity data on CKN were analysed in terms of the "jump-relaxation model" [116, 117] and indeed a good agreement with theoretical predictions was stated. In the present work, we refrain from a detailed analysis of the ionic conductivity in CKN. At high frequencies, the conductivity contribution is of less importance. Here, $\varepsilon''(\nu)$ in CKN has a shallow minimum, similar to the findings in the molecular glass-formers glycerol and PC (Figs. 5.2b and 5.3b).

As discussed in Chap. 3, the use of the modulus representation was proposed [112] to suppress the contributions from conductivity and electrode polarization. In Fig. 5.6 the imaginary part of the electric modulus is shown for various
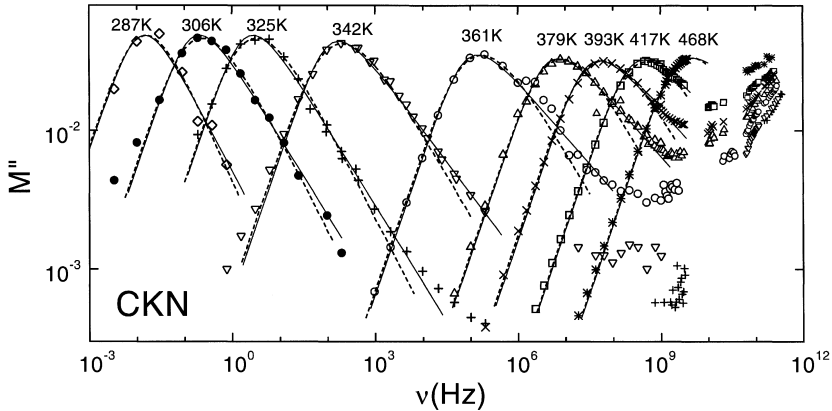
Fig. 5.6. Imaginary part of the electric modulus of CKN for various temperatures [43, 92]. The *solid lines* are fits of the α-peak with the CD function, the *dashed lines* are fits with the Fourier transform of the KWW law

temperatures as calculated from the measured $\varepsilon'(v)$ and $\varepsilon''(v)$. Figure 5.6 reveals overall characteristics, quite similar to that found in the molecular glass formers, Figs. 5.2–5.4. Well pronounced α-peaks show up and a minimum is revealed at high frequencies. The high-frequency deviations from the CD-fits (solid lines), seen, e.g. at 325 K, may also indicated the presence of an excess wing. In addition to the CD-fits, fits with the Fourier transform of the KWW-function are also included in Fig. 5.6 (dashed lines), which lead to a somewhat better description near the peak, but exhibit stronger deviations at high frequencies. More information on the α-process in CKN can be found in [43, 92]. The results in the minimum region will be discussed in Sect. 5.5.1. In Fig. 5.6 infrared data are missing and therefore the boson peak is not seen. Infrared data on CKN, up to 1.5 THz, were reported in [14] and indeed a saturation of $\varepsilon''(v)$ at highest frequencies, indicative of the presence of a boson peak was observed.

In Fig. 5.7 the frequency dependent dielectric loss of plastic-crystalline *ortho*-carborane is shown. In plastic crystals (also called rotor crystals or glassy crystals) the centres of mass of the molecules form a regular crystalline lattice but the molecules are disordered with respect to the orientational degrees of freedom. The carborane molecule, $B_{10}C_2H_{12}$, forms an almost regular shaped icosahedron whose corners are occupied by ten boron and two carbon atoms. The icosahedron is surrounded by 12 outward-bonded hydrogen atoms. For *ortho*-carborane the two carbon atoms occupy adjacent positions. Overall, the carborane molecules are nearly spherically shaped and therefore experience little steric hindrance for reorientational processes, thus favouring the forming of a plastic-crystalline phase. Near 275 K, *ortho*-carborane undergoes a phase transition where the reorientational motion is partly restricted [119–123]. The complete orientational order reported at $T \leq 165$ K [121, 124] can be easily suppressed by moderate cooling rates, i.e. the spectra at $T \leq 165$ K have been measured in a supercooled orientationally disordered state. From the temperature
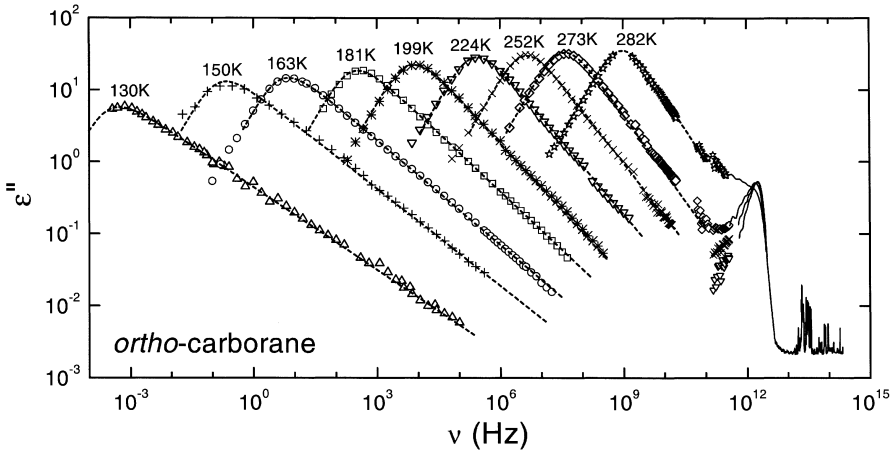
Fig. 5.7. Dielectric loss of *ortho*-carborane for various temperatures [66, 67, 100, 139]. To maintain readability, at $\nu > 400$ MHz the data are shown as *solid lines* and at $\nu > 3$ THz only data for 282 K are shown. The *dashed lines* are fits of the α-peak with the CD function

dependence of the α-relaxation time [89] and from calorimetric [124] measurements a "glass" temperature, $T_g \approx 134$ K can be deduced.

The spectra in Fig. 5.7 reveal well developed α-relaxation peaks, shifting through the frequency window with temperature. However, there is no trace of an excess wing or a β-peak! In contrast, the high frequency power law of the α-peaks extends over up to eight decades of frequency. The dashed lines are fits with the CD-function, which leads to a very good description of the data up to 10 GHz. More details on the α-relaxation in *ortho*-carborane can be found in [89]. Similar to the structurally disordered materials (Figs. 5.2, 5.3 and 5.5), $\varepsilon''(\nu)$ of *ortho*-carborane exhibits a minimum near some 100 GHz. In addition, a nearly temperature independent peak near 2 THz shows up, in analogy to the boson peak observed in the structural glass formers glycerol and PC (Figs. 5.2 and 5.3). These high-frequency features will be discussed in Sect. 5.5. Finally, at frequencies above 10 THz sharp resonance-like peaks show up which can be ascribed to intramolecular excitations of the carborane molecule [119].

Overall, the dielectric loss spectra presented in this section reveal a variety of features that seem to be common to all supercooling materials: the α-relaxation peak, the minimum, the excess wing (with the exception of the plastic-crystalline *ortho*-carborane) and the boson peak. In the following sections the latter three features will be discussed in more detail.

5.4
The Excess Wing

As noted in Sect. 5.3, a well developed excess wing shows up in the spectra of glycerol and PC (Figs. 5.2 and 5.3). In contrast, this feature is only weakly seen in

the modulus spectra of CKN (Fig. 5.6). In ethanol (Fig. 5.4) it is obviously due to a β-relaxation and in the plastic crystalline *ortho*-carborane there is no excess wing at all (Fig. 5.7). Therefore in the following we will mainly discuss the results in glycerol and PC.

5.4.1
Scaling and Divergent Susceptibility

As mentioned in Sect. 5.2, it has been demonstrated [9] that the excess wing and α-peak region in the dielectric loss spectra of many glass-forming liquids exhibit quite intriguing scaling properties. Nagel and co-workers found that the $\varepsilon''(\nu)$-curves for different temperatures and different materials, including the wing, can be scaled onto one master curve by plotting $Y := w^{-1} \log_{10} [\varepsilon'' \nu_p /(\Delta\varepsilon\, \nu)]$ vs $X := w^{-1}(1 + w^{-1}) \log_{10} (\nu/\nu_p)$. Here w denotes the half-width of the loss peak, normalized to that of the Debye-peak, ν_p is the peak frequency and $\Delta\varepsilon$ the relaxation strength. One has to state clearly that the Nagel-scaling is phenomenological with no underlying physical model. In addition, during the last years some criticism of the Nagel-scaling arose concerning its validity [63–67] and accuracy [64, 65, 68, 69] and also some minor modifications of the original scaling procedure have been proposed [64]. Nevertheless, it is clear that the Nagel scaling indeed works quite well in many materials.

As an example, in Fig. 5.8 the Nagel scaling is applied to the loss data in glycerol and PC shown in Figs. 5.2 and 5.3. To maintain readability, for each material curves for three different temperatures only are shown. In addition, only data points up to the onset of the $\varepsilon''(\nu)$ minimum are included. The present data have not been corrected for conductivity contributions, the correct procedure being controversially discussed in the context of small deviations from a master curve, reported for low values of X [70–73]. Figure 5.8 reveals a good scaling of the data in glycerol and PC up to $X \approx 9$. Only at very high values of X, small deviations from a single master curve show up (inset), admittedly of somewhat restricted significance (see error bars in the inset of Fig. 5.8). Further broadband mea-

Fig. 5.8. Frequency dependent dielectric loss of glycerol at 195 K, 223 K and 363 K (*circles*) and PC at 158 K, 173 K and 253 K (*triangles*) [69], scaled according to Nagel and co-workers [9]. For the meaning of the axes, see text. The *inset* shows a magnified view of the high-frequency region. (From [69] with permission from Taylor and Francis Ltd., www.tandf.co.uk/journals)
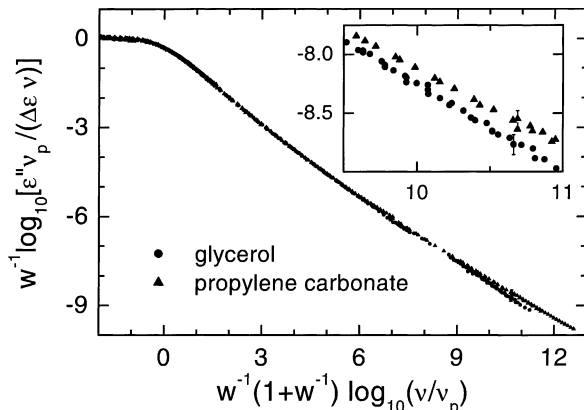
surements in other glass-forming liquids shall clarify if these deviations indicate a general failing of the Nagel-scaling at high frequencies.

The presence of a second power law, $\varepsilon'' \sim \nu^{-b}$, at the high frequency flank of the α-peak is a prerequisite for the applicability of the Nagel scaling. Therefore the ethanol data of Fig. 5.4 at $T \geq 126$ K that reveal a clear shoulder cannot be scaled in this way. However, the low-temperature data also cannot be scaled [93] and ethanol seems to be an example of a glass-forming liquid where the Nagel scaling clearly fails. The spectra of plastic crystalline *ortho*-carborane (Fig. 5.7) also do not follow the Nagel scaling as was demonstrated in [67, 69]. This behaviour is due to the complete absence of the excess wing in this material, also corroborated by recent NMR experiments [125]. Interestingly it was found that the excess wing is absent in various other plastic crystals, too [66, 100]. Up to now, to our knowledge there is only one report of the successful scaling of dielectric loss data in a plastic crystal (cyclo-octanol) [75]. However, it was shown [126] that in cyclo-octanol the apparent excess wing was due to a secondary relaxation. Only if data up to sufficiently high frequencies are used are deviations from the ν^{-b} power law detected [126] and a failing of the scaling revealed [67]. Overall the excess wing in its original sense – a second high-frequency power law as part of the α-peak – seems to occur in structurally disordered materials only. However, even there this notion can be doubted as will be seen in Sect. 5.4.2.

The scaling of α-peak and excess wing in various glass-forming liquids suggests a close correlation of both features. Especially, making certain assumptions, it was suspected [13, 18] that the wing exponent b should become zero for a limiting relative half width $w \approx 2.6$ or an α-peak exponent $\beta \approx 0.38$. Interestingly such a constant loss behaviour at high frequencies and low temperatures was already predicted by Angell and co-workers [55, 127, 128], based on an interpolation of conductivity results from low frequency dielectric spectroscopy and far-infrared experiments. By a low-temperature extrapolation of $w(T)$ and $b(T)$ curves of various glass formers, Nagel and co-workers argued, that a constant loss should be reached near the Vogel-Fulcher temperature T_{VF} [13, 18]. If one assumes that the excess wing is a part of the α-peak, such a behaviour would imply a divergence of the static susceptibility, which is proportional to the area under the α-peak. This would support speculations about a phase transition from the liquid to the glass state, underlying the glass transition. However, in the next section we will show that it is not so clear that the excess wing is caused by the same dynamic process as the α-peak. In addition, one has to be aware that there are problems concerning the Kramers-Kronig consistency of a constant loss behaviour and that one may expect a "nearly constant loss" at best.

In Fig. 5.9 the present data on glycerol and PC are checked for a possible development of the excess wing into a constant loss near T_{VF}. The open circles show the parameter β_{CD} from the fits of the α-peak with the CD-function (Figs. 5.2 and 5.3), which gives a good estimate of the frequency exponent β at $\nu > \nu_p$. A linear extrapolation of $\beta(T)$ leads to values of $\beta(T_{\mathrm{VF}})$ clearly larger than 0.38 and a rather abrupt change of temperature characteristics at low temperatures has to be assumed to reach this limit. The above approach uses the close correlation of β and b, implied by the Nagel scaling, to deduce the low-tempera-
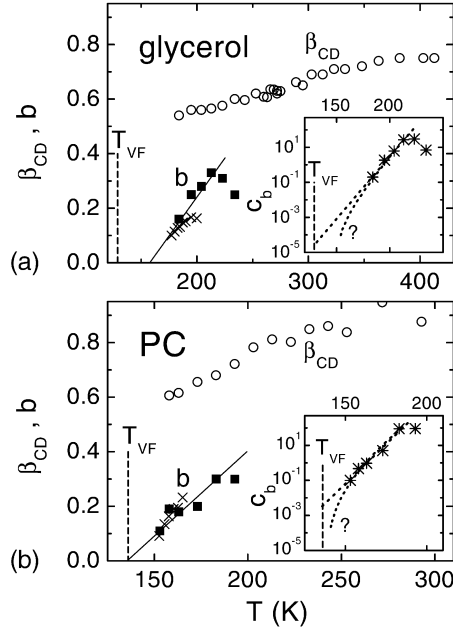
Fig. 5.9. Temperature dependence of the α-peak width-parameter β_{CD} (*circles*) and the excess-wing exponent b (*squares*) for: **a** glycerol; **b** PC [69]. b is obtained from fits with a phenomenological ansatz comprising a sum of two power laws for the high-frequency wing of the α-peak and some additional contributions for the $\varepsilon''(\nu)$-minimum [62]. The *crosses* show the results reported in [18]. The *solid lines* demonstrate possible low-temperature extrapolations of $b(T)$. T_{VF} is indicated by the *dashed lines*. The *insets* show the prefactor of the power law $c_b \nu^{-b}$ used for the description of the excess wing. The *dotted lines* in the insets demonstrate that it is not possible to draw definite conclusions concerning a non-zero value of c_b at T_{VF}

ture behaviour of b from an experimental determination of β. A more direct way is the investigation of the temperature dependence of the exponent b itself. To allow for an unambiguous determination of b at high temperatures, where α-peak, wing, and the minimum strongly overlap, a parameterisation using the sum of power laws can be used [62]. The resulting $b(T)$ is shown in Fig. 5.9 together with the results of Leheny and Nagel [18]. Due to the larger frequency range available and the different evaluation procedure we were able to extend the results of these authors to considerably higher temperatures. For PC (Fig. 5.9b) $b(T)$ can be reasonably well extrapolated to zero at T_{VF}, while this seems not to be the case for glycerol (Fig. 5.9a). However, as already noted in [18], even if b becomes zero, a divergent susceptibility will only be reached, if the prefactor of the ν^{-b} power law, $c_b(T)$, does not approach zero for $T \rightarrow T_{VF}$. The quantity $c_b(T)$ for both materials is shown in the insets of Fig. 5.9. As indicated by the dotted lines, a definite statement concerning this point is not possible. The same conclusion can be drawn from the results on c_b shown in [18]. Overall, no clear evidence for a divergent susceptibility at low temperatures can be deduced from an investigation of the temperature evolution of the excess wing.

5.4.2
The Excess Wing – a β-Relaxation?

Comparing the typical loss spectra of glass-formers showing an excess wing with those showing a β-relaxation (Fig. 5.1a,b), it seems natural to explain both on the same footing: in materials with an excess wing, a β-relaxation could be present, too, although with a relaxation time that is much closer to the α-relaxation time than in materials with a well resolved β-peak. Then the excess wing may be simply the high-frequency flank of the β-peak which itself is submerged under the much stronger α-peak. Such a scenario was considered in some earlier publications [12, 76–80, 92, 129]. Some hints for the validity of this scenario can be obtained from the results in glass-forming ethanol [93]. As mentioned in Sect. 5.3, in this material the excess wing seen at low temperatures (Fig. 5.4) is revealed to be due to a β-relaxation by the occurrence of a shoulder in the high-temperature spectra. In this way glass-forming ethanol seems to represent a limiting case between the schematic spectra shown in Fig. 5.1a,b. However, one should be aware that for the explanation of dielectric results in other primary alcohols an alternative assignment of the various relaxation processes was proposed [109–111].

In materials following the behaviour depicted in Fig. 5.1a, of course α-peak and excess wing can always formally be fitted by a sum of two relaxation peaks [12, 77–79, 92, 130]. However, such fits cannot *prove* that a relaxation process causes the excess wing. An experimental proof for a second relaxation can only be provided by the detection of a shoulder or even a second peak in the loss spectra. A possible way to check for the presence of a β-peak in excess-wing systems as glycerol and PC is the measurement of dielectric spectra at low temperatures, extending to very low frequencies. It is a well-established experimental fact that in materials with a well resolved β-relaxation, its time scale successively separates from that of the α-relaxation with decreasing temperature. However, in glass formers without a well resolved β-peak, very low temperatures, below T_g, may be necessary to observe this separation. However, below T_g, aging effects start to play a role. Aging occurs when the sample has fallen out of thermodynamic equilibrium, i.e. simply stated, after cooling, the molecules move so slowly that they do not reach a new equilibrium position during reasonable observation times. Therefore in those materials, only after very long aging times below T_g may the α-peak have shifted to sufficiently low frequencies for a β-peak to become visible.

In Fig. 5.10 loss spectra for PC and glycerol are shown at a temperature somewhat below T_g for different times after reaching this temperature [81]. In the frequency window of Fig. 5.10, mainly the excess wing is seen, the α-peak leading to the somewhat steeper increase observed at the lowest frequencies (compare Figs. 5.2 and 5.3). During aging, when thermodynamic equilibrium is being approached, the α-peak can be assumed to shift to lower frequencies. Finally, in equilibrium, when the maximum separation of α- and β-peaks is reached, the presence of a β-peak may become more clearly visible. Indeed in Fig. 5.10 after the maximum aging times of five weeks, the excess wing has developed into a shoulder! This behaviour strongly supports the assumption that a β-relaxation

Fig. 5.10. Frequency dependent dielectric loss of: **a** PC; **b** glycerol for different aging times t, indicated in the legend [81]. The *lines* connect the *symbols* for $t \leq 10^6$ s. The spectra for the maximum aging time of $10^{6.5}$ s have been taken in an extended frequency range. (From [81]. Copyright (2000) by the American Physical Society)
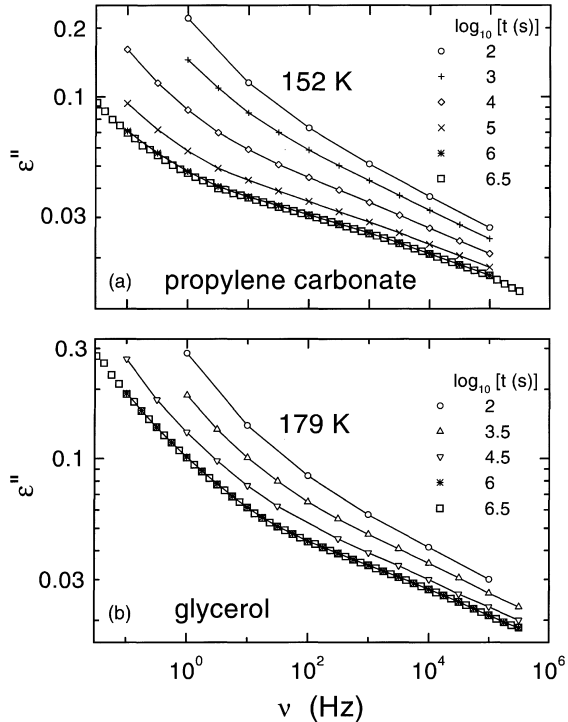
is responsible for the excess wing in glycerol and PC. In Fig. 5.11 it is shown for PC that the $\varepsilon''(\nu)$ curve at 152 K, obtained after maximum aging time (Fig. 5.10a), can be successfully described assuming the sum of a CD (for the α-peak) and a CC function (for the β-peak). Also the spectra at higher temperatures can be described in this way as demonstrated for two temperatures in Fig. 5.11. For glycerol similar results have been obtained [81]. Very recently a similar aging experiment was also performed for glass-forming propylene glycol [130]. Again, under aging the excess wing was observed to develop into a shoulder, caused by a β-relaxation.

Further evidence supporting the explanation of the excess wing by a β-relaxation can be found in the literature. For example, some admittedly vague indications for a shoulder in the excess wing region can be found in the low temperature spectra reported in [12, 18, 46, 47, 68, 80, 131]. However, often it is not clear if equilibrium was indeed reached in these studies. In this context it is of interest that there are some recent reports of strong β-relaxations being detected after rapid quenches into a non-equilibrium low-temperature state [80, 132]. Therefore it is very important to state that the shoulders observed in the wing region in glycerol and PC (Fig. 5.10) were measured in thermodynamic equilibrium [81]. Using a "difference isochrone" method, Johari and Pathmanathan [133] also found evidence for a β-relaxation in various glass formers with an excess wing. And finally also from other experimental methods such as calorime-

Fig. 5.11. Frequency dependence of ε'' of PC for three temperatures. The *solid lines* are fits with the sum of a CD and a CC function [81]. The *dashed lines* are the CD, the *dotted lines* the CC contributions to the total fit curves
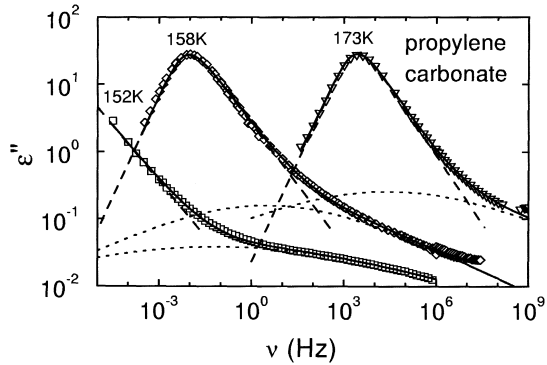
try [134] and nuclear magnetic resonance [135] β-relaxations in excess-wing glass formers were found.

Fits of the loss spectra in glycerol and PC with the sum of a CD or KWW and a CC function reveal a β-relaxation time $\tau_\beta(t)$ that shows significant deviations from Arrhenius behaviour [92, 130]. This is astonishing as the β-relaxation times, determined in glass formers with well resolved β-peaks ("type B" [19]), are believed to follow commonly an Arrhenius behaviour. However, it may be remarked that this notion to a large extend is based on non-equilibrium results, obtained below T_g. Irrespective of this objection, there is no principal reason that the β-process dynamics should always show Arrhenius behaviour. If the excess wing is indeed due to a β-relaxation, the difference between glass formers showing a well pronounced β-relaxation and those showing an excess wing ("type B" resp. "A" in [19]) may be caused just by the temperature evolution of the β-dynamics: in the first materials it is rather weak, presumably Arrhenius, leading to a clear separation of both relaxation times at low temperatures which enables a clear detection of the β-peak. In contrast, in the latter materials the relaxation time of the β-process may more closely follow that of the α-process (which is non-Arrhenius, Chap. 4) and only the high-frequency flank of the β-peak – the excess wing – is visible (except at low temperatures after aging). Such an uncommon temperature dependence of τ_β was already suspected by Johari and Goldstein to explain the apparent absence of a β-relaxation in some glass-formers [23].

In this context it shall be mentioned that the above scenario is consistent with the recently found correlation of $\tau_\beta(T_g)$ and the Kohlrausch-exponent $\beta_{KWW}(T_g)$ describing the width of the α-peak [136]: glass formers without a well-resolved β-relaxation ("type A") have relatively large β_{KWW} which, within this correlation, implies a close vicinity of τ_α and τ_β – the β-peak becomes submerged under the α-peak. In [136] a possible explanation of this correlation within the framework of the coupling model was proposed and even the Nagel-scaling may be explained in this way [78]. Finally, a recent extension of the Weiss mean-field theory for finite systems using the model of dynamically correlated domains [21, 137] also seems to be able to explain the present spectra, including the excess wing. Interestingly, within this framework the occurrence of an excess wing is

attributed to a superposition of peaks or shoulders, which are present in addition to the α-peak, in good accord with the scenario developed above.

5.5
The High-Frequency Response

5.5.1
The $\varepsilon''(\nu)$-Minimum

As mentioned in Sect. 5.3, irrespective of any theoretical models, a minimum in $\varepsilon''(\nu)$ always can be expected at frequencies between the excess wing or β-peak region and the well known excitations in the infrared region (boson peak and intramolecular excitations) [48–55]. It was noted in the introduction, that this region found much interest during recent years due to new developments in the theory of the glass transition, the most prominent being the MCT of the glass transition [25–28] (see also Chap. 4, Sect. 4.2). However, for dielectric spectroscopy the relevant frequency region of 1 GHz–1 THz is difficult to access. Consequently, mainly the susceptibility deduced from light and neutron scattering experiments was used for a comparison with the theoretical predictions (e.g. [34–38]). Indeed evidence for the presence of a fast process in this region and partly a good agreement of the susceptibility spectra with the MCT predictions was found. However, the applicability of the MCT for glass-forming materials, especially at low temperatures near T_g, is still a matter of debate. The MCT predicts that for all experimental methods that couple to density fluctuations, a shallow susceptibility minimum should be present, exhibiting some universal properties (see Sect. 5.5.1.2). Therefore the absence of a high-frequency minimum in dielectric spectra up to some 10 GHz [11, 12, 138] was one of the main points of criticism concerning the MCT and even led to the conjecture that there might be no $\varepsilon''(\nu)$-minimum at all [5, 11, 14, 138]. However, more recent investigations in an extended frequency range [14, 42, 44, 45, 90] provided clear evidence for the existence of a minimum in $\varepsilon''(\nu)$ of glass-forming materials in the GHz–THz range, which now is a well established experimental fact. However, the true question of course should not be the occurrence of a minimum per se, which is a natural consequence of the existence of excitations in the sub-MHz and the THz range, but its spectral form, which will be analysed in detail in the two following subsections.

For the ionically conducting glass former CKN, the question arises what representation, dielectric permittivity or modulus is best suited for an analysis of the high-frequency response. There are some reasons speaking in favour of an analysis of the dielectric permittivity: the results from light and neutron scattering reported in literature are usually analysed in terms of a susceptibility and not in terms of a modulus. In addition, to enable a comparison with the results for molecular glass formers, where the permittivity is usually considered as the appropriate quantity, the permittivity should be preferred. Therefore, in the following also for the ionically conducting glass formers, only the permittivity will be considered.

5.5.1.1
Phenomenological Description

The most naive assumption for the spectral form of the dielectric loss in the minimum region is a simple crossover from the α-peak or the excess wing to the boson peak. For the low frequency wing of the minimum a sublinear power law describing the excess wing (or the high-frequency flank of a β-peak) can be assumed. For the low frequency wing of the boson peak a linear or steeper increase of $\varepsilon''(\nu)$ [or $\chi''(\nu)$, determined from scattering experiments] is commonly found for a variety of glass formers [35, 36, 48, 50]. Also, $\chi''(\nu)$ must increase steeper than linearly towards the boson peak, in order for a peak to appear in the scattering function, $S \sim \chi''/\nu$, from light or neutron scattering experiments where the boson peak was first observed [36]. Therefore the ansatz

$$\varepsilon'' = c_b \nu^{-b} + c_n \nu^n \tag{5.1}$$

with $b < 1$ and $n \geq 1$ can be used. In the insets of Figs. 5.12 and 5.13 the region of the $\varepsilon''(\nu)$-minimum is analysed using this ansatz with the smallest possible value of $n = 1$. Clearly the experimentally observed minimum is too shallow to be explained in this way. If larger values for n are chosen, the fits will become

Fig. 5.12. Dielectric loss of: **a** glycerol; **b** PC in the minimum and boson peak region [42, 45–47, 94]. The *solid lines* are fits with the MCT prediction, Eq. (5.4), with $a = 0.325$, $b = 0.63$ for glycerol and $a = 0.29$, $b = 0.5$ for PC. For the lowest temperatures, the increase towards the boson peak approaches power laws $\varepsilon'' \sim \nu^3$ for glycerol and $\varepsilon'' \sim \nu$ for PC as indicated by the *dashed lines*. The *dotted line* in b is drawn to guide the eyes. The *insets* demonstrate for two temperatures each, that the simple superposition ansatz, Eq. (5.1), is not sufficient to explain the shallow minimum
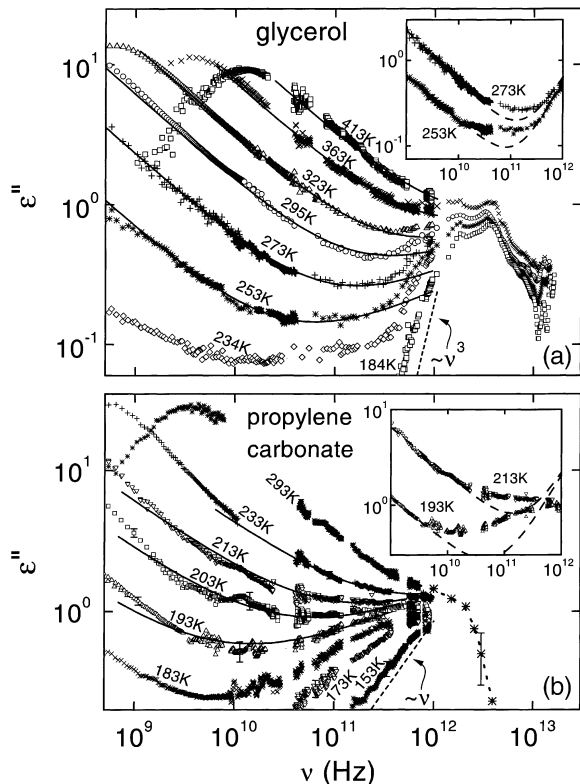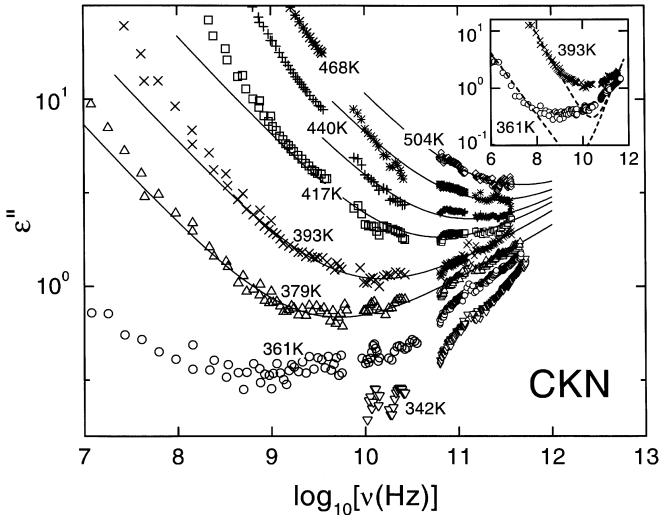
Fig. 5.13. Dielectric loss of CKN at high frequencies for various temperatures [43, 44]. The *solid lines* are fits with MCT, Eq. (5.4), with $a = 0.3$ and $b = 0.54$. In the *inset* it is demonstrated that the superposition ansatz, Eq. (5.1), cannot take account of the shallow minimum

even worse. This empirical finding clearly proves, independent from any model assumptions, that in the region of the $\varepsilon''(v)$-minimum an additional fast process contributes significantly to the dynamics of the investigated structural glass formers.

In the plastic crystalline *ortho*-carborane (Fig. 5.7), an evaluation with Eq. (5.1) reveals small deviations in the minimum region, which may be indicative of contributions by a fast process also in this orientationally disordered material [100, 139]. However, due to the somewhat restricted database in the minimum region, it is difficult to make a clear statement. In plastic crystalline cyclo-octanol, a somewhat stronger evidence for a fast process has been found [126, 140].

The simplest way to take account of the detected additional intensity in the minimum region of glass formers is the addition of a constant loss, ε_c, to Eq. (5.1):

$$\varepsilon'' = c_b v^{-b} + \varepsilon_c + c_n v^n \tag{5.2}$$

The introduction of a constant loss was early promoted by Angell and co-workers [51, 127, 128] who composed broadband absorptivity plots from dielectric and far infrared experiments and concluded that there is a background absorption, linear in frequency, which corresponds to a constant loss contribution in $\varepsilon''(v)$. Indeed many indications for an approach of a constant loss at high frequencies and low temperatures were found in various, mainly ionically conducting, glass formers [e.g. 52, 141–150], but also in crystalline materials [e.g. 141, 142, 151–153]. Despite a variety of explanations for the constant loss being proposed [e.g. 52, 143, 145, 146, 149, 150], it has to be stated that the microscopic

origin of this phenomenon is still unclear (it should be noted that due to the already mentioned problems concerning the Kramers-Kronig consistency, in fact only an approximate constant loss behaviour can be expected). Usually, the constant loss is detected at relatively low temperatures, below T_g, only. For the explanation of the shallow $\varepsilon''(\nu)$-minimum it has to be assumed that the constant loss is still important, even well in the liquid region. Here it may be superimposed by the α- and boson peak wings, which prevents its detection in "pure" form and leads to the observed shallowness of the minimum (compared with Eq. 5.1). This hypothetical contribution obviously cannot be identified with the constant loss that was assumed to be approached by the excess wing for much lower temperatures near T_{VF} [13, 18] (see Sect. 5.4.1).

For glycerol and CKN it was shown in [42, 45] that the minimum region of $\varepsilon''(\nu)$ can be reasonably well described by Eq. (5.2) at high temperatures. However, for low temperatures a description of the minimum region with Eq. (5.2) fails: the transition from the minimum to the boson peak is too smooth to be fitted by a sum of the constant loss and a relatively steep ν^n-increase towards the boson peak. For PC the situation is similar. A way out of this problem is the addition of another power-law increase with an exponent near 0.3. Such a power law was found in some glass formers, in addition to the constant loss [145, 146, 150, 154] and claimed to be ubiquitous, at least in glassy ionic conductors [150]. If one finally assumes a sum of a CD and a CC function for the description of the α-peak and the β-peak/excess-wing region (see Sect. 5.4.2), one arrives at

$$\varepsilon'' = CD + CC + \varepsilon_c + c_3\nu^{0.3} + c_n\nu^n \tag{5.3}$$

Here "CD" and "CC" schematically denote $\varepsilon''(\nu)$, obtained from the CD and CC formulae (Chap. 3, Sect. 3.2).

In Fig. 5.14, fits with Eq. (5.3) are shown as solid lines for PC [92]. Equation (5.3) enables a good description of the experimental data, extending over the impressive range of 17 decades of frequency. Also for glycerol, fits with similar quality can be obtained [92]. For CKN the $\varepsilon''(\nu)$-minimum can well be described with the last three terms in Eq. (5.3) [92]; at lower frequencies conductivity contributions become dominant. In [129] the CKN data from our group have been analysed in a similar way. However, one has to state that the number of parameters involved in the fitting with Eq. (5.3) is quite large and, while it cannot be excluded that this simple superposition ansatz is correct, the success of these fits does not provide a real proof for its validity. Also, one should mention that it is not so clear if a simple *additive* superposition of different contributions to $\varepsilon''(\nu)$ is really justified [155–157].

5.5.1.2
Mode-Coupling Theory

The mode-coupling theory ([25–27], for reviews see [28, 158, 159]) is based on a generalized oscillator equation of motion for the density autocorrelation func-
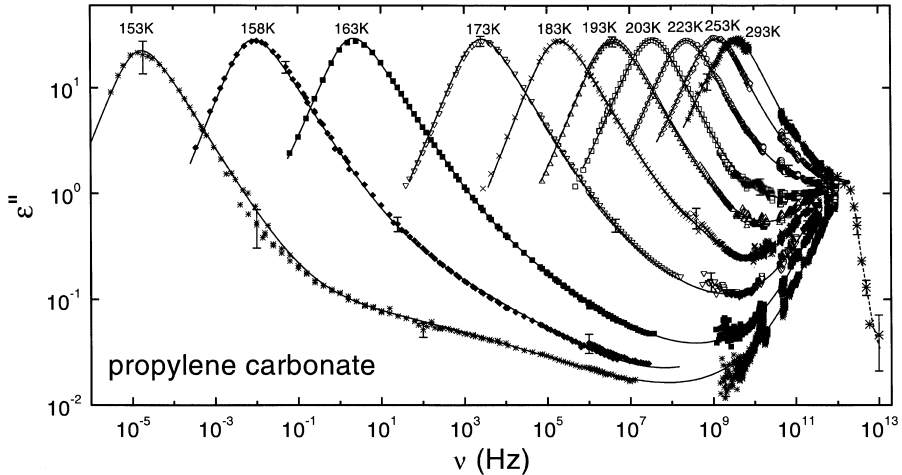
Fig. 5.14. Frequency dependence of ε'' of PC for various temperatures [45, 47]. The *dashed line* in the infrared region is drawn to guide the eye. The *solid lines* are fits with Eq. (5.3) [92]

tion $\Phi_q(t)$ (see Chap. 4, Sect. 4.2). The damping term comprises a contribution that itself depends on the autocorrelation function, which leads to a non-linear feedback mechanism. The MCT equations are solved self-consistently after making some approximations for the damping term. For details on the theoretical basis of MCT the reader is referred to the review articles [28, 158, 159]. MCT explains the glass transition in terms of a dynamic phase transition at a critical temperature T_c, significantly *above* the glass temperature T_g. For temperatures $T > T_c$, the presence of two dynamic processes, with quite different time scales, is predicted. The fast process can be roughly ascribed to the "rattling" movement of a particle in the transient "cage" formed by its neighbours. The slow process corresponds to the well-known α-relaxation, associated with the forming and decay of the cage involving the cooperative movement of many particles. For all experimental methods sensitive to density fluctuations, both processes should be visible in the spectra of the imaginary part of a generalized susceptibility χ'' (ε'' for dielectric spectroscopy). For $T < T_c$, the original version of MCT, the socalled idealized MCT, predicts a transition into a nonergodic "glass" state with a complete arrest of the α-relaxation. However, this is at variance with the experimental observations where the α-relaxation is detected well down to T_g and below. Therefore, in the so-called extended MCT additional hopping processes are considered that enable a diffusive motion out of the cages even below T_c, thereby restoring ergodicity. Within extended MCT, the meaning of T_c is a crossover-temperature between the dominating cage effect well in the liquid state and activated hopping processes in a more solid-like state below T_c. What makes MCT (and especially its simplest form, the idealized MCT) so attractive for the experimentalist is the large range of rather simple predictions, covering almost all aspects of the dynamic response of glass-forming materials. This should allow for rigid experimental tests of its validity.

One of the main outcomes of the MCT is the prediction of additional contributions in the region of the $\varepsilon''(\nu)$-minimum, due to the cage effect. Within idealized MCT, for T above but near T_c, the minimum region can be approximated by the sum of two power laws:

$$\varepsilon'' = \frac{\varepsilon_{\min}}{a+b}\left[a\left(\frac{\nu}{\nu_{\min}}\right)^{-b} + b\left(\frac{\nu}{\nu_{\min}}\right)^{a}\right] \tag{5.4}$$

where $\nu_{\min}$ and $\varepsilon_{\min}$ denote position and amplitude of the minimum, respectively. The power law ν^{-b} is often referred to as the von-Schweidler law, the power law ν^{a} as the critical law. Within MCT, the temperature independent exponents a and b are related to each other by the exponent parameter λ and the exponent a is restricted to values below 0.4. Thus at frequencies above the minimum, $\varepsilon''(\nu)$ should show a significantly sublinear increase. Within MCT, the minimum region is denoted as the β-relaxation window, despite no peak (as for conventional relaxation contributions) being expected. This MCT β-relaxation regime should not be confused with the much slower Johari-Goldstein β-relaxations and therefore often the term *fast β-process* is used to denote the MCT-related phenomenon.

In Figs. 5.12 and 5.13 the high frequency region of ε'' is shown for glycerol, PC and CKN, fitted with the MCT prediction, Eq. (5.4). For PC (Fig. 5.12b), a consistent description of the $\varepsilon''(\nu)$-minima at $T \geq 193$ K is possible with $\lambda = 0.78$ [45, 47], independent of temperature, which implies $a = 0.29$ and $b = 0.5$ (solid lines in Fig. 5.12b). The fits provide a good description of the data from 1–2 decades below $\nu_{\min}$ up to the boson peak frequency. The critical law is nicely seen between $\nu_{\min}$ and the boson peak frequency. The deviations of experimental data and fits, seen at low frequencies, can be ascribed to the growing importance of the α-relaxation. The simple interpolation formula, (Eq. 5.4), is only valid in the vicinity of the minimum. For $T < 193$ K the increase towards the boson peak becomes too steep to be fitted with the constraint $a < 0.4$. As mentioned above, Eq. (5.4) should be valid at $T > T_c$ only, which gives a first hint on the magnitude of T_c. Recently a more sophisticated analysis of the present data has been performed, using a schematic two-correlator model within the framework of extended MCT [160]. The value $\lambda = 0.75$ obtained from this analysis is of similar magnitude as the present result.

In Fig. 5.12a the MCT-fits of $\varepsilon''(\nu)$ of glycerol are shown with $\lambda = 0.705$ ($a = 0.325$, $b = 0.63$) [42, 45]. The MCT fits seem to be limited at high frequencies by a superimposed very steep increase towards the boson peak, which is not taken into account by the MCT interpolation formula, Eq. (5.4) [42, 45]. In PC this contribution seems to be of less importance. This is in accord with the finding of Sokolov et al. [161] that the amplitude ratio of boson peak and fast process is largest for strong glass formers (within the classification scheme introduced by Angell [95], glycerol being significantly stronger than PC. From Fig. 5.12a it seems likely that in glycerol, at least at low temperatures, position and amplitude of the minimum are only weakly influenced by these contributions. For glycerol an evaluation of the light and neutron scattering results with idealized MCT is

hampered by the even stronger boson peak contribution [97]. However, in [162] light scattering results [97] were analysed using a more sophisticated MCT approach, including the boson peak.

In CKN, consistent fits of the experimental data with Eq. (5.4) are possible, too [44] (Fig. 5.13), leading to $\lambda = 0.76$ ($a = 0.3$, $b = 0.54$). The deviation of experimental data and fits at low frequencies can be ascribed to conductivity contributions in this ionic conductor, which lead to a divergence of ε'' for low frequencies. For all materials investigated, the values of λ deduced from the present results are of similar magnitude as the results from other experimental techniques [98, 99, 162–164].

In contrast to light or neutron scattering, by dielectric spectroscopy also the real part of the susceptibility, ε', is directly accessible. A calculation of $\varepsilon'(v)$ from $\varepsilon''(v)$, which can be done using the Kramers-Kronig relation, is always ambiguous as in principle it requires an infinite frequency range. Therefore the $\varepsilon'(v)$ data provide valuable additional information about the high frequency dynamics. As an example, in Fig. 5.15, $\varepsilon'(v)$ is shown for the high frequency region in glycerol. The lines are fits with the MCT prediction,

$$\varepsilon' = f_e + \frac{\varepsilon_{\min}}{a+b} \left[a \cot (b\pi/2) \left(\frac{v}{v_{\min}} \right)^{-b} - b \cot (a\pi/2) \left(\frac{v}{v_{\min}} \right)^{a} \right] \tag{5.5}$$

with f_e a constant. In the fitting procedure, for a, b, $v_{\min}$ and $\varepsilon_{\min}$ the values obtained from the fits of $\varepsilon''(v)$ were used. As seen in Fig. 5.15, despite f_e being the only free fitting parameter, a good agreement of experimental data and fits can be stated. Also in PC and CKN the experimental data are consistent with the theoretical prediction [92].

MCT predicts a critical temperature dependence of the $\varepsilon''(v)$-minimum near T_c. For $T > T_c$, according to idealized MCT, the following relations should hold:

Fig. 5.15. $\varepsilon'(v)$ of glycerol at high frequencies [92]. The *solid lines* are fits with the MCT prediction, Eq. (5.5) with f_e the only free parameter. The other parameters have been taken from the fits of $\varepsilon''(v)$ (Fig. 5.12a)
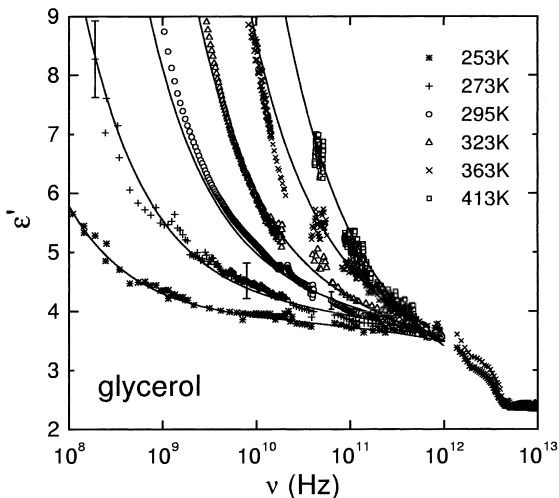
$$\nu_{min} \sim (T - T_c)^{1/(2a)} \tag{5.6}$$

$$\varepsilon_{min} \sim (T - T_c)^{1/2} \tag{5.7}$$

In addition, the α-relaxation rate should also exhibit critical behaviour

$$\nu_\tau \sim (T - T_c)^\gamma \quad \text{with} \quad \gamma = \frac{1}{2a} + \frac{1}{2b} \tag{5.8}$$

In Fig. 5.16, the temperature dependencies of ε_{min}^2, ν_{min}^{2a} and $\nu_\tau^{1/\gamma}$ are shown for glycerol, PC and CKN. According to Eqs. (5.6)–(5.8), these representations can be expected to lead to straight lines extrapolating to T_c. Indeed, for the investigated materials all three data sets can be consistently described with $T_c \approx 187$ K for PC [45, 47], $T_c \approx 262$ K for glycerol [42, 45] and $T_c \approx 375$ K for CKN [44] as indicated by the solid lines. For temperatures near T_c, the data partly deviate from the predicted behaviour. Within MCT this can be ascribed to a smearing out of the critical behaviour due to hopping processes, which are considered in extended versions of MCT.

The present results for T_c are located within the range of values determined with other techniques [98, 99, 164–166], except for glycerol, where a T_c lying between 223 and 233 K was stated in [162]. In addition, a recent more sophisticated analysis of the present results in PC led to a T_c of 180 K [160]. As mentioned above, the relations at Eqs. (5.6)–(5.8) should hold only for $T > T_c$. However, crit-
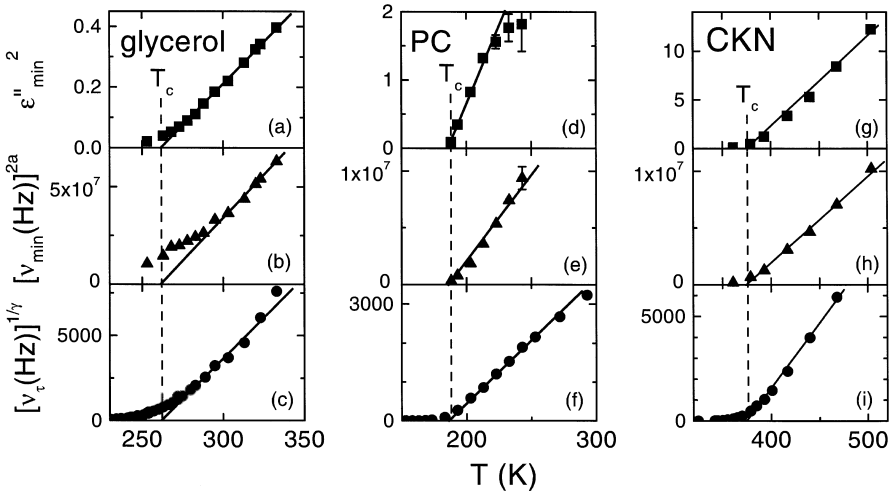

Fig. 5.16. Temperature dependence of: **a, d, g** the amplitude ε_{min}; **b, e, h** the position ν_{min} of the $\varepsilon''(\nu)$-minimum; **c, f, i** the α-relaxation rate ν_τ of glycerol, PC, and CKN [42, 44, 45, 47, 94]. ε_{min} and ν_{min} have been taken from the fits with Eq. (5.4), shown in Figs. 5.12 and 5.13. Representations have been chosen that should result in straight lines according to the predictions of the MCT, Eqs. (5.6), (5.7) and (5.8). The *solid lines* demonstrate a consistent extrapolation for all three quantities to a T_c of 262 K for glycerol, 187 K for PC and 375 K for CKN

ical laws are well known to fail too far above the critical temperature. Therefore it is difficult to choose the correct temperature range to be used for the determination of T_c, which may lead to some uncertainties concerning the value of T_c. In addition, as mentioned above, Eqs. (5.4) and (5.5) are approximations only and the temperature and frequency region where their application is justified is difficult to determine [99, 160, 167]. Therefore, overall the significance of the parameters obtained from the above presented most simple kind of analysis within MCT should not be overemphasized.

Finally, it should be mentioned that idealized MCT predicts a significant change in the behaviour of $\varepsilon''(v)$ at T_c [28]: for $T < T_c$, instead of a minimum, $\varepsilon''(v)$ should follow two power laws, $\varepsilon'' \sim v^a$ for $v > v_k$ and $\varepsilon'' \sim v$ for $v < v_k$. This so-called "knee" should also exhibit critical behaviour. There was considerable controversy in literature concerning the presence or absence of this unusual feature in neutron and light scattering data [138, 168–171]. In the present results in all materials investigated no evidence for a knee is obtained. In [171] the absence of the knee was ascribed to hopping processes, which are not included in idealized MCT.

5.5.1.3
Other Models

It was mentioned in the introduction that fast processes are also considered in some other models for the dynamic response of glass formers. In the CM of Ngai [29–31] the molecular units are predicted to exhibit a transition from an exponential fast relaxation to a slower KWW relaxation due to the onset of cooperative motion at a crossover time t_c. Continuity of the relaxing function (the polarization in our case) at t_c implies a correlation of the relaxation times of both processes and the relaxation time of the fast process can be calculated from the KWW parameters of the α-process. It was shown [47, 92] that for glycerol, PC and CKN the fast process of CM is located at much lower frequencies than the $\varepsilon''(v)$-minimum and therefore additional contributions, e.g. a constant loss (Sect. 5.5.1.1), have to be invoked for the explanation of the excess intensity in this region.

In the FLD model [22, 32] a "narrowly avoided critical point" at a temperature T^* above the melting point is postulated. The theory is based on the assumption that there is a locally preferred structure (LPS) that, however, is not able to tile space periodically. Without this geometrical constraint the system would condense into the LPS at T^*. In real systems somewhat below T^*, frustration-limited domains with the LPS are formed. In the FLD model the α-relaxation is identified with the restructuring of the FLDs and occurs on a length scale given by their characteristic size. Within the FLD framework there is a second length scale, the correlation length ξ of the locally preferred structure. It was argued [22, 32] that the experimentally observed fast β-processes may be ascribed to fast relaxations taking place on this smaller length scale of the FLD model. However, up to now a theoretical elaboration of the fast processes within FLD theory is missing.

Recently, a model was proposed considering a low-frequency relaxation-like part of the vibration susceptibility function, assumed to be responsible for the boson peak [33]. This relaxation-like response was shown to arise from the anharmonicity of vibrations. For the imaginary part of the susceptibility it should lead to an additional peak with $\varepsilon'' \sim \nu^\alpha$ and $\varepsilon'' \sim \nu^{-1}$ at its low and high frequency side, respectively. For the absolute value of the exponent α, reasonable values ranging between 0.375 and 1 were given in [33], depending on the system. While no peak is seen between α- and boson peak in the present spectra, its ν^{-1}-wing may be obscured by the dominating boson peak at higher frequencies. Indeed, the spectra in glycerol give the impression of a boson peak with a steep ($\sim \nu^3$) low-frequency wing, superimposed to a more shallow power law (Fig. 5.12a). In contrast in PC (Fig. 5.12b) a smooth transition of $\varepsilon''(\nu)$ from the minimum to the boson peak with only one power law ($\sim \nu^n$, $n \leq 1$) is observed, which seems unlikely to result from the superposition of the ν^α-wing of the fast β-process and the low frequency wing of the boson peak (steeper than ν^1, see above).

Very recently, by extending the Weiss mean-field theory to finite systems (clusters) and combining it with a model for the size dependence of the relaxation rate [20], it was possible to explain a considerable part of the present spectra of glycerol, including the $\varepsilon''(\nu)$-minimum [21]. Within this framework it is assumed that the basic thermodynamic units, the so-called aggregates, are subdivided into strongly interacting clusters which are statistically indistinguishable. From the distribution of the aggregate sizes and the size dependence of the relaxation rate of particles in an aggregate, a non-Debye α-peak and an excess wing are predicted. In addition, peaks or shoulders can arise at high frequencies due to the fact that only integer values of m, the number of molecules per cluster, are possible. This means that these high frequency features reflect the dynamic response of dimers, trimers, quadrimers, etc. [137].

5.5.2
Comparison with Light and Neutron Scattering

The present high frequency dielectric results enable a direct comparison of the dielectric susceptibility with that determined from the scattering experiments. Of the glass formers investigated in the present work, susceptibility data from scattering experiments are available for glycerol, PC and CKN. In Fig. 5.17 the dielectric loss spectra of glycerol and PC are compared with the imaginary part of the susceptibility, determined from neutron and light scattering data [97–99, 172]. As the scattering results give no information on the absolute magnitudes of χ'', the data sets have been arbitrarily scaled to yield a comparable height of the α-peak. The dielectric and light scattering results are qualitatively similar showing an α-peak, a minimum and a boson peak. The frequency range of the neutron scattering results is somewhat restricted but the minimum also is nicely seen. For CKN, $\varepsilon''(\nu)$ is compared to $\chi''(\nu)$ from neutron [173] and light scattering [164] in Fig. 5.18. As no α-peak is seen in $\varepsilon''(\nu)$, the curves were scaled to a similar amplitude of the minimum. Again the data from the different methods agree qualitatively (except for the missing α-peak in $\varepsilon''(\nu)$).

Fig. 5.17. Frequency dependence of the imaginary part of the susceptibility of: **a** glycerol; **b** PC as obtained with different experimental methods. The *symbols (except for the lozenges)* represent the present dielectric results, those from light scattering are shown as *solid lines* [97, 98, 172]. The *lozenges* show the neutron scattering results from [97, 99]. The light and neutron scattering data sets have been vertically shifted to give a comparable intensity of the α-peak
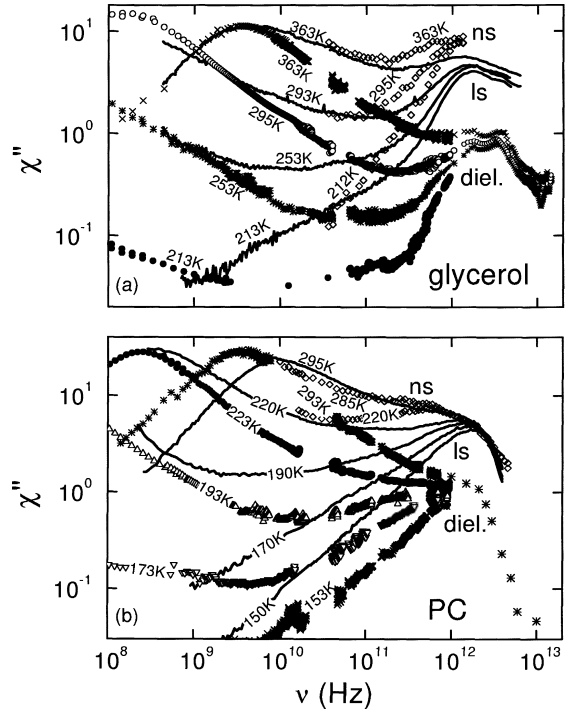
In Fig. 5.17a, for glycerol the α-peak frequencies at 363 K from light scattering and dielectric spectroscopy are nearly identical. In contrast, for PC (Fig. 5.17b) the α-peaks from dielectric spectroscopy are located at a significantly lower frequency. Also earlier investigations of glycerol revealed very similar α-relaxation times from different methods [174–177]. In contrast, in glass-forming PC there is a difference in the absolute values of the α-relaxation times determined from different experimental methods [98]. Presumably the hydrogen bonds between neighbouring molecules in glycerol lead to a strong coupling of reorientational and translational motions of the molecules. In contrast, in the van-der-Waals bonded glass former PC, reorientational and translational degrees of freedom seem to decouple partly. However, the different relaxation times in PC exhibit a common temperature behaviour, i.e. can be transferred into each other by a temperature independent factor [98]. This finding is in agreement with the prediction of MCT that in Eq. (5.8) only the prefactor should depend on the experimental probe. For both materials the α-peak determined from light scattering is broader and exhibits a larger asymmetry.

Figure 5.17 reveals that for glycerol and PC the peak seen in the dielectric loss at some THz is approximately located at the same frequency as that detected by neutron and light scattering. Therefore, as mentioned above, this peak can be identified with the boson peak. However, for the dielectric results the ratio of the boson peak and α-peak amplitudes is much smaller than for the scattering results. A similar behaviour was also found in our experiments on Salol

Fig. 5.18. Frequency dependent dielectric loss of CKN, compared to the imaginary part of the susceptibility as determined from light (*solid lines*) [164] and neutron scattering (*dashed lines*) [173]. The data sets from neutron and light scattering have been vertically shifted to yield a comparable intensity in the minimum region
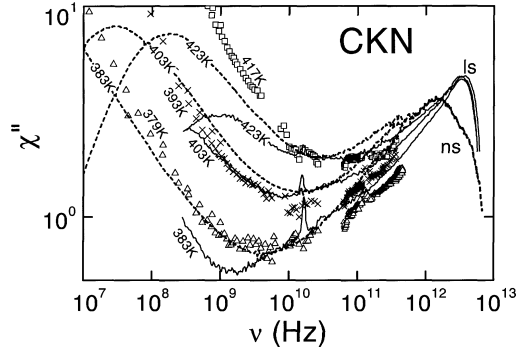
[91] and in numerical molecular-dynamics simulations of various glass-forming systems [178–180]. In addition, the position of the minimum differs between the different methods, also in accordance with results from molecular dynamics simulations [178, 180]. In contrast to the two molecular glass formers investigated, in CKN the $\chi''(\nu)$-minimum seems to be roughly located at the same frequency for all experimental methods (Fig. 5.18). In all glass formers investigated, the increase towards the boson peak seems to be quite similar for all experimental methods, including the much stronger steepness of this increase in glycerol.

Concerning the MCT, it is one of its main predictions that the same parameters T_c and λ should arise from all observables coupling to the density fluctuations [28, 158, 159]. This is indeed the case for PC and CKN, but so-far unclarified for glycerol (see Sect. 5.5.1.2). In glycerol and PC, dielectric spectroscopy mainly probes orientational degrees of freedom, which are not taken into account by MCT in its original form. In contrast, in CKN all experimental probes can be assumed to couple to translational motions. Therefore it may be suspected that the differences between the results from the different experimental methods, seen in glycerol and PC, are due to the coupling to different degrees of freedom and to the different tensorial properties of the experimental probes [178]. In recent theoretical works, MCT was generalized by incorporating orientational degrees of freedom [167, 181, 182]. It was shown, that the larger ratio of α- and boson peak amplitude revealed by the dielectric results, the larger width of the α-peak seen in light scattering and the differences in the α-peak frequency in PC can be qualitatively understood in this way [167, 182]. In addition, very recently a simultaneous analysis of the present results in PC and those from light and neutron scattering was performed [160]. Using a schematic two-correlator model within the framework of extended MCT including hopping processes, it was shown that it is possible to explain the different minimum positions obtained from different experimental methods, as observed in Fig. 5.17 [160].

5.5.3
The Boson Peak

Here we will refrain from comparing the experimental results with the many different theoretical models dealing with the boson peak, mentioned in Sect. 5.2. However, some interesting experimental facts shall be emphasized in the following. The high-resolution FIR measurements performed in glycerol seem to reveal a double-peak structure in the boson peak region, with peaks located at about 1.8 THz and 3.5 THz (Fig. 5.12a). In the FIR absorbance-spectra of glycerol, reported in [53], there are indications for a double peak, too (in $\alpha(\nu)$ in fact the first peak shows up as shoulder only) and also the "fine structure" above about 5 THz is observed. To a lesser extend the double-peak structure is also seen in the light [97] (Fig. 5.17a) and the neutron scattering results [97]. Also in many other (but not all, e.g. PC [98, 99]) glass-forming materials such a two-peak structure in the THz region has been observed using scattering methods (e.g. [36, 37, 183–185]). In addition, in glycerol, at the low frequency flank of the boson peak two regimes can be distinguished: just above ν_{min}, there is a rather shallow increase of $\varepsilon''(\nu)$, which at high temperatures can be described by the critical law of MCT (Fig. 5.12a). However, at higher frequencies a very steep increase appears, approaching $\varepsilon'' \sim \nu^3$ for $T \to T_g$ (dashed line in Fig. 5.12a). In contrast, in PC only one power law, $\varepsilon'' \sim \nu^{-a}$, is seen simultaneously forming the high-frequency wing of the minimum and the low-frequency wing of the peak at 1 THz. It seems that in glycerol the fast process, giving rise to the shallow minimum in $\varepsilon''(\nu)$ is obscured at higher frequencies by a strong boson peak contribution and that this is not the case for PC. This behaviour may be related to the empirical finding by Sokolov et al. [161] that for stronger glass formers ($m \approx 53$ for glycerol and $m \approx 104$ for PC [96]) the amplitude-ratio of boson peak and fast process is higher.

In the plastic crystal *ortho*-carborane at about 1.7 THz a boson peak is observed, too (Fig. 5.7). It is remarkable that its high frequency flank is extremely steep. *Ortho*-carborane has a cubic crystal structure and therefore its phonon spectrum should exhibit contributions from acoustic phonons only. If one assumes a disorder-induced coupling of the electromagnetic waves to *all* phonons within the Brillouin zone [48, 49, 82], it may be suspected that the boson peak in *ortho*-carborane is disorder allowed and reflects the complete phonon density of states. In supercooled liquids and glasses sound waves still exist and can propagate. However, these acoustic modes are strongly coupled to relaxational excitations. It is this hybridisation which makes the acoustic phonon density of states accessible for dielectric spectroscopy and which yields a strongly enhanced density of states at low frequencies. In harmonic solids, assuming that the Debye approximation is valid, a quadratic frequency dependence is expected. This certainly is not the case in disordered solids and any coupling with relaxations or low level molecular excitations will yield a strongly enhanced density of states, which shows up as an excess heat capacity (close to 30 K) in thermodynamic experiments and which certainly will contribute to the boson peak. Of course numerous models exist which also can explain the boson peak. However, already the above naive and rather hand waving

arguments give a reasonable explanation for both the existence of the boson peak and its "dipolar" character.

5.6
Conclusions

In the present chapter, dielectric permittivity spectra of various members of quite different classes of glassy materials have been presented. By the combination of a large variety of dielectric and optic techniques, broadband spectra covering up to 19 decades of frequency were obtained. A rich variety of universal dynamic features is revealed by these spectra, which reflects the "zoo" of different dynamic processes that play a role in glassy dynamics. In the present chapter we have concentrated on the processes at frequencies beyond the α-relaxation, including the excess wing, the $\varepsilon''(\nu)$-minimum and the boson peak, which have attracted increasing interest in recent years. By dielectric spectroscopy it is possible to follow the development of all these features, from temperatures deep in the liquid state down to below T_g, using one experimental probe only.

The following picture of glassy dynamics evolves from these results: aside of the α-relaxation, with its tremendous continuous slow down when approaching T_g, in most structural glass formers at $T > T_g$ there is either the clear signature of a slow β-relaxation peak ("type B" [19]) or an excess wing ("type A"). Our results, obtained in glycerol and PC after long-time aging at $T < T_g$ (Sect. 5.4.2), strongly suggest that the excess wing observed in "type A" glass formers is due to a β-relaxation, which is a common feature in these materials, too. There are also materials that cannot be clearly classified as "type A" or "B", e.g. glass-forming ethanol. Here the excess wing, observed in certain temperature regions, can be clearly identified to be due to a β-relaxation, too.

The β-relaxation, causing the excess wing, can be assumed to be of the Johari-Goldstein type [23, 24], inherent to the structurally disordered state. However, in materials without a well developed β-relaxation peak, the relaxation time of the β-process may more closely follow that of the α-process (and thereby exhibit marked deviations from Arrhenius behaviour) than in "type B" systems and therefore show up as an excess wing only. Various microscopic explanations of the β-relaxation phenomenon have appeared (e.g. [19, 20, 23, 24, 78, 136]) and also for the different separation of α- and β-peak in "type A" and "type B" glass formers a theoretical explanation has been proposed [78, 136]. Even for the so-far unexplained scaling, introduced by Nagel and co-workers [9], by which the α-peak and the excess wing in many (but not all) "type A" glass formers can be collapsed onto one master curve, an explanation assuming a β-relaxation as the true origin of the excess wing seems possible [78]. Some plastic crystals also show clear signatures of β-relaxations [100, 126, 139, 186, 187], however, usually with rather weak amplitudes only, but in others there is neither a β-relaxation nor an excess wing [66]. Obviously, in this kind of disordered materials the occurrence of a Johari-Goldstein β-relaxation is not a common property and also the Nagel-scaling is violated [69, 139]. It seems that structural disorder is closely related to the occurrence of both phenomena.

At frequencies beyond the excess wing, respectively the slow β-relaxation regime, in the GHz–THz frequency range, an $\varepsilon''(\nu)$-minimum appears. In the structural glass formers there is clear evidence for additional intensity in this region, indicating the presence of a fast process, sometimes called fast β-process (Sect. 5.5.1). A phenomenological ansatz, involving the sum of power laws, including a constant loss contribution can take account of the observed spectra, but a theoretical foundation of this model is still in its beginning stages. The MCT provides a microscopic explanation for the fast process in all glass formers investigated. Already the idealized version of the MCT can partly describe the experimental results and for PC it was shown that a more sophisticated analysis is able to describe the experimental data in an impressively wide frequency and temperature range [160]. Also the differences, revealed by the susceptibilities from dielectric, neutron and light scattering experiments (Sect. 5.5.2) in the investigated molecular glass formers seem to be understandable within recent extensions of MCT that take into account orientational degrees of freedom [167, 181, 182]. Another microscopic approach of the high-frequency dynamics in glass formers is provided by an extension of the Weiss mean-field theory for finite systems using predictions of the dynamically correlated domain model [21]. Within this framework, recently part of the present spectra of glycerol were successfully described [21] and also our results in PC seem to be consistent with this model [137].

At frequencies around THz the boson peak shows up. However, in glycerol (Fig. 5.12a) and other glass formers [36, 37, 183–185] in this region in fact a double-peak structure is observed. Also there are marked differences in the increase of $\varepsilon''(\nu)$ towards the boson peak for different glass formers (e.g. Fig. 5.12). In the plastic crystalline *ortho*-carborane the boson peak may simply reflect the acoustic-phonon density of states. Further systematic experimental work is necessary to clarify whether the boson peak is indeed a universal property of glass-forming materials or if there may be different microscopic origins for the appearance of one or several peaks at frequencies around THz.

Overall, broadband dielectric results on glass-forming materials reveal many characteristic, partly intriguing properties of glass-forming materials, e.g. the excess wing with its scaling properties, the additional intensity in the minimum region and the boson peak. The microscopic understanding of many of these phenomena is still controversially discussed, and much work, both experimental and theoretical, will have to be done to reach a consensus. In our view, MCT provides the most consistent picture of glassy dynamics, offering explanations for the largest variety of experimental facts, including the high-frequency processes. Even so, certainly many questions need to be addressed in more detail, e.g. the behaviour near and below T_c, or the occurrence of Johari-Goldstein β-relaxations. However, also more experimental work is needed, e.g. concerning the boson peak region and the filling of the "gaps" in the GHz region at low temperatures. Nevertheless, the recent tremendous theoretical and experimental progress in this very lively field of solid state physics gives rise to the hope that these and other open questions will be solved in due course, finally arriving at a consistent picture of the glass transition and glass dynamics.

List of Abbreviations and Symbols

a	exponent of MCT critical law
b	power-law exponent of excess wing; also exponent of von-Schweidler law
c_b	prefactor of excess-wing power law
c_n	prefactor of left wing of boson peak
c_3	prefactor of $\nu^{0.3}$ power law
m	fragility parameter
n	power-law exponent of left wing of boson peak
S	scattering function
T	temperature
t_c	CM crossover time
T_c	MCT critical temperature
T_g	glass temperature
T_{VF}	Vogel-Fulcher temperature
w	half width of loss peak
β	power-law exponent of α-peak at $\nu > \nu_p$
β_{CD}	width parameter of CD function
γ	MCT critical exponent
$\Delta\varepsilon$	relaxation strength
ε_c	constant loss
ε_{min}	amplitude of loss minimum
ε'	real part of dielectric permittivity
ε''	imaginary part of dielectric permittivity (dielectric loss)
λ	MCT exponent parameter
ν	frequency
ν_k	MCT knee frequency
ν_{min}	frequency of loss minimum
ν_p	α-peak frequency
ν_τ	$1/(2\pi \langle \tau_\alpha \rangle)$
σ_{dc}	d.c. conductivity
σ'	real part of conductivity

τ_α α-relaxation time
τ_β β-relaxation time
χ'' imaginary part of susceptibility

CC   Cole-Cole
CD   Cole-Davidson
CKN $[Ca(NO_3)_2]_{0.4}[KNO_3]_{0.6}$
CM   coupling model
FIR   far infrared
FLD   frustration-limited domain
KWW   Kohlrausch-Williams-Watts
LPS   locally preferred structure (FLD theory)
MCT   mode-coupling theory
PC   propylene carbonate
VFT   Vogel-Fulcher-Tammann

References

1. Cable M (1991) In: Zarzycki J (ed) Materials science and technology, vol 9: glasses and amorphous materials. VCH, Weinheim, p 1
2. Zarzycki J (1991) Glasses and the vitreous state. Cambridge University Press, Cambridge
3. Höchli UT, Knorr K, Loidl A (1990) Adv Phys 39:405
4. Anderson PW (1995) Science 267:1615
5. Ediger MD, Angell CA, Nagel SR (1996) J Phys Chem 100:13,200
6. Angell CA, Ngai KL, McKenna GB, McMillan PF, Martin SW (2000) J Appl Phys 88:3113
7. Ngai KL (2000) J Non-Cryst Solids 275:7
8. Böttcher CJF, Bordewijk P (1978) Theory of electric polarization. Elsevier, Amsterdam
9. Dixon PK, Wu L, Nagel SR, Williams BD, Carini JP (1990) Phys Rev Lett 65:1108
10. McCrum NG, Read BE, Williams G (1991) Anelastic and dielectric effects in polymeric solids. Dover, New York
11. Schönhals A, Kremer F, Hofmann A, Fischer EW, Schlosser E (1993) Phys Rev Lett 70: 3459
12. Hofmann A, Kremer F, Fischer EW, Schönhals A (1994) In: Richert R, Blumen A (eds) Disorder effects on relaxational processes. Springer, Berlin Heidelberg New York, p 309
13. Menon N, Nagel SR (1995) Phys Rev Lett 74:1230
14. Ngai KL, Cramer C, Saatkamp T, Funke K (1996) In: Giordano M, Leporini D, Tosi MP (eds) Proceedings of the Workshop on Non-Equilibrium Phenomena in Supercooled Fluids, Glasses, and Amorphous Materials, Pisa, Italy, 1995. World Scientific, Singapore, p 3
15. Lunkenheimer P, Schneider U, Brand R, Loidl A (2000) Contemp Phys 41:15
16. Davidson DW, Cole RH (1951) J Chem Phys 19:1484
17. Lunkenheimer P, Pimenov A, Schiener B, Böhmer R, Loidl A (1996) Europhys Lett 33:611
18. Leheny RL, Nagel SR (1997) Europhys Lett 39:447
19. Kudlik A, Benkhof S, Blochowicz T, Tschirwitz C, Rössler E (1999) J Mol Structure 479:201
20. Chamberlin RV (1993) Phys Rev B 48:15,638
21. Chamberlin RV (1999) Phys Rev Lett 82:2520
22. Tarjus G, Kivelson D, Kivelson S (1997) In: Fourkas JT, Kivelson D, Mohanty U, Nelson KA (eds) Supercooled liquids, advances and novel applications. American Chemical Society, Washington, DC, ACS Symposium Series 676, p 67
23. Johari GP, Goldstein M (1970) J Chem Phys 53:2372

24. Johari GP (1976) In: Goldstein M, Simha R (eds) The glass transition and the nature of the glassy state. Annu New York Acad Sci 279:117
25. Bengtzelius U, Götze W, Sjölander A (1984) J Phys C 17:5915
26. Leutheuser E (1984) Phys Rev A 29:2765
27. Götze W (1985) Z Phys B 60:195
28. Götze W, Sjögren L (1992) Rep Progr Phys 55:241
29. Ngai KL (1979) Comments Solid State Phys 9:127
30. Ngai KL (1994) In: Richert R, Blumen A (eds) Disorder effects on relaxational processes. Springer, Berlin Heidelberg New York, p 89
31. Ngai KL, Rendell RW (1997) In: Fourkas JT, Kivelson D, Mohanty U, Nelson KA (eds) Supercooled liquids, advances and novel applications. American Chemical Society, Washington, DC, ACS Symposium Series 676, p 45
32. Kivelson D, Kivelson SA, Zhao X-L, Nussinov Z, Tarjus G (1995) Physica A 219:27
33. Novikov VN (1998) Phys Rev B 58:8367
34. Cummins HZ, Li G, Du WM, Hernandez J, Tao NJ (1995) Transp. Theory Statist Phys 24:981
35. Petry W, Wuttke J (1995) Transp Theory Stat Phys 24:1075
36. Cummins HZ, Li G, Hwang YH, Shen GQ, Du WM, Hernandez J, Tao NJ (1997) Z Phys B 103:501
37. Rössler E, Novikov VN, Sokolov AP (1997) Phase Transitions 63:201
38. Götze W (1999) J Phys Condens Matter 11:A1
39. Volkov AA, Goncharov YG, Kozlov GV, Lebedev SP, Prokhorov AM (1985) Infrared Phys 2:369
40. Volkov AA, Kozlov GV, Lebedev SP, Prokhorov AM (1989) Infrared Phys 29:747
41. Schneider U, Lunkenheimer P, Pimenov A, Brand R, Loidl A (2001) Ferroelectrics 249:89
42. Lunkenheimer P, Pimenov A, Dressel M, Goncharov YG, Böhmer R, Loidl A (1996) Phys Rev Lett 77:318
43. Pimenov A, Lunkenheimer P, Rall H, Kohlhaas R, Loidl A, Böhmer R (1996) Phys Rev E 54:676
44. Lunkenheimer P, Pimenov A, Loidl A (1997) Phys Rev Lett 78:2995
45. Lunkenheimer P, Pimenov A, Dressel M, Gorshunov B, Schneider U, Schiener B, Loidl A (1996) In: Fourkas JT, Kivelson D, Mohanty U, Nelson KA (eds) Supercooled liquids, advances and novel applications. American Chemical Society, Washington, DC, ACS Symposium Series 676, p 168
46. Schneider U, Lunkenheimer P, Brand R, Loidl A (1998) J Non-Cryst Solids 235/237:173
47. Schneider U, Lunkenheimer P, Brand R, Loidl A (1999) Phys Rev E 59:6924
48. Angell CR, Wong J, Edgell WF (1969) J Chem Phys 51:4519
49. Strom U, Hendrickson JR, Wagner RJ, Taylor PC (1974) Solid State Commun 15:1871
50. Strom U, Taylor PC (1977) Phys Rev B 16:5512
51. Liu C, Angell CA (1990) J Chem Phys 93:7378
52. Cole RH, Tombari E (1991) J Non-Cryst Solids 131/133:969
53. Perova TS, Vij JK (1996) J Mol Liq 69:1
54. Perova TS, Vij JK, Christensen DH, Nielsen OF (1999) J Mol Structure 479:111
55. Wong J, Angell CA (1976) Glass: structure by spectroscopy. Dekker, New York
56. Karpov VG, Klinger MI, Ignatiev FN (1983) Sov Phys JETP 57:439
57. Buchenau U, Galperin YM, Gurevich VL, Parshin DA, Ramos MA, Schober HR (1992) Phys Rev B 46:2798
58. Elliott SR (1992) EuroPhys Lett 19:201
59. Malinovsky VK, Novikov VN, Sokolov AP (1987) J Non-Cryst Solids 90:485
60. Schirmacher W, Diezemann G, Ganter C (1998) Phys Rev Lett 81:136
61. Götze W, Mayr MR (2000) Phys Rev E 61:587
62. Lunkenheimer P, Schneider U, Brand R, Loidl A (1999) In: Tokuyama M, Oppenheim I (eds) Slow dynamics in complex systems. 8th Tohwa University International Symposium. AIP, New York, AIP Conference Proceedings 469, p 433
63. Schönhals A, Kremer F, Schlosser E (1991) Phys Rev Lett 67:999

64. Dendzik Z, Paluch M, Gburski Z, Ziolo J (1997) J Phys Condens Matter 9:L339
65. Paluch M, Dendzik Z, Gburski Z (1998) J Non-Cryst Solids 232/234:390
66. Brand R, Lunkenheimer P, Schneider U, Loidl A (1999) Phys Rev Lett 82:1951
67. Lunkenheimer P, Brand R, Schneider U, Loidl A (1999) Phil Mag B 79:1945
68. Kudlik A, Benkhof S, Lenk R, Rössler E (1995) Europhys Lett 32:511
69. Schneider U, Brand R, Lunkenheimer P, Loidl A (2000) Eur Phys J E 2:67
70. Menon N, Nagel SR (1993) Phys Rev Lett 71:4095
71. Schönhals A, Kremer F, Stickel F (1993) Phys Rev Lett 71:4096
72. Leheny RL, Menon N, Nagel SR (1996) Europhys Lett 36:473
73. Kudlik A, Blochowicz T, Benkhof S, Rössler E (1996) Europhys Lett 36:475
74. Menon N, O'Brian KP, Dixon PK, Wu L, Nagel SR, Williams BD, Carini JP (1992) J Non-Cryst Solids 141:61
75. Leslie-Pelecky DL, Birge NO (1994) Phys Rev Lett 72:1232
76. Olsen NB (1998) J Non-Cryst Solids 235/237:399
77. Jiménez-Ruiz M, González MA, Bermejo FJ, Miller MA, Birge NO, Cendoya I, Alegriá A (1999) Phys Rev B 59:9155
78. León C, Ngai KL (1999) J Phys Chem B 103:4045
79. León C, Ngai KL, Roland CM (1999) J Chem Phys 110:11,585
80. Wagner H, Richert R (1999) J Chem Phys 110:11,660
81. Schneider U, Brand R, Lunkenheimer P, Loidl A (2000) Phys Rev Lett 84:5560
82. Zallen R (1983) The physics of amorphous solids. Wiley, New York
83. Lovesey SW (1984) Theory of neutron scattering from condensed matter, vol 1. Clarendon Press, Oxford, p 301
84. Chantry GW, Gebbie HA (1965) Nature 208:378
85. Poley JP (1955) Appl Sci Res B 4:337
86. Vij JK, Hufnagel F (1985) In: Evans MW (ed) Dynamical processes in condensed matter. Wiley, New York
87. Hill NE (1963) Proc Phys Soc 82:723
88. Coffey WT, Corcoran PM, Vij JK (1987) Proc R Soc London A 412:339
89. Lunkenheimer P, Loidl A (1996) J Chem Phys 104:4324
90. Lunkenheimer P, Pimenov A, Dressel M, Schiener B, Schneider U, Loidl A (1997) Progr Theor Phys Suppl 126:123
91. Lunkenheimer P, Pimenov A, Dressel M, Gorshunov B, Schneider U, Schiener B, Böhmer R, Loidl A (1997) In: Angell CA, Ngai KL, Kieffer J, Egami T, Nienhaus GU (eds) Structure and dynamics of glasses and glass formers. Material Research Society, Pittsburgh, MRS Symposium Proceedings 455, p 47
92. Lunkenheimer P (1999) Dielectric spectroscopy of glassy dynamics. Shaker, Aachen
93. Brand R, Lunkenheimer P, Schneider U, Loidl A (2000) Phys Rev B 62:8878
94. Lunkenheimer P, Schneider U, Brand R, Loidl A (2000) Phys Bl 56:35
95. Angell CA (1985) In: Ngai KL, Wright GB (eds) Relaxations in complex systems. NRL, Washington, DC, p 3
96. Böhmer R, Ngai KL, Angell CA, Plazek DJ (1993) J Chem Phys 99:4201
97. Wuttke J, Hernandez J, Li G, Coddens G, Cummins HZ, Fujara F, Petry W, Sillescu H (1994) Phys Rev Lett 72:3052
98. Du WM, Li G, Cummins HZ, Fuchs M, Toulouse J, Knauss LA (1994) Phys Rev E 49:2192
99. Wuttke J, Ohl M, Goldammer M, Roth S, Schneider U, Lunkenheimer P, Kahn R, Rufflé B, Lechner R, Berg MA (2000) Phys Rev E. 61:2730
100. Brand R (2001) Breitbandige dielektrische Spektroskopie zur Untersuchung der Glasdynamik plastischer Kristalle. Pro Business, Berlin
101. Hassion FX, Cole RH (1955) J Chem Phys 23:1756
102. Benmore CJ, Loh YL (2000) J Chem Phys 112:5877
103. Fayos R, Bermejo FJ, Dawidowski J, Fischer HE, González MA (1996) Phys Rev Lett 77:3823
104. Ramos MA, Vieira, S, Bermejo FJ, Dawidowski J, Fischer HE, Schober H, González MA, Loong CK, Price DL (1997) Phys Rev Lett 78:82

105. Fischer HE, Bermejo FJ, Cuello GJ, Fernández-Diáz MT, Dawidowski J, González MA, Schober H, Jiménez-Ruiz M (1999) Phys Rev Lett 82:1193
106. Miller MA, Jiménez-Ruiz M, Bermejo FJ, Birge NO (1998) Phys Rev B 57:13,977
107. Benkhof S, Kudlik A, Blochowicz T, Rössler E (1998) J Phys Condens Matter 10:8155
108. Jiménez-Ruiz M, González MA, Bermejo FJ, Miller MA, Birge NO, Cendoya I, Alegriá A (1999) Phys Rev B 59:9155
109. Garg SK, Smyth GP (1965) J Phys Chem 69:1294
110. Hansen C, Stickel F, Berger T, Richert R, Fischer EW (1997) J Chem Phys 107:1086
111. Kudlik A, Tschirwitz C, Benkhof S, Blochowicz T, Rössler E (1997) Europhys Lett 40:649
112. Macedo PB, Moynihan CT, Bose R (1972) Phys Chem Glasses 13:171
113. Ross Macdonald J (1987) Impedance spectroscopy. Wiley, New York
114. Elliott SR (1989) Phil Mag B 60:777
115. Elliott SR (1990) J Non-Cryst Solids 116:179
116. Funke K (1986) Solid State Ionics 18/19:183
117. Funke K (1993) Phil Mag A 68:711
118. Funke K, Hermeling J, Kümpers J (1988) Z Naturforsch 43a:1094
119. Leites LA (1992) Chem Rev 92:279
120. Baugham RH (1970) J Chem Phys 53:3781
121. Leffler AJ (1975) J Chem Phys 63:3971
122. Bukalov SS, Leites LA (1982) Chem Phys Lett. 87:327
123. Bukalov SS, Leites LA (1989) Bull Acad Sci USSR, Physical Series 53:61
124. Yamamuro O, private communication
125. Böhmer R, private communication
126. Brand R, Lunkenheimer P, Loidl A (1997) Phys Rev B 56:R5713
127. Boehm L, Smith DL, Angell CA (1987) J Mol Liq 36:153
128. Angell CA, Boehm L, Oguni M, Smith DL (1993) J Mol Liq 56:275
129. Casalini R, Ngai KL, Roland CM (2000) J Chem Phys 112:5181
130. Ngai KL, Lunkenheimer P, León C, Schneider U, Brand R, Loidl A (2001) J Chem Phys 115:1405
131. Leheny RL, Nagel SR (1998) Phys Rev B 57:5154
132. Hansen C, Richert R (1997) J Phys: Condens Matter 9:9661
133. Johari GP, Pathmanathan K (1986) J Chem Phys 85:6811
134. Fujimori H, Oguni M (1994) J Chem Thermodyn 26:367
135. Schnauss W, Fujara F, Sillescu H (1992) J Chem Phys 97:1378
136. Ngai KL (1998) Phys Rev E 57:7346
137. Chamberlin RV, private communication
138. Dixon PK, Menon N, Nagel SR (1994) Phys Rev E 50:1717
139. Brand R, Lunkenheimer P, Loidl A (to be published)
140. Lunkenheimer P, Brand R, Schneider U, Loidl A (1999) In: Tokuyama M, Oppenheim I (eds) Slow dynamics in complex systems. 8th Tohwa University International Symposium, AIP, New York, AIP Conf Proc 469, p 671
141. Jonscher AK (1983) Dielectric relaxations in solids. Chelsea Dielectrics Press, London
142. Lee WK, Liu JF, Nowick AS (1991) Phys Rev Lett 67:1559
143. Ngai KL, Strom U, Kanert O (1992) Phys Chem Glasses 33:109
144. Lim BS, Vaysleyb AV, Nowick AS (1993) Appl Phys A 56:8
145. Elliott SR (1994) Solid State Ionics 70/71:27
146. Cramer C, Funke K, Saatkamp T (1995) Phil Mag 71:701
147. Lunkenheimer P, Gerhard G, Drexler F, Böhmer R, Loidl A (1995) Z Naturforsch 50a:1151
148. Sidebottom DL, Green PF, Brow RK (1995) Phys Rev Lett 74:5068
149. Sidebottom DL, Green PF, Brow RK (1995) J Non-Cryst Solids 203:300
150. Ngai KL, Jain H, Kanert O (1997) J Non-Cryst Solids 222:383
151. Böhmer R, Lotze M, Lunkenheimer P, Drexler F, Gerhard G, Loidl A (1994) J Non-Cryst Solids 172/174:1270
152. Dumm M, Dressel M, Nicklas M, Lunkenheimer P, Loidl A, Weiden M, Steglich F, Assmann B, Homborg H, Fulde P (1998) Euro Phys J B 6:317

153. Pimenov A, Ullrich J, Lunkenheimer P, Loidl A, Rüscher CH (1998) Solid State Ionics 109:111
154. Le Stanguennec M, Elliott SR (1994) Solid State Ionics 73:199
155. Colmenero J, Arbe A, Alegía A (1993) Phys Rev Lett 71:2603
156. Alvarez F, Hoffman A, Alegía A, Colmenero J (1996) J Chem Phys 105:432
157. Arbe A, Richter D, Colmenero J, Farago B (1996) Phys Rev E 54:3853
158. Schilling R (1994) In: Richert R, Blumen A (eds) Disorder effects on relaxational processes. Springer, Berlin Heidelberg New York, p 193
159. Cummins HZ (1999) J Phys Condens Matter 11:A95
160. Götze W, Voigtmann T (2000) Phys Rev B 61:4133
161. Sokolov AP, Rössler E, Kisliuk A, Quitmann D (1993) Phys Rev Lett 71:2062
162. Franosch T, Götze W, Mayr MR, Singh AP (1997) Phys Rev E 55:3183
163. Ma J, Vanden Bout D, Berg M (1996) Phys Rev E 54:2786
164. Li G, Du WM, Chen XK, Cummins HZ, Tao NZ (1992) Phys Rev A 45:3867
165. Börjesson L, Elmroth M, Torell LM (1990) Chem Phys 149:209
166. Börjesson L, Howells WS (1991) J Non-Cryst Solids 131/132:53
167. Götze W, Singh AP, Voigtmann T (2000) Phys Rev E 61:6934
168. Zeng CZ, Kivelson D, Tarjus G (1994) Phys Rev E 50:1711
169. Cummins HZ, Li G (1994) Phys Rev E 50:1720
170. Gapinski J, Steffen W, Patkowski A, Sokolov AP, Kisliuk A, Buchenau U, Russina M, Mezei F, Schober H (1999) J Chem Phys 110:2312
171. Barshilia HC, Li G, Shen GQ, Cummins HZ (1999) Phys Rev E 59:5625
172. Wuttke J, private communication
173. Knaak W, Mezei F, Farago B (1988) Europhys Lett 7:529
174. Birge NO (1986) Phys Rev A 34:1631
175. Jeong YH, Nagel SR, Bhattacharya S (1986) Phys Rev A 34:602
176. Ngai KL, Rendell RW (1990) Phys Rev B 41:754
177. Wu L, Dixon PK, Nagel SR, Williams BD, Carini JP (1991) J Non-Cryst Solids 131/133:32
178. Lebon MJ, Dreyfus C, Guissani Y, Pick RM, Cummins HZ (1997) Z Phys B 103:433
179. Wahnströhm G, Lewis LJ (1997) Progr Theor Phys Suppl 126:261
180. Kämmerer S, Kob W, Schilling R (1998) Phys Rev B 58:2141
181. Franosch T, Fuchs M, Götze W, Mayr MR, Singh AP (1997) Phys Rev E 56:5659
182. Schilling R, Scheidsteger T (1997) Phys Rev E 56:2932
183. Steffen W, Patkowski A, Gläser H, Meier G, Fischer EW (1994) Phys Rev E 49:2992
184. Li G, Du WM, Sakai A, Cummins HZ (1992) Phys Rev A 46:3343
185. Rössler E, Sokolov AP, Kisliuk A, Quitmann D (1994) Phys Rev B 49:14,967
186. Pathmanathan K, Johari GP (1985) J Phys C Solid State Phys 18:6535
187. Gangasharan, Murthy SSN (1993) J Chem Phys 99:9865

6 Molecular Dynamics in Confining Space

F. Kremer · A. Huwe · A. Schönhals · S.A. Różański

6.1
Introduction

The molecular and collective dynamics in confining space is determined by the counterbalance between surface- and confinement effects [1]. The former results from interactions of a host system with guest molecules which take place at the interface between both, the latter originates from the inherent length scale on which the underlying molecular fluctuations take place. Surface effects cause a decrease while confinement effects are characterised by an increase of the molecular dynamics with decreasing spatial dimensions of the confining space (Fig. 6.1). Hence in glass-forming systems [2–7] for the calorimetric glass transition temperature an increase resp. a decrease is observed. It is evident that this counterbalance must depend sensitively on the type of confined molecules (glass-forming liquids, polymers, liquid crystals), on the properties of the (inner) surfaces (wetting, non-wetting) and on the architecture of the molecules with respect to the walls (grafted, layered or amorphous systems).

   Confining geometries [8–23] can be realised in various ways: by containing the system under study in zeolites, in nanoporous sol-gel glasses, in mesoporous

Fig. 6.1. Scheme of the molecular dynamics in confining space as a counterbalance between surface and confinement effects
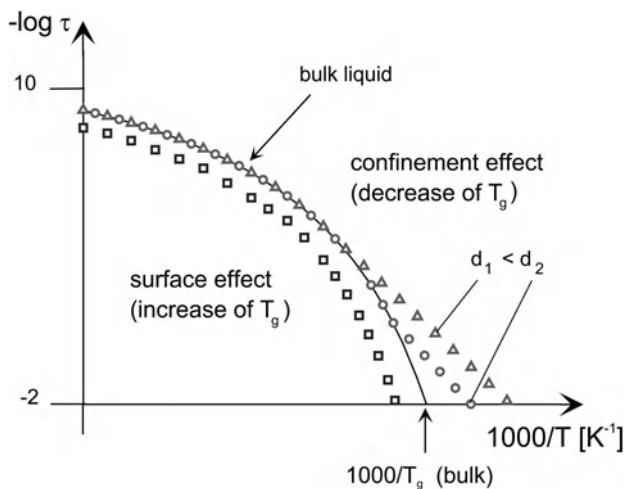
membranes, in block copolymers, etc. With its extraordinary dynamic range (in frequency *and* intensity) broadband dielectric spectroscopy enables one to unravel the subtle interplay between surface- and confinement effects and to contribute to basic questions such as for instance (i) is there an inherent lengthscale of cooperativity in glass forming liquids and how does it vary with temperature, (ii) what is the effect of a lubricant layer in order to decouple the dynamics of a liquid from a solid wall, (iii) what is the difference between H-bond forming and van-der-Waals liquids, (iv) what is the dynamics of polymers in confining space and (v) how is the molecular and collective dynamics of liquid crystals influenced in mesoporous membranes?

6.2
H-Bond Forming and van-der-Waals Liquids in Zeolitic and Nanoporous Media

6.2.1
Glycols in Zeolites and Nanoporous Sol-Gel Glasses

Zeolites [24, 25] offer the unique possibility to vary the dimension and the topology of spatial confinement on a sub-nanometer scale in controlled manner. Silica sodalite consists of identical, so-called β-cages, with an inner diameter of 0.6 nm. Ethylene glycol (EG) is one of the structure-directing agents which control the formation of silica sodalite [26, 27]. Exactly *one* EG molecule becomes occluded in *one* sodalite cage during synthesis and cannot escape from it unless the cage is thermally decomposed [27]. Silicalite-I, zeolite beta and AlPO$_4$-5 have channel-like pore systems (see Fig. 6.2). In silicalite-I, consisting of pure SiO$_2$, rings of ten Si and ten O atoms form a three-dimensional pore system with two types of elliptical channels having cross-sections of 0.56–0.53 nm and 0.55–0.51 nm [24]. In zeolite beta (12-ring system) the channels in [100] and [10] directions have a cross-section area of 0.76 nm × 0.64 nm, whereas the channels in the [1] direction have smaller pores (0.55 nm × 0.55 nm) [28]. The Si:Al ratio of the sample was 40 to reduce the number of counter-ions in the channels. AlPO$_4$-5 has a one-dimensional pore system. In this aluminophosphate, the channels with diameters of 0.73 nm are arranged in a hexagonal array. To realise larger pore diameters, sol-gel glasses (Geltech Inc., USA) with pore sizes of 2.5 nm, 5.0 nm, 7.5 nm and 20 nm and a narrow pore size distribution can be used.

Besides sodalite which is already loaded with EG after synthesis, all nanoporous hosts are heated to 600 K with a temperature increase of 20 K h^{-1} and evacuated at 10^{-5} mbar for 36 h to remove water and other volatile impurities. Afterwards the zeolitic host systems are filled with EG from the vapour phase in a closed vacuum chamber at 448 K. The samples are cooled down to room temperature and remain in the vacuum chamber for 24 h before the dielectric measurements are carried out.

Isothermal data (Fig. 6.3) of the dielectric loss ε'' are fitted by a superposition of a Havriliak and Negami (HN) relaxation function and a conductivity contri-
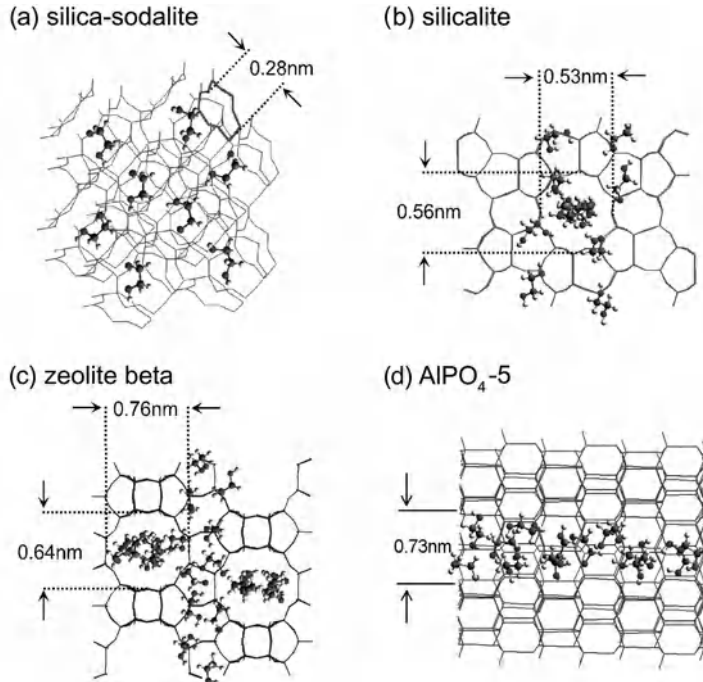
Fig. 6.2. Scheme of the zeolitic host systems in which the guest molecule ethylene glycol was confined: **a** silica sodalite (SiO_2) has cubic cages with a lattice constant of 0.89 nm. The cages are connected by channels with a diameter of 0.28 nm. Only *one* molecule is confined to each cage; **b** silicalite consists of pure SiO_2 and has a three-dimensional pore system with two different types of elliptical channels having cross sections of 0.56 nm × 0.53 nm and 0.55 nm × 0.51 nm; **c** zeolite beta is an aluminosilicate with a three-dimensional pore system having cross sections of 0.76 nm × 0.64 nm in the [100] and [010] directions and a diameter of 0.55 nm in the [001] direction; **d** $AlPO_4$-5 is an aluminophosphate with one-dimensional channels (diameter 0.73 nm) arranged in hexagonal array. Taken from [1] with permission

bution [29, 30]

$$\varepsilon'' = \frac{\sigma_0}{\varepsilon_0}\frac{a}{\omega^s} + \mathrm{Im}\left[\frac{\Delta\varepsilon}{(1+(i\omega\tau)^\alpha)^\gamma}\right] \tag{6.1}$$

In this notation, ε_0 is the vacuum permittivity, σ_0 the d.c.-conductivity and $\Delta\varepsilon$ the dielectric strength. α and γ describe the symmetric and asymmetric broadening of the relaxation peak. The exponent $s = 1$ holds for pure electronic conduction; deviations ($s < 1$) are observed for ionic charge carriers which cause electrode polarisation or Maxwell-Wagner polarisation effects. The factor a has the dimension $(Hz)^{-1}$ $(rad\ Hz)^s$. The uncertainty in the determination of $\log\tau$ is ≤ 0.1 decades and less than 5% for $\Delta\varepsilon$. Due to the fact that ε' and ε'' are con-
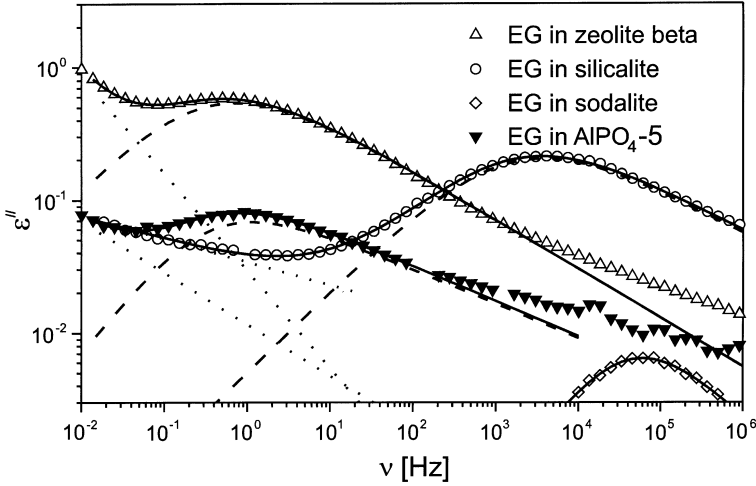
Fig. 6.3. The dielectric loss ε'' vs frequency for ethylene glycol (EG) being confined to zeolitic host systems as indicated. The *solid lines* are a superposition of a Havriliak-Negami-relaxation (*dashed line*) and a conductivity contribution (*dotted line*). Taken from [1] with permission

nected by the Kramers-Kronig relations, a fit in ε' does not improve the accuracy. From the fits according to Eq. (6.1) the relaxation rate $1/\tau_{max}$ can be deduced which is given at the frequency of maximum dielectric loss ε'' for a certain temperature. A second way to interpret the data is the use of a relaxation time distribution function $L(\tau)$ of Debye relaxators with relaxation times τ. The imaginary part of the dielectric function is expressed by

$$\varepsilon'' = (\varepsilon_s - \varepsilon_\infty) \int \frac{L(\tau)}{1+\omega^2\tau^2} \, d\tau \tag{6.2}$$

where ε_s and ε_∞ denote the low- and high-frequency limit of the permittivity. $L(\tau)$ can be extracted numerically from the data [31] or calculated (analytically) from the fit with HN-functions [29, 30]. To characterise the temperature dependence of the relaxation behaviour, the averaged logarithmic relaxation time $\log\tau_{med}$ is calculated

$$\log \tau_{med} = \langle \log\tau \rangle = \left(\int\limits_{-\infty}^{+\infty} \log\tau\, L(\tau)\,d\tau \right) \Big/ \left(\int\limits_{-\infty}^{+\infty} L(\tau)\,d\tau \right) \tag{6.3}$$

$\log\tau_{med}$ equals $\log\tau_{max}$ if the peak of a relaxation process is symmetrically broadened. The calculation of $\log\tau_{med}$ can be done only with high accuracy if the relaxation time distribution function is known in a broad range. For that reason $\log\tau_{max}$ is determined for molecules confined to zeolites (where the frequency range is limited) and $\log\tau_{med}$ is calculated if the nanoporous sol-gel glasses are used as host.

Figure 6.3 shows the dielectric spectra for ethylene glycol (EG) confined to different zeolitic host systems at 160 K. The relaxation rates τ_{max}^{-1} for EG in the

Fig. 6.4. The relaxation rate vs inverse temperature for ethylene glycol being confined to different zeolitic host systems as indicated. The errors are smaller than the size of the symbols. Taken from [1] with permission
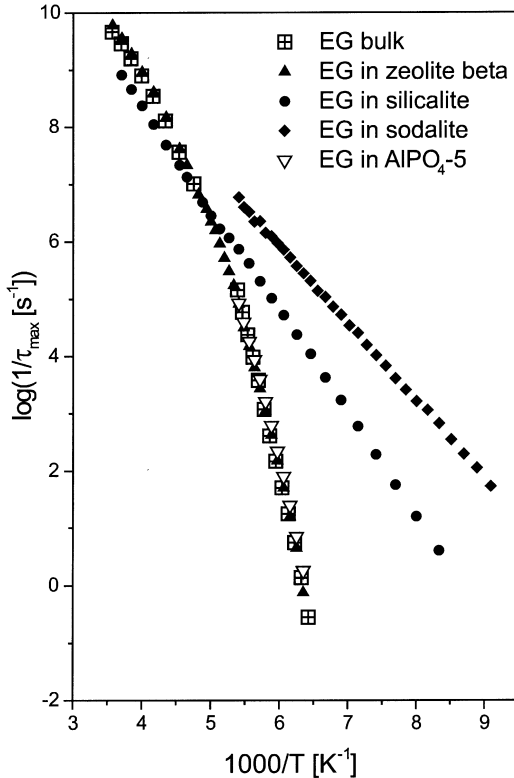

zeolitic host systems differ by up to six orders of magnitude: In zeolites with smaller pores (silicalite and sodalite) the relaxation rates of EG are significantly higher compared to zeolite beta and $AlPO_4$-5. Especially for EG in sodalite, the relaxation strength is comparatively weak. This is caused by EG molecules which are immobilised due to the interaction with the zeolitic host matrix. Figure 6.4 shows the relaxation rate as a function of inverse temperature for EG as bulk liquid and confined to zeolites. EG in zeolite beta (solid triangles) and in $AlPO_4$-5 (open triangles) has a relaxation rate like the bulk liquid (squares) following the temperature dependence according to the empirical Vogel-Fulcher-Tammann – (VFT-) equation [32–34]

$$\frac{1}{\tau} = A \exp\left(\frac{-DT_0}{T - T_0}\right) \tag{6.4}$$

where A is a prefactor, D is the fragility parameter and T_0 is the Vogel temperature. The relaxation rates of EG in silicalite and sodalite show an Arrhenius-type temperature dependence.

The single molecule relaxation of EG in sodalite is at $T \approx 155$ K about six orders of magnitude faster compared to the bulk liquid. Its activation energy is 26 ± 1 kJ mol^{-1} and corresponds to the value for bulk EG at high relaxation rates

Fig. 6.5. Normalized relaxation process for a Debye process (*solid line*), for EG bulk (*solid squares*) and confined to zeolite beta (*open triangles*), silicalite (*open circles*), sodalite (*open diamonds*) and AlPO$_4$-5 (*solid triangles*) at 165 K. The curves are calculated from the Havriliak-Negami-fit parameters. Taken from [1] with permission
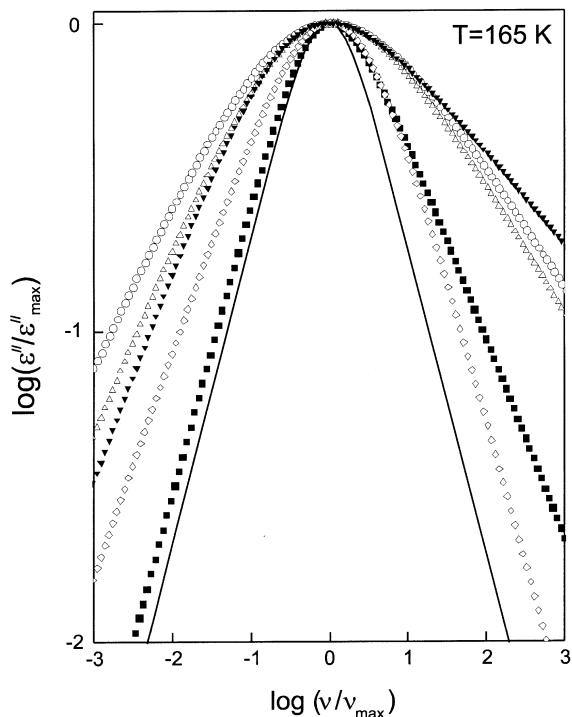
$(29 \pm 2$ kJ mol$^{-1})$ [35]. The relaxation process of EG in silicalite has a larger activation energy $(35 \pm 2$ kJ mol$^{-1})$ which is still smaller than the apparent activation energy (tangent to the VFT-temperature dependence) of the bulk liquid close to T_g. Its Arrhenius-like temperature dependence resembles the single molecule relaxation of EG in sodalite.

Figure 6.5 shows the normalised relaxation peaks for all samples at 165 K as calculated from the fits. Compared to a Debye process (solid curve) even the bulk liquid and the single molecule relaxation (EG in sodalite) are broadened. The distributions for EG in the other zeolitic host systems show very pronounced broadening at both low and high frequencies.

To study the molecular arrangement of the molecules in confining space, the molecular simulation program Cerius^2 is used on a Silicon Graphics workstation to model a finite zeolite crystal with four unit cells surrounded by vacuum. By "filling" the pores with EG a completely loaded nanoporous host/guest-system can be simulated and structural parameters like distance between molecules, density and length of H bonds can be determined. The simulations were carried out using three different force fields: The *Dreiding* force-field [36], the force-field *Burchardt-universal* [37, 38] and the *consistent force-field cff 91*. The three force-fields provide the same results within the uncertainty for the quantities shown in Table 6.1.

The computer simulations of EG in zeolitic host systems show that in silicalite the molecules are aligned almost single-file-like along the channels and that in zeolite beta and in AlPO$_4$-5 two EG molecules are located side by side in the chan-

Table 6.1. Distance between the molecules, average length of hydrogen-bonds (O-H ··· O bonds with a length up to 0.3 nm) and density as calculated from the molecular simulations for ethylene glycol confined to zeolite beta and silicalite and for the bulk liquid. For the simulation of the bulk liquid a limited volume (6.64 nm³) was filled with EG molecules until the bulk density of 1.113 g cm⁻³ was reached. In contrast the densities of EG confined in zeolites are results of the simulation. The error is mainly caused by the uncertainty in calculating the accessible volume of the zeolitic channels

	Distance between molecules (nm)	Average length of H-bonds (nm)	Density (g cm⁻³)
Bulk liquid	0.42 ± 0.01	0.23 ± 0.02	1.113
Zeolite beta	0.41 ± 0.01	0.25 ± 0.02	1.0 ± 0.1
Silicalite	0.42 ± 0.01	0.24 ± 0.02	1.0 ± 0.1

nels (Fig. 6.6). However, neither for the distance between molecules nor for the average length of hydrogen-bonds or the density is a significant change found between the bulk liquid and the molecules in the restricting geometry (Table 6.1). However, for the number of neighbouring molecules (coordination number) a pronounced difference is observed (Fig. 6.7): the coordination number of 11 corresponds to the maximum value in the case of the random close packing model [39] and is found for the bulk liquid within a radius of $r = 0.66$ nm. Within that EG in zeolite beta and in AlPO$_4$-5 has only five neighbouring molecules. As AlPO$_4$-5 has one-dimensional channels and no intersections between them in contrast to zeolite beta the dimensionality of the host system seems to play only a minor role for the dynamics of H-bonded guest molecules. Further reduction in the channel size (as in the case of silicalite) decreases the average number of neighbouring molecules by about 1. This results in a sharp transition from a liquid like dynamics to that of single molecules. In AlPO$_4$-5 only two molecules are located side by side in the one-dimensional channels, hence the interactions are dominated by the nearest neighbouring molecules and an ensemble as small as six EG molecules is sufficient to show a liquid-like dynamics.

In order to analyse the dielectric properties of the heterogeneous systems under study, effective medium theory has to be applied ([40], Chap. 13). It takes into account that the local electric field and the polarisation depend not only on the external electric field but also on the microstructure (topology, filling factor) of the sample. For spherical inclusions in a diluted system (having two components with dielectric functions ε_1^* and ε_2^*) with a volume filler factor f the Maxwell-Garnett formula is used [41]

$$\varepsilon^* = \varepsilon_1^* \frac{2\varepsilon_1^* + \varepsilon_2^* + 2f(\varepsilon_2^* - \varepsilon_1^*)}{2\varepsilon_1^* + \varepsilon_2^* - f(\varepsilon_2^* - \varepsilon_1^*)} \tag{6.5}$$

For ellipsoidal particles the depolarisation factor A has to be taken into account [42]

$$\varepsilon^* = \varepsilon_1^* \frac{\varepsilon_1^* + [A(1-f) + f](\varepsilon_2^* - \varepsilon_1^*)}{\varepsilon_1^* + A(1-f)(\varepsilon_2^* - \varepsilon_1^*)} \tag{6.6}$$
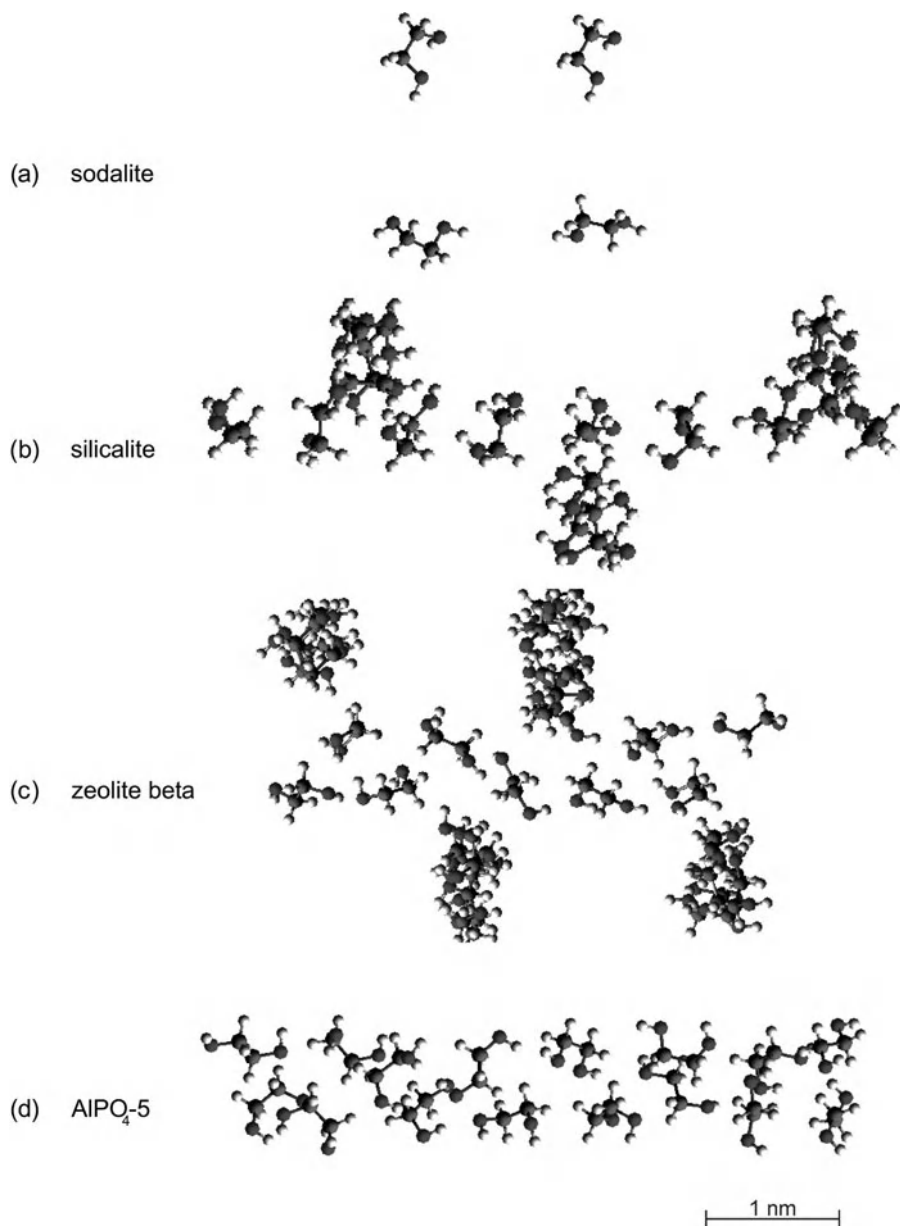
Fig. 6.6. Results of computer simulations of the arrangement of ethylene glycol molecules confined in zeolites. For better visibility the framework of the zeolites is omitted: **a** sodalite; **b** silicalite; **c** zeolite beta; **d** AlPO$_4$-5. The orientation has been chosen for picture **b** and **c** so that one of the channels runs along the horizontal direction of the paper plane. In adjacent channels perpendicular to the paper plane, the molecules appear as stacked on top of one another

Fig. 6.7. The average number of neighbouring molecules (coordination number) as a function of the radius of a surrounding sphere as calculated from the simulations for EG bulk liquid (*squares*), EG confined to zeolite beta (*triangles*), to silicalite (*circles*) and to AlPO$_4$-5 (*solid triangles*). Taken from [1] with permission
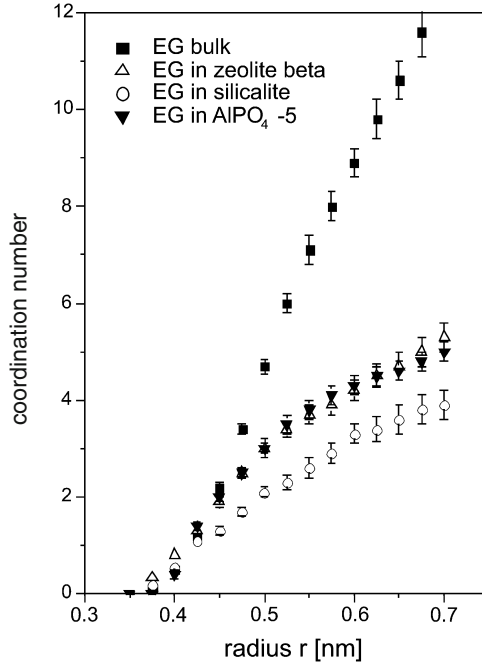
If the axes of an ellipsoid are *a, b* and *c,* the depolarisation factor along the *a*-axis A_a is defined as

$$A_a = \frac{abc}{2} \int_0^\infty \frac{ds}{(s+a^2)\sqrt{(s+a^2)(s+b^2)(s+c^2)}} \tag{6.7}$$

If the inclusions are randomly distributed cylinders, the dielectric function for all three orientations has to be superposed. One of them is parallel to the electric field ($A = 0$) and two are perpendicular ($A = 1/2$)

$$\varepsilon^* = \frac{1}{3}\varepsilon^*(A=0) + \frac{2}{3}\varepsilon^*(A=0.5) \tag{6.8}$$

For higher concentrations ($f > 0.2$) the Hanai-Bruggeman equation is valid [43]

$$\frac{\varepsilon_2^* - \varepsilon^*}{\varepsilon_2^* - \varepsilon_1^*}\left(\frac{\varepsilon_1^*}{\varepsilon^*}\right)^{1/3} = 1 - f \tag{6.9}$$

It can be solved analytically. As it is not symmetric in ε_1^* and ε_2^* it will certainly fail for $f > 0.5$. *Kamiyoshi* modified Rayleigh's approach, which gives similar results to the Maxwell-Garnett formula, with an expression for ε^* which is symmetric in ε_1^* and ε_2^*. It was deduced especially for powder samples and agrees well

with experimental results (e.g. for $f = 0.5$) [44]:

$$\varepsilon^* = \frac{2\varepsilon_I^* \varepsilon_{II}^*}{\varepsilon_I^* + \varepsilon_{II}^*} \quad \text{with} \quad \varepsilon_I^* = \varepsilon_1^* \left(1 + 3f \middle/ \left(\frac{2\varepsilon_1^* + \varepsilon_2^*}{\varepsilon_2^* - \varepsilon_1^*} - f - 0.525 \frac{3(\varepsilon_2^* - \varepsilon_1^*)}{4\varepsilon_1^* + 3\varepsilon_2^*} f^{10/3}\right)\right)$$

$$\text{and} \quad \varepsilon_{II}^* = \varepsilon_2^* \left(1 + 3(1-f) \middle/ \left(\frac{2\varepsilon_2^* + \varepsilon_1^*}{\varepsilon_1^* - \varepsilon_2^*} - (1-f) - 0.525 \frac{3(\varepsilon_1^* - \varepsilon_2^*)}{4\varepsilon_2^* + 3\varepsilon_1^*} (1-f)^{10/3}\right)\right)$$

$$(6.10)$$

The zeolitic samples consist of three components (see Fig. 6.8). The guest molecules are confined in the channels of the zeolites and the sample itself contains about 50 vol.% air between the grains of the zeolites. Therefore an effective-medium analysis in two steps has to be employed: first the guest molecules in the zeolitic host system are described and in the second step the air is taken into account. In the first step, Eqs. (6.8), (6.9) and (6.10) are used while in the second step the assumptions underlying Eq. (6.10) are well fulfilled. The topology of the pores in zeolite beta and in silicalite cannot be described by a simple model (see Fig. 6.2).

Figure 6.9a shows the dielectric loss spectra of EG in $AlPO_4$-5 for the three different models and the experimental data. All calculations deliver a Maxwell-Wagner process at low frequencies. Figure 6.9b presents the peak of the dynamic glass transition normalised to the maximum of the dielectric loss. Equations (6.9) and (6.10) show comparable loss spectra whereas Eq. (6.8) results in a bimodal relaxation peak in contrast to the experimental findings. Figure 6.10a,b shows the relaxation rates and the dielectric strength vs inverse temperature for the models and the experimental data. The error bars result from the uncertainty in the sample thickness and the volume filler factor of the zeolitic microcrystals which has a strong influence on the calculated air content of the samples. Equation (6.8) predicts a relaxation rate which is slightly higher than the experimental data. For Eqs. (6.9) and (6.10) this shift is about one decade similar as in [45, 46]. The molecules show a molecular dynamics which is slower than calculated. This might be caused by the interaction of the guest molecules with the host system. For the dielectric strength, Eqs. (6.9) and (6.10) agree with the experimental data. The model for cylindrical inclusions (6.8) predicts a dielectric strength which is slightly larger.

In summary the models assuming spherical inclusions (Eqs. 6.9 and 6.10) fit better the experimental data. For ethylene glycol in zeolite beta comparable results are obtained. There is a difference in the relaxation rates of about one

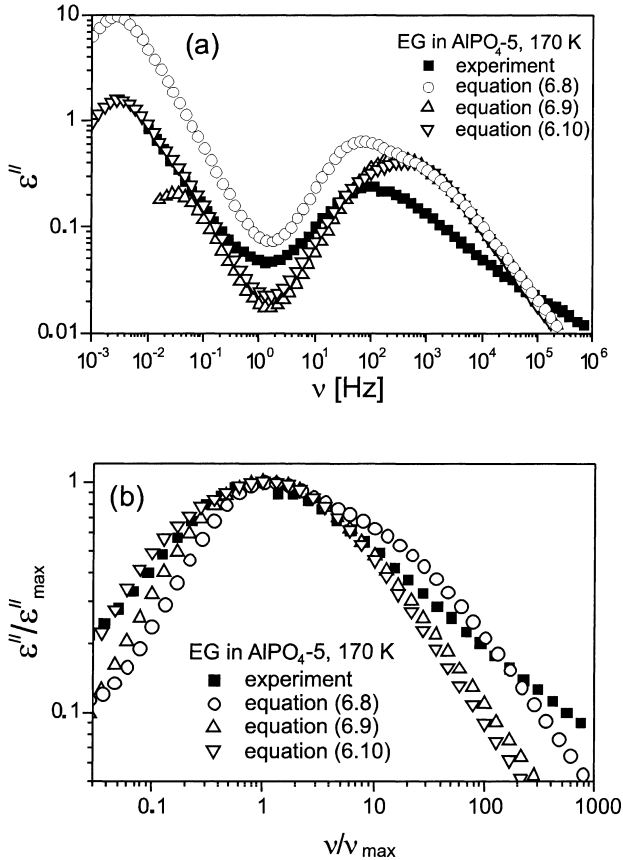**Fig. 6.8.** Scheme of the sample capacitor with the zeolitic sample filled with ethylene glycol
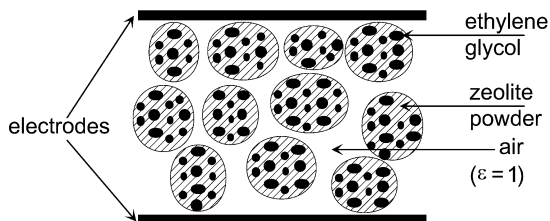
Fig. 6.9. **a** Dielectric spectra of ethylene glycol in AlPO$_4$-5 calculated for three different effective medium models and experimental results as indicated at 170 K. **b** Normalized peak of the dynamic glass transition of the spectra shown in **a**

decade indicating a surface effect. The dielectric strength coincides with the calculations. In general the intrinsic relaxation rate of a filler particle is shifted to higher relaxation rates in heterogeneous media by not more than one decade.

Hence, the experimental results for silicalite and sodalite cannot be explained on the basis of an effective medium approach. The dramatic change of the relaxation rate of ethylene glycol in silicalite and sodalite is not an effect of the heterogeneous mixtures but it is caused by the transition from the liquid state to that of a single molecule. Effective medium theory predicts for ethylene glycol in silicalite and sodalite a dielectric strength which is much larger than observed. The spectra cannot be described by using bulk data and applying effective medium models. This shows that ethylene glycol in silicalite and sodalite has lost its bulk like properties.

Controlled porous glasses (Geltech Inc., USA) offer another possibility to realise a confining space [3–13]. They are available with pore sizes of 2.5 nm,
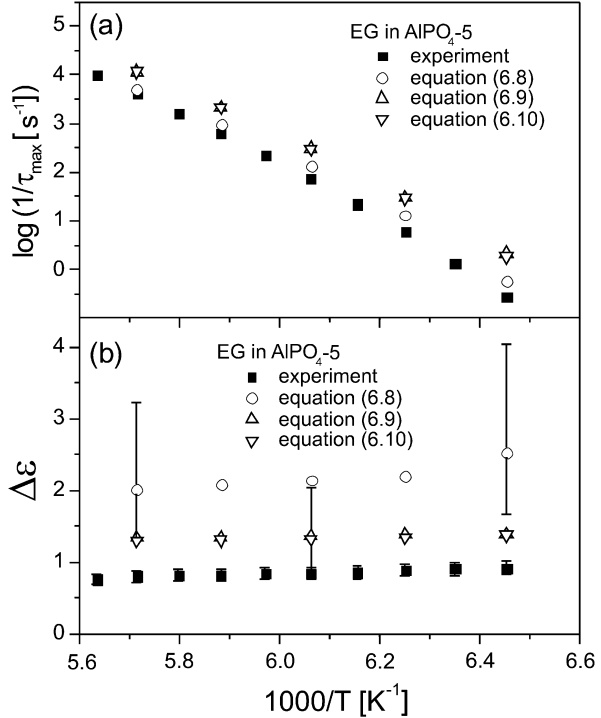
5.0 nm and 7.5 nm and a narrow pore size distribution. The porous glass is disc-shaped (diameter 10 mm, thickness 0.2 mm) so the outer surface is negligible compared to the huge inner surface (520–620 m^2g^{-1}). After evacuating the porous glasses to 10^{-5} mbar at 570 K for 24 h to remove water and other volatile impurities, the pores were filled by capillary wetting during 48 h at a temperature of about 20 K above the melting point of the liquids. For that purpose the glass-forming liquid was injected in the (closed) vacuum chamber by use of a syringe. Both sides of the sample disks were covered with aluminium foil (thickness 800 nm) to ensure a homogenous field distribution and were mounted between gold plated brass electrodes of the capacitor. As H-bond forming liquids the homologous sequence of propylene-, butylene- and pentylene glycol (PG, BG, PeG) were used having an averaged molecular radius or $r_m = 0.306$ nm, $r_m = 0.329$ nm and $r_m = 0.349$ nm, respectively.

Figure 6.11a–c shows the relaxation rates of the α-relaxation of the bulk and confined liquids. No effect of confinement is observed on the relaxation rates of PG and BG in 7.5 nm and 5.0 nm pores. For PeG the α-relaxation in 7.5 nm and 5.0 nm pores becomes slightly faster compared to the bulk at low temperatures. In 2.5 nm pores the relaxation rate is slowed down compared to the bulk; this effect is more pronounced for the larger molecules. The volume corrected dielectric strengths of the α-relaxation of bulk and confined PG, BG, and PeG are shown in Fig. 6.11d–f. For all liquids the absolute value of the dielectric strength $\Delta\varepsilon$ decreases with decreasing pore sizes, indicating the existence of a fraction of
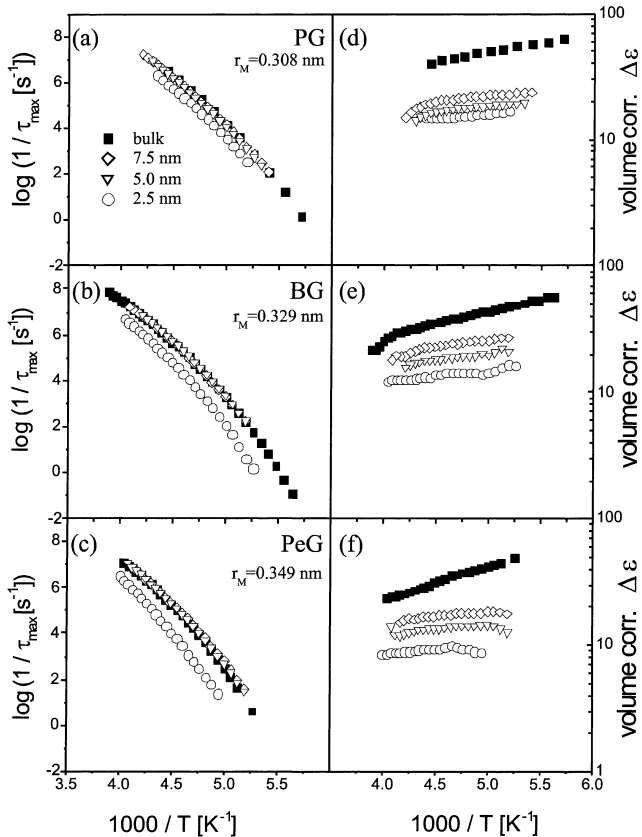
Fig. 6.11. Depiction of: **a–c** relaxation rate $1/\tau_{max}$; **d–f** volume corrected relaxation strength $\Delta\varepsilon$ of the α-relaxation of PG, BG and PeG in pores vs the inverse temperature T. Pore sizes: 2.5 nm (*circles*), – 5.0 nm (*triangles*), 7.5 nm (*diamonds*) and bulk (*filled squares*). The error is smaller than the size of the symbols. r_M is the mean van-der-Waals radius of the molecules. Taken from [9] with permission

immobilised molecules which is dielectrically inactive (complete pore filling was checked by weighing). This layer is caused by H-bonds formed between the glycol molecules and the inner surface of the sol-gel glass.

For confined PG and BG, the temperature dependence of $\Delta\varepsilon$ is comparable to that of bulk liquids while for PeG, $\Delta\varepsilon$ decreases for low temperatures for all pore sizes. This decrease resp. increase of the relaxation rate may be comprehended by assuming exchange between the molecules bound to the pore surface (solid-like layer) and molecules in the centre of pores.

More instructive than the HN-parameters τ_{HN}, α and γ is the relaxation time distribution function $L(\tau)$. It can be deduced from the dielectric spectra (see Chap. 3) either analytically from the HN-fit parameters [29, 30] or by a regularisation technique [31]. Figure 6.12 shows the relaxation time distributions of confined PG at different temperatures. On the long term side a broadening is ob-
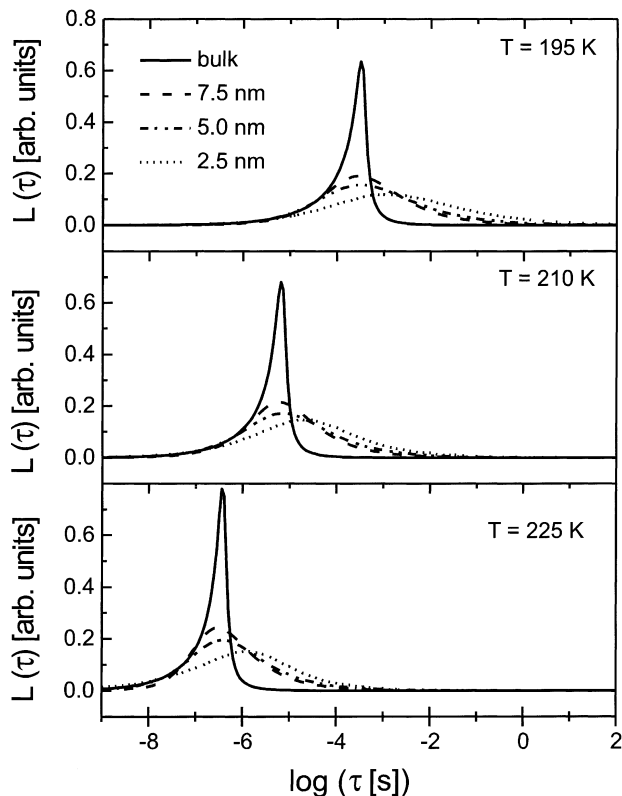
Fig. 6.12. Relaxation time distribution of the α-relaxation as calculated from Havriliak-Negami-fits for bulk and confined PG at 195 K, 210 K and 225 K (*solid line*: bulk; *dashed line*: 7.5 nm; *dash-dotted line*: 5.0 nm; *dotted line*: 2.5 nm pore diameter). Taken from [9] with permission

served with decreasing pore size. For 2.5 nm pores even the maximum is shifted to lower relaxation times.

The confined molecules can be classified (Fig. 6.13a) according to their dynamics into three fractions: (i) liquid-like with relaxation rates as in the bulk, (ii) interfacial with reduced mobility and (iii) immobilised. Assuming that the density of the molecules in confinement is only negligibly influenced and that the dielectric strength is proportional to the number of molecules participating in a relaxation process, a quantitative three layer model (Figs. 6, 13b and Table 6.2) can be deduced. Hereby the fraction of immobilised molecules is estimated from the difference in the dielectric strength which is expected from the filling factor of the confined molecules and which is measured as the contribution of the interfacial and bulk-like molecules. Considering spherical or cylindrical shape for the pores delivers similar results. Within the experimental accuracy, no significant temperature dependence of the layer structure is found. The layer thicknesses r_s and r_i have only a weak pore size dependence while the radius r_b of the

Fig. 6.13. a Relaxation time distribution of an H-bonded liquid (bulk and confined to nanopores). *Shaded area with horizontal lines*: bulk-like molecules; *shaded area with inclined lines*: interfacial molecules. **b** Sketch of the presumed spatial relaxation time distribution in the pores. *Checked*: solid-like molecules (thickness r_s), *inclined lines*: interfacial layer (thickness r_i), and *horizontal lines*: bulk-like molecules (radius r_b). Taken from [9] with permission
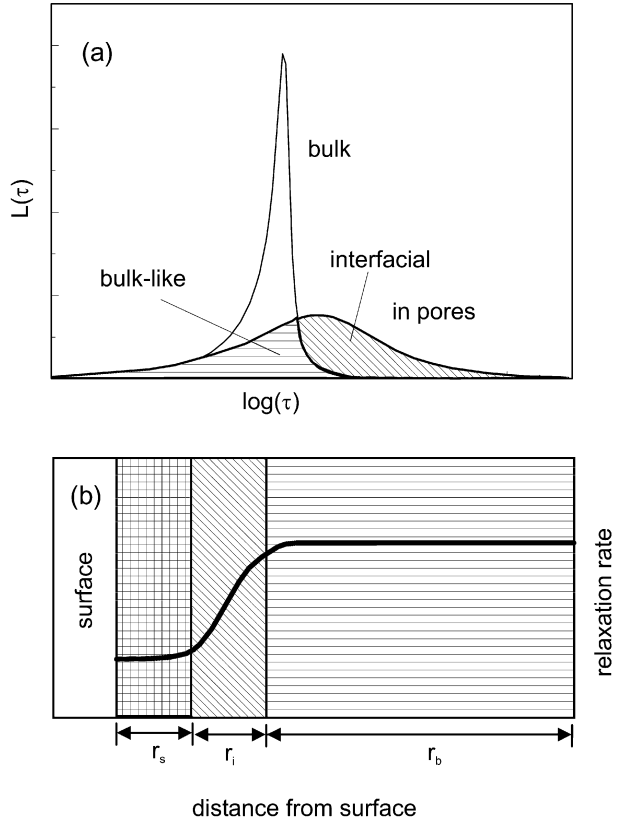

Table 6.2. Thickness of the solid-like layer r_s and the radius of the bulk-like phase r_b of molecules of PG, BG, and PeG for three different temperatures. The interfacial layer $r_i = R - r_b - r_s$ is ≈ 0.3 nm for all samples. The absolute error of r_s, r_i and r_b is 0.2 nm

Temperature (K)	Pore size	PG		BG		PeG	
	R (nm)	r_b (nm)	r_s (nm)	r_b (nm)	r_s (nm)	r_b (nm)	r_s (nm)
225	7.5	2.5	0.8	2.8	0.5	2.8	0.6
	5.0	1.5	0.7	1.8	0.5	1.7	0.5
	2.5	0.7	0.3	0.7	0.4	0.6	0.4
210	7.5	2.5	0.8	2.8	0.6	2.6	0.8
	5.0	1.5	0.7	1.6	0.5	1.6	0.7
	2.5	0.7	0.4	0.6	0.4	0.6	0.5
195	7.5	2.4	0.9	2.8	0.6		
	5.0	1.5	0.7	1.6	0.5		
	2.5	0.6	0.4	0.6	0.4		

Fig. 6.14. Scheme of propylene glycol in the neighbourhood of an uncoated SiO$_2$ surface (*top*) and a silanized SiO$_2$ surface (*bottom*)

uncoated:

coated:
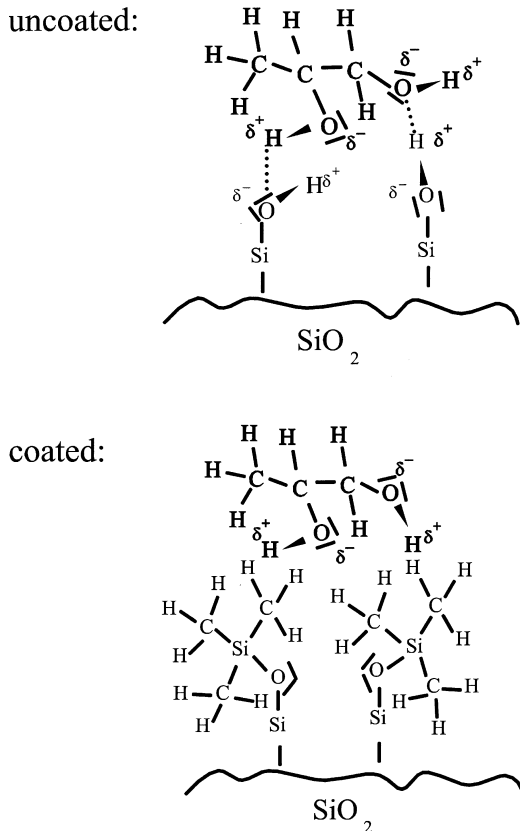
bulk-like phase scales roughly with the pores. From the mean van-der-Waals radius r_m and r_b the number of bulk-like molecules in the pores can be derived. As in the experiments with zeolitic host systems it turns out that the number of molecules which is necessary to perform a bulk-like dynamics is small.

Propylene glycol (PG) is an H-bonded glass forming liquid. Due to the fact that a freshly prepared SiO$_2$ surface is hydrophilic one has to expect that the PG molecules form H-bonds with the solid surfaces of the nanoporous system. This surface interaction can be hindered by a silanization as shown schematically in Fig. 6.14.

For PG in uncoated nanopores – compared to the bulk liquid – there is a pronounced broadening of the width of the dielectric loss curve and the relaxation time distribution function (Figs. 6.15a,b, 6.16). Silanization of the inner surfaces counteracts this (Figs. 6.15c, 6.16) effect which is – as expected – strongly temperature dependent and weakens with increasing thermal activation (Fig. 6.16): at a temperature of 185 K the low-frequency broadening of the relaxation time distribution function for PG in uncoated pores is completely removed and the mean relaxation time for PG in coated nanopores becomes even faster than in the bulk. The broadening is interpreted as caused by interactions
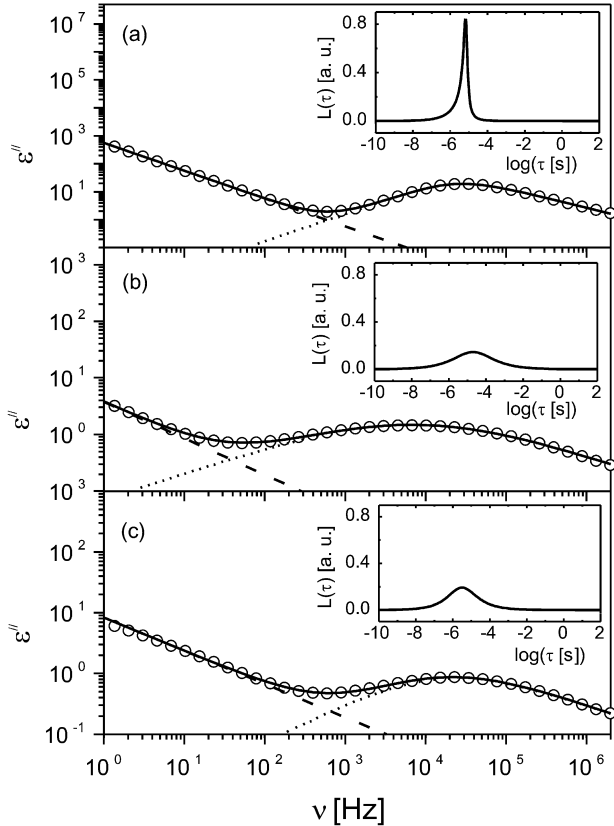
Fig. 6.15. The dielectric loss of PG at a temperature $T = 210$ K: **a** bulk PG; **b** PG confined to 2.5 nm uncoated pores; **c** PG confined to 2.5 nm coated pores. The error of the measured data is smaller than the size of the symbols, *solid line*: superposition of a Havriliak-Negami-relaxation function (*dotted line*) and conductivity contribution (*dashed line*). The *inset* shows the resulting relaxation time distribution function $L(\tau)$. Taken from [9] with permission

of the molecules with the surface [3]. The lubrication hinders the formation of H-bonds to the solid wall of the nanoporous ambience, hence decoupling its dynamics.

To characterise the temperature dependence of the relaxation rate the averaged relaxation time $\log \tau_{med}$ is calculated as defined in Eq. (6.3). The temperature dependence follows for all (uncoated and coated) pores the well known VFT-law (Fig. 6.17). The difference in the relaxation rate of PG in uncoated and coated pores is maximal for the smallest pore size (2.5 nm) and lowest temperature (≈ 190 K). Despite the fact that due to the silane layer having a thickness of about 0.4 nm the space for the PG molecules becomes even more confining one finds a dynamics which is – within experimental accuracy – identical to that of the bulk liquid.

Fig. 6.16. Relaxation time distribution function vs relaxation time for propylene glycol as a bulk liquid (*solid line*), in uncoated (*dashed line*) and in coated (*dotted line*) pores at different temperatures
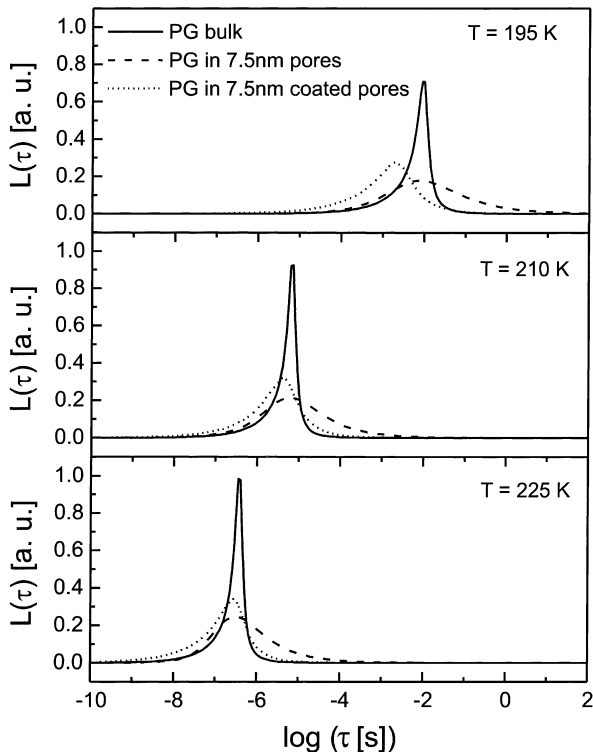
It is well known that for glass forming liquids the product of temperature T and dielectric strength $\Delta\varepsilon$ increase with decreasing temperature [47] (according to the Langevin function it should be constant, neglecting density effects). This effect vanishes for the dynamic glass transition if it takes place in the nanoporous systems (Fig. 6.18). The fact that the dielectric strength becomes smaller with decreasing pore diameter is attributed to the change in the surface to volume ratio of the nanoporous system.

6.2.2
Salol in (Lubricated) Nanoporous Sol-Gel Glasses

Salol (phenyl salicylate) is one of the most studied organic glass forming liquids. It is regarded as a "quasi"-van-der-Waals molecule despite the fact that it can form (mainly intramolecular) H-bonds (see scheme in Fig. 6.19). In nanoporous sol-gel glasses with hydrophilic inner surfaces an interfacial layer (Fig. 6.19) of molecules in the neighbourhood of the solid wall is established having a dynamics which is slowed down compared to the bulk liquid [11a,b].

In the experiment two molecular relaxation processes (I and II) are observed which can be separated in frequency and fitted by generalised relaxation func-

Fig. 6.17. The mean relaxation rate of propylene glycol vs inverse temperature for the bulk liquid (*open circles, solid curve*: VFT-fit) and for propylene glycol being confined to uncoated (*solid diamonds*) and coated pores (*open triangles*) of different pore diameters as indicated
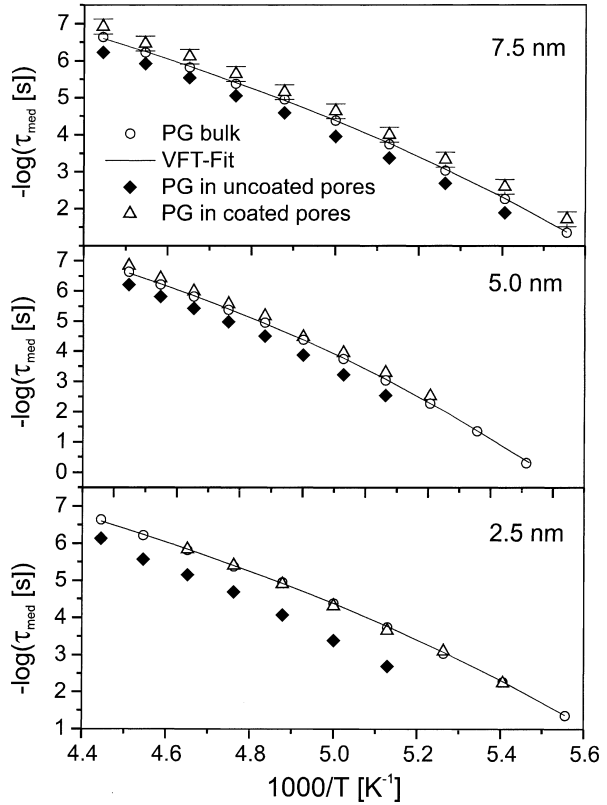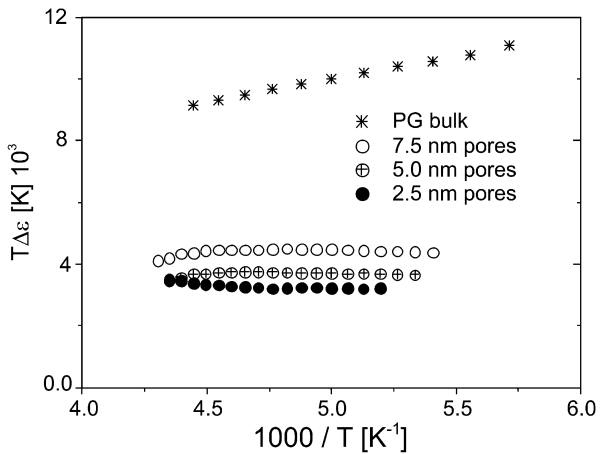

Fig. 6.18. Dielectric strength $\Delta\varepsilon$ times temperature T vs inverse temperature for propylene glycol as a bulk liquid (*stars*) and confined to silanized pores of a sol-gel glass having different diameters of 7.5 nm (*open circles*), 5.0 nm (*cross centred circles*) and 2.5 nm (*filled circles*)
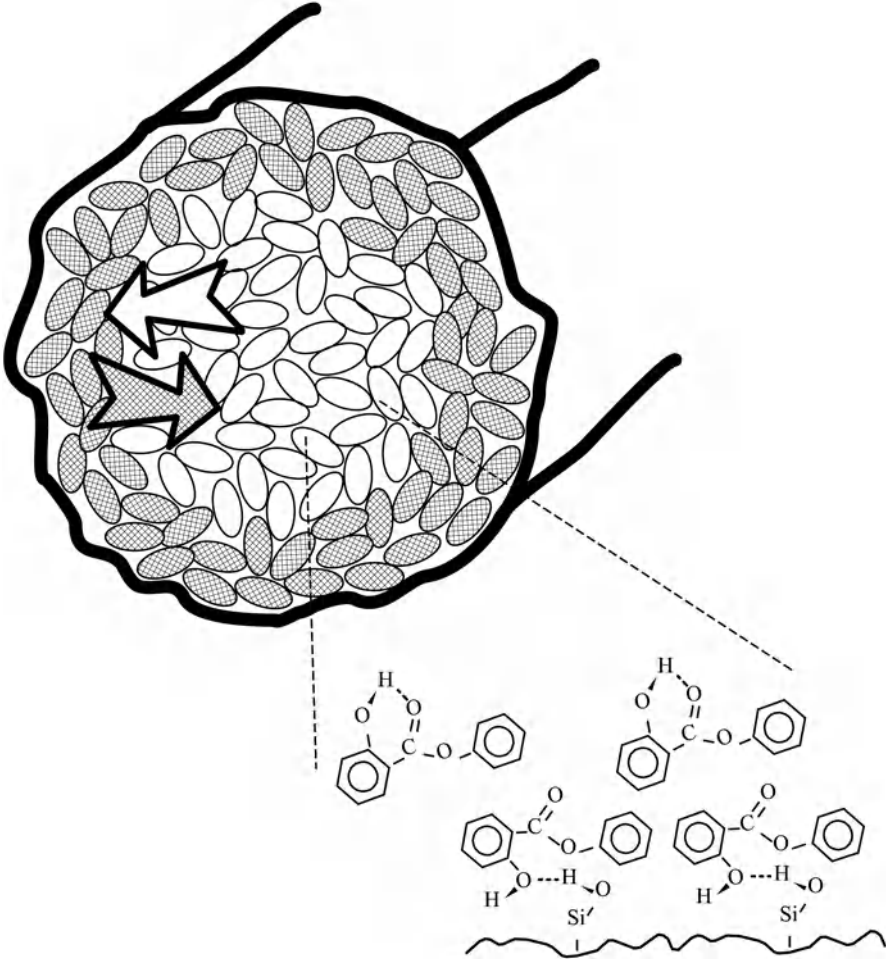
Fig. 6.19. Schematic view of a pore filled with a glass forming liquid. The pore walls are covered by a surface bound layer of molecules, the remaining volume is filled with bulk-like molecules. Due to H-bonding the salol molecules can directly bind to the SiO$_2$ surface of the inner walls of the nanoporous system

tions according to Havriliak-Negami (inset in Fig. 6.20). The dielectric spectra can be interpreted in terms of a two state model with dynamic exchange between a bulk-like phase in the pore volume and an interfacial phase close to the pore wall [10].

The formulae describing the change of polarisation p_i in subsystem i form a set of coupled linear first-order differential equations if $p_i(t)$ are purely exponential and if the jump rate c_{ij} is time independent

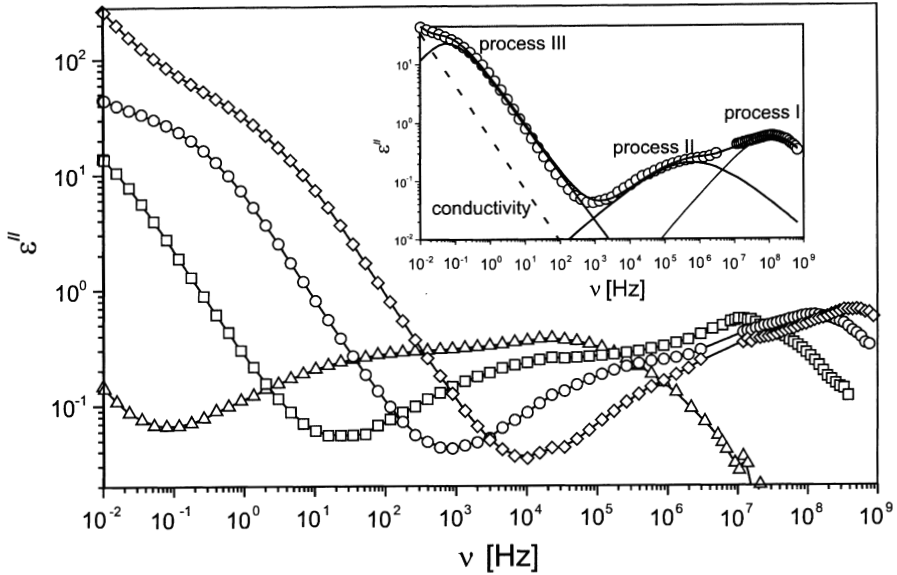$$\frac{dp_i(t)}{dt} = c_{ij}p_j, \qquad i = 1, 2 \tag{6.11}$$

Fig. 6.20. Dielectric loss ε'' of salol in 7.5 nm pores vs frequency: 245 K (*triangles*), 265 K (*squares*), 285 K (*circles*), 305 K (*diamonds*). The error of the measured data is smaller than the size of the symbols. The *inset* illustrates the deconvolution of the data for $T = 285$ K. Relaxation process I is assigned to fluctuations of bulk-like molecules, process II originates from molecules close to the inner walls and process III is caused by Maxwell-Wagner-polarization. Taken from [10] with permission

The polarisation in subsystem 1 changes by internal relaxation with the function $p_1(\text{t})$ and by transfer to and from state 2 as a consequence of jumps

$$\frac{dp_1}{dt} = -s_1 p_1 - c_{12} p_1 + c_{21} p_2$$

The polarisation in state 2 is described analogously

$$\frac{dp_2}{dt} = -s_2 p_2 - c_{21} p_2 + c_{12} p_1$$

The number of jumps per unit time is $c_{ij} N_i$, where N_i is the number of particles in system i; the transferred polarisation for a single particle is p_i/N_i. The constant s_i $(i = 1, 2)$ describe the relaxation rates in the uncoupled system. Both equations are collected to construct the relaxation matrix

$$c_{ij} = \begin{pmatrix} -s_1 - c_{12} & c_{21} \\ c_{12} & -s_2 - c_{21} \end{pmatrix} = \begin{pmatrix} -s - c - \Delta s - \Delta c & c - \Delta c \\ c + \Delta c & -s - c + \Delta s + \Delta c \end{pmatrix}$$

with

$$s = \frac{s_1 + s_2}{2} \qquad \Delta s = \frac{s_1 - s_2}{2} \qquad c = \frac{c_{12} + c_{21}}{2} \qquad \Delta c = \frac{c_{12} - c_{21}}{2}$$

and eigenvalues

$$u_1 = -r + Q \quad \text{(slow process)}$$
$$u_2 = -r - Q \quad \text{(fast process)}$$
$$Q^2 = c^2 + \Delta s^2 + 2\Delta s \cdot \Delta c$$
$$r = s + c$$

Diagonalizing Eq. (6.11) delivers

$$\begin{pmatrix} \dot{\beta}_1 \\ \dot{\beta}_2 \end{pmatrix} = \begin{pmatrix} u_1 & 0 \\ 0 & u_2 \end{pmatrix} \begin{pmatrix} \beta_1 \\ \beta_2 \end{pmatrix} \tag{6.12}$$

with $\beta_i = D_{ij}\, p_j$ and the diagonalization matrix

$$D_{ij} = \frac{1}{2Q(c - \Delta c)} \begin{pmatrix} -\Delta s - \Delta c + Q & c - \Delta c \\ \Delta s + \Delta c + Q & -c + \Delta c \end{pmatrix}$$

$$D_{ij}^{-1} = \begin{pmatrix} c - \Delta c & c - \Delta c \\ \Delta s + \Delta c + Q & \Delta s + \Delta c - Q \end{pmatrix}$$

The solution of Eq. (6.12) is

$$\beta_i = e^{u_i t}\, \beta_i(0) \quad \text{with} \quad \beta_i(0) = D_{ij}\, p_j(0)$$

Inserting the relative population numbers $p_{\{1,2\}}(0) = \dfrac{1}{2} \mp \dfrac{\Delta c}{c}$ one finds

$$\begin{pmatrix} \beta_1 \\ \beta_2 \end{pmatrix} = \frac{1}{4cQ} \begin{pmatrix} (Q + c - \Delta s)\, e^{-(r-Q)t} \\ (Q - c + \Delta s)\, e^{-(r+Q)t} \end{pmatrix} \tag{6.13}$$

and after transformation back to $p_i = D_{ij}^{-1}\beta_j$ the relaxation functions for states 1 and 2 [10] are obtained:

$$p_1(t) = \frac{c - \Delta c}{4cQ} \left[(Q + c - \Delta s)\, e^{-(r-Q)t} + (Q - c + \Delta s)\, e^{-(r+Q)t} \right]$$

$$p_2(t) = \frac{c + \Delta c}{4cQ} \left[(Q + c + \Delta s)\, e^{-(r-Q)t} + (Q - c - \Delta s)\, e^{-(r+Q)t} \right] \tag{6.14}$$

Their sum $p(t)$ is the total relaxation function of the system

$$p(t) = \left(\frac{1}{2} + \frac{C}{2Q} + \frac{\Delta s \Delta c}{2cQ} \right) e^{-(r-Q)t} + \left(\frac{1}{2} - \frac{C}{2Q} - \frac{\Delta s \Delta c}{2cQ} \right) e^{-(r+Q)t} \tag{6.15}$$

Identical results are obtained by calculating the probability of a particle remaining in its original state 1 or jumping to state 2.
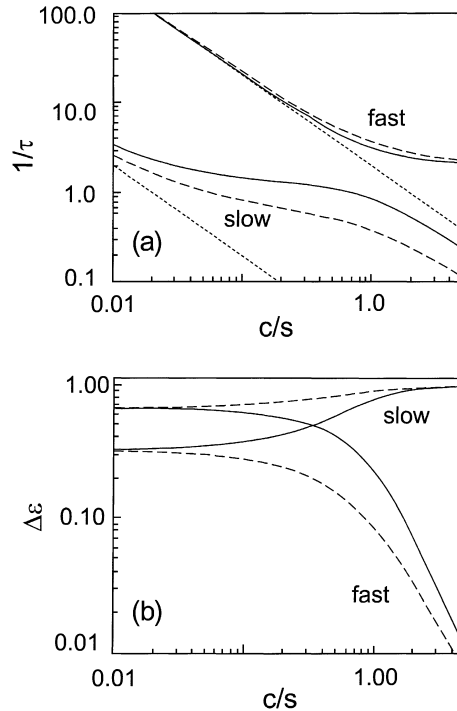
Fig. 6.21. **a** Apparent relaxation rate $1/\tau$ (in arbitrary units) of two relaxation processes with relaxation time ratio $s_2/s_1 = 100$ at fixed exchange rate c, and s slowing down from left to right. The *dotted lines* visualize the assumed exponential decrease of the undisturbed rate s_2 and s_1. The relative strengths of the original fast and slow processes are 1:2 (*dashed line*) and 2:1 (*solid line*) respectively. $(\Delta c/c = (n_1 - n_2)/(n_1 + n_2) = \pm 1/2)$. **b** The apparent relaxation strengths $\Delta\varepsilon$, notation as above. The relative strength of the slow process approaches 1, the fast process strength decays to zero with increasing exchange, irrespective of the strengths of the uncoupled processes. Taken from [11a] with permission

Typical graphs are shown in Fig. 6.21 where the apparent relaxation rate $1/\tau_i$ and the apparent relaxational strengths $1/2 \mp (c/2Q + \Delta c \Delta s/2Qc)$ are shown in dependence on c/s.

Keeping the exchange rate constant and lowering the relaxation rates s_1, $s_2 = 100 \, s_1$ exponentially from left to right (dotted lines) allows one to model the typical slowing down of relaxation rates with temperature. In Fig. 6.21a the single relaxation rates and in Fig. 6.21b the corresponding relaxation strengths $1/2 \mp (c/2Q + \Delta c \Delta s/2Qc)$ are shown on logarithmic scale. The apparent shift to higher relaxation rates is of course only an effect of the artificial separation of the relaxation processes. Molecules starting in the fast relaxation state do not relax faster by exchange with a slower state. This is easily verified from calculating the time derivatives of $p_i(t)$.

These theoretical results are used to interpret the experimental dielectric data of salol confined in porous sol-gel glasses (Fig. 6.22). In bulk salol, one observes

Fig. 6.22. a Relaxation rate $1/\tau_{max}$. **b** Volume corrected dielectric strength $\Delta\varepsilon$ of salol in pores vs inverse temperature. Pore sizes: 2.5 nm, *solid symbols*; 5.0 nm, *cross centred symbols*; and 7.5 nm, *open symbols*. Different processes: dynamic glass transition, *circles*; interfacial relaxation process, *squares*. Bulk salol, *stars*
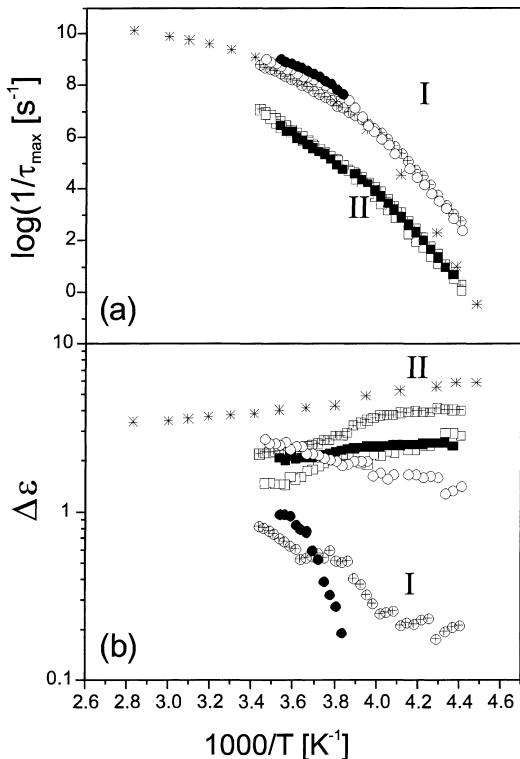
a single relaxation process. Its relaxation rate decreases with lower temperatures (according to the VFT equation). When salol is brought into porous glasses with nanometer pore diameters, new characteristic features are observed. One process, which can obviously be attributed to the free salol in the pores, shows at high temperatures a relaxation rate equal to that of the bulk, but with decreasing temperature it becomes faster than the bulk relaxation at the same temperatures. A second process, attributed to a layer of surface bound salol, appears at relaxation rates which are almost two decades slower. At lower temperatures, it gradually approaches the bulk rate. (A third process at low frequencies, due to Maxwell-Wagner polarisation, will not be considered here and has been omitted in the representation.) As temperature decreases, the fast (volume) process loses its dielectric strength while the second (surface) process gains such that the sum of both processes roughly follows the temperature curve of the bulk value.

Comparison with Fig. 6.21 suggests the following interpretation: both, the surface and volume relaxation rates in the pores are fast compared to the molecular exchange process between surface bound and free salol at high temperatures. Their ratio is roughly 1:100. On the basis of relation of pore radii and molecular sizes (≈ 0.5 nm), one expects that the ratio of free salol in the pores compared to the amount of molecules bound in a monomolecular surface layer is 1:2 and 1:3 for pore diameters of 2.5 nm and 7.5 nm, respectively. This is roughly
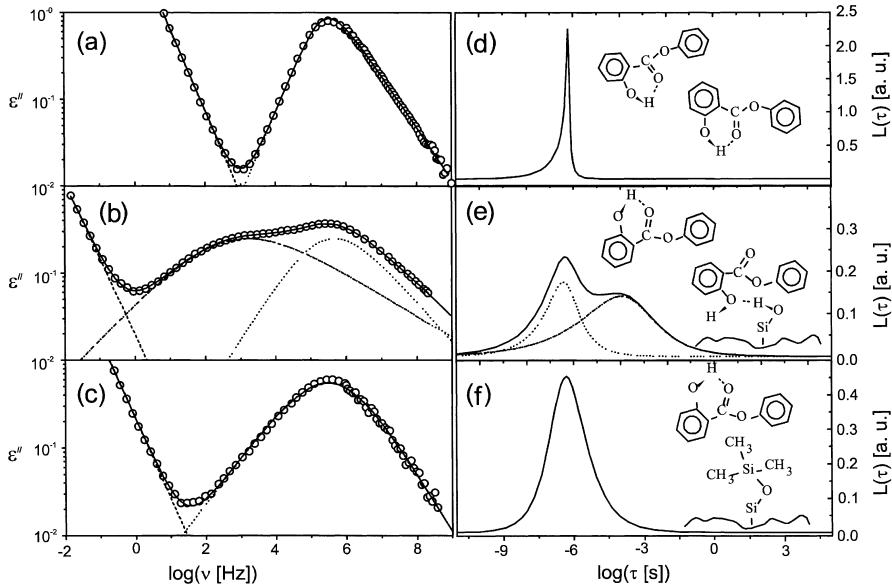
Fig. 6.23. Dielectric loss ε'' of salol at a temperature $T = 253$ K. The error of the measured data (*circles*) is smaller than the size of the symbols. The *dotted and dashed-dotted lines* indicate fits to the data according to Havriliak-Negami functions. The *dashed lines* correspond to conductivity contributions and loss processes caused by polarisation effects. **a** Bulk salol: the molecules form intra-molecular H-bonds, one relaxation process having the characteristic shape of $L(\tau)$ for a bulk glass-forming liquid is observed. **b** Salol confined to 7.5-nm uncoated pores: salol molecules in the direct vicinity of the surface form H-bonds to the pore surface resulting in an additional interfacial relaxation process (*dashed-dotted lines*) next to the relaxation of unbound molecules (*dotted lines*). The corresponding $L[(\tau)]$ has a bimodal shape (*solid line*). **c** Salol confined to 7.5-nm coated pores: the formation of H-bonds is strongly suppressed. The resulting unimodal $L(\tau)$ is shifted to shorter relaxation times with respect to the bulk phase. **d, e, f** The plots on the right hand side show the relaxation time distributions $L(\tau)$ that correspond to the relaxational processes. The sketches illustrate possible conformations of the molecules. Taken from [11b] with permission

equal to the respective experimental high temperature ratios of the dielectric strengths. As the temperature is lowered towards the calorimetric glass transition, dielectric relaxation rates reach the order of magnitude of the exchange rate between free and surface bound salol, which has a weaker temperature dependence. With decreasing temperature, random exchange between surface layer and free molecules leads to an apparently faster relaxation of the volume process compared to the bulk curve, and also to an increased rate of the surface process, which gradually approaches the bulk curve. The measured relaxation strengths show exactly the predicted behaviour; the slow process apparently gains intensity from the fast process. In summary, it is shown that the experimental data obtained for salol in nanoporous sol-gel glasses must be interpreted in terms of a surface volume exchange of salol molecules on the characteristic time scale of the dielectric experiment.

Fig. 6.24. Relaxation time distribution $L(\tau)$ for salol confined to 7.5 nm (*circles*), 5.0 nm (*cross centred circles*), 2.5 nm (*solid circles*) pores with a hydrophobic coating and bulk salol (*solid line*) at different temperatures: **a** 305 K; **b** 243 K; **c** 223 K. Taken from [11b] with permission
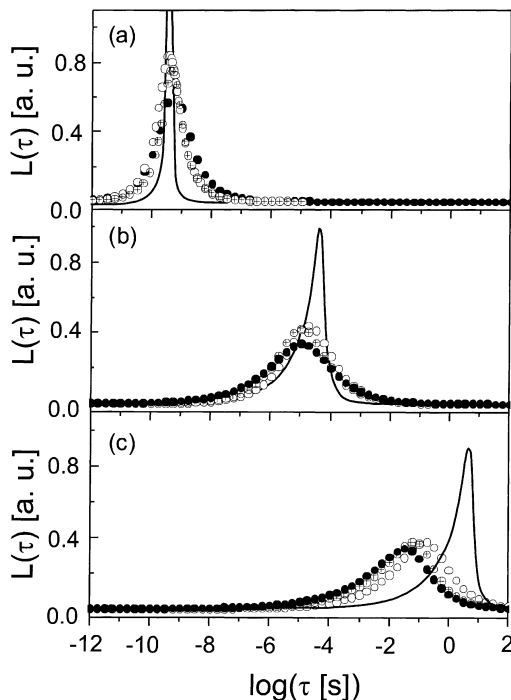
In order to suppress the formation of an interfacial layer of molecules the inner surfaces of the nanoporous sol-gel glasses can be silanized [11b]. By that the formation of H-bonds between the salol molecules and the solid surfaces is strongly hindered. For the dynamics it means that the corresponding interfacial relaxation process (process II) is no longer observed (compare Fig. 6.23a and e). It is remarkable that the relaxation time distribution function of unbound molecules in the silanized pores is only weakly broadened (Fig. 6.23f) compared to the bulk liquid (Fig. 6.23b). Figure 6.24 shows the relaxation time distribution of salol confined to silanized pores of different diameter and at varying temperatures. A broadening is observed at high temperatures due to the various unspecific influences of the random confinement. With decreasing temperature $L(\tau)$ shifts to short relaxation times for confined salol. This effect is more pronounced for smaller pores. The analysis of the dielectric strengths shows that the silane layer has a thickness of 0.38 ± 0.02 nm in all pore sizes.

In order to characterise the temperature dependence, the averaged relaxation time $-\log \tau_{med}$ is calculated according to Eq. (6.6). The activation plot of the relaxation rate $-\log \tau_{med}$ is compared for bulk and confined salol in Fig. 6.25. At high temperatures the relaxation rates of the confined liquids are identical to the bulk liquid in all pore sizes while with decreasing temperatures the molecules in the confining geometry fluctuate faster compared to the bulk liquid: i.e. the glass transition temperature of the confined liquids is shifted to lower temperatures. This shift is more pronounced for smaller pores. A comparable effect is observed by means of DSC [11b]. The calorimetric glass transition temperature in the
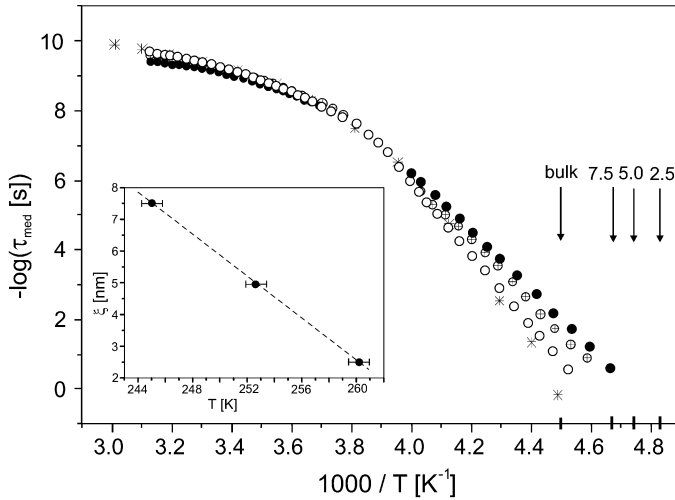
Fig. 6.25. Activation plot for salol confined to coated pores. 7.5 nm (*circles*), 5.0 nm (*cross centred circles*), 2.5 nm (*solid circles*), bulk salol (*stars*). The error of the data is smaller than the size of the symbols. The *arrows* indicate the calorimetric glass transition temperatures for salol in pores of different sizes and bulk salol. *Inset*: size of cooperatively rearranging domains ξ vs temperature. Taken from [11b] and modified. The dashed line is a fit

confining geometry is shifted 8, 11 and 15 K to lower temperatures in the 7.5, 5.0 and 2.5 nm pores, respectively (indicated by arrows in Fig. 6.25).

The confinement effect can be unambiguously explained on the basis of the cooperativity of molecular reorientations in glass-forming van-der-Waals liquids: At high temperatures the range of cooperativity ξ is smaller than the extension of the nanoporous restrictions. Hence, no difference between molecules in the bulk and in confining space has to be expected. With decreasing temperature deviations from the Arrhenius-type temperature dependence occur indicating the onset of cooperativity. The correlation length ξ increases until it becomes limited by the pore diameter ("hindered glass transition") [3, 4]. Because of the lubricant coating of the inner surfaces, the cooperatively rearranging molecules in the pores are decoupled from the solid walls and may reorient within the pore volume. In contrast, the reorientational dynamics in the bulk liquid is increasingly retarded due to the unhindered growth of ξ. This leads to a faster dynamics of the confined molecules compared to the bulk liquid.

Following the simple model described above the temperature dependence of the length scale of cooperativity can be estimated from the pore size dependence of the shift of the relaxation rate: it starts to increase compared to the bulk rate when the length scale of cooperativity ξ reaches the size of the confining geometry. For the 2.5 nm pores deviations from the bulk rate are observed at 250 K. At lower temperatures even for salol in 7.5 nm pores a significant increase of the relaxation rate compared to bulk salol is observed so one can estimate the length scale ξ of cooperativity to be greater than 7 nm in the vicinity of the calorimetric glass transition temperature.
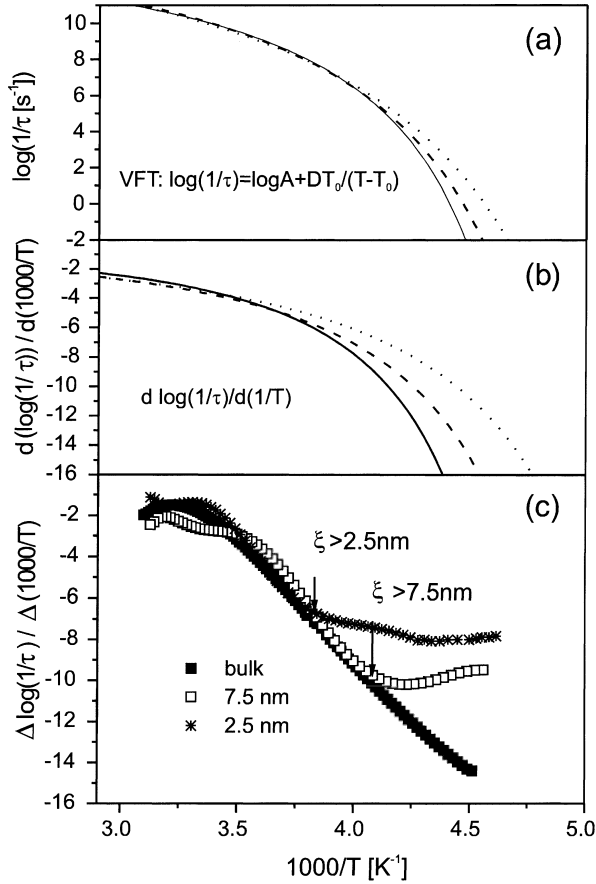
Fig. 6.26. **a** The calculated dependence of the mean relaxation rate vs inverse temperature assuming a VFT-law, where T_0 is shifted according to the calorimetrically measured shift of T_g. *Solid line*: bulk liquid $T_g = 222$ K; *dashed line*: salol confined to a silanized sol-gel glass having a mean diameter of 7.5 nm: $T_g = 214$ K; *dotted line*: salol confined to a silanized sol-gel glass having a mean diameter of 2.5 nm: $T_g = 207$ K. **b** The calculated derivative $d(\log(1/\tau))/d(1000/T)$ assuming the temperature dependence shown in a. The units are omitted due to graphical reasons. They are the same like in part c of this figure. **c** The experimentally determined difference quotient $\Delta(\log(1/\tau))/\Delta(1000/T)$ for the data shown in Fig. 6.25 for the bulk liquid (*solid squares*), salol confined to silanized nanopores of 7.5 nm (*open squares*) and salol confined to silanized nanopores of 2.5 nm (*stars*). Taken from [1] with permission

The question arises of whether the confinement effect could be caused by a pore-size dependent decrease of the density of the confined liquid. This conjecture can be ruled out based on the following consideration: Assuming that the density and hence the mean relaxation rate $1/\tau$ obeys a VFT law where the Vogel temperature varies with the pore size in a similar way as the measured calorimetric glass transition temperature (Fig. 6.26a) the derivative $d(\log(1/\tau))/d(1000/T)$ delivers a temperature dependence as shown in Fig. 6.26b. This can be

compared with the difference quotient as determined *experimentally* from the relaxation rate *measured* in temperature steps of 0.5 K (Fig. 6.26c). It turns out that the difference quotient behaves qualitatively different. In the temperature interval between 333 K and 260 K, the apparent activation energies for the bulk and the confined (2.5 nm and 7.5 nm) liquid coincide within experimental accuracy. However, for lower temperatures, suddenly the charts bend off; this takes place for the 2.5-nm pores at 256 ± 3 K and for 7.5-nm pores at 245 ± 3 K. The temperature dependence is in sharp contrast to the results (Fig. 6.26b) which one would expect from a dependence like that displayed in Fig. 6.26a, assuming a weakly varying temperature dependence of the density. In reverse a non-monotonous change of the density seems to be unreliable: instead it is suggested that the measured confinement effects are caused by the cooperative nature of the dynamic glass transition. With decreasing temperature the size of cooperatively rearranging domains is growing and the apparent activation energy increases. If, due to the confinement of the nanoporous system, further growth is prohibited, the VFT dependence turns suddenly into an Arrhenius-like thermal activation.

6.3
Polymers in Zeolitic and Nanoporous Media

6.3.1
Poly(vinylether) in Mesoporous MCM

It is possible to synthesize poly(vinylether)s directly in the channels of nanoporous zeolites and mesoporous MCM-materials. MCM-materials possess pores with a diameter in the range from 2 nm up to 8 nm with a narrow pore size distribution. The framework of these porous materials is an amorphous aluminosilicate. To study the molecular dynamics of polymers in confining space the following host systems (Fig. 6.27 and Table 6.3) were used: MCM-41 with one-dimensional channels and a pore diameter of 3.6 nm and MCM-48 having pores with a pore size of 2.5 nm and a cubic structure [48, 49].

The polymerisation is started either by an initiator or by silanol groups at the inner surface of the host system. Figure 6.28 shows how the surface induced polymerisation works. In both cases the pores are filled only partially by the

Table 6.3. Pore diameter, inner surface, specific pore volume, specific channel length, loading ratio and ratio contour length of the polymer compared to the channel length for the MCM-41 and MCM-48 materials which are filled with poly(isobutyl vinylether)

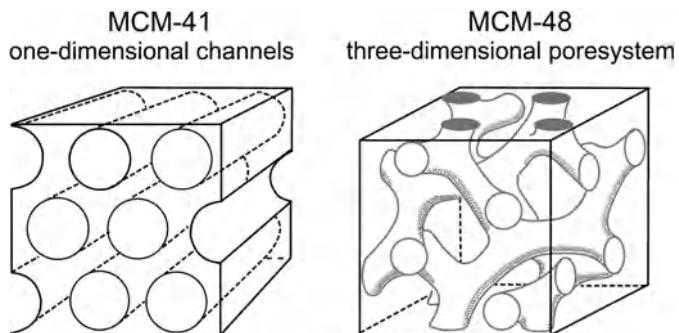|	MCM-41	MCM-48
Pore diameter (nm)	3.6	2.5
Inner surface ($m^2 \, g^{-1}$)	770	1840
Specific pore volume ($cm^3 \, g^{-1}$)	1.25	1.34
Specific channel length ($10^{10} \, m \, g^{-1}$)	11.6	27.3

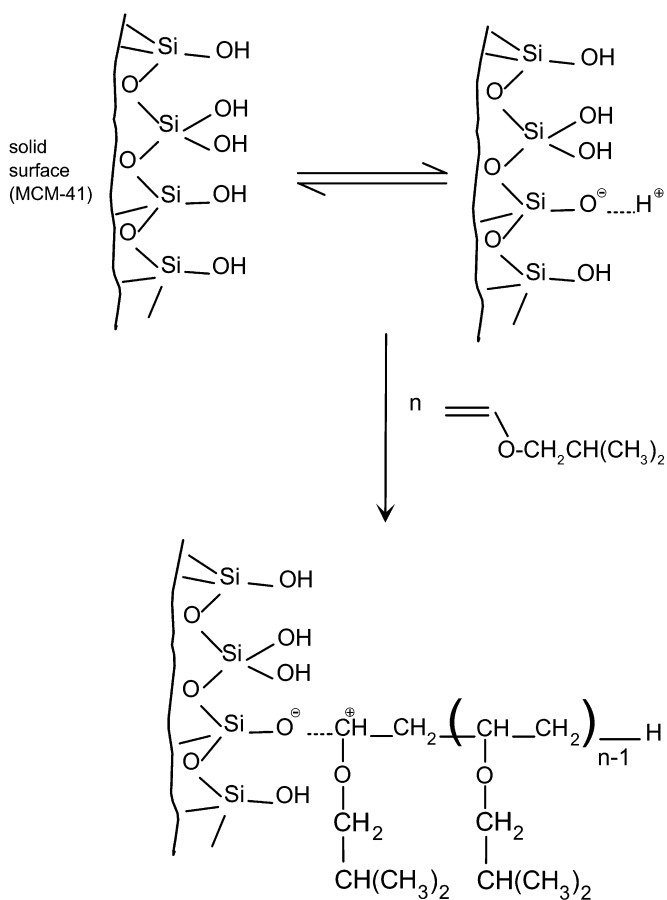**Fig. 6.27.** Structure of mesoporous MCM-41 and MCM-48

Fig. 6.28. Scheme of surface induced polymerization of poly(isobutyl vinylether) (PIBVE) in mesoporous MCM-41
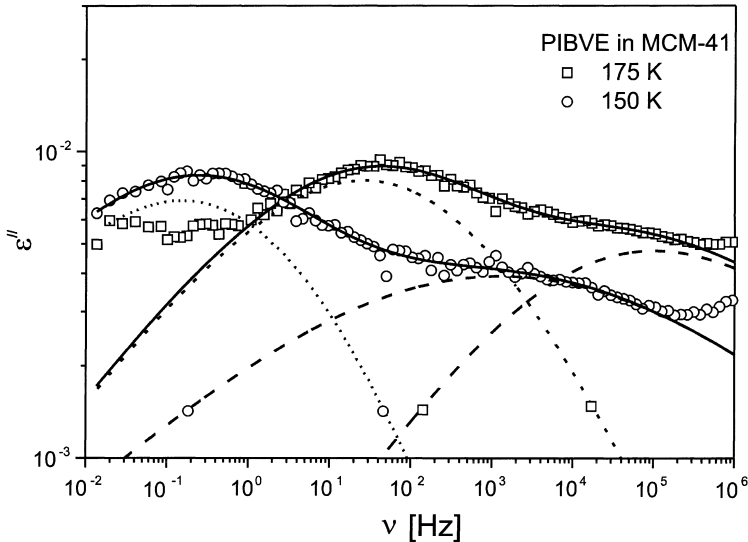
Fig. 6.29. Dielectric spectra of PIBVE confined in MCM-41 at 175 K (*squares*) and 150 K (*circles*). The *solid line* is a superposition of the HN-fits for the α- (*dotted line*) and β- (*dashed line*) relaxation at the indicated temperatures

polymer. For the polymer in MCM-materials the filling ratio is comparatively large (up to 43 vol.%) and the dielectric spectra has distinct relaxation processes. Figure 6.29 shows the dielectric spectra of poly(isobutyl vinylether) (PIBVE) in MCM-41 for two different temperatures.

Figure 6.30 displays the relaxation rates and the dielectric strength for PIBVE in the bulk and in the confining space of MCM-41. One process has a relaxation rate similar to the β-relaxation of the bulk polymer with an Arrhenius-like temperature dependence. It corresponds to the β-relaxation of the confined polymer and is assigned to fluctuations of the ether group [50]. The second process also has an Arrhenius-type temperature dependence. It is much faster compared to the α-relaxation of the bulk polymer. After annealing the sample its relaxation rate slows down and approaches the dynamic glass transition of the bulk sample. This process is assigned to the α-relaxation of the confined polymer. The relaxation rate of the β-relaxation is almost uninfluenced by the confinement and the thermal treatment. The relaxation strength of both processes decreases after annealing. Comparing the molecular dynamics of PIBVE in MCM-41 and in MCM-48, faster relaxation rates are observed (Fig. 6.31) in the smaller pores of MCM-48. Hence, similar to EG in zeolites and salol in silanized sol-gel glasses, PIBVE in MCMs shows a confinement effect.

The slowing down of the α-relaxation after annealing the sample was found to be a solvent effect. Figure 6.32 shows the relaxation rate of the α-relaxation after annealing and after the subsequent uptake of a solvent. Annealing results in a decrease of the relaxation rate. After the uptake of solvents it increases. If polar solvents are used the relaxation rate reaches the values of a sample which was

Fig. 6.30. Relaxation rate $1/\tau_{max}$ and dielectric strength $\Delta\varepsilon$ vs inverse temperature for PIBVE in the bulk and in MCM-41. The *solid symbols* correspond to the α-relaxation, the *open symbols* to the β-relaxation. The thermal treatment of the samples is indicated in the figure
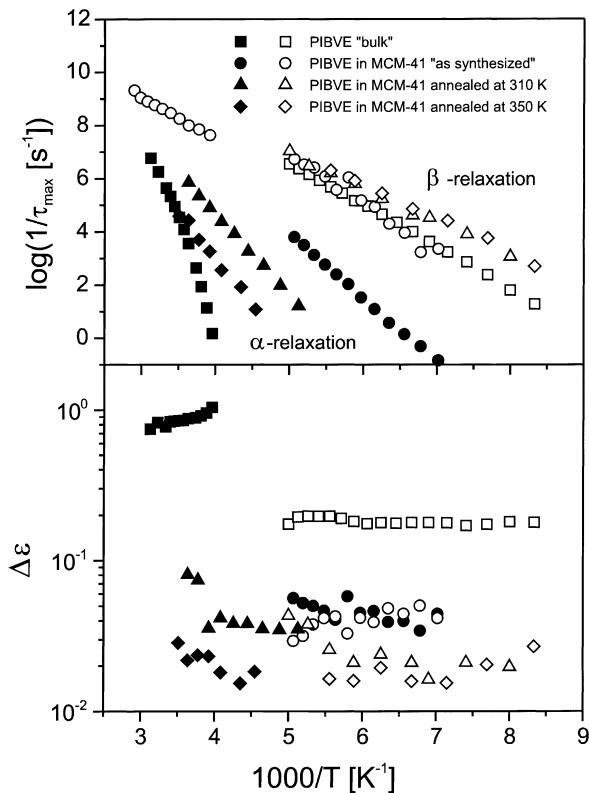

measured without any treatment "as synthesised". Furthermore, the dielectric strength which decreases after annealing increases as well. The desorption and absorption of solvent and the effect on the dielectric spectra is completely reversible.

6.3.2
Poly(propylene glycol) in Nanoporous Sol-Gel Glasses

Poly(propylene glycol) (PPG) is the polymeric pendant to propylene glycol (PG) which has been discussed already in Sect. 6.2.1. The question arises how the *polymer* properties of PPG influences its molecular dynamics in confinement [51, 52] in comparison to PG. Poly(propylene glycol) is a "type-A" polymer [53, 54] having molecular dipole components perpendicular and parallel to the polymer backbone. The latter adds up to a dipole moment which is proportional to the end-to-end vector of the chain. Hence two dielectric active relaxation processes are observed: a segmental relaxation (dynamic glass transition or α-relaxation) and a so-called normal mode process (see Chap. 7). Evidently both processes take place on different length scales. While the dynamic glass transi-

Fig. 6.31. Relaxation rate vs inverse temperature for PIBVE in the bulk (*squares*), in MCM-41 (*upright triangles and diamonds*) and in MCM-48 (*circles and inverted triangles*) as indicated. The *solid symbols* correspond to the α-relaxation, the *open* symbols to the β-relaxation
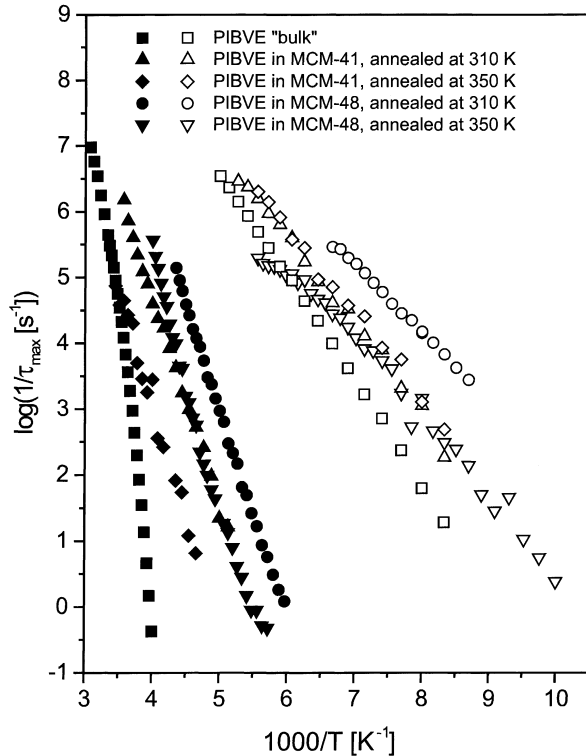
tion is related to fluctuations of a few polymer segments the normal mode process senses the global chain dynamics [55a].

In Fig. 6.33 the dielectric loss of PPG in the bulk and in native (uncoated) nanoporous sol-gel glasses is compared in its temperature dependence at a fixed frequency. Two relaxation processes can be identified: The segmental relaxation at low and the normal mode process at higher temperatures. The temperature position of the former is weakly influenced by the confinement while the latter shifts strongly to higher temperatures with decreasing pore size connected with a pronounced broadening.

The measurements are analysed by fitting the HN-equation (Eq. 6.1) to the data and the relaxation rate at maximal loss $v_{max} = (2\pi\,\tau_{max})^{-1}$ is extracted. Unfortunately both processes do strongly overlap in their relaxation time distribution. This prevents a reliable estimation and analysis of their dielectric strengths.

In the activation plot (Fig. 6.34) the pore size dependence of the relaxation rate of the segmental and the normal mode relaxation is analysed. Both processes can be described in their temperature dependence by the VFT-equation (Eq. 6.4). For high temperatures the data for bulk and confined PPG coincide which proves the molecular assignment of the relaxation process in the pores. While the normal mode shows a continuous decline of its dynamics, the

Fig. 6.32. Relaxation rate vs inverse temperature for PIBVE in MCM-48 as synthesized (*filled squares*), annealed at 350 K (*open circles*), after the uptake of dichloromethane (*filled circles*), annealed at 350 K (*open triangles*), after the uptake of cyclohexane (*filled triangles*), annealed at 350 K (*open diamonds*), after the uptake of water (*filled diamonds*)
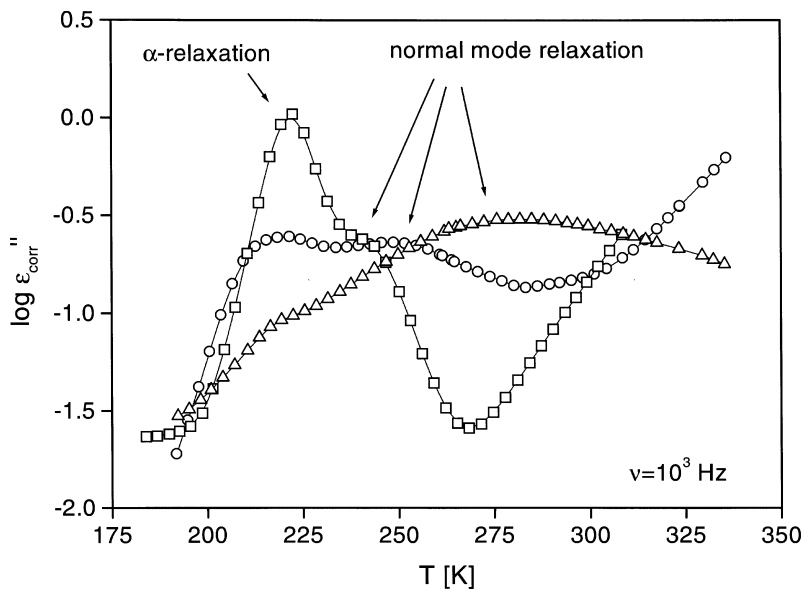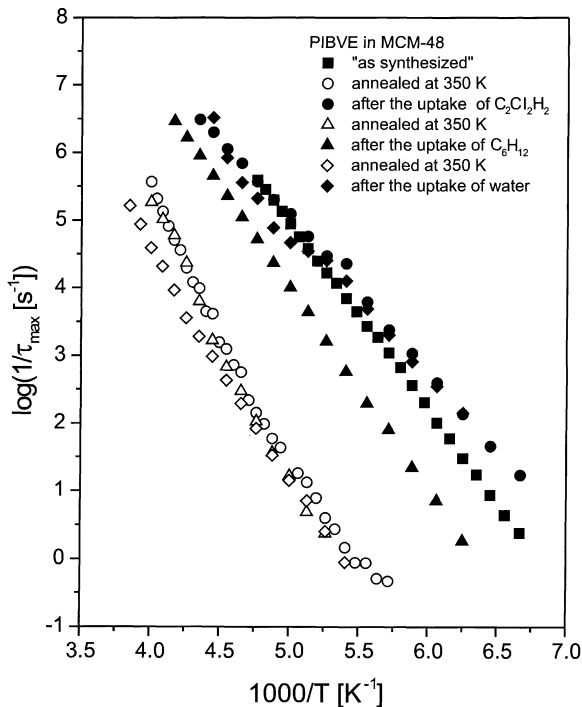

Fig. 6.33. Dielectric loss ε'' (corrected for the pore volume) vs temperature at a frequency of 10^3 Hz for PPG (molecular weight $M_w = 3000$ g mol^{-1}) in the bulk (*open squares*) and in uncoated pores of different pore sizes: 7.5 nm (*open circles*), 2.5 nm (*open triangles*)
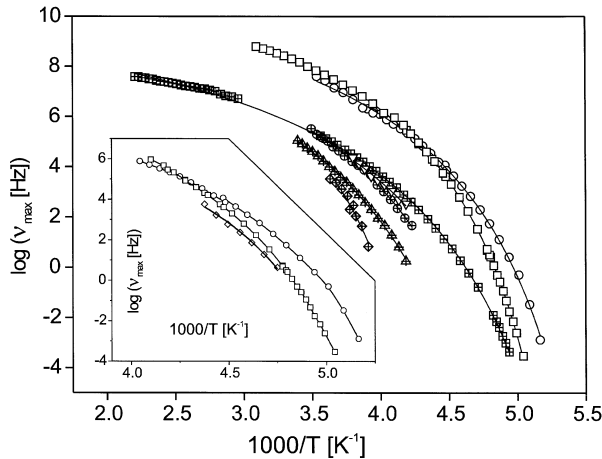
Fig. 6.34. Relaxation rate v_{max} vs inverse temperature for PPG ($M_w = 3000$ g mol^{-1}) in the bulk (*open squares*) and in uncoated pores of different size: 20 nm (*inverted open triangles*), 7.5 nm (*open circles*), 5 nm (*open triangles*), 2.5 nm (*open lozenges*). *Open symbols* denote the segmental relaxation (dynamic glass transition), *crossed symbols* the normal mode relaxation. The *lines* are fits of the VFT-equation (Eq. 6.4) to the data. In the *inset* the segmental relaxation is enlarged

segmental relaxation shows a non-monotonous dependence on confinement (see inset Fig. 6.34). For pore sizes down to 7.5 nm the dynamics becomes faster but it slows down for smaller pores. The estimated VFT-parameters are used to calculate the dielectrically determined glass transition temperature $T_g^{Diel} = T(v_{max} = 10^{-2}$ Hz) and to discuss its pore size dependence (Fig. 6.35). In contrast to the monomer PG where only an adsorption effect is found in the polymeric pendant PPG the counterbalance between surface and confinement effects determines the pore size dependence of the dynamic glass transition.

This is attributed to the different capability of the molecules to form hydrogen bonds with the walls of the pores: PG can form two primary H-bonds per molecule while for PPG due to its chain structure this is possible only at the chain ends.

The effect of surface treatment (silanization) on the two relaxation processes in PPG reveals a strong effect on the normal mode relaxation (see Fig. 6.36). Obviously the surface treatment damps the global chain fluctuations while the local segmental relaxation is even slightly amplified. Compared to the bulk both processes broaden with decreasing pore size (Fig. 6.37). This prevents a reliable estimation of the relaxation rates of the normal mode process for smaller pore sizes.

Figure 6.38 compares the temperature dependence of the relaxation rate v_{max} for the dynamic glass transition in uncoated and coated pores. While close to T_g the segmental fluctuations in 2.5 nm coated pores are slightly faster compared to native ones; for 7.5 nm pores there is no effect of the silanization on the temperature dependence of the dynamic glass transition. Thus, for the polymer PPG
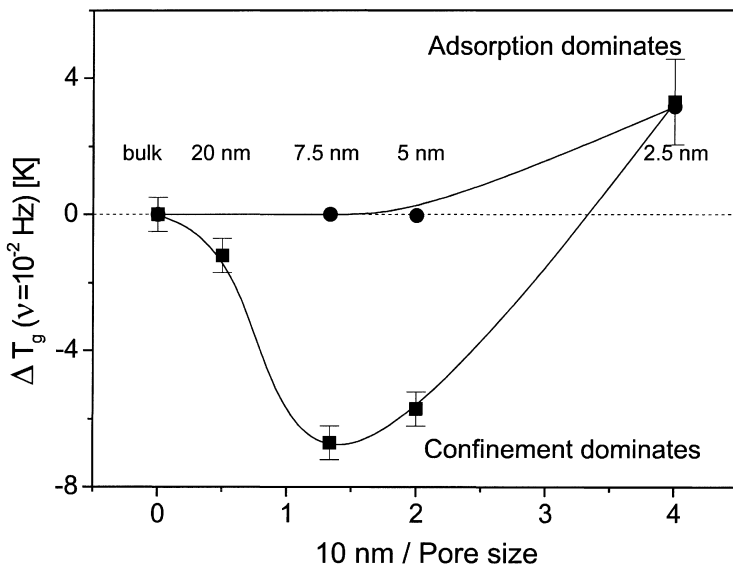
Fig. 6.35. $\Delta T_g = T_g^{\text{Diel}}$ (pore) $- T_g^{\text{Diel}}$ (bulk) vs inverse pore size: *filled circles* – PG, *filled squares* – PPG ($M_w = 3000$ g mol^{-1}). *Lines* are guides for the eyes

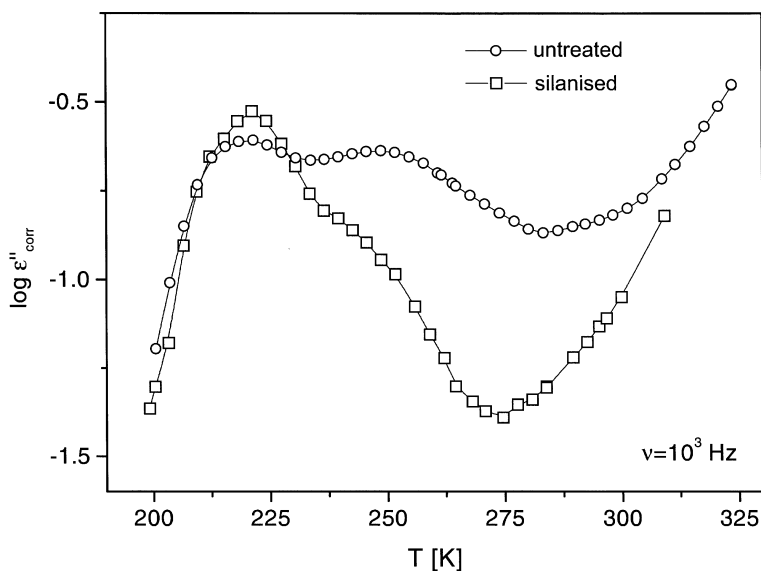**Fig. 6.36.** Dielectric loss ε'' (corrected for the pore volume) vs temperature at 10^3 Hz for PPG ($M_w = 3000$ g mol^{-1}) in untreated and silanized pores for a pore size of 7.5 nm. *Lines* are guides for the eyes
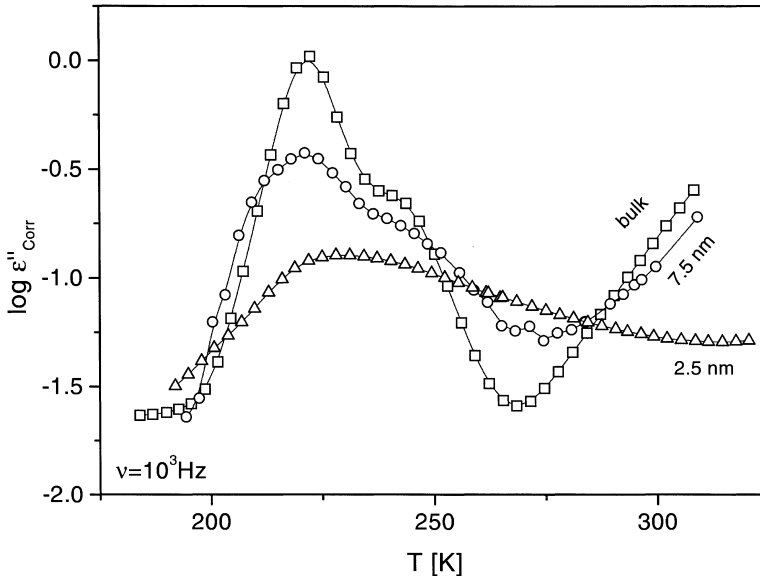
Fig. 6.37. Dielectric loss ε'' (corrected for the pore volume) vs temperature at a frequency of 10^3 Hz for PPG ($M_w = 3000$ g mol^{-1}) in the bulk (*open squares*) and in silanized pores of different sizes: 7.5 nm (*open circles*), 2.5 nm (*open triangles*). *Lines* are guides for the eyes

the effect of a surface treatment is much weaker than for the monomeric pendant.

Temperature modulated differential scanning calorimetry (TMDSC) measurements were carried out to reveal the thermal relaxation at the dynamic glass transition in addition to the dielectric experiments [51]. By the variation of the modulation frequency (or modulation time) the temperature dependence of the relaxation rates due to enthalpy (entropy) fluctuations can be estimated and compared to the corresponding dielectric data (see inset Fig 6.38). Both methods are in accord with each other in the absolute value of the relaxation rates and in the apparent activation energy. The increment of the specific heat capacity Δc_p due to the glass transition decreases strongly with decreasing pore size (see inset Fig. 6.39) which agrees with the dielectric measurements (compare Fig. 6.33). Δc_p vanishes at a value of about 1.8 nm (see Fig. 6.39). For smaller pores no glass transition takes place in the system. Therefore the estimated value can be regarded as the minimal length scale of cooperativity for the glass transition of PPG.

6.3.3
Poly(dimethyl siloxane) in Nanoporous Sol-Gel Glasses

Poly(dimethyl siloxane) PDMS is compared to PPG a more fragile glass forming system (see Chaps. 4 and 5). It has *one* dielectrically active relaxation process
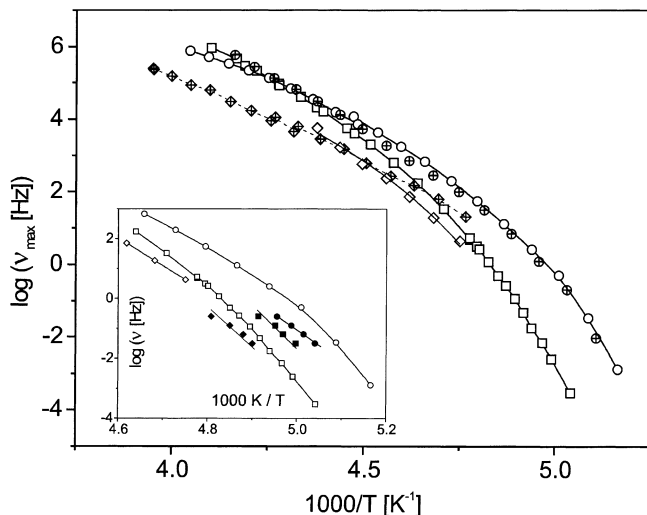
Fig. 6.38. Relaxation rate ν_{max} vs inverse temperature for PPG ($M_w = 3000$ g mol^{-1}) in the bulk (*open squares*) and in uncoated (*open symbols*) and coated (*crossed symbols*) pores of different sizes: 7.5 nm (*open circles*), 2.5 nm (*open lozenges*). The *lines* are VFT-fits. The *inset* compares the dielectric data with that obtained by TMDSC (*solid symbols*) for uncoated pores
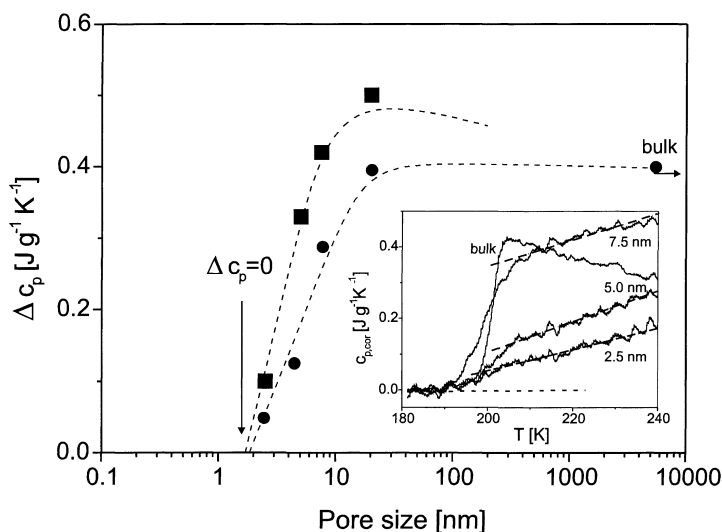
Fig. 6.39. Δc_p vs pore size for PPG ($M_w = 2000$ g mol^{-1}) in uncoated (*filled circles*) and silanized (*filled squares*) pores. The *lines* are guides for the eyes. The *inset* shows the real part of the complex heat capacity obtained by TMDSC for PPG at the indicated pore sizes. The temperature was modulated with a modulation time of 200 s and an amplitude of 0.5 K. The heating rate was 0.25 K min^{-1}. The specific heat $c_{p,corr}$ was reduced for the weight of the confined polymer and the value in the glassy state. Δc_p was taken at T_g for the given modulation time. *Lines* are guides for the eyes
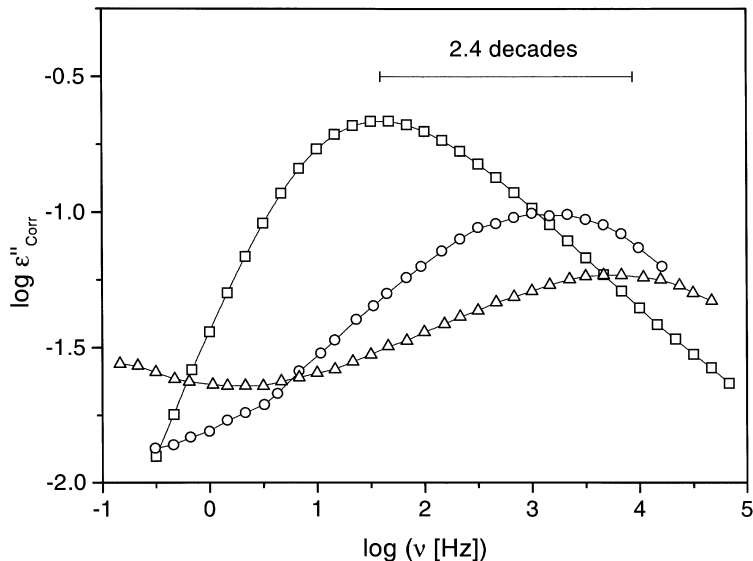
Fig. 6.40. Dielectric loss ε'' (corrected for the pore volume) vs frequency at $T = 157.5$ K for PDMS ($M_w = 1400$ g mol^{-1}) in the bulk (*open squares*) and in uncoated pores of different sizes: 20 nm (*open circles*), 7.5 nm (*open triangles*). The *lines* are guides for the eyes [55b]
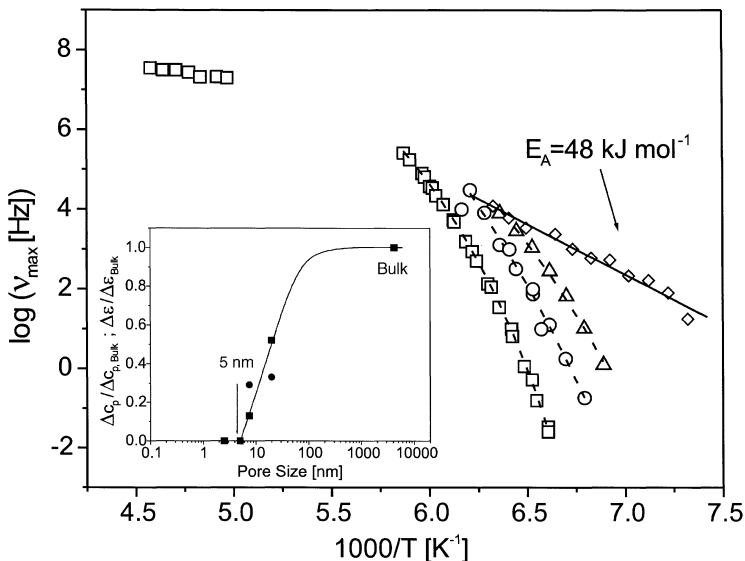
Fig. 6.41. Relaxation rate ν_{max} vs inverse temperature for PDMS ($M_w = 1400$ g mol^{-1}) in the bulk (*open squares*) and in uncoated pores of different sizes: 20 nm (*open circles*), 7.5 nm (*open triangles*), 5 nm (*open lozenges*). The *dashed lines* are fits of the VFT-equation (Eq. 6.4) to the data, *solid line* is an Arrhenius fit. The *inset* shows the ratio of $\Delta c_p / \Delta c_{p,corr}$ (*filled squares*) and $\Delta \varepsilon / \Delta \varepsilon_{bulk}$ (*filled circles*) vs pore size [55b]

which originates from segmental fluctuations corresponding to the dynamic glass transition of the polymer. Embedded in nanoporous sol-gel glasses, PDMS shows a much faster dynamics (Fig. 6.40) with broadened relaxation time distribution functions.

The temperature dependence of the relaxation rates (Fig. 6.41) switches from a VFT-like dependence for pores ≥ 7.5 nm to an Arrhenius-like behaviour for 5.0-nm pores. This reflects the transition from a cooperative dynamics taking place on a minimal length scale of about 5 nm to localised fluctuations. It is observed as well in the pore size dependence of the dielectric strength and the increment of the specific heat capacity (see inset in Fig. 6.41). Hence, similar to ethylene glycol in zeolites a pronounced confinement effect is observed for PDMS in sol-gel glasses, but on a larger length scale [55b].

6.4
Liquid Crystals in Confining Space

Liquid crystals are characterized by their ability to form mesophases in which molecular orientational order is realised in one, two or three dimensions (see Chap. 10). This can take place on extended macroscopic length scales up to the micrometer range. The question of how an external geometric confinement influences order, thermodynamics and molecular mobility of liquid crystals was studied [56] for a variety of different systems such as porous filters [57, 58], polymer matrices [59], porous glasses [60, 61], silica gels, aerosils [62] and molecular sieves [63a, 63b]. Besides calorimetric and spectroscopic methods especially NMR, light scattering and dielectric spectroscopy were employed. It is the purpose of this section to exemplify the effect of geometrical confinement on the dynamics of a nematic and a ferroelectric liquid crystalline system being embedded in Anopore (Fig. 6.42 a) and Synpor (Fig. 6.42 b) membranes.

6.4.1
Nematic Liquid Crystals in Mesoporous Membranes

The dielectric properties of the nematic liquid crystal 5 CB (4-*n*-pentyl-4′-cyanobiphenyl) in the bulk and confined to Anopore membranes (pore diameter: 0.2 μm, 0.1 μm and 0.02 μm) were measured in the frequency range from 10^6 Hz to 10^9 Hz at temperatures between 285 K and 320 K [57, 58a,b]. In order to modify the interaction between the liquid crystals and the inner surfaces, the latter were treated with a 2 wt% solution of decanoic acid ($C_9H_{19}COOH$) in methanol. The acid head group binds chemically to the surface and the aliphatic chains form a compact array perpendicular to the inner surfaces. By that, a homeotropic orientation of the director at the wall is induced, leading to three basic types of nematic director field configuration, i.e. the planar-radial, planar-polar and escaped radial.

For a study of the orientational order of the director field dielectric spectra of 5 CB in the bulk and adsorbed to treated and untreated Anopore membranes were measured (Fig. 6.43). In the isotropic phase *one* relaxation process is ob-

Fig. 6.42. Scanning electron microscope images of: **a** an Anopore membrane with pore diameter 0.2 µm; **b** a nitro-cellulose membrane Synpor with mean pore diameter 0.60 µm. Taken from [69] with permission
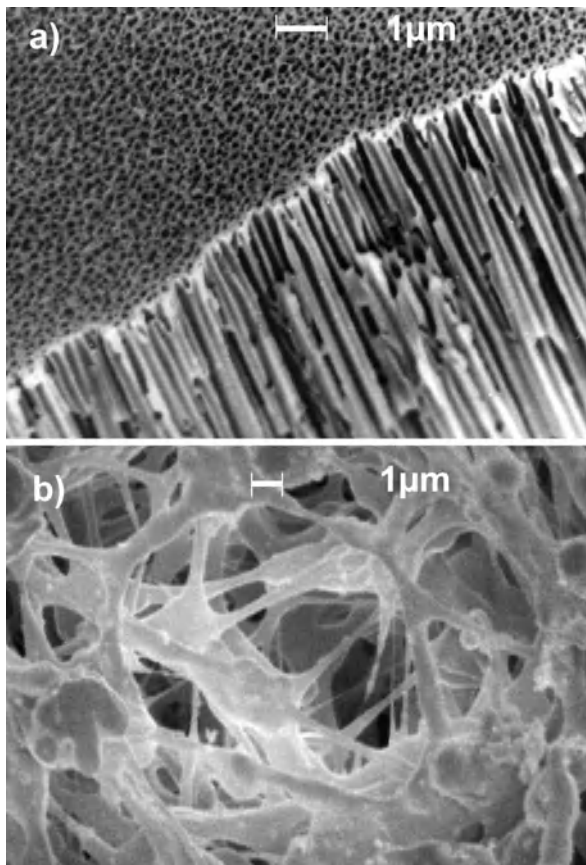
served while in the nematic phase *two* relaxation processes occur: the first is connected with hindered rotation of the molecules around their short molecular axis ("δ-relaxation") and the second is assigned to a tumbling libration ("tumbling mode") with small angular excursion around the short molecular axis. The dielectric strength of the δ-relaxation is comparable to the static dielectric anisotropy of 5 CB, the dielectric strength of the second process is one order of magnitude lower than the first one.

In the confined mesophase, the nematic director is aligned perfectly parallel to the pore walls of the membrane (axial configuration). The fast process is weakened in the dielectric spectra of the axially confined sample. In this configuration mainly the process connected with flips of the molecules around their short axis (δ-relaxation) is effective. However, in Anopore membranes chemically modified with decanoic acid, the slow process is weakened. This indicates that the nematic director inside the treated membranes is oriented nearly perpendicular to the axis of the channels (planar-polar or planar-radial configuration).
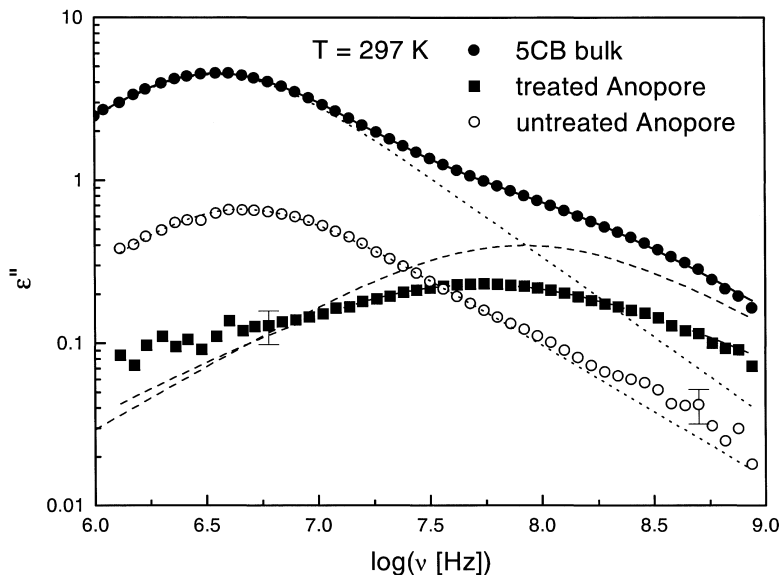
Fig. 6.43. Dielectric loss ε'' vs frequency for 5 CB in the bulk (*filled circles*) and in untreated (*open circles*) and treated (*filled squares*) Anopore membranes at 297 K. The *solid line* is a superposition of two Havriliak-Negami fits, being assigned to the δ-relaxation (---) and the tumbling mode (– – –). In the confined system either the δ-relaxation (untreated pores) or the tumbling mode (treated pores) prevails
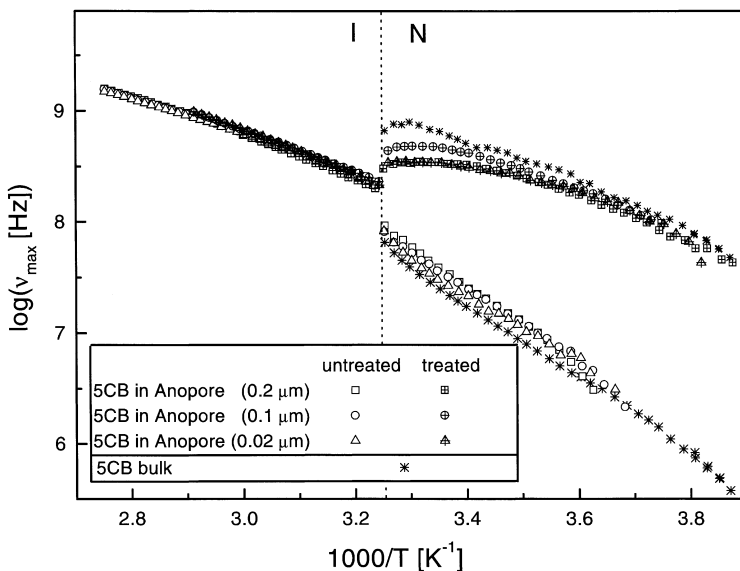
Fig. 6.44. Activation plot: relaxation rate vs inverse temperature for 5 CB in the bulk and confined to untreated and treated Anopore membranes of different diameters as indicated
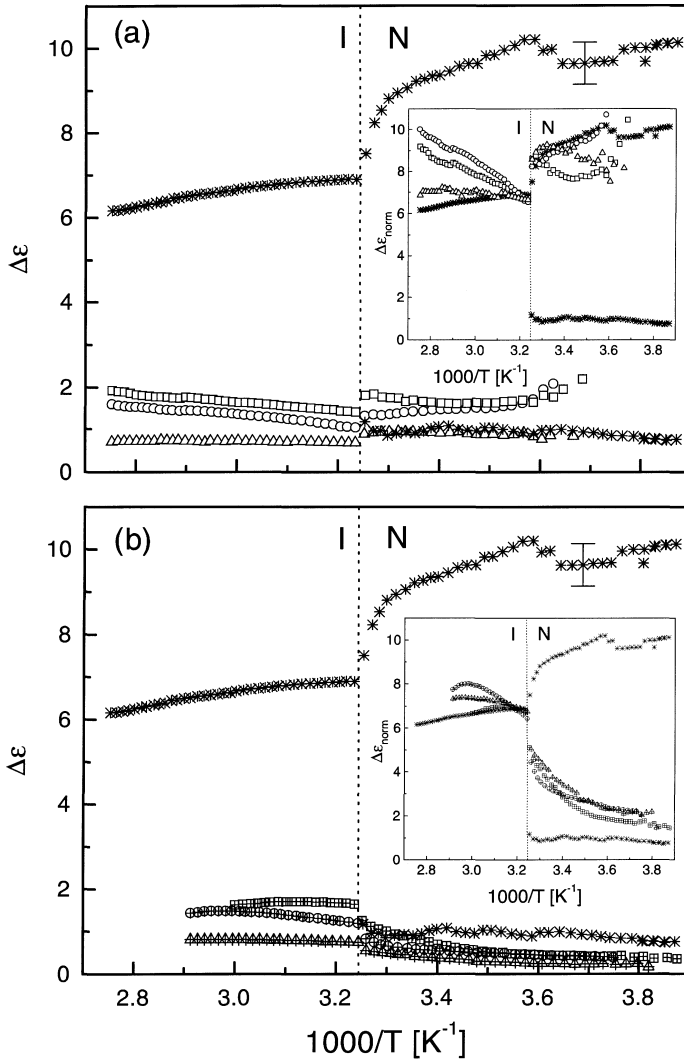
Fig. 6.45. Dielectric strength for the data shown in Fig. 6.44: **a** untreated Anopore membranes. In the *inset* the dielectric strength of the δ-relaxation in the confined system is normalised with respect to the dielectric strength in the bulk close to the phase transition I/N; **b** treated Anopore membranes. *Inset*: normalised dielectric strength of the δ-relaxation, analogously to **a**

The activation plot (Fig. 6.44) shows that in the isotropic phase the bulk and the confined sample have nearly identical relaxation rates. At the phase transition I/N in the bulk sample *two* well separated relaxation modes occur, the δ-relaxation and the tumbling mode. In contrast, in the confined system *one* process prevails, for untreated samples the δ-relaxation while in the surface treated matrix the tumbling mode dominates being by two orders of magnitude faster. For

the latter strong pretransitional effects are observed and the phase transition is smeared out. The effect of the channel dimensions on the relaxation rate is negligible.

The dielectric strength of the δ-relaxation of the axially confined 5 CB in the (untreated) Anopore membranes (Fig. 6.45a) is one order of magnitude lower than in the bulk and it decreases with smaller channel dimensions. The main influence comes from the different amounts of liquid crystal inside the pores which prevent a comparison of the absolute values of the dielectric losses measured in the different samples. In the isotropic phase the ratio of dielectric strength of different samples should depend on the filling factor only. Assuming the latter to be independent of temperature, it is possible to scale the absolute data (inset in Fig. 6.45a). It proves that the dielectric strength in the confined system decreases with decreasing channel diameter. This is caused by the growing fraction of molecules being immobilised by interactions with the solid inner surfaces. At the phase transition I/N the dielectric strength increases. This effect is less pronounced for the small channel diameters.

The dielectric strength of the tumbling mode in treated Anopore membranes (Fig. 6.45b) decreases at the phase transition I/N. This might be due to a slight escape of the director field towards an axial orientation in the centre of the Anopore channels, although a low frequency contribution from configuration in the pore centres (director along the electric field direction) is not resolvable in the dielectric spectra. It fits that for the smallest channel diameter of 0.02 μm the change in the dielectric strength is weakest. The rescaled dielectric strengths prove that in the surface treated channels the amount of immobilised LC molecules is smaller compared to the untreated Anopore membranes (inset in Fig. 6.45b).

The orientation of the nematic molecules inside the treated and untreated Anopore membrane allows for separate measurements of the dielectric dispersion of the real parts of $\varepsilon_{\parallel}$ resp. $\varepsilon_{\perp}$ of the permittivity tensor (parallel resp. perpendicular to the director) in 5 CB. If a simple ansatz of rotational diffusion in a cosine potential $V = V_0 \cos(\vartheta)$ is assumed, where ϑ is the angle between director and molecular long axis (roughly the direction of the dipolar moment of 5 CB), one can estimate the ratio between the dynamics of the fast process (in the potential minimum) and the slow process (crossing of the potential barrier). $\tau_{\mathrm{slow}}/\tau_{\mathrm{fast}} = I_0^2 (V_0/k_B T)$ decreases with the square of the modified Bessel function of order zero. The corresponding values for V_0 which yield the experimental ratios are 2.44 $k_B T$ at the high temperature the end ($\tau_{\mathrm{slow}}/\tau_{\mathrm{fast}} = 0.1$) and 4.0 $k_B T$ at the low temperature end ($\tau_{\mathrm{slow}}/\tau_{\mathrm{fast}} = 0.08$). In the Maier-Saupe theory one would expect order parameters of 0.638 and 0.793, respectively, with these values for the mean field potentials. Compared to order parameters from other experiments [64–66], the potential barriers estimated from the relaxation time ratios are slightly too high but, in view of the rough estimates, in a reasonable order of magnitude. Moreover, in the polar liquid crystal 5 CB, short range dipolar antiparallel ordering may be responsible for a deviation from Maier-Saupe mean field predictions. For further details see [57].

In the cellulose nitrate membrane (Synpor) the cavity surfaces are distributed randomly (Fig. 6.42b). The nematic director is aligned at the inner surfaces and hence oriented isotropically [67]. Considering the results obtained for Anopore

Fig. 6.46. Dielectric loss ε'' vs frequency for 5 CB in the bulk and in untreated Synpor membranes of 0.85 μm mean diameter. The *solid line* is a superposition of two Havriliak-Negami relaxation processes being assigned to the δ-relaxation (---) and the tumbling mode (---). In the con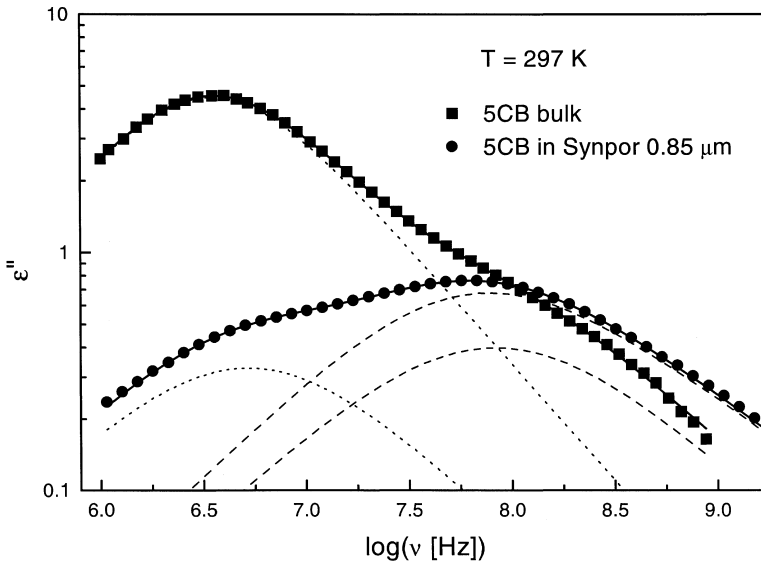fined system both relaxation processes are observable as well, but the δ-relaxation with decreased dielectric strength

membranes two relaxation processes, the δ-relaxation and the tumbling mode have to be expected (Fig. 6.46).

Compared to the bulk the δ-relaxation is strongly reduced in the confining system. This is not surprising because in the bulk phase the liquid crystalline material is oriented rather perpendicular to the electrode planes. Hence the angle between the director and the field axis is close to zero. In that geometry the reorientation of the 5 CB molecules about their short axes, the δ-relaxation, is dielectrically observable. The relaxation rates are nearly independent of the pore diameters (Fig. 6.47a). The temperature dependence is Arrhenius-like in both phases except in the vicinity of the phase transition. The activation energy in the isotropic phase is 37 kJ mol^{-1}. In the nematic phase it is 67 kJ mol^{-1} for the δ-relaxation and 23 kJ mol^{-1} for the tumbling mode. The dielectric strength of 5 CB in the Synpor membranes is in the isotropic phase smaller compared to the bulk due to immobilised molecules (Fig. 6.47b). In the nematic phase the situation is more complex: While the δ-relaxation is weakened the tumbling mode becomes stronger in the confinement. This shows up nicely if the dielectric strength is normalised analogously as in Fig. 6.45 and evidences that the geometry of the porous material determines the orientational order of the confined molecules while it leaves – at least at that level of constraint – phase transitions, order parameters and relaxation rates unchanged.
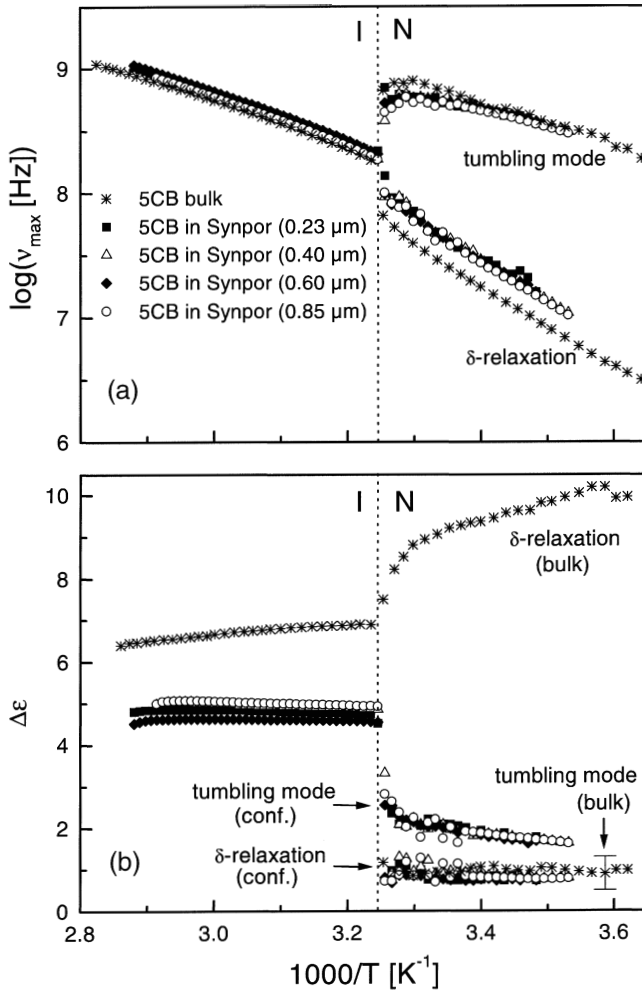
Fig. 6.47. a Activation plot: relaxation rate vs inverse temperature for 5 CB in the bulk and confined to untreated Synpor membranes of diameters as indicated. **b** Dielectric strength vs inverse temperature for the data shown in **a**

6.4.2
Ferroelectric Liquid Crystals in Mesoporous Membranes

In ferroelectric liquid crystals collective relaxation processes (Goldstone- and soft mode) exist besides the molecular fluctuations (see Chap. 10). The question arises of how especially the former are influenced by a spatial confinement.

The comparison (Fig. 6.48) shows for the example of the chiral liquid crystal 4-octyloxy-4-(2-methylbutyloxy)-carbonyl-phenylbenzoate a strong effect [68]: in the bulk sample (Fig. 6.48a) in the smectic SmC* phase the Goldstone mode is

Fig. 6.48. Three-dimensional representation of the temperature and frequency dependence of the dielectric loss ε'' for: **a** the bulk ferroelectric liquid crystal; **b** the ferroelectric liquid crystal embedded in untreated Anopore membranes of 0.2 µm diameter; **c** the ferroelectric liquid crystal embedded in untreated Synpor membranes with pore diameters between 0.23 and 0.85 µm
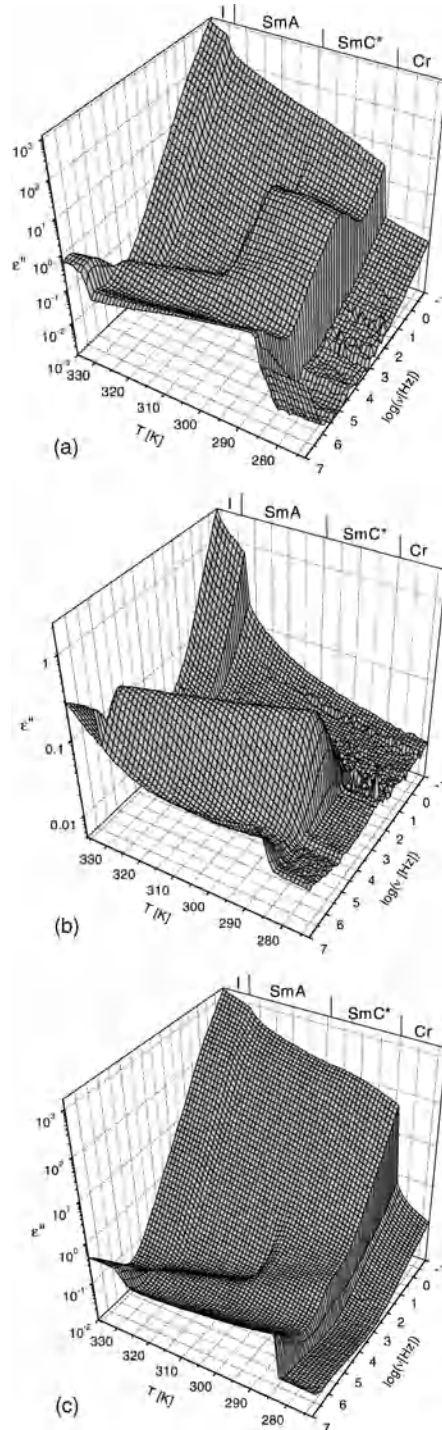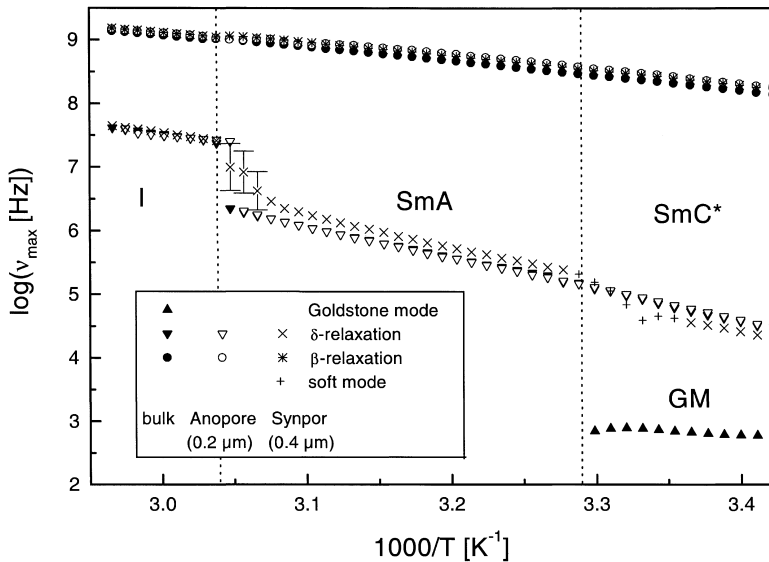
Fig. 6.49. Activation plot: relaxation rate vs inverse temperature for the bulk FLC (*solid symbols*), the FLC in untreated Anopore membranes of 0.2 μm diameter (*open symbols*) and the FLC in untreated Synpor membranes with 0.4 μm diameter (*crossed symbols*). The transition temperature from SmA to SmC* phase is shifted by about 4 K compared to the bulk FLC

observed. It is a strong dielectric loss process being assigned to the fluctuations of the phase of the helical superstructure (phason). In the (non-ferroelectric) smectic SmA phase this collective process no longer exists and only the δ-relaxation remains below 10^7 Hz. In the high frequency regime a further molecular fluctuation takes place, the β-relaxation corresponding to librations around the long molecular axis. At the transition to the isotropic (I) phase the δ- and β-relaxations merge. In the crystalline state both the molecular and the collective dynamics are blocked. In the FLC/Anopore system (Fig. 6.48b) the overall dielectric dynamics is one order of magnitude weaker. The Goldstone mode is not observed; instead as molecular fluctuations the δ- and β-relaxations become measurable. The former has – compared to the bulk system – an increased dielectric strength. This is caused – analogously to the nematic LC/Anopore system – by the aligning effect of the Anopore channels. In the SmC* phase the ferroelectric helix exists in the cylindrical channels and is parallel to its axis. Hence, the observation of the Goldstone mode is prevented by the orientation of the FLC in the Anopore membrane. In the FLC/Synpor system (Fig. 6.48c) no collective fluctuations are observed as well and only the δ- and β-relaxations exist, with the exception that at the phase transition SmC*/SmA indications for a soft mode contribution can be found in a discontinuous change of the relaxation rate (Fig. 6.49). Unfortunately, the overall conductivity in the FLC/Synpor membrane is by two order of magnitude higher than in the FLC/Anopore system (presumably caused by spurious ionic impurities of the Synpor matrix). This prevents a

Fig. 6.50. Dielectric strength vs inverse temperature for the data shown in Fig. 6.48. FLC bulk: Goldstone mode (GM) (*filled triangles*), β-relaxation (*filled circles*), δ-relaxation (*inverted filled triangles*); FLC in Anopore (0.2 µm): β-relaxation (*inverted open triangles*), δ-relaxation (*open circles*); FLC in Synpor (0.4 µm): β-relaxation (*asterisks*), δ-relaxation (*crosses*), soft mode (*plus signs*)
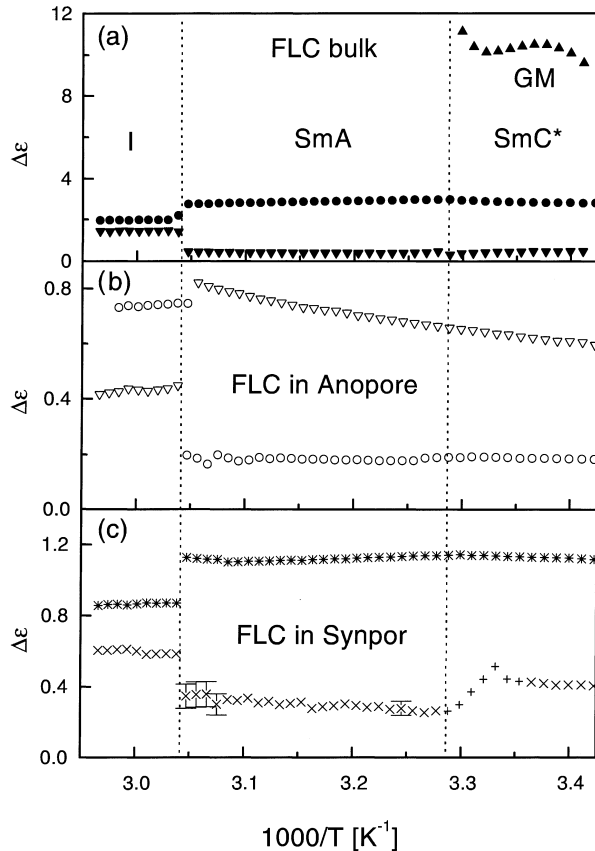
more detailed analysis. In the FLC/Synpor system no Goldstone mode is observed. This is explained – in contrast to the FLC/Anopore system – as a direct effect of the random geometrical confinement, which inhibits the formation of a helical superstructure. The size of the inner cavities is comparable to the pitch length. Hence the irregular cavity boundaries (Fig. 6.42b) create defects in the director or layer structures and pin the director orientation. In Figs. 6.49 and 6.50 the relaxation rates resp. the dielectric strengths are compared for the systems shown in Fig. 6.48a–c.

The collective and molecular dynamics of FLC in confining space is the result of a detailed balance in the host/guest interactions. For the long pitch material DOBAMBC (2-methylbutyl-4-(4-decyloxybenzylideneamino)-cinnamate) neither in Anopore nor in Synpor membranes a Goldstone mode could be observed. In contrast, for the low pitch material C 7 (4-(3-methyl-2-chloropentanoyloxy)-4′-heptyloxybiphenyl) a phason fluctuation was observed in Synpor membranes but with considerably reduced dielectric strength [69]. In the system C 7/Anopore an additional process attributed to the flexoelectric polarisation was observed [70].

6.5
Conclusions

Broadband dielectric spectroscopy enables one to unravel in detail the counterbalance between surface- and confinement effects determining the molecular dynamics in confining space. This is exemplified for a variety of different host/guest systems:

1. Ethylene glycol (EG) in zeolitic host systems shows a pronounced confinement effect. Beyond a threshold channel size, the liquid character is lost as indicated by a dramatically increased relaxation rate and an Arrhenius-like temperature dependence. Computer simulations of the molecular arrangement in a confining space prove that an ensemble as small as six molecules is sufficient to exhibit the dynamics of a bulk liquid.

2. Propylene-, butylene- and pentylene glycol (PG, BG, PeG) in nanoporous sol-gel glasses show for (untreated) hydrophilic inner surfaces a surface effect which can be fully removed by making the boundary layer between the guest molecules and the solid host system hydrophobic. From an analysis of the relaxation time distribution a quantitative three layer model can be deduced with immobilised, interfacial and bulk like molecules.

3. The quasi-van der Waals liquid salol shows in (untreated) hydrophilic sol-gel glasses a dynamics which must be interpreted in terms of a two-state model with exchange between a bulk-like phase in the pore volume and an interfacial phase close to the pore wall. This enables one to analyse the interplay between the molecular dynamics in the two subsystems, and hence their growth and decline in dependence on temperature and strength of the molecular interactions. Analogously to system 2 the surface induced relaxation process can be fully removed by silanization of the walls of the solid host system. Under these conditions a confinement effect for the dynamics of the embedded salol molecules is observed. It is proven by calorimetric studies as well. A refined analysis (Figs. 6.25 and 6.26) enables one to estimate the size of cooperatively rearranging domains and its temperature dependence.

4. Cationic host-guest polymerisation enables the synthesis of poly (isobutyl vinylether) in nanoporous channels of MCMs with different topology. In full accord with the results for low molecular weight systems the interplay between confinement and surface-effects is observed.

5. Poly(propylene glycol) PPG is a type-A polymer which has two dielectrically active relaxation processes, a segmental mode (dynamic glass transition) corresponding to fluctuations of a few polymer segments and a normal mode fluctuation of the end to end vector. In the confinement of nanoporous sol-gel glasses both relaxation processes behave differently: while the normal mode slows down with decreasing pore size, the segmental mode shows a non-monotonous dependence on the pore diameter – in contrast to the monomeric Propylene glycol (PG). This is attributed to the subtle interplay between surface and confinement effects mediated by the formation of H-bonds with the solid walls.

6. Comparing the dielectric data with measurements obtained by Temperature Modulated Differential Scanning Calorimetry (TMDSC) delivers similar re-

sults for the relaxation rates. From the pore size dependence of the increment of the specific heat capacity the minimal length scale of cooperativity of the dynamic glass transition is obtained. It has for PPG a value of about 1.8 nm.

7. For poly(dimethyl siloxane) a confinement effect is observed where – with decreasing pore size (pore sizes ≥ 7.5 nm) – the VFT-dependence changes into an Arrhenius-like behaviour at pores of 5 nm. Exactly at this transition the increment of the heat capacity vanishes delivering a value of 5 nm as minimal length scale of cooperativity for PDMS.

8. The liquid crystal 4-n-pentyl-4'-cyanobiphenyl (5 CB) has two dielectrically active relaxation processes in the nematic phase: (i) a δ-relaxation, corresponding to flips of the mesogene and (ii) a "tumbling mode" being assigned to librations around the short molecular axis. Under the confinement of ordered cylindrical channels of Anopore membranes, the nematic director is aligned axially or radially depending upon their surface preparation (untreated resp. treated with decanoic acid). Consequently it is possible to study each of the two relaxation processes separately by appropriate surface treatment of the pores. The frequencies of both processes are found to be unchanged with respect to the bulk phase with the exception of the region of the phase transition isotropic/nematic which becomes smeared out with increasing confinement. In the randomly disordered cellulose nitrate membrane Synpor 5 CB exhibits – as expected – both relaxation processes.

9. Chiral liquid crystals have collective modes besides molecular relaxations. They correspond to fluctuations of the phase and amplitude of the helical superstructure (Goldstone – and soft mode). Under conditions of confinement (Anopore or Synpor membranes) the latter are suppressed while the former (β-relaxation, δ-relaxation) are influenced weakly only.

List of Abbreviations and Symbols

a	Constant
A	Constant
c_{ij}	Jump rate between substems i and j
D	Fragility parameter
f	Volume filler factor
$L(\tau)$	Relaxation time distribution function
p_i	Polarisation in a subsystem
s	Constant
T_0	Vogel temperature

$\varepsilon^{*}, \varepsilon', \varepsilon''$ Complex dielectric function, real and imaginary part

ε_0 Dielectric permittivity of vacuum ($\varepsilon_0 = 8.854 \times 10^{-12}$ AsV^{-1}m^{-1})

$\varepsilon_s, \varepsilon_\infty$ $\varepsilon_s = \lim_{\omega\tau \ll 1} \varepsilon'(\omega); \; \varepsilon_\infty = \lim_{\omega\tau \gg 1} \varepsilon'(\omega)$

$\Delta\varepsilon$ Dielectric strength

ν Frequency, relaxation rate

ν_{max} Relaxation rate of maximum dielectric loss

$\sigma^{*}, \sigma', \sigma''$ Complex conductivity, real and imaginary part

σ_0 Direct current (d.c.) conductivity

τ Relaxation time

τ_{max} relaxation time a maximum dielectric loss

ω Angular frequency

BG   Butylene glycol

C 7   Liquid crystal (4-(3-methyl-2-chloropentanoyloxy)-4'-heptyloxy-biphenyl)

5 CB   Liquid crystal (4-n-pentyl-4'-cyanobiphenyl)

Cr   Crystalline

d.c.   Direct Current

DSC   Differential Scanning Calorimetry

EG   Ethylene glycol

FLC   Ferroelectric Liquid Crystals

GM   Goldstone mode

HN   Havriliak Negami

I   Isotropic

LC   Liquid Crystals

MCM   Mesoporous material ("Mobil Composition of Matter")

N   Nematic

PeG   Pentylene glycol

PDMS   Poly(dimethyl siloxane)

PG   Propylene glycol

PIBVE   Poly(isobutyl vinylether)

PPG   Poly(propylene glycol)

TMDS   Temperature modulation differential scanning calorimetry

SmA   Smectic A

SmC* Smectic C*

VFT   Vogel-Fulcher-Tammann (see Eq. 6.4)

References

1. Kremer F, Huwe A, Arndt M, Behrens P, Schwieger W (1999) J Phys Cond Matter 11:A175
2. Adam G, Gibbs JH (1965) J Chem Phys 43:139
3. Donth E (1981) Glasübergang. Akademie, Berlin
4. Donth E (1992) Relaxation and thermodynamics in polymers, glass transition. Akademie Verlag, Berlin
5. Fischer EW, Donth E, Steffen W (1992) Phys Rev Lett 68:2344

6. Fischer EW (1993) Physica A 201:183
7. Sappelt D, Jäckle J (1993) J Phys A 26:7325
8. Huwe A, Kremer F, Behrens P, Schwieger W (1999) Phys Rev Lett 82:2338
9. Gorbatschow W, Arndt M, Stannarius R, Kremer F (1996) Europhys Lett 35:719
10. Arndt M, Stannarius R, Gorbatschow W, Kremer F (1996) Phys Rev E 54:5377
11. a Stannarius R, Kremer F, Arndt M (1995) Phys Rev Lett 75:4698; b Arndt M, Stannarius R, Groothues H, Hempel E, Kremer F (1997) Phys Rev Lett 79:2077
12. Barut G, Pissis P, Pelster R, Nimtz G (1998) Phys Rev Lett 80:3543
13. Pissis P, Kyritsis A, Daoukaki D, Barut G, Pelster R, Nimtz G (1998) J Phys Cond Matter 10:6205
14. Daoukaki D, Barut G, Pelster R, Nimtz G, Kyritsis A, Pissis P (1998) Phys Rev B 58:5336
15. Pissis P, Kyritsis A, Barut G, Pelster R, Nimtz G (1998) J Non-Cryst Solids 235/237:444
16. Wendt H, Richert R (1999) J Phys Cond Matter 11:A199
17. Schönhals A, Stauga R (1998) J Non-Cryst Solids 235–237:450
18. Schönhals A, Stauga R (1998) J Chem Phys 108:5130
19. Rittig F, Huwe A, Fleischer G, Kärger J, Kremer F (1999) Phys Chem Chem Phys 1:519
20. Liu G, Li Y, Jonas J (1991) J Chem Phys 95:6892
21. Zhang J, Liu G, Jonas J (1992) J Chem Phys 96:3478
22. Streck C, Mel'nichenko YB, Richert R (1996) Phys Rev B 53:5341
23. Schüller J, Mel'nichenko YB, Richert R, Fischer EW (1994) Phys Rev Lett 73:2224
24. Meier WM, Olson DH, Baerlocher C (1996) Atlas of zeolite structure types. Elsevier, Amsterdam
25. Kärger J, Ruthven DM (1992) Diffusion in zeolites and other microporous solids. Wiley, New York
26. Bibby M, Dale MP (1985) Nature 317:157
27. Braunbarth CM, Behrens P, Felsche J, van de Goor G (1997) Solid State Ionics 101/103: 1273
28. Newsam JM, Treacy MMJ, Koetsier WT, de Gruyter CB (1988) Proc R Soc (London) 420:375
29. Havriliak S, Negami S (1966) J Polym Sci C 14:99
30. Havriliak S, Negami S (1967) Polymer 8:161
31. Schäfer H, Sternin E, Stannarius R, Arndt M, Kremer F (1996) Phys Rev Lett 76:2177
32. Vogel H (1921) Phys Zeit 22:645
33. Fulcher GS (1925) J Am Ceram Soc 8:339
34. Tammann G, Hesse G (1926) Anorg Allgem Chem 156:245
35. Jordan BP, Sheppard RJ, Szwarnowski S (1978) J Phys D 11:695
36. Mayo SL, Olafson BD, Goddard WA III (1990) J Phys Chem 94:8897
37. Rappe AK, Casewit CJ, Colwell KS, Goddard WA III, Skiff WM (1992) J Am Chem Soc 114:10,024
38. Burchart E (1992) Thesis, Technische Universiteit Delft
39. Cusack NE (1987) The physics of structurally disordered matter. Adam Hilger, Bristol
40. van Beek LKH (1967) In: Birks JB (ed) Progress in dielectrics. Heywood, London, vol 7, p 69
41. Maxwell JC (1892) Electricity and magnetism. Clarendon, Oxford 1:452
42. Sillars RW (1937) J Inst Elect Engrs 80:378
43. Hanai T (1968) Electrical properties of emulsions. In: Sherman P (ed) Emulsion science. Academic Press, New York, pp 353–478
44. Kamiyoshi K (1950) Sci Rep Res Inst Tohoku Univ 26:318
45. Pelster R (1999) Phys Rev B 59:9214
46. Yan X, Streck C, Richert R (1997) In: Drake JM, Klafter J, Kopelman R (eds) Dynamics in small confining systems III. Materials Research Society, Pittsburgh, Pennsylvania 464:33
47. Schönhals A, Kremer F, Hofmann A, Fischer EW, Schlosser E (1993) Phys Rev Lett 70:3459
48. Kresge CT, Leonowicz ME, Roth WJ, Vartuli JC, Bech JS (1992) Nature 359:710
49. Beck JS, Vartuli JC, Roth WJ, Leonovicz ME, Kresge CT, Schitt KD, Chu CTW, Olson DH, Shappard EW, McCullen SB, Higgins JB, Schlenker JL (1992) J Am Chem Soc 114: 10,834

50. Casalini R, Fioretto D, Livi A, Lucchesi M, Rolla PA (1997) Phys Rev B 56:3016
51. Schönhals A, Goering H, Schick C (2002) J Non-Cryst Solids (in press)
52. Petychakis L, Floudas G, Fleischer G (1997) Europhys Lett 40:685
53. Stockmayer WH (1967) Pure Appl Chem 15:539; Stockmayer WH, Burke JJ (1969) Macromolecules 2:647
54. Adachi K, Kotaka T (1993) Prog Polym Sci 18:585
55. a Appel M, Fleischer G, Kärger J, Chang I, Fujara F, Schönhals A (1997) Colloid Polym Sci. 275:187; Fleischer G, Appel M (1995) Macromolecules 28:7281; b Schönhals A, Goering H, Schick C (2002) In preparation
56. Crawford GP, Zumer S (1996) Liquid crystals in complex geometries. Taylor and Francis, London Bristol
57. Rozanski SA, Stannarius R, Groothues H, Kremer F (1996) Liq Cryst 20:59
58. a Sinha GP, Aliev FM (1998) Phys Rev E 58:2001; b Aliev I, Sinha GP (2001) Mol Cryst Liq Cryst 364:435
59. Różański SA, Kremer F, Groothues H, Stannarius R (1997) Mol Cryst Liq Cryst 303:319
60. Goleme A, Zumer S, Allender DW, Doane JW (1988) Phys Rev Lett 61:1937
61. Cramer C, Cramer T, Kremer F, Stannarius R (1997) J Chem Phys 106:3730
62. Cramer C, Cramer T, Arndt M, Kremer F, Naji L, Stannarius R (1997) Mol Cryst Liq Cryst 303:209
63. a Frunza S, Frunza L, Schönhals A, Zubova H-L, Kosslick H, Carius HE, Fricke R (1999) Chem Phys Lett 307:167; b Frunza S, Frunza L, Schönhals A (2000) J Phys IV 10:115
64. Won APY, Kim SB, Goldburg WI, Chan WHM (1993) Phys Rev Lett 70:954
65. Tschierske S, Yaroshchuk OV, Kresse H (1995) Cryst Res Technol 30:571
66. Buka A, de Jeu WH (1982) J Physique 43:361
67. Różański SA, Stannarius R, Kremer F (1999) Z Phys Chem 211:147
68. Różański SA, Stannarius R, Kremer F (2001) IEEE Trans Dielectr Electr Insul 8:488
69. Różański SA, Stannarius R, Kremer F (2001) Liq Cryst 28:1071
70. Różański SA, Stannarius R, Kremer F (2001) XIV Conference on Liquid Crystals, 3–7 September 2001, Zakopane, Poland, Abstract p A28

7 Molecular Dynamics in Polymer Model Systems

A. Schönhals

7.1
Introduction

It has been proven (see for instance [1–11]) that dielectric spectroscopy is a useful tool to study the molecular dynamics of polymers. This is due to the fact that a broad dynamical range from the milli- to the Giga-Hertz region can be covered by this method in its modern form (see Chap. 2). Therefore motional processes which take place for polymeric systems on extremely different time scales can be investigated in a broad frequency and temperature range. Moreover the motional processes depend on the morphology and micromorphology of the system under investigation. Therefore information on the structural state of the material can be indirectly extracted by taking the molecular mobility as a probe for the structure.

Polymeric materials are rather complex systems. For an isolated macromolecule a large number (typically hundreds to millions) of atoms are covalently bonded and therefore macromolecular chains can have an even larger (almost unlimited) number of conformations in space and time. Most of the polymer properties like chain flexibility, the mean-square end-to-end vector of the chain or the mean-square dipole moment are due to this large number of conformations. Using methods of statistical mechanics, the *Rotational Isomeric State* (RIS)-model – mainly developed by Flory [12, 13], awarded with the Nobel Prize in chemistry in 1974- is able to predict equilibrium conformational properties of macromolecular chains.

Related to the huge number of conformations the behaviour and the properties of macromolecules in solutions and in the undiluted state are complex. For instance in the bulk a polymeric system can behave as a solid, as a rubbery (viscoelastic) material which is highly deformable or as a melt[1] in dependence on temperature. This is demonstrated in Fig. 7.1 where the temperature dependence of the shear modulus is sketched for an amorphous polymer. At low temperatures the system behaves like a glassy solid where the shear modulus is in the order of magnitude of 10^9 Pa s. At the glass transition the shear modulus drops down by three orders of magnitude and the system has viscoelastic properties. From this step-like change the glass transition temperature T_g can be estimated which corresponds to the value measured by calorimetry. At still higher temper-

---

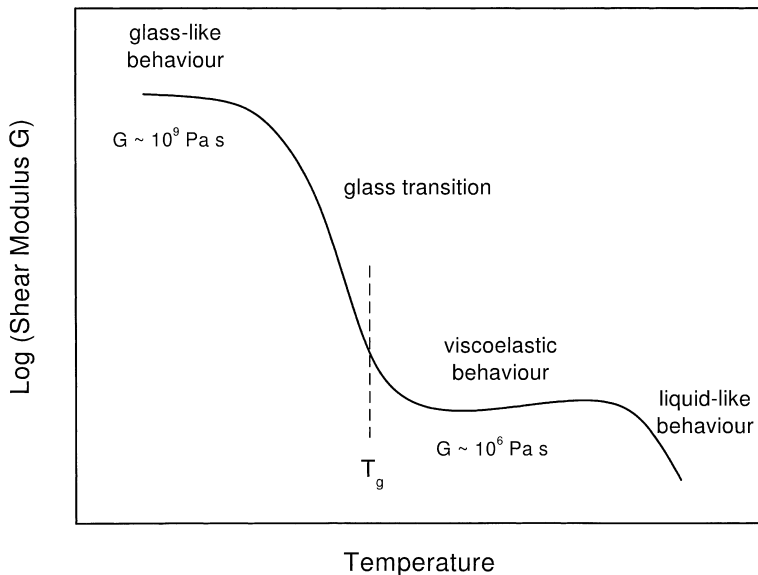[1] This is only true if the macromolecules are not crosslinked.

Fig. 7.1. Schematic temperature dependence of the shear modulus for an amorphous polymer

atures the chains have a further more increased mobility and the systems flows like an ordinary liquid, i.e. the shear modulus is approximately zero.

The morphology of macromolecular materials in the bulk can be amorphous (no long-range order), liquid crystalline (see for instance Chap. 10) or semicrystalline. The type of observed morphology depends on the chemical composition of the chain.

As was discussed above, a large number of properties of polymers depends on the molecular weight. However, there are also some properties which become independent of molecular weight if its value is sufficiently high. Effects related to chain ends become less important for longer chains or topological interactions (entanglements) are different for long and short chains. A measure for this molecular weight threshold is the critical molecular weight M_C which is in the order of 10^4 g mol^{-1} for most flexible polymers.

One has to keep in mind that depending on the synthesis of polymers the molecular weight has a distribution which will additionally influence the properties of macromolecules to some extent. Choosing different routes of synthesis means that distribution can be broader or narrower. In most cases the influence of this distribution is omitted here for sake of brevity[2].

---

[2] For a discussion of the molecular weight distribution, its characterization and similar effects like branching the reader is referred to textbooks of macromolecular science like [275]. Besides the distribution of molecular weight linear chain structures can also have some unwanted defects like branches due to chemical reaction.

Fig. 7.2. Model for an idealized flexible chain molecule. A_i represent the centers of gravity of the monomeric units and l_i the bonds. The end-to-end vector r of the chain is defined by the vector between A_0 and A_{N-1}
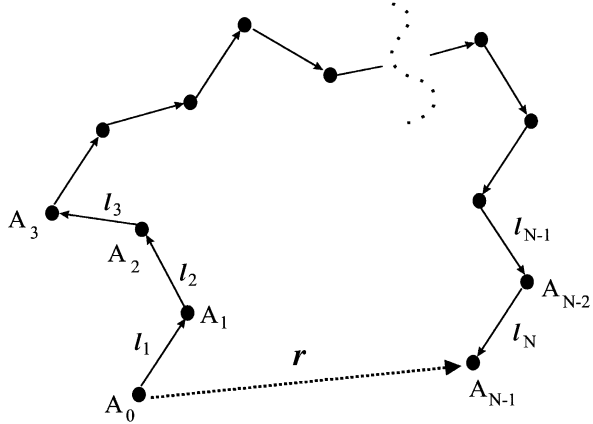
In addition to linear chains macromolecular systems can be synthesized in a wide variety of molecular architectures like comb-like and branched structures, stars (also with chemically different arms), cycles, copolymers (statistical-, di- or multiblock copolymers), physically or chemically bonded networks, hyper-branched polymers or dendrimers [16]. These novel molecular architectures cause new morphologies like liquid-crystalline phases, phase or microphase separated structures. Some of this new architecture and its dielectric properties will be discussed at the end of this chapter.

7.2 Theoretical Considerations

In this section some basic theoretical concepts and ideas to describe polymers are introduced to discuss the dielectric properties of macromolecular systems from a general point of view.

7.2.1
Conformations of Polymeric Chains

Besides the molecular weight M of a macromolecule, its spatial dimension characterized for instance by the end-to-end vector r is one of the most important quantity. The definition of r for an idealized chain gives Fig. 7.2. Due to molecular motions r fluctuates and its mean quadratic value $\langle r \cdot r \rangle = \langle r^2 \rangle$ has to be considered where the brackets indicate the ensemble (or time) average.

To calculate $\langle r^2 \rangle$ one has to decide between stiff, rod like and flexible chain structures. The following discussion will focus on the latter one. For an idealized chain (see Fig. 7.2)

$$\langle r^2 \rangle = \left\langle \sum_{i,j=1}^{N} l_i \cdot l_j \right\rangle = \sum_{i=1}^{N} l_i^2 + 2 \sum_{1 < i < j < N} \langle l_i \cdot l_j \rangle \tag{7.1}$$

holds where l measures the length of a bond and N counts its numbers ($N \sim M$). The simplest model for an isolated macromolecule is that of a freely joined chain. Two assumptions are made: (i) the bonds can cross each other and (ii) no correlation exists between different bonds ($\langle l_i \cdot l_j \rangle = l^2 \delta_{ij}$, δ_{ij} – Kronnecker symbol). With these assumptions Eq. (7.1) simplifies to

$$\langle r^2 \rangle_0 = l^2 N \sim M \tag{7.2}$$

From a mathematical point of view this corresponds to a random walk [15] (Gaussian statistics) and such a chain is called a Gaussian one.

For a real chain neither the rotational angle ϕ around each bond nor the valence (bond) angle $\gamma(\theta = 180° - \gamma)$ can be regarded as free (for definitions see Fig. 7.3a). These effects lead to a greater stiffness of the chain which can be expressed by

$$\langle r^2 \rangle = C_\infty \langle r^2 \rangle_0 \tag{7.3}$$

where C_∞ is the characteristic ratio [3]. It measures the flexibility of a chain structure in comparison to the freely joined chain model. One extension of the freely joined chain model is the free rotational one where the bond angle θ is fixed while the rotational angle ϕ is regarded as free. For the tetrahedral bond angle ($\theta = 70.53°$) $C_\infty = 2$ is estimated. More refined calculations of conformational properties can be carried out in the frame work of the RIS-model [12, 13, 16]. In this approach the large number of conformations of two consecutive bonds is modelled by a limited small number of discrete ones having statistical weights σ_i according to $\sigma_i = \exp(-E_{\alpha\beta}/k_B T)$. $E_{\alpha\beta}$ is the conformational energy of the rotational state β of the bond i provided that the bond $i-1$ is in the state α (see Fig. 7.3b). Usually these states are called gauche(–), trans and gauche(+). Defining a transfer matrix $\tilde{T}_i$ by

$$\tilde{T}_i = \begin{bmatrix} \cos\theta & \sin\theta & 0 \\ \sin\theta\cos\phi & -\cos\theta\cos\phi & \sin\phi \\ \sin\theta\sin\phi & -\cos\theta\sin\phi & -\cos\phi \end{bmatrix}_i \tag{7.4}$$

a bond l_{i-1} can be transformed to the bond l_i by $l_i = \tilde{T}_i l_{i-1}^T$ where l_i^T denotes the transpose vector to l_i. Using this technique in combination with averaging procedures the statistical properties of a chain- for instance realistic values of C_∞ for real chains – can be calculated [12, 13, 17].

The bonds of real chains cannot cross each other. This leads to additional interactions of chain segments which are distant along the chain but can become close in space (long range repulsive interactions, excluded volume effect [12, 15]) which can cause an expansion of the coil. The model of a random walk (where the path can be crossed, see Eq. (7.2)) has to be replaced by a self-avoid-

---

[3] For sufficiently long chains C_∞ is independent of the chain length [12].

(a)

(b)

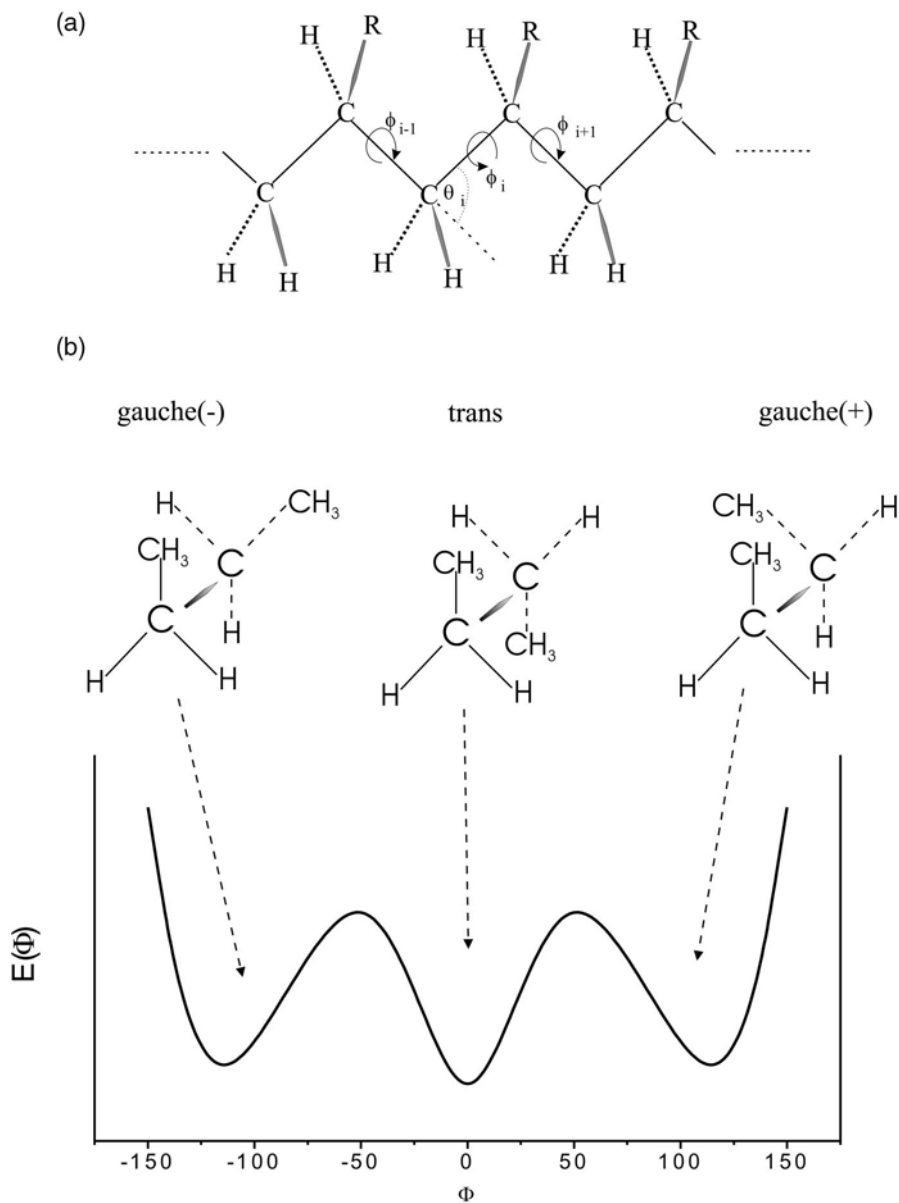gauche(-)　　　　　　　trans　　　　　　　　gauche(+)

Fig. 7.3. Atomistic model for a polymeric chain: **a** definition of the bond angle ϕ and the valence angle θ; **b** rotational potential for n-butane to explain the basics of the RIS model for a polymer chain. The minima in the potential are due to the discrete isomeric rotational states called gauche (–)-, trans- and gauche(+)-conformation

ing random walk [15]. This corresponds to a polymeric chain in a good solvent where due to the solvent-polymer interaction the coil is expanded. One obtains

$$\langle r^2 \rangle = C_\infty M^{2\nu_{Coil}} \tag{7.5}$$

For the scaling exponent ν_{Coil} a value of $\nu_{Coil} = 3/5$ is found. This value can also be calculated in the framework of a simple scaling model [12, 15]. For bad solvents the coil collapses which leads to $\nu_{Coil} < 0.5$. For $\nu_{Coil} = \nu_\theta = 0.5$ (see Eq. 7.2) the excluded volume effect (repulsive interaction) and the attractive interaction compensate each other. The chain dimensions $\langle r^2 \rangle_\Theta$ are then called "undisturbed" (θ-condition) [12, 15]. A change of the chain dimensions with the solvent quality can be described by the expansion factor

$$\alpha = \frac{\langle r^2 \rangle}{\langle r^2 \rangle_\Theta} \tag{7.6}$$

Also for a polymer chain in an undiluted melt or in the amorphous glassy state $\nu_{Coil} = 0.5$ was found (see for instance [18]) which can be explained by screening arguments [15].

To consider the conformational properties of stiff or rod-like chain structures the concept of the persistence length is used leading to the model of worm like chains [19] which is not discussed further in this chapter.

7.2.2
Dipole Moments of Polymeric Chains

According to Chap. 1 the dielectric properties of a polymeric chain depend on the polarization P which is the dipole density in a unit volume V

$$P = \frac{1}{V} \sum_{chain} \sum_{repeating\ unit} \boldsymbol{\mu}_i \tag{7.7}$$

where $\boldsymbol{\mu}_i$ is the dipole moment of the repeating unit i. In more detail, the mean square dipole moment

$$\langle \boldsymbol{\mu}^2 \rangle = \sum_{i=1}^{N} \langle \boldsymbol{\mu}_i^2 \rangle + 2 \sum_{i=1}^{N} \sum_{j<i} \langle \boldsymbol{\mu}_i \boldsymbol{\mu}_j \rangle \tag{7.8}$$

has to be considered. The first part of Eq. (7.8) denotes the self correlation of the dipole moment of a repeating unit whereas the second part represents the cross correlations of dipoles between different repeating units.

In contrast to low molecular weight molecules, where the dipole moment can be well represented by a rigid vector [20], for long chain molecules there are different possibilities for the orientation of a molecular dipole vector with respect to the polymer backbone (see Fig. 7.4). According to Stockmayer [21], macro-
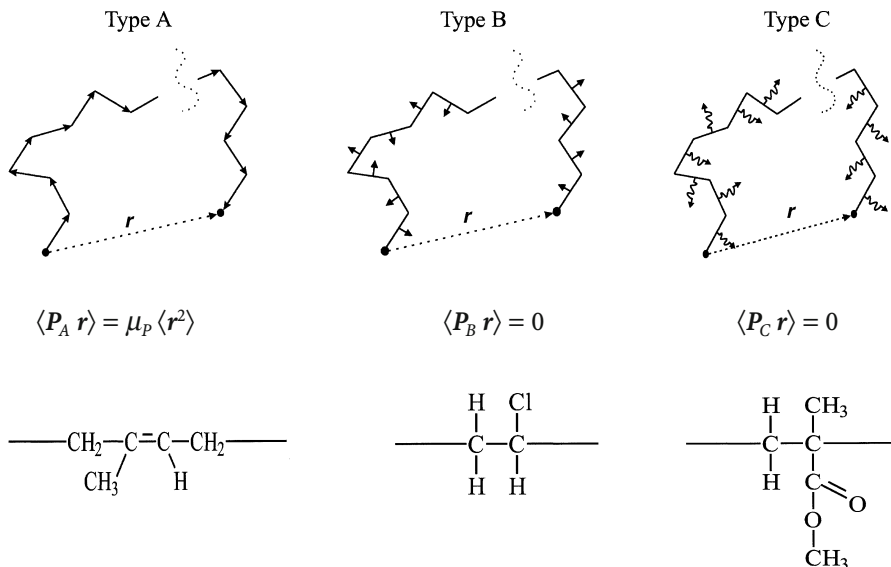
Type A   Type B   Type C

$$\langle P_A\, r\rangle = \mu_P \langle r^2\rangle \qquad\qquad \langle P_B\, r\rangle = 0 \qquad\qquad \langle P_C\, r\rangle = 0$$

$$—CH_2—C\!\!=\!\!C—CH_2—$$
$$CH_3 \quad H$$

H   Cl
| |
—C—C—
| |
H   H

H   CH$_3$
| |
—C—C—
| |
H   C
     O
     |
     O
     |
     CH$_3$

Fig. 7.4. The different geometric possibilities for the location of molecular dipoles with respect to the polymer chain. Examples: Type-A – poly(*cis*-1,4-isoprene); Type-B – poly(vinyl chloride); Type-C – poly(methyl methacrylate)

molecules with molecular dipoles fixed parallel to the backbone are called Type-A polymers. For the dipole moment P_A of the whole chain one gets

$$P_A = \mu_p r \tag{7.9a}$$

where r is the end-to-end vector of the chain and μ_p is the component of the dipole moment of the repeating unit parallel to the chain contour. For the mean square value

$$\langle P_A^2\rangle = \mu_p^2 \langle r^2\rangle \tag{7.9b}$$

is obtained. For Type-B polymers the dipole moment is rigidly attached perpendicular to the chain skeleton. Therefore for the dipole moment P_B of a type B polymer

$$\langle P_B \cdot r\rangle = 0 \tag{7.10}$$

holds. There is no correlation between the dipole moment and the chain contour (no long range correlations of the dipole moments of different repeating units). Most of the synthetic macromolecules are of Type-B. The fluctuation of the dipole moment of Type-B polymers are due to conformational transitions which are related to segmental mobility. Although there is no polymer which is solely of Type-A there are several examples of macromolecules like poly(*cis*-1,4-isoprene) [22] having components of the dipole moment parallel and perpendicu-

lar to the chain. These polymers are also called Type-A- or Type-AB polymers [7]. Various classifications of Type A and Type AB polymers are discussed in detail by Adachi and Kotaka [7].

Chain molecules having the dipoles in a more or less flexible side chain like the poly(n-alkyl methacrylate)s are called to be of Type-C[4]. Also in that case the classification is not straightforward. If the side group can rotate on a shorter time scale than the segmental dynamics one the macromolecule is classified as Type-C polymer. In the opposite case it should be regarded as a structure of Type-B [8].

In the following only Type-B polymers will be considered. Equation (7.8) can be rewritten as

$$\langle \mu^2 \rangle = \sum_{i=1}^{N} \langle \boldsymbol{\mu}_i^2 \rangle + 2 \sum_{i=1}^{N} \sum_{j<i} \langle |\boldsymbol{\mu}_i| |\boldsymbol{\mu}_j| \cos\theta_{ij} \rangle$$

or   (7.11)

$$\langle \mu^2 \rangle = \sum_{i=1}^{N} |\boldsymbol{\mu}_i|^2 + 2 \sum_{i=1}^{N} \sum_{j<i} |\boldsymbol{\mu}_i| |\boldsymbol{\mu}_j| \langle \cos\theta_{ij} \rangle$$

where θ_{ij} is angle between bonds i and j. $|\boldsymbol{\mu}| = m$ denotes the norm of the dipole moment perpendicular to the chain. For the freely joined chain model $\langle \cos\theta_{ij} \rangle = 0$ holds. For real chain structures this is of course not the case. Short range intramolecular correlations contribute to the mean square dipole moment described by the intramolecular dipolar correlation coefficient g_{intra} defined as[5]

$$g_{\text{intra}} = \frac{\langle \mu^2 \rangle}{\sum\limits_{i=1}^{N} m_i^2} = 1 + 2 \sum_{i=1}^{N} \sum_{j<i} \langle \cos\theta_{ij} \rangle$$ (7.12)

It should be noted that the dipolar correlation coefficient is in fact the Kirkwood/Fröhlich correlation factor for an isolated chain (see Chap. 1). For a freely joined chain $g_{\text{intra}} = 1$ holds. Therefore g_{intra} is a measure for the correlations between dipole moments of neighboured repeating units. Calculations of g_{intra} were started by Debye and Bueche [24]. More detailed estimations can be done in the framework of the RIS-model [12, 13]. Using the technique of transfer matrix one can write

$$\mu^2 = \sum_{i=1}^{N} \boldsymbol{\mu}_i^2 + \sum_{i=1}^{N} \sum_{j\neq i} \boldsymbol{\mu}_i \tilde{T}_i \tilde{T}_{i+1} ... \tilde{T}_j \boldsymbol{\mu}_j^T$$ (7.13)

Since the statistical weights are known in the RIS-model average values can be calculated. Detailed considerations and calculations for different chain struc-

---

[4] It should be noted that a dipole in a side chain usually implies both a dipole component that contributes to the polarization by main chain reorientations and a component whose reorientation is due to local side chain motions [23].

[5] It was assumed that all dipole moments have the same value.

tures (including main chain and side group polymers) have been summarized by Riande and Saiz [8].

For rod like polymers like poly(n-alkyl isocyanate)s or poly(γ-benzyl-L-glutamate) which can also form suprastructures like helices, due to intramolecular correlations the dipole moment adds up to give giant values (see for instance [23]).

7.2.3
Motional Processes in Isolated Chains

As it was discussed in detail in Chap. 1 the dielectric relaxation behaviour is due to the time dependent dipole-dipole correlation function $\Phi_\mu(t)$ which may be written as

$$\Phi_\mu(t) = \frac{\sum_i \langle \mu_i(0)\mu_i(t) \rangle + 2 \sum_i \sum_{i<j} \langle \mu_i(0)\mu_j(t) \rangle}{\langle (\sum_i \mu_i)^2 \rangle} \tag{7.14}$$

The first part corresponds to the self correlation function and the second to contributions of cross correlation terms.

Macromolecules are complicated many-body systems and so the analytic calculation of $\Phi_\mu(t)$ is impossible even for an isolated chain with a simple structure. However, for polymeric systems motional processes which lead to dipole fluctuations take place at very different length and time scales. Such motional processes can be localized fluctuations within a backbone segment or local rotational fluctuations of a short side chain. On a larger spatial and longer time scale the so called segmental motion becomes relevant. At a more extended length scale the translatorial motion of the whole chain characterized by the end-to-end vector takes place. Therefore the fluctuation of the net dipole moment given by Eq. (7.8) can be due to different motional processes which give rise to distinct parts in the decay of $\Phi_\mu(t)$. In a first rough approximation one can consider the processes as statistically independent which leads to $\Phi_\mu = \Phi_{\text{Local}} + \Phi_S + \Phi_{\text{Ch}}$. Φ_{Local} is the part of Φ_μ due to localized motions, Φ_S is due to the segmental motion and Φ_{Ch} is the part of the correlation function related to global chain dynamics. For each of these motional processes models have been developed taking into consideration their specific peculiarities. For local motional processes often transitions in a double minimum potential have been assumed (see Chap. 1). For the segmental as well as for the chain motion the situation is more complex. Models for these two motional processes will be discussed in the next two sections.

7.2.3.1
Segmental Motion

The segmental motion in an isolated macromolecular chain is related to conformational changes. The RIS-model relates these transitions to a limited number of energetically favoured states. As discussed these transitions are not indepen-

dent from each other and many degrees of freedom are involved in such a process. One suggestion to understand this type of motion is based on correlated transitions of a limited number of segments assuming that the first and the last of the involved segments are in the same state at the beginning and at the end of the correlated transitions. Examples for such models are the Shatzki crankshaft [25] or the Three-Bond-Motion developed by Monnerie and coworkers [26]. A critical discussion of these models can be found in [27]. The current understanding of the segmental motion in isolated chains is based on ideas of Helfand et al. [27] and Skolnik and Yaris [28]. They describe the segmental motion as a damped diffusion of conformational states along the chain. The idea is as follows. A conformational transition can occur spontaneously and isolated. Such a conformational change disturbs the bond length and also the angles. Therefore the probability that a neighboured segment will also undergo a conformational transition is enhanced. So a given conformational change seems to diffuses along the chain. Because only the probability for a conformational change is enhanced not every transition of one segment will lead to a transition of the neighboured one. Therefore the diffusion of conformational states along the chain is damped.

In an idealized model with conformational states "0" and "1" the probability $\tilde{P}$ that a segment marked by the coordinate x is in state "1" at the time t is modelled by

$$\frac{\partial \tilde{P}(x,t)}{\partial t} = -\frac{1}{\tau_0}\tilde{P}(x,t) + D_{\text{Con}}\frac{\partial^2 \tilde{P}(x,t)}{\partial x^2} \tag{7.15}$$

where τ_0 is a time constant describing that a conformational state disappears by direct coupling with the heat bath. D_{Con} is a formal diffusion coefficient of conformational states along the chain which can be calculated using the transition probabilities given by the RIS-model [12]. It can be written as $D_{\text{Con}} = \text{const}/\tau_1$. τ_1 is a further time constant for the diffusion of conformational states. By averaging over all coordinates the correlation function for segmental dynamics can be calculated as

$$\Phi_S(t) = \exp(-t/\tau_0)\exp(-t/\tau_1)I_0(t/\tau_1) \tag{7.16}$$

where I_0 is the Bessel function of 0-th order [34]. For short and long times power laws $\Phi_S(t) \sim t^{-0.5}$ (for $t \ll \tau_1$) and $\Phi_S(t) \sim t^{-1}$ (for $t \gg \tau_1$) hold respectively. The exponent 0.5 is characteristic for the diffusive character of the process.

The discussed model for the local chain dynamics (segmental dynamics) is in agreement with both experimental results (see for instance [30–33]) and computer simulations [34]. A more recent discussion about this model can be found in [35].

7.2.3.2
Chain Motion

The simplest model to describe the chain motion is the bead-spring model pioneered by Rouse [36] (Fig. 7.5). In this approach a macromolecule is modelled

Fig. 7.5. Schematic illustration of the Rouse model. A_i denotes the beads, k_B is Boltzmann's constant and f_i are the stochastic forces
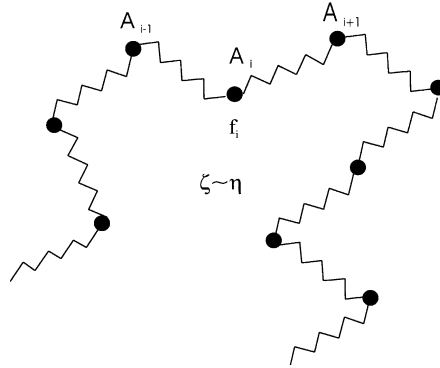
as a chain formed by beads connected by springs taking into account both connectivity and entropic forces. The stochastic motion of this system is considered in an environment characterized by a "solvent" viscosity η_S which can also be expressed by the friction coefficient per bead (monomeric friction coefficient ζ) [37].

The global motion of the chain described by the time correlation function Φ_{Ch} of the end-to-end vector r [7, 36, 37] is calculated to

$$\Phi_{Ch}(t) = \frac{\langle r(0)\,r(t)\rangle}{\langle r^2\rangle} = \frac{8}{\pi^2}\sum_{p=1}^{N}\frac{1}{p^2}\,\exp\left(-t/\tau_p\right) \tag{7.17}$$

where τ_p is the relaxation time of the mode p. The Rouse model (free draining model) gives

$$\tau_p = \frac{\zeta N^2 b^2}{3\pi^2 k_B T p^2},\quad p=1,\,3\,\dots \tag{7.18}$$

where N is the number of beads and b describes the average distance between the beads (Kuhns segment length [37]).

Zimm extended the Rouse model to include hydrodynamic interaction (nondraining model) [38]. The functional shape of $\Phi_{Ch}(t)$ (Eq. (7.17)) is maintained but the relaxation times have to be changed to

$$\tau_p = \frac{\pi^{3/2}\eta_S b^3 N^{3/2}}{12^{1/2} k_B T \lambda_p} \tag{7.19}$$

where λ_p is the p-th eigenvalue ($\lambda_1 = 4.04$, $\lambda_2 = 24.2$, $\lambda_3 = 53.5 \dots$ [38]) of the diagonalization matrix. For Type-A polymers the fluctuation of r leads to a fluctuation of the corresponding dipole moment (see Eq. 7.9b) and so the global chain dynamics can be detected by dielectric spectroscopy and is called in this case normal mode relaxation.

7.3
Dielectric Properties of Polymers in Solution

Compared to the high number of publications dealing with the dielectric behaviour of bulk polymeric systems dielectric data for solutions are rare. From a historical point of view one has to quote the basic work of Stockmayer [21] and of North [39]. Block [23] also reviews – besides other points – some aspects of dielectric properties of polymers in solution. For Type-B polymers the relaxation process due to the segmental motion is observed at frequencies above 1 MHz. One reason for the limited number of data may be that equipment to measure the dielectric properties at high frequencies routinely is available only for a short time. Time-domain reflectometry studies dealing with aqueous solutions and solutions of polyelectrolytes and biopolymers were presented by Mashimo [40].

7.3.1
Dilute Solutions

7.3.1.1
Segmental Motion

Dielectric relaxation spectroscopy can be used to verify the models discussed in Sect. 7.2.3.1 for segmental motions in isolated chains. Also other methods like NMR [41] or fluorescence depolarisation [42–44] have been applied to unravel the mechanism of segmental motion. Comparing different experimental methods one has to bear in mind that dielectric spectroscopy measures quantities related to the first Legendre polynomial Λ_1

$$\Phi_S(t) = \Lambda_1(t) = \langle \cos\theta(t) \rangle \tag{7.20}$$

whereas NMR or fluorescence depolarisation are sensitive to the second Legendre polynomial Λ_2

$$\Phi_S(t) = \Lambda_2(t) = \frac{3\langle \cos^2\theta(t) \rangle - 1}{2} \tag{7.21}$$

(see Chap. 1). cos $(\theta(t))$ is the projection of the dipole moment vector at time t on its direction at $t = 0$.

According to the RIS-model the dielectric relaxation properties should depend strongly on the barrier height for internal rotation as well as on the energy difference between rotational isomeric states. Based on Florys ideas [12] Bahar and Erman developed a time-dependent RIS theory [45]. The temperature dependence of the segmental relaxation time τ_S should be described by the Kramers theory [46] in the high friction limit which leads to [47]

$$\tau_S \sim \eta_S \exp\left[\frac{E_A}{k_B T}\right] \tag{7.22}$$

where η_S is the solvent viscosity and E_A is the barrier height.

Dielectric experiments on a variety of chain structures show [33, 48–53] that the measured barrier heights are in the range from 5 kJ mol^{-1} up to 20 kJ mol^{-1} where most values are around 8 to 10 kJ mol^{-1}. Because the barrier height for a rotation around a single carbon-carbon σ-bond is about 10.5 kJ mol^{-1} [53] these experimental results exclude the Shatzki crankshaft [25] as a mechanism for segmental dynamics.

The characteristic ratio C_∞ is a measure of chain stiffness which is according to the RIS model closely related to the barrier heights. Therefore a correlation should exist between the segmental relaxation time in dilute solution τ_S and C_∞. This is demonstrated by the inset of Fig 7.6 where τ_S is plotted vs C_∞. The relaxation time τ_S depends not only on the energy difference between rotational isomeric states but also on the shape and the bulkiness of the repeating unit. Moreover it is believed that the segmental dynamics is the elementary process which is responsible for the glass transition in polymeric systems. Therefore a correlation should also exist between τ_S in dilute solution and the glass transition temperature T_g of the bulk system. This was reported recently by Adachi [54]. Figure 7.6 shows this correlation for a variety of different chain structures.

Equation (7.22) predicts a proportionality between τ_S and η_S. This was confirmed by Mashimo [48]. Also the experiments using fluorescence depolarisation spectroscopy by Yamamoto et al. [44] gave the same result. In contrast Ediger and co-workers report $\tau_S \sim \eta_S^{0.74}$ [43].
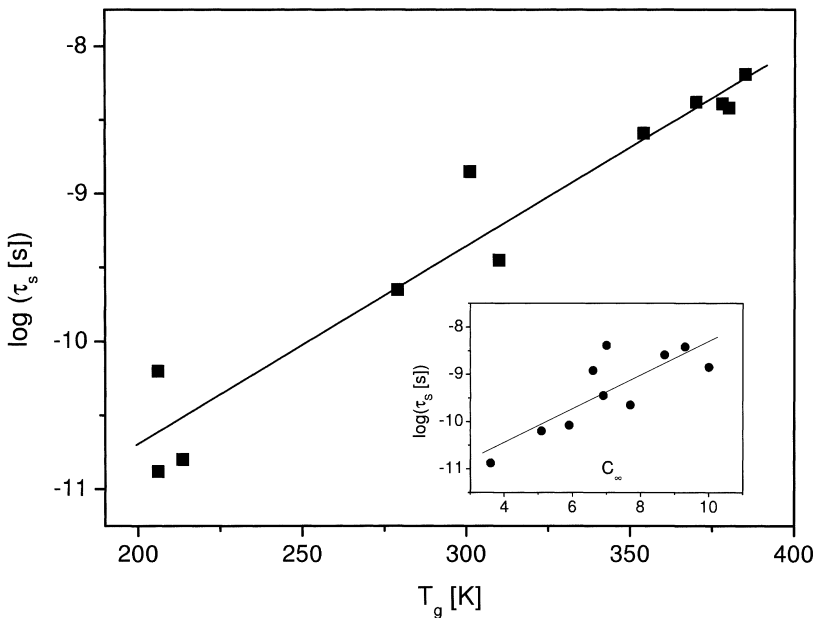

Fig. 7.6. Correlation of the segmental relaxation time τ_S in dilute solution and the glass transition temperature of the bulk system. The *inset* shows the segmental relaxation time τ_S vs the characteristic ratio C_∞. The *lines* are linear regressions through the points. The data were taken partly from [54] and represent different chain structures

7.3.1.2
Chain Motion

Dielectric experiments on dilute solutions of Type-A polymers like poly(*cis*-1,4-isoprene) or poly(*ε*-caprolactone) can be used to test the Rouse or the Zimm model (see Sect. 7.2.3.2). It can be shown that the mean relaxation time τ_n extracted from the position of maximal dielectric loss for the chain dynamics (normal mode relaxation) corresponds closely to the longest relaxation times τ_1 of the Rouse or Zimm theory [7]. Most experiments have been carried out on poly(*cis*-1,4-polyisoprene). Both good and θ-solvents have been used [7]. For the latter the data can be described by the Zimm theory [38] and $\tau_n \sim M^{1.5}$ holds approximately (see Eq. (7.19)). For thermodynamically good solvents a slightly stronger dependence of the relaxation time on molecular weight ($\sim M^{1.77}$) was found which can be explained by excluded volume effects leading to an expansion of the chain dimensions. It has been known for a long time that the excluded volume effect can be involved by rewriting Eqs. (7.18) and (7.19) in terms of the intrinsic viscosity $[\eta] = \lim\limits_{c \to 0} \dfrac{\eta - \eta_S}{c \, \eta_S}$ where η is the viscosity of the polymer solution and c its concentration. According to both the Rouse and the Zimm theory τ_n should scale according to

$$\tau_n = A \, \frac{\eta_S \, [\eta] \, M}{RT} \tag{7.23}$$

where A is constant. Equation (7.23) was fulfilled for a variety of polymer structures in different solvents as shown in Fig. 7.7. The data are taken from [54]. For A a value of 1.4 [54] was found which is larger than the values given by both the Rouse ($A = 1.22$) and the Zimm theory ($A = 0.85$).

7.3.2
Concentrated Solutions

7.3.2.1
Segmental Motion

The concentration dependence of the segmental motion is related to the glass transition in dense systems. This is supported by the correlation of the relaxation time for segmental motion in dilute solution and the glass transition temperature (see Fig. 7.6 and [54]). The dynamic glass transition or the dielectric α-relaxation will be discussed below (Sect. 7.4.1.2). Here it should only be mentioned that concepts which are used for the description of the dielectric α-relaxation like the free volume approach [55] are also applied to model the concentration dependence of the segmental motion [56, 57]. Furthermore the time-dependent RIS model [45] has been extended taking into account intermolecular interactions [58].

Recently Adachi and coworkers report measurements on concentrated solutions of poly(vinyl acetate) and poly(vinyl octanoate) [59, 60]. These measure-
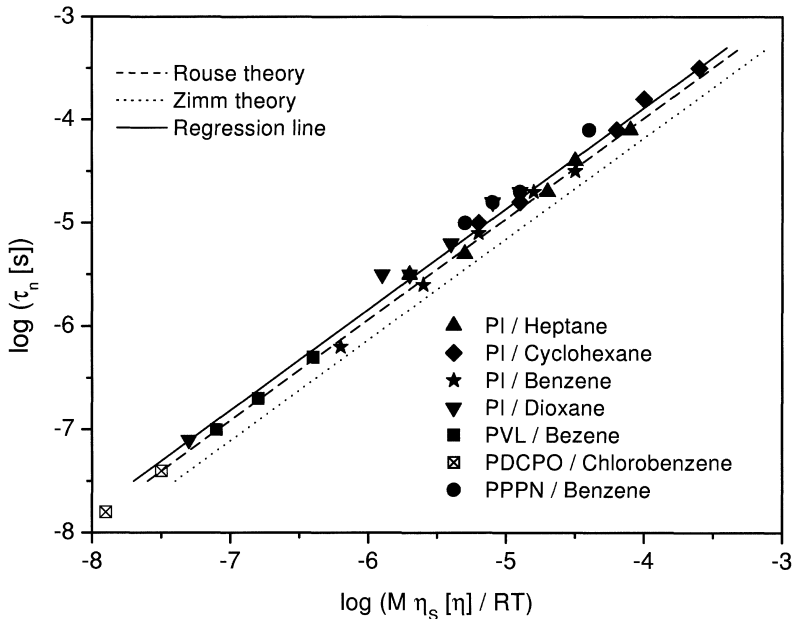
Fig. 7.7. Correlation of the relaxation time τ_n of the normal mode process vs $\dfrac{M\eta_s[\eta]}{RT}$ for different systems: PI – poly(*cis*-1,4-isoprene); PVL – poly(valerolacetone); PDCPO – poly(2,6-dichloro-1,4-phenyle oxide); PPPN – poly(phenoxy phosphazene). Data are taken from [54]

ments show that the segmental dynamics is influenced by local heterogeneities due to concentration fluctuations. The underlying theoretical approach will be discussed in greater detail in Sect. 7.4.3.2.

7.3.2.2
Chain Motion

In diluted polymer solutions the coils are isolated. The change from isolated coils to overlapping ones (semi dilute solutions) is often characterized by the overlapping concentration $C^* \sim \dfrac{3M}{4\pi\,N_A\langle r^2\rangle^{3/2}}$ where N_A is the Avogadro number [15]. For approximately $10 \cdot C^*$ the coils will penetrate each other (concentrated solution). Dielectric experiments on Type-A polymers [7, 61–67] agree with the concentration dependence of τ_n predicted by the Muthukumar/Freed theory [68] in the crossover regime between dilute and semi diluted solution and also with a scaling theory developed by de Gennes for semi diluted solutions [15, 69].

7.3.3
Rod-Like Systems

The relaxational behaviour of polymers with a stiff backbone in solution is different from that of flexible polymers because the energy barriers for segmental transitions are essentially higher. In many cases a suprastructure like a helix is formed which stabilizes additionally the rod-like shape of the whole macromolecule. Examples for such systems are poly(n-alkyl isocyanates), poly(γ-benzyl L-glutamate), polypeptides and also biological systems like DNA. It should be noted that these polymers are Type-A polymers because of the helical structure. So the correlation function of the end-to-end vector is measured. Dielectric investigations on such systems in dilute solutions are rare. Some results can be found for poly(n-alkyl isocyanates) [70–72], for poly(γ-benzyl L-glutamate)s [73] and for DNA [74].

In the limit of small molecular weights rotational fluctuations of the whole rod around its centre of mass should be the dominating motional process in dilute solution of stiff polymers. It was shown by Kirkwood and coworkers that the characteristic relaxation time τ_{Rod} scales with the cube of the rod length, i.e. $\tau_{Rod} \sim M^3$. Since the energy barriers for segmental transitions are not infinitely high some flexibility is maintained which leads to deviations from the rod-like shape. At high molecular weights (i.e., the chain length exceeds the persistence length)
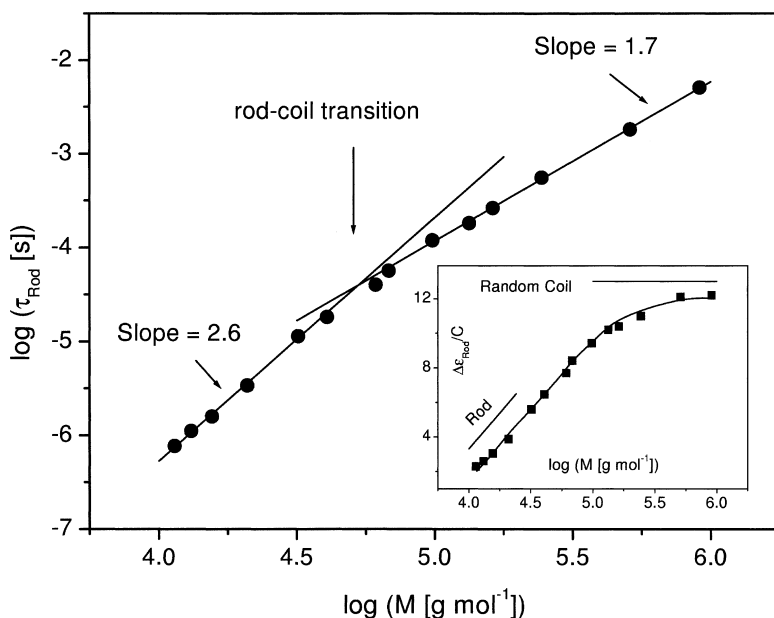

Fig. 7.8. Dependence of the relaxation time for global chain dynamics on molecular weight for poly(hexyl isocyanate) in toluene at 289 K. *Lines* are linear fits through the corresponding data points. The *inset* shows the dependence of the dielectric relaxation strength on molecular weight. The *line* is a guide for the eyes. The data were taken from [72]

the characteristic behaviour of a coil should be recovered. This so-called rod-coil-transition is demonstrated in Fig. 7.8 where both the relaxation time for overall chain dynamics τ_{Rod} and the corresponding dielectric relaxation strength $\Delta\varepsilon_{Rod}$ are plotted vs molecular weight for dilute solutions of poly(hexyl isocyanate) in toluene at 289 K. The data are taken from [72]. For low molecular weights $\tau_{Rod} \sim M^{2.6}$ holds where the exponent is in agreement with 3 predicted for a rod by Kirkwood et al. [75]. For higher molecular weights the exponent decreases to 1.7 which is close to the value given by the Zimm theory for a coil (see Eq. (7.19)). Also the dependence of $\Delta\varepsilon_{Rod}$ on M shows a transition from a behaviour characteristic for a rod to a constant value which corresponds to a coil.

If the concentration of the solution is increased the molecular dynamics of the molecules is increasingly restricted. Dielectric studies on such systems are rare. Some results for poly(n-alkyl isocyanates) can be found in [76–78]. For even higher concentration rod like polymers can form lyotropic liquid crystalline materials which can be also biphasic. A detailed discussion of such systems is beyond the scope of this chapter. For further information see [79].

7.4
Dielectric Properties of Polymeric Systems in the Bulk State

In the following section the essential properties of bulk polymer systems will be discussed from a fundamental point of view. This regards first of all amorphous and semicrystalline systems. Some features of polymer blends are discussed briefly. The dielectric properties of polymeric liquid crystals are discussed in detail in Chap. 10. At the end of this section the dielectric properties of polymers with novel architectures are summarized.

In general, for dense polymeric systems one has to bear in mind that the dynamics of segments or whole chains is not only influenced by intramolecular but also by intermolecular correlations. In order to calculate the mean square dipole moment (see Eq. (7.8)) or the corresponding correlation function one has to sum up over all chains in the system.

7.4.1
Amorphous Polymers

It is well known that most amorphous polymers exhibit a secondary- or β- and a principal- or α-relaxation located at lower frequencies or higher temperatures than the β-process. For type A polymers at frequencies below the α-relaxation a further process called α'- or normal mode relaxation can be observed which corresponds to the overall chain dynamics. As an example the dielectric loss for poly(propylene glycol) ($M = 2000$ g mol^{-1}) in the frequency range from 10^{-4} Hz to 10^9 Hz is given in Fig. 7.9. Two relaxation processes indicated by peaks in ε'' are visible. The process at higher frequencies is the α-relaxation which is related to the dynamic glass transition whereas the peak at lower frequencies corresponds to the normal mode process because poly(propylene glycol) is a Type-A polymer.
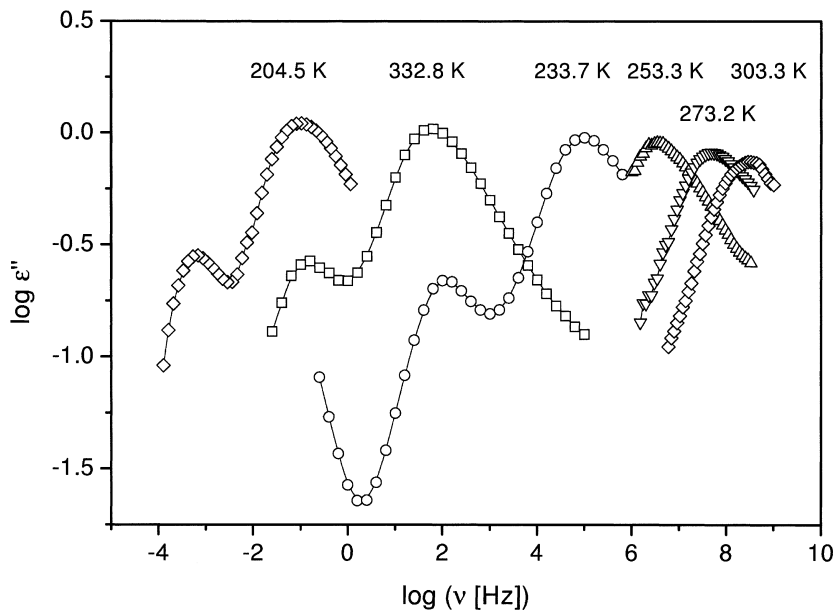
Fig. 7.9. Dielectric loss ε'' for poly(propylene glycol) ($M = 2000$ g mol^{-1}) vs logarithm of frequency at the labelled temperatures. *Lines* are guides for the eyes

In the following the characteristic and fundamental peculiarities of the β-, α- and the normal mode relaxation of amorphous polymers are discussed. Apart from these processes amorphous polymers can also exhibit further dielectrically active relaxation processes.

7.4.1.1
β-Relaxation

Most authors agree that the dielectric β-relaxation of amorphous polymers arises from localized rotational fluctuations of the dipole vector. For the first time Heijboer [80] developed a nomenclature for the molecular mechanisms which can be responsible for this process. According to this approach fluctuations of localized parts of the main chain, the rotational fluctuations of side groups or parts of them are discussed. Investigations on model systems (see for instance [81–84]) support this picture. Experiments on poly(*n*-alkyl methacrylate)s in dependence on the length of the alkyl side chain seem to favour this idea [84–88] as well. However, it has to be noted that the relaxation behaviour of the poly(*n*-alkyl methacrylate)s is quite unusual compared to other polymers. This concerns the relaxation strength which will be discussed later. Also a degeneration of the calorimetric glass transition with increasing length of the side chains [89] and indications for a nanophase separation [90] are observed.

Another approach to the β-relaxation was outlined by Goldstein and Johari [91, 92]. They argued that the β-relaxation is a generic feature of the glass tran-

sition and the amorphous state. Therefore such β-relaxation processes could be observed except from polymeric systems for a great variety of glass-forming materials like low molecular weight glass-forming liquids and rigid molecular glasses [92]. Also for polymers in which the dipoles are rigidly attached to the main chain [2] the dielectric β-relaxation was well known long before Johari and Goldstein observed it for low molecular weight systems. Recently the discussion of the β-relaxation is renewed because it is supposed that the investigation of this process can help to understand the nature of the dynamic glass transition (α-relaxation) which is an unsolved problem of condensed matter physics [93, 94] up to now. Some further discussions can be found in Sect. 7.4.1.3 and in Chaps. 4, 5 and 18 of this book. As a general conclusion one can state that the β-relaxation can be of intra- and/or intermolecular nature.

In the following some peculiarities of the β-relaxation in terms of its relaxation rate, its dielectric strength and the shape of the relaxation function will be discussed.

Relaxation rate. The temperature dependence of the relaxation rate $v_{p\beta}$ (or time) of the β-relaxation can be described in general by an Arrhenius law

$$v_{p\beta} = v_{\infty\beta} \exp\left[-\frac{E_A}{k_B T}\right] \tag{7.24}$$

where $v_{\infty\beta}$ is the preexponential factor. For localized motional processes $v_{\infty\beta}$ should be in the order of 10^{12} to 10^{13} Hz. The activation energy E_A depends on both the internal rotational barriers and the environment of a fluctuating unit. The influence of the molecular environment was also discussed in terms of matrix rigidity for acrylic polymers [95]. Typical values for E_A are 20 to 50 kJ mol^{-1}.

Dielectric strength. For most polymers of Type-B (a dipole moment is rigidly attached to the main chain) like polycarbonate [82], poly(vinyl chloride) [96, 97], poly(propylene glycol) [98] or poly(chloroprene) [96] for the relaxation strength of the β-relaxation $\Delta\varepsilon_\beta \ll \Delta\varepsilon_\alpha$ holds where $\Delta\varepsilon_\alpha$ is the dielectric strength of the α-process. This is also true for semi-rigid polymer structures like poly(ethylene terephthalate) [99, 100] or poly(ethylene-2,6-naphthalene dicarboxylate) [101] which can crystallize. For some polymers containing flexible side groups like poly(methyl acrylate) [102] or higher poly(n-alkyl acrylate)s [103] $\Delta\varepsilon_\beta \leq \Delta\varepsilon_\alpha$ is observed. Exceptions are poly(n-alkyl methacrylate)s for which $\Delta\varepsilon_\beta > \Delta\varepsilon_\alpha$ is measured [2, 87, 104, 105]. The reason for this behaviour is unclear up to now. Because the main dipole moment is located in the side group only small fluctuations of it can contribute significantly to the dielectric loss. However, there is some evidence from NMR-measurements that the motion of the main and the side chain are coupled [106]. A recent discussion on the relaxational properties of the poly(n-alkyl methacrylate)s can be found elsewhere [107].

Generally $\Delta\varepsilon_\beta$ increases with temperature. According to the Onsager/Kirkwood/Fröhlich theory (see Chap. 1) which predicts

$$\Delta\varepsilon \sim F_{\text{Onsager}} \, g \, \frac{\mu^2}{k_B T} \frac{N_p}{V} \tag{7.25}$$

($F_{\mathrm{Onsager}} \approx 1$, internal field or Onsager factor) this can be understood assuming that either the number of contributing dipoles N_P or the angular extension of the fluctuations increases with temperature. The suggestion that the Kirkwood/ Fröhlich correlation factor $g = g_{\mathrm{intra}} + g_{\mathrm{inter}}$ (for bulk polymers g is the sum of intra- and intermolecular contributions[6]) increases with temperature is unlikely for the β-relaxation because a reorientation of larger parts of the molecular dipole vector, which is necessary for a change of g, does not seem to be possible at least below T_g.

Shape of the relaxation function. Generally the width of the relaxation function measured for instance by the half height width of the loss peak is broad (4–6 decades) but mostly symmetric. With increasing temperature the width of the β-peak decreases. It is often assumed that the shape of the relaxation function for the β-relaxation is due to a distribution of both the activation energy and the preexponential factor, related to a distribution of molecular environments of the relaxing dipole. It is difficult to extract information on the basic mechanisms of motion from such broad peaks.

7.4.1.2
Dynamic Glass Transition (α-Relaxation)

The understanding of the α-process or the dynamic glass transition which is related to the calorimetric glass transition is an actual problem of condensed matter physics [93, 94]. If a glass-forming system is supercooled the time scale of the relevant motional processes increases by more than twelve decades. Near the calorimetric glass transition temperature T_g its magnitude is greater than 1 s (see Chap. 4 for a deeper discussion). Most workers agree that for polymers the glass transition corresponds to the segmental motion. Conformational changes like gauche-trans transitions (see Sect. 7.2.3.1) lead to rotational fluctuations of a dipole around the chain to which it is perpendicular (rigidly) attached. This is supported by a correlation of the dielectric segmental relaxation time in dilute solution with T_g [54] (see Fig. 7.6). Therefore models developed for the segmental motion in isolated chains (see Sect. 7.2.3.1) should be applied also in the dense state. However for bulk polymers a test segment fluctuates in a dense environment of surrounding segments of other chains. Hence besides the intramolecular cooperativity (see Sects. 7.2.3.1 and 7.3.1.1) an intermolecular one is introduced. As for the β-relaxation the α-relaxation is discussed in terms of its relaxation rate, its dielectric strength and the shape of the relaxation function.

Relaxation rate. The temperature dependence of the relaxation rate of the α-relaxation $v_{p\alpha}$ cannot be parameterized by an Arrhenius law. Close to the glass transition temperature it can be described by the Vogel/Fulcher/Tammann/

---

[6] It should be noted that Williams generalized the Onsager/Kirkwood/Fröhlich theory by considering intra and intermolecular terms in the g-factor for the first time [2].

Hesse (VFT) [108–110] equation

$$\log v_{p\alpha} = \log v_{\infty\alpha} - \frac{A}{T - T_0} \tag{7.26}$$

where $\log v_{\alpha\infty}$ ($v_{\alpha\infty} \approx 10^{10}$–$10^{12}$ Hz) and A are constants. T_0 is the so-called ideal glass transition or Vogel temperature which is found to be 30–70 K below T_g. Empirically it was shown that the glass transition temperature corresponds to relaxation rates of 10^{-3} to 10^{-2} Hz. Therefore a dielectric glass transition temperature T_g^{Diel} can be defined by $T_g^{\text{Diel}} = T(v_{p\alpha} \approx 10^{-3}\ldots10^{-2}$ Hz).

Formally an apparent, temperature dependent activation energy can be calculated from Eq. (7.26). However, near the glass transition this apparent activation energy is much greater than the binding energy for a C-C σ-bond. That may reflect the cooperativity of the underlying molecular motions. Several models have been proposed to understand the physical origin of the VFT equation and of T_0 (For detailed discussion see Chaps. 4 and 5). In the free volume approach of Cohen and Turnbull [111] the fractional free volume becomes zero at T_0. Adam and Gibbs [112] were the first who treated the α-relaxation as a cooperative process. This cooperativity sets in well above T_g and increases with decreasing temperature. In this kinetic approach [112] and in the later fluctuation model of Donth [113, 114] the volume of the cooperatively rearranging region (CRR), defined as the smallest volume element that can relax to a new configuration independently, diverges at $T = T_0$. The lattice theory of the glass transition developed by DiMarzio [115] predicts a second-order phase transition at T_0 which is believed to overcome the Kauzman paradox [116, 117]. Although the meaning of T_0 is not yet clear the universality of the VFT equation near T_g suggests that T_0 is a significant temperature for the dynamics of the glass transition.

An analogous representation for the temperature dependence of the relaxation rate of the α-relaxation is the Williams/Landel/Ferry (WLF) relation [37]

$$\log \frac{v_{p\alpha}(T)}{v_{p\alpha}(T_{\text{Ref}})} = -\frac{C_1(T - T_{\text{Ref}})}{C_2 + T - T_{\text{Ref}}} \tag{7.27}$$

where T_{Ref} is a reference temperature and $v_{p\alpha}(T_{\text{Ref}})$ is the relaxation rate at this temperature. C_1 and $C_2 = T_{\text{Ref}} - T_0$ are so called WLF-parameters. It has been argued that these parameters should have universal material independent values if $T_{\text{Ref}} = T_g$ is chosen [37]. However it was found experimentally that these estimates are only rough approximations. Equations (7.26) and (7.27) are mathematically equivalent.

Figure 7.10 shows a fit of Eq. (7.26) to the data of poly(vinyl acetate) (PVAC), poly(propylene glycol) (PPG) and poly(dimethyl siloxane) (PDMS). At temperatures close to T_g the data can be well described by the VFT-equation. For significantly higher temperatures ($T = T_g + 80 \ldots 100$ K) deviations are observed. These deviations are more pronounced for PDMS which is known as a more fragile glass forming system than PPG. (For a recent discussion of the fragility concept to the glass transition see [117] or Chap. 4). With a derivative technique discussed in Chap. 4 it could be shown that the high temperature data can be approximated by a second VFT-law with a higher T_0 even for PPG [118]. A charac-
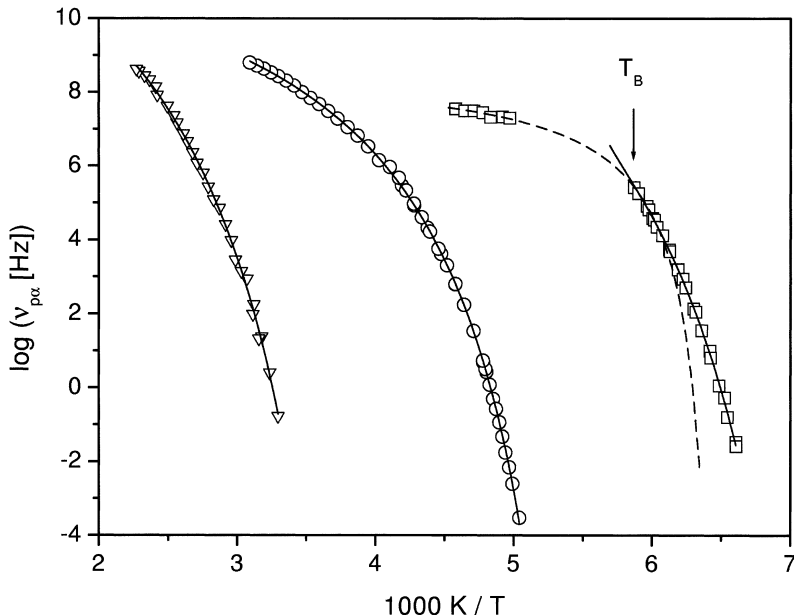
Fig. 7.10. Relaxation rates $\nu_{p\alpha}$ for the α-relaxation of PDMS (*open squares*), PPG (*open circles*) and PVAC (*inverted open triangles*). *Lines* are fits of Eq. (7.26) to the data. The *dashed line* is a fit of Eq. (7.26) to the high temperature data of PDMS

teristic crossover temperature T_B can be defined by the intersection of the two VFT-laws where $T_B \approx 1.2 \dots 1.3 \times T_g$ holds (see Chap. 4). With regard to the temperature dependence of the relaxation rate of the α-relaxation there is no essential difference between polymers and low molecular glass forming liquids [119]. This indicates that the (essential) underlying phenomena responsible for the dynamic glass transition must be the same for both classes of materials.

Dielectric strength. The dielectric relaxation strength of the α-relaxation $\Delta\varepsilon_\alpha$ decreases with increasing temperature. This is shown in Fig. 7.11 where $\Delta\varepsilon_\alpha$ for poly(propylene glycol) is plotted vs temperature. However, Fig. 7.11 indicates further that the temperature dependence of $\Delta\varepsilon_\alpha$ is much stronger than predicted by the Onsager/Kirkwood/Fröhlich theory (see Eq. 7.25 and inset of Fig. 7.11). Close to T_g the increase of $\Delta\varepsilon_\alpha$ with decreasing temperature is pronounced.

This also becomes clear from Fig. 7.12 where the product $T\Delta\varepsilon_\alpha$ (normalized to the maximal value) is plotted vs T for several polymers. According to Eq. (7.25) $T\Delta\varepsilon_\alpha$ should be independent of temperature but obviously it decreases with increasing temperature. The stronger temperature dependence of $\Delta\varepsilon_\alpha$ than predicted by Eq. (7.25) (see also [120–122]) cannot be explained by the increase of the density with decreasing temperature. Also its modelling by a temperature dependent g-factor remains formal because g was introduced to describe direct correlations between dipoles like association (see Chap. 1). Because apart from polymers similar temperature dependencies of $\Delta\varepsilon_\alpha$ are also found for low
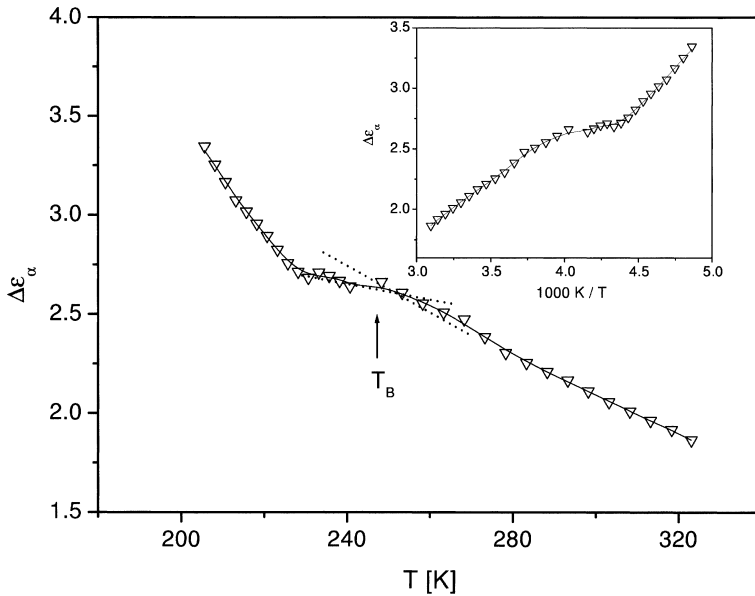
Fig. 7.11. Temperature dependence of $\Delta\varepsilon_\alpha$ for poly(propylene glycol). The *inset* shows $\Delta\varepsilon_\alpha$ vs $1/T$ for PPG as well. The data were taken from [98]. *Lines* are guides for the eyes
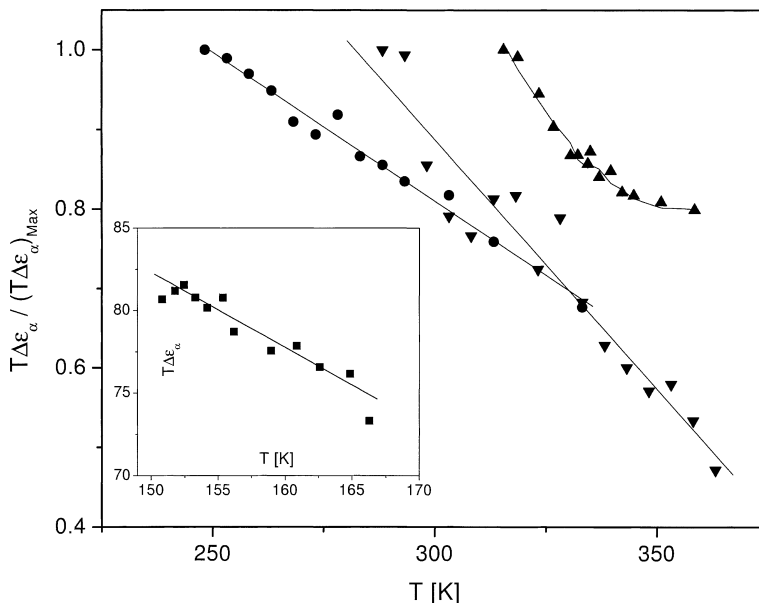

Fig. 7.12. Values of $(T\Delta\varepsilon_\alpha)$ reduced by the value $(T\Delta\varepsilon_\alpha)_{max}$ at the lowest measured temperature vs temperature: *filled triangles* – poly(vinyl acetate). The data were taken from Mashimo and Nozaki [121]. *Inverted filled triangles* – poly(methyl acrylate), *filled circles* – poly(vinyl isobutylether). The data were taken from A. Hoffmann (1993), PhD thesis, University Mainz. The *inset* shows data for poly(dimethyl siloxane). *Lines* are guides for the eyes

molecular weight glass forming systems (see [119, 123] and Chap. 4) it must be considered as a general feature of the α-relaxation. It can be argued that this temperature dependence results from an increasing influence of (intermolecular) cross-correlation terms to μ^2 with decreasing temperatures. In other words the reorientation of a test dipole is influenced increasingly by its environment with decreasing temperature. In the framework of the cooperativity concept to the α-relaxation $\Delta\varepsilon_\alpha$ should be related to an effective dipole moment μ_{eff} which is due to the CRR. With decreasing temperature the size of the CRR and therefore μ_{eff} increases. For a detailed discussion see Chap. 4 or [123].

Shape of the relaxation function. In general the α-process shows in the frequency domain a broad (the width ranges from 2 up to 6 decades depending on structure) and asymmetric peak. It is well known (see Chap. 1) that the functional shape of the relaxation function can be well described by the model function of Havriliak/Negami [124]

$$\varepsilon_{HN}^*(\omega) = \varepsilon_\infty + \frac{\Delta\varepsilon}{(1 + (i\omega\tau_{HN})^\beta)^\gamma} \tag{7.28}$$

where τ_{HN} is a characteristic relaxation time. The fractional shape parameters β and γ ($0 < \beta, \beta\gamma \leq 1$) due to the symmetric and asymmetric broadening of the complex dielectric function are related to the behaviour of $\varepsilon''(\omega)$ at low and high frequencies:

$$\varepsilon'' \sim \omega^m \quad \text{for} \quad \omega \ll 1/\tau_{HN} \qquad \text{with} \quad m = \beta \tag{7.29a}$$

$$\varepsilon'' \sim \omega^{-n} \quad \text{for} \quad \omega \ll 1/\tau_{HN} \qquad \text{with} \quad n = \beta\gamma \tag{7.29b}$$

This nomenclature was first introduced by Jonscher [125]. Generally it is assumed that in contradiction to the β-process the shape of the relaxation function of the dynamic glass transition is not related to a distribution of relaxation times due to local spatial heterogeneities (see Chap. 14). Rather this broad, asymmetric loss peak is an intrinsic feature of the dynamics of glass-forming systems. Recently the picture of dynamical heterogeneity introduced by Schmidt-Rohr and Spiess for polymers has been reviewed for low molecular weight glass forming systems [126] and also for polymers [127]. The spatial extent of this dynamical heterogeneity, its temperature dependence and the relationship to the cooperativity approach to the glass transition is subject of controversial debate. However using the concept of dynamical heterogeneity a characteristic length scale for the glass transition in the range of a few nm can be expected for poly (vinyl acetate) [128, 129].

The width of the α-peak for polymers depends on various factors such as temperature, structure of the chain or crosslinking density. It becomes narrower with increasing temperature and broadens dramatically with crosslinking.

The parameters m and n are plotted in Fig. 7.13 for a considerable number of polymers and for several low molecular weight glass-forming liquids. For polymers n is found to be between $n = 0$ and $n = 0.5$. This behaviour is quite differ-

ent compared to low molecular weight materials where (depending on temperature) $n = 1$ (Debye relaxation) can be observed [119].

For low molecular weight systems the elementary type of motion are rotational fluctuations of a rigid dipole (see Chap. 1, rotational diffusion model). For polymers the elementary type of motion is the local chain dynamics discussed in Sect. 7.2.3.1. This is supported by the correlation of the glass transition temperature with the relaxation time for segmental chain dynamics in dilute solution (see Fig. 7.6). However, in contrast to isolated chains in undiluted systems the local chain dynamics is influenced by the environment of the segments. That modifies the mechanism of damped diffusion of conformational states (see Sect. 7.2.3.1) to hindered one. In analogy to Eq. (7.15) one can write [130]

$$\frac{\partial \tilde{P}(x,t)}{\partial t} = -\frac{1}{\tau_0} \tilde{P}(x,t) + \int_0^t \dot{D}_{\mathrm{Con}}(t-\tau) \frac{\partial^2 \tilde{P}(x,\tau)}{\partial x^2} \, d\tau \tag{7.30}$$

where $\dot{D}_{\mathrm{Con}} = \dfrac{\partial D_{\mathrm{Con}}(t)}{\partial t}$. Equation (7.30) is a generalized master equation which gives the wave equation for $\dot{D}(t) = $ const and the diffusion equation for $\dot{D}(t) = D_0 \delta(t)$ ($\delta(t)$ – Dirac function). To model the segmental dynamics in the bulk state (hindered damped diffusion of conformational states) $\dot{D}(t) \sim D_0 t^{-\lambda}$ ($-1 \leq \lambda \leq 1$) is chosen for several reasons which are discussed in detail in [123]. The important point is that the diffusion in inhomogeneous media can be described by a power law with $-1 \leq \lambda \leq 0$ [131, 132]. With this ansatz the correlation function for the segmental dynamics in the bulk state can be calculated for a static environment of a test segment [130]. Moreover one has to consider that the molecular environment of a selected segment also fluctuates. Because a greater length scale is involved this motional process takes place on a longer time scale. To incorporate these fluctuations of environment a treatment similar to that developed by Dissado and Hill [133] is used [130]. For the dielectric loss functional dependencies according to Eq. (7.29) are obtained where the exponent $n = \dfrac{1+\lambda}{2}$ ($-1 \leq \lambda \leq 0$) is related to the modified segmental dynamics and the parameter m ($0 < m \leq 1$) to the fluctuations of the environment of a segment taking place on a larger length scale than the segmental dynamics. An appropriate interpretation scheme for the shape of the dielectric α-relaxation is given in Fig. 7.14.

The model is supported by Fig. 7.13 where for the parameter n $0 < n \leq 0.5$ holds for polymers. A much greater compilation of data also supporting this fact as well is given in [134]. In Fig. 7.15a the shape parameters n and m for poly(propylene glycol) are compared to that of the monomeric counterpart propylene glycol. The data are plotted vs log $v_{p\alpha}$ to compare the data with respect to their different glass transition temperatures. For propylene glycol n increases with temperature close to unity but for the polymer poly(propylene glycol) n is restricted to values below 0.5.

In general the parameter n should depend on temperature. For temperatures close to the glass transition temperature the chains are more densely packed and therefore the hindrance of the segmental dynamics is stronger than for higher
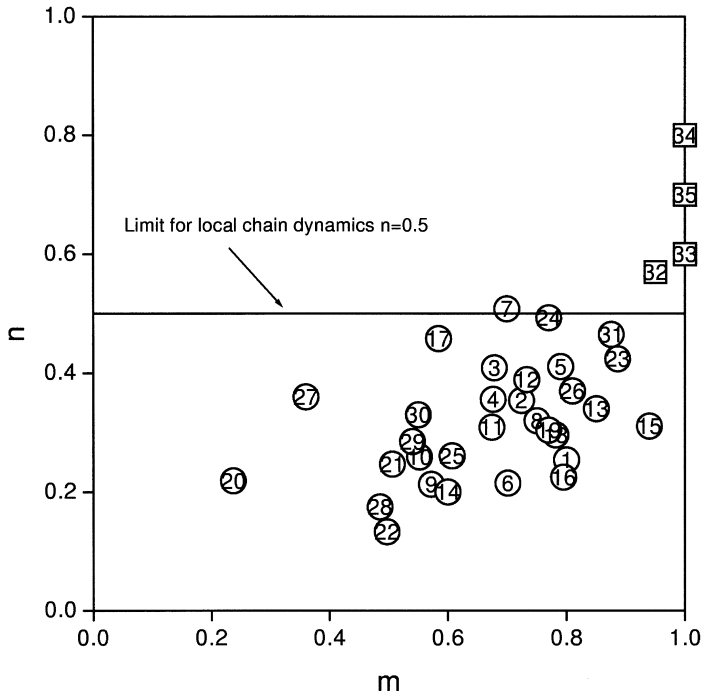
Fig. 7.13. Shape parameter *n* and *m* for different polymers (*open circles*) and low molecular weight glass-forming systems (*open squares*). The *line* is the limit for local chain dynamics. (The relationship of the points to the numbers is given in the Appendix)

temperatures where the amount of free volume is greater. For $T \gg T_g$ n should approach the value $n = 0.5$. This is shown in Fig. 7.15b where the shape parameters m and n are plotted vs $\log v_{p\alpha}$ for poly(vinyl acetate) and poly(chloro styrene). The parameter n increases with $\log v_{p\alpha}$ (and therefore with temperature) up to $n = 0.5$ as a limiting value. Some similar results are presented for instance for poly(n-butyl acrylate) by Fioretto et al. [135].

According to the considerations presented above the low frequency shape parameter m should vary with the intermolecular interactions. With increasing temperature these intermolecular interactions should decrease in strength and therefore m should increase. This statement is justified by Fig. 7.15 where m increases with $\log v_{p\alpha}$ and approaches $m \approx 1$ at high temperatures for poly(propylene glycol) (Fig. 7.15a), poly(vinyl acetate) and poly(chloro styrene) (Fig. 7.15b). For poly(n-butyl acrylate) a similar behaviour is observed [135].

The relationship between the shape parameter m and motional modes on a larger length scale can be tested by a direct modification of these modes in a chemical or physical way. This can be done for instance by crystallization. Figure 7.16a gives the reduced dielectric loss for amorphous and semicrystalline polycarbonate according to [136]. The high frequency behaviour of the loss peak is not changed whereas the low frequency part is dramatically broadened by the
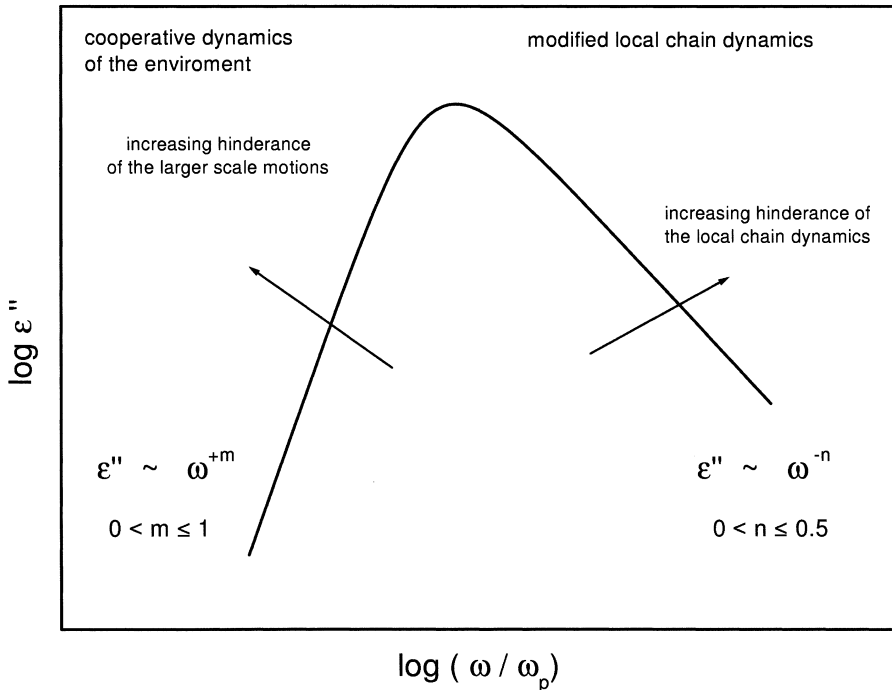
Fig. 7.14. Interpretation scheme for the shape of the dielectric α-relaxation

crystallization. Similar results were obtained for poly(ethylene terephthalate) [137].

Besides crystallization motional modes on a greater length scale can be also influenced by crosslinking. Figure 7.16b shows the dependence of the shape parameters m and n on crosslinking for a styrene-butyl acrylate copolymer crosslinked with divinyl benzene [138]. With increasing degree of crosslinking the parameter m decreases strongly whereas the parameter n related to the local chain dynamic remains unchanged.

In the same sense the model was used to interpret the dielectric behaviour of polyurethane network systems [139]. It was further applied to discuss the dynamic glass transition of semi crystalline polymers [140–142].

7.4.1.3
Relationship Between the β- and the α-Relaxation – the $(\alpha\beta)$-Process

Because $\log \nu_{p\alpha}$ increases more rapidly with increasing temperature than $\log \nu_{p\beta}$ the α- and the β-processes merge at higher temperatures and form the so called $(\alpha\beta)$- or α-process. In a very recent publication on the glass transition [143] this process was named the Williams-process because it was first discussed by Williams et al. [144] as a separate process. In other words with decreasing tem-
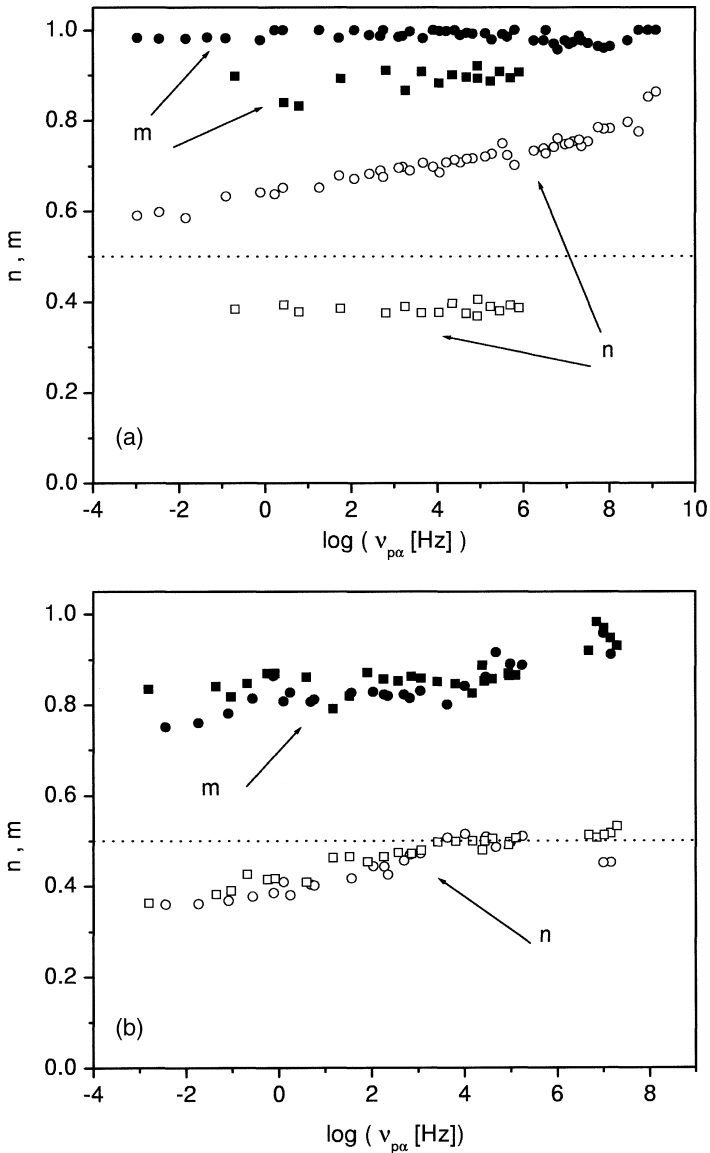
Fig. 7.15. a Shape parameter *m* and *n* vs log $\nu_{p,\alpha}$ for propylene glycol (*filled circles, open circles*) and the polymeric counterpart poly(propylene glycol) (*filled squares, open squares*). **b** Shape parameter *m* and *n* vs log $\nu_{p,\alpha}$ for poly(vinyl acetate) (*filled squares, open squares*) and for poly(chloro styrene) (*filled circles, open circles*)
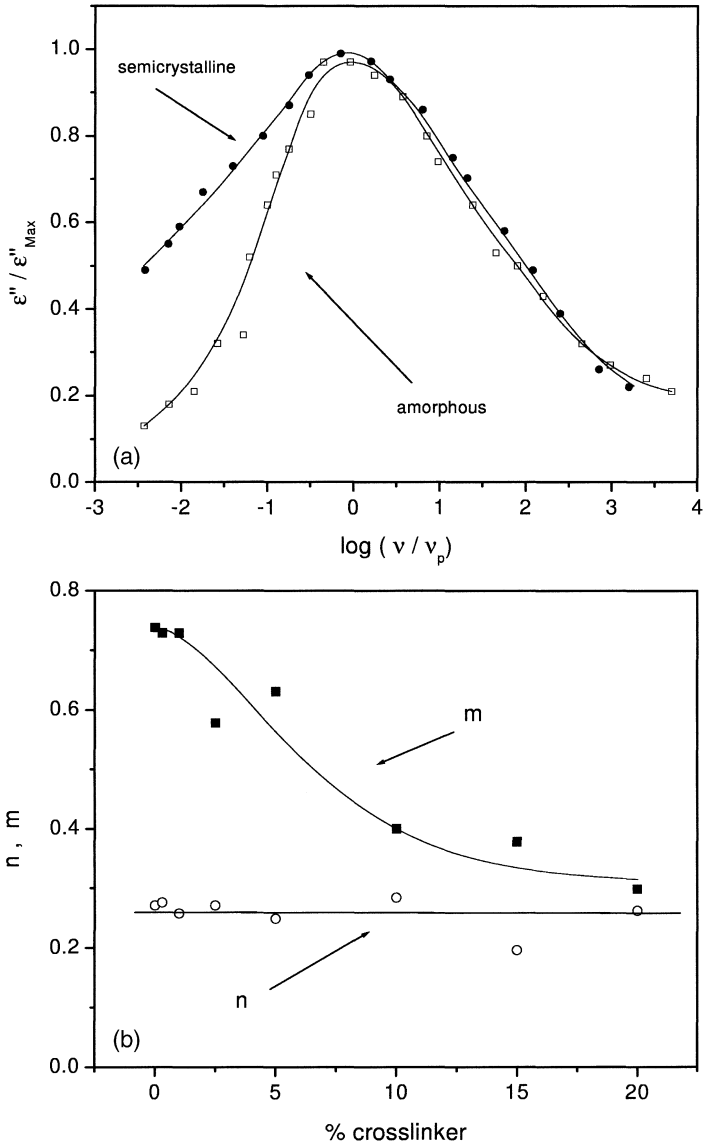
Fig. 7.16. a Normalized dielectric loss for amorphous (*open squares*) and semicrystalline (*filled circles*) polycarbonate [136]. **b** Shape parameter *m* (*filled squares*) and *n* (*open circles*) for a styrene-butyl acrylate copolymer crosslinked with divinyl benzene vs the concentration of divinyl benzene [138]

peratures the α- and the β-process will separate from each other in a certain temperature region called splitting region S according to Donth and coworkers [87, 143, 145, 146]). Figure 7.17 gives three different scenarios for this separation:

1. Goldstein and Johari suggested the merging of the α- and β-relaxation at high temperatures whereas $\log \nu_{p(\alpha\beta)}$ should have an Arrhenius-like temperature dependence with the same activation energy as the low temperature β-process (Fig 7.17a). There are experiments which support this picture [91, 92], but recent dielectric investigations have shown that $\log \nu_{p(\alpha\beta)}$ cannot be described by an Arrhenius law in general (see Chap. 4 for a detailed discussion) even at very high temperatures compared to T_g.
2. From a theoretical approach to the glass transition [143] a separate onset of the α-relaxation (Fig. 7.17b) is predicted and found for poly(n-butyl methacrylate) [146] and other poly(n-alkyl methacrylate)s [87]. Also for a series of poly(n-butyl methacrylate-$stat$-styrene) with varying composition such a separate onset of the dynamic glass transition was found [147]. It is characterized by a (splitting) temperature T_S for which the extrapolated temperature dependence $\Delta\varepsilon_\alpha$ vanishes, i.e. $\Delta\varepsilon_\alpha(T_S) \approx 0$. Thermal heat spectroscopy also shows that the relaxational part of the heat capacity for the glass transition $\Delta c_{p\alpha}$ vanishes for $T = T_S$ [145]. At present it is still an open question if this behaviour is characteristic for polymers with bulky side chains. However, recently a similar behaviour for a low molecular weight model compound was observed [83]. Also for a mixture of water with an oligomeric poly(ethylene glycol) a separate onset of the α-relaxation with $\Delta\varepsilon_\alpha(T_S) \approx 0$ has been reported recently [148].
3. A scheme according to Fig. 7.17c is expected if the high temperature α-relaxation (or a-process) in a certain temperature range is a precondition for the β-process. This scenario is found for many materials including low molecular weight glass forming liquids and amorphous polymers [83, 98, 149–153]. It should be noted that again the splitting temperature T_S coincides with the temperature T_B where the temperature dependence of the relaxation rate of the α-relaxation changes [98, 119] (see Fig. 7.11). Moreover the temperature dependence of the dielectric strength shows a change (see Chap. 4 and [119]) at this temperature as well. Therefore besides the Vogel temperature T_0 T_B should be regarded as a characteristic temperature for the dynamic glass transition. It should be further noted that in the same temperature range a decoupling of rotational and translatorial diffusion (see for instance [154–157]) is observed.

7.4.1.4
Normal Mode Relaxation

For melts of Type-A polymers the normal mode process can be observed as a separate relaxation region at frequencies below the α-process (Fig. 7.9). Because the overall chain dynamics is reflected by this process its properties depend strongly on molecular weight, i.e. chain dimensions. Figure 7.18 shows the di-

Fig. 7.17. Three different scenarios for the separation of the α- and β-relaxation: **a** merging of the α- and β-relaxation where the $(\alpha\beta)$-process has the same activation energy as the low temperature β-relaxation; **b** separate onset of the α-relaxation according to [146]; **c** separation of the α- and β-relaxation where the high temperature process is regarded as a precondition for the β-process
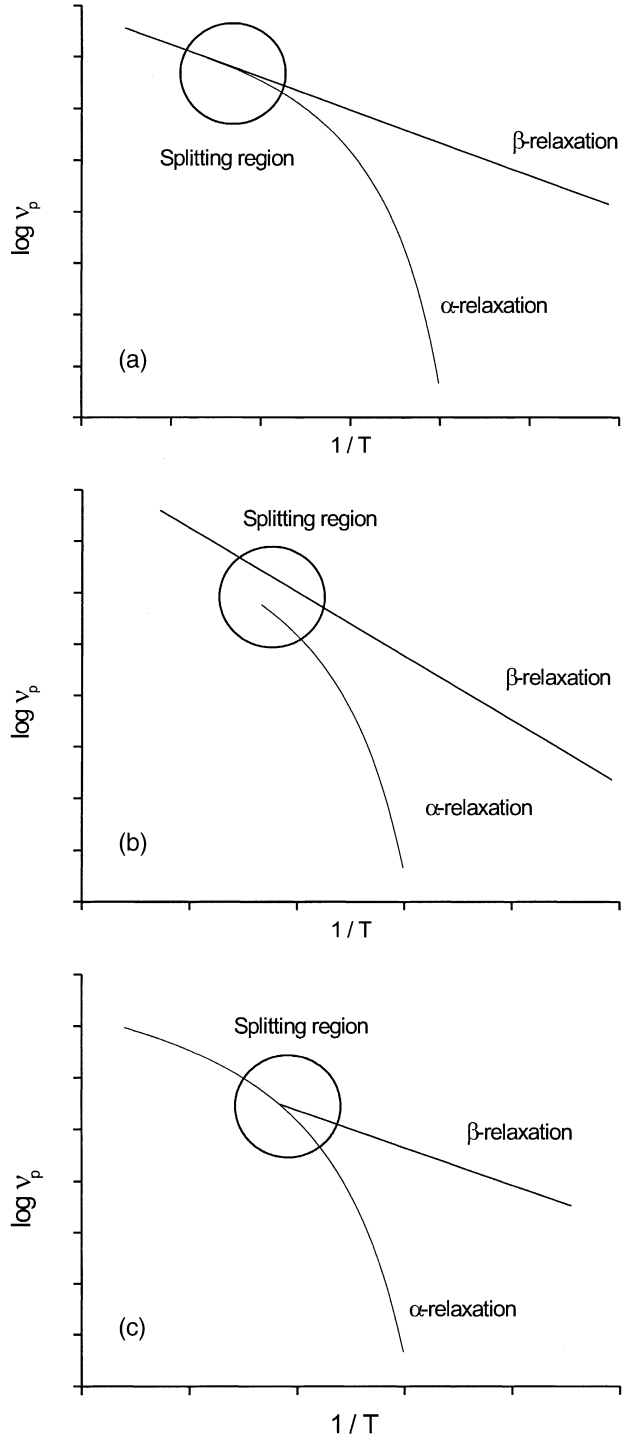
electric loss vs temperature at a fixed frequency for poly(cis-1,4-isoprene) of different molecular weights. The low temperature (high frequency) α-relaxation shows only a weak dependence on M whereas the high temperature peak, caused by the normal mode process depends strongly on the molecular weight. The theory outlined in Sect. 7.2.3.2 (Eq. (7.17)) remains valid to describe the normal mode relaxation also for the undiluted melt.

Relaxation rate. The global chain dynamics in undiluted melts depends strongly on molecular weight. For $M < M_C$ ($M_C \approx 10^4$ g mol^{-1}, depending on structure [37]) τ_p can be calculated in the framework of the Rouse theory [7, 36] because the excluded volume effects and hydrodynamic interactions are screened out [15]. Therefore Eq. (7.18) remains valid for τ_p where the monomeric friction coefficient is related to the viscosity of the melt. For $M > M_C$ the polymeric chains are entangled [15, 37]. Due to topological constraints the dynamical behaviour of the chains is restricted compared to the disentangled state. The functional shape of Eq. (7.17) is maintained but the expression for the relaxation times is changed to

$$\tau_p = \frac{\zeta N^3 b^4}{\pi^2 k_B T a^2 p^2} \tag{7.31}$$

Equation (7.31) is calculated in the framework of the reptation or tube model [15, 159] where it is assumed that a test chain is confined within a tube with a diameter a formed by neighboured chains.

Because of the factor $1/p^2$ in Eq. (7.17) it becomes clear that only the modes with $p = 1$ and 3 contribute significantly to the dielectric response. Therefore the relaxation time extracted from the maximum position of the dielectric loss $\tau_n = 1/(2\pi \nu_{pn})$ for the normal mode process corresponds approximately to the mode with $p = 1$. Figure 7.19 shows τ_n at a fixed temperature for poly(cis-1,4-isoprene) vs M. The data were taken from different authors. For low molecular weights ($M < M_C$) a Rouse-behaviour $\tau_n \sim M^2$ is fulfilled. At $M_C \approx 10^4$ g mol^{-1} a change to a stronger dependence on the molecular weight is observed. The linear regression to the data points gives a slope of 4.1 (Fig. 7.19). This value is larger than predicted by the reptation model which gives $\tau_n \sim M^3$ (see Eq. (7.31)). Mechanical experiments [163] give a value of 3.4 (see also Chap. 17). The difference between 3 and 3.4 can be understood in the frame of the theory of contour length fluctuation [164] or of the constrain-release-model [165, 166]. It is not clear if these models can be applied to explain dielectric experiments and so the value of approximately 4 is not well understood yet.

The inset of Fig. 7.19 gives ν_{pn} for oligomeric ($M < M_C$) poly(propylene glycol) as a function of molecular weight at $T = 222$ K. The estimated slope of 2.5 is slightly larger than given by the Rouse theory but may be caused by hydrogen bonding which can lead to transient entanglements.

To check the statement that the normal mode process is due to the overall chain dynamics the following consideration can be made. In the Rouse theory the self-diffusion coefficient D of a chain is related to the 0-th Rouse mode
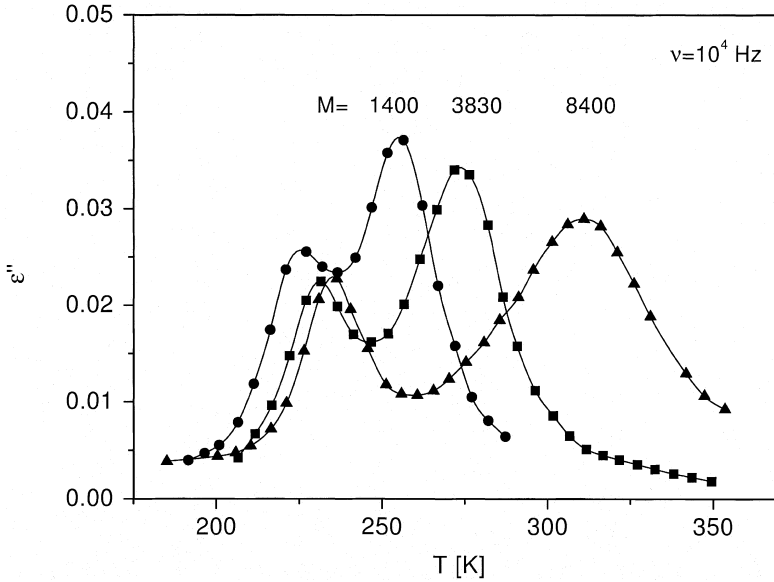
$$D = \frac{k_B T}{\zeta N} \tag{7.32}$$

Fig. 7.18. Dielectric loss vs temperature at a frequency of 10^4 Hz for poly(*cis*-1,4-isoprene) of different molecular weights: *filled circles* – $M = 1400$ g mol^{-1}, *filled squares* – $M = 3830$ g mol^{-1}, *filled triangles* – $M = 8400$ g mol^{-1}. The figure was adapted from [158]
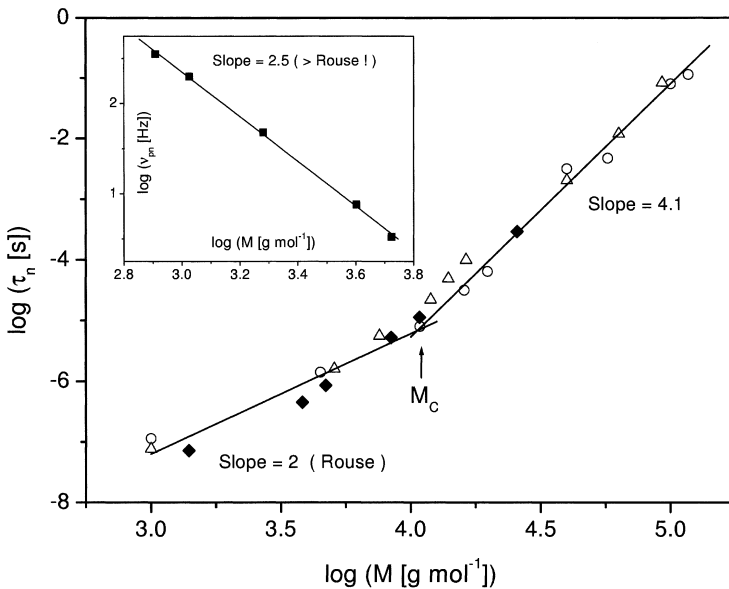

Fig. 7.19. Relaxation time τ_n of the normal mode process for poly(*cis*-1,4-polyisprene) at $T = 320$ K as a function of *M*: *open circles* – values taken from [160], *open triangles* – values taken from [161], *filled diamonds* – own measurements [162]. The *inset* gives ν_{pn} for poly(propylene glycol) vs molecular weight at $T = 222$ K [162]. The *lines* are linear regression through the data points in the corresponding regions

For the product $\tau_p D$ one obtains with Eq. (7.18) and $\langle r^2 \rangle = b^2 N$

$$\tau_p D = \frac{\langle r^2 \rangle}{3\pi^2 p^2} \tag{7.33}$$

If $\langle r^2 \rangle$ is known D can be calculated from dielectric data using Eq. (7.33). On the other hand side D can be also measured directly by, e.g. pulsed field gradient NMR (Chap. 18). Corresponding investigations have been carried out for poly(propylene glycol) with a molecular weight of 4000 g mol^{-1} [167] and for poly(cis-1,4-isoprene) [168]. Figure 7.20 shows the results for poly(propylene glycol) and in the inset the data for poly(cis-1,4-isoprene). It becomes clear that the absolute values as well as the temperature dependence agree well. The small difference in the temperature dependence can be explained by the temperature dependence of $\langle r^2 \rangle$ which has been omitted for sake of simplicity. So it can be concluded that for Type-A polymers the overall chain dynamics can be monitored by dielectric spectroscopy.

According to Eq. (7.18) (or Eq. (7.31)) the temperature dependence of the relaxation rate of the normal mode relaxation is due to the temperature dependence of the monomeric friction coefficient ζ. For bulk melts the temperature
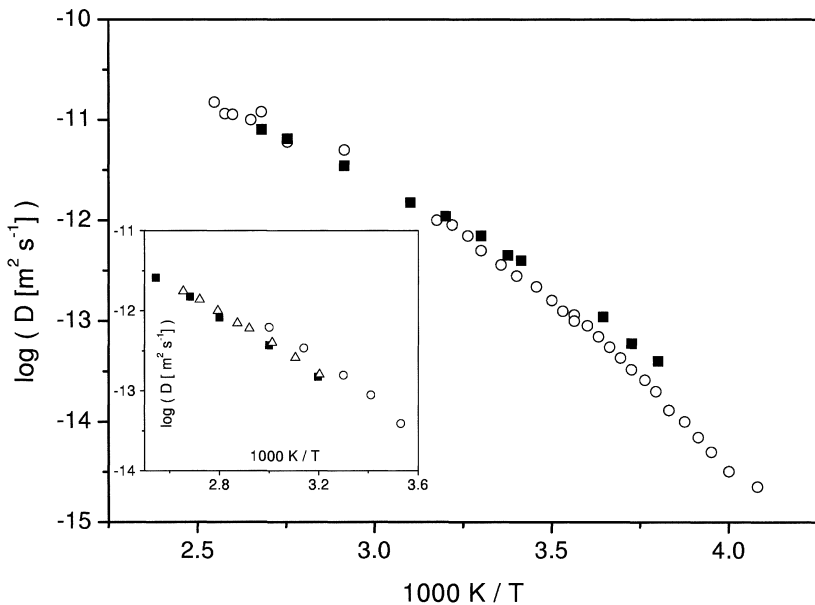

Fig. 7.20. Temperature dependence of the self diffusion coefficient for poly(propylene glycol) with a molecular weight of 4000 g mol^{-1}. *Filled squares* – measured by pulsed field gradient NMR, *open circles* – calculated with Eq. (7.33) from the relaxation rate of the dielectric normal mode relaxation. The *inset* shows values for poly(cis-1,4-isoprene) with (*filled squares*) measured by pulsed field gradient NMR $M = 8400$ g mol^{-1}, *open symbols* calculated with Eq. (7.33) from the relaxation rate of the dielectric normal mode relaxation, *open circles* – 8400 g mol^{-1}, *open triangles* 10,800 g mol^{-1}

dependence of ζ is determined by the segmental dynamics and therefore the relaxation rates of the α- and the normal mode relaxation should have the same temperature dependence. Figure 7.21a shows the temperature dependencies of both, the relaxation rates of the α- and the normal mode relaxation for poly(propylene glycol) of different molecular weights. The figure gives that close to T_g the temperature dependence of the α- relaxation is much stronger than that of the normal mode process. Fitting of the VFT-equation (Eq. (7.26)) to both the α- and the normal mode relaxation leads to $T_{0\alpha} > T_{0n}$, where $T_{0\alpha}$ and T_{0n} are the corresponding Vogel temperatures. To characterize the temperature dependence of both processes in more detail the ratio of their relaxation rates is plotted vs temperature in Fig. 7.21b. According to the Rouse theory this ratio should be independent of temperature. At high temperatures this is true but for temperatures close to T_g this ratio decreases dramatically. A similar behaviour was found by Floudas et al. [169] also for poly(propylene glycol) and for poly(cis-1,4-isoprene) [158, 170]. Using creep measurements Plazeck et al. have reported an analog effect for the shift factors of the segmental and terminal relaxation (global chain dynamics) for polystyrene [171], poly(vinyl acetate) [172], polypropylene [173] and poly(diphenyl siloxane) [174]. The change in the temperature dependence indicates that the underlying motional processes alters. At the moment there is no generally accepted model for this phenomenon. One interpretation based on the coupling scheme developed by Ngai (Chap. 1) is presented in [174, 175]. Recently Loring et al. presented a disordered Rouse model to explain this experimental result [176]. However, because $\nu_{p\alpha}$ corresponds to a rotational diffusion process (rotation of a dipole around the backbone) and ν_{pn} is related to translational diffusion the observed behaviour is quite similar to the decoupling of the rotational and translational diffusion reported for low molecular weight compounds and also polymers [154–157]. Moreover a strong decrease of the intensity of the overall chain motion was observed close to T_g by mechanical and dielectric measurements [174]. Some further discussion can be found in chapter 8 where the influence of pressure is analysed on both the dielectric α- and normal mode relaxation.

Dielectric strength. Because for Type-A polymers the whole dipole moment parallel to the chain skeleton is obtained by integration over the chain length the relaxation strength of the normal mode relaxation $\Delta\varepsilon_n$ is proportional to the mean end-to-end vector of the chain $\langle r^2 \rangle$. If the dipole moment μ_p parallel to the repeating unit and the molecular structure is known, the mean end-to-end vector can be calculated from $\Delta\varepsilon_n$ by

$$\Delta\varepsilon_n = \frac{4\pi N_A \mu_p^2 F_{\text{Onsager}}}{3 k_B T M} \langle r^2 \rangle \tag{7.34}$$

It was argued that the Onsager-factor F_{Onsager} is close to one also for chain dynamics [7]. For poly(cis-1,4-isoprene) the molecular weight dependence of $\langle r^2 \rangle$ obtained by dielectric spectroscopy is in good agreement with that measured by scattering techniques [177].
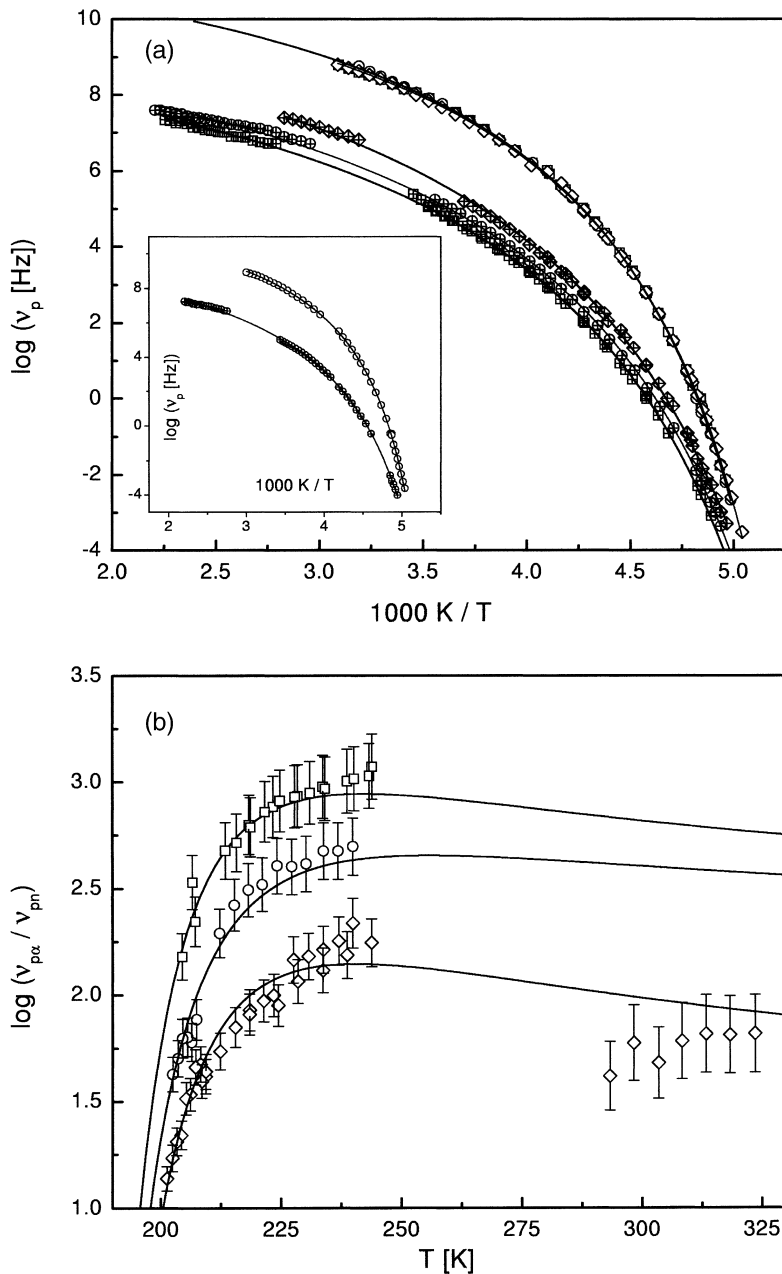
Fig. 7.21. a Relaxation rates of α-process $\nu_{p\alpha}$ (*open symbols*) and the normal mode relaxation ν_{pn} (*crossed symbols*) vs $1/T$ for poly(propylene glycol): *squares* $M = 4000$ g mol^{-1}, *circles* $M = 3080$ g mol^{-1}, *diamonds* $M = 1970$ g mol^{-1}. The *inset* shows the same for $M = 5300$ g mol^{-1}. **b** Ratio $\log(\nu_{p\alpha}/\nu_{pn})$ vs temperature: *open squares* $M = 4000$ g mol^{-1}, *open circles* $M = 3080$ g mol^{-1}, *open diamonds* $M = 1970$ g mol^{-1}. *Lines* are calculated according to the estimated VFT parameters

Shape of the relaxation function. From Eq. (7.17) one can estimate that the shape parameters of the normal mode peak should be described by $m = 1$ and $n \approx 0.7$ [158] independent of molecular weight. Experimentally it is found that for samples with very narrow distribution[7] of molecular weights the loss peaks are much broader than predicted by the theory [7, 158, 161]. Especially the high frequency parameter n is much smaller than predicted by the Rouse theory. This is true for molecular weights below and above M_c. Figure 7.22a shows the dielectric loss for a poly(*cis*-1,4-isoprene) with a molecular weight of 70,000 g mol^{-1}. The data were analysed by two HN-functions where the shape of the low frequency one is fixed to the Rouse-shape. The figure shows that the high frequency tail is much broader than predicted by the Rouse theory. Moreover the shape of the loss peak seems to depend on molecular weight [7, 158, 179] as it becomes clear from Fig. 7.22b where the shape parameter n for the normal mode process is plotted vs molecular weight.

Similar results are also obtained by means of mechanical spectroscopy [180]. There are several theoretical considerations to understand this dependency on the molecular weight. One model is based on the coupling scheme [181] (for a general discussion of the coupling scheme see Chap. 1). Ngai and coworkers have also presented a Focker/Planck approach to the chain dynamics of polymers [182]. Computer simulations for cooperative relaxation in dense macromolecular systems carried out by Pakula and Geyler [183] show that the time correlation function of the end-to-end vector has a strong non-exponential behaviour which depends on molecular weight. More recently Schweitzer developed a mode coupling approach for the chain dynamics which has not yet been compared with experimental results [184].

7.4.2
Semicrystalline Polymers

In this section the dielectric properties of semicrystalline polymers will be summarized briefly. Dielectric investigations on semicrystalline polymers were pioneered by Hoffman et al. [185] and Ashcraft et al. [186]. Because there are several reviews [10, 187–189] available in the literature no attempt is made to be complete here. Many useful details can be found in these overviews. This section will focus on recent developments like real time dielectric spectroscopy to follow the crystallization behaviour (see for instance [140, 141]) or a direct combination of structural with dielectric relaxation studies (e.g. [140, 142]).

The dielectric properties of semicrystalline polymers cannot be understood without a knowledge of their morphology. Therefore structural aspects will be summarized first. A more detailed discussion of the crystalline state of polymers can be found in [190].

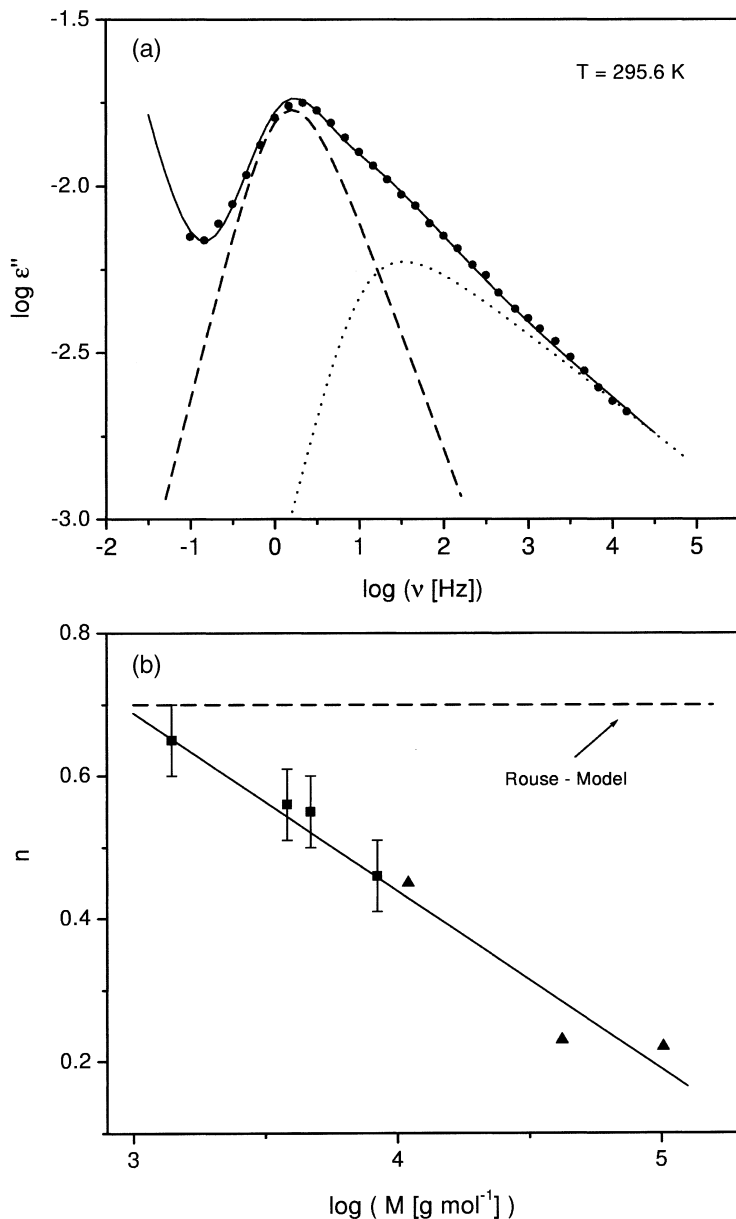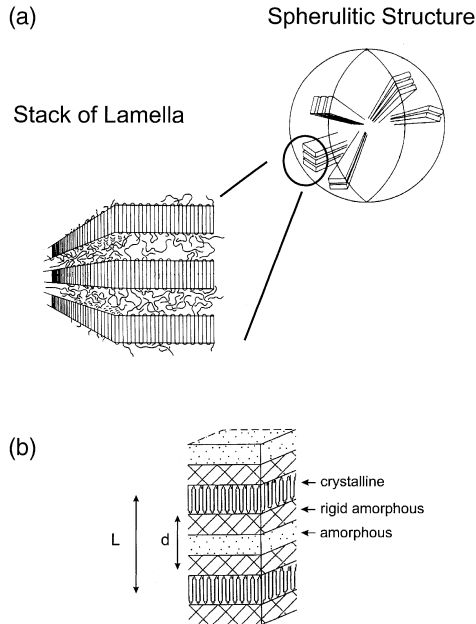[7] It should be noted that the distribution of molecular weights can be estimated from dielectric measurements [7, 178].

Fig. 7.22. a Dielectric loss vs frequency for the normal mode relaxation of poly(*cis*-1,4-iso-prene) with a molecular weight of $M = 70,000$ g mol^{-1} at $T = 295.6$ K described by a combination of two HN-functions. The *dashed line* corresponds to a Rouse-like behaviour with $m = 1$, $n = 0.7$ (fit parameter $\Delta\varepsilon = 0.048$, log $\tau_{HN} = -0.88$) The *dotted line* corresponds to a second function with $m = 1$ (fit parameter $\Delta\varepsilon = 0.03$, $n = 0.204$, log $\tau_{HN} = -1.75$). **b** Dependence of the parameter n for the normal mode relaxation on molecular weight for poly(*cis*-1,4-isoprene): *filled squares* – [158], *filled triangles* – [179]. The line is a linear regression through all data points which gives $n(M) = 1.435 - 0.249$ log M

Fig. 7.23. **a** Spherulitic morphology in a semicrystalline polymer. **b** Three phase model of a semicrystalline polymer

(a)   Spherulitic Structure

Stack of Lamella

(b)   ← crystalline
                                       ← rigid amorphous
L   d   ← amorphous

7.4.2.1
Morphology of Semicrystalline Polymers

Polymers with a regular chain structure like polyethylene or polypropylene can easily form crystalline structures. However, also other effects like hydrogen bonding (see for instance the class of polyamides [2]) can lead to crystalline polymers. Moreover different types of semi-rigid main chain polymers like polyesters (e.g. poly(ethylene terephthalate) (PET) [99, 189] or poly(ethylene-2,6-naphthalene dicarboxylate) (PEN) [101, 191]) and corresponding copolymers [142, 192]) or polyketones [140, 141, 193]) can be crystallized.

The true thermodynamic equilibrium state of crystalline polymers is the extended chain crystal which can be obtained for polyethylene under very special conditions like extremely high pressure [190]. Because of the high molecular weight of polymers it is kinetically difficult to form large extended crystals. Under conventional conditions polymers crystallize from the melt in the form of lamella which are often organized in spherulites[8] on a larger special length scale (see Fig. 7.23a).

The thickness of the lamella is in the order of several 10 nm where the chain is oriented normal to the lamella (see Fig. 7.23a). In the lateral directions the crystals are much more extended. These results and data obtained for polymeric single crystals crystallized from dilute solution led to the folded chain model of

---

[8] Besides spherulites other structures like fibres can also be obtained under special conditions like melt spinning, orientation, etc. Also fibrils and dendritic structures are known.

semicrystalline polymers [190]. Ideally in that model the polymeric chain is folded back and forth with hairpin turns. This leads to adjacent re-entries of a selected chain into the same lamella which have been proven by neutron and infrared experiments. A different set of experiments favours the switchboard model [194]. In that model the chains do not have a re-entry by regular chain folding. They enter the lamella more or less randomly. Both the folded chain model and the switchboard model can be regarded as limiting cases for the crystallization of polymers.

Because the thickness of the lamella is much smaller than the extended length of a macromolecule a selected chain can be a part of different adjacent lamellae. Therefore a 100% crystalline material cannot be obtained by crystallization in the bulk and a crystalline polymer is always semicrystalline. Moreover a stack layered structure (see Fig. 7.23a,b) is formed consisting of lamellae and more or less amorphous material in between. Thus semicrystalline polymers can be used as model systems to investigate the influence of a nanometer confinement on the molecular dynamics because the amorphous phase is confined between the crystalline lamella (see for instance Chap. 6).

Semicrystalline polymers are at least biphasic materials consisting of amorphous and crystalline regions. This has several implications for dielectric measurements. First, the dielectric response can be due to relaxation processes taking place in the amorphous or crystalline phase. In most cases the crystalline phase is regarded as immobile so that no relaxation process can take place. Second, because a semicrystalline polymer is a composite material, in general the mixing rules developed for such systems (see Chap. 13) should be applied bearing in mind that the dielectric permittivities of the amorphous and the crystalline regions are different. Using a stack-like layered structure Boyd developed a composite model of the upper and the lower bond of the measured permittivity [195]. Third, due to the biphasic structure of semicrystalline polymers separation of charges can take place at boundaries of the crystalline and amorphous phase which can lead to Maxwell/Wagner polarization effects (see Chap. 3).

The degree of crystallinity x_c can be estimated for instance from calorimetric experiments considering the melting enthalpies, density measurements or from wide angle X-ray scattering [190]. Moreover small angle X-ray scattering allows one to estimate the long period L (see Fig. 7.23b) which is defined as the distance between lamellae. Using the model sketched in Fig. 7.23b the thickness of the amorphous regions d can be estimated to d = Lx_c. It can be expected that the dielectric behaviour of polymers with a high degree of crystallinity (e.g. above 80%, high density polyethylene) is different to that obtained for a polymer with medium degree of crystallinity around 50% (for instance PET) because the amorphous phase is more restricted in the first case as it was discussed by Williams [10].

7.4.2.2
Polymers with a Medium Degree of Crystallinity

In general the crystalline phase is rigid and shows no dielectric relaxation processes. Therefore the observed dielectric relaxation behaviour is assigned to
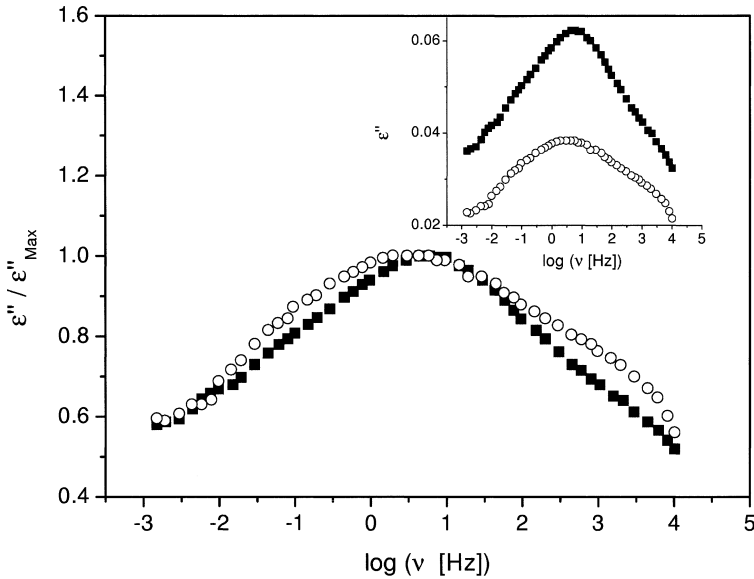
Fig. 7.24. Normalized dielectric loss vs frequency for semicrystalline (*open circles*) and amorphous (*filled circles*) PET at $T = 203$ K. The data are taken from [189]. The *inset* shows the unreduced dielectric spectra

the amorphous phase and shows in principle a similar pattern as observed for amorphous polymers. So most semicrystalline polymers show a β-relaxation at low temperatures (high frequencies) and an α-process related to the dynamic glass transition at higher temperatures (lower frequencies). Up to now no normal mode relaxation was found for a semicrystalline polymer of Type-A [196]. Probably due to the incorporation of the chain into the crystallites the end-to-end vector of the chain cannot fluctuate.

One of the most extensively investigated semicrystalline polymer is PET [99, 137, 189] because it easily crystallizes. For that reason mainly the dielectric properties of PET are discussed as an example here. Most of the described results are general features of the dielectric response of semicrystalline polymers.

β-relaxation. The inset of Fig. 7.24 compares the dielectric loss of amorphous and semicrystalline PET for the β-relaxation. Where the dielectric strength due to the reduced amount of the amorphous fraction is strongly decreased with regard to both the position and the shape of the relaxation function there is no significant difference between both samples (see Fig. 7.24 where the dielectric loss normalized to its maximum). The temperature dependence of the relaxation rate for the semicrystalline material can be described by an Arrhenius law with slightly higher activation energy than for the amorphous polymer [189].

To discuss the dependence of the relaxation strength on the degree of crystallinity it is useful to consider its value normalized by that measured for the
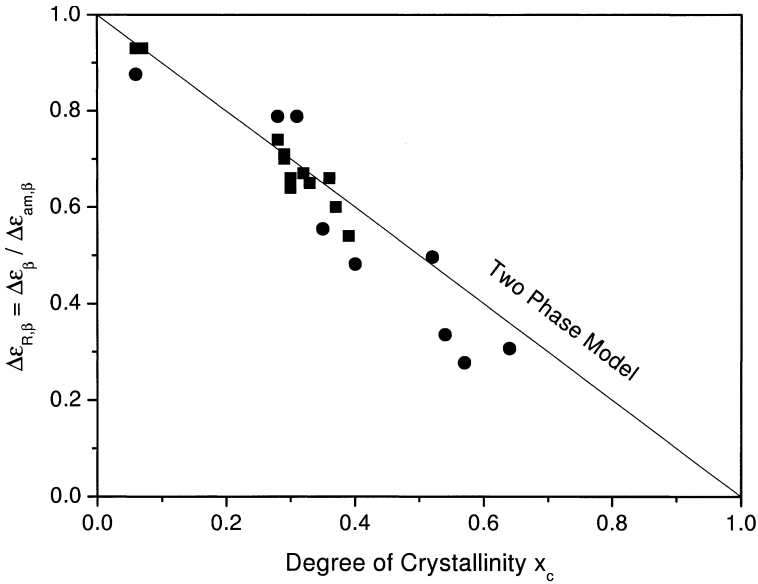
Fig. 7.25. Normalized dielectric relaxation strength for the β-relaxation $\Delta\varepsilon_{R,\beta}$ vs degree of crystallization for PET: *filled circles* – data taken from [189], *filled squares* – data taken from [197]. The *line* is due to a two phase model

complete amorphous state

$$\Delta\varepsilon_{R,i} = \frac{\Delta\varepsilon_i}{\Delta\varepsilon_{\text{am},i}} \; (i = \alpha, \beta) \tag{7.35}$$

In Fig. 7.25 this ratio is plotted for two sets of data of PET [189, 197]. As expected $\Delta\varepsilon_{R,\beta}$ decreases with x_C and obeys a dependence as predicted by a simple two phase model ($\Delta\varepsilon_{R,\beta} \approx 1 - x_C$). This means that the whole amorphous fraction contribute to the β-relaxation.

α-relaxation. In contrast to the β-relaxation the influence of the crystals on the molecular motions responsible for the α-process is strong. Mainly three effects are observed: (i) a decrease of the dielectric strength, (ii) a shift of the relaxation rate to lower values and (iii) a considerable broadening of the relaxation function [9]. This is illustrated by Fig. 7.26 where the dielectric loss for poly(aryl ether ketone ketone) is plotted vs frequency for different crystallization times t_c using real time dielectric spectroscopy [140]. The continuous variation of the dielectric function with t_c shows that crystallization does not induce a new amorphous phase but that its properties are influenced more and more by the crystallites.

In the following the dependence of the dielectric relaxation strength $\Delta\varepsilon_\alpha$ on the degree of crystallization is discussed using its normalized value $\Delta\varepsilon_{R,\alpha}$ defined by Eq. (7.35). Figure 7.27a shows $\Delta\varepsilon_{R,\alpha}$ vs x_C for PET using the corre-
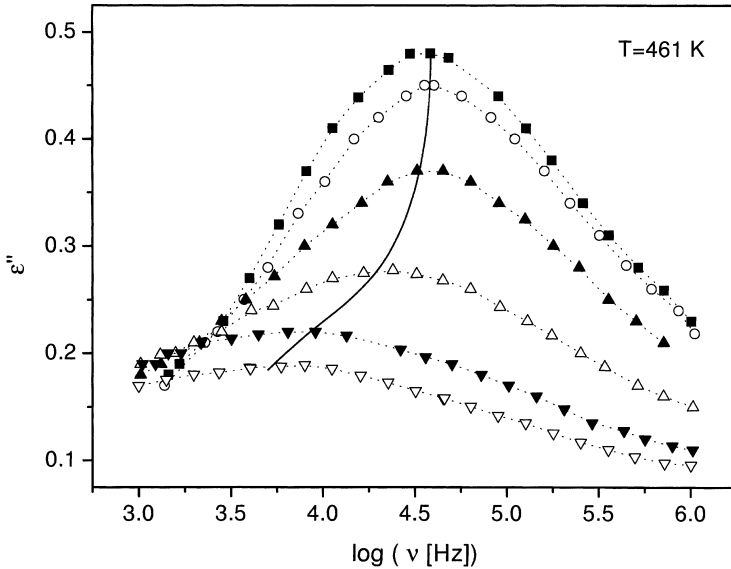
Fig. 7.26. Dielectric loss for poly(aryl ether ketone ketone) vs frequency for different crystallization times t_c: *filled squares* – $t_c = 0$ s, *open circles* – $t_c = 4.314 \times 10^3$ s, *filled triangles* – $t_c = 7.032 \times 10^3$ s, *open triangles* – $t_c = 9.594 \times 10^3$ s, *inverted filled triangles* – $t_c = 1.812 \times 10^4$ s, *inverted open triangles* – $t_c = 5.4804 \times 10^4$ s. The data are taken from [140]. The *solid line* indicates the shift of the position of maximum loss and the *dotted lines* are guides for the eyes

sponding data sets as in Fig. 7.25. In contrast to the β-relaxation the dependence of $\Delta\varepsilon_{R,\alpha}$ on x_C does not follow a two-phase model. The extrapolation of $\Delta\varepsilon_{R,\alpha}$ to zero reads a value which is smaller than 1. This means that not the whole amount of the amorphous phase contributes to the α-relaxation. A part of the amorphous phase is amorphous in structure but it is rigid with regard to the molecular mobility which is responsible for the dynamic glass transition. Therefore this part of the amorphous phase is called rigid amorphous phase (RAP). Probably the RAP is located close to the crystallites as it is sketched schematically in Fig. 7.23b. By analysing the normalized step height of the specific heat capacity measured by calorimetry a similar dependence on x_C is obtained [137].

In Fig 7.27b $\Delta\varepsilon_{R,\alpha}$ is plotted vs the degree of crystallinity for poly(aryl ether ketone ketone) [140] and for a set of different semicrystalline copolyesters [142]. For all of these quite different polymer structures a similar behaviour is obtained. $\Delta\varepsilon_{R,\alpha}$ goes to zero at a value of x_C smaller than 1. Such an amorphous phase restricted in mobility was also observed by means of dielectric spectroscopy for a number of other semicrystalline polymers [198–202]. That means that existence of the RAP is quite general where its amount depends on the polymer under consideration [201].

For amorphous polymers $\Delta\varepsilon_\alpha$ decreases with increasing temperature whereas for semicrystalline polymers $\Delta\varepsilon_\alpha$ often increases [198–201, 203]. This is shown in Fig. 7.28 where $\Delta\varepsilon_\alpha$ is compared for amorphous and semicrystalline PET. Because $\Delta\varepsilon_\alpha$ is proportional to the number of contributing dipoles this

Fig. 7.27. a Normalized dielectric relaxation strength for the α-relaxation $\Delta\varepsilon_{R,\alpha}$ vs degree of crystallinity for PET: *filled circles* – data taken from [189], *filled squares* – data taken from [197]. The *solid line* is due to a two-phase model. The *dotted line* is a linear regression the data taken from [197] whereas the *dashed line* is due to a linear regression to the data taken from [189].
b Normalized dielectric relaxation strength for the α-relaxation $\Delta\varepsilon_{R,\alpha}$ vs degree of crystallinity for two systems: *filled squares* – poly(aryl ether ketone ketone) [140] where the *dotted line* is a linear regression through the data; *open circles* – a set of copolyesters [142] whereas the *dashed line* is a linear fit to the data. The *solid line* is due to a two phase model
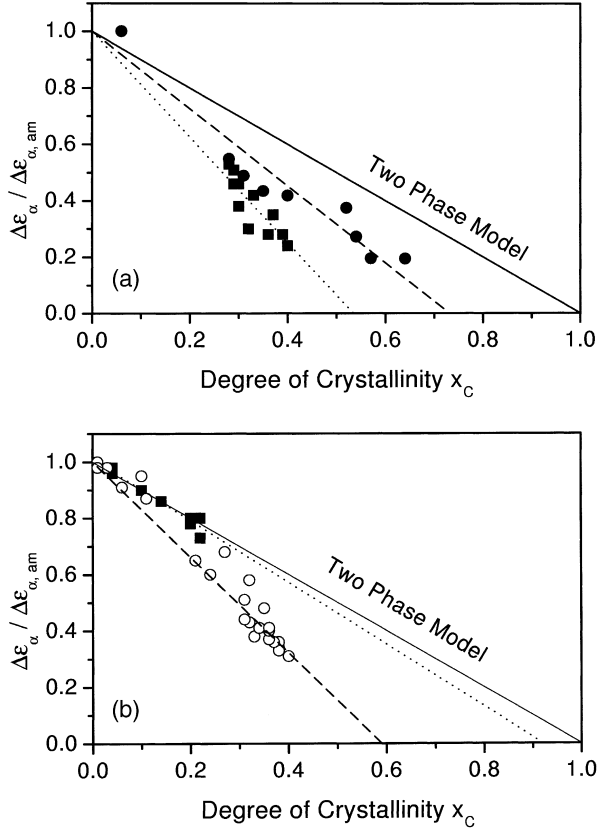
means that the amount RAP decreases with increasing temperature [203]. This result is not only found for PET but also for a number of other semicrystalline polymers [198–201].

Often the kinetics of crystallization is described or modelled by the Avrami equation [190]. Using real time methods – which are pioneered by Williams [204] – it is possible to follow the kinetics of the crystallization process by dielectric spectroscopy [140, 141]. The Avrami equation can be adapted to describe the time dependence of the dielectric strength of the α-relaxation during crystallization

$$\Delta\varepsilon_\alpha(t_C) = \Delta\varepsilon_\alpha(0) - \delta\varepsilon\left[1 - \exp\left[-\left(\frac{t_C}{\tau_{\mathrm{Crys}}}\right)^{n_A}\right]\right] \tag{7.36}$$

where $\delta\varepsilon$ is the change of dielectric relaxation strength during crystallization, τ_{Crys} is a time constant for it and n_A is a parameter characterizing the kind of the crystals. Figure 7.29 gives the dependence of $\Delta\varepsilon_\alpha$ on the crystallization time for poly(aryl ether ketone ketone) [140]. The main part of the time dependence of
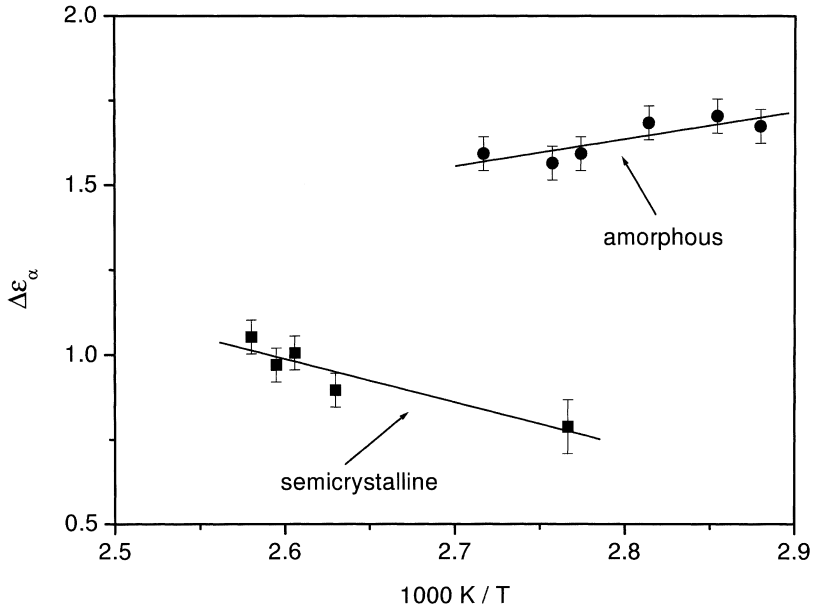
Fig. 7.28. $\Delta\varepsilon_\alpha$ vs inverse temperature for amorphous (*filled circles*) and semicrystalline (*filled squares*, $x_C = 0.29$) PET. The *lines* are linear fits through the data. The data are taken from [203]
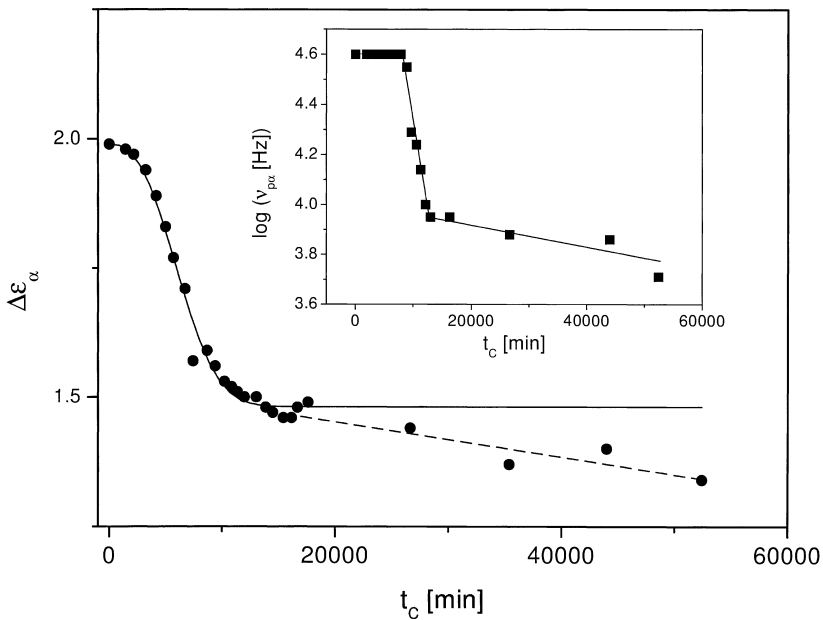

Fig. 7.29. $\Delta\varepsilon_\alpha$ vs crystallization time t_C for poly(aryl ether ketone ketone) at $T = 461$ K. The data are taken from [140]. The *solid line* is a fit of Eq. (7.36) to the data with $\Delta\varepsilon_\alpha(0) = 1.99$, $\delta\varepsilon = 0.509$, $\tau_{\text{Crys}} = 7074$ min and $n_A = 2.6$. Secondary crystallization is indicated by the *dashed line*. In the *inset* the change of the relaxation rate of the α-process with t_C is shown. The *lines* are guides for the eyes
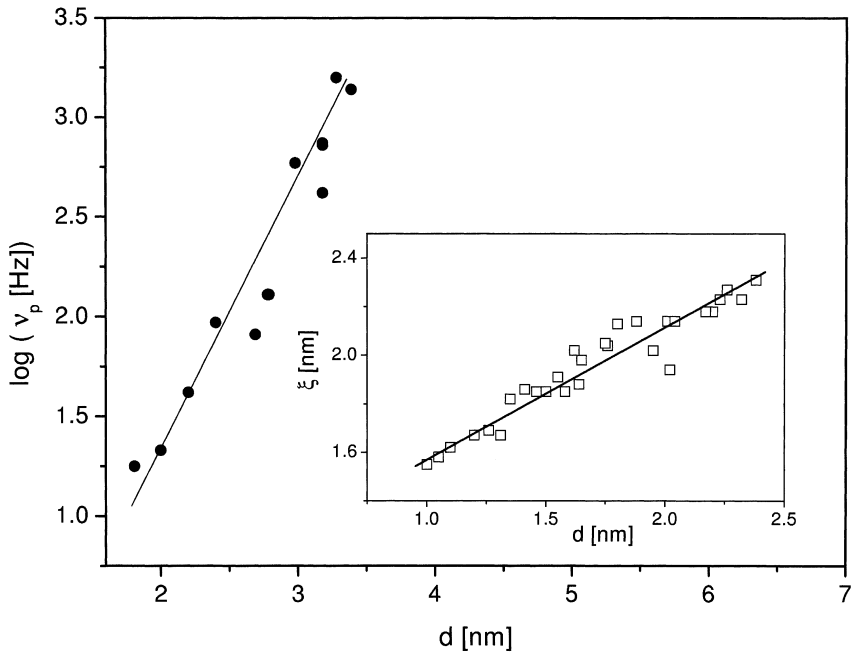
Fig. 7.30. Dependence of the relaxation rate of the α-relaxation on the thickness of the amorphous regions for PET at 383 K. The data are taken from reference [197]. The *line* is a guide for the eyes. The *inset* shows the characteristic length ξ for the glass transition estimated from calorimetric measurements vs the thickness of the amorphous regions. The *line* is a guide for the eyes. The data are taken from [205]

$\Delta\varepsilon_\alpha$ can be well described by the Avrami equation. For n_A a value of $n_A = 2.6$ is obtained which indicates a spherulitic crystallization between 2 or 3 dimensions. For longer times ($t_C > 2 \times 10^4$ min) there are systematic deviations from the Avrami equation which indicates a secondary crystallization process.

The inset of Fig. 7.29 shows the dependence of the relaxation rate $\nu_{p\alpha}$ on t_C. It is interesting to note that a significant change in $\nu_{p\alpha}$ is observed after a decrease in $\Delta\varepsilon_\alpha$ of approximately 70 %. This might be understood considering the dependence of relaxation rate on the thickness d of the amorphous layers as it is plotted for PET in Fig. 7.30. For large d the segmental dynamics is only weakly influenced. If the thickness of the amorphous layer decreases the crystallites act more and more as confining geometry which slows down the molecular mobility (Fig 7.30). This line of argumentation is supported by a correlation of the characteristic length scale of the molecular motions responsible for the glass transition and the thickness of the amorphous layer [205] as it is shown in the inset of Fig. 7.30.

7.4.2.3
Polymers with a High Degree of Crystallinity – Polyethylene

For a high degree of crystallinity the amount of the amorphous phase and also the thickness of the amorphous layer is strongly reduced. Because the relaxation processes discussed in Sect. 7.4.2.1 originate from the amorphous phase it is difficult to observe and to analyse them for polymers with a high degree of crystallinity. On the other hand it possible to observe dielectric relaxation processes taking place in the crystalline phase.

Among others like polyoxymethylene, poly(trimethylene oxide) or poly-(tetrafluoro ethylene) for polyethylene a very high degree of crystallinity can be obtained because of its simple chain structure consisting only of CH_2 units. This is especially true for high density polyethylene which contains in addition a low degree of chain branching. Generally the dielectric response of pure polyethylene should be very small because the CH_2 groups carry only a weak dipole moment. However, due to oxidation processes commercial polyethylene contains a number of carbonyl groups which can be used as a dielectric probe to reveal the molecular motions in both the amorphous and the crystalline regions. Titanium dioxide fillers can also be applied to enhance oxidation [206]. In addition slightly chlorinated polyethylenes and copolymers of ethylene and carbon monoxide [186] have been used to monitor the dielectric relaxation processes in polyethylene.

Discussing the dielectric behaviour of polyethylene it should be noted that the nomenclature of relaxation processes for polyethylene or other semicrystalline polymers with a high degree of crystallinity [2] is different from that of amorphous polymers. The γ-process in polyethylene corresponds to the β-relaxation discussed for amorphous polymers; the β-relaxation is due to the segmental motions in the amorphous regions similar to the α-relaxation discussed in Sect. 7.4.1. In addition to these both processes in polyethylene a so-called α- or α_C-relaxation is observed due to molecular motions within the crystals. Some peculiarities of these relaxation processes will be discussed for polyethylene as model system. The results can be transferred to similar systems.

γ-process. The temperature dependence of the relaxation rate of the γ-process shows an Arrhenius-like behaviour with an activation energy around 45 kJ mol^{-1} which is typical for local motional processes. As shown by the pioneering studies of Ashcraft and Boyd [186] the γ-process arises from the amorphous regions. A combination of dielectric, mechanical and NMR experiments shows that chain segments close to the surface of the lamella also contribute to the γ-process [207]. This is in agreement with results found for semicrystalline polymers with a medium degree of crystallinity where the β-relaxation also takes place in the restricted amorphous phase close to the crystallites (see Fig. 7.23). The relaxation function is found to be extremely broad which is explained by a broad distribution of energy barriers [186].

β-process. The β-process originates from molecular fluctuations of the chain segments in the amorphous phase and corresponds to the dynamic glass transi-

tion of the system. This becomes clear from investigations which have shown that the dielectric strength of the β-process is higher for low density polyethylene having a lower degree of crystallinity. Very often the temperature dependence of the relaxation rate of the β-relaxation was described by an Arrhenius law with a high apparent activation energy of 220 kJ mol^{-1} which indicates a cooperative process. A recent study on low density polyethylene filled with titanium dioxide reveals [206] that the temperature dependence of the relaxation rate follows a Vogel/Fulcher/Tammann dependence (see Eq. (7.26)) which is characteristic for the glass transition.

α- or α_C-process. The α-process is assigned to the crystalline lamella where a rotational-translation of chain segments was assumed assisted by a chain twisting. Conformational energy calculations for the twisted assisted chain reorientation mechanism [208] show that the process is accompanied by a twisted region of approximately 12 CH$_2$ groups along the chain. This model leads to an activated temperature dependence of the relaxation rate. Experimentally an activation energy of approximately 100 kJ mol^{-1} was found by dielectric spectroscopy which agree with that found by mechanical measurements [190]. Also NMR investigations support the twisted assisted chain reorientation mechanism and yield similar activation energies [209]. Moreover recently 180° chain flips in polyethylene crystallites have been observed directly by ^{13}C NMR [210].

7.4.3
Polymer Blends

Because recent reviews about the dielectric properties of polymeric blends are available [211, 212] in this section only fundamental and the most important aspects will be summarized focusing on binary blends of amorphous polymers. For an overview about the large number of published experimental data the reader is referred to the mentioned reviews [211, 212].

Dielectric spectroscopy can be used to detect and to define criteria of miscibility on a molecular level [213]. In general both components of a blend will have different polarities. One component can be dielectrically more visible than the other one (limiting case: one component can be dielectrically invisible). Furthermore by blending a Type-A and a Type-B polymer the overall chain dynamics (normal mode, see Sects. 7.2.3.2 and 7.4.1.4) can be studied only for the polymer of Type-A by dielectric spectroscopy. Because the chain dynamics of Type-B polymer is dielectrically invisible one can ask the question how the global chain motion of the Type-A polymer is influenced by the second component. The normal mode relaxation proves a larger length scale than the segmental one. Thus information about composition fluctuations on different length scales can be deduced. Such investigations have been carried out for instance for blends of polybutadiene and poly(*cis*-1,4-isoprene) [7], polystyrene and poly(*cis*-1,4-isoprene) [214] or blends of poly(*n*-butyl acrylate) and poly(propylene glycol) [215, 216].

7.4.3.1
General Considerations

For polymers the contribution of the entropy of mixing ΔS_M to the free enthalpy of mixing ΔG_M is small. According to the lattice model of Flory/Huggins [217] ΔG_M can be estimated to

$$\Delta G_M = -kT\Delta S_M + \kappa \Phi_1 \Phi_2$$

with

$$\Delta S_M = -\left[\frac{\Phi_1}{N_1}\ln\Phi_1 + \frac{\Phi_2}{N_2}\ln\Phi_2\right]$$

(7.37)

where Φ_1 are the volume fractions, N_i the degrees of polymerization and κ denotes the Flory/Huggins interaction parameter[9]. Based on the principle of thermodynamics the conditions for miscibility, the critical (solution) temperature for phase separation T_C or the binodals can be calculated from Eq. (7.37). At temperatures above T_C the two components are miscible on a molecular level whereas below T_C phase separation occurs. The composition of these phases follows the binodal. That means even in the phase separated state a certain degree of mixing (depending on κ and on N_i) is observed which leads to a component 1 and to a component 2 rich phase.

In general the β-, the α- and even the normal mode process will be modified in the case of miscible blends or in systems with partial miscibility. Only for completely phase separated materials (as the limiting case) is the relaxational characteristic of both compounds fully maintained. This is demonstrated for the α-relaxation in Fig. 7.31 schematically. Figure 7.31a shows the relaxation map for a miscible system where a single α-process is observed which is located – depending on the composition – between the traces obtained for each component. There are many models for the dependence of the glass transition temperature on the composition for a homogeneous blend which can be found in standard textbooks of polymer science (see for instance [190, 217]). For a phase separated blend with a partial miscibility two α-processes will be observed where the location of both processes depends on the composition of both phases. Therefore dielectric spectroscopy is expected to provide valuable information on the local fluctuations of concentrations and on the local miscibility. In the following we will focus on characteristics of the α-relaxation of blends only.

7.4.3.2
Miscible Blends – Concentration Fluctuations

It has been known for a long time [218] that the relaxation function measured for a miscible blend is considerable broadened compared to the spectra of the

---

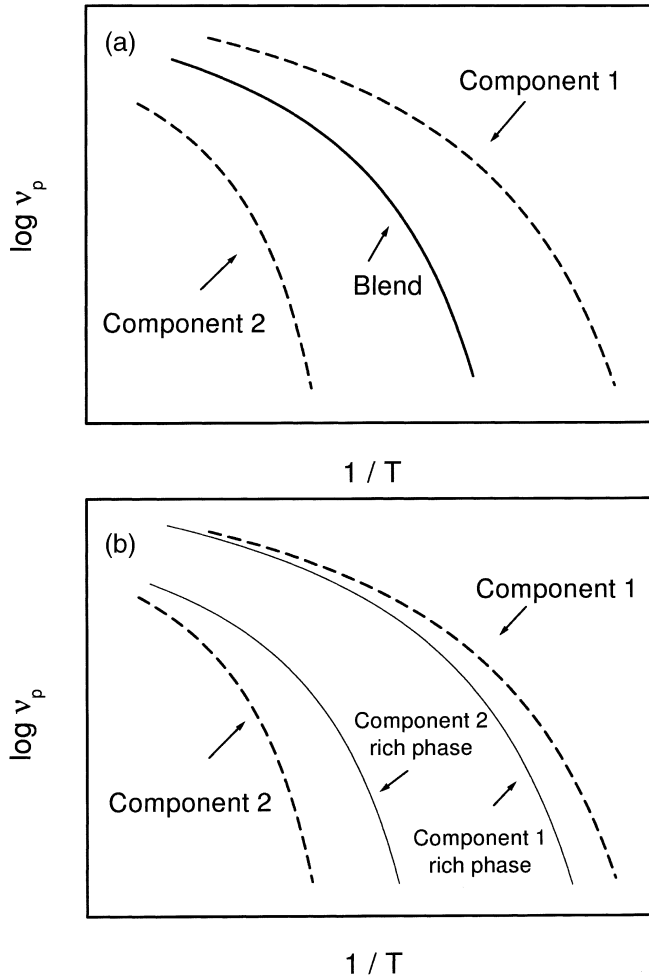[9] It should be noted that the Flory/Huggins theory can describe only systems with a lower critical solution temperature.

Fig. 7.31. Schematic representation of the relaxation rate of the α-relaxation for binary polymeric blends: **a** miscible blend; **b** immiscible blend with a partial miscibility of both compounds

pure polymers [4, 57, 82, 213, 219–221]. As an example this is shown for a miscible blend of polystyrene (PS) and poly(vinyl methylether) (PVME) in Fig. 7.32. For the blend (Fig. 7.32b) the loss peak is much broader than for the single component PVME (see Fig. 7.32a). Recently the behaviour of the PS/PVME systems was investigated by a combination of dielectric, NMR and neutron scattering investigations using deuterated polystyrene [223]. In miscible blends the broadening of the α-relaxation increases with the difference of the glass transition temperatures. It is also a characteristic of miscible blends that the loss peak narrows as temperature increases [4, 222].

In recent theoretical approaches to the dielectric relaxation of miscible blends it was assumed that the broadening of the dielectric relaxation function

Fig. 7.32. a Dielectric loss vs frequency for poly(vinyl methylether) for different temperatures. **b** Dielectric loss vs frequency for a blend of polystyrene and poly (vinyl methylether) for a volume fraction of polystyrene of $\Phi_{PS} = 0.4$. All lines are guides for the eyes. The data were taken from [222]
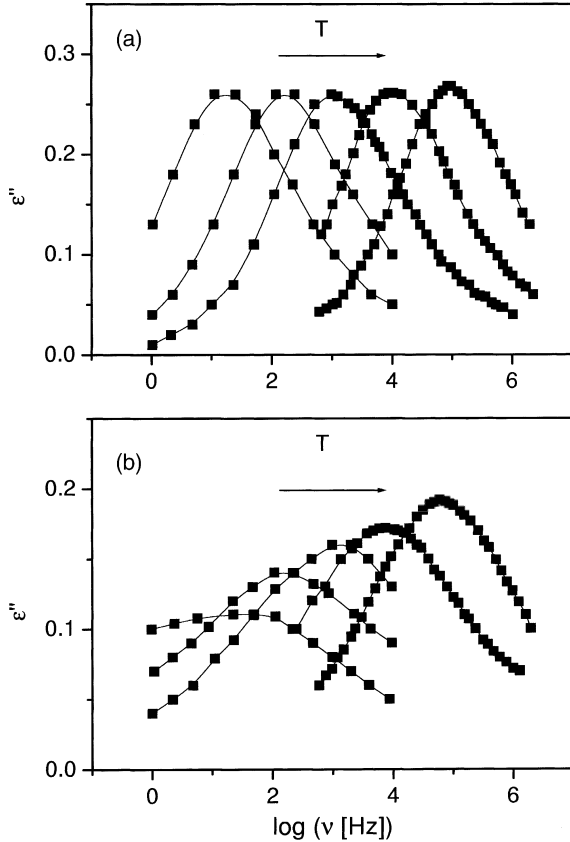
of the blend compared to that of the pure components is due to composition or concentration fluctuations [59, 60, 220, 224]. The theoretical treatment is simplest if one component is dielectric invisible as it is nearly the case for polystyrene. Assuming that the lifetime of the composition fluctuations is much longer than the relaxation time for the α-relaxation one can write [220, 224]

$$\varepsilon''_{\text{Blend}}(\omega) = \int_0^\infty \tilde{c}(\tau)\, \varepsilon''_{\text{Vis}}(\omega\tau)\, d\tau \qquad (7.38)$$

where $\tilde{c}$ is the distribution function of the composition fluctuations and $\varepsilon''_{\text{Vis}}(\omega)$ is the relaxation function of the dielectrically visible component. Often $\tilde{c}$ is assumed to be Gaussian with a variance $s = \sqrt{\langle \delta\Phi^2 \rangle}$. $\langle \delta\Phi^2 \rangle$ is the mean square composition fluctuation which can be estimated by fitting Eq. (7.38) to the loss data of a miscible blend. It is found that $\langle \delta\Phi^2 \rangle$ increases with increasing temperature [220, 222] which can be understood in the framework of the cooperativity approach to the glass transition [220]. The same procedure was also applied to describe the dielectric behaviour of a solvent/polymer system in the concentrated regime [59, 60].

Recently for the dielectric function of a miscible blend

$$\varepsilon^*_{\text{Blend}}(\omega) = \Phi_1 \varepsilon^*_1\left(\frac{\zeta_{\text{Blend}}}{\zeta_1}\omega\right) + \Phi_2 \varepsilon^*_2\left(\frac{\zeta_{\text{Blend}}}{\zeta_2}\omega\right) \tag{7.39a}$$

was suggested by Adachi and coworkers [216]. This formula is based on the idea that the dipole moment of the mixture is a weighted sum of the dipole moment of each compound and that the segmental mobility in the blend can be described by a common friction coefficient ζ_{Blend} [37, 216]. According to this assumption the segmental relaxation time τ_i for the pure component i has to be changed to $\tau_i \dfrac{\zeta_{\text{Blend}}}{\zeta_i}$. For the friction coefficient

$$\ln \zeta_{\text{Blend}} = \Phi_1 \ln \zeta_1 + \Phi_2 \ln \zeta_2 + k\Phi_1\Phi_2 \tag{7.39b}$$

was supposed where k is a parameter which characterizes the interaction between both components. It was shown that this model can qualitatively describe the data [216].

7.4.3.3
Immiscible Blends

Immiscible blends are inhomogeneous systems. For dielectric spectroscopy this fact – like for semicrystalline polymers – has several implications. First, appropriate mixing rules for the dielectric permittivity have to be applied (see Chap. 13). Second, due to the phase separated structure migrating charge carriers can be blocked at the phase boundaries which can give rise to a Maxwell/Wagner polarization process (see Chap. 3). Analysing this effect by invoking model considerations information about the phase morphology and the structure of the phase boundaries can be extracted (Chap. 13).

In the simplest case of a completely phase separated structure and if both components having approximately the same dipole moment one can write for the dielectric function of the blend

$$\varepsilon^*_{\text{Blend}}(\omega) = \Phi_1\varepsilon^*_1(\omega) + \Phi_2\varepsilon^*_2(\omega) \tag{7.39c}$$

However in most cases a limited miscibility (depending on N_i and κ) is observed which leading to two phases enriched in one component which can be described by a concentration C_i. Following the ideas developed in Sect. 7.4.3.2 the dielectric properties of each of these phases can be modelled by the approaches developed for miscible blends. By analysing the frequency position of the α-relaxation and its dielectric strength the unknown concentration of each compound can be estimated in principle assuming appropriate mixing rules. In practice this can be difficult. Of special interest is again the case where one component is dielectrically invisible as it is discussed for a blend of polystyrene and poly(methylphenyl siloxane) [225].

7.4.4
Novel Polymeric Architectures

7.4.4.1
Rings

As was pointed out earlier, with increasing molecular weight the influence of chains ends having a higher mobility becomes less important. For instance the dependence of the T_g on molecular weight can be described by the Fox/Flory equation [217]

$$T_g(M) = T_{g,\infty} - \frac{\tilde{K}}{M} \tag{7.40}$$

($T_{g,\infty}$ – glass transition temperature for $M \to \infty$, $\tilde{K}$– constant) which is based on free volume considerations and describes well the experimental observations for linear chains. In comparison to linear chains for rings or cycles the conformational degrees of freedom are reduced. For small rings this can lead to a complete frustration of the segmental motions. In contrast to linear chains an increase of T_g is observed with decreasing molecular weight for several systems [226–228]. Because the segmental motion is strongly affected in cyclic polymers dielectric spectroscopy is suitable to study the influence of the ring size on the molecular dynamics. Such investigations are carried out for linear and cyclic poly(dimethyl siloxane) [229]. Figure 7.33 compares the dependence of the dielectric glass transition temperature $T_g^{\mathrm{Diel}}(\tau_{\mathrm{HN}} = 1\,\mathrm{s})$ on the molecular weight for cyclic and linear PDMS. For the latter a dependence according to the Fox/Flory equation is obtained. For rings a quite different dependence is obtained. For high molecular weights approximately the same T_g^{Diel} is observed as for the linear polymers. With decreasing M, in contrast to linear macromolecules, T_g^{Diel} increases. At low molecular weights there are indications for a weak maximum. These experimental results can be understood in the framework of a modified Gibbs/DiMarzio theory [230, 231] and they are also in agreement with molecular simulations [229].

The dielectric strength $\Delta\varepsilon$ decreases with molecular weight for both the linear and the cyclic macromolecules (see inset of Fig. 7.33). However, for the rings this dependence is much stronger than for the linear chains. For tight rings ($M_n = 296\,\mathrm{g\,mol^{-1}}$) no α-relaxation can be detected. This indicates, further, that the conformational degrees of freedom are strongly reduced for rings.

7.4.4.2
Stars and Block Copolymers

Together with rings star-like polymers can be regarded as one of the simplest case where the architecture of the whole molecule will influence its molecular dynamics in comparison to linear chains. Because the differences in architecture become relevant at length scales much larger than that of a segment the global chain dynamics should be mainly changed when linear and star-like structures
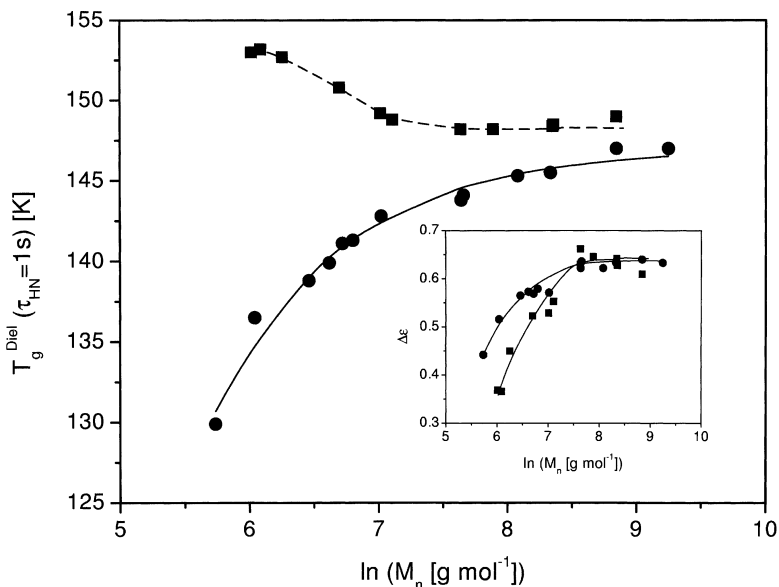
Fig. 7.33. $T_g^{\text{Diel}}(\tau_{\text{HN}} = 1\ s)$ vs molecular weight: *filled circles* – linear chains, *filled squares* – rings whereas the *solid line* is a fit of Fox/Flory equation to the data ($T_{g,\infty} = 147\,\text{K}, \widetilde{K} = 5057\ \text{K}$ mol g^{-1}) The *dashed line* is a guide for the eyes. The *inset* shows $\Delta\varepsilon$ vs molecular weight at $T = 298\ \text{K}$: *filled circles* – linear chains, *filled squares* – rings whereas *lines* are guides for the eyes. All data are taken from [229]

of the same monomer are compared. First dielectric investigations on star-branched poly(propylene oxide) were reported by Stockmayer et al. [21]. Adachi and Kotaka presented results for branched poly(2,6-dichloro-1,4-phenylene oxide) in solution [232]. Dielectric properties of linear and star-like poly(*cis*-1,4-isoprene)s are discussed in [233–235]. Both the number and the molecular weight of the arms were changed. No significant differences in the segmental motion of linear chains and star-like macromolecules are observed as it is expected. Since poly(*cis*-1,4-isoprene) is a Type-A polymer the normal mode process of the arms can be studied by dielectric spectroscopy and compared to that of linear chains. First, there is no influence of the number of arms on the normal mode relaxation. Second, for stars the relaxation time τ of an arm is much slower as for a linear chain of a comparable molecular weight (see inset of Fig. 7.34). For stars one chain-end of the arm is fixed (tethered chain) and cannot contribute to the global chain motion as for linear chains. In a model of Graessley [166]

$$\tau_{\text{tethered}} \approx 4\,\tau_{\text{linear}} \tag{7.41}$$

is obtained for the retardation of the normal mode relaxation for a tethered chain. The corresponding motional process can be regarded as a breathing motion of the contour length of the arm. In solutions similar processes are known
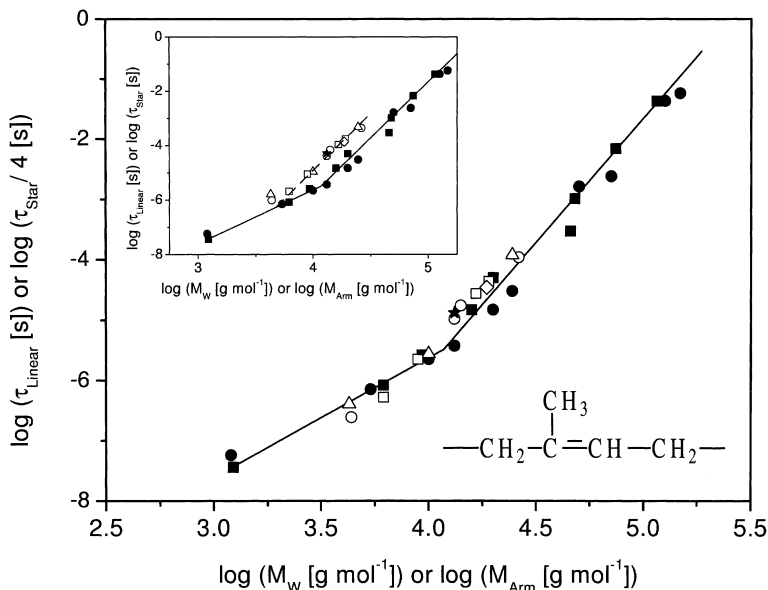
Fig. 7.34. τ_{Linear} and $\tau_{\text{Star}}/4$ vs molecular weight of the chain or the arm of different linear and star-like poly(*cis*-1,4-isoprene)s at $T = 320$ K. The *inset* shows τ_{Linear} and τ_{Star} vs molecular weight of the chain or the arm. *filled squares* [234], *filled circles* [22] linear chains, *open circles* – 18-arm star, *open triangles* – 12-arm star, *open squares* – 8-arm star, *open diamonds* – 4-arm star, *stars* – 3-arm star. The *solid lines* are linear fits for $M < M_C$ (Slope 2.0, Rouse behaviour) and $M > M_C$ (Slope 3.7, reptation behaviour). The *dashed line* is a parallel shift of the line obtained for the reptation behaviour through the data of the stars. The data are taken from [233, 234]

as elastic modes [236]. For stars Eq. (7.41) is proved by plotting $\tau_{\text{Star}}/4$ vs molecular weight (Fig. 7.34). All data points for the stars collapse approximately to that obtained for the linear chains.

There is an increasing interest in the investigation of block copolymers in recent years [237] where the simplest case is that of diblocks. Due to a subtle counterbalance of chain connectivity (entropic forces) and enthalpy effects block copolymers can undergo a microphase separation at temperatures below the order to disorder transition temperature T_{ODT}. The control parameter is κN (κ-Flory/Huggins interaction parameter, N-whole degree of polymerization). There are two limiting cases: the strong segregation limit for $\kappa N \gg V(c)$[10] [238] at temperatures well below T_{ODT} and the weak segregation limit at temperatures close to T_{ODT} for $\kappa N \approx > V(c)$ where $V(c)$ is a critical value which depends on the composition c of the diblock. For $\kappa N < V(c)$ a homogeneous system (disordered state) is observed. Theoretical approaches to the weak segregation limit of diblock copolymers are due to Leibler [239] and were extended by Fredrickson et al. [240] by including concentration fluctuations. For bulk systems in the mi-

---

[10] For diblock copolymers of a 50/50 composition $V(c) = 10.5$ holds [239].

crophase separated state a variety of structures like spheres, cylinders, lamellas or cubes are observed depending on the composition and on the molecular weight [190, 237, 238].

There is a considerable body of work concerning dielectric spectroscopy on block copolymers [241–255]. Therefore only the most important aspects will be summarized. Discussing the dielectric properties of copolymers one can focus on the global chain dynamics which proves greater length scales or on local segmental fluctuations. The latter is discussed at first considering mainly diblock copolymers.

Segmental Motion (α-relaxation). As for miscible blends a considerable broadening of the dielectric α-relaxation compared to the corresponding homopolymers is observed in the disordered state [241, 245, 251]. In the fluctuation approach to copolymer melts [240] a considerable amount of concentration fluctuations are possible in the disordered state which should increase with increasing κN. Therefore also for disordered copolymer melts the increased width of the α-relaxation should be related to concentration fluctuations in the sense of the approach developed for blends [224] (see Sect. 7.4.3.2).

The average segmental dynamics should be influenced by both segments characterized by their monomeric friction coefficients. Figure 7.35 shows the relaxation time τ_α for the α-relaxation of a poly(cis-1,4-isoprene)-b-polystyrene (PI-b-PS) diblock copolymer in the disordered state vs molecular weight of the polyisoprene block which reveals the composition (fixed molecular weight of the PS block) [245]. With increasing PI content τ_α decreases strongly because the monomeric friction coefficient of PI is much lower than that of PS. In the limiting case these data correspond to τ_α of PI-b-PS diblock copolymers in the phase separated state [246]. The absolute values are slightly slower than for pure poly (cis-1,4-isoprene) indicating a small partial mixing of isoprene and styrene segments even in the phase separated state.

If the slow concentration fluctuations in the disordered state are larger, careful investigations have shown two segmental relaxation processes for a PI-b-PS [244] and a poly(cis-1,4-polyisoprene)-b-poly(1,2-butadien) diblock copolymer [243]. This is observed as well for a PS-b-PI-b-PS-b-PI tetrablock copolymer which does not undergo any phase separation [256].

Disordered diblock copolymers exhibit two distinct glass transitions close to the glass transition temperatures of the constituent homopolymers. If both monomeric units have a dipole moment two α-relaxation processes can be observed in the ordered state as for phase separated blends. If one component is nearly dielectric invisible (e.g. polystyrene) the combination of dielectric spectroscopy with another method like light scattering can be quite useful to investigate the α-relaxation of blocks. In the ordered state sometimes a speeding up of the α-relaxation is observed close to T_g for the nanodomains with the higher glass transition temperature [242, 257]. This is accompanied by a weaker temperature dependence than the VFT one measured for the corresponding homopolymer. Quite similar results are found for the dynamics of molecules in confining geometries (see Chap. 6). Thus one can argue that the structure formed in ordered copolymers acts as a kind of confinement on the molecular motions [242].
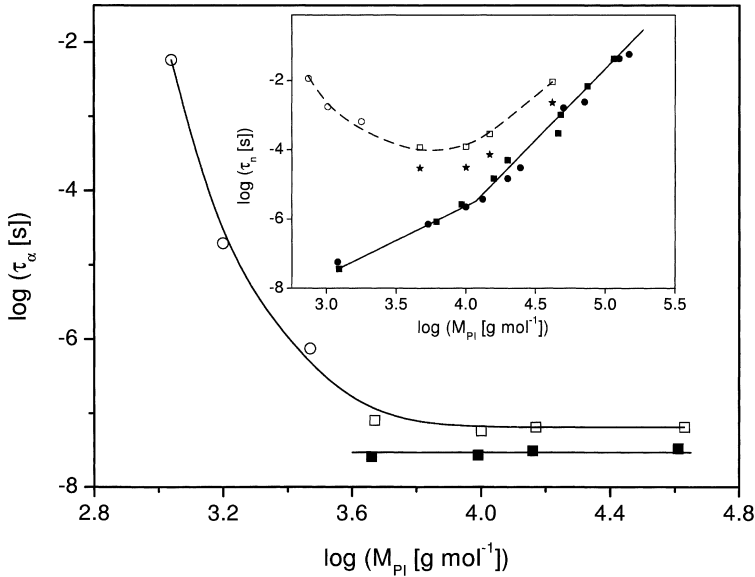
Fig. 7.35. τ_α vs molecular weight M_{PI} of the PI-block for PI-*b*-PS diblock copolymers at $T = 273$ K: *open circles* – disordered state [245], *open squares* – ordered state [246], *filled squares* – pure poly (*cis*-1,4-isoprene) [246]. *Lines* are guides for the eyes. The *inset* shows τ_n vs M_{PI} for PI-*b*-PS diblock copolymers at $T = 320$ K: *open circles* – disordered state [245], *open squares* – ordered state [246], *filled squares* – [234] and *filled circles* – [22] pure poly (*cis*-1,4-isoprene). For the *solid lines* see Fig. 7.34. The *dashed line* is a guide for the eyes. Stars are the relaxation times for the normal mode in the ordered state divided by 4

Global Chain Dynamics (Normal Mode Relaxation). For block copolymers having a Type-A part like the PI-*b*-PS systems in addition to the segmental relaxation also the global chain motion of the Type-A block can be studied by dielectric spectroscopy. The inset of Fig. 7.35 compares the relaxation time τ_n for the PI-block of a PI-*b*-PS copolymers with that of pure poly(*cis*-1,4-isoprene). In the disordered state τ_n decreases with increasing polyisoprene content [245]. At first glance this can be attributed only to the reduction of the monomeric friction coefficient due to the increasing isoprene content. However, a careful analysis of τ_n with respect to the corresponding α-relaxation results in an additional slowing down of the global chain dynamics. This can be understood by considering that the segmental motion proves local fluctuations whereas the normal mode process averages over larger length scales [245]. Furthermore an unexpected temperature dependences of τ_n is observed. Close to T_g of the system a bend from a VFT-like to a weaker temperature dependence is observed [245]. It is argued that this effect is due to the different freezing of PS and PI-rich nanodomains which are created by slow composition fluctuations. This line of argumentation is also supported by a light scattering study [244]. A careful analysis of the molecular weight dependence of the dielectric strength provides evidence that the conformation of the chains deviates from that of a Gaussian coil even in the disordered state.

In the phase separated state the molecular weight dependence of τ_n follows that of the bulk poly(*cis*-1,4-isoprene) but the absolute value is slower [246] (see inset of Fig. 7.35). This can be understood considering that the phase separation is not complete. Regarding the boundary of PS and PI phase separated regions as stiff a factor of 4 should be observed between the relaxation times the homo- and the block copolymer (see Eq. 7.41). The observed ratio is only a little bit larger (see inset of Fig. 7.35). This is also observed for another PI-*b*-PS diblock system [248] and for a triblock copolymer [253]. An analysis of the distribution function of the relaxation times of the normal mode relaxation which is broader than for the homopolymers reveals a spatial heterogeneity of the global chain motion [246, 248] also due to slow composition fluctuations [251].

To study the influence of the phase separation on the global chain dynamics directly a PS-*b*-PI diblock copolymer was investigated having a T_{ODT} in a frequency and a temperature window which is accessible by X-ray and dielectric spectroscopy [248]. Close to the T_{ODT} in the weak segregation limit a speeding up of τ_n compared to its extrapolated temperature dependence in the disordered state is observed. This can be quantitatively described by a free volume model of the monomeric friction coefficient which depends on composition. The stretching of the chain at the phase transition was directly observed, too. A more recent investigation [258] shows that the behaviour close to the ODT can be more complex in the disordered as well as in phase separated state. Furthermore an investigation of the normal mode relaxation in a PS-PI-PS triblock copolymer in the disordered state with a well defined laminar structure shows that the phase boundaries are not completely stiff but fluctuate [252].

Dielectric investigations on more complex block copolymer architectures can be found in [259–261]. This includes also studies of blends of copolymers with constituent homopolymers [262] and dielectric studies of solutions as well [247, 255].

7.4.4.3
Dendrimers

Dendrimers are a novel type of macromolecular architecture which opens new perspectives in material science [263]. They are distinguished from other types of macromolecules by their well defined highly branched structure. Starting from a central point with a certain functionality f_{Den} linear segments of uniform length are attached. The end of each block presents a new branching point where the addition of each branching layer completes a generation g_{Den}. In this nomenclature $g_{Den} = 0$ represents only the functional core and f_{Den} arms.

Dielectric investigation on dendritic model systems are sparse up to now [264–268]. Depending on the core, the generation and the nature of the terminal groups dendrimers can have a complex supramolecular structure. For instance carbosilane dendrimers with flexible perfluorinated end groups can have a liquid crystalline ($g_{Den} = 1$) or amorphous structure ($g_{Den} > 1$) [264]. Therefore the dielectric properties are also complex. In general an α-relaxation is observed [264, 265] which is related to the dynamic glass transition. The temperature de-

pendence of the relaxation time exhibits a VFT-like behaviour. Moreover a splitting of the single α-relaxation into two branches is observed [264] which may indicate a para liquid crystalline structure (see Chap. 10). In addition to the α-process a β-relaxation assigned to local motional processes can be measured [264–266]. A careful analysis allows one to distinguish between different end groups [265, 266]. This was also possible for hyperbranched polyesters [269].

For dendrimers with mesogenic end groups a characteristic liquid crystalline relaxation pattern was observed [267, 268] (see Chap. 10).

7.4.4.4
Networks

In general the segmental dynamics of crosslinked polymers is nearly identical to that of amorphous uncrosslinked systems with the exception that the α-relaxation shows a considerable broadening compared to the corresponding uncrosslinked system (see for instance Fig. 7.16b). A more interesting case is the situation where the global chain can be proved and a comparison between entanglements (physical crosslinks) and covalent bonded networks can be made. This was done by end-linking linear and three armed poly(oxypropylene) as a Type-A polymer [270]. It was found that the molecular dynamics between covalent cross-links and entanglements is nearly identical but is changed by end-linking.

Another interesting case are thermoreversible networks. In such systems the crosslinks are not fixed and can be changed by temperature. The macroscopic properties of these networks are governed by the dynamics of this reversible junctions. On timescales shorter than the life of the junctions, the network shows the viscoelastic properties of a covalent bonded system whereas at longer times only entanglements determine the mechanical behaviour. Dielectric investigation on such a model system are carried out for polybutadiene where a low concentration of 4-phenylurazol units (PU) are attached to the polymer chain [271]. Thermoreversible junctions are formed by binary hydrogen bond complexes of two PU units. The overall relaxation will be governed by the lifetime of the binary complex and the chain dynamics as predicted in the framework of a hindered reptation theory [272]. The corresponding relaxation process was detected by both mechanical [273] and dielectric spectroscopy [271]. The observed differences between the mechanical and the dielectric results can be understood by a recent theoretical approach [274].

7.5
Conclusion

Because of the very broad accessible frequency range dielectric spectroscopy is a powerful method to investigate the molecular dynamics of polymeric systems which take place on a hierarchy of different length and timescales. Depending on the polymer under investigation local relaxation processes due to molecular

groups, the segmental relaxation on a larger spatial scale and the global chain dynamics corresponding to the size of the whole macromolecule can be studied. Moreover the different kinds of molecular motions can be taken as a probe for structure of the system under investigation.

Appendix. Shape Parameter *m* and *n* for Different Monomers and Polymers: Coordinates for Fig. 7.13

Nr.	Material	$T[K]$	m	n	Ref.
1	Poly(methyl acrylate)	303.2	0.8	0.254	[3]
2	Poly(isobutyl methacrylate)	375.9	0.724	0.354	[3]
3	Poly(n-hexyl methacrylate)	305.8	0.678	0.409	[3]
4	Poly(n-butyl methacrylate)	332.1	0.676	0.356	[3]
5	Poly(nonyl methacrylate)	315.9	0.790	0.411	[3]
6	Poly(cyclohexyl methacrylate)	394.2	0.701	0.215	[3]
7	Polyacetaldehyde	276.6	0.699	0.508	[276]
8	Polystyrene	>377.0	0.75	0.320	[277]
9	Poly(methyl methacrylate)	345.1	0.572	0.213	[278]
10	Oligo(methyl methacrylate)	283.2	0.552	0.259	[278]
11	Oligo(vinyl acetate)	275.9	0.674	0.309	[278]
12	Poly(*p*-chloro styrene)	412.2	0.733	0.389	[279]
13	Poly(*o*-chloro styrene)	>404	0.850	0.340	[277]
14	Poly(para-chloro styrene)	>366	0.600	0.200	[280]
15	Copolymer from phenyl methacrylate and acrylnitrile	418.1	0.940	0.311	[280]
16	Poly(bisphenol-A-carbonate)	437	0.795	0.225	[124]
17	Poly(vinyl formal)	403.1	0.584	0.458	[281]
18	Poly(vinyl acetal)	373.1	0.782	0.296	[281]
19	Poly(vinyl butyral)	358.1	0.770	0.304	[282]
20	Epoxy resin 1	373.1	0.237	0.219	[283]
21	Epoxy resin 2	291.1	0.506	0.247	[283]
22	Epoxy resin 3	328.1	0.497	0.133	[283]
23	Poly(vinyl octanoate)	267.1	0.886	0.424	[284]
24	Poly(vinyl decanate)	270.9	0.770	0.493	[284]
25	Poly(bisphenol-A-isophthalate)	464.1	0.607	0.261	[124]
26	PET amorphous	350.8	0.810	0.370	[203]
27	PET crystalline, 29%	361.4	0.360	0.360	[203]
28	Polyurethane 1	264.9	0.485	0.175	[139]
29	Polyurethane 2	304.4	0.435	0.150	[139]

30	Polyurethane 3	341.3	0.540	0.285	[139]
31	Poly(vinyl acetate)	342	0.875	0.465	[121]
32	Glycerol	200	0.97	0.58	[285]
33	Propylene glycol	175	1	0.61	[285]
34	Salol	290	1	0.8	[286]
35	Propylene carbonate	175	1	0.7	[286]

List of Abbreviations and Symbols

b	Kuhn segment length
c	Concentration
c^*	Overlapping concentration
C_∞	Characteristic ratio
C_1, C_2	Parameters of the WLF-equation
d	Thickness of the amorphous layers in semicrystalline polymers
D	Self diffusion coefficient
D_{Con}	Diffusion coefficient for conformational states
E_A	Activation energy, barrier heights
g, g_{intra}, g_{inter}	Dipolar correlation coefficients
ΔG_M	Free energy of mixing
k_B	Boltzmann constant, $k_B = 1.380662 \times 10^{-23}$ J K^{-1}; $k = R/N_A$
l	Bond length in simple chain models
L	Long period in semicrystalline polymers
m, n	Low and high frequency slope of the HN-function, $m = \beta, n = \beta\gamma$
M, M_N, M_W	Molecular weight, number average, weight average
M_C	Critical molecular weight for the formation of entanglements or the disappearance of chain end effects
n_A	Avrami exponent
N	Number of bonds or beads in simple chain models; degree of polymerisation
N_A	Avogadro number, $(N_A = 6.022 \times 10^{23}$ mol$^{-1})$
$\boldsymbol{P}$	Polarization
$\boldsymbol{r}; \langle r^2 \rangle, \langle r^2 \rangle_0$	End-to-end vector of a chain; mean quadratic end-to-end vector; the index 0 refers to the undisturbed dimension
$\langle r(0)r(t) \rangle$	Time correlation function of the end-to-end vector
R	Gas constant $R = 8.314$ kJ mol^{-1}
ΔS_M	Mixing entropy
t_C	Crystallization time
T	Temperature
T_0	Vogel temperature, ideal glass transition temperature
T_g	Glass transition temperature
T_{ODT}	Order-to-Disorder Transition temperature
$\tilde{T}_i$	Transfer matrix in the RIS model
x_c	Degree of crystallinity
α	Expansion coefficient

β, γ	Shape parameter of the HN-function
θ, ϕ, γ	Bond and rotational angle of a model chain, γ-valence angle, $\theta = 180\text{-}\gamma$
$\Gamma()$	Gamma function
$\delta\varepsilon$	Change of $\Delta\varepsilon$ during crystallization
$\varepsilon^*, \varepsilon', \varepsilon''$	Complex dielectric function, real and imaginary part
$\Delta\varepsilon_i$	Dielectric relaxation strength, $i = \beta, \alpha, n$, Rod for the different processes
$\Delta\varepsilon_{R,i}$	Normalized dielectric relaxation strength ($i = \alpha, \beta$)
ζ	Monomeric friction coefficient
η	Viscosity
η_S	Solvent viscosity
$[\eta]$	Intrinsic viscosity
κ	Flory/Huggins interaction parameter
λ_i	Eigenvalues of the Zimm model [39]
Λ_i	Legendre polynomial Λ_i of order i
$\boldsymbol{\mu}$	Dipole moment
ν	Frequency
ν_{pi}	Relaxation rate at maximal loss, $i = \beta, \alpha, n$
$\nu_{\infty i}$	Preexponential factor, $i = \beta, \alpha, n$
ν_{Coil}	Scaling exponent
τ_p	Relaxation time of the p-th mode in the Rouse or Reptation model
τ_{HN}	Relaxation time of the HN-function
τ_{Crys}	Time constant for crystallization
CRR	Cooperatively rearranging region
RAP	Rigid amorphous phase
PDMS	Poly(dimethyl siloxane)
PEN	Poly(ethylene-2,6-naphthalene dicarboxylate)
PET	Poly(ethylene terephthalate)
PI	Poly(*cis*-1,4-isorene)
PPG	Poly(propylene glycol)
PS	Polystyrene
PVAC	Poly(vinyl acetate)
PVME	Poly(vinyl methylether)
VFT	Vogel/Fulcher/Tammann
WLF	Williams/Landel/Ferry

References

1. Fuoss RM, Kirkwood JG (1941) J Am Chem Soc 63:385
2. McCrum NG, Read BE, Williams G (1967) Anelastic and dielectric effects in polymeric solids. Wiley, New York (reprinted by Dover Publications 1991)
3. Ishida Y, Yamafuji K (1961) Kolloid Z 177:97; Ishida Y, Matsuo M, Yamafuji K (1969) Kolloid Z 180:108; Ishida Y (1969) J Polym Sci A-2 7:1835
4. Hedvig P (1977) Dielectric spectroscopy of polymers. Adam Hilger, Bristol
5. Karasz FE (ed) (1972) Dielectric properties of polymers. Plenum, New York

6. Blythe AR (1979) Electrical properties of polymers. Cambridge University Press, Cambridge
7. Adachi K, Kotaka T (1993) Prog Polym Sci 18:585
8. Riande E, Saiz E (1992) Dipole moments and birefringence of polymers. Prentice Hall, Englewood Cliffs, New Jersey
9. Williams G (1979) Adv Polym Sci 33:60
10. Williams G (1989) In: Allen G, Bevington JC (eds) Comprehensive polymer science, vol II. Pergamon Press; Williams G (1993) In: Thomas EL (ed) Structure and properties of polymers, vol 12. Materials Science & Technology Series, p 471, VCH Publications
11. Runt JP, Fitzgerald JJ (eds) (1997) Dielectric spectroscopy of polymeric materials. American Chemical Society, Washington, DC
12. Flory JP (1989) Statistical mechanics of chain molecules. Hanser Verlag, München
13. Volkenstein MV (1963) Configurational statistics of polymeric chains. Wiley Interscience, New York
14. Vogel O (1996) Pure Appl Chem A33:963; Vogel O, Jaycox GD (1999) Prog Polym Sci 24:3
15. de Gennes PG (1979) Scaling concepts in polymer physics. Cornell University Press, Ithaca, New York
16. Mattice WL, Suter UW (1994) Conformational theory of large molecules; the rotational isomeric state model in macromolecular science. Wiley Intersience, New York
17. Flory JP (1974) Macromolecules 7:381
18. Cotton JP, Decker D, Benoit H, Farnoux B, Higgins J, Jannink G, Ober R, Picot C, des Cloizeaux J (1974) Macromolecules 7:863; Kirste RG, Kruse WA, Ibel K (1975) Polymer 16:120
19. Elias HG (1990) Makromoleküle. Hüthig & Wepf, Basel Heidelberg New York
20. Debye P (1929) Polar molecules. Chemical catalog, reprinted by Dover
21. Stockmayer WH (1967) Pure Appl Chem 15:539; Stockmayer WH, Burke JJ (1969) Macromolecules 2:647
22. Adachi K, Kotaka T (1985) Macromolecules 18:466
23. Block H (1979) Adv Polym Sci 33:94
24. Debye P, Bueche F (1951) J Chem Phys 7:589
25. Shatzki TF (1962) J Polym Sci 57:496
26. Valeur B, Jarry JP, Geny F, Monnerie J (1975) J Polym Sci Polym Phys Ed 13 667; Valeur B, Monnerie J, Jarry JP (1975) J Polym Sci Polym Phys Ed 13:675
27. Hall C, Helfand E (1982) J Chem Phys 77:3275
28. Skolnik J, Yaris R (1982) Macromolecules 15:1041
29. Abramowitz M, Stegun IA (1965) Handbook of mathematical functions. Dover Press, New York
30. Viovy JL, Monnerie L, Brochon, JC (1983) Macromolecules 16:1845
31. Hateley F, Cox M (1973) Polymer 18:1141
32. Waldow DA, Johnson BS, Ediger MD, Kitano T, Ito K (1989) Macromolecules 22:1345
33. Mashimo S, Chiba A (1973) Polymer J 5:41
34. Helfand E, Wassermann ZR, Weber TA (1980) Macromolecules 13:526
35. Adolf AD, Ediger MD (1991) Macromolecules 24:5834; Adolf AD, Ediger MD (1992) Macromolecules 25:1074
36. Rouse PE (1953) J Chem Phys 21:1272
37. Ferry JD (1980) Viscoeleastic properties of polymers, 3rd edn. Wiley, New York
38. Zimm BH (1956) J Chem Phys 24:269
39. North AM (1972) Chem Soc Rev 1:49
40. Mashimo S (1997) In: Runt JP, Fitzgerald JJ (eds) Dielectric spectroscopy of polymeric materials. ACS-Books, Washington DC, p 201
41. Glowinkowski S, Gisser DJ, Ediger MD (1990) Macromolecules 23:3520
42. Ediger MD (1991) Annu Rev Phys Chem 42:225
43. Adolf BD, Ediger MD, Kitono T, Ito K (1992) Macromolecules 25:867
44. Ono K, Ueda K, Yamamoto M (1994) Polymer J 26:1345
45. Bahar I, Erman B (1987) Macromolecules 20:1368

46. Kramers HA (1940) Physica 7:284
47. Helfand EJ (1971) J Chem Phys 54:4651
48. Mashimo S (1976) Macromolecules 9:91
49. Davies M, Williams G, Loveluck GD (1960) Z Elektrochem 64:575
50. Matsumo K, Stockmayer WH, Mashimo S (1982) Macromolecules 15:606
51. Cole RH, Mashimo S, Windsor P (1980) J Chem Phys 84:786
52. Mashimo S, Windsor P, Cole RH, Matsuo K, Stockmayer WH (1983) Macromolecules 16:965
53. Lister DG, Macdonald JN, Owen NL (1998) Internal rotation and inversion. Academic, Orlando, chap 5, p 105
54. Adachi K (1997) In: Runt JP, Fitzgerald JJ (eds) Dielectric spectroscopy of polymeric materials. ACS-Books, Washington DC, p 261
55. Cohen MH, Turnbull D (1959) J Chem Phys 31:1164; Doolittle AK (1951) J Appl Phys 22:1471
56. Mashimo S (1977) J Chem Phys 67:2651
57. Floudas G, Higgins JS, Kremer F, Fischer EW (1992) Macromolecules 25:4955
58. Bahar I, Erman B, Kremer F, Fischer EW (1992) Macromolecules 25:816
59. Yada M, Nakazawa M, Urakawa O, Morishima Y, Adachi K (2000) Macromolecules 33:3368
60. Nakazawa M, Urakawa O, Adachi K (2000) Macromolecules 33:7898
61. Jones AA, Stockmayer WH, Molinari RJ (1976) J Polym Sci Polym Symp 54:227
62. Patel SS, Takahashi KM (1992) Macromolecules 25:4382
63. Urakawa O, Adachi K, Kotaka T (1993) Macromolecules 26:2042
64. Urakawa O, Adachi K, Kotaka T, Takemoto Y, Yasuda H (1994) Macromolecules 27:7410
65. Baysal B, Stockmayer WH (1993) J Mol Liq 56:175
66. Adachi K, Kotaka T (1988) Macromolecules 21:157
67. Adachi K, Imanishi Y, Kotaka T (1989) J Chem Soc Faraday Trans 1 85:1065
68. Muthukumar M, Freed KF (1978) Macromolecules 11:843; Muthukumar M (1984) Macromolecules 17:971
69. de Gennes PG (1976) Macromolecules 9:594
70. Bur AJ, Roberts DE (1969) J Chem Phys 51:406
71. Bur AJ, Fetters LJ (1976) Chem Rev 76:727
72. Takada S, Itou T, Chikiri H, Einaga Y, Teramoto A (1989) Macromolecules 22:973
73. Block H, Hayes EF, North AM (1970) Trans Faraday Soc 66:1095
74. Eisenberg H (1970) Faraday Soc 55:572
75. Kirkwood JG, Auer PL (1951) J Chem Phys 19:281; Rieseman J, Kirkwood JG (1950) J Chem Phys 18:512
76. Moscicki JK, Aharoni SM, Williams G (1981) Polymer 22:571
77. Moscicki JK, Aharoni SM, Williams G (1981) Polymer 22:1361
78. Moscicki JK, Aharoni SM, Williams G (1982) Macromolecules 15:1982
79. Moscicki JK (1992) In: Collyer AA (ed) Liquid crystal polymers – from structure to applications. Elsevier, p 143
80. Heijboer J (1978) In: Meier DJ (ed) Molecular basis of transition and relaxation. Gordon and Branch, New York
81. Buerger DE, Boyd RH (1989) Macromolecules 22:2649
82. Katana G, Kremer F, Fischer EW, Plaetscke R (1993) Macromolecules 26:3075
83. Corezzi S, Campani E, Rolla AP, Capaccioli S, Fioretto D (1999) J Chem 111:9343
84. Tetsutani T, Kakizaki M, Hideshima T (1982) Polymer J 14:305
85. Tetsutani T, Kakizaki M, Hideshima T (1982) Polymer J 14:471
86. Gomes Ribelles JL, Diaz Calleja RJ (1985) J Polym Sci Polym Phys Ed 23:1297
87. Garwe F, Schönhals A, Beiner M, Schröter K, Donth E (1996) Macromolecules 29:247
88. Zeeb S, Höring S, Garwe F, Beiner M, Schönhals A, Schröter K, Donth E (1997) Polymer 38:4011
89. Hempel E, Beiner M, Renner T, Donth E (1996) Acta Polym 47:525
90. Beiner M, Schröter K, Reissig S, Hempel E, Donth EJ (1999) Macromolecules 32:6278
91. Johari GP, Goldstein MJ (1970) J Chem Phys 53:2372

92. Johari GP (1973) J Chem Phys 28:1766
93. Anderson PW (1995) Science 267:1615
94. Angell CA (1995) Science 267:1924
95. Havriliak S, Havriliak S (1992) Polymer 33:938
96. Matsuo M, Ishida Y, Yamafuji K, Takayanagi M, Irie F (1965) Kolloid-Z und Z für Polymere 201:7
97. Colmenero J, Arbe A, Alegria A (1993) Physica A 201:447
98. Schönhals A, Kremer F (1994) J Non-Cryst Solids 172/174:336
99. Coburn J, Boyd RH (1986) Macromolecules 19:2238
100. Hofmann A, Kremer F, Fischer EW (1993) Physica A 201:106
101. Hardy L, Stevenson I, Boiteux G, Seytre G, Schönhals A (2001) Polymer 42:5679
102. Kremer F, Hofmann A, Fischer EW (1992) ACS-Polymer Preprints 33:96
103. Williams G, Watts DC (1971) Trans Faraday Soc 67:2793
104. Williams G, Edwards DA (1966) Trans Faraday Soc 62:1329
105. Sasabe H, Saito S (1968) J Polym Sci Part A-2 6:1401
106. Kulik AS, Beckham HW, Schmidt-Rohr K, Radloff D, Pawelzik U, Boeffel C, Spiess HW (1994) Macromolecules 27:4746
107. Beiner M (2001) Macromol Chem Rapid Comm 22:869
108. Vogel H (1921) Phys Z 22:645
109. Fulcher GS (1925) J Am Ceram Soc 8:339
110. Tammann G, Hesse W (1926) Z Anorg Allg Chem 156:245
111. Grest GS, Cohen MH (1981) Adv Chem Phys 48:455
112. Adam G, Gibbs JH (1965) J Chem Phys 43:139
113. Donth EJ (1982) J Non-Cryst Solids 53:325
114. Donth EJ (1992) Relaxation and thermodynamics in polymers. Glass transition. Akademie-Verlag, Berlin
115. DiMarzio EA (1981) Ann NY Acad Sci 371:1; Gibbs JH, DiMarzio EA (1958) J Chem Phys 28:373; DiMarzio EA, Gibbs JH (1963) J Polym Sci A1:1417
116. Angell CA, Rao KJ (1972) J Chem Phys 57:470
117. Richert R, Angell CA (1998) J Chem Phys 108:9016
118. Schönhals A (2002) in preparation
119. Schönhals A, Kremer F, Hofmann A, Fischer EW, Schlosser E (1993) Phys Rev Lett 70:3459
120. Alegria A, Colmenero J, del Val JJ, Barandiaran JM (1985) Polymer 26:913
121. Nozaki R, Mashimo S (1987) J Chem Phys 87:2271
122. Schlosser E, Schönhals A (1991) Polymer 32:2135
123. Schönhals A (2001) Europhys Lett 56:815
124. Havriliak S, Negami S (1966) J Polym Sci Part C 16:99; Havriliak S, Negami S (1967) Polymer 8:161
125. Jonscher AK (1983) Dielectric relaxation in solids. Chelsea Dielectrics Press, London
126. Sillescu H (1999) J Non-Cryst Solids 243:81
127. Ediger MD (2000) Annu Rev Phys Chem 51:99
128. Tracht U, Wilhelm M, Heuer A, Feng H, Schmidt-Rohr K, Spiess HW (1998) Phys Rev Lett 81:2727
129. Vidal Russell E, Israeloff NE, Walther LE, Alvarez Gomariz H (1998) Phys Rev Lett 81:1461; Vidal Russell E, Israeloff NE (2000) Nature 408:695
130. Schönhals A, Schlosser E (1989) Colloid Polym Sci 267:125
131. Montroll EW, Lebowitz JL (1979) Studies in statistical mechanics. North-Holland Publishing Company, Amsterdam
132. Webman J, Klafter J (1982) Phys Rev B 26:5950
133. Dissado LA, Hill RM (1983) Proc R Soc London 390:131
134. Havriliak S, Havriliak SJ (1994) J Non-Cryst Solids 172/174:297
135. Fioretto D, Livi A, Rolla AP, Socino G, Verdini L (1994) J Phys Condens Matter 6:1
136. Matsuoka S, Ishida Y (1966) J Polym Sci Part C 14:247
137. Dobbertin J, Hensel A, Schick C (1996) J Therm Anal 47:1027; Hensel A, Dobbertin J, Schawe JEK, Boller A, Schick C (1996) J Therm Anal 46:935

138. Glatz-Reichenbach JKW, Sorriero LJ, Fitzgerald JJ (1994) Macromolecules 27:1338
139. Schlosser E, Schönhals A (1989) Colloid Polym Sci 267:133
140. Ezquerra TA, Majszczyk J, Baltà-Calleja FJ, López-Cabarcos E, Gardner KH, Hsiao BS (1994) Phys Rev B 50:6023
141. Ezquerra TA, Liu F, Boyd RH, Hsiao BS (1997) Polymer 38:5793
142. Nogales A, Ezquerra TA, Garicia JM, Baltà-Calleja FJ (1999) J Polym Sci B Polym Phys 37:37
143. Donth EJ (2001) The glass transition. Springer, Berlin Heidelberg New York
144. Williams G, Watts DC (19971) In: Nuclear magnetic resonance, basics, principles and progress, vol 4. NMR of polymers. Springer, Berlin Heidelberg New York
145. Beiner M, Kahle S, Hempel E, Schröter K, Donth EJ (1998) Europhys Lett 44:321
146. Garwe F, Schönhals A, Beiner M, Schröter K, Donth EJ (1994) J Phys Condens Matter 6:6941
147. Kahle S, Korus J, Hempel E, Unger R, Höring S, Schröter K, Donth EJ (1997) Macromolecules 30:7214
148. Sudo S, Shimomura M, Saito T, Shinyashiki N (2001) 1st International Conference on Dielectric Spectroscopy in Physical, Chemical and Biological Applications, Jerusalem, March 12–15
149. Wu L (1991) Phys Rev B 43:9906
150. Matsuoka S, Johnson GE (1994) ACS-PMSE Preprints 70:369
151. Pschorn U, Rössler E, Sillescu H, Kaufmann S, Schaefer D, Spiess HW (1991) Macromolecules 24:389
152. Rössler E (1992) Phys Rev Lett 69:1620
153. Murty SSN (1989) J Mol Liq 44:51
154. Rössler E (1990) Phys Rev Lett 65:1595
155. Ehlich D, Sillescu H (1990) Macromolecules 23:1600
156. Cicerone MT, Blackburn FR, Ediger MD (1995) J Chem Phys 102:471
157. Fujara F, Geil B, Sillescu H, Fleischer G (1992) Z Phys B Condensed Matter 88:195
158. Schönhals A (1993) Macromolecules 26:1309
159. Doi M, Edwards SF (1986) The theory of polymer dynamics. Clarendon, Oxford
160. Adachi K, Kotaka T (1985) Macromolecules 18:466
161. Boese D, Kremer F (1990) Macromolecules 23:829
162. Schönhals A (1996) Habilitation thesis. Technical University Berlin
163. Matsuoka S (1992) Relaxation phenomena in polymers. Hanser Verlag, München
164. Doi M (1983) J Polym Sci Polym Phys Ed 21:667
165. Klein J (1978) Macromolecules 11:852
166. Graessley WW (1982) Adv Polym Sci 47:68
167. Appel M, Fleischer G, Kärger J, Chang I, Fujara F, Schönhals A (1997) Colloid Polym Sci 275:187
168. Fleischer G, Appel (1995) Macromolecules 28:7281
169. Nicolai T, Floudas G (1998) Macromolecules 31:2578
170. Adachi K, Hirano H (1998) Macromolecules 31:3958
171. Plazek DJ, O'Rouke M (1971) J Polym Sci A2 9:209
172. Plazek DJ (1980) Polymer J (Japan) 12:43
173. Roland CM, Ngai KL, Santangelo PG, Qiu XH, Ediger MD, Plazek DJ (2001) Macromolecules 34:6159
174. Plazek DJ, Schlosser E, Schönhals A, Ngai KL (1993) J Chem Phys 98:6488
175. Ngai KL, Schönhals A, Schlosser E (1992) Macromolecules 25:4915
176. Ilan B, Loring RF (1999) Macromolecules 32:949
177. Adachi K, Nishi I, Itoh S, Kotaka T (1990) Macromolecules 23:2550
178. Fodor JS, Hill DA (1994) J Phys Chem 98:7674
179. Adachi K, Kotaka T (1987) J Mol Liq 36:75
180. Winter HH (1994) J Non-Cryst Solids 172/174:1158
181. Ngai KL, Rendell RW (1987) Macromolecules 20:1066
182. Ngai KL, Peng SL, Skolnick J (1992) Macromolecules 25:2184

183. Pakula T, Geiler S (1987) Macromolecules 21:2909
184. Schweitzer KS (1993) Physica Scripta T 49:99
185. Hoffman JD, Williams G, Passagglia E (1966) J Polym Sci Part C 14:173
186. Ashcraft CR, Boyd RH (1976) J Polym Sci Polym Phys Ed 14:2153
187. Boyd RH (1985) Polymer 26:323
188. Boyd RH (1985) Polymer 26:1123
189. Boyd RH, Liu F (1997) In: Runt JP, Fitzgerald JJ (eds) Dielectric spectroscopy of polymeric materials. ACS-Books, Washington DC, p 107
190. Strobl GR (1996) The physics of polymers. Springer, Berlin Heidelberg New York
191. Nogales A, Denchev Z, Sics I, Ezquerra TA (2000) Macromolecules 33:9367
192. Carius HE, Schönhals A, Guigner D, Sterzynski T, Brostow W (1996) Macromolecules 29:5017
193. Ezquerra TA, Zolotukhin M, Privalko VP, Balta-Calleja FJ, Nequlqueo G, Garcia C, de la Campa JG, de Abajo J (1999) J Chem Phys 22:10,134
194. Flory JP (1962) J Am Chem Soc 84:2857
195. Boyd RH (1983) J Polym Sci Polym Phys Ed 21:205
196. Grimau M, Laredo E, Pérez MC, Belloa (2001) J Chem Phys 114:6417
197. Dobbertin J (1995) Untersuchungen zum Einfluß der Größe der glasbildenden Bereiche auf das dielektrische Relaxationsverhalten von teilkristallinem Polyethylterephthalat (PET)
198. Huo P, Cebe P (1992) Macromolecules 25:902
199. Huo P, Cebe P (1992) J Polym Sci Phys Ed 30:239
200. Huo P, Cebe P (1993) Polymer 34:696
201. Cebe P, Huo P (1994) Thermochim Acta 238:229
202. Kalika DS, Krishnaswamy RK (1993) Macromolecules 26:4252
203. Schlosser E, Schönhals A (1989) Colloid Polym Sci 267:963
204. Williams G (1979) Adv Polym Sci 33:60
205. Donth E, Hempel E, Schick C (2000) J Phys Condens Matter 12:L281
206. Frübing P, Blischke D, Gerhard-Multhaupt R, Salah Khalil M (2001) J Appl Phys D 30:3051
207. Kakizaki M, Kakudate T, Hideshima T (1985) J Polym Sci Phys Ed 23:787; Kakizaki M, Kakudate T, Hideshima T (1985) J Polym Sci Phys Ed 23:809
208. Mansfield M, Boyd RH (1978) J Polym Sci Phys Ed 16:1227
209. Schmidt-Rohr K, Spieß HW (1991) Macromolecules 24:5288
210. Hu WG, Boeffel C, Schmidt-Rohr K (1999) Macromolecules 32:1611
211. Simon GP, Schönhals A (2002) In: Polymeric blends. ACS-books, Washington DC (in press)
212. Runt JP (1997) In: Runt JP, Fitzgerald JJ (eds) Dielectric spectroscopy of polymeric materials. ACS-Books, Washington DC, p 283
213. Zetsche A, Kremer F, Jung H (1990) Polymer 31:1988
214. Se K, Takayanagi O, Adachi K (1997) Macromolecules 30:4877
215. Hayakawa T, Adachi K (2000) Macromolecules 33:6834
216. Hayakawa T, Adachi K (2000) Macromolecules 33:6840
217. Sperling LH (1986) Introduction to physical polymer science. Wiley, New York
218. Wetton RE, MacKnight WJ, Fried JR, Karasz FE (1978) Macromolecules 11:158
219. Kantana G, Zetsche A, Kremer F, Fischer EW (1992) ACS Polymer Preprints 33 (1):122
220. Kantana G, Fischer EW, Hack T, Abetz V, Kremer F (1995) Macromolecules 28:27
221. Miura N, MacKnigght W, Matsuoka S, Karasz FE (2001) Polymer 40:6129
222. Fischer EW, Zetsche A (1992) ACS Polymer Preprints 33(1):78
223. Cendoya I, Alegria, A, Alberdi JM, Colmenero J, Grimm H, Richter D, Frick B (1999) Macromolecules 32:4065
224. Zetsche A, Fischer EW (1994) Acta Polym 45:168
225. Karatasos K, Valaachos G, Vlassopoulos D, Fytas G, Meier G, Du Chesne A (1998) J Chem Phys 108:5997
226. Clarson SJ, Semlyen JA, Dodgson K (1991) Polymer 32:283

227. Hogen-Esch TE, Toreki W, Butler GB (1987) ACS Polymer Preprints 28:343; Hogen-Esch TE, Toreki W, Butler GB (1987) ACS Polymer Preprints 30:129
228. Clarson SJ, Dodgson K, Semlyen JA (1985) Polymer 19:930
229. Kirst U, Kremer F, Pakula T, Hollinghurst J (1994) Colloid Polym Sci 272:1024
230. DiMarizio EA, Guttman CM (1987) Macromolecules 20:1403
231. Yang AJM, DiMarizio EA (1991) Macromolecules 24:6012
232. Adachi K, Kotaka T (1983) Macromolecules 16:1936
233. Boese D, Kremer F, Fetters LJ (1988) Makrom Chem Rapid Commun 9:367
234. Boese D, Kremer F (1990) Macromolecules 23:829
235. Boese D, Kremer F, Fetters LJ (1990) Polymer 31:1831
236. Grest GS, Kremer K, Milner ST, Witten TA (1989) Macromolecules 22:1904
237. Bates FS, Fredrickson GH (1990) Annu Rev Phys Chem 41:525 (and references therein)
238. Helfand E, Wasserman ZR (1982) In: Goodman I (ed) Developments of copolymers I. Applied Science, London
239. Leibler L (1980) Macromolecules 13:1602
240. Fredrickson GH, Helfand EJ (1987) J Chem Phys 87:697
241. Quan X, Johnson GE, Anderson EW, Bates FS (1989) Macromolecules 22:2456
242. Vogt S, Gerharz B, Fischer EW, Fytas G (1992) Macromolecules 25:5986
243. Kannetakis J, Fytas G, Kremer F, Pakula T (1992) Macromolecules 25:3484
244. Fytas G, Alig I, Rizos A, Kanetakis J, Kremer F, Roovers J (1992) ACS Polymer Preprints 33:86
245. Alig I, Kremer F, Fytas G, Roovers J (1992) Macromolecules 25:5277
246. Yao ML, Watanabe H, Adachi K, Kotaka T (1991) Macromolecules 24:2955
247. Yao ML, Watanabe H, Adachi K, Kotaka T (1992) Macromolecules 25:1699
248. Stühn B, Stickel F (1992) Macromolecules 25:5306
249. Anastasiadis SH, Fytas G, Vogt S, Gerharz B, Fischer EW (1993) Europhys Lett 26:619
250. Jian T, Anastasiadis SH, Fytas G, Adachi K, Kotaka T (1993) Macromolecules 26:4706
251. Karatasos K, Anastasiadis SH, Semenov AN, Fytas G, Pitsikalis M, Hadjichristidis N (1994) Macromolecules 27:3543
252. Alig I, Floudas G, Avgeropoulos A, Hadjichristidis N (1997) Macromolecules 30:5004
253. Kyritsis A, Pissis P, Mai SM, Booth C (2000) Macromolecules 33:4581
254. Moreno S, Rubio RG, Luengo G, Ortega F, Prolongo MG (2001) Eur Phys J E4:173
255. Adachi K, Hirano H, Freire JJ (1999) Polymer 40:2271
256. Schönhals A, Fytas G, Lodge T (in preparation)
257. Rizos AK, Fytas G, Roovers J (1992) J Chem Phys 97:6925
258. Karatasos K, Anastasiadis SH, Floudas G, Fytas G, Pispas S, Hadjichristidis N, Pakula T (1996) Macromolecules 29:1326
259. Floudas G, Paraskeva S, Hadjichristidis N, Fytas G, Chu B, Semenov AN (1997) J Chem Phys 107:5502
260. Alig I, Floudas G, Avgeropoulos A, Hadjichristidis N (1998) J Non-Cryst Solids 235/237:485
261. Floudas G, Hadjichristidis N, Iatrou H, Pakula T (1996) Macromolecules 29:3139
262. Floudas G, Mermvelitaki, Hadjichristidis N (1999) Macromolecules 32:7496
263. Newkome GR, Moorefield C, Vögtle F (1998) Dentritic molecules – concepts, synthesis, perspectives. Verlag Chemie, Weinheim, Germany; Frey H, Lach C, Lorenz K (1998) Adv Mater 10:279
264. Trahasch B, Stühn B, Frey H, Lorenz K (1999) Macromolecules 32:1962
265. Huwe A, Appelhans D, Prigann J, Voit BI, Kremer F (2000) Macromolecules 33:3762
266. Emran SK, Newkome GR, Weiss DW, Harmon JP (1999) J Polym Sci Polym Phys Ed 37:2025
267. Trahasch B, Frey H, Lorenz K, Stühn B (1999) Colloid Polym Sci 277:1186
268. Örtegren J, Tidlund J, Nykvist M, Busson P, Hult A, Sen S, Boyd RH, Gedde UW (2001) Polymer 42:10,027
269. Malström E, Liu F, Boyd RH, Hult A, Gedde UW (1997) Polymer 38:4873
270. Nicolai T, Prochazka F, Durand D (1999) Phys Rev Lett 82:863

271. Müller M, Kremer F, Stadler R, Fischer EW, Seidel U (1995) Colloid Polym Sci 273:38
272. Leibler L, Rubinstein M, Colby RH (1991) Macromolecules 24:4701
273. Müller M, Seidel U, Stadler R (1995) Polymer 36:3143
274. Müller M, Stadler R, Kremer F, Williams G (1995) Macromolecules 28:6942
275. Cowie JMG (1991) Polymers: chemistry and physics of modern materials. Chapman and Hall, London, UK
276. Strella S, Chinai SN (1958) J Polymer Sci 31:45
277. Alexandrovish PS, Karasz FE, McKnight WJ (1980) Polymer 21:488
278. Ikada E, Sugimura T, Watanabe T (1975) Polymer 15:201
279. Schlosser E (1982) Polymer Bull 8:461
280. Curtis A (1962) SPE Trans 2:82
281. Funt BL, Sutherland TH (1952) Can J Chem 30:940
282. Dittmer M (1969) PhD Thesis University Leipzig
283. Schlosser E (1968) Plaste Kautschuk 15:652
284. Bure JA (1962) PhD Thesis, Penn State University
285. Schönhals A, Kremer F, Schlosser E (1991) Phys Rev Lett 67:999
286. Schönhals A, Kremer F, Hofmann A, Schlosser E, Fischer EW (1993) Phys Rev Lett 70:3459

8 Effect of Pressure on the Dielectric Spectra of Polymeric Systems

G. Floudas

8.1
Introduction

Pressure is one of the essential thermodynamic variables that control the structure and the associated dynamics of polymers and glass-forming systems. The pressure dependence of the viscoelastic relaxation times is of paramount importance because hydrostatic pressure is encountered in the extrusion and molding processes [1]. Dielectric spectroscopy was among the first dynamic techniques to take advantage of pressure through the recognition of the fact that the dynamic state of a glass-forming system can only be completely defined if *T and P* are specified [2]. This observation motivated studies of the effect of pressure on the dielectric α- and β-processes in a number of systems in the early 1960s [3–6]. The main concern in these pioneering studies was to unravel the effect of pressure on separating mixed processes. Since then, there have been reports on the effect of pressure on the relaxations of oxidized polyethylene [7], on the plasticization of poly(ethyl methacrylate) by sorbed carbon dioxide [8] and on the dynamics of a liquid crystalline siloxane polymer [9].

However, the lack of a versatile experimental set-up has put a halt to these studies and made pressure, for a number of years, the "forgotten" variable. During the past 20 years polymer chemistry has produced an unparalleled number of polymeric compounds with unmatched physical properties ranging from polymer blends with a well-defined thermodynamic state to block copolymers with well-controlled nanostructures. Moreover, the interest in traditional fields such as polymer crystallization has been rejuvenated through the possibility of new experimental probes and novel synthesis. Pressure, however, was not applied until recently, in systems where the thermodynamic state of the system is of importance.

In this chapter we will review some of the early work in this field and provide new experimental results in systems of current interest where the thermodynamics also play a role. We will study the effect of pressure on length scales starting from the segment up to the end-to-end vector. Then we will comment on the effect of pressure on the dynamic miscibility of athermal diblock copolymers and homogeneous polymer blends. Finally, we will review recent experimental reports on the effect of pressure on the crystallization process with emphasis on the in situ monitoring of the process.

8.2
Theoretical Background

8.2.1
Transition State Theory

Eyring et al. [10] derived the rate at which species relax from A_1 to A_2 via an activated state A^* according to the scheme

$$A_1 \Leftrightarrow A^* \Leftrightarrow A_2 \qquad (8.1)$$

where A_1 and A_2 are non-activated species. From the equilibrium $A \leftrightarrow A^*$ using the condition for the chemical potentials: $\mu_A = \mu_{A*}$ and the definition of ΔV ($= V_{A*}(T,P) - V_A(T,P)$) as the difference in the molar volumes of activated and non-activated species at T and P, one can show that [10, 11]

$$\Delta V = RT \left(\frac{\partial \ln \tau}{\partial P} \right)_T \qquad (8.2)$$

Thus the linear dependence of $\ln \tau$ with P can be used to define an activation volume ΔV. As we will see below, a linear relation between $\ln \tau$ and P can result through a completely different approach.

8.2.2
Models Based on Free Volume Theories

The starting point in theories of free volume [12, 13] is the introduction of the fractional free volume, $f = V_f/V_o$, where V_f is the available or "free" volume and V_o is the total volume. The fractional free volume, which in general depends on T and P, determines the viscosity and dynamics (relaxation times) of the system above the glass transition temperature T_g. For example, according to the empirical Doolittle equation [14]

$$\eta = \eta^* \exp \left(\gamma \frac{V_o}{V_f} \right) \qquad (8.3)$$

where η^* and γ are constants (γ is very close to 1 [1]), the viscosity or the relaxation times decrease exponentially with the increase of f. For thermorheologically simple systems [1], a shift factor $\alpha = (\eta T_o \rho_o)/(\eta_o T \rho)$ or $\alpha = \tau/\tau_o$ (where η_o, ρ_o, and τ_o are the values of the viscosity, density, and relaxation times at a reference temperature T_o) can be defined which is

$$\ln a_{T,P} = \left(\frac{1}{f} - \frac{1}{f_o} \right) + \ln \left(\frac{T_o \rho_o}{T \rho} \right) \qquad (8.4)$$

where f_o is the fractional free volume at a reference temperature or pressure (in this case at T_o, P_o). In practice, the slow temperature variation of the product $T\rho$

is neglected and the following equation is mainly used

$$\ln a_{T,P} = \left(\frac{1}{f} - \frac{1}{f_o} \right) \tag{8.5}$$

According to a free volume theory [1], increasing T and P produce opposite effects on the fractional free volume and within the range where β_f is constant

$$f_{T,P} = f_o + \alpha_f (T - T_o) - \beta_f (P - P_o) \tag{8.6}$$

where $\alpha_f (= 1/V_o(\partial V_f/\partial T)_P)$ and $\beta_f (= -1/V_o(\partial V_f/\partial P)_T)$ are the thermal expansion coefficient and compressibility of the free volume, respectively. We should mention here that in general the compressibility of free volume can be different from the total compressibility. Measurements of β and calculations of β_f have shown that β_f is less than half of $\beta (= -1/V_o(\partial V_o/\partial P)_T)$ and the main part of change of volume upon compression is due to the reduction of the occupied volume [1]. On the contrary, the thermal expansion is mainly due to the increase of free volume (i.e., $\alpha \approx \alpha_f$).

According to Eq. (8.6), we can have a situation of increasing both T and P at constant free volume, then

$$\left(\frac{\partial T}{\partial P} \right)_f = \frac{\beta_f}{\alpha_f} \tag{8.7}$$

If the glass transition is regarded as controlled by relaxation processes whose rates are constant at constant fractional free volume then

$$\left(\frac{\partial T}{\partial P} \right)_\tau = \frac{\beta_f}{\alpha_f} = \frac{\Delta \beta}{\Delta \alpha} \tag{8.8}$$

where $\Delta \beta$ and $\Delta \alpha$ are, respectively, the excess compressibility and thermal expansion of the rubbery state over the glassy state. Equation (8.8) is reminiscent of the Prigogine and Defay equation ($\mathrm{d}T/\mathrm{d}P = \Delta \beta / \Delta \alpha$) [15] obtained for a second order transition and suggests that the equilibrium quantity $\mathrm{d}T/\mathrm{d}P$ and the dynamic quantity $(\partial T/\partial P)_\tau$ are related. However, the relation is not a simple one since the dynamic quantity depends strongly on τ [4]. Returning to Eq. (8.8), the meaning is that the T- or P-dependence of relaxation times at constant free volume is zero, i.e.,

$$\left(\frac{\partial \ln a_T}{\partial T} \right)_f = 0 \tag{8.9}$$

This does not necessarily mean that this holds for constant total volume since at constant total volume the fractional free volume increases (since β_f is a small part of β whereas α_f is about equal to α).

A key parameter in the discussion of the effect of P on the relaxation times is the free volume compressibility β_f. If the free volume compressibility depen-

dence is analogous to the total compressibility, then the expectation is that, it will be a decreasing function of P. For small intervals of pressure, however, we can assign a constant β_f which gives rise to the following model.

8.2.3
Model of Constant Free Volume Compressibility

For temperature variation alone, we can assume (due to the very small values of a and a_f) that f increases linearly with T as $f = f_o + a_f (T-T_o)$, which together with Eqs. (8.3) and (8.5) result in the well-known Williams-Landel-Ferry (WLF) equation [16]

$$\ln a_T = -\frac{c_1 (T - T_o)}{c_2 + (T - T_o)}$$

(8.10)

where $c_1 = 1/f_o$ and $c_2 = f_o/\alpha_f$. Defining $T_\infty = T_o - c_2$, at which $\ln a_T$ becomes infinite, results in the Vogel-Fulcher-Tammann (VFT) equation

$$\ln \tau = A_T + \frac{B_T}{T - T_\infty}$$

(8.11)

where $A_T = \ln \tau_o - c_1$ and $B_T = c_1 c_2$.

For pressure variation alone, i.e., at constant T and for the limited pressure range where β_f can be considered as constant, the variation of f with P can be expressed as $f_P = f_o - \beta_f (P - P_o)$. With the use of Eqs. (8.3) and (8.5) the following shift factor is obtained for pressure-dependent measurements

$$\ln a_P = \frac{\dfrac{1}{f_o}(P - P_o)}{\dfrac{f_o}{\beta_f} - (P - P_o)}$$

(8.12)

which is reminiscent of the corresponding WLF equation ($c_1 = 1/f_o, c_2 = f_o/\beta_f$). At vanishing pressure, the above equation reduces to $(\partial \ln a_P/dP)_T = \beta_f/f_o^2$, and shows that the effect of P on t will become insignificant at high T due to the dominance of the f_o^2 term. In analogy to the T-variation, we can define a pressure P_∞ where the fractional free volume is equal to zero: $P_\infty = P_o + f_o/\beta_f$ which results in

$$\ln a_P = \frac{1}{\beta_f (P_\infty - P)} - \frac{1}{f_o}$$

(8.13)

and

$$\ln \tau = A_P + \frac{B_P}{P_\infty - P}$$

(8.14)

where $A_P = \ln \tau_o - 1/f_o$ and $B_P = c_1 c_2$. Notice the similarity of the $\tau(T)$ and $\tau(P)$ dependencies.

8.2.4
Models of Variable Free Volume Compressibility

Models have been proposed which take into account that the free volume compressibility can decrease significantly with increasing pressure. Two such models are discussed here: the exponential and Tait models from the dependence of the shift factor.

The *exponential model* is based on the frequently observed linear dependence of the logarithm of the shift factor on pressure, i.e.,

$$\ln a_P = \Lambda(P - P_o) \tag{8.15}$$

where $\Lambda \neq \Lambda(P)$. Using this form for the shift factor and Eq. (8.5) results in the following expression for the dependence of the fractional free volume on pressure [17]:

$$f_P = \frac{f_o \dfrac{1}{f_o \Lambda}}{\dfrac{1}{f_o \Lambda} + P - P_o} \tag{8.16}$$

where $\Pi = 1/f_o \Lambda$ is an empirical constant related to the internal pressure. The compressibility of free volume [1]:

$$\beta_f = -\left(\frac{\partial f_P}{\partial P}\right)_T = \frac{f_P}{\dfrac{1}{f_o \Lambda} + P - P_o} \tag{8.17}$$

is now a decreasing function of pressure. Interestingly, the non-linear f_P dependence creates a linear dependence of $\ln a_P$ on P. Due to the form of Eq. (8.15) being similar to Eq. (8.2), the coefficient Λ has been interpreted as an apparent activation volume, i.e., $\Lambda = \Delta V/RT$.

The *Tait model* assumes that the free volume compressibility can be described by an equation analogous to the corresponding equation used to describe the specific volume. The shift factor in this model is [18]

$$a_P = \left(1 + \frac{P - P_g}{B}\right)^{\theta_c} \tag{8.18}$$

taking as a reference the pressure at the glass transition, B depends on the polymer and $\theta_c = C/f_g^2$, where $C = 0.0894$ and $f_g \approx 0.025$ for many polymers. It is worth noticing that the Tait model reduces to the exponential model when $(P - P_g)/B \ll 1$ since

$$\ln a_P = \theta_c \ln\left(1 + \frac{P - P_g}{B}\right) \approx \frac{\theta_c}{B}(P - P_g) \tag{8.19}$$

which is of the form of Eq. (8.15). Thus, for small pressures the Tait model reduces to the exponential model.

8.2.5
Problems Related to Free Volume Theories

In some cases it is of interest to obtain the activation energies under constant volume conditions; for example, computer simulations produce activation energies that are constant volume quantities. This quantity can also be obtained in DS provided that volumetric data exist. We can define constant pressure and constant volume apparent activation energies as $Q_P(T,P) = -2.303\, RT^2\, (\partial \log \tau/\partial T)_P$ and $Q_V(T,V) = -2.303\, RT^2(\partial \log \tau/\partial T)_V$, respectively, which are related through [3, 5]

$$\left(\frac{\partial \log \tau}{\partial T}\right)_V = \left(\frac{\partial \log \tau}{\partial T}\right)_P + \left(\frac{\partial \log \tau}{\partial P}\right)_T \left(\frac{\partial P}{\partial T}\right)_V \tag{8.20}$$

where $(\partial P/\partial T)_V$ is given by the ratio of the thermal expansion coefficient α and the compressibility $\beta(T)$. Then Eq. (8.20) can be written as

$$Q_V(T,V) = Q_P(T,P) - T\frac{\alpha}{\beta(T)}\Delta V(T,P) \tag{8.21}$$

where $\Delta V = 2.303\, RT\, (\partial \log \tau/\partial P)_T$ is the activation volume. It follows from Eq. (8.21) that $Q_V < Q_P$ and in practice $Q_V/Q_P \approx 0.7 - 0.8$ for the dielectric α-process in amorphous polymers [3, 5]. This finding is inconsistent with free vol-
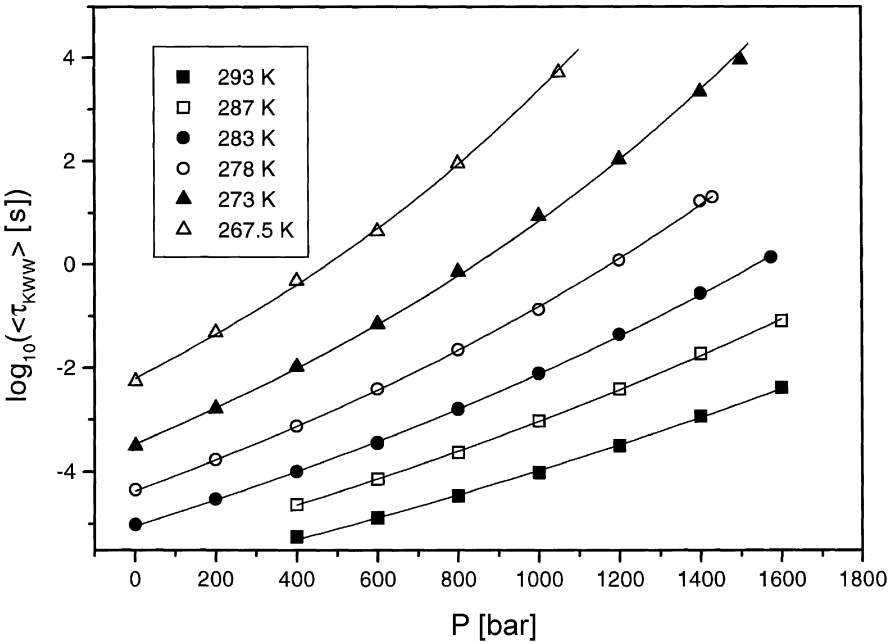
Fig. 8.1. Average Kohlraush-Williams-Watts (KWW) relaxation times for poly(bisphenol A-*co*-epichlorohydrin) glycidyl end capped (PBG) shown for different temperatures as a function of pressure. The *solid lines* are fits to the data using Eq. (8.22) (taken from [19])

ume theories (which in the simplest free volume theory would predict $Q_V = 0$) and emphasizes that the rate of relaxation is largely determined by the thermal energy kT. Raising the temperature at constant macroscopic volume increases the rate of relaxation through the increase of thermal energy and not, primarily, through the change in free volume.

8.2.6
Scaling of the α-Process: an Example

An example of the scaling of the α-process is provided for the fragile liquid poly(bisphenol A-co-epichlorohydrin) glycidyl end capped (PBG) [19]. The Kohlrausch-Williams-Watts (KWW) relaxation times exhibit a steep pressure dependence as shown in Fig. 8.1. The relaxation times can be fitted to the VFT equation in the form

$$\tau = \tau_\alpha \exp\left(\frac{D_P P}{P_o - P}\right) \tag{8.22}$$

where τ_α is the relaxation time measured at atmospheric pressure, P_o is the pressure of the ideal glass transition at a constant temperature, and D_P is a dimen-
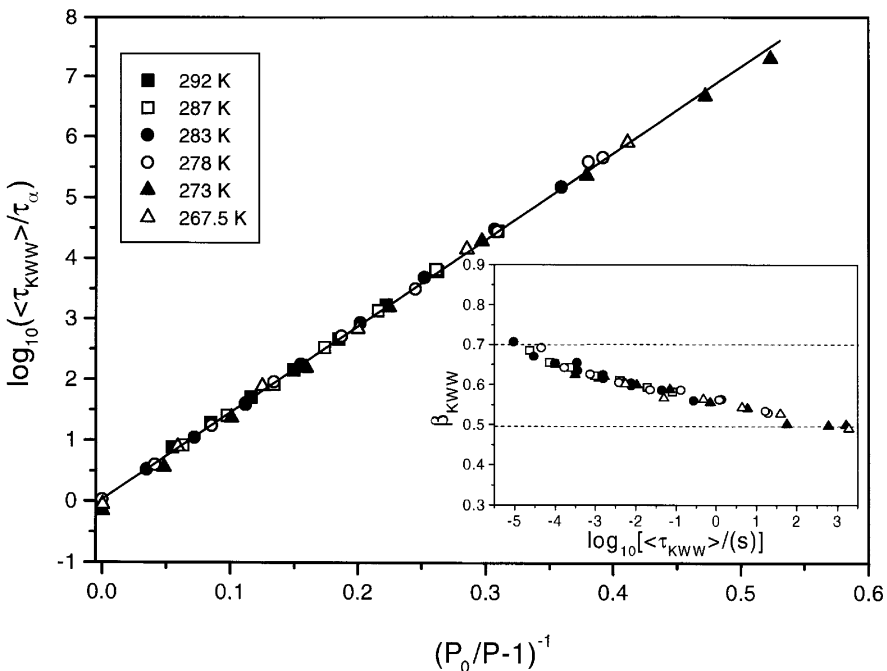
Fig. 8.2. Normalized relaxation times for PBG plotted vs reduced pressure. Notice the good superposition for the different temperatures. In the *inset* the Kohlrausch-Williams-Watts exponent is plotted as a function of the relaxation times (taken from [19])

sionless fitting parameter. The relaxation times obtained at the different temperatures and pressures can all be superimposed when using the following reduced variables for the time as τ/τ_α and the pressure: $(P_o/P - 1)^{-1}$. The result of the superposition is shown in the Fig. 8.2 and reveal that all data can effectively superimpose. Implicit in using Eq. (8.22) is the notion of a constant free volume compressibility.

8.3
Effect of Pressure on the Separation of the α- and β-Processes

It is well known that amorphous polymers exhibit multiple relaxation processes ranging from local, known as the β-process to the segmental or α-process at higher temperatures and to the end-to-end vector relaxation, giving rise to even slower dynamics referred to as normal modes. Not all molecular processes are dielectrically active unless they involve the reorientation of the dipole-moment vector. For the majority of amorphous polymers containing dipoles rigidly attached to the main chain, the dielectric strength of the α-process exceeds that of the β-process (i.e., $\Delta\varepsilon_\alpha \gg \Delta\varepsilon_\beta$) [20]. Certain polymers with flexible dipolar side-groups (poly(vinyl acetate), poly(methyl methacrylate) (PMMA)) also show $\Delta\varepsilon_\alpha > \Delta\varepsilon_\beta$. In addition, the higher members of the poly(n-alkyl methacrylates) have $\Delta\varepsilon_\alpha > \Delta\varepsilon_\beta$ such as poly(n-hexyl methacrylate), poly(n-nonyl methacrylate), poly(n-decyl methacrylate), poly(n-lauryl methacrylate). In contrast, polymers with flexible dipolar side groups (i.e., atactic PMMA and poly(n-ethyl methacrylate) (PEMA)) show $\Delta\varepsilon_\beta > \Delta\varepsilon_\alpha$ under certain temperature and pressure conditions [20].

The existing pressure studies on the α-process in polymers and some glass forming liquids are summarized in Table 8.1. The studies on the lower members of poly(n-alkyl methacrylates) have shown [5, 6] that the total dielectric strength $\Delta\varepsilon$ is partitioned between the α- and β-relaxations, i.e.,

$$\Delta\varepsilon = \Delta\varepsilon_\alpha + \Delta\varepsilon_\beta \tag{8.23}$$

Since $\Delta\varepsilon$ is proportional to the product $C\langle\mu^2\rangle$, where C is the concentration of dipoles and $\langle\mu^2\rangle$ is the apparent mean-square dipole moment of a group, the case $\Delta\varepsilon_\alpha \gg \Delta\varepsilon_\beta$ means that the β-process relaxes only a small part of $\langle\mu^2\rangle$ and the remaining is relaxed through the α-process. Conversely, $\Delta\varepsilon_\alpha < \Delta\varepsilon_\beta$ means that the β-process relaxes most of $\langle\mu^2\rangle$. Within a temperature range, the α- and β-processes coalesce into a single ($\alpha\beta$)-process which already implies that the three processes are interrelated [27].

A key experiment that verifies Eq. (8.23) and shows that the α- and β-processes are indeed interrelated was made with the help of pressure. It was shown that pressure affects the two relaxations in a different way [5]. When the two processes are well separated, pressure was found to shift the α-process to lower frequencies whereas the β-process was much less affected. The intensities of the two processes did not show a considerable change. At temperatures where the two processes approach, pressure was found to increase the strength of the

Table 8.1. Polymers and glass-forming liquids studied by dielectric spectroscopy under pressure

Substance	Reference
Poly(vinyl acetate) (PVAc)	O'Reilly 1962 [17]
	Heinrich et al. 1985 [21]
Poly(vinyl chloride) (PVC)	Koppelman et al.1961 [22]
	Saito et al. 1968 [23]
	Williams and Watts 1971 [24]
	Sasabe 1971 [25]
	Heinrich et al. 1985 [21]
Poly(ethylene terephthalate) (PET)	Williams 1966 [26]
	Saito et al. 1968 [23]
Poly(methyl acrylate) (PMA)	Williams 1964 [3, 4]
Poly(ethyl acrylate) (PEA)	Williams 1966 [5]
Poly(methyl methacrylate) (PMMA)	Sasabe and Saito 1968 [6]
	Sasabe 1971 [25]
Poly(n-ethyl methacrylate) (PEMA)	Williams 1966 [5]
	Sasabe and Saito 1968 [6]
	Sasabe 1971 [25]
	Kamiya 1990 [8]
Poly(n-butyl methactylate) (PnBMA)	Williams et al. 1965 [27]
	Sasabe and Saito 1968 [6]
	Sasabe 1971 [25]
Poly(n-octyl methacrylate) (PnOMA)	Sasabe and Saito 1968 [6]
	Sasabe 1971 [25]
Poly(n-nonyl methacrylate) (PnNMA)	Williams and Watts 1971 [28]
Poly(n-lauryl methacrylate) (PnLMA)	Sasabe and Saito 1968 [6]
	Williams and Watts 1971 [28]
Polyethylene (PE), linear-oxidized	Sayre et al. 1978 [7]
Polysiloxane liquid crystal	Moura-Ramos et al. 1991 [9]
Poly(n-octadecyl methacrylate) (PnODMA)	Mierzwa et al. 2000 [29]
Polyisoprene (PI)	Floudas et al. 1999 [30, 31]
Polyvinylethylene (PVE)	Floudas et al. 2000 [32]
Poly(isoprene-b-ethylene) (PI-PVE)	Floudas et al. 1999 [33]
Polystyrene-poly(vinyl methyl ether) (PS/PVME)	Floudas and Mierzwa 2000 [34]
Poly(norbornene diethylester) side-chain polymer liquid crystal	Mierzwa et al. 2001 [35]
Poly(norbornene diethylester-b-octene)	Mierzwa et al. 2001 [36]
Poly(propylene oxide) (PPO)	Williams 1965 [37]
	Freeman et al. 1990 [38]
	Anderson et al. 1998 [39]
Poly(propylene glycol)/LiCF$_3$SO$_3$	Fontanella 1999 [92]
Poly[(phenyl glycidyl ether)-co-formaldehyde]	Paluch et al. 1999 [40]
Poly(bisphenol A-co-epichlorohydrin)	Paluch et al. 1999 [41]
Polyurethane elastomer	Cheng et al. 1999 [42]
Salol, orthoterphenyl	Paluch et al. 1999 [43]
Di-isobutyl phthalate	Paluch et al. 1996 [44]
Diglycidyl ether of bisphenol A	Corezzi et al. 1999 [45]
NAFION	Fontanella et al. 1996 [93]
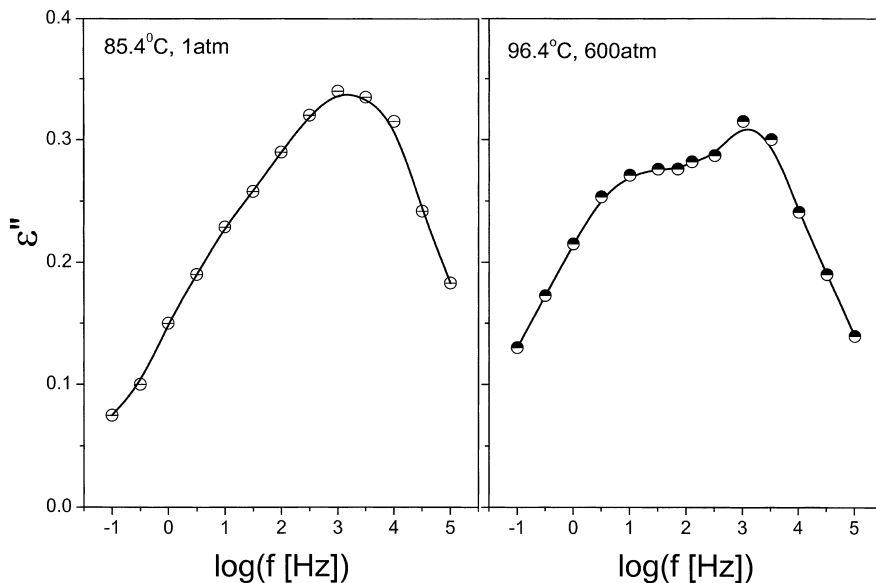
Fig. 8.3. Effect of pressure on the dielectric loss spectra of PEMA at two temperatures. At the lowest temperature ($\theta = 85.4$°C) two separate relaxations contribute to the dielectric loss. Increasing pressure results in the separation into α- and β-processes as can be seen in the spectrum taken under $\theta = 96.4$°C, $P = 600$ atm (reproduced in part from [5])

α-process at the expense of that for the β-process. Furthermore, in the vicinity of the single ($\alpha\beta$)-process, pressure leads to the decomposition of the mixed relaxation to separate α- and β-processes. These findings are shown in Fig. 8.3 and 8.4. Figure 8.3, gives the effect of pressure on the ε' and ε'' of PEMA at two temperatures. At the lowest temperature ($\theta = 85.4$°C) two separate relaxations can be seen at atmospheric pressure. Increasing pressure results in a better separation of the two modes mainly through the significant slowing-down of the α-process. Notice, that the strength of the α-process increases at the expense of the faster β-process. The situation at the higher temperatures is shown in the same figure. At atmospheric pressure at $\theta = 96.4$°C, the system exhibits a single ($\alpha\beta$)-process. Increasing pressure results in the separation into α- and β-processes. The separation, again, effectively is produced by the α-process becoming very slow whereas the β-process is much less affected. These results are nicely depicted in Fig. 8.4 in the usual Arrhenius representation. It is seen that the ($\alpha\beta$)-process lies between the extrapolated α- and β-processes and the effect of pressure is to shift the β-process slowly whereas the effect on the α-relaxation is more important. As a result, the emerging of the ($\alpha\beta$)-relaxation at a given pressure occurs at a location largely determined by the location of the α-process at that pressure.

These key experiments performed on the lower members of the poly(n-alkyl methacrylate) series have shown that:
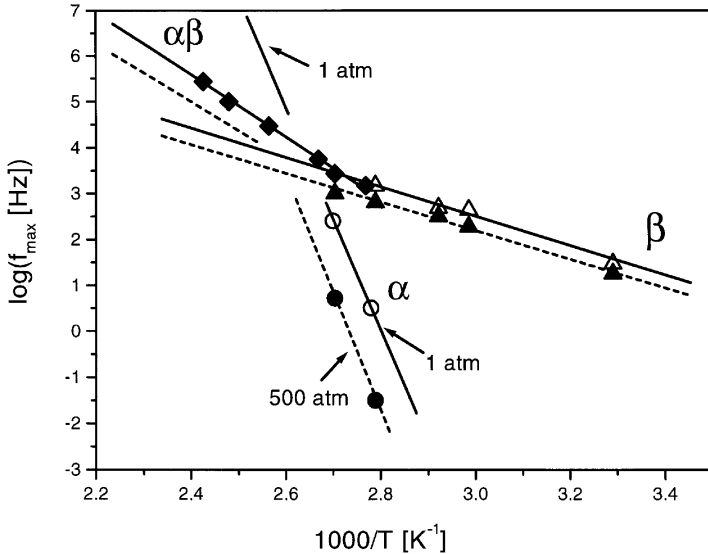
Fig. 8.4. Arrhenius representation of the relaxation times corresponding to the three processes in PEMA: *open and filled circles* correspond to the α-process at 1 and 500 atm, respectively; *open and filled triangles* correspond to the β-process at 1 and 500 atm, respectively; *filled rhombus* corresponds to the ($\alpha\beta$)-process at 1 atm. *Solid and dashed lines* give the positions of the three relaxations at 1 and 500 atm, respectively. The ($\alpha\beta$)-process lies between the extrapolated α- and β-processes and the effect of pressure is to shift the β-process slowly whereas the effect of the α-relaxation is more important. As a result, the emerging of the ($\alpha\beta$)-relaxation at a given pressure occurs at a location which is largely determined by the location of the α-process at that pressure (reproduced from [5])

1. The α- and β-processes are interrelated via the conservation relation $\Delta\varepsilon = \Delta\varepsilon_\alpha + \Delta\varepsilon_\beta$, and the decrease of $\Delta\varepsilon_\beta$ in these flexible side-chain polymers arises from the reduction of the free volume which effectively "blocks" the β-process. The conservation relation can be understood in terms of $[\langle\mu\rangle^2]\,\varphi_\alpha(t) + [\langle\mu^2\rangle - \langle\mu\rangle^2]\,\varphi_\beta(t)$ and when pressure has the effect of decreasing the strength of the β-process there is a corresponding increase of the strength of the α-process in order to conserve the relaxation of all of $\langle\mu^2\rangle$.
2. The ($\alpha\beta$)-process at higher temperatures is a "mixed" process which relaxes the whole of $\langle\mu^2\rangle$ whereas the individual α- and β-processes relax only a part of the $\langle\mu^2\rangle$.

8.4
Effect of Pressure on the Local and Global (Chain) Dynamics

It is well known that the local segmental and global chain motions control the mechanical response of polymers above their glass transition temperature (T_g).

The latter can be reached by lowering temperature (T) at a given pressure (P), or by increasing P at a given T. As we discussed before, the effect of pressure on the local segmental dynamics and on sub-T_g relaxations has been studied in detail. It was found that pressure exerts a stronger influence on the segmental as compared to the local sub-glass relaxations and is the right variable if a separation of the two modes is needed. On the other hand, the effect of pressure on the global chain dynamics that control the flow regime and thus of interest in polymer processing only recently has started to be explored [30, 31, 39].

Herein we review the results of recent studies [30, 31] treating the effect of pressure on the segmental and chain dynamics as a function of polymer molecular weight. The polymer is polyisoprene which has been extensively studied before as a function of temperature for different molecular weights [46–49]. Being a type-A polymer (according to Stockmayers classification [50]) it has components of the dipole moment both parallel and perpendicular to the chain giving rise, respectively, to end-to-end vector and local segmental dynamics. A study of the effect of pressure on the segmental and normal mode dynamics requires polymer chains of variable lengths and M/M_e ratios: 1/5, 1/2, 2/3, 2, and 5, i.e., from unentangled to well entangled chains. The aim is to investigate the effect of P on M_e. This question is not only of fundamental importance but has industrial implications as well (i.e., in polymer processing).

For this purpose five *cis*-polyisoprenes (PI) have been used: PI-1200, PI-2500, PI-3500, PI-10600, and PI-26000 g mol^{-1} with the numbers indicating number averaged molecular weights and with polydispersity of less than 1.1. The entanglement molecular weight of PI is 5400 g mol^{-1}; thus the first three samples are unentangled. A typical set-up [51] for the pressure dependent dielectric measurements consists of the following parts: temperature controlled sample cell, hydraulic closing press with pump, and pump for hydrostatic test pressure. Silicone oil is used as the pressure transducing medium. The sample cell consists of two electrodes 20 mm in diameter and the sample has a thickness of 50 μm. The sample capacitor is sealed and placed inside a Teflon ring to separate the sample from the silicon oil. The dielectric measurements were made at different temperatures in the range 273 to 306 K and for frequencies in the range from 10^{-2} to 10^6 Hz using a Novocontrol BDS system composed from a frequency response analyzer (Solartron Schlumberger FRA 1260) and a broad band dielectric converter. The complex dielectric permittivity $\varepsilon^* = \varepsilon' - i\varepsilon''$, where ε' is the real and ε'' is the imaginary part, is a function of frequency ω, temperature T and pressure P, $\varepsilon^* = \varepsilon^*(\omega, T, P)$.

Representative dielectric loss spectra for a PI with molecular weight of 1200 are shown in Fig. 8.5 under isothermal (top) and isobaric (bottom) conditions (here we refer to isothermal and isobaric in a broad sense; strictly speaking all spectra are under isothermal/isobaric conditions). Both sets of spectra display two modes which become slower with increasing pressure and decreasing temperature. The fastest of the two modes corresponds to the local segmental mode whereas the slower mode corresponds to a spectrum of normal modes. From the broad spectrum of normal modes in the following we only discuss the longest normal mode which for homopolymers corresponds to the position of the maximum loss. Note that within the δT and δP shown, temperature is more effective
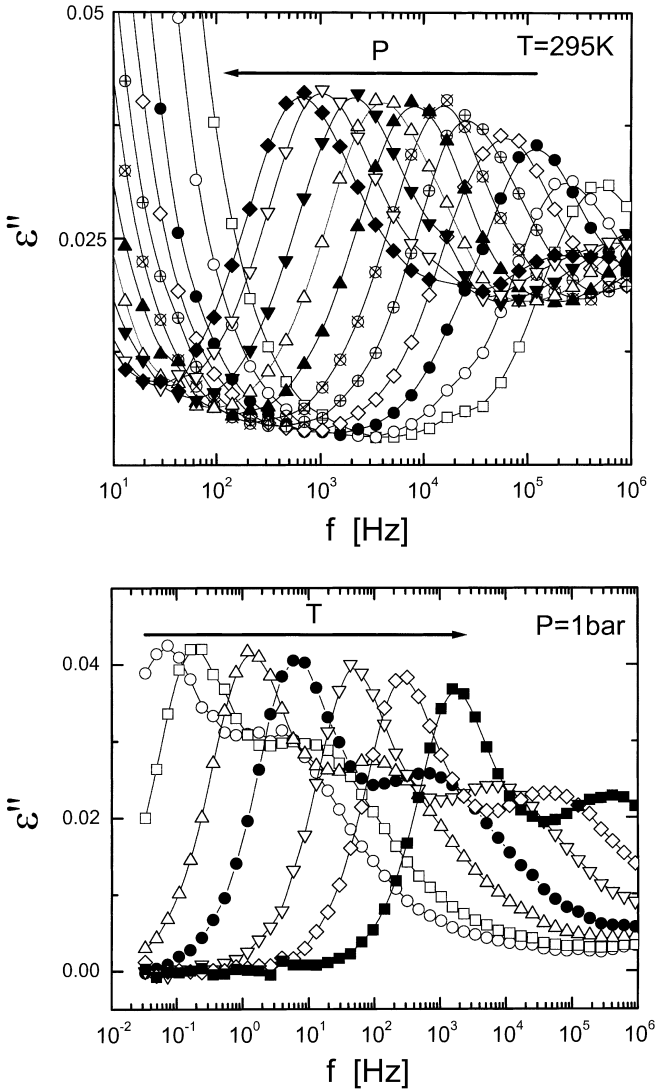
Fig. 8.5. Dielectric loss for PI-1200 plotted under isothermal conditions (*top*) at 295 K, and under isobaric conditions (*bottom*) at 1 bar. The corresponding pressures to the isothermal spectra are: (*open squares*): 1 bar, (*open circles*): 0.3 kbar, (*filled circles*): 0.6 kbar, (*open lozenges*): 0.9 kbar, (*circled plus signs*): 1.2 kbar, (*circled multiplication signs*): 1.5 kbar, (*filled triangles*): 1.8 kbar, (*open triangles*): 2.1 kbar, (*inverted filled triangles*): 2.4 kbar, (*inverted open triangles*): 2.7 kbar, (*filled lozenges*): 3.0 kbar. The temperatures for the isobaric spectra are: (*open circles*): 205 K, (*open squares*): 208 K, (*open triangles*): 213 K, (*filled circles*): 218 K, (*inverted open triangles*): 225 K, (*open lozenges*): 233 K, (*filled squares*): 243 K. The symbols "*s*" and "*n*" indicate the segmental and normal modes, respectively (from [31])

is slowing-down both modes, i.e., with an increase in T from 205 to 243 K the spectrum shifts by nearly five decades whereas increasing the pressure isothermally, from $P = 1$ bar up to $P = 3$ kbar, results in a shift of only three decades.

In Fig. 8.6 the same spectra are now shifted horizontally to the corresponding data at a reference pressure ($P_{ref} = 1.5$ kbar) (top) and temperature ($T_{ref} = 213$ K) (bottom) and allow a reasonable superposition of the normal mode spectra. This shows that the spectrum of normal modes in not affected by changes in T and P, that is, the intensity and characteristic times of each one of the normal modes have the same T and P dependence, i.e., the spectral shape is invariant. However, on the segmental level, the superposition breaks-down and this is more pronounced under isobaric conditions (Fig. 8.6, bottom). This break-down of the time-temperature (tTs) and time-pressure superposition (tPs) reflects on the distinctly different T- and P-dependence of the two modes. There is a steeper dependence of the shift factors on T and the more pronounced deviations from tTs indicates that, within the δT and δP shown, temperature is more efficient in inducing the proximity of the two modes. In other words, to produce a similar shift of the two modes as a change of T by 40 K one would have to go to very high pressures which are not accessible with the current experimental set-up.

Typically the analysis of the DS spectra obtained under pressure can be made as with the spectra obtained by changing temperature, that is, using the empirical equation of Havriliak and Negami (HN) [52]:

$$\frac{\varepsilon^*(T,P,\omega) - \varepsilon_\infty(T,P)}{\Delta\varepsilon(T,P)} = \frac{1}{[1 + (i\omega\tau_{HN}(T,P))^\alpha]^\gamma} \tag{8.24}$$

$\tau_{HN}(T, P)$ is the characteristic relaxation time in this equation, $\Delta\varepsilon(T, P) = \varepsilon_S - \varepsilon_\infty$ is the relaxation strength of the process under investigation, and α, γ describe, respectively, the symmetrical and asymmetrical broadening of the distribution of relaxation times. In the fitting procedure both the ε' and ε'' values at every temperature and pressure can be used and a typical fit is shown in Fig. 8.7 for PI-1200 at $T = 277$ K and $P = 2.4$ kbar. From the fits to the real and imaginary part of the $\varepsilon^*(f)$ we can extract the dielectric strength ($\Delta\varepsilon$), the distribution parameters (α, γ), and the characteristic times for each process. The distribution parameters assume the values $\alpha_S = 0.55 \pm 0.05$, $\gamma_S = 0.7 \pm 0.05$, and $\alpha_n = 1.0$ (fixed), $\gamma_n = 0.5 \pm 0.05$ for the segmental and normal modes, respectively, without displaying any pressure dependence. The rise of the ε'' at lower frequencies is caused by the conductivity ($\varepsilon'' \sim (\sigma_o/\varepsilon_o)\omega^{-1}$, where σ_o is the d.c.-conductivity and ε_o is the permittivity of free space) which usually is included in the fitting procedure.

The dependence of the relaxation times for both the segmental and longest normal mode can be described by the VFT equation ($\log\tau = \log\tau_o + B/(T - T_\infty)$) where $\log\tau_o$ is the limiting value at high T, B is the apparent activation energy and T_∞ is the "ideal" glass transition temperature. For example, the following parameters have been obtained for the PI-1200 segmental and normal modes, respectively: $-\log(\tau_o[s]) = 13.9$, $B = 664 \pm 40$ K and $T_\infty = 153 \pm 1$ K and $-\log(\tau_o[s]) = 10.84$, $B = 646 \pm 30$ K and $T_\infty = 149 \pm 1$ K and the higher T_∞ value for the segmental mode indicates that the modes cross. The corresponding crossing of the
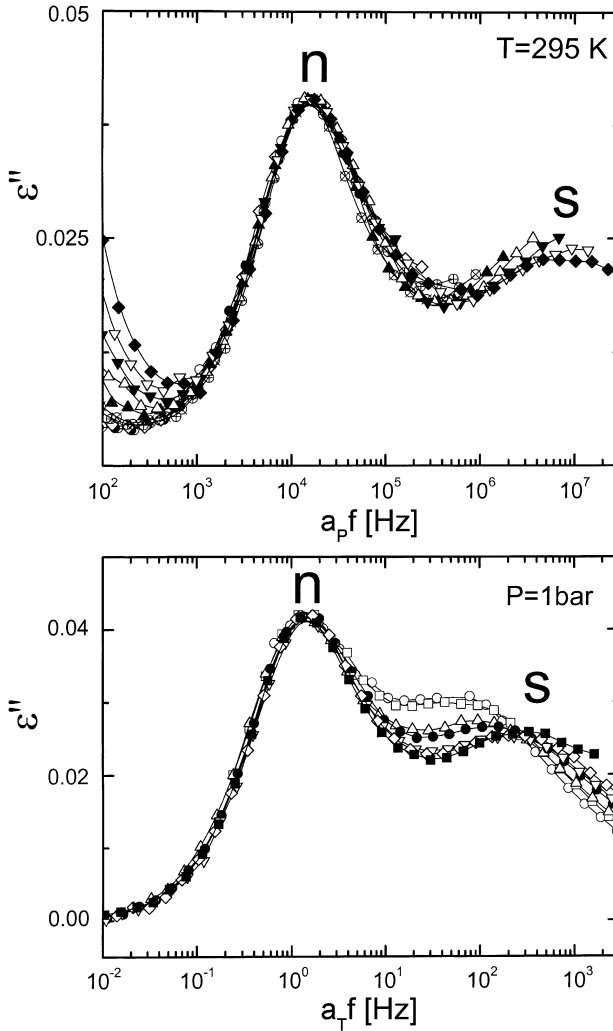
Fig. 8.6. "Master-curves" obtained by shifting the spectra of Fig. 8.5 to the peak of the normal mode spectra by applying a horizontal pressure-shift factor (a_P) (*top*) and a temperature shift factor (a_T) (*bottom*). The corresponding reference spectra are at $P_{ref} = 1.5$ kbar and $T_{ref} = 213$ K. The key to the symbols is the same as in Fig. 8.5 (from [31])

modes by decreasing T under isobaric conditions ($P = 1$ bar) has been discussed before in terms of the breakdown of the Rouse model [53–56].

The relaxation times obtained by varying T and P can be discussed in two representations: $\tau(T, P)$ and $\tau(T, \rho)$ which provide complementary information. The pressure dependence of the relaxation times corresponding to the segmental and longest normal mode are shown in the $\tau(T, P)$ representation in Fig. 8.8 for the PI-1200 at four temperatures as indicated. Within the investigated pres-
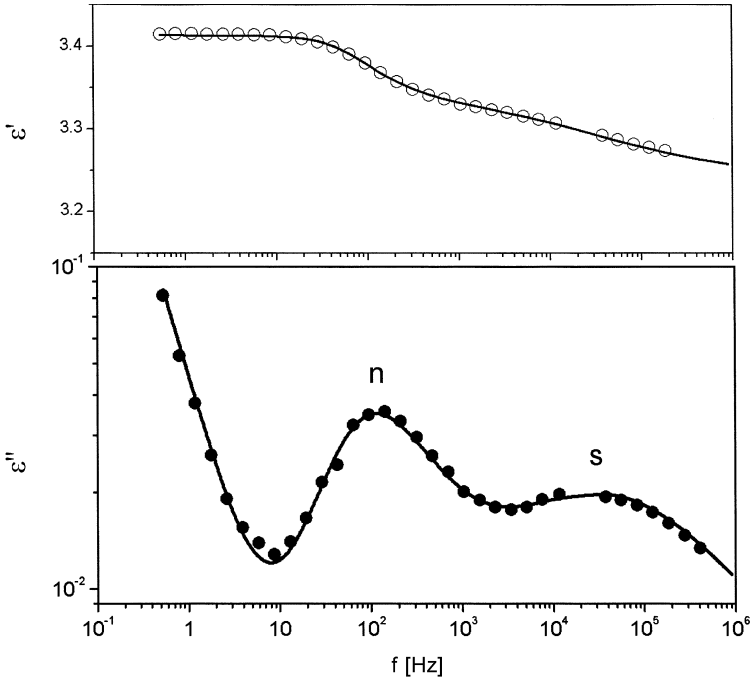
Fig. 8.7. Representative spectrum of the real (*top*) and imaginary (*bottom*) parts of the dielectric permittivity for the PI-1200 plotted as a function of frequency at $T = 277$ K and $P = 2.4$ kbar. The spectrum is fitted using two HN functions and a conductivity contribution. The *solid line* is the result of the fit

sure range the relaxation times exhibit a linear P-dependence, i.e.,

$$\log\left(\frac{\tau_p}{\tau_o}\right) = \Lambda(T)(P - P_o) \tag{8.25}$$

where τ_P and τ_o are the characteristic times at pressures P and P_o, respectively and the coefficient $\Lambda(T)$ is independent of pressure and is proportional to the activation volume as discussed earlier. Notice that the two modes have distinctly different P-dependencies. For example, at $T = 283$ K, $-\log\tau_S = 8.8 - 1.156 \times 10^{-3} P$ and $-\log\tau_n = 6.03 - 1.029 \times 10^{-3} P$ (P in bars) for the segmental and normal modes, respectively, which implies that the two modes will cross at a finite pressure ($P \approx 22$ kbar). Based on the discussion in Sect. 8.2, we can define an apparent activation volume ΔV as

$$\Delta V = 2.303 RT \left(\frac{\partial \log \tau}{\partial P}\right)_T \tag{8.26}$$

The extracted activation volumes from the different PI's are plotted in Fig. 8.9 as a function of the temperature difference from the respective T_g (the calorimet-
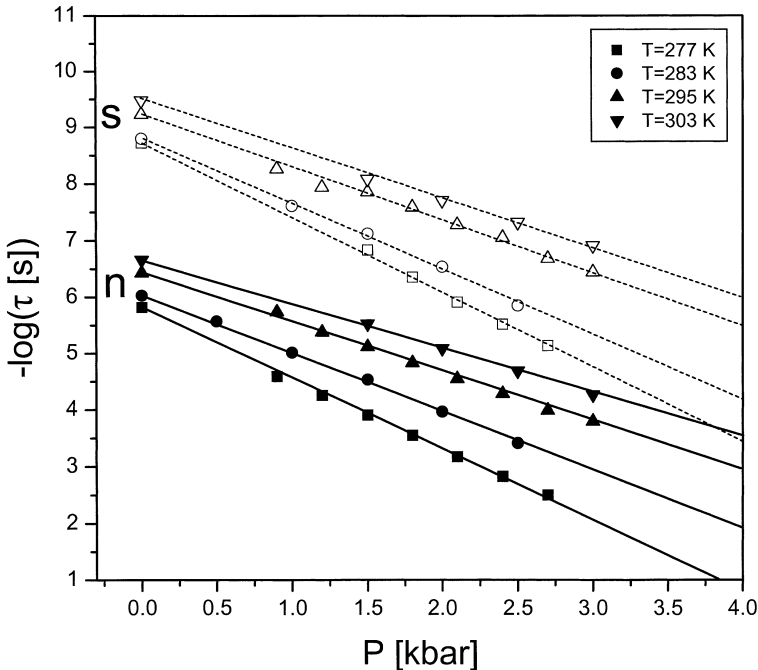
Fig. 8.8. Pressure dependence of the relaxation times corresponding to the segmental (*open symbols*) and longest normal mode (*filled symbols*) of PI-1200 at different temperatures as indicated. The *lines* are linear fits to the data (from [31])

ric T_g values used were 191, 199, 200, 204, and 208 K for the PI-1200, PI-2500, PI-3500, PI-10600, and PI-26000, respectively). First, note that the activation volumes from the different molecular weights collapse on a single curve when scaled as $T - T_g$ and second, the strong T-dependence which is reminiscent to the postulated T-dependence of the cooperative volume [57]. The dashed line in the figure gives the monomer volume and shows that at approximately 80 K above T_g the activation volume of PI is comparable to the monomer volume.

　　The T- and P-effects on the relaxation times can be cast together using the density as a variable in a $\tau(T, \rho)$ representation. For this purpose the Tait equation can be employed [58]:

$$V(P, \theta) = V(0, \theta) \left\{ 1 - 0.0894 \ln\left(1 + \frac{P}{C(\theta)}\right) \right\} \tag{8.27}$$

where $C(\theta)$ is the Tait parameter which depends only on T according to $C(\theta) = C_o \exp(-C_1\theta)$ and $V(0, \theta) = A_o + A_1\theta + A_2\theta^2$. For PI the above parameters are: $C_o = 202$ MPa, $C_1 = 4.653 \times 10^{-3}\,°C$ and $A_o = 1.0943$ cm^3 g^{-1}, $A_1 = 0.6293 \times 10^{-3}$ cm^3 g$^{-1}\,°C^{-1}$, $A_2 = 0.6231 \times 10^{-6}$ cm^3 g$^{-1}\,°C^{-2}$. Based on the Tait equation the corresponding volume for the isobaric and isothermal experiments can be calculated and the result for the segmental and normal modes are shown in Fig. 8.10 in the
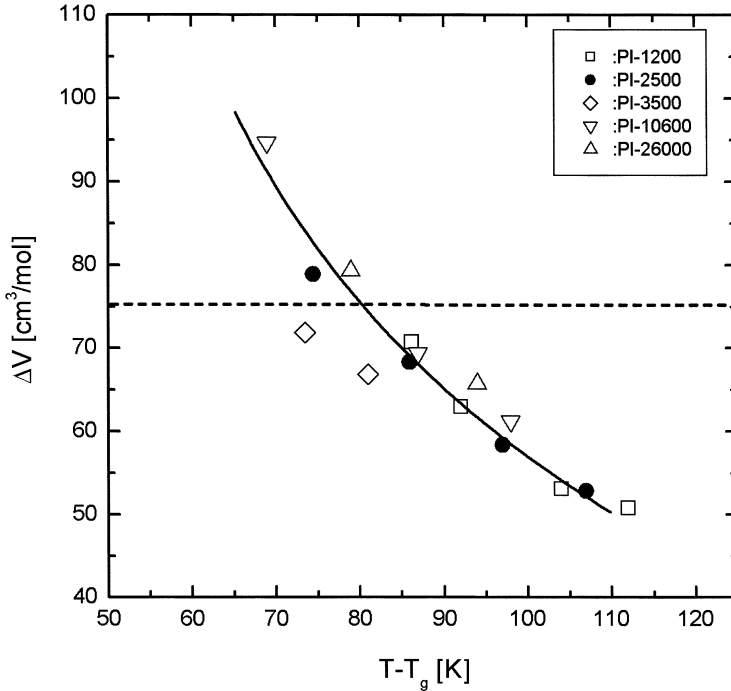
Fig. 8.9. Activation volume of the different polyisoprenes plotted as a function of the temperature difference from the respective T_g. The *solid line* is a guide for the eye. The *dashed line* indicates the monomer volume (from [31])

$-\log\tau$ vs ρ representation. Notice that the isobaric data (at 1 bar) in this representation resemble the same data in the $-\log\tau$ vs T^{-1} representation. The resemblance calls for a modified VFT equation

$$\log\tau = \log\tau_o + \frac{D}{\rho - \rho_g} \qquad (8.28)$$

where D is a constant and ρ_g is the density at T_g. Applying the same function to both modes (at $P = 1$ bar) we obtain $\rho_g^{\mathrm{nor}} = 0.972$ g cm^{-3} as compared to $\rho_g^{\mathrm{seg}} = 0.969$ g cm^{-3}, that is, the two modes cross also in this representation. The crossover is expected since $T_\infty^{\mathrm{nor}} < T_\infty^{\mathrm{seg}}$ and ρ is – to a first approximation – inversely proportional to T. In the same figure the isothermal relaxation times corresponding to the segmental and normal modes at two temperatures are plotted. Because of the functional form of the Tait equation the isothermal data show a curvature in the $-\log\tau$ vs ρ representation and can be fitted to the modified VFT equation. The resulted values of ρ_g for the two modes are consistently $\rho_g^{\mathrm{nor}} > \rho_g^{\mathrm{seg}}$ but the glasses made by pressurizing the samples under isothermal conditions possess a much higher density than the glasses prepared under isobaric conditions since they are prepared at elevated pressures. This shows that T at a given
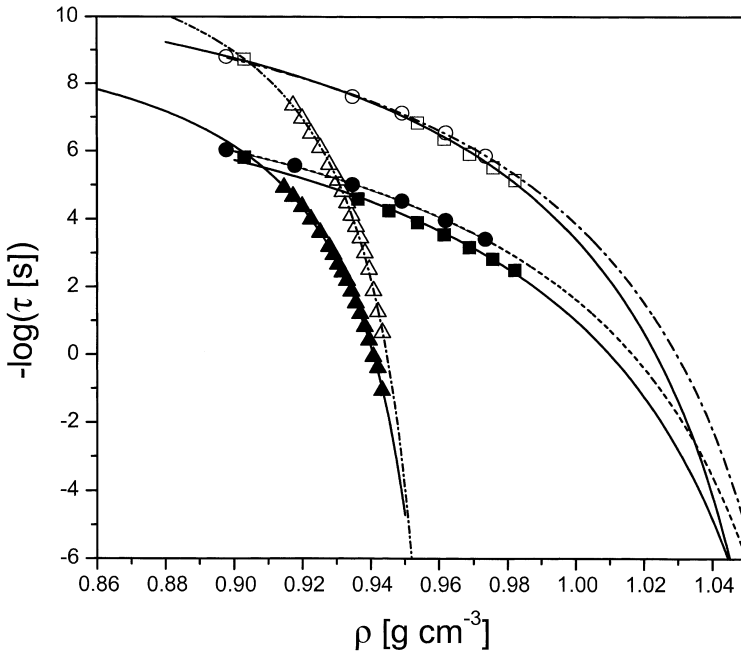
Fig. 8.10. Relaxation map for the PI-1200 as a function of density showing both the segmental (*open symbols*) and longest normal (*filled symbols*) modes. *Triangles* correspond to relaxation times measured under isobaric conditions (at $P = 1$ bar) by changing the temperature. *Squares and circles* correspond to relaxation times measured isothermally at 277 and 283 K, respectively, by changing pressure. The *lines* are fits to Eq. (8.28) (from [31])

P is more effective in shifting the two modes and in inducing a glass transition and this is consistent with the fact that pressure shift factors exhibit a weaker dependence on P and ρ than the temperature shift factors on T and ρ.

We now turn our attention to the molecular weight dependence of the segmental and longest normal modes. Figure 8.11 gives the two processes in the different samples as a function of pressure, at 320 K. As discussed earlier, the segmental modes through the higher activation volume exhibit a stronger P-dependence than the corresponding normal modes. At any given P, the longest normal mode times exhibit a weak molecular weight dependence for $M < M_e$ ($\tau \sim M^2$) and a stronger dependence for $M > M_e$ ($\tau \sim M^{3.4}$) in qualitative agreement with the Rouse and reptation models [59], respectively. Notice the additional molecular weight dependence for the smaller molecular weights due to chain-end effects. To make the comparison with theory more quantitative we normalize the longest normal mode times to the corresponding segmental times and the result is shown in Fig. 8.12. The reduced quantity plotted in the figure is now free from chain-end effects. Two regimes are clearly seen with distinctly different slopes below and above M_e; however, the point of intersection of the lines is not much influenced by pressure. The weak P-dependence of the normalized relaxation times is better depicted in the inset where the slopes are plotted as a function of
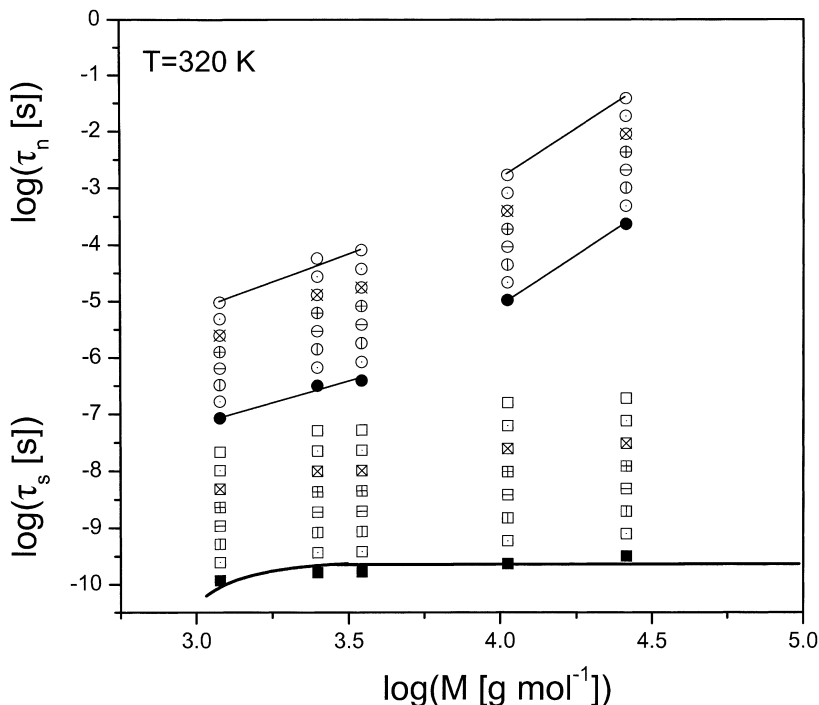
Fig. 8.11. Molecular weight dependence of the segmental (*squares*) and longest normal mode (*circles*) for the five PIs investigated plotted for different pressures at 320 K. The shortest time corresponds to the data at 1 bar and the rest are interpolated data shown at intervals of 0.5 kbar. The *line* through the segmental times at atmospheric pressure is a guide for the eye. The lines for the normal mode at 3.5 kbars represent linear fits to the $M < M_e$ and $M > M_e$ regimes (from [31])

applied P. For $M > M_e$, the slope changes from 3.1 to about 3.2 whereas a weaker P-dependence is found for $M < M_e$. Nevertheless, increasing pressure does not change significantly the picture from atmospheric pressure and this signifies that there is a minor, if any, dependence of M_e on P.

In conclusion, the study [30, 31] of the effect of pressure on the segmental and normal modes of the type-A polymer polyisoprene as a function of molecular weight, from unentangled to well-entangled chains, revealed that the spectral shape of the normal modes and of the segmental mode is invariant under variation of T *and* P. Both time-temperature superposition and time-pressure superposition fail due to the higher sensitivity of the segmental mode to T and P variations, respectively. The latter implies a higher activation volume for the segmental mode. The activation volume of the segmental mode for the different molecular weights exhibits a strong T-dependence and scales as $T - T_g$. Lastly, M_e does not show a significant pressure dependence.
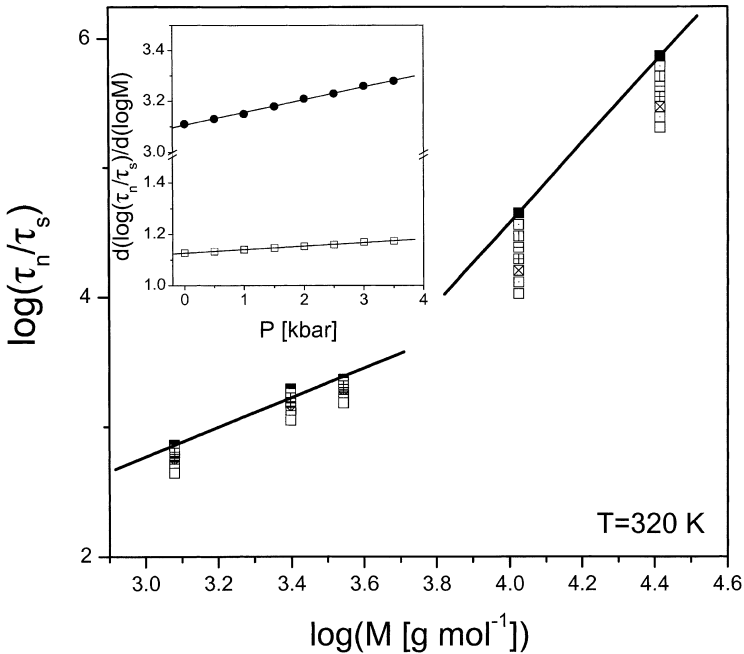
Fig. 8.12. Molecular weight dependence of the longest normal mode relaxation time normalized to the corresponding segmental mode relaxation time at the same pressure. The *filled squares* correspond to the data at 1 bar and the rest are interpolated data shown in increments of 0.5 kbar and the *lines* are fits to the $P = 1$ bar data. In the inset, the pressure dependence of the two slopes for $M < M_e$ (*open squares*) and $M > M_e$ (*filled circles*) are shown (from [31])

8.5
Effect of Pressure on the Miscibility of Blends/Copolymers

Block copolymers and polymer blends are polymeric composites with many interesting properties (optical, mechanical, electrical, ionic, barrier, etc.) and potential applications. Polymer blends [60] phase separate on a macroscopic scale (macrophase separation) by heating or cooling. Block copolymers [61], i.e., a sequence of two homopolymers linked together with a covalent bond, cannot macrophase separate, but instead, micro-phase separate into a variety of complex nano-structures, mainly because of enthalpic reasons. The phase behavior of blends and copolymers can be discussed in terms of phase diagrams [62] composed of the following parameters: the product of the overall degree of polymerization N with the interaction parameter χ, (χN) and the composition f_A $(= N_A/N)$. A typical phase diagram for a diblock copolymer and a blend of two homopolymers are shown in Fig. 8.13. There are different regimes where the system may exist in the thermodynamically "homogeneous" state or in the phase separated state. Herein we will review the effect of pressure on the dynamic miscibility of the "athermal" diblock copolymer poly(isoprene-*b*-vinylethylene)
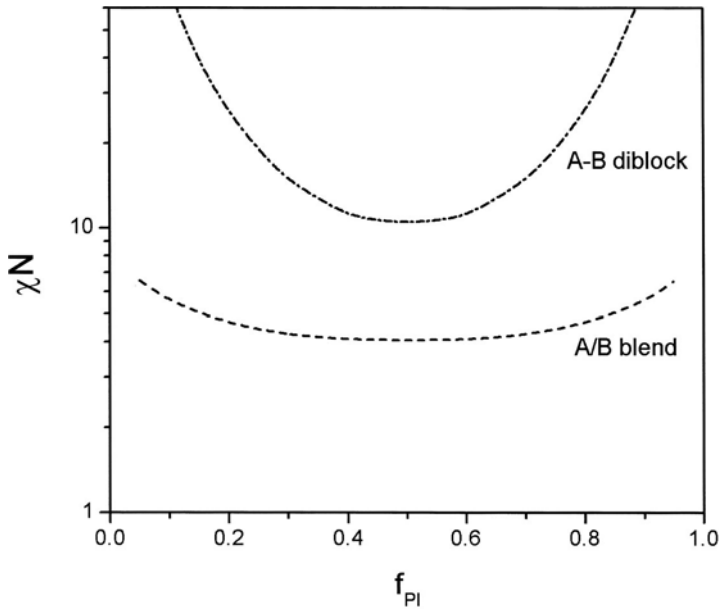
Fig. 8.13. Schematic phase diagrams for polymer blends and diblock copolymers

[33] and the homogeneous blend polystyrene-poly(vinyl methyl ether) [34] by exploring the dynamics at the segmental level.

   Homogeneous blends and disordered diblock copolymers can be dynamically heterogeneous exhibiting two segmental (α-) relaxations [63–67] that underlie the single – albeit broad – calorimetric glass transition measured by differential scanning calorimetry (DSC). The dynamic heterogeneity is further asymmetric with respect to the segmental dynamics of the pure components [68–72]. The segmental dynamics of the high T_g component in the blend is effectively plasticized by the presence of the low T_g component and relates to the composition average T_g. On the other hand, the segmental dynamics of the low T_g component is much less affected becoming somewhat slower as compared to the bulk homopolymer. The origin of this phenomenon, with impact to the mechanical behavior and flow of multi-component polymer systems, can be intramolecular due to chain connectivity [68, 71] and intermolecular [72, 73] due to spatial composition heterogeneities. The presence of composition fluctuations within a small composition dependent volume $V(\phi)$ of the "cooperatively rearranging regions" can drive the effective local composition ϕ away from the mean. The distribution of motional times $F(\ln \tau)$ with the appropriate mapping between ϕ and the relaxation time τ captures the main experimental findings [74].

8.5.1
The PI-*b*-PVE Athermal Diblock Copolymer

Measuring selectively the individual component dynamics has either led to a single or double segmental relaxation for each species in the blend. Specifically, for the athermal (nearly ideal $\chi \approx 0$) [75] polyisoprene-poly(vinylethylene) (PI-PVE) system (either as a blend or a diblock) species selective techniques, unequivocally show a unimodal distribution of segmental times for each component in the mixed system. For PI/PVE with a $\Delta T_g \approx 70$ K, $F(\ln \tau)$ becomes unimodal by considering chain connectivity effects which set a low intramolecular cutoff in the accessible compositions sampled by each component, i.e., $2b/\xi < \phi_{PI} < 1$, with b being the segmental length and $\xi = V^{1/3}$.

Vitrification of a single component fluid occurs not only by decreasing temperature T but also by increasing pressure P, the influence of P on the dual segmental relaxation spectrum of PI-*b*-PVE can be examined using dielectric spectroscopy. Since the "slow" and "fast" peaks in the DS spectra correspond solely to the high and low-T_g components (the PVE and PI glass temperatures are at 272 and 208 K, respectively) then depending on the activation volume (ΔV) of each species, pressure can give rise to the following scenarios: (i) enhance dynamic symmetry and therefore induce local mixing (when $\Delta V_{fast} > \Delta V_{slow}$), (ii) unaltered dynamics ($\Delta V_{fast} \approx \Delta V_{slow}$), (iii) enhance dynamic asymmetry and therefore induce local demixing (when $\Delta V_{fast} < \Delta V_{slow}$). Studies on the effect of P on the segmental dynamics of PI [30, 31] and PVE [32] homopolymers and on the chain dynamics of PI with DS, have shown that the homopolymers possess significantly different activation volumes. Evidently, the small selectivity of the T-dependent DS – through the different amplitudes of the "fast" and "slow" components (for example in the PI-PVE system the dielectric strength ($T\Delta\varepsilon$) of PI and PVE, is 24 and 33, respectively) – can be significantly enhanced by selecting homopolymers with different activation volumes. Here we employ an example from a system exhibiting the first scenario, i.e., $\Delta V_{fast} > \Delta V_{slow}$ and show that P, can induce dynamic homogeneity.

The samples employed were prepared via anionic polymerization and size exclusion chromatography resulted in a polydispersity of less than 1.1. The PI composition in the PI-*b*-PVE diblock was 0.495 and the sample had a total weight averaged molecular weight of 3.16×10^5 g mol^{-1}. The PVE homopolymer had a number averaged molecular weight of 6.7×10^4 g mol^{-1} and the two PIs 1.06×10^4 g mol^{-1} and 2.6×10^4 g mol^{-1}. Both T- and P-dependent measurements were made for the diblock copolymer at three temperatures (279, 294, and 309 K) and for different pressures in the range (1 bar to 3.15 kbar).

Some typical dielectric loss spectra at different temperatures and at ambient pressure shown in Fig. 8.14. The spectra reveal a double peak structure originating from the fast PI segmental relaxation (notice that the PI chain relaxation, i.e., the end-to-end vector relaxation through the cumulative dipole moment along the chain contour, is too slow for the present molecular weight) and a slower PVE segmental relaxation. In the inset, the same spectra are shown but now shifted with a horizontal shift factor a_T and a vertical shift factor b_T to the reference spectrum at 258 K. While the double peak structure is preserved, a
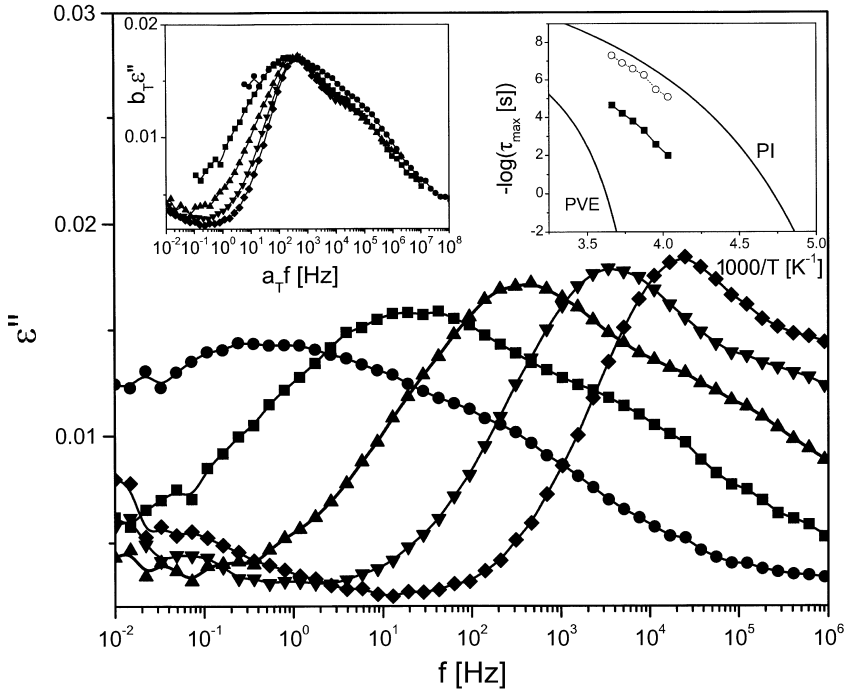
Fig. 8.14. Dielectric loss spectra ε'' as a function of frequency for the symmetric PI-*b*-PVE diblock copolymer shown at different temperatures: (*open circles*): 238 K, (*open squares*): 248 K, (*filled triangles*): 258 K, (*open inverted triangles*): 268 K, (*open lozenges*): 278 K at ambient pressure. The reduced spectra ($T_{ref} = 258$ K) are shown in the *upper left inset*. The *T*-dependence of the characteristic times of the fast (*circles*) and slow (*squares*) relaxation processes are also plotted as an *inset* in the usual Arrhenius representation together with the PI and PVE homopolymer relaxations in the bulk (*solid lines*) (from [33])

symmetric spectral broadening (at low frequencies) is evident with decreasing *T*. The representation of the ε'' spectra proceeds via a double Havriliak-Negami function keeping the distribution parameters of the "fast" segmental relaxation fixed to the values of the bulk PI homopolymer ($\alpha = 0.5$ and $\gamma = 0.7$, independent of *T*). Then the low frequency slope of the "slow" relaxation was found to vary from 0.53 ± 0.02 at 273 K to 0.32 ± 0.02 at 248 K. The slow process due to PVE corresponds qualitatively to the average T_g of the mixed glass whereas the fast process due to PI is slightly slower than the PI homopolymer at the same *T* as shown in the upper right inset to Fig. 8.14.

Isothermal dielectric loss spectra for different pressures are shown in Fig. 8.15 at 309 K. The bimodal appearance of the $\varepsilon''(f)$ spectra become less apparent with increasing *P* as also seen in the reduced plots in the inset. In fact, as seen in the shifted data, the spectra become more symmetric with increasing *P*. Since *T* and *P* can influence differently the two segmental relaxations, one can compare the loss spectra under iso-kinetic conditions; i.e., at (*T*, *P*) conditions with the same relaxation time for the main ("slow") process. For example,
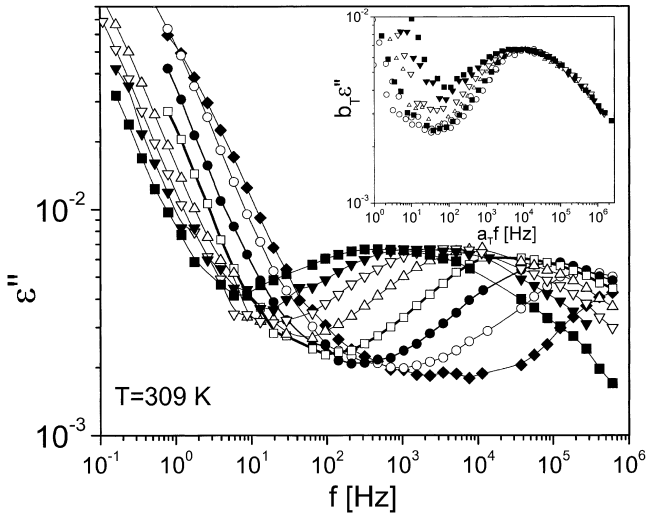
Fig. 8.15. Dielectric loss spectra as a function of pressure shown at $T = 309$ K ((*filled lozenges*): $P = 1$ bar, (*open circles*): $P = 0.5$ kbar, (*filled circles*): $P = 1$ kbar, (*open squares*): $P = 1.5$ kbar, (*open triangles*): $P = 2$ kbar, (*inverted open triangles*): $P = 2.4$ kbar, (*filled inverted triangles*): $P = 2.77$ kbar and (*filled squares*): $P = 3.15$ kbar. In the inset these spectra have been shifted to the spectrum at a reference pressure ($P = 2$ kbar at 309 K) and allow a direct comparison of the spectral shape (from [33])

Fig. 8.16 compares two spectra taken at different (T, P) where the main peak for both sets corresponds to 0.2 ms. Notice that this representation leads to a good superposition at low frequencies; however, at high frequencies the two sets of spectra are quantitatively different. The successful overlapping of the main low frequency peak suggests that at these two (T, P) conditions in each case the lower frequency process is the same distance $T - T_g(P)$ from the T_g. Then, the disparity in the high frequency part of the spectrum of the pressurized sample can arise from the distinctly different P-dependence of the "fast" process.

The strong P-dependence of the main process due to the "slow" PVE relaxation in the copolymer is shown in Fig. 8.17 for three temperatures. Up to the highest applied pressure the plots of $-\log\tau$ against P are linear for each temperature which implies that $\log(\tau_P/\tau_o) = \Lambda(T)(P - P_o)$, can be employed. The data have been parameterized as, $-\log(\tau\,[s]) = 5.14 - 2.06 \times 10^{-3}\,P$ at $T = 279$ K, $-\log(\tau\,[s]) = 6.08 - 1.23 \times 10^{-3}\,P$ at $T = 294$ K and $-\log(\tau\,[s]) = 6.85 - 1.0 \times 10^{-3}\,P$ (P in bars) at $T = 309$ K. From the slopes of the data in Fig. 8.17 the following activation volumes have been deduced: 61, 71, and 112 cm^3 mol^{-1} at 309, 294, and 279 K, respectively. The activation volume in the copolymer has a strong T-dependence and increases with decreasing T in a qualitatively similar way with the cooperative volume.

It is meaningful, therefore, to compare ΔV in the diblock and the pure homopolymers at T equidistant from T_g as shown in the inset to Fig. 8.17. Notice that the homopolymers have significantly different activation volumes and that this is also reflected in the monomer volumes implying local packing effects.
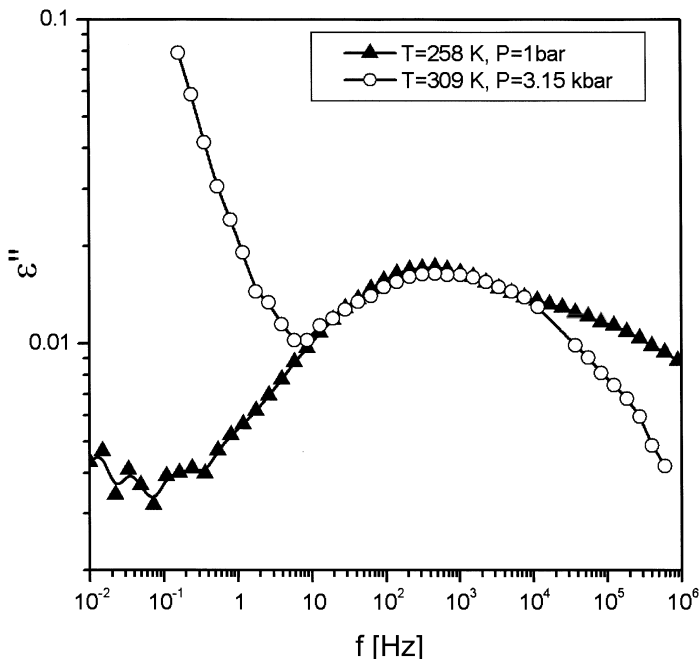
Fig. 8.16. Comparison of the measured dielectric loss spectra under iso-kinetic conditions: (*filled triangles*): $T = 258$ K and $P = 1$ bar, and (*open circles*): $T = 309$ K, $P = 3.15$ kbars. The main peak for both spectra corresponds to about 0.2 ms (from [33])

The observed similarity of ΔV in the diblock with the pure PVE corroborates the notion that the main relaxation in the former is due to the hard component (PVE) that is noticeably characterized by a lower ΔV, as compared to the soft block (PI) under similar ΔT_g. For independent component dynamics, pressurization of the copolymer would slow down more efficiently the fast (PI) rather than the slow (PVE) component simply because of the higher ΔV requirement in the latter. In fact, the spectrum of Fig. 8.16 at 3.15 kbar and 309 K can be rationalized by estimating the relative slowing down of the two components from: $\Delta \log (\tau_{\mathrm{PI}}/\tau_{\mathrm{PVE}}) = (\Delta V_{\mathrm{PI}} - \Delta V_{\mathrm{PVE}}) \Delta P/(2.303\ RT) \approx 1.6$ which is about the required frequency shift for successful overlapping of the two processes of Fig. 8.16. In this estimation we have assumed $T_g = 233$ K for both components in the diblock and the ΔV values at $\Delta T_g = 76$ K. The utilization of ΔV of the bulk PI instead of the corresponding quantity of the fast process in the diblock, is justified by the observation that the characteristic times of the latter are in close proximity to the bulk PI.

   In conclusion, decreasing T and increasing P produce qualitatively similar broadening at low frequencies; however, P unlike T has an additional function; high P induces dynamic homogeneity in contrast to temperature. The former is a property of the concentration fluctuations and the strong non-Arrhenius dependence of the primary process, whereas the latter is a result of the different ac-
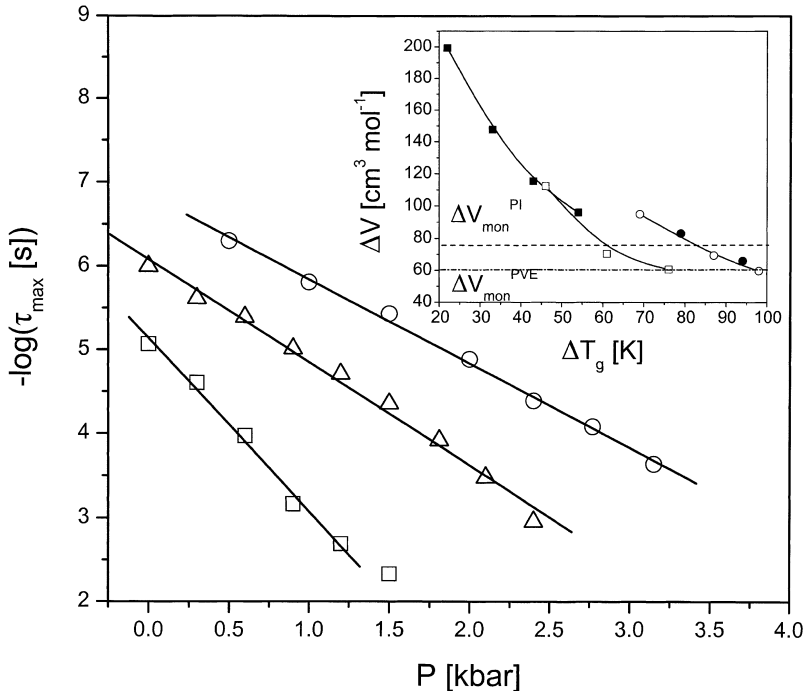
Fig. 8.17. Pressure dependence of the characteristic times corresponding to the main relaxation in the PI-*b*-PVE shown at three temperatures: (*open squares*): $T = 279$ K, (*open triangles*): $T = 294$ K, (*open circles*) $T = 309$ K. The *lines* are linear fits to the experimental times. In the *inset* the activation volume for the segmental relaxation of PI ((*open circles*): $MW = 2.6 \times 10^4$ g mol^{-1}, (*filled circles*): $MW = 1.06 \times 10^4$ g mol^{-1}) and PVE (*filled squares*) homopolymers as well as of the PI-*b*-PVE copolymer (*open squares*) are plotted at temperatures equidistant from the corresponding T_g's. For the T_g the following values were used: 272, 208 and 233 K for PVE, PI and PI-*b*-PVE respectively and correspond to the temperature where the maximum relaxa-tion time in DS is 10 s. The *lines* are linear fits (from [33])

tivation volumes of the species. As we will see below it is not always the soft component that is the one with the highest activation volume.

8.5.2
The PS/PVME Homogeneous Blend

The dynamics in the miscible blend PS/PVME have attracted many investigations with a variety of techniques ([70] and references therein). Rheology has been used and found that the time-temperature superposition principle fails in the blends, meaning that the system is thermorheologically complex at both the segmental and terminal regimes. DS has also been employed to probe the dynamics at the segmental level [70, 73]. Due to the much higher dipole moment of PVME as compared to PS, DS allows the selective probing of the PVME dynamics in the blends. The blend spectra were found to be asymmetrically broadened
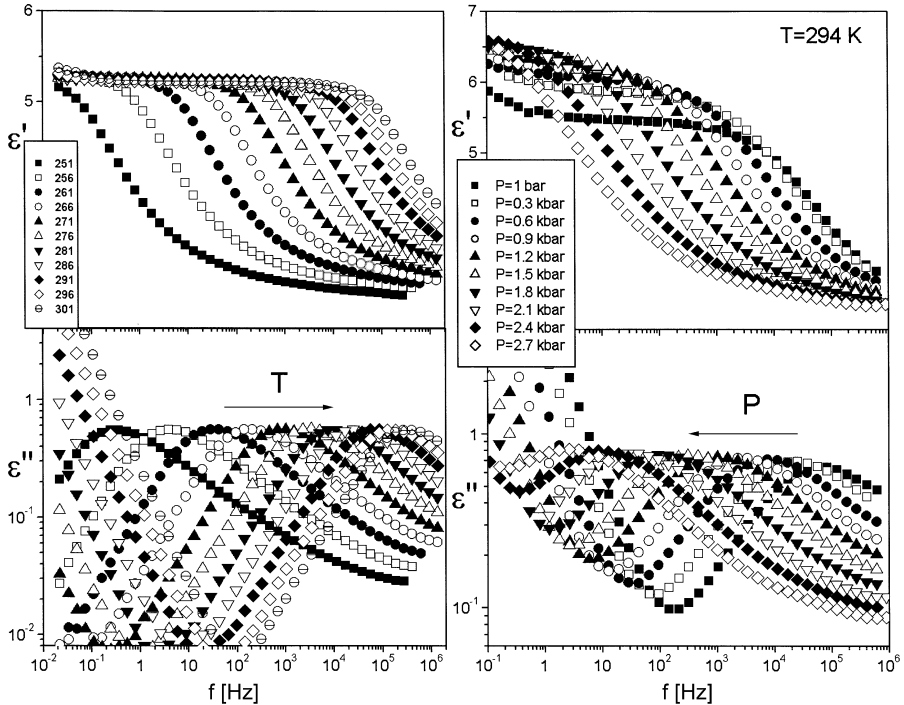
Fig. 8.18. Dielectric loss spectra for pure PVME as a function of temperature at 1 bar (*top*) and as a function of pressure at 294 K (*bottom*). The corresponding temperatures to the data taken at 1 bar are: (*filled squares*): 251 K, (*open squares*): 256 K, (*filled circles*): 261 K, (*open circles*): 266 K, (*filled triangles*): 271 K, (*open triangles*): 276 K, (*inverted filled triangles*): 281 K, (*inverted open triangles*): 286 K, (*filled lozenges*): 291 K and (*circled minus sign*): 301 K. The corresponding pressures to the data taken at 294 K are: (*filled squares*): 1 bar, (*open squares*): 0.3 kbar, (*filled circles*): 0.6 kbar, (*open circles*): 0.9 kbar, (*filled triangles*): 1.2 kbar, (*open triangles*): 1.5 kbar, (*inverted filled triangles*): 1.8 kbar, (*inverted open triangles*): 2.1 kbar, (*filled lozenges*): 2.4 kbar and (*open lozenges*): 2.7 kbar (from [34])
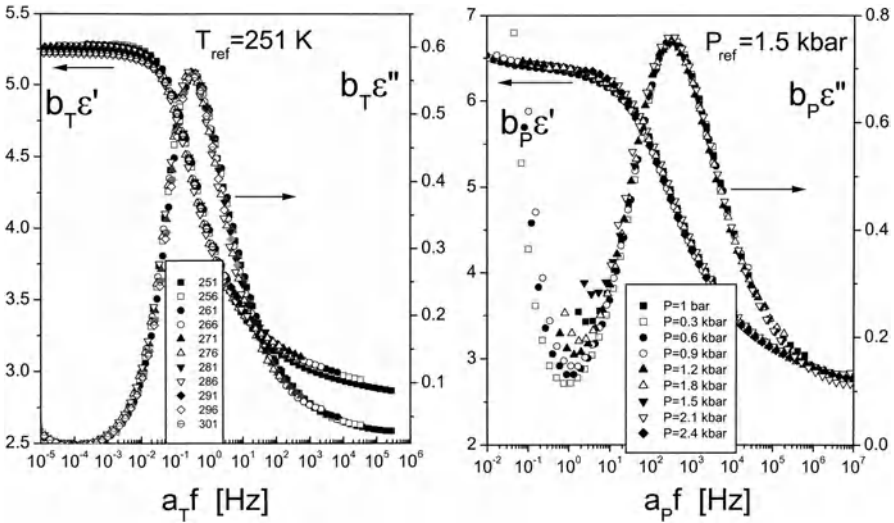
Fig. 8.19. "Master curves" obtained by applying vertical (b) and horizontal (a) shift factors to the data shown in Fig. 8.18. The corresponding temperatures to the data taken at 1 bar are: (*filled squares*): 251 K, (*open squares*): 256 K, (*filled circles*): 261 K, (*open circles*): 266 K, (*filled triangles*): 271 K, (*open triangles*): 276 K, (*inverted filled triangles*): 281 K, (*inverted open triangles*): 286 K, (*filled lozenges*): 291 K and (*circled minus signs*): 301 K. The corresponding pressures to the data taken at 294 K are: (*filled squares*): 1 bar, (*open squares*): 0.3 kbar, (*filled circles*): 0.6 kbar, (*open circles*): 0.9 kbar, (*filled triangles*): 1.2 kbar, (*open triangles*): 1.5 kbar, (*inverted filled triangles*): 1.8 kbar, (*inverted open triangles*): 2.1 kbar, (*filled lozenges*): 2.4 kbar and (*open lozenges*): 2.7 kbar. On the *left*, the spectra taken at different temperatures were shifted to the spectrum at 251 K, and on the *right*, the spectra taken at the different pressures at 294 K, were shifted to the spectrum at 1.5 kbar (from [34])

towards the low frequency side and models based on concentration fluctuations have been employed to account for the spectral shape. Here we review the effect of pressure on the dynamic miscibility in PS/PVME blends [34]. Representative dielectric spectra for the pure PVME are shown in Fig. 8.18 as a function of temperature and pressure. In Fig. 8.19 use of the time-temperature (tTs) and time-pressure (tPs) superposition allows "master curves" to be constructed from the data shown in Fig. 8.18. The *tTs* allows the frequency dependence of the complex permittivity ε^* at any temperature to be determined from a master curve at a reference temperatures T_{ref} according to

$$\varepsilon^*(f;T) = b_T \, \varepsilon^*(a_T f; T_{ref}) \tag{8.29}$$

Similarly, the use of the *tPs* allows the frequency dependence of the complex permittivity ε^* at any pressure to be determined from a master curve at a reference temperature P_{ref} according to

$$\varepsilon^*(f;P) = b_P \, \varepsilon^*(a_P f; P_{ref}) \tag{8.30}$$

It is evident that at each temperature (pressure), a single frequency-scale shift factor a_T (a_P) and a single permittivity-scale shift factor b_T (b_P) allow superposi-
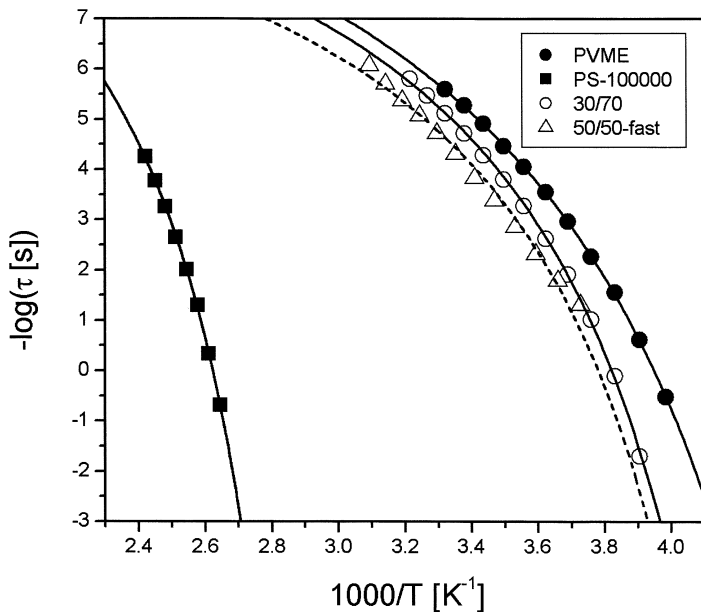
Fig. 8.20. Temperature dependence of the relaxation times corresponding to the maximum dielectric loss in the usual activation plot. The key to the symbols are: (*filled squares*): bulk PS, (*filled circles*): bulk PVME, (*open circles*): PS/PVME (30/70) and (*open triangles*): PS/PVME (50/50). The *lines* are fits to the VFT equation (Eq. 8.11) (from [34])

tion of all dielectric spectra at temperature T (pressure P) with the spectra at the reference temperature T_{ref} (P_{ref}). Since T and P completely define the thermodynamic state of the system we conclude that the PVME relaxation is described by a distribution function whose shape is independent of the thermodynamic state of the system. However, in the blends, tTs and tPs fail due to the broadening of the spectra towards the low-frequency side.

In Fig. 8.20 the relaxation times corresponding to the maximum loss are plotted in the usual Arrhenius representation. Notice that the relaxation processes in the blends are located in the vicinity of the pure PVME relaxation. The times have been fitted to the VFT equation with parameters -12.1, 720 ± 70 K, 322 ± 3 K and -11.8, 622 ± 24 K, 200 ± 2 K for the PS and PVME homopolymers, respectively. The corresponding parameters for the 30/70 and 50/50 blends are: -11, 480 ± 30 K, 218 ± 2 K and -10.3, 460 ± 30 K, 220 ± 2 K, respectively.

The pressure dependence of the relaxation times corresponding to the maximum loss of the two homopolymers is shown in Fig. 8.21. The relaxation times display a linear dependence within the investigated pressure range with different slopes for the PVME and PS. For example, at 294 K (i.e., $\Delta T = T - T_\infty = 94$ K), an increase of pressure by 1 kbar results in a slowing down of the PVME relaxation times by about 1.5 decades, whereas the same pressure applied at 418 K (i.e., $\Delta T = T - T_\infty = 96$ K), results in the retardation of the PS times by about 3.5 decades. The corresponding relaxation times in the blends were found to have a
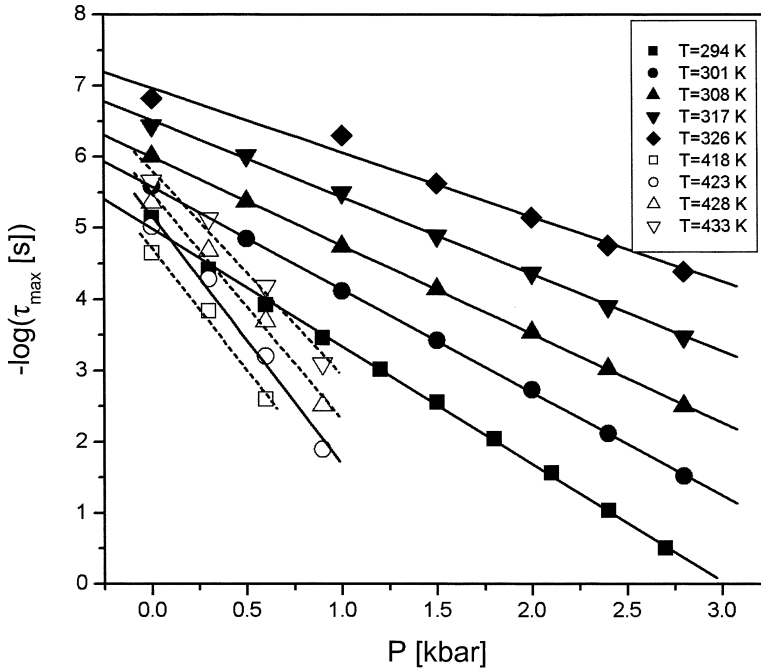
Fig. 8.21. Pressure dependence of the relaxation times at maximum loss for the homopolymers: *filled symbols*: PVME, *open symbols*: PS shown at different temperatures: (*filled squares*): 294 K, (*filled circles*): 301 K, (*filled triangles*): 308 K, (*inverted filled triangles*): 317 K, (*filled lozenges*): 326 K, (*open squares*): 418 K, (*open circles*): 423 K, (*open triangles*): 428 K, (*inverted open triangles*): 433 K. The *solid and dashed lines* are linear fits to the PVME and PS relaxation times, respectively (from [34])

similar P-dependence as with the PVME. The corresponding activation volumes are plotted in Fig. 8.22 for the PS, PVME homopolymers and their blends. In order for this comparison to be meaningful the volumes are compared at temperatures equidistant from the respective "ideal" glass transition temperatures. The result shows that the apparent activation volume of the process corresponding to the maximum loss in the blends exhibit similar values and identical T-dependence with the pure PVME being much smaller than the corresponding volume in the PS.

To make the comparison between the homopolymers and their blends more quantitative the various $T_g(P)$ dependencies are compared in Fig. 8.23. Here T_g is operationally defined as the T corresponding to a relaxation time of 100 s and involves extrapolations from the isothermal and isobaric data. The P-dependence of the glass transition temperatures can be parameterized as $T_g^{PS}(K) = 373.4 + 22.8\ P$ (kbar), $T_g^{PVME}(K) = 249 + 9.21\ P$ (kbar), $T_g^{70/30}(K) = 258 + 9.6\ P$ (kbar), and $T_g^{50/50}(K) = 264.6 + 9.0\ P$ (kbar). The slopes dT_g/dP are also plotted in the inset and confirm the assignment of the peak maximum as reflecting mainly PVME relaxing segments in the blends. The concentration fluctuation model employed earlier to account for the affect of blending on the shape of the
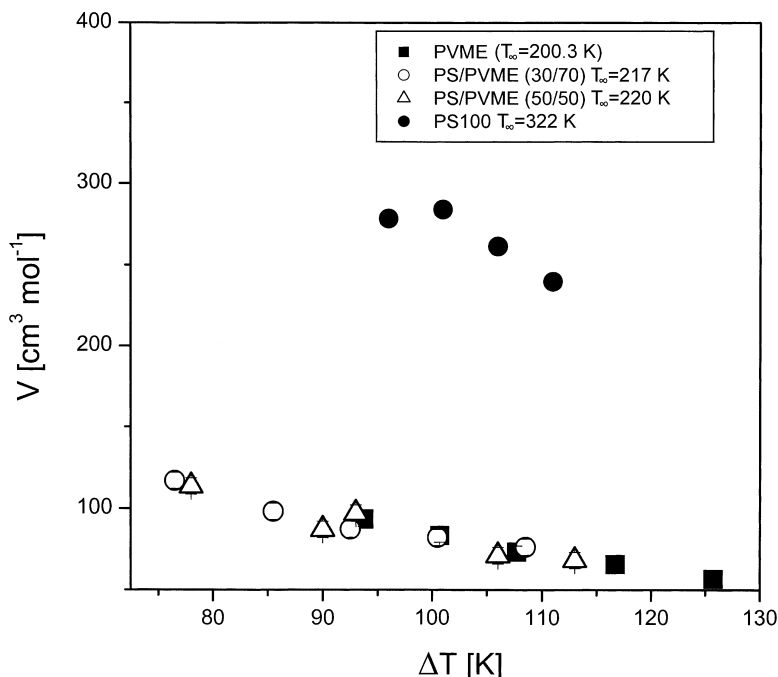
Fig. 8.22. Activation volumes of the homopolymers PS (*filled circles*) and PVME (*filled squares*) and of the blends PS/PVME (30/70) (*open circles*) and PS/PVME (50/50) (*open triangles*) plotted as a function of the temperature difference ($\Delta T = T - T_\infty$) from the respective "ideal" glass temperature. The following T_∞ values have been used: PVME: 200.3 K, PS: 322 K, PS/PVME (30/70): 217 K and PS/PVME (50/50): 220 K (from [34])

segmental relaxation as a function of T [73, 76] can also be applied here to describe the effect of P on the concentration fluctuations.

8.6
Effect of Pressure on Polymer Crystallization

Pressure like temperature can induce polymer crystallization. Although the effect of pressure on the segmental relaxation of amorphous polymers has been investigated, the corresponding effect on the complex relaxation spectra of semicrystalline polymers is relatively unexplored. Pressure might also have additional functions than temperature alone. For example, the densification of the system may influence the dynamics and the crystallization kinetics. Such investigations require a polymer with strong dipole moment that undergoes crystallization/melting at a convenient temperature range. Moreover, for intensity reasons, the dipole ideally should be located near but outside the crystal.

A good example of a homopolymer undergoing crystallization which fulfill these requirements is the semicrystalline polymer poly(*n*-octadecyl methacry-
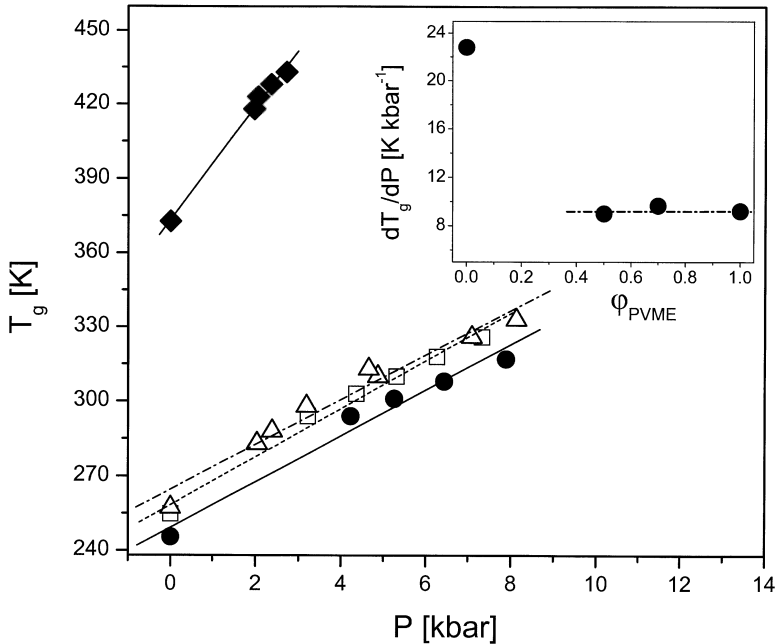
Fig. 8.23. Pressure dependence of the glass temperature for the homopolymers PS (*filled lozenges*) and PVME (*filled circles*) and of the blends PS/PVME (30/70) (*open squares*) and PS/PVME (50/50) (*open triangles*). For the T_g definition we have used the temperature at which the relaxation times are 100 s. In the *inset* the dT_g/dP is shown as a function of the PVME volume fraction (from [34])

late) (PnODMA) with a melting temperature of 308 K [29]. PnODMA is a nice probe for sidechain crystallization by using dielectric spectroscopy; being a member of the poly(*n*-alkyl methacrylate) series has a strong dipole moment which is located in the vicinity of both the backbone and the crystallizing units. Static experimental probes can account for the morphology (wide-angle X-ray scattering (WAXS), differential scanning calorimetry (DSC)) and dynamic probes (DS) to monitor the relaxations in the melt and crystal states. For PnODMA earlier WAXS [77, 78] and infra-red (IR) studies [79] have shown that – at atmospheric pressure – part of the side-chains composed of about ten methylene units crystallize in a lattice with a hexagonal symmetry. Can pressure affect the crystal characteristics such as crystal thickness and overall crystallinity and influence the macroscopic properties of the material?

Some structural information is needed before the DS study. The (apparent) melting temperature T'_m and the heat of fusion have been determined with DSC and amount to 308 K and 45 J·g^{-1}, respectively. WAXS measurements revealed that the degree of crystallinity is about 50%. From the WAXS diffraction peaks, the heat of fusion, the degree of crystallinity, and FTIR spectroscopy on monomolecular layers, the following model has been proposed. According to the model, shown in Fig. 8.32 (below), crystallites are formed by intercalating side

chains pointing in opposite directions. The "amorphous" phase is composed of the chain backbone and some portion of the side chains in their vicinity composed of five to seven methylene units. The latter act as spacers to adjust for the density difference between the hexagonally packed side-chains and the steric requirements imposed up on the side-chains by fixing them to the polymer backbone. This leaves about ten methylene units within the crystallites.

Figure 8.24 gives some representative dielectric loss spectra of PnODMA obtained by increasing T at atmospheric pressure (top) or by increasing pressure at 321 K (bottom). Below the melting temperature (T_m^o) for a given pressure or above the critical pressure (P_c) at a given temperature, upon crystallization, the dielectric spectra undergo significant changes: first they shift to lower frequencies and broaden considerably towards the lower frequency side. In addition, there is a loss of the crystal phase intensity relative to the melt which is both T- and P-dependent.

DS apart from the dynamics provides valuable information through the intensity of the process under investigation. The dielectric strength for segmental dynamics depends on T and P and is given by

$$\Delta\varepsilon\,(T,P) \approx \frac{\rho(T,P)}{k_B T}\, F(T,P)\, g(T,P)\, \mu^2 \qquad (8.31)$$

where $\rho(T,P)$ is the mass density and $g(T,P)$ is the Kirkwood correlation function which takes into account the short-range orientation correlations between a reference molecule and its nearest neighbors. $F(T,P)$ is the local field which is given by

$$F(T,P) = \frac{\varepsilon_S(T,P)(\varepsilon_\infty(T,P)+2)^2}{3(2\varepsilon_S(T,P)+\varepsilon_\infty(T,P))} \qquad (8.32)$$

Since T and P enter in the expression through different factors we plot in Fig. 8.25 the normalized quantity, $T\Delta\varepsilon/\rho F$, which is proportional to $g(T,P)$. In the melt, the increase of the normalized strength with P signifies a strong $g(T = \text{constant}, P)$ dependence and the highest value of the orientation correlations is obtained at the transition point. In the crystal state, the opposite trend results from the decrease in the number of mobile dipoles through the incorporation of methylene units to the crystal which tends to increase the crystal thickness. Temperature has a similar effect on the normalized strength. In the melt, increasing T weakens the strong pair orientation correlations between adjacent dipoles. The effect is spectacular: decreasing T within 40 K doubles the value of $g(T, P = \text{constant})$. This strong T-dependence indicates that, by cooling towards the transition temperature, dipoles become increasingly correlated, i.e., there exists a *pre-ordering* mechanism before the onset of crystallization. This could originate from the extension of the sidechains prior to crystallization which tend to increase $g(T,P)$ but does not involve complete ordering and thus is not observable in the diffraction experiments. Thus, DS through the intensity of the process can provide valuable information which is not accessible by static experiments.

The loss of crystal phase intensity with decreasing T is better shown in Fig. 8.26 (top). Here the assumption is that the intensity in the semicrystalline
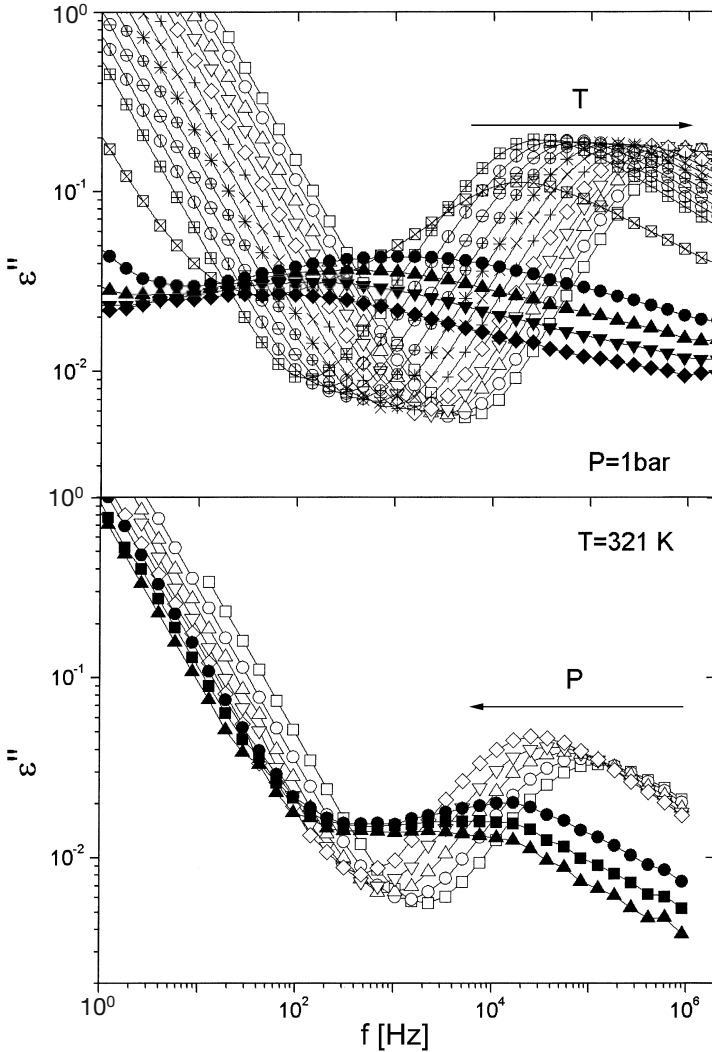
Fig. 8.24. Dielectric loss spectra for PnODMA under isobaric (*top*) and isothermal (*bottom*) conditions. The *open and filled symbols* correspond to spectra taken within the melt and crystal phases, respectively. The corresponding temperatures for the isobaric spectra are: (*filled lozenges*): 278 K, (*inverted filled triangles*): 283 K, (*filled triangles*): 288 K, (*filled circles*): 293 K, (*squared multiplication signs*): 298 K, (*squared plus signs*): 303 K, (*open circles with vertical lines*): 308 K, (*open circles with horizontal lines*): 313 K, (*circled plus signs*): 318 K, (*stars*): 323 K, (*X*): 328 K, (*plus signs*): 333 K, (*open lozenges*): 338 K, (*inverted open triangles*): 343 K, (*open triangles*): 348 K, (*open circles*): 353 K, (*open squares*): 358 K. The pressures for the isothermal spectra are: (*open squares*): 1 bar, (*open circles*): 0.3 kbar, (*open triangles*): 0.6 kbar, (*inverted open triangles*): 0.9 kbar, (*open lozenges*): 1.2 kbar, (*filled circles*): 1.5 kbar, (*filled squares*): 1.8 kbar, (*filled triangles*): 2.1 kbar (from [29])
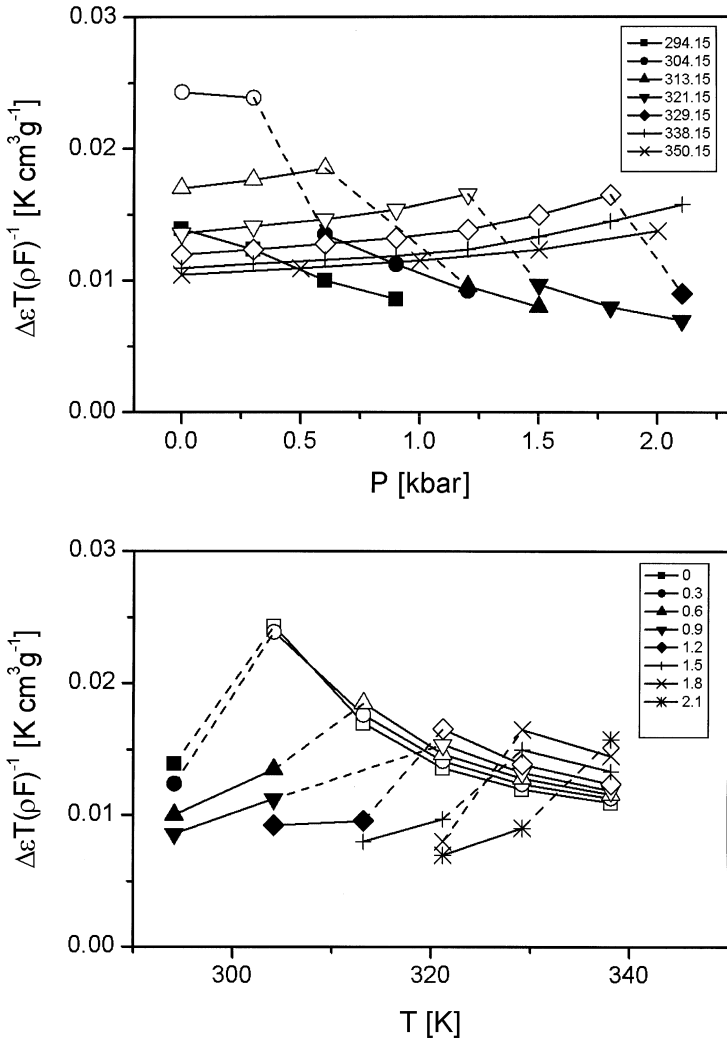
Fig. 8.25. Pressure (*top*) and temperature (*bottom*) dependence of the normalized relaxation strength $T\Delta\varepsilon/\rho F$, shown for different temperatures: (*filled squares*): 294 K, (*filled circles*): 304 K, (*filled triangles*): 313 K, (*inverted filled triangles*): 321 K, (*filled lozenges*): 329 K, (*plus signs*): 338 K, (*X*): 350 K and different pressures: (*filled squares*): 1 bar, (*filled circles*): 0.3 kbar, (*filled triangles*): 0.6 kbar, (*inverted filled triangles*): 0.9 kbar, (*filled lozenges*): 1.2 kbar, (*plus signs*): 1.5 kbar, (*X*): 1.8 kbar, (*stars*): 2.1 kbar. The *open and filled symbols* correspond to the melt and crystal states, respectively. The *lines* are guides to the eye (from [29])

Fig. 8.26. Temperature-
(*top*) and pressure-
(*bottom*) dependence of the
ratio of the crystal to melt
dielectric strength. In the
latter the intensity ratio is
plotted as a function of
pressure difference from the
critical pressure $P_c(T)$
needed to induce the crys-
tallization. The different
data sets in the latter corre-
spond to different tempera-
tures: (*filled squares*): 304 K,
(*filled circles*): 313 K, (*filled
triangles*): 321 K and (*in-
verted filled triangles*):
329 K. The *lines* are guides
to the eye (from [29])
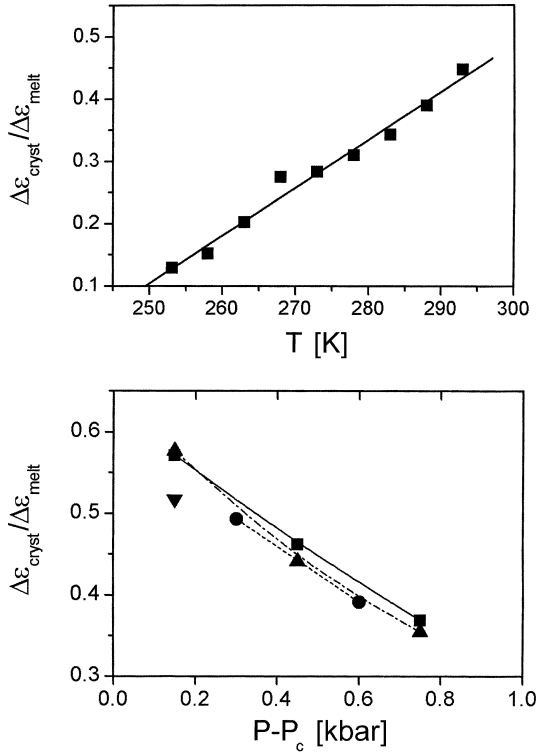
material results solely from dipoles excluded from the crystals, i.e., dipoles lo-
cated within the amorphous phase. This assumption seems realistic; the dielec-
tric relaxation within the crystal structure would be very slow and of extremely
low intensity since the dipole moment of PnODMA is located near the backbone
and this is excluded from the crystallizing units. In Fig. 8.26 we plot the ratio of
the dielectric strength in the semicrystalline material to the corresponding
quantity in the melt state (obtained by extrapolation). The intensity ratio at the
transition is about 0.5 which is in accordance with the crystallinity of 50 % as ob-
tained from WAXS. However, by decreasing T this ratio displays a linear decrease
at constant crystallinity. A two-phase system composed from amorphous and
crystalline phases cannot explain the strong T-dependence of the ratio.
Alternatively, it has been proposed that the ratio provides a direct measure of the
material located within the interface, i.e., within the rigid amorphous phase
(RAP) [80–83]. The latter has a strong T-dependence originating from a T-de-
pendent number of dipoles that freeze by lowering T. At 250 K, most of the amor-
phous phase is composed from the RAP, whereas at the melting temperature the
RAP vanishes. At intermediate temperatures, the single but very broad relax-
ation process originates from "fast" and "slow" dipoles located within the *mobile
amorphous* and *rigid* amorphous phases, respectively. However, there is no tem-
perature where a dual relaxation could be found, that is, separate relaxations of

the two fractions. As we will see below with respect to the kinetic studies, the appearance of a dual relaxation process depends strongly on the annealing at the crystallization temperature T_c.

The effect of pressure on the number of mobile dipoles is also shown in Fig. 8.26 (bottom) where the same ratio is now plotted as a function of the pressure difference from the critical pressure for crystallization. The overall effect of increasing P is qualitatively similar to that of decreasing T. For a more quantitative comparison a relation between δT and δP (where d is the variation in T or P) is required. Anticipating the result (see below), regarding the shift of the crystallization temperature with pressure, we find that an increase of pressure of 2 kbars corresponds to a 35 K increase in temperature. By comparing the fractions of the RAP produced by lowering T and increasing P we find that decreasing T is more effective than increasing P in inducing the RAP.

The T- and P-dependence of the relaxation times is shown in Fig. 8.27. Within the investigated T- and P- ranges both relaxation times, in the crystal and melt states, display a nearly linear dependence on T^{-1} and P, and these dependencies are consistently stronger in the crystal state. For a purely activated process we can define the activation volume which is always higher in the crystal state as compared to the melt. At the same time the apparent activation energy at a constant pressure ($E = 2.303R\,(\partial \log \tau / \partial T^{-1})_P$) is also higher in the crystal as compared to the melt state. The dependencies of the activation volume and activation energy on P and T, respectively, are shown in Fig. 8.28. The melt activation energies and activation volumes display a weak T- and P-dependence which together with the narrow distribution of relaxation times (which is T- and P-independent) signify a small cooperativity. In the crystal state, the activation volume and apparent activation energies are consistently higher which is suggestive of a hindered and thus a more cooperative relaxation within the restricted amorphous phase.

The different $\tau(T,P)$ dependencies of the melt and crystal states can also be discussed in terms of the "fragility plot" [84] where the relaxation times are plotted as a function of reduced temperature. This representation for the lower members of the series have shown a systematic dependence of the "steepness index" and thus of the fragility on the length of the alkyl side chain. The "steepness index" [85] defined as

$$m = \frac{\mathrm{d}\,(\log \tau_{\max})}{\mathrm{d}\,(T_g/T)}\bigg|_{\text{at } T \approx T_g} \tag{8.33}$$

was found [86] to change systematically from 92 in poly(methyl methacrylate) to 36 in poly(n-decyl methacrylate). The investigation of the static structure factor revealed that this dynamic behavior reflected on the increased intersegmental distances [86]. For the T_g definition, the T corresponding to a relaxation time of 100 s was used and the extrapolations were made using both the isobaric (Fig. 8.27, top) and isothermal (Fig 8.27, bottom) melt and crystal state relaxation times. With the above definitions of T_g the "fragility plot" has been constructed in Fig. 8.29. The steepness index is 19.7 and 28.2 for the melt and crystal states, respectively, independent of pressure. These values are characteristic of "strong" liquids with the melt value being one of the lowest reported.
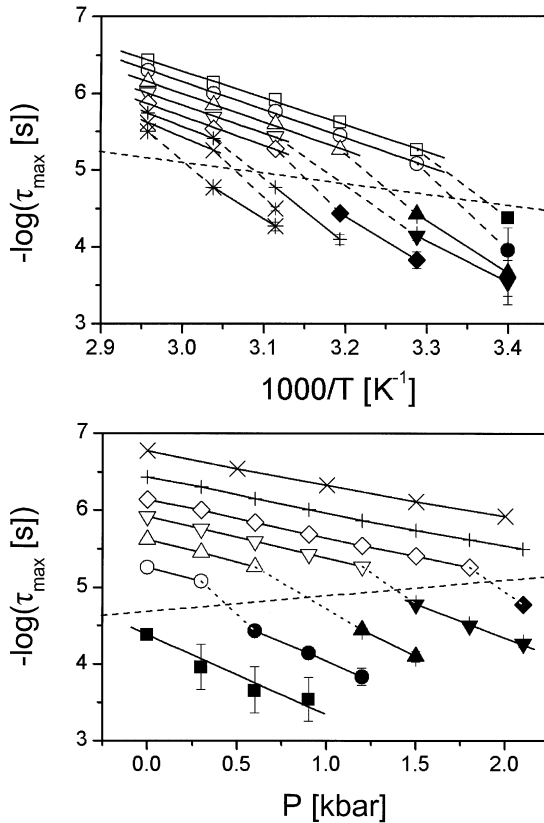
Fig. 8.27. Temperature (*top*) and pressure (*bottom*) dependence of the relaxation times corresponding to the maximum loss. The different pressures are: (*open squares*): 1 bar, (*open circles*): 0.3 kbar, (*open triangles*): 0.6 kbar, (*inverted open triangles*): 0.9 kbar, (*open lozenges*): 1.2 kbar, (*plus signs*): 1.5 kbar, (*X*): 1.8 kbar, (*stars*): 2.1 kbar and the different temperatures: (*filled squares*): 294 K, (*filled circles*): 304 K, (*filled triangles*): 313 K, (inverted *filled triangles*): 321 K (*filled lozenges*): 329 K, (*plus signs*): 338 K and (*X*): 350 K. The *open and filled symbols* correspond to the melt and crystal states, respectively and the *solid lines* are the result from the linear fits (see text). *Error bars* are visible only when exceed the symbol size. The *dashed lines* indicate the transition from the melt to the crystal states (from [29])

The T- and P-dependencies of the relaxation times can be combined in a single variable: the density ρ in a $\tau(\rho)$ representation. We have used the Tait equation (crystal: $A_o = 0.983$ cm^{3}g^{-1}, $A_1 = 4.14 \times 10^{-4}$ cm^{3}g^{-1}K^{-1} and melt: $A_o = 1.002$ cm^{3}g^{-1}, $A_1 = 5.45 \times 10^{-4}$ cm^{3}g$^{-1}\cdot$K^{-1}). The volume was then calculated from the isothermal and isobaric experiments and the $\tau(\rho)$ dependence is shown in Fig. 8.30. The open and filled symbols signify the melt and crystal states, respectively, and the long connecting lines result from the densification up on crystallization. There are some points to be noticed: (i) variation of T is more effective than P in shifting the relaxation times, (ii) melts prepared by T or

Fig. 8.28. Apparent activation energies and activation volumes plotted vs P and T, respectively for the melt (*open symbols*) and crystal (*filled symbols*) states, respectively. Notice that the crystal state possess higher activation energies and activation volumes. The error bars for the melt data are smaller than the symbol size (from [29])
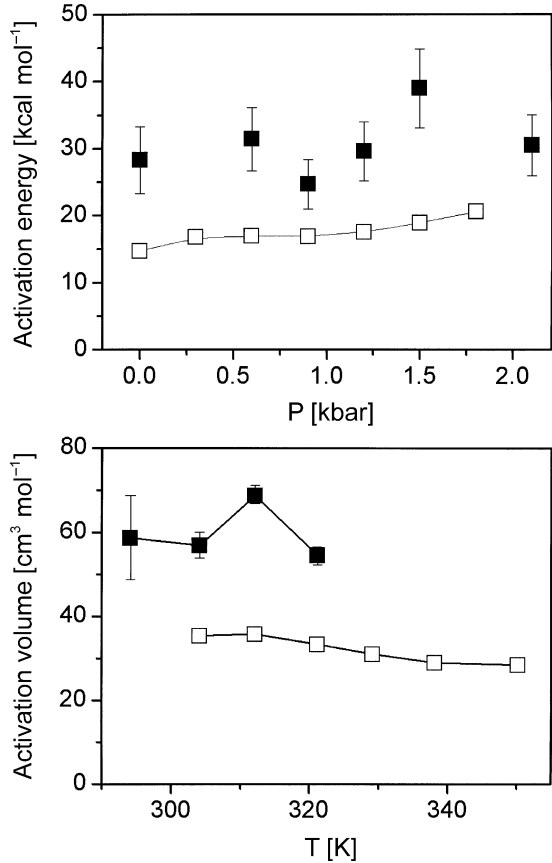
Fig. 8.29. T_g-scaled plot of the melt (*open symbols*) and crystal (*filled symbols*) relaxation times. The $T_g(P)$ is operationally defined as a temperature corresponding to 100 s. *Dash-dotted and dashed lines* are linear fits to the melt and crystal data points [29]
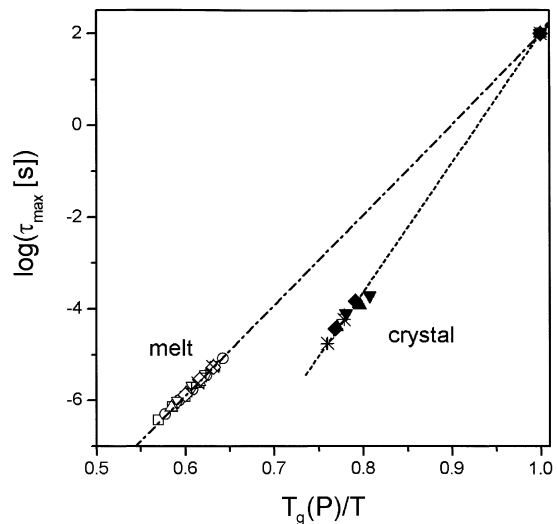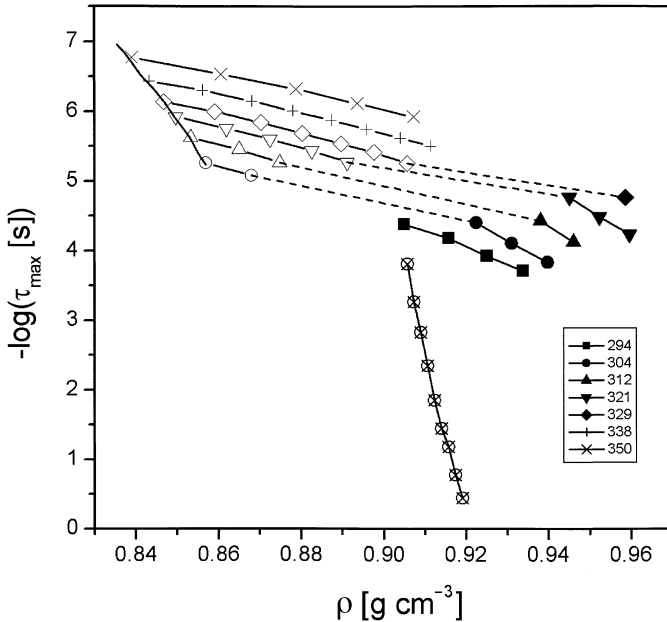
Fig. 8.30. Relaxation map for the PnODMA as a function of density. The points are from a compilation of data taken under isobaric and isothermal conditions. The (*circled multiplication signs*) data points correspond to the isobaric data ($P = 1$ bar) in the crystal state. Again, the *open and filled symbols* correspond to the melt and crystal states, respectively: (*filled squares*): 294 K, (*filled circles*): 304 K, (*filled triangles*): 312 K, (*inverted filled triangles*): 321 K, (*filled lozenges*): 329 K, (*plus signs*): 338 K, (*X*): 350 K. *Solid lines* are only guides for the eye and *dashed lines* indicate the transition regimes (from [29])

P variations and compared under conditions of constant density differ in their dynamics by one to two decades, but crystals compared under the same conditions can differ as much as four decades. This happens despite the higher activation volume of the crystal as compared to the melt state and results largely from the higher activation *energy* in the crystal state obtained under isobaric conditions ($P = 1$ bar). Therefore, density is not the controlling parameter for the segmental dynamics in the melt state and this is also true for the segmental relaxation in semicrystalline polymers.

From the pressure dependence of the crystallization temperature we can draw conclusions about morphological changes occurring in PnODMA. The $T_g(P)$ and $T_c(P)$ dependencies are shown in Fig. 8.31. For the glass transition, both the segmental relaxation in the melt and crystal states were used to define $T_g^{melt}(P)$ and $T_g^{crystal}(P)$, respectively. In both cases, $T_g(P)$ was obtained by extrapolating the melt and crystal dynamics obtained at different temperatures and pressures from both the isothermal and isobaric relaxation times. For the glass transition temperature the operational definition was used (as the temperature where the relaxation times attain a value of 100 s). For the $T_c(P)$ definition, the crystallization temperature (T_c) and pressure (P_c) at which the crystallization times be-
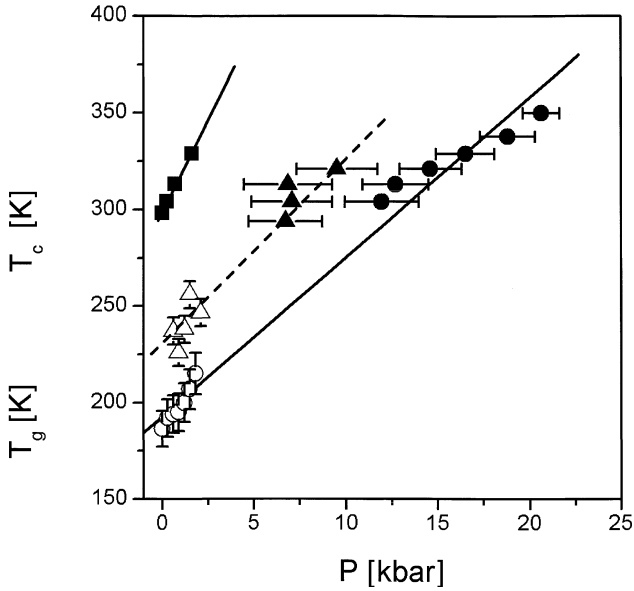
Fig. 8.31. Dependence of the melt glass transition temperature T_g^{melt} (*circles*) and of the glass transition temperature corresponding to the amorphous phase in the semicrystalline material T_g^{crystal} (*triangles*) and of the crystallization temperature T_c (*squares*), on pressure. The T_g is defined as the temperature corresponding to a relaxation time of 100 s. Both the isothermal (*filled symbols*) and isobaric (*open symbols*) relaxation data were used in the extrapolations. Notice the stronger P-dependence of the crystallization temperature (from [90])

come very slow with characteristic times of the order of 10^4 s were used. The latter is not precisely the P_m^o but is close to the true equilibrium pressure. The $T_g^{\text{melt}}(P)$, $T_g^{\text{crystal}}(P)$, and $T_c(P)$ dependencies shown in the figure display a linear dependence as

$$T_g^{\text{melt}}(\text{K}) = 192.8 + 8.25\,P(\text{kbar})$$

$$T_g^{\text{crystal}}(\text{K}) = 228 + 10.5\,P(\text{kbar}) \tag{8.34}$$

$$T_c(\text{K}) = 298.7 + 19.1\,P(\text{kbar})$$

These dependencies show a higher glass temperature for the amorphous polymer in the semicrystalline state reflecting the restriction imposed by the presence of crystals. At atmospheric pressure the restricted amorphous phase in the semicrystalline state has a glass temperature some 35 K higher with respect to the melt T_g. Furthermore, the crystallization temperature displays a much stronger dependence with $dT_c/dP \approx 2.3\,dT_g^{\text{melt}}/dP$, which can be traced back to the transition being of first order giving rise to a different crystal structure. Note that although $T_g^{\text{crystal}}(P) > T_g^{\text{melt}}(P)$ the $dT_g^{\text{crystal}}/dP \approx dT_g^{\text{melt}}/dP$ implying that the effect of restriction is mainly on the absolute value of the transition temperature the slope being determined by the melt dynamics.

P = 1 bar   P = 2 kbar
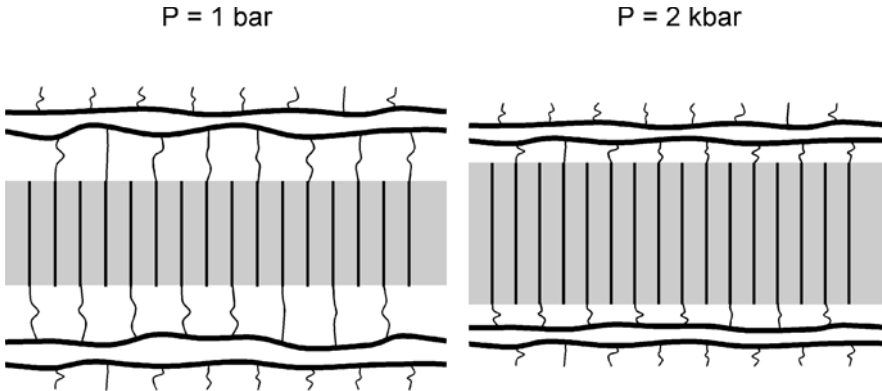
Fig. 8.32. Schematic representation of the structural changes imposed by a pressure of 2 kbars (from [29])

From the linear increase of the T_c with P the slope dP/dT can be defined and the Clausius-Clapeyron equation can be employed:

$$\frac{dP}{dT} = \frac{\Delta H}{T \Delta V} \tag{8.35}$$

where ΔH is the latent heat of the transition and ΔV is the change in volume. Using $dP/dT = 0.0579$ kbar K^{-1}, $\Delta V = 0.0574$ cm^3 g^{-1} [87] and $T = 296$ K we deduce a latent heat of 98 J g^{-1}. The latter is much higher than the latent heat obtained from DSC at atmospheric pressure (45 J g^{-1}). The higher latent heat results from the incorporation of additional CH$_2$ units within the crystal phase. Given that each methylene unit of lower alkanes contributes about 10 J g^{-1} to the latent heat [88] we deduce that a pressure of 2 kbars results in the incorporation of four to five additional methylene units in the sidechain crystal phase, thus increasing the crystal thickness as shown in Fig. 8.32. Thus, pressure has a dual function, not only slowing down the dynamics but also inducing morphological changes to the semicrystalline polymer PnODMA. Interestingly, these morphological changes can be obtained from dynamic data alone using DS.

The main results from the T- and P-dependent DS experiments on the semicrystalline polymer PnODMA undergoing side-chain crystallization are as follows:

1. Time-Temperature-superposition (*tTs*) and time-Pressure-superposition (*tPs*) works in the melt state and only approximately in the crystal state.
2. The T- and P-dependent crystal to melt intensity ratio suggests the existence of a rigid amorphous phase.
3. The T- and P-dependencies of the characteristic relaxation times revealed that the (single) relaxation process in the semicrystalline state possesses higher activation energy, higher activation volume and a higher steepness index as compared to the melt.

4. Melts with the same density prepared by varying T and P differ in their re-
   laxation times by two decades while crystals of the same density can differ
   even more.
5. Pressure increases the number of the crystallizing methylene units thus in-
   creasing the crystal thickness.
6. There is a strong increase of the pair correlations with decreasing T and in-
   creasing P as the transition from the melt state indicative of pre-transitional
   ordering is approached.

8.6.1
Crystallization Kinetics

DS under pressure can also be employed to follow the crystallization process, i.e.,
the crystallization kinetics. Despite the recent progress in understanding the
morphological changes during crystallization there is very little knowledge about
the associated dynamical changes during the crystallization process. The few ex-
perimental reports [2, 82, 83, 89] are mainly through dielectric spectroscopy at at-
mospheric pressure. PnODMA offers the possibility of investigating the crystal-
lization kinetics. The advantage of using P-instead of T-jump experiments is that
the former can be considered as "instantaneous" thus allowing the investigation
of the "fast" crystallization dynamics. Furthermore, the pressure effect might be
considerably different to T, since P was found to affect the crystal morphology
and overall crystallinity. The evolution of the crystallization process can be stud-
ied in real-time by recording the changes in the dielectric spectrum [90].

The crystallization kinetics of PnODMA were obtained by performing T- and
P-jumps from an initial state corresponding to the melt to different final crys-
tallization temperatures and pressures. Figures 8.33 and 8.34 show the time-evo-
lution of the dielectric permittivity and loss for a temperature jump from 308 to
295 K at atmospheric pressure and for a pressure jump from 1 to 400 bar at
304 K. The spectra shown correspond to the isothermal crystallization at the fi-
nal temperature and pressure, respectively. Notice that all spectra get progres-
sively broad from the low frequency side and for long crystallization times they
appear as bimodal. The decrease of the intensity near the maximum at 2×10^4 Hz
correspond to the decrease in the number of dipoles within the amorphous ma-
terial whereas the increasing intensity near the minimum, at about 20 Hz, corre-
spond to a new process (called α') originating from the increasing number of
dipoles in the restricted amorphous phase [2]. The appearance of the latter
process depends strongly on the final temperature and crystallization times as it
reflects the dynamics of dipoles in the vicinity of the crystallizing side-chains.
Apparently, long "equilibration" times are necessary for the appearance of the
slow α' process. It is worth noting that at a frequency of about 1 kHz the two ef-
fects seem to be compensated; an isochronal measurement at this frequency
would conceal all the spectral changes occurring during the crystallization
process. Such isosbestic points have first been observed in the dielectric loss
spectra of side-chain liquid crystalline polymers and have been treated theoret-
ically [91]. An integration of the spectra in the vicinity of the maximum and
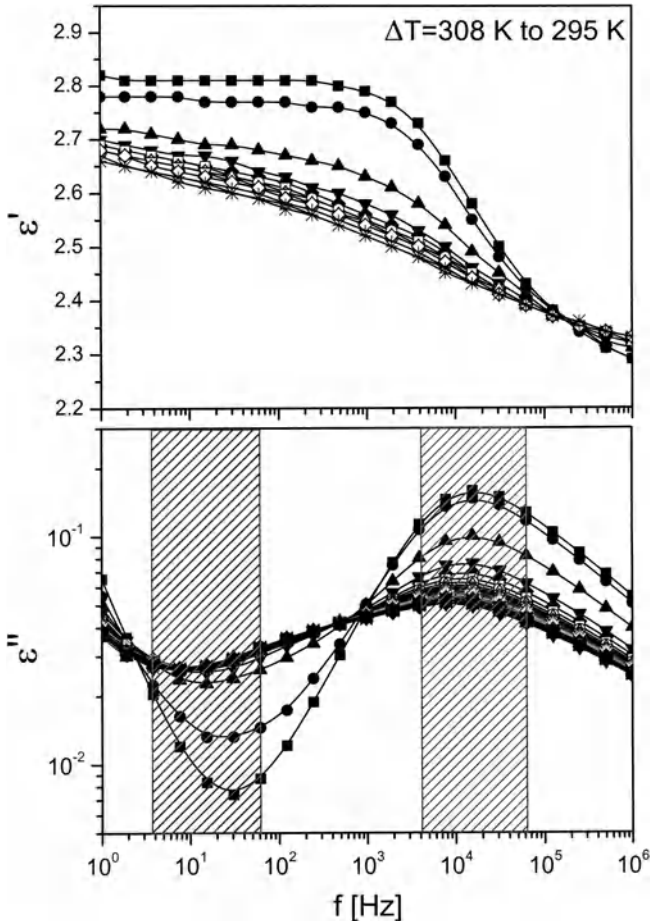
Fig. 8.33. Time evolution of the dielectric permittivity (*top*) and loss (*bottom*) spectra following a temperature jump from 308 to 295 K. The key to the symbols: (*filled squares*): 222 s, (*filled circles*): 422 s, (*filled triangles*): 621 s, (*inverted filled triangles*): 822 s, (*filled lozenges*): 1020, (*open squares*): 1220 s, (*open circles*): 1420 s, (*open triangles*): 1620 s, (inverted *open triangles*): 1820 s, (*open lozenges*): 2020 s, (*plus signs*): 4020 s, (*X*): 6020 s and (*stars*): 8020 s. The *hatched areas* indicate the frequency ranges around the minimum and maximum of the dielectric loss used in the integration (see text) (from [90])

minimum dielectric loss will reveal the characteristics of the processes a and α', respectively.

The evolution of the integrated intensities are shown in Fig. 8.35 for the three crystallization temperatures. The higher the crystallization temperature the longer it takes for the side-chains to crystallize; a decrease of the undercooling $\Delta T = T_m^o - T_c$ from 3 to 2 K slows down the kinetics by one decade ($T_m^o = 299$ K, as at this temperature the kinetics are extremely slow). Furthermore, identical kinetics for the min and max were found implying that the same dipoles are responsible for the loss of the intensity of the α-process and the concomitant in-
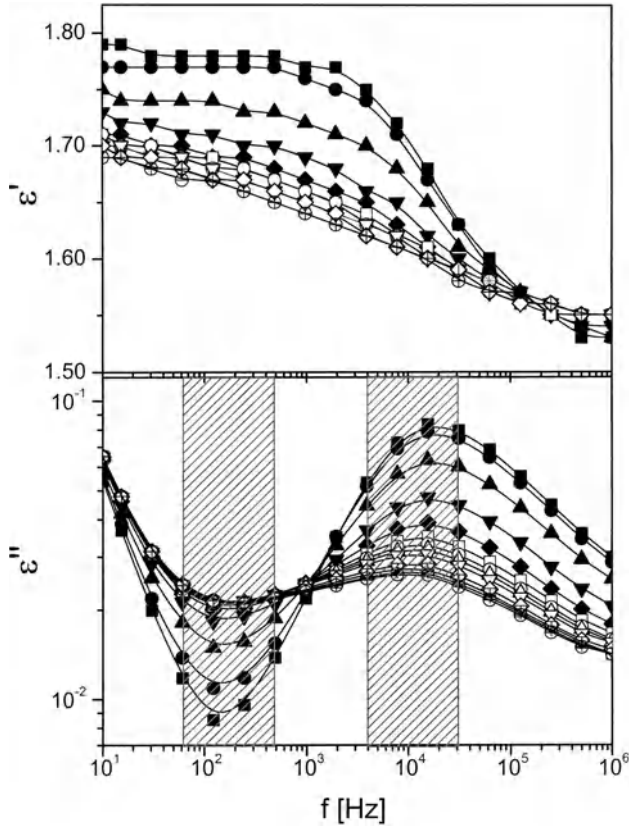
Fig. 8.34. Time evolution of the dielectric permittivity (*top*) and loss (*bottom*) spectra following a pressure jump from 1 to 400 bar at 304 K. The *hatched areas* indicate the frequency ranges around the minimum and maximum of the dielectric loss used in the integration (see text) (from [90])

crease of the slower α'-process. The evolution of the integrated intensities can be represented by the well-known KWW equation:

$$\sum \varepsilon'' \Delta f = A \exp(- ((t - t_0)/\tau)^{\beta_{KWW}}) + c \tag{8.36}$$

where A is the amplitude, t_0 is an initial time required for the temperature equilibration, τ is the characteristic crystallization time, and β_{KWW} is the KWW exponent. The result reveal that the isothermal crystallization following a T-jump gives rise to slow processes with a stretched exponential relaxation typical of the melt relaxation dynamics. The fractional exponents seem to indicate a strong effect of the crystallization mechanism on the transport and packing of chains. The formation of crystals at atmospheric pressure inhibits the transport of chains which have to move in a highly cooperative way.

Pressure has considerably different functions on the side chain crystallization of PnODMA. First, the $T_c(P)$ is much stronger than $T_g(P)$ (Fig. 8.31). Further-

Fig. 8.35. Time evolution of the integrated intensities corresponding to the maximum (*top*) and minimum (*bottom*) of the relaxation spectra obtained during the *T*-jump from 308 to different crystallization temperatures; *squares*: 297 K, *circles*: 296 K, and *triangles*: 295 K. The *lines* are fits according to Eq. (8.36) [90]
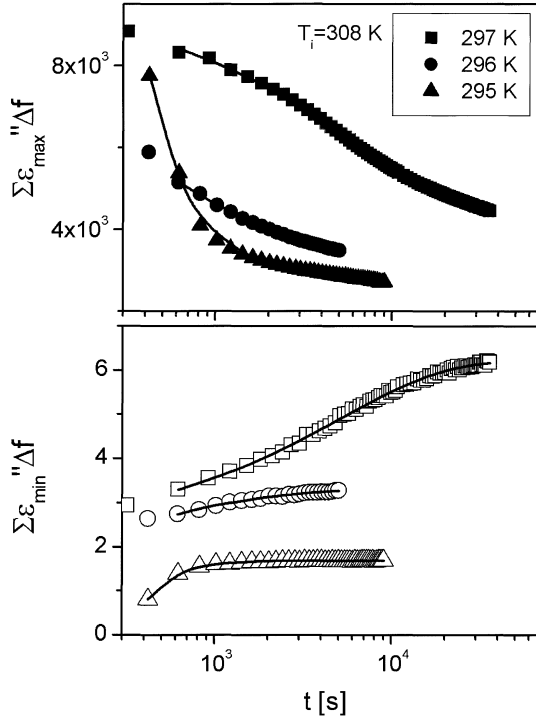
more, pressure results in a higher crystallinity through the incorporation of additional methylene units to the side-chain crystals. Therefore inducing the crystallization by pressure jumps is expected to result in considerably different kinetics.

Figure 8.36, gives the evolution of the dielectric susceptibility and loss following a *P*-jump from 1 bar to 400 bar at 304 K. As described above, at this temperature it would not be possible for the chains to crystallize without the assistance of pressure. At first glance the spectra evolution seem very similar to the corresponding *T*-jump experiments; the spectra get broader with time especially from the low frequency side. Again at a frequency of 1 kHz no significant changes occur. In contrast to the *T*-induced kinetics, the analysis of the integrated intensities at minimum and maximum positions have shown a completely different dependence of the crystallization kinetics. The integrated intensities *cannot* be described by a KWW function since they exhibit a stronger dependence on time. Instead, the evolution can now be described by the well-known Avrami equation

$$\sum \varepsilon'' \Delta f = A \exp\left(-zt^n\right) + \mathrm{d} \tag{8.37}$$

where A is the contrast factor, z is the crystallization rate, and n is the Avrami exponent which is a function of the type of the nucleation process (i.e., homogeneous vs heterogeneous) and the dimensionality of growth. The characteristic

Fig. 8.36. Time evolution of the integrated intensities corresponding to the maximum (*top*) and minimum (*bottom*) of the relaxation spectra obtained during the *P*-jump from 1 bar to different crystallization pressures: (*filled squares*): 350, (*filled circles*): 400, (*filled triangles*): 450 and (inverted *filled triangles*): 500 bar. The *lines* are fits according to Eq. (8.37) (from [90])
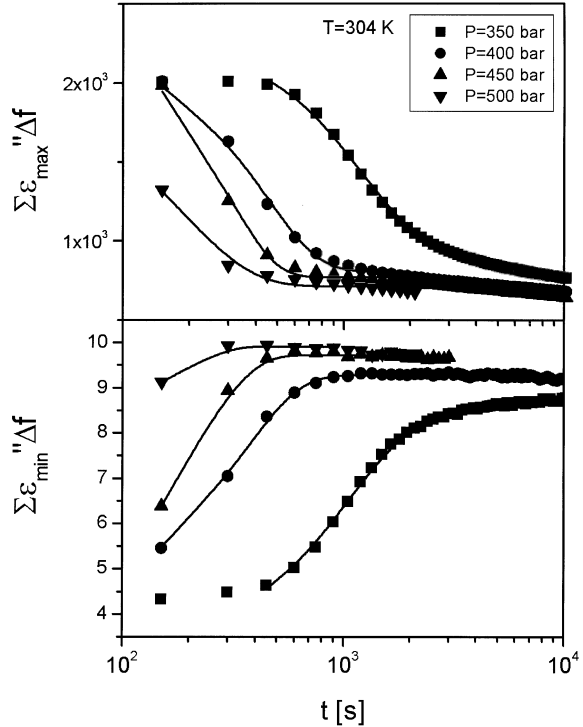
crystallization half-times are obtained as $t_{1/2} = (\ln 2/z)^{1/n}$. The resulted parameters for the different crystallization temperatures are plotted in Fig. 8.37 as a function of the final crystallization pressure.

The Avrami exponent has a strong *P*-dependence; the lower the final crystallization pressure (or the under-pressure) the lower the exponent which attains values in the range from 1 to 3. Such drastic change of the exponent implies changes of the crystallization mechanism (a change from homogeneous to heterogeneous nucleation can only increase the value of the exponent by 1) but additional changes on the dimensionality of crystal growth have to be invoked to explain the higher values. For example, the results at higher under-pressures suggest a nucleation and growth mechanism with a spherulitic superstructure whereas the result at lower under-pressure are suggestive of a fibrilar growth instead. A possible explanation for the different dimensionality of growth can be provided through an apparently "paradoxical" increase of mobility with increasing pressure. According to Fig. 8.31, increasing pressure results in an increase of the temperature difference $\Delta = T_c - T_g^{melt}$; at atmospheric pressure this difference is about 106 K, whereas at 2.5 kbars it is 133 K. The increase of Δ at elevated pressures implies that in the super-pressurized melt and just before the onset of crystallization, the chains are more mobile than at atmospheric pressure. This increase in mobility might be responsible for the more isotropic growth of crystals.
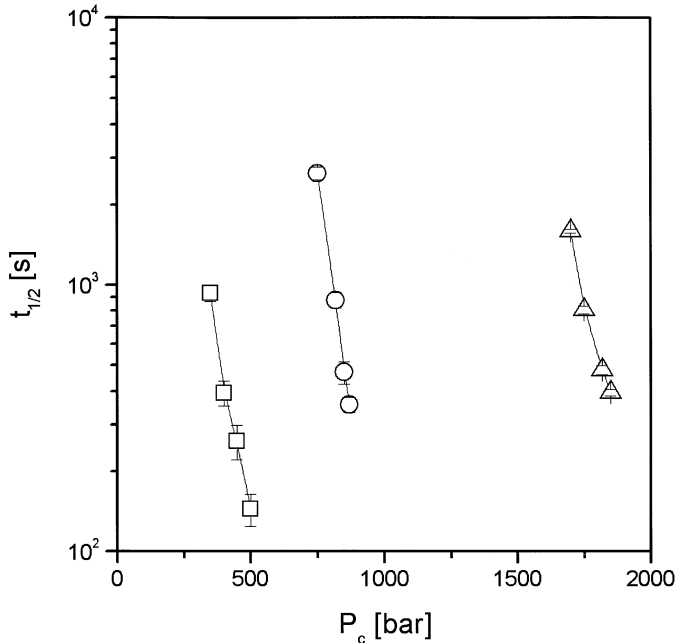
Fig. 8.37. Characteristic crystallization times as a function of crystallization pressure P_c for three different temperatures: (*open saquares*): $T = 304$ K, (*open circles*): $T = 313$ K, and (*open triangles*): $T = 329$ K (from [90])

As with the T-induced kinetics, the characteristic crystallization times exhibit a strong P-dependence. In analogy to the equilibrium melting temperature at atmospheric pressure one can define the corresponding equilibrium melting pressure as the pressure where the crystallization time becomes infinite. Based on this analogy, an undercooling of 1 K results in the same dynamics as an overpressure of 0.2 K kbar^{-1}, i.e., $\delta T/\delta P \approx 5$ K kbar^{-1}, a value close to the $\mathrm{d}T_g^{\mathrm{melt}}/\mathrm{d}P$ which suggests a strong influence of the transport term in the kinetics.

In conclusion, the crystallization and subsequent melting of PnODMA in real time induced by temperature and pressure jump experiments can be followed by DS. In both experiments, the single α-process in the melt was found to split in two processes (α and α') reflecting the dynamics of the relatively mobile and restricted dipoles. In the isothermal/isobaric crystallization experiments induced by T-jumps the kinetics follow a stretched exponential relaxation whereas in the corresponding P-jump experiments the kinetics follow the typical nucleation and growth kinetics with a spherulitic structure at higher under-pressures. The distinctly different dimensionality of growth could be explained by the apparently "paradoxical" situation of increasing chain mobility with increasing pressure.

8.7
Conclusion

In this chapter we have reviewed earlier work on the effect of pressure on separating mixed processes and provided recent examples from systems where the thermodynamic state of the system is of importance. Pressure is the ideal variable if a separation of mixed processes is needed. As an example, earlier pioneering work has shown that pressure can separate the local β-process from the segmental process. The effect of pressure in slowing down the segmental mode is strong and results in the approach with the longest normal mode process, at high pressures. However, the entanglement molecular weight is not affected by compression, which is of importance in polymer processing. Pressure was shown to affect the spectrum of concentration fluctuations and to induce dynamic mixing in certain polymer blends. Finally, pressure is sensitive to the ordering prior to crystallization and consequently is a sensitive probe of the crystallization process. As such it can be used to monitor the crystallization process.

The above are only some examples where the application of pressure can elucidate the structure and dynamic behavior of polymeric systems using DS. There are many other cases where pressure can be employed to elucidate the complex dynamic behavior; one example is systems exhibiting orientational order such as stiff backbone polymers and liquid crystalline polymers. More work is expected in these areas in the near future.

List of Abbreviations and Symbols

A	Constant
A_T	VFT-parameter
B_T	VFT-parameter
C_0, C_1, C_2	Constants
c_1, c_2	WLF-coefficients
D	Constant
F	Local field
f	Fractional free volume
g	Kirkwood correlation function
M	Molecular weight
M_e	Entanglement molecular weight
m	Steepness index
P	Pressure
Q	Apparent activation energy
V	Volume
T	Temperature (in Kelvin)

$t_{1/2}$	Crystallization half-time
T_c	Crystallization temperature
T_g	Glass temperature
T_∞	"Ideal" glass temperature
T_m^0	Equilibrium melting temperature
T_0	Reference temperature in WLF
α	Shift factor
α_f	Thermal expansion coefficient of free volume
β_f	Isothermal compressibility of free volume
β_{KWW}	Exponent of the KWW function
γ	Constant
$\Delta\varepsilon$	Dielectric strength
ΔV	Activation volume
ε^*	Complex dielectric function
θ	Temperature (in °C)
τ	Relaxation time
η	Viscosity
ρ	Density

VFT	Vogel-Fulcher-Tammann
WLF	Williams-Landel-Ferry
RAP	Restricted amorphous phase
DSC	Differential scanning calorimetry
WAXS	Wide-angle X-ray diffraction
PVAc	Poly(vinyl acetate)
PVC	Poly(vinyl chloride)
PET	Poly(ethylene terephthalate)
PMA	Poly(methyl acrylate)
PEA	Poly(ethyl acrylate)
PMMA	Poly(methyl methacrylate)
PEMA	Poly(n-ethyl methacrylate)
PnBMA	Poly(n-butyl methactylate)
PnODMA	Poly(n-octyl methacrylate)
PnNMA	Poly(n-nonyl methacrylate)
PnLMA	Poly(n-lauryl methacrylate)
PnODMA	Poly(n-octadecyl methacrylate)
PI	Polyisoprene
PVE	Poly(vinylethylene)
PI-PVE	Poly(isoprene-b-ethylene)
PS-PVME	Polystyrene-poly(vinyl methyl ether)
PPO	Poly(propylene oxide)

References

1. Ferry JD (1970) Viscoelastic properties of polymers, 2nd edn. Wiley, New York
2. Williams G (1979) Adv Polym Sci 33:60
3. Williams G (1964) Trans Faraday Soc 60:1548
4. Williams G (1964) Trans Faraday Soc 60:1556
5. Williams G (1966) Trans Faraday Soc 62:2091
6. Sasabe H, Saito S (1968) J Polym Sci Part A 2 6:1401
7. Sayre JA, Swanson SR, Boyd RH (1978) J Polym Sci Polym Phys 16:1739
8. Kamiya Y, Mizoguchi K, Naito Y (1990) J Polym Sci Polym Phys 28:1955
9. Moura-Ramos JJ, Williams G (1991) Polymer 32:909
10. Glasstone, Laidler, Eyring (1941) Theory of rate processes. McGraw Hill
11. Guggenheim (1937) Trans Faraday Soc 33:607
12. Turnbull D, Cohen MH (1961) J Chem Phys 34:120
13. Cohen MH, Grest GS (1979) Phys Rev B 20:1077
14. Doolittle AK, Doolittle DB (1957) J Appl Phys 28:901
15. Prigogine I, Defay R (1950) In: Desoer (ed) Thermodynamique Chimique
16. Williams ML, Landel RF, Ferry JD (1955) J Am Chem Soc 77:3701
17. O'Reilly JM (1962) J Polym Sci 57:429
18. Ramos AR, Kovacs AJ, O'Reilly JM, Tribone JJ, Greener J (1971) J Polym Sci Polym Phys Ed A2(9):731
19. Paluch M, Patkowski A, Fischer EW (2000) Phys Rev Lett 85:2140
20. McCrum NG, Read BE, Williams G (1991) Anelastic and dielectric effects in polymeric solids, 2nd edn. Dover, New York
21. Heinrich W, Stoll B (1985) Colloid Polym Sci 263:873
22. Koppelman J, Gielessen J (1961) Elektrochemistry 65:689
23. Saito S, Sasabe H, Nakajima T, Yada K (1968) J Polym Sci A 2 6:1297
24. Williams G, Watts DC (1971) Trans Faraday Soc 67:1971
25. Sasabe H (1971) Research of the Electrotech Lab, Tokyo Japan Publication 721
26. Williams G (1966) Trans Faraday Soc 62:1321
27. Williams G, Edwards DA (1966) Trans Faraday Soc 62:1329
28. Williams G, Watts DS (1971) Trans Faraday Soc 67:2793
29. Mierzwa M, Floudas G, Stepanek P, Wegner G (2000) Phys Rev B 62:14,012
30. Floudas G, Reisinger T (1999) J Chem Phys 111:5201
31. Floudas G, Gravalides C, Reisinger T, Wegner G (1999) J Chem Phys 111:9847
32. Floudas G (unpublished results)
33. Floudas G, Fytas G, Reisinger T, Wegner G (1999) J Chem Phys 111:9129
34. Floudas G, Mierzwa M (to be published)
35. Mierzwa M, Floudas G, Wewerka A (2001) Phys Rev E 64:031,703
36. Mierzwa M, Floudas G, Wewerka A (2002) J Non-Cryst Solids (in press)
37. Williams G (1965) Trans Faraday Soc 61:1564
38. Freeman BD, Bokobza L, Sergot P, Monnerie L, De Schryver FC (1990) Macromolecules 23:2566
39. Andersson SP, Andersson O (1998) Macromolecules 31:2999
40. Paluch M, Hensel-Bielowka S, Ziolo J (2000) Phys Rev E 61:526
41. Paluch M, Hensel-Bielowka S, Ziolo J (1999) J Chem Phys 110:10,978
42. Cheng Z-Y, Gross S, Su J, Zhang QM (1999) J Polym Sci Polym Phys 37:983
43. Paluch M, Ziolo J, Rzoska SJ (1999) Phys Rev B 60:2979
44. Paluch M, Dendzik Z, Rzoska SJ, Habdas P (1996) Phys Rev E 54:4008
45. Corezzi S, Capaccioli S, Casalini R, Fioretto D, Paluch M, Rolla PA (2000) Chem Phys Lett 320:113
46. Adachi K, Kotaka T (1985) Macromolecules 18:466
47. Adachi K, Kotaka T (1988) Macromolecules 21:157
48. Adachi K, Hirano H (1998) Macromolecules 31:3958
49. Adachi K, Kotaka T (1990) Macromolecules 23:829

50. Stockmayer WH, Bauer ME (1964) J Am Chem Soc 86:3485
51. Reisinger T, Zarski M, Meyer WH, Wegner G (1997) Dielectrics Newsletter, Nov; Mierzwa M, Floudas G, Wegner G (2000) Dielectrics Newsletter, June
52. Havriliak S, Negami S (1967) Polymer 8:161
53. Plazek DJ, Schlosser E, Schönhals A, Ngai KL (1993) J Chem Phys 98:6488
54. Ngai KL, Schönhals A, Schlosser E (1992) Macromolecules 25:4915
55. Schönhals A (1993) Macromolecules 26:1309
56. Nicolai T, Floudas G (1998) Macromolecules 31:2578
57. Fischer EW, Donth E, Steffen W (1992) Phys Rev Lett 68:2344
58. Yi XY, Zoller P (1993) J Polym Sci Polym Phys Ed 31:779
59. Doi M, Edwards S (1986) The theory of polymer dynamics. Clarendon, Oxford
60. Utracki LA (1990) Polymer alloys and blends: thermodynamics and rheology. Carl Hanser, Munich
61. Bates FS, Fredrickson GH (1990) Annu Rev Phys Chem 41:525
62. Leibler L (1980) Macromolecules 13:1602
63. Colby RH (1989) Polymer 30:1275
64. Miller JB, McGrath KJ, Roland CM, Trask CA, Garroway AN (1990) Macromolecules 23:4543
65. Roland CM, Ngai KL (1991) Macromolecules 24:2261
66. Quan X, Johnson GE, Anderson EW, Lee HS (1991) Macromolecules 22:2451
67. Rizos AK, Fytas G, Roovers JEL (1992) J Chem Phys 97:6925
68. Chung GC, Kornfield JA, Smith SD (1994) Macromolecules 27:964, 5729
69. Alegria A, Colmenero J, Ngai KL, Roland CM (1994) Macromolecules 27:4486
70. Pathak JA, Colby RH, Floudas G, Jerome R (1999) Macromolecules 32:2553
71. Khokhlov AR, Erukhimovich I (1993) Macromolecules 26:7155
72. Wetton RE, MacKnight WJ, Fried JR, Karasz FE (1978) Macromolecules 11:158
73. Zetsche A, Fischer EW (1994) Acta Polym 45:168
74. Kamath S, Colby RH, Kumar SK, Karatasos K, Floudas G, Fytas G, Roovers JEL (1999) J Chem Phys 111:6121
75. Roland CM (1987) Macromolecules 20:2557
76. Katana G, Fischer EW, Hack T, Abetz V, Kremer F (1995) Macromolecules 28:2714
77. Hsieh HWS, Post B, Morawetz H (1976) J Polym Sci Polym Phys Ed 14:1241
78. Plate NA, Schibaev VP, Petrukhin BS, Zubor YA, Kargin VA (1971) J Polym Sci Part A 1 9:2291
79. Duda G, Scouten AJ, Arndt T, Lieser G, Schmidt GF, Bubeck C, Wegner G (1988) Thin Solid Films 159:221
80. Huo P, Cebe P (1992) Macromolecules 25:902
81. Kalika DS, Krishnaswamy RK (1993) Macromolecules 26:4252
82. Nogales A, Ezquerra TA, Batallan F, Frick B, Lopez-Carbarcos E, Balta-Calleja FJ (1999) Macromolecules 32:2301
83. Ezquerra TA, Majszczyk J, Balta-Calleja FJ, Lopez-Cabarcos E, Gardner KH, Hsiao BS (1994) Phys Rev B 50:6023
84. Angell CA (1991) J Non-Cryst Solids 131:13
85. Bohmer R, Ngai KL, Angell CA, Plazek DJ (1993) J Chem Phys 99:4201
86. Floudas G, Stepanek P (1998) Macromolecules 31:6951
87. Roger SS, Mandelkern L (1957) J Phys Chem 61:985
88. Wunderlich B (1990) Thermal properties. Academic, San Diego
89. Fukao K, Miyamoto Y (1997) Phys Rev Lett 79:4616
90. Mierzwa M, Floudas G (2001) IEEE Trans Dielectrics EI 8:359
91. Attard GS, Araki K, Williams G (1987) Br Polym J 19:119
92. Fontanella JJ (1999) J Chem Phys 111:7103
93. Fontanella JJ, Edmondson CA, Wintersgill MC, Wu Y, Greenbaum SG (1996) Macromolecules 29:4944

9 Dielectric Spectroscopy of Reactive Network-Forming Polymers

J. Mijovic

9.1
Introduction

There are very good reasons for the current surge of interest in fundamental and applied aspects of dielectric spectroscopy (DS) of polymeric materials. Fundamental investigations of the dielectric response yield a wealth of information about different molecular motions and relaxation processes. A unique characteristic of DS is the wide frequency range, from 10^{-5} Hz to 10^{11} Hz, over which polymers respond to an applied electric field. This remarkable breadth is the key feature that enables one to relate the observed dielectric response to slow (low frequency) and/or fast (high frequency) molecular events. Complementary information to DS studies can be obtained from nuclear magnetic resonance (NMR), dynamic mechanical analysis (DMA), quasi-elastic light scattering (QELS), quasi-elastic neutron scattering (QENS), transient fluorescence depolarization, and ultrasonic measurements, but none of those techniques can cover as wide a frequency range. A strong industrial interest in dielectric and electrical properties of polymers reflects the growing use of these materials in electronic interconnect devices, optoelectronic switches, printed board circuitry, microwave assemblies for radar, batteries, fuel cells, and so on.

Detailed accounts of the basic aspects of dielectric behavior of polymeric materials can be found in this book and several other books and key reviews [1–10], although the information in those sources pertains almost exclusively to the systems that do not change with time. Systematic studies by DS of systems characterized by a temporal evolution of structure have a more recent origin. The great potential of dielectric spectroscopy in such investigations has been pointed out in an excellent recent article by Williams [11]. Examples include systems that undergo a chemical and/or physical change as a result of chemical reaction, crystallization, vitrification, phase separation, etc. In this chapter we shall focus attention on the use of dielectric measurements to follow cross-linking or cure, i.e., the conversion of (usually) liquid prepolymers into a three-dimensional thermoset polymer network.

The principle objective of this chapter is to present an overview of the effect of network formation on two principal polarization mechanisms in polymers, namely charge migration and dipole orientation. We shall begin in Sects. 9.2 and 9.3 by briefly recapping the origins of polarization in polymers and the relevant experimental aspects. The major portion of this chapter is devoted to the de-

scription of how the advancement of cure affects charge migration (Sect. 9.4) and dipole reorientation (Sect. 9.5). In Sects. 9.4 and 9.5 we shall summarize the fundamental background, review the published information, and present a few selected examples.

9.2
Polarization Mechanisms

When an electric field is applied across the faces of a parallel plate capacitor containing a dielectric, the atomic and molecular charges in the dielectric are displaced from their equilibrium positions and the material is said to be polarized. There are two major polarization mechanisms in polymeric materials that are studied by dielectric spectroscopy: 1) polarization due to charge migration, and 2) polarization due to orientation of permanent dipoles. Migration of charges gives rise to conductivity [12]. The measured conductivity encompasses contributions from *extrinsic* migrating charges (e.g., ionic impurities) and *intrinsic* migrating charges (e.g., proton transfers along hydrogen bonds). Extrinsic conductivity is commonly assumed to be inversely proportional to viscosity according to the viscous model for charge transfer (Stokes law), implying that highly viscous materials should exhibit zero conductivity, which is never the case. This means that the origin of conductivity in highly cross-linked polymer networks could be traced, at least partly, to the intrinsic migrating charges, whose existence in solids is documented in the literature [14–17]. However, while extrinsic conductivity decreases during reaction as a result of the increase in viscosity, intrinsic conductivity can follow a more complex pattern, and hence the trend exhibited by the overall (measured) conductivity will depend on which mechanism (extrinsic or intrinsic) dominates the dielectric response. As a direct consequence of this interplay between extrinsic and intrinsic contributions, the measured value can display different trends, as was exemplified elsewhere [18]. In Sect. 9.4 we shall describe how the progress of network formation affects polarization by charge migration.

When materials that contain permanent dipoles are placed in the electric field, dipole orientation or dipole polarization is produced as a result of the alignment of dipoles in the direction of the applied field. The orientation of permanent dipoles involves cooperative motions of molecular segments in a viscous medium with time scales measurable by dielectric spectroscopy. The time-dependent loss of orientation of dipoles upon removal of the electric field is called dipole relaxation. In Sect. 9.5 we shall discuss the effect of cross-linking and network formation on dipole dynamics.

There are two additional aspects of induced polarization that one should recognize and account for in the interpretation of experimental results. The first is electrode polarization, which results from the accumulation of ions at the polymer-electrode interface. The second aspect is the polarization due to the build-up of charges at the interface (or in the interphase) between components in heterogeneous systems. This polarization is known as interfacial, space charge, or Maxwell-Wagner-Sillars polarization.

9.3
Experimental

9.3.1
Principles of Measurements

Derived complex quantities that can be obtained from dielectric spectroscopy include impedance, admittance, dielectric modulus, dielectric constant, and susceptibility. The interrelations between all these parameters are tabulated elsewhere (e.g., [19]).

9.3.2
Instrumentation

By a broad definition, the frequency range of dielectric measurements varies from 10^{-5} Hz to 10^{11} Hz. Early descriptions of methodology and instrumentation for dielectric measurements can be found in the classic text by McCrum et al. [1] and the book by Hedvig [3], while a treatment of dielectrics at microwave frequencies can be found in the book by Metaxas and Meredith [20]. More recently, an excellent review of the instrumentation for broadband dielectric spectroscopy was written by Kremer and Arndt [21].

9.3.3
Cells and Sensors

In the course of a dielectric measurement voltage is applied across the sample between two conductive electrodes. The most commonly used types of electrodes are parallel plate and comb. Acquisition and interpretation of data is readily achieved with parallel plate electrodes but the control of plate area and spacing must be extremely accurate for quantitative analysis. The reproducibility of data obtained with comb electrodes may be superior but these are typically larger than the parallel plate electrodes. In either case, a bridge is designed to calculate the impedance (or admittance) between the electrodes when the field is applied. The signal is then processed and the dielectric constant calculated from the measured values of impedance.

A simultaneous use of DS and another technique can be quite revealing. For example, there have been reports of simultaneous dielectric and dynamic mechanical analysis (e.g., [22]), and dielectric and dynamic light scattering measurements (the latter example is discussed in Sect. 9.5.2). However, particularly revealing results can be obtained from the simultaneous dielectric/infrared (IR) spectroscopy. One such set up, designed in our laboratory, had as the common element a disposable sample cell composed of two glass slides separated by a Teflon spacer, with thin aluminum electrodes placed on the inside surface of each glass slide [23]. A special high-temperature adhesive was used to bond Teflon to glass and a guarded electrode was introduced to minimize the fringe

fields and eliminate the possibility of surface conduction. The receiving and transmitting legs of the optical fiber were inserted through the Teflon spacer and centered inside the cell just above the electrodes. The measurements were conducted in the transmission mode using a near-IR source and select results were published elsewhere (e.g., [24, 25]).

The use of sensors is an attractive feature of dielectric measurements and is conducive to in situ real time monitoring of chemical and physical processes. In the early 1980s, a technique for in situ measurements of dielectric properties has been developed and termed microdielectrometry [26]. The microdielectrometer sensor is a comb electrode fitted with a pair of field-effect transistors that combines the best features of parallel plate and comb electrodes. The sensor is fabricated in silicon and consists of an aluminum interdigitated electrode on SiO_2. When placed in the electric field, this sensor measures the so-called complex transfer function (which is related to the admittance) from which the dielectric function is calculated. The sensor has dimensions 2.5×5 mm and is packaged in a flexible polyimide ribbon cable, 9 mm wide and 0.4 mm thick. The sensor also includes a thermal diode that records temperature. Further details about this sensor, including schematics and photos, are available in the literature [27–29]. Another sensor for in situ monitoring of dielectric response, known as frequency-dependent electromagnetic sensor (FDEMS), has been developed by Kranbuehl et al. [30–32]. This capacitative interdigitated sensor, commercially available as DekDyne microsensor, has an area of ca. 2.5×1.2 cm^2 and is about 125 μm thick. The conductor part is copper and the substrate is polyimide. The sensor produces an approximately 30 μm deep fringing electric field over its active surface. Further details regarding this sensor are available elsewhere [30–32]. Similar sensors for in situ monitoring of cure at microwave frequencies are not currently available, although the concept of microwave dielectrometry has been put forward.

9.3.4
In Situ Real Time Monitoring of Cure

In situ dielectric monitoring of processes holds great appeal for materials and process engineers, with the principal advantages being threefold. First, the in situ acquired information eliminates the need for off-line collection and analysis of control samples. Second, dielectric measurements have a distinct advantage over other characterization techniques of being able to monitor cure continuously, as the resin changes from viscous liquid to gel to cross-linked glass. Third, the fundamental character of the sensed information allows a continuous verification of chemical and physical changes inside the reactor against a known processing model and provides an input for "smart" closed-loop process control. The key characteristic of a smart system is its ability to self-adjust to the variations in the material and/or processing parameters and thus guide the process along an optimum path.

Over the years, thermocouples and pressure transducers were almost exclusively used for in situ monitoring of cure. Precise monitoring of temperature is

particularly important in thick samples, such as polymer composites, where high reaction exotherms and low heat dissipation rates could result in considerable temperature gradients within the sample, but the knowledge of temperature as a function of time and location offers little insight into the *molecular* nature of cure. The pressure gradient across the thickness of the composite is important in the analysis of resin flow but alone, like temperature, reveals little about what happens on the molecular level. Dielectric measurements have the advantage of providing a more fundamental response that could be related to the two main processing parameters, namely degree of cure and viscosity. Naturally, the use of dielectric measurements is not limited to in situ monitoring of processing of polymers and composites. Attractive possibilities for their use exist in diverse fields, including the microelectronic and semiconductor industry; the pharmaceutical industry for measurements of dissolution rates of tablets and capsules, studies of electrolytes, polyelectrolytes, and salt/metal complexes; the chemical industry for polymerization, separation, extraction, and catalytic processes, and so on.

9.4
Polarization Due to Migrating Charges

9.4.1
Modeling Concepts – Equivalent Circuits

One attractive feature of dielectric spectroscopy lies in its applicability to the studies aimed at the development of direct correlation between the response of a real system and an idealized model circuit composed of discrete electrical components. In such modeling studies one seeks to match experimental impedance with the impedance of an equivalent circuit composed of ideal resistors and capacitors. General accounts of models based upon equivalent circuitry have been given in several key references [19, 33–35], but their use in the studies of polymers has a much more recent origin.

Phenomenologically, a resistance R is taken to represent the dissipative component of the dielectric response, while a capacitance C describes the storage component, i.e., the ability to store the electric field. Resistance(s) and capacitance(s) can be combined in a variety of forms, leading to an array of phenomenological models that can describe various combinations of polarization mechanisms in dielectric materials. Inductance L requires the storage of energy in a magnetic field but there is no appreciable a.c. magnetic field energy present in the low current (mA) DS measurements.

The simplest equivalent circuits are obtained by combining resistance and capacitance in parallel or series.

An *R-C* parallel circuit (Fig. 9.1A), its simplicity notwithstanding, is often an adequate model of polarization by charge migration over a given frequency range. A single resistance that encompasses the dissipative contributions of all migrating charges, extrinsic and intrinsic alike, is all that is needed to describe the overall loss because the dissipative contributions due to electrode polariza-

tion and dipole relaxations occur at lower and higher frequencies respectively. The lone capacitance, on the other hand, embodies the overall ability of the dielectric to store the electric field by all polarization mechanisms. The overall impedance of a parallel circuit, (equal to the reciprocal overall admittance, Y^*), is given by the sum of the contributions from resistance and capacitance:

$$Z^* = \frac{1}{Y^*} = R_1 + \frac{1}{i\omega C_1} \tag{9.1}$$

where $i = (-1)^{1/2}$ and ω is the angular frequency, $\omega = 2\pi f$.

The real and imaginary components of impedance are given by

$$Z' = \frac{R_1}{1 + (\omega C_1 R_1)^2} \tag{9.2}$$

and

$$Z'' = \frac{\omega C_1 R_1^2}{1 + (\omega C_1 R_1)^2} \tag{9.3}$$

where RC is equal to τ, the circuit characteristic time. In the case of dipole polarization, τ represents the relaxation time. Two (or more) charge-migration mechanisms that are well separated in the frequency domain can be modeled by a series of two (or more) R-C parallel circuits.

When resistance and capacitance are placed in series (Fig. 9.1B), the resulting combination leads to the classic Debye equations for a single dipole or many dipoles with a single relaxation time. In reality, however, the contribution to stored energy from atomic and electronic polarization is always reflected in the measured dielectric response, and that is accounted for in the models by introducing an additional capacitance (C_1) in parallel with the dipole contribution (C_2-R series). The overall impedance of that circuit (Fig. 9.1C) is given as

$$Z^* = (i\omega C_2)^{-1} + \left[\frac{i\omega C_1 (1 - i\omega\tau)}{1 + (\omega\tau)^2} \right] \tag{9.4}$$

where $\tau = R_1 C_1$. This expression is often reported in terms of the complex dielectric function $\varepsilon^* = Y^*/(i\omega\varepsilon_0)$

$$\varepsilon^* = \varepsilon_\infty + \frac{\varepsilon_s - \varepsilon_\infty}{1 + i\omega\tau} \tag{9.5}$$

By separating Eq. (9.5) into its real and imaginary components we obtain

$$\varepsilon'(\omega) = \varepsilon_\infty + \frac{\varepsilon_s - \varepsilon_\infty}{1 + (\omega\tau)^2} \tag{9.6}$$

$$\varepsilon''(\omega) = \frac{(\varepsilon_s - \varepsilon_\infty)\omega\tau}{1 + (\omega\tau)^2} \tag{9.7}$$
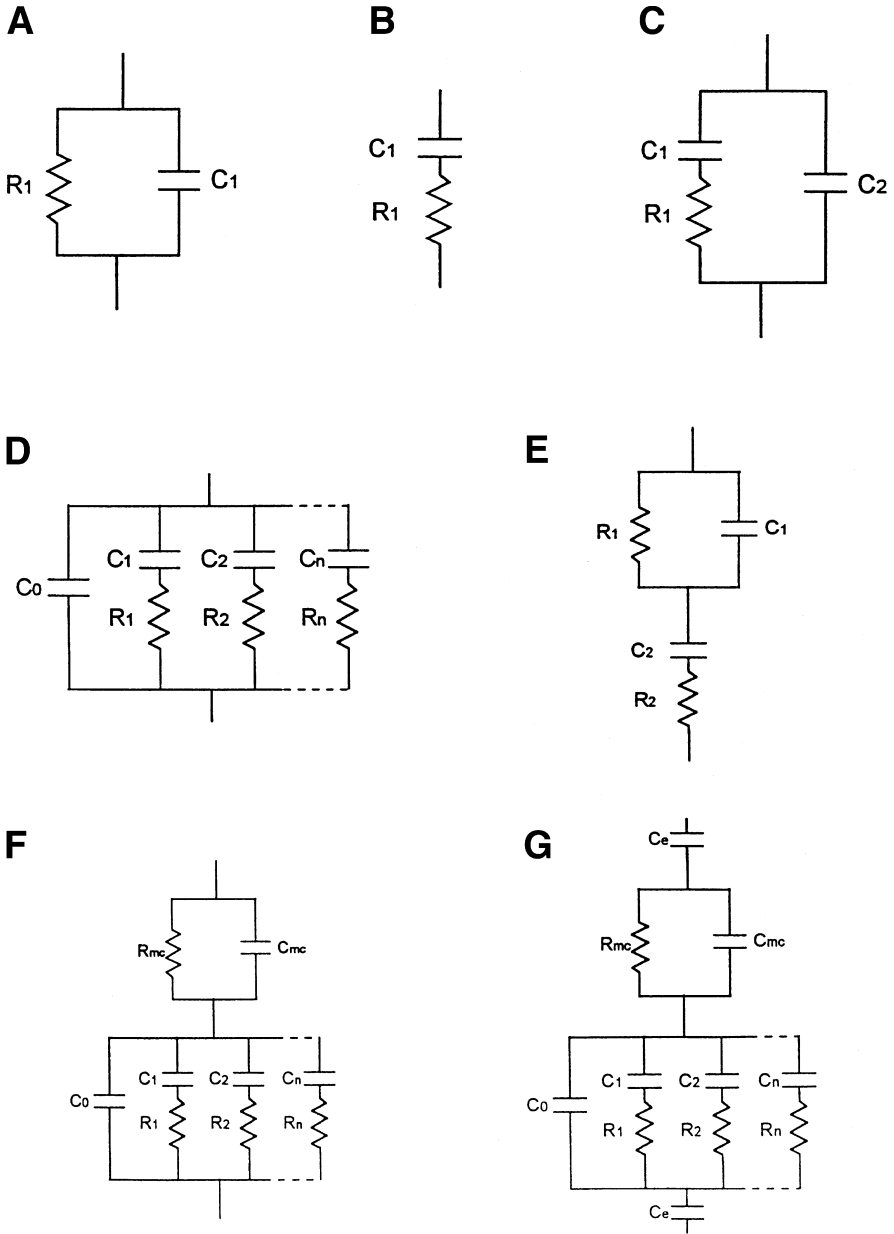
Fig. 9.1A–G. Equivalent circuit diagrams for modeling of material properties

Equations (9.6) and (9.7) are commonly referred to as Debye equations. When plotted in the complex plane (ε'' vs ε'), Eqs. (9.6) and (9.7) yield a semicircle of radius ($\varepsilon_s - \varepsilon_\infty$)/2 known as the Cole-Cole plot [36].

Inherent in Eqs. (9.6) and (9.7) is the assumption of a single relaxation time. In polymeric materials, however, the mobility of different dipoles depends upon the local restrictions imposed by their immediate surroundings. The spatial variations of these restrictions result in a distribution of relaxation times. An equivalent circuit that accounts for the distribution of relaxation times is shown in Fig. 9.1D. Analytically, a distribution of dipole relaxation times can be taken into account in different ways, as described in Sect. 9.5.

Let us now consider several equivalent circuits characterized by the presence of two or more polarization mechanisms. For example, the elements of the circuit in Fig. 9.1E represent the following dielectric events: capacitance C_{mc} includes the contributions of atomic and electric polarization, as well as the capacitance (i.e., non-lossy contribution, *if any*) inherent in polarization due to migrating charges; resistance R_{mc} represents the dissipative component of polarization due to migrating charges; capacitance C_2 and resistance R_2 describe dipole(s) with a single relaxation time. An equivalent circuit that, in addition to the above phenomena, also accounts for a distribution of relaxation times, can be modeled as shown in Fig. 9.1F. Finally, particularly at low frequencies it is often important to take into account the presence of the electrode-blocking layers, which introduce an infinite resistance to the passage of current and can be modeled with two additional capacitances C_e in series, shown as identical in Fig. 9.1G.

9.4.2
Graphical Representation and Evaluation of Characteristic Parameters

We shall now briefly describe the various methods of graphical representation of impedance data and the quantitative evaluation of circuit parameters of an *R-C* parallel circuit. The first representation is based on the plots of imaginary vs real impedance, often referred to as Nyquist plots. An R-C parallel equivalent circuit yields a semicircle in the complex plane: the resistance is obtained from the intersection of the semicircle and the Z' axis. The second representation of impedance data consists in plotting the absolute value of impedance, $|Z^*| = [(Z')^2 + (Z'')^2]^{1/2}$, as a function of the logarithm of frequency. The resulting Bode plot is used to obtain the value of resistance from the intersection of the extrapolated (low) frequency-independent horizontal line and the $\log|Z|$ axis. At higher frequency the dielectric response is purely capacitive and impedance is directly proportional to frequency with slope of –1. The third graphical representation is based on the plots of imaginary impedance in the frequency domain. In general, three zones characterize this type of plot: a low frequency zone where electrode polarization dominates, an intermediate frequency zone where polarization by migration charges plays a major role, and a high frequency zone where dipole relaxation takes place. In many instances, the dielectric response in a frequency range dominated by charge migration (dipole loss

is negligible) reduces to a single R-C parallel model whose imaginary impedance is given by Eq. (9.3). Taking the derivative of Z'' with respect to angular frequency, we get

$$\frac{dZ''}{d\omega} = \frac{CR^2(1-(\omega RC)^2)}{1+(\omega CR)^2} \tag{9.8}$$

Equation (9.8) is equal to zero at the peak in the Z'' vs frequency plot and that condition is met for $\omega = 1/RC$. By combining Eqs. (9.3) and (9.8) we obtain

$$Z''_{max} = R/2 \tag{9.9}$$

which enables one to calculate the unknown resistance directly from the plot ($R = 2\,Z''_{max}$).

Naturally, the numerical values of the elements of the model circuit change in the course of chemical reaction. The progress of reaction is followed by frequency sweeps over the broadest possible frequency interval. It is important to ensure that the time scale of the experiment is negligible in comparison with the time scale of the structural changes in the system, so that each measurement can be taken to represent an iso-structural state. As an illustration of the changes in Z'' vs frequency as the material cures, we present Fig. 9.2, where changes in both the Z''_{max} peak location and peak intensity can be observed.

Reverting to the methodology described above and utilizing spectra obtained at various stages of cure, we calculate resistance from Eq. (9.9) as a function of reaction time. Next, the resistivity, ρ (or its reciprocal – conductivity, $\rho = 1/\sigma$) is calculated from the following equation

$$\rho = RS/L \tag{9.10}$$

where S/L is the cell constant. The extent of reaction (or degree of cure), α, is then obtained from resistivity using an empirical equation that often takes the

Fig. 9.2. Three-dimensional plot of imaginary part of impedance as a function of frequency and cure time for a reactive system
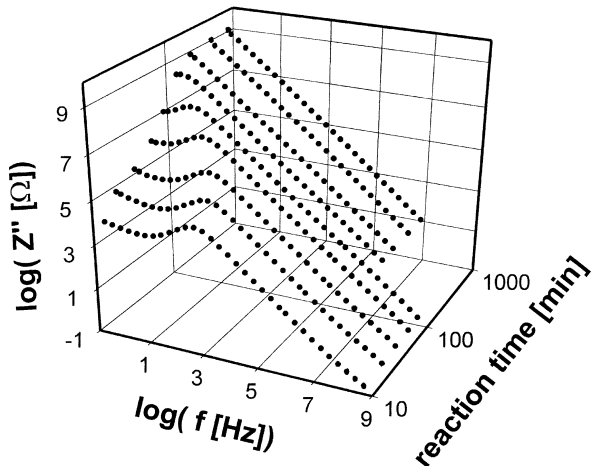
following form:

$$\frac{\alpha}{\alpha_m} = \frac{\log(\rho) - \log(\rho_0)}{\log(\rho_m) - \log(\rho_0)} \tag{9.11}$$

Here, α_m denotes the maximum value of extent of reaction attainable at a given cure conditions prior to vitrification [37], ρ_m is the corresponding resistivity, while the subscript 0 denotes initial conditions. There are numerous example in the literature of the plots of extent of reaction vs time for various thermosetting polymers, including comparative studies of cure kinetics by DS and other techniques, such as FTIR spectroscopy, GPC, and so on (see, e.g., [38]).

Finally, Eq. (9.11) (or another empirical equation) could be substituted into any suitable chemorheological expression that enables one to calculate viscosity during cure (e.g., [39–41]). An example is Eq. (9.12) proposed by Opalicki and Kenny [42]

$$\eta = \eta_{g0} \exp\left[\frac{C_{1\eta}[T - T_g(\alpha)]}{C_{2\eta} + T - T_g(\alpha)} \right] \left[\frac{\alpha_g}{\alpha_g - \alpha} \right]^n \tag{9.12}$$

where η_{g0}, C_{1n}, C_{2n}, and n are parameters to be obtained by fitting procedure and α_g is the extent of cure at gelation. These authors reported good agreement between the measured viscosity and the prediction of phenomenological models based on dielectric results for both isothermal and non-isothermal cure of a tetraglycidyl diaminodisphenyl methane (TGDDM) epoxy and diphenyl diaminosulfone (DDS) amine.

9.4.3
Examples of In Situ Dielectric Cure Monitoring

We begin this section by emphasizing that an early review of the dielectric analysis of thermoset cure was written by Senturia and Sheppard in the mid-1980s [43] and several reviews have appeared subsequently [38, 44]. Most recently, Kranbuehl [45] wrote an excellent article on the dielectric monitoring of polymerization and cure, in which he showed a number of examples of the use of sensors to monitor the dielectric response during cure in molds, autoclaves, adhesives, films and, coatings. Consequently, our goal here is not to be comprehensive but rather to highlight the most interesting aspects of this subject.

Following the introduction of dielectric sensors in the 1980s, a number of investigators [46–53] and particularly Kranbuehl and coworkers [54–56] have continued to use sensors for in situ monitoring of processing. The emphasis in those studies, however, was predominately on the application of sensors and instruments to a growing number of different materials while the essential features of sensors and the sensing methodology have remained unchanged.

The starting point in the analysis of dielectric data is the following equation:

$$\varepsilon'' = \frac{(\varepsilon_s - \varepsilon_\infty)\omega\tau}{1+(\omega\tau)^2} + \frac{\sigma}{\omega\varepsilon_0} \tag{9.13}$$

The main premise in this approach is that at some experimental frequency the contribution of dipole loss to the total loss is negligible and hence

$$\frac{(\varepsilon_s - \varepsilon_\infty)\omega\tau}{1+(\omega\tau)^2} \ll \frac{\sigma}{\omega\varepsilon_0} \tag{9.14}$$

With this inequality Eq. (9.13) becomes

$$\varepsilon'' = \frac{\sigma}{\omega\varepsilon_0} \tag{9.15}$$

The apparent conductivity, which is of interest and is referred to in the literature as "ionic conductivity", can then be calculated from

$$\sigma = \omega\varepsilon_0\varepsilon'' \tag{9.16}$$

This apparent conductivity has been identified as the dielectric parameter of interest because it can be related, at least qualitatively, with the fundamental processing parameters of thermoset networks before gelation. Specifically, ionic conductivity is inversely proportional to viscosity, while the time derivative of ionic conductivity mimics the rate of cure. Also, the temperature dependence of ionic conductivity can be modeled by the classic WLF equation. In practice, the inequality expressed by Eq. (9.14) is met at some frequency that is not known a priori. Two methods for the calculation of ionic conductivity of thermoset polymers based on this approach have been described by Senturia and coworkers (e.g., [27–29]) and Kranbuehl and coworkers [30–32]. Fundamentally, the two methods differ little and were contrasted from the point of view of accuracy and reproducibility in the fine paper by Ciriscioli and Springer [57].

At this point it is appropriate to comment briefly on the usefulness and limitations of the use of ionic conductivity for in situ monitoring of cure. It is our opinion that the following three principal requirements must be met before a complete and successful implementation of this methodology is possible:

1. The availability of sensors and instruments for fast, reliable and reproducible measurements of the dielectric response during cure
2. The development of fundamental understanding of the nature of measured conductivity
3. The development of models that relate the measured dielectric response to the chemorheological characteristic of the resin

What is the current status? The first requirement has been largely met, the second and third not yet. Ionic conductivity is calculated assuming that some ions are initially present in the resin formulation. Although that is probably true, neither the type and concentration of such ions nor their effect on the measured re-

sponse have been identified, much less systematically studied, while the contribution of intrinsic conductivity, with a few exceptions, has been all but ignored. When one considers a large variety of resin formulations and the inevitable vicissitudes of the batch-to batch characteristics and their hygro-thermal histories, it is clear that any presently used model based on the measured conductivity is bound to be empirical and batch-specific. Current work by a group in Lyon is interesting and worth mentioning [58]. These authors are using time of flight (TOF) technique, which measures only the changing mobility of ionic species, along with dielectric spectroscopy (DS), which measures the product of the concentration, charge, and mobility. Thus, by contrasting the results of TOF and DS, they hope to identify both the changing concentration and mobility of ionic species during cross-linking in different polymer networks. Further research along these lines is warranted. Nonetheless, it is also true that, notwithstanding the lack of understanding of fundamental nature of the measured conductivity, dielectric spectroscopy is the only currently available technique for in situ monitoring of kinetics and rheology of cure.

9.5
Polarization by Dipole Orientation

A distinct advantage of broad-band dielectric relaxation spectroscopy (DRS) is its ability to probe molecular dynamics (of dipoles) at all times during cure: from the early stages of a high temperature cure, where the dipolar relaxation times are on the order of tens of picoseconds ($f_{max} \sim 10$ GHz) to the late stages of cure (after gelation) through the vitrification process where the glassy state relaxation times are tens or hundreds of seconds. Throughout cure, accompanying the relaxation time changes, are changes in static dielectric constant, high frequency dielectric constant (index of refraction), the shape parameters of the relaxation spectrum, and the separation of secondary, high frequency, local relaxation processes. We will discuss these changes in turn and show examples of how cure may be monitored by experimental observation of them.

9.5.1
Dipolar Relaxation Processes – Classification Scheme

The major dielectric relaxation in polymers is termed α relaxation – its molecular origin lies in the segmental motions. Since the principal role in determining the glass transition is played by the time scale for segmental motions, and not the Rouse or sub-Rouse modes, α relaxation is associated with the "dielectric glass transition". Secondary relaxations, labeled β, γ, and so on, in the order of decreasing temperature (at constant frequency) or increasing frequency (at constant temperature) are associated with localized motions in the glassy state. Secondary processes generally have the following characteristics: located at high frequencies (short time scales $< 10^{-5}$ s), broad dispersions, Arrhenius temperature dependence, low activation energy, low intensity, and are present above and

below T_g. The origin of these so-called β relaxations remains elusive, but appeals have been made in the literature to explanations ranging from far-IR phonon excitations [59], cage-rattling motions [60, 61], a universal glassy state phenomenon [62], and various types of local/side-chain motions [1, 63]. For the purpose of this chapter we rest with providing an operational definition of the process. At high temperatures (and therefore frequencies) the α and β processes merge: the faster moving (with temperature) α process catches up with and merges with the slower moving (with temperature) β process to become the $\alpha\beta$ process. It is also important to point out that α and β relaxations have different length and time scales but are interrelated since often the same dipoles contribute to both processes.

In some polymers it is also possible to distinguish between different types of dipoles (or components of the same dipole) on the basis of their location and orientation in the electric field. Stockmayer [64] has classified all dipoles into three categories: type A – oriented parallel to the chain contour; type B – oriented perpendicular to the main chain; and type C – located in the side chain. A well-known and widely studied example is *cis*-polyisoprene, which contains type A and B dipoles whose relaxations can be resolved in the frequency domain [65–71]. The important point here is that the relaxation of type B dipoles in polymers is associated with segmental motions and is therefore synonymous with the α process. Type A dipoles give rise to a relaxation at lower frequency (at constant temperature) with the characteristic relaxation time that is affected by the fluctuations of the end-to-end vector and is therefore a function of the molecular weight. This relaxation is referred to as normal mode. Another relaxation at lower frequency (at constant temperature) than the α process was reported in crystalline polymers and is assigned to the molecular motions of amorphous entities within the crystalline phase.

A prerequisite for the use of DRS in the studies of molecular dynamics is that the materials under study contain a permanent dipole. In network-forming polymers, however, the type and concentration of dipoles can vary during cross-linking. To systematize the various scenarios possible, a classification scheme was recently proposed [72] based on four general classes of cross-linking reactions that result in network formation and can be probed by DRS. Class 1: dipoles present in the reactants are not involved in the chemical reaction so that the product contains the same concentration (normalized for density changes) and type of dipolar groups (e.g., telechelic polymer chains with low polarity reactive end groups and dipolar groups in the polymer backbone – such as vinyl-terminated siloxane polymers). Class 2: dipoles present in the reactants (though not necessarily all of them) are involved in the reaction and a new type of dipoles is formed (e.g., a reactive mixture of epoxide- and amine-containing molecules which react to form secondary and tertiary amines and hydroxyl groups). Class 3: dipoles present in the reactants (not necessarily all of them) react to form nonpolar groups (e.g., cyanate ester resins which cross-link to form symmetric nonpolar triazine rings). Class 4: no dipoles are present among the reactants but are formed during the reaction (e.g., oxidation of polyethylene by radiation cross-linking). General examples of all of these classes are illustrated in Fig. 9.3.

Class 1: Dipoles Not Involved In Reaction
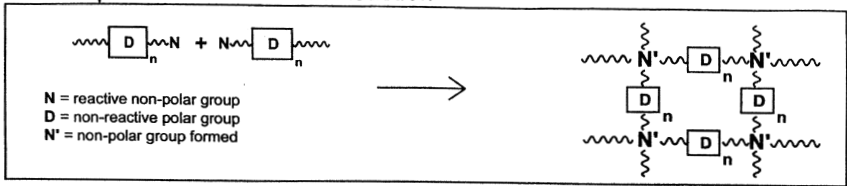
Class 2: Dipoles Reacting To Form New Dipoles
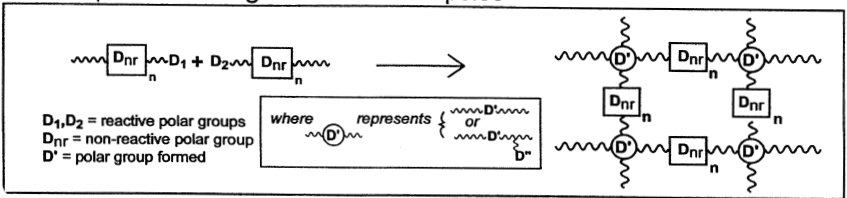
Class 3: Dipoles Reacting To Form Nonpolar Groups
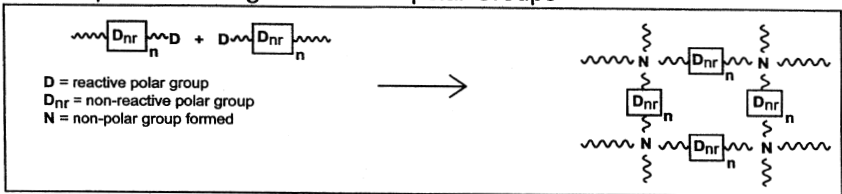
Class 4: Nonpolar Reactants Becoming Polar

Notes:

Fig. 9.3. Classification scheme for the compositional changes of dipolar groups during cross-linking

Note that the above scheme encompasses only systems that undergo chemical cross-linking and does not include physical and thermoreversible cross-linking (e.g., [73, 74]), hydrogen bonded structures, reversible gels, or linear polymers (e.g., [75–78]).

9.5.2
Changes In Relaxation Time (τ) During Network Formation

In order to monitor and analyze effectively and accurately the time-dependent change in a material during chemical reaction (or crystallization or phase separation), a measurement must be made of a fundamental material property, independent of the specific type of test. The dipolar relaxation time, a fundamental material parameter, will be shown to be an effective tool for the study of reactive systems. The knowledge of relaxation time serves a twofold purpose: 1) it can be used to describe the dynamics of networks at various stages of cure, and 2) it can be used in conjunction with an appropriate kinetic model to relate molecular dynamics to chemical kinetics. Both aspects are discussed below.

Epoxy-amine formulations are by far the most widely studied (by DRS) generic group of network-forming materials. According to the classification scheme of Fig. 9.3, these are class 2 systems. Consider a typical epoxy-amine mixture undergoing isothermal cure. We present in Fig. 9.4 dielectric permittivity and loss in the frequency domain with extent of cure (obtained by simultaneous FTIR measurements) as a parameter.

Similar dielectric results were reported by several groups [79–81] and the general features of the underlying physics can be described as follows. During cross-linking, as molecular weight and connectivity increase and the accompanying bulk physical properties develop (T_g rises, etc.), the dipolar dynamics encounter the three regimes illustrated in Fig. 9.4. They are: regime I – early cure, merged $\alpha\beta$ process, picosecond relaxation time; regime II – the α and β processes separate with the α process shifting to lower frequencies; and regime III – towards the completion of cure, at which time the α process shifts to very low frequency (indicating glass formation), while the secondary β process remains at high frequencies. An interpretation of the corresponding microscopic events is as follows. The unreacted mixture response (the $\alpha\beta$ process) is essentially of a local nature due to a large degree of thermal kinetic energy; all motions are within domains of similar size and the number of atoms involved in the relaxation (number of atoms per domain) is small. As the reaction progresses, the increasing molecular connectivity leads to a wider distribution of domain sizes and an increase in the number of atoms per domain. When the domain size is much larger than the scale of local motions, we observe the splitting into distinct α and β processes; beyond this time in the reaction the α process continues to evolve to longer relaxation times. To indicate more clearly the divergence of the $\alpha\beta$ process we extract from Fig. 9.4 the relaxation times, τ ($\tau = 1/2\pi f_{max}$), where f_{max} is the frequency of loss maximum, and plot in Fig. 9.5 log τ as a function of conversion for all of the above regimes.
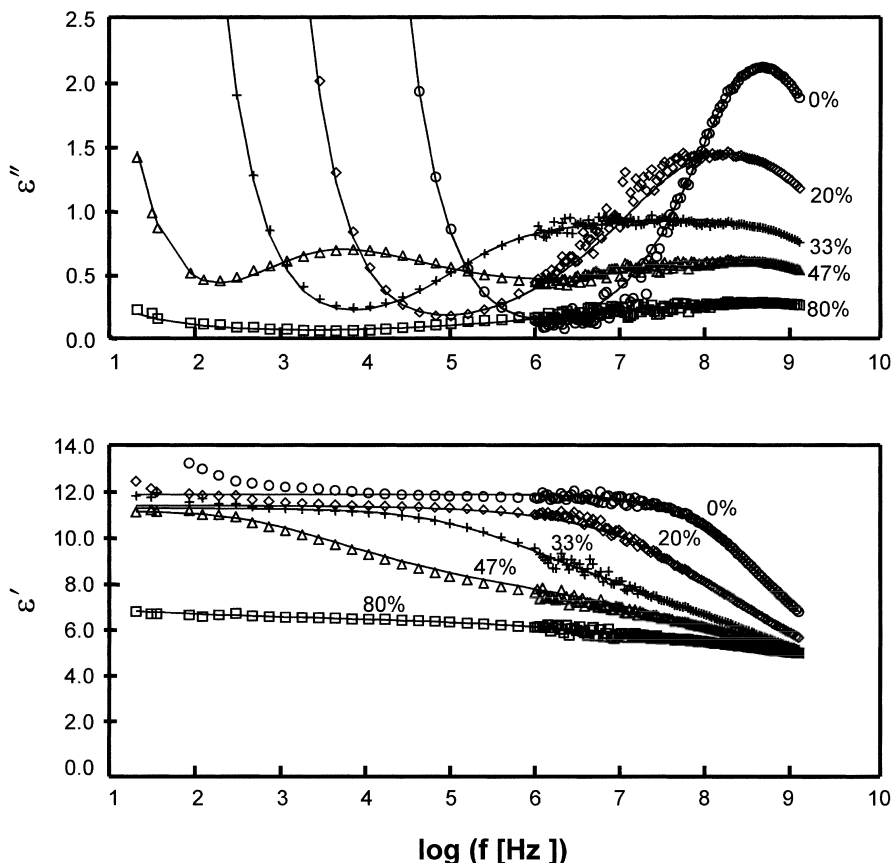
Fig. 9.4. Dielectric loss and permittivity in the frequency domain at different extents of cure for DGEBA/DETA isothermal reaction at 50 °C. The *solid line* is a fit to a two-term Havriliak-Negami (HN) function

The curve running through the data is a modified version of the VFT functional form:

$$\tau_\alpha = \tau_{0\alpha} \exp\left(\frac{F_1}{\% - \%(0)}\right) \tag{9.17}$$

The β process is described by an Arrhenius-like equation:

$$\tau_\beta = \tau_{0\beta} \exp(F_2^* \%) \tag{9.18}$$

In Eqs. (9.17) and (9.18), % denotes extent of reaction, and τ_0, F_1, and F_2 are best-fit parameters to the data in Fig. 9.5. We point out that τ, for α and β processes, does not diverge to infinity at the gel point, as translational processes do, since the segmental α process becomes independent of molecular weight above a material-dependent critical chain length.

Fig. 9.5. Apparent relaxation time extracted from data of Fig. 9.4 vs extent of cure
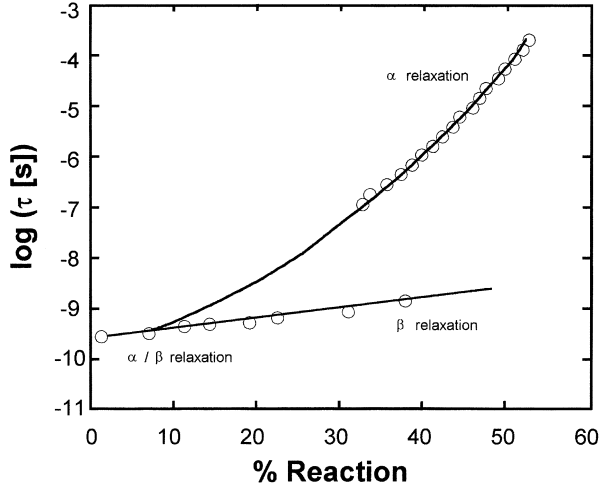
We have recently gained further insight into dynamics of epoxy-amine networks by contrasting the changes in the α relaxation time with conversion obtained from the dielectric (DRS) and dynamic light scattering (DLS) data [82]. We obtain τ_{DRS}, as stated above, i.e., from the reciprocal of the ε'' peak frequencies. For the DLS data we use the following well-known relation to connect the apparent relaxation time to the KWW τ^*

$$\langle \tau_{app} \rangle = \frac{\tau^*}{\beta} \Gamma \left(\frac{1}{\beta} \right) \tag{9.19}$$

where Γ is the Gamma function. As seen in Fig. 9.6, the agreement in relaxation times between the two techniques is excellent, leading us to suggest that the underlying origin of the α process as probed by the two technique is the same.

In the conversion range where the α process has an associated time scale slow enough to be found within the DLS autocorrelation time window, the DLS experiment is measuring the longitudinal density fluctuations (at lower conversions we measure a different process – concentration fluctuations, not considered here). At any given instant, the fluctuating density will be frozen, and a hypothetical instantaneous microscopic snapshot is that of a distribution of domains of various densities (the macroscopic density being the ensemble average of these subsystems). We note that the connection between the micro-Brownian α process, the glass transition, and density fluctuations observed via DLS has been amply demonstrated in the literature. Regions of higher density are assumed to relax more slowly, lower density more quickly; the distribution of density domains thus yields the distribution of relaxation times. That dipole dynamics exhibit the same α relaxation characteristics as time-dependent density fluctuations suggests that the α process as measured by DRS is also broadened by the density domain heterogeneity. The factors influencing the density domains are evidently also those that govern both the distribution of dipolar re-

Fig. 9.6. Apparent relaxation time from DLS and DRS experiments vs extent of cure for DGEBA/DETA reaction at 50 °C
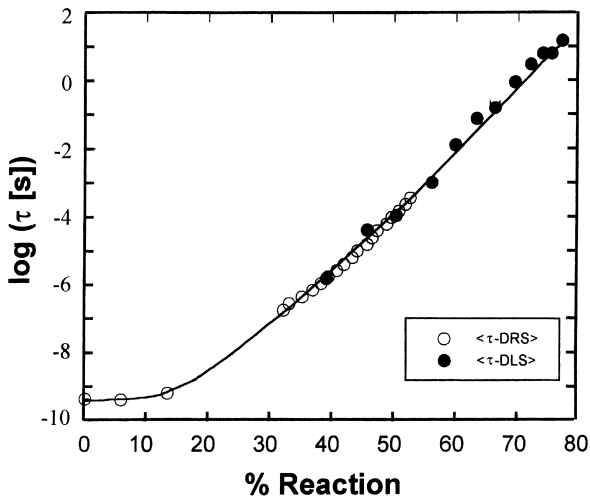
laxation times and the mean of the relaxation times for the α process. Interestingly, there exists conflicting evidence in the literature for other comparisons between DRS and DLS data. For some polymers, including PPG, PVAc, PS, and PEA, it was found that when comparing data at the same temperature $\tau_{DRS} < \tau_{DLS}$ and the KWW parameter $\beta_{DLS} < \beta_{DRS}$ [83]. For other polymers, including PMPS [84], PHMA [85], and poly(n-laurel methacrylate) [86], and for low molecular weight liquids BKDE and BCDE [87], the α processes have equivalent DRS and DLS τ and KWW β parameters.

9.5.3
Correlation Between Chemical Kinetics and Molecular Dynamics During Network Formation

The primary requirement for monitoring a chemical reaction using dipolar relaxation spectroscopy is, of course, that there be present some polar portion of one of the reactants and/or products. That requirement being met, there are four chemical reaction possibilities that lead to networks, as schematically shown in Fig. 9.3. Historically, the types of chemical reactions most often monitored by DRS are those in which the reactants are low molecular weight liquids and on exposure to appropriate conditions (usually heating or exposure to radiation (UV or microwave) or the addition of a catalyst) react to form various polymeric structures: linear and branched polymers and cross-linked networks with various physical states: viscous liquids, rubbery gels, amorphous solids or semicrystalline solids. This diversity is governed by the structure and functionality of the reactants and the thermodynamic and kinetic considerations.

Fundamental studies aimed at *correlating* dipole dynamics with the kinetics of network formation have a recent origin. Early attempts at modeling of cure from dielectric measurements of dipole relaxation were reported in several pa-

pers by Seferis and coworkers [88–90]. They recognized and clearly expressed the need to relate the dielectric signal to the change of some fundamental property of polymer network during cure. The essential feature of their model is correlation between dielectric function (dielectric permittivity and loss) and network parameters (viscosity and degree of cure). The average relaxation time was tracked during cure and related to viscosity. The viscosity, in turn, was correlated to the degree of cure by a multi-parameter equation reported earlier by Dusi et al. [91]. Good agreement was found between the measured and predicted results, despite the empirical nature of the model and an oversimplified physical picture. In the early 1990s Johari and coworkers initiated a series of comprehensive dielectric studies of curing kinetics [92–94]. They used the complex electrical modulus formalism to describe d.c. conductivity and dipolar relaxation. The decrease in d.c. conductivity obeyed a power law form used to describe critical phenomena and approached a negligible value at gelation. That led to a controversial and harshly criticized [95] conclusion that gelation could be characterized by dielectric measurements. The isothermal spectra of dielectric permittivity were fitted to a KWW functional form with stretch exponent termed γ(to distinguish it from the KWW β) that varied with curing temperature and molecular architecture, and was identified as a curing parameter for the vitrification of thermosets. The following equations have been applied to isochronal cure data [94], where a modified version of the normalized complex permittivity ($\omega\tau_0$ is substituted for ω) is used:

$$\varepsilon''(\omega\tau_0) = \varepsilon_\infty + (\varepsilon_s - \varepsilon_\infty) \int\limits_0^\infty \exp(i\omega\tau) \left(-\frac{\partial\phi}{\partial t}\right) dt \qquad (9.20)$$

and

$$\phi(t) = \exp\left[-\left(\frac{t}{\tau_0}\right)^\gamma\right] \qquad (9.21)$$

where ϕ is the polarization decay function, τ_0 is the modified KWW function relaxation time, and the other variables have their usual meanings. In this isochronal method of data fitting the γ parameter represents an average of the KWW β parameter that would be found from a frequency sweep over the experimental time range of the isochronal ε'' peak. It is a less precise shape parameter determination than the frequency domain method; however, it may be necessary to undertake under constrained experimental situations, and can still be somewhat revealing. This work was later extended to cover non-isothermal cure of thermosets and a general expression for dielectric properties during cure was written. To calculate dielectric permittivity and loss from Eq. (9.20) one needs to know the relaxation time τ, which, in turn, is a function of the degree of cure α. Thus a kinetic equation is needed that relates τ to α. Parthun and Johari [94] used a general kinetic expression proposed by Barton [96], assumed a simple first order reaction mechanism, and reported a good agreement with experimental results for a DGEBA-EDA mixture cured at two heating rates. An important contribution to this field of study was made by Fournier et al. [97],

who generated 3-D plots of dielectric permittivity (and dielectric loss) against the curing time and frequency, and developed a theoretical working model that allows DRS to predict the course of the reaction in the vitrification range. A strategy for the monitoring of cure via τ dynamics can be briefly outlined as follows (additional details may be found in the recent literature [97, 98]). Usually, the first step is to perform a series of kinetic and DRS measurements on the material at selected isothermal reaction temperatures. From the kinetic data (obtained by DSC, FTIR, titration, GPC, etc.) one generates the plots of extent of reaction vs reaction time. A kinetic equation is then derived that describes the reaction mechanism and accounts for the presence (when necessary) of diffusion control [99–103]. The rates and mechanisms of cross-linking reactions vary as a function of chemical composition and many such studies have been reported in the literature. For example, the widely studied epoxy-amine mixtures are almost always characterized by autocatalytic kinetics and the interested reader is referred to several comprehensive reviews of this subject [104–106]. Utilizing an appropriate kinetic equation, the temperature dependent reaction rate constants and the activation energy are obtained. Next, the DRS data are analyzed. The frequency of maximum loss, f_{max}, is related to the average relaxation time, τ, by

$$f_{max} = 1/(2\pi\tau) \tag{9.22}$$

The increase in molecular weight and cross-link density is accompanied by a concomitant decrease in the molecular mobility and an increase in the relaxation time. An exponential dependence (experimentally observed) of the relaxation time on reaction time affords a good description of the process and hence we write

$$\tau = \tau_0 \exp(k t_{max}) \tag{9.23}$$

or

$$f_{max} = f_{max}(0) \exp(-k t_{max}) \tag{9.24}$$

where the time of maximum dielectric loss, t_{max}, is chosen to define an operational reaction time with respect to the measuring frequency, $f_{max}(0)$ is the frequency of the maximum loss for the uncured material, and k is a constant for a given reaction temperature. The next step is to introduce the kinetic information into Eq. (9.24). First we write the rate of polymerization $d\alpha/dt$, in the following general form

$$\frac{d\alpha}{dt} = k f'(\alpha) f''(\alpha) \tag{9.25}$$

where $f'(\alpha)$ defines the kinetic expression and $f''(\alpha)$ is the diffusion control factor. For further treatment of diffusion-controlled kinetics the reader is referred to the literature (e.g., [99–103]). Equation (9.25) can be rewritten to yield the time $t(\alpha)$ needed to reach a given extent of reaction:

$$t(\alpha) = \int_0^\alpha \frac{d\alpha'}{f'(\alpha')f''(\alpha')} \tag{9.26}$$

When Eqs. (9.25) and (9.26) are combined, the frequency at maximum loss for a fixed reaction temperature can be expressed as a function of the degree of cure as follows:

$$\ln f_{max} = \ln f_{max}(0) - k \int_0^\alpha \frac{d\alpha'}{f'(\alpha')f''(\alpha')} \tag{9.27}$$

Equation (9.27) relates molecular dynamics to chemical kinetics. In the conversion range where diffusion control is absent, the second term under the integral is equal to unity ($f''(\alpha) = 1$).

The following equation was reported by Fournier et al. [97] in their study of the cure of DGEBA-PACM system:

$$\log(f_{max}(\alpha)) = \alpha(T)\left[\log(f'_{max}(0)) - \frac{k\alpha}{\ln(10)}\right]\left[\frac{2}{1+\exp\left[\dfrac{\alpha - \alpha_f(T)}{0.01}\right]} - 1\right] + c(T) \tag{9.28}$$

The plots of $\log f_{max}$ vs α gave important information. For example, the slopes of the straight lines $\log f_{max}$ vs α in the kinetically controlled region were seen to decrease with increasing temperature of cure T_{cure}. At higher T_{cure}, the loss peak remains at high frequency until vitrification, and then decreases abruptly. The rapid decrease of f_{max} indicates that α is always close to α_f in the diffusion-controlled region. Building upon the original work of Fournier et al. [97], Andjelic and Mijovic obtained similar results in their study of dynamics and kinetics of a carbonyl-modified-epoxy/amine network [98].

We now turn our attention to polymers that belong to class 1 cross-linking systems (see Fig. 9.3). We begin by presenting the results of Roland, who used DRS to study constraints on local segmental motions in poly(vinyl ethylene) (PVE) networks [107]. Different cross-linked densities were realized by adding varying quantities of dicumyl peroxide to PVE. No KWW fits were possible and the relaxation time was calculated from the frequency at maximum loss. Roland observed an increase in relaxation time and glass transition temperature with increasing cross-link density. Fragility (or cooperativity) plots were characterized by a systematic increase in temperature sensitivity with increasing cross-link density, suggesting that segmental relaxation in the more densely cross-linked networks is associated with stronger intermolecular coupling. That led to the argument that the junctions and the chains emanating from them are effectively constraining the motions of segments well removed from junctions. Glatz-Reichenbach et al. [108] also studied dielectric relaxation of class 1 networks obtained by cross-linking styrene-butyl acrylate (SB) copolymer with divinyl benzene (DVB). Relaxation time and glass transition temperature were found to increase with increasing cross-linking and it was speculated that the segments near the chain ends may have a different activation energy than those further away. We shall return to the arguments of Roland and Glatz-Reichenbach et al. later in the text in conjunction with the effect of cross-links on the breadth and shape of the distribution spectrum, but first we present the results for an end-

group functionalized network-forming poly(methylphenylsiloxane) (PMPS). Three cross-linked PMPS networks were prepared and investigated [72], with the extent of cross-linking varying as follows: PMPS374 > PMP747 > PMPS149. Dielectric permittivity and loss were measured for each network composition across a wide frequency and temperature range. Because permittivity and loss are directly related via the Kramers-Kronig relations, for simplicity only the loss data are presented in Fig. 9.7.

The solid curves are HN function fits with the low conductivity contribution subtracted. Since the τ_{HN} is not equivalent to the apparent relaxation time (recall that $\tau_{app} = \tau = 1/2\pi f_{max}$), we must calculate it from

$$\tau = \frac{1}{2\pi f_{max}} = \tau_{HN}\left[\sin\left(\frac{a\pi}{2+2b}\right)\right]^{1/a}\left[\sin\left(\frac{ab\pi}{2+2b}\right)\right]^{-1/a} \tag{9.29}$$

The temperature dependence of τ for selected compositions is shown in Fig. 9.8.

Data of Boese et al. [109] on a higher molecular weight linear PMPS sample are included for comparison. Also included are several high frequency data points, omitted in Fig. 9.7 for clarity. The solid curves in Fig. 9.8 are VFT fits. While different PMPS networks have different T_gs, evidenced by the low temperature τ behavior, the trends are similar. This is verified when scaling τ by T_g^*/T (where T_g^* is the operational definition of T_g – the temperature at which τ_{max} is 100 s), as shown in Fig. 9.9.

The solid line in the main plot of Fig. 9.9 is the Arrhenius limiting case. The inset of Fig. 9.9 shows a magnified portion of the low-temperature region of the main plot. We point out the apparent high fragility of PMPS, intuitively unexpected considering the flexibility of Si-O backbone and a low T_g. The high fragility is not caused by secondary relaxations; the secondary process of interest is the phenyl ring flip but this process is not dielectrically active and the low temperature dielectric data (where secondary relaxations would be most noticeable) are featureless for all compositions. However, let us for the moment change the discussion from the topic of fragility and focus our attention on the implications of changing cross-link density on the length scale of the segmental dynamics. First, the fragility index of PMPS has been shown to be independent of cross-link density, molecular weight, and T_g. Also independent of these variables is the relaxation shape (characterized by a KWW β parameter). The fact that no change in the fragility index was found may not be significant, since several dissimilar materials were found to have equivalent indices. However, the fragility information taken together with the unchanged relaxation shape suggests the following conclusion. Since these segmental dynamics measures are not sensitive to the different PMPS structures examined, gels and linear chains, this implies that the relaxing segments are smaller than the distance between cross-links (approximately 14 repeat units). An understanding of primitive segmental dynamics is, unfortunately, not directly accessible through a DRS test, as the dipole-containing segments are relaxing within cooperatively rearranging domains. It is not possible to predict how the domains ought to behave on the
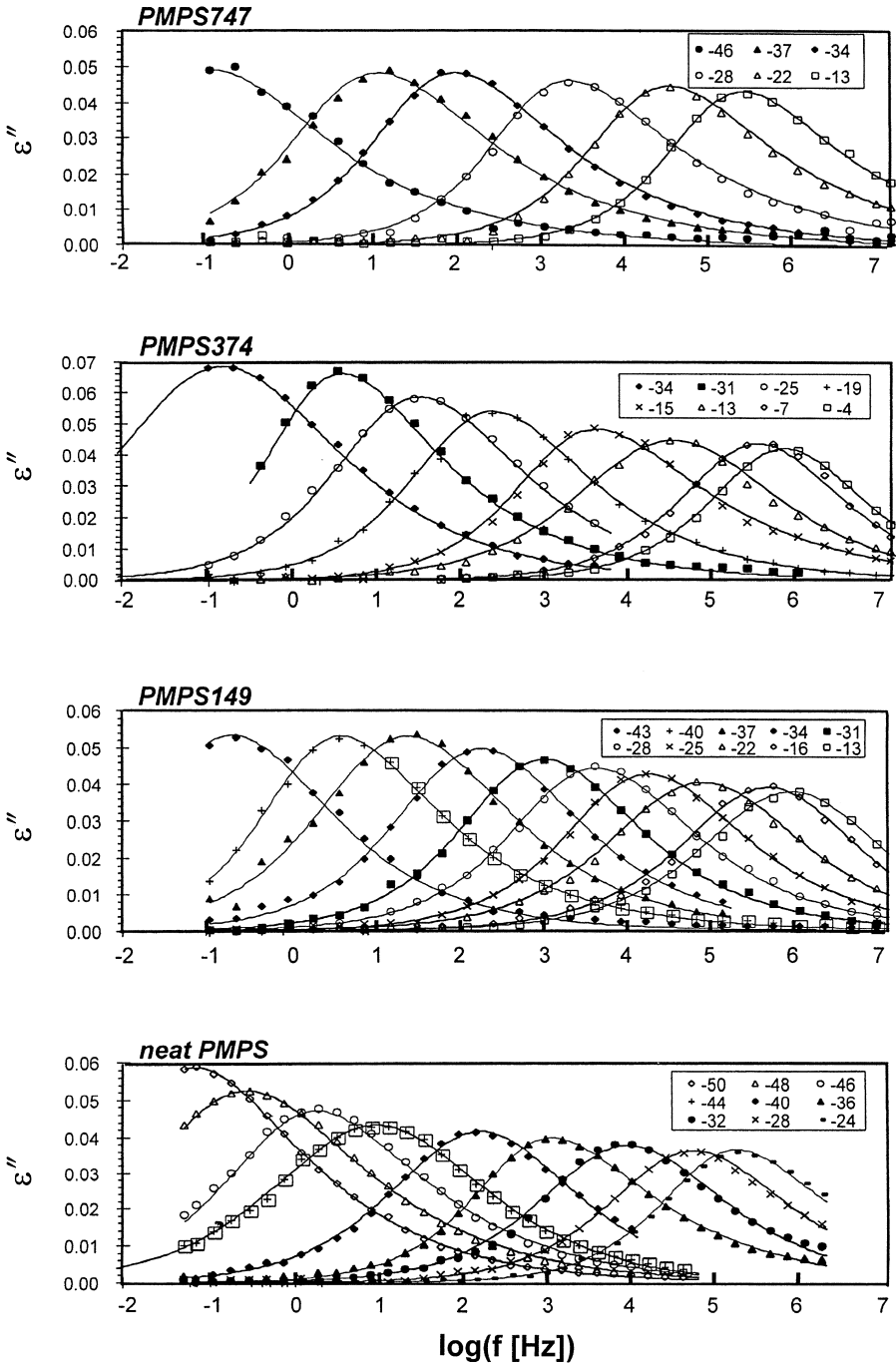
Fig. 9.7. Dielectric loss in the frequency domain at specified temperatures for indicated PMPS networks

Fig. 9.8. Temperature dependence of apparent relaxation time, τ, for various PMPS networks
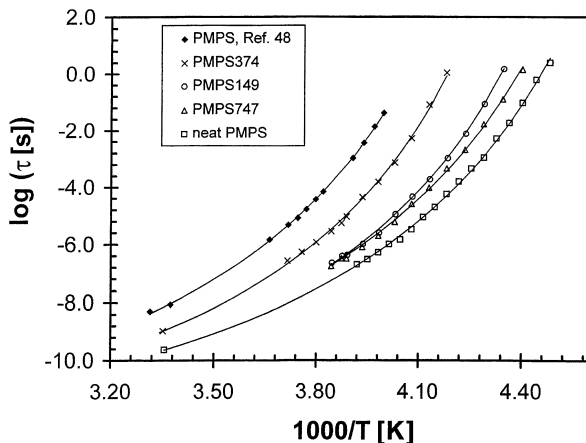
basis of the molecular structure at present, although a recent attempt has been made [110]. Nevertheless, if the domain size distribution had been affected by cross-linking, one of the manifestations in a DRS test would be through the relaxation distribution (KWW β parameter). Since this is not the case for the PMPS network here, we may infer that the characteristic domain size is smaller that the distance between cross-links. In other terminology, although density fluctuations are quenched in regions very close to cross-links, fluctuations in density *between* the cross-links are not significantly disturbed. In this respect, there is an apparent difference in the effect of cross-linking on segmental relaxation in cross-linked PVE [107], SBDVB [108], and PMPS [72] networks. If the characteristic domain size were larger than this distance, upon cross-linking all fluctuations on this scale would be quenched and only local (non-cooperative) modes would be observed [111]. We conclude that the distance between cross-links (28 skeletal Si-O bond lengths, approximately 50 Å) is greater than the length of the primitive segment and the cooperatively rearranging domain; therefore, the length scale of the α process in PMPS networks is less than 5 nm. The upper length bound would be somewhat smaller than 5 nm if there is some immobilization near the cross-links. This size is in agreement with the value of about 2–5 nm, recently reported in several investigations of the cooperative length scale in polymers and molecular liquids (e.g., [112]).

9.5.4
Changes in Relaxation Strength During Network Formation

Another approach to cure monitoring based on dipole polarization is the characterization of the extremes in dielectric constant: static, ε_s, and high frequency, ε_∞, or the difference $\Delta\varepsilon = \varepsilon_s - \varepsilon_\infty$, relaxation strength. The motivation behind this approach is, as we shall see, a direct relationship between a materials dipole composition and the static permittivity, ε_s. When the dipolar composition changes in the course of network formation in a systematic manner, measure-
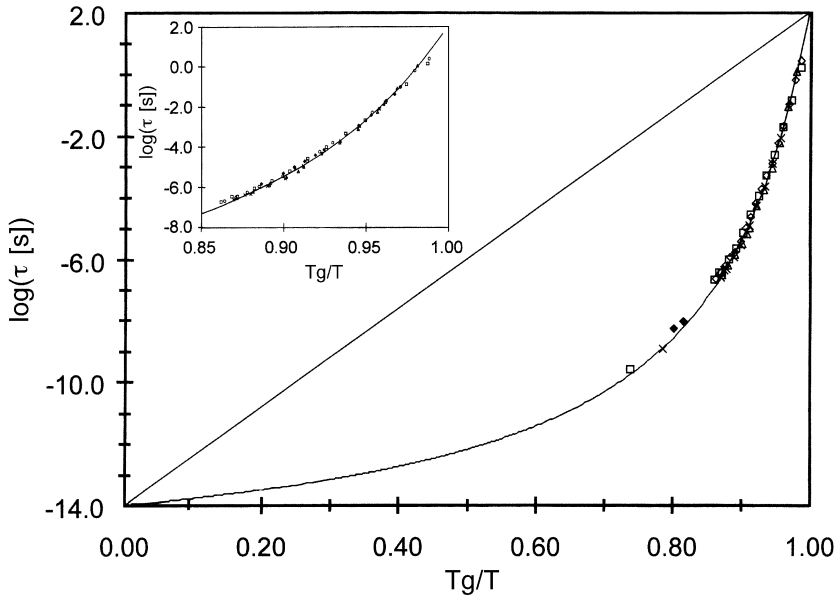
Fig. 9.9. T_g/T scaled temperature dependence of apparent relaxation time for all compositions. *Inset* shows magnification of T_g/T range from 0.85 to 1

ment of ε_s will give fundamental information on the makeup of the reactive system at any time during cure.

Accompanying the chemical change and increase of molecular weight is usually a density increase and therefore an increase in dipole density that should result in an increase in dipolar relaxation strength. However, an increase in permittivity is usually not observed for reactive systems because in most instances product dipoles are less polar or not polar entities. An exception has recently been found [18] where the product dipoles are of a higher dipole moment than the reactants via a possible specific interaction induced molecular conformation.

The relaxation between relaxation strength and a material's constituent dipoles has been derived from fundamental principals by Debye and later modified by Fröhlich [113] as

$$\frac{(\varepsilon_s - \varepsilon_\infty)(2\varepsilon_s - \varepsilon_\infty)}{\varepsilon_s(\varepsilon_\infty + 2)^2} = \frac{4\pi}{9kT}\sum N_i\langle \mu_i^2 \rangle \tag{9.30}$$

where ε_s and ε_∞ are the limiting low and high frequency dielectric permittivity, N_i is the concentration of dipoles of type i in the material, μ_i the type i dipole moment, k the Boltzmann constant, and T the absolute temperature. In situations where the reactant dipole moments are greater than the products, which is the case for most epoxy-amine systems, a systematic decrease in ε_s or $\Delta\varepsilon$ will be found.

In the early stages of cure the decrease in ε' is gradual; later when the system vitrifies an abrupt drop is observed. In the early reaction stages (pre-vitrification) what is being measured are changes in the material's ε_s. However, in the

Fig. 9.10. A Illustration of dielectric permittivity vs frequency with cure time as a parameter. **B** Extracted dielectric permittivity at frequency (f_1) vs cure for material in A
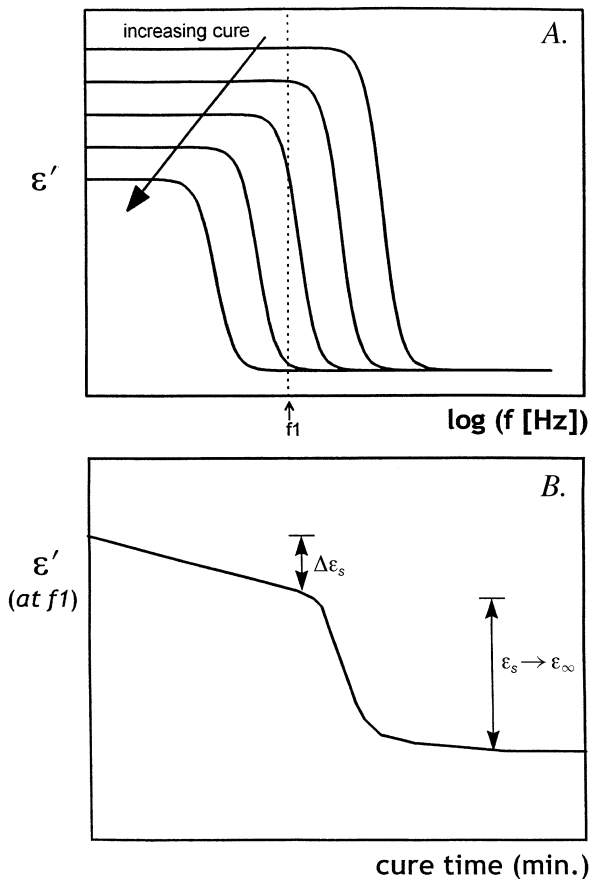
reaction time window of vitrification, we are instead measuring a continuous change from ε_s to ε_∞ (the material's lowest permittivity value, ignoring for the moment any β relaxations, as they have for the present purpose negligible relaxation strength). As the foregoing isochronal approach is a typical (prevailing) one in the literature it will be useful to explore these ideas further using a series of illustrations. We show in Fig. 9.10A a set of frequency sweeps that represent qualitatively the general trend for dielectric permittivity changes during cure, while in Fig. 9.10B we extract isochronal information as a function of cure time.

We point out the ε_s changes can only be monitored while the majority of the relaxation process remains in the available experimental frequency window. That condition fails eventually because the lowest measured frequency must be kept sufficiently high so that the measurement time is short compared with chemical changes. It is this vitrification time period in cure where modeling approaches are needed to account for the dependence of the α relaxation on T_g including the relaxation strength, relaxation time, and shape parameters. We dis-

cuss these features in the following section. It should be also mentioned that care must be exercised when presenting isochronal data to avoid choosing a frequency which includes interfacial or electrode blocking influences, as discussed in the previous section on polarization by migrating charges.

In an industrial application, microwave frequency measurements are often useful for both cure monitoring and for material characterization (particularly necessary when processing materials with microwave heating). As mentioned in the charge migration polarization section (Sect. 9.4), typically at frequencies greater than 1 MHz the only relevant polarization mechanisms are the dipolar relaxation and faster resonance processes. For this reason electrode effects and conductivity contributions to the measurement are avoided.

Great strides have been made in high frequency instrumentation and signal analysis techniques [114, 115] that result in rapid and accurate microwave band frequency measurements on reactive systems. For industrial processing purposes it may be sufficient to monitor a dielectric response at a single microwave frequency if the material permittivity changes during cure are systematic. The types of probes used are either flat surface strip-line measurements [116], coaxial airlines filled with sample [81, 117–119], open-ended semi-rigid coaxial lines terminated by a volume of the sample [120], or resonant cavities tuned to a specific frequency band and adjusted to obtain the samples permittivity [121, 122]. While such isochronal measurements reveal little about the underlying molecular nature of the relaxation process and are batch-specific, they can be useful for industrial cure monitoring.

9.5.5
Changes in Relaxation Spectrum During Network Formation

Another approach to the analysis of cure data is to examine changes in the shape parameters of a fit relaxation function. The most robust and general function is the well-known Havriliak-Negami (HN) equation [123]

$$\varepsilon^*(\omega) = \frac{\varepsilon_s - \varepsilon_1}{[1 + (i\omega\tau_\alpha)^{1-a_\alpha}]^{b_\alpha}} + \frac{\varepsilon_1 - \varepsilon_\infty}{[1 + (i\omega\tau_\beta)^{1-a_\beta}]^{b_\beta}} + \varepsilon_\infty - i\left(\frac{\sigma}{\omega\varepsilon_0}\right)^d \qquad (9.31)$$

where both the α and β processes are accounted for (see appropriate subscripts) and ω is the angular frequency, i is $(-1)^{1/2}$, $\varepsilon_s - \varepsilon_1$, and $\varepsilon_1 - \varepsilon_\infty$ are the relaxation strengths of the α and β processes, τ_α and τ_β are their relaxation time, a_α, b_α, a_β, b_β are the processes shape parameters. The final term in Eq. (9.31) accounts for conductivity (σ), ε_0 is the permittivity of free space, and d is a scaling constant, usually with a value of one for migrating charge polarization. In Fig. 9.4 we have applied this functional form to the data. It is apparent that one of the strengths of this analysis is the ability to deconvolute distinct but overlapped processes. We hasten to add that as the nature of the β process is poorly understood, so to the nature of the merging region of α and β processes (e.g., [124]), therefore the linear deconvolution may eventually be found to be in error. However, trends in the behavior of the relaxation times beyond this region where the processes ap-

pear to be distinct are reasonable; until these issues are resolved its continued use for this purpose is warranted.

Other functional forms such as the Kohlrauch-Williams-Watts (KWW) [125] stretched-exponential functional form are also often applied:

$$\phi(t) = A \exp\left[-\left(\frac{t}{\tau^*}\right)^\beta\right] \tag{9.32}$$

where τ^* is the relaxation time and β is the stretching exponent ranging from 0 to 1. There are several different fundamental physical arguments for the description of the α process [126–128] that arrive at a functional form for the relaxation phenomena in the form of a stretched-exponential (KWW). One of the most accessible arguments is the work of Ngai and Roland [129], in which systematic changes to polymer structures were observed to result in systematically altered α process T_g-reduced temperature dependencies. The trends, as predicted from the fundamental argument, become visually convincing when presented in the cooperativity plot (or fragility plot [130]) in which log τ is presented as a function of T_g/T. Actually, the cooperative nature of a reactive system was first considered by Matsuoka et al. [131], who proposed a model for the curing reactions of epoxy resins based on the similarity between chemical cross-linking and structural relaxation in glassy thermoplastics. During cross-linking, the configurational entropy will decrease while the temperature below which the equilibrium state cannot be reached (T^*) and the relaxation time (τ) will both increase. The authors calculate T^* by assuming that it varies in proportion with the degree of cure and then substitute the calculated value in the Adam-Gibbs expression [132], in order to obtain the relaxation time. The relaxation time, on the other hand, is contained within an "apparent" rate constant and is thus related to the reaction kinetics (simple first-order kinetics is assumed). The Adam-Gibbs expression and a distribution spectrum obtained from dielectric relaxation of poly(vinyl acetate) were employed to model the curing process for both isothermal and nonisothermal histories. Additional details regarding cooperativity dynamics in epoxy-amine system may be found in the recent literature [23].

We mention finally the two power-law form of Jonscher [6]:

$$\varepsilon'' \sim \omega^m \qquad\qquad \omega \ll \omega_0 \tag{9.33}$$

$$\varepsilon'' \sim \omega^{-n} \qquad\qquad \omega \gg \omega_0 \tag{9.34}$$

where $\omega_0 = 1/\tau$. It has been explored recently in the context of curing systems [133, 134] in an attempt to ascribe significance to the slope (m and $-n$) on either side of the relaxation peak in terms of length scales of motion being probed, i.e., low frequency side applying to long length scales and the high frequency side to short. The short time n parameter arrived at by a percolation model for the glass transition [135] was found to be in agreement with their experimental findings. Historically, the interpretation of shape parameters in terms of the length-scale

of the relaxation originated with the work of Schönhals and Schlosser [136] on non-reactive amorphous polymer systems.

In general, after the splitting of the $\alpha\beta$ peak early in cure, the α peak tends to broaden as cross-linking develops. Let us examine the changes in model parameters with cure using the familiar epoxy/amine reactive system. The HN parameters (Eq. 9.31) show the following trends: the $1 - a_\alpha$ linearly decreases, the b_α is insensitive to cure, and the $1 - a_\beta$ and $1 - a_\beta$ both increase and then decrease in a parabolic trend with minima occurring at the same cure time. Interpretation of these complex trends is avoided by the other models with fewer parameters. Nevertheless, the pattern in HN relaxation time change with cure accurately reflects the apparent relaxation times gleaned from the frequency sweep data and therein lies the utility of the model. The trend in the Jonscher model m and n parameters are a constant linear decrease in m with cure from 1 to 0.5 up to 65 % of conversion and a linear decrease in n but with a more gradual slope from 0.4 to 0.2. In this way the systematic broadening of the α process is quantified. Finally, the KWW β parameter reveals the same broadening trend, while containing only one parameter. KWW β decreases from 0.5 to 0.32 up to 65 % conversion. For this system the linear changes in the shape parameter allow for the direct monitoring of conversion to just beyond the gel point. The limitation to the highest extent of cure that can be covered by the relaxation peak shape analysis comes from an experimental concern: the low frequency measurement time cannot exceed appropriate values determined by the system's chemical kinetics.

The use of changes in a model parameter to monitor cure is not appropriate for all types of reactive mixtures. In some reactive systems the changes are too small to be accurately monitored. A reactive urethane system, for example, exhibits a very small change in the Jonscher m and n parameters: m decreases from approximately 0.85 to 0.8, while n increases from 0.2 to 0.25 [137]. In this system the product of the reaction is a lightly cross-linked rubber, where the final T_g of the system is much lower than the reaction temperature, and the relaxation time of the α remains in the MHz region at completion of cure. In this case the broadening of the α process due to cooperativity on approaching the glass transition does not play a role.

As a final example we examine the broadening of the α process during network growth in a cyanate ester resin. As conversion increases, the α process appears to broaden, while its intensity decreases. It is well known that the loss shape can be temperature dependent. To assess the influence of a temperature-dependent change of shape on the increasing breadth of the α process, we replot the original data at an "isomobility" temperature, i.e., at a temperature where the loss has a convenient loss maximum of 10^4 Hz. These plots are shown in Fig. 9.11 (raw data), and the normalized spectra are shown in Fig. 9.12, illustrating that with increasing conversion the α loss peak indeed becomes more broad.

No significant influence from conductivity was found in the frequency region near the loss peak and hence the foregoing analyses lead us to conclude that the broadening is a real feature of the relaxation itself. The shapes of the peaks in Fig. 9.12 are characterized and quantified by the Jonscher model. The Jonscher parameters $m = 0.62$ and $n = 0.55$ for the neat resin are comparable to those of

Fig. 9.11. Dielectric loss spectra for 0, 10, 20, 30, and 40% samples at an "isomobility" temperature (temperature where the frequency of ε''_{max} is 10 kHz). *Solid lines* are fits to the Jonscher model
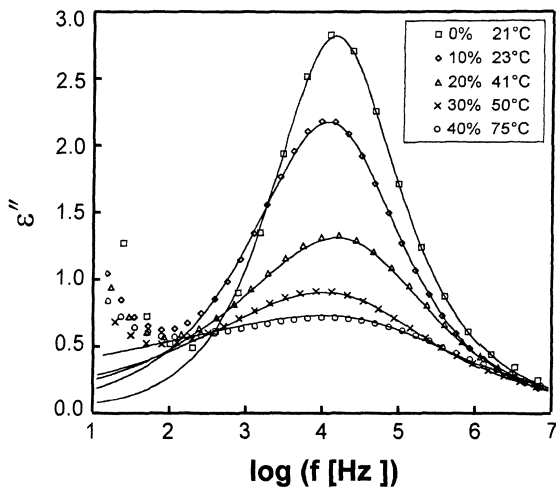
many polymers and low molecular weight materials; however, with increasing conversion both parameters decrease, but the m parameter becomes smaller than n, This behavior is unusual. In Jonscher's monograph [6] where the parameters are given for 65 different materials, only 18 have smaller m's than n's. The broadening of the α process with cross-linking is not a new finding, but precisely why the broadening occurs remains unclear. We envision two aspects of the broadening of the α process. First is broadening due to microscale composition variations (concentration fluctuations). Such broadening phenomena have been studied for polymer blends using DSR by Katana et al. [138], who investigated the binary blend of bisphenol A polycarbonate (BPAPC) and tetramethyl bisphenol A polycarbonate (TMBAPC) and found a maximum in the broadening of the α process at approximately 40 mol% of TMBAPC but, interestingly, found no difference in ΔT_g (temperature range of calorimetrically determined glass transition) or $\Delta Cp(T_g)$ (extrapolated heat capacity difference between liquid and glass) for these blends. Kumar et al. [139] developed a mathematical model based on nanoscale concentration fluctuations, predicting a broadening of ΔT_g and width of the α process for miscible polymer blends. Arguments along similar lines have been set forth by Roland and Ngai [140], though they refer to the phenomenon generically as heterogeneous broadening. We acknowledge a contribution to the broadening in cross-linked cyanate ester networks due to these compositional fluctuations; however, it appears that the severity of the broadening for our network's α process must have an additional explanation. We have shown above (Sect. 9.5.3) that the breadth of the α process in PMPS networks remains unchanged when the distance between cross-links is greater than the length scale of the cooperatively rearranging domain (CRD). In the cyanate ester network, consisting of rigid cross-link nodes and rigid sections connecting those nodes, we propose that the CRD is relatively large and of the order of (or larger than) the distance between the cross-links (approximately 18 Å). In this case the α dynamics will become increasingly disturbed and heterogeneous
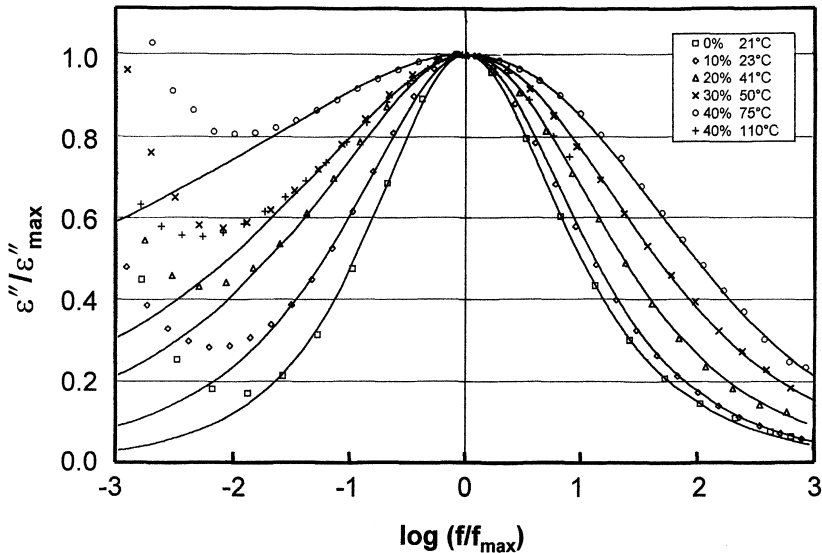
Fig. 9.12. Normalized dielectric loss spectra for 0, 10, 20, 30, and 40% samples at an "isomobility" temperature (temperature where the frequency of ε''_{max} is 10 kHz). *Solid lines* are fits to the Jonscher model

with the progress of cross-linking, with an ultimate disappearance of the α process in perfect networks of this kind. We assert that this influence on the broadening of the α process is greater than the influence of concentration fluctuations mentioned above.

9.6
Conclusions

In this chapter we have demonstrated how dielectric spectroscopy can be used to monitor network formation in chemically reactive systems. The two major polarization mechanisms that are studied by dielectric spectroscopy are (1) polarization due to charge migration and (2) polarization due to orientation of permanent dipoles. Migration of charges gives rise to conductivity that is affected by network formation and hence can serve as an indicator of the progress of cure. Phenomenological models that match experimental impedance with the impedance of an equivalent circuit composed of resistors and capacitors are used to describe polarization due to migrating charges. The study of dipole reorientation provides a more fundamental insight into molecular the dynamics of network-forming polymers. Depending on the type and destiny of dipoles present, there are four classes of cross-linking reactions that result in network formation and can be probed by DRS. Common to all these classes, however, is the change in the segmental relaxation (the α process) during network formation. The advancement of network formation can be quantified and modeled by

following the change in the relaxation time, the breadth of the relaxation spectrum, the spectral shape parameters, and the dielectric relaxation strength.

List of Abbreviations and Symbols

C	Capacitance
f	Frequency
k	Kinetic rate constant
L	Inductance
m,n	Power-law parameters
N	Concentration of dipoles
R	Resistance
T	Temperature
T_g	Glass transition temperature
T_g^*	T at which $\tau = 100$ s
Y^*	Admittance
Z^*	Impedance
β	KWW exponent
Γ	Gamma function
ε^*	Complex dielectric function
ε'	Dielectric permittivity (real part)
ε''	Dielectric loss (imaginary part)
ε_s	Limiting low-frequency ε'
ε_∞	Limiting high-frequency ε'
$\Delta\varepsilon$	$\varepsilon_s - \varepsilon_\infty$
Φ	Polarization decay function
η	Viscosity
τ	Average relaxation time
ω	Angular frequency

CRD	Cooperatively rearranging domain
DETA	Diethylene triamine
DGEBA	Diglycidylether of bisphenol A
DLS	Dynamic light scattering
DRS	Dielectric relaxation spectroscopy
DS	Dielectric spectroscopy
HN	Havriliak-Negami
KWW	Kohlrausch-Williams-Watts
PMPS	Poly(methylphenylsiloxane)
VFT	Vogel-Fulcher-Tammann

References

1. McCrum NG, Read B, Williams G (1967) In: Anelastic and dielectric effects in polymeric solids. Wiley, NY
2. Karasz FE (ed) (1972) Dielectric properties of polymers. Plenum Press, NY
3. Hedvig P (1977) Dielectric spectroscopy of polymers. Adam Hilger, Bristol
4. Böttcher CJF, Bordewijk P (1978) Theory of electric polarization. Elsevier, Amsterdam
5. Williams G (1979) Adv Polym Sci 33:60
6. Jonscher AK (1983) Dielectric relaxation in solids. Chelsea Dielectric Press, London
7. Ku CC, Liepins R (1987) Electrical properties of polymers. Hanser, Munich
8. Owen J (1988) In: Allen G, Bevington JC (eds) Comprehensive polymer science, vol 2. Pergamon Press, Oxford, pp 669–686
9. Williams G (1988) In: Allen G, Bevington JC (eds) Comprehensive polymer science, vol 2. Pergamon Press, Oxford, pp 601–632
10. Riande E, Saiz E (1992) Dipole moments and birefringence of polymers. Prentice Hall, NY
11. Williams G (1997) In: Riande E (ed) Keynote lectures in selected topics of polymer science, chap 1. CSIC, Madrid, pp 1–40
12. Conductive polymers, where charge carriers are electrons and electron holes, will not be discussed here and the reader is referred to the excellent article by Block [13]
13. Block H (1979) Adv Polym Sci 33:93
14. Bockris JO'M, Reddy AKN (1970) Modern electrochemistry, vols 1 and 2. Plenum Press, NY
15. Barker RE Jr (1976) Pure Appl Chem 46:157
16. Seanor DA (ed) (1982) Electrical properties of polymers. Academic Press, NY
17. Gray FM (1991) Solid polymer electrolytes. VCH, New York
18. Gallone G, Levita G, Mijovic J, Andjelic S, Rolla P (1998) Polymer 39:2095
19. Macdonald JR (1987) Impedance spectroscopy. Wiley, New York
20. Metaxas AC, Meredith RJ (1983) Industrial microwave heating. Peregrinus, London
21. Kremer F, Arndt M (1997) In: Runt JP, Fitzgerald JJ (eds) Dielectric spectroscopy of polymeric materials, chap 2. Amererican Chemical Society, Washington, DC, p 67
22. Gotro J, Yandrasits M (1989) Polym Eng Sci 29:278
23. Andjelic S, Fitz B, Mijovic J (1997) Macromolecules 30:5239; Fitz B, Andjelic S, Mijovic J (1997) Macromolecules 30:5227
24. Mijovic J, Andjelic S (1995) Macromolecules 28:2787
25. Mijovic J, Andjelic S (1995) Polymer 36:3783
26. Sheppard NF, Garverick SL, Day DR, Senturia SD (1981) SAMPE Int Symp 26:65
27. Senturia SD, Sheppard NF Jr, Lee HL, Day DR (1982) J Adhesion 15:69
28. Day DR, Lewis TJ, Lee HL, Senturia SD (1985) J Adhesion 18:73
29. Bidstrup WW, Sheppard NF Jr, Senturia SD (1986) Polym Eng Sci 26:358
30. Kranbuehl DE, Delos SE, Jue PK (1986) Polymer 27:11
31. Kranbuehl DE, Delos SE, Hoff M, Weller L, Haverty L, Seeley J (1987) SAMPE Int Symp 32:338
32. Kranbuehl DE, Hoff M, Haverty L, Loss A, Freeman T (1988) SAMPE Int Symp 33:1276
33. Sluyters-Rehbach M, Sluyters JH (1977) In: Bard AJ (ed) Electroanalytical chemistry, vol 4. Marcel Dekker, New York, pp 1–127
34. Archer WI, Armstrong RD (1980) Electrochemistry 7:157
35. Walter GW (1986) Corrosion Sci 26:681
36. Cole RH, Cole KS (1941) J Chem Phys 9:341
37. Kenny JM, Trivisano A (1991) Polym Sci Eng 31:19
38. Mijovic J, Bellucci F (1996) Trends Polym Sci 4:74
39. Tajima YA (1982) Polym Composites 3:162
40. Koike T (1993) J Appl Polym Sci 50:1943
41. Maistros GM, Bucknall CB (1994) Polym Eng Sci 34:1517
42. Opalicki M, Kenny JM (1993) Makromol Chem Makromol Symp 68:41

43. Senturia SD, Sheppard NF (1986) Adv Polym Sci 80:1
44. Mijovic J, Kenny JM, Maffezzoli A, Trivisano A, Bellucci F, Nicolais L (1993) Comp Sci Tech 49:277
45. Kranbuehl DE (1997) In: Runt JP, Fitzgerald JJ (eds) Dielectric spectroscopy of polymeric materials. American Chemical Society, Washington, DC, Chap 11, p 303
46. Sanjana ZN (1986) Polym Eng Sci 26:373
47. Zukas WX, Wentworth SE (1987) Polym Composites 8:232
48. Day DR, Sheppard DD (1989) Mater Res Soc Symp Proc 142:227
49. Day DR (1989) Polym Eng Sci 29:334
50. Day DR, Sheppard DD (1991) Polym Composites 12:87
51. Mathieu C, Boiteux G, Seytre G, Villain R, Dublineau P (1994) J Non-Cryst Solids 172/174:1012
52. Maistros GM, Partridge IK (1995) Comp Sci Tech 53:355
53. Maistros GM, Partridge IK (1998) Composites Part B 29B:245
54. Kranbuehl DE, Eichinger D, Hamilton T, Clark R (1991) Polym Eng Sci 31:5
55. Kranbuehl DE (1991) J Non-Cryst Solids 131/133:930
56. Kranbuehl DE, Kingsley P, Hart S, Hasko G, Dexter B, Loos A (1994) Polym Composites 15:297
57. Ciriscioli PR, Springer GS (1989) SAMPE J 25:35
58. Ulanski J, Friedrich K, Boiteux G, Seytre G (1997) J Appl Polym Sci 65:1143
59. Angell CA, Boehm L, Oguni M, Smith DL (1993) J Mol Liq 56:275
60. Johari GP (1984) In: Ngai K, Wright GB (eds) Relaxations in complex systems. National Technical Information Service, US Department of Commerce, Springfield, VA
61. Lewis LJ, Wahnstrom G (1994) Phys Rev E 50:3865
62. Johari GP, Goldstein M (1970) J Chem Phys 53:2372
63. Meier G, Fujara F, Petry W (1989) Macromolecules 22:4421
64. Stockmayer WH (1967) Pure Appl Chem 15:539
65. Imanishi Y, Adachi L, Kotaka T (1988) J Chem Phys 89:7585
66. Adachi K, Yoshida H, Fukui F, Kotaka T (1990) Macromolecules 23:3138
67. Boese D, Kremer F (1990) Macromolecules 23:8298
68. Boese D, Kremer F, Fetters LJ (1990) Macromolecules 23:1826
69. Adachi K, Kotaka T (1993) Prog Polym Sci 18:585
70. Watanabe H, Urakawa O, Yamada H, Yao M-L (1996) Macromolecules 29:755
71. Pakula T, Geyler S, Edling T, Boese D (1996) Rheol Acta 35:1
72. Fitz BD, Mijovic J (1999) Macromolecules 32:3518
73. Müller M, Stadler R, Kremer F, Williams G (1995) Macromolecules 28:6942
74. Müller M, Kremer F, Stadler R, Fischer EW, Seidel U (1995) Colloid Polym Sci 273:38
75. Carlini C, Rolla PA, Tombari E (1990) J Appl Polym Sci 41:805
76. Tombari E, Johari GP (1993) J Chem Soc Faraday Trans 89:3477
77. Carlini C, Livi A, Rolla PA, Fioretto D (1994) J Non-Cryst Solids 172/174:569
78. Fournier J, Williams G, Holmes PA (1997) Macromolecules 30:2042
79. Casalini R, Corezzi S, Fioretto D, Livi A, Rolla PA (1996) Chem Phys Lett 258:470
80. Wasylyshyn DA, Johari GP, Tombari E, Salvetti G (1997) Chem Phys 223:313
81. Mijovic J, Fitz B (1998) Polym Adv Tech 9:721
82. Fitz BD, Mijovic J (1999) Macromolecules 32:4134
83. Ngai KL, Mashimo S, Fytas G (1988) Macromolecules 21:3030
84. Boese D, Momper B, Meier G, Kremer F, Hagenah J, Fischer E (1989) Macromolecules 22:4416
85. Hwang Y, Patterson GD, Stevens J (1996) J Polym Sci Part B Polym Phys 34:2291
86. Floudas G, Placke P, Stepanek P, Brown W, Fytas G, Ngai KL (1995) Macromolecules 28:6799
87. Meier G, Gerharz B, Boese D, Fischer, E (1991) J Chem Phys 94:3050
88. Lane JW, Seferis JC, Bachmann MA (1986) Polym Eng Sci 26:346
89. Lane JW, Seferis JC, Bachmann MA (1986) J Appl Polym Sci 31:1155
90. Nass KA, Seferis JC (1989) Polym Eng Sci 29:315

91. Dusi MR, May CA, Seferis JC (1983) In: May CA (ed) Chemorheology of thermosetting polymers. Am Chem Soc Symp Ser 227, p 301
92. Mangion M, Johari GP (1990) J Polym Sci Part B Polym Phys 29:1127
93. Parthun MG, Johari GP (1992) Macromolecules 25:3254
94. Parthun MG, Johari GP (1992) Macromolecules 25:3149
95. Zukas W (1992) Macromolecules 26:2390
96. Barton JM (1985) Adv Polym Sci 72:111
97. Fournier J, Williams G, Duch C, Aldridge GA (1996) Macromolecules 29:7097
98. Andjelic S, Mijovic J (1998) Macromolecules 31:8463
99. Deng Y, Martin GC (1994) J Polym Sci Part B Polym Phys 32:2115
100. Deng Y, Martin GC (1994) Macromolecules 27:5141
101. Deng Y, Martin GC (1994) Macromolecules 27:5147
102. Huguenin FGAE, Klein MT (1985) Ind Eng Chem Prod Res Dev 24:166
103. Kenny JM, Apicella A, Nicolais L (1989) Polym Eng Sci 29:972
104. Dusek K (1986) Adv Polym Sci 78:1
105. Rozenberg BA (1985) Adv Polym Sci 75:113
106. Tanaka Y, Bauer RS (1988) In: May CA (ed) Epoxy resins chemistry and technology, 2nd edn. Marcel Dekker, New York, chap 3, pp 285–464
107. Roland CM (1994) Macromolecules 27:4242
108. Glatz-Reichenbach JKW, Sorriero LJ, Fitzgerald JJ (1994) Macromolecules 27:1338
109. Boese D, Momper B, Meier G, Kremer F, Hagenah J, Fischer EW (1989) Macromolecules 22:4416
110. Matsuoka S (1997) J Appl Polym Sci 64:77
111. The phenomenon of a network relaxation becoming entirely local because of the network's disturbance of the cooperative domain size is the subject of current research in our laboratory. The effect is similar to the situation of amorphous polymer confined within a thin space between crystalline lamellar walls; e.g., Schick C, Donth E (1991) Phys Scr 43:423; Arndt M, Stannarius R, Groothues H, Hempel E, Kremer F (1997) Phys Rev Lett 79:2077; Sy JW, Mijovic J (2000) Macromolecules 33:933
112. Sillescu H (1999) J Non-Cryst Solids 243:81
113. Fröhlich H (1949) Theory of dielectrics. Oxford University Press, London
114. Wei Y, Sridhar S (1989) Rev Sci Instr 60:3041
115. Stuchly M, Stuchly S (1980) IEEE Trans on Instr Meas IM29, p 176
116. Das NK, Voda SM, Pozar DM (1987) IEEE Trans Microwave Theory and Techniques MTT35, p 636
117. Cole RH, Mashimo S, Windsor P IV (1980) J Phys Chem 84:786
118. Carrozzino S, Levita G, Rolla PA, Tombari E (1990) Polym Eng Sci 30:366
119. Fioretto D, Livi A, Rolla PA, Socino G, Vardini G (1994) J Phys Condensed Matter 6:5294
120. Baker KR, Graybeal JD (1991) In: Symposium on Polymer Radiation Chemistry. American Chemical Society, p 470
121. Marand E, Baker K, Graybeal J (1992) Macromolecules 25:2243
122. Jow J, Hawley M, Finzel M, Kern T (1988) Polym Eng Sci 28:1450
123. Havriliak S, Negami S (1966) J Polym Sci C14:99
124. Arbe A, Richter D, Colmenero J, Farago B (1996) Phys Rev E 54:3853
125. Williams G, Watts D (1970) Trans Farad Soc 66:80
126. Bendler JT, Shlesinger MF (1987) J Mol Liq 36:37
127. Ngai KL, Rendell RW (1991) J Non-Cryst Solids 131/133:233
128. Chamberlin RV, Kingsbury DW (1994) J Non-Cryst Solids 172/174:318
129. Ngai KL, Roland M (1992) Macromolecules 24:5315
130. For a review see: Angell CA (1995) Science 267:1924
131. Matsuoka S, Quan X, Bair HE, Boyle DJ (1989) Macromolecules 22:4093
132. Adam G, Gibbs J (1965) J Chem Phys 43:139
133. Casalini R, Livi A, Rolla PA (1996) Phys Rev B 53:564
134. Andjelic S, Mijovic J (1998) Macromolecules 31:2872
135. Langier JM, Luck JM (1987) J Phys A 20:L885

136. Schönhals A, Schlosser E (1989) Colloid Polym Sci 267:125
137. Tabellout M, Randrianantoandro H, Emery JR, Durand D, Hayward D, Pethrick RA (1995) Polymer 36:4547
138. Katana G, Kremer F, Fischer E, Plaetschke R (1993) Macromolecules 26:3075
139. Kumar S, Colby R, Anastasiadis S, Fytas G (1996) J Chem Phys 105:3777
140. Ngai KL, Roland MC (1993) Macromolecules 26:6824

10 Molecular and Collective Dynamics of (Polymeric) Liquid Crystals

F. Kremer · A. Schönhals

10.1
Introduction

Thermotropic liquid crystals form a class of matter which is located between the crystalline and the isotropic state [1, 2]: In crystals molecules have maximal (positional and translational) order and minimal mobility while in liquids the reverse is the case. In liquid crystals (LC) aspects of both states are combined and – so-called – mesomorphic phases are developed in which order and mobility compete. The former results in anisotropic (optical) properties, the latter enables one to modify (to "switch") the orientation of the molecules by use of external electric or magnetic fields. Broadband dielectric spectroscopy has turned out to be a versatile tool to study the dynamics in these systems.

   The literature concerning the dielectric properties of (low molecular weight and polymeric) liquid crystals is vast. (For reviews see for instance [3–7].) It would be far beyond the scope of this contribution to discuss it in detail. Thus the present chapter is written out of the personal perspective of the authors mainly based on their own experiments.

10.2
Molecular and Mesomorphic Structures of Liquid Crystals

10.2.1
Low Molecular Weight Systems

Numerous organic molecules form due to their shape anisotropy liquid crystalline phases [7, 8]. Most of them are rod-like, but also bent-shaped and disc-like molecules can show liquid crystalline properties. The mesophases can be divided into nematics and smectics.

   The nematic phase is the liquid crystalline state with the lowest order and it appears usually at temperatures just below the isotropic state. The molecules have all translational degrees of freedom and therefore no long range positional order [1] exists. Their long axes are preferentially aligned with respect to a common unit vector n, the director (see Fig. 10.1a). For uniaxial molecules $n = -n$ (uniaxial nematic phase). For chiral molecules the spatial variation of n leads to a helical superstructure (with pitch p_H) in the so-called cholesteric phase.

For smectic phases, in addition to the orientational, a positional order is observed. Therefore on time-average the centres of mass of the molecules are fixed and equidistant layered structures are developed. The mean orientation of the molecules within the layers can be parallel (smectic A) or tilted (smectic C) with respect to the direction of the layer normal (Fig. 10.1a). For smectic A and C phases there is no positional order of the molecules within a layer and they can be regarded as a two-dimensional fluid. For higher organized smectic phases (B, E, F, ...) an increasing positional order of the molecules within a layer (and also between neighboured layers) is established which is accompanied by a reduced rotational and translational mobility. For chiral molecules with tilted smectic phases – as in cholesterics – a helical superstructure is formed (see Sect. 10.5).

The degree of orientation of the molecules is described by the order parameter S defined as

$$S = \frac{1}{2} \langle 3\cos\theta - 1 \rangle \tag{10.1}$$
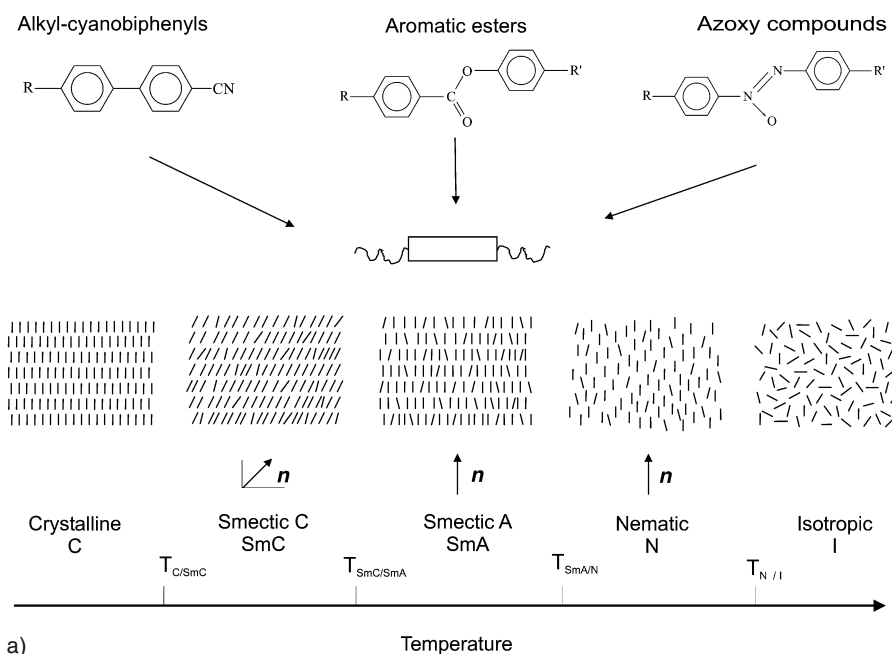
Fig. 10.1. **a** Some examples for rod-like molecules forming mesomorphic phases. n indicates the direction of the director and $T_{x/y}$ symbolizes the phase transition temperatures. **b** Some examples for disk-like mesogens which can form nematic and columnar liquid crystalline phases. **c** Some examples of architectures for polymeric liquid crystals. The basic units are monomers with rod- or disk-like mesogens which are attached via a spacer as a side group or which may form part of the main chain

Hexa-alkanoates
of benzene

triphenylene
structures

b)   nematic phase

columnar phase

Side Chain
Liquid Crystalline Polymers

Main Chain
Liquid Crystalline Polymers

"end on"

"side on"

Combined Main Side Chain Polymers
Staistical Copolymers
Blockcopolymers
Networks
.
.
.

c)
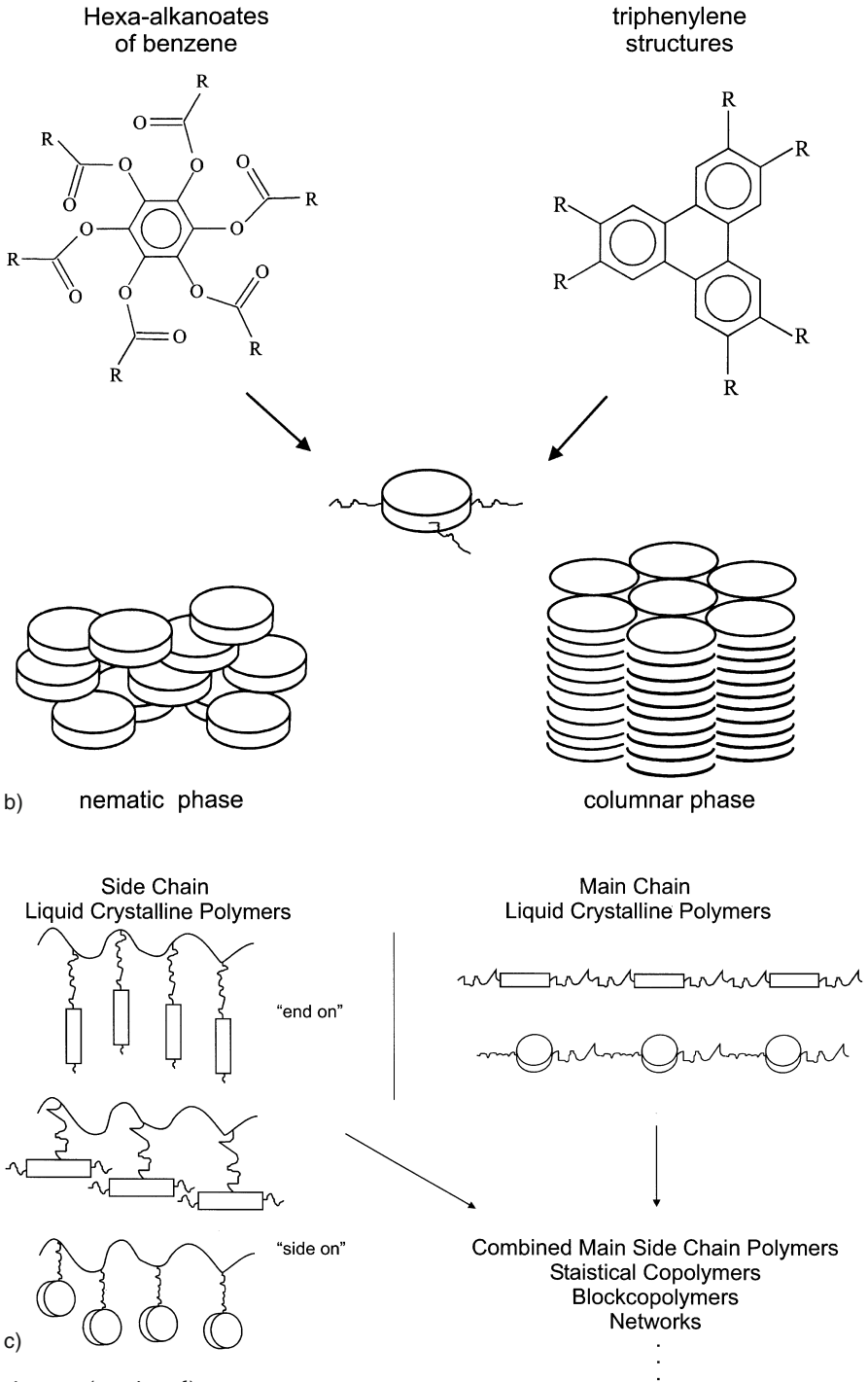
Fig. 10.1 (continued)

where θ is the angle between the direction of the long axis of the molecule and the director **n**; the brackets denote the statistical average. For an isotropic liquid $S = 0$ holds and for a fully aligned LC phase $S = 1$.

Also disc-shaped molecules (see for instance [9, 10]) like hexa-alkanoate or benzene and triphenylene derivatives can form mesomorphic phases (see Fig. 10.1b). In columnar discotic phases superstructures – analogous to smectics – can be observed.

10.2.2
Polymeric Systems

Liquid crystals can be readily combined with polymers of different architecture by use of a flexible spacer which decouples the mesogenic moieties from the polymer chain ([7, 11], see Fig. 10.1c). In side chain liquid crystal polymers (SCLCP) [12] which have received much attention since their first synthesis [13, 14] the mesogenic units are located in a side chain of the polymer backbone. For rod-like mesogenic moieties the coupling with regard to the spacer groups can be parallel or perpendicular. It is expected that such materials can be applied as active components for optical data storage, holographic applications and electro-optical devices [15]. In main chain liquid crystalline polymers (MCLCP) the mesogenic moiety is part of the polymeric backbone. Due to the stiffness of the mesogenic building blocks, materials of extraordinary mechanical properties can be realized. In addition to SCLCP and MCLCP, combined side chain/main chain [16, 17] systems or liquid crystalline copolymers [12] or networks [18] can be synthesized.

10.3
Theoretical Considerations

The theoretical treatment of the static dielectric properties of LCs was pioneered by Maier and Saupe (see for instance[19–22]). They introduced an additional contribution to the interaction energy of the system depending on the orientation of the molecules, the nematic potential U_i [2]. For that is assumed in a mean field approximation $U_i \sim S\left(\dfrac{3\cos\theta_i - 1}{2}\right)$ where θ_i is the angle between the direction of the long axis of the molecule and the director **n** and S the order parameter. In a simplified version neglecting internal field and polarization effects for the mean square dipole moments parallel $\langle\mu_{\parallel}^2\rangle$ and perpendicular $\langle\mu_{\perp}^2\rangle$ to the director [2]

$$\langle\mu_{\parallel}^2\rangle = \frac{\mu^2}{3k_BT}\left[1-(1-3\cos^2\Psi)S\right]E \tag{10.2a}$$

$$\langle\mu_{\perp}^2\rangle = \frac{\mu^2}{3k_BT}\left[1+\frac{1}{2}(1-3\cos^2\Psi)S\right]E \tag{10.2b}$$
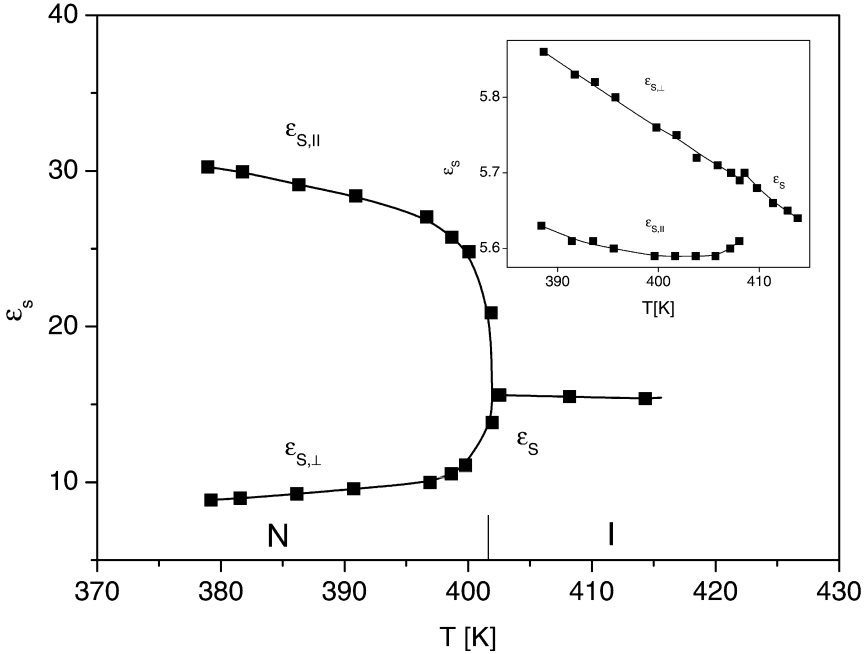
Fig. 10.2. Temperature dependence of the quasi-static permittivities parallel and perpendicular to the director $\varepsilon_{S,\parallel}$ and $\varepsilon_{S,\perp}$ for p–n–alkoxy benzoic acid ($\delta\varepsilon > 0$). The *inset* shows the same for $n(4'$-ethoxybenzylide) 4-aminobenzonitrile ($\delta\varepsilon < 0$). All *lines* are guides for the eyes. The figures are redrawn from [1]

is obtained where Ψ is the angle between the dipole moment $\boldsymbol{\mu}$ and the long axis of the molecule (k_B is the Boltzman constant and T the temperature). Equations (10.2a) and (10.2b) give for the difference in the quasi static permittivities parallel $\varepsilon_{S,\parallel}$ and perpendicular $\varepsilon_{S,\perp}$ to the director ($\varepsilon_S = \lim\limits_{\omega\tau \ll 1} \varepsilon'(\omega)$, see Chap. 1)

$$\delta\varepsilon = \varepsilon_{S,\parallel} - \varepsilon_{S,\perp} = -\frac{\mu^2}{2k_B T \varepsilon_0} \frac{N}{V} (1 - 3\cos^2\Psi)S \tag{10.2c}$$

where N is the number of dipoles, V the volume of the system and ε_0 the permittivity of free space. The sign of the dielectric anisotropy $\delta\varepsilon$ is positive if Ψ is small. Otherwise the sign of $\delta\varepsilon$ is negative[1]. In Fig. 10.2 the temperature dependence of the dielectric anisotropy is presented for two low molecular weight LC having a positive and a negative value of $\delta\varepsilon$. In the isotropic state $\delta\varepsilon$ vanishes for both materials.

---

[1] The corresponding materials are called dielectric positive ($\delta\varepsilon > 0$) or dielectric negative ($\delta\varepsilon < 0$).
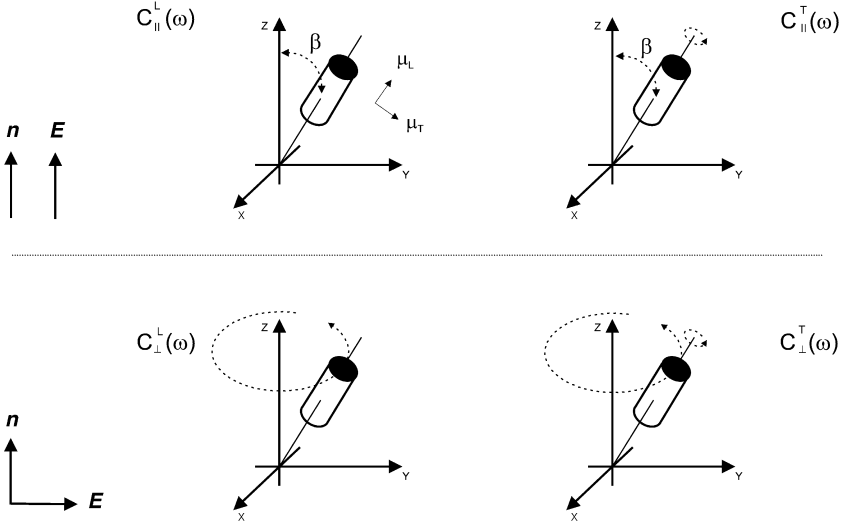
Fig. 10.3. Possible relaxation modes for a mesogenic unit in an uniaxial nematic phase depending on its orientation with regard to an outer electric field (redrawn from [6])

The extension to dynamical properties was initiated by the work of Nordio et al. [23] and continued by Attard et al. [24] and Araki et al. [25] who developed an approach without prior specification of the character of the motions involved. The starting point is the consideration that each mesogenic unit has two components of its molecular dipole vector longitudinal and transverse to its long axis μ_L and μ_T respectively. From a microscopic point of view the dielectric properties are determined by the correlation functions of the polarization fluctuations parallel and perpendicular to the nematic director. These can be expressed by four different molecular relaxation modes given by correlation functions of the longitudinal and transverse component of the molecular dipole vector projected parallel and perpendicular to the nematic director (see Fig. 10.3). In that semi-microscopic treatment the measured dielectric function parallel $\varepsilon_{\parallel}^*(\omega)$ and perpendicular $\varepsilon_{\perp}^*(\omega)$ to n comprises different weighted sums of the four underlying relaxation modes depending on the macroscopic orientation of the sample

$$\varepsilon_{\parallel}^*(\omega) = \varepsilon_{\infty,\parallel} + \frac{G}{3k_BT}\left[(1+2S)\mu_L^2 C_{\parallel}^L(\omega) + (1-S)\mu_T^2 C_{\parallel}^T(\omega)\right] \tag{10.3a}$$

$$\varepsilon_{\perp}^*(\omega) = \varepsilon_{\infty,\perp} + \frac{G}{3k_BT}\left[(1-S)\mu_L^2 C_{\perp}^L(\omega) + \left(1+\frac{S}{2}\right)\mu_T^2 C_{\perp}^T(\omega)\right] \tag{10.3b}$$

where $\varepsilon_{\infty,\parallel}$ and $\varepsilon_{\infty,\perp}$ are the limiting high frequency permittivities parallel and perpendicular to the local director n and G is a constant. $C_j^i(\omega)$ ($i = L, T; j = \parallel, \perp$) denote the one-sided Fourier transformations (see Chap. 1) of the correlation functions of the longitudinal and transverse component of μ projected parallel

and perpendicular to n. It could be shown that Eq. (10.3) can be derived by assuming small step rotational diffusion [26] but also without an assumption about the underlying motional process [27, 28]. Four different relaxation modes are predicted according to the four different correlation functions.

For the corresponding relaxation rates v_j^i holds:

$$v_{\parallel}^L < v_{\parallel}^T \leq v_{\perp}^T \leq v_{\perp}^L. \tag{10.4}$$

According to this approach, depending on the orientation of the sample with regard to the outer electrical field, different relaxations should be observed. If E is parallel to the director two modes are possible. The correlation function $C_{II}^L(\omega)$ involves fluctuations of μ_L around the short axis of the mesogenic unit and is also called δ-process. Using polar coordinates $C_{\parallel}^L(\omega)$ is expressed by

$$C_{\parallel}^L(\omega) = 1 - i\omega\, FT\left(\langle \cos(\beta(0) \cdot \cos(\beta(t)) \rangle \right) \tag{10.5}$$

where FT indicates the Fourier transform, β is the angle between the long axis of the molecule and the z-axis (see Fig. 10.3) and the brackets denote the ensemble average. $C_{\parallel}^T(\omega)$ is due to fluctuations of μ_T projected to the direction of E which can only be observed for $S < 1$ (see Eq. 10.3). In the opposite case if E is perpendicular to n, $C_{\parallel}^T(\omega)$ is connected with fluctuations of the longitudinal component of the dipole moment μ_L around the long axis of the mesogen and is observed only for $S < 1$. $C_{\perp}^T(\omega)$ involves reorientations around the short axis of the mesogenic unit. The complex dielectric function of an unaligned sample corresponds to the average

$$\bar{\varepsilon}^*(\omega) = \frac{1}{3}\left[\varepsilon_{\parallel}^*(\omega) + 2\varepsilon_{\perp}^*(\omega)\right] \tag{10.6}$$

For a partially aligned LC sample of uniaxial symmetry the complex dielectric function is given by [24]

$$\varepsilon^*(\omega) = \frac{1}{3}\left[(1+2S_D)\varepsilon_{\parallel}^*(\omega) + 2(1-S_D)\varepsilon_{\perp}^*(\omega)\right] \tag{10.7}$$

where S_D is the director order parameter which describes the average orientation of the director with respect to the measuring field direction. S_D is equal to 0 for an unaligned (see Eq. 10.6), sample and equal to 1 for homeotropic and to $-1/2$ for planar alignment.

For applications in display technology liquid crystals must be aligned. Hereby the exerted dielectric torque is proportional to $\delta\varepsilon$. Sometimes it is of advantage to apply an a.c. voltage in order to avoid a disturbance of the orientation due to polarization effects. Because of the frequency dependence of $\varepsilon_{\parallel}^*(\omega)$ and $\varepsilon_{\perp}^*(\omega)$ the kind of orientation (homeotropic or planar) depends on the applied frequency of the a.c. field. A positive dielectric material ($\delta\varepsilon > 0$) will be aligned homeotropically at low frequencies and planarly at high frequencies [5, 24, 25]. The kind of the electrically induced alignment changes at a certain critical frequency v_c which is similar to the isosbestic point well known in optical spec-

troscopy. It can be estimated from a diagram where ε' of a homeotropic, of a planar and of an unaligned sample is plotted vs frequency. At v_c all three ε' traces cross each other. Of course v_c depends on temperature. This is the principle of two frequency addressing [30].

10.4
Molecular Dynamics

10.4.1
Low Molecular Weight Systems

As suitable model systems alkyl-cyanobiphenyls, like heptyl-cyanobiphenyl (7CB), can be used having a dipole moment parallel to the long axis only. For an unaligned sample of 7CB in the nematic state two relaxation processes indicated by peaks in ε'' can be observed (Fig. 10.4, see also Fig. 10.5) which are assigned to the tensorial components of the complex dielectric function parallel and perpendicular to the director (see Eqs. 10.3 and 10.4). The process assigned parallel to the director corresponds to rotational fluctuations of the molecule around the short axis (δ-process, correlation function $C_\parallel^\dagger(\omega)$, see Fig. 10.3). Above the clearing temperature the two processes collapse into one broadened relaxation
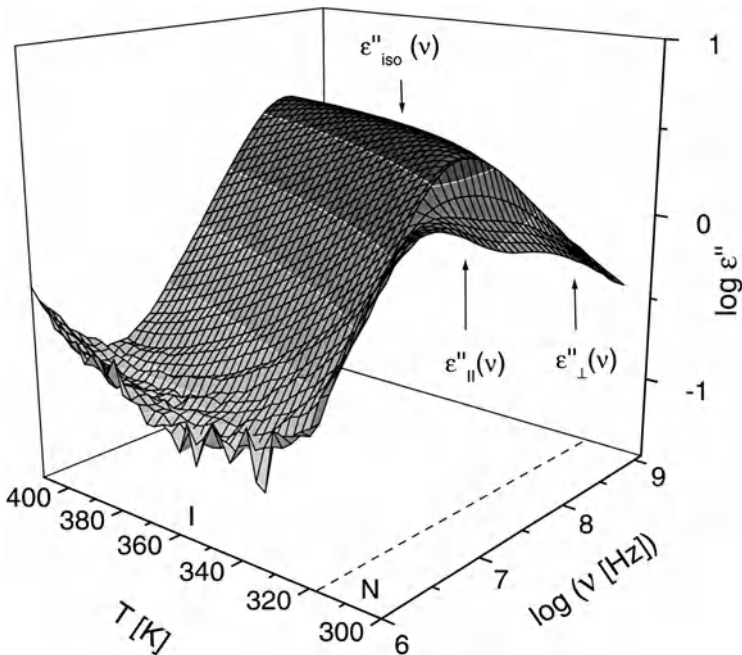
Fig. 10.4. Dielectric loss vs frequency and temperature for 7CB. The phase transition from the nematic to the isotropic phase takes place at $T = 317$ K
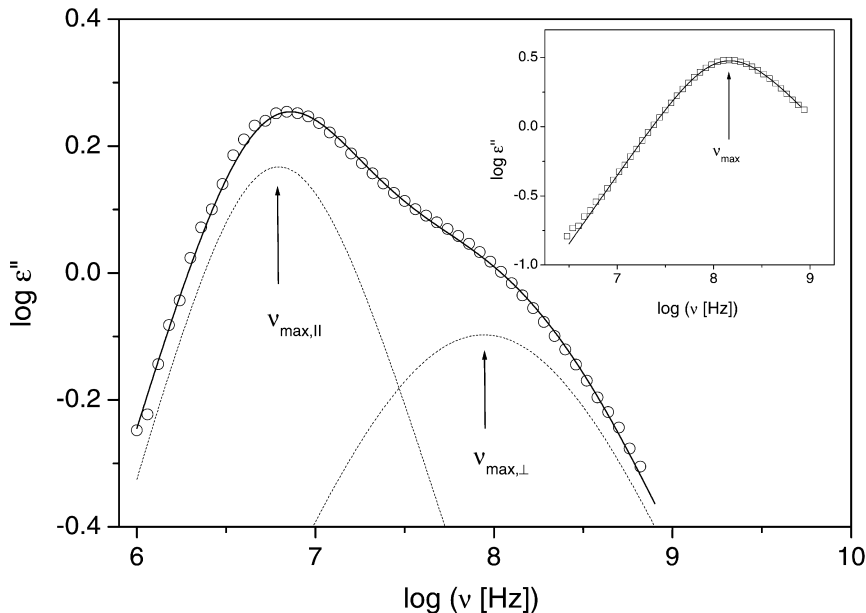
Fig. 10.5. Fit of two Havriliak/Negami (HN) model functions to the dielectric loss in the liquid crystalline state of 7CB at $T = 310.6$ K. $\varepsilon''_{\parallel}$ (*dotted line*): $\Delta\varepsilon = 7.5$, log (v_{HN} [Hz]) = 6.76, $\beta_{HN} = 1$, $\gamma_{HN} = 0.908$; $\varepsilon''_{\perp}$ (*dashed line*): $\Delta\varepsilon = 2.6$, log (v_{HN} [Hz]) = 7.94, $\beta_{HN} = 0.7$, $\gamma_{HN} = 0.7$. The *solid line* is the superposition of both fit functions. The *inset* shows the fit of one HN-function in the isotropic state of 7CB at $T = 360.3$ K. $\Delta\varepsilon = 6.855$, log ($v_{HN}$ [Hz]) = 8.075, $\beta_{HN} = 0.99$, $\gamma_{HN} = 0.766$

(Fig. 10.4 and inset Fig. 10.5). Additionally, a β-relaxation takes places in systems having a dipole component perpendicular to the long axis of mesogen assigned to librational fluctuation of the molecule around its long axis [29].

The relaxation rate at maximal loss (mean relaxation rate) v_{max} is extracted by fitting model functions of Havriliak/Negami [31] to the data which reads

$$\varepsilon^*_{HN}(v) = \varepsilon_\infty + \frac{\Delta\varepsilon}{(1+(iv/v_{HN})^{\beta_{HN}})^{\gamma_{HN}}}$$

(10.8)

where v_{HN} is a relaxation rate connected with the peak frequency v_{max}, β_{HN} and γ_{HN} are shape parameters ($0 < \beta_{HN}$, $\gamma_{HN}\beta_{HN} \leq 1$) due to the symmetric and asymmetric broadening of the loss peak and $\Delta\varepsilon$ is the relaxation strength (for details see Chap. 3.). Figure 10.5 shows an example for a fit in the nematic as well as in the isotropic state.

Figure 10.6 gives the temperature dependence of the relaxation rates v_{max} in the different states where data for aligned samples [3, 32] were also included. Both sets of data agree well with each other proving the assignment of the relaxation process for the unaligned sample.
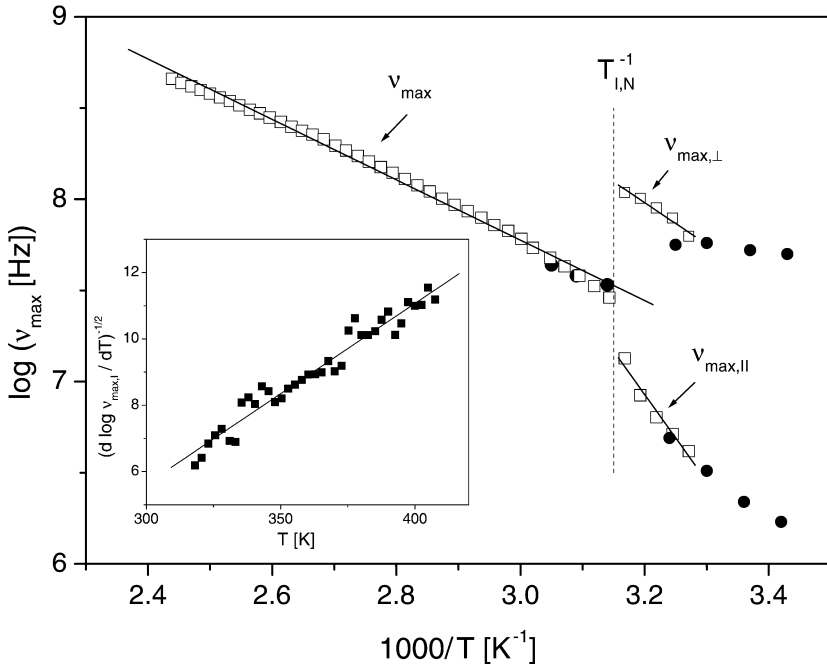
Fig. 10.6. Temperature dependence of the relaxation rates of 7CB. *Open symbols* are own measurements. The data for the *filled symbols* are taken from [32]. The *lines* are fits of the Arrhenius equation to the data. The *inset* shows $(\mathrm{d}\log \nu_{max}/\mathrm{d}T)^{(-1/2)}$ vs T for the isotropic state. The *line* is a linear regression to the data

The Arrhenius equation

$$\nu_{max} = \nu_\infty \exp\left[-\frac{E_A}{k_B T}\right] \tag{10.9}$$

where E_A is activation energy and ν_∞ is a prefactor, can be used to describe the temperature dependence of the relaxation rates (see Fig. 10.6 and Table 10.1). The activation energy estimated for the δ-process is high because of the nematic potential. The shape of the relaxation function is nearly Debye-like (see also [33]) as predicted by theory. The activation energy for $\varepsilon^L_\perp(\omega)$ is lower related to molecular fluctuations of the long axis of the molecule inside the nematic po-

Table 10.1. Activation parameter for the different processes observed for 7CB

	$\log(\nu_\infty \text{ [Hz]})$	$E_A \text{ [kJ mol}^{-1}\text{]}$
Parallel	22.2	91.1
Perpendicular	15.3	43.8
Isotrop	12.7	31.7

tential (correlation function $C_\perp^L(\omega)$). The shape of the relaxation function is broadened indicating a distribution of relaxation times.

A more detailed analysis of the temperature dependence of the relaxation rate in the isotropic state $v_{\mathrm{max,I}}$ by the derivative technique (see Chap. 4) shows that the data can be better described by the Vogel/Fulcher/Tammann/Hesse (VFT) [34–36] equation (see inset of Fig. 10.6):

$$\log v_{\mathrm{max}} = \log v_\infty - \frac{A}{T - T_0}$$

$$\left[\frac{\mathrm{d}\log v_{\mathrm{max}}}{\mathrm{d}T}\right]^{-1/2} = A^{-1/2}(T - T_0) \tag{10.10}$$

where v_∞ and A are constants and T_0 is the Vogel temperature.

Deviations from the Arrhenius-like dependence of the relaxation rate in the temperature range of mesophases were first reported by Zeller for pentyl-cyanaobiphenyl (5CB) [37] and later also found for other nematic and smectic liquid crystals [38]. Based on the free volume concept Diogo and Martins [39] derived for $v_{\mathrm{max,\parallel}}$

$$\log v_{\mathrm{max,\parallel}} = \log v_\infty - \frac{\tilde{A}S^2}{T - T_0} \tag{10.11}$$

where $\tilde{A}$ is a proportionality constant. Equation (10.11) describes the temperature dependence of dielectric relaxation rates [38] as well as of viscosity coefficients [39] for different systems. A temperature dependence according to Eq. (10.10) or (10.11) is in general characteristic for glass forming systems [40, 41] (for details see Chaps. 4 and 5).

Generally the relaxation rates $v_{\mathrm{max,\parallel}}$ and $v_{\mathrm{max,\perp}}$ in the liquid crystalline state can be related to that in the corresponding extrapolated isotropic phase $v_{\mathrm{max,I}}$ by reduction factors $\gamma_\parallel(S)$ and $\gamma_\perp(S)$:

$$v_{\mathrm{max,\parallel}} = \gamma_\parallel(S)v_{\mathrm{max,I}} ; v_{\mathrm{max,\perp}} = \gamma_\perp(S)v_{\mathrm{max,I}} \tag{10.12}$$

In principle the dependence of the reduction parameters on the order parameter S can be calculated in the frame of the Maier/Saupe theory [19–22] where some approximate relationships are given in [42–44]. For instance, Eq. (10.12) is used to calculate the order parameter from dielectric measurements which agrees well with theoretical predictions [32, 45]. Strobl and coworker developed a method to measure the rotational viscosity of both molecular LCs [33, 46] and liquid crystalline polymers [42, 47] by application of dielectric relaxation spectroscopy.

10.4.2
Polymeric Systems

10.4.2.1
Side Chain Polymers

Dielectric spectroscopy on liquid crystalline side chain polymers (SCLCP) was pioneered by Kresse and coworkers (see for instance [48–52]), followed by the work of Haase et al. [53, 54] and by extensive studies of the group around Williams (see for instance [5] and the references quoted therein). Zentel et al. [55] developed a nomenclature for dielectric relaxation processes of SCLCP. Several recent reviews are also available [3–6, 56].

In SCLCP the mesogens are decoupled from the main chain by a spacer, which is usually made out of aliphatic segments. The molecular dynamics in these systems is the result of a complicated interplay between the polymer backbone which forms a glassy melt and the liquid crystalline moieties in their different mesophases. In Fig. 10.7a SCLCP based on a poly(methacrylate)/poly(arylate) main chain is sketched. (For details of the synthesis and the characterization see [57–60].) Already small variations in the residues R_1 to R_4 and/or in the number of aliphatic units have a strong impact (Tables 10.2 and 10.3) on the thermodynamics of the system as manifested in the existence of mesophases or its sequence.

The overall molecular dynamics (Fig. 10.8) is characterized by three relaxation processes, the high-frequency β-, the α- and the δ-relaxation. In the following these processes will be discussed in detail[2] for a set SCLCP based on a poly(methacrylate)/poly(acrylate) main chain.

β-Relaxation. The β-relaxation[3] corresponds to librational fluctuations of the mesogen around the long molecular axis as proven by a manifold of dielectric [3, 6, 16, 55, 61], NMR [62] and combined dielectric/NMR [63] studies. The temperature dependence of its relaxation rate $\nu_{max,\parallel}^{(\beta)}$ is Arrhenius-like (see Eq. (10.9), Fig. 10.9). Details of the structure of the mesogenic group (compare the values for the samples P4 and P5) or of the main chain have a weak influence only on its librational dynamics (Table 10.2). Analysing the activation energy $E_A^{(\beta)}$ and the prefactor $\nu_\infty^{(\beta)}$ of the Arrhenius equation delivers only for the non liquid crystalline polymer P1 values which are in accord with the interpretation of a single fluctuating mesogen in a potential formed by its neighbours. For the systems with mesophases for both $E_A^{(\beta)}$ and $\nu_\infty^{(\beta)}$ extraordinary high values are obtained which increase sensitively with the order of the mesophase in which it

---

[2] In addition to these, other processes like a γ-relaxation related to rotational fluctuations of the tail or terminal groups can be observed depending on the system under investigation. For more details see [6].

[3] This well defined β-relaxation should not be interchanged with the general nomenclature in amorphous systems where "β-relaxation" simply means some secondary relaxation (see Chaps. 4, 5 and 7).
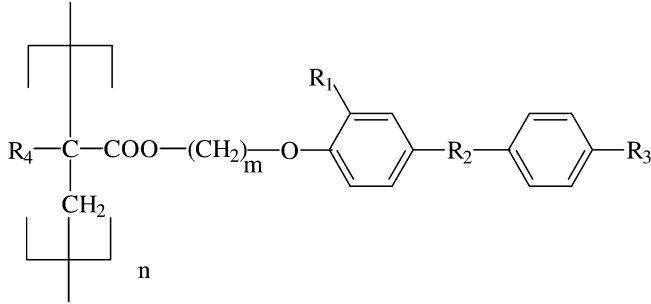
Fig. 10.7. Molecular structure of the liquid crystalline poly(methacrylate)s/poly(acrylate)s The definition of the R_1 groups is given in Tables 10.2 and 10.3
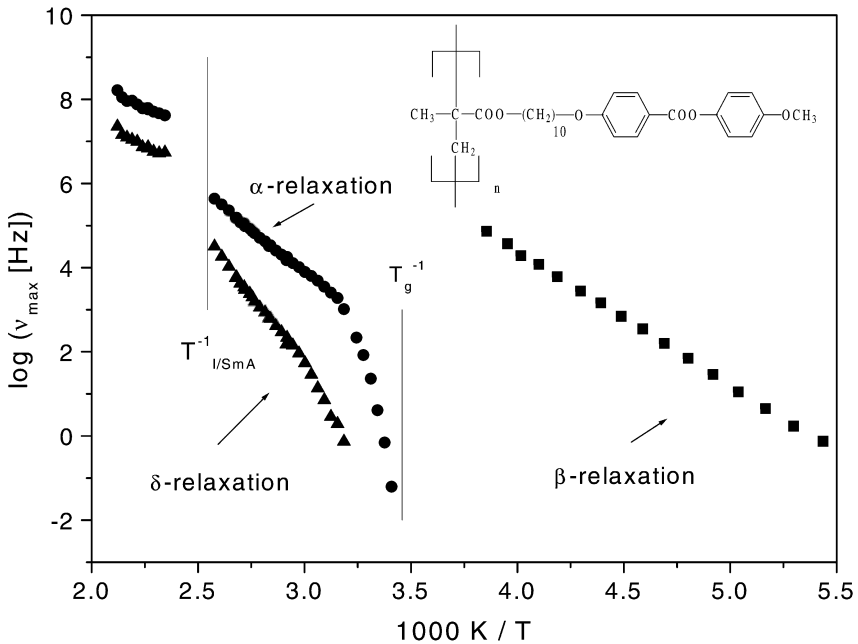
Fig. 10.8. Relaxation rates of the different processes vs reciprocal temperature for the sample P13 (see Fig. 10.7 and Table 10.2): (*filled squares*) β-, (*filled circles*) α- and (*filled triangles*) δ-relaxation

is measured (Fig. 10.10) indicating that the picture of a single mesogen librating in the potential formed by its surrounding molecules cannot be correct. Instead it is suggested that neighbouring molecules are involved as well in the librational dynamics of the β-relaxation [58, 59, 64]. This interpretation is also supported by the finding that with increasing spacer length $E_A^{(\beta)}$ and $\nu_\infty^{(\beta)}$ increase (inset A of Fig 10.10) [60] because of the better formation of smectic phases in the system (see Table 10.3). The increase of $\nu_\infty^{(\beta)}$ with decreasing mean lateral distance

Table 10.2. Structure, phase transition temperatures and activation parameters of the β-relaxation of the studied polymers having phenyl benzoate as mesogenic unit: I, N, SmX means the isotropic, the nematic and the smectic state ($X = A, B, C$). The at the glass transition temperature frozen in phase is indicated in bold

	R_1	R_2	R_3	R_4	m	T_g [K]	$T_{\text{Phase Transitions}}$ [K]	$\log(\nu_\infty^{(\beta)}$ [Hz])	$E_A^{(\beta)}$ [kJ mol^{-1}]
P1	G^1	COO	OCH$_3$	CH$_3$	6	322	**I**	12.8	45.7
P2	H	COO	OCH$_3$	CH$_3$	4	318	**N/I** 377	13.8	46.5
P3	H	COO	OCH$_3$	H	2	343	**N/I** 390	14.8	53.3
P4	H	COO	OCH$_3$	CH$_3$	6	314	**SmA/N** 345 N/I 383	16.5	57.5
P5	H	OOC	OCH$_3$	CH$_3$	6	311	**SmA/I** 370	16.4	56.4
P6	H	COO	OC$_4$H$_9$	CH$_3$	6	315	**SmA/N** 380 N/I 384	17.1	61.0
P7	H	COO	OCH$_3$	H	6	297	**SmA/N** 367 N/I 394	17.5	62.8
P8	H	OOC	OC$_4$H$_9$	CH$_3$	10	304	**SmB/SmA** 318 SmA/I 394	18.2	63.2
P9	H	OOC	OC$_6$H$_{13}$	CH$_3$	6	295	***SmA/SmC*** 349 SmC/SmA 358 SmA/I 401	18.5	64.9
P10	H	OOC	OC$_6$H$_{13}$	CH$_3$	10	296	**SmB/SmC** 320 SmC/SmA 330 SmA/I 399	19.4	68.9
P11	Br	COO	OCH$_3$	CH$_3$	6	323	**I**	–	–
P12	H	COO	OCH$_3$	CH$_3$	8	307	**SmA/N** 283 N/I 390	–	–
P13	H	COO	OCH$_3$	CH$_3$	10	289	**SmA/I** 395	16.5	55.3
P14	H	COO	OCH$_3$	CH$_3$	2	343	**N/I** 390	–	–

^{1} G-represents a OCH$_3$ group. Note that the molar masses are sufficient high and comparable for all samples.

Table 10.3. Structure, phase transition temperatures and activation parameters of the β-relaxation of the studied polymers having azobenzene as mesogenic unit: I, N, SmX means the isotropic, the nematic and the smectic state $(X = A, B, C)$. The phase which is frozen in at the glass transition temperature is indicated in bold

	R_1	R_2	R_3	R_4	m	T_g [K]	$T_{\text{Phase Transitions}}$ [K]		$\log(\nu_\infty^{(\beta)}$ [Hz])	$E_A^{(\beta)}$ [kJ mol^{-1}]
A_1	H	N=N	OCH$_3$	CH$_3$	6	343	**SmA**/N	365	18.2	66.8
							N/I	405		
A_2	H	N=N	OCF$_3$	CH$_3$	2	346	**SmA**/I	417	13.6	41.6
A_3	H	N=N	OCF$_3$	CH$_3$	3	348	**SmA**/I	395	15.7	51.0
A_4	H	N=N	OCF$_3$	CH$_3$	4	340	**SmA**/N	369	17.9	58.9
							N/I	387		
A_5	H	N=N	OCF$_3$	CH$_3$	5	339	**N**/SmA	395	17.5	57.9
							SmA/I	405		
A_6	H	N=N	OCF$_3$	CH$_3$	6	331	**N**/SmA	363	16.8	56.0
							SmA/I	382		

Note that the molar masses are sufficient high and comparable for all samples.
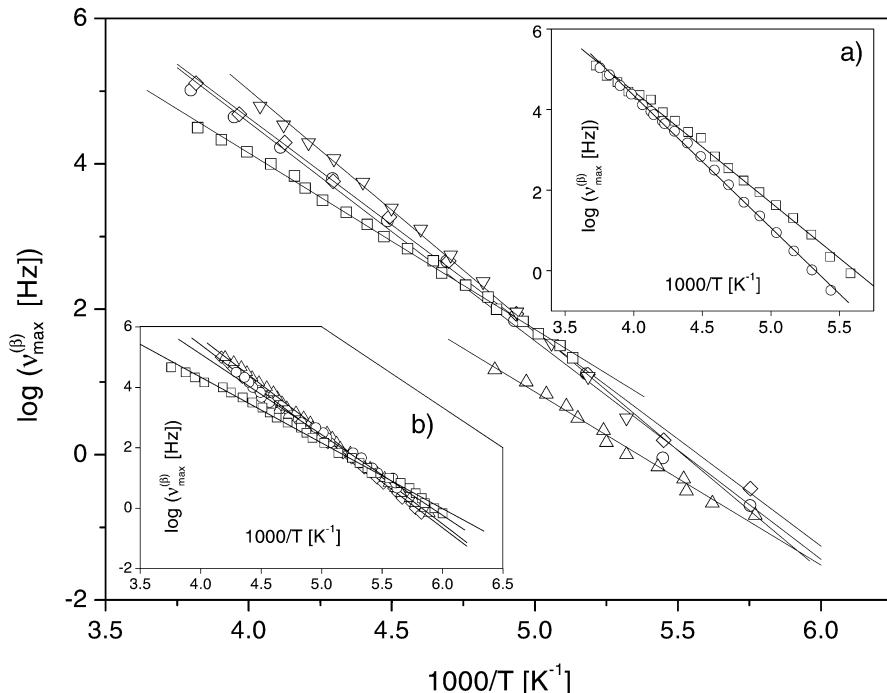
Fig. 10.9. Arrhenius diagram for the β-relaxation for different poly(methacrylate) samples given in Fig. 10.7 and Tables 10.2 and 10.3: (*open triangles*)-P1; (*open squares*)-P2; (*open circles*)-P4; (*open diamonds*)-P5; (*open inverted triangles*)-P8. The inset *a* shows data for the poly(acrylate)s: (*open squares*)-P3; (*open circles*)-P7. The inset *b* shows data for samples having azobenzene in the side group: (*open squares*)-A2; (*open circles*)-A3; (*open triangles*)-A4; (*open diamonds*)-A5. *Lines* are fits of the Arrhenius equation to the data. The fit parameters are given in Tables 10.2 and 10.3. (Reproduced from [56] with permission)

of the mesogens d extracted from X-ray measurements supports this conclusion as well (inset b in Fig. 10.10).

α-Relaxation. The α-relaxation[4] is assigned to fluctuations of segments of the polymer main chain between structural substates as they are observed in glass forming systems (see Chaps. 4 and 5). Its relaxation rate $v_{max}^{(\alpha)}$ shows a temperature dependence according to the VFT-equation (Eq. 10.10). For the polymers P1 and P11 which do not form mesophases (Table 10.2) the VFT-temperature dependence is observed as expected for an isotropic melt (Fig. 10.11). For the similar sample P4 having a nematic and a smectic A phase the relaxation rate is identical in the isotropic state to $v_{max}^{(\alpha)}$ of the polymers P1/P11 but it becomes

---

[4] In this chapter only the peculiarities for the samples having phenylbenzoate in the side group is discussed. A detailed discussion of the samples having fluorinated azobenzene in the side group can be found elsewhere [60].
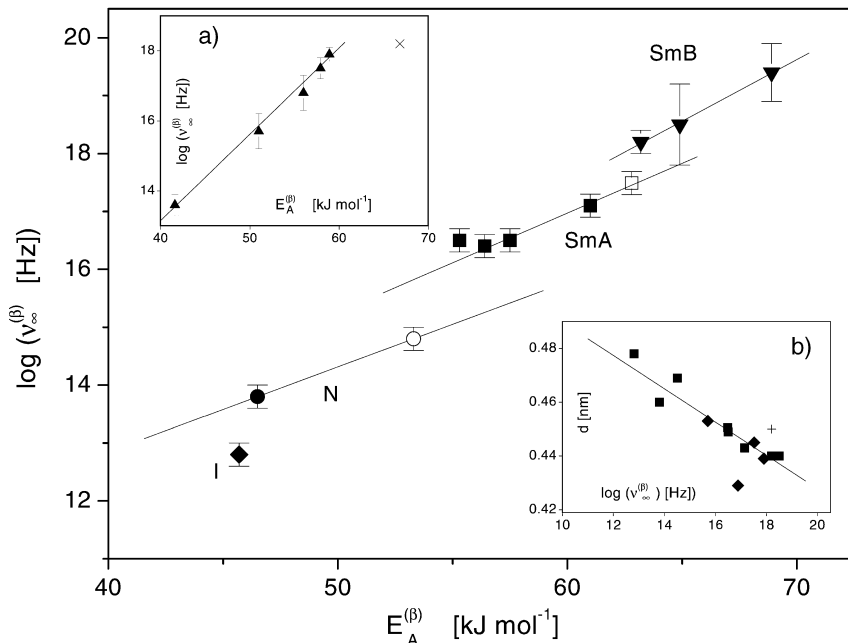
Fig. 10.10. Prefactor $\log \nu_\infty^{(\beta)}$ vs activation energy $E_A^{(\beta)}$ for the different samples: (*filled diamonds*) isotropic state; (*open circles, filled circles*)-nematic phase; (*open squares, filled squares*)-smectic A phase; (*filled inverted triangles*)-smectic B phase. *Solid symbols* – poly(methacrylate)s; *open symbols* – poly(acrylate)s. *Inset a*: data for poly(methacrylate)s having azobenzene in the side group: (*multiplication sign*) A1; (*filled triangles*) A2-A6. The *lines* are linear regressions through the data. *Inset b*: lateral distance of the mesogenic units d vs prefactor $\nu_\infty^{(\beta)}$: (*filled squares*) poly(methacrylate)s having phenylbenzoate in the side group; (*filled diamonds*) poly(methacrylate)s having fluorinated azobenzene in the side group; (*plus sign*) sample A1 (see Table 10.3). The *solid line* is a linear regression through all data points

higher in the temperature range of the mesophases. This is explained by the microphase separation between the mesogens and the polymer backbone which takes place at the phase transition [65]. Thereby the local concentration of stiff moieties in the neighbourhood of the main chain segments is strongly reduced resulting in an increased segmental mobility and hence in a decrease of T_g. (Fig. 10.11) [57]. The possibility of an additional confinement effect (see Chap. 6) cannot be excluded.

With increasing spacer length m the dynamic glass transition of the polymer chain becomes faster (Fig. 10.12). This results in a pronounced decrease of T_g because the segregation of the mesogenic units into the liquid crystalline structures increases with *m* and enhances the internal plasticizer effect of the aliphatic spacer groups on the comparably stiff poly(methacrylate) chain.

For a detailed analysis of the temperature dependence of $\nu_{max}^{(\alpha)}$ derivative plots are employed [66] (see Chap. 4). As exemplified for sample P2 and P13 at high temperatures $\nu_{max}^{(\alpha)}$ follows an Arrhenius equation (Fig. 10.13a) which turns into
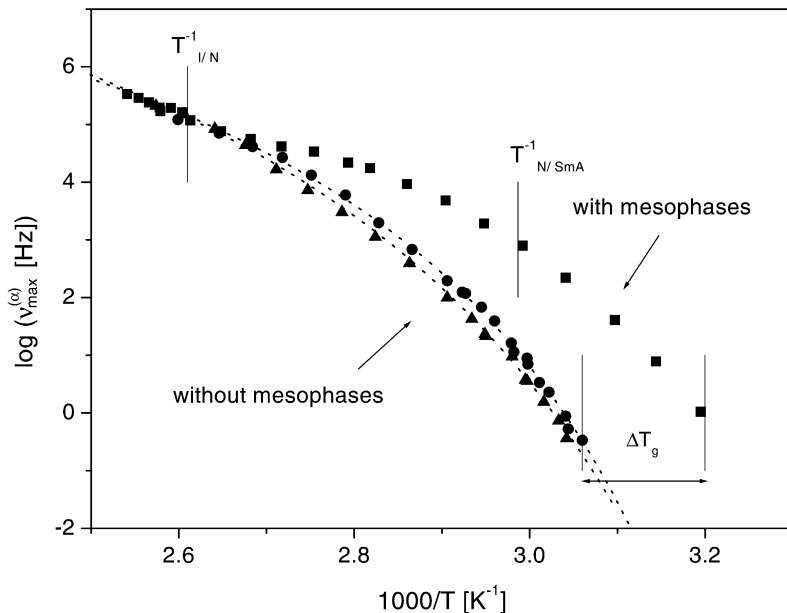
Fig. 10.11. $\log \nu_{max}^{(\alpha)}$ vs inverse temperature T^{-1}: (*filled squares*) sample P4 (liquid crystalline); (*filled circles*) sample P1, (*filled triangles*) sample P11 (polymeric melt without mesophases). The *dotted lines* are fits of the VFT-equation to the data. (Reproduced from [56] with permission)
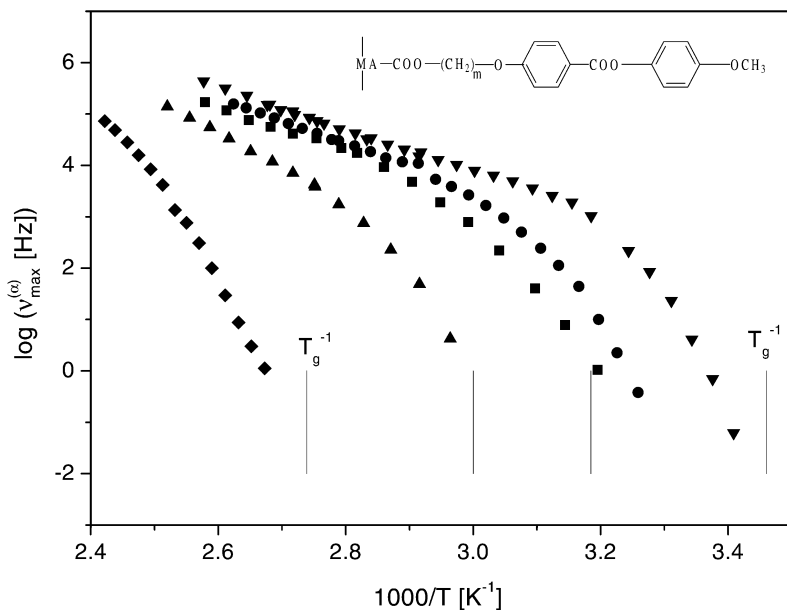
Fig. 10.12. $\log \nu_{max}^{(\alpha)}$ vs T^{-1} for different poly(methacrylate)s having a similar mesogenic core but different spacer length:(*filled diamonds*) P14 (*m* = 2); (*filled triangles*) P2 (*m* = 4); (*filled squares*) P4 (*m* = 6); (*filled circles*) P12 (m = 8); (*filled inverted triangles*) P13 (*m* = 10). *Lines* indicate T_g as estimated by DSC. (Reproduced from [56] with permission)
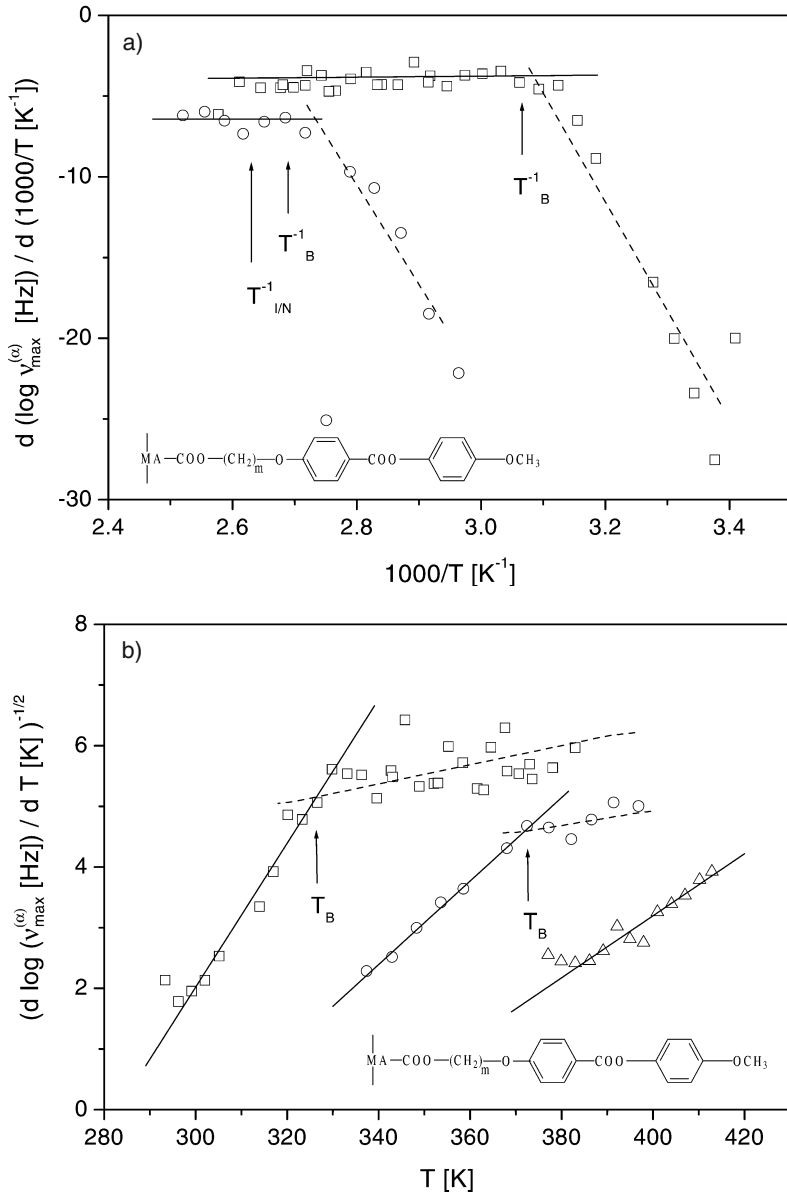
Fig. 10.13. a $d(\log v_{max}^{(\alpha)})/d(T^{-1})$ vs $1/T$ for the polymers P2 (*open circles*) and P13 (*open squares*). The *solid lines* are the average values in the high temperature range while the *dashed lines* are a guide for the eyes. The intersection of both lines defines a characteristic temperature T_B. Due to the derivation procedure the data show a large scatter. Reproduced from [67] with permission. **b** $\left[\dfrac{d\log v_{max}^{(\alpha)}}{dT}\right]^{-1/2}$ vs temperature for the liquid crystalline polymers: (*open triangles*) $m = 2$ (P14), (*open circles*) – $m = 4$ (P2), (*open squares*) $m = 10$ (P13). The *solid lines* are linear fits to the low temperature data where *dashed lines* are fits to the Arrhenius equation
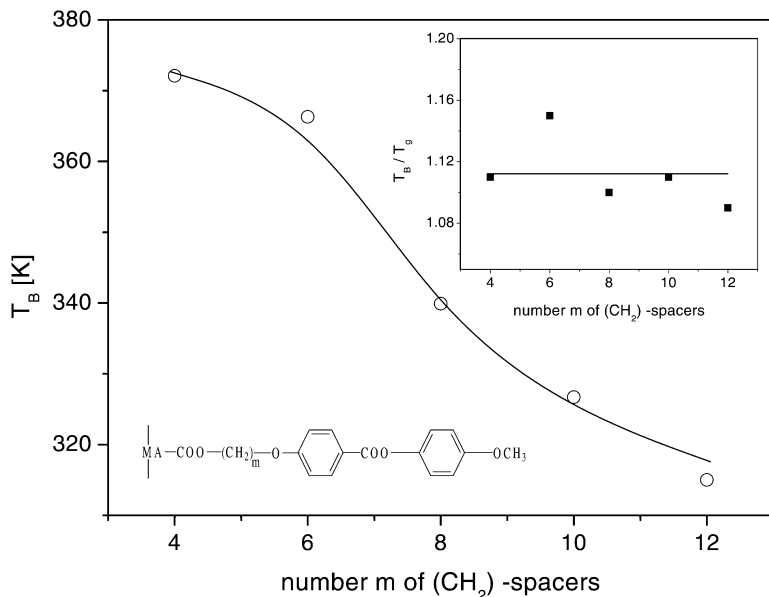
Fig. 10.14. Crossover temperature T_B vs number m of (CH$_2$) spacers. The *line* is a guide for the eyes. The *inset* shows the ratio T_B/T_g vs number m of (CH$_2$) spacers. The *line* is the mean value of all data

a VFT-like dependence (Fig.10.13b) at a temperature T_B. That indicates a change in the molecular dynamics of the system.

The temperature T_B decreases with increasing spacer length (Fig. 10.14). In no case does T_B agree with a phase transition temperature of the system while the ratio T_B/T_g is constant for all polymers in the homologous series (inset Fig. 10.14). As for conventional glass forming systems this temperature T_B might be interpreted as the temperature at which cooperative fluctuations start to develop (Chap. 4). Some further discussion can be found in [67].

The Vogel temperature T_0 obtained from the dielectric data (Fig. 10.13b) correlates well with the glass transition temperature measured by calorimetric methods (Fig. 10.15). This and the fact that the latter depends in a similar way on the number of aliphatic spacers for non-LC poly(n-alkyl methacrylate) and for the corresponding SCLCP (see inset of Fig. 10.15) is a further prove for a similar glassy dynamics related to segmental motions in both systems [67].

The dielectric strength $\Delta\varepsilon^{(\alpha)}$ of the α-relaxation shows (Fig. 10.16) a temperature dependence which is characteristic for the dynamic glass transition (see Chaps. 4 and 7, [68]) with no discontinuity at the phase transition [73]. In contrast the δ-relaxation behaves completely different (see. inset of Fig. 10.16): $\Delta\varepsilon^{(\delta)}$ is constant in the isotropic phase but decreases to zero with decreasing temperature in the nematic phase.

Temperature modulated differential scanning calorimetry (TMDSC) allows one – unlike dielectric spectroscopy – to sense entropy fluctuations in their frequency dependence. In this method a periodically modulated (with frequency ν)
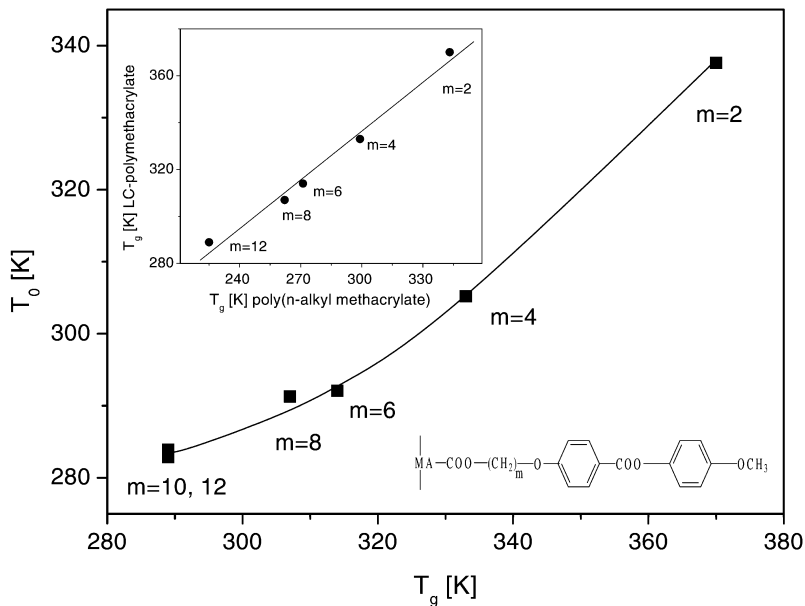
Fig. 10.15. The Vogel temperature T_0 estimated from dielectric measurements vs glass transition temperature T_g from calorimetric experiments. The *line* is a guide for the eyes. The *inset* shows T_g of the liquid crystalline poly(methacrylate)s vs T_g of the poly(*n*-alkyl methacrylate)s. The *solid line* is the linear regression through all data points
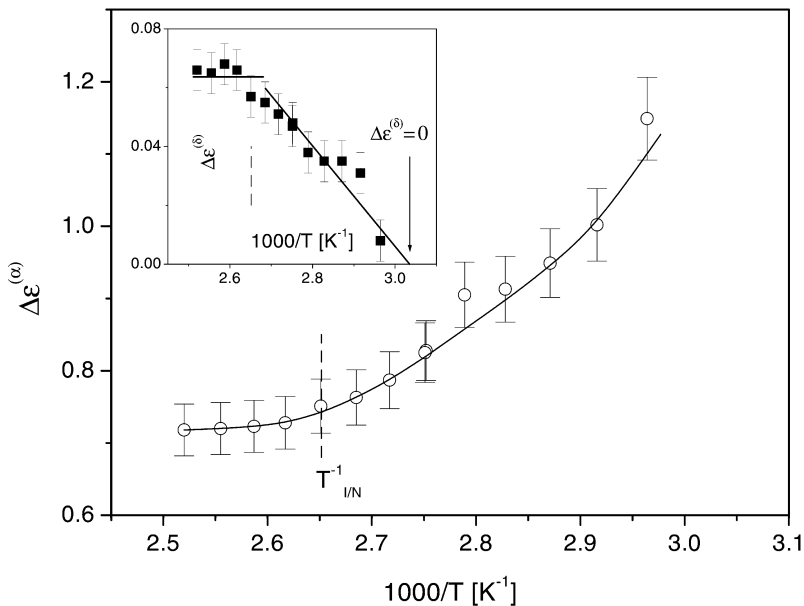
Fig. 10.16. $\Delta\varepsilon^{(\alpha)}$ vs inverse temperature for the sample P2. The *line* is a guide for the eyes. The *dashed line* indicates the phase transition temperature. The *inset* gives $\Delta\varepsilon^{(\delta)}$ vs inverse temperature. Reproduced from [69] with permission
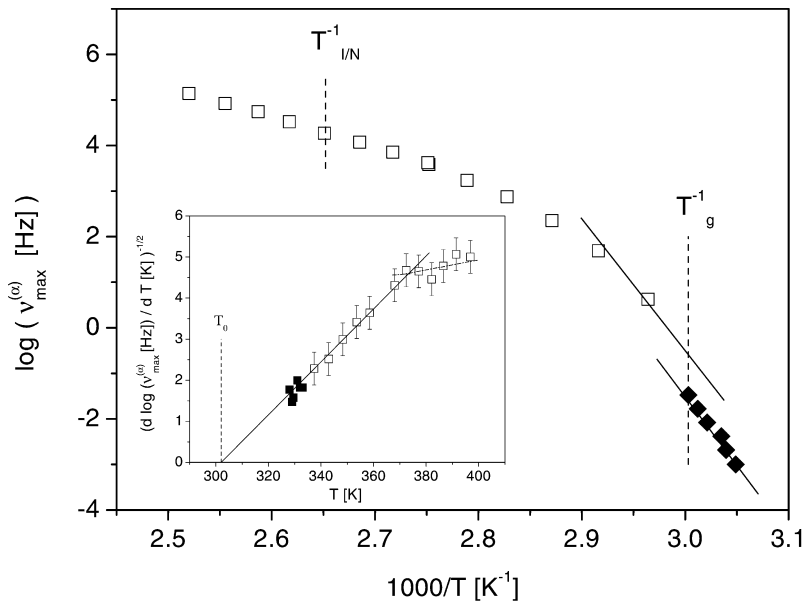
Fig. 10.17. $\log v_{max}^{(\alpha)}$ vs inverse temperature for the sample P2: (*open squares*) dielectric α-relaxation; (*filled squares*) dynamic glass transition measured by TMDSC taken from the maximum value of tan δ_{DSC} vs temperature for different frequencies. *Lines* are guides for the eyes. *Inset* $[d \log v_{max}^{(\alpha)}/dT]^{-1/2}$ vs temperature: (*open squares*) dielectric α-relaxation; (*filled squares*) dynamic glass transition measured by TMDSC. The *solid line* is a linear fit to the low temperature dielectric data. The *dashed dotted line* is a fit according to the Arrhenius equation. The *dashed line* indicates the Vogel temperature T_0

temperature is added to a linear cooling or heating ramp and the resulting response, the complex heat capacity $C_p^*(v) = C_p'(v) - iC_p''(v)$, is measured. The comparison[5] with the dielectric α-relaxation shows that both methods measure the same process [69] (Fig. 10.17). Derivative plots allow again a more detailed analysis of the dynamics. The thermal and dielectric data obey a VFT law with the same Vogel temperature (inset Fig. 10.17).

δ-Relaxation. The δ-relaxation is assigned – similar to that in low molecular weight LCs – to librational fluctuations of the mesogen around the short molecular axis. Presumably it is rather a multistep process with motional averaging [70] rather than a 180° flip-flop jump of the mesogen.

The temperature dependence of its relaxation rate $v_{max}^{(\delta)}$ (Fig. 10.18) shows some resemblance to that of the α-relaxation[6] in the shift with increasing spacer

---

[5] Both quantities can be compared because they are both generalized compliances (see Chap. 1).

[6] In the literature it was argued sometimes that the temperature dependence of the relaxation rate of the δ-relaxation seems to be Arrhenius-like (for an overview see [3]). At least the estimated activation energies must be regarded as apparent ones.
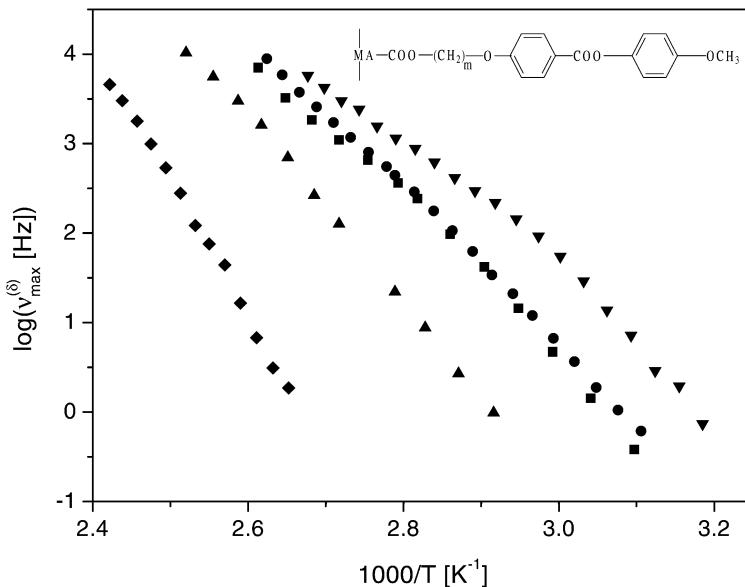
Fig. 10.18. $\log \nu_{max}^{(\delta)}$ vs T^{-1} for different poly(methacrylate)s having a similar mesogenic core but different spacer length: (*filled diamonds*) P14 ($m = 2$); (*filled triangles*) P2 ($m = 4$); (*filled squares*) P4 ($m = 6$); (*filled circles*) P12 ($m = 8$); (*filled inverted triangles*) P13 ($m = 10$)

length (compare Figs. 10.12 and 10.18) but it can be described neither by an Arrhenius-nor by a VFT-law (compare as well Fig. 10.8).

As a process originating from fluctuations of the mesogen and depending on the microviscosity of its surrounding molecules, the δ-relaxation reflects the interplay between mesogens and the polymer chain. In order to analyse this in more detail a comparison of the $\dfrac{\nu_{max}^{(\alpha)}}{\nu_{max}^{(\delta)}}$ vs T for the non-LC polymers P1 and P11 and the LC polymer P4 is instructive (Fig. 10.19). While the former are nearly independent on temperature the latter strongly changes with temperature showing a discontinuity at the phase transition *N/I* (Fig. 10.19). This is related to an increase of order with decreasing temperature [67]. From the ratio $\dfrac{\nu_{max}^{(\alpha)}}{\nu_{max}^{(\delta)}}$ (T) the molecular order parameter can be calculated using a modified Maier/Saupe theory [57]. Good agreement with NMR-measurements [71] is obtained (Fig. 10.20).

Polysiloxanes (Fig. 10.21a)[7] form a class of SCLCPs which has – due to the high flexibility of the main chain – lower glass transition temperatures compared to poly(methacrylate)s/poly(acrylate)s. In principle the dynamics is comparable, thus a β-, an α- and a δ-relaxation have to be expected. The α-relaxation scales with the glass transition T_g and also with the relaxation rates of entropy fluctuations [72]. At the phase transition SmC/I it shows no discontinuity in con-

---

[7] The material is obtained from Merck, catalogue no LC1
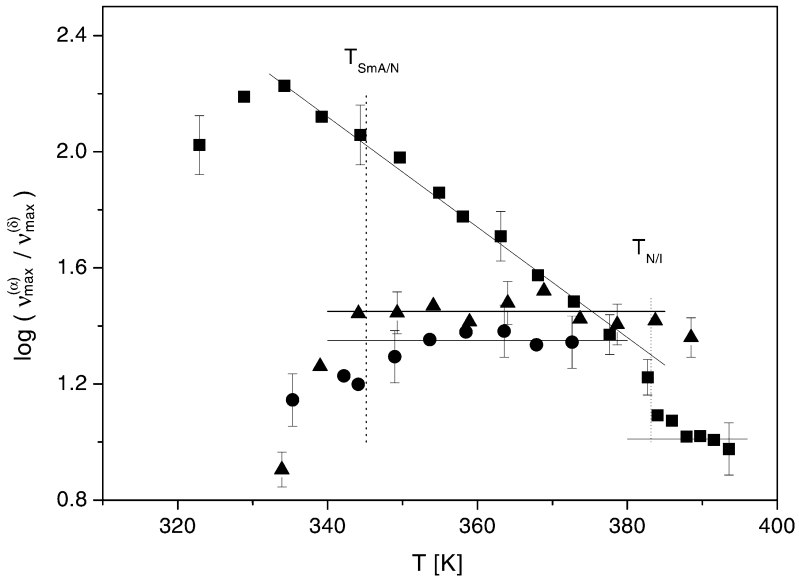
Fig. 10.19. $\log(\nu_{max}^{(\alpha)}/\nu_{max}^{(\delta)})$ temperature for amorphous polymers P1 (*filled circles*) and P11 (*filled triangles*) as well as for the liquid crystalline sample P4 (*filled squares*). *Solid lines* are guides for the eyes. The *dashed lines* indicate the phase transition temperatures
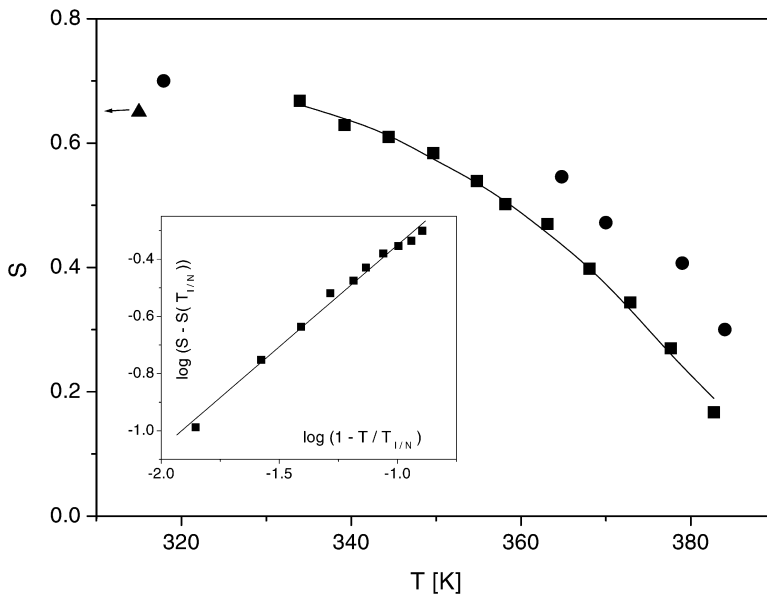
Fig. 10.20. Temperature dependence of the order parameter *S* for polymer P11 (*filled squares*) estimated from the temperature dependence of $\nu_{max}^{(\alpha)}/\nu_{max}^{(\delta)}$, (*filled circles*) estimated from NMR measurements [71], (*filled triangles*) estimated from NMR measurements in the glassy state. The *line* is a guide to the eyes. The *inset* shows the power law dependence of S near the phase transition. Reproduced from [57] with permission
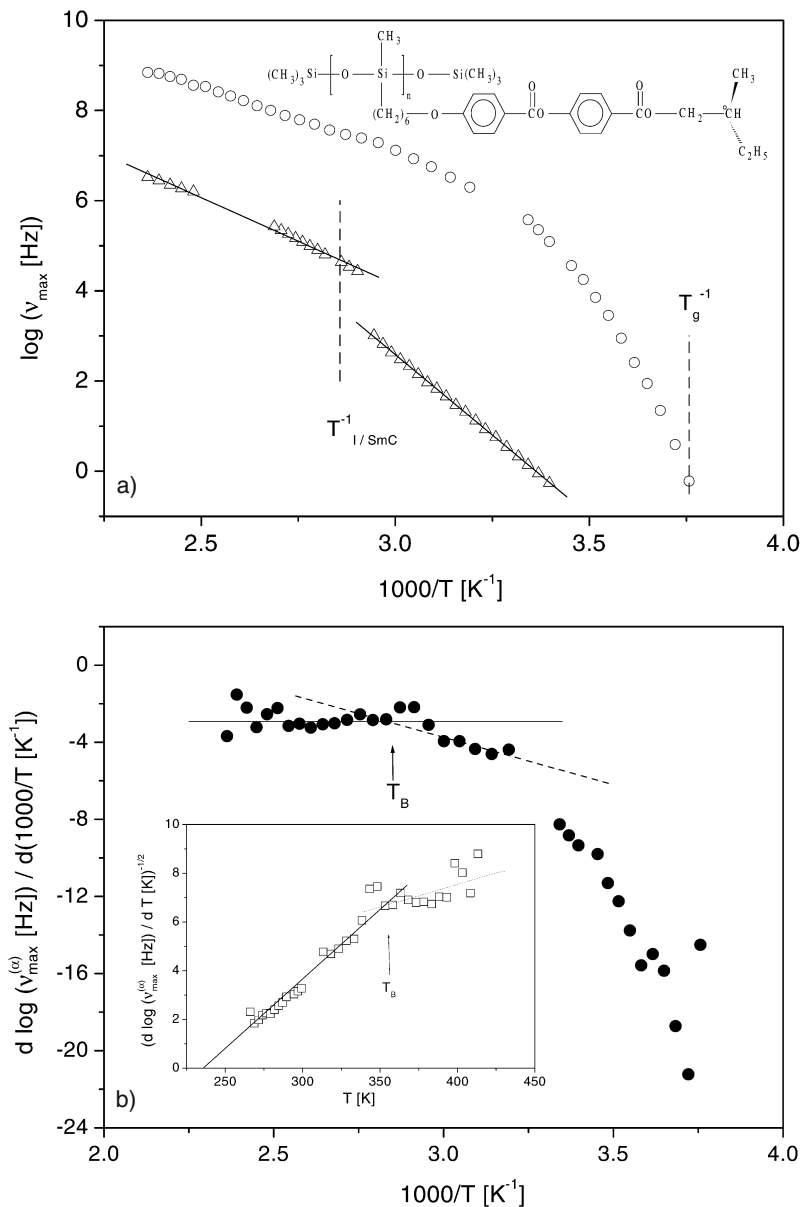
Fig. 10.21. **a** log ν_{max} vs inverse temperature for the α- (*open circles*) and for the δ- (*open triangles*) process of the liquid crystalline polysiloxane LCP1. $T_g = 266$ K; $T_{SmC/I} = 350$ K. These temperatures are indicated by *dashed lines*. The *solid lines* are fits of the Arrhenius equation to the data of the δ-process. **b** d$(\log(\nu_{max}^{(\alpha)})/\mathrm{d}(1/T)$ vs inverse temperature for the liquid crystalline polysiloxane LCP1. The *lines* are guides for the eyes. The *inset* shows $\left[\dfrac{\mathrm{d}\log\nu_{max}^{(\alpha)}}{\mathrm{d}T}\right]^{-1/2}$ vs temperature. The *solid line* is a linear fit to the low temperature branch of the data. The *dashed line* is a guide for the eyes
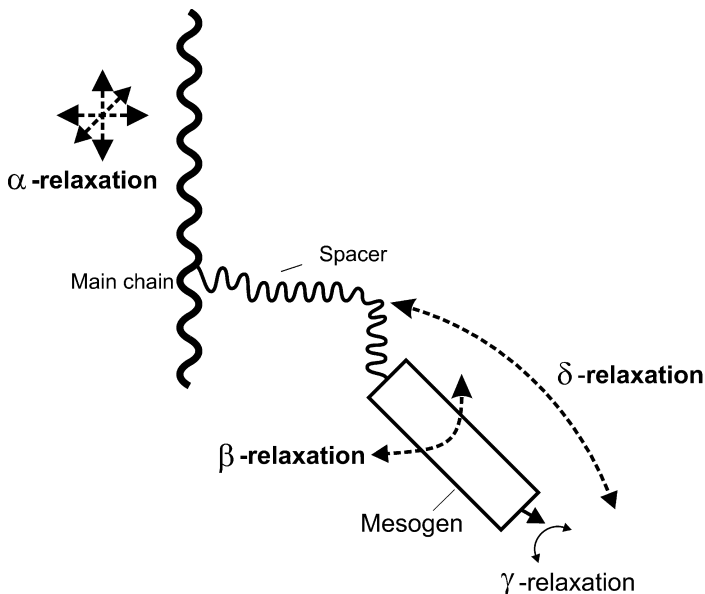
Fig. 10.22. Scheme of liquid crystalline side chain polymers. Possible dielectric relaxation processes are indicated by *arrows*

trast to the δ-relaxation which has an Arrhenius-like temperature dependence with an activation energy of 88 kJ mol^{-1} in the isotropic and 136.7 kJ mol^{-1} in the SmC phase. The temperature dependence of the α-relaxation can be analysed in more detail by the derivative technique. Clear indications for an Arrhenius-dependence at high temperatures and a VFT-dependence below a transition temperature T_B are found (Fig. 10.21b). So similar features are observed as in poly(methacrylate)s/poly(acrylate)s.

Based on the concept outlined in Sect. 10.3 and refined investigations on aligned polysiloxanes (see [4, 5, 25, 73, 74] and references quoted therein) the α-relaxation was interpreted in a different way and assigned to fluctuations of both the transverse and the longitudinal dipole moment of the mesogenic unit. For clarification broadband dielectric investigation on aligned samples are needed.

In conclusion the molecular dynamics in liquid crystalline side chain polymers is characterized by tree major processes[8] – the β-, α- and the δ-relaxation in order of decreasing frequency (Fig. 10.22). It reflects the result of a delicate interplay between the dynamics the polymer backbones which form a glassy melt and the mesogenes in the their liquid crystalline phases. While the processes (β-, δ-relaxation) originate from fluctuations the mesogenes the α-relaxation corresponds mainly to that of the polymer backbone.

---

[8] In several systems further secondary processes (γ-relaxation) can be observed.
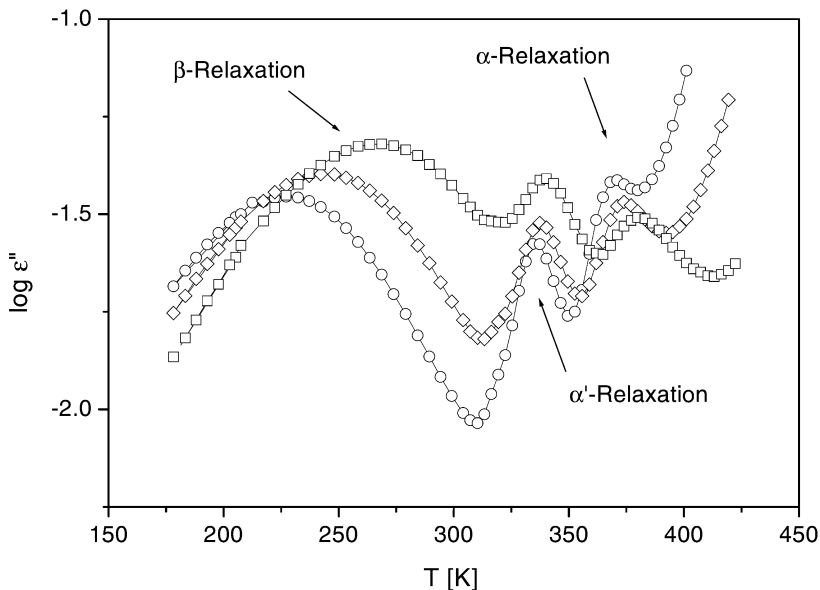
Fig. 10.23. Dielectric loss vs temperature at different frequencies for PET/0.5PHB: (*open circles*) 147 Hz, (*open diamonds*) 10^3 Hz, (*open squares*) 10^4 Hz. Reproduced from [56] with permission

10.4.2.2
Main Chain Polymers

Main chain liquid crystalline polymers are widely applied because of their outstanding mechanical properties[9]. In comparison to the numerous dielectric studies on SCPLC, systematic investigations on MCPLC are rare and limited mainly to ester systems (see for instance [3, 6, 76–78]). The molecular fluctuations of the mesogenic unit around its short axis (δ-relaxation) is not possible because they are incorporated in the main chain. In principle the dielectric response is similar to other semi flexible chains (see Chap. 7) showing a local β-relaxation and the dynamic glass transition (α-relaxation). However, compared to that they can have microphase separated structures where the morphology depends on the concentration of mesogens as well as on thermal history [79–83]. Moreover transester reactions cannot be excluded at high temperatures.

To illustrate the dielectric response of an MCLCP isochronal spectra of the random copolyester PET/xPHB (PET – poly(ethylene terephthalate), PHB – *p*-hydroxybenzoic acid, $x = 0.5$) is plotted vs temperature (Fig. 10.23). These copolymers form liquid crystalline phases for $x > 0.25$ with a hierarchical structure. At low temperatures (high frequencies) the β-process takes place.

---

[9] Recently it has also been demonstrated that main chain liquid crystalline polymers can be used as active material in light emitting diodes [75]. They can have also ferroelectric properties (see Sect. 10.5)

Furthermore the systems shows two dynamic glass transitions (α' and α-relaxation) which are also confirmed by DSC measurements. The α'-process is assigned to the segmental dynamics in amorphous microphases rich in PHB while the α-peak is due to PET-rich islands [81].

10.5
Collective Dynamics in Ferroelectric Liquid Crystalline Systems

In 1975 Meyer et al. [84] predicted and proved experimentally that smectic phases of chiral liquid crystals exhibit ferroelectric properties (FLC). This discovery initiated a dramatic development leading to a manifold of low molecular weight, polymeric and elastomeric ferroelectric liquid crystalline systems [85–88]. Moreover in recent years antiferroelectric liquid crystalline (AFLC) systems were found. Dielectric spectroscopy is, besides NMR and dynamic light scattering, the main experimental tool to analyse the dynamics in these systems.

The ferroelectricity in FLC is a local property restricted to a single smectic layer. Due to interactions between the mesogenic molecules in the tilted smectic phase the distribution of lateral dipole moments becomes anisotropic ("biased"), hence giving rise to a polarization vector P_L which is perpendicular to the layer normal. In order to minimise the free energy of the system as a whole the c_L director resp. the polarisation vector P_L form a helical superstructure having a pitch p_H in the micron range. By that an incommensurable (liquid) crystal is formed (Fig. 10.24a). In order to make the microscopic ferroelectricity of the single smectic layers macroscopically observable the helical superstructure has to be "unwound" (Fig. 10.24b). This can be achieved for instance by applying an external electric field or by surface effects. Net polarisation vectors of a magnitude between 1 and 1000 nC cm^{-2} can be realised.

The supermolecular arrangement of the molecules gives rise to collective motions of the polarisation vector in addition to the usual molecular fluctuations. Broadband dielectric spectroscopy is an ideal tool to unravel this dynamics.

10.5.1
Low Molecular Weight Systems

In order to orient the FLC in the so-called bookshelf geometry (where the external electric field is oriented perpendicular to the normal of the smectic layers) the metal electrodes (diameter: 5 mm, spacing: 10 µm) are coated with crosslinked polyimide which was rubbed. Such a sample cell (Fig. 10.25a,b) can be used in the entire frequency range from 10^{-2} Hz to 10^{10} Hz, hence enabling one to study both collective and molecular dynamics in the same probe [89–95]. The measured net polarisation in such a sample cell compares well with that observed in commercial sample cells used for electro-optical studies.

The dielectric properties of FLC in the frequency range below 1 MHz are dominated by one huge loss process – the Goldstone-mode (Fig. 10.26) It is restricted to the ferroelectric SmC-phase and vanishes above and below the phase
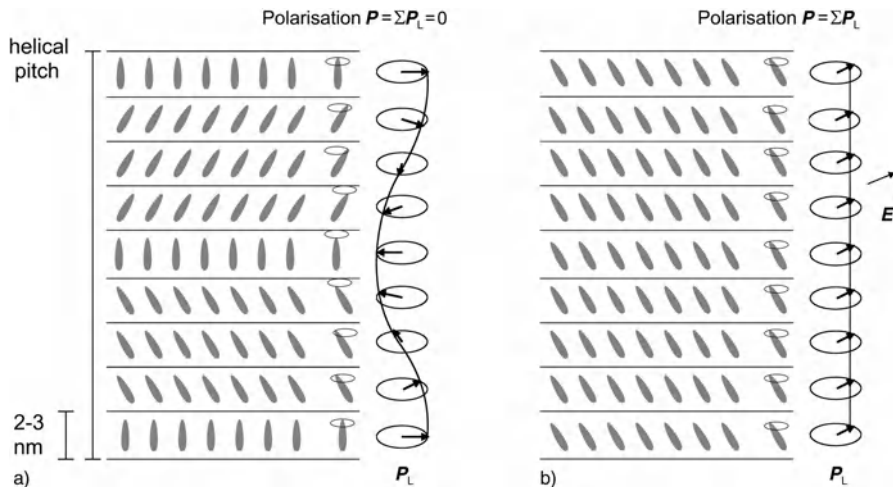
Fig. 10.24. a Scheme of ferroelectric liquid crystals in the smectic mesophase. In order to decrease the free energy of the system the polarisation vector of the single smectic layers (thickness: 2–3 nm) forms a helical superstructure (pitch: ~ μm). Hence the whole ensemble can be regarded as an incommensurable liquid crystal. **b** Applying an external electric field E in the plane of the smectic layers enables one to "unwind" the helical superstructure. By that the (local) ferroelectricity of the single smectic layers becomes macroscopically observable ("induced spontaneous polarization")
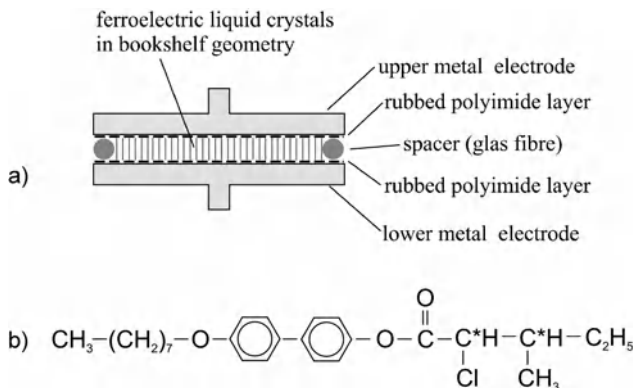
Fig. 10.25. a Scheme of the sample cell orienting the ferroelectric liquid crystalline system in bookshelf geometry. A spacing of 10 μm is maintained by use of glass fibres. The surfaces of the electrodes are coated with rubbed polyimide. The sample cell can be used in the entire frequency range between 10^{-2} Hz to 10^{10} Hz. **b** Chemical structure of sample FLC1. The phase sequence is $C \xleftrightarrow{322K} SmC^* \xleftrightarrow{328K} SmA \xleftrightarrow{338K} I$
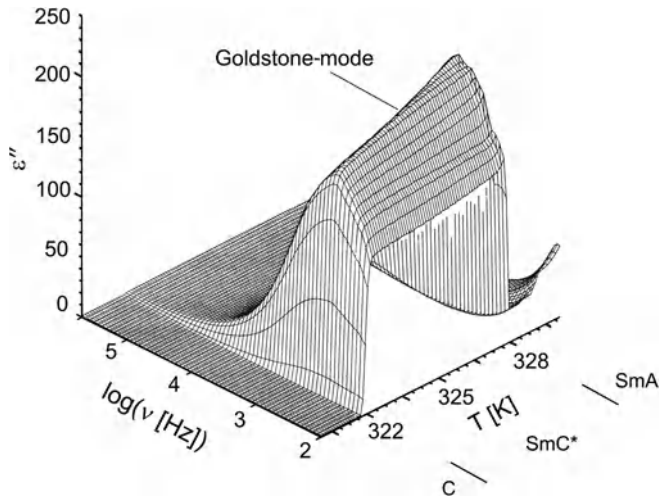
Fig. 10.26. Dielectric loss ε'' vs frequency and temperature of sample FLC1. Sample thickness 10 μm; a.c.-field strength 1000 V cm^{-1}; d.c.-field strength: 0 V cm^{-1}

transitions to the SmA resp. the crystalline phase. The Goldstone-mode has a negligible temperature dependence which proves that it cannot be comprehended as a simple relaxation process. Instead it is assigned to fluctuations of the phase of the helical superstructure (phason). It is a non-ideal zero-frequency mode which approaches zero if the wave vector k of the helical pitch with $|k| = \dfrac{2\pi}{p_H}$ goes to zero.

Applying a superimposed d.c.-bias field to the measuring a.c.-field enables one to suppress continuously the helical superstructure (Fig. 10.27a,b). By that the strength of the Goldstone-mode contribution decreases strongly (Fig. 10.28) and a second collective mode becomes observable; the soft mode. It is characterised by a critical slowing down of the relaxation rate (frequency at maximum dielectric loss) and the inverse of the dielectric strength (Fig. 10.29a,b).

The soft mode corresponds to motions of the amplitude of the helical superstructure (amplitudon). It shows a negligible d.c.-bias field dependence only. Both the Goldstone- and soft-mode are well known from the theory of incommensurable crystals [96].

For frequencies above 1 MHz only the β-relaxation is observed which corresponds to librations (hindered rotations) around the long molecular axis of the mesogenes. This fluctuation was assumed to be – if hindered – the origin of the spontaneous polarisation [97, 98]. Dielectric spectroscopy in the microwave range is especially suitable to analyse this process in detail. Employing the identical sample cell as used in the low frequency experiments the molecular dynamics can be measured in its frequency and temperature dependence. For both the chiral sample (Fig. 10.30) and its racemic mixture (Fig. 10.31a,b) a very similar behaviour is found.
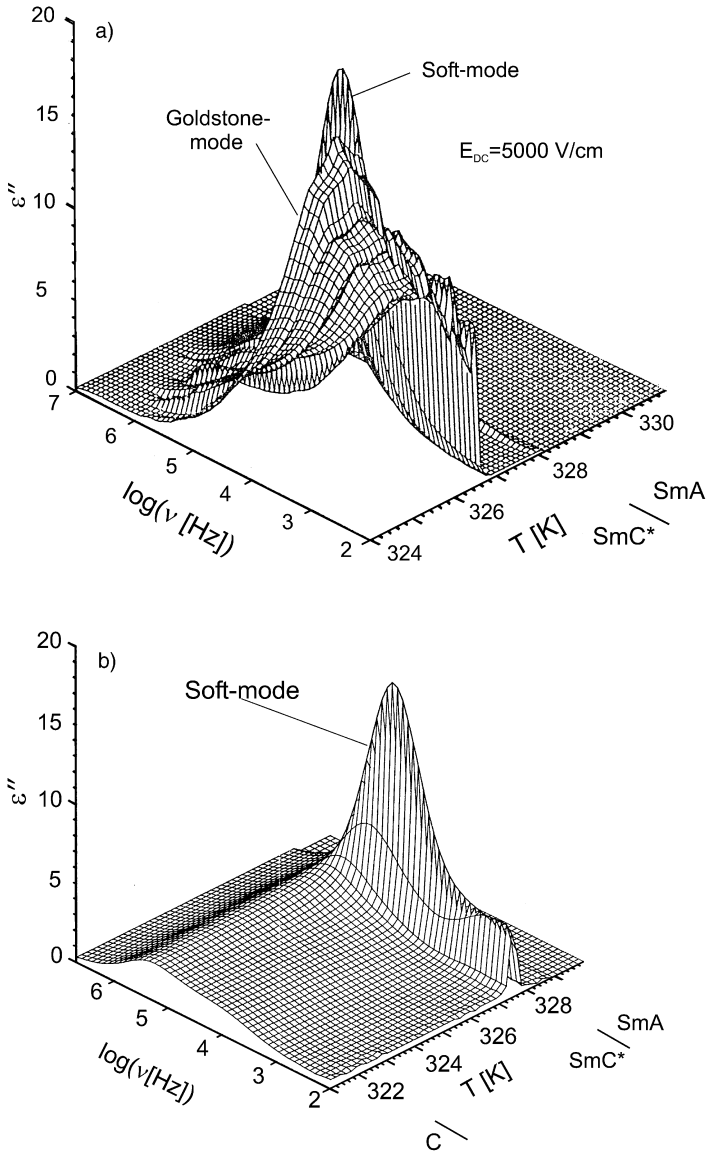
Fig. 10.27. **a** Dielectric loss ε'' vs frequency and temperature after application of a d.c.-bias field of 5000 V cm^{-1}. Otherwise as Fig. 10.26. **b** As a but with a d.c.-bias field of 8000 V cm^{-1}. Otherwise as Fig. 10.26

Fig. 10.28. Dielectric loss ε'' vs frequency at a fixed temperature of 326.4 K. Sample FLC1, sample thickness: 10 μm. Applying a d.c.-bias field between 0 and 8000 V cm^{-1} enables to suppress the Goldstone-mode. The a.c.-field strength: 1000 V cm^{-1}. *Inset*: field dependence of the dielectric loss ε'' at a frequency of 2.51 kHz and a temperature of 326.4 K
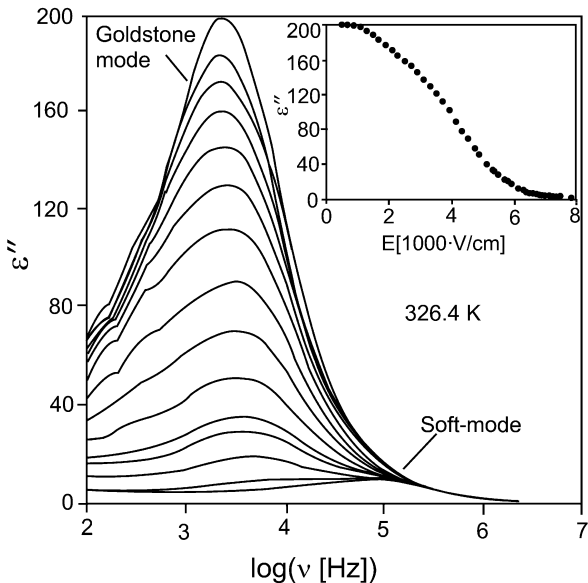
By fitting the data using the Havriliak/Negami equation [31] the mean relaxation rate and the dielectric strength $\Delta\varepsilon$ can be determined (Fig. 10.32a,b). At the phase transition SmA/SmC* resp. SmA/SmC neither for the chiral resp. for the racemic sample any discontinuity is observed. Hence the conjecture that the β-relaxation is slowed down in the ferroelectric phase is *not* correct. As expected one finds the dielectric strength to increase in steps at the phase transition I/SmA. This is caused by the change in the molecular order influencing the component of the dipole moment which interacts with the external electric field. At the transition to the crystalline state the dielectric strength of the β-relaxation vanishes, because the corresponding molecular fluctuation becomes arrested. It is worth mentioning that the β-relaxation does not show any indications of a splitting or discontinuous broadening at the phase transition SmA/SmC*. This was predicted by theories based on an extended Landau expansion of the free energy [99, 100].

Superimposing a d.c.-bias electric field to the measuring a.c.-field enables one to increase the dielectric strength (Figs. 10.33 and 10.34). In order to rule out the possibility that alignment effects influence this finding it was shown that by applying both positive and negative d.c.-bias fields similar results are obtained.

The d.c.-bias field dependence of the dielectric strength increases with decreasing temperature (Fig. 10.35). This is due to the fact that the net polarisation increases with decreasing temperature in the SmC*-phase. After the transition to the non-ferroelectric N*-phase the d.c.-bias field dependence vanishes. In the racemic mixture neither in the SmC- nor in the SmA-phase any d.c.-bias field dependence is found.

The β-relaxation is a molecular fluctuation which is assigned to a hindered rotation (libration) of the mesogenes around the long mesogenic axis. This process takes place in a similar way in the ferroelectric and in the non-ferro-
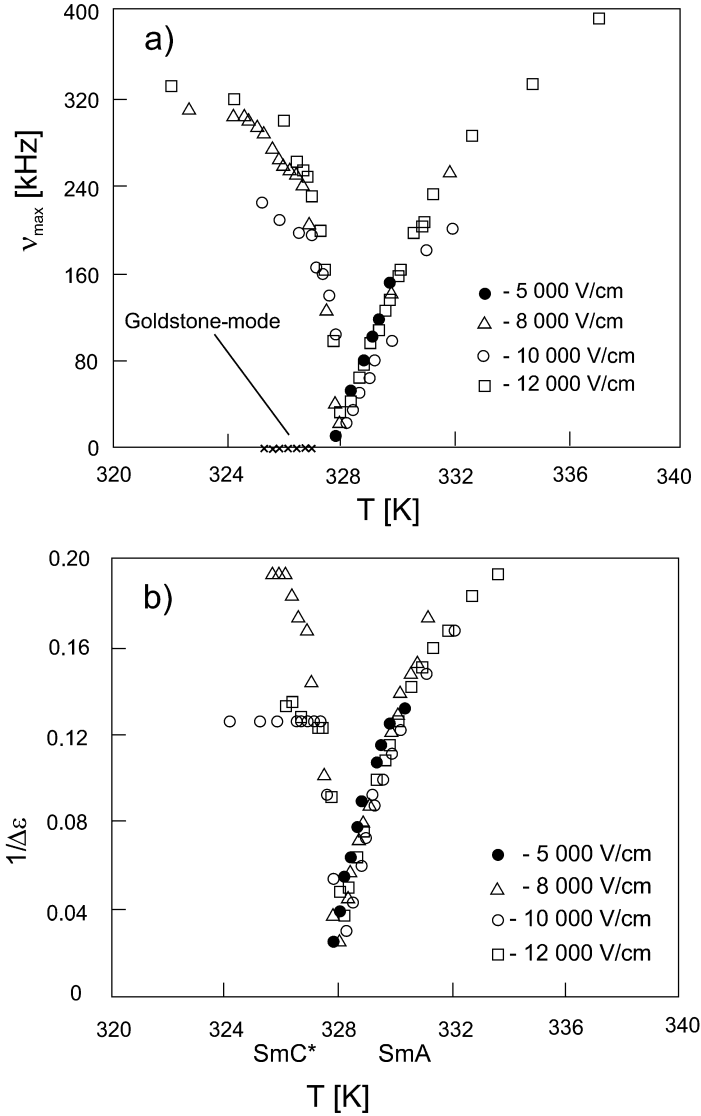
Fig. 10.29. Critical slowing down of: **a** the relaxation rate at maximum loss; **b** the inverse of the dielectric strength at the phase transition $\text{SmA} \xleftarrow{\ 338K\ } \text{SmC}^*$. Sample FLC1, sample thickness: 10 μm; a.c.-field strength: 1000 V cm^{-1}. The effect of a superimposed d.c.-bias field is indicated as well
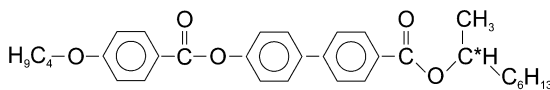
Fig. 10.30. Chemical structure of sample FLC2. Its phase sequence is

$\text{C} \xleftarrow{\ 325K\ } \text{SmC}^* \xleftarrow{\ 358K\ } \text{SmA} \xleftarrow{\ 366K\ } \text{I}$

Fig. 10.31. Dielectric loss ε'' vs frequency and temperature for: **a** the chiral sample FLC2; **b** its racemic counterpart. The samples were aligned in bookshelf geometry. Sample thickness: 10 μm, diameter of sample capacitor: 5 mm
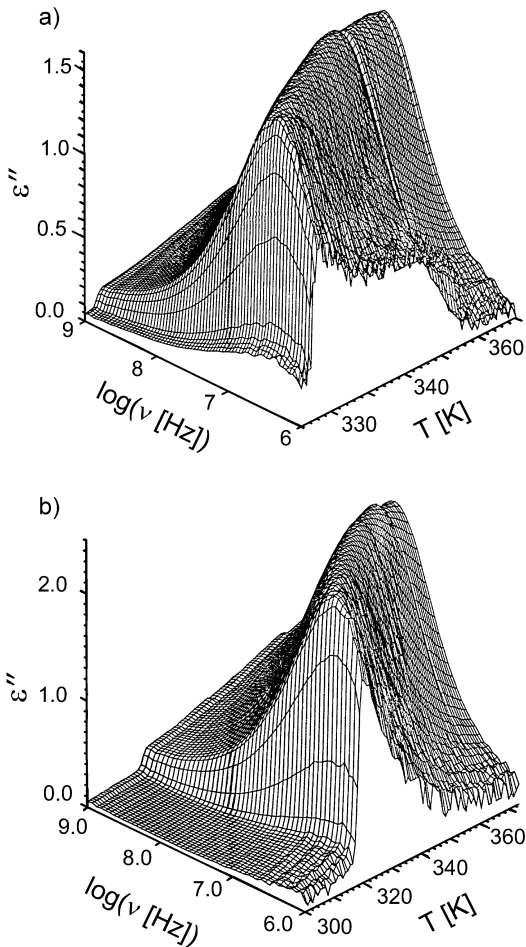
electric phase as well as in chiral FLC and racemic mixtures. However, while in the non-ferroelectric state (SmA isotropic) the angular distribution of the lateral dipole moments is isotropic, it becomes strongly anisotropic (biased) in the ferroelectric SmC*-phase (Fig. 10.36). This anisotropy is induced by the chirality and the tilt of the mesogenes. Applying an external d.c.-bias field increases this anisotropy while in parallel the helical superstructure and hence the Goldstone-mode is suppressed. Such a counteracting dependence is observed indeed (Fig. 10.37).

In summary, one finds in low molecular weight FLCs three dielectric loss processes (Fig. 10.38) which are quite different in their physical origin. Below 10^6 Hz two collective processes, the Goldstone-mode and the soft-mode, are observed. While the Goldstone-mode can be comprehended as a driven oscillator, the soft-mode corresponds to a fluctuation which exhibits critical behaviour when approaching the phase transition SmA/SmC*.
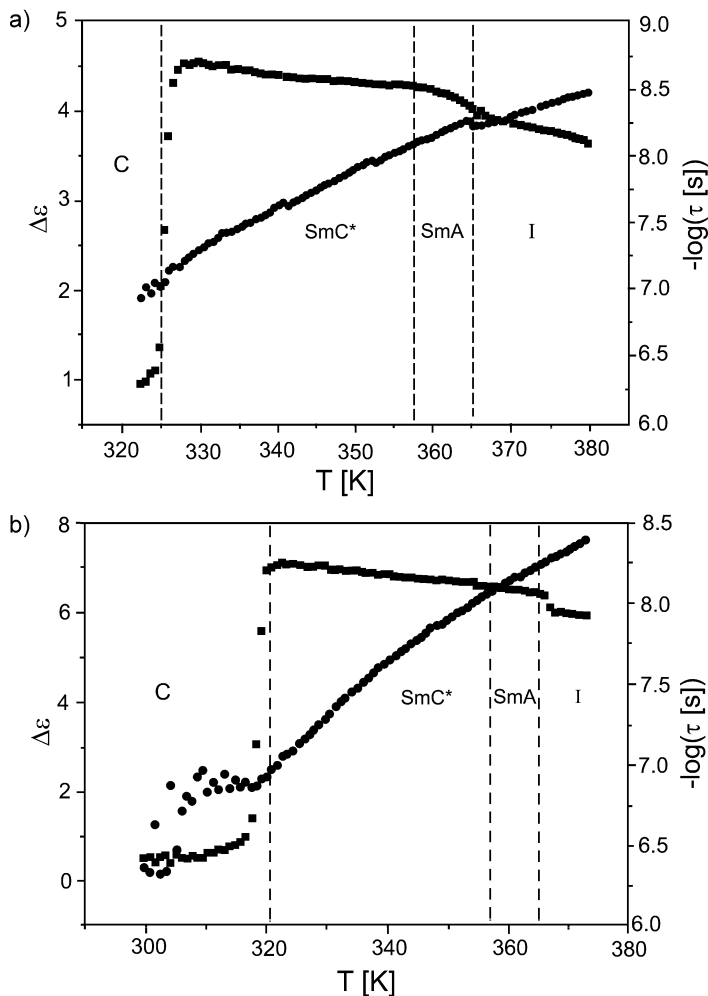
Fig. 10.32. Dielectric strength (*filled squares*) and relaxation rate (*filled circles*) vs temperature for the measurements: **a** in Fig. 10.31a (chiral FLC); **b** in Fig. 10.31b (racemic sample). The phase transition temperatures determined by polarised microscopy are indicated
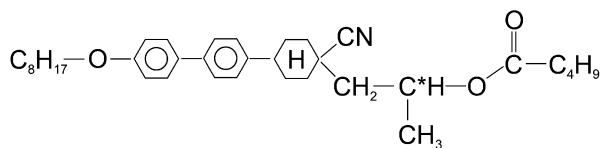
Fig. 10.33. Chemical structure of sample FLC3. The phase sequence is

$$C \xleftarrow{305K} SmC^* \xleftarrow{328K} N \xleftarrow{341K} I$$
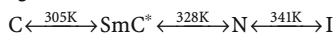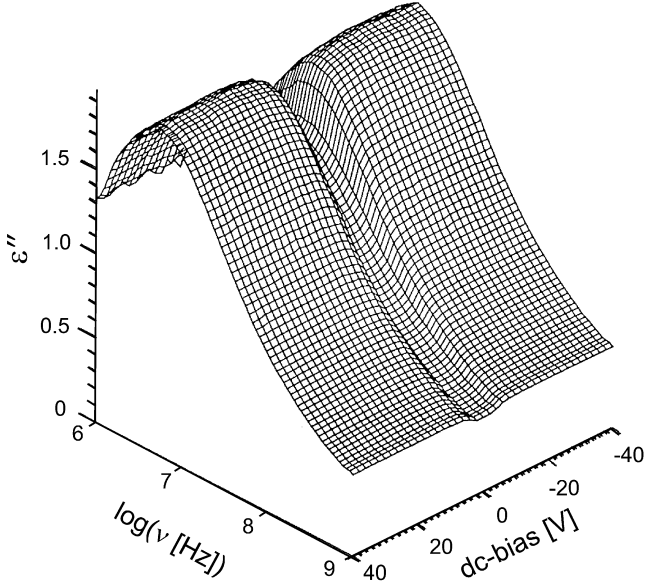
Fig. 10.34. Dielectric loss ε'' vs frequency for varying d.c.-bias fields; sample FLC3, sample thickness: 10 μm, Sample diameter: 3 mm, a.c.-field strength: 1000 V cm^{-1}
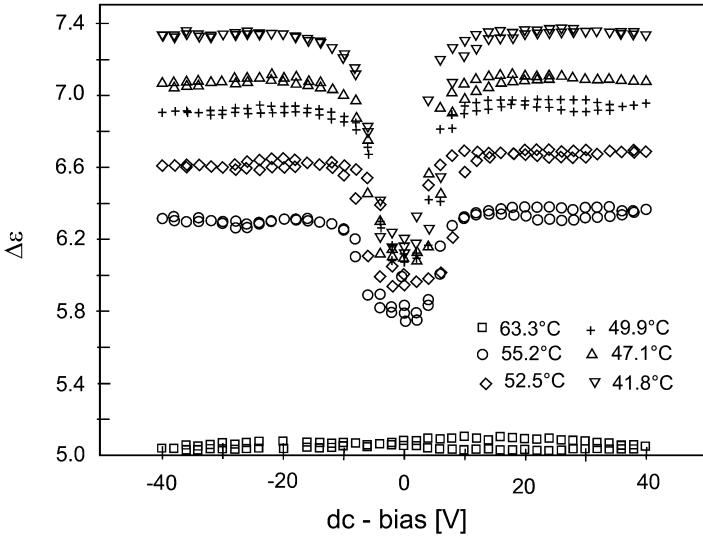
Fig. 10.35. Dielectric strength of the β-relaxation vs d.c.-bias field at different temperatures as indicated in the SmC* and N*. Sample FLC3

Fig. 10.36. Scheme of the distribution of the lateral dipole moments in the SmA and the SmC* phase

non-ferroelectric
phase

ferroelectric
phase
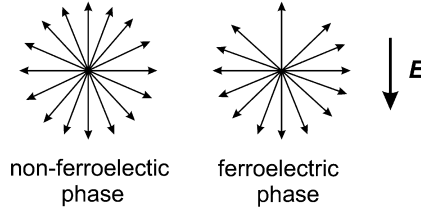
Fig. 10.37. Comparison of the d.c.-bias field dependence of the maximum dielectric loss $\varepsilon''^{(GM)}_{max}$ of the Goldstone-mode and of the strength of the β-relaxation. Sample FLC3
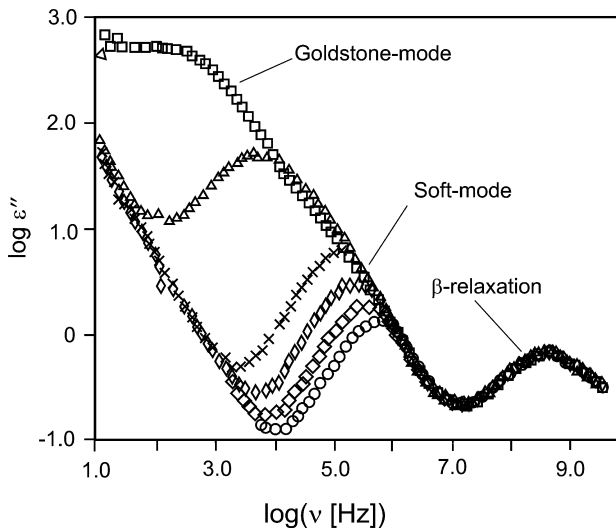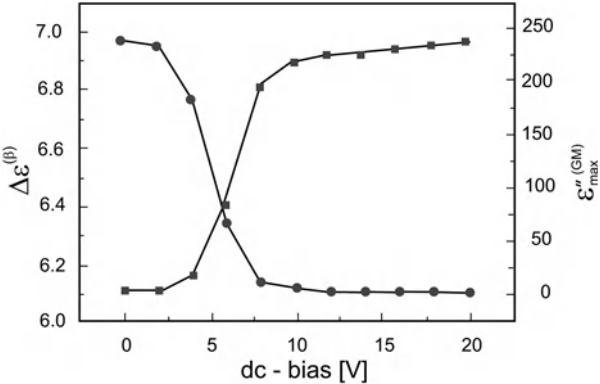
Fig. 10.38. Dielectric loss ε'' vs frequency for different temperatures slightly below and above the phase transition SmC*/SmA for sample FLC1 (*open circles*) 331.3 K, (*open diamonds*) 330.4 K, (*open asymmetric diamonds*) 329.4 K, (*crosses*) 328.5 K, (*open triangles*) 327.5 K, (*open squares*) 326.5 K. The contributions of the collective processes (Goldstone- and soft-mode) and the molecular β-relaxation are well separated
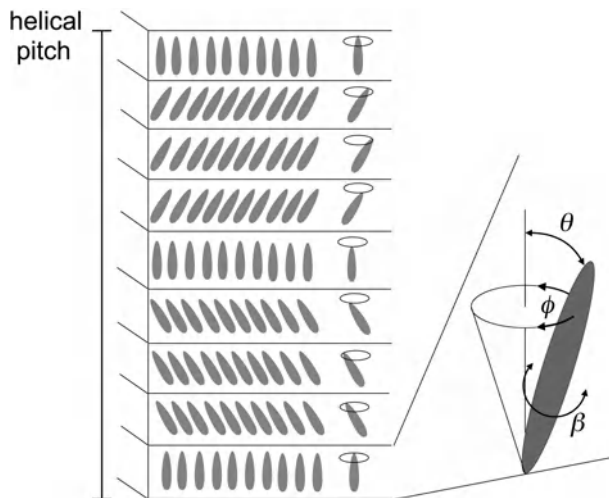
Fig. 10.39. Scheme of the collective and molecular dynamics in FLC: The Goldstone-mode corresponds to fluctuations of the phase ϕ (phason) and the soft-mode of the amplitude θ (amplitudon) of the helical superstructure. The high frequency β-relaxation is assigned to librations of the mesogen around its long molecular axis

In the frequency regime between 10^6 Hz and 10^{10} Hz *one* dielectric loss process is observed, the β-relaxation, which is assigned to the libration of the mesogenic groups around their long molecular axis. This process is a local fluctuation which is not directly influenced by the collective rearrangements which take place at the phase transition SmA/SmC*. The experimental results lead to a precise picture for the origin of ferroelectricity in chiral liquid crystals. It is caused by the anisotropy in the distribution of the lateral orientation of the molecular dipole moments induced by the chirality and the tilt of the mesogenes. A slowing down of molecular fluctuations at the phase transition SmA/SmC* is *not* observed (Fig. 10.39).

10.5.2
Polymeric Systems

Ferroelectric liquid crystals can be incorporated into a variety of different polymeric architectures, e.g. side-group liquid crystalline polymers [12], main chain polymers [101], combined side group/main chain systems [102, 103], or elastomers [104–107]. The collective and molecular dynamics remains well comparable to low molecular weight systems. Two collective modes are observed (Goldstone- and soft-mode) and one molecular relaxation, the β-process being assigned to librations around the long molecular axis.

Siloxane main chains are, because of their high flexibility (and hence low glass transition temperature), suitable systems for polymeric FLC. In side chain

polymers the chiral mesogene is decoupled from the main chain by a flexible alkyl spacer (Fig. 10.40). The density of the mesogenic side groups can be continuously varied by changing the ratios $y:x$ in the copolymer.

Measuring the collective and molecular dynamics in this system (Fig. 10.41) delivers a similar performance as in low molecular weight FLC (Fig. 10.38). Below 1 MHz two collective modes are observed, the Goldstone- and soft-mode and above 1 MHz the β-relaxation takes place (Table 10.4).

Applying a d.c.-bias electric field enables one to suppress continuously the Goldstone mode, which is in contrast to low molecular weight systems shifted to lower frequencies by about three decades (Fig. 10.42). If the helical superstructure is suppressed, a second collective process – the soft-mode – becomes observable. As is to be expected, it shows in the frequency position at maximum loss and in the inverse of the dielectric strength a slowing down with a minimum at the phase transition temperature SmA/SmC* (Fig. 10.43). In contrast to low molecular weight systems (Fig. 10.29) the relaxation rate (Fig. 10.43a) does not increase in the SmC* phase. This might be caused by the strongly enhanced viscosity of the polymeric system compared to low molecular weight FLC.

In the high frequency regime above 1 MHz the β-relaxation is observed (Fig. 10.44). As expected it shows an Arrhenius-like temperature dependence and no discontinuity at the phase transition SmA/SmC*.
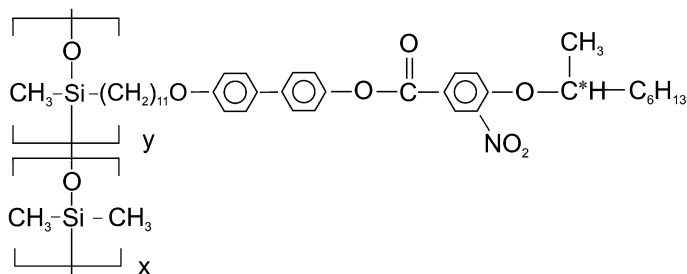
Fig. 10.40. Chemical structure of the side-group polymer FLCP1 under study. The phase transition temperatures for the different mol-(%) fractions y are indicated in Table 10.4

Table 10.4. Composition of the copolymer sample FLCP1. M_w and M_n are weight- and number-averaged molecular weights, respectively. P_s is the spontaneous polarization

Sample	x	y	M_w [10^{-3} g mol^{-1}]	M_n [10^{-3} g mol^{-1}]	P_s [nC cm^{-2}]	Phase sequence [K]
FLCP1a	3.2	1	23	14	104	g, 273; SmX, 319; SmC*, 371; SmA, 417 I
FLCP1b	1.1	1	53	27	130	g, 286; SmX, 327; SmC*, 397; SmA, 441 I
FLCP1c	0.5	1	51	29	161	g, 293; SmX, 345; SmC*, 411; SmA, 455 I
FLCP1d	0	1	28	13	211	g, 294; SmX, 330; SmC*, 434; SmA, 456 I
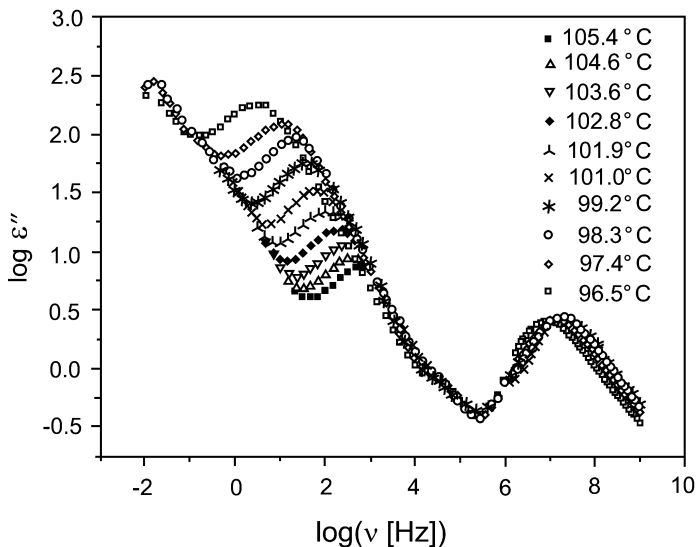
Fig. 10.41. Dielectric loss ε'' vs frequency for sample FCLP1a at different temperatures (see Table 10.4) slightly below and above the phase transition SmC*/SmA; sample thickness 10 μm, sample diameter: 3 mm; a.c.-field strength 1000 V cm^{-1}
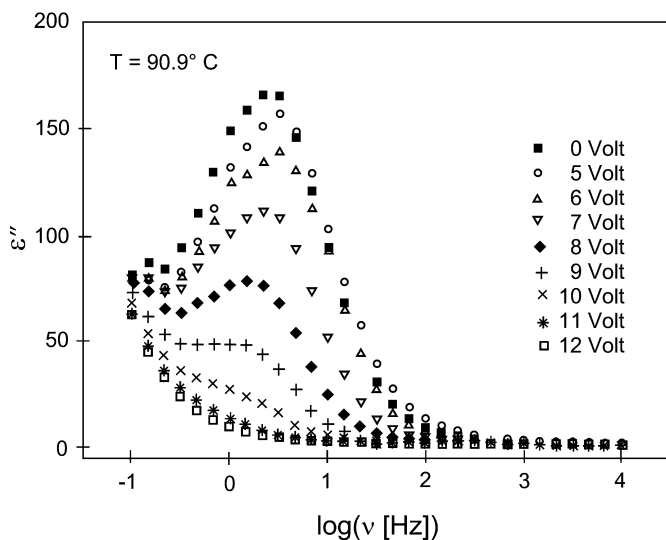
Fig. 10.42. Dielectric loss ε'' vs frequency for different d.c.-bias fields for sample FLCP1a, otherwise as Fig. 10.41
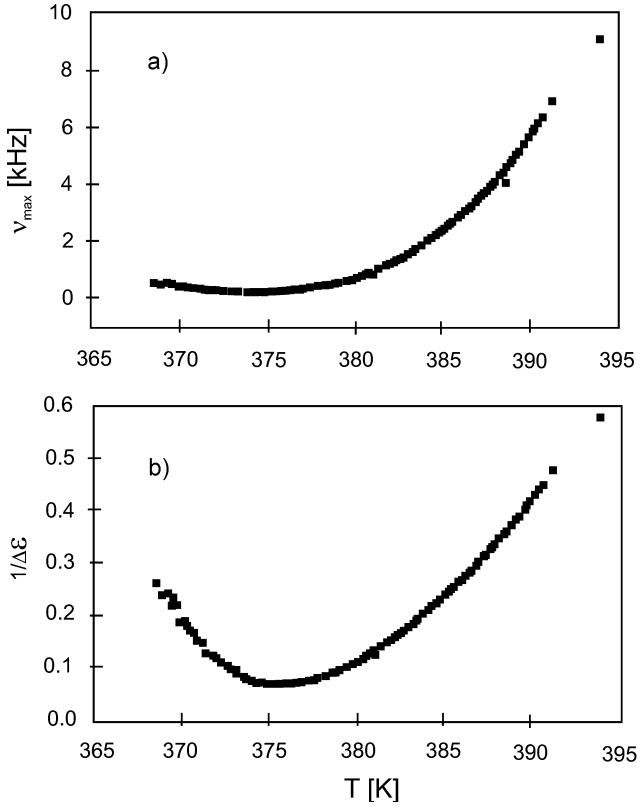
Fig. 10.43. Critical slowing down of: **a** the relaxation rate at maximum loss; **b** the inverse dielectric strength at the phase transition SmA/SmC*. Sample FLCP1a from Table 10.4; otherwise as Fig. 10.41
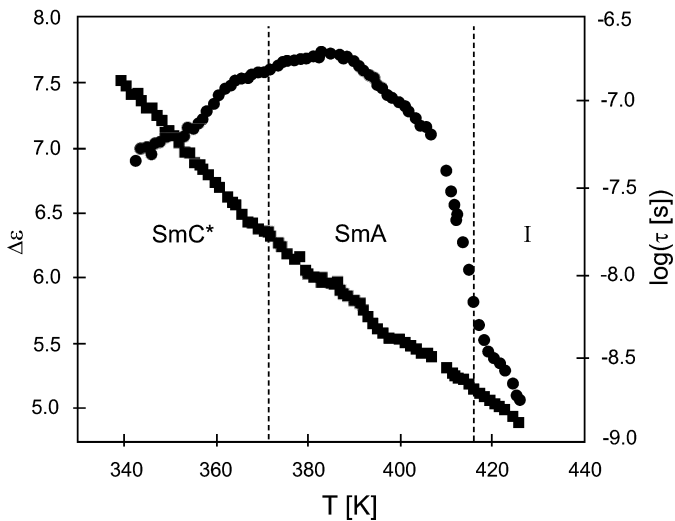
Fig. 10.44. Dielectric strength and relaxation time for the β-relaxation of sample FLCP1a from Table 10.4; otherwise as Fig. 10.41
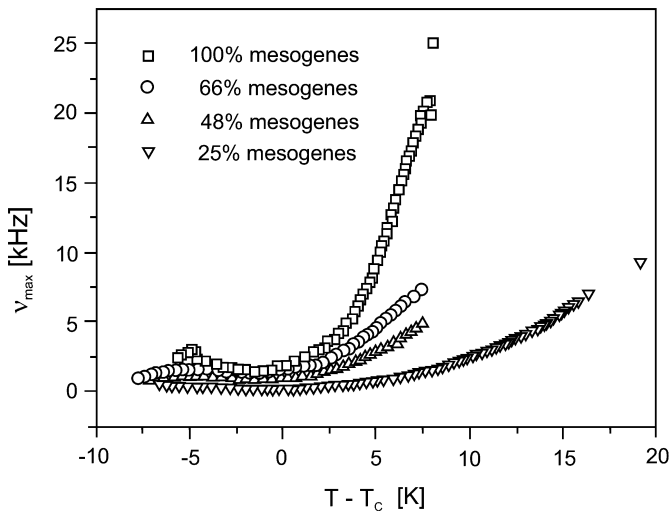
Fig. 10.45. Critical slowing down of the soft-mode relaxation rate for the copolymer sample FLCP1a with varying content of chiral mesogenes. Sample thickness: 10 μm, sample diameter: 3 mm; a.c.-field strength: 1000 V cm^{-1}
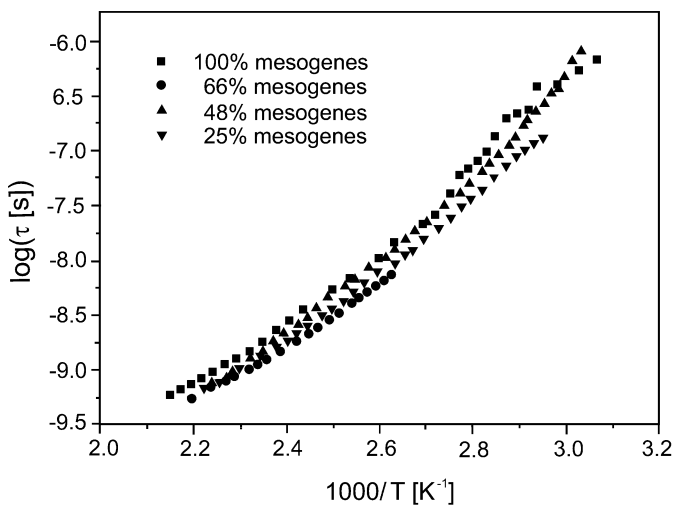
Fig. 10.46. Relaxation time vs inverse temperature for the β-relaxation of the copolymer sample FLCP1a with varying content of chiral mesogenes; otherwise as Fig. 10.45

Diluting the mesogenes by changing the ratio $y:x$ decreases the net polarization of the system (Table 10.4). In the slowing down of the relaxation rate of the soft-mode this is reflected as a decrease in the critical behaviour (Fig. 10.45). In contrast the local β-relaxation is nearly uninfluenced by the dilution of the mesogenes (Fig. 10.46). In the 25% diluted system it is slightly faster compared to the undiluted side chain polymer.
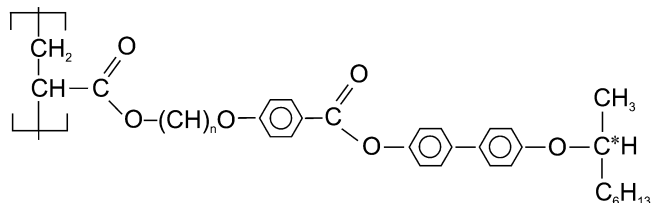
Fig. 10.47. Chemical composition of the side-group polymer (sample FLCP2) with varying spacer length. The phase transition temperatures are indicated in Table 10.5
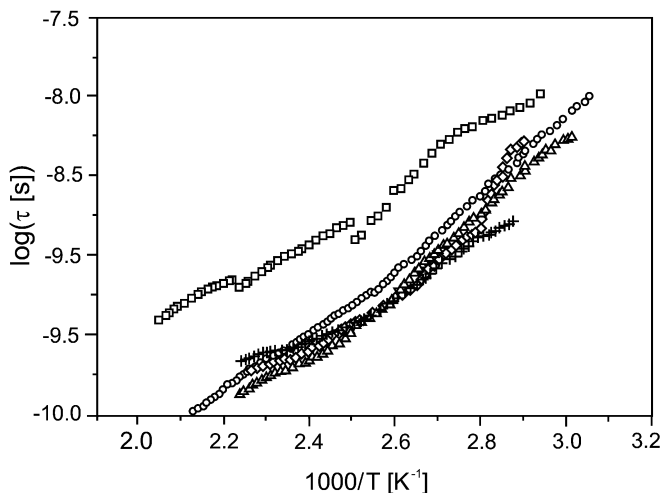
Fig. 10.48. Relaxation time vs inverse temperature for the β-Relaxation of sample FLCP2 with varying spacer length: (*open squares*) FLCP2a, (*open circles*) FLCP2b, (*open triangles*) FLCP2c, (*open diamonds*) FLCP2d, (*plus signs*) FLCP2e

Table 10.5. Number of (CH_2) spacers n and weight-averaged molecular weight M_w for the side group polymer sample 5

Sample	n	$M_w \, [\text{g mol}^{-1}]$
FLCP2a	2	117,000
FLCP2b	6	83,000
FLCP2c	8	27,000
FLCP2d	11	38,000
FLCP2e	11	240,000

It is an interesting question as to how long the alkyl-spacer has to be in order to decouple the β-relaxation dynamics from the main chain (Fig. 10.47). To analyse this for a polyacrylate main chain the spacer length was systematically varied between 2 and 11 alkyl units (see Table 10.5). As shown in the activation plot for the β-relaxation (Fig. 10.48) a twofold spacer decreases the relaxation rate by almost half a decade compared to a sixfold or longer spacer.

10.6
Conclusions

In low molecular weight liquid crystals the following relaxation processes are typically observed which depend strongly on the mesophase in which they take place: (i) the β-relaxation which is assigned to librational fluctuations of the mesogen around the long molecular axis; (ii) the δ-relaxation which corresponds to librational fluctuations around the short molecular axis. In the nematic phase a further relaxation is observed corresponding to small angular fluctuations around the short molecular axis.

In side chain liquid crystalline polymers the molecular dynamics of the mesogens is decoupled from the main chain by use of a flexible (aliphatic) spacer. Three relaxation processes are observed: the β-relaxation and the δ-relaxation having the same assignment as for low-molecular weight systems and additionally an α-relaxation corresponding to the dynamic glass transition of the main chain. The latter may be enhanced in its dielectric strength by contributions from polar components of the mesogens.

In main chain liquid crystalline polymers beside the β- and α-relaxation a further α' process is often observed which corresponds to the dynamic glass transition in a microphase separated state. No δ-relaxation takes place.

The collective and molecular dynamics (10^{-2} Hz to 10^{10} Hz) in (low molecular weight and polymeric) ferroelectric liquid crystals (FLC) is characterized by two collective and *one* molecular process. Below 1 MHz the Goldstone- and the soft-mode are observed. The Goldstone-mode is assigned to fluctuations respectively modulations of the phase angle of the helical superstructure (phason). The soft mode corresponds to fluctuations of the amplitude (amplitudon) of the helical superstructure. It has a negligible a.c.- and d.c.-field dependence. In the frequency regime from 10^6 to 10^{10} Hz *one* relaxation process takes place, the β-relaxation, which corresponds to the libration of the chiral mesogene around its long molecular axis. This process is not directly involved in the molecular rearrangements which take place at the phase transition.

Incorporating chiral mesogenic groups into polymeric architectures (side chain, main chain, combined side group/main chain systems, copolymers, networks) it is possible to combine the electric and dielectric properties of ferroelectric liquid crystals with the viscoelastic properties of polymers. By that means new materials can be tailored (e.g. photochromic, ferroelectric polymers, single crystal, ferroelectric liquid crystalline rubbers, etc.) with completely new technological perspectives.

List of Abbreviations and Symbols

A	Constants
$c_p^*(v)$	Complex heat capacity
c_p'	Real part
c_p''	Imaginary part
$C_j^i(\omega)$	Fourier transform of the correlation function
E_A	Activation energy
k_B	Boltzmann constant
M_w, M_n	Weight- and number-average molecular weight
$\boldsymbol{n}$	Director
S	Molecular order parameter
S_D	Director order parameter
T	Temperature
T_0	Vogel temperature
T_g	Glass transition temperature
T_B	Characteristic temperature
V	Volume
β_{HN}, γ_{HN}	Shape parameters of the Havriliak/Negami function
$\delta\varepsilon$	Dielectric anisotropy
$\Delta\varepsilon$	Dielectric strength
ε_0	Permittivity of the free space
ε_s	$\lim_{\omega\tau\ll 1}\varepsilon'(\omega)$
ε_∞	$\lim_{\omega\tau\gg 1}\varepsilon'(\omega)$
$\varepsilon^*, \varepsilon', \varepsilon''$	Complex dielectric function, real part and imaginary part
ϑ	Tilt angle
μ	Dipole moment
v	Frequency
v_{max}	Relaxation rate at maximum dielectric loss
v_∞	Relaxation rate for $T \to \infty$
τ	Relaxation time
ω	Angular frequency
C	Crystalline
5 CB	Pentyl-cyanobiphenyl
7 CB	Heptyl-cyanobiphenyl
DSC	Differential Scanning Calorimetry

FLC	Ferroelectric liquid crystal
FT	Fourier transform
HN	Havriliak/Negami
I	Isotropic
L	Longitudinal (subscript)
LC	Liquid crystal
MCLCP	Main chain liquid crystalline polymers
N	Nematic
PET	Poly(ethylene terephthalate)
PHB	p-Hydroxybenzoic acid
SCLCP	Side chain liquid crystalline polymers
SmX	Smectic X (X = A, B, C, …) phase
T	Transversal (superscript)
TMDSC	Temperature modulated differential scanning calorimetry
VFT	Vogel/Fulcher/Tammann

References

1. de Gennes PG (1975) The physics of liquid crystals. Clarendon Press, Oxford
2. Chandrasekhar S (1992) Liquid crystals. Cambridge University Press
3. Moscicki JK (1992) In: Collyer AA (ed) Liquid crystal polymers – from structure to applications. Elsevier, p 143
4. Haws CM, Clark MG, Attard GS (1989) Dielectric relaxation spectroscopy of liquid crystalline side chain polymers. In: McArdle CB (ed) Side chain liquid crystal polymers. Blackie, Glasgow/London, p 196
5. Williams G (1989) In: Allen G, Bevington JC (eds) Comprehensive polymer science, vol II. Pergamon Press; Williams G (1993) In: Thomas EL (ed) Structure and properties of polymers. materials science and technology series, vol 12. VCH Publications, p 471
6. Simon GP (1997) Dielectric properties of polymeric liquid crystals. In: Runt JP, Fitzgerald JJ (eds) Dielectric spectroscopy of polymeric materials. ACS-Books, Washington DC, p 329
7. Demus D, Goodby J, Gray GW, Spiess HW, Vill V (eds) (1998) Handbook of liquid crystals. Wiley-VCH, Weinheim
8. Demus D, Demus H, Zaschke H (1974) Flüssige Kristalle in Tabellen, Deutscher Verlag für Grundstoffindustrie, Leipzig; Demus D, Zaschke H (1984) Flüssige Kristalle in Tabellen, vol II, Deutscher Verlag für Grundstoffindustrie, Leipzig
9. Chandrasekhar S, Sandashiva BK, Suresh KA (1977) Pramana 9:471
10. Groothues H, Kremer F, Schouten G, Warman JM (1995) Adv Mater 7:283
11. Brostow W (1990) Polymer 31:979
12. McArdle CB (1989) Side chain liquid crystal polymers. Blackie Publishing Group, Glasgow
13. Shibaev VP, Platé N, Freidzon, Ya S (1979) J Polym Sci Chem 17:1655
14. Finkelmann H, Ringsdorf H, Wendorff JH (1978) Makromol Chem 179:273
15. Eich M, Wendorff JH, Reck B, Ringsdorf H (1987) Makromol Chem Rapid Commun 8:59; Eich M, Wendorff JH (1987) Makromol Chem Rapid Commun 8:467
16. Kremer F, Vallerien SU, Zentel R, Kapitza H (1989) Macromolecules 22:4040
17. Enders BW, Ebert M, Wendorff JH, Reck B, Ringsdorf H (1990) Liq Cryst 7:217
18. Gleim W, Finkelmann H (1989) Side chain liquid crystalline elastomers. In: McArdle CB (ed) Side chain liquid crystal polymers. Blackie, Glasgow/London, p.287
19. Martin AJ, Meier G, Saupe A (1971) Chem Soc Faraday Symp 5:119
20. Maier W, Meier G (1961) Z Naturforsch 16a:262

21. Maier W, Meier G (1961) Z Naturforsch 16a:470
22. Saupe A (1960) Z. Naturforsch 15a:810; Saupe A (1960) Z Naturforsch 15a:815
23. Nordio PL, Rigatti G, Serge U (1973) Mol Phys 25:129
24. Attard GS, Araki K, Williams G (1987) Br Polym J 19:119
25. Araki K, Attard GS, Kozak GS, Williams G, Gray GW, Lacey D, Nestor G (1988) J Chem Soc Faraday Trans II 84:1067
26. Attard GS (1986) Mol Phys 58:1087
27. Kozak A, Moscicki JK, Williams G (1991) Mol Cryst Liq Cryst 201:1
28. Kozak A, Moscicki JK (1992) Liq Cryst 12:377
29. Bucher HK, Klingbiel RT, van Meter JP (1974) Appl Phys Lett 5:186
30. Kresse H, Weissflog W, Kremer F, Schönfeld A (1992) Cryst Res Technol 27:K5
31. Havriliak S, Negami S (1966) J Polym Sci C 16:99; Havriliak S, Negami S (1967) Polymer 8:161
32. Davies M, Moutran R, Price AH, Beevers MS, Williams G (1976) J Chem Soc Faraday II 72:1447
33. Christoph G, Stille W, Strobl G (1993) J Chem Phys 99:3075
34. Vogel H (1921) Phys Z 22:645
35. Fulcher GS (1925) J Am Ceram Soc 8:339
36. Tammann G, Hesse W (1926) Z Anorg Allg Chem 156:245
37. Zeller HR (1982) Phys Rev Lett 48:334
38. Benguigui L (1984) Mol Cryst Liq Cryst 114:51
39. Diogo AC, Martins AF (1982) J Phys (Paris) 43:779
40. Anderson PW (1995) Science 267:1615
41. Angell CA (1995) Science 267:1924
42. Götz S, Stille W, Strobl G, Scheuermann H (1993) Macromolecules 26:1520
43. Marrucci G (1982) Mol Cryst Liq Cryst Lett 72:153
44. Tseber AO (1978) Magn Gidrodin 3:3
45. Bauman D, Jadzyn J, Czechowski (2001) IEEE Trans Dielectr Electr Insul 8:381
46. Raviol A, Stille W, Strobl G (1995) J Chem Phys 103:3788
47. Seiberle H, Stille W, Strobl G (1990) Macromolecules 23:2008
48. Kresse H, Talroze RV (1981) Macromol Chem Rapid Commun 2:369
49. Kresse H, Kostromin SG, Shibaev VP (1982) Macromol Chem Rapid Commun 3:509
50. Kresse H, Shibaev VP (1983) Z Phys Chem (Leipzig) 264:161
51. Kresse H, Shibaev VP (1984) Macromol Chem Rapid Commun 5:63
52. Kresse H, Trennstedt E, Zentel R (1995) Macromol Chem Rapid Commun 6:261
53. Haase W, Bormuth FJ, Pfeifer M, Jakob E (1991) Ber Bunsenges Phys Chem 95:1050
54. Haase W, Pranoto H, Bormuth FJ (1985) Ber Bunsenges Phys Chem 89:1229
55. Zentel R, Strobl G, Ringsdorf H (1985) Macromolecules 18:960
56. Schönhals A, Carius HE (2000) Int J Polym Mater 45:239
57. Schönhals A, Geßner U, Rübner J (1995) J Macromol Chem Phys 196:1671
58. Schönhals A, Wolff D, Springer J (1995) Macromolecules 28:6254
59. Schönhals A, Wolff D, Springer J (1997) Polym Adv Technol 7:853
60. Schönhals A, Ruhmann R, Thiele T, Prescher D (1997) In: Jenekhe SA, Wynne KJ (eds) Photonic and opto-electronic polymers. ACS Symposium Series p. 280
61. Schönhals A, Wolff D, Weidner S, Springer J (1999) ACS Polym Prepr 40:502
62. Pschorn U, Spiess HW, Hisgen B, Ringsdorf H (1986) Makromol Chem 187:2711
63. Vallerien SU, Kremer F, Boeffel C (1989) Liq Cryst 4:9
64. Ngai KL, Schönhals A (1998) J Polym Sci Phys Ed 36:1927
65. Lipatov SY, Tsukruk VV, Shilov VV (1983) Polym Commun 24:75
66. Stickel F, Fischer EW, Richert R (1995) J Chem Phys 102:6251
67. Schönhals A, Wolff D, Springer J (1998) Macromolecules 31:9019
68. Schönhals A, Kremer F, Hofmann A, Fischer EW, Schlosser E (1993) Phys Rev Lett 70:3459
69. Schick C, Sukhorukov D, Schönhals A (2001) Macromol Chem Phys 202:1398
70. Baehr C, Glüsen B, Wendorff JH (1994) Makromol Chem Rapid Commun 15:327

71. Böffel C, Spiess HW (1989) NMR methods for studying molecular order and motion in liquid crystalline side group polymers. In: McArdle CB (ed) Side chain liquid crystal polymers. Blackie, Glasgow/London, p.224
72. Mano JF, Alves NM, Meseguer Dueñas JM, Gómez Ribelles JL (1999) Polymer 40:6545
73. Attard GS (1986) Mol Phys 58:1087
74. Attard GS, Williams (1986) Liq Cryst 1:253
75. Lüssem G, Festag R, Greiner A, Schmidt C, Unterlechner C, Heitz W, Wendorff JH, Hopmeier M, Feldmann J (1995) Adv Mater 7:923
76. Gedde UW, Liu F, Hult A, Gustafsson A, Jonsson H, Boyd RH (1991) Polymer 32:1218
77. Takase Y, Mitchell RG, Odayima A (1986) Polym Commun 27:76
78. Gedde UW, Buerger D, Boyd RH (1987) Macromolecules 20:988
79. Brostow W, Hess M, Lopez B (1994) Macromolecules 27:2262
80. Yoon DY, Maschiochi N, Depero LE, Viney C, Parrish W (1990) Macromolecules 23:1793
81. Carius HE, Schönhals A, Guigner D, Sterzynski T, Brostow WK (1996) Macromolecules 29:5017
82. Chen D, Zachmann HG (1991) Polymer 32:1612
83. Ahumada O, Ezquerra TA, Nogales A, Balta-Calleja FJ, Zachmann HG (1995) Macromol Chem Rapid Commun 16:899
84. Meyer RB (1977) Mol Cryst Liq Cryst 33:40
85. Lagerwall ST (1999) Ferroelectric and antiferroelectric liquid crystals. Wiley-VCH Weinheim
86. Musevic I, Blinc R, Zeks B (2000) The physics of ferroelectric and antiferroelectric liquid crystals. World Scientific, Singapore
87. Vij JV (ed) (2000) Advances in liquid crystals. A special volume of advances in chemical physics, vol 113. Wiley, New York
88. Kitzerow HS, Bahr C (eds) (2001) Chirality in liquid crystals. Springer, Berlin Heidelberg New York
89. Vallerien SU, Kremer F, Kapitza H, Zentel R, Frank W (1989) Phys Lett A 138:219
90. Kremer F, Vallerien SU, Kapitza H, Zentel R, Fischer EW (1990) Phys Rev A 42:2482
91. Vallerien SU, Kremer F, Geelhaar T, Wächtler AE (1990) Phys Rev A 42:2482
92. Kremer F, Schönfeld A, Vallerien SU, Hofmann A, Schwenk N (1991) Ferroelectrics 121:13
93. Schönfeld A, Kremer F, Hofmann A, Kühnpast K, Springer J, Scherowsky G (1993) Makromol Chem 194:1149
94. Schönfeld A, Kremer F (1993) Liq Cryst 13:403
95. Schönfeld A, Kremer F (1993) Ber Bunsenges Phys Chem 97:1237
96. Toledano JC, Toledano P (1987) The Landau theory of phase transitions. World Scientific, Lecture Notes in Physics, vol 3
97. Bereshnev LA, Blinov LM (1981) Ferroelectrics 33:129
98. Lagerwall ST, Dahl I (1984) Mol Cryst Liq Cryst 114:151
99. Carlsson T, Zeks B, Levstik A, Filipic C, Levstik J, Blinc R (1987) Phy Rev A 36:1484
100. Carlsson T, Zeks B, Filipic C, Levstik A (1990) Phys Rev A 42:877
101. Chiellini E, Laus M (1998) Main chain liquid crystalline polymers. In: Demus D, Goodby J, Gray GW, Spiess HW, Vill V (eds) Handbook of liquid crystals, vol III. Wiley-VCH, Weinheim
102. R. Zentel (1989) Angew Chem Adv Mater 101:1437
103. Vallerien SU, Zentel R, Kremer F, Kapitza H, Fischer EW (1989) Makromol Chem Rapid Commun 10:333
104. Semmler H, Finkelmann H (1994) Polym Adv Technol 5:231
105. Meier M, Finkelmann H (1990) Macromol Chem Rapid Comm 11:599
106. Vallerien SU, Kremer F, Fischer EW, Kapitza H, Zentel R, Poths H (1990) Makromol Chem Rapid Comm 11:593
107. Gebhard E, Brehmer M, Zentel R, Reibel J, Decher G, Brodowsky HM, Kremer F (1997) In: Nijenhuis K, Mijs W (eds) The Wiley Polymer Networks Group Review, vol 1. Wiley, Chichester, UK

11 Molecular Dynamics in Thin Polymer Films

L. Hartmann · K. Fukao · F. Kremer

11.1
Introduction

The structural and dynamic properties of thin supported and freely standing polymer films are in the focus of scientific discussion [1–4]. Up to now, broadband dielectric spectroscopy has turned out to be a convenient experimental access which enables one to measure directly the molecular fluctuations of polar moieties in these systems in an extraordinary broad frequency and temperature range. A further benefit results from the fact that its sensitivity increases with decreasing sample thickness and hence with decreasing amount of sample material.

Many studies pursue the question if the glass transition in the confinement of thin supported or freely standing polymer films is altered in comparison to that in the bulk material. This was done for instance by ellipsometry [5, 6], neutron and X-ray reflectivity measurements [7], positron annihilation life time spectroscopy (PALS) [8], thermal probe measurements [9], capacitive scanning dilatometry [11–13], thermal expansion spectroscopy [10, 14] and, in case of freely standing films, Brillouin light scattering [15, 16]. Both increases and decreases of the glass transition temperature T_g were found which are attributed to strong or weak interactions between the polymer and its boundary. Recently, several attempts were made to explain these observations within the scope of theoretical models [17–19] and computer simulations [20–22]. Based on the results for freely standing polystyrene films of high molecular weight, it was proposed by de Gennes [23, 24] that an additional mode besides the dynamics known from the bulk polymer is active in films with a thickness being comparable to the radius of gyration. This "sliding motion" of the polymer chains along their own contour originates from an enhanced mobility of chain segments if they are close to a free surface.

This chapter is structured as follows: Details of the preparation are given in Sect. 11.2. The results for thin films of two typical glass forming polymers, namely poly(methyl methacrylate) (PMMA) and polystyrene (PS) are discussed in Sect. 11.3. Whereas in thin films of PS only a dielectrically active α-relaxation is observable, in the case of PMMA the secondary β-relaxation can be studied as well. In Sect. 11.4 the application of dielectric spectroscopy to investigate the molecular dynamics in thin grafted films of poly(γ-benzyl-L-glutamate) (PBLG) is demonstrated. The techniques to graft polymers on surfaces have been devel-

oped recently and so far only information concerning the structure is available. Again, dielectric spectroscopy is used to provide a deeper insight into the molecular dynamics in such films.

11.2
Preparation and Methodical Aspects

11. 2.1
Preparation of Thin Polymer Films

Thin polymer films (Table 11.1) were prepared from solutions of the polymer in toluene or chloroform by use of the spin coating technique on aluminium-coated glass substrates. The film thickness was controlled by changing the concentration of the solution. Subsequently, the films were annealed above T_g under vacuum for several days to remove solvents and to let the as-spun films equilibrate.

An array of sample capacitors was obtained by evaporation of aluminium stripes being perpendicular to the ground electrodes onto the polymer film. Typical arrangements of sample capacitors are given in Fig. 11.1.

The film thickness was determined using the formula for the capacity of a flat-plate capacitor, $C' = \varepsilon' \varepsilon_0 A/d$, where ε' is the real part of the permittivity of the polymer, ε_0 is the permittivity of the vacuum, A is the area of electrodes (2.3 mm^2 and 8 mm^2 for thin films of isotactic PMMA and atactic PS respectively as well as 0.8 cm^2 and 3.1 cm^2 for bulk samples) and d is the film thickness. For the determination of d the limit of ε' at high frequencies, ε_∞, is used which is assumed to be independent of the film thickness. Respective values for ε' are found in [25, 26]. To determine the glass transition temperature T_g, supplemen-

Table 11.1. Molecular weight M_w, polydispersity index M_w/M_n, radius of gyration R_g and bulk glass transition temperature T_g^{bulk} of the glass forming polymers PS and PMMA. Data are taken from [12–14, 27, 34]

Polymer	M_w [g mol^{-1}]	M_w/M_n	R_g [nm]	T_g^{bulk} [K]
a-PS	6.67×10^6 [a]	1.22	79	373
	1.80×10^6 [b]	1.03	41	373
	2.80×10^5 [c]	– [d]	16	373
	3.60×10^4 [a]	1.06	6	370
	3.60×10^3 [a]	1.06	2	341
a-PMMA	4.90×10^5 [c]	4.11	18.6	373
i-PMMA	1.65×10^5 [a]	1.30	4.7	331
	4.50×10^4 [a]	1.21	8.9	331

[a] Polymer Source Inc.
[b] Aldrich Co. Ltd.
[c] Scientific Polymer Products, Inc.
[d] Data not available.
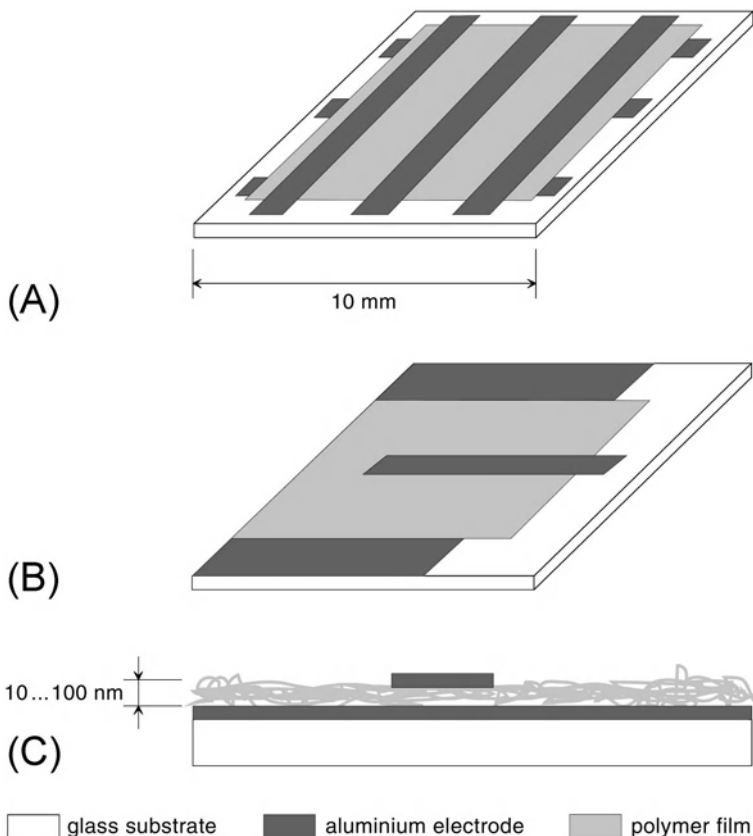
Fig. 11.1. A, B Arrangements of sample capacitors as used for the studies on thin films of iso-tactic poly(methyl methacrylate) [27] (A) and of atactic polystyrene, poly(vinyl acetate) and atactic poly (methyl methacrylate) [12–14, 34] (B), respectively. **C** Vertical section through the sample capacitor

tary ellipsometric studies were carried out on thin films of isotactic PMMA pre-pared on the SiO_x surface layer of silica wafers. This substrate had to be used since the results of ellipsometric measurements on aluminium do not allow an unambiguous determination of T_g for two reasons: (i) the contrast in the real part of the refractive indices of i-PMMA ($n \approx 1.4$) and aluminium ($n = 1.3 \ldots 1.4$ for $\lambda = 500 \ldots 600$ nm) is too low and (ii) the evaporated aluminium shows a quite uneven surface. Details of the ellipsometric studies on thin i-PMMA films on SiO_x are given in [27, 31, 32].

A detailed description of the preparation of grafted films is beyond the scope of this chapter; it can be found in [28]. Instead, we focus here on an alternative way to prepare the upper electrode, which has been successfully applied for the investigation of the dynamics in films of grafted PBLG [29]. The direct evapora-tion of the upper electrode has the drawback that a metal layer of about 70 nm

has to be deposited on an underlying organic film with a thickness in the order of 10 nm. Therefore, one cannot rule out that the films will be damaged by this treatment and show afterwards defects such as pinholes and cracks or artefacts caused by Schottky contacts. These disadvantages can be circumvented by use of freshly cleaved lamellae of mica being evaporated with aluminium as upper electrodes. This technique is demonstrated to be equivalent to the direct evaporation of upper electrodes [29].

Details concerning the measurement technique used in the studies which are summarized in this chapter can be found in [27, 34]. It should be noted that the resistance of the aluminium electrodes cannot be neglected because it forms a series circuit together with the sample capacitor. This causes an artificial loss process at frequencies typically greater than 10^5 Hz. Since this artefact can be described in the frequency domain by a simple Debye-type ansatz, the data can be corrected for it [30].

11.2.2
Thermal Expansion Spectroscopy

The experimental setup used for dielectric relaxation spectroscopy (DRS) can be employed as well for thermal expansion spectroscopy (TES) [11, 14]. The latter technique allows for investigation of the slow dynamics of the thermal expansivity and for the determination of T_g in both bulk [10, 11] and thin films [12–14]. Compared to ellipsometry, the combination of dielectric spectroscopy and thermal expansion spectroscopy offers the advantage to determine T_g and to investigate the α-relaxation at long relaxation times in thin polymer films on the identical sample. The determination of T_g can be carried out in two ways. In a ramping experiment the temperature dependence of the film thickness, $d(T)$, can be recorded. T_g is then defined as the temperature at which a kink occurs in $d(T)$ due to the change in the thermal expansion coefficient from the value of the glassy state to that of the liquid (capacitive scanning dilatometry, CSD [11–13]). The determination of T_g can be done as well by TES, i.e. by probing the dilatometric dynamics on a time scale of 100 s. The corresponding temperature is considered as T_g. For this purpose, the dependence of the thermal expansion coefficient on a sinusoidal modulation of the sample temperature $T(t) = \langle T \rangle + \Delta T_{\omega_T} e^{i\omega_T t}$ [11, 14] is measured. The response in capacitance with the same angular frequency ω_T as the temperature modulation is monitored within a linear approximation as

$$C'(t) = \langle C' \rangle - \Delta C'_{\omega_T} e^{i(\omega_T t + \theta)} \tag{11.1}$$

where $\omega_T = 2\pi\nu_T$ with ν_T being the frequency of temperature modulation, $\langle T \rangle$ is the average temperature, $\langle C' \rangle$ is the averaged capacitance, ΔT_{ω_T} is the amplitude of the temperature modulation with an angular frequency ω_T, $\Delta C'_{\omega_T}$ is the amplitude of the capacitive response with the same angular frequency ω_T and θ is the phase lag between the temperature modulation and the change in the capacitance.

For a flat-plate capacitor the geometrical capacitance in dependence on a temperature change ΔT is given by

$$C_0(T) \equiv \varepsilon_0 \frac{A}{d} \sim \varepsilon_0 \frac{A_0}{d_0}(1 + (2\alpha_t - \alpha_n)\Delta T) \tag{11.2}$$

and the real part of the permittivity is expressed by

$$\varepsilon'(\omega_E, T) = \varepsilon_\infty(T) + \Delta\varepsilon(\omega_E, T) \tag{11.3}$$

where ε_∞ is the real part of the permittivity in the high frequency limit, ω_E is the angular frequency of the electrical field, α_t and α_n are the linear thermal expansion coefficients parallel and normal to the surface of the thin polymer film, $\Delta T = T - T_s$ and T_s is a reference temperature. The term $\Delta\varepsilon$ in Eq. (11.3) is related to the dispersion of the dielectric loss due to molecular relaxation processes. The detection frequency, i.e. the frequency ν_E ($\omega_E = 2\pi\nu_E$) of the electrical field which is necessary to monitor the capacitance, has to be set to such a value that no relaxation process is present in a wide temperature range. Thus, the contribution $\Delta\varepsilon$ can be neglected in Eq. (11.3) and the temperature dependence of ε' is given by

$$\varepsilon'(T) = \varepsilon_\infty(T) \sim \varepsilon_\infty(T_s)(1 - \eta_0\alpha_n\Delta T) \tag{11.4}$$

where

$$\varepsilon_\infty(T_s) = \frac{1 + 2\xi_0}{1 - \xi_0} \tag{11.5}$$

$$\eta_0 \equiv \frac{3\xi_0}{(1 - \xi_0)(1 + 2\xi_0)} \tag{11.6}$$

$$\xi_0 \equiv \frac{1}{3\varepsilon_0}\sum_j N_j(T_s)\overline{\alpha_j} \tag{11.7}$$

Here, $N_j(T)$ is the number density at a temperature T and $\overline{\alpha_j}$ is the polarization of the j-th atom. Furthermore, the Clausius-Mossotti relation, $(\varepsilon_\infty - 1)/(\varepsilon_\infty + 2) = 1/3\varepsilon_0 \cdot \sum_j N_j \overline{\alpha_j}$ with $N_j(T) = N_j(T_s)(1 - \alpha_n\Delta T)$ is used and it is assumed that the films are constrained along the surfaces. Hence, for α_t and α_n holds

$$\alpha_t = 0 \quad \text{and} \quad \alpha_n = \frac{1 + \mu}{1 - \mu}\alpha_\infty \tag{11.8}$$

where μ is the Poisson ratio and α_∞ is the bulk linear coefficient of thermal expansion [13]. For example, in the literature [25] one finds for atactic polystyrene $\mu = 0.325$ and $\alpha_\infty = 0.57 \cdot 10^{-4}\,\text{K}^{-1}$ for $T < T_g$ and $\mu = 0.5$ and $\alpha_\infty = 1.7 \cdot 10^{-4}\,\text{K}^{-1}$ for $T > T_g$. Combining Eqs. (11.2), (11.4) and (11.8) one obtains the following relation for the linear thermal expansion coefficient normal to the

film surface α_n:

$$\alpha_n = -\zeta \frac{1}{C'(T_s)} \frac{dC'}{dT} = \zeta \frac{1}{C'(T_s)} \frac{\Delta C'_{\omega_T}}{\Delta T_{\omega_T}} e^{i\theta} \qquad (11.9)$$

where $C'(T)$ is the capacitance at a temperature T and T_s is a standard temperature. For atactic polystyrene $\zeta \approx 0.5$ was found [13].

As long as the response obeys the change in the external field without any delay, the phase lag θ in Eq. (11.1) is zero. However, in presence of a relaxation process with a characteristic time in the order of $1/\omega_T$ the phase lag θ is unequal to zero and α_n becomes a complex number which is denoted by $\alpha_n^* = \alpha'_n - i\alpha''_n$. Here, α'_n and α''_n are the real and the imaginary part of the complex thermal expansion coefficient.

Both DRS and TES measure the complex capacitance of thin films and can therefore be employed to obtain dynamical properties from the identical sample in a frequency range from 10^{-3} Hz to 10^4 Hz [14]. If $v_T = 0$ and v_E is varied at a fixed temperature, the complex dielectric permittivity is obtained. Thermal expansion spectroscopy is performed when v_T is varied at a given temperature and v_E is fixed to a value distinct from the rate $1/\tau_{\max}$ of any dielectric relaxation. For the measurements on atactic polystyrene which are presented in Sect. 11.3.2, the average temperature $\langle T \rangle$ is controlled to increase with a constant rate of 0.1 Kmin^{-1} or 0.5 Kmin^{-1}. The amplitude ΔT_{ω_T} is set between 0.2 K and 0.6 K. For the capacitance measurements in the TES measurements the frequency v_E is set to 100 kHz.

11.3
Thin Films of Glass Forming Polymers

11.3.1
Poly(methyl methacrylate) (PMMA)

Studies on PMMA in thin films revealed that the thickness dependence of the glass transition temperature, $T_g(d)$, as determined by ellipsometry [6, 31] or thermal probe analysis [9], is strongly influenced by the interaction of PMMA with the underlying substrate. With decreasing film thickness, Keddie et al. found a decrease in T_g of PMMA films on gold, whereas T_g remains almost constant with tendency for a slight increase if the films were deposited on SiO$_x$ [6]. Grohens et al. demonstrated that T_g increases in thin films of atactic and isotactic PMMA (a- and i-PMMA) while it decreases in case of syndiotactic PMMA (s-PMMA) [31, 32]. These findings do not depend on the substrates used in these studies (silicon- or aluminium-wafers). In case of i-PMMA an increase of T_g of 40 K was found for a film thickness of 20 nm. At this film thickness, the value of the T_g shift in all other studies was about 15 K for both increases or decreases of T_g. Fryer et al. proved that the increase in T_g in thin films on SiO$_x$ can be switched to a decrease by a treatment of the substrate surface with hexamethyldisilazane (HMDS) (silanisation). Prucker et al. found a de-

crease of T_g in thin films of PMMA on silanised SiO_x substrates independent on the inner architecture of the PMMA film [33]. In this study, spin-cast, grafted and Langmuir-Blodgett-Kuhn films were compared by measuring the temperature dependence of the refractive index and the film thickness by means of optical waveguide spectroscopy.

A recent dielectric study analyses the influence of a confinement given by the thin film geometry on both the α- and the β-relaxation in films of a-PMMA (Table 11.1) [34]. The molecular mechanism of both relaxation processes in the bulk is elucidated by multi-dimensional NMR measurements (see Chap. 18). For thin films of a-PMMA it is found that the temperatures T_α and T_β corresponding to the maximum of the dielectric loss ε''_{max} at a given frequency of the electrical field decrease linearly by about 20 K below a critical film thickness d_c. Above d_c, almost no change is found with respect to the bulk values. It is expected that the thickness dependence of T_g is qualitatively the same like the thickness dependence of T_α. The surprising decrease of T_β is attributed to a strong correlation between the α- and the β-relaxation despite the fact that both processes are well separated in the activation plot. The same value of the critical thickness d_c holds for both relaxation processes and compares well to the radius of gyration R_g of the bulk polymer ($d_c \approx R_g = 18.6$ nm). The change of the thickness dependence of T_α at d_c is explained by assuming that the "sliding motion" of the polymer chains along their own contour as proposed by de Gennes [23, 24] becomes important for thicknesses below d_c. This motion can be prevented in the bulk due to blocked end monomers whereas it is not impeded in thin films where monomers close to free surfaces possess a high mobility. However, the dependences of T_α and T_β on the molecular weight M_w in thin films of a-PMMA have still to be measured in order to prove this conjecture [34]. The findings for T_α and T_β are consistent with the result that in the activation plot both processes are shifted to higher values of the relaxation rate with decreasing film thickness. While the β-process is found to be only weakly broadened in both the frequency and the temperature domain, a considerable broadening is found for the α-process in the temperature domain in accordance with results for thin films of atactic polystyrene (a-PS) and poly(vinyl acetate) (PVAc) [14, 34]. For the β-relaxation in a-PMMA as the dominating process with respect to the dielectric strength $\Delta\varepsilon$ it is found that $\Delta\varepsilon$ decreases with decreasing film thickness. The same tendency holds for the α-relaxation in thin films of PVAc. However, the α-process in thin films of a-PMMA has not been analysed in the frequency domain in terms of fits according to the empirical fit function of Havriliak and Negami (Eq. 11.10) since it is weak compared to the β-relaxation.

Therefore, i-PMMA has been chosen to study its dynamics in thin films since the α-process is dominating with respect to the dielectric strength. Although it is known that i-PMMA tends to crystallize for low molecular weights [35], no hint of crystallisation was found by DSC measurements on bulk samples of the molecular weights used in this study.

Figure 11.2 displays the dielectric loss ε'' vs frequency for a film of 20 nm thickness of i-PMMA with a molecular weight of $M_w = 164,700$ g mol^{-1}. Dielectric data were analysed only up to 10^5 Hz since for higher frequencies an additional loss peak dominates the spectra which is due to the non-negligible re-
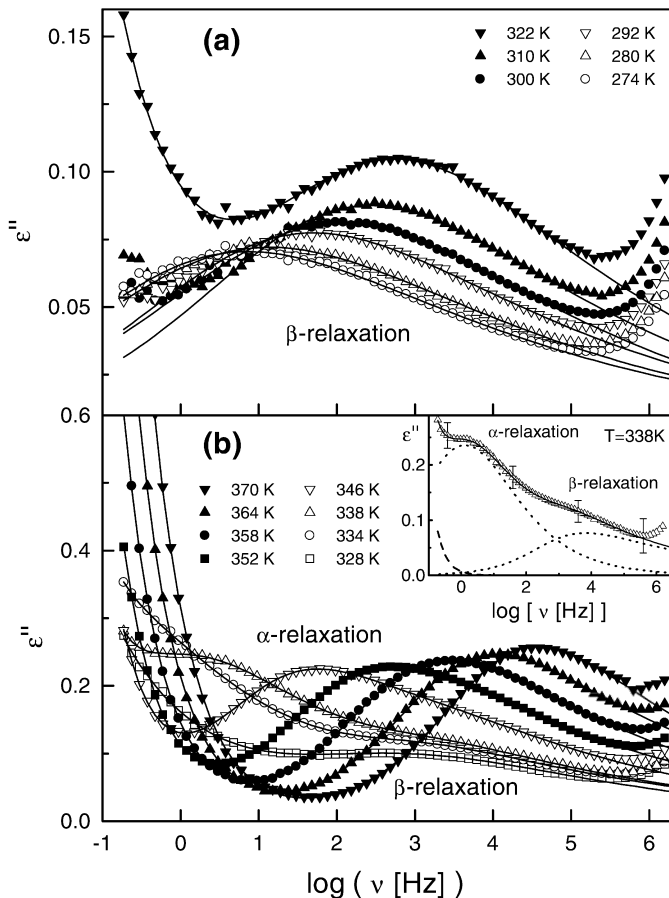
Fig. 11.2. Dielectric loss ε'' vs frequency for i-PMMA (sample thickness $d = 20$ nm, $M_w = 164{,}700$ g mol^{-1}) at temperatures as indicated: **a** only the β-relaxation is present. For $T = 322$ K the high frequency wing of the α-relaxation appears; **b** spectra at temperatures within and above the merging region. *Solid lines* represent fits according to the Havriliak-Negami equation (Eq. 11.10). The *inset* illustrates the superposition (*solid lines*) of the α- and the β-relaxation (*dotted lines*) and a conductivity contribution (*dashed line*) for $T = 338$ K. Note the different scales for ε'' in Fig. 2a,b

sistance of the evaporated aluminium electrodes [30]. However, this artefact process turns out to have only a weak influence on the molecular relaxation processes. For elevated temperatures ($T \geq 340$ K) a conductivity contribution at low frequencies has to be considered. At low temperatures ($T < 330$ K, Fig. 11.2a) the spectra are characterised by a weak and broad β-relaxation. Above T_g, the β-relaxation appears as a shoulder of the comparatively stronger α-relaxation. At around 350 K both processes have merged to one process whose amplitude increases while its width tends to decrease with increasing temperature

(Fig. 11.2b). Solid lines in Fig. 11.2 are fits according to the empirical fit function of Havriliak and Negami (HN-equation) [36]:

$$\varepsilon''(\omega) = \frac{\sigma_0}{\varepsilon_0}\frac{a}{\omega^s} - \sum_{\alpha,\beta\text{-relax.}} \mathrm{Im}\left[\frac{\Delta\varepsilon}{(1+(i\omega\tau_{\mathrm{HN}})^{\alpha_{\mathrm{HN}}})^{\gamma_{\mathrm{HN}}}}\right] \tag{11.10}$$

Here, $\Delta\varepsilon$ denotes the dielectric strength, τ_{HN} is an apparent relaxation time, α_{HN} and γ_{HN} are shape parameters describing the symmetric and the asymmetric broadening of the loss peak. σ_0 is the d.c. conductivity, ε_0 is the permittivity of the vacuum and $\omega = 2\pi v$ is the angular frequency of the applied electrical field. The exponent s equals one for ohmic behaviour; deviations ($s < 1$) are caused by electrode polarization and a is a factor having the dimension $(\mathrm{Hz})^{-1}(\mathrm{rad\ Hz})^s$. A superposition of two peaks according to Eq. (11.10) as proposed in [37, 38] is used to fit the data in the merging region of the α- and the β-relaxation, whereas one process is sufficient for spectra above and below this region.

To extend the analysis of the α-relaxation towards T_g one has to obtain spectra which do not show the conductivity contribution. This is achieved by applying a data transformation proposed in [39]:

$$\varepsilon''_{\mathrm{deriv}}(\omega) = -\frac{\pi}{2}\frac{\partial\varepsilon'(\omega)}{\partial\ln\omega} \tag{11.11}$$

Figure 11.3a demonstrates the application of Eq. (11.11) for films of various film thickness at a constant temperature. The low frequency wing of the α-relaxation can now be analysed. Solid lines represent HN-fits according to Eq. (11.10); for $d = 20$ nm the decomposition into the α- and the β-relaxation is demonstrated. A weak shoulder at around 100 Hz in some curves in Fig. 11.3a is caused by the differentiation of noisy data of $\varepsilon'(\omega)$ and has no physical meaning. The solid vertical line indicates the maximum position of the α-relaxation for the bulk sample. The corresponding value for thin films of i-PMMA is shifted to higher frequencies when the film thickness decreases. Furthermore, it is found that the dielectric strength $\Delta\varepsilon$ of the α-relaxation is reduced in thin films whereas that of the β-relaxation remains almost constant. In Fig. 11.3b, relaxation time distributions $g(\log(\tau))$ are given for the spectra of Fig. 11.3a. They are related to the dielectric loss ε'' by

$$\varepsilon''(\omega) = \Delta\varepsilon \int_{-\infty}^{\infty} \frac{g(\log(\tau))\omega\tau}{1+\omega^2\tau^2}\,\mathrm{d}(\log\tau) \tag{11.12}$$

and can be either calculated from a set of HN-fit parameters [40] or can be extracted directly from the data using the Tikhonov regularization algorithm [41]. The inset in Fig. 11.3b shows the relaxation time distribution obtained by both techniques as a check of consistence. In Fig. 11.3b, the distributions reveal two peaks corresponding to the α- and β-relaxation. The latter is not influenced by the decrease of the film thickness whereas the maximum position of the former is shifted to shorter times and its strength $\Delta\varepsilon$ is decreased when the film thick-
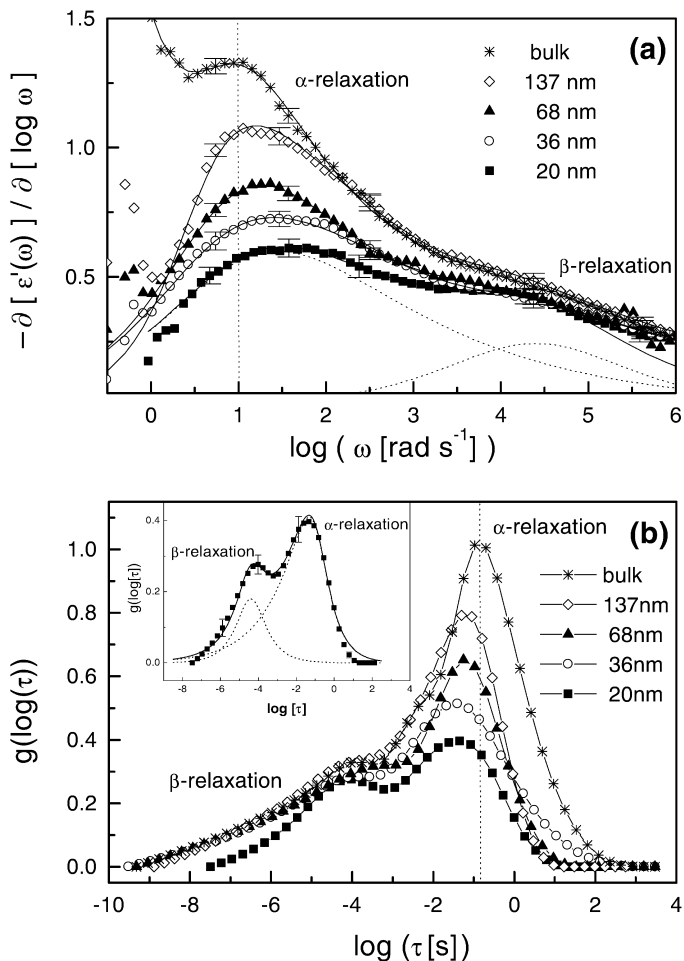
Fig. 11.3. **a** Derivative $-\partial\varepsilon'(\omega)/\partial\log\omega$ vs frequency according to Eq. (11.11) for i-PMMA (M_w = 164,700 g mol^{-1}) at 339 K for thicknesses as indicated. The *solid lines* are HN-fits according to Eq. (11.10); for d = 20 nm the decomposition into the α- and the β-relaxation is shown. **b** Relaxation time distributions obtained by the *Tikhonov* regularization for the spectra shown in (a). The *inset* compares for d = 20 nm the *Tikhonov* distribution (*symbols*) to that calculated by use of the HN fit parameters. The *dotted lines* correspond to the individual relaxation processes, their sum is given by the solid line. *Vertical dotted lines* are used to indicate the maximum values for the bulk

ness is reduced. It turns out that the decrease of $\Delta\varepsilon$ affects mainly the long term wing (i.e. $\tau \geq \tau_\alpha^{max}$ where τ_α^{max} is the maximum of the α-relaxation in the bulk) whereas the short term wings ($\tau \geq \tau_\alpha^{max}$) of all distributions nearly coincide. Thus, the shift of the maximum corresponding to the α-relaxation is related to a weakening of the relaxation time distribution at long times τ. This behaviour is different from findings for low molar mass glass forming liquids where an anal-
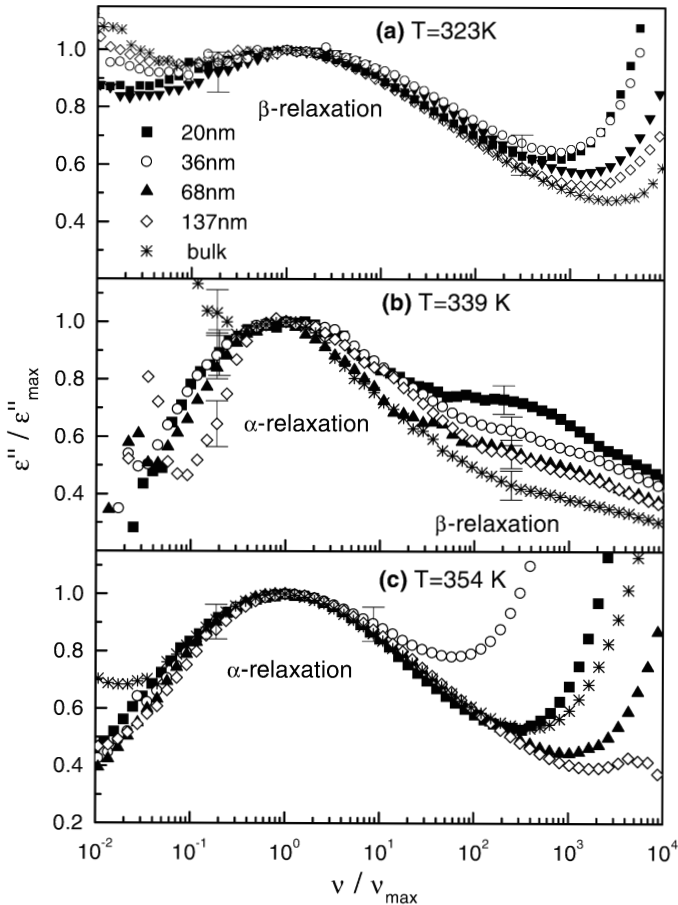
Fig. 11.4. Dielectric spectra of i-PMMA, normalized with respect to the maximum frequency ν_{max} and the maximum of the dielectric loss, ε''_{max}: **a** 323 K, β-relaxation; **b** 339 K, α- and β-relaxation; **c** 354 K, α-relaxation (M_w = 164,700 g mol^{-1}). The increase of $\varepsilon''/\varepsilon''_{max}$ at high frequencies is an artefact due to the non-negligible resistance of electrodes

ogous analysis yields a dynamics being on an absolute scale faster in the confinement than in the bulk (see [42] and references therein).

Figure 11.4 displays spectra for various values of the film thickness which are normalized with respect to their maximum position at three different temperatures which are representative for the β-relaxation (Fig. 11.4a), the merging region (Fig. 11.4b) and the α-relaxation above the merging region (Fig. 11.4c). In Fig. 11.4b a broadening of the α-relaxation is observed which has been found in other studies as a typical feature of the dynamics in confinement for both low molar mass substances [42] and polymers [12–14, 34].

Figure 11.5 shows the activation plot for films of various thickness of two molecular weights. The β-relaxation obeys the Arrhenius law and no depen-
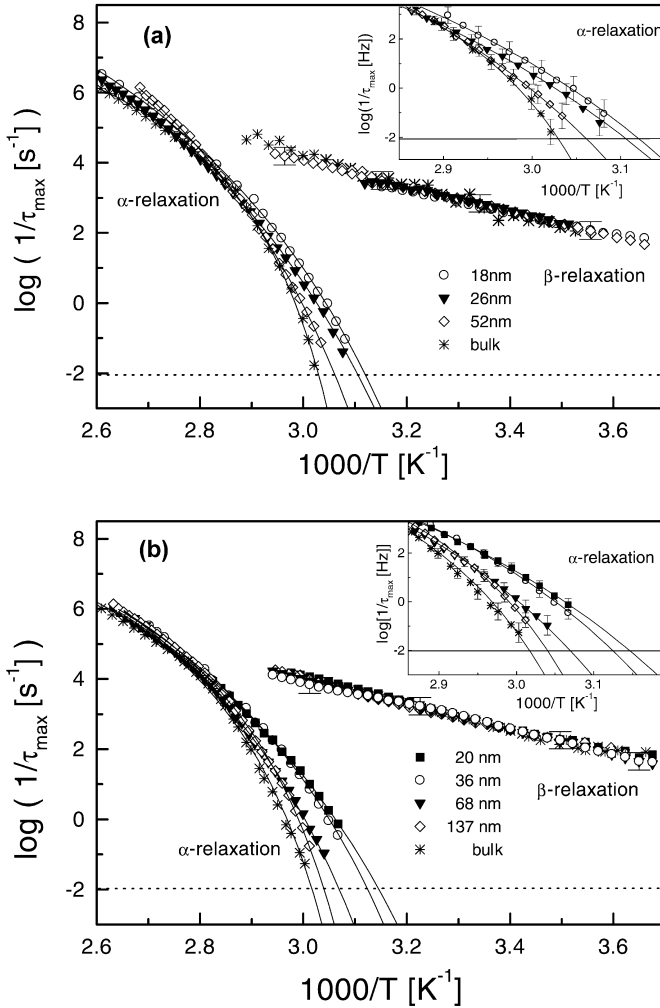
Fig. 11.5. Activation plot: logarithm of the relaxation rate $1/\tau_{max}$ vs 1000/T for i-PMMA in thin films of thicknesses as indicated: **a** $M_w = 44{,}900 \text{ g mol}^{-1}$; **b** $M_w = 164{,}700 \text{ g mol}^{-1}$. The *solid lines* represent fits according to the VFT equation (Eq. 11.13). In the *insets* the α-relaxation around T_g is enlarged in order to demonstrate the shift of the relaxation time τ_{max} to shorter times with decreasing film thickness. T_g is determined as the temperature at which the VFT fits yield $\tau_{max} = 100 \text{ s}$

dence on the film thickness was found confirming the local character of this relaxation process. The traces of the α-relaxation can be well fitted to the Vogel-Fulcher-Tammann (VFT) equation [43–45]

$$\log(1/\tau_{max}) = \log(1/\tau_0) - \frac{U}{T - T_0} \tag{11.13}$$
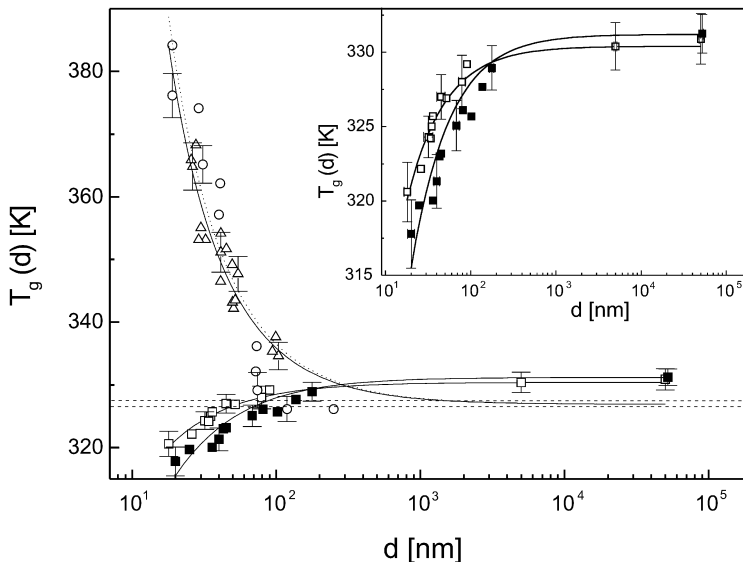
Fig. 11.6. Thickness dependence of the glass transition temperature T_g as obtained by ellipsometry (*open circles, open triangles*) and dielectric spectroscopy (*open squares*) for i-PMMA ($M_w = 44{,}900$ g mol^{-1}). (*Open triangles*) represent our own ellipsometric measurements whereas (*open circles*) are taken from [32]. Additionally, the dielectric results for the higher molecular weight of $M_w = 164{,}700$ g mol^{-1} are shown (*filled squares*). The *inset* magnifies the dielectric data for both molecular weights in order to show more details. The *solid and dotted lines* are fits according to Eq. (11.15), values for the fit parameters are shown in Table 11.2. The *dashed horizontal lines* indicate the glass transition temperature of the bulk samples as measured by DSC (*upper line*: $M_w = 164{,}700$ g mol^{-1}, *lower line*: $M_w = 44{,}900$ g mol^{-1})

where U denotes a constant which is related to the fragility, T_0 is the Vogel-Fulcher temperature and τ_0 is the relaxation time in the limit of high temperatures. Only data below the merging region were considered for the VFT-fits. For each film of a thickness d, the glass transition temperature T_g is defined as the temperature where the relaxation time τ_{max} is equal to 100 s. This way to determine T_g of thin polymer films has already been applied in previous studies [14, 18]. It should be noted that the determination of T_g by use of capacitive scanning dilatometry [11] or thermal expansion spectroscopy [14] fails in case of i-PMMA due to the presence of the dielectrically active β-relaxation.

From Fig. 11.5 it can be seen that in the vicinity of the bulk glass transition temperature the time τ_{max} of the α-relaxation is shifted to shorter times, while at high temperatures the traces for all films and for bulk coincide. This decrease of τ_{max} whose origin has been discussed with respect to Fig. 11.3, leads to a shift of T_g to lower temperatures with decreasing film thickness. For the higher molecular weight this shift is more pronounced and it already sets in at higher temperatures.

Figure 11.6 summarizes the thickness dependences of T_g obtained for two molecular weights by dielectric spectroscopy and ellipsometry, respectively. For

details of the latter see [27, 31, 32]. Against the background of the apparently contradicting thickness dependences in Fig. 11.6, the differences concerning the polymer-substrate interfaces have to be pointed out: while the polymer is embedded by aluminium for dielectric measurements, it forms interfaces with a SiO$_x$ layer and with air in case of the ellipsometric measurements. For i-PMMA on SiO$_x$ an increase of T_g of about 70 K for a film thickness of about 20 nm is found by means of ellipsometry. In this case, our ellipsometric measurements confirm analogous studies of Grohens et al. [31, 32]. In contrast, the dielectric studies for supported capped films of i-PMMA on aluminium lead to a decrease of T_g of about 10 K for the thinnest films. At the moment we can only attribute this different behaviour to a pronounced change of the interaction between i-PMMA and the substrate when the latter is changed from SiO$_x$ to aluminium. In case of both PS and PMMA it has been shown that chemically different substrates [6], surface modification [9] or variation of tacticity [31, 32] strongly influence the value of the T_g shift and its sign. Moreover, AFM measurements on both substrates reveal a higher mean roughness for the evaporated aluminium (2.6 nm) than for the Si wafer (1 nm). This difference can weaken the strong adsorption which was observed for i-PMMA on SiO$_x$.

Here, we will focus on the results of dielectric measurements which raise the question for the molecular origin of the decrease of T_g in thin films with respect to the bulk value. This question is discussed in conjunction with a model recently developed by Herminghaus et al. [18]. The authors explain the shift of T_g found for thin films of amorphous a-PS of low molecular weight ($M_w \sim 10^3$ g mol^{-1}), i.e. the radius of gyration is small compared to the film thickness even for the thinnest films. Furthermore, the polymer has to be amorphous and should not show any tendency to crystallize. Since both requirements are fulfilled for i-PMMA of the molecular weights used in this study, the model of Herminghaus should be applicable to describe the dependence of T_g as revealed by dielectric spectroscopy. In previous studies [13, 16] no significant difference in the thickness dependence of T_g for supported films which are covered by an evaporated layer of the substrate material (supported *capped* films [16]) and films with a free surface (supported *uncapped* films [16]) was found. Thus, the adoption of this model is not affected by the presence of an upper electrode evaporated onto the films.

The model is described in detail in [18]. It relates the thickness dependence of the glass transition temperature T_g to Young's elastic modulus E and to the surface tension σ of the polymeric material in the thin film:

$$T_g(d) = T_g^{\text{bulk}} \left(1 + \frac{1.16\sigma}{dE} \right)^{-1} \tag{11.14}$$

where T_g^{bulk} is the bulk glass transition temperature and σ was set to 40 mN m^{-1} [26]. In several previous studies [13, 32, 46] the dependence of T_g on the thickness d was described phenomenologically by

$$T_g(d) = T_g^{\text{bulk}} (1 + \xi/d)^{-1} \tag{11.15}$$

For the fitting parameter ξ it was assumed up to now that it is related to the segment length of the polymer. Within the framework of the model given by Herminghaus et al. [18], ξ is now given by the ratio σ/E with E being the only fit parameter in Eq. (11.14). For PS of several molecular weights, ξ was obtained in the range between 0.33 nm and 0.82 nm [13, 18, 46], but no significant dependence of ξ on the molecular weight was found.

The solid lines in Fig. 11.6 are obtained by fitting Eq. (11.14) respectively Eq. (11.15) to the data. By changing the sign of the term ξ/d in Eq. (11.15), an increase of T_g can be described as well. For the fitting procedure, T_g^{bulk} was fixed either to the value obtained from dielectric measurements on bulk samples or, for the ellipsometric data sets, to the value obtained by DSC measurements. Results of fits to both the dielectric and the ellipsometric data sets are listed in Table 11.2. The fit parameters obtained for the ellipsometric measurements are in agreement with those given in [32]. Thus, we can state that the values obtained for ξ in the case of the dielectric measurements are well comparable to those given in the literature for PS of comparable molecular weight.

Further on, the values obtained for the modulus E are in the same order of magnitude (some ten MPa) like those obtained by Herminghaus et al. [18] for a-PS. It should be noted here that this model predicts, if any, a weak dependence of $\xi \sim \sigma/E$ on the molecular weight M_w, since E depends weakly on M_w. This forecast is confirmed by experiments [13, 18]. Since the values for ξ in case of thin films of i-PMMA are comparable to those of a-PS (with similar errors), we follow the conclusion given in [13] that ξ is independent on the molecular weight within experimental uncertainty. It turns out to be difficult to investigate further molecular weights since for smaller values of M_w crystallization becomes important while higher molecular weights of *isotactic* PMMA are not available to our best knowledge.

Recently, Long and Lequeux proposed a thermodynamic model which describes the glass transition by percolation of small domains of slow dynamics [19]. Thus, the heterogeneous dynamics in the bulk and increases or decreases of T_g in films which interact strongly or weakly with an underlying substrate are explained. This model requires two independent fit parameters: the volume of

Table 11.2. The values for the parameters T_g^{bulk}, ξ and E resulting from the best fit to Eq. (11.14) and Eq. (11.15), respectively for the thickness dependence of the glass transition temperature $T_g(d)$ as found for thin films of i-PMMA by dielectric spectroscopy and ellipsometry

Dielectric data, $\sigma = 40$ mN m^{-1}

M_w [g mol^{-1}]	T_g^{bulk} [K]	ξ [nm]	E [MPa]
44,900	330.6	0.56 ± 0.10	71.2 ± 4.5
164,700	331.2	0.86 ± 0.15	46.6 ± 5.8

Ellipsometric data, $M_w = 44,900$ g mol^{-1} ($T_g^{\text{bulk}} = 326.9$)

Source	ξ [nm]
[32]	2.9 ± 0.2
Present data	2.7 ± 0.1

small viscous domains and the number of monomers which is necessary to ensure that a domain is in the viscous state. It is possible to reproduce the thickness dependence of T_g as measured by dielectric relaxation spectroscopy resulting in fit parameters comparable to those given in [19]. However, this model fails to describe the increase of T_g by a single set of fit parameters for all thicknesses in case of the ellipsometric measurements performed on thin i-PMMA films on SiO_x.

In Fig. 11.7 the thickness dependence of the dielectric strength, $\Delta\varepsilon(d)$, as obtained from HN fits (Eq. 11.10) is displayed for both the α- and the β-relaxation. In consistence with the spectra shown in Fig. 11.3, the β-relaxation turns out to be uninfluenced by geometric confinement: $\Delta\varepsilon^{(\beta)}$ is independent of the film thickness. Above the merging region, the values of $\Delta\varepsilon^{(\alpha)}$ for the α-relaxation decrease with decreasing film thickness. For all values of the film thickness d, the dielectric strength $\Delta\varepsilon^{(\beta)}$ is proportional to the inverse temperature according to the Onsager equation with the approximation of $\Delta\varepsilon \approx \varepsilon_\infty$:

$$\Delta\varepsilon^{(\alpha)} = \frac{2}{5}(\varepsilon_\infty + 2)^2 \frac{n\, g_{KF}\, \mu^2}{9\varepsilon_0\, k_B T} \tag{11.16}$$

Here, n is the number density of dipoles, μ is the molecular dipole moment, k_B is the Boltzmann constant, g_{KF} is the Kirkwood-Fröhlich correlation factor, ε_∞ is the high frequency limit of the permittivity, ε_0 is the vacuum permittivity and T is the temperature. The results for $\Delta\varepsilon^{(\alpha)}$ and $\Delta\varepsilon^{(\beta)}$ may be interpreted in the picture of cooperative motion for the α-relaxation in an analogous manner to that given in [34]. It is assumed for the α-relaxation that N neighbouring dipoles relax cooperatively. The number N is expected to be proportional to the dimension of regions in which this cooperative motion takes place. Replacing n and μ in Eq. (11.16) by n/N and $N\mu$, respectively yields $\Delta\varepsilon^{(\alpha)}_{coop} = N\Delta\varepsilon^{(\alpha)}$ for the relaxation strength in case of cooperative motions. These cooperative motions are restricted in the regions close to the electrodes. Therefore, the intrinsic length scale of the α-relaxation and the number N may be decreased in the interfaces. Thus, the dielectric strength $\Delta\varepsilon^{(\alpha)}$ in these regions is expected to be smaller than in the bulk. This picture can be considered by describing the thin film as a sequence of three layers. A layer of totally immobilized chains forms each interface. The total (temperature-independent) thickness of both layers is d_i and their permittivity is equal to ε_∞. Between these immobilized layers there is a layer of a thickness $d - d_i$ possessing a permittivity of $\varepsilon_\infty + \Delta\varepsilon_{bulk}$. The calculation of the total dielectric strength $\Delta\varepsilon(d)$ of the α-relaxation yields

$$\Delta\varepsilon(d) = \Delta\varepsilon_{bulk}\left(1 - \frac{d_i}{d}\left(1 + \frac{\Delta\varepsilon_{bulk}}{\varepsilon_\infty}\right)\right) \tag{11.17}$$

In Eq. (11.17) it is assumed that $d_i \Delta\varepsilon/d\varepsilon_\infty \ll 1$. In Fig. 11.7, the temperature dependences of the dielectric strength of the bulk are fitted to a linear function as justified by Eq. (11.16). The solid lines to describe the dielectric strength of the thin films are reproduced by combining Eq. (11.17) with the temperature dependences of $\Delta\varepsilon_{bulk}$. Results for the thickness of the immobilized layers are given in Table 11.3. The fact that $\Delta\varepsilon^{(\beta)}$ does not depend on the film thickness is consistent with the local character of this relaxation process.
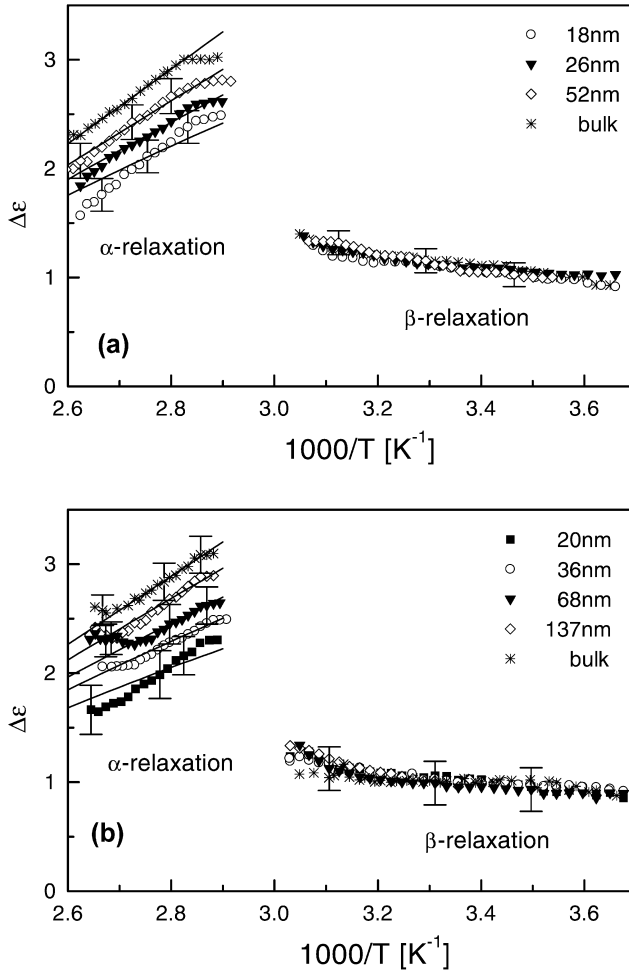
Fig. 11.7. Dielectric strength $\Delta\varepsilon$ of i-PMMA as obtained from HN fits to the isothermal dielectric loss data: **a** M_w = 44,900 g mol^{-1}; **b** M_w = 164,700 g mol^{-1}. The data for the β-relaxation coincide within the experimental uncertainty for all values of the film thickness d, whereas the α-relaxation displays a pronounced thickness dependence. This allows for the calculation of a total thickness d_i of immobilized layers according to Eq. (11.17). The *solid lines* describing the temperature dependence of $\Delta\varepsilon$ of thin films are obtained by combining Eq. (11.17) and linear fits to $\Delta\varepsilon$ of the bulk. Within the merging region of the α- and β-relaxation only ambiguous fit results for $\Delta\varepsilon$ were obtained which are omitted in this figure

Table 11.3. Values for the thickness d_i of layers of immobilized chains and corresponding thicknesses of films of i-PMMA (M_w = 164,700 g mol^{-1} and M_w = 44,900 g mol^{-1}). The values for d_i were obtained from fitting the temperature and thickness dependence of the dielectric strength $\Delta\varepsilon$ to Eq. (11.17)

M_w = 164,700 g mol^{-1}		M_w = 44,900 g mol^{-1}	
D [nm]	d_i [nm]	d [nm]	d_i [nm]
137	9.5 ± 1.2	–	
68	9.5 ± 1.2	52	5.3 ± 0.5
36	8.7 ± 0.9	26	4.5 ± 0.4
20	6.9 ± 0.8	18	4.5 ± 0.4

In the activation plot it is found that the traces of the α-relaxation split for the different film thicknesses. It is therefore expected that also the fragility m as a measure of the non-Arrhenius character [47] is dependent on the film thickness d. The fragility m is defined as

$$m = \left(\frac{\mathrm{d}\log\tau_\alpha(T)}{\mathrm{d}(T_g/T)} \right)_{T=T_g} \tag{11.18}$$

Here, the inverse of the relaxation rate $1/\tau_{\max}$ is chosen as $\tau_\alpha(T)$ and T_g is the temperature at which $\tau_\alpha(T)$ = 100 s is satisfied.

Figure 11.8 displays the Angell plot for the α-relaxation in thin films of i-PMMA of various film thickness. In this representation the fragility m is obtained as the slope of the curves in the point ($T = T_g$; $\tau_\alpha(T)$ = 100 s). A further analysis yields that m decreases with decreasing film thickness. Values for the fragility index m are given in Table 11.4. A similar result is obtained for the α-relaxation in thin films of atactic polystyrene (Fig. 11.13). The findings concerning the thickness dependence of the fragility index m are interpreted below as tendency of the thermal activation towards an Arrhenius dependence.

Compared to a recent dielectric study on thin films of a-PMMA [34] one has to state that there are some pronounced differences between both studies with respect to their results. The thickness dependence of T_g is a continuous decrease for thin films of i-PMMA which can be described by Eq. (11.15). In contrast, the temperature T_α in [34] which should behave qualitatively similar to T_g is almost constant above a critical film thickness d_c whereas T_α decreases linearly for below d_c. It is found for the β-relaxation that both the relaxation time and the dielectric strength depend on the film thickness whereas these quantities remain uninfluenced in thin films of i-PMMA.

Studies on freely standing films [17] of atactic polystyrene reveal that the dependence of T_g on the film thickness strongly depends on the molecular weight. A consistent result concerning the dynamics of the α-relaxation in thin films is obtained by means of dielectric spectroscopy [12–14, 34] for supported films of atactic polystyrene and poly(vinyl acetate) as described below. It is therefore
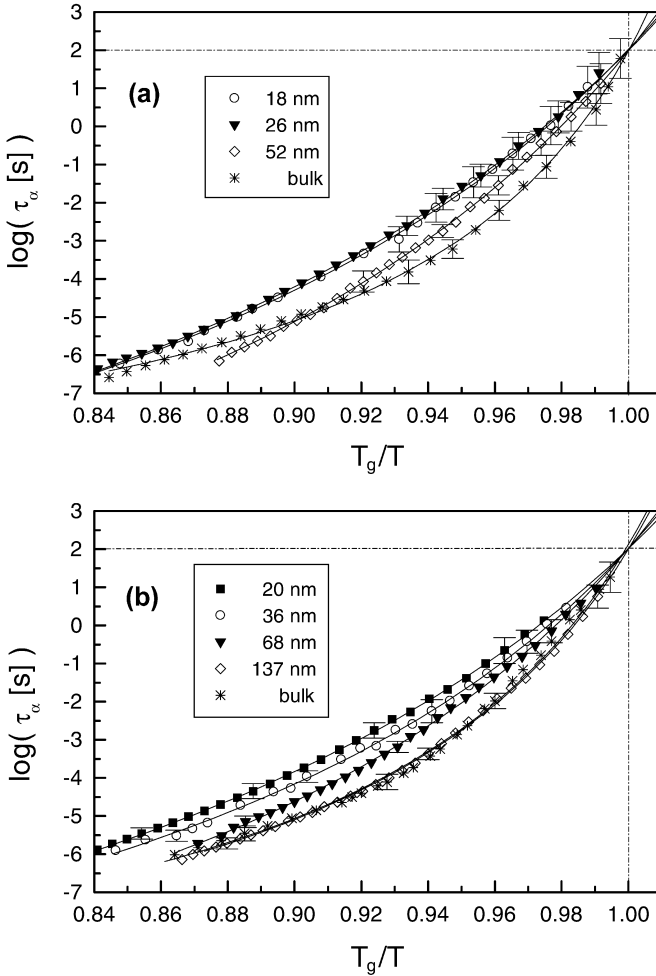
Fig. 11.8. The dependence of $\log \tau_\alpha$ on the inverse of the reduced temperature T_g/T for thin films of i-PMMA: **a** $M_w = 44{,}900$ g mol^{-1}; **b** $M_w = 164{,}700$ g mol^{-1}. The values of T_g are obtained by the relation $\tau_\alpha(T_g) = 100$ s. The fragility index m can be determined from this plot as the derivative $\left(\dfrac{\mathrm{d} \log \tau_a(T)}{\mathrm{d}\,(T_g/T)} \right)_{T=T_g}$ *Dashed-dotted lines* represent the values $\tau_\alpha = 100$ s and $T = T_g$, respectively

Table 11.4. Values for the fragility index m in dependence on the film thickness for thin films of i-PMMA ($M_w = 164{,}700$ g mol^{-1} and $M_w = 44{,}900$ g mol^{-1}). The quantity m is determined from data represented in Fig. 11.8 according to Eq. (11.18)

$M_w = 164{,}700$ g mol^{-1}		$M_w = 44{,}900$ g mol^{-1}	
d [nm]	m	d [nm]	m
20	96	–	–
36	105	18	93
68	114	26	88
137	128	52	109
Bulk	138	Bulk	139

assumed that the different experimental results are due to the differences in the molecular weight (Table 11.1), due to the different tacticity of the investigated PMMA and due to the fact that in case of a-PMMA film thicknesses above and below the radius of gyration R_g were obtained whereas for i-PMMA only films with a thickness greater than R_g could be investigated.

11.3.2
Atactic Polystyrene (a-PS)

Atactic polystyrene (a-PS) is the best explored polymer concerning its static and dynamic properties in thin freely standing or supported films [1–4]. In these studies, typically the temperature dependence of the film thickness, $d(T)$, and thus the glass transition temperature T_g was determined as described above. This was accomplished by experimental techniques such as ellipsometry [5, 6], X-ray and neutron reflectivity measurements [7] or, in case of freely standing films, by Brillouin light scattering [15, 16]. For a-PS it was found consistently by these different methods that T_g decreases when the film thickness is reduced. However, these studies yield macroscopic quantities only and do not lead to an understanding of the microscopic mechanism. This shortcoming is partially removed by the combination of TES and DRS which allows one to determine the glass transition temperature of thin a-PS films as well. At the same time, these techniques grant access to the dynamics of the α-relaxation over a wide frequency range on the identical sample [12–14].

Figure 11.9 displays spectra of the dielectric loss ε'' vs frequency ν for the α-relaxation of a-PS at various temperatures for three different values of the film thickness d. To study the relaxation behaviour of the α-relaxation in thin films in more detail, spectra are normalized with respect to both the maximum position ν_{max} and the peak height ε''_{max} (Fig. 11.10). Thus, for each film thickness the spectra of various temperatures above T_g can be reduced to a single master curve.

In Fig. 11.10 the arrows indicate the value $\varepsilon''/\varepsilon''_{max} = 0.5$ for each thickness and thus the full width at half maximum (FWHM) of the corresponding loss peak. To investigate the thickness dependence of the width quantitatively, each
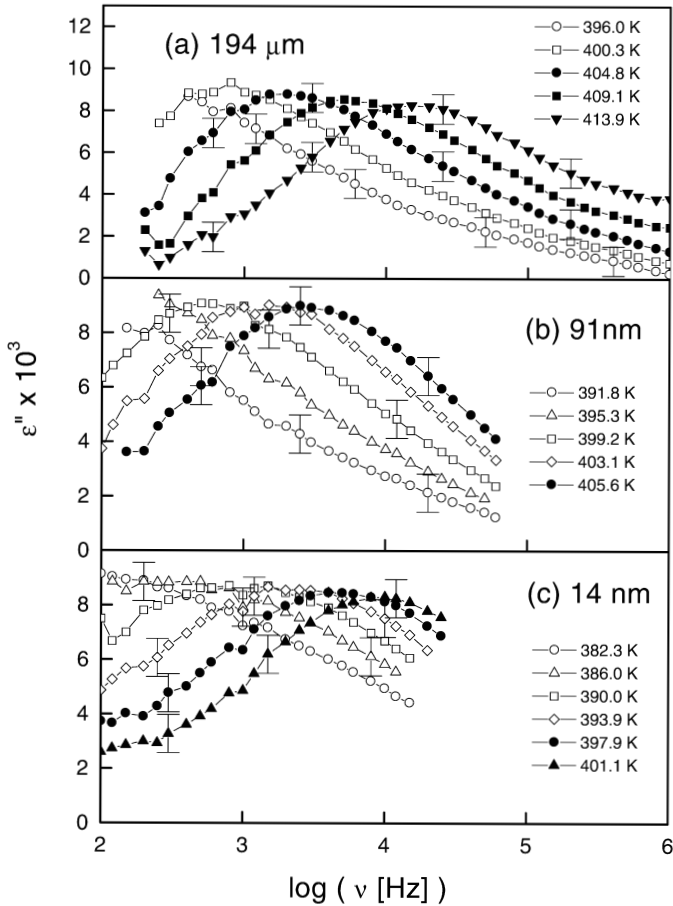
Fig. 11.9. Dielectric loss ε'' vs frequency for thin films of a-PS ($M_w = 1.8 \times 10^6$ g mol^{-1}) of various film thickness at temperatures as indicated: **a** $d = 194$ μm (bulk sample); **b** $d = 91$ nm; **c** $d = 14$ nm

master curve in Fig. 11.10 has been fitted to the HN-equation (Eq. 11.10). Further on, the data $\varepsilon''(\omega)$ can be converted from the frequency domain into the time domain by

$$\phi(t) = \frac{2}{\pi} \int_0^\infty \frac{\varepsilon''(\omega)}{\Delta\varepsilon} \cos\omega t \, d\omega \tag{11.19}$$

For each thickness d it is found that the respective relaxation function $\phi(t)$ can be well fitted to the Kohlrausch-William-Watts (KWW) equation

$$\phi(t) = \phi_0 \exp\left[-\left(\frac{t}{\tau_{KWW}} \right)^{\beta_{KWW}} \right] \tag{11.20}$$
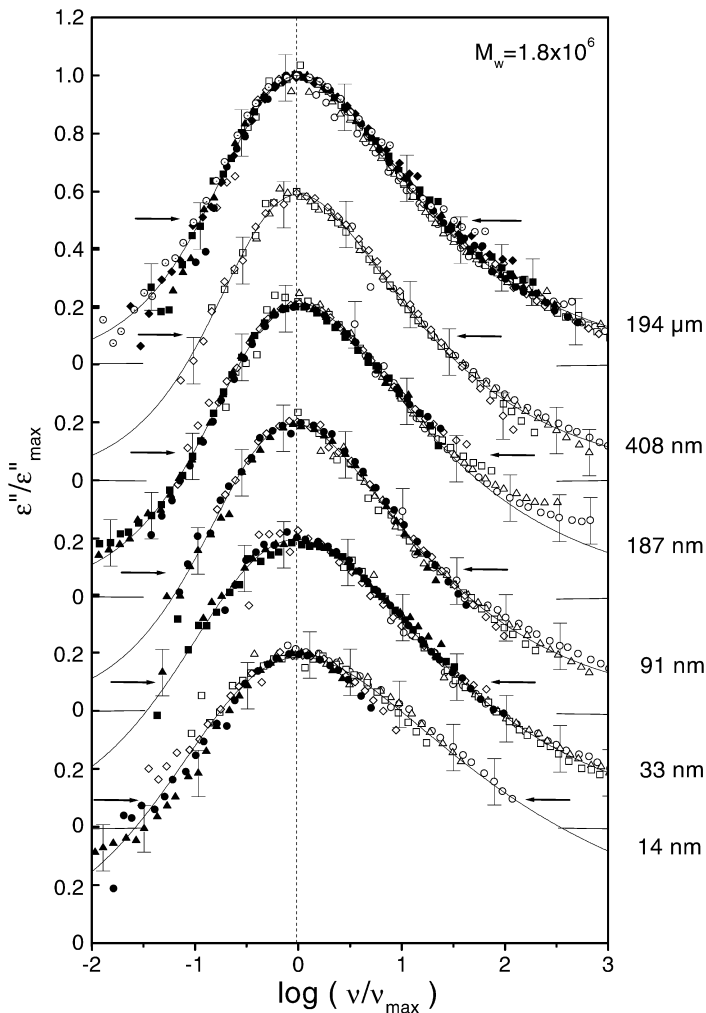
Fig. 11.10. Normalized dielectric loss ($\varepsilon''/\varepsilon''_{max}$) vs normalized frequency $\log(\nu/\nu_{max})$ for thin films of a-PS ($M_w = 1.8 \times 10^6$ g mol^{-1}) at thicknesses as indicated. The *solid lines* are HN-fits. *Arrows* indicate the full width of the peaks at $\varepsilon''/\varepsilon''_{max} = 0.5$ (FWHM). The *vertical dashed line* describes the maximum position of the normalized loss curves. For $d = 194$ μm, the symbol (*open circles*) corresponds to 396.0 K, (*open squares*) to 400.3 K, (*filled circles*) to 404.8 K, (*filled squares*) to 409.1 K and (*inverted filled triangles*) to 413.9 K. For $d = 408$ nm, the symbol (*open circles*) corresponds to 393.5 K, (*open triangles*) to 397.5 K, (*open squares*) to 401.3 K, and (*open diamonds*) to 404.3 K. For $d = 187$ nm, the symbol (*open circles*) corresponds to 388.5 K, (*open triangles*) to 392.4 K, (*open squares*) to 396.3 K, (*open diamonds*) to 400.4 K, (*filled circles*) to 404.3 K, (*filled triangles*) to 407.6 K, and (*filled squares*) to 408.1 K. For $d = 91$ nm, the symbol (*open circles*) corresponds to 391.8 K, (*open triangles*) to 395.3 K, (*open squares*) to 399.2 K, (*open diamonds*) to 403.1 K and (*filled circles*) to 405.6 K. For $d = 33$ nm, the symbol (*open circles*) corresponds to 380.5 K, (*open triangles*) to 384.5 K, (*open squares*) to 388.4 K, (*open diamonds*) to 392.4 K, (*filled circles*) to 396.4 K, (*filled triangles*) to 399.9 K, and (*filled squares*) to 400.6 K. For $d = 14$ nm, the symbol (*open circles*) corresponds to 382.3 K, (*open triangles*) to 386.0 K, (*open squares*) to 390.0 K, (*open diamonds*) to 393.9 K, (*filled circles*) to 397.9 K and (*filled triangles*) to 401.1 K

Table 11.5. The values of the broadening parameters α_{HN} and β_{HN} as well as of the stretching parameter β_{KWW} resulting from the best fits of Eq. (11.10) and Eq. (11.20), respectively to the loss spectra measured on thin films of a-PS with $M_w = 1.8 \times 10^6$ g mol^{-1}

d [nm]	α_{HN}	γ_{HN}	β_{KWW}
194×10^3	0.78 ± 0.01	0.46 ± 0.01	0.419 ± 0.012
408	0.78 ± 0.01	0.48 ± 0.02	0.435 ± 0.017
187	0.75 ± 0.01	0.46 ± 0.03	0.399 ± 0.021
91	0.75 ± 0.01	0.47 ± 0.01	0.406 ± 0.014
33	0.62 ± 0.01	0.51 ± 0.02	0.344 ± 0.017
14	0.60 ± 0.02	0.37 ± 0.03	0.271 ± 0.019

The broadening parameter β_{KWW} obtained for films of various thickness turns out to be proportional to the inverse film thickness d [13]. The values for the parameters α_{HN}, β_{HN} and β_{KWW} of the best fits are given in Table 11.5. They confirm that the width remains constant down to a thickness of 91 nm whereas it increases considerably for the two thinnest films of $d = 14$ nm and $d = 33$ nm.

In the temperature representation of the dielectric loss (i.e. the plot of the dielectric loss ε'' vs temperature for a fixed frequency) an increased broadening of the loss peak is found as well when the film thickness decreases [13]. From evaluation of the thickness dependences of T_α (i.e. the temperature at which ε'' realizes its maximum in the temperature representation), of ΔT_α being related to the width of the loss peak in the temperature representation and of the broadening parameter β_{KWW} length scales of the dynamics in thin films of a-PS can be extracted. Their values are related to the heterogeneous film structure within a three layer model including a layer of immobilized molecules, a layer of bulk-like dynamics and a layer near the film surface showing a higher mobility of the polymer chains than in the bulk [13].

Since a-PS is a weakly polar material, it is difficult to obtain significant dielectric loss signals at low frequencies by DRS. It is therefore demonstrated how information on the dynamics of the α-relaxation in this frequency range can be completed by TES. Figure 11.11 displays the temperature dependence as obtained by TES of the real (α'_n) and the imaginary part (α''_n) of the thermal expansion coefficient normal to the film surface for thin films of a-PS of two values of the film thickness d and at two frequencies ν_T of temperature modulation. The solid curves in Fig. 11.11 are obtained by combining the HN-equation (Eq. 11.10) modified for $\alpha_n^*(\omega)$ [14] with the Vogel-Fulcher-Tammann (VFT) dependence (Eq. 11.13). It is assumed here that $\tau_{HN} = \tau_\alpha$ and that all parameters apart from the relaxation time are independent of temperature. The fit parameters resulting from this procedure are given in Table 11.6.

From Fig. 11.11b it can be seen that for constant frequency ν_T of temperature modulation the peak temperature T_α at which α''_n realizes its maximum is shifted to lower temperatures when the film thickness is reduced from 247 nm to 18 nm. Also in the temperature domain the width of the transition region between the glassy and the liquid state increases as the thickness decreases. This corresponds to an increase of the width of the relaxation time distribution with decreasing
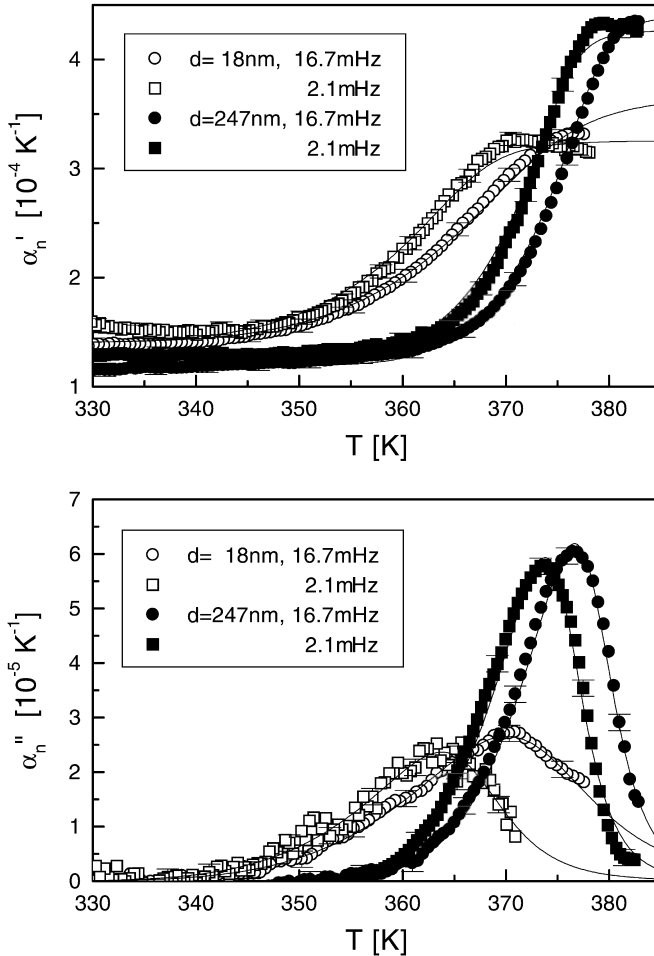
Fig. 11.11. Temperature dependence of complex linear thermal expansion coefficient α_n^* for a-PS films ($M_w = 6.7 \times 10^6$ g mol^{-1}) with a thickness of 18 nm (*open symbols*) and 247 nm (*full symbols*). The temperature dependence for two values of the frequency ν_T of temperature modulation are given: $\nu_T = 16.7$ mHz (*circles*); $\nu_T = 2.1$ mHz (*squares*). The *upper figure* shows the real part of α_n^* and the *lower one* the imaginary part. *Solid lines* are calculated by combining the HN equation and the VFT equation. Corresponding fit parameters are displayed in Table 11.6

film thickness and is in agreement with the results of dielectric measurements as discussed above.

Figure 11.12 displays the activation plot, i.e. the dependence of the relaxation rate ν_{max} of the α-process ($\nu_{max} = 1/2\pi\tau_\alpha$; τ_α is the relaxation time) on temperature for thin films of a-PS of various thickness and of two different molecular weights. The temperature T_α, where the peak in either α_n'' or ε'' realizes its maximum, was measured at a fixed frequency ν_{max} (equal to ν_E for DRS or to ν_T for TES). Thus the

Table 11.6. Values for the broadening parameters α_{HN} and γ_{HN}, the constant U of the VFT-equation (Eq. (11.13)) and the Vogel-Fulcher temperature T_0 resulting from best fits for the results of TES measurements in Fig. 11.11. Additionally, the stretching parameter β_{KWW} is calculated

D [nm]	f_T [Hz]	α_{HN}	γ_{HN}	β_{KWW}	U [K]	T_0 [K]
18	1.67×10^{-2}	0.40 ± 0.05	0.22 ± 0.03	0.19	1887	312.7
18	2.1×10^{-3}	0.38 ± 0.07	0.23 ± 0.04	0.20	1887	312.7
247	1.67×10^{-2}	0.20 ± 0.05	0.29 ± 0.03	0.30	1733	324.0
247	2.1×10^{-3}	0.23 ± 0.06	0.27 ± 0.04	0.27	1733	324.0
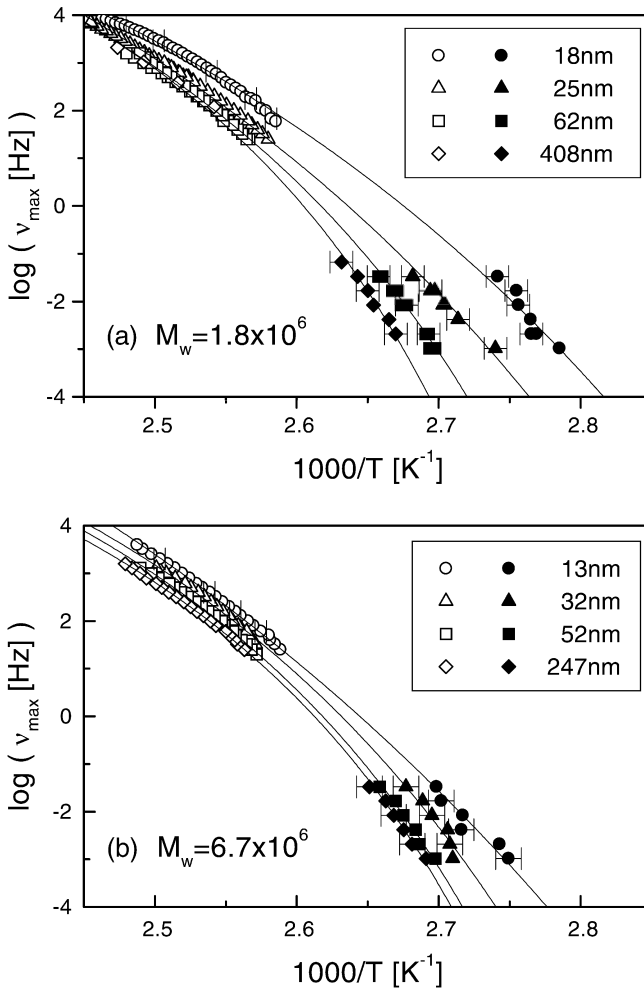
Fig. 11.12. Activation plot: logarithm of the relaxation rate ν_{max} vs $1000/T$ for a-PS films of thicknesses as indicated. *Full and open symbols* describe TES and DRS measurements, respectively. The *solid lines* are VFT-fits: **a** $M_w = 1.8 \times 10^6$ gmol^{-1}; **b** $M_w = 6.7 \times 10^6$ gmol^{-1}

relaxation rate ν_{max} is obtained in a wider frequency range from 10^{-3} Hz to 10^4 Hz. It can be seen from Fig. 11.12 that the relaxation rate ν_{max} increases with decreasing film thickness for both molecular weights $M_w = 6.7 \times 10^6$ g mol^{-1} and $M_w = 1.8 \times 10^6$ g mol^{-1}. The shift of ν_{max} to higher values of the relaxation rate for the same decrease of the film thickness d is more pronounced at temperatures near T_g than at higher temperatures. Hence, the thickness at which finite size effects on the dynamics of the α-relaxation appear increases when the glass transition temperature T_g is approached. This finding is in qualitative agreement with the model of CRRs by Adam and Gibbs [49]. The size ξ_{CRR} of CRRs is predicted to increase as the temperature nears T_g from high temperatures. According to this picture, the dynamics of a glass-forming liquid being geometrically confined should deviate significantly from that of the bulk for the smallest possible size of confinement. This deviation is expected to be more pronounced when T_g is approached as it is found in case of thin films of a-PS. Investigations on low molecular substances confined to nanoporous host systems by dielectric relaxation spectroscopy ([42] and references therein) and inelastic neutron scattering [48] have led to similar findings like those presented in Fig. 11.12. This indicates that the size- and temperature-dependence of ν_{max} as described above are not restricted to thin polymer films but hold for the molecular dynamics in confinement of quite different glassformers.

A further evaluation of the results displayed in Fig. 11.12 allows for the investigation of the thickness dependence of the Vogel-Fulcher temperature T_0 and of the fit parameter U [14]. T_0 depends in a similar manner on the film thickness d like the glass transition temperature T_g as discussed below. The quantity $1/U$ turns out to be proportional to the inverse film thickness $1/d$. Both parameters can be related to the thermal expansion coefficient of the free volume within the theory of Cohen and Turnbull [50]. It is found that this quantity decreases with decreasing film thickness in accordance with the results of PALS measurements [8] on thin films of a-PS.

From the fact that the parameter U depends on the film thickness one has to expect that the fragility m as defined in Eq. (11.18) shows a thickness dependence as well. The relaxation time τ_α in Eq. (11.18) is obtained via the relation $2\pi\nu_{max}\tau_\alpha = 1$ from the observed relaxation rate ν_{max}. T_g is redefined as the temperature at which the relation $\tau_\alpha(T_g) = 10^2$ s is fulfilled.

Figure 11.13 shows the Angell plot [47] for the α-relaxation in thin films of a-PS of various values of film thickness d. It can be seen that with decreasing film thickness the fragility m decreases as well, i.e. the films become less fragile when the film thickness is reduced. If the origin of the VFT law is attributed to the cooperativity in the dynamics of the α-relaxation, the observed approach to an Arrhenius dependence leads to the conjecture that the dynamics of the α-process in thin films of a-PS tends from the cooperative dynamics of the bulk liquid to a dynamics which is typical for a single molecule [14]. This conjecture is in accord with findings for low molar liquids confined to porous host systems [42, 51].

The glass transition temperature T_g for thin a-PS films of three different molecular weights has been determined by TES measurements as the temperature T_α which is obtained for a frequency of temperature modulation of $\nu_T = 8.3$ mHz. For this frequency the corresponding relaxation time is on a macro-
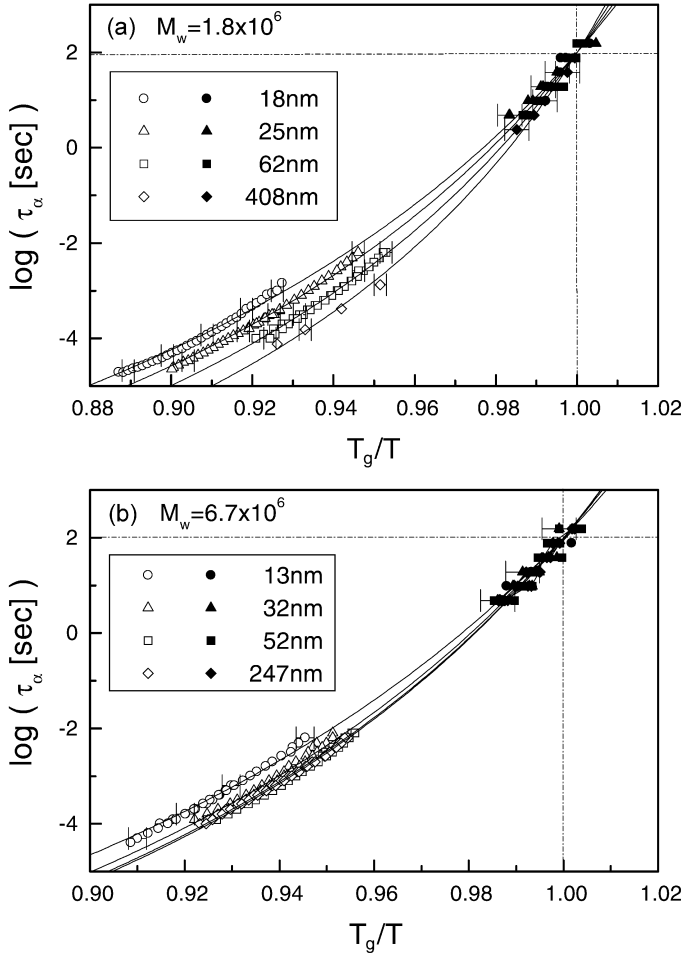
Fig. 11.13. Dependence of log τ_α on the inverse of reduced temperature T_g/T for thin films of a-PS: **a** $M_w = 1.8 \times 10^6$ g mol^{-1}; **b** $M_w = 6.7 \times 10^6$ g mol^{-1}. The values of T_g are obtained by the relation $\tau_\alpha(T) = 100$ s. Otherwise as Fig. 12. *Dashed-dotted lines* represent the values $\tau_\alpha = 100$ s and $T = T_g$, respectively

scopic time scale. This definition of T_g is justified by a variety of experimental results, e.g. [11, 52].

Figure 11.14 displays the thickness dependence of T_g for three different molecular weights. Down to a critical film thickness d_c there is only a slight decrease of T_g with decreasing film thickness. Below d_c a much stronger decrease of T_g with decreasing film thickness is found for all molecular weights which can be well fitted by a linear function. The values for d_c show a distinct dependence on the molecular weight M_w: they change with M_w in accordance with the radius of gyration, R_g [14]. The thickness dependence of T_g presented in Fig. 11.14 is similar to that obtained for freely standing films of a-PS in the regime of high mol-
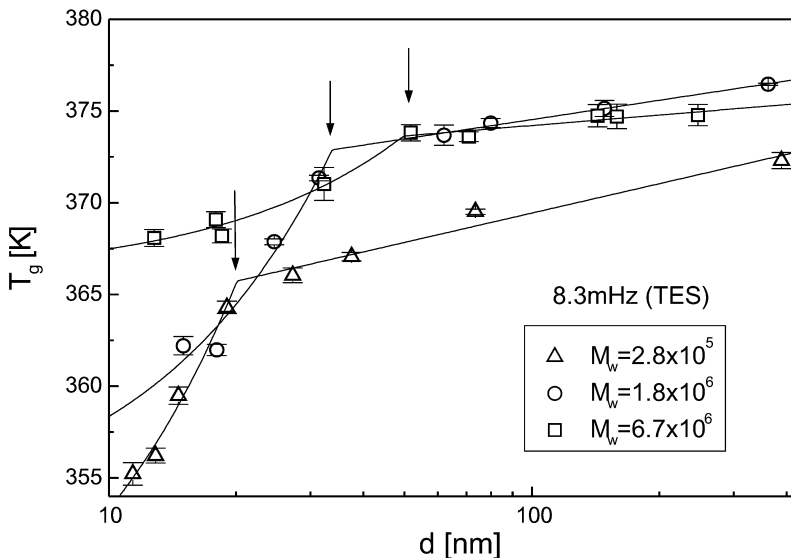
Fig. 11.14. Glass transition temperature T_g vs logarithm of the film thickness d for thin films of a-PS of molecular weights as indicated. The value of T_g is measured as the temperature T_α at which the imaginary part of thermal expansion coefficients has its peak value for the modulation frequency 8.3 mHz in TES measurements. The *arrows* show the crossover thickness d_c, below which T_g decreases abruptly with decreasing film thickness. The *lines* are linear fits to $T_g(d)$ above and below d_c

ecular weights ($M_w \geq 5 \times 10^5$ g mol^{-1}) [15, 53]. Furthermore, it compares well to the thickness dependence of T_α in supported films of a-PS as obtained by dielectric relaxation spectroscopy [12, 13]. Based on these experimental results, the M_w and d dependence of T_g in Fig. 11.14 is ascribed to the confinement of polymer chains in the thin film geometry. This effect is characteristic for the dynamics of the α-process in thin films of a-PS whereas no counterpart has been found for small molecules in confinement. Despite these similarities between supported and freely standing films there are also considerable differences which are not yet understood: the T_g reduction is much smaller for supported films than for freely standing films of a-PS. This finding can presumably be explained by the presence of free surfaces instead of any substrate. The absence of a substrate might also be the reason for the different slopes in the thickness dependences of T_g in the linear region below d_c: in case of freely standing films the slope increases with increasing M_w [54]. The reverse tendency is found for supported films by TES [14].

On the other hand, measurements of T_g by capacitive scanning dilatometry (CSD) [12, 13] and ellipsometric measurements of T_g on thin films of a-PS [5, 6] yield a qualitatively different dependence of T_g on the film thickness d: T_g decreases gradually with decreasing film thickness d and no critical thickness d_c could be found at which the thickness dependence changes qualitatively. Moreover, a qualitatively similar thickness dependence was reported for T_g of

freely standing films of a-PS in the regime of low molecular weights [17] as well as for T_α of thin films of PVAc. In all these cases, no molecular weight dependence was found for $T_g(d)$ and for $T_\alpha(d)$, respectively. The gradual decrease of T_g can be described by an empirical fit formula:

$$T_g(d) = T_g^{\text{bulk}} \left[1 - \left(\frac{a}{d} \right)^\delta \right] \tag{11.21}$$

For $\delta = 1$ and $a \ll d$ one obtains Eq. (11.15). T_g^{bulk} is the glass transition temperature of the bulk polymer and a is a length which shows no dependence on the molecular weight and is in the same order like the statistical segment length of a-PS [13]. For the exponent δ different values are reported in literature: Keddie et al. found $\delta = 1.28 \pm 0.20$ [55] in case of ellipsometric studies, whereas $\delta = 1$ is obtained by CSD [13] for supported films of a-PS. In case of thin films of PVAc $\delta = 0.77 \pm 0.04$ is found by dielectric relaxation spectroscopy for $T_\alpha(d)$ [34].

Based on the results for thin films of a-PS, it is assumed [4, 13, 17] that there are two regimes of the molecular weight M_w in which different dependences of T_g (or T_α) on the film thickness d are found. For low values of M_w ($M_w < 5 \times 10^5$ g mol^{-1}), the *effect of chain confinement* is not important for the reduction of T_g whereas *finite size effects* due to an intrinsic length scale of the glass transition are dominant. Therefore, no dependence of $T_g(d)$ on the molecular weight is found. The effect of chain confinement determines the thickness dependence of T_g in the regime of high molecular weights. In this regime $T_g(d)$ is characterized by the presence of a critical thickness d_c which scales with the molecular weight and consequently with the radius of gyration.

The difference in the findings for $T_g(d)$ on thin films of a-PS of the same molecular weight as obtained by means of CSD [12, 13] and TES [14] are not yet fully understood in the moment [56]. The value for T_g depends on the unambiguous determination of a peak maximum in case of TES, whereas it is determined as "kink temperature" in case of CSD. The latter depends on the contrast of the glass transition, i.e. the difference between the thermal expansion coefficients of the liquid and the glassy state. This contrast becomes weaker when the film thickness is reduced. Therefore, any dependence of $T_g(d)$ on the molecular weight might be covered by experimental errors in case of dilatometric experiments but can still be revealed by TES measurements. However, in analogy to calorimetry which can also be performed in the ramping mode or in the mode of temperature modulation, the values for T_g obtained by CSD are expected to coincide with those obtained by TES [10, 57, 58].

Similar results as for a-PS were obtained for thin films of PVAc [34]. In both the frequency and the temperature representation of the data of the dielectric loss ε'' a pronounced broadening of the loss peaks is obtained. For the relaxation time distribution, a shift of the maximum to shorter times with respect to the bulk was found for thin films besides the broadening. This leads to an activation plot which is quite similar to that of a-PS (Fig. 11.12), i.e. the relaxation rate $\nu_{\max}$ increases with decreasing film thickness. The thickness dependence of T_α, which

is assumed to be similar to that of T_g, is well comparable to that obtained from thin films of a-PS. They were found to be consistent under the assumption that the investigated molecular weights of PVAc are too small to observe chain confinement effects.

11.4
Thin Films of Grafted Polymers: Poly(γ-benzyl-L-glutamate) (PBLG)

While the structure of grafted polymers is well explored by a variety of experimental techniques (ellipsometry [59], neutron-reflectivity [60] and X-ray-reflectivity measurements [61]), little is known about the molecular dynamics in these systems. Recently, dielectric relaxation spectroscopy has been applied to tackle the question to which extent the molecular dynamics is changed with respect to that of the bulk when polymers are prepared as thin grafted films [29, 62, 63]. In case of poly(γ-benzyl-L-glutamate) (PBLG) a new experimental approach to form electrical contacts to the thin films besides the conventional evaporation of metal electrodes has been developed [29, 62]. Results obtained by this new preparation technique are compared to those obtained by evaporating the upper electrode directly on the polymer film as well as to measurements on the bulk material. Furthermore, the molecular dynamics after swelling the grafted polymer film is studied.

The rigid rodlike polymer PBLG (Fig. 11.15a) carries a large dipole moment parallel to its helical axis. By grafting one end of the helix to a surface one has to expect a considerable net dipole moment perpendicular to the surface. Thus, the possibility is given to control the structure, orientation and dynamic properties by an external electrical field. This could lead to possible applications in the areas of non-linear optics, liquid crystal displays, separation membranes or biosensors. Grafted films of PBLG have already been studied with regard to the molecular orientation [64], the electromechanical properties [65] and the formation of microstructured layers [28]. In particular, the molecular dynamics of polyglutamates in the bulk is well understood. It is known that PBLG has two dielectrically active relaxation processes which are assigned to the (restricted) fluctuation of the helical main chain as a whole (chop stick motion) and to the fluctuation of the side groups [66, 67].

Details about the preparation of grafted films of PBLG may be found elsewhere [28, 62]. In order to circumvent artefacts which may appear in case of direct evaporation of metal electrodes of about 50 nm thickness onto an organic film of comparable thickness, a new preparation technique was applied. To prepare the grafted polymer in a capacitor arrangement, the grafted film is covered with a freshly cleaved lamella of mica which was previously evaporated with aluminium stripes. Thus, a sample capacitor with an area of 2 mm^2 is formed (Fig. 11.15b). Mica offers the advantage that it shows atomically flat surfaces after cleaving. Further details can be found in [62].

Figure 11.16 displays spectra for both the side chain relaxation and the chop stick motion as obtained for the bulk and for the grafted film. For the latter, results of both techniques to contact the film are presented. Since in the
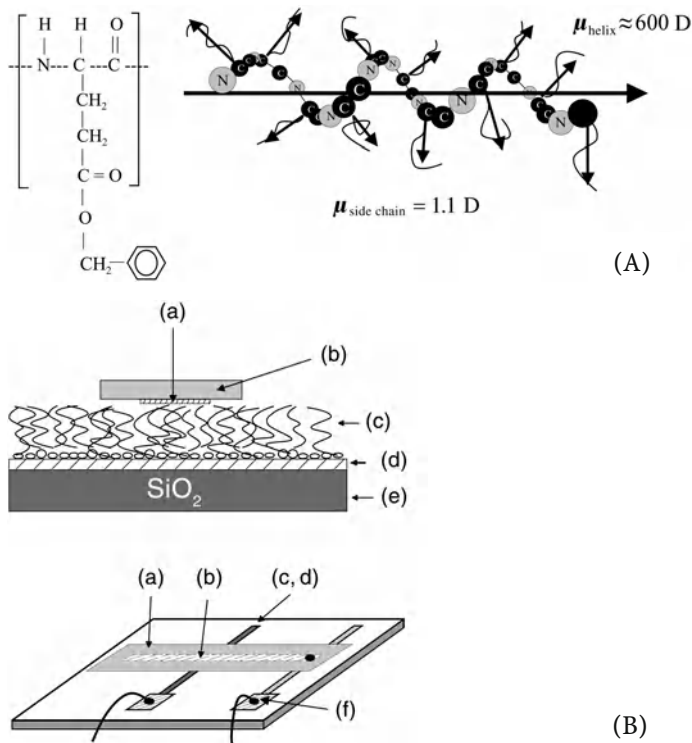
Fig. 11.15. A Primary and secondary structure of poly(γ-benzyl-L-glutamate) (PBLG). **B** Sketch of contacting the sample by use of a solid mica-electrode. An aluminium stripe (a) is evaporated onto a sheet of freshly cleaved mica (b), thus forming the upper electrode. For the baseplate, aluminium stripes (d) are evaporated onto cleaned glass plates (e). PBLG-films (c) are grafted subsequently on the aluminium stripes and are contacted by applying the evaporated side of the mica sheet, thus composing one sample capacitor. Wires are electrically connected to contact pads by use of silver paint (f)

case of the mica electrode a contact to the film is not given over the whole area of the electrode, the data for ε'' have to be rescaled with the ratio $\varepsilon_\infty^{bulk}/\varepsilon_\infty^{grafted}$, where $\varepsilon_\infty^{bulk}$ and $\varepsilon_\infty^{grafted}$ are the high frequency limits of ε' of the bulk and of the grafted polymer, respectively. This data treatment is based on the assumption that ε_∞ is only specific for the polymer and does not depend on film thickness or on inner film structure. In Fig. 11.16, the side chain motion in the grafted films is found to be broadened and to be slightly slowed down with respect to the bulk spectrum. These findings are presumably caused by the influence of the underlying substrate on the dipole fluctuations. The chop stick motion is found to be faster in the grafted layer depending on its thickness with respect to the bulk reference (Fig. 11.17). This faster relaxation in the grafted layer cannot be explained by a difference in the molecular weight since M_w was found to be almost the same for the bulk sample and for the grafted films. However, the behaviour of the chop stick motion can be quali-
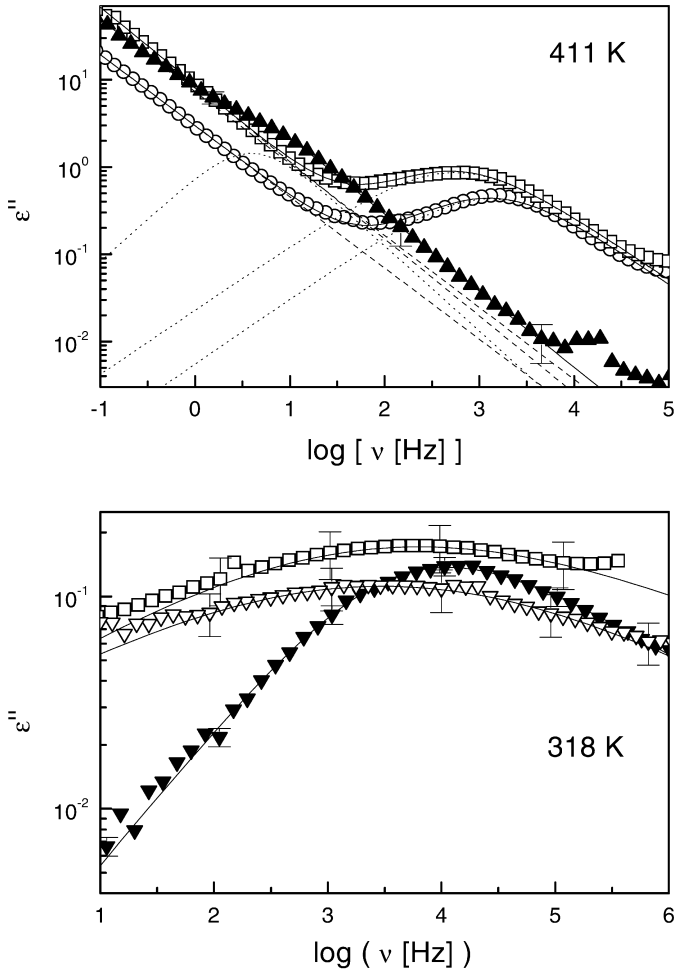
Fig. 11.16. Dielectric loss ε'' vs frequency for a bulk sample cast from solution and for a grafted layer of PBLG at 411 K and 318 K with fits according to the HN-equation (Eq. 11.10). The relaxation process at 411 K corresponds to the restricted motion of the helical main chains ("chop stick motion") in the bulk (*filled triangles*) and in layers of grafted PBLG of two different thicknesses: (*open squares*) 57 nm, (*open circles*) 22 nm. The spectra at 318 K correspond to the motion of the side chains: *inverted filled triangles*) bulk, (*inverted open triangles*), (*open squares*) grafted PBLG layer contacted by a solid top electrode and by evaporation of aluminium, respectively. *Solid lines* indicate the superposition of a conductivity contribution (*dashed lines*) and a relaxation process (*dotted lines*) according to the HN-equation (Eq. 11.10). Two typical sets of fit parameters are given for the bulk sample: 318 K: $\Delta\varepsilon = 0.66$, $\tau = 1.4 \times 10^{-5}$ s, $\alpha = 0.65$, $\gamma = 0.496$; 411 K: $\Delta\varepsilon = 2.496$, $\tau = 0.0245$ s, $\alpha = 1$, $\gamma = 1$, $\sigma_0 = 3.93 \times 10^{-10}$ S m^{-1}, $s = 0.82$
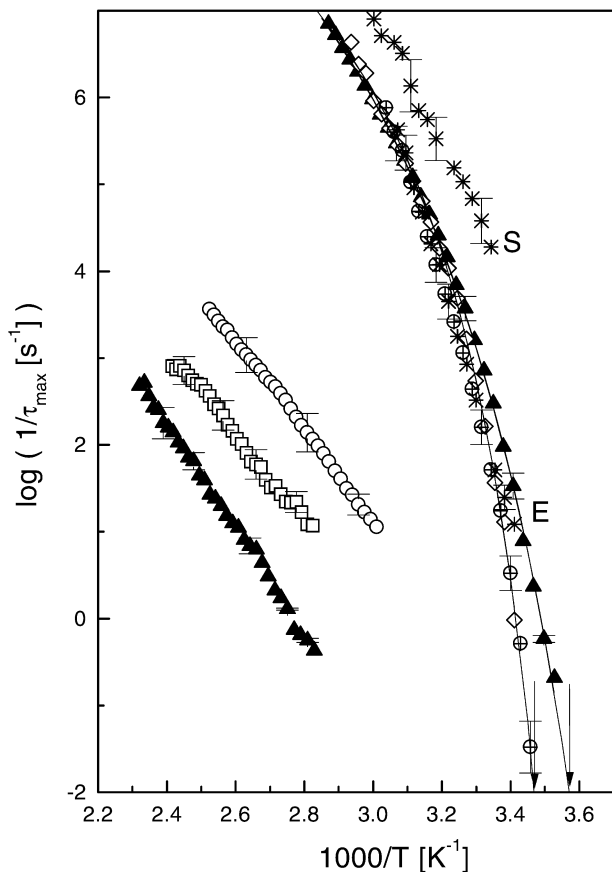
Fig. 11.17. Activation plot for the two relaxation processes of PBLG in the dried and in the swollen state of thin grafted layers and of the (unswollen) bulk (*filled triangles*). The measurements on the grafted layer are denoted by *open symbols*: (*open squares*) and (*open circles*) are used to mark the fluctuation of the helical main chains within a grafted layer of 57 nm and 22 nm thickness, respectively (evaporated electrodes). (*circled plus signs*) and (*open diamonds*) indicate the data of the side chain motion obtained by use of evaporated electrodes and of the "mica method", respectively. (*asterisks*) is used to denote the side chain fluctuation after the swelling procedure. In this case, S denotes the starting point and E the end of the measurement on the swollen sample. Fits according to the VFT-law are shown by *solid lines* for the bulk and for the grafted layer before the swelling procedure. The following fit parameters were obtained for the bulk: $\log(1/\tau_0) = 10.3$, $U = 670.8$ K, $T_0 = 264.5$ K and for the grafted layer: $\log(1/\tau_0) = 11.9$, $U = 1270.2$ K, $T_0 = 240.3$ K. *Arrows* indicate the glass transition temperature T_g, i.e. the temperature which corresponds to a relaxation time of $\tau_{max} = 100$ s: $T_g^{bulk} = (280 \pm 2)$ K, $T_g^{layer} = (287 \pm 2)$ K

tatively understood within the scope of the model of Wang and Pecora [68] as discussed below. Since the differences between the bulk and the grafted layer were obtained independently from the preparation of the bulk sample and from the way of contacting the thin films, they have to be attributed either to the different structure of both films or to the decreased thickness of the grafted layer. To decide this question, further investigations on grafted films with different thicknesses and on spin coated films of PBLG have to be done.

In Fig. 11.17 the activation plot is shown as obtained for PBLG in the bulk and as grafted layer for both techniques to contact the grafted film. The thermal activation of the side chain relaxation process would be expected to show an Arrhenius-like temperature dependence. This was indeed found for glutamates with short methyl side chains [69]. However, for PBLG or similar substances with longer side chains the thermal activation of the corresponding relaxation can be well described by the VFT law (Eq. 11.13) indicating that the side chains undergo a glass transition [30, 66]. The slower side chain relaxation in the thin grafted films of PBLG leads to a higher glass transition temperature with respect to the bulk as indicated in Fig. 11.17. To improve the contact between the grafted film and the upper (mica-) electrode, the grafted PBLG has been swollen in a chloroform atmosphere for several hours. As result of this procedure, a higher capacitance being in better agreement with calculated values is achieved. Furthermore, the side chain fluctuation becomes faster in the swollen sample. Since the content of chloroform decreases with increasing temperature, the relaxation rate tends to the values of the unswollen sample. Dielectric measurements while cooling the sample yield the same thermal activation as for the unswollen sample, thus indicating that the swelling process is fully reversible. The chop stick motion is not affected by the swelling procedure.

Figure 11.18 displays the dielectric strength $\Delta\varepsilon$ of the side chain fluctuation which can be well described by Eq. (11.16) for both the bulk and the grafted film being contacted by the mica-electrode. For the calculation of $\Delta\varepsilon$ according to Eq. (11.16) it is assumed that $\mu = 1.1$ D [65], $g_{KF} = 1$ and $n = 5 \times 10^{21}$ cm^{-3}. The latter value is based on an estimation taking into account approximate values for the chain length (≈ 60 nm) and the grafting density (≈ 0.005 Å^{-2}). While there is a good agreement of the calculation and the measurements on the bulk and the grafted layer prepared according to the mica technique, $\Delta\varepsilon$ is higher when the electrodes are evaporated. This difference is attributed to changes within the grafted layer during the evaporation of aluminium.

In Fig. 11.19 the dielectric strength of the chop stick motion for the bulk and for the grafted layer with evaporated electrodes is shown. Concerning the chop stick motion it has to be considered that this motion is restricted by interactions between neighbouring chains and by fixing one end of the chains to the electrode surface. This situation corresponds to the model of Wang and Pecora [68], which describes the restricted rotational diffusion of rodlike molecules. In this model the fluctuation of the molecule length axis is constrained to a cone with an apex angle θ_0 (inset in Fig. 11.19). In the scope of this model it is possible to deduce a relation connecting $\Delta\varepsilon_{rod}$ for the free fluctuation of the helical main
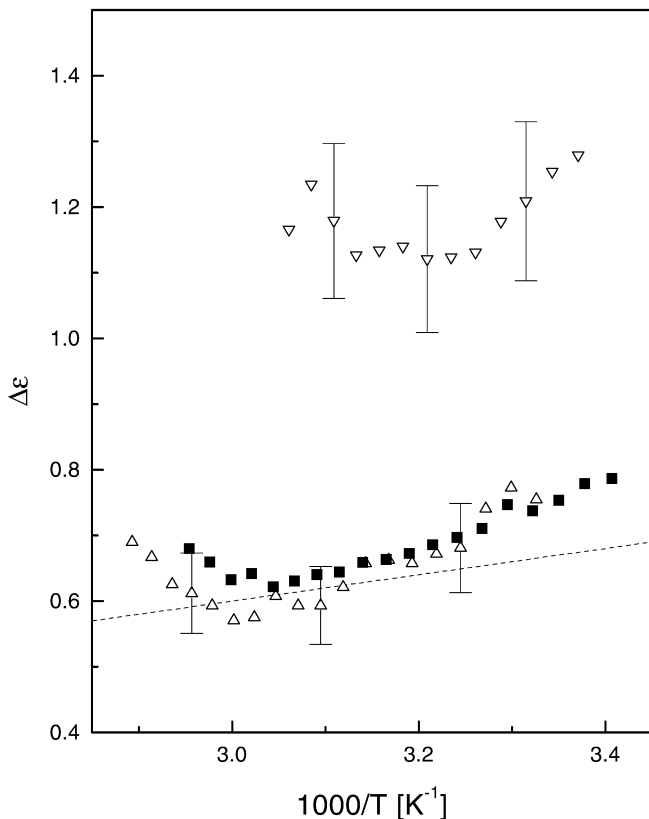
Fig. 11.18. Relaxation strength $\Delta\varepsilon$ of the side chain fluctuation for the grafted layer of PBLG (corrected values: (*inverted open triangles*) evaporated electrodes, (*open triangles*) mica technique) and for the bulk (*filled squares*). Calculated values according to Eq. (11.16) are given by the *dashed line*

chains as expected from Eq. (11.16) and the values $\Delta\varepsilon_{csm}$ obtained for the chop stick motion from the (corrected) HN-fits [66]:

$$\Delta\varepsilon_{csm} = \Delta\varepsilon_{rod}\left(1 - \frac{1}{4}(1+\cos\theta_0)^2\right) \tag{11.22}$$

Application of Eq. (11.22) to the data delivers an angle θ_0 of approximately 2° in good agreement with previous results [66]. There, similar glutamic acid containing polymers have been investigated by means of dielectric spectroscopy; for the evaluation of the bulk data the model of Wang and Pecora has been applied as well. Both the increase of the relaxation time of the chop stick motion and the decrease of its dielectric strength in the grafted films with respect to values of the bulk can be explained consistently by the assumption that the angle θ_0 is smaller in the grafted film than in the bulk [70–72].
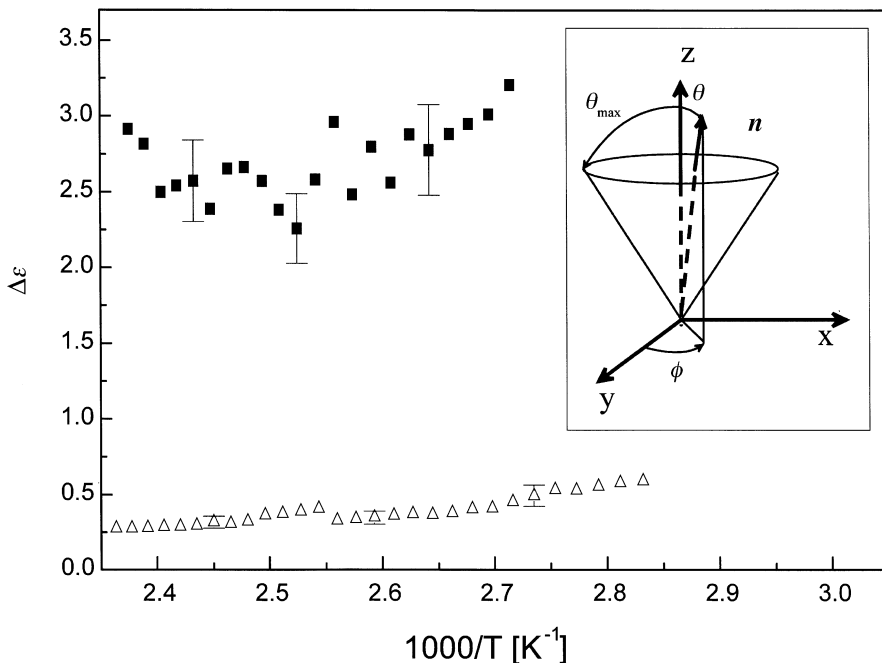
Fig. 11.19. Relaxation strength $\Delta\varepsilon$ of the fluctuation of the helical main chains of PBLG: (*open triangles*) denotes the corrected values of $\Delta\varepsilon$ for the grafted layer contacted by the "mica method". (*Filled squares*) are used to denote values of the bulk sample. The *inset* illustrates the restricted "chop-stick-motion" according to the model of Wang and Pecora [68]: **n** indicates the length axis of the rod-like molecule and θ_{max} the apex angle of the cone which restricts the fluctuation of the rodlike molecule having a tilt angle θ

In summary, a novel method is introduced which enables to our best knowledge for the first time to study the molecular dynamics in (ultra-) thin layers of grafted PBLG. The results are compared to measurements on the bulk sample and on grafted PBLG layers contacted by evaporating metal electrodes. Two relaxation processes are observed which are assigned to (restricted) fluctuations of the helical main chains as a whole (chop stick motion) and to the dynamic glass transition of the side chains. The latter shows a VFT-temperature dependence which scales well with calorimetric measurements [67]. For grafted layers this process is broadened with respect to the bulk and its relaxation rate τ_{max} is slightly shifted to longer times. The dielectric strength of the side chain relaxation can be described by Eq. (11.16). With decreasing film thickness, the chop stick motion is shifted to shorter relaxation times. The changes of the relaxation rate of the chop stick motion can be qualitatively explained by the model of Wang and Pecora [68] and the results obtained for its dielectric strength $\Delta\varepsilon$ are in good agreement with calculations based on this model. Swelling the polymer with chloroform leads to a faster motion of the side chains. This effect is reversible.

11.5
Conclusions

Dielectric spectroscopy is an ideal tool to study the molecular dynamics in thin polymer films. It has the extraordinary advantage that its sensitivity increases with decreasing thickness and decreasing amount of sample material, respectively.

The molecular dynamics in thin polymer films is determined by an interplay of different, in part counteracting effects:

1. Confinement effects make the dynamic glass transition faster compared to the bulk. This is the more pronounced the smaller the confining length scale is. As a result a strong decrease in the glass transition temperature T_g is observed.
2. Surface effects cause a decrease of the relaxation rate of the dynamic glass transition provided that an attractive interaction of the polymers with the solid boundaries is present. This is accompanied by an increase of T_g with decreasing thickness of the polymer layer.
3. If the length scale of the confinement becomes comparable to the radius of gyration of the polymer chain, additional effects on its structure, architecture and mode spectrum have to be expected.

The above-mentioned counterbalance is exemplified for three different polymeric systems:

1. In isotactic poly(methyl methacrylate) (i-PMMA) two dielectric relaxation processes are observed, the dynamic glass transition and a secondary β-relaxation. The former shows a confinement effect, i.e. the relaxation rate is increased with decreasing film thickness, which depends weakly only on the molecular weight. The secondary β-relaxation is for thin films of i-PMMA not influenced by the confinement whereas this is the case for a-PMMA. From the dielectric strength of the α-relaxation in thin films of i-PMMA a three-layer model can be deduced which enables to determine the amount of immobilized chain segments at the boundary with the electrodes. In contrast to the confinement effect found in dielectric studies, ellipsometric measurements on i-PMMA films on silica wafers reveal an increase of T_g with decreasing film thickness. This is attributed to an altered interaction of polymer chains with the substrate surface compared to the dielectric experiment.
2. In thin films of atactic polystyrene (a-PS) the dynamic glass transition shows a pronounced confinement effect, i.e. the relaxation rate increases strongly with decreasing thickness of the polymer film. This finding is supported by thermal expansion spectroscopy (TES) which enables to determine directly the glass transition temperature T_g from the dilatometric dynamics at low frequencies. The observed decrease of T_g with decreasing film thickness of the polymer film shows a dependence on the molecular weight which resembles to that found in ellipsometric and light scattering studies on freely standing films of a-PS. The combination of dielectric measurements and capacitive scanning dilatometry (CSD) allows one to deduce quantitatively a three-layer model for the heterogeneous dynamics in thin films of a-PS.

3. In order to study the molecular dynamics in grafted layers of poly(γ-benzyl-L-glutamate) (PBLG) a novel method to contact thin polymer films has been employed besides the conventional evaporation of electrodes. Two relaxation processes are observed which originate from fluctuations of the helical main chains as a whole (chop stick motion) and from dynamic glass transition of the side groups. The latter shows a VFT dependence which scales well with calorimetric measurements. Its relaxation time distribution is broadened in case of the grafted layer with respect to the bulk and its relaxation rate is slightly shifted to longer times. In contrast, the chop stick motion shows an increase in the relaxation rate for the grafted system which is presumably caused by the different molecular architecture compared to that of the bulk. Its dielectric strength can be well comprehended by a model for restricted rotational diffusion as developed by Wang and Pecora.

List of Abbreviations and Symbols

a	Fit parameter
A	Area of a capacitor
$C^* = C' - iC''$	Complex capacitance
C_0	Capacitance of the empty sample capacitor
$\langle C' \rangle$	Time averaged sample capacitance
$\Delta C'_{\omega_T}$	Amplitude of the sample capacitance
d	Film thickness
d_c	Critical film thickness
E	Young's elastic modulus
$g(\log(\tau))$	Relaxation time distribution
m	Fragility index
$\mathbf{n}$	Preferred orientation of rod-like molecules
M_w	Mass averaged molecular weight
M_n	Number averaged molecular weight
N_j	Number density of j-th atom
R_g	Radius of gyration
s	Exponent
t	Time
T	Absolute temperature
ΔT	Temperature difference
$\langle T \rangle$	Time averaged temperature
T_0	Vogel-Fulcher temperature
T_α	Temperature position of the maximum of the α-process at constant frequency
T_β	Temperature position of the maximum of the β-process at constant frequency
T_g	Glass transition temperature
T_g^{bulk}	Bulk glass transition temperature
T_S	Standard temperature
ΔT_{ω_T}	Amplitude of temperature modulation

U	Fit parameter in the VFT-equation
$\alpha_n^* = \alpha_n' - i\alpha_n''$	Complex thermal expansion coefficient normal to the film surface
α_t	Thermal expansion coefficient parallel to the film surface
α_{bulk}	Bulk thermal expansion coefficient
α_{HN}, γ_{HN}	HN shape parameters
$\overline{\alpha_j}$	Polarizability of j-th atom
β_{KWW}	KWW exponent
δ	Fit parameter
$\Delta\varepsilon$	Dielectric strength
$\varepsilon^* = \varepsilon' - i\varepsilon''$	Complex dielectric function
ε''_{max}	Maximum of the dielectric loss peak
ε_0	Dielectric permittivity of the vacuum
ε_∞	High frequency limit of ε'
η_0, ξ_0, ζ	Auxiliary variables
θ	Phase lag
θ, θ_{max}	(Maximal) tilt angle
μ	Poisson ratio
ν	Frequency
ν_{max}	Frequency corresponding to the maximal dielectric loss or relaxation rate
ξ	Fit parameter
ξ_{CRR}	Size of CRR
σ	Surface tension
σ_0	Direct current (d.c.) conductivity
τ_0	Relaxation time at high temperatures
τ_α	Relaxation time of the α-relaxation
τ_α^{max}	Maximum of $g(\log(\tau))$ corresponding to the α-relaxation
τ_{HN}	Relaxation time (HN-fit)
τ_{KWW}	Relaxation time (KWW-fit)
$\phi(t)$	Relaxation function
$\omega_T = 2\pi\nu_T$	(Angular) frequency of temperature modulation
$\omega_E = 2\pi\nu_E, \omega = 2\pi\nu$	(Angular) frequency of the electrical field in TES or DRS measurements

CRR	Cooperatively rearranging region
CSD	Capacitive scanning dilatometry
DRS	Dielectric relaxation spectroscopy
DSC	Differential scanning calorimetry
HN	Havriliak Negami
KWW	Kohlrausch Williams Watts
PALS	Positron annihilation life time spectroscopy
PBLG	Poly(γ-benzyl-L-glutamate)
a-, i-, s- PMMA	a-, iso- and syndiotactic poly(methyl methacrylate)
a-PS	Atactic polystyrene
PVAc	Poly(vinyl acetate)
TES	Thermal expansion spectroscopy
VFT	Vogel-Fulcher-Tammann

References

1. Dutcher JR, Dalnoki-Veress K, Forrest JA (1999) In: Warr G, Manne S (eds) Supramolecular structure in confined geometries. American Chemical Society Symposium Series
2. Forrest JA, Jones RAL (2000) In: Karim A, Kumar S (eds) Polymer surfaces, interfaces and thin films. World Scientific, Singapore
3. Frick B, Zorn R, Büttner H (2000) Proceedings of International Workshop on Dynamics in Confinement. J Phys IV:10
4. Forrest JA, Dalnoki-Veress K (2001) Adv Coll Int Sci 94:167
5. Keddie JL, Jones RAL, Cory RA (1994) Europhys Lett 27:59
6. Keddie JL, Jones RAL, Cory RA (1994) Faraday Discuss Chem Soc 98:219
7. Wallace WE, van Zanten JH, Wu WL (1995) Phys Rev E52:R3329
8. de Maggio GB, Frieze WE, Gidley DW, Zhu M, Hristov HA, Yee AF (1997) Phys Rev Lett 78:1524
9. Fryer DS, Nealey PF, de Pablo J (2000) Macromolecules 33:6439
10. Bauer C, Richert R, Böhmer R, Christensen T (2000) J Non-Cryst Solids 262:276
11. Bauer C, Böhmer R, Moreno-Flores S, Richert R, Sillescu H, Neher D (2000) Phys Rev E61:1755
12. Fukao K, Miyamoto Y (1999) Europhys Lett 46:649
13. Fukao K, Miyamoto Y (2000) Phys Rev E61:1743
14. Fukao K, Miyamoto Y (2001) Phys Rev E64:011803
15. Forrest JA, Dalnoki-Veress K, Stevens JR, Dutcher JR (1996) Phys Rev Lett 77:2002
16. Forrest JA, Dalnoki-Veress K, Dutcher JR (1997) Phys Rev E56:5705
17. Mattsson J, Forrest JA, Börjesson L (2000) Phys Rev E62:5187
18. Herminghaus S, Jacobs K, Seemann R (2001) Eur Phys J E 5:531
19. Long D, Lequeux F (2001) Eur Phys J E 4:371
20. Binder K, Baschnagel J, Bennemann C, Paul W (1999) J Phys Cond Mat 11:A47
21. Baschnagel J, Mischler C, Binder K (2000) Dynamics of confined polymer melts: recent Monte Carlo simulation results. In: Frick B, Zorn R, Büttner H (eds) International Workshop on Dynamics in Confinement. EDP Sciences, Les Ulis, J Phys IV 10:Pr7–9
22. Khare R, de Pablo J, Yethiraj A (2001) J Chem Phys 114:7593
23. de Gennes PG (2000) CR Acad Sci Paris 1/IV:1179
24. de Gennes PG (2000) Eur Phys J E 2:201
25. Brandrup J, Immergut EH, Grulke EA (eds) (1999) Polymer handbook, 4th edn. Wiley, New York, p V/77
26. Mark JE (ed) (1996) Physical properties of polymers handbook. AIP Press, Woodbury, New York
27. Hartmann L, Gorbatschow W, Hauwede J, Kremer F (2002) Eur Phys J E 8(2) (in print)
28. Kratzmüller T, Appelhans D, Braun HG (1999) Adv Mater 11:555
29. Hartmann L, Kratzmüller T, Braun HG, Kremer F (2000) Macromol Rapid Commun 21:814
30. Blum G, Kremer F, Jaworek T, Wegner G (1995) Adv Mater 7:1017
31. Grohens Y, Brogly M, Labbe C, David MO, Schultz J (1998) Langmuir 14:2929
32. Grohens Y, Hamon L, Carriere P, Holl Y, Schultz J (2000) MRS Spring Meeting Symposium Proceedings, vol 629
33. Prucker O, Christian S, Bock H, Rühe J, Frank CW, Knoll W (1998) Macromol Chem Phys 199:1435
34. Fukao K, Uno S, Miyamoto Y, Hoshino A, Miyaji H (2001) Phys Rev E 64:051807
35. Ute K, Miyatake N, Hatada K (1995) Polymer 36:1415
36. Havriliak S, Negami S (1967) Polymer 8:161
37. Garwe F, Schönhals A, Lockwenz H, Beiner M, Schröter K, Donth E (1996) Macromolecules 29:247
38. Bergman R, Alvarez F, Alegria A, Colmenero J (1998) J Chem Phys 109:7546
39. Wübbenhorst M, van Turnhout J (2000) Dielectrics Newsletter 11:1
40. Nozaki R, Mashimo S (1987) J Chem Phys 87:2271

41. Schäfer H, Sternin E, Stannarius R, Arndt M, Kremer F (1996) Phys Rev Lett 76:2177
42. Kremer F, Huwe A, Schönhals A (2002) Molecular dynamics in confining space. In: Kremer F, Schönhals A (eds) Broadband dielectric spectroscopy. Springer, Berlin Heidelberg New York, chap 6
43. Vogel H (1921) Phys Z 22:645
44. Fulcher GS (1925) J Am Ceram Soc 8:339
45. Tammann G, Hesse G (1926) Anorg Allg Chem 126:245
46. Kim JH, Jang J, Zin WC (2000) Langmuir 16:4064
47. Böhmer R, Angell CA (1992) Phys Rev B45:10,091
48. Zorn R, Hartmann L, Frick B, Richter D, Kremer F (2002) J Non-Cryst Solids (accepted)
49. Adam G, Gibbs J (1965) J Chem Phys 43:139
50. Cohen MH, Turnbull J (1959) J Chem Phys 31:1164
51. Kremer F, Huwe A, Arndt M, Behrens P, Schwieger W (1999) J Phys Condens Matter 11:A175
52. Hensel A, Schick C (1998) J Non-Cryst Solids 235/237:510
53. Dalnoki-Veress K, Murray C, Gigault C, Dutcher JR (2001) Phys Rev E63:1801
54. Dalnoki-Veress K, Forrest JA, de Gennes PG, Dutcher JR (2000) Glass transition reductions in thin freely-standing polymer films: a scaling analysis of chain confinement effects. In: Frick B, Zorn R, Büttner H (eds) International Workshop on Dynamics in Confinement EDP Sciences, Les Ulis, J Phys IV 10:Pr7–221
55. Keddie JL, Jones RAL (1995) Israel J Chem 35:21
56. Fukao K (2001) private communication
57. Schick C, Merzlyakow M, Hensel A (1999) J Chem Phys 111:2695
58. Donth E (2001) The glass transition: relaxation dynamics in liquids and disordered materials. Springer, Berlin Heidelberg New York
59. Heise A, Menzel H, Yim H, Foster MD, Wieringa RH, Schouten AJ, Erb V, Stamm M (1997) Langmuir 13:723
60. Lambooy P, Russell TP, Kellog GJ, Mayes AM, Gallagher PD, Satija SK (1994) Phys Rev Lett 72:2899
61. Tourillon G, Fontaine A, Garrett R, Sagurton M, Xu P, Williams GP (1987) Phys Rev B (Condensed Matter) 35:9863
62. Hartmann L, Kremer F, Kratzmüller T, Braun HG (2001) IEEE Trans Dielectr Electr Insul 8:390
63. Hartmann L, Kremer F, Leger L et al. (to be published)
64. Chang YC, Frank CW, Forstmann GG, Johannsmann D (1999) J Chem Phys 111:6136
65. Jaworek T, Neher D, Wegner G, Wieringa RH, Schouten AJ (1998) Science 279:57
66. Schmidt A, Lehmann S, Georgelin M, Katana G, Mathauer K, Kremer F, Schmidt-Rohr K, Boeffel C, Wegner G, Knoll W (1995) Macromolecules 28:5487
67. H Block (1983) Poly(γ-benzyl-L-glutamate) and other glutamic acid containing polymers, 1st edn. Gordon and Breach Science Publishers, New York
68. Wang CC, Pecora R (1980) J Chem Phys 72:5333
69. Tsujita Y, Uematsu I (1974) Polym J 6:274
70. Moscicki JK, Williams G (1983) J Polym Sci Polym Phys Ed 21:197
71. Moscicki JK, Williams G (1983) J Polym Sci Polym Phys Ed 21:213
72. Moscicki JK, Williams G (1983) J Polym Sci Polym Phys Ed 21:2017

12 The Dielectric Properties of Semiconducting Disordered Materials

F. Kremer · S.A. Różański

12.1
Introduction

In Maxwell's equations the current density J and the time derivative of the electric displacement $\dfrac{\partial D}{\partial t}$ are additive quantities. Hence for sinusoidal electric fields the complex conductivity σ^* and the complex dielectric function ε^* are related by $\sigma^* = i\omega\varepsilon_0\varepsilon^*$ (ε_0 being the permittivity of the free space). Both quantities σ^* and ε^* are key features of (semi)-conducting (disordered) materials. Measured over a wide enough frequency – and temperature – range it enables one to analyse the underlying mechanisms of charge transport. Thereby it reflects a continuous process. At high frequencies ($\geq 10^{10}$ Hz) the charge carriers are driven by the external electric field over distances corresponding to atomic length scales, while in the direct current (d.c.) limit of $\omega \to 0$ they propagate on some percolation path from one side of the sample to the other. Thus with decreasing frequency a length scale is involved going from microscopic to macroscopic dimensions.

In disordered systems the charge transport takes place due to hopping conduction of which many different versions are known. To name a few: variable range hopping, phonon-assisted hopping, trigger induced hopping, nearest neighbour hopping etc. [1–17]. The motion of a charge in disordered systems is accompanied by an electrical relaxation. An ionic or electronic (in case of a polaron) charge is surrounded by negative or positive counter charges. A hop to a new site can lead to a successful charge transport only if the polarisation cloud follows, otherwise the charge carrier will – with high probability – jump back. This mutual electric relaxation requires a relaxation time τ_σ. If the external electric field has a frequency which is much higher than $1/\tau_\sigma$ its effect on the charge transport averages out. In contrast for $\omega \ll 1/\tau_\sigma$ it supports the charge transport and causes a contribution to the electrical relaxation which increases with decreasing frequency. This is the essence of the Debye-Hückel-Falkenhagen theory [18–20] of the dispersion of the dielectric function of electrolyte systems.

It is remarkable that the complex conductivity σ^* is similar in its frequency – and temperature (resp. charge carrier concentration) – dependence for a variety of quite different materials, e.g. ionic glasses [21–31] (Fig. 12.1a), ion conducting polymers [7, 32–46] (Fig. 12.1b), electron-conducting conjugated polymers [47–52] (Fig. 12.1c) or electron conducting carbon black composites [53–56] (Fig. 12.1d). In all cases the real part of the conductivity σ' has a plateau on the

a) 50LiF-30KF-20Al(PO₃)₃

b) 100 mol%

c)
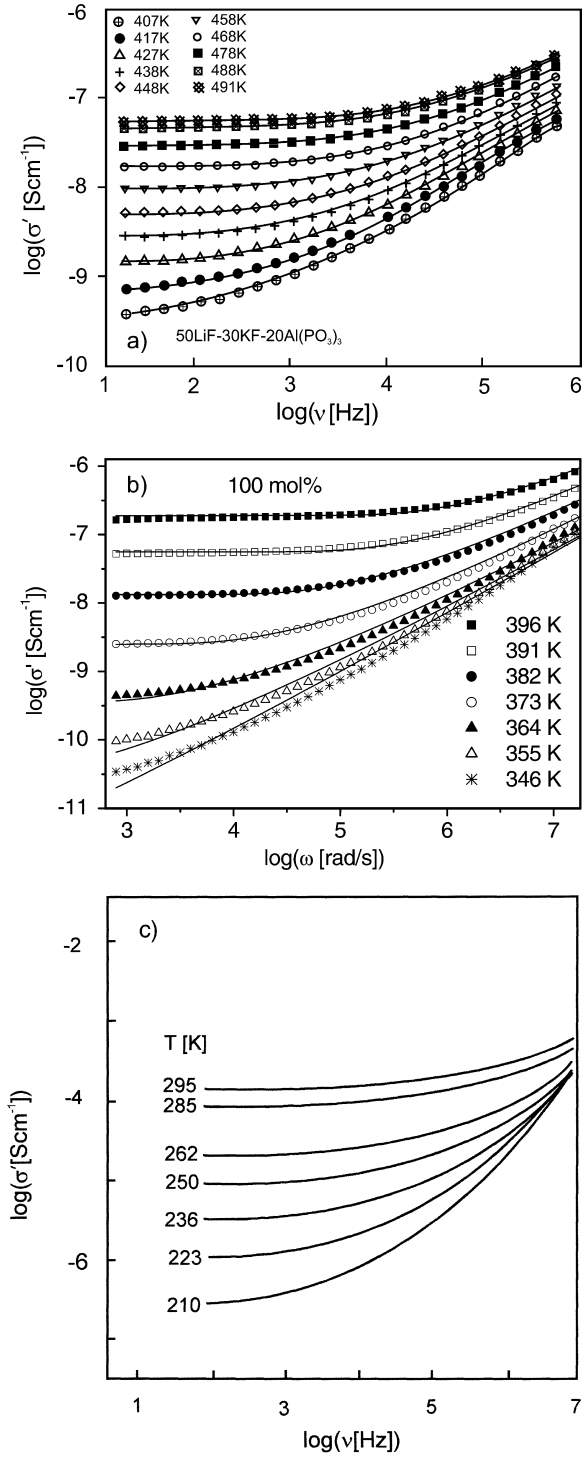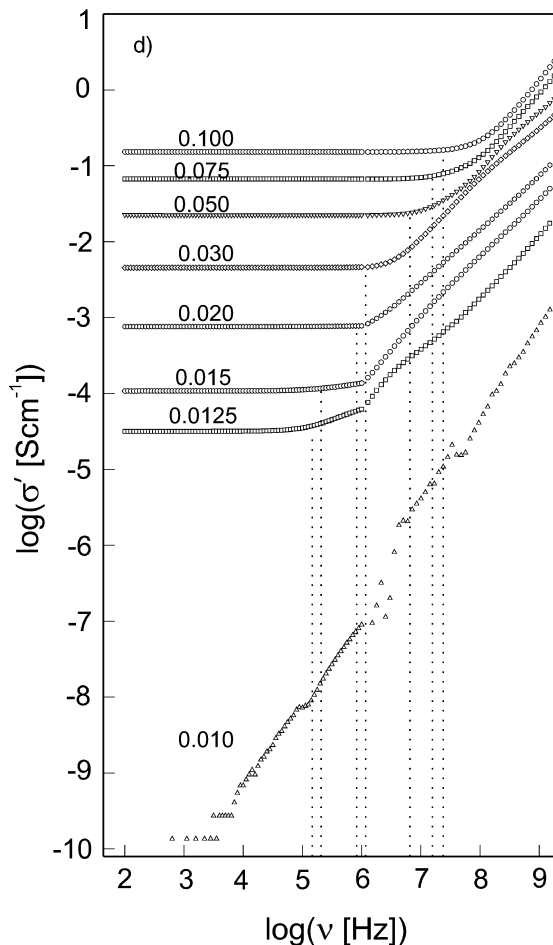
Fig. 12.1. A.c. conductivity of typical ion or electron conducting disordered materials. Each figure shows in log-log representation the frequency dependence of the real part of the complex conductivity $\sigma^*(\omega, T) = i\omega\varepsilon_0\varepsilon^*(\omega, T)$ at different temperatures or concentrations as indicated. **a** Mixed alkali glass 50LiF-30KF-20Al(PO$_3$)$_3$ glass [76]. **b** Zwitterionic polymer **P3** at 200 mol% NaI (see Sect. 12.3). **c** Poly(methyl-thiophene) [77]. **d** Composite of highly structured carbon black (CB) within an amorphous polymer, poly(ethylene terephthalate). The numbers indicate the various concentrations of CB in volume content [55]

low frequency side which bends off at a certain critical frequency ω_c and results for $\omega \gg \omega_c$ in a power law dependence of the type $\sigma' \sim \omega^s$ ($s \leq 1$). ω_c is determined by calculating the maximum in the second derivative of σ' with respect to ω[1]. In good approximation a "master function" can be constructed for the normalised conductivity $\sigma'(\omega)/\sigma'(0)$ with respect to ω/ω_c (Fig. 12.2a–d).

_____

[1] To determine ω_c by calculating the second derivative of $\sigma'(\omega)$ with respect to ω requires averaging of the data.
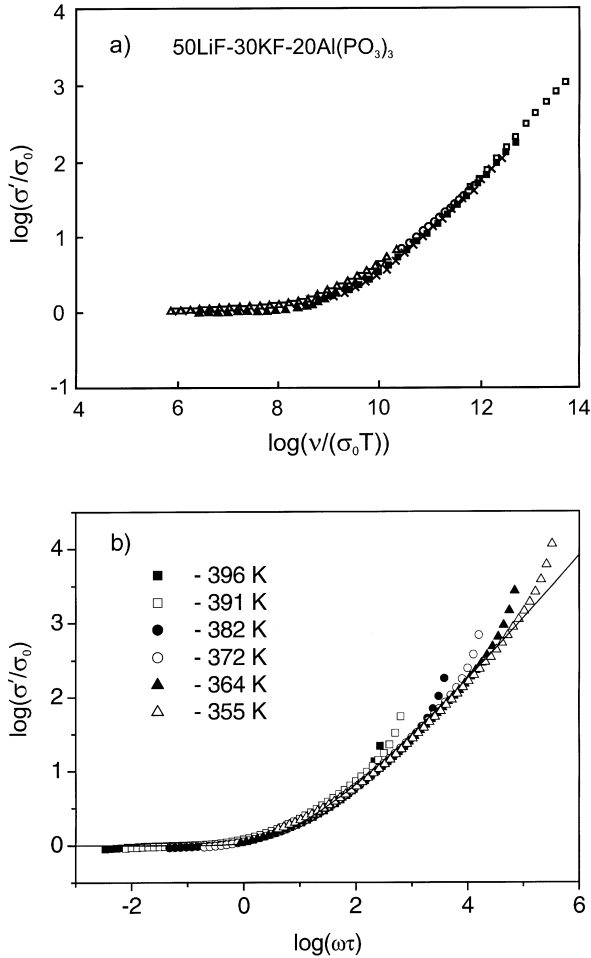
Fig. 12.2. A.c. conductivity master plots for the data shown in Fig. 12.1: **a** 50LiF-30KF-20Al(PO$_3$)$_3$ glass in the temperature range 407–401 K [76]; **b** Zwitterionic polymer **P3** at 100 mol% NaI (see Sect. 12.3)

The plateau value *and* the critical frequency ω_c decrease with decreasing temperature (resp. charge carrier concentration). This finding (Fig. 12.3) is know as the experimentally observed Barton-Nakajima-Namikawa (BNN)-relationship [57–59]

$$\sigma(0) \sim \omega_c \tag{12.1}$$

It indicates that the d.c. – and a.c. – conductivity are closely related to each other and based on the same mechanism of charge transport. Hence any separation into d.c.- and a.c.-like charge carriers is artificial and without physical meaning.
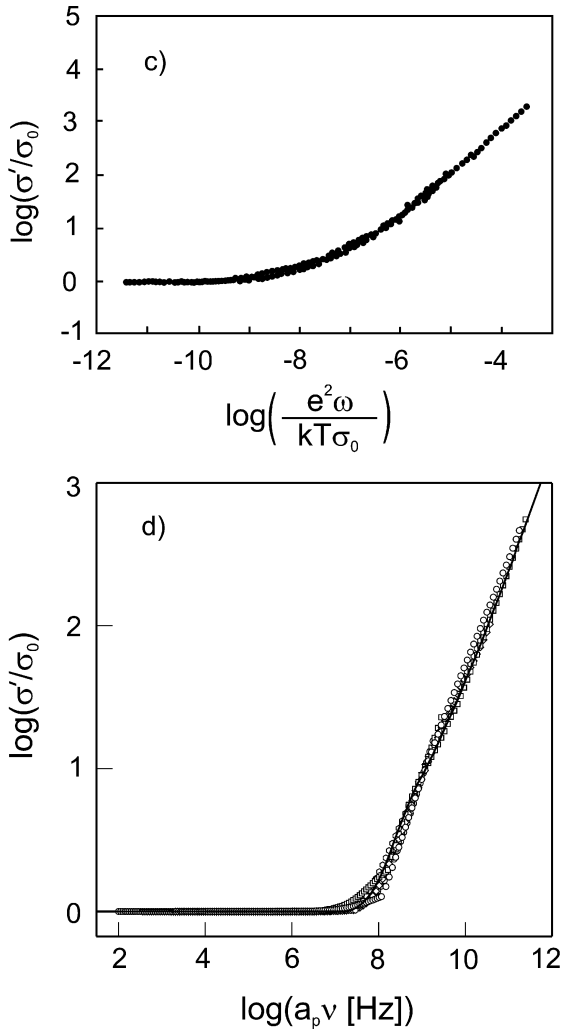
Fig. 12.2 (continued). **c** poly(methyl-thiophene) [77]; **d** composite of highly structured carbon black (CB) within amorphous poly(ethylene terephthalate) [55]

This chapter is organised in the following sections. In Sect. 12.2 the similarities of the frequency and temperature (resp. charge carrier concentration)-dependence of the complex conductivity will be discussed in detail. In Sect. 12.3 – as an example for an ion conducting polymers – relaxation and charge transport in mixtures of zwitterionic polymers and inorganic salts will be discussed. In Sect. 12.4 conclusions will be drawn and it will be discussed from which physical quantities which information can be deduced best concerning the charge transport in semiconducting disordered systems.

Fig. 12.3. BNN-plot for the data shown in Fig. 12.1a–d and Polymer P3 at 0 and 100 mol% NaI
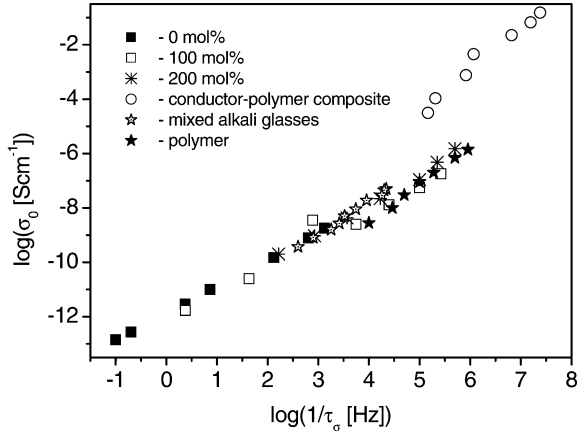
12.2
Similarities[2] in the a.c. Conductivity of Semiconducting Disordered Materials

The observed frequency – and temperature (charge carrier concentration) – dependence of the real part of the conductivity σ' is characterised by the following features [16, 60]:

1. For elevated temperatures (resp. charge carrier concentration[3]) σ' has a plateau for frequencies ω smaller than a certain critical frequency ω_c.
2. For frequencies $\omega > \omega_c$ a gradual dispersion sets in resulting in a power law dependence

$$\sigma(\omega) \sim \omega^s \tag{12.2}$$

with $0.5 \leq s \leq 1$.
3. s increases with decreasing temperature and increasing frequency.
4. For frequencies $\omega < \omega_c$ the temperature dependence of σ' is much more pronounced than for $\omega > \omega_c$.
5. In good approximation it is possible to assume time-temperature superposition and to scale the normalised conductivity $\sigma'(\omega)/\sigma'(0)$ with respect to the normalised frequency ω/ω_c.

---

[2] Sometimes instead of similarities the term "universalities" is used. In view of the fact that the observed scaling of the conductivity is a good approximation only and by no means strict we prefer the term "similarities".
[3] The number density of the charge carriers is in disordered systems a thermally activated usually Arrhenius-like process. In this sense temperature and charge carrier concentration are equivalent. In the following the later will be omitted.

6. The frequency ω_c satisfies the Barton-Nakajima-Namikawa (BNN)-relation [57–59]

$$\sigma'(\omega \to 0) \sim \omega_c \tag{12.3}$$

On the basis of what models can these features be described? The fluctuation-dissipation theorem expresses the frequency-dependent conductivity $\sigma^*(\omega)$ in terms of the equilibrium (i.e. zero-field) current autocorrelation function [61]

$$\sigma^*(\omega) = \frac{Nq^2}{k_BT} \int_0^\infty \langle v(0)\, v(t) \rangle\, e^{-i\omega t} dt \tag{12.4}$$

where q is the charge of a single charge carrier, $v(t)$ its velocity projected onto a fixed direction in space and N the number density. For the frequency dependent diffusion constant $D^*(\omega)$ with

$$D^*(\omega) = \int_0^\infty \langle v(0)\, v(t) \rangle\, e^{-i\omega t}\, dt \tag{12.5}$$

from Eq. (12.4) follows

$$\sigma^*(\omega) = \frac{Nq^2}{k_BT} D^*(\omega) \tag{12.6}$$

which reduces to the well-known "Nernst-Einstein" equation for $\omega \to 0$

$$\sigma(\omega \to 0) = \frac{Nq^2}{k_BT} D(\omega \to 0) \tag{12.7}$$

For the mean-squared displacement $\langle [r(t) - r(0)]^2 \rangle$ of the charge carriers it follows

$$D^*(\omega) = -\frac{1}{6}\omega^2 \int_0^\infty e^{i\omega t} \langle [r(t) - r(0)]^2\, dt \rangle \tag{12.8}$$

Possible correlations between successive hops of mobile charge carriers or cross-correlations between adjacent charges are not taken into account here. They can be introduced on the right hand side of Eq. (12.6) by the Haven ratio f_H. Thus in order to describe the dispersion of the complex conductivity resp. the diffusion constant D^* the time dependence of the mean squared displacement of the charge carriers has to be modelled. In the low-frequency regime this is realised by macroscopic approaches. For frequencies above ω_c microscopic models are required[4].

The simplest macroscopic model for electrical conduction is based on percolation [62–64]. The "percolation threshold" p_c, where an infinite "percolation

---

[4] The reader is referred to the review article by Dyre JC and Schrøder TB (2000) Rev Mod Physics 72:873.

cluster" appears has in two dimensions a value of $p_c = 0.5$ and in three dimensions of $p_c = 0.2488$ [63]. The temperature dependence of the d.c.-conductivity $\sigma(0) = \exp(-E_c/k_B T)$ is Arrhenius-like with an activation energy E_c. As shown by [65–68] p_c and E_c are related according to

$$\int_0^{E_c} p(E)\mathrm{d}E = p_c \qquad (12.9)$$

where $p(E)$ is the activation energy probability distribution. E_c determines the bottlenecks in the charge transport and hence – in case of hopping conduction – it describes the largest barrier [16].

Another macroscopic ansatz treats the sample with its local inhomogeneities in conductivity as an "effective medium" [69, 70]. By that the sample is considered as a mixture of components having different dielectric properties. The averaged effective conductivity is calculated in a self consistent manner [71].

It is also possible to model the sample by equivalent electrical circuits of random resistors and capacitors [72, 73]. All capacitors are equal, proportional to ε' while each resistor is proportional to $1/\sigma'$ at a certain position in the network. When a potential difference is applied to two opposing boundaries the electrostatic potentials at the nodes are obtained by solving Kirchoff's equations. The resistor currents are related to the motion of free charges while the capacitor currents correspond to Maxwell's displacement [73]. Applying a periodic potential enables one to determine the conductivity $\sigma^*(\omega)$.

The effective medium approximation and the percolation approach are opposite approaches. The former views conduction as spatially homogeneous, the later treats it as strictly one-dimensional. In order to take into consideration the fractal structure of the diffusion cluster Dyre and Schrøder proposed a "diffusion cluster approximation" [16].

As a microscopic approach hopping conduction has to be considered. A variety of different models exist. The simplest is the random free-energy barrier model as developed by Dyre. This model assumes that conduction takes place by hopping of charge carriers which are subject to spatially randomly varying energy barriers. It is solved within the Continuous-Time-Random Walk (CTRW) approximation [74] with the result [9]

$$\sigma^*(\omega) = \sigma(0)\left[\frac{i\omega\tau_e}{\ln(1+i\omega\tau_e)}\right] \qquad (12.10)$$

where τ_e is the attempt frequency to overcome the largest barrier determining the d.c.-conductivity. Splitting Eq. (12.10) into real and imaginary parts delivers

$$\sigma'(\omega) = \frac{\sigma(0)\,\omega\tau_e\arctan(\omega\tau_e)}{\frac{1}{4}\ln^2(1+\omega^2\tau_e^2)+(\arctan\omega\tau_e)^2}$$

$$\sigma''(\omega) = \frac{\sigma(0)\,\omega\tau_e\ln(1+\omega^2\tau_e^2)}{\frac{1}{2}\ln^2(1+\omega^2\tau_e^2)+2(\arctan\omega\tau_e)^2}$$

$$(12.11)$$

For the exponent s one obtains [9]

$$s = 1 - 2/\ln(\omega\tau_e) \qquad (12.12)$$

Furthermore it is shown that the BNN relationship is fulfilled by the model.

In a recent review Dyre and Schrøder compared the above-mentioned macroscopic and microscopic models of the conduction with the result that all reproduce the above discussed characteristic features [16]. The frequency and temperature dependence of the conductivity proves to be determined by the weakest link ("the bottleneck") in the conductive path – irrespective of the nature of the charge carriers.

12.3
Relaxation and Charge Transport in Mixtures of Zwitterionic Polymers and Inorganic Salts

In zwitterionic polymers [45] each macromolecule bears the same number of cationic and anionic groups, hence the individual chains are uncharged in spite of the high concentration of ionic groups present. The high density in dipolar units results in a number of specific features of polyzwitterions: (i) very high glass transition temperatures, (ii) strong polarity and (iii) hygroscopy. Furthermore these polymers are strongly interacting with low-molecular weight cations and anions, both in solution and in the bulk. In selected cases these interactions enable the preparation of homogeneous mixtures of polyzwitterions with inorganic salts containing up to stoichiometric amounts of the salt. This behaviour was recently demonstrated for a number of zwitterionic poly(sulfobetaines) blended with $LiClO_4$, NaBr or NaI. Phase segregation is only observed in mixtures containing more than 125 mol% of salt. The chemical structure of the zwitterionic polymethacrylate poly{3-[N-(ω-methacryloyloxyalkyl)-N,N-dimethylammonio] propanesulfonate} where $m = 2$(**P1**), $m = 6$(**P2**), and $m = 11$(**P3**) is shown in Fig. 12.4.

In polymers **P2** and **P3**, the ionic groups are separated from the polymer backbone by long alkyl spacers ($m = 6$ and 11). In contrast, in polymer **P1** the ionic groups are attached closely to the backbone ($m = 2$). The dielectric properties of the ion-conducting system are characterised by a superposition of a dielectric relaxation process and a strong conductivity contribution. For elevated temperatures furthermore an electrode polarisation effect gives rise to a strong increase of
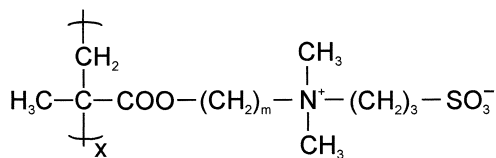
Fig. 12.4. Scheme of chemical structure of the zwitterionic polymethacrylate poly{3-[N-(ω-oxyalkyl)-N,N-dimethylammonio]propanesulfonate}

$\varepsilon'(\omega)$ and $\sigma''(\omega)$ at low frequencies. The different contributions can be (to a certain extent) separated by choosing an appropriate temperature range. At temperatures <243 K one relaxation process occurs. It can be quantitatively analysed using a generalised relaxation function according to Havriliak-Negami and by a superposition of a conductivity contribution as suggested by Dyre (Eq. 12.10)

$$\varepsilon^*_{total} = \frac{\sigma^*(\omega)}{i\omega\varepsilon_0} + \varepsilon^*_{HN}(\omega)$$

$$\varepsilon^*_{HN}(\omega) = \varepsilon_\infty + \frac{\varepsilon_s - \varepsilon_\infty}{(1 + (i\omega\tau)^\alpha)^\gamma}$$

(12.13)

$\Delta\varepsilon = \varepsilon_s - \varepsilon_\infty$ is the dielectric strength where ε_s is the value of ε' in the limit of $\omega \ll 1/\tau$ where τ is the relaxation time of the underlying process. The term ε_∞ describes the value of the real part ε' in the limit of high frequencies. The constant α and γ describe symmetric and asymmetric broadening of the relaxation time distribution.

Figure 12.5a,b shows the two contributions as separated according to Eq. (12.13). The fit parameters (Table 12.1) α and γ are nearly independent of the salt concentration. The relaxation process depends sensitively on the length of the spacer between the betaine groups and the polymer backbone. The process is shifted to higher temperatures with decreasing length of the alkyl spacer.

In contrast the amount of the NaI has a negligible influence on the relaxation process only (Fig. 12.6). The observed Arrhenius-type temperature dependence has an activation energy of $E_A = 47$ kJ mol^{-1}. With this value but also in its absolute frequency and temperature dependence it is comparable to the γ-relaxation in ionene glasses as observed by mechanical [32–34] and dielectric spectroscopy [37]. The γ-relaxation is assigned to fluctuations of the methylene groups which are transmitted to some extent to the polar ammonium moiety, which makes this relaxation dielectrically active. The strong dependence on the length of the spacer fits well to this interpretation.

The conductivity contribution can be best analysed in terms of $\sigma^*(\omega)$[5]. The data can be well described by the conductivity as suggested by Dyre (Eq. 12.10). On the low-frequency side deviations occur which are caused by electrode polarisation effects (Tables 12.2 and 12.3). The latter has its physical origin in the formation of a layer of counterions at the external electrodes. By that electric field energy is stored in the sample giving rise to a strong increase in $\varepsilon'(\omega)$ and a weak decline in $\varepsilon''(\omega)$. The electrode polarisation effect can be described by the empirical formula

$$\varepsilon' = A\omega^{-z}$$

(12.14)

where A and z are strongly temperature dependent fit parameters (see Chap. 3).

---

[5] This sounds trivial, but there is an ongoing debate in what terms conductivity spectra should be analysed in ε^*, σ^* or $M^* = 1/\varepsilon^*$? (see for instance a panel discussion at the 4th International Meeting on Relaxation in Disordered Systems, Heraklion, June 2001 or Roling B, Happe A, Funke K, Ingram MD (1997) Phys Rev Lett 78:2160, Sidebottom DL, Roling B, Funke K (2000) Phys Rev B 63:024,301, Sidebottom DL (1999) Phys Rev Lett 82:3653).

Fig. 12.5. Separation of the conductivity contribution and the relaxation process according to (Eq. 12.13): a sample **P3**. The relaxation process and the conductivity contribution add up to ε''_{total}; **b** influence of the spacer length m on the spectral position of the relaxation process. Otherwise as **a** for 224 K
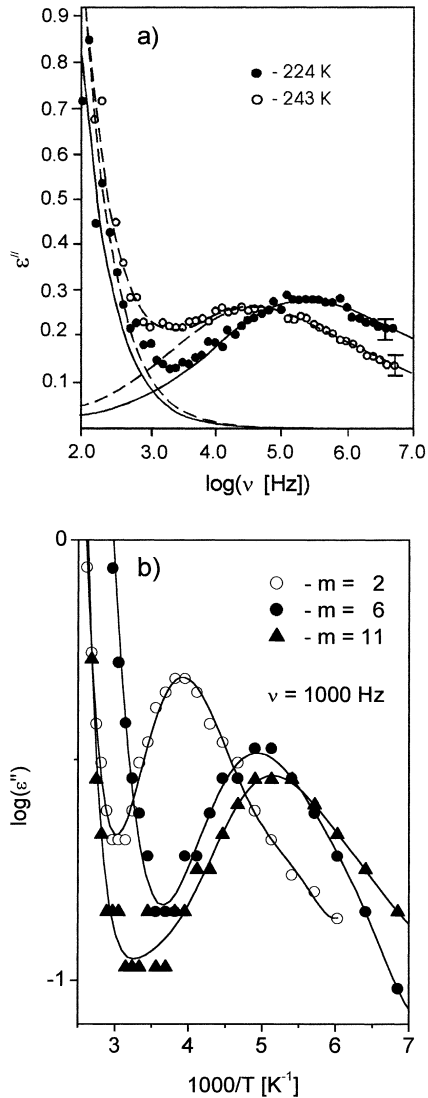
In Fig. 12.7 it is shown how well Eq. (12.10) describes the complex conductivity of the system. At elevated temperatures (≥ 382 K) electrode polarisation must be considered. The data of Fig. 12.7 are presented in terms of $\varepsilon^*(\omega)$ in Fig. 12.8. An electrode polarisation effect shows up as a steep increase in $\varepsilon'(\omega)$ with decreasing frequency for temperatures ≥ 382 K. The fits work equally well as in the $\sigma^*(\omega)$ representation.

Displaying the data in the complex modulus $M^* = \dfrac{1}{\varepsilon^*}$ delivers nearly perfect fits in M' while in M'' certain deviations occur (Fig. 12.9). The relaxation rates ω_M, ω_c and $1/\tau_e$ show very similar absolute values and a nearly identical temper-

Table 12.1. Fit parameters for the γ-relaxation according to the Harviliak-Nagami equation (Eq. 12.13). For ε_∞ values of 3.7 ± 0.3 (100 mol%) and 9.5 ± 0.3 (200 mol%) are obtained

Concentration [mol%]	Temperature [K]	$\Delta\varepsilon$	α	γ	τ [s]
0	214	1.904	0.420	0.524	9.2×10^{-5}
	224	1.692	0.475	0.524	1.8×10^{-5}
	233	1.762	0.465	0.524	6.7×10^{-6}
	243	1.684	0.506	0.524	2.6×10^{-6}
	253	1.684	0.530	0.524	1.1×10^{-6}
	262	1.783	0.502	0.524	5.7×10^{-7}
100	202	0.599	0.475	0.444	8.4×10^{-5}
	212	0.617	0.488	0.444	3.0×10^{-5}
	221	0.644	0.489	0.444	1.2×10^{-5}
	231	0.610	0.539	0.444	4.8×10^{-6}
	241	0.562	0.604	0.444	1.8×10^{-6}
	250	0.529	0.656	0.444	8.5×10^{-7}
	260	0.549	0.643	0.444	5.6×10^{-7}
200	193	1.245	0.454	0.529	7.0×10^{-5}
	203	1.299	0.458	0.529	2.5×10^{-5}
	212	1.266	0.491	0.529	8.8×10^{-6}
	222	1.239	0.521	0.529	3.5×10^{-6}
	232	1.196	0.555	0.529	1.5×10^{-6}
	241	1.215	0.558	0.529	7.7×10^{-7}
	251	1.270	0.542	0.529	4.3×10^{-7}
	261	1.318	0.529	0.529	2.4×10^{-7}

Table 12.2. Fit parameters σ_0 and τ_e as deduced from fits according to the Dyre conductivity (Eq. 12.10)

Temperature [K]	σ_0 [Scm^{-1}] 0 mol%	τ_e [s]	σ_0 [Scm^{-1}] 100 mol%	τ_e [s]	σ_0 [Scm^{-1}] 200 mol%	τ_e [s]
396	1.8×10^{-9}	7.5×10^{-4}	1.9×10^{-8}	3.6×10^{-6}	1.5×10^{-6}	1.7×10^{-6}
391	7.9×10^{10}	1.6×10^{-3}	5.6×10^{-8}	1×10^{-5}	5.0×10^{-7}	3.6×10^{-6}
382	1.5×10^{-10}	7.6×10^{-3}	1.3×10^{-8}	4×10^{-5}	1.1×10^{-7}	1×10^{-5}
373	1.0×10^{-11}	1.4×10^{-1}	2.5×10^{-9}	1.8×10^{-4}	2.2×10^{-8}	5×10^{-5}
364	2.9×10^{-12}	4.2×10^{-1}	3.5×10^{-10}	1.3×10^{-3}	4.5×10^{-9}	2.3×10^{-4}
355	2.7×10^{-13}	5	2.5×10^{-11}	2.3×10^{-2}	1.0×10^{-9}	9.8×10^{-4}
346	1.4×10^{-13}	10	2.8×10^{-13}	4	2.4×10^{-10}	4.4×10^{-3}

Table 12.3. Fit parameters A and z describing the electrode polarisation according to Eq. (12.14)

Temperature [K]	A [(Hz)^z] 100 mol%	z [/]	A [(Hz)^z] 200 mol%	z [/]
396	24×10^5	1.32	32×10^6	1.33
391	7×10^4	1.03	47×10^5	1.27
382	6×10^2	0.55	18×10^4	1.05

Fig. 12.6. Activation plot – log τ vs 1000/T for different ion concentrations
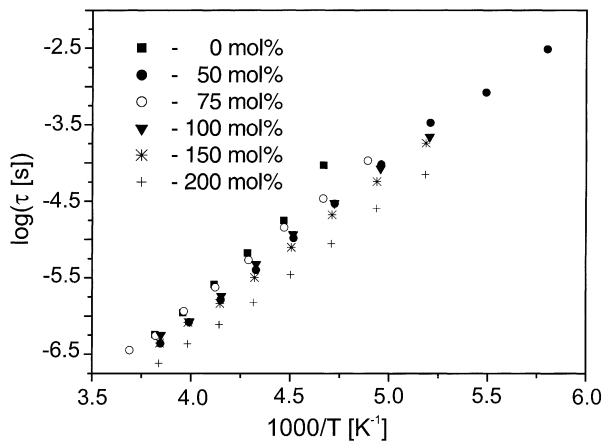
Fig. 12.7. Real and imaginary part of the conductivity σ^* vs frequency at temperatures as indicated. Sample **P3** at 200 mol% NaI. The *solid line* is a fit according to Eqs. (12.10), (12.13) and (12.14). The conductivity (—) and electrode polarisation effects (---) add up, while the relaxation process is negligible on this scale. The *inset* shows the quality of the fit. The fit parameters are contained in Tables 12.2 and 12.3
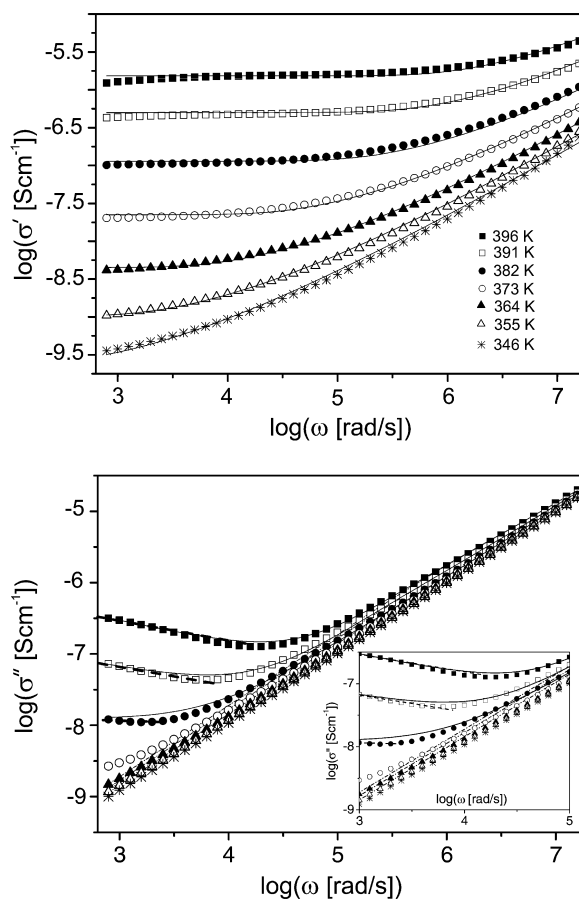
Fig. 12.8. Real and imaginary part of the complex dielectric function ε^* vs frequency for the data shown in Fig. 12.7
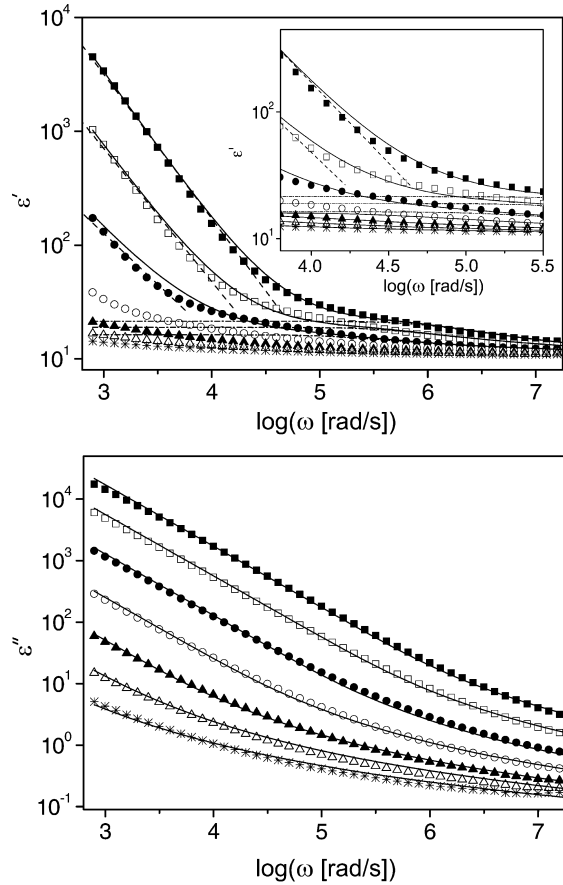
ature dependence (Fig. 12.10). The macroscopic electrical modulus relaxation time $2\pi/\omega_M$ is related to the microscopic electrical relaxation time by a factor proportional to $\varepsilon_\infty \dfrac{2\pi}{\omega_M}$. This was proven experimentally and theoretically by [75].

Master plots with respect to temperature and ion concentration (Fig. 12.11) can be constructed for both dependencies, but systematic deviations occur at the high frequency side (especially in the temperature dependence). This proves that the assumed time-temperature superposition is a good approximation of the data but by no means a fundamental law.

The temperature dependence of the fit parameters σ_0 and τ_e as obtained from fits using Eq. (12.10) is Arrhenius like with activation energies between 44 kcal mol^{-1} and 62 kcal mol^{-1} (Table 12.4). Displaying $\sigma(\omega = 0)$ vs τ_e^{-1} proves how well the BNN relationship is fulfilled by the data irrespective of the ion concentration (Fig. 12.12). The temperature dependence of the exponent parameter s shows (Fig. 12.13) that also this quantity is well described by the formula developed by Dyre.

Fig. 12.9. Real and imaginary part of the dielectric modulus M^* vs frequency for the data shown in Fig. 12.7
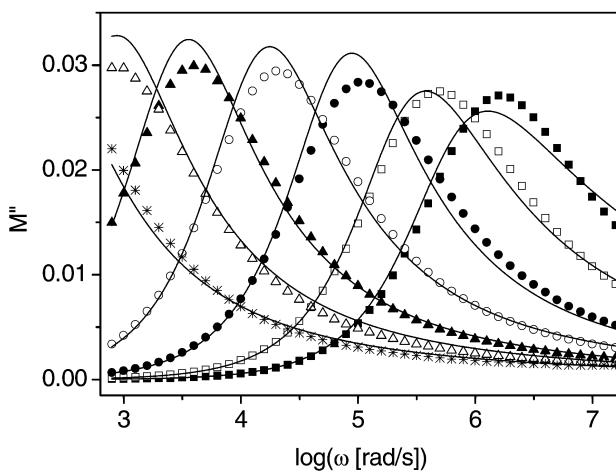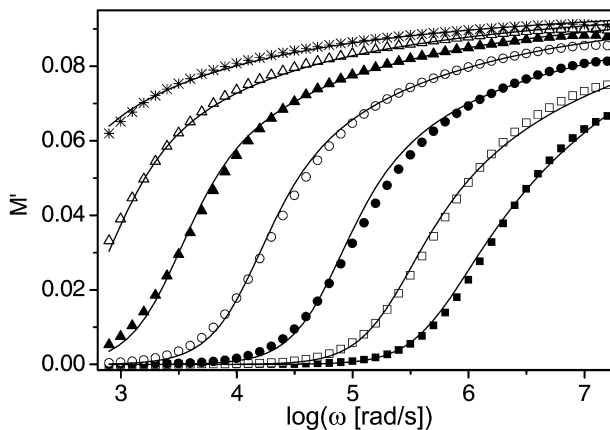
Fig. 12.10. Activation plot for different electrical relaxation rates ω_c (as obtained from σ^*) ω_M (as obtained from the maximum in $M''(\omega)$ and $1/\tau_e$ as taken from the fit using Eq. (12.10)
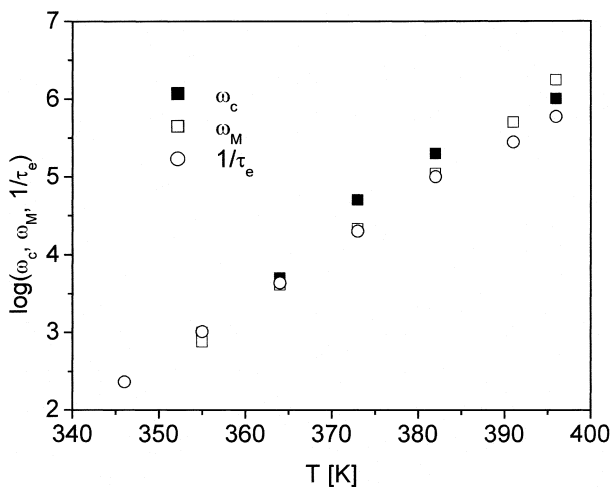
Fig. 12.11. Masterplots of the normalised conductivity σ'/σ_0 vs $\omega\tau_e$. σ_0 and τ_e are obtained from a fit using Eq. (12.10). The *solid lines* indicate the scaling of the conductivity predicted by Dyre: **a** for different temperatures as indicated, sample: **P3**; **b** for different ion concentrations at a fixed temperature of $T = 396$ K
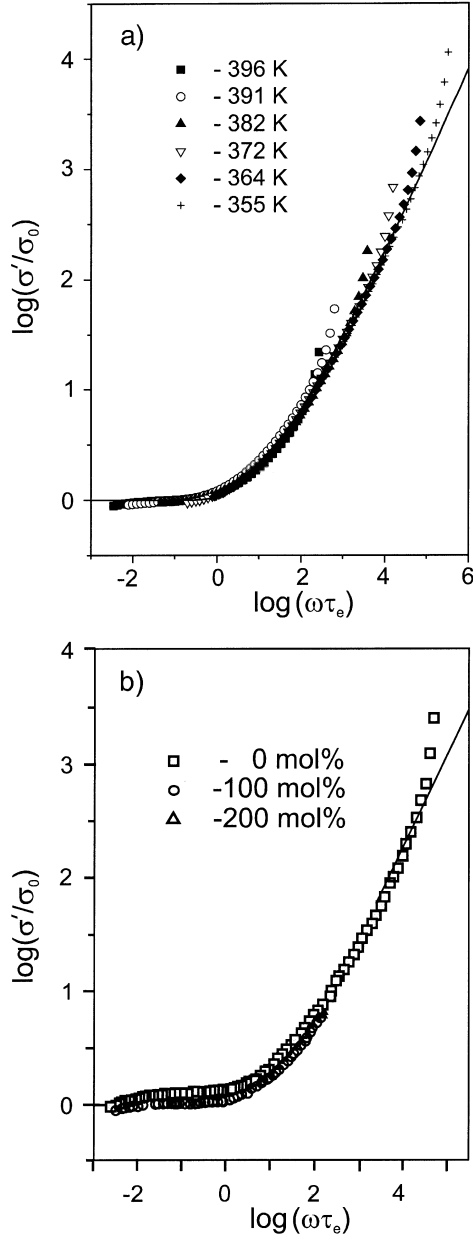
Table 12.4. Activation energies E_A of the d.c. conductivity σ_0 and τ_e for different salt concentrations

Concentration [mol%]	E_A for σ_0 [kcal mol^{-1}]	E_A for $1/\tau_e$ [kcal mol^{-1}]
0	55	56
100	61	62
200	48	44

Fig. 12.12. BNN-plot: $\log \sigma_0$ vs $\log (1/\tau_e)$ for the ion concentrations as indicated. σ_0 and τ_e were obtained from fits using Eq. (12.10)
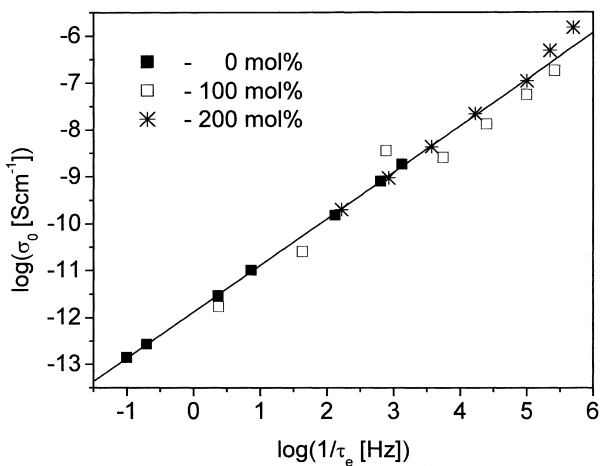
Fig. 12.13. Exponent parameter s vs T at different ion concentrations as indicated. The corresponding *open symbols* describe the predictions according the Eq. (12.12)
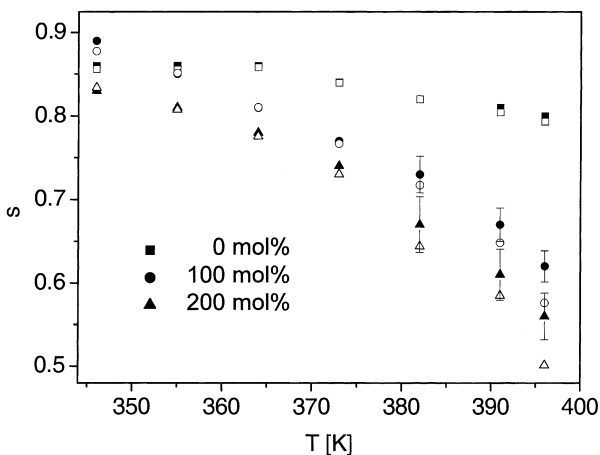
In summary one has to state that in the system under study (zwitterionic polymers with inorganic salts) the dielectric data can be well described by a superposition of a generalised relaxation function a conductivity contribution as developed by Dyre and a term describing electrode polarisation.

12.4
Conclusions

The dielectric properties of semiconducting disordered materials have characteristic features in the real *and* imaginary part of the conductivity σ^*, the dielectric function ε^* or the electrical modulus M^*. All these representations are completely equivalent but they emphasize of course different aspects of the underlying mechanisms of charge transport. Based on hopping conduction with increasing frequency the entire range from macroscopic to microscopic length scales is covered. As an example fits of the *complex* quantities are presented for zwitterionic polymers using a conductivity formula as derived by Dyre in the framework of a random free energy barrier model.

Electrode polarization effects occur for ionic charge carriers and result in a huge effective increase of ε' or σ'' with decreasing frequency. Furthermore possible contributions due to underlying relaxation processes or infrared absorption bands have to be taken into consideration.

List of Abbreviations and Symbols

A, z	Fit parameters
$\boldsymbol{D}$	Dielectric displacement
$D^*(\omega)$	Frequency dependent diffusion constant
E_A	Activation energy
k_B	Boltzmann constant
$M^* = M' + iM''$	Complex electric modulus, real and imaginary part
N	Number density
q	Charge of a single charge carrier
s	Exponent characterising the frequency dependence of the a.c. conductivity
$v(t)$	Velocity projected onto a fixed direction in space
t	Time
T	Temperature measured in Kelvin [K]
α, γ	Shape parameters of Havriliak-Negami function
$\Delta\varepsilon = \varepsilon_s - \varepsilon_\infty$	Dielectric strength
$\varepsilon^* = \varepsilon' - i\varepsilon''$	Complex dielectric function or permittivity, real and imaginary part

$\varepsilon_s, \varepsilon_\infty$	Static permittivity $\varepsilon_s = \lim \varepsilon'(\omega)$ if $\omega \ll 1/\tau$; high frequency permittivity $\varepsilon_\infty = \lim \varepsilon'(\omega)$ if $\omega \gg 1/\tau$
ε_0	Permittivity of the free space
σ_0	Direct current (d.c.)-conductivity
$\sigma^* = \sigma' + i\sigma''$	Complex conductivity, real and imaginary part
τ	Relaxation time
τ_e	Attempt time to overcome the largest barrier determining the d.c.-conductivity
τ_σ	Conductivity relaxation time
ω	Radial frequency
ω_c	Critical radial frequency
BNN	Barton-Nakajima-Namikawa

References

1. Stevels JM (1957) The electrical properties of glass. In: Flügge S (ed) Handbuch der Physik. Springer, Berlin Heidelberg New York, p 350
2. Macedo PB, Moynihan CT, Bose RA (1972) Phys Chem Glasses 13:171
3. Pollak M, Pike GE (1972) Phys Rev Lett 28:1449
4. Jonscher AK (1977) Nature 267:673
5. Mott NF, Davis EA (1979) Electronic processes in non-crystalline materials. Clarendon Press, Oxford
6. Long AR (1982) Adv Phys 31:553
7. Shklovskii BI, Efros AL (1984) Electronic properties of doped semiconductors. Springer, Berlin Heidelberg New York
8. Boettger H, Bryksin VV (1985) Hopping conduction in solids. Akademie, Berlin
9. Dyre JC (1988) J Appl Phys 64:2456
10. Elliot SR (1990) Physics of amorphous materials, 2nd edn. Longman Scientific, London
11. Funke K, Hoppe R (1990) Solid State Ionics 40/41:200
12. Dieterich W (1990) Solid State Ionics 40/41:509
13. Hunt A (1991) Philos Mag B 64:579
14. Maass P, Meyer M, Bunde A (1995) Phys Rev B 51:8164
15. Rinn B, Dieterick W, Mass P (1998) Philos Mag B 77:1283
16. Dyre JC, Schrøder TB (2000) Rev Mod Physics 72:873
17. León C, Rivera A, Várez A, Sanz J, Santamaria J (2001) Phys Rev Lett 86:1279
18. Debye P, Hückel E (1923) Phys Z 24:185
19. Debye P, Falkenhagen H (1928) Phys Z 29:121, 401
20. Falkenhagen H (1971) Theorie der Elektrolyte. S. Hirzel, Leipzig
21. Angell CA (1983) Solid State Ionics 9/10:3
22. Angell CA (1990) Chem Rev 90:523
23. Elliot SR, Owens AP (1991) Ber Bunsenges Phys Chem 95:987
24. Nowick AS, Lim BS (1994) J Non-Cryst Solids 172/174:1389
25. Murawski L, Barczyński RJ (1995) J Non-Cryst Solids 185:84
26. Bazan JC, Duffy JA, Ingram MD, Mallace MR (1996) Solid State Ionics 86/88:497
27. Murawski L, Barczyński RJ (1996) J Non-Cryst Solids 196:275
28. León C, Santamaría J, París MA, Sanz J, Ibarra J, Torres LM (1997) Phys Rev B 56:5302
29. Sidebottom DL (1999) Phys Rev Lett 82:3653
30. Rivera A, Santamaría J, León C (2001) Appl Phys Lett 78:610
31. Murawski L, Barczyński RJ (2001) IEEE Trans Dielectr Electr Insul 8:442
32. Tsutsui T, Sato T, Tanaka T (1975) J Polym Sci Polym Phys Ed 13:2091
33. Tsutsui T, Tanaka R, Tanaka T (1976) J Polym Sci Polym Phys B 14:2259

34. Tsutsui T, Tanaka R, Tanaka T (1976) J Polym Sci Polym Phys B 14:2273
35. Tsutsui T, Tanaka T (1977) Polymer 18:817
36. Ratner MA, Nitzan A (1988) Solid State Ionics 28:3
37. Kremer F, Dominguez L, Meyer WH, Wegner G (1989) Polymer 30:2023
38. Köberle P, Laschewsky A, Lomax TD (1991) Macromol Chem Rapid Commun 12:427
39. Meyer WH, Perchez J, Mathy A, Wegner G (1991) Adv Mater 3:153
40. Kremer F, Klee J (1992) Polymer 33:5364
41. Tsuruk V, Mischenko N, Köberle P, Laschewsky A (1992) Macromol Chem 193:1829
42. Rietz RR, Schaefer D, Meyer WH (1992) Electrochim Acta 37:1491
43. Meyer WH (1993) Makromol Chem Macromol Symp 69:35
44. Rietz RR, Schmidt-Rohr K, Meyer WH, Spiess HW, Wegner G (1994) Solid State Ionics 68:151
45. Różański SA, Kremer F, Köberle P, Laschewsky A (1995) Macromol Chem Phys 196:877
46. Köberle P, Laschewsky A (1994) Macromolecules 27:2165
47. Kivelson S, Epstein AJ (1984) Phys Rev B 29:3336
48. Epstein AJ (1986) AC conductivity of polyacetylene: distinguishing mechanisms of charge transport. In: Skotheim TA (ed) Handbook of conducting polymers, vol 2. Marcel Dekker, New York, p 1041
49. Ngai KL, Rendell RW (1986) In: Skotheim TA (ed) Handbook of conducting polymers, chap 28, p 967
50. Ulanski J, Glatzhofer DT, Przybylski M, Kremer F, Gleitz A, Wegner G (1987) Polymer 28:859
51. Rühe J, Kröhnke C, Ezquerra M, Kremer F, Wegner G (1987) Ber Bunsenges Phys Chem 91:885
52. Kremer F, Rühe J, Meyer WH (1990) Macromol Chem Macromol Symp 37:115; Kubo R (1957) J Phys Soc Jpn 12:570
53. Kremer F, Ezquerra M, Mohammadi W, Bauhofer W, Vilgis TA, Wegner G (1988) Solid State Commun 66:153
54. Pelster R, Marquardt P, Nimtz G, Enders A, Eifert H, Friedrich K, Petzholdt F (1992) Phys Rev B45: 8929
55. Connor MT, Roy S, Ezquerra TA, Baltá-Calleja FJ (1998) PRB 57:2286
56. Pelster R, Simon U (1999) Colloid Polym Sci 277:2
57. Barton JL (1966) Verres Refract 20:328
58. Nakajima T (1971) Annual Report, Conference on Electric Insulation and Dielectric Phenomena. National Academy of Sciences, Washington DC
59. Namikawa H (1975) J Non-Cryst Solids 18:173
60. Kremer F, Dominguez L, Meyer WH, Wegner G (1989) Polymer 30:2023
61. Kubo R (1957) J Phys Soc Jpn 12:570
62. Broadbent SR, Hammersley JM (1957) Proc Cambridge Philos Soc 53:629
63. Isichenko MB (1992) Rev Mod Phys 64:961
64. Stauffer D, Aharony A (1992) Introduction to percolation theory, 2nd edn. Taylor and Francis, London
65. Ambegaokar V, Halperin BI, Langer JS (1971) Phys Rev B 4:2612
66. Shklovskii BI, Efros AL (1971) Zh Eksp Teor Fiz 60:867
67. Tyè S, Halperin BI (1989) Phys Rev B 39:877
68. Dyre JC (1994) Phys Rev B 49:11,709
69. Landauer R (1978) In: Garland JC, Tanner DB (eds) Electrical transport and optical properties of inhomogeneous media. AIP Conf Proc 40:2, New York
70. Bergman DJ, Stroud D (1992) Solid State Phys 46:147
71. Bruggeman DAG (1935) Ann Phys (Leipzig) 24:636
72. Fishchuk II (1986) Rev Mod Phys 70:653
73. Dyre JC (1993) Phys Rev B 48:12,511
74. Montroll E, Weiss GH (1965) J Math Phys 6:167
75. Ngai KL, Léon C (1999) Phys Rev B 60:9396
76. Kulkarni AR, Lunkenheimer P, Loidl A (1998) Solid State Ionics 112:69
77. Rehwald W, Kiess H, Binggeli B (1987) Z Phys B 68:143

13 Dielectric Properties of Inhomogeneous Media

P. A. M. Steeman · J. van Turnhout

13.1
Introduction

Inhomogeneous media present an interesting class of materials for dielectric research. Differences in conductivity of the phases of an inhomogeneous medium give rise to interfacial polarization, the build-up of space charges near the interfaces between the various phases. Such a polarization usually occurs at frequencies lower than the time scales typical of dipolar polarizations. Moreover, the contribution of interfacial polarization to the dielectric properties of a material is often much larger than the dipolar contributions.

Numerous authors have studied the dielectric behaviour of heterogeneous materials. Several excellent reviews on the subject can be found in the literature [1–9]. It was soon recognized that the observed polarization and loss effects in inhomogeneous media could not be derived from dipolar polarization phenomena, especially since often strong effects are observed. Extremely large contributions to the real part of the dielectric function or permittivity along with anomalous dispersions are detected in biological materials [6], porous media [10, 11], emulsions and related colloidal systems [12]. It was understood that the strong polarization effects are of macroscopic nature and caused by charge build-up at the boundaries between the various components in the material.

Theories about the dielectric properties of inhomogeneous media have been developed to a high level; much work was done already in the first half of the twentieth century. Van Beek [1] presented an early detailed review of the classical theories and validated them against examples of experimental data. With the advent of fully automated broadband dielectric spectrometers, which in most cases are also capable of performing dynamic dielectric measurements at low to very low (mHz range) frequencies, a detailed study of interfacial polarization mechanisms has become possible.

13.2
Theory

13.2.1
Two-Phase Heterogeneous Materials

The simplest case of an inhomogeneous medium in which interfacial polarization shows up is a layered structure of two materials (Fig. 13.1) with frequency-independent dielectric constants ε_1 and ε_2, in which only one medium is electrically conductive with a conductivity σ.

The dielectric function $\varepsilon^*(\omega)$ of such a laminate becomes complex and frequency dependent and is given by the well-known Debye relaxation equation, which is also the basic equation for dipolar relaxation processes:

$$\varepsilon^*(\omega) = \varepsilon'(\omega) - i\varepsilon''(\omega) = \varepsilon_\infty + \frac{\varepsilon_s - \varepsilon_\infty}{1 + i\omega\tau} \tag{13.1}$$

in which

$$\varepsilon_\infty = \frac{\varepsilon_1 \varepsilon_2}{\varepsilon_1(1-\varphi) + \varepsilon_2\varphi} \tag{13.2}$$

is the high frequency limit of the real part of $\varepsilon^*(\omega)$ (see footnote 4)

$$\varepsilon_s = \frac{\varepsilon_1}{\varphi} \tag{13.3}$$

is the low frequency limit or static dielectric constant

and

$$\tau = \varepsilon_0 \frac{\varepsilon_1(1-\varphi) + \varepsilon_2\varphi}{\sigma\varphi} \tag{13.4}$$

is the relaxation time of the interfacial polarization.

The relaxation time of the process is inversely proportional to the conductivity of the conducting layer, while the low frequency dielectric constant is a function of the volume fraction and the dielectric constant of the insulating layer. Because of the latter dependence very strong interfacial polarization mechanisms may arise if the fraction of the non-conductive component is small. This example illustrates how a frequency-dependent polarization may emerge in an inhomogeneous medium, even if the components of that medium do not show any dipolar polarization mechanism. The more complicated case in which both

Medium 1: ε_1, fraction φ	Direction of
Medium 2: ε_2, σ, fraction $1-\varphi$	electrical field
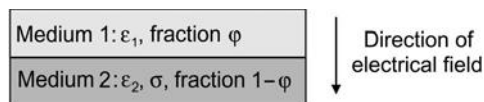
Fig. 13.1. Layered heterogeneous dielectric consisting of an insulating and a conducting layer with different dielectric constants

media are electrically conductive has been described in detail in many text-books [1, 13] and results in similar equations, with the major difference that the composite medium also becomes electrically conducting. This d.c.-conductivity contributes with $\sigma/\varepsilon_0\omega$ to the measured total loss ε'' and may thus obscure the energy loss caused by the interfacial polarization, as will often be the case in practice. However, in the dielectric constant ε' the contribution of the interfacial polarization will remain visible. Using the Kramers-Kronig transform [14] the conductivity and frequency-dependent polarization effects can be separated. The polarization losses ε''_p calculated from ε' are also called ε''_{KK}-losses [58] [1].

Maxwell [15] was the first to derive a *mean-field* theory for materials containing dispersed dielectric spheres in a dielectric medium, whereby a volume fraction φ_f of filler particles with a frequency-independent dielectric constant ε_f is dispersed in a (matrix) medium with a dielectric constant ε_m c.f. Fig. 13.2. His approach was later generalized by Wagner [16], who included the effects of conducting phases. Finally, Sillars [17] extended the theory to filler particles of a more general, ellipsoidal shape. The resulting theory is known as the *Maxwell-Wagner-Sillars* (MWS) theory. Similar to layered structures, it predicts a polarization process due to differences in conductivity and permittivity of the constituents. Therefore, interfacial polarization is commonly called MWS-polarization.

More general, if filler particles with a *complex*, frequency-dependent permittivity $\varepsilon_f^*(\omega)$ and volume fraction φ_f are dispersed in a matrix material with a complex permittivity $\varepsilon_m^*(\omega)$, then according to the MWS-theory the complex dielectric function $\varepsilon_c^*(\omega)$ of the heterogeneous mixture (Fig. 13.2) can be calculated from

$$\varepsilon_c^*(\omega) = \varepsilon_m^*(\omega)\frac{[n\varepsilon_f^*(\omega) + (1-n)\varepsilon_m^*(\omega)] + (1-n)[\varepsilon_f^*(\omega) - \varepsilon_m^*(\omega)]\,\varphi_f}{[n\varepsilon_f^*(\omega) + (1-n)\varepsilon_m^*(\omega)] - n\,[\varepsilon_f^*(\omega) - \varepsilon_m^*(\omega)]\,\varphi_f} \qquad (13.5)$$

in which n, with $0 \leq n \leq 1$, is the shape factor of the dispersed particles in the direction of the electrical field lines. For ellipsoidal particles with axes a,b,c the shape factor n_a in the direction of the a-axis is given by

$$n_a = \frac{4}{3}\pi abc \int_0^\infty \frac{d\xi}{(\xi + a^2)V(\xi)} \qquad (13.6)$$

with:

$$V(\xi) = \frac{4}{3}\pi\sqrt{(\xi + a^2)(\xi + b^2)(\xi + c^2)} \qquad (13.7)$$

For spherical particles $n_a = n_b = n_c = 1/3$. For prolate spheroids (rod-like) $0 \leq n \leq 1/3$, with the limiting case of a needle $n_a = 0$ and $n_b = n_c = 1/2$. For oblate spheroids (disc-like) $1/3 \leq n \leq 1$, with the limiting case of a plate-like particle $n_a = 1$ and $n_b = n_c = 0$. For more details see, e.g. [1].

---

[1] Another option to eliminate the conduction losses is the use of $d\varepsilon'/d\ln\omega$. This quantity too is a measure of ε''_p.

Fig. 13.2. Heterogeneous material of the matrix-inclusion type, wherein filler and matrix both have complex permittivities. This configuration is used in the MWS-theory, in which the filler particles may have an ellipsoidal instead of a spherical shape
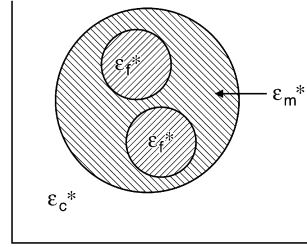
If the filler particles simply have a real, frequency-independent, dielectric constant ε_f and conductivity σ_f and the matrix also has a real, frequency-independent, dielectric constant ε_m and conductivity σ_m, then the MWS-response too reduces to a Debye-type of relaxation process. The following equation applies for $\varepsilon'_c(\omega)$ of the composite:

$$\varepsilon'_c = \varepsilon_\infty + \frac{\Delta\varepsilon}{1+(\omega\tau)^2} \tag{13.8}$$

with

$$\varepsilon_\infty = \varepsilon_m \frac{[n\varepsilon_f + (1-n)\varepsilon_m] + (1-n)[\varepsilon_f - \varepsilon_m]\varphi_f}{[n\varepsilon_f + (1-n)\varepsilon_m] - n[\varepsilon_f - \varepsilon_m]\varphi_f} \tag{13.9}$$

$$\Delta\varepsilon = \frac{n(\varepsilon_f\sigma_m - \varepsilon_m\sigma_f)^2\varphi_f(1-\varphi_f)}{[(1-n)\varepsilon_m + n\varepsilon_f + n(\varepsilon_m - \varepsilon_f)\varphi_f][(1-n)\sigma_m + n\sigma_f + n(\sigma_m - \sigma_f)\varphi_f]^2} \tag{13.10}$$

$$\tau = \varepsilon_0 \frac{(1-n)\varepsilon_m + n\varepsilon_f + n(\varepsilon_m - \varepsilon_f)\varphi_f}{(1-n)\sigma_m + n\sigma_f + n(\sigma_m - \sigma_f)\varphi_f} \tag{13.11}$$

where ε_∞ is the high frequency limit of the dielectric constant, $\Delta\varepsilon = \varepsilon_s - \varepsilon_\infty$ the relaxation strength of the interfacial polarization and τ its retardation time. ε_0 is the permittivity of vacuum, which is equal to 8.854 pF/m. Once again, the retardation time of the interfacial polarization is inversely proportional to the conductivity of the phases. At higher conductivities the loss maximum will shift to higher frequencies. For instance interfacial losses due to occluded (electrically conductive) water droplets in an insulating matrix are usually detected in the MHz region [1].

The Maxwell approach is applicable to low filler volume fractions (below 20%)[2]. Bruggeman [18] introduced an *asymmetrical integration technique* in order to derive a relation that can be used up to high filler volume fractions. He

---

[2]　Note that the role of the components in a mixture might be interchanged. After this exchange, Eq. (13.5) holds from 100 down to say 80 vol.% of filler.

assumed that the Maxwell equation could be used to calculate the infinitesimal increment of the mixture's dielectric constant after adding an infinitesimal amount of filler particles to the material at a random position. These increments of the filler volume fraction are integrated to obtain a relation for the dielectric constant of the heterogeneous material. Hanai [19] extended Bruggeman's differential approach to dynamic fields and conducting components. Later the approach was further extended to ellipsoidally shaped filler particles [2]. The following relation was obtained for the complex dielectric function of a two-component matrix-inclusion type of heterogeneous mixture:

$$\frac{\varepsilon_c^*(\omega)-\varepsilon_f^*(\omega)}{\varepsilon_m^*(\omega)-\varepsilon_f^*(\omega)}\left(\frac{\varepsilon_m^*(\omega)}{\varepsilon_c^*(\omega)}\right)^n = (1-\varphi_f) \tag{13.12}$$

in which $\varepsilon_i^*(\omega)$ with $i = m, f, c$ stands for the complex dielectric function at an angular frequency ω of the matrix, the filler and the composite respectively, φ_f is the volume fraction of the filler particles and n the shape factor of the filler particle as discussed before (Eq. 13.6). A further extension of this equation to randomly oriented ellipsoidal filler particles was given by Boned and Peyrelasse [2, 20].

Like before, in the simple case of a filler with a frequency-independent dielectric constant ε_f and conductivity σ_f, and a matrix material with dielectric constant ε_m and conductivity σ_m, again a relaxation process is found in the complex dielectric function $\varepsilon_c^*(\omega)$ of this matrix-inclusion kind of heterogeneous material. However, the relaxation process is no longer of the Debye type but somewhat broadened [4]. The following relations can be derived for the low and high frequency limits of the dielectric constant, ε_s and ε_∞:

$$\frac{\varepsilon_\infty-\varepsilon_f}{\varepsilon_m-\varepsilon_f}\left(\frac{\varepsilon_m}{\varepsilon_\infty}\right)^n = (1-\varphi_f) \tag{13.13}$$

and

$$\varepsilon_s\left[\frac{1}{\sigma_s-\sigma_f}-\frac{1}{n\sigma_s}\right]=\left[\frac{\varepsilon_m-\varepsilon_f}{\sigma_m-\sigma_f}+\frac{\varepsilon_f}{\sigma_s-\sigma_f}\right]-\frac{\varepsilon_m}{n\sigma_m} \tag{13.14}$$

in which the conductivity σ_s follows from

$$\frac{\sigma_s-\sigma_f}{\sigma_m-\sigma_f}\left(\frac{\sigma_m}{\sigma_s}\right)^n = (1-\varphi_f) \tag{13.15}$$

where σ_s is the static or d.c.-electrical conductivity of the heterogeneous material and $n = 1/3$ for spherical filler particles. No explicit analytical description of the interfacial polarization process as a function of the angular frequency can be given, as it was possible for the MWS theory [4].

Fig. 13.3. Bruggeman's symmetrical effective-medium approach for a mixture of two components with complex permittivities

Effective medium ε_c^*

Component 1: ε_1^* Component 2: ε_2^*
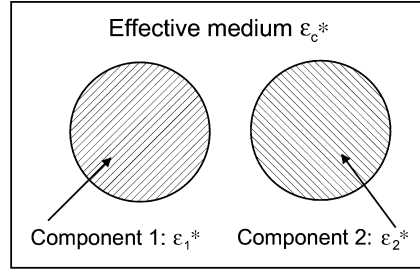
The MWS and Bruggeman/Hanai theory are applicable to matrix-inclusion type heterogeneous materials. These theories belong to the group of *asymmetrical* mixture equations.

A whole family of solutions based on another pioneering development of Bruggeman the *effective medium approach* [7, 21] is known from the literature. Two calculation schemes are applied, depending on the microstructure or morphology of the mixture. In the first scheme, being a *symmetrical* method, which is applicable to mixtures in which no clear assignment of a matrix component and a filler component can be made, both components (1 and 2) of the mixture are embedded in an effective medium with properties of the mixture. Figure 13.3 illustrates this symmetrical approach.

It is assumed that the average dipolar field due to the inclusions vanishes. With this assumption the Bruggeman/Böttcher [22] equation for the complex dielectric function $\varepsilon_c^*(\omega)$ of the mixture is obtained

$$\frac{[\varepsilon_1^*(\omega) - \varepsilon_c^*(\omega)]\,\varphi_1}{\varepsilon_c^*(\omega) + [\varepsilon_1^*(\omega) - \varepsilon_c^*(\omega)]\,n_1} + \frac{[\varepsilon_2^*(\omega) - \varepsilon_c^*(\omega)]\,\varphi_2}{\varepsilon_c^*(\omega) + [\varepsilon_2^*(\omega) - \varepsilon_c^*(\omega)]\,n_2} = 0 \tag{3.16}$$

in which n is the shape factor of the (ellipsoidal) inclusions in the direction of the field lines. Later this approach was extended to randomly oriented ellipsoids [2].

If one component (e.g. component 1) is electrically conducting and the other component is not, this model predicts a *percolation* threshold for conduction near $\varphi_1 \approx n_1$. By contrast, the MWS-theory predicts no electrical conduction of the composite material at any filler volume fraction, for conductive filler particles in an insulating matrix. The filler particles are always completely enclosed by non-conductive matrix material. Hanai's theory forms an intermediate between these two theories and predicts electrical conduction of the heterogeneous material albeit at higher filler volume fractions [2].

Looyenga [23] introduced a *symmetrical integration technique*, similar to the asymmetrical integration technique developed by Bruggeman. Starting from Böttcher's equation and generalizing it to ellipsoidal shapes, the following asymmetrical mixture formula for *oriented* ellipsoids can be derived:

$$\varepsilon_c^*(\omega)^{1-2n} = \varphi_1 \varepsilon_1^*(\omega)^{1-2n} + \varphi_2 \varepsilon_2^*(\omega)^{1-2n} \tag{13.17}$$

Fig. 13.4. Asymmetrical effective-medium approach in which the filler particles are surrounded by matrix material. Both filler and matrix have a complex permittivity. The radii of the spheres are determined by the volume fractions

Effective medium ε_c^*

Filter: ε_f^* Matrix: ε_m^*
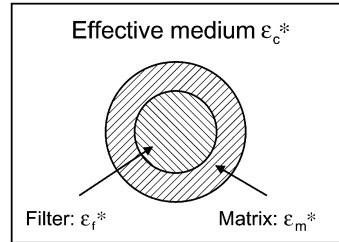
If one component is electrically conductive, the Looyenga model predicts for $n < 0.5$ a non-zero electrical conductivity of the heterogeneous material, even at the smallest volume fractions of the conductive component. However, for $n > 0.5$ no electrical conductivity is predicted at any volume fraction of the conducting component.

For spherical inclusions and for *randomly* oriented ellipsoids, independent of their shape, the following equation was found:

$$\varepsilon_c^*(\omega)^{1/3} = \varphi_1 \varepsilon_1^*(\omega)^{1/3} + \varphi_2 \varepsilon_2^*(\omega)^{1/3} \tag{13.18}$$

Both Looyenga [23] and Landau and Lifshitz [24] derived this equation independently. In fact, a whole set of solutions with different powers is known from the literature, of which the Davies equation [25] with exponent 1/5 is often used for mechanical calculations on composites.

The second effective-medium scheme, the *asymmetrical* approach, is applicable to mixtures in which one component can be assigned as the matrix and the second component as being the filler, a two-phase element consisting of a filler particle surrounded by a layer of matrix material is embedded in an effective medium with properties of the mixture. Figure 13.4 illustrates this asymmetrical approach.

Again, it is assumed that the average dipolar field due to the inclusion vanishes. For spherical particles this approach leads to results identical to the Maxwell-Wagner solution [26]. For ellipsoidal filler particles, however, a modification of Sillars's relation is found [27], which also takes the shape factor of the *matrix* material into account. Just as the MWS and Hanai solutions, these asymmetrical solutions are applicable to matrix inclusion type mixtures only.

13.2.2
Heterogeneous Materials Containing More than Two Phases

The effective medium approach can easily be extended to mixtures of more than two components. Assume a symmetrical mixture containing i components with volume fraction φ_i, complex dielectric function $\varepsilon_i^*(\omega)$ and shape factor n_i, respectively. In the symmetrical approach inclusions of all i components are embedded in an effective medium having the dielectric function of the mixture $\varepsilon_c^*(\omega)$. The imposed condition that the average dipolar field vanishes results in

the following equation, from which the complex dielectric function of the mixture can be calculated:

$$\sum_i \frac{[\varepsilon_i^*(\omega) - \varepsilon_c^*(\omega)]\, \varphi_i}{\varepsilon_c^*(\omega) + [\varepsilon_i^*(\omega) - \varepsilon_c^*(\omega)]\, n_i} = 0 \qquad (13.19)$$

In the case of a multi-component asymmetrical mixture of the matrix-inclusion type, two-phase inclusions consisting of the different filler types surrounded by a layer of matrix material are embedded in the effective medium. Again the induced dipolar field of all inclusions, averaged with weight factors according to the volume fractions of the phases, is assumed to vanish. The effective complex dielectric function of the two-phase elements, which should be *inserted* in Eq. (13.19) as $\varepsilon_i^*(\omega)$, can be calculated using the equation derived by Bilboul [27]:

$$\varepsilon_c^*(\omega) = \varepsilon_m^*(\omega) \frac{[\varepsilon_{fi}^*(\omega) - \varepsilon_m^*(\omega)][n_{fi} - \varphi_{fi} n_{mi} + \varphi_{fi}] + \varepsilon_m^*(\omega)}{[\varepsilon_{fi}^*(\omega) - \varepsilon_m^*(\omega)][n_{fi} - \varphi_{fi} n_{mi}] + \varepsilon_m^*(\omega)} \qquad (13.20)$$

in which φ_{fi} is the volume fraction, $\varepsilon_{fi}^*(\omega)$ the complex dielectric constant and n_{fi} the shape factor of filler type i and n_{mi} the shape factor of the matrix surrounding the filler i. A detailed description of this *two-step* procedure can be obtained from Lamb et al. [28].

The same approach can be used for randomly oriented ellipsoidal filler particles. In that case it can be shown that the averaged squared cosines of the angles between the main axes of the ellipsoid and the electrical field are equal to 1/3 ($\langle \cos^2 \alpha_i \rangle = 1/3$, with $i = x, y, z$), i.e. all directions are equally important [2]. Randomly oriented filler particles can therefore be treated as three different filler types, one for each main direction. The mixture dielectric properties can be calculated using the same procedure as discussed above for multi-component heterogeneous materials.

13.2.3
Heterogeneous Materials with an Interfacial Layer

Heterogeneous materials of the matrix-inclusion type, wherein between the filler particles and the matrix material an interfacial layer is present, present a special case. Analogous to a method used by Fröhlich and Sack [29], van der Poel [30] and Maurer [31] for the analysis of the viscosity and the shear modulus of particulate composites with and without interlayer, the asymmetric effective medium approach can also be used for this case. Figure 13.5 shows schematically the asymmetric effective-medium model used.

The solution for a heterogeneous material with an interfacial layer between filler particles and matrix, also known as the *interlayer model* [32], is in the generalized case of ellipsoidal filler particles given by

$$\varepsilon_C^*(\omega) = \frac{\varepsilon_f^*(\omega)\, \varphi_f + \varepsilon_\ell^*(\omega)\, \varphi_\ell R^* + \varepsilon_m^*(\omega)\, \varphi_m S^*}{\varphi_f + \varphi_\ell R^* + \varphi_m S^*} \qquad (13.21)$$

Fig. 13.5. Asymmetrical effective-medium approach for a material with an interfacial layer between filler and matrix. A layered ellipsoidal structure instead of a spherical one is also possible
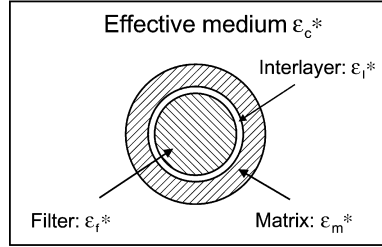
with

$$R^* = \frac{[(1-n)\varepsilon_\ell^* + n\varepsilon_f^*]}{\varepsilon_\ell^*} \tag{13.22}$$

$$S^* = \frac{[n\varepsilon_\ell^* + (1-n)\,\varepsilon_m^*][n\varepsilon_f^* + (1-n)\,\varepsilon_\ell^*] + dn\,(1-n)(\varepsilon_\ell^* - \varepsilon_m^*)(\varepsilon_f^* - \varepsilon_\ell^*)}{\varepsilon_\ell^* \varepsilon_m^*} \tag{13.23}$$

$$d = \frac{\varphi_f}{\varphi_f + \varphi_\ell} \tag{13.24}$$

where n is the depolarization factor of the filler particle in the field direction. The equation can be used for calculating the dielectric properties of the composite in the direction of any of the principle axes, by inserting the depolarization factor for that direction. As could be expected Eq. (13.21) reduces to Eq. (13.5) for $\varphi_l \to 0$ and $\varepsilon_l \to \varepsilon_m$.

13.3
Experimental Results

13.3.1
Polymeric Blends

In the past decades much attention has been paid to the development of polymeric blends. Blends offer the possibility of combining the unique properties of the components and thus of producing materials with tailor-made properties. This often has advantages over the synthesis of completely new polymers. In the recycling of polymeric materials, blends of several polymers are usually obtained as well.

Two types of blends can be distinguished, depending on whether the components are *miscible* or *immiscible* on a molecular scale. Materials from the second class of blends are inhomogeneous, thus interfacial or MWS-polarization might be expected. Besides commonly used blend characterization techniques such as (electron) microscopy, thermal analysis and dynamic mechanical analysis, dielectric spectroscopy potentially provides additional information about the *microstructure* of the material from specific interfacial polarization phenomena.

Many dielectric studies have been performed on miscible blends. In most cases, blend miscibility is investigated by comparing the dipolar losses at the glass transition with those of the components. It was shown how both the glass transition temperatures and the width of the loss peaks are affected by the miscibility of the components [33–36].

For immiscible blends on the other hand strong conduction and low frequency polarization effects have been found. These polarization effects have often been attributed to Maxwell-Wagner polarization (MWS) [37–41]. Some authors have managed to describe them quantitatively with the MWS theory [42, 43]. Maistros et al. [44] have shown how dielectric spectroscopy can be used to detect the demixing of non-reactive rubber (impact modifier) into domains during the cure of the epoxy matrix. The occurrence of interfacial polarization at low frequencies coincides with a change in turbidity of the material, as was simultaneously detected optically. Similarly, the appearance of phase separation during the cure of thermoplastic modified epoxy resins was demonstrated by MacKinnon et al. [45], whereas Dionisio et al. [46] used MWS-polarization to prove the existence of phase separation in polymer blends.

Recently, Boersma and van Turnhout studied blends of a thermotropic liquid crystalline polymer (LCP) dispersed in polypropylene during extrusion. They demonstrated that interfacial polarization effects, detected with dielectric measurements, could be used to monitor the change in shape, as well as the co-continuity of the LCP phase with increasing extrusion speed [47]. Additionally, they were able to follow the fibre break-up mechanism [48] and could interpret their results in terms of interfacial tension [49] and particle *size* effects [50]. The latter was made possible by incorporating *diffusion* in the theory, so that the formation of double layers near the interfaces could be accounted for.

Much work has been performed on the morphology and mechanical properties of the immiscible blend of the ductile BisPhenol-A PolyCarbonate (BPA-PC) and the brittle Styrene-AcryloNitrile copolymer (SAN) [51–54]. Dielectric experiments on this blend showed that the information obtained is complementary to the results obtained from dynamic mechanical measurements [55, 56]. Whereas mechanical measurements are most sensitive to the high T_g component (i.e. PC) and are used to determine the extent of continuity of this phase in the blend, the dielectric properties are mainly governed by the low T_g component (SAN) [57].

Figure 13.6a,b shows the real part ε' and the imaginary part ε'' of the complex dielectric function of a blend of 60 wt% PC with 40 wt% ABS (acrylonitrile-butadiene-styrene; a SAN matrix with poly-butadiene (PB) rubber inclusions), as a function of temperature at a series of frequencies between 0.5 and 8.2 kHz [57]. The frequencies were chosen in a geometric series such that the polarization losses, i.e. the dielectric losses *without* the contribution from ohmic conduction, could be easily calculated from the real part of the dielectric function data using a fast numerical Kramers-Kronig transform [58][3]. In Fig. 13.6b the solid lines depict the polarization loss calculated, while the dashed lines depict the total loss measured (including the conductive loss).

---

[3] Alternatively, the ohmic conduction could – even more simply – have been eliminated by differentiating the ε'-data, cf. footnote 1.

Fig. 13.6. Dielectric permittivity ε', total loss ε'' (*dashed lines*) and polarization loss ε''_p (*solid lines*) of a 60/40 PC/ABS blend at various frequencies (from *left* to *right* 0.5 Hz, 2 Hz, 8 Hz, 32 Hz, 128 Hz, 512 Hz, 2048 Hz and 8196 Hz) as a function of temperature. The ε' and ε''-data were measured, the ε''_p-data calculated
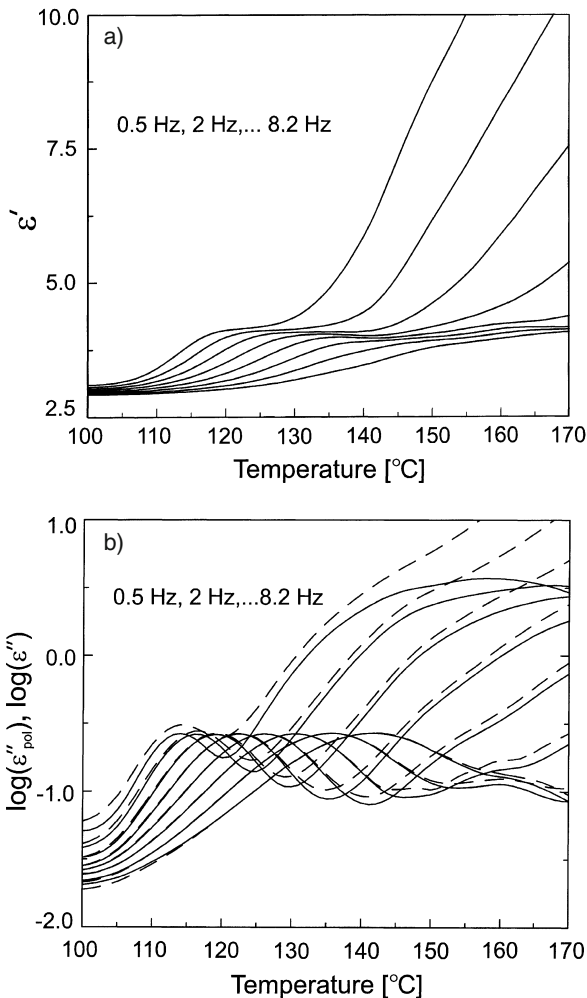
Between 100 and 130 °C the curves show the glass transition of the polar SAN component like it is also found in pure ABS. Above 150 °C the glass transition of the less polar BPA-PC can be seen at the highest frequencies, both from a small additional increase in the dielectric constant and from weak loss peaks, again in agreement with the results for the pure PC component. However, after passing the glass transition of the SAN a strong additional polarization process is found from a sharp increase in the dielectric losses and in the real part of the permittivity at the lowest frequencies, which cannot be attributed to a dipolar polarization process in one of the components. Up to about 140 °C the polarization loss and the measured loss are nearly equal. Thus, despite the fact that the SAN component becomes electrically conductive above its T_g, the 60/40-blend does not. This suggests that the ABS phase is completely included in a non-conduc-

Fig. 13.7. Dielectric permittivity ε', total loss ε'' and polarization loss of a 60/40 PC/ABS blend predicted with the Hanai-model. (in **b**: *dashed lines* = ε'', *solid lines* = polarization loss calculated from ε')
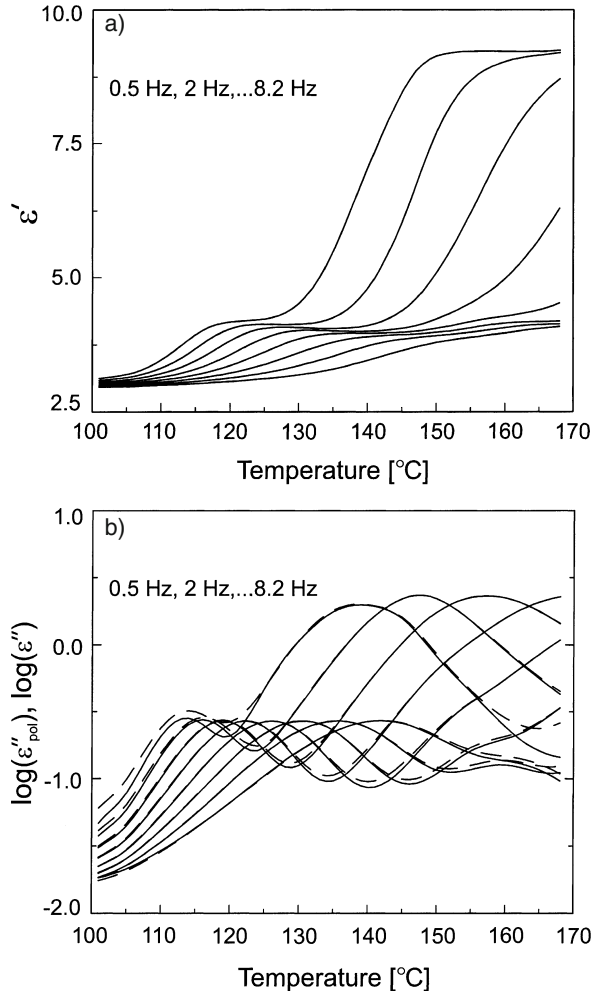
tive PC matrix. Therefore, the strong low frequency polarization process found is expected to be of interfacial origin.

The dielectric properties of the blend were modelled with the asymmetrical Hanai-model, assuming the ABS phase as ellipsoidal inclusions in a PC matrix and with the symmetrical Looyenga-equation, which does not presume one component to form the matrix phase. The shape factor of the ABS domains was used as fit factor to obtain the best possible description of the dipolar losses in the glass transition regions of both components.

Figure 13.7a,b shows the results of calculations with the Hanai-model, using a shape factor $n = 0.60$. A good description of the glass transition regions of both components is obtained. The model predicts a strong interfacial polarization in the frequency and temperature interval where it is experimentally observed. However, ε' reaches a plateau which is experimentally not observed.

Fig. 13.8. ε', ε'' and polarization loss of a 60/40 PC/ABS blend predicted with the Looyenga-model (in **b**: *dashed lines* = ε'', *solid lines* = calculated polarization loss)
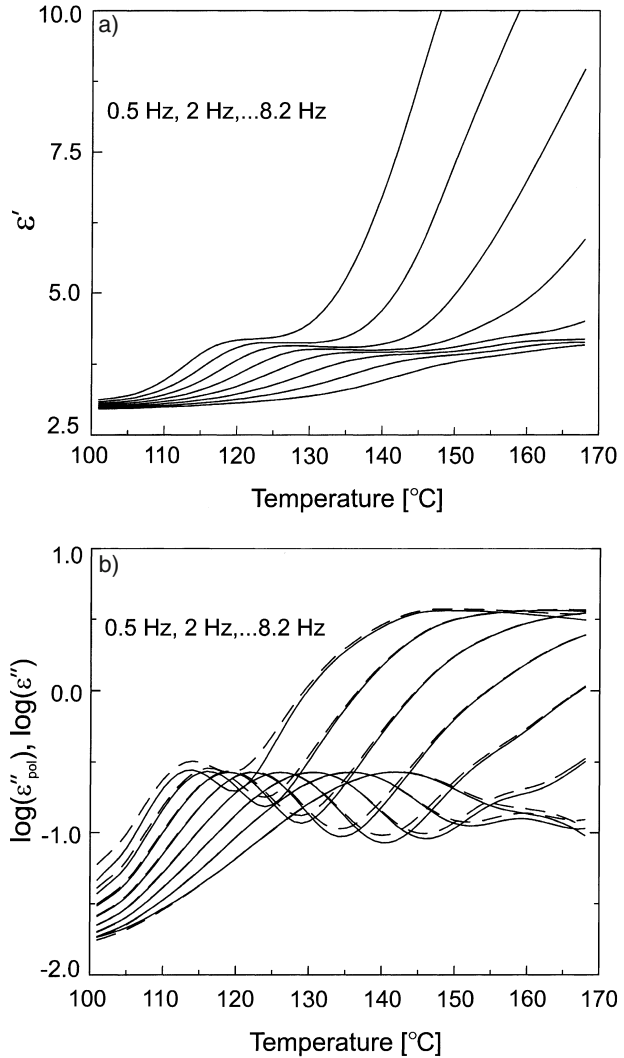
Similarly, Fig. 13.8a,b shows the results of the calculations according to the Looyenga model, using $n = 0.65$. Again, a good description of the glass transition regions is found, while the model now also correctly predicts the magnitude of the interfacial polarization.

From these figures it is concluded that the symmetrical approach of Looyenga applies better to the morphology of the 60/40 PC/ABS blend. However, both models predict that the blend is not electrically conductive, while experimentally a small contribution from conduction to the loss is found above 140°C, slightly below the T_g of the PC component. This indicates that probably a percolating conductive network of the ABS component is present in the blend.

Microscopic analysis showed that the morphology of this blend consists of disc-like ABS structures embedded in PC with lateral dimensions of about 10 μm and a thickness of 2–3 μm [57]. The (ellipsoidal) shape factor of such structures amounts to $n = 0.65$–0.70, in agreement with the optimal shape factor for the Looyenga-model. These results confirm the validity of the model calculations and show that dielectric spectroscopy can indeed be used as a sensitive tool for studying blend morphology, even during processing as was demonstrated by Boersma and van Turnhout [47].

13.3.2
Filled Polymers

Often polymers are filled with rigid particles to enhance the mechanical properties of the materials, e.g. to increase the modulus or the failure stress. Typical inorganic fillers include minerals like chalk, mica, clay, etc. or carbon black and glass. Many filler types such as spherical or ellipsoidal particles or fibres may be used.

The use of filler particles frequently introduces a water sensitive component into the polymer. For example, glass fillers are well known to adsorb water on their surface. Since water has a high dielectric constant and a high electrical conductivity, strong dielectric effects are to be expected. Several authors have reported an increase in the dielectric constant and the loss of composites after the absorption of water [59–65]. The composites considered are made up of a matrix material with filler particles or fibres dispersed in it. The dielectric loss effects due to absorbed water seem to be dominant at low frequencies and are often related to the absorption of water into the interfacial regions of filler/fibre and matrix. Plueddemann [66] states that even if a glass-based composite is prepared with perfectly dry glass, water will be able to reach the interface by diffusion through the polymer. Moreover, imperfections or micro-cracks in the composites formed through stresses generated by differential shrinkage allow water to get to the interface even more rapidly.

The composite can be considered as a three-component system in which the adsorbed water forms an interlayer between the filler particles and the matrix material. This conductive *interlayer* between the glass filler and the matrix material gives rise to an interfacial dielectric loss process, which can be detected by low frequency dielectric measurements. Bánhegyi and Karasz [59, 60] observed a low frequency, low temperature loss process in $CaCO_3$ filled polyethylene due to absorbed water. The high frequency dielectric constant could be well described by the models proposed for heterogeneous mixtures as discussed before, but the frequency dependent dielectric losses could not be interpreted on the basis of a sole interfacial loss mechanism. However, the authors were able to describe their results with the 'universal response theory'. Because of its universality this model was unable to describe the effects in terms of structural characteristics.

Woo and Piggott [64] stated that the absorbed water in glass-epoxy composites is concentrated in the interfacial regions, which are interconnected by disc-shaped water clusters providing conducting paths. Paquin et al. [65] studied the dielectric properties of polymer composites containing plasma treated mica.

The detected low frequency dispersion was ascribed to the intrinsic dispersive properties of the mica filler. Additionally, a broad audio frequency loss peak was observed probably due to Maxwell-Wagner-Sillars losses from water absorbed at the filler surface.

In most cases the structure of the composites is rather complex and the absorbed water is not only present at the filler-matrix interface. Therefore, low concentrated glass-filled high-density polyethylene composites were prepared [67, 68]. Glass beads with an average diameter of 10–13 μm were added to a melt of high-density polyethylene on a two-roll open mill to obtain a 20 vol.% filled HDPE composite [67]. Samples of these materials were exposed to environments with varying relative humidity (RH 14–100%) to allow different equilibrium water uptakes ranging from 0.09 to 0.27 wt%. The high-density polyethylene does not absorb a measurable amount of water; thus all the water absorbed can be assumed to be present at the surface of the filler particles. Moreover, the HDPE matrix shows a nearly frequency-independent dielectric constant of about 2.4 and no dielectric losses.

Figure 13.9a,b shows ε' and ε'' of the samples measured after equilibrium water uptake as a function of the frequency, at room temperature. The sample with the lowest water content exhibits only at the lowest frequencies some signs of a very low frequency polarization process. However, all the other samples clearly reveal a polarization process in the frequency interval studied. In view of the fact that the matrix and the bulk of the filler absorb no water, the observed polarization effects are expected to be of interfacial origin.

If a water layer is present on the surface of the filler particles it will become electrically conductive. Since the matrix material is not electrically conducting, this will give rise to interfacial polarization. This was theoretically investigated by using Eq. (13.21) for non-conductive spherical filler particles covered with a thin electrically conductive interfacial layer, embedded in a non-conductive matrix. In that case it could be derived [32] that the complex dielectric function of the composite $\varepsilon_c^*(\omega)$ shows a Debye-type relaxation process with

$$\varepsilon_c^*(\omega) = \varepsilon_\infty + \frac{\varepsilon_s - \varepsilon_\infty}{1 + i\omega\tau} \tag{13.25}$$

in which

$$\varepsilon_s = \varepsilon_m \left(\frac{1 + 2\varphi_f}{1 - \varphi_f} \right) \tag{13.26}$$

$$\varepsilon_\infty = \varepsilon_m \left(\frac{(\varepsilon_f + 2\varepsilon_m) + 2(\varepsilon_f - \varepsilon_m)\varphi_f}{(\varepsilon_f + 2\varepsilon_m) - (\varepsilon_f - \varepsilon_m)\varphi_f} \right) \tag{13.27}$$

$$\tau = \left(\frac{\varphi_f}{1 - \varphi_f} \right) \left(\frac{3\varepsilon_0}{2\sigma_\ell \varphi_\ell} \right) [(\varepsilon_f + 2\varepsilon_m) - (\varepsilon_f - \varepsilon_m)\varphi_f] \tag{13.28}$$

Fig. 13.9. ε' and ε'' of a 20 vol.% glass-beads filled HDPE composite, measured at various humidities, as a function of frequency
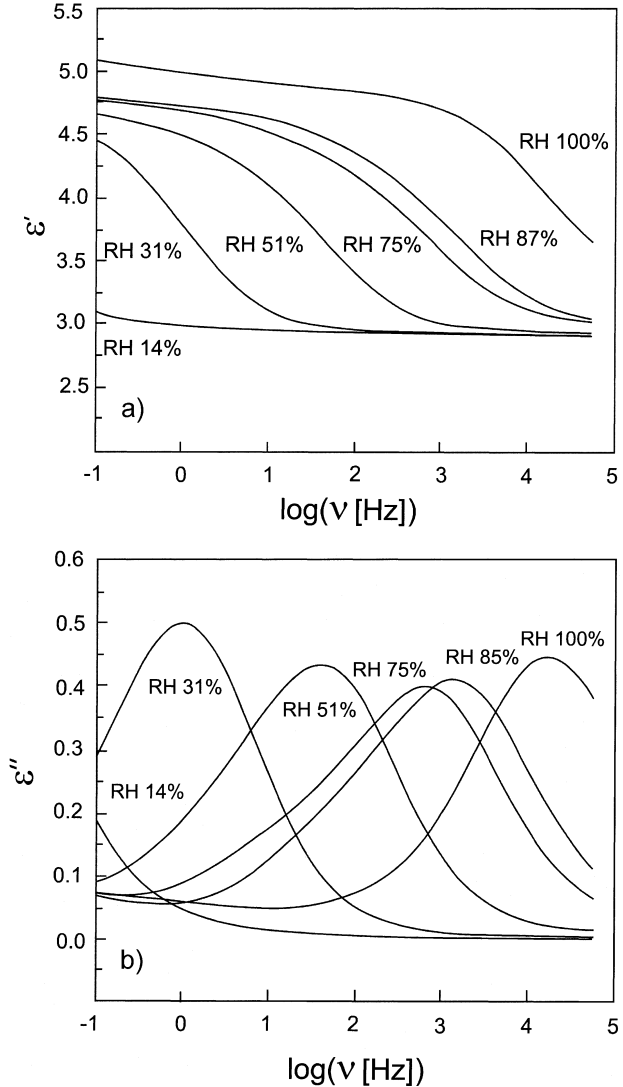
where ε_s is the low-frequency limit of the composite dielectric function, ε_∞ the high-frequency limit of the composite dielectric constant and τ the retardation time of the interfacial polarization process.

The low-frequency limit of the dielectric function of the composite is solely determined by the dielectric permittivity of the matrix material and the volume fraction of the filler, similar to what was found for the simple two-layer composite. The conducting interfacial layer shields the filler particles from the electrical field. In fact, the composite is similar to a material with highly conductive spheres dispersed in it. The high-frequency limit of the dielectric function

equals that of a composite of non-conductive filler particles in a non-conductive matrix. The conductive interfacial layer does not enter in the equations since it does not affect the properties at high frequencies. Finally, Eq. (13.28) implies that the frequency of maximum dielectric loss of the interfacial polarization mechanism is proportional to both the volume fraction and the conductivity of the interfacial layer. In the case of an interfacial water layer it is therefore expected that the frequency of the maximum dielectric loss will shift to higher values with increasing water content.

The influence of a conductive (water) interlayer on the dielectric properties of a 20 vol.% glass-beads filled high density polyethylene composite was simulated with Eqs. (13.25)–(13.28). The dielectric constant of the HDPE matrix is

Fig. 13.10. ε' and ε'' of a 20 vol.% glass-beads filled HDPE composite predicted with the interlayer model for various volume fractions of a conducting interfacial water layer
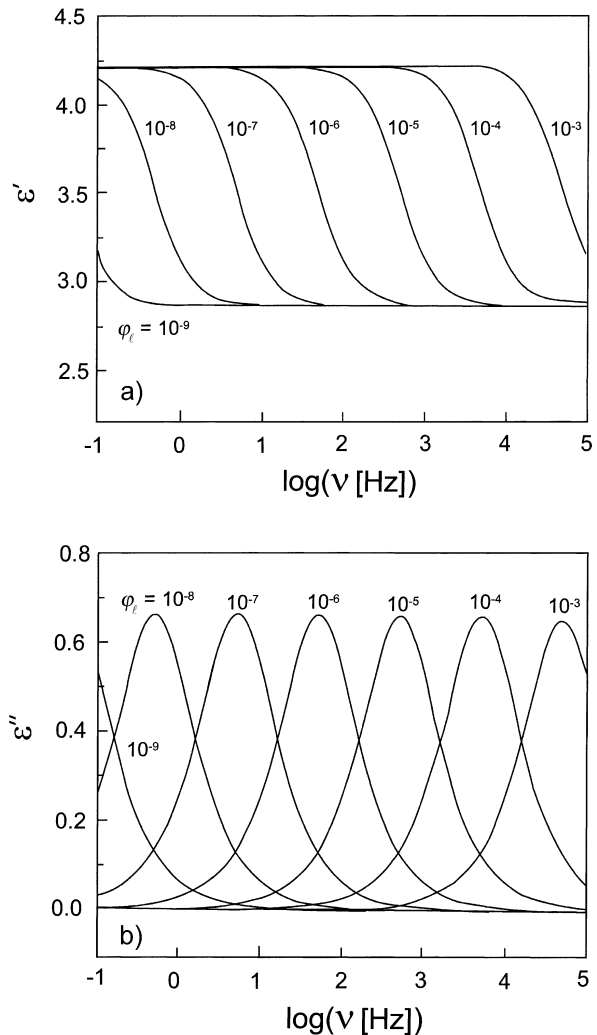
about 2.4 and of the glass filler particles about 5.5, both independent of the frequency and thus with negligible dielectric loss. The only remaining variables in Eq. (13.28) are the conductivity σ_ℓ and the volume fraction φ_ℓ of the layer. For the simulations σ_ℓ was set to an arbitrary value of 10^{-2} Sm^{-1}, while the volume fraction φ_ℓ was varied between 10^{-9} and 10^{-3}. The results of these calculations given in Fig. 13.10a,b show for $10^{-8} < \varphi_\ell < 10^{-3}$ an interfacial polarization process with accompanying loss peaks in the frequency domain from 100 mHz to 100 kHz. The calculated relaxation curves are similar to the experimental results. The frequency of maximum dielectric loss is proportional to the volume fraction of the interfacial layer, or more general (according to Eq. 13.28) to the product of layer volume fraction and conductivity. The shape of the relaxation curves is the same for all layer volume fractions, which to some extent is also experimentally observed. However, the theoretical relaxation process is Debye-like and much sharper along the frequency axis than the experimental results. Such an experimental broadening is quite often observed and attributed to a distribution of relaxation times instead of a single relaxation time as predicted theoretically. In this case it may for instance be attributed to a distribution of layer volume fractions caused by various filler particle sizes.

The volume fraction of the interfacial (water) layer can be found from the amount of water absorbed by the composite. Thus, the conductivity of the water layer can be calculated. For the various water contents studied the conductivity ranges from 3×10^{-9} to 8×10^{-4} Sm^{-1} [67]. The lowest values are lower than the conductivity of pure water, which due to the H_3O^+/OH^- dissociation equilibrium is about 5×10^{-6} Sm^{-1} at room temperature. Probably, the thinnest water layers are tightly bound to the glass surface and therefore show a reduced ionic mobility.

Similar dielectric effects were found in glass fibre and glass fabric filled HDPE composites after water absorption [32]. The magnitude of the polarization process was found to depend on the shape of the filler. For glass fabrics (shape factor $n > 1/3$) the dielectric effects are smaller than for glass beads, while for glass fibres (shape factor $n < 1/3$) a much stronger interfacial polarization is found. Moreover, glass fibres have the tendency to form an electrically continuous phase already at low volume fraction. Continuity of the conductive filler surface causes additional strong conduction effects, which do not occur for fabrics and for beads, and may be even stronger than the interfacial polarization.

13.3.3
Semi-Crystalline Polymers

Semi-crystalline polymers can be expected to show strong interfacial polarization effects at temperatures above the glass transition of the amorphous domains. While the crystallites are not electrically conducting, the conductivity of the amorphous domains increases with increasing temperature, especially after passing T_g. In the literature strong polarization processes above the glass transition are well documented [69–74] for polyamides, polyesters and polyurethanes.

For polyamides it has for instance been shown that in the range 40–70°C, depending on the type of polyamide, a strong polarization process is found which corresponds to the glass-rubber transition of the amorphous phase. At higher temperatures the materials become electrically conductive and show a sharp increase in the dielectric function [75, 76]. This is thought to be due to an interfacial or MWS-type of polarization process caused by trapping of free charge carriers at the boundaries between crystalline and amorphous regions. The electrical conductivity of the crystalline phase is much lower than the conductivity of the amorphous phase. Free charge carriers (ions) moving through the amorphous phase of the sample, are hindered in their motion by the crystalline domains and pile up near the interfaces between the amorphous and the crystalline phases. Space-charge effects as detected by the thermally stimulated discharge (TSD) technique [77] are probably related to this MWS-polarization mechanism.

A three-phase morphology with amorphous material included in crystallites which are embedded in amorphous material seems to be a good approach for modelling the interfacial polarizations in semi-crystalline materials. However, as several authors have discussed [76, 78, 79], the morphology of semi-crystalline polymers is too complicated to allow a description based on simple models and so one is limited to qualitative results.

Figure 13.11a,b show the real and the loss part of the complex dielectric function of a dry polyamide-4,6 measured as a function of temperature, at various frequencies between 0.5 Hz and 8.2 kHz [80]. Again, the frequencies were chosen such that the fast numerical Kramers-Kronig transform [58] could be used to calculate the polarization losses from the frequency dependence of the real part of the dielectric function. The calculated polarization losses ε_p'' are depicted in Fig. 13.11b with full lines, while the measured dielectric loss ε'', which includes apart from ε_p'' the contribution from ohmic conduction, is plotted with dashed lines. Between 75 and 100°C the glass transition of the amorphous phase is found, which results in an increase of the dielectric constant from about 3.5 to 12. At higher temperatures a strong polarization process appears due to which the dielectric constant increases further to 80 or more. This strong relaxation process cannot be related to a molecular mobility of the polyamide chains, while its relaxation time is inversely proportional to the conductivity of the material. These observations clearly hint at an interfacial origin of the relaxation process.

While the actual morphology of semi-crystalline materials is too complex to be described with mixture theories, two limiting cases of the morphology may be considered above the glass transition temperature of the amorphous phase. One consists of non-conductive crystalline domains embedded in an electrically conductive amorphous matrix, and the second of conductive amorphous domains embedded in a non-conductive crystalline matrix. The actual morphology is probably a mix of these two phase-inverted structures. Because of the high volume fractions of the components, the Hanai theory was used to model the dielectric properties of these sample morphologies. The dielectric permittivity of the amorphous polyamide-4,6 was taken from [76] and assumed to be about 20. Its high conductivity was taken into account by setting the low frequency loss to an arbi-

Fig. 13.11. $\varepsilon', \varepsilon''$ and polarization loss of dry polyamide-46 at various frequencies, as a function of temperature (in **b**: *dashed lines* = measured ε'', *solid lines* = calculated polarization loss)
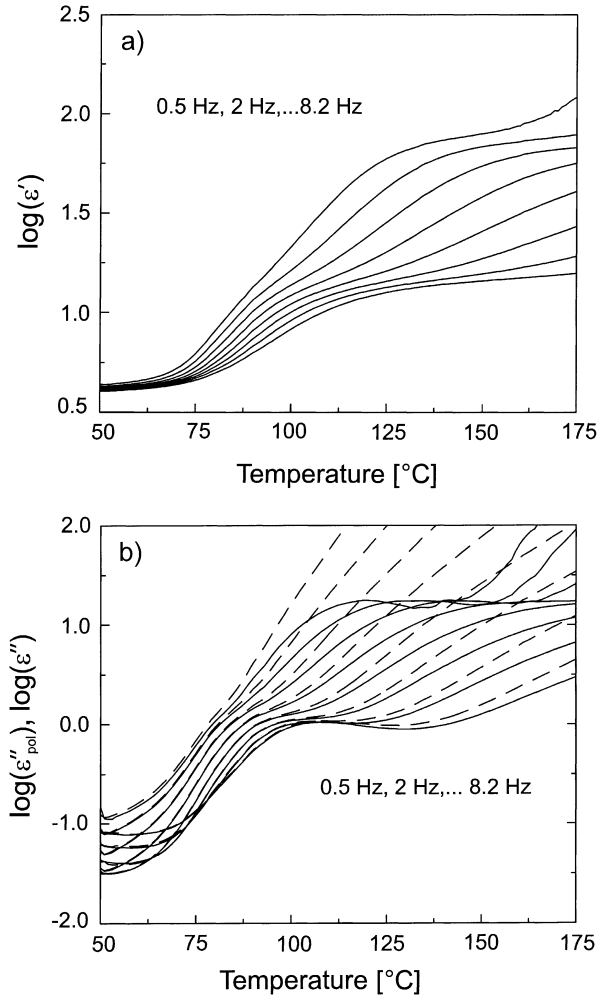
trary high value of 10^6 and the high frequency loss to zero. At very low temperatures the dielectric constant of the glassy polyamide-4,6 is about 3.3, which value was taken as a first estimate for the dielectric constant of the crystalline phase.

Figure 13.12 shows the dielectric increment, the increase of the low-frequency dielectric constant due to interfacial polarization, as calculated with the Hanai theory for a conductive amorphous matrix with non-conductive crystalline inclusions. The calculations were performed for different shape factors of the (ellipsoidal) inclusions, ranging for $n = 0$ (needle-like) to $n = 1$ (plate-like). It is found that only for inclusion structures with shape factor close to plate-like and at high volume fractions (φ_m) of the amorphous phase are dielectric effects of the experimentally observed magnitude of about 70 to be expected. This seems unlikely because of the high crystallinity of polyamide-4,6 [80].

Fig. 13.12. Dielectric increment $\Delta\varepsilon$ due to interfacial polarization predicted with Hanai's theory for a morphology of insulating crystallites in a conductive amorphous matrix. Volume fraction of amorphous phase as indicated
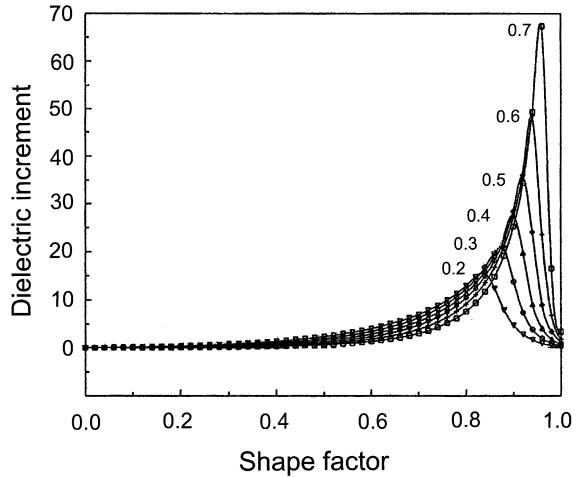
Fig. 13.13. Dielectric increment due to interfacial polarization predicted with Hanai's theory for a morphology of conductive amorphous inclusions in an insulating crystalline matrix. Volume fraction of the amorphous phase as indicated
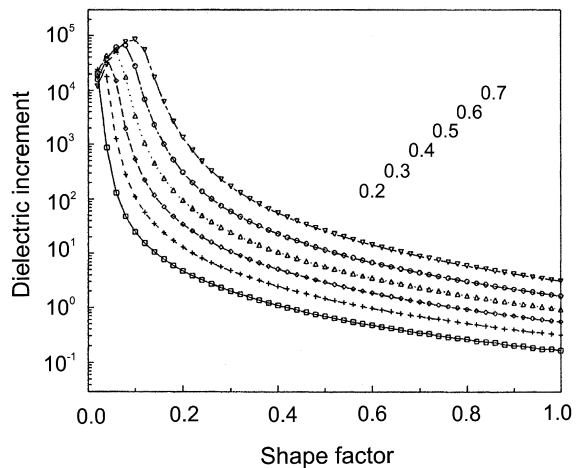
Figure 13.13 shows the results of similar calculations with the Hanai theory, but now rather for a non-conductive crystalline matrix with conductive amorphous inclusions. Again, the calculations were performed for various shape factors of the (ellipsoidal) inclusions. In this case it turns out that the experimentally observed dielectric increment of 70–100 is predicted for inclusions with shape factor 0.2–0.4 over a broad composition (φ_f) range. A shape factor of 0.2–0.4 agrees with well-known semi-crystalline morphologies consisting of spherulites and axialites. It is therefore concluded that in particular the morphology of conductive amorphous inclusions in non-conductive crystalline domains is able to describe the dielectric behaviour observed experimentally.

13.3.4
Effect of Processing on Material Homogeneity

A final example to be discussed relates to the effect of processing on sample homogeneity and how this affects the dielectric properties of emulsion-polymerized poly(vinylchloride). PVC is a strongly polar polymer due to the presence of the polar C-Cl bonds exhibiting very pronounced dipolar polarization processes. These mechanisms have been the subject of studies by many authors [81–86]. A detailed description of the dipolar polarization mechanisms in PVC can be obtained from McCrum et al. [69]. The most important dipolar transitions are the secondary β-transition found in the glassy state and the main α-transition, the glass rubber transition of the material.

Figure 13.14a,b shows ε' and ε'' of a compression moulded sample of suspension polymerized poly(vinylchloride) with a weight average molar mass of about 65 kg mol^{-1} (K-value 80), measured as a function of the frequency, at various temperatures in the glass transition range and higher [87].

Fig. 13.14. ε' and ε'' of poly(vinylchloride) with K-value 80, measured at various temperatures, as a function of frequency
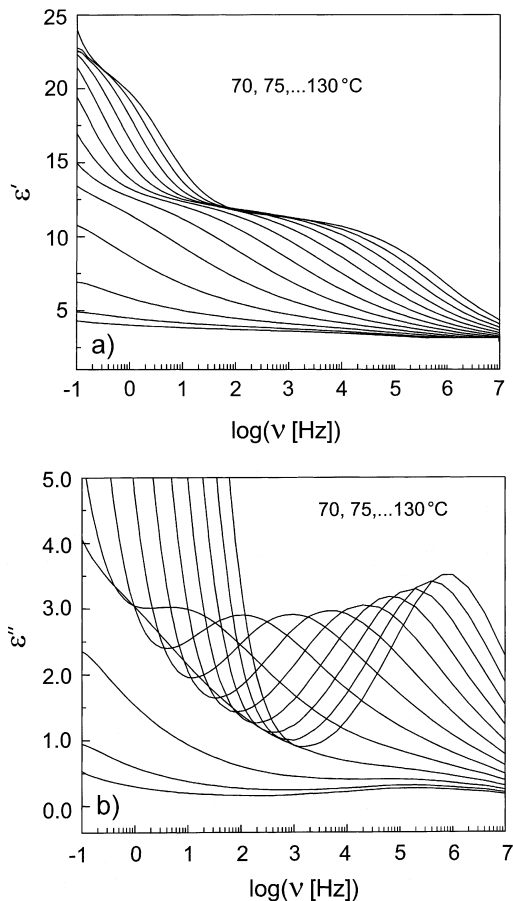
At the lowest temperatures, the loss peaks of the β-transition are visible around 100 kHz–1 MHz. At higher temperatures the loss peaks and the sharp increase of the dielectric constant (to about 12), due to the glass-rubber (α) transition become apparent. At the lowest frequencies the dielectric loss increases according to a power law, which is attributed to the contribution of ohmic conduction losses to the measured loss. Finally, at the highest temperatures (in the rubbery state) and the lowest frequencies an unexpected, additional relaxation process appears, due to which the dielectric permittivity increases further to about 22. However, the loss peaks of this process cannot be seen in the measured ε''-data, since these are dominated by conduction losses. Figure 13.15 shows the polarization losses calculated with the numerical Kramers-Kronig transform [58] from the frequency dependence of the dielectric constant. In this figure the loss peaks from the additional polarization process appear well resolved. The unexpected dispersion cannot be attributed to permanent dipoles in the polymer molecules. Moreover, it was shown that the frequency of maximum dielectric loss is proportional to the electrical conductivity of the material [87]. Both results point in the direction of an interfacial or macroscopic polarization process, which should be related to some interface of unknown origin in the material.

Dielectric measurements on bulk polymerized poly(vinylchloride) do not show this interfacial polarization process. Besides, a study of suspension polymerized poly(vinylchloride) samples with varying molar masses revealed that the mechanism is only found in samples of high molecular weight [87]. The latter observation leads to the conclusion that the interfacial polarization might be related to the *processing* conditions, in view of the fact that the high Mw samples are more highly viscous. Compression moulding is known to be a rather mild processing technique. Therefore, the PVC sample was subjected to 6 min of kneading before compression moulding. Figure 13.16 shows the dielectric properties of the material after kneading. Clearly, the interfacial polarization process has disappeared.

Fig. 13.15. Polarization loss of poly(vinylchloride) with K-value 80, calculated from measured ε'-data at various temperatures, as a function of frequency
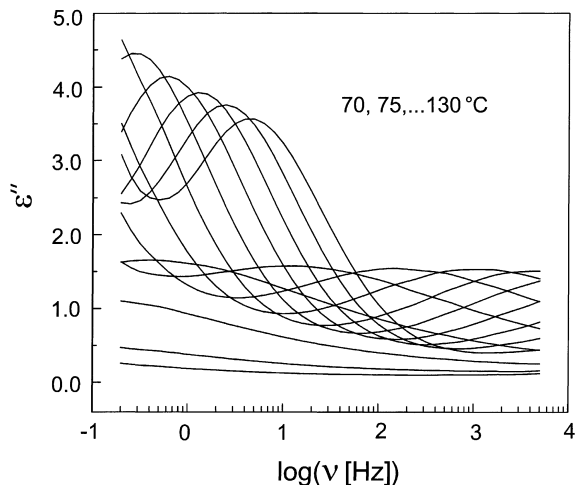
Fig. 13.16. ε' of poly(vinyl-chloride) with K-value 80 after kneading for 6 min at 170 °C, measured at several temperatures, as a function of frequency
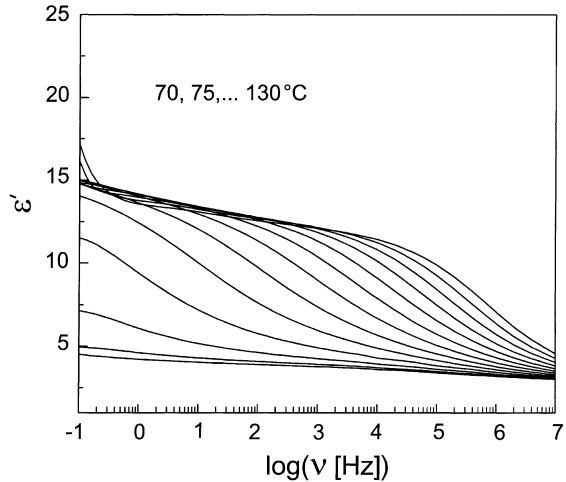
According to Allsopp [88], the 100–200 micron sized suspension PVC grain particles contain 10 µm sized agglomerates of 1–2 microns measuring primary particles. These primary particles are the original growth sites during the polymerization reaction. The outer surface of the grain particles is covered by a 1–2 µm thick shell of polymeric material, which was formed at the surface of the original suspended vinylchloride (MVC) droplets. This shell is formed by the precipitation of PVC molecules on the poly(vinylacetate)-poly(vinylalcohol) emulsifier interface [89]. During compression moulding this particle shell may remain intact and cause a grain boundary structure to be present in the sample. At these boundaries the material is discontinuous, which may block transport of charge carriers, thus causing interfacial polarization. Such boundaries were indeed observed with phase contrast microscopy in the not-kneaded sample, while they are absent in the kneaded one.

In order to determine whether such boundaries can cause the experimentally found dielectric effects, Wagner's theory was used to model the dielectric strength of an interfacial polarization process due to air inclusions in the material. As a result of the compression moulding, these boundaries and the included air are expected to be flat voids with a depolarization factor close to 1. The calculations with the Wagner-model, with low volume fraction of the inclusions and flat geometries indicate that for a shape factor $n > 0.98$, it is possible to have a dielectric increment of 10 or more, as found experimentally. Figure 13.17 shows a typical result of the calculations with the Wagner-model, in which the dielectric data of the kneaded sample were used as matrix, with 1 vol.% air present with a shape factor of 0.98.

The calculated curves of the dielectric permittivity are similar to the curves found experimentally for the not-kneaded material. This demonstrates that it is indeed likely that a residual grain boundary structure is present in the latter material, which causes interfacial polarization due to charge build-up at the discontinuities in the material. Though these defects are hard to detect opti-

Fig. 13.17. Dielectric permittivity ε' of kneaded poly(vinylchloride) estimated with the Wagner theory assuming 1 vol.% air inclusions with shape factor 0.98

70, 75,...130 °C

ε'

log(ν [Hz])
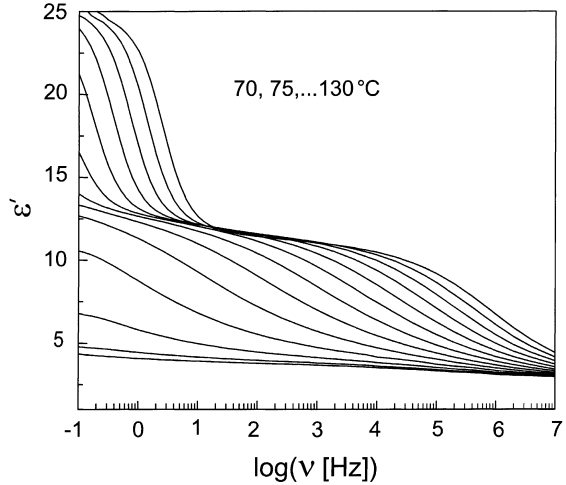
cally, the dielectric properties show large effects from interfacial polarization that occurs at the boundaries. Since the ultimate mechanical properties of the material may be highly dependent on the presence of defects, this again points to the usefulness of dielectric spectroscopy as a tool to study the homogeneity of materials.

13.4
Conclusions

In this chapter the basic theories for the dielectric properties of heterogeneous materials were reviewed. It was made clear that many polymer systems such as blends, filled polymers, semi-crystalline polymers, but also imperfectly processed amorphous polymers show interfacial polarization processes. Dielectric mixture theory may be used to investigate the morphological cause of the observed processes. Dielectric spectroscopy was shown to be a valuable tool in molecular and morphological characterization of polymeric materials.

List of Abbreviations and Symbols

n_i	Depolarization or shape factor in direction i
T	Temperature
T_g	Glass transition temperature
ε_0	Permittivity of vacuum, $\varepsilon_0 = 8.854$ pF/m
ε_s	Static dielectric permittivity
ε_∞	High-frequency limit of dielectric permittivity
$\Delta\varepsilon$	Dielectric relaxation strength, $\Delta\varepsilon = \varepsilon_s - \varepsilon_\infty$

$\varepsilon_i^*(\omega)$	Complex dielectric function of component i [4]
ε'	Real part of complex dielectric function
ε''	Imaginary part of complex dielectric function
σ_i^*	Complex conductivity of component i
σ_s	Static or d.c. conductivity
τ	Retardation or relaxation time
φ_i	Volume fraction of component i
ω	Angular frequency
ν	Frequency

ABS	Acrylonitrile-butadiene-styrene
HDPE	High density polyethylene
LCP	Liquid crystalline polymer
MWS	Maxwell-Wagner-Sillars
PA	Poly(amide)
PB	Poly(butadiene)
PC	Poly(carbonate)
PVC	Poly(vinylchloride)
SAN	Styrene-acrylonitrile

References

1. van Beek (1967) Dielectric behaviour of heterogeneous systems. In: Birks JB (ed) Progress in dielectrics, vol 7. Heywood, London, pp 69–114
2. Bánhegyi G (1986) Colloid Polym Sci 264:1030–1050
3. Hale DK (1976) J Mater Sci 11:2105–2141
4. Hanai T (1968) Electrical properties of emulsions. In: Sherman P (ed) Emulsion science. Academic Press, New York, pp 353–478
5. Dukhin SS, Shilov VN (1974) Dielectric phenomena and the double layer in disperse systems and polyelectrolytes. Wiley, New York
6. Takashima S (1989) Electrical properties of biopolymers and membranes. Hilger, Bristol
7. Landauer R (1978) In: Garland JC, Tanner DB (eds) Proceedings Electrical Transport and Optical Properties of Inhomogeneous Media (ETOPIM Conference). American Institute of Physics, New York, pp 2–45
8. Clausse M (1983) Dielectric properties of emulsions and related systems. In: Becher P (ed) Encyclopedia of emulsion technology, vol 1. Dekker, New York, pp 481–715
9. Priou A (ed) (1992) Dielectric properties of heterogeneous materials. Elsevier, Amsterdam
10. Hilfer R (1996) Transport and relaxation phenomena in porous media. In: Prigogine I, Rice SA (eds) Advances in chemical physics, vol 92. Wiley, New York, pp 299–424
11. Hilfer R (1991) Phys Rev B44:60–75
12. Feldman Y, Skodvin T, Sjöblom J (2000) Dielectric spectroscopy on emulsion and related colloidal systems – a review. In: Sjöblom J (ed) Encyclopedic handbook of emulsion technology. Dekker, New York
13. Whitehead JB (1927) Lectures on dielectric theory and insulation. McGraw-Hill, New York
14. Böttcher CJF, Bordewijk P (1978) Theory of electric polarization, vol 2. Elsevier, Amsterdam
15. Maxwell JC (1892) Treatise on electricity and magnetism, vol 1. Dover (reprint), New York

---

[4] The real part $\varepsilon'(\omega)$ of the dielectric function $\varepsilon^*(\omega)$ is often named "dielectric constant".

16. Wagner KW (1914) Arch Elektrotech 2:371–387
17. Sillars RW (1937) J Inst Electr Eng 80:378–394
18. Bruggeman DAG (1935) Ann Phys Leipzig 24:636–664
19. Hanai T (1961) Bull Inst Electr Eng Kyoto Univ 39:341; Hanai T (1960) Koll Zeitschr 171:23–31
20. Boned C, Peyrelasse (1983) Colloid Polym Sci 261:600–612
21. Bruggeman DAG (1935) Ann Phys Leipzig 24:665, 25:645
22. Böttcher CJF (1945) Rec Trav Chim 64:47–51
23. Looyenga H (1965) Physica 31:401–406
24. Landau LD, Lifshitz EM (1960) Electrodynamics of continuous media. Pergamon, London
25. Davies WEA (1971) J Phys D 4:318–328; Davies WEA (1974) J Phys D 7:120, 1016–1029
26. Smith GB (1977) J Phys D 10:L39–L42
27. Bilboul RR (1969) J Phys D 2:921–923
28. Lamb W, Wood DM, Ashcroft NW (1978) In: Garland JC, Tanner DB (eds) Proceedings ETOPIM Conference. American Institute of Physics, New York, pp 240–254
29. Fröhlich J, Sack R (1946) Proc R Soc A185:415–430
30. van der Poel C (1958) Rheol Acta 1:198–205
31. Maurer FHJ (1986) In: Sedlacek B (ed) Polymer composites. de Gruyter, Berlin, pp 399–411
32. Steeman PAM, Maurer FHJ (1990) Colloid Polym Sci 268:315–325; Steeman PAM, Maurer FHJ (1992) Colloid Polym Sci 270:1069–1079
33. Zetsche A, Kremer F, Jung W, Schulze H (1990) Polymer 31:1383–1387
34. Pathmanathan K, Cavaille JY, Johari GP (1988) Polymer, 29:311–319
35. Malik TM, Prud'homme RE (1984) Polym Eng Sci 24:144–152
36. Rellick GS, Runt J (1986) J Polym Sci Polym Phys 24:279–302, 313–324
37. La Mantia FP, Valenza A, Acierno D (1985) Colloid Polym Sci 263:726–729
38. Rellick GS, Runt J (1986) J Polym Sci Polym Phys 26:1425–1488
39. Pillai PK, Gupta BK, Goel M (1981) J Polym Sci Polym Phys 19:1461–1470
40. Pratt GJ, Smith MJA (1989) Polymer 30:1113–1116
41. Pillai PK, Khurana P, Taripathi A (1986) J Mater Sci Lett 5:629–632
42. North AM, Pethrick RA, Wilson D (1978) Polymer 19:913–930
43. Lei D, Runt J, Safari A, Mewnham RE (1986) Macromolecules 20:1797–1801
44. Maistros GM, Block H, Bucknall CB, Partridge IK (1992) Polymer 33:4470–4478
45. MacKinnon AJ, Jenkins SD, McGrail PT, Pethrick RA (1995) J Appl Polym Sci 58:2345–2355
46. Dionisio MCS, Moura Ramos JJ, Fernandes AC (1996) J Appl Polym Sci 60:903–909
47. Boersma A, van Turnhout J (1999) Polymer, 40:5023–5033
48. Boersma A, Wübbenhort M, van Turnhout J (1997) Macromolecules 2915–2922
49. Boersma A, van Turnhout J (1998) J Polym Sci Polym Phys 36:815–825
50. Boersma A, van Turnhout J (1998) J Polym Sci Polym Phys 36:2835–2848
51. Quitens D, Groeninckx G, Guest M, Aerts L (1990) Polym Eng Sci 30:1474–1490; Quitens D, Groeninckx G, Guest M, Aerts L (1991) 31:1207–1221
52. Gregory BL, Siegmann A, Im J, Baer E (1987) J Mater Sci 22:532–538
53. Keitz JD, Barlow JW, Paul DR (1984) J Appl Polym Sci 29:3131
54. Maurer FHJ, Palmen JHM, Booij HC (1985) Rheol Acta 24:243–249
55. Daly JH, Guest MJ, Hayward D, Pethrick RA (1991) In: Proceedings 3rd European Symposium on Polymer Blends. Plastics Rubber Inst., London, B20, pp 1–5
56. Guest MJ, Aerts LM (1991) Compalloy Europe '91, pp 167–177
57. Steeman PAM, Maurer FHJ, van Turnhout J (1994) Polym Eng Sci 34:697–706
58. Steeman PAM, van Turnhout J (1997) Colloid Polym Sci 275:106–115
59. Bánhegyi G, Karasz FE (1986) J Polym Sci 24:209–228
60. Bánhegyi G, Karasz FE (1986) Colloid Polym Sci 265:394, 266:701–715
61. Bunsell AR (1984) In: Pritchard G (ed) Developments in reinforced plastics, vol 3. Applied Science, London, pp 1–24
62. Cotinaud M, Bonniau P, Bunsell AR (1982) J Mater Sci 17:867–877
63. Reid JD, Lawrence WH (1986) J Appl Polym Sci 31:1771–1784
64. Woo M, Piggott R (1988) J Compos 10:16–19

65. Paquin L, St-Onge H, Wertheimer MR (1982) IEEE Trans Electr Insul EI-17:399–404
66. Plueddemann EP (1982) Silane coupling agents. Plenum Press, New York
67. Steeman PAM, Maurer FHJ, van Es MA (1991) Polymer 32:523–530
68. Steeman PAM, Maurer FHJ, Baetsen JFH (1992) Polym Eng Sci 32:351–356
69. McCrum NG, Read BE, Williams G (1967) Anelastic and dielectric effects in polymeric solids. Wiley, London
70. Hedvig P (1977) Dielectric spectroscopy of polymers. Hilger, London
71. Hirota S, Saito S, Nakajima T (1966) Kolloid Z Z Polym 213:109–115
72. Hirota S, Saito S, Nakajima T (1967) Rep Progr Polym Phys Jpn 10:425–428
73. Michel R, Seytre G, Maitrot M (1975) J Polym Sci Polym Phys 13:1333–1346
74. North AM, Pethrick RA, Wilson AD (1978) Polymer 19:923–930
75. Baird ME, Goldsworthy GT (1968) J Polym Sci B6:737–742
76. Baird ME, Goldsworthy GT (1971) Polymer 12:159–175
77. Gil-Zamrano JL, Juhasz C (1982) J Phys D, Appl Phys 15:119–128
78. North AM, Pethrick RA, Wilson AD (1978) Polymer 19:913–922
79. Keith HD (1969) Kolloid Z Z Polym 231:421–428
80. Steeman PAM, Maurer FHJ (1992) Polymer 33:4236–4241
81. Reddish W (1966) J Polym Sci C 14:123–137
82. Kopac Z, Schworer U, Stoll B (1976) Colloid Polym Sci 254:957–963, 1053–1058
83. Utracki LA, Jukes JA (1984) J Vinyl Technol 6:85–93
84. Naoki M (1989) J Chem Phys 91:5030–5036
85. Havriliak S Jr, Shortridge TJ (1990) Macromolecules 23:648–653
86. Del Val JJ, Alegria A, Comenero J (1989) Makromol Chem 190:893–905, 3257–3267
87. Steeman PAM, Gondard C, Scherrenberg RL (1994) J Polym Sci Polym Phys 32:119–130
88. Allsopp MW (1981) Pure Appl Chem 53:449–465
89. Clark M (1982) In: Butter G (ed) Particulate nature of PVC. Applied Science Publishers, London

14 Principles and Applications of Pulsed Dielectric Spectroscopy and Nonresonant Dielectric Hole Burning

R. Böhmer · G. Diezemann

14.1
Introduction

Nowadays dielectric relaxation measurements can be carried out almost routinely in broad frequency ranges continuously covering ten to fifteen decades and more [1]. This allows one to track the time scale on which dipolar motions occur in a wide temperature interval and to investigate in detail the shape of permittivity and dielectric loss spectra. Early on it has become clear that at a given temperature and pressure the molecular motion in most dielectric materials cannot be characterized by a unique time constant. In order to describe the experimentally observed relaxations intrinsic non-exponential as well as distributed processes have been considered. For a long time the distribution concept was quite popular in the description of dielectric phenomena [2–4]. It was often based on the assumption that environments differing from site to site lead to locally varying time constants. However, the alternative option which starts from the consideration of nonexponential responses [5] has also gained considerable attention [6–9]. To justify these approaches theoretically it has been pointed out that the interactions which exist between dipolar molecules should render a description in terms of a simple distribution of relaxation times at least questionable.

Experimental methods which allow one to test the assumptions underlying each of these theoretical approaches directly were missing for a long time. However, during the past decade several measuring techniques were devised that allow one to resolve this issue not only using computer simulations (for reviews, see [10, 11]), but also via laboratory experiments. Among these are multi-dimensional NMR [12, 13], dedicated optical techniques [14, 15] as well as dielectric approaches [16–18]. The main idea on which most of these methods rest is as follows. If a distribution of relaxation times exists then it should be possible to select (or selectively address) a subensemble which exhibits properties that are different from those of the overall ensemble. Such a selection can proceed either in the spectral (i.e., frequency or time) domain or in real space. Using dielectric techniques the latter option was implemented using atomic force noise microscopy. This method was shown to be sensitive to polarization fluctuations in a mesoscopic region [about $(50 \text{ nm})^3$] and was applied to amorphous polymers [17]. Frequency domain selectivity (which does not necessarily imply *spatial* heterogeneity) was demonstrated using nonresonant spectral hole burning (NHB). Principles and some applications of this technique constitute the

main subject of the present chapter [16]. Procedures for successfully measuring nonresonant spectral hole burning, based on the notion of a local fictive temperature, were first proposed by Chamberlin who already reviewed several aspects of this technique [19, 20].

At first glance, NHB may appear as a variant of the well known magnetic resonance or optical hole burning techniques. By employing monochromatic irradiation the latter methods can be used to decide whether a magnetic or optical resonance absorption line is predominantly homogeneously broadened (e.g., due to lifetime broadening) or predominantly inhomogeneously broadened. The latter type of broadening can arise if the transition (or resonance) frequencies which reflect (static) molecular orientations or local configurations or deformations exhibit a strong spatial variation. Although resonant hole burning was first demonstrated using magnetic resonance [21], its optical counterpart is more often employed to study a host of properties, particularly in amorphous systems at low temperatures [22] and in single molecule spectroscopy [23]. It has yielded information not only on the dominant type of broadening but also, e.g., on homogeneous line widths and on the dynamical processes responsible for hole refilling.

Nonresonant dielectric hole burning is related to conventional spectral hole burning in the sense that both methods are designed to reveal why spectra are broadened. In many respects, however, NHB is distinctively different from the resonance techniques. This is primarily because in the regime of orientational polarization, which is of interest here, we deal with relaxation rather than with resonance phenomena. Consequently, the theoretical framework available for the treatment of the mechanisms responsible for various features such as spectral selectivity and hole refilling needs to be carefully reconsidered for NHB.

The limiting cases for the broadening of dielectric loss spectra are usually termed the *homogeneous* (intrinsic nonexponential relaxation) vs the *heterogeneous* (distribution of relaxation times) scenario, cf. Fig. 14.1. In the linear response regime the two cases cannot be distinguished. Nevertheless it is worthwhile to review briefly some aspects of linear response in dipolar systems

Fig. 14.1. Homogeneous **a** vs heterogeneous **b** broadening of dielectric loss spectra represented as *solid lines*. The *dotted lines* are a meant to reflect the line shapes of elementary processes
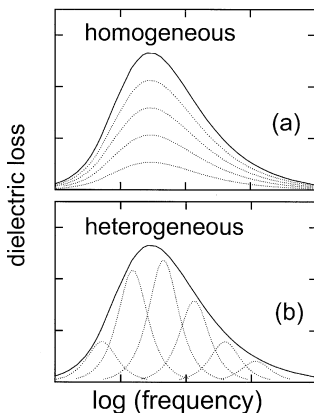
(Sect. 14.2.1) which are important in view of the extension of these experiments into the weakly non-linear domain. The principles of this weakly non-linear technique, NHB, are dealt with in Sect. 14.2. In Sect. 14.3 experimental aspects are discussed. In Sect. 14.4 NHB is demonstrated to provide compelling evidence that the slow response of most disordered materials studied so far is *dynamically heterogeneous*, according to the criterion formulated in [24].

14.2
Theoretical Concepts

14.2.1
Macroscopic Linear Response

Following the treatment of Böttcher and others [4, 25] we will formulate the general framework for the computation of dynamic variables such as the macroscopic dipole moment which is closely related to the experimentally accessible electric polarization. In a classical description of (charged) particles any dynamic variable $S(p,q)$ may be specified by the phase space coordinates q and the conjugated momenta p via

$$\langle S(t)\rangle = \iint S(p,q,t)\, \rho(p,q,t)\, \mathrm{d}p\mathrm{d}q \tag{14.1}$$

Here $\rho(p,q,t)\, \mathrm{d}p\mathrm{d}q$ is the probability to find the particles in a volume element $\mathrm{d}p\mathrm{d}q$ around the point (p,q). The phase space density $\rho(p,q,t)$ obeys the Liouville equation $\partial\rho(p,q,t)/\partial t = i\mathsf{L}\rho(p,q,t)$ and using Eq. (14.1) allows one to compute any dynamic variable. The Liouville operator L is related to the Hamiltonian H via the Poisson bracket, $\{S,\mathsf{H}\} = -i\mathsf{L}S$, known from classical mechanics [26]. This gives $\dot{S}(t) = -i\mathsf{L}S(t)$ and hence $S(t) = e^{-i\mathsf{L}t}\,S(0)$ for the time evolution of the dynamic variable. Under the influence of a time-dependent electric field $E(t)$ the Hamiltonian is $\mathsf{H}(p,q) = \mathsf{H}_0(p,q) - M(p,q)E(t)$ with $M(p,q)$ being the electric dipole moment. Note that in the present chapter a scalar formulation is given, i.e., fields, dipole moments, etc. will be described in terms of their projection onto the axis of the external electrical field.

The perturbation induced by the electric field leads to deviations from the equilibrium phase space density ρ_0 (corresponding to the non-perturbed Hamiltonian H_0) which can be written as the series

$$\rho(p,q,t) = \rho_0(p,q) + \rho_1(p,q,t) + \rho_2(p,q,t) + \dots \tag{14.2}$$

The phase space density increments ρ_i depend on the electrical field in i-th order. For sufficiently small external fields the terms with $i > 1$ can be neglected. This gives the linear contribution

$$\rho_1 = \frac{\rho_0(p,q)}{k_B T} \int_{-\infty}^{t} \exp[i(t-t')\,\mathsf{L}_0]\,\dot{M}(p,q,t')\,E(t')\,\mathrm{d}t' \tag{14.3}$$

where k_B is the Boltzmann constant and T denotes temperature. Exploiting that $iL_0 M(p,q,t) = -\dot{M}(p,q,t)$ and performing the phase space integration prescribed by Eq. (14.1), the time evolution of the dynamic variable can be expressed as $\langle S(t) \rangle = \langle S(t=0) \rangle + (k_B T)^{-1} \int_{-\infty}^{t} E(t') \langle S(t) \dot{M}(p,q,t') \rangle \, dt'$. When the thermal expectation value of $M(p,q,t)$, i.e., the orientational polarization $P(t)$ is chosen as dynamic variable, then this relation can be written via the convolution integral as

$$P(t) = \varepsilon_0 \chi_s \int_{-\infty}^{t} E(t') \, \partial_t \Phi(t-t') \, dt' \tag{14.4}$$

Here $\Phi(t) \equiv \langle M(p,q,t) M(p,q,0) \rangle / \langle M(p,q,0) M(p,q,0) \rangle$ is the dipolar correlation function. Furthermore, χ_s denotes the static dipolar susceptibility and ε_0 is the permittivity of free space. Equation (14.4) is sometimes designated Boltzmann's superposition principle. It allows one to calculate the polarization provided a sufficiently small field $E(t)$ (with an arbitrary time dependence) is given.

Non-exponential step response functions may be expressed as $\Phi(t) = \exp[-t \, W(t)]$ using a time dependent rate, $W(t) = 1/\tau(t)$, sometimes referred to, e.g., in the treatment of generalized master equations [27]. This approach and the memory function approach [28] were occasionally associated with intrinsic non-exponential response functions, since in these cases a recourse to a superposition of exponentials is not required.

Alternatively, $\Phi(t)$ can explicitly be represented by a continuous distribution of relaxation times $g(\tau)$ or equivalently, in a discrete description, by appropriately chosen weighting factors g_i

$$\Phi(t) = \int_0^{\infty} g(\tau) \, e^{-t/\tau} d\tau = \sum_i g_i \, e^{-t/\tau_i} . \tag{14.5}$$

Numerous types of distributions of relaxation times are available to describe relaxation data [3, 4, 29]. In the linear regime the polarization response to field sequences with an arbitrary time dependence can explicitly be written in terms of $g(\tau)$ as [30]

$$P(t) = \varepsilon_0 \chi_s \int_0^{\infty} g(\tau) \, A(\tau) \, e^{-t/\tau} d\tau \tag{14.6}$$

Here $A(\tau)$ has been termed amplitude function. If $E(t)$ is proportional to the Heaviside function then $A(\tau)$ is constant. Other cases with stepwise constant fields have been dealt with in [30]. One interesting application is based on pulsed electric fields (Sect. 14.3). For continuous field variations the amplitude function is given by [31]

$$A(\tau) = \tau^{-1} \int_{-\infty}^{t} E(t') \, e^{t'/\tau} \, dt' \tag{14.7}$$

The advantage of this approach is that effective distributions $g_{\text{eff}}(\tau) \equiv A(\tau) g(\tau)$ exhibiting specified properties can easily be generated. In particular, it is possi-

ble to suppress or emphasize specific parts of the dielectric response by choosing $E(t) = \int \tau^{-1} A(\tau) \, e^{-t/\tau} \, d\tau$ appropriately. It should be kept in mind, however, that the ability to modify the strength of (seemingly) slow or fast parts of the response does *not* necessarily imply the (physical) existence of a distribution of relaxation times. This is because the description in terms of Eq. (14.4) is completely equivalent to that using Eq. (14.6). In other terms, in the linear response regime homogeneous and heterogeneous relaxation processes cannot be distinguished. Therefore, an extension into the non-linear response regime is required if we want to address the question regarding the nature of the broadening of dielectric loss spectra.

Also in the following the treatment will be kept in the time domain since only in the linear response regime can the Fourier transformation $-\int_{-\infty}^{\infty} \dot{\Phi}(t) \, e^{-i\omega t} \, dt$ be identified with a complex, frequency dependent susceptibility $\chi(\omega)$.

14.2.2
Microscopic Reorientation Models

When proceeding to a more microscopic formulation we have to recognize the following (i) The internal electric fields in condensed systems generally are different from the ones applied externally – this is often accounted for by Lorentz field corrections or more elaborate approaches; (ii) Then, before we have discussed the macroscopic step response function $\Phi(t) \sim \langle M(t) M(0) \rangle$. However, for the description of the behavior of microscopic dipole moments the appropriate step response function involves not only self-terms but also cross-terms. In the following treatment we will neglect the latter to keep the discussion as simple as possible. Thus the microscopic response is given by the autocorrelation function $\langle \mu(t)\mu(0) \rangle / \langle \mu^2(0) \rangle$ and after carrying out the ensemble average we need not distinguish the latter function from $\Phi(t)$. This, however, holds only if with respect to point (i) we take Cole's optimistic view that the local or internal field problem is primarily reflected in magnitude rather than in time dependences [32, 33].

With internal field and correlation effects thus neglected, in a statistical description the microscopic motion can be specified by the conditional probability $G(w_2, t_2 | w_1, t_1)$ to find a permanent dipole moment pointing along direction w_2 at t_2 under the condition that it pointed along w_1 at t_1. Here the orientation $w = \{\phi, \theta\}$ is specified by the polar angle, θ, which the dipole moment axis encloses with the direction of the external electric field and the azimuthal angle, ϕ.

In order to make the connection to the previous section we note that the expectation value of the dipole moment is obtained from

$$\langle \mu(t) \rangle = \int dw \, \mu(w) \, p(w, t) \tag{14.8}$$

Here $\mu(w) = \mu \cos\theta$ and $p(w, t)$ is the probability to find the orientation w at time t. The polarization is related to Eq. (14.8) via $P(t) = N \langle \mu(t) \rangle$ with N denoting the number or, more properly, the number density of dipoles. $p(w, t)$ corresponds to

the phase space density $\rho(p,q,t)$ in the general formalism and is related to $G(w_2,t_2|w_1,t_1)$ by

$$p(w_2,t_2) = \int dw_1 G(w_2,t_2|w_1,t_1)\, p(w_1,t_1) \tag{14.9}$$

In equilibrium one has $p(w,0) \equiv p_0(w)$ and therefore $p(w,t) = p_0(w)$. Equation (14.4) then follows from an expansion of $p(w,t)$ in linear order in the field and the dipole correlation function is given by

$$\langle \mu(t_2)\mu(t_1)\rangle = \int dw_2 \int dw_1\, G(w_2,t_2|w_1,t_1)\, \mu(w_2)\, \mu(w_1)\, p_0(w_1) \tag{14.10}$$

This relation clearly reveals the importance of the conditional probability.

In most cases of relevance the reorientational motion is non-Markovian [12], but for simplicity here we focus only on Markovian models. Then $G(w_2,t_2|w_1,t_1)$ obeys a so-called master equation [34, 35] which can be assumed to be

$$\dot{G}(w_2,t_2|w_1,t_1) = \int dw\, \Pi(w_2|w)\, G(w,t_2|w_1,t_1) \tag{14.11}$$

Here $\Pi(w_2|w_1) = \lim\limits_{t_2 \to t_1} \dot{G}(w_2,t_2|w_1,t_1)$ defines the rate for a transition between two orientations w_1 and w_2. Equation (14.11) has then to be solved with the initial condition $G(w_2,t_1|w_1,t_1) = \delta(w_2 - w_1)$.

Two classes of models for reorientational motions may be distinguished. One assumes that the molecules reorient via rotational diffusion (infinitesimally small angular displacements), while the other starts from finite angular displacements. Both approaches yield single exponential responses in the time domain, corresponding to the so called Debye relaxation in the frequency domain [36]. Therefore in this respect these models cannot be discerned by carrying out measurements in the linear response regime. It should be emphasized from the outset that, when dealing with amorphous materials, all these and other models which we will mention in the following are to be considered as simplifications. To illustrate this situation a sketch of a more realistic scenario is depicted in Fig. 14.2. It summarizes results from experimental magnetic resonance studies [37].

Let us first consider rotational diffusion. The corresponding differential equation for isotropic liquids reads [36]

$$\nabla^2_{w_2} G(w_2,t_2|w_1,t_1) = D_r^{-1} \dot{G}(w_2,t_2|w_1,t_1) \tag{14.12}$$

with $\nabla^2_w = \frac{1}{\sin^2\theta}\left[\sin\theta \frac{\partial}{\partial\theta}(\sin\theta \frac{\partial}{\partial\theta}) + \frac{\partial^2}{\partial\phi^2}\right]$ denoting the angular part of the Laplace operator, and D_r the rotational diffusion coefficient. Equation (14.12) is obtained from the master equation by the replacement $\Pi(w_2|w_1) = D_r \nabla^2_{w_2}\delta(w_2 - w_1)$ and is solved by

$$G(w_2,t_2|w_1,t_1) = G(w_2,t_2-t_1|w_1,0)$$
$$= \sum_{l=0}^{\infty}\sum_{m=-l}^{l} Y_{lm}(w_2)Y_{lm}^*(w_1)\exp[-l(l+1)(t_2-t_1)D_r] \tag{14.13}$$
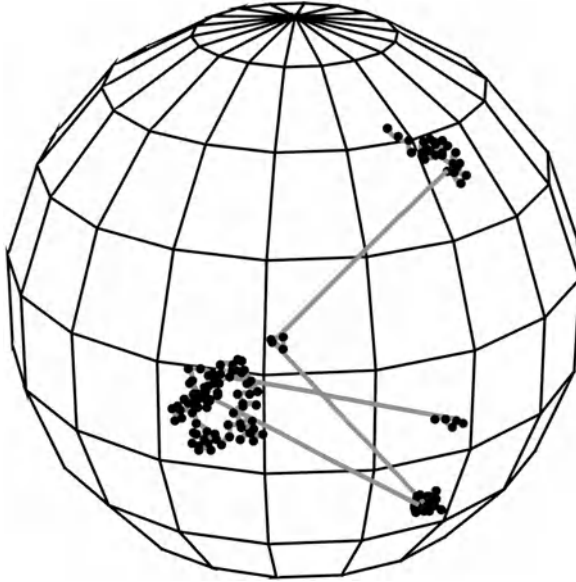
Fig. 14.2. Fragment of a trajectory where each *dot* on the sphere surface marks a molecular orientation. This is a pictorial representation of the distribution of large and small jump angles that characterize the molecular reorientation in supercooled liquids and the segmental motion in amorphous polymers. This scenario was inferred from magnetic resonance experiments carried out slightly above T_g [37]

where $Y_{lm}(w)$ denotes a spherical harmonic. From this equation the auto-correlation functions of the various Legendre polynomials of rank l,
$P_l(\cos\theta) = \sqrt{\frac{4\pi}{2l+1}} Y_{l0}(w)$ can be computed as

$$\langle P_l[\cos\theta(t)] \, P_l[\cos\theta(0)] \rangle$$
$$= \int dw_2 \int dw_1 \, G(w_2, t_2 - t_1 \,|\, w_1, 0) \, P_l[\cos\theta(t)] \, P_l[\cos\theta(0)] \, p_0(w_1) \qquad (14.14)$$

In conventional dielectric spectroscopy one measures $\Phi(t) \sim \langle P_1[\cos\theta(t)] \, P_1[\cos\theta(0)] \rangle$, cf. Eq. (14.10) with $\mu(w) = \mu\cos\theta = \mu P_1(\cos\theta)$. For the model of isotropic rotational diffusion this function decays as $\Phi(t) \sim \exp(-t/\tau_1)$ with $\tau_l = [l(l+1)D_r]^{-1}$. Therefore, using dielectric spectroscopy the characteristic time for the loss of dipolar (i.e., vectorial) autocorrelation is given by $\tau_1 = 1/(2D_r)$. Based on this simple approach one may expect a faster decay, $\tau_2 = 1/(6D_r)$, for techniques sensitive to the decorrelation of tensorial properties corresponding to $l = 2$ (e.g., transient Kerr effect [38], magnetic resonance, depolarized light scattering and photobleaching [39]).

The other approach which involves *finite* angular jumps in random directions can be implemented in a number of ways. One scenario is that a dipole can jump from one orientation to any other with equal probability. Then $\Pi(w_2|w_1)$ is in-

dependent of w_2 as well as of w_1 and is given by $\Pi(w_2|w_1) = \tau_J^{-1}[(4\pi)^{-1} - \delta(w_2 - w_1)]$ with τ_J denoting the average time between consecutive jumps. τ_J is called jump correlation time. The conditional probability is then found to be given by $G(w_2,t_2|w_1,t_1) = (4\pi)^{-1} + \exp[-(t_2 - t_1)/\tau_J][\delta(w_2 - w_1) - (4\pi)^{-1}]$. This random jump model was explicitly applied to dielectric spectroscopy quite some time ago [40]. This model, like the approach of rotational diffusion, yields single exponential response functions.

Yet another option is that finite jump angles are involved which leads to the definition of the Anderson model [41]. For this approach $G(w_2,t_2|w_1,t_1)$ is given by the same expression as in the model of rotational diffusion, Eq. (14.13), but with the replacement $l(l + 1) D_r \rightarrow \tau^{-1}[1 - P_l(\cos\varphi)]$ where φ denotes the jump angle. Note that in the limit of small jump angles one recovers the results for rotational diffusion with $D_r = (\varphi/2)^2\tau^{-1}$ [because then $P_l(\cos\varphi) \rightarrow 1 - l(l + 1)(\varphi/2)^2$].

When comparing the dipole correlation times from the Anderson model with those from the random jump model one finds $\tau_1/\tau_J = 1 - \cos\varphi$. This relation expresses the fact that in the random jump model each rotational jump leads to a complete decorrelation of the orientations. In the Anderson model, on the other hand, a number of jumps (depending on the magnitude of φ) have to take place before decorrelation is complete.

Finally, also models which only allow transitions between a set of K orientations were considered. These models are most appropriate for the description of crystalline solids. When the symmetry of the jump process is fully exploited it is found that in general $\Phi(t)$ does not decay to zero but to some constant, $\Phi(t \rightarrow \infty)$ [25]. Of course, in the usual treatment one subtracts out this constant, i.e., one considers only the time dependent response and this assumption was implicitly also made in Sect. 14.2.1. Nevertheless $\Phi(t \rightarrow \infty)$ can easily be understood by noting that (also for $t \rightarrow \infty$) the probability of finding a particle in a specific orientation w is just K^{-1}. This scenario is most appropriately formulated in terms of a set of coupled rate equations. These are obtained directly from the general master equation, Eq. (14.11) by the following substitutions: now the orientations are specified by $i = 1, 2, \dots K$. Then the conditional probabilities are written as $G_{ik}(t) = G(w_i,t_i|w_k,t_k)$ and the rates for the transition from state "1" to state "2" as $\Pi(w_2|w_1) = \Pi_{21}$. Using the "sum rule" $\Pi_{ii} = -\sum_k\Pi_{ki}$, which expresses the conservation of probability, one finds

$$\dot{G}_{ij}(t) = -\sum_k \Pi_{ki} G_{ij}(t) + \sum_k \Pi_{ik} G_{kj}(t) \tag{14.15}$$

By relating the conditional probability $G_{ij}(t)$ to the populations $p_i(t) = \sum_k G_{ik}(t) p_k(0)$ this equation can be cast into an even more transparent form as

$$\dot{p}_i(t) = -\sum_k \Pi_{ki} p_i(t) + \sum_k \Pi_{ik} p_k(t) \tag{14.16}$$

This equation has a simple interpretation. The first term on the right hand side represents the loss in probability to find the dipole moment in orientation w_i. This loss is due to jumps which lead away from w_i. The second term describes the gain in probability due to jumps into orientation w_i. Thus Eq. (14.16) is a typ-

Fig. 14.3. Schematic representation of an asymmetric double well potential (ADWP). The barrier height V, the overall asymmetry Δ, and the rates Π_{ij} connecting the two states "1" and "2" are indicated. For comparison, the *dotted line* depicts a symmetric DWP
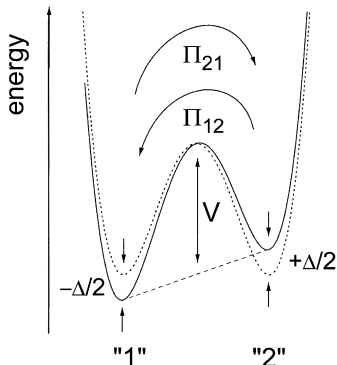
ical gain-loss master equation as it appears in many fields of condensed matter physics and physical chemistry.

The most simple case for this discrete master equation approach which we will treat here is that of an asymmetric double well potential (ADWP) [42, 43]. A schematic representation of an ADWP is given in Fig. 14.3. By definition, in this model there are only two orientations θ_1 and $\theta_2 = \theta_1 + \pi$. If we assume thermally activated jumps over the barrier V, the transition rates in the presence of an arbitrary electrical field are given by

$$\Pi_{12} = W\exp[-(\Delta + \mu E\cos\theta)/(2k_BT)] \tag{14.17a}$$

$$\Pi_{21} = W\exp[+(\Delta + \mu E\cos\theta)/(2k_BT)] \tag{14.17b}$$

It should be noted that for a double well there is some ambiguity in the definition of the dipole moment: One can either locate each of the charges in one well or, alternatively, fix one charge in the center of the double well and put the other into one of the wells. In accord with [42] we employ the latter option, but keep μ to denote the dipole moment. In Eq. (14.17) the expression $W = \nu_0\exp[-V/(k_BT)]$ denotes the hopping rate for vanishing asymmetry Δ. The attempt frequency ν_0 is on the order of a typical vibrational frequency of about 10^{13} s^{-1}. Since now there are only two orientations the summation in the rate equations (Eq. 14.16) is restricted to a single term and reads as

$$\dot{p}_1(t) = -\Pi_{21}p_1(t) + \Pi_{12}p_2(t) \tag{14.18a}$$

$$\dot{p}_2(t) = -\Pi_{12}p_2(t) + \Pi_{21}p_1(t) \tag{14.18b}$$

Thus here one has $\dot{p}_2(t) = -\dot{p}_1(t)$. The polarization can then be written as $P(t) = \langle\mu(t)\rangle = \sum_{i=1}^{2}\mu(\theta_i)p_i(t) = N\mu\cos\theta\,[p_1(t) - p_2(t)]$ suggesting to define the difference in the populations as

$$n(t) \equiv N[p_1(t) - p_2(t)], \tag{14.19}$$

so that $P(t) = \mu \cos\theta\, n(t)$. With additional abbreviations for the relaxation time τ, the reduced asymmetry δ, and the reduced electric field $e(t)$ given by

$$\tau^{-1} \equiv 2W \cosh[\Delta/(2k_B T)] \tag{14.20a}$$

$$\delta \equiv \tanh[\Delta/(2k_B T)] \tag{14.20b}$$

$$e(t) \equiv \mu E(t) \cos\theta/(2k_B T) \tag{14.20c}$$

from a combination of Eqs. (14.17)–(14.19) one finds the "equation of motion"

$$\dot{n}(t) = \tau^{-1}\{\sinh[e(t)] + \delta \cosh[e(t)]\} N - \tau^{-1}\{\cosh[e(t)] + \delta \sinh[e(t)]\}\, n(t) \tag{14.21}$$

Via Eq. (14.19) the solution of this equation, cf. Appendix 14.1, directly yields the polarization. For arbitrary fields it may be solved numerically [44]. If we restrict ourselves to the case of weak external fields, $|e(t)| \ll 1$, then from Eq. (14.21) in linear order in $e(t)$ we have

$$\dot{n}(t) = \tau^{-1}[e(t) + \delta]\, N - \tau^{-1}[1 + e(t)\delta]\, n(t). \tag{14.22}$$

As we are dealing mainly with overall isotropic systems we always perform powder averages, i.e., integrations over the entire solid angle. For a variable x the powder average is defined as $\langle x \rangle \equiv \frac{1}{4\pi} \int_0^{2\pi} d\phi \int_0^\pi d\theta\, x(\phi,\theta) \sin\theta$. When performing the average over the orientations of the dipoles with respect to the external field we have $\langle \cos^k\theta \rangle = (k+1)^{-1}$ for even k and $\langle \cos^{2k+1}\theta \rangle = 0$.

It is instructive to discuss some implications of Eq. (14.22). Let us start with the simplest case of a symmetric double well potential (DWP), $\Delta = 0$. Then this equation yields the one commonly associated with the Debye model [36]

$$\dot{P}(t) = \chi_{\text{DWP}} \tau^{-1} E(t) - \tau^{-1} P(t) \tag{14.23}$$

which yields a single exponential response function. In Eq. (14.23) the susceptibility of DWPs characterized by the polar angle θ is given by $N\mu^2 \cos^2\theta/(2k_B T)$ and after performing the powder average becomes $\chi_{\text{DWP}} = \frac{1}{6} N\mu^2/(k_B T)$.

For finite Δ it is seen from Eq. (14.22) that via the term $e(t)n(t)\delta$ higher orders in the field enter [since $n(t)$ itself depends linearly on $e(t)$]. Furthermore, in the absence of an external electrical field one finds a finite equilibrium value for the population difference of a single ADWP: $n_{\text{eq}} \equiv n(t \to \infty) = N\delta$. This can be rationalized by noting that in equilibrium the lower minimum in the ADWP is energetically favored. In an isotropic system the equilibrium polarization nevertheless vanishes because $\langle \cos\theta \rangle = 0$. In simple terms this means that for each ADWP with positive Δ, there is another one with negative Δ.

For later use we give the expression for the time dependent solution of Eq. (14.22) starting from an arbitrary population difference $n(0)$. For the case of a static field E_S, if one retains only terms linear in $e_S \equiv \mu E_S \cos\theta/(2k_B T)$, from

Eq. (14.22) one has the following result:

$$n(t) = n(0)[1 - e_S \delta t/\tau]\, e^{-t/\tau}$$
$$+ N[\delta(1 - e^{-t/\tau}) + e_S \delta^2\, e^{-t/\tau} t/\tau + e_S(1 - \delta^2)(1 - e^{-t/\tau})] \tag{14.24}$$

From this equation the step response with the initial condition $n(0) = N\delta$ follows as

$$P(t) = \chi_{\mathrm{DWP}} E_S (1 - \delta^2)(1 - e^{-t/\tau}) \tag{14.25}$$

Also the solution of Eq. (14.22) in the absence of an external electrical field will be used later. With $E_S = 0$ from Eq. (14.24) one has

$$n(t) = n(0)\, e^{-t/\tau} + N\delta(1 - e^{-t/\tau}) \tag{14.26}$$

It is clear that if the system was in equilibrium initially [$n(0) = N\delta$], then Eq. (14.26) yields a population difference which is independent of time [i.e., $n(t)$ equals $N\delta$ as well]. However if the initial population difference $n(0)$ deviated from the equilibrium value this is no longer true and Eq. (14.26) has to be employed explicitly.

It should be pointed out that by taking the ADWP approach it is a simple matter to model a heterogeneous dielectric response. Analogous to Eq. (14.5) this can be achieved by defining distributions of barrier heights and asymmetries. We mention that in the context of disordered crystals this is quite similar to the concept of so-called random fields. The latter lead to a distribution of asymmetries $\Delta \sim \mu E_{\mathrm{RF}} \cos\vartheta$ with ϑ denoting the angle enclosed by directions of μ and E_{RF}. Here the direction and the amplitude of E_{RF} are chosen according to some distribution function.

An aspect that we have not mentioned so far is the possibility that with the presence of a heterogeneous distribution of relaxation rates temporal fluctuations of the latter can occur. These "fluctuations of rates" may be described in terms of environmental fluctuation models [45]. This type of model was recently applied to the dipolar dynamics of systems in which the molecules can exchange from the surface to the inner regions of mesoscopic pores [46].

14.2.3
Stochastic Dynamics in Moderately Large Electric Fields

As outlined in Sect. 14.2.1 it is not possible to distinguish between the homogeneous and the heterogeneous scenario in the linear response regime. However, as the calculations presented in this section confirm, this becomes possible in the non-linear regime. Non-linear experiments can be performed in many different ways. The most common modes are based on large amplitude continuous wave excitation and on the superposition of a.c. fields with large d.c. bias fields. For a description of the more conventional non-linear response theory the reader is referred to the literature [47–50]. The approach implemented in NHB is different in that it employs a pump, wait, and probe scheme. Consequently this three-step procedure will also be reflected by the computations that we present further below in this section.
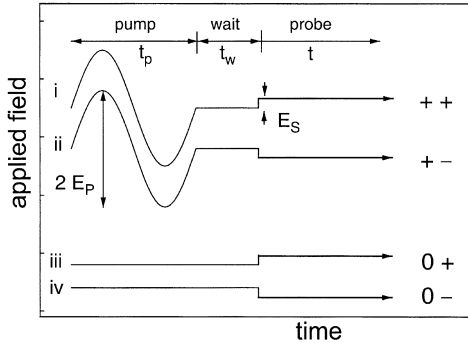
Fig. 14.4. Pump, wait, and probe sequence used for NHB experiments. In the preparation period (duration $2\pi N_\Omega/\Omega$ for N_Ω cycles with pump frequency Ω) a pump field $E_P(t)$ is applied to the sample (*traces* i *and* ii). The modified polarization can (partially) re-equilibrate during t_w and is then detected as the step response in the linear response regime. For comparison the equilibrium response is also measured (*traces* iii *and* iv). On the *right hand side* a short hand notation for each scan is introduced. In the experiment usually another four scans are performed

One of the key ingredients of NHB, which has to be considered as a difference spectroscopy, is the phase cycle schematically depicted in Fig. 14.4. With each pump, wait, and probe scan (e.g., traces i or ii in Fig. 14.4) a non-linear signal will be generated, i.e., one which can be expanded in general powers of the external field. Usually the perturbation is kept so small that only terms up to quadratic order need to be taken into account. Although this restriction is not necessarily required, it simplifies the development of the theory and the interpretation of the experimental results considerably. Then, the decisive trick of NHB is to subtract the linear contribution that can be probed, e.g., by a simple step response (cf. traces iii or iv in Fig. 14.4).

14.2.3.1
The Model of Asymmetric Double Well Potentials

Analogous to the phase space description summarized in Sect. 14.2.1 the NHB signal can be given in terms of the appropriate (higher-order) Liouville operators [51]. Based on these very general considerations reorientational models can be formulated along the lines presented in the previous section [52]. The treatment of these nonlinear models is, however, somewhat more involved as compared to what we have seen above. Therefore, in the following we will restrict discussion to the relatively simple case of an ADWP. Nevertheless, we will present the derivations in a way from which the general principles should become clear. It is obvious that an ADWP is not suited as a starting point for the description of, e.g., a supercooled liquid. It has to be emphasized that this model is only the simplest out of a class of more realistic approaches which are discussed elsewhere [51, 52].

The three-step procedure of NHB is taken into account as follows. First, during the pump process the signal can be calculated for the ADWP from

Eq. (14.22). Below this will be carried out to second order in the pump field $E_P(t)$. Thus, after a pump of duration t_p one gets the *modified* population difference $n(t_p)$. Second, during the waiting time, t_w, i.e., in the absence of an external field, we can use Eq. (14.26) with $n(t_p)$ as initial distribution to obtain $n(t_w)$. Finally, in the third step the modified response, $P^*(t) \sim n(t)$, is calculated according to Eq. (14.24) with the initial population difference now given by $n(0) = n(t_w)$. Thus one needs to compute the sequence of population differences briefly summarized by $n_{eq} \rightarrow n(t_p) \rightarrow n(t_w) \rightarrow n(t)$ [or formally more correct: $n_{eq} \rightarrow n(t_p) \rightarrow n(t_p + t_w) \rightarrow n(t_p + t_w + t)$]. We note that in the present context, accordingly, $p_i(t_p)$ should be read as a *modified* population of the orientation w_i. Therefore, speaking in more general terms, the effect of the pump process is to create a modified orientational distribution.

Since during the wait and the probe steps only small (or no) fields are involved, it is the calculation of $n(t_p)$ from Eq. (14.22) which is the crucial step. In Appendix 14.1 we outline how to solve this equation in quadratic order. The result for a pump field $e_P(t)$ [cf. Eq. (14.20c)] is

$$n(t_p) = N\delta + N(1 - \delta^2) \left[\frac{\mu \cos\theta}{2k_B T} Y(\Omega) - \delta \left(\frac{\mu \cos\theta}{2k_B T} \right)^2 X(\Omega) \right] \tag{14.27}$$

with the definitions

$$Y(\Omega) \equiv \tau^{-1} \int\limits_0^{t_p} dt\, E_P(t) \exp[-(t_p - t)/\tau] \tag{14.28a}$$

$$X(\Omega) \equiv -\tau^{-2} \int\limits_0^{t_p} dt_1 \int\limits_0^{t_1} dt_2 E_P(t_1) E_P(t_2) \exp[-(t_p - t_1)/\tau]. \tag{14.28b}$$

When deriving these expressions we have restricted ourselves to pump sequences which are cyclic in the sense that $\int_0^{t_p} dt E_P(t) = 0$. It is important to realize that $Y(\Omega)$ is linear in the pump field while for $X(\Omega)$ it enters quadratically. For reasons that will become obvious shortly $X(\Omega)$ is called excitation profile. Furthermore, $Y(\Omega) = \exp(-t_p/\tau) A_p(\tau)$ is directly related to the amplitude function of the pump field, $A_p(\tau) = \tau^{-1} \int_0^{t_p} E_P(t') e^{t'/\tau} dt$, cf. Eq. (14.7).

By plugging the results from Eq. (14.27) into Eq. (14.26) and in turn using them as the initial condition for Eq. (14.24) the resulting polarization is

$$P'(E_S, E_P; t) \equiv P(E_S; t) + \Delta P'(E_S, E_P; t) \tag{14.29a}$$

$$P(E_S; t) = \chi_{DWP} E_S (1 - \delta^2)(1 - e^{-t/\tau}) \tag{14.29b}$$

$$\Delta P'(E_S, E_P; t) = \chi_{DWP}(1 - \delta^2) Y(\Omega) \exp[-(t + t_w)/\tau]$$
$$+ \zeta E_S \delta^2 (1 - \delta^2) X(\Omega) \frac{t}{\tau} \exp[-(t + t_w)/\tau] \tag{14.29c}$$

with $\zeta \equiv N\mu^4 \langle \cos^4\theta \rangle / [(2k_B T)^3] = N\mu^4/[40(k_B T)^3]$. The phase cycle can now be understood to involve two steps. First, one subtracts the results from

scans i and ii (cf. Fig. 14.4) and obtains the modified polarization $P^*(E_S, E_P; t) = \frac{1}{2}[P'(+E_S, E_P; t) - P'(-E_S, E_P; t)]$. This eliminates contributions which are linear in the pump field, i.e., the term $Y(\Omega)$ which represents the polarization after-effect of the pump cycle. Then by subtracting the term $P(E_S; t)$ [cf. Eq. (14.25)] which is linear in the probe field (implemented by scans iii and/or iv) one arrives at the NHB signal $\Delta P_{ADWP}(t) = P^*(E_S, E_P; t) - P(E_S; t)$. This central result of our computation can be written as

$$\Delta P_{ADWP}(t) = C_{ADWP}(\delta, E_S) X(\Omega) \frac{t}{\tau} \exp[-(t + t_w)/\tau] \qquad (14.30)$$

with $C_{ADWP}(\delta, E_S) \equiv \zeta E_S \delta^2 (1 - \delta^2)$. In the following we will discuss in turn the amplitude coefficient $C_{ADWP}(\delta, E_S)$, the excitation profile $X(\Omega)$, as well as the t and t_w dependences of $\Delta P_{ADWP}(t)$. The amplitude coefficient shows that the NHB signal is proportional to the probe field E_S. Note that for small δ one has $C_{ADWP} \sim \Delta^2$, cf. [53], thus C_{ADWP} vanishes for Δ (or δ) $\to 0$.

The meaning of the term excitation profile is best illustrated when applying N_Ω cycles of a sinusoidal pump field, $E_P(t) = E_{P,0} \sin(\Omega t)$. In this case Eq. (14.28b) yields

$$X_{SIN}(\Omega) = \frac{3}{2} E_{P,0}^2 \, \varepsilon''(\Omega\tau)\varepsilon''(2\Omega\tau)\{1 - \exp[-2\pi N_\Omega/(\Omega\tau)]\} \qquad (14.31)$$

with $\varepsilon''(k\Omega\tau) = k\Omega\tau/[1 + (k\Omega\tau)^2]$ and $k = 1,2$. Figure 14.5 reveals that $X_{SIN}(\Omega)$ is strongly peaked. This implies that the modification of polarization is maximum only for $\Omega\tau \approx 1$. Thus if the response is dynamically heterogeneous, then frequency selective changes can be achieved using NHB. In other terms, slower and faster relaxations are much less affected by the pump and the respective modification tends to vanish if τ is not close to Ω^{-1}. We should mention that intrinsic nonexponential responses can also be considered. In the fully homogeneous sce-
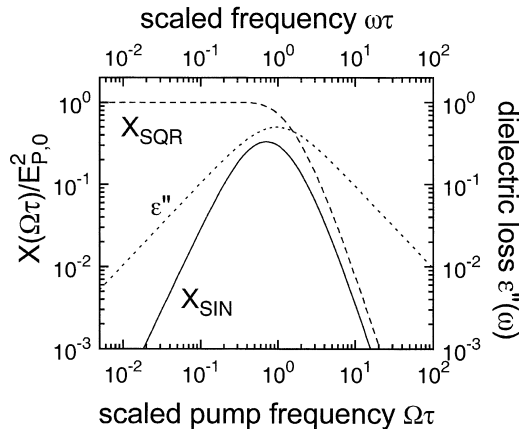
Fig. 14.5. Scaled excitation profiles $X(\Omega)/E_{P0}^2$ for a single cycle of a sine wave (*solid line*), Eq. (14.31), and of a square wave (*dashed line*), Eq. (14.32), pump field. Less suitable for frequency selective NHB experiments is $X_{SQR}(\Omega)$ since square wave excitation addresses the entire frequency range below about $\Omega\tau \approx 1$. On the high frequency side both profiles exhibit a Ω^{-2} dependence. For comparison $\varepsilon''(\omega) = \omega\tau/(1 + \omega^2\tau^2)$ is also shown (*dotted line*)

nario no spectral selectivity can be achieved [31]. This was recently demonstrated explicitly by considering time dependent relaxation rates [51]. In such a case broadened spectral holes arise which for variable pump frequencies all exhibit the same shape and only differ in their amplitudes.

From Eq. (14.31) it is seen that $X_{\mathrm{SIN}}(\Omega)$ is determined by the absorbed energy per cycle $[\sim \varepsilon''(\Omega\tau)E_{P0}^2]$. This insight forms an essential input into the approach discussed in Sect. 14.2.3.2. The term $\varepsilon''(2\Omega\tau)\{1 - \exp[-2\pi N_\Omega/(\Omega\pi)]\}$ can be interpreted to arise from a non-monochromatic excitation [53]. For $\Omega\tau \ll 1$ one has $X_{\mathrm{SIN}}(\Omega) \sim \Omega^2$ independent of N_Ω. Up to $\Omega\tau = 1$ the deviations between the $X_{\mathrm{SIN}}(\Omega)$ curves for all N_Ω are smaller than 0.2%. On the high-frequency side $X_{\mathrm{SIN}}(\Omega) \sim \Omega^{-3}$ for $N_\Omega = 1$. For $N_\Omega \to \infty$ one finds $X_{\mathrm{SIN}}(\Omega) \sim \varepsilon''(\Omega\tau)\varepsilon''(2\Omega\tau)$ which is peaked at $(\Omega\tau)_m = 1/\sqrt{2}$ with $X_{\mathrm{SIN}}[(\Omega\tau)_m] = 1/3$. The appearance of higher harmonics of the driving frequency resembles results known from other non-linear spectroscopies [54, 55], e.g., from second harmonic generation. It should be noted that, when viewed on a double logarithmic plot, the excitation profile X_{SIN} is narrowest for $N_\Omega = 1$ and slightly broader for $N_\Omega \to \infty$; however, in both cases the full width at half maximum is about 0.8 decades.

For a square wave excitation defined by $E_P(t) = +E_{P0}$ for $t \le t_p/2$ and $E_P(t) = -E_{P0}$ for $t_p/2 < t \le t_p$, one finds from Eq. (14.28b)

$$X_{\mathrm{SQR}}(\Omega) = E^2_{P,0}\{1 - (t_p/\tau)\exp[-t_p/(2\tau)] - \exp(-t_p/\tau)\} \tag{14.32}$$

The associated frequency, $\Omega = 2\pi/t_p$, is used in the latter expression in order to facilitate comparison with $X_{\mathrm{SIN}}(\Omega)$, cf. Fig. 14.5. For the square wave excitation one addresses essentially all relaxation processes that are slower than about $t_p/2\pi$. This remotely resembles the low-pass filtering used in multidimensional NMR [12, 13]. However, since in all experiments to described below sinusoidal pump fields were employed, we will not discuss square wave and other pump field sequences further.

The dependence of $\Delta P_{\mathrm{ADWP}}(t)$ on the detection time t is given by $(t/\tau)\exp[-t/\tau]$. This expression is proportional to $\mathrm{d}\exp(-t/\tau)/\mathrm{d}\ln t \sim \exp(-t/\tau) - \exp(-t/\tau^*)$ for τ unequal but close τ^*. In Appendix 14.2 we define this modified relaxation time τ^* more precise-ly and show that for the situation we discuss here (and $t_w = 0$) it is given by $\tau^* = \tau[1 - \zeta\delta^2 X(\Omega)/\chi_{\mathrm{DWP}}] < \tau$. This demonstrates that for the ADWP model the modified polarization response is $P^*(t) = \chi_{\mathrm{DWP}}E_S(1 - \delta^2)(1 - e^{-t/\tau^*})$. This corresponds to a simple shift of the polarization along the logarithmic time axis.

To make the small differences between $P^*(t)$ and $P(t)$ clearly visible one can not only plot the vertical difference, $\Delta P_{\mathrm{ADWP}}(t)$, but also the horizontal one. The latter can be defined by $\Delta(t) \equiv (t^* - t)/[t\ln(10)]$, where t^* has to be evaluated from the condition $P^*(t^*) = P(t)$, cf. Appendix 14.2. An example for $P(t)$ and $P^*(t)$ is depicted in Fig. 14.6a. In Fig. 14.6b,c we show $\Delta P_{\mathrm{ADWP}}(t)$ and $\Delta(t)$, respectively. Note that, unlike in the case of a distribution of relaxation times, in the situation considered here $\Delta(t)$ is obviously not explicitly time dependent. Our notation $\Delta(t)$ is thus only intended to avoid confusion with the asymmetry Δ. The maximum in the vertical difference (Fig. 14.6b) shows up at $t = \tau$; thus $\Delta P_{\mathrm{ADWP}}(t = \tau) = \zeta E_S\delta^2 X(\Omega)e^{-1}$, cf. Eq. (14.30). In Appendix 14.2 we show that

Fig. 14.6. Schematic representation of: **a** step response function $\Phi(t)$ and modified response $\Phi^*(t)$; **b** horizontal difference $\Delta\Phi(t)$; **c** vertical difference $\Delta(t)$ with the ordinate scales in arbitrary units. $\Delta\Phi(t)$ exhibits a maximum for $t = \tau$ and is 0.94 decades wide
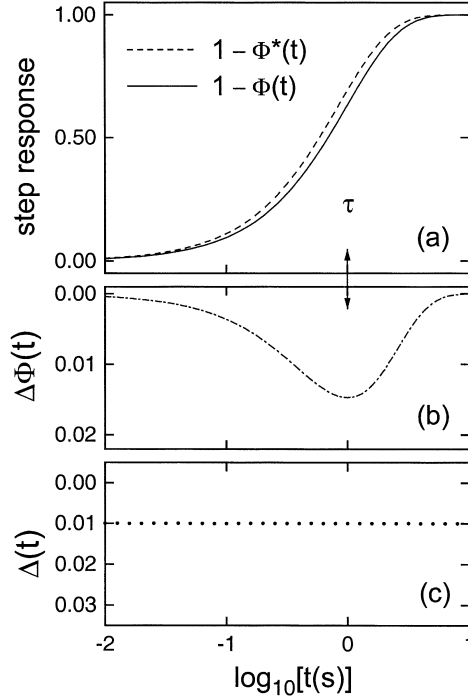
$\Delta(t) = \zeta\delta^2 X(\Omega)/[\chi_{DWP}\ln(10)]$ which gives $\Delta(t) = \Delta P_{ADWP}(t = \tau)\, e/[\chi_{DWP}E_S\ln(10)]$.

In view of the non-exponential polarization responses almost ubiquitously found in experiments it is worthwhile to mention briefly that in the presence of a distribution of relaxation times $\Delta(t)$ becomes explicitly time dependent; see Appendix 14.2. In the limit of a completely homogeneous response, on the other hand, the horizontal difference is again time independent. The NHB signal at a single Ω thus suffices to distinguish the two opposite scenarios using the $\Delta(t)$ representation, while several pump frequencies are required if the $\Delta P(t)$ format is chosen. Then the homogeneous case is recognized from NHB signals which only shift in amplitude but not in shape and they always display a maximum at the same time t, if Ω is varied. The heterogeneous scenario reveals itself by spectral selectivity, i.e., the maximum in $\Delta P(t)$ depends on the pump frequency.

Returning to the ADWP model, the dependence on the waiting time which variously has been called hole refilling, re-equilibration, or recovery is simply described by the factor $\exp(-t_w/\tau)$ appearing in Eq. (14.30). This means that dipolar reorientation and hole refilling are both governed by the same time constant τ, implying that at least in the framework of the nonlinear ADWP model presented in this section, the waiting period does not contain information that is not already available from the detection time dependence, $\Delta P_{ADWP}(t)$. Thus, if this model applies (which may not be always the case, cf. Sect. 14.4.3) then NHB is not able to contribute significantly to the question regarding the heterogeneity lifetime. Under these circumstances one merely measures the decay of the

non-equilibrium orientational distribution which has been generated by the pump process.

The origin of this modified orientational distribution may be understood as follows. The NHB effect is quadratic in the pump field amplitude and the distribution thus created is proportional to $\cos^2\theta$ [or $P_2(\cos\theta)$]. It should be noted that prior to the burn cycle one has $p_0(w) = 1/(4\pi)$ for an isotropic system. The modified response $\Delta P^*(t)$ involves terms proportional to $\cos^4\theta$ because (i) another factor $\cos\theta$ arises from the (linear order in the) step field and (ii) yet another one from the fact that the expectation value of $\mu(w) = \mu\cos\theta$ is calculated. Based on these consideration it becomes clear that, within the present approach, the recovery taking place during t_w traces essentially the decay of a $\cos^2\theta$ [or $P_2(\cos\theta)$] distribution. The associated time scale hence is τ_2. Depending on the motional model this time constant may or may not be (slightly!) different from τ_1 [56]. These calculations in the framework of the ADWP model thus show that NHB can be understood as a linear response experiment, however, not starting from an equilibrium orientational distribution, but from one which has been modified in a frequency selective way.

Aspects related to dynamic exchange [45] obviously cannot be addressed when dealing with two-site models. These features, which are known to play a prominent role particularly in glass-forming liquids [57], require a more sophisticated treatment [52].

Broadened susceptibility spectra occurring in solids are often ascribed to random fields. In the presence of random fields, i.e., with a distribution of asymmetries (and barrier heights) $f(\delta,V)$ the relaxation times $\tau = \tau(V,\delta)$ are also distributed. Thus the shape of the NHB can be written as $\int d\delta \int dV f(\delta,V) \Delta P_{\mathrm{ADWP}}(t,\delta,V)$. Of course $f(\delta,V)$ cannot be chosen at will but has to be adjusted such that it reproduces the step response as well. The spectral selectivity also of this random field scenario implies that only relaxation processes for which $\Omega\tau \approx 1$ are affected by the pump process. This means that recovery proceeds on the time scale set by Ω^{-1}.

Finally, we would like to discuss briefly how the present approach relates to the standard treatment of nonlinear phenomena. In the latter case for isotropic systems an expansion of the (quasi-static) response involves only odd powers of the external field [47] while a prominent feature of the calculated NHB signal is that it exhibits an even (i.e., quadratic) dependence on the pump field. This seeming problem can be resolved by noting that according to Eqs. (14.30) and (14.31) or (14.32) $\Delta P_{\mathrm{ADWP}}(t)$ is also cubic as in ordinary non-linear response theory, albeit in a particular fashion, $\Delta P_{\mathrm{ADWP}}(t) \sim E_S E_{P,0}^2$. Furthermore, it is clear that unlike conventional cubic non-linearities, NHB signals cannot be generated by a static field. Rather they appear as a consequence of the application of particular sequences of time-dependent fields. Thus NHB may be considered as a dynamic effect.

Keeping these considerations in mind it is nevertheless instructive to compare the *magnitudes* of typical static non-linear and of NHB effects. For the former one has $P = \chi_1 E + \chi_3 E^3 + \ldots = P_1 + P_3 + \ldots$ This particular dynamic non-linearity can show up in a regime in which the Langevin function can be approximated linearly to any desired level. In this limit these non-linearities will of course not be observable in a real experiment for purely practical reasons

with the linear and non-linear susceptibilities given by $\chi_1 = \frac{1}{3}N\mu^2/(k_BT)$ and $\chi_3 = -\frac{1}{45}N\mu^4/(k_BT)^3$, respectively [47]. Thus the static third-order non-linearity is $s \equiv |P_3/P_1| = \frac{1}{15}[\mu E/(k_BT)]^2$ and for the DWP a similar expression can be derived. This result can be compared with the magnitude of the NHB signal $s_{NHB} \equiv \Delta P_{ADWP}(t = \tau)/|P(t \to 0) - P(t \to \infty)|$ in its maximum which corresponds to $X(\Omega) = \frac{1}{3}E_{P,0}^2(=\frac{1}{3}E^2)$, cf. Eq. (14.31). Using Eqs. (14.25) and (14.30) one can thus estimate that $s_{NHB} = E^2\delta^2\zeta/(3\chi_{DWP}e) = [\delta^2/(20\,e)]\,[\mu E/(k_BT)]^2$. Thus for $\delta \approx 1$ one finds that the magnitudes of both effects, i.e., s and s_{NHB}, are very similar.

In the present section we have considered a simple stationary Markovian model as the simplest example out of a family of more realistic scenarios [51, 52]. Since it is known that, e.g., in supercooled liquids the reorientational dynamics is non-Markovian [12, 57], it may be worthwhile to discuss alternative descriptions.

14.2.3.2
The Box Model

Previously, a specific model has turned out useful for the analysis of NHB results of supercooled liquids and other materials. Since this so-called "box model" has been discussed previously [31, 58] here we will only outline some of its features and briefly compare the results obtained in this framework with those of the formulation presented above. The box model is based on the notion of spectrally distinguishable features (these are the "boxes", cf. Fig. 14.3 of [31]) which may or may not be associated with nanoscopic spatial regions in disordered materials. One of the starting points of the model is that, in addition to the thermodynamic temperature T, each box i is characterized by a non-thermodynamic quantity T_i which has the dimensions of a temperature. This quantity has variously been called local "fictive" [59], "internal" [60], "structural" [61], or "effective" temperature [62]. Via a modified Arrhenius or more precisely Tool-Narayanaswamy [63] relationship $\tau_i \sim \exp(B/T_i)$ any change ΔT_i leads to a modification of the effective relaxation time τ_i of box i via

$$\Delta \ln(\tau_i/s) = -B\Delta T_i/T^2. \tag{14.33}$$

Here the activation barrier B for simplicity was chosen to be independent of i and of T_i. It should be realized that the features described so far may be related to the notions advanced by several authors for a description of supercooled liquids [20, 64–67]. Furthermore, direct evidence for a distribution of time-dependent local temperatures exists for a crystalline model glass, cf. Sect. 14.5 [68].

The following two points are more specific for the present context: (i) energy input is regarded as spectrally selective, with the time derivative of the amount of energy absorbed by box i from a sinusoidal field of amplitude $E_{P,0}$ assumed to be given by

$$\dot{Q}_i = \pi\varepsilon_0\,\varepsilon''(\Omega\tau_i)\,\Omega E_{P,0}^2\sin^2(\Omega\tau) \tag{14.34}$$

and (ii) flow of energy between box i and the thermal bath proceeds at a rate κ_i and that between different boxes with rates κ_{ij}. With the (constant) bath temperature denoted as T_B and the heat capacity of the boxes given by Δc_p the pump process may be described by a rate equation for each box [31]

$$\dot{T}_i(t) = \dot{Q}_i(t)/\Delta c_p - \kappa_i[T_i(t) - T_B] \tag{14.35}$$

if the rates κ_{ij} are set to zero. Effects of incorporating them in various ways have been discussed [31]. Also several choices for the rates κ_i were considered [16, 31, 58], among them $\kappa_i = 0$ and $\kappa_i = 1/\tau_i$, corresponding to absence of energy flow out of the boxes and the existence of a unique time scale for each box, respectively.

  If the above view of glass formers is adopted, then Eq. (14.35) may be accepted as defining a simple model. Following the computations presented in Sect. 14.2.3.1 [51] the concept of energy selectivity is well justified (see also Fig. 14.3 in [31]). A detailed analysis shows that the simple form for $\dot{Q}(t)$, Eq. (14.34), is only recovered for this model if three ad hoc assumptions are made. The feedback between polarization and dielectric displacement (which may lead to an unphysical potential decrease of fictive temperature) is neglected. Likewise the slight decrease in $\ln\tau_i$ associated with the small increase in T_i during the pump is disregarded. Finally, since the above expression is usually derived for the steady state, it becomes clear that transient contributions are omitted. Taking the latter into account one finds that after one sinusoidal pump cycle the absorbed energy as compared to Eq. (14.35) is reduced by a factor $b_i \equiv (4\pi)^{-1}(2\Omega/\kappa_i)^3[1 + (2\Omega/\kappa_i)^2]^{-1}[1 - \exp(-2\pi\kappa_i/\Omega)]$. This factor is about 0.13 for $\kappa_i = \Omega$ and approaches unity for $\kappa_i \to 0$. The latter implies that in the absence of hole refilling and with transient effects neglected the energy absorption per cycle, $Q = \pi\varepsilon_0\varepsilon''(\Omega\tau_i)\Omega E_{P0}^2$, is recovered.

  The solution of Eq. (14.35) yields a time dependent $\tau_i(t) \sim \exp[B/T_i(t)]$. Now, in order to calculate the polarization it is assumed to obey $\dot{P}_i^*(t) = \chi\tau_i^{-1}(t)E(t) - \tau_i^{-1}(t)P_i^*(t)$, cf. Eq. (14.23). Since $\tau_i(t)$ is a function of $E(t)$ [via $\dot{Q}$ in Eq. (14.35)] this latter equation is not independent of Eq. (14.35). Thus these two differential equations have to be solved simultaneously in quadratic order in the pump field amplitude. Such a calculation for an integer number, N_Ω, of pump cycles yields for the modified response function $\Phi_i^*(t) = \Phi_i(t) + \Delta\Phi_i(t)$ with $\Phi_i(t) = \exp(-t/\tau_i)$ and

$$\Delta\Phi_i(t) = -\frac{B\varepsilon_0 E_{P,0}^2}{\Delta c_p T_B^2}\varepsilon''(2\Omega\,\tau_i)\,\varepsilon''[\Omega/(\kappa_i N_\Omega)]^2\,[1 - \exp(-2p\kappa_i N_\Omega)]$$
$$\times (\kappa_i\tau_i)^{-1}[1 - \exp(-\kappa_i t)]\exp(-t/\tau_i)\exp(-\kappa_i t_w) \tag{14.36}$$

The waiting time dependence implied by this model is easy to understand. Subsequent to the pumping period Q is zero and the first term on the right hand side of Eq. (14.35) vanishes so that equilibrium is approached as $\exp(-\kappa_i t_w)$. A comparison of Eq. (14.36) with the corresponding expressions for the ADWP model, Eqs. (14.30) and (14.31), shows that for $\kappa_i = \tau_i^{-1}$ the NHB signal computed for the current approach behaves very similar to that dealt with in Sect. 14.2.3.1,

thus suggesting that the assumptions made here are not critical. If one attempts to describe the recovery process only (and thus to circumvent possible problems associated with a detailed description of the pump process) it may be worthwhile to parameterize the shape of the NHB signal, $\Delta\Phi$, in terms of a distribution of effective temperatures T_i. The correlation between the shape of $\Delta\Phi(t) = \Sigma_i \Delta\Phi_i(t)$ and the hole refilling time which may be anticipated on the basis of this suggestion [69] can be checked experimentally [70].

If reorientation and hole refilling are governed by the same mechanism, then the condition $\kappa_i = \tau_i^{-1}$ is expected to hold. It is easy to imagine scenarios for which this is not the case, i.e., for which relaxation time and recovery time are not strictly correlated [51]. Of course for $E_P \rightarrow 0$, the relation $\kappa_i = \tau_i^{-1}$ should be valid in any case.

14.3
Experimental Aspects

Pulsed dielectric spectroscopy and nonresonant spectral hole burning are time-domain techniques which can be carried out in several ways. An important distinction is whether the polarization is detected under conditions of constant voltage or under conditions of constant charge. A sketch of the general set-up used in the first case is shown in Fig. 14.7a. It is essentially based on the time-honored Sawyer-Tower circuit [71]. The desired field sequence is produced using an arbitrary function generator and then passed through a high-voltage amplifier. The voltage across the very low-loss reference capacitor (with $C_{sample} \lll C_{ref}$) is essentially proportional to the dielectric displacement and hence the polarization of the sample. The reference voltage is detected using a high-impedance amplifier and then digitized. This allows for a straightforward implementation of the pump, wait, and probe scheme depicted in Fig. 14.4.

Measurements under constant-charge conditions can be performed using the circuit adapted from [72] (cf. Fig. 14.7b). In the pump and wait parts of the experiment the sample is connected to the high-voltage amplifier. Then, immediately (< 0.5 ms) after the application of the detection voltage, a fast relay switches the capacitor to the high-impedance device. For electrically conducting samples this set-up is to preferred over the one presented above. This is because it avoids space charge effects which otherwise would hamper proper signal detection during long acquisition times.

For both approaches essentially the same dedicated components (a high-voltage and a high-impedance amplifier) are used. It should be mentioned that for pulsed dielectric spectroscopy the high-voltage amplifier will usually not be required. Suitable bipolar high-voltage amplifiers are commercially available. Concerning high-impedance amplifiers for many applications it is preferable to work with battery powered devices in terms of signal to noise ratio. The use of home-built impedance transformers is advisable in view of the dielectric breakdown which occasionally may occur, particularly in the study of supercooled liquids. Such events not only call for a replacement of the sample but usually also of the high-impedance amplifier.

(a)

(b)
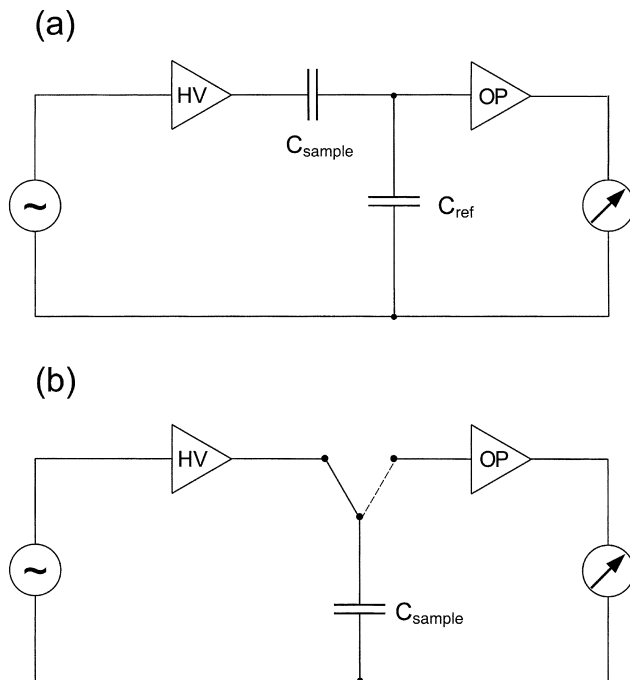
Fig. 14.7. Schematic representation of two types of NHB spectrometers. In both set-ups a digital to analog converter (located in a computer) drives the high-voltage (×1000) amplifier. The detection circuits consist of a high-impedance (10^{15} Ω) operational amplifier and a fast volt meter. Circuit: **a** is employed for the experiments that require detection under a constant field; **b** for detection under constant charge conditions. In (b) C_{sample} is connected to the high-voltage amplifier during the pump and wait periods. Almost immediately after the application of the pump voltage a high-resistance relay connects C_{sample} to the detection circuit (cf. the *dashed line*)

Most NHB experiments were carried out in the time range between about 10^{-3} s and 10^2 s. However, it does not present any difficulties to extend the range towards shorter times by improving on the high-voltage amplifier and/or the switching devices, and to extend towards longer times by further minimizing the unavoidable leakage currents appearing in the detection circuit.

For the experimental protocol of NHB phase cycling is essential, since the hole burning signal is obtained as the difference between step response and modified response. A minimum of four scans is required as sketched in Fig. 14.4. However, in order to recognize and eliminate possible artifacts it has proven useful to employ an eightfold cycle as summarized in Table 14.1. Note that each of the scans comes as a positive and negative pair with the correspondences being 1 and 8, 2 and 7, 3 and 6, 4 and 5, and also 1 and 2 (as well as 7 and 8). The redundancy inherent in the extended cycle allows one to check thoroughly the reproducibility of the measurements. Furthermore, this phase cycle efficiently suppresses slight asymmetries which may sometimes be present in the output of the driving amplifier. An experimental example of the various scans is shown for

Table 14.1. Signs of pump and probe voltages. The zero implies that no pump voltage is applied at all. To obtain the final NHB signal the scans have to be co-added taking into account the signs given in the last row

Step #	1	2	3	4	5	6	7	8
Pump	0	0	+	+	−	−	0	0
Probe	+	−	+	−	+	−	+	−
Detect	+	−	+	−	+	−	+	−

cyclo-octanol [73] in Fig. 14.8, from which the symmetry of the phase cycle becomes obvious.

Prior to NHB measurements a number of checks should be performed. First the recycle delay, t_d, between each scan of the phase cycle has to be chosen sufficiently long. In the case of the supercooled liquids, supercooled plastic crystal and the ion conductor this was particularly simple to achieve since one only needs to set t_d to 3…5 times the mean primary or conductivity relaxation time, respectively. For the relaxor materials the recycle delay was chosen such that the results did not depend on t_d. If t_d is chosen too short then, even in practically exponentially relaxing model systems, aging effects can be produced which at first glance can look somewhat similar to NHB [74, 75].

Another important issue is to ascertain that one works in the linear regime with respect to the step field. In view of the considerations outlined in Sect. 14.2.3, above, the NHB investigations should be done in the quadratic pump field regime. Since NHB is a difference spectroscopy the effective signal is often relatively small. Then large pump fields are required to achieve a satisfactory signal to noise ratio. To illustrate this point we compile typically employed pump fields in Table 14.2. In order to generate these fields, thin samples have been used in the studies of the liquids glycerol and propylene carbonate (50 µm) [16], of the glassy ionic conductor $2\,Ca(NO_3)_2 \cdot 3\,KNO_3$ (25 µm) [76], as well as of the supercooled plastic crystal cyclo-octanol (10 µm) [73].

By comparing with the expressions for the magnitudes for the NHB signals, as given in Sect. 14.2.3, one recognizes that the magnitude of the hole depths can also be affected by several other factors. An important question is how pronounced the temperature dependence of the mean relaxation time is. At least for supercooled liquids this property is directly related to their kinetic fragility [77].

Table 14.2. Typical values for pump fields, maximum dielectric losses, energy absorptions ($\sim\varepsilon'' E_{P0}^2$), and hole depths (measured in terms of Δ_m) for some materials for which NHB experiments were carried out

Material	Glycerol	CKN	90PMN-10PT
E_{P0} [V/mm]	20,000	10,000	50
ε''_{max}	25	1.5	3000
$\varepsilon'' E_{P0}^2$ [(kV/mm)^2]	10,000	150	7.5
Δ_m [decades]	0.03	0.01	1.5

Fig. 14.8. Polarization $P(t)$ of cyclo-octanol monitored subsequent to applying various field sequences, cf. Fig. 14.4. The step response functions (0+ and 0−) are characterized by $\langle \tau \rangle = 0.13$ s and $\beta = 0.74$. Note that the cycles with positive pump fields [traces (i) and (ii) in Fig. 14.4], and hence with $E_P < 0$ in the second half cycle, yield $P(t \rightarrow 0) < 0$. For further details see [73]
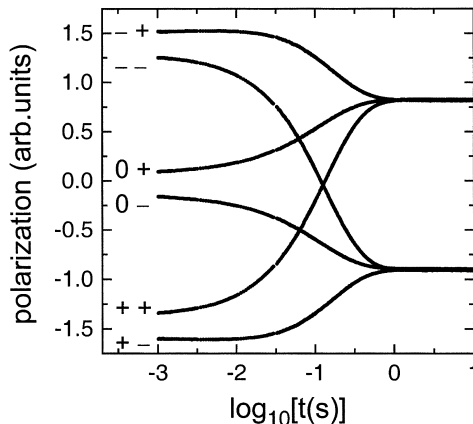
On the other hand, one should realize that very strongly temperature dependent relaxation times impose also more stringent conditions on the stability of the sample temperature. Furthermore, the specific heat contributions, Δc_p, of the degrees of freedom addressed by the pump, cf. Eq. (14.35), may be quite different in different situations. It is well known that Δc_p associated with the primary relaxation of supercooled liquids is readily accessible with standard methods. However, the much smaller contributions which are due to the arrest of "decoupled" processes has only been studied occasionally, e.g., for the freezing of ions in glassy networks [78] or for the slow-down of secondary processes in disordered crystals [79]. Then, the considerations near the end of Sect. 14.2.3.1 raise the possibility that also non-linear susceptibilities play a role. When using large electrical fields, a proper experimental determination in supercooled liquids [80] may be more difficult than it is for rigid solids [81].

Finally, we should note that unless explicitly stated otherwise all experiments reviewed in this chapter were collected after excitation with $N_\Omega = 1$ cycle of a sinusoidal pump field. Also, if below we do not give explicit values for the waiting time, this always should be read as the shortest waiting time (of $t_w = 1$ ms) that can conveniently be implemented by our current dielectric apparatus.

14.4
Applications

14.4.1
Supercooled Liquids and Plastic Crystals

14.4.1.1
Pulsed Dielectric Spectroscopy

The main advantage of pulsed dielectric spectroscopy is that it allows one to emphasize (or suppress) specific regimes of the dielectric response. This can be

Fig. 14.9. Normalized polarization $P(t)/P_0$ of propylene carbonate as measured at $T = 160.0$ K subsequent to the application of an electrical pulse of length t_1 as shown as *inset*. For the longest t_1 the step response function is measured. The *double bar* indicates the acquisition period. Reproduced from [30]
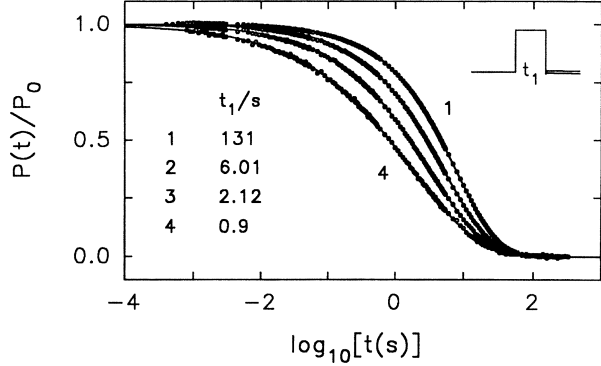
useful for supercooled monohydric alcohols for which a strong Debye-type relaxation dominates other high-frequency contributions [82]. However, also for other viscous liquids one finds simultaneously a strong dielectric loss peak and a weak so-called wing region at high-frequencies [1]. Under these circumstances one may aim at emphasizing the short-time contributions to the response. This can be achieved using the single-pulse experiment in which an electric field of constant magnitude, ΔE, is switched on for a time interval t_1. In Fig. 14.9 corresponding experimental results for supercooled propylene carbonate just above its glass transition [83] are shown. If t_1 is chosen sufficiently long then one measures the structural relaxation which in this example can be parameterized using $P(t)/P_0 = \Phi(t) = \exp[-(t/\tau)^{\beta}]$ with $\langle\tau\rangle = 9.9$ s and $\beta = 0.71$. For pulse lengths comparable to or shorter than the relaxation time τ it is seen that the response functions decay considerably faster, with effective relaxation times τ_S. Adopting the distribution picture this is due to the fact that the amplitude function here is given by $A_S(\tau) = [1 - \exp(-t_1/\tau)]\Delta E$. In other words one may then say that while, near the end of the pulse, the faster dipoles are already oriented by the electric field the slow ones did essentially not respond. Recourse to the distribution concept is, however, not necessary since the effective response functions $\Phi_S(t)$ are fully described by Eq. (14.4) which simply reads here $\Phi_S(t) = \Phi(t) - \Phi(t + t_1)$. This expression immediately shows that for $t_1 \to 0$ the impulse response, $-t_1 \partial\Phi(t)/\partial t$, is obtained. For finite t_1 the effective relaxation times are given by

$$\langle\tau_S\rangle = \frac{1}{1 - \Phi(t_1)}\int_0^{t_1}\Phi(t)\,\mathrm{d}t = \langle\tau\rangle\,P(\beta^{-1}, \zeta)\,(1 - e^{-\xi}) \tag{14.37}$$

The latter equality with $\xi \equiv (t/\tau)^{\beta}$ and $P(\beta^{-1}, \xi)$ denoting the incomplete Gamma function [84] only holds if $\Phi(t)$ is of the Kohlrausch form. In Fig. 14.10 we demonstrate that the theoretical results based on these considerations compare favorably with the experimental data.

Various other applications of pulsed dielectric spectroscopy are described in [30]. Here we only mention a method allowing to map out distributions of relaxation times directly from time domain measurements. The pulse sequence is schematically depicted in Fig. 14.11. After an electric pulse of duration t_1, a wait-

Fig. 14.10. Normalized non-equilibrium relaxation times $\langle \tau_S(t_1) \rangle / \langle \tau \rangle$. The *solid line* has been calculated according to Eq. (14.37). For illustration purposes the *dashed line* shows results for $\beta = 0.5$. Adapted from [30]

$\beta = 0.71$

$\beta = 0.5$

$\langle \tau_E \rangle = 9.9\,s$
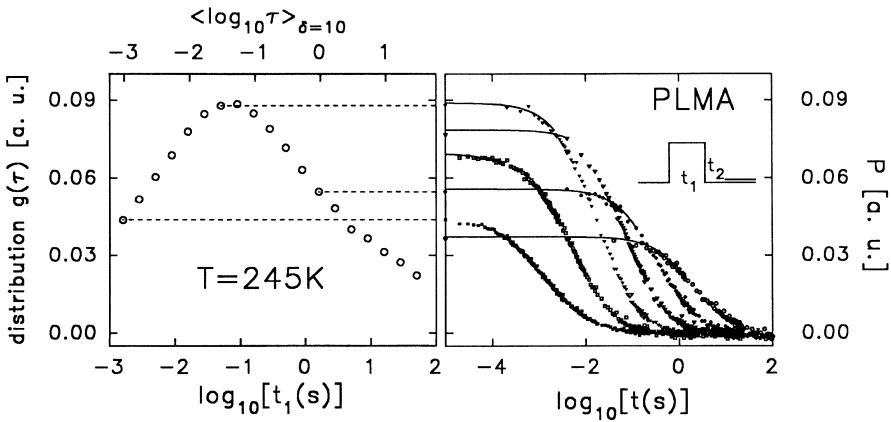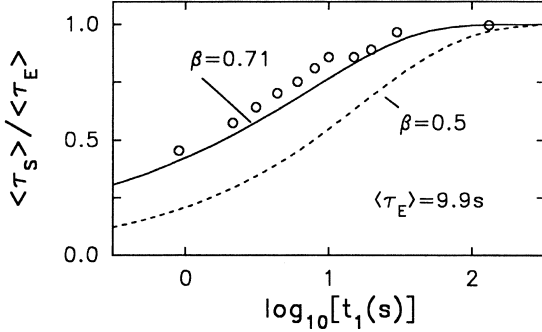
Fig. 14.11. The time dependent polarization of poly(lauryl methacrylate) (PLMA) is shown in the *frame on the right hand side* for pulse durations (*from left to right*) $t_1 = 1.6, 8.9, 50, 281, 1580,$ and 8900 ms. The employed electric field sequence is schematically depicted as *inset*. The *left part* of the figure presents the distribution of relaxation times $g(\tau)$ as a function of $\log_{10}(t_1/s)$ (*lower axis*) and $\langle \log_{10}(\tau/s) \rangle$ (*upper axis*). Reproduced from [30]

ing interval t_2 at zero field is inserted before the acquisition of the polarization $P(t)$ is started. For sufficiently broad distributions $g(\tau)$ one finds that $P_0 \equiv P(t \to 0)$ as measured as a function of t_1 (with the ratio t_1/t_2 kept fixed) is proportional to the distribution. More precisely one has $g(\langle \log_{10} \tau/s \rangle) \sim P_0(\log_{10} t_1/s)$ [30]. Corresponding experimental results for a polymeric material are shown in Fig. 14.11. For these measurements we have chosen $t_1/t_2 = 10$ which implies that the associated amplitude function $A_B(\tau) = \exp(-t_2/\tau) [1 - \exp(-t_1/\tau)] \Delta E$ is peaked near $\tau \approx 0.6\, t_1$. Hence there is a slight shift of 0.23 decades between top and bottom axes in Fig. 14.11. For $t_1/t_2 = 10$ the full width at half maximum of $A_B(\tau)$ is only slightly larger than the Debye width of 1.14 decades. The ability to map out $g(\tau)$ may be rationalized by noting that the slowest dipoles are not aligned by the electric field during t_1 while the fastest have already relaxed during t_2. Thus only a band of intermediately fast relaxations contributes to the sub-

sequently measured polarization response. This statement alludes to the notion of a distribution of dipolar relaxation times. However, according to the discussion in Sect. 14.2.1 up to this point it has remained open whether the distribution concept is more than a matter of mathematical convenience. It has to be reiterated that the results from frequency selective NHB, which we describe next, indeed demonstrate that it *is* more than that.

14.4.1.2
Nonresonant Spectral Hole Burning

For our initial NHB experiments we have chosen propylene carbonate and glycerol. Both supercooled liquids are well studied using dielectric and other techniques [1, 37]. They exhibit a sizable maximum dielectric loss (ε_m'' in the range of 20–30) which is, however, only moderately broadened. While the large ε_m'' is favorable if the NHB effects are related to the absorbed energy, the broadening of about 1.5 decades implies that the pump frequency cannot reasonably be varied over very wide ranges. Propylene carbonate has the advantage that it is quite fragile [77], i.e., a given temperature variation is associated with a particularly pronounced change in relaxation time.

In Fig. 14.12 we show NHB results obtained for propylene carbonate just above T_g. In the upper part of this figure we compare the step response with the

Fig. 14.12. **a** Equilibrium and modified responses of propylene carbonate represented in terms of the dielectric relaxation constant. (**b, c**) The NHB signals $\Delta\varepsilon(t)$ **b** and $\Delta(t)$ **c** are defined here as the logarithmic difference in the times between modified and step responses. In frame (a) the lower and upper pair of curves have been offset for clarity. Adapted from [16]
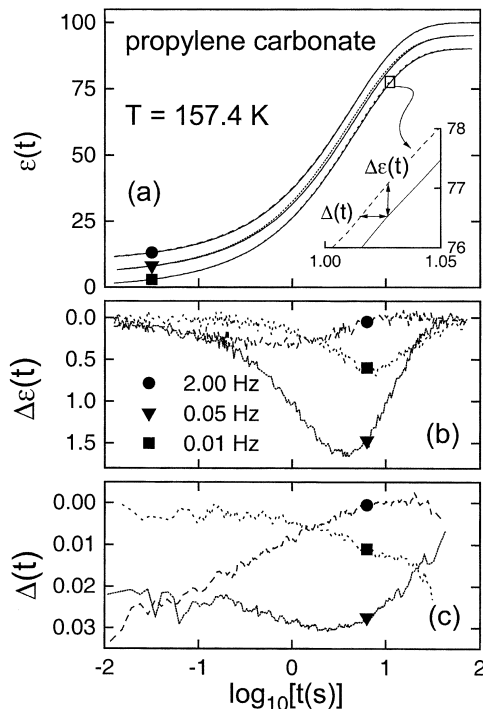
modified response. Both are plotted in terms of the dielectric constant for several pump frequencies Ω. Already in the raw data it is seen that the large pump frequency modifies the dielectric response most at short times and vice versa. This finding reveals not only the spectral selectivity of NHB, but it also provided the first direct experimental evidence that the dipolar relaxation of a supercooled liquid is heterogeneously broadened. As we have pointed out previously the finding of *dynamic* heterogeneity not necessarily implies the existence of *spatial* heterogeneity. In this context it is interesting to mention that experimental evidence for spatial heterogeneity of a glass-forming substance, slightly above T_g, was recently obtained using multidimensional NMR techniques [85].

Returning to the data shown in Fig. 14.12 one recognizes that even with the relatively large pumping fields of $U_P = 900$ V across the capacitor gap of 50 μm (in conjunction with the likewise quite sizable probe voltage of $U_S = 150$ V) the NHB effect here is smaller than about 1.5 % (cf. Fig. 14.12b). In order to bring out the deviations between step response and modified response more clearly in Fig. 14.12b,c we plot the vertical differences, $\Delta\varepsilon(t)$, and the horizontal ones, $\Delta(t)$, respectively (cf. Fig. 14.12a). The maximum modification $\Delta\varepsilon_m$ as seen in the vertical difference signal strongly depends on Ω (Fig. 14.12b). It is largest where the slope $d\varepsilon(t)/d\log t$ is largest.

Each one of the representations chosen in Fig. 14.12b,c has specific advantages and drawbacks. $\Delta\varepsilon$ (or ΔP or $\Delta\Phi$) can be evaluated directly if, within a phase cycle, data are recorded using the same timing scheme, whereas for the determination of $\Delta(t)$ a (straightforward) interpolation procedure is required. The assignment of a reference time becomes ambiguous if $\Delta(t)$ turns larger than 0.1 decades, say. In view of the small NHB effects in supercooled liquids this is not an issue. The main advantage of the $\Delta(t)$ representation is that it allows for an unambiguous distinction of homogeneous from heterogeneous responses, even if a measurement at a single pump frequency is carried out. This is because for completely homogeneous relaxations the modified and the step responses are related by a mere shift along the logarithmic time axis, cf. Appendix 14.2. Thus, the horizontal difference is constant, i.e., it does not depend on time [86]. However, in the heterogeneous case $\Delta(t)$ is not constant (cf. Fig. 14.12c). Furthermore, via $\Delta T_f(t) \approx -\Delta(t)\ln(10)(k_B T)^2/B$, [cf. Eq. (14.33)] the increase in fictive temperature can directly be obtained from the horizontal difference $\Delta(t)$. For propylene carbonate a change in $\Delta(t)$ of about 1% thus corresponds to a $\Delta T_f(t)$ variation of roughly 20 mK. From Fig. 14.12c one may infer that the experimental uncertainty in ΔT_f is about 5 mK. When working very close to T_g one may also express ΔT_f using the liquid fragility, $m = B(T_g)/[T_g\ln(10)]$, here written in terms of the temperature scaled effective barrier [77]. With $\Delta T_f(t) = -T_g\Delta(t)/m$ one recognizes that even for a low-fragility material like glycerol (with $m = 53$), for which $\Delta(t)$ was in the percent range [31] as well, $\Delta T_f/T_g$ is of the order of 10^{-5}. Thus for the NHB study of supercooled liquids stringent conditions have to be placed on the stability of the sample temperature which should be comparable in magnitude to $\Delta T_f/T_g$.

However, it is also important to check whether the conditions for the application of the theoretical frameworks outlined in Sect. 14.2 are fulfilled. Here it is important that the hole depths are proportional to E_S and to E_P^2. In Figs. 14.13

Fig. 14.13. Maximum spectral modification ΔP_m obtained for glycerol using $\Omega/2\pi = 0.5$ Hz. Note that in Fig. 14.8 of [31] corresponding data for $\Delta_m(U_P)$ were presented
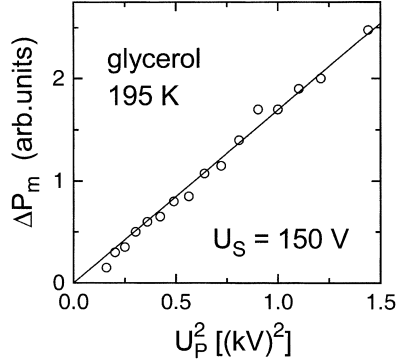
Fig. 14.14. Hole depths ΔP_m as a function of the probe voltage recorded for glycerol using $\Omega/2\pi = 0.5$ Hz
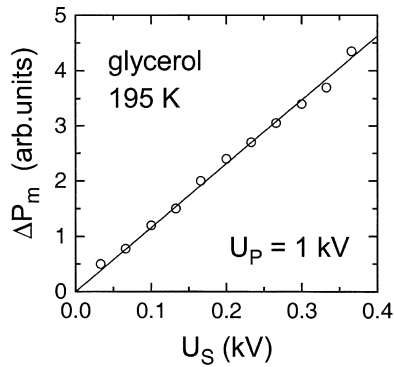
and 14.14 we present corresponding data for supercooled glycerol. Both conditions are nicely fulfilled, i.e., the NHB effect is proportional to the energy absorbed during the pump cycle (Fig. 14.13), and linear in the probing field (Fig. 14.14).

In order to address the question regarding the nature of the broadening of dielectric loss spectra it suffices to apply just $N_\Omega = 1$ pump cycle. However, it is also interesting to see what happens if one increases N_Ω. Corresponding data have been reported and analyzed for propylene carbonate elsewhere [24, 31]. In Fig. 14.15 we present corresponding data for glycerol in the format $\Delta P_m(N_\Omega)/\Delta P_m(N_\Omega \to \infty)$ for two pump frequencies. In order to compare these data to one another they are not simply plotted as a function of N_Ω, but displayed vs the total pumping time $2\pi N_\Omega/\Omega$. It is clearly seen that for a sufficiently large number of cycles the hole depths saturate.

Not only the build-up but also the refilling of the spectral holes has been studied for propylene carbonate and glycerol [16]. It was found that hole refilling and step response take place on the same time scale. Based on the considerations presented in Sect. 14.2.3.1 this is expected in the absence of extrinsic relaxation effects and implies that also build-up and refilling of the spectral holes should proceed on the same time scale. This expectation is seen to be confirmed by the
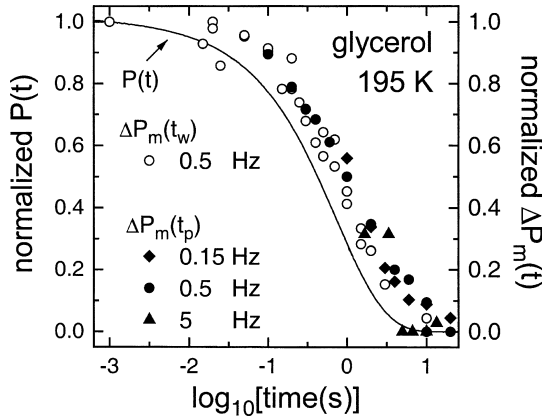
Fig. 14.15. The response functions measured for glycerol and scaled to decay from 1 to 0 is shown as *solid line*. These data are compared with the hole depths from the waiting time experiment $\Delta P_m(t_w)$ subsequent to pumping with one cycle, $N_\Omega = 1$. Also hole depths $\Delta P_m(t_p)$ with $t_p = 2\pi N_\Omega/\Omega$ recorded for variable N_Ω and for several Ω are included; t_p and t_w are simply denoted as "time" in this plot. This representation demonstrates that within experimental error the build-up $[\Delta P_m(t_p)]$ and the decay $[\Delta P_m(t_w)]$ of the spectral holes proceed on the same time scale which is somewhat longer than the α relaxation time. For these data we employed $U_S = 150$ V and $U_P = 1$ kV [87]

data shown in Fig. 14.15 [87]. The time variable appearing on the abscissa of this plot is to be understood either as the total pumping time $t_p = 2\pi N_\Omega/\Omega$ (corresponding to the build-up experiment), or as the waiting time t_w (for the recovery experiment), or simply as the running time (when referring to the step response). All data are scaled so that they represent a decay from 1 to 0. One clearly recognizes that the results for build-up and refilling coincide within (the considerable) experimental error. They reflect a dynamical process which is a factor of about 1.4 slower than the step response. Note that this result which is based on analyzing ΔP_m is slightly different from that obtained by evaluating $\Delta_m(t)$ [16]. In both cases, however, we may conclude that recovery and equilibrium response occur practically on quite similar time scales.

While the results described in the foregoing refer to the primary or α-relaxation, it is of course also of interest to check what the nature of the response of secondary processes is. About 30 years ago Johari and Goldstein [88] found a relaxation in the glassy state which today is often called the slow β-process. These processes are typically characterized by symmetrically broadened dielectric loss spectra that exhibit strongly temperature dependent widths. The dynamic heterogeneity in these degrees of freedom was confirmed by deuteron NMR [89]. Furthermore, using solvation spectroscopy the β-relaxation (of glassy D-sorbitol) was reported to be spatially uniform in the sense that no signs of "islands of mobility" could be detected [90]. The latter optical technique relies on the optical switching of the dipole moment of dye tracers. It may therefore be viewed as a local dielectric experiment which bears some resemblance to the electrical field relaxation experiment, i.e., the modulus technique [72].

Recently an NHB experiment was conducted for glassy D-sorbitol (T_g = 268 K) [91] with detection proceeding under constant charge conditions. This glass-former previously was studied not only for its relatively strong β-process [92] but also for its interesting aging kinetics [93]. The NHB investigation was conducted at a temperature of 204 K. Here the loss spectrum is centered at roughly 10^2 Hz and is about six decades wide. The results presented in [91] nicely demonstrate the dynamic heterogeneity of the β-process of this molecular glass-former and provide evidence for a pronounced spectral selectivity. The latter led to a shift in the hole positions that can be expressed as $t_m = 0.25 \, \Omega^{-\alpha}$ with $\alpha = 1$. Here the factor of 0.25 was ascribed to the fact that in these experiments the usual electrical field pump was used in conjunction with a detection under constant charge conditions. This fact has also to be taken into account in the interpretation of the recovery experiments presented in [91]. Recently, binary glass-formers composed of α-methyl-pyridine and polystyrene were investigated using NHB for various compositions [94]. In each case evidence for dynamic heterogeneity was found.

Cyclo-octanol belongs to the class of supercooled plastic crystals which bear a number of similarities to glass-forming liquids [95–97], except that they often exhibit a highly symmetrical center of mass lattice. In recent years the dielectric properties of cyclo-octanol were extensively studied using broadband dielectric spectroscopy [98, 99]. Near the freezing temperature defined by $\tau \approx 100$ s (for simplicity also called T_g; T_g = 168 K) the dielectric loss spectra of cyclo-octanol are about 1.5 decades wide ($\beta = 0.74$) and ε_m'' is around 10 [98].

NHB experiments were carried out on cyclo-octanol several degree above T_g. Some raw data are shown in Fig. 14.8. An analysis of the step response functions show that here the mean dipolar relaxation time is 0.13 s [73]. For this crystalline material the spectral selectivity, hence dynamic heterogeneity of the dipolar relaxation, as well as the E_p^2 dependence of the NHB effect were confirmed. In Fig. 14.16 we present some results from the hole refilling after pumping at 0.3 Hz. From these data it may be inferred that the recovery proceeds on about the same time scale as the dipolar step response, similar to what has been found for the supercooled liquids.

14.4.2
Ion Conducting Glasses

Also for ion conductors nonexponential relaxation phenomena are well known. A number of techniques are available for studying the electric relaxation associated with the migration of charge carriers. The measurements can be presented in various formats, e.g., as the frequency dependent complex conductivity, resistivity, or dielectric function, but also in the time domain as the (dis-)charging current or as the electrical modulus. Each specific representation emphasizes or suppresses certain aspects of the experimental results and there is an ongoing debate as to what is the most appropriate representation of electrical relaxation data [100]. However, there is also the more fundamental question concerning the proper theoretical description of ion transport [101]. When dealing with glassy

Fig. 14.16. Comparison of polarization response $P(t)/P(0)$ (*dots*) and hole refilling $\Delta P_m(t_w)/\Delta P_m(0)$ (*diamonds*) after pumping at 0.3 Hz. The *dotted line* represents an exponential fit. In the *inset* we show the spectral holes (in arbitrary units) at two different waiting times recorded using $U_S = 30$ V and $U_P = 300$ V. The *solid line* is drawn to guide the eye. Reproduced from [73]
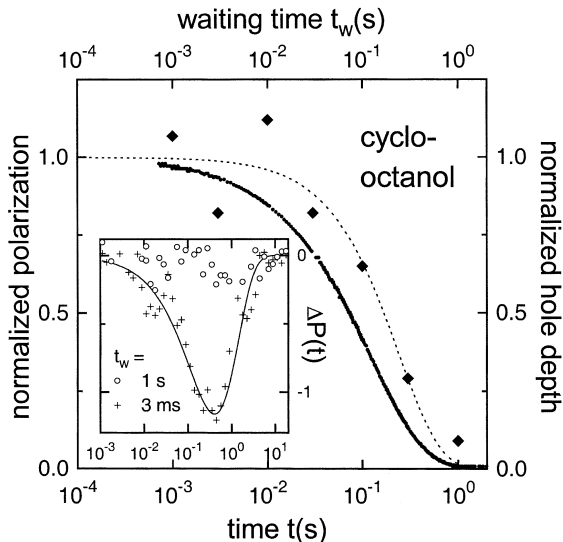
ionic conductors it is easy to imagine that the conductivity pathway is affected by the structural disorder of the vitreous matrix. On the other hand, depending, e.g., on the ion concentration Coulomb interactions among the mobile ions may or may not lead to an effective averaging over these structural inhomogeneities.

On the basis of a kinetic model it has been argued that such an averaging should be most pronounced in solid electrolytes for which there is a substantial decoupling of the electrical from the structural degrees of freedom [102]. While many fast ionic conductors are strongly decoupled [103], there is also a (small) number of solid electrolytes which exhibit less pronounced decoupling. Among the latter is the binary salt $2\,Ca(NO_3)_2 \cdot 3\,KNO_3$ (CKN) which has been thoroughly studied using impedance spectroscopy [104–106] and other techniques. Interestingly, in the vicinity of the glass transition ($T_g = 333$ K) of CKN it is possible to probe the structural relaxation via measurements of the d.c. conductivity [107].

According to the predictions put forward by Moynihan [102] more strongly coupled systems should be characterized by a more heterogeneous ion dynamics. The structural heterogeneity specifically of CKN [108] was already addressed using NMR in the liquid [109] as well as deep in the glassy states [110]. The electrical degrees of freedom can very effectively be probed by an experiment such as NHB. One should realize, however, that in this case the response functions reflect translational motions, while above we have primarily addressed reorientational ones. As mentioned in Sect. 14.3, above, this calls for a detection scheme which avoids excessive accumulation of charges near one of the sample electrodes.

In Fig. 14.17a we plot the so-called electric modulus $M(t)$, i.e., the electrical field relaxation of CKN as detected under constant charge conditions [76]. These experiments were carried out about 33 K below T_g implying that the ionic mo-

Fig. 14.17. a Time dependent field relaxation of CKN. The *line* represents a Kohlrausch fit with $\tau = 1.89$ s and $\beta = 0.79$. **b,c** The NHB signals are presented for $\Omega > \Omega_C$ and $\Omega < \Omega_C$, respectively. The *solid lines* in (c) correspond to homogeneous modifications ΔM_{hom}. Adapted from [76]
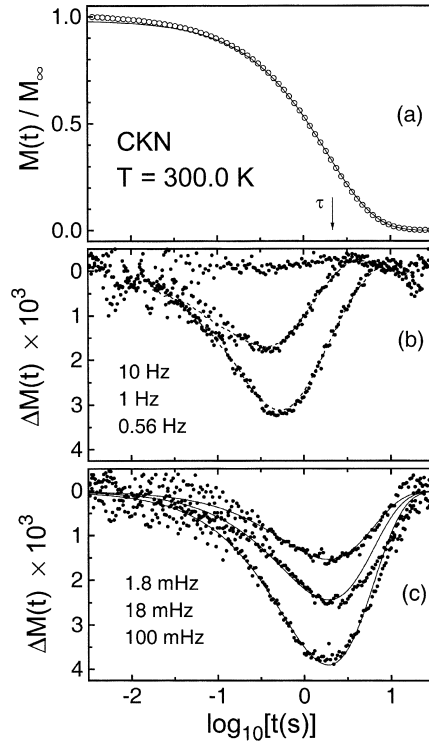
tions take place in an essentially rigid vitreous host. NHB signals recorded at 300 K are plotted for large pump frequencies in Fig. 14.17b and in Fig. 14.17c for relatively small ones. It is clearly recognized that the behavior in these two regimes is qualitatively different. When probing on a short time scale, $\Omega < \Omega_C$, (Fig. 14.17b) frequency selectivity is found, i.e., the maximum modifications shift with Ω. This is the hallmark of heterogeneous response. However, for low burn frequencies, $\Omega < \Omega_C$, the maximum modification appears always on the same time scale, irrespective of Ω. From the plot of the times of maximum modification, t_m, vs Ω, as shown in Fig. 14.18a, the crossover frequency Ω_C can easily be determined. Furthermore for $\Omega < \Omega_C$ it is seen that the maximum modifications always occur near $t_m = \tau$.

This latter behavior can be understood if one assumes that when probed on long time scales electrical relaxation is dynamically *homo*geneous. As mentioned above this scenario is associated with a uniform shift of the response function along the logarithmic time axis. For small shifts the shape of the corresponding NHB signal ΔM_{hom} is thus nothing else than the derivative $\Delta M_{hom}(t) = \Delta \ln(\tau/s)\partial[M(t)/M_\infty]/\partial\ln(t/s)$. If one assumes that $M(t)M_\infty = \exp[-(t/\tau)^\beta]$ then $|\Delta M_{\mathrm{hom}}(t)| = [(\beta B \Delta T/T^2) \times (t/\tau)^\beta \times M(t)/M_\infty]$ is maximum for $t = \tau$. Here we have again used Eq. (14.33) which thus allows one to associate the shift on the logarithmic time scale with a fictive or effective temperature change. With

Fig. 14.18. a The *open circles* show the frequency dependent resistivity of CKN measured at $T = 300$ K [72]. The *other symbols* reflect the times, t_m, of maximum modification as a function of Ω for pump fields ranging from 4.0 to 9.6 kV·mm^{-1}. The *dashed line* represents the relation $t_m \sim \Omega^{-\alpha}$ with $\alpha = 0.5$. The *horizontal line* corresponds to $t_m = \tau$. **b** *Symbols* correspond to hole depths ΔM_m as a function of Ω. The *curve* represents the dispersive component of the dielectric loss. On its high frequency wing it shows good agreement with the Ω dependence of ΔM_m. Adapted from [76]
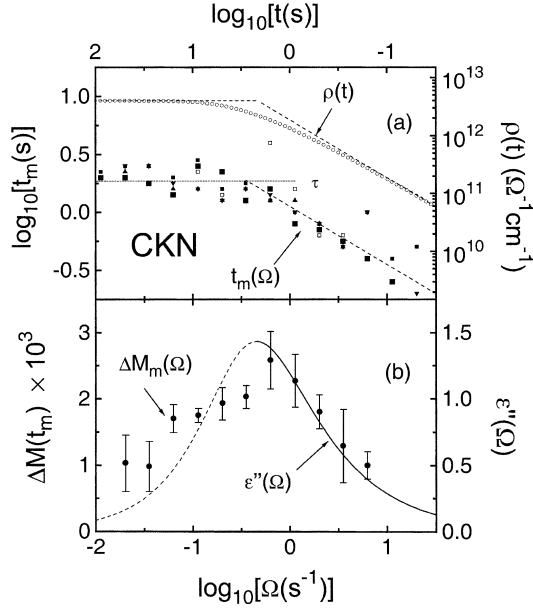
$B = 4980$ K, $T = 300$ K, ($\tau = 1.89$ s), and $\beta = 0.79$ fictive temperature changes of up to about 0.25 K can be inferred from the data presented in Fig. 14.17c. As Fig. 14.18b shows, ΔT_f (i.e., ΔM_m) depends on the pump frequency, however, in a manner which for $\Omega < \Omega_C$ is currently not fully understood. In the heterogeneous regime, $\Omega > \Omega_C$, the magnitude of the hole burning effects is proportional to the dielectric loss of CKN as one may have expected.

In order to understand better why at low pump frequencies evidence for homogeneous electrical relaxation is observed, it is instructive to compare the NHB data with results from the electrical resistivity, $\rho(t) = \varepsilon_0^{-1} \int_0^t M(t')\mathrm{d}t'$ of CKN. From Fig. 14.18a one recognizes that the crossover from d.c. to a.c. resistivity, i.e., from dispersive to steady state ionic transport occurs right at the crossover frequency Ω_C. This coincidence can be interpreted as follows. When addressing short time scales (via high pump frequencies) dynamic heterogeneity is observed in accord with the expectations formulated in [102]. However, when viewed at longer time scales the ions can visit a representative set of sites along their conductivity pathway and thus effectively perform a spatial averaging. In other words, under these circumstances the dynamics looks homogeneous. Such a scenario is consistent with models of hopping conductivity [101].

The question regarding the number of sites required to be visited by ions before homogenization is attained, i.e., the issue of a characteristic length scale is very interesting. It has been addressed using conductivity measurements in the linear [111] as well as in the non-linear regime [112–114]. Another possibility would be to count the number of jumps that can occur on the time scale set by $1/\Omega_C$. This requires to measure directly the time scale associated with single

ion jumps. In principle this is possible using recently developed NMR methods [115, 116].

14.4.3
Crystals with Frozen-In Disorder

There is a wide variety of dielectric crystals which are orientationally disordered down to the lowest temperatures. As one example in Sect. 14.4.1 we have discussed cyclo-octanol which exhibits self-induced order, only. Then there is the family of orientational glasses [96, 117]. Here anisotropic interactions together with the presence of static random fields originating from local concentration fluctuations lead to frustration effects. Depending on the degree of disorder and on the strength of the interactions between the orientable moieties these substances may also exhibit relaxor behavior [118–120]. Relaxors are materials characterized by nanoscopic domains which presumably are distributed in size. Each internally ordered domain is thought to be subjected to strong random fields, so that relatively well defined domain walls exist. In some of these materials, called quantum paraelectrics, quantum mechanical tunneling may counteract the disorder, at least at very low temperatures [121].

The relaxor ferroelectrics involve highly polar nano-domains and due to the resulting large dielectric constants and piezoelectric coefficients they have found numerous technical applications [122, 123]. The mechanism governing the dynamics of this materials is, however, only incompletely understood, so far. One of the problems one encounters here is the strong disorder which can lead to an extremely broad dielectric response. A typical example is $PbMg_{1/3}Nb_{2/3}O_3$ (PMN) which crystallizes in the perovskite structure. For NHB studies PMN ceramics doped with 10% $PbTiO_3$ (90PMN-10PT) were used [70]. In Fig. 14.19 we show that the step response of this material exhibits an almost logarithmic time dependence. This is characteristic for a practically constant dielectric loss in the dynamic range covered by these experiments. Consequently using pulsed dielectric spectroscopy an exceedingly slow approach of equilibrium showed up for 90PMN-10PT [124].

Some results from spectral hole burning are also included in Fig. 14.19. When varying the pump frequency from 0.1 to 10 Hz it is seen that the maximum modification shifts by two decades as well. The position of the maximum modification occurs at $t_m = \Omega^{-1}$ as indicated by the arrows in Fig. 14.19. Thus we are able to address those contributions to the dielectric response which are characterized by an intrinsic response time of about $\tau_\Omega = \Omega^{-1}$. This finding confirms dynamic heterogeneity for 90PMN-10PT as expected on the basis of the strong static random fields present in this material. The experiments presented in Fig. 14.19 were conducted in a regime for which the response is proportional to E_S and to E_P^2. Corresponding results were given in [124]. Here we only show that the peak positions, t_m, do not depend on the employed voltages if they are confined to the specified regime (cf. Fig. 14.20). For 90PMN-10PT the relationship $t_m = \Omega^{-1}$ with $\alpha = 1$ is nicely obeyed in an Ω range of more than three decades. Interestingly, also for the dilute quantum paraelectric $Sr_{0.998}Ca_{0.002}TiO_2$ dynamic

Fig. 14.19. Step response function $P(t)$ (*solid line*) and modified response functions $P^*(t)$ (*symbols*) measured for 90PMN-10PT with U_S = 2.5 V and U_P = 25 V. The time scales associated with the pump frequencies of 10 Hz and 0.1 Hz are marked by the *arrows*. Adapted from [70]
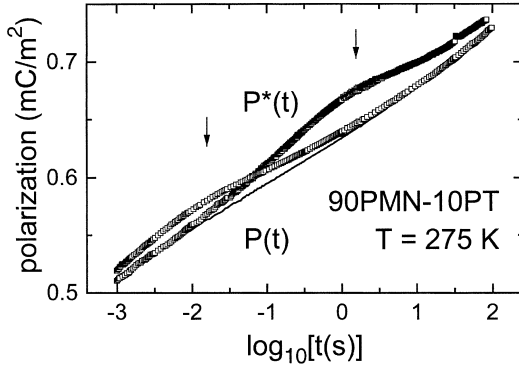
Fig. 14.20. The times of maximum modification, t_m, for various pump frequencies Ω. The pump (and probe) voltages are indicated. The *lines* represent the relation $t_m \sim \Omega^{-\alpha}$ with α = 1 for 90PMN-10PT [70] and α = 0.5 for PLZT 9/65/35 [126]
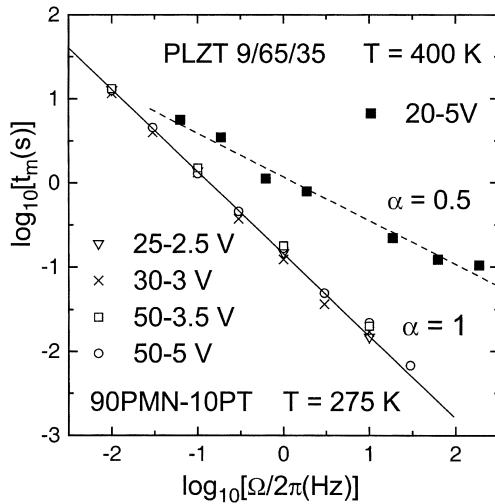
heterogeneity could be confirmed at liquid helium temperatures and the spectral holes were reported to shift by about one decade when changing the pump frequency by a factor of ten [125]. Results on yet another relaxor ferroelectric, PLZT 9/65/35, are included in Fig. 14.20. While frequency selectivity is also found here, it is clearly seen that the exponent α is not universal for relaxor ferroelectrics [126].

It has also been demonstrated that it is possible to pump at two different frequencies Ω_1 and Ω_2 simultaneously [70]. The experiments were performed by first subjecting the sample to a one-cycle pump at $\Omega_1 < \Omega_2$ followed by another cycle at Ω_2. The pump period was designed such that both cycles involved the same maximum amplitude and they were terminated at the same time. The measurements are shown in Fig. 14.21, cf. the lowest curve which corresponds to a very short waiting time, $t_w \approx 1$ ms, between pump and probe. The structure of these data clearly reflects the ratio $\Omega_2/\Omega_1 = 10^3$ chosen for these experiments.
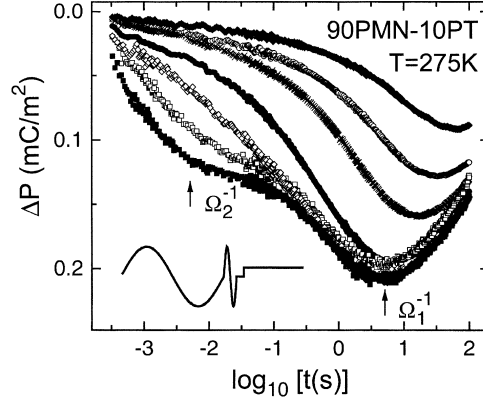
Figure 14.21 also contains data recorded at longer waiting times up to $t_w = $
30 s. One recognizes that the high-frequency hole refills first and only then the
modification induced at lower frequencies starts to recover. When plotted
against the waiting time the maximum modifications $\Delta P_m \equiv \Delta P(t_m)$ reveal a
characteristic re-equilibration time scale τ_{req}. In Fig. 14.22 data recorded for a
wide range of pump frequencies are displayed as a function of the scaled wait-
ing time $t_w\Omega$. It is seen that in such a representation all data superimpose within
experimental error. Thus, for the re-equilibration time one has $\tau_{req} \sim \Omega^{-1}$ as,
more qualitatively, already inferred from Fig. 14.21. The recovery data $\Delta P_m(t_w)$
can be parameterized using $\exp[-(t_w/\tau_{req})^\beta]$ with an exponent $\beta = 0.36$ and a
mean re-equilibration time scale of $\langle\tau_{req}\rangle = 44\, t_\Omega$.

The latter result implies that the time scale for dipolar relaxation and that for
hole refilling are vastly different. This has been taken as evidence for the exis-
tence of a long-lived heterogeneity in 90PMN-10PT and strongly suggests that
that two different relaxation mechanisms are active in this material [70]. Before
providing a somewhat more detailed interpretation, it is helpful to outline some
factors on which the separation of time scale, $\langle\tau_{req}\rangle/\tau_\Omega$, can depend. In Fig. 14.23
we show $\langle\tau_{req}\rangle/\tau_\Omega$ as a function of temperature. It is obvious that $\langle\tau_{req}\rangle/\tau_\Omega$ be-
comes significantly smaller for higher temperatures. However, also for decreas-
ing pump field amplitudes $\langle\tau_{req}\rangle/\tau_\Omega$ decreases and in the limit of small E_P^2 ap-
proaches unity.

These findings can be rationalized by assuming that the application of larger
and larger pump fields leads to an increasingly more effective depinning of do-
main walls. Hence, only at the largest pump fields can sizable pinning barriers
be surmounted. During the waiting time, i.e., in the absence of an external elec-
tric field the return to the equilibrium domain wall distribution is slowed down
more, if larger energy barriers have to be traversed back. Such a picture also ren-
ders the decrease of $\langle\tau_{req}\rangle/\tau_\Omega$ with temperature plausible not only because of the
concomitant increase in thermal energy, but also because the pinning energies
decrease. The latter may be inferred from the decrease of the coercive field with
increasing temperatures that is usually observed, also for relaxor ferroelectrics.

Fig. 14.22. Waiting time dependence of the normalized hole depths $\Delta P_m(t_w)/\Delta P_m(0)$ vs the scaling variable $t_w\Omega$. The *solid line* represents a Kohlrausch fit with the specified parameters. Results from double-hole experiments [with frequency separations $\log_{10}(\Omega_2/\Omega_1)$ given in *brackets*] and from an analysis of the hole refilling in the $\Delta(t)$ representation are also included (*crosses*). Adapted from [70]
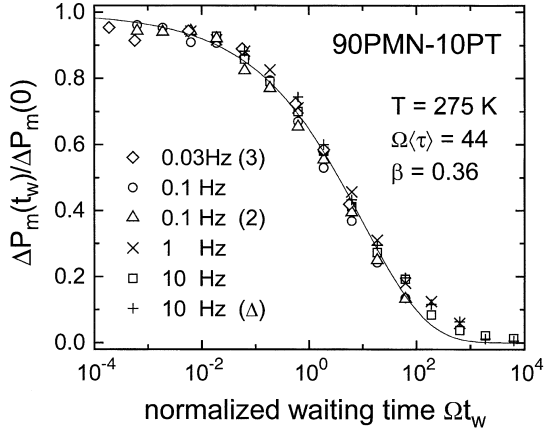
Fig. 14.23. Separation of time scales, $\langle\tau_{req}\rangle/\tau_\Omega$ obtained from master plots such as shown in Fig. 14.22. The temperature dependent data were acquired at a field of 38.5 V mm^{-1}. The *inset* shows the quadratic dependence on the pump field amplitude at 275 K. *Lines* are drawn to guide the eye. Adapted from [124]
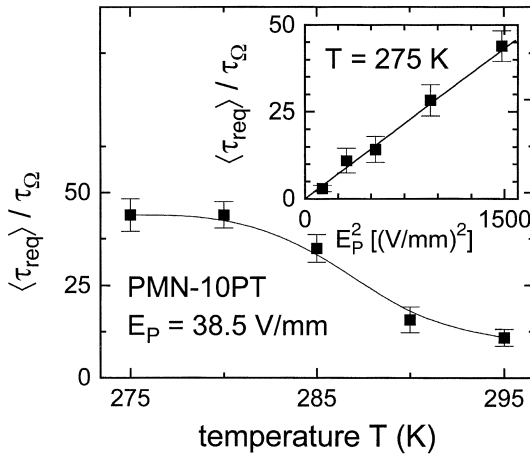
It should be noted that the above picture also means that a strict dependence $\Delta\Phi \sim E_P^2$ does not hold in this regime. A similar situation is encountered in a domain theory for spin-glasses [127]. There the response is cubic in the field but an additional non-linearity enters via the field dependence of the relaxation times. Finally we point out that additional non-linearities were also suggested as a source of the relatively broad spectral holes that show up in crystals with frozen-in disorder [69].

14.5
Related Experimental Methods

Most closely related to nonresonant dielectric spectral hole burning is the magnetic variant of this experiment which has been applied to a single-crystal whisker of iron [19] and to the spin-glass Au:Fe [68]. The experimental procedure used in the latter case is slightly different to the ones described above. At constant mag-

netic field H the sample is cooled through its spin-glass transition ($T_g = 21.6$ K) to the temperature at which the experiments are conducted. Then the pump field of amplitude H_0 is superposed onto H and detection is performed using a time domain SQUID magnetometer in zero field. Furthermore, prior to each scan of a phase cycle the sample is heated to above T_g. The spin-glass study revealed evidence for dynamic heterogeneity and a recovery which in our terms could be described by $\exp[-(t_w/\tau_{\mathrm{req}})^\beta]$ with $\beta = 0.6$ and $\langle\tau_{\mathrm{req}}\rangle = 12\,\tau_\Omega$. In this context it may be interesting to note that the widths of the spectral holes are significantly broader than those seen for the supercooled liquids (see Fig. 14.12). However, they are narrower than those reported for 90PMN-10PT (cf. Figs. 14.19 and 14.21).

A particularly interesting result was obtained for the spin-glass Au:Fe by carrying out the magnetic spectral hole burning experiments very close to (but below) T_g [68]. As Fig. 14.24 shows for small pump fields and consequently for small changes in effective temperature, spectral holes emerge which are characterized by the usual quadratic pump field dependence. However, above a certain threshold it has been reported that most of the sample remains a spin glass, while some of the slow response is no longer seen in the (very wide) experimental time window: These contributions were obviously pumped to above T_g. Their relaxation time is by orders of magnitude faster than at the base temperature. Remarkably, their recovery behavior was also found to be very different from what we have described above. With a pump frequency of 0.1 Hz selective local "heating" was achieved that persisted for several minutes [68].
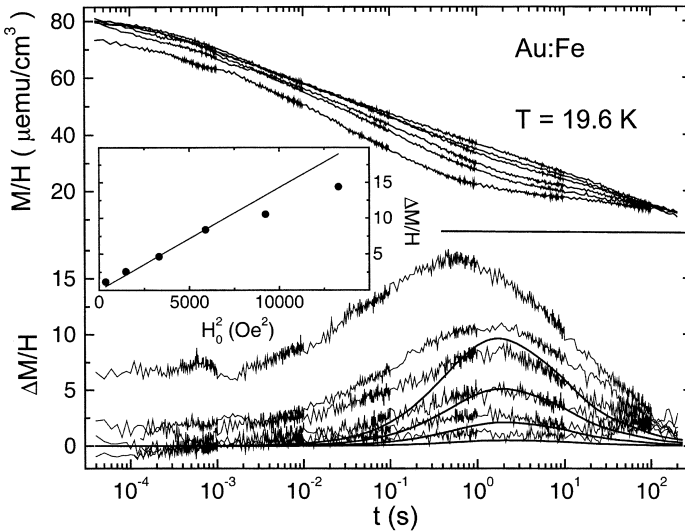
Fig. 14.24. Magnetic relaxation (*upper frame*) and difference spectra (*lower frame*) recorded for Au:Fe at a base temperature of 19.6 K and various pump fields. The *inset* demonstrates that the hole depths increase quadratically for moderately large pump fields. For the largest pump amplitude an offset at short time reveals that some of the response has been "pushed" outside the experimental time window. The *lines* are calculated using the model defined by Eq. (14.35). Adapted from [68] and reproduced by permission

One of the main characteristics of NHB is spectral selectivity and this feature is shared by several other experimental techniques such as multidimensional NMR [12, 37] and optical deep bleaching [14]. However, there are several distinctive features of NHB. Both other methods involve a low-pass (or high-pass) selection scheme. Although band-pass selection, required for highest spectral selectivity, should also be possible using NMR [128], to our knowledge it has not been implemented, so far. With NHB, on the other hand, it was demonstrated experimentally and theoretically (cf. Fig. 14.5) that a relatively narrow spectral range is addressed. Another advantage of NHB is that it does not require to admix probe molecules that allow for a coupling to an external perturbation with which the spectral selection is achieved.

In the NHB studies discussed above the perturbation induced by the pump process is usually kept so small that one operates in the weakly non-linear regime. For supercooled liquids we have previously emphasized that this corresponds to working in the domain of *linear structural* response [31]. When using very large external perturbations one can, however, drive the system out of equilibrium. This so-called aging regime [129] is characterized by a breakdown of the fluctuation-dissipation-theorem already for linearly responding materials [130]. Non-equilibrium or aging phenomena in relation with driving systems non-linearly have been reported from mechanical spectroscopy [131–133] and recently from a computer simulation (cf. Fig. 14.7 in [74]). Under these circumstances one may rely on empirical constitutive equations in attempts to disentangle non-linear effects from non-equilibrium ones [134].

It is important *not* to confuse non-equilibrium results with those obtained from NHB. This note of caution is very important since several viscoelastic studies on polymers revealed that strongly non-linear mechanical perturbations can lead to a seeming acceleration of response ("rejuvenation") which tends to diminish upon increasing the time interval between the application of a large strain (or stress) and a small "tickle" deformation ("fading memory") [131–133]. At first glance, both effects, "rejuvenation" and "fading memory", look somewhat similar to the speed-up seen in modified NHB responses (Figs. 14.6 and 14.12) and to hole filling, respectively. However, the pronounced decrease of the relaxation strengths showing up in the modified (or incremental [131, 133]) viscoelastic responses is just one observation which is quite different from the NHB signatures presented in previous sections.

Other distinctive features of NHB are that spectral hole burning does not require one to invoke non-equilibrium effects or empirical constitutive equations (see, e.g., Sect. 14.2.3.1). Furthermore, when performing mechanical NHB experiments it will be essential to check whether one operates in the quadratic pump and the linear probe regimes, and to ensure that the results do not depend on the time delay between subsequent scans within a phase cycle. Since the cited viscoelastic studies were carried out prior to the development of NHB it is not surprising that none of these features were tested. Furthermore, the large pulse strains applied in the quoted mechanical spectroscopy studies are not associated with a peaked excitation profile. This may be just one of the reasons why in these investigations no signs of frequency selectivity are apparent.

Apart from spectral selectivity NHB, mainly via its phase cycle, additionally features the ability to generate symmetric orientational dipole distributions. To appreciate this point more fully it should be realized that for overall isotropic equilibrium systems conventional (also non-linear) spectroscopy only allows one to generate dipolar distribution functions which can be expanded in terms of $P_l(\cos\theta)$ with odd l. With NHB, on the other hand, distributions characterized by even l (> 0) can be achieved. In the weak non-linear limit in which most previous experiments were carried out, the term with $P_2(\cos\theta)$ should be most prominent. While this appears as a peculiarity in the framework of (non-linear) dielectric spectroscopy, the generation of symmetrical orientational distribution is well known for many optical techniques. Here we may think of photobleaching [39, 135–138] and Kerr effect methods [40, 50, 139, 140]. Those optical methods are to be distinguished from NHB since they lack spectral selectivity. One of the reasons for this difference is due to the fact that these latter optical methods, like, e.g., neutron scattering [141], rely on the detection of two-point response or correlation functions.

14.6
Conclusions

Nonresonant spectral hole burning is a powerful dielectric technique which already has yielded valuable insights into the dynamics of a diverse variety of disordered materials. In this review we have presented results obtained for supercooled liquids and plastic crystals, for glassy ion conductors, and for relaxor-ferroelectrics as well as for spin-glasses. In most of the materials studied so far evidence for dynamically heterogeneous responses was obtained. Together with results from other dynamically selective techniques these studies have provided clues to resolve long standing issues concerning the nature of dielectric (or magnetic) relaxations.

We have also reviewed some theoretical concepts that are useful in order to describe NHB. While more general theoretical considerations have been presented elsewhere here we have focused on a relatively simple ADWP model which provides useful insights into the fundamentals of NHB. In particular, it helps one to gain a basic understanding of homogeneous types of relaxations and of spectral selectivity. The latter is also an important ingredient of the box model that we have discussed above. Clearly, further complex models for the weakly non-linear dielectric effects which play an important role in NHB spectroscopy need to be developed. One of the reasons being that several experimentally observed effects currently still require a phenomenological treatment. Here we mainly think of the extrinsic relaxation mechanisms that have been invoked to rationalize the recovery behavior in the relaxor materials.

It is also reassuring that experimental evidence for dynamically homogeneous relaxation could be achieved. This observation, made in the non-dispersive regime of glassy CKN, does not really come unexpected. However, so far it could not be achieved with any other technique. A particularly impressive piece of experimental evidence is provided by the "local heating" experiments performed on a magnetic spin glass.

Many further applications of NHB can be conceived. When suitably adapted to the degree of freedom that relaxes, this new method can be a useful tool for all kinds of materials characterized by non-exponential response functions. An obvious extension, that we have already mentioned above, would be into the field of mechanical spectroscopy. For materials in which, e.g., dielectric and mechanical degrees of freedom are coupled it should be possible to carry out cross-experiments which involve pumping on one channel and detecting on the other. Such NHB studies would allow one to find out just how well various degrees of freedom are coupled to one another.

Appendix 14.1

The solution of Eq. (14.22) as given by Eqs. (14.24), (14.27), and (14.28) is straightforward. However, since it is central to the theoretical development outlined in the present chapter, we nevertheless briefly recall the two-step strategy to solve this linear differential equation. With $a(t) \equiv -\tau^{-1}[1 + e(t)\delta]$ and $b(t) \equiv \tau^{-1}[e(t) + \delta] N$ it is seen that Eq. (14.22) is of the standard form

$$\dot{n}(t) = a(t)\, n(t) + b(t) \tag{A1.1}$$

The homogeneous part of this equation [i.e., with $b(t)$ set to zero], written as $\frac{dn}{n} = a(t)dt$, can immediately be integrated to yield the general solution (of the homogeneous part)

$$n(t) = n(t_0)\exp\int_{t_0}^{t} a(t')\,dt' \tag{A1.2}$$

In the second step one treats the constant $n(t_0)$ as a variable. With the replacement $n(t_0) \to c(t)$ the derivative of Eq. (A1.2) can be compared with Eq. (A1.1) to yield a differential equation for $c(t)$. By solving this equation in combination with Eq. (A1.2) one obtains the solution of the inhomogeneous equation as

$$n(t) = \exp\left[\int_{t_0}^{t} a(t')dt'\right]\left\{n(t_0) + \int_{t_0}^{t} dt'\, b(t')\exp\left[-\int_{t_0}^{t'} a(t'')\,dt''\right]\right\} \tag{A1.3}$$

To obtain closed analytical expressions one can expand the inner integrals in terms of the (pump) field amplitude $e_P(t)$ up to the quadratic order. Together

with the (convenient) condition $\int_0^{t_p} dt\, e_P(t) = 0$ (implying here $t_0 = 0$), the solution (Eq. A1.3) can be rearranged into the form given by Eqs. (14.27) and (14.28). Alternatively these equations can be obtained by solving the more general Eq. (14.21) and expanding the results for $n(t)$ up to the terms which are quadratic in $e(t)$.

In the linear response regime the general solution, in the presence of a constant field e_S, is obtained from Eq. (A1.3) by replacing $a(t) \to a \equiv -\tau^{-1}[1 + e_S\delta]$, $b(t) \to b \equiv \tau^{-1}[e_S + \delta]N$, and by expanding the field-dependent terms in linear order in e_S. This yields Eq. (14.24).

Appendix 14.2

In terms of response functions Eqs. (14.29) and (14.30) can be summarized for $t_w = 0$ as $\Phi^*(t) = \Phi(t) + \Delta\Phi(t)$ with $\Phi(t) = e^{-t/\tau}$ and $\Delta\Phi(t) = -X_n(\Omega)\frac{t}{\tau}\, e^{-t/\tau}$ with the normalized excitation profile $X_n(\Omega) = \zeta\delta^2 X(\Omega)/\chi_{\mathrm{DWP}}$. Thus the modified response is $\Delta\Phi^*(t) = e^{-t/\tau}[1 - X_n(\Omega)\frac{t}{\tau}]$. Recognizing that $X_n(\Omega) \ll 1$ one can interpret the expression in the square brackets as the first term in the expansion of an exponential function giving $\Delta\Phi^*(t) \approx \exp\{-[1 + X_n(\Omega)]\frac{t}{\tau}\} \equiv \exp(-t/\tau^*)$. The latter equation simply expresses the definition of a modified relaxation time $\tau^* = \tau/[1 + X_n(\Omega)] \approx \tau[1 - X_n(\Omega)]$. Hence the normalized change in relaxation time $(\tau^* - \tau)/\tau \equiv \Delta\tau/\tau = \Delta\ln(\tau/s)$ is $\Delta\ln(\tau/s) = -X_n(\Omega)$.

Via the Arrhenius expressions $\tau^* = \tau_0\exp(B^*/T)$ or $\tau^* = \tau_0\exp(B/T^*)$ the modified relaxation time may either be connected with a modified (lowered) barrier B^* or a modified *effective* (non-thermodynamic) temperature T^*. Both approaches can be interpreted to indicate that the occupation or Boltzmann factor of the ADWP has effectively been changed by the pump process. Assuming, e.g., that B remains invariant one has $T^* = T + X_n(\Omega)T^2/B$. This result can of course also be obtained by combining $\Delta\ln(\tau/s) = -X_n(\Omega)$ with Eq. (14.33) to yield a change in effective temperature $\Delta T_i = X_n(\Omega)T^2/B$.

Now the defining condition for $\Delta(t)$ is $\Phi^*(t^*) = \Phi(t)$ and it has to be solved for t^* or equivalently for $\Delta t \equiv t^* - t$. On the logarithmic scale this gives $\Delta t/t \approx \Delta\ln(t/s) \equiv \ln(10)\Delta(t)$, as desired, provided Δt is small. For a single ADWP the formulated condition leads to $\exp(-t^*/\tau^*) = \exp(-t/\tau)$ or $t^*/t = \tau^*/\tau$. Using the above result this directly yields $1 + \Delta t/t = 1 - X_n(\Omega)$ and hence $\Delta(t) = -X_n(\Omega)/\ln(10)$. This shows that $\Delta(t)$ is not explicitly time dependent if only a single relaxation time exists. In the presence of a distribution of relaxation times $g(\tau)$ it will, however, depend on time because $\Delta(t) = -[\int d\ln\tau\, e^{-t/\tau}X_n(\Omega\tau)g(\tau)]/[\ln(10)\int d\ln\tau\, e^{-t/\tau}g(\tau)]$, cf. Appendix B of [31]. Here we have explicitly written out that $X_n(\Omega\tau) \equiv X_n(\Omega)$ depends on the relaxation time as well.

Finally we note that the arguments presented here remain valid if $\Phi(t)$ is not given by the exponential $e^{-t/\tau}$ [51, 52].

List of Abbreviations and Symbols

$A(\tau)$	Amplitude function
B	Energy barrier
D_r	Rotational diffusion coefficient
$Y_{lm}(w)$	Spherical harmonic
E_P	Pump field
E_S	Probe field
$e(t)$	Normalized field
g_i	Weighting factor
$g(\tau)$	Distribution of relaxation times
$G_{ik}(t)$	Conditional probability
$G(w_i,t_i|w_k,t_k)$	Conditional probability
H	Magnetic field step
H_0	Magnetic pump field amplitude
H	Hamilton operator
L	Liouville operator
m	Fragility index
$M(p,q,t)$	Electric dipole moment
$M(t)$	Electric modulus
n	(Modified) population difference
n_{eq}	Equilibrium population difference
N_Ω	Number of pump cycles
N	Number of dipoles
p_i	(Modified) population of state i
$p(w,t)$	Probability to find w at time t
P_l	Legendre polynomial of rank l
p,q	Phase space coordinates
Q	Absorbed energy
s	Magnitude of non-linear effects
$S(t)$	Dynamic variable
t_p	Duration of pump cycle
t_w	Duration of waiting time
t	(Probe) time
T_g	Glass transition temperature
U_P	Pump voltage
U_S	Probe (or step) voltage
w	Orientation
W	Hopping rate
$X(\Omega)$	Excitation profile
α	Pump frequency exponent
β	Stretching exponent
δ	Normalized asymmetry
Δ	Asymmetry of ADWP
$\Delta(t)$	Horizontal spectral modification
ε	Dielectric function
ζ	Non-linear coefficient

θ	Polar angle
κ	Rate
μ	Dipole moment
ν_0	Attempt frequency
Π_{ij}	Transition rate
$\Pi(w_i \| w_j)$	Transition rate
$\rho(p,q,t)$	Phase space density
$\rho(t)$	Resistivity
τ	Relaxation time
τ^*	Modified relaxation time
τ_J	Jump angle correlation time
φ	Jump angle
Φ	Step response function
χ	Susceptibility
ω	Angular frequency
Ω	Pump frequency
ADWP	Asymmetric double well potential
NMR	Nuclear magnetic resonance
NHB	Nonresonant spectral hole burning
PDS	Pulsed dielectric spectroscopy

References

1. Lunkenheimer P, Schneider U, Brand R, Loidl A (2000) Contemp Phys 41:15 (see also Chaps. 2, 4, and 5)
2. Wagner KW (1913) Ann Phys (Leipzig) 40:817
3. Cole KS, Cole RH (1941) J Chem Phys 9:341
4. Böttcher CJF, Bordewijk P (1973) Theory of electric polarization, vol 2. Elsevier, Amsterdam
5. Kohlrausch R (1854) Pogg Ann Phys 91:179
6. Williams G, Cook M, Hains PJ (1972) J Chem Soc Faraday Trans II 68:1045
7. Ngai KL (1979) Comments Solid State Phys 9:127
8. Jonscher AK (1983) Dielectric relaxation in solids. Chelsea Dielectrics Press, London
9. Palmer G, Stein D, Abrahams E, Anderson PW (1984) Phys Rev Lett 53:958
10. Poole PH (1998) Curr Opin Solid State Mater Sci 3:391
11. Kob W (1999) J Phys Condensed Matter 11:R85
12. Schmidt-Rohr K, Spiess HW (1991) Phys Rev Lett 66:3020
13. Böhmer R, Hinze G, Diezemann G, Geil B, Sillescu H (1996) Europhys Lett 36:55
14. Cicerone MT, Ediger MD (1995) J Chem Phys 103:5684; Ediger MD (2000) Annu Rev Phys Chem 51:99
15. Richert R (1997) J Phys Chem B 101:6323 (see also Chap. 15)
16. Schiener B, Böhmer R, Loidl A, Chamberlin RV (1996) Science 274:752
17. Vidal Russell E, Israeloff NE, Walther LE, Alvarez Gomariz H (1998) Phys Rev Lett 81: 1461
18. Vidal Russell E, Israeloff NE (2000) Nature 408:695
19. Chamberlin RV (1998) Phase Trans 65:169
20. Chamberlin RV (2002) ACS Sym Ser 820:228
21. Bloembergen N, Purcell EM, Pound RV (1948) Phys Rev 73:679

22. Friedrich J, Haarer D (1984) Angew Chem 96:96 [Angew Chem Int Ed Engl 23:113]; Friedrich J, Haarer D (1988) In: Moerner WE (ed) Persistent spectral hole burning: science and applications. Springer, Berlin Heidelberg New York

23. Basché T, Moerner WE, Orrit M, Wild UP (eds) (1997) Single-molecule optical detection, imaging and spectroscopy. Wiley-VCH, Weinheim

24. Böhmer R, Chamberlin RV, Diezemann G, Geil B, Heuer A, Hinze G, Kuebler SC, Richert R, Schiener B, Sillescu H, Spiess HW, Tracht U, Wilhelm M (1998) J Non-Cryst Solids 235/237:1

25. Williams G (1978) Chem Soc Rev 7:89

26. For a definition of the Poisson bracket see, e.g., Chap. X of [4]

27. Rajagopal AK, Ngai KL, Rendell RW, Teitler S (1988) Physica 149A:358

28. Fournier J, Williams G (1996) J Chem Phys 104:5690 and references cited therein

29. Chamberlin RV (1993) Phys Rev B 48:15,638

30. Böhmer R, Schiener B, Hemberger J, Chamberlin RV (1995) Z Phys B Condensed Matter 99:91; Böhmer R, Schiener B, Hemberger J, Chamberlin RV (1996) Z Phys B Condensed Matter 99:624

31. Schiener B, Chamberlin RV, Diezemann G, Böhmer R (1997) J Chem Phys 107:7746

32. Cole RH (1981) In: Goodman CHL (ed) Inst Phys Conf Series 58:1

33. Madden PA, Kivelson D (1984) Adv Chem Phys 56:467

34. van Kampen NG (1981) Stochastic processes in physics and chemistry. North Holland Publishing Company, Amsterdam

35. Diezemann G, Sillescu H (1999) J Chem Phys 111:1126

36. Debye P (1929) Polare Molekeln. S. Hirzel, Leipzig, chap V

37. Böhmer R, Diezemann G, Hinze G, Rössler E (2001) Prog NMR Spectrosc 39:191 and references cited therein; Böhmer R, Kremer F (2002) Broadband dielectric spectroscopy. Springer, Berlin Heidelberg New York, chap 17

38. Rosato V, Williams G (1981) Faraday Trans II 77:1761

39. Kozak A, Williams G (1989) Mol Phys 67:1065

40. Beevers MS, Crossley J, Garrington DC, Williams G (1976) J Chem Soc Faraday II 72:1482

41. Anderson JE (1972) Faraday Symp Chem Soc 6:82

42. Fröhlich H (1949) Theory of dielectrics. Oxford University Press, New York

43. Note that ADWPs have also been used in the context of the frequency-dependent conductivity in glasses; see, e.g., Pollak M, Pike GE (1972) Phys Rev Lett 28:1449

44. Wagner A, Kliem H (1999) J Chem Phys 111:1043

45. Anderson JE, Ullman R (1967) J Chem Phys 47:2178

46. Stannarius R, Kremer F, Arndt M (1995) Phys Rev Lett 75:4698

47. Böttcher CJF (1973) Theory of electric polarization, vol 1. Elsevier, Amsterdam

48. Morita A (1986) Phys Rev A 34:1499

49. Alexiewicz W, Derdowska-Zimpel H (1995) Physica A 214:9

50. Déjardin JL, Debiais G (1995) Adv Chem Phys 91:241

51. Diezemann G (2001) Europhys Lett 53:604

52. Diezemann G (to be submitted) J Chem Phys

53. Kircher O, Chamberlin RV, Diezemann G, Böhmer R (2000) J Chem Phys 113:6449

54. Mills DL (1991) Nonlinear optics: basic concepts. Springer, Berlin Heidelberg New York

55. Glazounov AE, Tagantsev AK (2000) Phys Rev Lett 85:2192

56. Diezemann G, Sillescu H, Hinze G, Böhmer R (1998) Phys Rev E 57:4398

57. Sillescu H (1999) J Non-Cryst Solids 243:81

58. Chamberlin RV, Schiener B, Böhmer R (1997) Mat Res Soc Symp Proc 455:117

59. Rather than expressing the change in properties that depend on Boltzmann factors, $\exp(-B/k_BT)$, by modified (fictive, effective) temperatures T in some cases modified energy barriers B may be preferable

60. Baschnagel J, Binder K, Wittmann HP (1993) J Phys C 5:1597

61. Moynihan CT (1998) Solid State Ionics 105:175

62. Nieuwenhuizen TM (1998) Phys Rev Lett 80:5580

63. For a review, see Hodge IM (1994) J Non-Cryst Solids 169:211

64. Adam G, Gibbs JH (1965) J Chem Phys 28:373
65. Moynihan CT, Schroeder J (1993) J Non-Cryst Solids 160:52
66. Donth E (1982) J Non-Cryst Solids 53:325; Donth E (1999) Acta Polym 50:240
67. Chamberlin RV (1999) Phys Rev Lett 82:2520; see also Chamberlin RV (2000) Nature 408:337
68. Chamberlin RV (1999) Phys Rev Lett 83:5134
69. Chamberlin RV (private communication)
70. Kircher O, Schiener B, Böhmer R (1998) Phys Rev Lett 81:4520
71. Sawyer CB, Tower CH (1930) Phys Rev 35:269
72. Wagner H, Richert R (1999) J Appl Phys 85:1750
73. Kircher O, Wirsch C, Böhmer R (unpublished)
74. Cugliandolo LF, Iguain JL (2000) Phys Rev Lett 85:3448
75. Diezemann G, Böhmer R (2001) Phys Rev Lett; 87:129602
76. Richert R, Böhmer R (1999) Phys Rev Lett 83:4337
77. Böhmer R, Ngai KL, Angell CA, Plazek DJ (1993) J Chem Phys 99:4201
78. Hanaya M, Nakayama M, Hatate A, Oguni M (1995) Phys Rev B 52:3234 and references cited therein
79. Mizukami M, Fujimori H, Oguni M (1996) Solid State Commun 100:83
80. Wu L (1991) Phys Rev B 43:9906
81. Hemberger J, Böhmer R, Loidl A (1998) Phase Trans 65:233
82. Schiener B, Böhmer R (1995) J Non-Cryst Solids 182:180 and references cited therein
83. Angell CA, Boehm L, Oguni M, Smith DL (1993) J Mol Liq 56:275; Takahara S, Yamamuro O (1995) J Phys Chem 99:9589
84. Abramowitz M, Stegun IA (eds) (1972) Handbook of mathematical functions. Dover Publications, New York
85. Tracht U, Wilhelm M, Heuer A, Feng H, Schmidt-Rohr K, Spiess HW (1998) Phys Rev Lett 81:2727
86. From a mathematical viewpoint $\Delta(t)$ vanishes in the limits of times that are very much shorter or very much longer than the mean correlation time. With finite signal to noise ratios these time regimes are not expected to be accessible experimentally
87. Schiener B, Böhmer R (unpublished)
88. Johari GP, Goldstein M (1970) J Chem Phys 53:2372
89. Schnauss W, Fujara F, Hartmann K, Sillescu H (1990) Chem Phys Lett 166:381. For references to more recent work see Böhmer R, Hinze G, Jörg T, Qi F, Sillescu H (2000) J Phys Condensed Matter 12:A383
90. Wagner H, Richert R (1998) J Non-Cryst Solids 242:19
91. Richert R (2001) Europhys Lett 54:767
92. Wagner H, Richert R (1999) J Phys Chem B 103:4071
93. Olsen NB (1998) J Non-Cryst Solids 235/237:399
94. Blochowicz T, Rössler E (unpublished)
95. Angell CA, Dworkin A, Figuière P, Fuchs A, Szwarc H (1985) J Chim Phys 82:773
96. Loidl A, Böhmer R (1994) In: Richert R, Blumen A (eds) Disorder effects on relaxational processes. Springer, Berlin Heidelberg New York, p 659 and references cited therein
97. Jiménez-Ruiz M, González MA, Bermejo FJ, Miller MA, Birge NO, Cendoya I, Alegría A (1999) Phys Rev B 59:9155
98. Leslie-Pelecky DL, Birge NO (1994) Phys Rev B 50:13,250
99. Brand R, Lunkenheimer P, Loidl A (1997) Phys Rev B 56:R5713
100. Dyre JC (1988) J Appl Phys 64:2456; Proceedings of the International Conference on Structure and Dynamics of Ionic Glasses: Experiments, Models and Applications [(1998) Solid State Ionics 105].
101. Dyre JC, Schrøder TB (2000) Rev Mod Phys 72:873 and references cited therein
102. Moynihan CT (1998) J Non-Cryst Solids 235/237:781
103. Angell CA (1990) Chem Rev 90:523
104. Howell FS, Bose RA, Macedo PB, Moynihan CT (1974) J Phys Chem 78:631

105. Pimenov A, Lunkenheimer P, Rall H, Kohlhaas R, Loidl A, Böhmer R (1996) Phys Rev E 54:676
106. Lunkenheimer P, Pimenov A, Loidl A (1997) Phys Rev Lett 78:2995 and references cited therein
107. Pimenov A, Loidl A, Böhmer R (1997) J Non-Cryst Solids 212:89
108. Machavariani VS, Voronel A (2000) Phys Rev E 61:2121
109. Sen S, Stebbins JF (1997) Phys Rev Lett 78:3495
110. Zürn C, Titze A, Diezemann G, Böhmer R (1999) J Phys Chem B 103:4109
111. Roling B, Martiny C, Funke K (1999) J Non-Cryst Solids 249:201
112. Isard JO (1996) J Non-Cryst Solids 202:137
113. Barton JL (1996) J Non-Cryst Solids 203:280
114. Roling B (private communication)
115. Xu Z, Stebbins JF (1995) Science 270:1332
116. Böhmer R, Jörg T, Qi F, Titze A (2000) Chem Phys Lett 316:417
117. Höchli UT, Knorr K, Loidl A (1990) Adv Phys 39:405
118. Korner N, Pfammatter C, Kind R (1993) Phys Rev Lett 70:1283
119. Levstik A, Kutnjak Z, Filipic C, Pirc R (1998) Phys Rev B 57:11,204
120. Kutnjak Z, Filipic C, Pirc R, Levstik A, Farhi R, El Marssi M (1999) Phys Rev B 59:294
121. Kleemann W, Albertini A, Chamberlin RV, Bednorz JG (1997) Europhys Lett 37:145
122. Cross LE (1994) Ferroelectrics 151:305 and references cited therein
123. Uchino K (1994) In: Swain MV (ed) Materials science and technology, vol 11: structure and properties of ceramics. VCH, Weinheim, p 635
124. Kircher O, Diezemann G, Böhmer R (2001) Phys Rev B 64:054,103
125. Kleemann W, Bobnar V, Dec J, Lehnen P, Pankrath R, Prosandeev SA (2001) Ferroelectrics 261:43
126. El Goresy T, Kircher O, Böhmer R (2002) Solid State Commun 121:485
127. Koper JM, Hilhorst HJ (1988) J Phys (France) 49:429
128. Tracht U, Heuer A, Spiess HW (1998) J Non-Cryst Solids 235/237:27
129. Struik LCE (1978) Physical ageing in amorphous polymers and other materials. Elsevier, Amsterdam
130. Grigera TS, Israeloff NE (1999) Phys Rev Lett 83:5038
131. McKenna GB, Zapas LJ (1986) Polym Eng Sci 26:725
132. Yee AF, Bankert RJ, Ngai KL, Rendell RW (1988) J Polym Sci Polym Phys Ed 26:2463
133. Waldron WK Jr, McKenna GB (1995) J Rheol 39:471
134. Larson RG (1988) Constitutive equations for polymer melts and solutions. Butterworth, Boston
135. Jones P, Darcy P, Attard GS, Jones WJ, Williams G (1989) Mol Phys 67:1053
136. Jones P, Jones WJ, Williams G (1990) J Chem Soc Faraday Trans 86:1013
137. Cicerone MT, Ediger MD (1993) J Phys Chem 97:10,489
138. Kanetakis J, Sillescu H (1996) Chem Phys Lett 252:127
139. Beevers MS, Elliott DA, Williams G (1980) J Chem Soc Faraday II 76:112
140. Torre R, Bartolini P, Pick RM (1998) Phys Rev E 57:1912
141. Arbe A, Colmenero J, Monkenbusch M, Richter D (1998) Phys Rev Lett 81:590

15 Local Dielectric Relaxation by Solvation Dynamics

R. Richert

15.1
Introduction

This chapter is concerned with a method of measuring dielectric relaxation phenomena locally, in order to complement the information regarding the dynamics of molecules inferred from the various macroscopic dielectric techniques outlined in previous chapters. In a simplified picture, these solvation dynamics experiments measure the dielectric relaxation of a liquid as a response to a step in the dielectric displacement of a molecule rather than the macroscopic effects following a field step applied to a capacitor. The time dependent dielectric polarization in the immediate vicinity of a probe molecule gives rise to a Stokes-shift of the luminescence. This tendency of the emission wavenumbers $\bar{v}$ to shift towards the red is monitored by recording the emission spectra $I(\bar{v})$ as a function of time using straightforward techniques of optical spectroscopy. The key quantity for assessing the dynamics of the liquid is the time dependent average emission energy $\langle \bar{v}(t) \rangle$ [1].

Although dielectric relaxation and solvation dynamics effects are highly related phenomena, there are differences in the experimental conditions under which the dielectric polarization is measured. Disregarding the more subtle features, the solvation energy is a measure of the local electric field relaxation at a constant dielectric displacement, and therefore better represented by the dielectric modulus $M(t)$ than by $\varepsilon(t)$. Because the spatial resolution inherent in this experimental approach is of the order of a few molecular diameters only, its application is advantageous wherever a spatial variation of dynamics or polarity is anticipated.

For many materials, the interactions between a guest molecule and its liquid host environment involve electrostatic forces. In the absence of ions it is mainly the dipole-dipole coupling which determines the energy required to remove entirely the guest or probe molecule from its solvent. In the case of dipolar systems, this free energy of solvation depends on the dipole moment of the solute and on that of the solvent constituents, where the latter is directly related to the dielectric constant ε of the liquid. The solvation free energy also depends on the mutual orientation of the dipoles, which gives rise to inhomogeneous broadening of the optical lines in disordered materials. A simple way of envisioning the solvated state is to consider the solvent dipoles being in equilibrium with the electric field which arises from the dipole moment of the guest molecule. In the pre-

sent context, the interesting aspect of dipolar solvation is the possibility of altering the solutes permanent dipole moment from the ground state to the excited state value, $\mu_G \rightarrow \mu_E$, by electronic excitation at $t = 0$. As a consequence, the solvent is suddenly removed from its equilibrium state because the local electric field has changed. This situation induces a dielectric relaxation process aimed at attaining equilibrium conditions with respect to the excited state of the solute. As with the macroscopic dielectric properties, the time scale of this relaxation is determined by the orientational correlation time in the system and hence often coupled to the viscosity [2].

Time resolved studies of dipolar solvation have initially been advanced using fluorescent probe molecules with typical excited state lifetimes τ_{fl} between 10^{-12} s and 10^{-9} s [3]. Due to signal intensity limitations, solvent dynamics are observable in a time range of approximately $10^{-2} \, \tau_{ex} \leq t \leq 10 \, \tau_{ex}$, where τ_{ex} is the lifetime of the excited state. Accordingly, fluorescence solvation dynamics studies are typically limited to liquids of low viscosity associated with orientational correlation times of ≈ 10 ns or faster [4]. In contrast, triplet state lifetimes τ_{ph} of phosphorescent chromophores are between 10^{-3} s and 1 s, such that analogous experiments focusing on the dynamics in the viscous regime of supercooled liquids near their glass transition temperature T_g have become available [5, 6].

The following sections are organized as follows: Section 15.2 describes the experimental approach to phosphorescence solvation dynamics including the requirements regarding probe molecules and properties of the liquids. In Sect. 15.3 the relevant optical transitions and their dependence on the dielectric properties of the liquid are outlined more quantitatively in order to clarify the relation between dielectric polarization and solvation coordinate. Finally, Sect. 15.4 is devoted to the experimental results by demonstrating the extent to which solvation data can be rationalized in terms of the liquids dielectric function $\varepsilon^*(\omega)$ and by discussing several applications which exploit the local nature of this technique.

15.2
Experimental Techniques

The perturbation of the system which initiates the solvation relaxation process is the electronic excitation of a probe molecule present at a low concentration in the liquid under study. In general, such an electronic transition is accompanied by a change in the permanent dipole moment from μ_G in the ground state to μ_E in the excited triplet state of the solute. Because the oscillator strength of the direct $S_0 \rightarrow T_1$ transition is practically zero, the first excited triplet state T_1 is populated via a singlet $S_0 \rightarrow S_1$ absorption followed by intersystem crossing. The sequence of transitions are schematically shown in the energy level diagram in Fig. 15.1. The time scale of this process is around 1 ns and can be considered instantaneous for what follows. An electronic transition is accompanied by a dipole moment change $\Delta\mu = \mu_E - \mu_G$ which initiates the solvation process. This process of the solvent approaching the equilibrium state with respect to the ex-
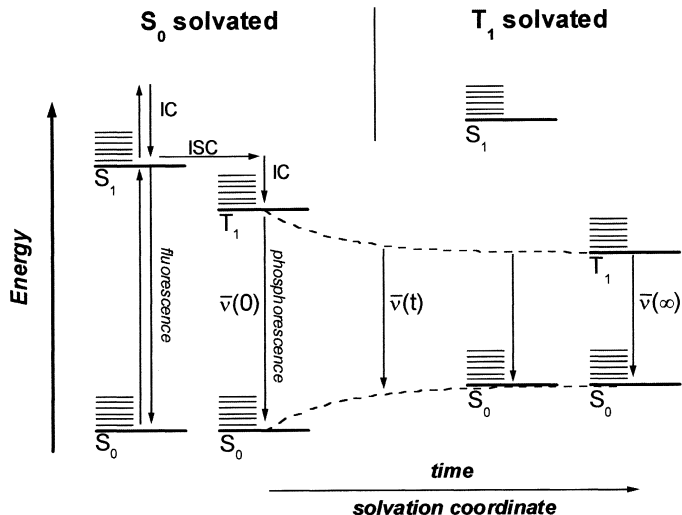
Fig. 15.1. Schematic energy level diagram for the electronic states S_0, S_1, and T_1 comparing the situations where the ground state S_0 is solvated (*left*) and where the excited state T_1 is solvated (*right*). The *dashed curves* indicate the gradual process along the solvation coordinate. The T_1 population proceeds via internal conversion (IC) and intersystem crossing (ISC). Reprinted with permission from The Journal of Chemical Physics, Copyright 2000, American Institute of Physics [50]

cited state of the solute lowers the energy level of the excited state T_1 and in parallel increases that of the ground state S_0, as indicated in Fig. 15.1. The aim of the experiment is to record this time dependent change in the $S_0 \leftarrow T_1$ emission energies along the solvation coordinate.

The requirement regarding the solvents usable for solvation studies is their transparency at the wavelength of the exciting light source and at the emission wavelength of the dye molecules. Appropriate probe molecules are those with a significant change $\Delta\mu$ in their permanent dipole moment upon electronic excitation. On the other hand, extreme values of $\Delta\mu$ often exhibited by charge-transfer states are likely to induce dielectric saturation in their immediate vicinity [7]. Rigid probe molecules are preferred in order to keep intramolecular structural relaxations from interfering with solvation processes. Since exciton migration is an effective route for lowering the average energy of the excited states, any donor-acceptor coupling has to be avoided in order to assure that only solvation processes are responsible for the red-shift. For this reason, the electronic energy levels of the solvent molecules should exceed those of the dye. Furthermore, the dye concentration should be sufficiently low such that energy transfer among the dye molecules remains negligible. Due to the short ranged exchange interaction of triplet excitations the allowable chromophore concentration can be as high as 10^{-4} mol mol^{-1}. Highly purified materials should be used for a phosphorescence solvation experiment, because impurity luminescence can easily interfere with the low level emission from the triplet state of the probe molecule.

The experimental methods used to study the dynamics of solvation consist of the basic techniques of time resolved optical emission spectroscopy. For phosphorescent chromophores one observes the $S_0 \leftarrow T_1$ (0 – 0) emission spectrum which is related to long excited state lifetimes τ_{ph}, typically between 1 ms and 1 s. In order to observe Stokes shift dynamics in such a time range, the solvent has to exhibit orientational relaxation processes which occur within the time window of the excited state lifetime. Therefore, most probe molecules will limit the observation of phosphorescence solvation dynamics to the viscous regime of glass-forming materials near their glass transition [8].

For observing dipolar solvation, the most appropriate phosphorescent dye molecules should exhibit both a high quantum yield and a significant change in their permanent dipole moment upon electronic excitation. The triplet solvation probes examined thus far are quinoxaline (QX, $\Delta\mu = 1.31$ D, $\tau_{ph} = 0.31$ s), quinoline (QI, $\Delta\mu \approx 0$, $\tau_{ph} = 1.11$ s), and naphthalene (NA, $\Delta\mu \approx 0$, $\tau_{ph} = 2.27$ s). For these molecules, the phosphorescence quantum yields are fairly high (≥ 0.5), but only QX is associated with a significant change $\Delta\mu$ for the $S_0 \rightarrow T_1$ transition.

The following experimental setup has been employed for the solvation results described further below. The sample cell is made of cooper or brass having a sapphire window which is vacuum sealed by a Kalrez O-ring. The cell is mounted to the cold stage of a closed cycle He refrigerator (Leybold, RDK 10–320, RW 2) and temperature stability within ± 30 mK can be achieved by a temperature controller (Lake Shore, LS 330) equipped with calibrated diode sensors. An excimer laser (Radiant Dyes, RD-EXC-100) operated at 308 nm with pulse width ≈ 25 ns and pulse energy 120 mJ serves as excitation light source. The repetition rate should not exceed values corresponding to ≈ $3\tau_{ph}$. The incident laser beam has to be attenuated sufficiently in order to avoid photoinduced degrading of the sample. The phosphorescence emission is coupled via fiber optics to a triple grating monochromator (EG&G, 1235) and registered by a micro-channel-plate (MCP) intensified diode array camera (EG&G, 1455B-700-HQ) with controller (EG&G, 1471A), gating options (EG&G, 1304), and synchronization facilities (SRS, DG-535). The spectra, consisting of 730 channels with a resolution of 0.04 nm/channel for the 1800 g mm^{-1} holographic grating, were wavelength calibrated with Xe and Kr calibration lamps. The time resolution is defined by gating the camera with gate widths between 100 ns and 10 ms. For the probe molecule QX the usable time range is limited to 10 μs $\leq t \leq 2$ s. An alternative technique to the time resolved detection outlined above is to scan the temperature for a fixed position of the detection time window. This allows for a faster overview of the solvation effects over a large temperature range, but without showing the details of the dynamics.

In the low temperature/high viscosity regime where phosphorescence solvation is applied, the vibrational bands are often well resolved and homogeneous contributions to the line broadening remain small. A representative set of $S_0 \leftarrow T_1$ (0 – 0) emission data for QX in 2-methyltetrahydrofuran (MTHF) is shown in Fig. 15.2 as a function of wavenumber $\bar{v}$ and time t. The decay of the overall intensity as time increases is due to the phosphorescence lifetime $\tau_{ph} = 0.31$ s of QX, whereas the gradual shift of the emission band towards lower energies indi-

Fig. 15.2. Altitude map of the $S_0 \leftarrow T_1 (0 - 0)$ emission intensity (in arbitrary units) on energy and evolution time in the ranges 20900 cm$^{-1} \leq \bar{v}$ $\leq$ 21900 cm^{-1} and $0 \leq t \leq 0.6$ s for QX in MTHF at $T = 93.9$ K. Also shown are the limiting values of the average emission energy, $\bar{v}(0)$ and $v(\infty)$, and the resulting $C(t)$ decay pattern. Reprinted with permission from The Journal of Chemical Physics, Copyright 2000, American Institute of Physics [50]
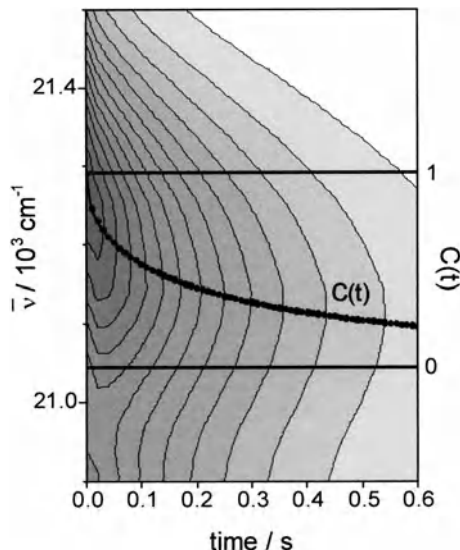
cates the solvation process. For inhomogeneously broadened lineshapes, Gaussian profiles are the rule, i.e., the intensity $I(\bar{v})$ follows

$$I(\bar{v}) = \frac{1}{\sigma\sqrt{2\pi}} \exp\left[-\frac{(\bar{v} - \langle\bar{v}\rangle)^2}{2\sigma^2}\right] \tag{15.1}$$

The line shape is thus characterized by the average energy $\langle\bar{v}\rangle$ and the Gaussian width σ. In a solvation dynamics experiment, $\langle\bar{v}\rangle$ is commonly observed to vary non-exponentially with time, such that a single $\langle\bar{v}(t)\rangle$ sweep is insufficient for unambiguously defining the limiting values attained at short and long times, $\langle\bar{v}(0)\rangle$ and $\langle\bar{v}(\infty)\rangle$. Their difference, $\Delta\bar{v} = \langle\bar{v}(0)\rangle - \langle\bar{v}(\infty)\rangle$, quantifies the energy change associated with the entire Stokes shift. The limiting values of $\langle\bar{v}(t)\rangle$ for $t \rightarrow 0$ and $t \rightarrow \infty$ are required for constructing the solvation time correlation function $C(t)$:

$$C(t) = \frac{\langle\bar{v}(t)\rangle - \langle\bar{v}(\infty)\rangle}{\langle\bar{v}(0)\rangle - \langle\bar{v}(\infty)\rangle} \tag{15.2}$$

which is the appropriate normalized decay function for focusing on the dynamical aspects of the solvation process, while disregarding the absolute energy scale. The relation between the resulting $C(t)$ curve and the original data set is represented graphically in Fig. 15.2. A typical set of $C(t)$ decays obtained for QX in the polar non-associating solvent MTHF is compiled in Fig. 15.3 as master plot $C(t)$ vs t/τ_{KWW}. These measurements cover the range 91 K $\leq T \leq$ 97 K or $T_g \leq T \leq T_g + 6$ K or 3×10^{-3} s $\leq \langle\tau\rangle \leq$ 54 s, in which $\beta_{KWW} = 0.5$ is temperature invariant.
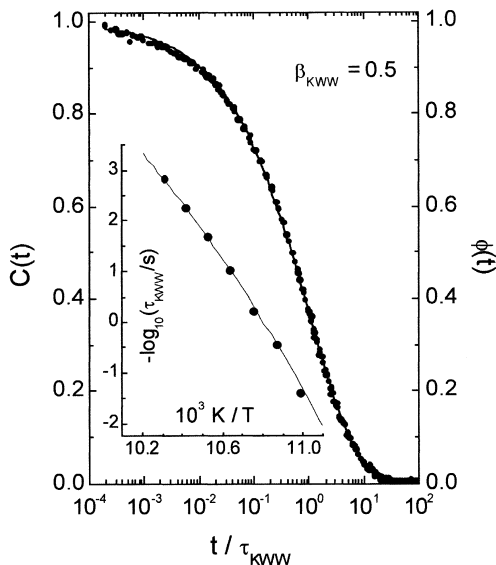
15.3
Dielectric Aspects of Solvation

The dipole moment change $\Delta\mu = \mu_E - \mu_G$ resulting from the excitation of the chromophore implies a change ΔE in the inhomogeneous electric field around the probe molecule. This process of locally perturbing the system thus corresponds to applying a field step to a capacitor in the classical time domain dielectric experiment [9]. In a given electronic state of a molecule, however, it is the charge distribution rather than the electric field which remains constant or polarization invariant. Additionally, the assumption of a homogeneous field as in the case of a macroscopic capacitor is certainly not appropriate for the field created by a molecular dipole.

The dielectric polarization process $P(t)$ depends on the experimental condition, e.g., the constant charge vs constant field case. While $P_D(t) \sim \varepsilon(t)$ holds for the constant field case with $E(t) = E_0$, the condition of a constant charge or of a polarization invariant dielectric displacement D leads to $P_E(t) \sim M(t)$, where $M(t)$ is the electric modulus. The special situation of a Debye type dielectric has been treated already by Fröhlich [10], with the result that an exponential constant field polarization $P_D(t) \sim \exp(-t/\tau_D)$ with dielectric time constant τ_D corresponds to a constant charge response $P_E(t) \sim \exp(-t/\tau_E)$ which is again exponential but with a time constant τ_E given by

$$\tau_E = \frac{\varepsilon_\infty}{\varepsilon_s}\tau_D \tag{15.3}$$

Due to the inequality $\varepsilon_s \geq \varepsilon_\infty$, the decay associated with the constant charge time constant τ_E is always faster than its constant field counterpart τ_D. In the context

of time dependent solvation effects, the time constant τ_E is often referred to as the longitudinal time τ_L. The above simple relation between τ_E and τ_D holds only for Debye type systems, characterized by a single exponential dielectric response. For the experimentally more relevant non-Debye systems associated with a distribution of relaxation times, the separation between the average longitudinal, $\langle \tau_E \rangle$, and average dielectric, $\langle \tau_D \rangle$, time scales becomes even more pronounced [9]. In a simple approximation, the time dependent changes in the average emission energy are governed by the electrostatic interaction energy of a permanent dipole μ with the local electric field, $W = - \boldsymbol{\mu} E_{\mathrm{loc}}(t)$. Therefore, this optical technique measures the electric field $E_{\mathrm{loc}}(t)$ or the electric modulus $M_{\mathrm{loc}}(t)$ ($\sim E_{\mathrm{loc}}(t)$ in the constant charge case) at the location of the probe molecule [9, 11].

It remains to establish a relation between the time dependent local field $E_{\mathrm{loc}}(t)$ and the macroscopic dielectric properties of the liquid, usually characterized by the frequency or time dependent dielectric function, $\varepsilon^*(\omega)$ or $\varepsilon(t)$, respectively. In a continuum approximation, one attempts to cast the entire behavior of the solvent into $\varepsilon^*(\omega)$, while disregarding the microscopic structure of the liquid. This is appropriate only when the constituents forming the dielectric body are much smaller than the length scales associated with the spatial inhomogeneities of the electric field. Consequently, the first solvent shell surrounding the probe molecule may be only poorly represented by the continuum model, although these nearest neighbors are dominant regarding the interaction energies [12].

The Mean Spherical Approximation (MSA) in its dynamic (d-MSA) version advanced by Rips et al. [11] is one of the theories which go beyond the continuum picture in order to predict the solvation on the basis of the dielectric function $\varepsilon^*(\omega)$. Although more sophisticated approaches to this problem have been worked out [7], we focus on the d-MSA because it yields the results in terms of closed analytic expressions while capturing the important deviations from the continuum model. It should be noted that the complex relaxation dynamics of liquids and supercooled liquids including the temperature dependence are not predicted by the d-MSA. These properties are an input to this electrostatic calculation in terms of $\varepsilon^*(\omega)$ in order to solve for the time dependent solvation free energies. The system considered is a solute represented by a point dipole of moment μ centered in a non-polarizable hard sphere of diameter D and solvent molecules represented by point dipoles centered in hard spheres of diameter d. In the following, the case $d = D$ will be discussed only, i.e., assuming solute and solvent molecules of equal sizes. For this model, the MSA integral equation has been solved to yield the steady state solvation free energies $E_s(\varepsilon_s)$ [13]:

$$E_s(\varepsilon_s) = \frac{\mu^2}{4\pi\varepsilon_0 \, k_B T \, D^3} \alpha_s(\varepsilon_s) \tag{15.4a}$$

with

$$\alpha_s(\varepsilon_s) = \frac{8(\varepsilon_s - 1)}{2u\rho^3 + 2\varepsilon_s[1 + (1 - 2u)]^3 + [1 + \rho]^3} \tag{15.4b}$$

$$\rho = \frac{1-u}{1-2u}, \quad u = \frac{3\xi}{1+4\xi}, \quad \xi = \frac{1}{2}\left[1 - \frac{9}{4 + f^{1/3} + f^{-1/3}}\right] \quad \text{and} \tag{15.4c}$$

and

$$f = 1 + 54\sqrt{\varepsilon_s}\left[1 - \sqrt{1 + \frac{1}{27\sqrt{\varepsilon_s}}}\right] \tag{15.4d}$$

For practical purposes, the resulting $E_s(\varepsilon_s)$ is well approximated by the empirical relation

$$E_s(\varepsilon_s) \approx \frac{\mu^2}{4\pi\varepsilon_0 k_B T D^3} \frac{\ln(\varepsilon_s)}{3} \tag{15.5}$$

In the continuum limit corresponding to $d \to 0$, the classical result of Onsager (ONS) is recovered,

$$E_s^c(\varepsilon_s) = \frac{\mu^2}{4\pi\varepsilon_0 k_B T D^3}\left(8\frac{\varepsilon_s - 1}{2\varepsilon_s + 1}\right) \tag{15.6}$$

All of these relations between the solvation free energy and the static dielectric constant ε_s demonstrate that E_s is a pronounced nonlinear function of ε. Within this approach and for a given solute molecule and temperature, the energy E_s depends only on ε_s, i.e., solvent specific interactions of other that dipolar nature remain disregarded. As detailed below, it is this quantity $E_s(\varepsilon_s)$ which determines how the solvent affects the optical lineshapes, i.e., their spectral position and width.

Optical line shapes of an electronic two-level solute dissolved at infinite dilution in an equilibrium dipolar hard-sphere solvent have been addressed in a statistical mechanical approach by Loring [14]. As in Eq. (15.4a), the thermodynamic state of the solvent is entirely cast into the dimensionless function $\alpha_s(\varepsilon_s)$, whose explicit dependence on ε_s is a matter of the particular solvation theory used. The prediction for any linearized theory is a Gaussian line shape with variance σ_{inh}^2 and positioned at $\bar{v}_0 + \Delta\bar{v}$, where $\bar{v}_0$ is the gas phase emission energy and $\Delta\bar{v}$ is the Stokes shift. The steady state results for $\Delta\bar{v}$ and σ_{inh} are

$$\Delta\bar{v}_s = \bar{v}_s - \bar{v}_0 = \frac{2\mu_E(\mu_G - \mu_E)}{4\pi\varepsilon_0 ch D^3}\alpha_s(\varepsilon_s) \tag{15.7a}$$

$$\sigma_{inh}^2 = \frac{2(\mu_G - \mu_E)^2 k_B T}{4\pi\varepsilon_0 c^2 h^2 D^3}\alpha_s(\varepsilon_s) \tag{15.7b}$$

where ε_s again refers to the static ($t \to \infty$) dielectric constant. It is interesting to note that the ratio $\sigma_{inh}^2/\Delta\bar{v}$ in an equilibrated fluid no longer depends on the thermodynamic state of the solvent,

$$\frac{\sigma_{inh}^2}{\Delta\bar{v}_s} = \frac{(\mu_G - \mu_E)k_B T}{ch\mu_E} \tag{15.8}$$

This equation (Eq. 15.8) constitutes a special case of the fluctuation-dissipation theorem. For $\alpha_s(\varepsilon_s)$ we can directly use the static MSA solutions given in Eq. (15.4) or the continuum limit of Eq. (15.6), which then allows one to compare molecular approaches with continuum models as regards the steady state results of the solvation theory.

According to basic electrostatics [15], the electric field E of a point-sized particle with dipole moment μ_1 is

$$E(r) = -\boldsymbol{\mu}_1 \, r^{-3} + 3(\boldsymbol{\mu}_1 \, \boldsymbol{r}_0)\boldsymbol{r}_0 \, r^{-3} \tag{15.9}$$

where the particle 1 is assumed to be positioned at the origin and with $\boldsymbol{r} = r \, \boldsymbol{r}_0$. Being interested only in the radial dependence of the interaction energies w, we can focus on the equatorial plane with respect to $\boldsymbol{\mu}_1$, i.e. to $\boldsymbol{\mu}_1 \, \boldsymbol{r}_0 = 0$. The interaction energy of a dipole possessing a permanent moment $\boldsymbol{\mu}_2$ with the field $E(r)$ is given by $w = -\boldsymbol{\mu}_2 \, E(r)$. For the dipole pair we thus obtain $w_{\mu-\mu} \sim (\boldsymbol{\mu}_1 \, \boldsymbol{\mu}_2) \, r^{-3}$. At a certain distance r from the central dipole in a liquid, the number N of solvent dipoles increases as r^2, i.e., as the surface area of a sphere with radius r. For the equilibrium configuration of a disordered fluid we have to consider $\langle w_{\text{dip}} \rangle = -N\mu E \langle \cos\theta \rangle$, with $\langle \cos\theta \rangle$ being the ensemble average regarding the various orientations of dipoles with respect to the field of the central dipole. For non-interacting dipoles the Boltzmann distribution leads to $\langle \cos\theta \rangle = \mu E/3k_B T$ and thus $\langle w_{\text{dip}} \rangle = -N\mu^2 E^2 \, (3k_B T)^{-1}$, i.e., $\langle w_{\text{dip}} \rangle \sim r^{-4}$ for a solute dipole centered in a spherical shell of radius r of equilibrium solvent dipoles. If screening effects are ignored, i.e., for solvents of little polarity, integration from the solute radius $r = D/2$ up to the distance $r = x$ of the above results for $\langle w \rangle$ yields the energy $\langle W \rangle = \int\langle w \rangle \, dr$ related to the entire solvent within the radius x. For the radial dependence the result is $\langle W_{\text{dip}} \rangle \sim x^{-3}$, implying that approximately 90% of the contribution to the solvation free energy originates from the first solvent shell [12]. This limited spatial scale of the solute/solvent coupling has also been derived from simulation work [16].

In order to obtain the entire time dependence of the solvation process, the MSA equations have been solved using the frequency dependent dielectric function $\hat{\varepsilon}(p) = \varepsilon^*(\omega) \, [p = i\omega]$ instead of the static limit ε_s only [11]. We express the result in terms of the solvation time correlation function $C(t)$ in Eq. (15.2), the inverse Laplace transform L^{-1} of the normalized admittance $\hat{\chi}(p)$ of the system,

$$C(t) = L^{-1}\left[p^{-1} \frac{\hat{\chi}(p) - \hat{\chi}(0)}{\hat{\chi}(\infty) - \hat{\chi}(0)} \right] \tag{15.10a}$$

The d-MSA result for the dipole solvation dynamics reads

$$\hat{\chi}(p) = \frac{1}{2}\left(1 - \frac{9}{\hat{h}(p) + 4} \right), \quad \hat{h}(p) = \hat{f}^{1/3}(p) + \hat{f}^{-1/3}(p) \tag{15.10b}$$

$$\hat{f}(p) = \hat{g}(p) - \sqrt{\hat{g}^2(p) - 1}, \quad \hat{g}(p) = 1 + 54\sqrt{\hat{\varepsilon}(p)} \tag{15.10c}$$

Fig. 15.4. Solvation time correlation functions $C(t)$ as predicted by the d-MSA for the dipolar and ionic case on the basis of a Debye type $\varepsilon^*(\omega)$ with $\varepsilon_\infty = 2$, $\varepsilon_s = 30$, adapted from [11]. The dielectric function is plotted as $\varepsilon_n(t)$. The *dashed* lines refer to $\varepsilon_n(t)$ but rescaled in time by a factor of $(\varepsilon_S/\varepsilon_\infty)^{1/2}$ and $\varepsilon_S/\varepsilon_\infty$, respectively, with the latter case corresponding to the modulus $M_n(t)$. Reprinted with permission from The Journal of Chemical Physics, Copyright 2000, American Institute of Physics [50]
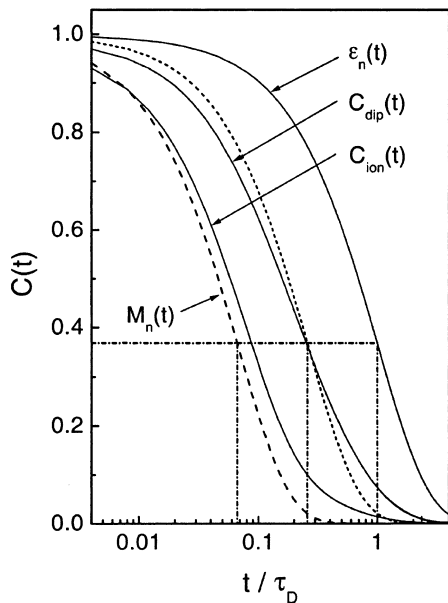
where a Debye type dielectric with relaxation time τ_D would enter the calculation as

$$\hat{\varepsilon}(p) = \varepsilon_\infty + \frac{\varepsilon_s - \varepsilon_\infty}{1 + p\tau_D} \tag{15.11}$$

Figure 15.4 compares the dipole solvation d-MSA prediction for $C(t)$ with the normalized constant field and constant charge dielectric polarization decays, and $\varepsilon_n(t) = [\varepsilon_s - \varepsilon(t)]/[\varepsilon_s - \varepsilon_\infty] = \exp(-t/\tau_D)$ and $M_n(t) = M(t)/M_\infty = \exp(-t/\tau_E)$, respectively. The parameters are adopted from Fig. 3 of [11] assuming a Debye type solvent of substantial polarity with $\varepsilon_\infty = 2$, $\varepsilon_s = 30$. Finally, we note that the d-MSA, as most other solvation theories, assumes that each solvent dipole is equally exhibiting the dynamics associated with the dielectric function $\varepsilon(t)$ or $\varepsilon^*(\omega)$. This picture of spatially homogeneous dynamics is not necessarily realistic in cases where non-Debye systems are considered.

15.4
Solvation Dynamics

In this section we explore the extent to which experimental phosphorescence solvation data can be rationalized in terms of the macroscopic dielectric properties of the solvent. The total Stokes shift $\Delta\bar{v}$ is a measure for the amplitude of the response to the electronic excitation of the solute molecule and represents the solvation analog of the dielectric relaxation strength $\Delta\varepsilon = \varepsilon_S - \varepsilon_\infty$. The theoretical relation between the steady state values $\langle\bar{v}(\infty)\rangle$ and ε_s is given by insert-

Fig. 15.5. Experimental results for the steady state gas-to-solvent shift, $\Delta \bar{\nu} = \bar{\nu}_0 - \bar{\nu}(\infty)$, obtained for QX in various solvents [17]. The predictions based on the Onsager (ONS) and MSA model as input to a lineshape theory are plotted vs the experimental data. The identity line indicates agreement between theory and observation, the line along the ONS data is a guide only. Reprinted with permission from The Journal of Chemical Physics, Copyright 2000, American Institute of Physics [50]
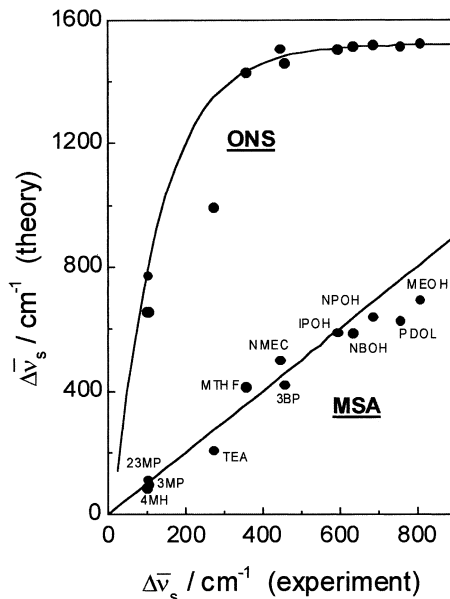
ing Eq. (15.4) into Eq. (15.7). Figure 15.5 tests the $\langle \bar{\nu}(\infty) \rangle$ data obtained for a series of solvents differing strongly in ε_s against both the Onsager (ONS) continuum model and the MSA results using the lineshape theory outlined above [14]. It is obvious that the linear correlation between theory and experiment is obtained for the MSA case only, while the continuum or Onsager approach fails to correlate the experimental results with the prediction properly [17].

Regarding the dynamics of solvation using phosphorescent probes, the initial attempt to associate the solvation dynamics with orientational solvent motion focused on the correlation of the onset of slow solvation effects with the structural relaxation of the solvent. It was observed for more than ten different glass forming liquids that the Stokes shift sets in at the glass transition temperature of each solvent [6]. Conversely, different probe molecules in the same solvent lead to almost identical dynamical responses, i.e., the observed solvation dynamics are independent of the particular probe molecule [6]. In a next step, we compare in Fig. 15.6 solvation and dielectric average time scales only, but over a large range of temperatures and response times for the solvent 2-methyltetrahydrofuran (MTHF). The $C(t)$ data have been obtained for various probe molecules with different excited state lifetimes, in order to cover decay times ranging from 10 ps to 100 s. Within these 12 decades in time, the Stokes-shift dynamics closely follow the course of the dielectric relaxation time, τ_D [18].

For a closer scrutiny of the $C(t) \leftrightarrow \varepsilon(t)$ relation, we select two temperatures in Fig. 15.6, $T = 94$ K and $T = 120$ K, for which the relaxation times differ by eight orders of magnitude. Figure 15.6 displays the typical temperature dependence of a fragile glass-forming liquid, characterized by a drastic increase of the apparent activation energy as the glass transition at $T_g = 91$ K is approached. In

Fig. 15.6. Activation plot of the average solvent relaxation times as derived from solvation dynamics experiments, $C(t)$ (*symbols*), and from dielectric relaxation, $\varepsilon^*(\omega)$ (*dashed line*) [18]. The various solvation time regimes are covered using three different probes: quinoxaline, Ru(bpy)$_2$(CN)$_2$, and 4-aminophthalimide (static and time resolved data). Reprinted with permission from The Journal of Chemical Physics, Copyright 2000, American Institute of Physics [50]
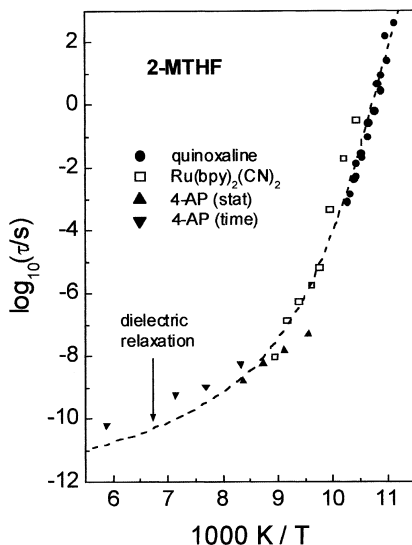
the domain of the phosphorescent probes, $\tau \geq 1$ ms, the relaxation time is extremely sensitive to temperature changes. Therefore, in order to avoid ambiguities, the dielectric relaxation experiment has been performed simultaneously with the optical data acquisition [5]. The dielectric data of the polar solvent MTHF are well represented by a Cole-Davidson type $\varepsilon^*(\omega)$ with $\gamma_{CD} = 0.49$, $\varepsilon_\infty \approx 3$, and $\varepsilon_s \approx 19$ near T_g. This result for $\varepsilon^*(\omega)$ is easily transformed to the respective normalized time domain representations,

$$\varepsilon_n(t) = \frac{\varepsilon_s - \varepsilon(t)}{\varepsilon_s - \varepsilon_\infty} \quad \text{and} \quad M_n(t) = \frac{M(t)}{M_\infty} \tag{15.12}$$

The upper panel of Fig. 15.7 confronts the experimental $C(t)$ results, $C(t)$, at $T = 94$ K, $\varepsilon_s \approx 18.4$, with the normalized dielectric retardation curve $\varepsilon_n(t)$, the equivalent relaxation $M_n(t)$, and the d-MSA prediction using $\varepsilon^*(\omega)$ as input. An analogous plot for the $T = 120$ K, $\varepsilon_s \approx 14.4$, case is shown in the lower part of Fig. 15.7. The relation among the various curves is very similar for the two examples plotted in the respective ranges 0–0.5 s and 0–10 ns [18]. The average time scales of the $C(t)$ results are close to those of the constant field polarization decay $\varepsilon_n(t)$, although a faster $C(t)$ according to $\tau_E = \tau_D \, \varepsilon_\infty/\varepsilon_s$ with $\varepsilon_\infty/\varepsilon_s \approx 5.5$ may be expected. In both cases the relaxation time dispersion, or deviation from exponentiality, is larger for the Stokes-shift dynamics relative to the macroscopic polarization curve. The simple continuum prediction, calculated as the constant charge polarization decay $M_n(t)$, yields decays which appear unreasonably fast. Also the d-MSA results for dipole solvation decay more rapidly than do the $C(t)$ measurements. However, the decay patterns of the d-MSA closely resembles those of the experimental $C(t)$ curves. This is demonstrated in Fig. 15.7 by rescaling the $C(t)$ data in time, which results in a good agreement between $C(t')$

Fig. 15.7. Plots of experimental $\log_{10}C(t)$ curves (*solid symbols*) and the scaled $\log_{10}C(\kappa t)$ data (*open symbols*) vs time, where $\kappa = (\varepsilon_s/\varepsilon_\infty)^{1/2}$ [18]. In each panel, the normalized dielectric response, $\varepsilon_n(t)$, as well as the MSA and ONS predictions are included as *solid lines* as indicated. *Upper panel*: data for QX in MTHF at $T = 94$ K for times $0 \leq t \leq 0.5$ s. *Lower panel*: data for 4AP in MTHF at $T = 120$ K for times $0 \leq t \leq 10$ ns. Reprinted with permission from The Journal of Chemical Physics, Copyright 2000, American Institute of Physics [50]
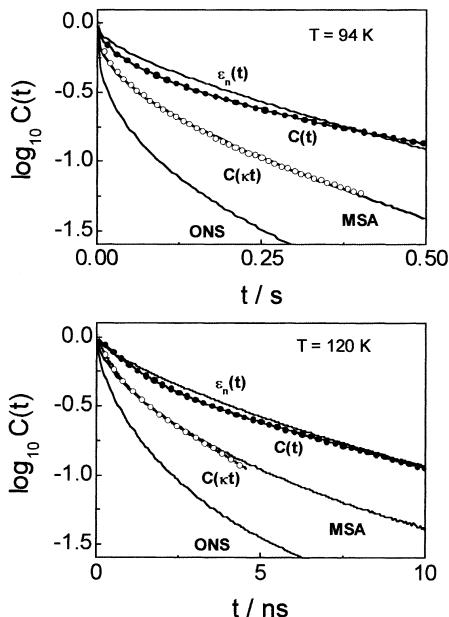
and the d-MSA $C(t)$ result. The scaling factors used in the plots are somewhat different for the two temperatures, but consistently given by $\sqrt{\varepsilon_\infty}/\sqrt{\varepsilon_s}(T)$ for both cases. This factor has been found to represent the ratio of the '1/e' times for the dipolar MSA result $C_{\mathrm{dip}}(t)$ and the $\varepsilon(t)$ decay, as indicated by the vertical dashed lines in Fig. 15.4 which are a factor of $\sqrt{\varepsilon_\infty}/\sqrt{\varepsilon_s}$ apart. Therefore, the $C(t)$ data agrees with the relaxation time dispersion of the d-MSA $C_{\mathrm{dip}}(t)$ prediction but exhibits the time scale of the constant field polarization decay, which corresponds to $C_{\mathrm{dip}}(t)$ only in the limit of non-polar solvents.

The above results concerning the solvation time correlation function $C(t)$ and the solvation amplitude $\Delta\bar{v}$ indicate clearly that solvation dynamics tracks the dielectric properties. However, as with the comparison between other relaxation methods, the quantitative relation between $C(t)$ and $\varepsilon(t)$ is not entirely understood. That a significant dipole moment change $\Delta\mu$ upon exciting the probe is crucial for a local measurement of the dielectric orientational polarization is emphasized in Fig. 15.8. This plot compares how the Stokes shift $\Delta\bar{v}$ increases with solvent polarity for the dipolar probe QX with $\Delta\mu \approx 1.3$ D, whereas the non-polar probe NA with $\Delta\mu \approx 0$ displays no coupling to the polarity or to the dielectric relaxation strength $\Delta\varepsilon$.

15.4.1
Dynamic Heterogeneity

The dispersive relaxation dynamics of supercooled liquids and polymers have been observed to originate from a distribution of site specific time scales. The

Fig. 15.8. Values of the total Stokes-shift $\Delta\bar{\nu}$ for the probes NA (*open symbols*) and QX (*solid symbols*) in various glass forming solvents near T_g [49]. The abscissa sorts the solvents according to their polarity in terms of E_T^N values at $T = 20\,°C$. *Lines* are meant to serve as guides only. Reprinted with permission from The Journal of Chemical Physics, Copyright 2000, American Institute of Physics [50]
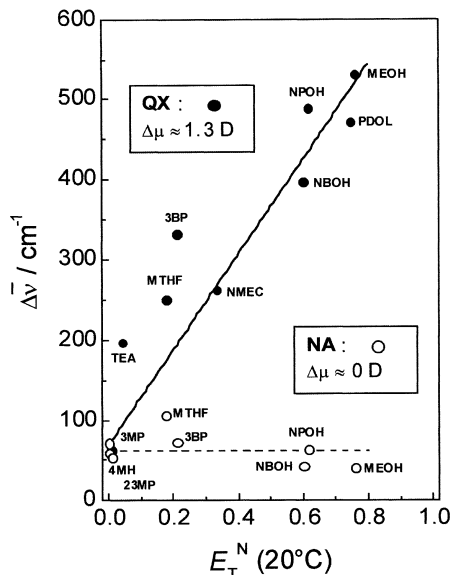
possibility of selecting a subensemble whose relaxation is slower or faster than the average is regarded as proof of this heterogeneity regarding the dynamics [19]. In fact, the initial experimental approaches to heterogeneity were based on techniques capable of employing dynamical selectivity, like multidimensional NMR methods [20–22], optical bleaching techniques [23–25], and non-resonant dielectric hole burning [26–28]. Instead of focusing on higher order time correlation functions, the solvation dynamics technique exploits the information contained in the higher moments of a two time correlation function. While a typical relaxation trace refers to the ensemble average, solvation data also contains information on the spatial variance of the relaxing quantity and is thereby directly sensitive to heterogeneity.

One advantage of the phosphorescence type solvation experiment is its capability of directly observing the inhomogeneous optical linewidth σ_{inh}, practically unobstructed by homogeneous broadening or unresolved vibronic structure. This linewidth is constant below the glass transition of the solvent, $\sigma_{inh}(T < T_g) = \sigma_o$. Its value reflects the frozen in disorder of solvent dipoles and the resulting spatial variation of the solvation free energy or of the local electric field at the sites of the probe molecules. Above T_g, σ_{inh} is observed to become time and temperature dependent, indicating a peak in the $\sigma_{inh}(t)$ curves but with $\sigma_{inh}(0) = \sigma_{inh}(\infty) = \sigma_o$ [29]. Within the framework of dipole solvation theories, no prediction for such time dependence of the linewidth has been advanced. In cases where the solvent dielectric properties enter solely in terms of $\varepsilon^*(\omega)$, as for the d-MSA, the dipole dynamics are assumed spatially homogeneous, i.e. the dynamical behavior of each dipole is identically determined by the macroscopic dielectric function $\varepsilon^*(\omega)$ or $\varepsilon(t)$. In this case, the emission spectrum is expected to shift as a whole while conserving its shape, resulting in $\sigma_{inh}(t) = \sigma_0$ for all times. An alternative picture is the situation that every site is associated with sin-

gle exponential dynamics but with the relaxation time being a spatially varying quantity [30, 31]. In what follows, we address the relation between dynamical heterogeneity and the inhomogeneous linewidth $\sigma_{\text{inh}}(t)$ in quantitative detail.

The solvation time correlation function $C(t)$ is usually non-exponential and often described by a KWW type decay, $C(t) = \exp[-(t/\tau_{\text{KWW}})^{\beta_{\text{KWW}}}]$. Let $\chi_i(t) = \exp[-(t/\tau_i)^{\beta_{\text{intr}}}]$ denote the decay intrinsic in the response of a specific site i, i.e., at a given probe molecule. Pure dynamical homogeneity is then described by $\chi_i(t) = C(t)$, with $\beta_{\text{intr}} = \beta_{\text{KWW}}$ and $\tau_i = \tau_{\text{KWW}}$, identically for all i. Heterogeneity is modeled by $\beta_{\text{intr}} > \beta_{\text{KWW}}$, i.e., the intrinsic decays are not as non-exponential as the ensemble average $C(t)$. In this case, a distribution of τ_i must account for the discrepancy between $C(t)$ and $\chi_i(t)$, and $C(t)$ can be written as

$$C(t) = \exp\left[-(t/\tau_{\text{KWW}})^{\beta_{\text{KWW}}}\right] = \int_0^\infty g(\tau)\exp\left[-(t/\tau)^{\beta_{\text{intr}}}\right]d\tau \tag{15.13}$$

The purely heterogeneous limit is reached when $\beta_{\text{intr}} = 1$, equivalent to local exponential decays and an accordingly broad probability density $g(\tau)$ characterizing the spatial variation of relaxation times.

For predicting $\sigma_{\text{inh}}(t)$ in the course of a solvation process associated with heterogeneous dynamics, both site specific quantities, the solvation free energy $\bar{v}_i$ and the characteristic time scale τ_i, need to be considered. For the equilibrated energies $\bar{v}_i(\infty)$ we assume a Gaussian distribution centered at $\bar{v}(\infty)$ and having a Gaussian width σ_0. The independent values of the τ_i are subject to a distribution according to $g(\tau)$ defined implicitly in Eq. (15.13). The energetic relaxation for site i, $\bar{v}_i(t)$, can be written as [32]

$$\bar{v}_i(t) = \bar{v}_i(\infty) + \Delta\bar{v}\exp\left[-(t/\tau_i)^{\beta_{\text{intr}}}\right] = \bar{v}_i(\infty) + \Delta\bar{v}\,\chi_i(t) \tag{15.14}$$

Since the quantities $\bar{v}_i(\infty)$ and $\chi_i(t)$ are independent random variables, the mean value $\bar{v}_i(t)$ and the variance $\sigma_{\text{inh}}^2(t)$ of $\bar{v}_i(t)$ can be obtained by adding the individual corresponding moments.

The mean, $\langle\chi(t)\rangle$, is directly given by Eq. (15.13), $\langle\chi(t)\rangle = C(t)$. The variance of $\chi(t)$, denoted $\rho(t)$, can be obtained accordingly,

$$\rho(t) = \langle(\chi(t) - \langle\chi(t)\rangle)^2\rangle = C(2^{1/\beta_{\text{intr}}}t) - C(2^{1/\beta_{\text{KWW}}}t) \tag{15.15}$$

with $\rho(t) = 0$ if $\beta_{\text{intr}} = \beta_{\text{KWW}}$ and with $\rho(t)$ attaining a maximum whenever $\beta_{\text{intr}} > \beta_{\text{KWW}}$. Inserting the results for $\langle\chi(t)\rangle$ and $\langle(\chi(t) - \langle\chi(t)\rangle)^2\rangle$ in Eq. (15.14) yields

$$\bar{v}(t) = \langle\bar{v}_i(t)\rangle = \bar{v}(\infty) + \Delta\bar{v}\,C(t) \tag{15.16}$$

$$\sigma_{\text{inh}}^2(t) = \langle(\bar{v}_i(t) - \bar{v}(t))^2\rangle = \sigma_0^2 + \Delta\bar{v}^2\rho(t) \tag{15.17}$$

with $\rho(t)$ stated in Eq. (15.15). A practical way of expressing the resulting relation between $\sigma_{\text{inh}}(t)$ and $C(t)$ is

$$\frac{\sigma_{\text{inh}}^2(t) - \sigma_0^2}{\Delta v^2} = \rho(t) = C(2^{1/\beta_{\text{intr}}}t) - C^2(t) \tag{15.18}$$

demonstrating the impact of β_{intr} on the observable $\sigma_{inh}(t)$, whereas $C(t)$ is independent of β_{intr}. The bounds of the time dependent width $\sigma_{inh}(t)$ are $\sigma_{inh}(t) = \sigma_o$ for the case of $\beta_{intr} = \beta_{KWW}$ and $\sigma_{inh}(t) \leq [\sigma_0^2 + \Delta\bar{\nu}^2/4]^{1/2}$ for other values of $0 < \beta_{KWW} < \beta_{intr} \leq 1$. Equation (15.18) relates the inhomogeneous linewidth $\sigma_{inh}(t)$ to the normalized Stokes shift response function $C(t)$. It predicts that an excess linewidth appears in the course of a solvation process if (and only if) the underlying dynamical processes exhibit a spatial variation of time scales.

In order to analyze the present solvation data along Eq. (15.18), it is convenient to have a simple analytical function which matches the $C(t)$ data, such that $C(2^{1/\beta_{intr}}t)$ can be obtained easily. Figure 15.3 demonstrates that a KWW decay with $\beta_{KWW} = 0.5$ is appropriate for handling $C(t)$ at arbitrary times. Furthermore, the observation of a temperature invariant β_{KWW} makes it sufficient to analyze the $\sigma(t) - C(t)$ relation on the basis of the master curves, where the variable t/τ_{KWW} is used instead of the absolute time. Figure 15.9 compares the experimental results $[\sigma_{inh}^2(t) - \sigma_0^2]/\Delta\bar{\nu}^2$ with the predictions, $C(2^{1/\beta_{intr}}t) - C^2(t)$, for various values of β_{intr}. In this plot the solid line refers to $\beta_{intr} = 1$, where $\rho(t) = C(2t) - C^2(t)$. This case corresponds to intrinsic relaxation patterns which are purely exponential and results in an excellent agreement with the experimental findings [33]. The dashed curves in Fig. 15.9 are for $\beta_{intr} = 0.9, 0.8$, and 0.7, where already $\beta_{intr} = 0.9$ is an inferior fit relative to $\beta_{intr} = 1$.

An unbiased approach for assessing the intrinsic relaxation pattern is a statistical analysis of the experimental data according to

$$\beta_{intr} = \beta_{KWW} \frac{\ln 2}{\ln\left[\frac{\ln(\rho(t) + \phi^2(t))}{\ln(\phi(t))}\right]} \tag{15.19}$$

Fig. 15.9. Master plot $\rho(t)$ (*symbols*) vs t/τ_{KWW} based on the $\sigma_{inh}(t)$ data of the system QX/MTHF at temperatures 91 K $\leq T \leq$ 97 K [33]. The *lines* are predicted $\rho(t)$ curves using $\phi(t) = \exp[-(t/\tau_{KWW})^{0.5}]$ for various values of $\beta_{intr} = 1.0, 0.9,$ 0.8, and 0.7, in the order from top to bottom curve. The homogeneous case $\beta_{intr} = \beta_{KWW} = 0.5$ leads to the prediction $\rho(t) \equiv 0$. Reprinted with permission from The Journal of Chemical Physics, Copyright 2000, American Institute of Physics [50]
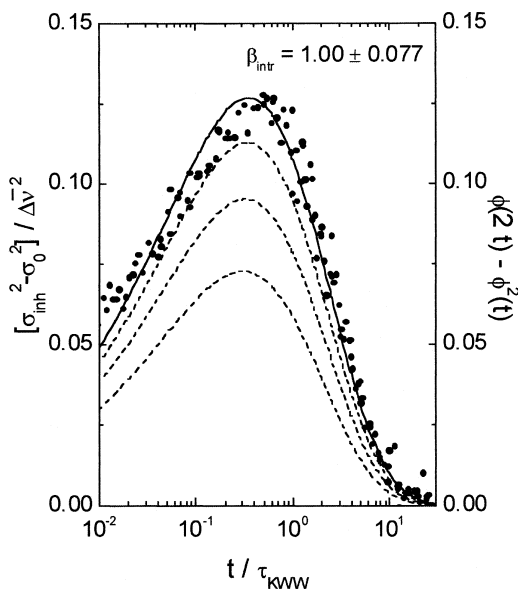
where β_{intr} is now expressed in terms of experimentally well defined quantities, β_{KWW}, $\rho(t) = [\sigma_{\mathrm{inh}}^2(t) - \sigma_0^2]/\Delta\bar{\nu}^2$, and $\phi(t) = C(t)$. The mean and standard deviation for β_{intr} have been computed in the range $2 \times 10^{-2} \leq t/\tau_{\mathrm{KWW}} \leq 2$ yielding $\beta_{\mathrm{intr}} = 1.001 \pm 0.077$ [33]. This result states unambiguously that the orientational correlation decays exponentially as far as the local response around a probe molecule is concerned. Within the present experimental range, $91\ \mathrm{K} \leq T \leq 97\ \mathrm{K}$ or $T_g \leq T \leq T_g + 6\ \mathrm{K}$ or $3 \times 10^{-3}\ \mathrm{s} \leq \langle\tau\rangle \leq 54\ \mathrm{s}$, no indication towards a systematic deviation from $\beta_{\mathrm{intr}} = 1$ can be found.

15.4.2
Confined Systems

Disordered materials are often studied under the constraints of spatial restrictions in order to understand the confinement and interfacial effects on the behavior of liquids [34], supercooled liquids [35, 36], liquid crystals [37, 38], polymers [39], and model systems [40]. Concerning the viscous regime of glass-forming materials, one is often interested in observing the competing effects of geometrical confinement and the length scale ξ of cooperativity. This latter scale can be pictured as the distance below which two molecules are dynamically coupled, i.e., the size of a 'cooperatively rearranging region' (CRR) or of domains [41]. This length scale ξ is assumed to attain values near 3 nm at the glass transition temperature T_g [42]. Porous systems are attractive materials for such studies because various pore diameters in the range of several nanometers are readily available. Phosphorescence solvation dynamics experiments are particularly useful for investigating the orientational relaxation of viscous liquids in the optically clear porous silica GelSil-glasses (GelTech) because the probe molecules are sensitive only to the local response without a significant spatial averaging.

The first solvation dynamics study of a supercooled liquid confined to nanopores has focused on the dipolar probe molecule quinoxaline dissolved in the polar glass-former MTHF [43]. Porous silica glasses with nominal pore diameters between 2.5 and 7.5 nm and with the native glass surfaces have been used for confining the liquid. The results have shown that the short time orientational correlation function in pores is the same as in the bulk situation. At times longer than a certain time t_e, however, the relaxation became non-ergodic, where t_e varied systematically with the pore size and with temperature. An example is shown in Fig. 15.10. The experimental findings are consistent with the idea that cooperativity of a certain length scale ξ couples an increasing fraction of the liquid to the boundary conditions as time proceeds [44]. These boundary conditions at the pore wall are defined by the surface properties, which are believed to be dominated by the silanol groups of a native silica glass surface. The pore size and temperature dependences were in accord with a cooperative length scale ξ which increases with decreasing temperature and which attains a value of $\xi \approx$ 3 nm at the glass transition temperature T_g. Consequently, the dynamics of molecules within the interfacial layer affect the remaining liquid to an extent which depends upon the length scale of cooperative motion. The above experiment has been repeated but using silanized porous glasses, in which a hydrophobic pore
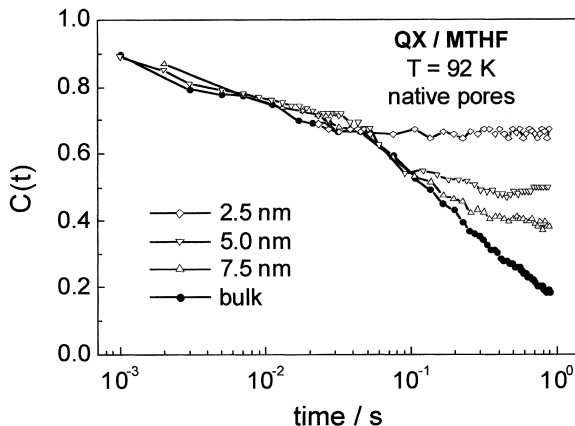
Fig. 15.10. Solvation dynamics $C(t)$ results for MTHF at $T = 92$ K [45]. The *curves* correspond to the bulk case (*solid symbols*) and to the cases of confinement in native pores (GelTech) of different diameter ϕ as indicated. The short time data is invariant to confinement effects, while the value of ϕ determines the time above which the process appears non-ergodic. Reprinted with permission from Journale de Physique IV France, Copyright 2000, EDP Sciences [46]

surface is achieved by passivating the silanol groups present on a native silica surface. Figure 15.11 displays the results for the solvation time correlation decay $C(t)$ observed in silanized pores. In contrast to the case of MTHF confined to pores with native surfaces, the relaxation dynamics in silanized pores as small as 2.5 nm is virtually identical to the behavior of the bulk liquid [45].

The data for native pores in Fig. 15.10 show unambiguously that geometrical confinement is capable of altering the relaxation dynamics of supercooled liquids in a qualitative fashion, such that the changes relative to the bulk relaxation can not be characterized by a shift of $\langle\tau\rangle$ or T_g alone. However, Fig. 15.11 indicates already that much of the bulk behavior can be restored by a surface treatment, i.e., by changing the properties of the interface only. Since the process of silanizing actually reduces the pore size slightly, the features seen for the native porous glass in Fig. 15.10 cannot be considered pure confinement effects. The non-ergodic component is rather a consequence of the special interactions between MTHF molecules and the silanol groups of a clean silica surface which appears to frustrate the reorientation in the interfacial layer considerably. It is then a matter of pore size and temperature to which extent dynamic cooperativity couples the remaining liquid within the pore to these boundary conditions.

For the silanized pores, the correlation decays $C(t)$ are well approximated by KWW functions as in Eq. (15.13), with a temperature invariant exponent β_{KWW} in the temperature range, 91 K $\leq T \leq$ 98 K, near the glass transition at $T_g = 91$ K. Therefore, temperature variations affect $C(t)$ only in terms of the characteristic time $\tau_{KWW}(T)$ without changing the functional form and a single master curve $C(t)$ vs t/τ_{KWW} covering six decades in reduced time can be constructed from a series of isothermal measurements according to the observation of the time-temperature superposition. Figure 15.12 compares the $C(t)$ results on reduced
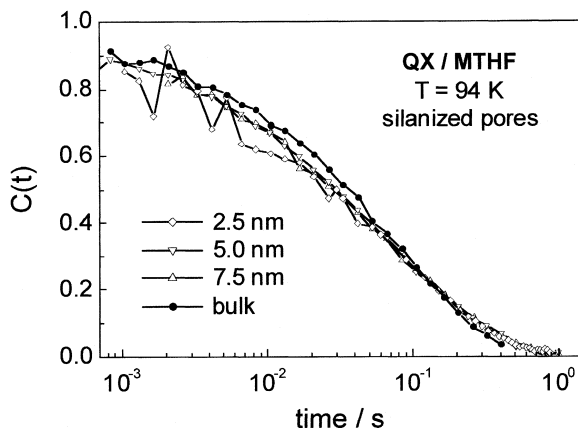
Fig. 15.11. Solvation dynamics $C(t)$ results for MTHF at $T = 94$ K [45]. The *curves* correspond to the bulk case (*solid symbols*) and to the cases of confinement in silanized pores (GelTech) of different diameter ϕ as indicated. The entire decays are independent of the pore size. Reprinted with permission from Journale de Physique IV France, Copyright 2000, EDP Sciences [46]
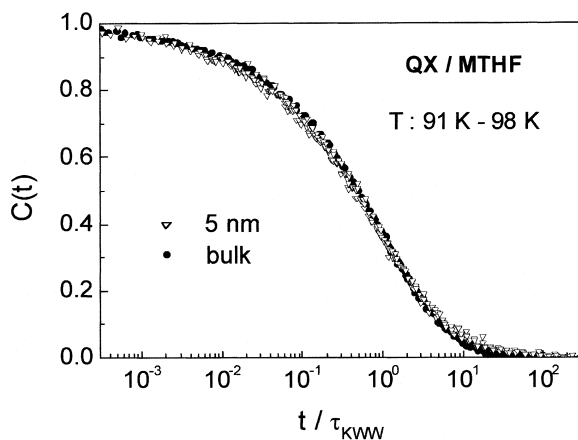
Fig. 15.12. Master curve for the Stokes-shift correlation functions $C(t)$ vs t/τ_{KWW} for QX in MTHF as derived from measurements at various temperatures in the range 91 K $\leq T \leq$ 98 K [46]. *Solid symbols* refer to the bulk liquid, *open symbols* are for the confinement to silanized pores of 5 nm diameter. Both data sets are well approximated by the Kohlrausch-Williams-Watts decay function with temperature independent exponents $\beta_{KWW} = 0.50$ and $\beta_{KWW} = 0.47$ for the relaxation in the bulk and in pores, respectively. Reprinted with permission from Journale de Physique IV France, Copyright 2000, EDP Sciences [46]

time scales for the case of the confinement to silanized pores of 5 nm nominal diameter with those for the bulk liquid [46]. The stretching exponents reflect the degree of deviations from an exponential decay pattern and are found to be very similar, $\beta_{KWW} = 0.47$ and $\beta_{KWW} = 0.50$ for the porous and bulk case, respectively. The total Stokes shift for the porous sample is $\Delta\bar{\nu} = \langle\bar{\nu}(0)\rangle - \langle\bar{\nu}(\infty)\rangle = 21342$ cm^{-1} – 21110 cm^{-1} = 232 cm^{-1}, whereas the bulk supercooled liquid MTHF displays a value of $\Delta\bar{\nu} = 21360$ cm^{-1} – 21113 cm^{-1} = 247 cm^{-1}.

In contrast to other techniques [44], the solvation dynamics method unambiguously identifies the amplitude of the relaxation function in porous media, because this value of $\Delta\bar{\nu}$ is inferred independently from the shift of the emission energy without referring to the number of emitting probe molecules. The total Stokes shift for the porous sample is $\Delta\bar{\nu} = 232$ cm^{-1}, and therefore only 5.6 % below that of the bulk liquid. Considering that some chromophores might be immobilized in the smallest pores of the existing pore size distribution or in the bottleneck between two pores, the bulk of the response amplitude is preserved inside the 5-nm pores. The normalized orientational correlation decays confronted in Fig. 15.12 are practically identical within the data scattering of the $C(t)$ results for the porous sample, although $\beta_{KWW} = 0.47$ vs $\beta_{KWW} = 0.50$ indicates a subtle increase in the relaxation time dispersion in silanized 5 nm pores over the bulk case. MTHF in silanized 5-nm pores appears to be an example of a confined liquid where the dynamics in the interfacial layer do not differ strongly from the bulk dynamics. This is the ideal situation for observing pure confinement effects, but they remain almost unnoticeable in the present case of MTHF in 5-nm pores.

The characteristic times of the KWW type $C(t)$ decays, τ_{KWW}, are strongly temperature dependent near T_g, because MTHF is a fragile liquid ($F_{1/2} = 0.73$) if classified within the strong-fragile pattern [47]. Figure 15.13 compiles the $\tau_{KWW}(T)$ data for the bulk and confined liquid as symbols in an activation plot. The line in this graph reflects the temperature dependence of the average dielectric relaxation time of bulk MTHF as seen in a macroscopic dielectric experiment. Above a temperature $T = 94$ K (10^3 K/$T = 10.6$) the relaxation times from the two experiments agree, but below 94 K the orientational correlation decays faster in the pores, which amounts to a factor of ≈ 4 at $T = T_g = 91$ K.

The above results emphasize the importance of the surface properties for the dynamics of molecules in porous media. A more detailed approach to discriminating interfacial from purely geometrical confinement effects requires a technique which facilitates the measurement of dynamics selectively in the interfacial layer. In what follows we briefly outline how solvation dynamics can be applied to achieve such a spatial selectivity [45]. The system used is QX in the nonpolar liquid 3-methylpentane (3MP) imbibed in native pores of 5 nm diameter. Figure 15.14 compares the temperature dependent average emission energies recorded at a fixed time $t_0 = 100$ ms for the porous and bulk case. In contrast to the QX/MTHF sample, the curves in Fig. 15.14 are offset by as much as $\Delta\bar{\nu} \approx 780$ cm^{-1} on the energy scale. This value agrees favorably with the Stokes shift observed only when the probe QX is dissolved in alcohols. Therefore, we conclude that the QX molecules are located at the pore walls, where the silanol groups are responsible for the 780 cm^{-1} energy offset. For both cases plotted in Fig. 15.14 the solvation dynamics near T_g lead to a Stokes shift of $\Delta\bar{\nu} \approx 70$ cm^{-1} .
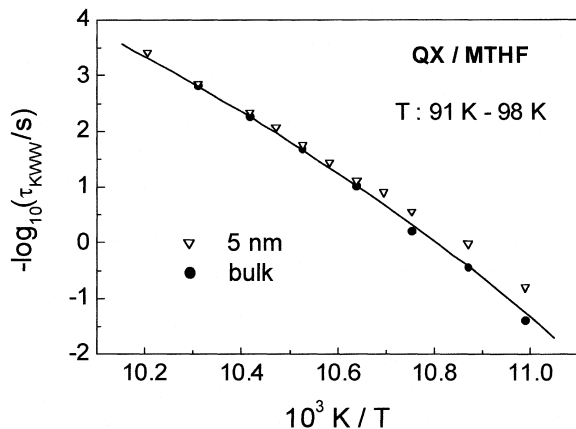
Fig. 15.13. Activation plot of $\tau_{KWW}(T)$ derived from fits to the Stokes-shift correlation function $C(t)$ for QX in MTHF [46]. The data is taken for temperatures between $T = 91$ K and $T = 98$ K. *Solid symbols* refer to the bulk liquid, *open symbols* are for the confinement to silanized pores of 5 nm diameter. The line is a Vogel-Fulcher fit to dielectric data of unconfined MTHF. The glass transition temperature of MTHF is $T_g = 91$ K ($10^3 K/T_g = 11.0$). Reprinted with permission from Journale de Physique IV France, Copyright 2000, EDP Sciences [46]
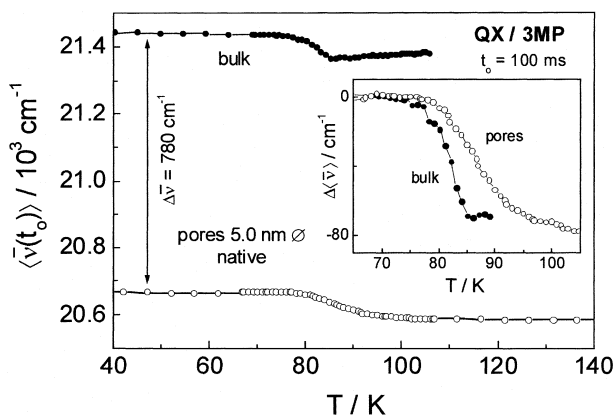
Fig. 15.14. Average emission energy $\langle \bar{v} \rangle$ of QX in 3MP recorded at a fixed time $t_0 = 100$ ms and as a function of temperature [45]. The *solid symbols* refer to the bulk 3MP liquid, *open symbols* are for 3MP in a native porous glass with 5 nm sized pores. At low temperatures, $T \leq 70$ K, the energy values are separated by $\Delta \bar{v}$. The *inset* shows the relative changes of $\Delta \langle \bar{v} \rangle$ on expanded scales. Reprinted with permission from Journale de Physique IV France, Copyright 2000, EDP Sciences [46]

The inset of Fig. 15.14 presents these solvation dynamics effects on enlarged scales.

Because 3MP is a non-dipolar liquid, the relaxations associated with the 70 cm^{-1} red-shift are due to mechanical responses of the environment rather than orientational motion as with dipolar solvation [48, 49]. The curve in the inset of Fig. 15.14 associated with the interfacial layer is shifted to higher temperatures and the transition is broader. In terms of the molecular dynamics, this implies that the relaxation at the interface is a factor of ≈ 10 slower, its distribution of relaxation times is broader, but there appears no qualitative difference like a motionally blocked interfacial layer. Note that a change in relaxation time by a factor of 10 amounts only to a fraction of the entire width of the broad relaxation time distributions typical for supercooled liquids.

15.5
Summary

This chapter has demonstrated that the optical technique of phosphorescence solvation dynamics is a versatile tool for assessing the local dynamics and polarity of molecules in soft condensed matter. The steady state as well as time dependent $S_0 \leftarrow T_1 \ (0 - 0)$ emission profiles originating from appropriate chromophoric guest molecules can be rationalized in a semi-quantitative fashion on the basis of the dielectric properties of the supercooled liquid, especially when going beyond continuum type approaches.

The close relation between the observed Stokes shift correlation function $C(t)$ and dielectric relaxation data $\varepsilon^*(\omega)$ allows one to exploit the local character of the solvation dynamics experiment in situations, where spatial heterogeneities regarding dynamics or polarity are anticipated. Two examples have been discussed, where local rather than macroscopic techniques are advantageous: detailed measurements of the dynamic heterogeneities intrinsic in the non-exponential orientational relaxations of supercooled liquids, and studies of liquid dynamics under geometrical confinement to pores in silica glasses with diameters of a few nanometers. A promising application of solvation dynamics is the possibility of tagging particular spatial regions of interest, like the interfacial layer of a liquid in porous glass, which are then measured selectively.

List of Abbreviations and Symbols

c	Vacuum speed of light
$C(t)$	Stokes shift correlation function
D	Dielectric displacement
D	Solute molecule diameter
d	Solvent molecule diameter
E	Electric field
E_{loc}	Local electric field
E_s	Solvation free energy
$F_{1/2}$	Fragility
h	Planck's constant
I	Emission intensity
k_B	Boltzmann's constant
$M(t)$	Electric modulus
$M_n(t)$	Normalized electric modulus
M_∞	High frequency electric modulus
M_{loc}	Local electric modulus
$P(t)$	Dielectric polarization
$P_D(t)$	Constant field polarization
$P_E(t)$	Constant charge polarization
S_0	Singlet ground state
S_1	First excited singlet state
T_1	First excited triplet state
T_g	Glass transition temperature
W	Interaction energy
α_s	Solvent state function
β_{intr}	Intrinsic non-exponentiality
β_{KWW}	KWW exponent
γ_{CD}	Cole-Davidson exponent
ΔE	Electric field change
$\Delta \mu$	Dipole moment change
$\Delta \bar{v}$	Total red shift
$\varepsilon(t)$	Dielectric function
$\varepsilon_n(t)$	Normalized dielectric function
ε_s	Static dielectric constant
ε_0	Permittivity of free space
ε_∞	High frequency dielectric constant
μ_E	Excited state dipole moment
μ_G	Ground state dipole moment
$\bar{v}$	Wavenumber
$\bar{v}_0$	Gas phase wavenumber
ξ	Cooperativity length scale
$\rho(t)$	Variance of relaxation function
σ	Optical linewidth
σ_{inh}	Inhomogeneous linewidth
τ_E	Modulus time constant

τ_{ex}	Excited state lifetime
τ_D	Dielectric time constant
τ_{KWW}	KWW time scale
τ_L	Longitudinal time constant
τ_{ph}	Phosphorescence lifetime
$\chi_i(t)$	Local response function

d-MSA	Dynamics MSA
KWW	Kohlrausch-Williams-Watts
3MP	3-Methylpentane
MSA	Mean spherical approximation
MTHF	2-Methyltetrahydrofuran
NA	Naphthalene
ONS	Onsager theory
QI	Quinoline
QX	Quinoxaline

References

1. Maroncelli M, Fleming GR (1987) J Chem Phys 86:6221
2. Ediger MD, Angell CA, Nagel SR (1996) J Phys Chem 100:13,200
3. Maroncelli M (1993) J Mol Liquids 57:1
4. Jarzeba W, Walker GC, Johnson AE, Barbara PF (1991) Chem Phys 152:57
5. Richert R (1992) Chem Phys Lett 199:355
6. Richert R, Wagener A (1991) J Phys Chem 95:10,115
7. Zhou HX, Bagchi B, Papazyan A, Maroncelli M (1992) J Chem Phys 97:9311
8. Richert R (1994) In: Richert R, Blumen A (eds) Disorder effects on relaxational processes. Springer, Berlin Heidelberg New York, p 333
9. Richert R, Wagner H (1995) J Phys Chem 99:10,948
10. Fröhlich H (1958) Theory of dielectrics. Oxford University Press, New York
11. Rips I, Klafter J, Jortner J (1988) J Chem Phys 89:4288
12. Richert R (1996) J Phys Condens Matter 8:6185
13. Wertheim MS (1971) J Chem Phys 55:4291
14. Loring RF (1990) J Phys Chem 94:513
15. Böttcher CJF (1983) Theory of electric polarization. Elsevier, Amsterdam
16. Papazyan A, Maroncelli M (1991) J Chem Phys 95:9219; 102:2888
17. Richert R, Wagener A (1993) J Phys Chem 97:3146
18. Richert R, Stickel F, Fee RS, Maroncelli M (1994) Chem Phys Lett 229:302
19. Böhmer R, Chamberlin RV, Diezemann G, Geil B, Heuer A, Hinze G, Kuebler SC, Richert R, Schiener B, Sillescu H, Spiess HW, Tracht U, Wilhelm M (1998) J Non-Cryst Solids 235/237:1
20. Schmidt-Rohr K, Spiess HW (1991) Phys Rev Lett 66:3020
21. Heuer A, Wilhelm M, Zimmermann H, Spiess HW (1995) Phys Rev Lett 75:285
22. Böhmer R, Hinze G, Diezemann G, Geil B, Sillescu H (1996) Europhys Lett 36:55
23. Cicerone MT, Ediger MD (1995) J Chem Phys 103:5684
24. Cicerone MT, Blackburn FR, Ediger MD (1995) Macromol 28:8224
25. Cicerone MT, Ediger MD (1996) J Chem Phys 104:7210
26. Schiener B, Böhmer R, Loidl A, Chamberlin RV (1996) Science 274:752
27. Schiener B, Chamberlin RV, Diezemann G, Böhmer R (1997) J Phys Chem 107:7746
28. Richert R, Böhmer R (1999) Phys Rev Lett 83:4337
29. Richert R (1997) J Phys Chem B 101:6323

30. Sillescu H (1999) J Non-Cryst Solids 243:81
31. Richert R, Blumen A (1994) In: Richert R, Blumen A (eds) Disorder effects on relaxational processes. Springer, Berlin Heidelberg New York, p 1
32. Richert R, Richert M (1998) Phys Rev E 58:779
33. Wendt H, Richert R (2000) Phys Rev E 61:1722
34. Drake JM, Grest GM, Klafter J, Kopelman R (eds) (1999) Dynamics in small confining systems IV. Materials Reseach Society, Pittsburgh
35. Jackson CL, McKenna GB (1991) J Non-Cryst Solids 131/133:22
36. Arndt M, Stannarius R, Gorbatschow W, Kremer F (1996) Phys Rev E 54:5377
37. Schwalb G, Deeg FW (1995) Phys Rev Lett 74:1383
38. Sinha GP, Aliev FM (1998) Phys Rev E 58:2001
39. Petychakis L, Floudas G, Fleischer G (1997) Europhys Lett 40:685
40. Donati C, Jäckle J (1996) J Phys Condens Matter 8:2733
41. Adam G, Gibbs JH (1965) J Chem Phys 43:139
42. Ediger MD, Angell CA, Nagel SR (1996) J Phys Chem 100:13,200
43. Streck C, Mel'nichenko YB, Richert R (1996) Phys Rev B 53:5341
44. Richert R (1996) Phys Rev B 54:15,762
45. Wendt H, Richert R (1999) J Phys Condens Matter 11:A199
46. Wendt H, Richert R (2000) J Phys IV France 10:67
47. Richert R, Angell CA (1998) J Chem Phys 108:9016
48. Fourkas JT, Benigno A, Berg M (1994) J Non-Cryst Solids 172/174:234
49. Wendt H, Richert R (1998) J Phys Chem A 102:5775
50. Richert R (2000) J Chem Phys 113:8404

16 Dielectric and Mechanical Spectroscopy – a Comparison

T. Pakula

16.1 Introduction

Mechanical spectroscopy is a technique of material characterization in which material deformation and flow behavior is analyzed by means of dynamic mechanical methods. As in dielectric spectroscopy, advantage is taken of the material reaction to periodic variation of the external field, however with the difference that the applied field is mechanical instead of the electrical one. Materials respond to the applied field (stress or strain) by dissipating the input energy in a viscous flow (non-reversible response), by storing the energy elastically (reversible response), or through a combination of both of these two extremes. Dynamic mechanical method makes it possible to detect variation of both contributions as a function of temperature or deformation rate and to determine in this way the spectra of relaxation processes which control the viscoelastic behavior of a given material. The mechanical behavior is often a key criterion for a possibility of application of the materials even if some other properties (e.g., optical or electrical) are effectively used. As a result mechanical spectroscopy is a widely used experimental technique both as a material testing method and as a tool for analysis of the dynamics in complex polymer systems.

A very large variety of very complex macromolecular systems with specific molecular structures is available both in nature and as synthetic materials. The molecular structures are formed in order to fulfill specific functions or to contribute to formation of larger complex aggregates in order to achieve specific material properties. Recent progress in scientific techniques in chemistry and physics have made it possible, with increasing success, to manipulate atoms and molecules to create such novel structures with desired properties. Especially, in macromolecular science and technology, a lot of systems have been developed in which a controlled molecular architecture leads to self-organization of molecules to various supramolecular structures with interesting properties. The materials under consideration are generally complex macromolecular fluids in which various kinds of interactions and a predetermined atomic order within molecules contribute under certain conditions to formation of specific supramolecular order. Generally, all kinds of interactions present in a given system, like excluded volume, intramolecular bonds, dipoles, charges or incompatibility of molecular segments, can contribute to the self organization processes. By a specific molecular design of atomic constitution and topology of bond

HOMOPOLYMERS

linear   cyclic   star   comb   microgel   network

BLOCK COPOLYMERS
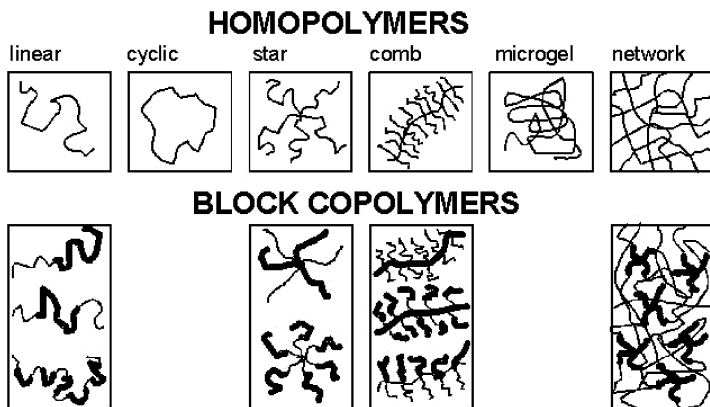
Fig. 16.1. Illustration of various macromolecular structures differing by the topology of bond skeletons and distributions of comonomers in copolymer systems

skeletons of molecules, contributions of various interactions can be controlled to a large extent. Some typical examples of such self assembling macromolecular structures are presented in Fig. 16.1, in which the topology of molecular skeletons and the atomic constitution within chains is varied. Various classes of systems can be generated by changing only these two parameters.

Figure 16.2 shows an example of structures to which a linear block copolymer system can organize in a condensed state. The hierarchical nature of order extending over many decades of the size scale, is illustrated. The broad size range of structures in such systems involves a broad variety of related relaxations which contribute to the dynamics extending over an extremely broad time range sometimes exceeding the observation possibilities. The dynamic spectrum of such materials becomes very important for understanding the correlation between parameters of the molecular and supramolecular structures on one hand, and macroscopic properties on the other. Analysis of these correlations appears to be extremely difficult and usually requires application of many experimental techniques for characterization of both the structure and the dynamics. In this chapter, dynamic mechanical measurements will be considered as a source of information about the dynamics consisting of relaxation processes in various polymeric systems.

Despite the structural and related dynamical complexity of polymeric materials, the phenomenological description of the mechanical behavior of the systems is rather simple and based on rather simple models [1, 2]. The two limiting behaviors – the elastic behavior of a solid and the viscous behavior of a liquid – are characterized by the well-known simple linear relationships between stresses and strains or strain rates and are given by Hooke's and Newton's laws, respectively. Polymers are usually considered as viscoelastic materials. The simplest viscoelastic behavior can be represented by a single relaxation time Maxwell model which describes the dynamic transition between the elastic and viscose regimes corresponding to times shorter (higher frequencies) and longer
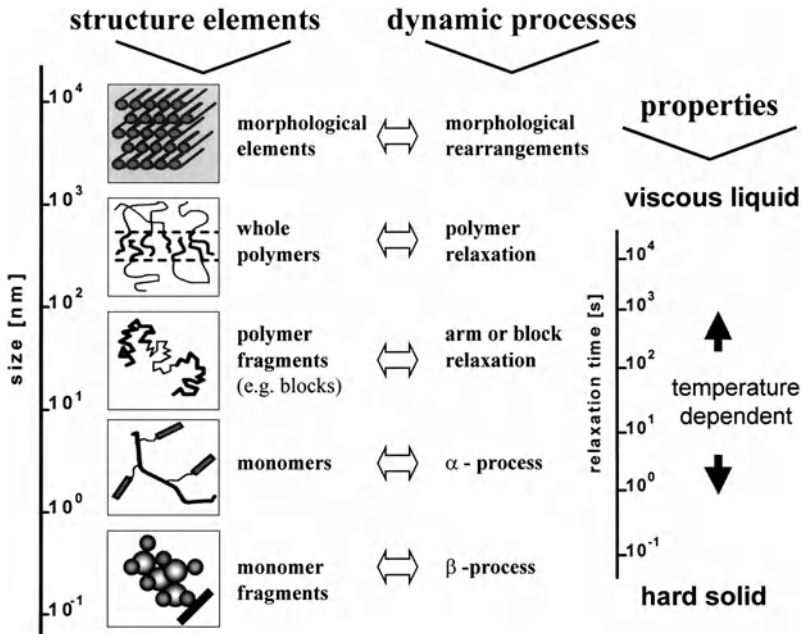
Fig. 16.2. Illustration of structures which can be detected at various size ranges in a block copolymer system and corresponding dynamic relaxation processes which extend over a very broad time range. The rates of relaxations and consequently the properties which can vary between a hard solid and a viscous liquid are additionally controlled by temperature

(lower frequencies) than the relaxation time, respectively. Polymers such as for example those illustrated in Figs 16.1 and 16.2 are characterized not by one but by several relaxation mechanisms with different relaxation times and can only be represented by a set of relaxing elements considered, for example, as connected in parallel when the assumption can be made that the interaction between the relaxation processes during the course of deformation is negligible. Each relaxation transition means usually a switching on and off a particular type of motion in the system and separates two dynamically different states of the material with different properties.

Formally there are many analogies between the behavior of materials in the electrical field and the above described cases of the mechanical responses. An ideal isolator can be regarded as analogue of the elastic solid and an electrical conductor as an analogue of the viscose liquid. Hence viscoelastic response has its analogy in dielectric relaxation, and both the experiments and the formalisms used to describe the results of dielectric and mechanical spectroscopies have many similarities. In this chapter mainly the mechanical spectroscopy technique and related results will be described but a correspondence to the results of the dielectric spectroscopy will be shown whenever possible. A comparison of these two techniques has already been considered earlier by other authors (e.g., [1, 3]), as well as, in the former chapters of this book (see Chaps. 1 and 3).

16.2
Principles of Mechanical Analysis

Force and deformation are the two physical quantities which accompany any mechanical testing of a material. The mechanical experiment consists usually in determination of a relationship between stress (force normalized with respect to the cross-section of the sample) and strain (deformation normalized with respect to the original shape or dimension of the specimen). Such relations are characteristic for materials and are called "constitutive relationships". Strains and stresses are generally tensors of the second rank each characterized by a number of components related to a given deformation state. Consequently, the quantities describing relations between strains and stresses are tensors of the fourth rank which in the most general case require specification of 36 components. Depending on the way in which the forces are applied to the material, various kinds of deformation can be distinguished and various components of the more general relations between strains and stresses can be determined. As examples, tension, simple shear and compression are illustrated in Fig. 16.3. For an elastic material, the three types of deformations allow one to determine the Young's modulus ($E_Y = \sigma/\varepsilon$), the shear modulus ($G = \sigma/\gamma$), and the compression modulus ($K = p/\Delta$) as ratios of corresponding stresses and deformations.

The procedure of properties analysis can generally be considered as an input-output system in which the input signal in the form of time dependent force or deformation is applied to a sample, which is kept under an environmental control (e.g., temperature, humidity, etc.), and the output signal as resulting deformation or exerted force, respectively, is monitored in time and related to the input signal. Various input functions including periodic ones have been applied in various variants of mechanical techniques.

The two simplest limiting behaviors, the elastic for solids and the viscous for liquids, are characterized by the simple linear relationships given by Hooke's law

$$\sigma = G \cdot \gamma \tag{16.1}$$

Fig. 16.3. Examples of various deformation modes (tension, shear, and compression) used in the mechanical analysis of materials. *Arrows* correspond to forces applied to the sample. *Dashed and solid lines* illustrate sample forms in the non deformed and deformed state, respectively

Tension σ – tensile stress

strain $\varepsilon = \Delta L/L_o$

Simple Shear σ – shear stress

shear $\gamma = \theta$

Compression p - pressure

compression $\Delta = \delta V/V$
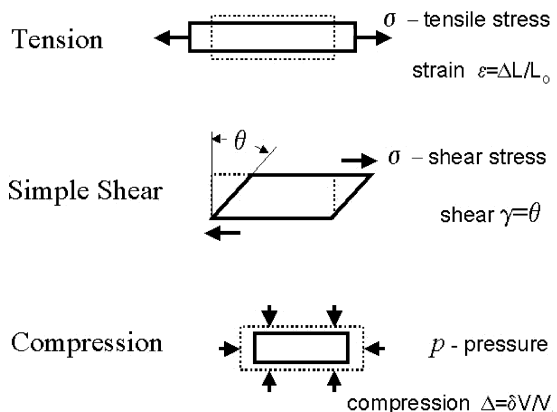
and Newton's law for fluids

$$\sigma = \eta \cdot \frac{\mathrm{d}\gamma}{\mathrm{d}t} \tag{16.2}$$

respectively. The corresponding material constants are the elasticity modulus G and the viscosity η. The simplest description of a viscoelastic behavior is provided by the Maxwell model with a single relaxation time:

$$\sigma(t) = \sigma_0 \cdot \exp\left(-\frac{t}{\tau}\right) \tag{16.3a}$$

which describes the time dependent stress relaxation related to the dynamic transition between the elastic and viscose regimes corresponding to times shorter and longer than the relaxation time τ, respectively. Considering an instantaneous deformation γ_0 related to the initial stress the behavior can be represented by means of a relaxation modulus

$$G(t) = \sigma(t) / \gamma_0 = G_0 \cdot \exp\left(-\frac{t}{\tau}\right) \tag{16.3b}$$

which describes the decay of perturbation introduced by the initial deformation. This formula goes beyond the Maxwell model, it corresponds to the Debye-relaxation function used in the dielectrics, and can be regarded as a basic relation for the simple relaxation process (see Chap. 3). An example of responses of the model materials to a single step stress function as an input is illustrated in Fig. 16.4. Immediate reaction and a unique correspondence of strain to stress is seen for the ideal elastic system whereas the viscous behavior is characterized by the irreversible response which can be considerably delayed with respect to the applied stress. In the case of the viscoelastic system much more complex strain functions are detected both at switching on and after switching off the stress.

Fig. 16.4. Mechanical experiment considered as an input-output system. Examples of responses (strain vs time) of various model materials (elastic, viscous, and linear viscoelastic) to a rectangular stress signal are shown
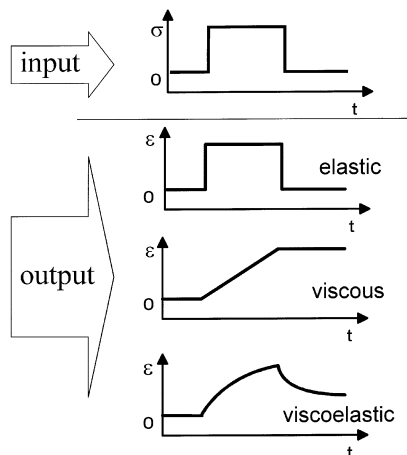
Fig. 16.5. Responses of the three model materials (elastic, viscous, and linear viscoelastic) to the sinusoidal deformation. The stress (output signal) is shown in comparison with the deformation (input signal)
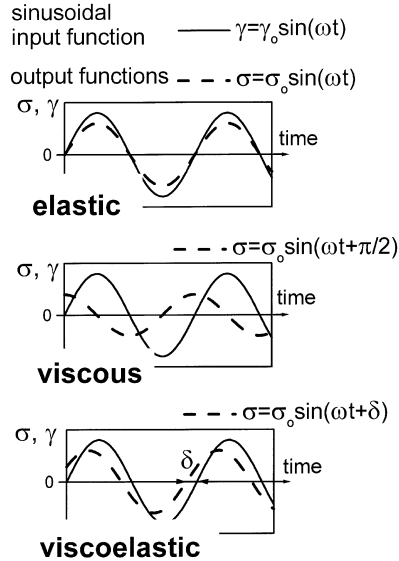
In a dynamic mechanical experiment, a sinusoidal strain is usually applied to a material and the resulting stress is measured. The stress signal is then separated into two components: an elastic component which is in phase with the applied strain, and a viscous component which is in phase with the strain rate, or 90° out of phase with the strain. In this way, both the stress-strain relation and the stress-strain rate dependence can be measured, giving information on both the elastic and viscous components of the properties. The input-output relations become in this case relatively simple. Illustration of responses for the three different types of material behavior are shown in Fig. 16.5. The behavior is considered as linear when the output functions remain sinusoidal and differ only by amplitude and phase shift from the sinusoid at the input.

16.3
Linear Viscoelastic Behaviour

Formally, the properties of linear viscoelastic materials are usually described by the storage G' and loss G'' moduli, representative for the elastic and viscous components, respectively. These properties of materials are usually determined by applying sinusoidal shear strain of amplitude γ_0 and frequency ω. The shear strain as a function of time is

$$\gamma(t) = \gamma_0 \sin(\omega t) \tag{16.4}$$

and the corresponding shear strain rate

$$\dot{\gamma}(t) = \gamma_0 \omega \cos(\omega t) \tag{16.5}$$

For the linear response the resulting shear stress will also be sinusoidal but can be shifted in phase as follows:

$$\sigma(t) = \sigma_0 \sin(\omega t + \delta) \tag{16.6}$$

where δ is the phase shift angle and σ_0 is the stress amplitude. The phase angle is limited ($0 < \delta < \pi/2$) and can be regarded as characterizing the distribution of the deformation energy into the two fractions: (1) the energy stored in the system as an elastic deformation and (2) the energy lost irreversibly due to flow. For purely elastic behavior δ is zero, and the ratio between shear stress and strain is constant in time. For viscous behavior $\delta = \pi/2$ and the ratio between the shear stress and strain rate becomes constant (Fig. 16.5).

The shear stress is usually written as a trigonometric identity as follows:

$$\sigma(t) = \gamma_0 [G'(\omega) \sin(\omega t) + G''(\omega) \cos(\omega t)] \tag{16.7}$$

The storage and loss moduli are also often considered as the real and imaginary parts of the complex dynamic modulus, $G^*(\omega) = G'(\omega) + iG''(\omega)$. Both real and imaginary parts of the complex modulus are functions of frequency with a characteristic behavior at frequencies around the relaxation frequency of structural units in a simple viscoelastic system. An example of such behavior is illustrated schematically in Fig. 16.6 by using the $G'(\omega)$ and $G''(\omega)$ dependencies determined for the simple Maxwell model which gives explicit formulas for these dependencies (e.g., [2]):

$$G'(\omega) = G_0 \omega^2 \tau^2 / (1 + \omega^2 \tau^2) \tag{16.8}$$
$$G''(\omega) = G_0 \omega \tau / (1 + \omega^2 \tau^2) \tag{16.9}$$

In the high frequency range the plateau of G' and the low G'/G'' ratio ($G' \gg G''$) are both characteristic for the elastic behavior (Hookean). The elastic shear modulus describing the material properties in this range is given by

$$G_0 = \lim_{\omega \to \infty} G'(\omega) \tag{16.10}$$

In the low frequency limit the behavior typical for the Newtonian flow is seen for which $G'' \gg G'$ and where G' and G'' obey the characteristic proportionalities to ω^2 and ω, respectively. Here the system can be characterized by the complex viscosity $\eta^*(\omega)$ given by

$$\eta^*(\omega) = \frac{G^*(\omega)}{i\omega} \tag{16.11}$$

The value of the complex viscosity $\eta^*(\omega)$ is equal to the kinematic viscosity η *only* if $G'' \gg G'$. Only in this range is the viscosity a meaningful material property and the complex viscosity can approach here the value of the zero shear viscosity

$$\eta_0 = \lim_{\omega \to 0} G''(\omega) / \omega \tag{16.12}$$

The two limiting types of behavior are separated by the intermediate cross-over region in which the system can be regarded as typically viscoelastic. The point at which G' and G'' cross each other determines the place (ω on the frequency scale) which is related to the relaxation time of the structural units constituting the system ($\tau = 1/\omega$). In the simple example of the relaxation represented by the Maxwell model, the G'' assumes a maximum and the lines $\log G'$ and $\log G''$ vs $\log \omega$ extrapolated from low to higher frequencies cross each other at the same frequency directly related to the relaxation time. These characteristic points in the G' and G'' vs ω dependencies are sometimes used to determine the relaxation times in real systems in which, however, the correspondence of these points to the relaxation times is only approximate. In real systems the relaxation is more complex and usually extends over a broader frequency range than in the simple example shown here, making an impression that they would consist of a variety of relaxation effects with various relaxation time spectra around the time corresponding to the cross-over point.

Figure 16.6 gives an example of a possible structural interpretation of the mechanically observed relaxation which can be considered for molecular or colloidal systems. For the dense system of spheres, which can be regarded as representing molecules or particles, there is the solid-like state at higher and the liquid-like state at low frequencies. The nature of these states is illustrated in the figure by particle trajectories. In the high frequency regime they indicate only vibrational motions and quasi localized positions of particles between the
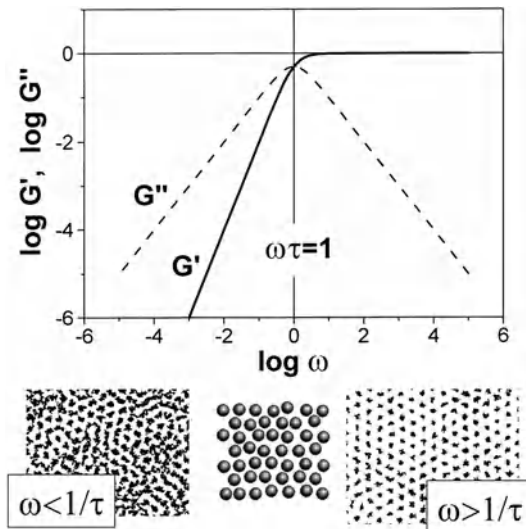
Fig. 16.6. Frequency dependencies of the real (G') and imaginary (G'') parts of the modulus and the viscosity (η) for the simplest relaxation model (Maxwell) with a single relaxation time (τ). Different behavior of elements in the systems of spherical particles below and above the frequency corresponding to $1/\tau$ is illustrated by trajectories of sphere centers in a short time interval. Ordered non-mobile systems (high frequencies) becomes mobile (low frequencies) due to the relaxation process involving longer range translations

neighbors, whereas at low frequencies displacements exceeding particle sizes make the system viscous – changing neighbors becomes possible. According to such a model, the relaxation is related to the position correlation of particles and the mechanical response can be considered as a Fourier transform of the position autocorrelation function with the characteristic relaxation time necessary for particles to escape from the surroundings of the initial neighbors. The single exponential correlation function ($\rho(t) = \exp(-t/\tau)$) constitutes the case equivalent to the Maxwell model when the relaxation is observed in the time domain.

If the considered structural units are bounded to or constitute fragments of some larger structure elements their complete relaxation with the single relaxation time is impossible. They can flow only locally within the size range controlled by the size and flexibility of the larger structure. In order to relax completely they have to wait until the larger structure with all constituting elements will become mobile. Such unrelaxed part manifests itself by a low frequency plateau in G' which can extend over a frequency range corresponding to the relaxation time of the larger structure.

In analogy to the described mechanical behavior, in dielectric experiments an alternating electric field (sinusoidal input function) with amplitude E_0

$$E(t) = E_0 \sin(\omega t) \tag{16.13}$$

produces an electric polarization which in the case of most polar materials will show a frequency dependent lag (δ) with respect to the applied field

$$P(t) = P_0 \sin(\omega t + \delta) \tag{16.14}$$

where P_0 is the frequency dependent polarization amplitude. The polarization results from displacements of charge clouds of opposite signs in response to the applied external field. In analogy to the formalism described above for the mechanical field we can define an electric modulus

$$M^*(\omega) = M'(\omega) + iM''(\omega) \tag{16.15}$$

with the frequency dependent real and imaginary parts $M'(\omega) = \varepsilon_0 (E_0/P_0) \cos \delta$ and $M''(\omega) = -\varepsilon_0 (E_0/P_0) \sin \delta$, respectively. ε_0 is the electric permittivity of the vacuum. At the relaxation processes, i.e., when the charges become in some way mobile, the electric modulus components should behave analogously to the example shown in Fig. 16.6 and such a process can in general be considered as a transition between an insulator at high frequencies and a conductor at low frequencies; however, the spatial range of charge motion can be limited. For most relaxation processes the charges get only a very local mobility because they remain bounded to molecular structures. In the case of materials with permanent dipoles the motion of charges involved by the external field results in a dipole reorientation (see discussion in Chap. 1).

16.4
Experimental Procedures and Typical Data Analysis

Dynamic mechanical measurements are usually performed by means of a mechanical spectrometer which, depending on the source of the instrument, can be used in various types of time dependent measurements. The most frequently used experimental arrangement is schematically illustrated in Fig. 16.7. The sinusoidal input signal is supplied to the motor and the resulting torque is measured by the transducer which in some spectrometers is also capable of measuring the normal force (the force in a direction normal to the plates) exerted by the sample subjected to shear between the parallel plates.

Depending on the sample state (solid, melt, or solution) various test geometries are used as illustrated in Fig. 16.8. The first two geometries plate-plate (a) and cone-plate (b) are typically used for melts, the rectangular bars (c) are used when materials under examination are solids, and the couette (d) geometry can be applied for polymer solutions or for liquids. The geometry can be varied for the same material when the properties change considerably as, for example, with changes of temperature.

Shear or in some cases tensile deformation can be applied under condition of controlled deformation amplitude, which should remain in the range of the linear viscoelastic response of studied samples. The storage (G') and loss (G'') shear modulus can be measured in various procedures, such as single point, frequency sweep, temperature sweep (both cooling and heating), amplitude or time sweep, etc. Experiments can usually be performed under dry nitrogen atmosphere. The typical frequency range accessible for the spectrometers is between 0.001 and 500 rad s^{-1}. The temperature can usually be varied in a broad range,
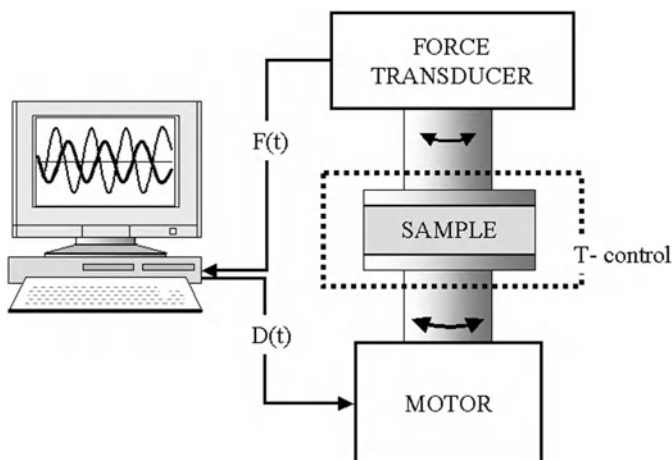
Fig. 16.7. A scheme of the dynamic mechanical spectrometer system. The sample is sheared between parallel plates by means of a motor controlling the deformation signal $D(t)$ and the resulting torque signal $F(t)$ is recorded and analyzed in comparison with the deformation. The sample is under environmental control
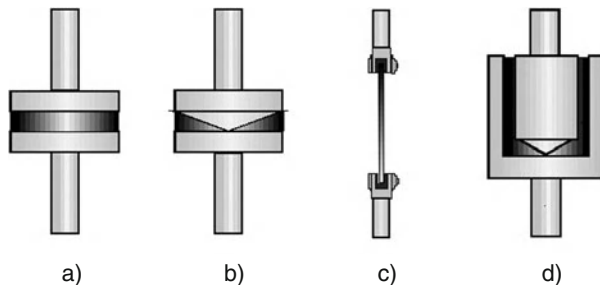
Fig. 16.8. Illustration of various sample geometries: **a** plate-plate; **b** cone-plate; **c** rectangular bar; **d** couette used in application to various states of materials (melt, solid, solution, etc.)

i.e., between −150 and 600 °C. In order to overcome the problem of very limited frequency range (especially in comparison with the dielectric spectroscopy), master curves are constructed which combine results of measurements performed at various temperatures to a single reference temperature but representing the material properties in a much broader frequency range (Fig. 16.9).

In order to do that, the frequency dependencies of G' and G'' measured, for example, within the frequency range 0.1–100 rad s^{-1} at various temperatures are used. In the construction of the master dependencies only shifts along the frequency scale should be performed under the condition that the geometry is adjusted with the temperature changes in order to account for the thermal expansion of the sample and the expansion of the tools. This procedure provides the broad range frequency dependencies of G' and G'', as well as a temperature dependence of shift factors (log a_T vs T). The low frequency range of the master dependence of G'' (with $G'' \sim \omega$, indicating the Newtonian flow range) can be used to determine the zero shear viscosity at the reference temperature ($\eta_0(T_{ref}) = G''/\omega$). Viscosity values related to other temperatures can be determined as $\eta_0(T) = \eta_0(T_{ref}) + \log a_T$.

The relaxation time corresponding to the transition between the Newtonian flow range at low frequencies and the rubbery plateau range at higher frequencies can usually be determined as $\tau(T_{ref}) = 1/\omega_c$, where ω_c is the frequency at which the G' and G'' dependencies cross each other. For the transition to the glassy range (high frequencies) the same procedure can be applied in order to get the segmental relaxation times at the reference temperature. Relaxation times at another temperatures are then given by $\tau(T) = \tau(T_{ref}) + \log a_T$.

The described procedure leading to the master curves has considerable limitations. It can be applied for a limited class of materials which are considered as rheologically simple and usually within a limited temperature and frequency range. It seems to work for various amorphous polymers at conditions allowing to detect segmental and slower relaxations. It does not work for materials changing structure or in the temperature-frequency range where relaxations with different temperature dependencies of relaxation times overlap.

An example of temperature dependencies of G' and G'' recorded with various deformation frequencies for a poly(methyl methacrylate) sample [4] is
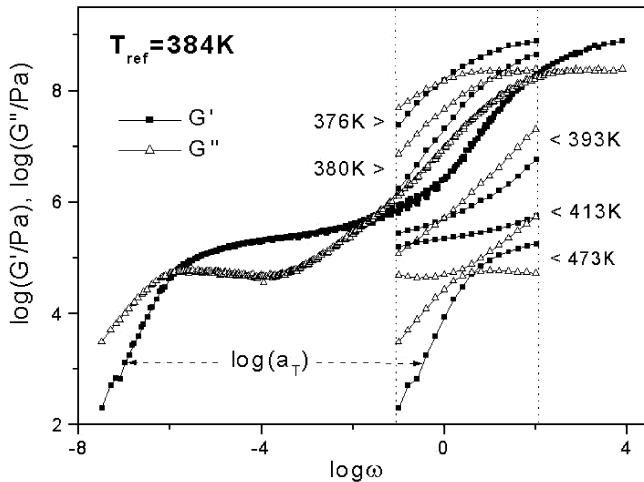
Fig. 16.9. Illustration of a construction of a master frequency dependencies of G' and G'' for a polystyrene melt ($M_w = 200{,}000$) taken as an example. Frequency dependencies of G' and G'' are measured at various temperatures in a frequency range indicated by the *vertical dotted lines*. One of these dependencies is taken as a reference and all other are shifted along the frequency scale only by $\log a_T$ to overlap with dependencies measured at adjacent temperatures and to form finally the continuous master curve corresponding to the reference temperature. The data measured at the reference temperature are not shifted. For the clarity of the figure only some data measured at various temperatures are shown

shown in Fig. 16.10. It is interesting to notice that the results for various frequencies have been obtained simultaneously using the so-called multiple frequency sweep technique in which the sample during a single temperature ramp is subjected to deformation being a superposition of sinusoidal signals of different frequencies. A strong effect of frequency on the relaxation rates is observed. Exceptionally in Fig. 16.10, the $\tan\delta$ values are included in order to demonstrate that the positions of the $\tan\delta$ maxima can be displaced considerably with respect to the maxima of G'' and cannot be taken as an indication of the positions of relaxation processes on the temperature scale. The maximum of $\tan\delta$ appears between two relaxation processes and only when a slower process exists. Therefore for the terminal relaxation (at higher temperature) $\tan\delta$ does not have a maximum.

Measurement techniques in dielectric spectroscopy have been discussed in various parts of this book (see Chap. 2). An analogy already mentioned earlier between dielectric and mechanical spectroscopy can clearly be seen. To some extent similar sample geometries, similar forms of signals at input and output, and similar data analysis are used. The procedure of master curve construction can also be applied to dielectric spectroscopy results but is not often used because of the extremely broad frequency range accessible to dielectric spectroscopy techniques at constant temperature. Nevertheless, an example of an attempt to construct a master dependencies of the electric modulus is illustrated in Fig. 16.11. It works reasonably in a limited frequency range but parts corre-
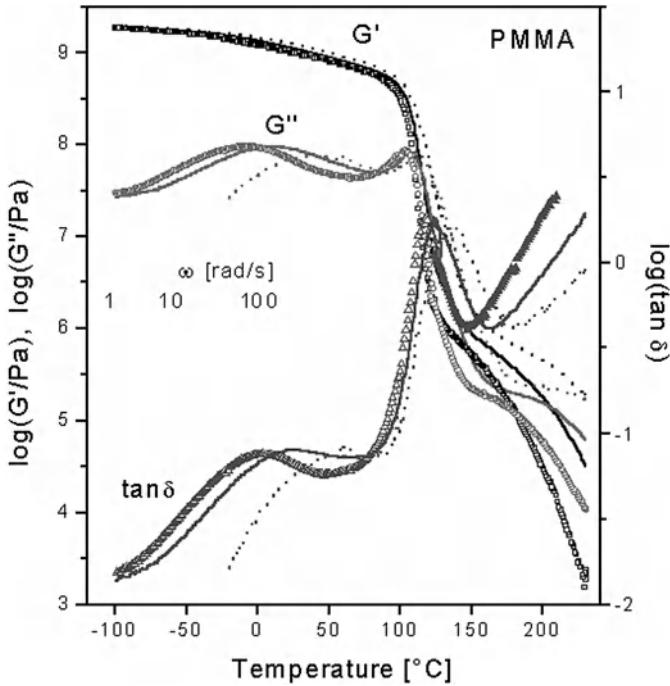
Fig. 16.10. Temperature dependencies of G', G'', and $\tan\delta$ for a PMMA bulk sample ($M_w =$ 100,000) at three different modulation frequencies applied simultaneously
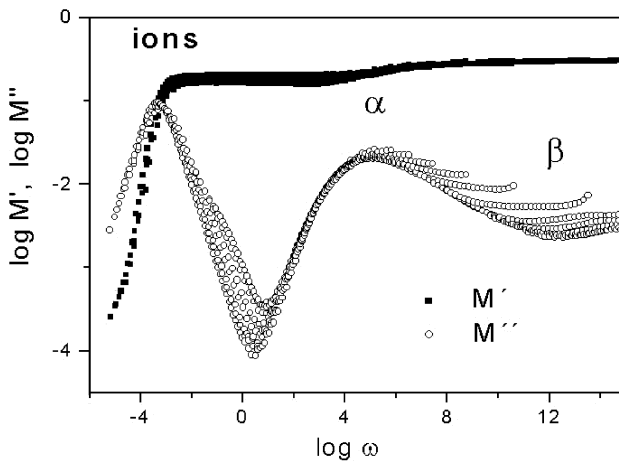
Fig. 16.11. An example of the electrical modulus spectrum as determined for a poly(n-butyl acrylate) melt ($M_w = 36,000$) at the reference temperature of 254 K. In order to obtain the master dependencies, both the real (M') and imaginary (M'') components measured at a given temperature have been shifted along the frequency scale simultaneously (in analogy to the procedure illustrated in Fig. 16.9)

sponding to different relaxations do not overlap, because of different temperature dependencies of the relaxation times for the different processes.

16.5
Differences in Data Treatment

Despite the analogies between dielectric and mechanical spectroscopy methods, different traditions in the representation of results have been developed in these two research techniques. As described in the former paragraph, the modulus has mainly been used for representation of results in mechanical spectroscopy, whereas, in dielectric spectroscopy the data have usually been represented as the dielectric permittivity (see, for example, Chaps. 1 and 3). The dielectric permittivity differs by 1 from the susceptibility which constitutes the reciprocal value of the electric modulus defined in the former section.

In order to compare results obtained by the two techniques, mechanical and dielectric, for a given material, at first, a common formalism should be considered. The modulus representation of the dielectric spectroscopy results has been suggested by Macedo et al. [5], mainly for highly conducting materials but it remains equally suitable for representing the dielectric relaxation [6] and it will be used throughout this chapter in order to avoid effects of data representation on the results when different methods are compared. It is known that the content of information in various representations is the same; nevertheless, this

Fig. 16.12. Frequency dependencies of: **a** real and imaginary components of the modulus; **b** real and imaginary parts of complex susceptibility for the Maxwell model
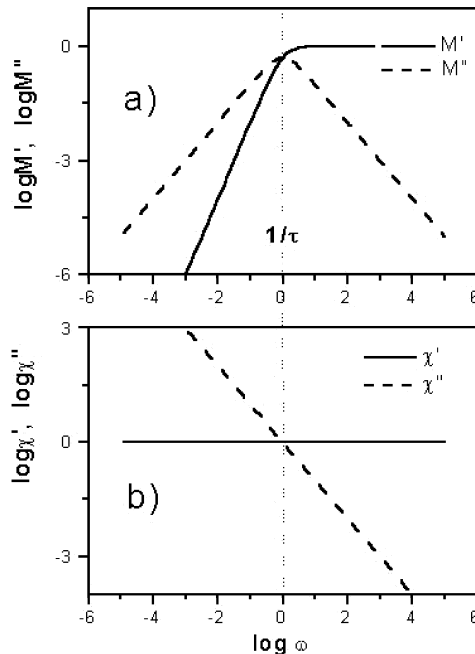
problem still constitutes a controversy both in mechanical and dielectric spectroscopy. It is important to recognize from other authors [1, 6] that the characteristic times determined from various representations of data have different meanings and can assume values which can considerably differ between each other. Taking into account the controversies and possible uncertainties in interpretation of results it is worthwhile to clarify this point here. For a single Maxwell relaxation process the modulus and susceptibility representations are compared in Fig. 16.12.

The complex modulus representation of such relaxation (Fig. 16.12a) has a number of characteristics which are clearly related to the relaxation rate. These are the maximum in the M'' and the cross-point of M' and M'' both at the $\omega\tau = 1$, the plateau of M' for $\omega \gg 1/\tau$, and the characteristic slopes 1 and 2 in the double logarithmic plots of M'' and M' vs ω, when $\omega \ll 1/\tau$. On the other hand, the complex susceptibility is rather featureless in this frequency range (Fig. 16.12b). The real part remains constant and the imaginary part keeps the constant slope of -1. There is no maximum in the imaginary part of susceptibility which could be related to the relaxation time and only the cross-point of the χ' and χ'' indicates the relaxation process. In the susceptibility representation only a superposition of two relaxation processes can create a maximum in the imaginary part as illustrated in Fig. 16.13.

Fig. 16.13. Frequency dependencies of: **a** the real and imaginary components of modulus; **b** the real and imaginary parts of complex susceptibility for a superposition of two relaxation processes differing by relaxation times (τ_1 and τ_2) and with a variable amplitude of the slower component. The three cases with different amplitude of the slower process are denoted as A, B, and C
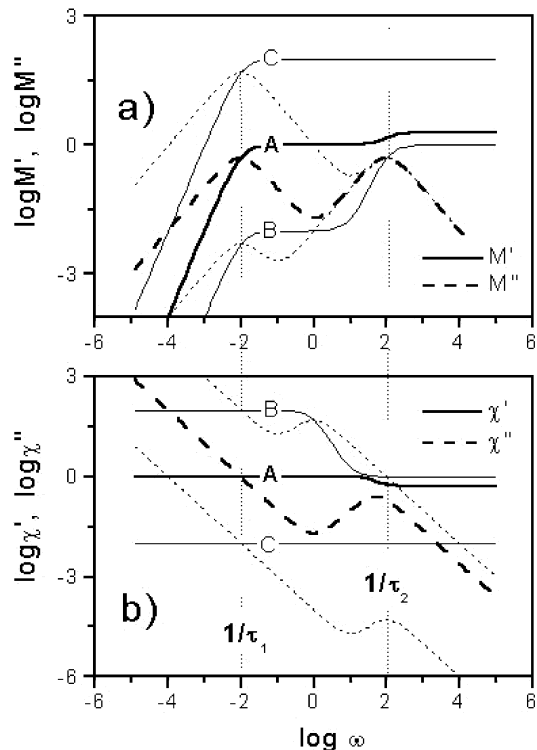
The susceptibility maximum appears only when a non relaxed part (in this case as a second slow relaxation process) is present. Moreover, the susceptibility maximum can coincide with the maximum in the imaginary modulus only when the amplitude of the faster relaxation is very small. Otherwise, the susceptibility maximum describes the retardation time which can differ considerably from the relaxation times of the assumed processes. The examples in Fig. 16.13 show the effect of amplitude of individual processes on their superposition. They illustrate that some arbitrary point will be considered as a relaxation when the susceptibility maximum is taken as an indicator. On the other hand, the assumed relaxations are very well distinguishable in the modulus representation of the superposition. Taking this into account, the modulus representation will be preferred here for both mechanical and dielectric spectroscopy.

16.6
Typical Behaviour of Polymeric Materials

16.6.1
Melts of Linear Polymers

In complex systems like bulk polymers, structural units of considerably different sizes, i.e., the monomers and polymer chains, relax with rates which can differ from each other by many orders of magnitude. Therefore, the observed frequency dependencies of G' and G'' indicate more than one relaxation region as illustrated already in Fig. 16.9. The two different relaxation ranges observed for the polymer melt at low and high frequencies correspond to structural rearrangements concerning the two different structural units, i.e., monomers and

Fig. 16.14. Depiction of: a electric; b mechanical modulus spectra (master curves) for a linear polyisoprene melt ($M_w = 50,000$). The *vertical dashed lines* indicate positions of M'' maxima
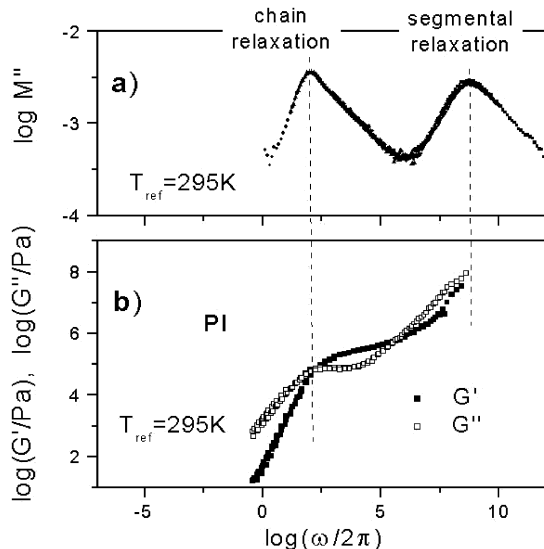
polymers, respectively. The ranges characteristic to flow and elastic response appear now at various deformation rates and correspond to different size scales in the examined system. The separation of the processes is strongly dependent on the molecular weight of the polymer.

For polymers having a segmental dipole moment which is oriented at some angle with respect to the polymer chain contour, the perpendicular and parallel components of the dipoles can reflect the segmental and chain relaxation, respectively. Figure 16.14 shows an example of results characterizing the viscoelastic behavior of a polyisoprene sample in comparison with the dielectric measurements represented as the frequency dependence of the electric modulus [7]. The dependencies shown, both dielectric and mechanical, are "master curves" which have been obtained by means of the procedure described in Sect. 16.4. Such results correspond to the behavior of the studied material at a chosen reference temperature T_{ref}. The shift factors are considered as reflecting differences in the elementary relaxation rates at the reference and the measurement temperatures. The procedure works well for melts of amorphous polymers in which temperature independent structure and temperature independent relaxation spectrum can be assumed or experimentally detected.

This result shows a good coincidence of the chain relaxation times but some differences in rates of relaxation of the polymer segments. This is more precisely seen in Fig. 16.15, in which the relaxation times determined from results of the two methods are presented. The comparison of temperature dependencies of the relaxation times obtained from the two methods indicates the very good coincidence of the terminal relaxation times determined from mechanical results and the normal-mode relaxation times determined from dielectric measurements [8]. Even though the results from different methods overlap only within a relatively narrow temperature range (determined by experimentally accessible conditions), they can be very well described by a single WLF-re-

Fig. 16.15. Temperature dependencies of the segmental and chain relaxation times determined from mechanical and dielectric spectra of the linear polyisoprene melt
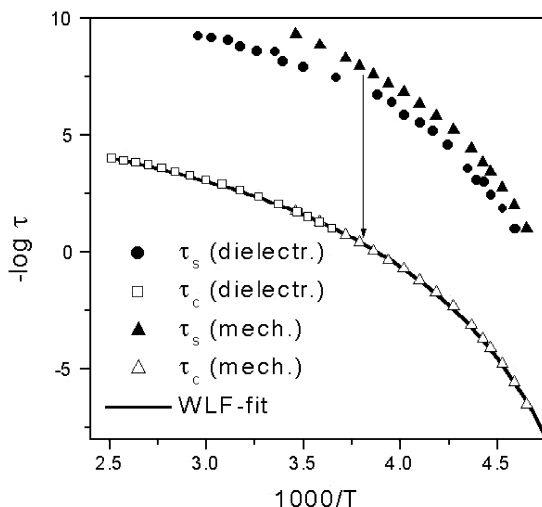
lation, shown by a solid line (WLF parameters: $T_{ref} = 250$ K, $C_1 = 7.05$, $C_2 = 77.7$ K, $f_{250} = 4.03$ Hz).

Despite the coincidence of chain relaxation times, there is a gap between relaxation times related to segmental processes determined by the two methods. The gap between the two relaxation times seems to be temperature independent and is attributed to the fact that the two methods detect relaxations of different units of the local chain structure. On the other hand, the observed coincidence of the terminal relaxation times determined by the two methods indicates that in both cases orientational relaxation of linear chains is detected. It should be mentioned that polyisoprene is a quite exceptional polymer for which the comparison of mechanical and dielectric results concerning both segmental and chain relaxation is possible, due to the location of segmental dipole moments within the backbone and their specific orientation with respect to the chain contour [9, 10]. For many other polymers, one or both relaxation modes observed here are non-active dielectrically because of a lack of dipoles or because of location of dipoles in side groups showing relaxation modes differing from these illustrated here.

16.6.2
Block Copolymer Systems

The specific property of polyisoprene allowing one to detect simultaneously both segmental and normal relaxation rates has been used in many cases to measure selectively relaxation of molecular fragments as, for example, in block copolymers [8, 11]. Using copolymers of polyisoprene and polybutadiene it was, for example, possible to detect relaxation times of polyisoprene blocks of various lengths located at various positions within linear chains. The dielectric spectroscopy has in this case been used for selectively sensing the relaxation of polyisoprene blocks and the mechanical spectroscopy, non selective, but providing information about the relaxation of whole copolymer chains [8], as shown in Fig. 16.16.

The interpretation of results concerning copolymers has been made under the assumption that the miscibility of polybutadiene and polyisoprene in the temperature range used created an average segmental mobility of both components. This was justified by single segmental relaxation processes observed in copolymers, independent of their composition, both by means of dielectric and mechanical measurements, as well as by a continuous shift of T_g of copolymers with their composition, within the range between the glass transitions temperatures of components. Under this assumption, the block relaxation times can be regarded as describing relaxation of fragments of a uniformly relaxing linear chain. Within the accuracy of this assumption the results have indicated that there is a considerable discrepancy between the experimental observations and predictions of the reptation theory which, however, does not indicate a non-validity of the reptation mechanism of chain motion, but rather is caused by an incomplete theoretical solution of the model postulated [8].

For disordered states of block copolymers, as in the case shown above, the viscoelastic behavior is usually similar to that observed for homopolymer melts.

Fig. 16.16. An example of frequency dependencies of viscoelastic (G' and G'') and electric (M'') quantities (master curves) for a tri-block copolymer melt with isoprene blocks at chain ends (IBI). Frequencies corresponding to segmental, block and chain relaxation are indicated
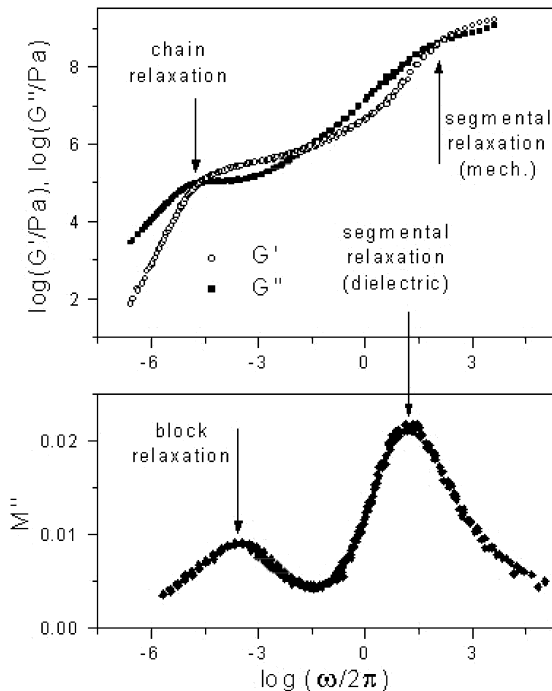
The two relaxation processes, the chain relaxation at low frequencies and the segmental relaxation at high frequencies, can be observed, although, in some cases, with a broadening or bifurcation in the range of segmental relaxation depending on the nature of comonomers. At temperatures higher than the order-disorder transition, the time temperature superposition (TTS) also usually works well and the moduli exhibit typical terminal behavior ($G' \sim \omega^2$ and $G'' \sim \omega$). When examined over a broad temperature range, however, TTS can be violated because of the order-to-disorder transition which drives the system from the disordered state to a microphase separated state [7, 12].

At temperatures smaller than the order-disorder transition temperature and at low frequencies, new ultra slow relaxation process related to morphological rearrangements appear and the moduli can exhibit weak frequency dependencies, which results from the plateau modulus of the slowest process. Unfortunately, quite often a complete relaxation of the microstructure of the copolymers cannot be observed within the accessible frequency and temperature window. An example of the behavior of such system is presented in Fig. 16.17 for the bulk styrene/isoprene diblock copolymer (SI) as characterized by means of the mechanical and dielectric spectroscopy.

Results for a nearly monodisperse sample ($M_w/M_n = 1.04$) with molecular weight $M_w = 65,000$ and 20.7 wt% of PS are reported. A spherical microdomain morphology has been detected for this system by means of the small angle X-ray scattering [7]. Two processes similar to those for the PI homopolymer (as in

Fig. 16.17. Frequency dependencies of: **a** the real and imaginary parts of the electric modulus; **b** the components of the shear modulus for the styrene isoprene block copolymer at indicated reference temperatures. *Vertical dashed lines* indicate the segmental and block relaxation processes of the isoprene component
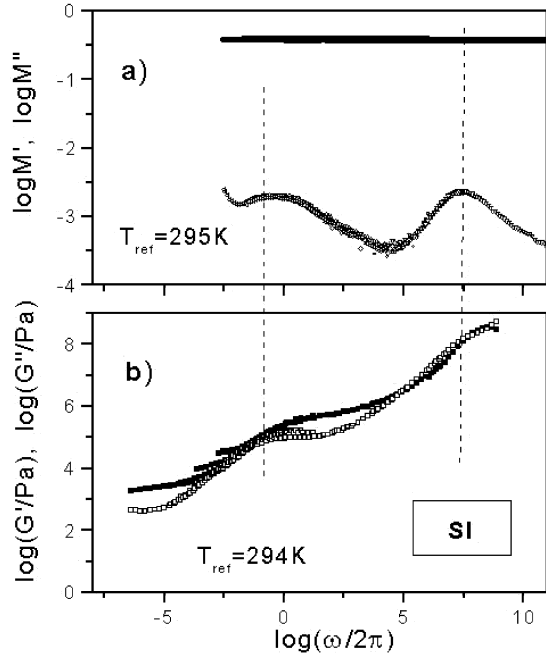
Fig. 16.14) are seen for the copolymer as well. In the case of the copolymer, they correspond to the segmental relaxation of the polyisoprene units (high frequency) and to the polyisoprene block relaxation in the microphase separated system (low frequency). Although the polyisoprene forms a continuous liquid matrix for the glassy PS microdomains, the copolymer sample does not flow at frequencies smaller than these corresponding to the polyisoprene block relaxation which means that no terminal relaxation process can be found besides the two relaxation processes attributed to the polyisoprene block chains.

This indicates a highly ordered phase of block copolymer micelles and the structural arrangement of the PS microdomains remaining maintained during the rheological experiment. This involves the clear plateau in the low frequency range for this sample. Such an effect can be considered as an example of the influence of the order-to-disorder transition on the frequency dependencies of G' and G'. It demonstrates the breakdown of TTS; the main effect is observed at low frequencies where the Newtonian behavior of the disordered state is replaced by a rubbery state related to non-relaxed morphology [7, 12].

Macroscopic flow of such material can be induced only by an increase of temperature above that of the presented measurements, where the microdomain structure could change to a more disordered state or by dilution of the micelles in a solvent or in the homopolymer matrix. An example of the later possibility is shown in Fig. 16.18 where the relaxation behavior of a homopolymer/copolymer mixture is presented. As in the two former cases, the two relaxation processes – the PI segmental relaxation and the relaxation of PI chains or blocks – are both detected also in the mixtures at characteristic frequencies. In the mixtures, how-

Fig. 16.18. Frequency dependencies of: **a** the imaginary part of the electric modulus; **b** the components of the complex shear modulus for the blend of a styrene-isoprene block copolymer and a polyisoprene at indicated reference temperatures. *Vertical dashed lines* indicate the PI segmental (τ_s), PI chain (τ_1) and structural (τ_2) relaxation processes; **c** the relaxation modulus $G(t)$ is shown as determined from the dynamic mechanical results presented in (b). The *solid line* in (c) represents the best fit of the sum of two stretched exponential decays, used to determine τ_1 and τ_2
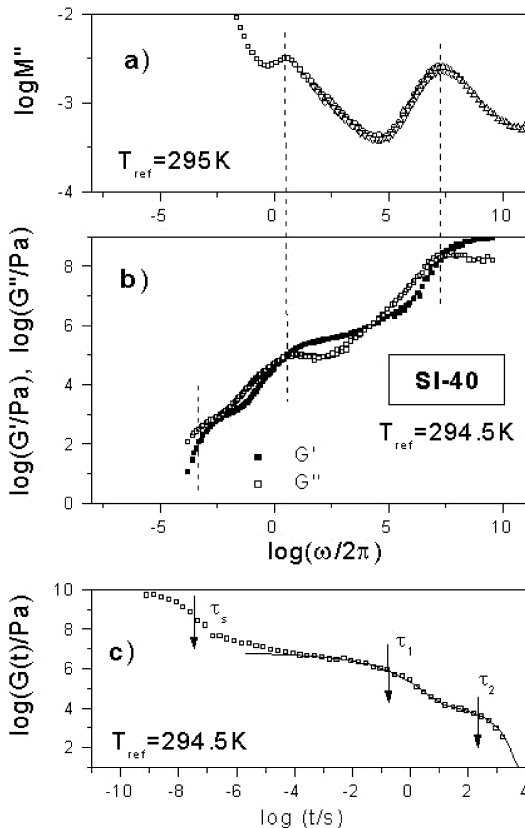
ever, a low frequency relaxation is additionally observed which partially overlaps with the PI chain relaxation for small copolymer concentrations but becomes well separated for higher copolymer content in the system. The appearance of this process is well correlated with the development of order between block copolymer micelles dispersed in the homopolymer matrix and can be attributed to a structural relaxation involving translational rearrangements of a certain number of micelles. This slow relaxation controls the cross-over to the terminal Newtonian flow regime of the mixture, and therefore it must be related to the onset of the global micellar mobility and can be regarded as the colloidal α-relaxation. Such mechanical response of the sample as that shown in Fig. 16.18 is to a large extent analogous to the behavior observed for other ordered melts as for example the melt of multiarm stars [13].

The two examples presented above of comparison of results from mechanical and dielectric spectroscopy have shown that such a comparison can considerably improve possibilities of assignment of observed relaxation processes. The unique assignment of the intermediate mode observed in the mechanical spectrum (Fig. 16.18b) to the relaxation of polyisoprene chains was only possible because of the specific localization of the dipole moments in the polymer chains

making the dielectric relaxation spectrum selectively sensitive to this type of motion. This appears particularly important for systems in which complex molecular architectures or complex morphologies make the response of materials to an external field rather complex.

16.6.3
Highly Branched Polymers

From the macromolecular structures shown in Fig. 16.1 the comb-like polymers, in a specific version known recently also as bottlebrush polymers [14], can be considered as more complex example of regularly branched macromolecules which, due to their specific architecture, assume a well defined shape with a characteristic intramolecular density distribution. They consist of a linear backbone with a high grafting density of side chains (usually one side chain per repeat unit of the backbone). It was reported that such macromolecules assume the shape of flexible cylinders with a large persistence length and a diameter related to density and length of side chains in solution. Bottle-brush polymers have also been directly visualized on surfaces by means of atomic force microscopy [15]. There is, however, little information about the dynamic behavior of such polymers in the condensed phase. Again here, an application of both discussed experimental techniques has helped in understanding the dynamic behavior of such systems. As an example, results of the dynamic behavior of poly (n-butyl acrylate) brushes are reported. The polymers have been synthesized by means of the grafting-from polymerization using controlled radical polymerization ATRP [16] with various macroinitiators and side chain monomers.

Three characteristic relaxation regimes can be distinguished in the polymer brush melt. They are indicated in Fig. 16.19 by arrows at frequencies that can be related to the corresponding relaxation times. The high frequency relaxation is identical with that observed in the melt of linear PnBA and is attributed to segmental relaxation, which is responsible for the solidification of the material to a glass at the highest frequencies. At low frequencies, on the other hand, a Newtonian flow regime is observed with the characteristic scaling of $G' \sim \omega^2$ and $G'' \sim \omega$. The transition to that flow regime is controlled by the slowest relaxation, which has to be attributed to the motion of entire brush molecules.

The relaxation, which can be distinguished in the intermediate frequencies must correspond to intramolecular relaxation of some well defined structural units and we attribute it to the side chain motion. A coincidence of the relaxation rate of that process with the rate of motion of linear chains having the length twice as large as the side chains in the bottle brush has been considered as supporting such an assignment. The deciding argument for the consideration of this process as a side chain motion came, however, from the dielectric spectrum illustrated in the insert of Fig. 16.19.

As can be seen, a process corresponding to the segmental relaxation is detected in this spectrum together with another strong slower relaxation which is attributed to motion of the bromine atoms present in this sample at the end of each side

Fig. 16.19. Frequency dependencies of the mechanical and electric modulus for a bottle brush poly(*n*-butyl acrylate) melt. *Lines* represent curves fitted to the data according to the formulas described in the text
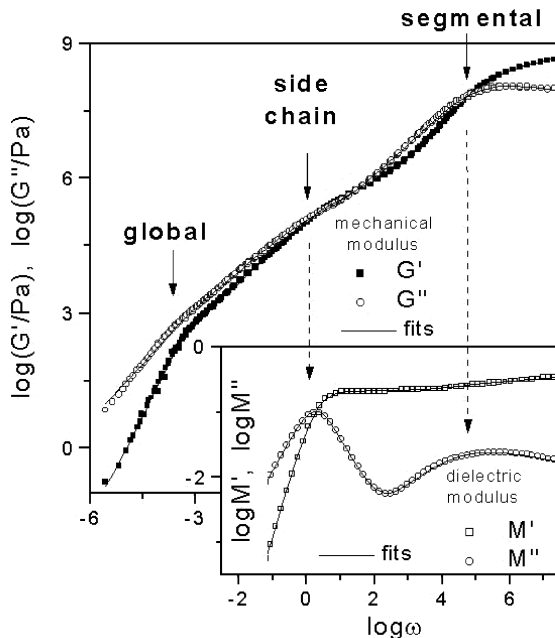
chain as a result of the polymerization mechanism in which the bromine atoms move with the side chains ends during their growth initiated at the linear backbone. It has also been observed that the length of side chains in the brush macromolecule influences both the intermediate and the terminal relaxation rate whereas changes of the backbone length affect only the terminal relaxation. Similar effects have been observed earlier for the multiarm polymer stars [13].

All this further suggests that the behavior of brush macromolecules at low frequencies can be regarded as analogous to the behavior of normal linear chains in melts with a shift on the size and time scales corresponding to the considerably larger "segment" of the brush. Instead of the series of monomers in normal linear polymers, in the brush one can consider a series of multiarm stars as macro-segments.

16.7
Suggested Analysis of Modulus Spectra

The possibility of description of the dynamic mechanical or dielectric results by means of analytical functions with a reasonably small number of parameters is of general interest because it simplifies the analysis of data on the one hand and allows one to use the functions in modeling of polymer behavior under various conditions on the other. Many empirical phenomenological relations have been suggested for description of both the mechanical and dielectric spectra considered in the frequency domain, but in the case of dielectric spectroscopy they are

usually expressed in terms of the dielectric permittivity. A comprehensive review is given in this book in Chap. 3. It will be shown here that a simple formula which has already been used for description of asymmetric loss peaks of the dielectric spectra [17, 18] can be used very successfully for description of frequency dependencies of the components the complex modulus usually used in representations of the dynamic mechanical spectra. For a single relaxation process the formula can be written in the following form:

$$G'(\omega) = A / [(\omega\tau)^{b1} + (\omega\tau)^{b2}] \qquad (16.16)$$

With the four parameters allowing one to represent most of the typical experimentally observed dependencies, it is interesting that this function can be used for representation of both the real and imaginary components of the complex modulus around the relaxation effects observed in the frequency domain. Examples of effects related to variation of the parameters $b1$ and $b2$ on the form of the function are shown in Fig. 16.20a,b. Figure 16.20c shows a single Debye relaxation represented by G' and G'' using the formula with the characteristic parameters:

$$G'(\omega) = A / [(\omega\tau)^{b1} + (\omega\tau)^{b2}]$$
$$G''(\omega) = A / [(\omega\tau)^{b3} + (\omega\tau)^{b4}] \qquad (16.17)$$

The value of τ corresponds to the relaxation time, the parameter A is related to the height of the plateaus of the real part of the modulus above the frequency corresponding to the reciprocal relaxation time, and the parameters $b1\ldots b4$ describe the slopes on both sides of the characteristic frequency.

Examples of application of these relations to fit the experimental results are shown in Fig. 16.19. In the case of the mechanical modulus the data are fitted with a three component function whereas for the electric modulus spectrum the two component function is used. In both cases simultaneous fitting of the real and imaginary frequency dependencies is performed which means that the amplitudes and relaxation times are common for both modulus components. In both cases, i.e., for the mechanical and the dielectric spectra, a very good fitting result is obtained. Because of a very broad range of changes of all variables in the spectra one has to take particular care for a proper form of data representation (logarithmic or linear) and a compatible definition of the fitting functions in fitting procedures.

16.8
Concluding Remarks

Only some aspects of application of mechanical spectroscopy to studies of polymeric materials have been discussed here and only some applications illustrated. The technique represents one of the relaxation spectroscopy methods which, because of a direct relation to mechanical properties of materials, is very useful. Some limitations of this technique however, such as, for example, low se-
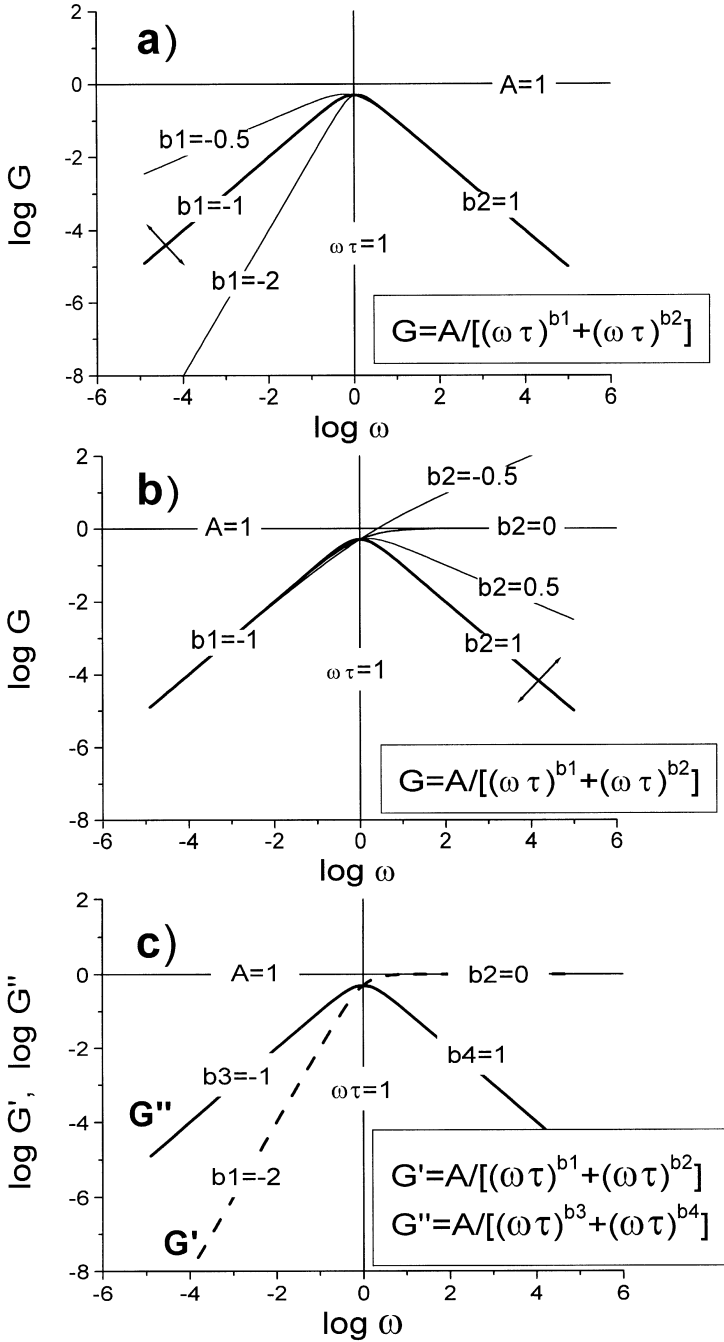
Fig. 16.20. Illustration of effects of parameter variation on the form of the function given by Eq. (16.16). **c** Real and imaginary parts of the complex modulus for the Maxwell model as described by the functions at Eq. (16.17) with the parameters shown

lectivity or relatively narrow frequency range, have to be compensated by other advantageous properties like very high sensitivity or by a combination with other techniques, such as for example dielectric spectroscopy, which are more selective or are operating in much broader frequency ranges and can improve in this way the possibilities of interpretation of the results.

It has been shown, for example, that by combination of results from dynamic, mechanical, and dielectric relaxation experiments for polyisoprene linear chains and for block copolymers of polyisoprene and polybutadiene, valuable details of the dynamic behavior of linear chains in the melt can be obtained. Both methods provided consistent results describing the orientational dynamics both on the segmental and polymer chain scales. In cases with more complex molecular structures the dielectric spectra usually help to assign relaxation of the molecular fragments bearing the dipole moments to the complex mechanical behavior.

Both discussed methods and especially a combined application of them can be considered as a valuable research tool for polymer chemists, polymer physicists, and for materials scientists and engineers.

List of Abbreviations and Symbols

A, b_1, b_2, b_3, b_4	Fitting parameters
a_T	Shift factor
$C1, C2$	Parameters in the WLF relation
D, F	Deformation, torque
E, E_0	Electric field, alternating electric field amplitude
G^*, G', G''	Shear complex modulus, real component, imaginary component
G, G_0, E_Y	Shear modulus, value at short time limit, Young's modulus
$L_0, \Delta L$	Initial length, length increment
M^*, M', M''	Complex modulus, real component, imaginary component
M_n, M_w	Number average molecular weight, weight average molecular weight
p, Δ, K	Pressure, compression, compression modulus
P, P_0	Electric polarization, amplitude of a periodic change
t, τ, τ_s, τ_c	Time, relaxation time, segmental relaxation, chain relaxation
T, T_{ref}, T_g	Temperature, reference temperature, glass transition temperature
$V, \partial V$	Volume, volume increment
α, β	Relaxation processes
γ, γ_0	Shear deformation, shear deformation amplitude
δ	Phase shift angle
ε	Strain
ε_0	Dielectric permittivity of the vacuum
η, η_0, η^*	Viscosity, zero shear viscosity, complex viscosity
θ	Angle
σ, σ_0	Stress, stress amplitude
χ^*, χ', χ''	Complex susceptibility (compliance), real component, imaginary component

ω	Angular frequency
IBI	Isoprene-butadiene-isoprene copolymer
PI	Polyisoprene
PnBA	Poly(n-butyl acrylate)
TTS	Time-temperature superposition
WLF	Wiliams-Landel-Ferry relation

References

1. McCrum NG, Read BE, Williams G (1991) Anelastic and dielectric effects in polymeric solid. Dover Publications, New York
2. Ferry JD (1970) Viscoelastic properties of polymers. Wiley, New York
3. Strobl G (1996) The physics of polymers. Springer, Berlin Heidelberg New York
4. Winkelhahn H-J, Pakula T, Neher D (1996) Macromolecules 29:6865
5. Macedo PB, Moynihan CT, Bose R (1972) Phys Chem Glasses 13:171
6. Wagner H, Richert R (1999) J Appl Phys 85:1750
7. Gohr K, Pakula T, Tsutsumi T, Schärtl W (1999) Macromolecules 32:7156
8. Pakula T, Geyler S, Edling T, Boese D (1996) Rheol Acta 35:631
9. Adachi K, Kotaka T (1993) Prog Polym Sci 18:589
10. Boese D, Kremer F (1990) Macromolecules 23:8298
11. Karatasos K, Anastasiadis SH, Pakula T, Watanabe H (2000) Macromolecules 33:523
12. Pakula T, Floudas G (2000) In: Balta Calleja FJ, Roslaniec Z (eds) Block copolymers. Marcel Dekker, New York
13. Pakula T, Vlassopoulos D, Fytas G, Roovers J (1998) Macromolecules 31:8931
14. Wintermantel M, Gerle M, Fischer K, Schmidt M, Wataoka I, Urakawa H, Kajiwara K, Tsukahara Y (1996) Macromolecules 29:978
15. Beers KL, Gaynor SG, Matyjaszewski K, Sheiko SS, Möller M (1998) Macromolecules 31:9413
16. Matyjaszewski K (1999) Chem Eur J 5:3095
17. Jonscher AK (1983) Dielectric relaxation in solids. Chelsea Dielectrics Press, London
18. Schönhals A, Schlosser E (1989) Colloid Polym Sci 267:125

17 Dielectric Spectroscopy
and Multidimensional NMR – a Comparison

R. Böhmer · F. Kremer

17.1
Introduction

Broadband dielectric spectroscopy (BDS) and solid-state nuclear magnetic resonance (NMR) are two of the working horses in modern materials research. Both methods are well suited to study the dynamics in disordered condensed matter in an extremely broad range of more than 15 decades in time and/or frequency. However, the strategies employed to retrieve information from a given substance are quite different for NMR as compared to BDS. To the practitioner of conventional dielectric spectroscopy, who is used to the relatively simple sampling of the electrical polarization in the frequency or time domains, the wealth of NMR techniques sometimes appears bewildering. Another difference between the two methods is that quantum effects are rarely needed explicitly in order to analyze a dielectric experiment, while in NMR at least some elementary knowledge of quantum mechanics is required from the outset. The benefits of the seeming complexity inherent in theory and experiment of NMR, as compared to BDS, are numerous: NMR is element specific and the selectivity to the dynamics of certain sites or groups within a molecule or to certain components within a mixture can often be enhanced further by spectral filtering or isotope labeling. Some of the more sophisticated NMR techniques, e.g., when performing multidimensional spectroscopy, due to limitations imposed by the requirement to achieve an acceptable signal to noise ratio, can be relatively time consuming as compared to experiments carried out using BDS. This advantage of the latter method may be viewed as arising at the expense of the fact that usually only an integral response of the subset of those degrees of freedom is measured which couple to charge carriers or dipole moments in the sample. Hence systematic (as a function of composition, say) BDS studies are often required to obtain firm assignments of relaxation processes as seen in, e.g., dielectric loss spectra. The combined application of experimental methods, and particularly of the two complementary ones dealt with in the present chapter, has greatly advanced our understanding of the molecular dynamics in disordered materials.

In this contribution we will focus on some similarities and differences between NMR and BDS. Certainly, there are numerous books dealing *either* with NMR *or* with BDS. An incomplete but useful list of BDS books is found in [1–6] and a much less complete list of NMR books in [7–11]. Fortunately, each one of these books, which contain numerous further references, provides a good start-

ing point to familiarize oneself with the two experimental methods. In this chapter we take a different perspective by trying to compare the two techniques. However, we wish to make clear from the beginning that the present chapter is highly selective in two respects: first we will only focus on very few NMR techniques and second on a few classes of amorphous or partly ordered materials. The choices we have made were guided by our anticipation of what kinds of techniques and experimental results could be most suitable for a comparison between NMR and BDS. However, probably even more so the choices made in this chapter reflect our own view of the field which is shaped by our previous scientific interests. This necessarily implies that in the present context we will not, or only very briefly, touch upon a number of interesting and exciting developments, such as multiple quantum spectroscopy, magic angle spinning techniques, and magnetic resonance imaging, to name a very few.

In Sect. 17.2, we review several aspects of spin-lattice relaxation and stimulated echo techniques with the additional restriction that we focus mostly on the nuclei ^1H, ^2H, and ^{13}C which are important in organic matter. First, some basic features of the still often employed spin-lattice relaxation time measurements are outlined in order to facilitate comparison with BDS. Then, in Sect. 17.2.2 the stimulated echo technique is presented. With respect to translational motions (Sect. 17.2.2.1) it is really complementary to incoherent neutron scattering and to conductivity spectroscopy. Rotational motions, which can be studied using two- and higher-dimensional NMR techniques, are then dealt with. Here some of the unique advantages of NMR show up since the wealth of geometrical information (e.g., on jump-angle distributions) that can be obtained via time domain (Sect. 17.2.2.2) and frequency domain (Sect. 17.2.3.1) techniques is not accessible directly using BDS. Next, we will give an introduction to some features of higher-order correlation functions in Sect. 17.2.3.2 as a basis for a comparison with recent non-conventional dielectric approaches. Then, in Sect. 17.3, we will discuss several combined dielectric and NMR studies as experimental examples: First, we will focus on low-molecular weight systems, i.e., on supercooled organic liquids as exemplified by glycerol and toluene (Sect. 17.3.1) and a glass forming, triphenylene based, discotic liquid crystal (Sect. 17.3.2). Then polymeric systems are dealt with. Here we particularly focus on the dynamics and time scale of the dynamics in poly(methyl methacrylate) (Sect. 17.3.3). In Sect. 17.3.4 we review experiments relating to the dynamic and spatial heterogeneity which was thoroughly studied in poly(vinyl acetate) and other systems. Magnetic field gradient experiments, useful to monitor translational diffusion processes in single phase and diblock copolymers, are briefly mentioned in Sect. 17.3.5. Finally results on an inorganic, ion conducting nitrate glass former are summarized in Sect. 17.3.6.

17.2
Selected NMR Methods

In this section we will focus on a few important, mostly standard NMR methods which are particularly suitable for comparison with dielectric techniques.

Before doing so some general remarks are in order. In the approximation of high magnetic fields, B_0, which are most frequently used in NMR, the populations of the nuclear-spin energy levels are given by a Boltzmann distribution. In the simplest case of a spin $-\frac{1}{2}$ system (e.g., protons which have the largest gyromagnetic ratio γ of all stable isotopes and thus the highest Larmor frequency $\omega_L = \gamma B_0$) the population difference of the spin-up and spin-down levels is given by $1 - \exp[-(\hbar \gamma B_0)/k_B T] \approx \hbar \omega_L/(k_B T)$. Inserting typical numbers (e.g., $B_0 = 14\ T$ and $T = 300$ K, corresponding to a proton frequency of $\omega_L = 600$ MHz and an equivalent thermal frequency of 300×20.8 GHz, respectively) gives 10^{-4}. Thus the sensitivity of solid state NMR, e.g., when trying to monitor a low concentration species, is often considered to be much smaller than it is for BDS [12].

17.2.1
Spin-Relaxation Techniques

Since the invention of NMR, spin-lattice relaxation has been used as a diagnostic of the dynamics in liquids and solids [7, 13]. Spin-lattice relaxation can be measured subsequent to perturbing the populations within the nuclear energy level scheme. At typical Larmor frequencies the spontaneous transitions between states with different magnetic quantum numbers are exceedingly rare ($\sim 10^{-25}$ s^{-1}). Therefore, transitions have to be induced by irradiating the spin system at or very close to the resonance (or Larmor) frequency. This can be done externally by applying radio frequency (RF) pulses. In the absence of external RF perturbations, equilibration of the spin system is attained through fluctuations of local magnetic fields, $B_{loc}(t)$, with spectral components near ω_L. Via the fundamental resonance condition, written here as $\omega_{eff}(t) = \gamma[B_0 + B_{loc}(t)]$, in this context one may alternatively talk about modulations of the effective NMR frequency. The magnitude of these fluctuation in a certain frequency interval is usually given in terms of the spectral density, $J(\omega)$, which under favorable circumstances can be related to the imaginary part of the dielectric susceptibility (see below). The fluctuation amplitude (i.e., the root mean square excursion of $B_{loc}(t)$ about its mean) is determined by the interactions of a tagged nuclear spin to its environment, e.g., to other spins. For example the spin-spin interaction, and hence the local field, depends on the relative distance of the spins *as well as* on the orientation of the internuclear vectors with respect to the external field. Situations in which the spectral density simultaneously samples orientation *and* distance information typically arises in proton NMR. One then has the problem to separate the contributions arising from reorientational and from translational motions. Therefore, it is sometimes more advantageous to work with nuclear probes for which local interactions dominate. This is usually the case for ^{2}H and ^{13}C (or also ^{31}P) isotopes.

^{13}C is a rare spin system (1.1 % natural abundance) and isotopic enrichment is often only employed up to a level at which the above-mentioned dipole-dipole interaction is much smaller than the chemical shift anisotropy (CSA) at the carbon site. The CSA arises from the distortion of the electronic 'cloud', i.e., from

the immediate chemical environment into which the probe nucleus is embedded. Hence, if the electronic environment of ^{13}C, or more loosely speaking the molecular orientation, fluctuates at a rate close to the Larmor frequency, the consequent modulation of ω_{eff} renders spin-lattice relaxation particularly effective. Translational motions remain undetectable under these circumstances, unless they are associated with a reorientation of the molecules. Similar considerations hold for the intramolecular dipole-dipole (DD) interaction. ^{1}H and also ^{13}C are among the simpler species in NMR since their spin is $I = \frac{1}{2}$. Quadrupolar (Q) interactions come into play for $I \geq 1$ probes such as ^{2}H.

In the present context let us focus on deuterons ($I = 1$) which play a prominent role in studies of organic matter. This is because here the quadrupolar interaction, which is due to the interplay of electric field gradient at the ^{2}H site with the quadrupole moment of that nucleus, is about a factor of 100 stronger than the DD interaction between the deuterons. Thus for the corresponding interaction energies (measured in frequency units) one has $\omega_{DD} \ll \omega_Q$. On the other hand, the quadrupolar interaction is still weak enough such as to fulfill two useful conditions. First, the quadrupolar interaction is very weak as compared to the Zeeman interaction in typical external magnetic fields, $\omega_Q \ll \omega_L$. This allows one to treat the former interaction as a small perturbation to the latter, unlike what is encountered for most other quadrupolar nuclei in solid-like samples. Second, in a covalent C-^{2}H bond, say, no other field gradients matter other than those originating from the bond in which the deuteron is located. Thus, essentially only the orientation with respect to the external magnetic field determines ω_Q. Hence, also in deuteron NMR one usually benefits from the advantages of a local (or single-particle) probe.

For a more quantitative description the reorientations of the corresponding nuclear (DD, CSA, or EFG) tensors needs to be specified. This can be accomplished using the normalized orientational autocorrelation functions, g_l [14], which for axially symmetric tensors can be cast into a particularly simple form:

$$g_l(t) = \langle P_l[\cos\theta(0)]\, P_l[\cos\theta(t)]\rangle / \langle P_l[\cos\theta(0)]^2 \rangle \qquad (17.1)$$

Here $P_l(\cos\theta)$ denotes a rank l Legendre polynomial of the cosine of the polar angle which is usually defined with respect to a laboratory-fixed axis. The $\langle\dots\rangle$ brackets indicate the average over all orientations (in the NMR context often called powder or ensemble average). For a variable that in isotropic systems only depends on θ it is given by $\langle x(\theta)\rangle \equiv \frac{1}{2}\int_0^\pi x(\theta)\sin\theta\, d\theta$.

In linear dielectric spectroscopy Eq. (17.1) with $l = 1$ corresponds to the customary step-response [$\sim 1 - g_l(t)$] if the so-called cross terms are disregarded [5, 6]. Furthermore, here $P_1(\cos\theta) = \cos\theta$ and θ is the angle enclosed by dipole moment and external electrical field. It is well known that in NMR (but also for Kerr effect studies [15, 16] and for other techniques which probe second rank tensors) θ designates the angle between the largest principal axis of the tensor and the relevant external field.

The spectral density corresponding to the fluctuation of rank l tensors is given by the Fourier transform of the correlation function as $J^{(l)}(\omega) = N \int g_l(t)\, e^{i\omega t} dt$ [14]. As a probability density $J^{(l)}(\omega)$ has to be properly normalized. This is ex-

pressed by the factor N. Via the fluctuation dissipation theorem, written as $\tilde{J}^{(1)}(\omega) \sim \chi''(\omega)/\omega \sim \varepsilon''(\omega)/(\omega\Delta\varepsilon)$, the rank one spectral density is directly related to the dielectric loss. Here $\Delta\varepsilon$ is the so-called dispersion step. It should be noted that the fluctuation dissipation theorem may not be obeyed in glassy, out-of-equilibrium systems. In order to test potential violations the spectral density can be determined directly by the measurement of polarization noise, as recently applied to various disordered systems [17–20].

In order to facilitate comparison with the dynamic structure factor, accessible directly via inelastic neutron scattering, the effective spectral density may be written as $\tilde{J}(\omega_L) = \sum_q A(q) S(q,\omega_L)$ with $S(q,\omega_L)$ denoting the dynamic structure factor [21]. The coupling coefficients $A(q)$ are known in special cases only. It should be noted that an NMR frequency of $\omega_L = 242$ MHz corresponds to an energy of $\hbar\omega_L = 1\,\mu\text{eV}$. Therefore, viewed from the perspective of inelastic neutron scattering, NMR is sometimes considered a 'zero frequency' technique.

Roughly speaking the spin-lattice relaxation rate, $1/T_1$, is proportional to the spectral density at the Larmor frequency or, more precisely,

$$1/T_1 = C_\lambda [J^{(2)}(\omega_L) + 4 J^{(2)}(2\omega_L)] \tag{17.2}$$

if one needs to consider only a single relaxation mechanism $\lambda \in \{DD, CSA, Q\}$ and hence a single coupling constant, C_λ. The latter can often be determined experimentally from corresponding NMR spectra. In favorable cases the knowledge of C_λ allows one to obtain information about motional processes, e.g., about the geometry of reorientations. This information is not necessarily available from $J(\omega)$ (and thus also not from $\chi''(\omega)$).

In the simplest case of a single exponential correlation function (CF) $g_l(t) = \exp(-t/\tau_{C,l})$ with a correlation time, $\tau_{C,l}$, the spectral density for isotropic systems in NMR is given by $J^{(2)}(\omega) = \tau_{C,2}/[1 + (\omega\tau_{C,2})^2]$. The latter expression when introduced into Eq. (17.2) yields the famous Bloembergen-Purcell-Pound (BPP) formula [22]. The BPP approach directly corresponds to the so-called Debye relaxation, $\chi''(\omega) = \omega\tau_{C,1}/[1 + (\omega\tau_{C,1})^2]$. A minor difference is that $\chi''(\omega)$ is maximum at $\omega\tau_{C,1} = 1$ while inserting $J^{(2)}(\omega)$ into Eq. (17.2) yields the minimum T_1 at $\omega\tau_{C,2} \approx 0.61$.

For the limiting scenarios of rotational diffusion and rotational random jumps, which both lead to single exponential $g_l(t)$, the expected ratio of $\tau_{C,1}/\tau_{C,2}$ is 3 and 1, respectively. In accord with many experimental observations, in more realistic models (e.g., [23]) this ratio is close to 1 even in the presence of a distribution of relaxation times. In dielectric spectroscopy such distributions are often used to describe the frequency dependence of the complex dielectric function. However, their width can be estimated even from scanning the temperature dependence of ε' and ε'' at a single, fixed frequency if the (apparent) activation energy is known. This is because the ratio of maximum dielectric loss, ε''_{max}, and dispersion step, $\Delta\varepsilon$, which equals $\frac{1}{2}$ for the Debye case, is well defined (and always $\leq \frac{1}{2}$). If specific functional forms are assumed such as given, e.g., by the Cole-Cole, Cole-Davidson, or Kohlrausch-Williams-Watts distributions then $\varepsilon''_{max}/\Delta\varepsilon$ may be computed; see Fig. 17.1a. Similarly in NMR for the BPP case the
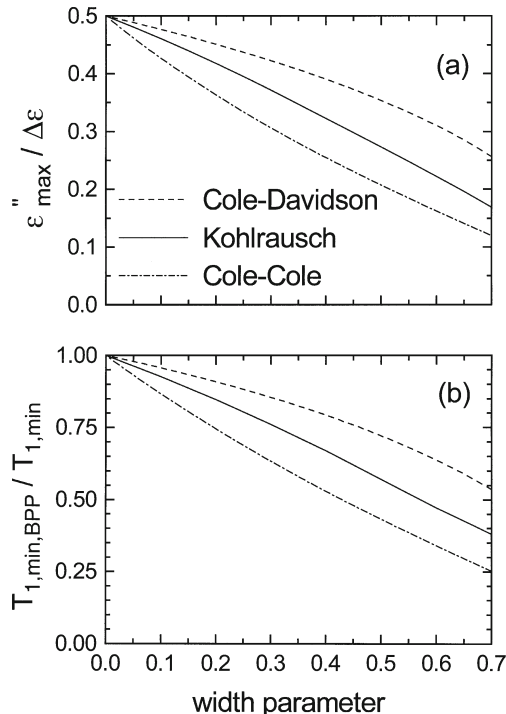
maximum spin-lattice relaxation rate, $1/T_{1,min,BPP}$, is well defined if the nuclear coupling constant C_λ is known (from the NMR spectrum). In Fig. 17.1b we show the decrease in rate if specific distribution functions are assumed. This plot allows a simple quantification of potential experimental deviations from the BPP case in a quantitative manner.

Above we have mentioned that the correlation times, τ_l, often depend only weakly on the rank l. Thus dropping the l dependence in the above expressions altogether, the effective spin-lattice relaxation rate is expected to be proportional to $\varepsilon''(\omega_L) + 4\varepsilon''(2\omega_L)$. Thus we may define a 'dielectric relaxation rate' as

$$\frac{1}{T_1^{diel}} \sim \frac{\varepsilon''(\omega_L) + 4\varepsilon''(2\omega_L)}{\omega_L \Delta\varepsilon} \tag{17.3}$$

cf. Eq. (17.2). Therefore, one may say that temperature dependent measurements of spin-lattice relaxation times at the Larmor frequency, ω_L, roughly correspond to a determination of the dielectric loss near ω_L. Frequency dependent measurements which are very common in BDS are performed only occasionally in NMR. This is because they require the use of different magnets, or dedicated techniques such as rotating frame measurements, $T_{1\rho}$ (essentially probing $J(\omega \approx 50\ kHz)$), multiple-pulse methods, or field cycling relaxometry [11].

For an analysis of temperature dependent spin-lattice relaxation times the use of empirical distributions of relaxation times, well known from dielectric spectroscopy, is common. Probably most popular are still those distributions invented by Cole and co-workers [24] but numerous other forms are also in use, see, e.g., those given in [25, 26]. Via $J(\omega) \sim \chi''(\omega)/\omega$ and Eq. (17.2) it is straightforward to derive corresponding expressions for the spectral density and T_1, see, e.g., [13, 27, 28]. For its numerical simplicity the Cole-Davidson distribution is quite often applied to parameterize not only BDS data but also NMR measurements on disordered materials. Such measurements often yield pronounced asymmetries in a representation of T_1 vs $1/T$. In the BPP case such a plot yields a symmetric V-shaped curve if the temperature dependence of the correlation time is given by an Arrhenius law. This situation is reminiscent of the symmetry and asymmetry of dielectric loss spectra, $\varepsilon''(\log \omega)$. This is because via $\log \omega \sim 1/T$ the logarithmic frequency scale can be mapped onto an inverse temperature axis. This mapping is often employed also in connection with other techniques, such as mechanical spectroscopy, for which measurements are sometimes acquired at a single frequency only [29].

At the temperature at which the T_1 minimum occurs the determination of distribution parameters is most precise. Potential temperature dependences of these parameters however, can hardly be mapped out from T_1 measurements at a single Larmor frequency because of the enormous variation of $\tau(T)$.

A particular advantage of NMR is that via isotope labeling or via spectroscopic means the selective study of intramolecular degrees of freedom becomes possible. This enables not only the study of side groups which change their dipole moment upon reorientation but also of side groups for which this is not the case, such as phenyl or methyl groups. The latter often can serve as built-in probes to monitor their local environment. Consequently, in glass-forming substances they have been utilized occasionally to investigate the energy landscape below the glass transition temperature. It has to be mentioned that the reorientation of such side groups becomes accessible also to dielectric spectroscopy if they are partially deuterated. The dipole moments of partially deuterated groups are of course relatively small [30].

17.2.2
Stimulated Two-Time Echo Spectroscopy

Spin-lattice relaxation provides a somewhat indirect perspective on the molecular dynamics since it probes the spectral density which is the Fourier transform of the underlying microscopic CF. Using stimulated-echo techniques various CFs can be probed directly. An example for a rotational CF which, as we will see, can be understood to involve the orientation dependent NMR frequencies at two times, has already been given as Eq. (17.1).

The stimulated echo can be generated using a sequence of three pulses as shown in Fig. 17.2. Its general functional form can be written as

$$F_2(t_p, t_m) = \langle \exp[i\omega(0) t_p] \exp[-i\omega(t_m) t_p] \rangle \tag{17.4}$$
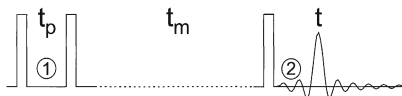
Fig. 17.2. Stimulated echo sequence consisting of ① dephasing and ② rephasing periods of length t_p with a mixing time t_m interleaved. This sketch only depicts the basic pulse sequence. Although important for practical implementations of the experiments, in the present context we will neither discuss spin-relaxation effects explicitly nor will we dwell on the necessity of phase cycling as well as cross-polarization and decoupling that are usually applied in ^{13}C NMR

and involves the correlation of the NMR frequencies prior and subsequent to a mixing time t_m [31]. The NMR frequencies are encoded as the (rotating frame) phases $\phi(0) = \omega(0)t_p$ and $\phi(t_m) = \omega(t_m)t_p$ in the dephasing and rephasing periods, respectively (with usually $t_p \ll t_m$). Depending on what is encoded in the NMR frequency, not only orientational CFs are accessible. For instance, if the NMR frequency depends on the spatial position then magnetic resonance imaging becomes possible, but also translational CFs can be measured [11, 32–34].

17.2.2.1
Translational Displacements

Dielectric spectroscopy as well as NMR have often been used to study transport and diffusion processes. Let us first focus on magnetic field gradient NMR [35] which is well suited to measure self-diffusion coefficients in a wide dynamic range. For this technique either static or pulsed field gradients are applied which lead to a spatial dependence of the NMR frequency. For a gradient along an axis r, say, superimposed onto the static field, $B_0 \| r$, one has $\omega(r) = \gamma B_0 + \gamma r g$ with the gradient strength $g = \partial B/\partial r$. Inserted into the right hand side of Eq. (17.4) this gives $\langle \exp[iqr(0)] \exp[-iqr(t_m)] \rangle$, which we may call $S_2(q,t_m)$, with the modulus of a generalized scattering vector $q = \gamma g t_p$. The 'intermediate incoherent scattering function' $S_2(q,t_m)$ can be measured by pulsed field gradient [36] and static field gradient NMR. A detailed description of these methods can be found in [33] and [38]. The NMR signal is usually generated by the stimulated-echo RF pulse sequence: $\pi/2 - t_p - \pi/2 - t_m - \pi/2 - t_p$ – echo, cf. Fig. 17.2.

The expression for $S_2(q,t_m)$ is completely analogous [37] to that for the incoherent intermediate scattering function, $S_{inc}(q,t) \sim \langle \exp[iqr(0)] \exp[-iqr(t)] \rangle$, known from neutron scattering. While in neutron scattering $|q^{-1}|$ typically is of the order of interatomic distances, in field gradient NMR (with g up to several hundred T/m) q^{-1} is typically 10^{-2} μm^{-1} to 10^2 μm^{-1}. Thus, incoherent neutron scattering and field gradient NMR can often be employed complementarily. In the case of spatially unrestricted diffusion single exponential 'scattering functions', or echo attenuations,

$$S_2(q,t_m) \sim \exp(-q^2 D_T t_m) \tag{17.5}$$

with decay times $\tau_q = D_T^{-1} q^{-2}$ result. From these the translational self-diffusion coefficient, D_T, sometimes also called tracer diffusion coefficient, can

be determined directly. If the field gradient is oriented along the z-direction, then the mean square displacement is given by $\langle z^2 \rangle = 2D_T t_m$ and hence $S_2(q, t_m) \sim \exp(-\frac{1}{2} q^2 \langle z^2 \rangle)$

If the local (or even the overall) diffusion is anisotropic then the scalar diffusion coefficient should be replaced by a diffusion tensor which, in its principal axis system, will be characterized by the eigenvalues D_{xx}, D_{yy}, and D_{zz}. This case can arise, e.g., in partially ordered systems such as liquid crystals. Let us consider an axially symmetric diffusion tensor with $D_\perp = D_{xx} = D_{yy}$ and $D_\parallel = D_{zz}$. If its main symmetry axis encloses the polar angle θ with the $(z\text{-})$ direction along which the external magnetic field gradient is oriented, then the above expression for the mean square displacement has to be written as $\langle z^2(\theta) \rangle = 2D_\perp t_m \sin^2\theta + 2D_\parallel t_m \cos^2\theta$. Carrying out the powder (or ensemble) average over $\exp(-\frac{1}{2} q^2 \langle z^2(0) \rangle)$ then yields [33]

$$S_2(q, t_m) \sim \exp(-q^2 D_\perp t_m) \int_0^1 \exp[-q^2(D_\parallel - D_\perp) t_m u^2)] \, du. \qquad (17.6)$$

from which the behavior for one-dimensional (1D) diffusion, $D_\perp \ll D_\parallel$, 2D diffusion, $D_\perp \gg D_\parallel$, and isotropic (3D) diffusion, $D_T = D_\perp = D_\parallel$, can easily be calculated.

Diffusion in spatially confined geometries and in particular in porous matrices is often of interest [32, 38]. Then, even for isotropic diffusion (upon which we will focus in the following) deviations from single exponential (with respect to t_m) and/or from q^{-2} behavior occur for $S_2(q, t_m)$ which can be cast into the form

$$S_2(q, t_m) = \int \exp(iqz) \, P(z, t_m) \, dz \qquad (17.7)$$

Here $P(z,t)$ is the so-called propagator [38] of the probability density for a displacement of a tagged particle (e.g., a polymer segment) over the distance z within the diffusion time t_m. It is well known that the expressions for free (spatially unrestricted) diffusion are recovered from Eq. (17.7) for a Gaussian propagator [32, 33, 38].

For illustrating the effects of geometrical restrictions let us briefly discuss here the instructive example of a system of mutually interconnected pores. The simplest approach is then to measure $S_2(q, t_m)$ at fixed (sufficiently long) t_m. This gives the structure factor of the pore space, cf. Fig. 17.3, from which the typical pore dimension, d, can be inferred. Apart from static properties dynamic information can be obtained from $S_2(q, t_m)$ as, e.g., measured for various (fixed) q. For $q^{-1} < d$, one focuses on only a small spatial spot. Thus one effectively samples the translational displacements within the pore and the spatial restrictions are not 'seen'. Sometimes so-called short time (or better small scale) diffusion coefficients D_s are extracted from experiments in this regime. If one sets $q^{-1} > d$, then the diffusing species effectively perform an average over the local topologies and the scattering function is again of the form $S_2(q, t_m) \sim \exp(-D_{eff} q^2 t_m)$, but now with an effective diffusion coefficient D_{eff}. The latter is always smaller than the diffusion coefficient, D_T, measured without geometrical restrictions. This is of-
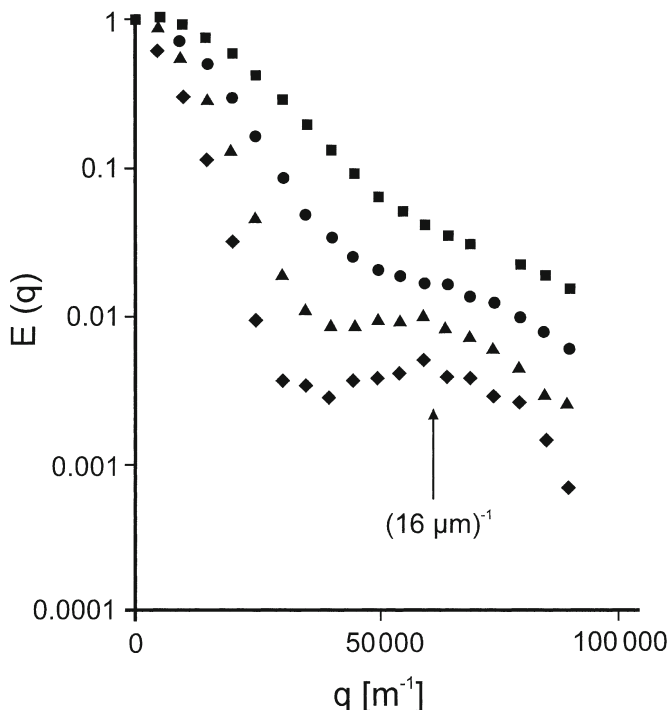
Fig. 17.3. Squared structure factor of liquid water filling the pore space in a random packing of spherical beads with a diameter of 15.8 μm for a series of diffusion times t_m (20, 40, 70, and 110 ms). For the longest t_m the peak at $q \approx 0.06$ μm^{-1}, corresponding to a typical pore separation of 16 μm, is clearly resolved. Reproduced from [195] with permission

ten expressed by the obstruction or tortuosity factor, $\Lambda = D_{eff}/D_T < 1$. Only for a few geometries is this factor known analytically and otherwise it can easily be computed numerically [39]. Finally, the regime defined by $qd \approx 1$ is useful to map out the characteristics of pore size distributions.

In studies of translational motions another option is to determine hopping rates. This requires that the NMR frequency changes if the translationally displaced particle jumps from one site to another. If one is able to determine the hopping rate $1/\tau_{hop}$ then knowledge of the jump distance, a, permits one to estimate the effective diffusion coefficient via the Einstein relationship, $D_E = fa^2/\tau_{hop}$. The factor f depends on the geometry; for unrestricted diffusion in three dimensions it is $f = 1/6$. There are a number of ways that can lead to a change of the NMR frequency upon translational displacements. Sometimes atomic or ionic jumps lead to significant variations in the isotropic chemical shift. This was demonstrated, e.g., for ^{6}Li in an ion conductor [40] or ^{129}Xe in a zeolite [41]. Quite often translational jumps are associated with a reorientation of the relevant interaction tensor at the nuclear site such as the CSA [42], the EFG [43], or the DD tensors [11]. This mechanism of reorientation mediated by translational

displacement (RMTD) is not only exploited using NMR but has occasionally also been employed in the context of BDS [44]. Its proper application evidently requires prior knowledge that on-site reorientations do not occur and that each translational jump alters the dipole orientation.

In the highly fluid state the translational diffusion coefficient can be related to the viscosity via the Stokes-Einstein relation, $D_T = k_B T/(6\pi \eta r_H)$. Here r_H is the apparent hydrodynamic radius which in supercooled liquids is often close but not identical to the van der Waals radius [45]. The rotational diffusion coefficient on the other hand is given by $D_R = k_B T/(8\pi \eta r_H^3) = 1/(2\tau_{C,1})$. The latter equality implies that the rotational correlation time is identified with an $l = 1$, e.g., a dielectric relaxation time. Thus, *if* rotational diffusion is the dominant mechanism then one may estimate D_T from $\tau_{C,1}$ via $D_T = \frac{3}{4} D_R r_H^2 = \frac{2}{3} r_H^2 / \tau_{C,1}$. It should be noted that this relation (cf. the one for D_E, above) can often only be considered as an approximation for several reasons. (i) The given numerical factors imply that particles diffusing in three dimensional space are spherical and that stick boundary conditions apply. (ii) The hydrodynamic radius is not well defined *a priori*. While these two factors still preserve the inverse relationship between τ_1 and D_T, it is (iii) often found to be violated in experimental studies of deeply supercooled liquids. This phenomenon has been denoted rotation-translation decoupling or translational enhancement [46]. Numerous authors have suggested models to rationalize this observation, see, e.g., [23] and the references cited therein.

In ion conducting materials translational displacements can be monitored using the electrical (d.c.) conductivity, σ [47]. Employing the Nernst-Einstein relation the associated diffusion coefficient $D_\sigma = \sigma k_B T/(ne^2)$ [48] is often found to be different from the self diffusion coefficient, $D_T (\approx D_E)$, as phenomenologically expressed by the Haven ratio, $H_R = D_T/D_\sigma$. The latter is usually considered as a measure for correlations of the ionic motions. For crystalline lattices it can be determined directly [49], while for amorphous ion conductors uncertainties in jump geometry and carrier concentration enter. Here it was estimated to be in the range $H_R \approx 0.1 \ldots 1$ [50].

For many solid electrolytes it is not clear whether variations in the ionic mobility, μ, or in the carrier density, n, affect the temperature dependence of the conductivity most. This issue is often discussed under the heading 'strong vs weak electrolyte model' [51]. The electrical conductivity is related to the above-mentioned quantities via $\sigma = ne\mu$. By combining the latter expression with the Einstein and the Nernst-Einstein relationships, and by further assuming that $H_R \approx 1$, the mobility $\mu = e/(k_B T) \times \frac{1}{6} a^2/\tau_{hop}$, which is independent of n, can be determined. However, this requires the hopping distances, a, and hopping times, τ_{hop}, to be known. In favorable cases τ_{hop} can be measured directly using the stimulated-echo techniques, if via an RMTD mechanism each translational jump alters the orientation of the interaction tensor (and thus the NMR frequency) at the nuclear sites [52].

Thus, from mapping out differences in the temperature dependences between σ (as obtained from impedance spectroscopy) and $\mu \sim (T\tau_{hop})^{-1}$ (from NMR) it should become clear whether the charge carrier concentration is approximately temperature independent or not. In order to estimate the diffusion coefficient

and mobility corresponding to a hopping rate of $\tau_{hop} = 1$ ms that is accessible via NMR we assume $a = 3$ Å and $T = 300$ K (corresponding to $\frac{1}{40}$ eV) thus giving $D_T = 1.5 \times 10^{-17}$ m^2 s^{-1} and $\mu = 60 \times 10^{-17}$ m^2 s^{-1} V^{-1}. Assuming a carrier concentration of $n = 10^{22}$ cm^{-3} we obtain a readily measurable conductivity of $\sigma = 10^{-8}$ Ω^{-1} cm^{-1}.

17.2.2.2
Reorientational Dynamics

The rotational analogue of the intermediate scattering function that we have dealt with in Sect. 17.2.2.1 can yield detailed insights into time scale and geometry of reorientational processes. In particular it allows one to extract information about the distribution of reorientation rates and of rotational jump angles, respectively. The stimulated echo time-domain technique to be described here is very well adapted to situations in which distributions of small jump angles (below about 20°) dominate. If well defined large jump angles are a concern, then frequency-domain methods are often more profitably applied, see Sect. 17.2.3.1. Here, we shall first discuss the application of the two-time stimulated echo to study geometry and time scale of the molecular motion. Then we will outline the conditions under which the stimulated echo can be used as a dynamic low-pass filter.

Above, we have emphasized the similarity between (the modulus of) the scattering vector, q, relevant for translational motions, and the preparation time, t_p, relevant for rotational motions. Large q are required in order to achieve a high spatial resolution. By analogy, this suggests that large t_p will be necessary to resolve small angle reorientations, cf. the discussion in connection with the CF presented as Eq. (17.4). Employing appropriate phase cycling the cos-cos version of this equation, i.e., $F_2^{COS}(t_p, t_m) = \langle \cos[\omega(0)t_p] \cos[\omega(t_m)t_p] \rangle$ can be measured, but also the sin-sin pendant

$$F_2^{SIN}(t_p, t_m) = \langle \sin[\omega(0)t_p] \sin[\omega(t_m)t_p] \rangle \tag{17.8}$$

becomes accessible. The general orientation dependence of the rotating frame NMR frequency for the (DD, CSA, or Q) interactions considered in this article is given by [9]

$$\omega = \frac{1}{2} \delta (3\cos^2\theta - 1 - \eta \sin^2\theta \cos^2\Phi) \tag{17.9}$$

Here the azimuthal angle, Φ, and the asymmetry parameter, η, specify the interaction tensor in addition to the polar angle, θ, and the anisotropy parameter, δ, which is a measure of the (dipolar, quadrupolar, etc.) coupling. For the practically often relevant axially symmetric tensors (with $\eta = 0$) the NMR frequency reduces to $\omega = \frac{1}{2} \delta (3\cos^2\theta - 1) = \delta \times P_2(\cos\theta)$.

The CF $g_2(t)$ (cf. Eq. 17.1) is thus seen to be experimentally accessible. In the limit $t_p \to 0$, Eq. (17.8) yields $F_2^{SIN}(t_p \to 0, t_m) = t_p^2 \langle \omega(0)\omega(t_m) \rangle$ which for $\eta = 0$ directly corresponds to $g_2(t)$ and thus allows one to measure the correlation time $\tau_{C,2}$.

In order for $g_2(t)$ of an isotropic system to decay to e^{-1}, say, of its initial value the molecules (or better: interaction tensors) have to reorient by about $40°$ on average [53]. This confirms that for many applications the angular resolution of the CF for $l = 2$ could be quite poor (of course that for $l = 1$ is even lower). Only for very large l one obtains sensitivity to small jump angles. However, when returning to the case of finite t_p, i.e., to Eq. (17.8) and related expressions one recognizes that a dependence on terms with larger l is implicit. This can be shown in a straightforward manner for $\eta = 0$ by expanding $\sin[\omega(0)t_p] = t_p\delta \times P_2(\cos\theta) - \frac{1}{6}[t_p\delta \times P_2(\cos\theta)]^3 + \dots$. The right hand side of this equation in turn can be written as a sum of higher rank Legendre polynomials. For instance, from the definitions of the Legendre polynomials one has $[P_2(\cos\theta)]^3 = \frac{1}{385}[22 + 165P_2(\cos\theta) + 108P_4(\cos\theta) + 90P_6(\cos\theta)]$ and, if the above series is carried further, correspondingly higher terms involving higher angular resolutions show up.

Thus $t_p\delta$ can be adjusted to achieve any desired, finite angular resolution, $\Delta\varphi$. In other terms, if one sets $t_p\delta$ larger than a certain threshold (e.g., $t_p\delta > 20$ for $\Delta\varphi \leq 10°$, cf. Fig. 17.4), then any jump should lead to a loss of correlation. Consequently, in the limit of very long t_p Eq. (17.8) defines the so-called angular jump relaxation function $F_2^{AJ}(t_m)$. This function decays with a time constant τ_{AJ} which in general is smaller than $\tau_{C,2}$. This becomes clear when considering a scenario for which small-angle jumps (of a few degree, say) dominate. A large number of such jumps (which in total of course take much longer than τ_{AJ}) are required to lead to a root mean square angular displacement of about $40°$ (roughly defining $\tau_{C,2}$).

Fig. 17.4. Double logarithmic plot of the normalized correlation times $\tau_2(t_p)/\tau_{C,2}$ as determined from random walk simulations (Adapted from [105]). It should be noted that similar results were also obtained using a semi-analytic approach [109]
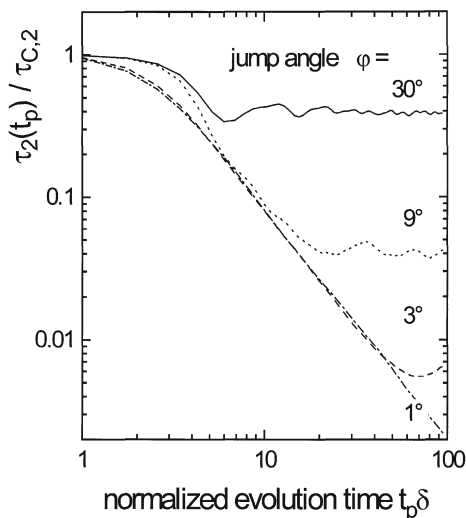
Based on the assumption that only a single jump angle φ is present, one can show that $\varphi = \arcsin[(2\tau_{AJ}/3\tau_2)^{1/2}]$ [54]. This result, but also the full $\tau_2(t_p)/\tau_{C,2}$ dependence, is borne out by random walk computations [55, 56], see Fig. 17.4. One major advantage of the latter numerical method with respect to analytical ones is that it can easily be adapted to situations in which a distribution of jump angles is present. Finally, apart from $\tau_2(t_p)$ the t_p dependent long mixing time limit, $F_2(t_p,t_m \to \infty)$, also contains valuable information concerning the overall reorientation geometry. However, here we will not dwell on this aspect, since the analogy between $F_2(t_p,t_m \to \infty)$ and the q dependent elastic incoherent structure factor from neutron scattering is well known [32, 57].

While further below we point out how, using NMR, $g_4(t)$ becomes accessible, it should be mentioned that in conventional dielectric spectroscopy explicitly l dependent CFs (apart from $l = 1$) are not measurable. However, there are several techniques which allow one to map out CFs with $l = 2$ by application of electrical fields. Apart from the well-known possibility to use the transient Kerr effect [15, 58], dynamic birefringence and polarizability spectroscopy (in connection with non-polar substances) [59–61], electric quadrupole spectroscopy [62, 63], and nonresonant spectral hole burning [64] may also be useful in this respect. It has to be noted that the angular resolution of time-domain NMR spectroscopy at large t_p is much higher than the one so far achieved using dielectric methods. Also the ability to map out angular jump functions, $F_2^{AJ}(t_m)$ is quite unique to NMR.

Angular jump functions form the basis for the construction of dynamic low pass-filters. This is because in the limit of very large evolution times, t_p, any molecules which in the dephasing period exhibited a frequency, $\omega_1 = \omega(0)$, that differs from the frequency in the rephasing period, $\omega_2 = \omega(t = t_m)$, will not contribute to the $F_2^{AJ}(t_m)$ echo. This is often expressed by saying that the molecules which have reoriented during t_m will be filtered out. If $F_2^{AJ}(t_m)$ acts as a dynamic low-pass (cf. Appendix 17.1), then the echo amplitude, $F_2^{AJ}(t_m)$, gives the fraction of 'molecules' that have not jumped during the mixing time t_m. Thus $1/t_m \equiv 1/t_{filter}$ defines the edge of a 'low-pass filter' and t_{filter} determines the filter efficiency $FE(t_{filter}) \equiv 1 - F_2^{AJ}(t_{filter})$ [65].

17.2.3
Multidimensional Techniques

17.2.3.1
Frequency-Domain Spectroscopy

Although in the present chapter our main focus is on time-domain NMR spectroscopy, now we will consider frequency-domain NMR. For the techniques mentioned here, which are more thoroughly treated elsewhere (see, e.g., [9]), hardly any comparable BDS method exists. They are nevertheless mentioned here in order to demonstrate some of the extraordinary potential of solid-state NMR.

The simplest way of recording an NMR spectrum is to apply a single (sufficiently short [66]) RF pulse and to record the subsequent free induction decay (FID) $F(t) = \langle \exp[i\phi(0,t)] \rangle$ (or the real or imaginary part of it) with $\phi(t_1,t_2) = \int_{t_1}^{t_2} \omega(t')\,dt'$. From the Fourier transform (FT) of $F(t)$ with respect to t the FID spectrum, $I(\omega) = \mathrm{FT}_t\{\langle \exp[i\phi(0,t)]\rangle\}$, is obtained. Thus, $I(\omega)$ tells which NMR frequencies are present with which weight. Depending on what is encoded via ω, one can get information on the spatial positions of the spins (which forms the basis of magnetic resonance imaging [33, 34]), on the kinds of chemical environments (useful, e.g., in analytical chemistry), and, as yet another example, on the occurrence of specific orientations (which can, e.g., be used to tell whether a sample is isotropic or whether orientational order parameters are non-zero [67]).

Often, FID spectra cannot be recorded reliably for technical reasons. The latter is often the case in deuterium NMR of disordered solids and usually is circumvented by application of the solid-echo technique. Solid echoes can be generated using two suitably phased RF pulses separated by an inter pulse delay t_p. The acquisition of the signal from the echo maximum onwards (which shows up at a time t_p after the second pulse) yields the solid-echo decay, $K(t,t_p) = \langle \exp[i\phi(0,t) - i\phi(t_p,t)]\rangle$, from which in turn the corresponding spectra, $S(\omega,t_p) = \mathrm{FT}_t\{K(t,t_p)\}$, can be obtained [68].

Solid-echo spectra can yield more information than FID spectra, but at the expense of being sometimes more difficult to interpret. For instance, if the time scale, τ, of the molecular dynamics is of the order of δ^{-1} (in ^{2}H NMR often about 1 µs) or longer, then $S(\omega,t_p)$ exhibits characteristic line shapes from which τ can be extracted. By recording solid-echo spectra as a function of t_p one may also get hints about the geometry of motion which already has been in focus in Sect. 17.2.2.2. Another way of obtaining such information is to carry out orientational NMR hole burning [69]. The most systematic approach, particularly if (a few) large jump angles are present, is via two-dimensional (2D) spectroscopy.

Figure 17.2 also displays the basic pulse sequence for this experiment. However, in the present context, not only the echo amplitude but also the entire magnetization subsequent to the echo maximum, i.e., the signal $F_2(t_p,t_m,t) = \langle \exp[i\omega(0)t_p] \exp[-i\omega(t_m)t]\rangle$ is recorded, cf. Eq. (17.4). Now an FT with respect to t is performed and yields, in the so-called direct dimension, the NMR frequencies $\omega_2 = \omega(t_m)$ which are present *subsequent* to the mixing time. In order to map out the frequencies, $\omega_1 = \omega(0)$, *prior* to t_m one has to acquire $F_2(t_p,t_m,t)$ for a number of preparation times, t_p. The frequencies, ω_1, in this so-called indirect dimension can then be obtained by performing an additional FT with respect to t_p. Thus executing the 2D FT properly [70] one obtains the 2D spectrum $S(\omega_1,\omega_2,t_m) = \mathrm{FT}_{tp}\{\mathrm{FT}_t\{F_2(t_p,t_m,t)\}\}$. It represents the joint probability to find an NMR frequency ω_2 (i.e., molecular orientation, etc.) subsequent to t_m if there was an NMR frequency ω_1 (originating from the same spin!) prior to t_m. Thus, the principle of two-dimensional exchange NMR in non-rotating solids can be summarized as follows: it consists of the detection of slow reorientations that occur during a mixing time by measuring the (here: angle-dependent) NMR frequencies before and after t_m [9, 71, 72]. If no reorientation, and consequently no
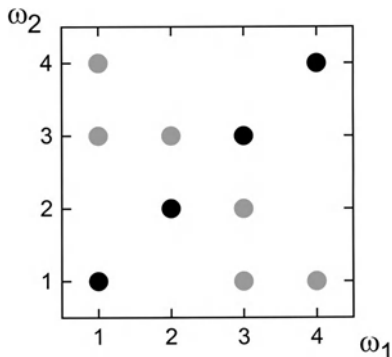
frequency change, takes place during t_m, the spectral intensity is confined to $\omega_1 = \omega_2$, the diagonal of the frequency plane. If frequency changes do occur during t_m off-diagonal intensity will appear in the spectrum.

As a simple example let us consider the case represented in Fig. 17.5 in which a diagonal spectrum with well resolved peaks is sketched (these may be imagined to be associated with different sites in a crystal). Then the exchange peaks directly reveal the connectivity among the sites. In a second example let a continuous distribution be present, e.g., an isotropic distribution of C-^{2}H bond orientations. If the motion of these bonds is characterized by a well defined reorientation angle, then a well defined relation between ω_1 and $\omega_2(\omega_1)$ exists. This situation can lead to the occurrence of elliptical exchange ridges from which the reorientation angle can be read off directly [9]. It should be noted that large-angle reorientations usually give rise to intensity far off the diagonal of a 2D spectrum [73]. Conversely, for reorientations by small angles, the signal appears close to the diagonal which can appear as a position-dependent broadening of the diagonal spectrum. This remark is intended to point out that, in general, it will be hard to perform an unambiguous determination of the underlying reorientation angle distribution, if small jump angles dominate.

Using 2D spectroscopy, irrespective of whether it is conducted in the time or in the frequency domain, one cannot distinguish between those spins which have not changed their NMR frequency, ω, during t_m and those which have switched to $\omega' \neq \omega$ and then returned to ω near the end of t_m. In order to discriminate between these two possibilities, e.g., in order to measure how large the fraction of molecules is which 'jump back' to their original orientation, one needs to know the NMR frequencies associated with a particular molecule for at least three points in time.

It is relatively straightforward to reach this goal using multidimensional spectroscopy since one of the advantages of this technique is its modularity, cf. Fig 17.6. This property allows one to design experiments yielding signals of the type $\langle \exp[i\omega_1 t_{p1}] \exp[-i\omega_2 t_{p2}] \exp[i\omega_3 t] \rangle$ [74] and even higher multiple-time correlations. One of the drawbacks of the experimental implementations is that an excessive number of spectra needs to be measured for an entire array of independently incremented evolution times t_{p1}, t_{p2}, t_{p3} (etc.). Therefore, 3D spectra of solids were reported only occasionally and, to our knowledge, no full but
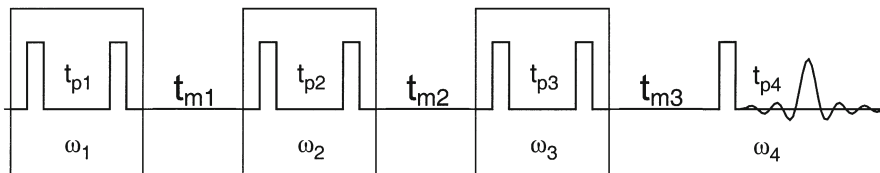
Fig. 17.6. Modular design of multidimensional NMR, here for the example of a 4D experiment. In frequency domain spectroscopy each relevant evolution time has to be incremented systematically in order to map out the frequencies, ω_i. In time domain spectroscopy some mixing times, t_{mi}, are varied with t_p kept fixed

only reduced 4D experiments have been performed to date (see Sect. 17.3.4, below).

Some of the information which these high-dimensional spectra contain can also be retrieved by analyzing higher-order signals in the time domain. Usually this is done by again focusing on echo signals which renders the corresponding experiments relatively time efficient. The significance of multiple-time correlation functions is discussed next.

17.2.3.2
Multiple-Time Correlations

In this subsection we deal with questions relating to the nature of the nonexponential relaxation or correlation functions in disordered materials. In the literature on BDS this issue is well known and has long been discussed in terms of, e.g., empirical distributions as well as defect diffusion [75] and environmental fluctuation models [76] and their impact on the shape of dielectric loss spectra. Since the seminal paper by Schmidt-Rohr and Spiess [77], who first studied multiple-time correlations in glass-forming materials, NMR and later other methods [64, 78, 79] have provided clues for our understanding of the origin of nonexponential responses [80–82]. Let us note that several properties of multiple-time CFs and experimental results relating to spatial and dynamical heterogeneities have been reviewed previously [83]. It should be noted that there are various notions around for the terms 'spatial heterogeneity' and 'dynamical heterogeneity'. In particular the latter is sometimes used to imply (i) the existence of a heterogeneity (or a distribution) in a dynamic (or kinetic) quantity or alternatively (ii) that this heterogeneity is not static but transient in nature. In this chapter we will conform to the definition that we have given previously. It states that a system will be called dynamically heterogeneous if it is possible to select a dynamically distinguishable subensemble by (computer) experiments [84].

In Sect. 17.2.2.2 we pointed out that for a proper choice of t_p the 2t-echo with a fixed mixing time can be considered as a low-pass filter (see also Appendix 17.1). This property of the stimulated echo, $F_2^{AJ}(t_{\text{filter}})$, is pictorially represented in Fig. 17.7a,b. Let us recall that this filter relies on probing the NMR
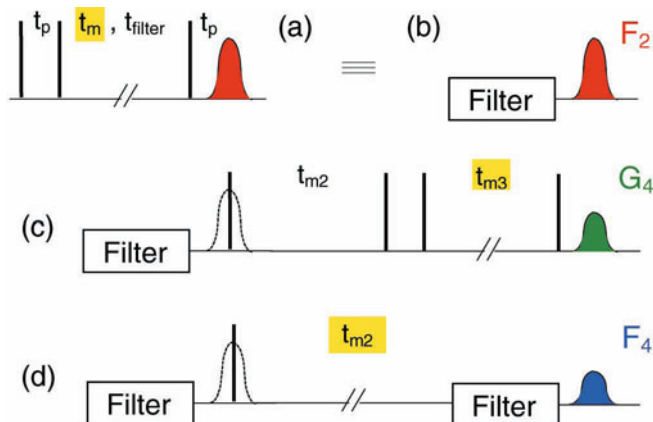
Fig. 17.7. a Three-pulse stimulated-echo sequence which allows one to measure the decay of rotational correlations when increasing the mixing time, $t_m = t_{m1}$. **b** This sketch expresses that for a proper setting of the evolution time, t_p, this sequence can act as a low-pass filter for fixed t_{filter}. **c** Sketch of the sequence for measuring the rotational decorrelation of a filtered subensemble. For t_{m2} (= t_{req}) → 0 this corresponds to $G_4(t_{m3})$. **d** Sketch of the double-filter approach useful for measuring $F_4(t_{m2})$. Note that variable mixing times are reproduced on *yellow background*. The *dashed echoes* are not detected but stored (i.e., transferred to longitudinal magnetization) by the pulse applied at its center

frequency at two points in time. In particular, above we have defined the filter efficiency, *FE*, as a measure of the fraction of 'molecules' (more precise: relevant nuclear interaction tensors) which have not reoriented during t_{filter}. Using an RF pulse the magnetization of this slow subensemble can then be stored for further analysis, cf. Fig. 17.7c,d. In the experiments, to be described in the following, this subensemble is probed at two additional points in time. Thus, in total, the NMR frequency reflecting the orientation of a molecule or molecular segment is monitored at four points in time. Using the notation for the times and frequencies as implied in Fig. 17.6 one of the relevant 4t-CFs can be written as

$$E_4(t_p, t_{m1}, t_{m2}, t_{m3}) = \langle \sin(\omega_1 t_p) \sin(\omega_2 t_p) \sin(\omega_3 t_p) \sin(\omega_4 t_p) \rangle. \tag{17.10}$$

It should be noted that the cosine counterpart of $E_4(t_p, t_{m1}, t_{m2}, t_{m3})$ as well as the difference version $\langle \cos[(\omega_1 - \omega_2)t_p] \cos[(\omega_3 - \omega_4)t_p] \rangle$ and related functions are also measurable. In this section we will first consider three types of 4t-CFs which all derive from the same general function $E_4(t_p, t_{m1}, t_{m2}, t_{m3})$ or related expressions. However, these functions differ with respect to which times are kept constant and which ones are varied. In the literature these functions are designated as $G_4(t_{m3})$, $F_4(t_{m2})$, and $L_4(t_{m2})$ with the written arguments indicating the *variable* mixing time. Finally, we will discuss another 4t-CF, called $F_4^{CP}(t_{m2})$, which previously has been used to map out spatial heterogeneity.

Conceptually the simplest function is $G_4(t_{m3})$. First, one filters a slow (on the scale set by $t_{m1} = t_{filter}$) subensemble with the re-equilibration time chosen close to zero ($t_{m2} = t_{req} \to 0$). Then the dynamics of the filtered slow molecules are probed by determining their motional correlation function, $G_4(t_{m3})$; see Fig. 17.7c.

Fig. 17.8. a In a dynamically heterogeneous system $F_2(t_m)$ probes the entire spectrum of reorientation rates. **b** $G_4(t_{m3})$, on the other hand, samples only the small rates, i.e., the effectively slow contributions. If the filter efficiency is larger, then fewer fast spectral components do contribute to $G_4(t_{m3})$
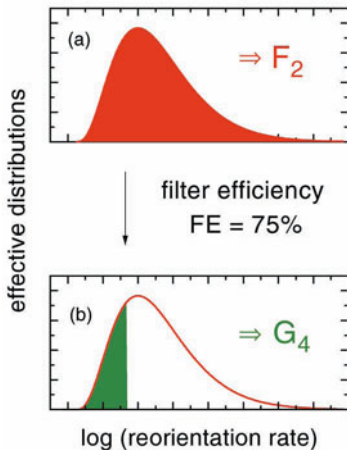
In this situation $G_4(t_{m3})$ reduces in fact to a three-time correlation function with two mixing time intervals t_{filter} (defining the filter efficiency) and t_{m3}. The latter is the relevant time variable for probing the dynamics of the slow subensemble. If the time scale on which $G_4(t_{m3})$ decays is denoted as τ_4 then, in a dynamically *heterogeneous* scenario for which it is possible to select only effectively slow contributions, one expects $\tau_4 > \tau_2$. For a heterogeneous system the action of the filter is sketched in Fig. 17.8. The τ_4/τ_2 ratio can easily be made quantitative in the *fully* heterogeneous case, corresponding to a distribution of exponentials, since here one has $G_4(t) = F_2(t + t_{\text{filter}})/F_2(t_{\text{filter}})$ [84]. The assumption $F_2(t) \sim \exp[-(t/\tau_2)^{\beta_2}]$, with the precautions formulated in Appendix 17.1 in mind, then yields the ratio of the corresponding time constants as

$$\tau_4/\tau_2 = [1 - \ln(1 - FE)]^{1/\beta_2} - [-\ln(1 - FE)]^{1/\beta_2} \tag{17.11}$$

For the fully homogeneous scenario, sometimes also expressed by saying that the intrinsic stretching is $\beta_{in} = 1$, no dynamic but only amplitude filtering may be expected so that one obtains $G_4(t) \sim F_2(t)$; hence $\tau_4/\tau_2 = 1$. Intermediate ratios have been considered elsewhere [84].

In order to address the question of how long it takes the sample to 'forget' the selection one could measure τ_4 for successively longer and longer t_{m2} until $\tau_4(t_{m2})$ approaches τ_2. Although the implementation of this idea is relatively time consuming, it has been demonstrated using a photobleaching technique [78]. In the context of NMR there is a more time efficient alternative by employing the same low pass filter twice, as sketched in Fig. 17.7d. With the requirements regarding the angular jump filter fulfilled (cf. Appendix 17.1), the four-time echo function, $F_4(t_{m2})$, will be maximum for $t_{m2} = 0$. This is because all molecules which have 'survived' the first low-pass filter, with no time allowed for exchange to take place, i.e., $t_{m2} = 0$, will still be slow when entering the second low-pass filter. However, if $t_{m2} \to \infty$ then there will be an effective exchange between slow and fast motions so that just prior to entering the second low pass, the selected subensemble will exhibit the same shape of the original distribution, albeit reduced in overall magnitude. This is sketched in Fig. 17.9 which reveals that the
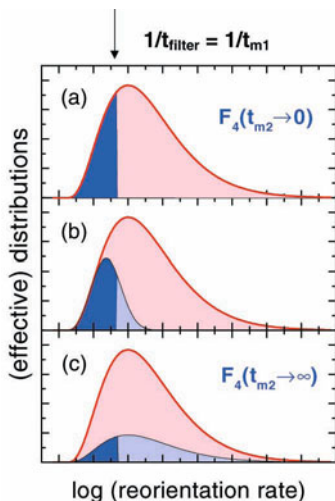
Fig. 17.9. Evolution of effective distributions in heterogeneous systems in relation to the $F_4(t_{m2})$ experiment. The amplitude of $F_4(t_{m2})$ is the smaller the smaller the dark blue area: **a** for short t_{m2} the slow fraction (dark blue) passes the filter twice; **b** partial re-equilibration during t_{m2} renders some 'slow' relaxations 'fast': the (dark *and* light) blue spectrum is the input to the second filter, but only the dark blue fraction can pass it; **c** the dynamic exchange is complete, i.e., red and blue spectra have the same shape but different amplitudes. It is seen that even in the limit of long t_{m2} a finite slow (dark blue) fraction remains. Thus for finite filter efficiencies $F_4(t_{m2})$ does not decay to zero

amplitude $F_4(t_{m2} \to \infty)$ will be smaller than $F_4(t_{m2} \to 0)$, but finite. From Fig. 17.9 one may also recognize that variations of the filter edge, $t_{m1} = t_{m3} \equiv t_{\text{filter}}$, will lead to related changes in $F_4(t_{m2} \to \infty)$. The decay of $F_4(t_{m2})$ directly yields the time scale on which the effective slow $\leftrightarrow$ fast exchange takes place. An even simpler scenario arises if rather than a more realistic, continuous distribution, a bimodal one is considered, cf. Fig. 17.10a. This will turn out helpful not only when dynamic but also when spatial aspects of heterogeneity are dealt with.

The third type of 4t-CF, denoted as $L_4(t_{m2})$, which does not directly address potential spatial heterogeneities is based on the same pulse sequence as $F_4(t_{m2})$, but with $t_p \to 0$ [85]. In this limit Eq. (17.10) can be used to define

$$L_4(t_{m2}) = \frac{E(t_p \to 0, t_{m1}, t_{m2}, t_{m3})}{E(t_p \to 0, t_{m1}, t_{m2} \to 0, t_{m3})} \tag{17.12}$$

and thus $L_4(t_{m2}) \sim \langle \omega_1 \omega_2 \omega_3 \omega_4 \rangle = (t_p \delta)^4 \langle P_2(\cos\theta_1) P_2(\cos\theta_2) P_2(\cos\theta_3) P_2(\cos\theta_4) \rangle$. For the latter equality axially symmetric tensors ($\eta = 0$, cf. Eq. 17.9) were assumed for simplicity. It should be noted that the proportionality sign in the above expression is justified by the fact that the term $E_4(t_p \to 0, t_{m1}, t_{m2} \to 0, t_{m3})$ appearing in the denominator of Eq. (17.12) is constant for fixed filter times $t_{m1} = t_{m3}$ (which we always consider in relation to $L_4(t_{m2})$). Furthermore, from Eq. (17.12) it is obvious that $L_4(t_{m2})$ approaches unity for $t_{m2} \to 0$. The CF $L_4(t_{m2})$ has some interesting properties. In [85] (see also Appendix 17.2) it was shown that $L_4(t_{m2})$ can be decomposed into three terms: one is proportional to $g_4(t)$, one is propor-

Fig. 17.10. Schematic representation of the timing scheme for: **a** the $F_4(t_{m2})$ experiments; **b** the $F_4^{CP}(t_{m2})$ experiments. The latter is designated here as $F_4^{\xi}(t_{m2})$. The simple case of a bimodal distribution of reorientation rates, k_{slow} and k_{fast}, is depicted. The exchange rate is denoted as Γ and the spin diffusion coefficient as D. Reproduced from [87] with permission
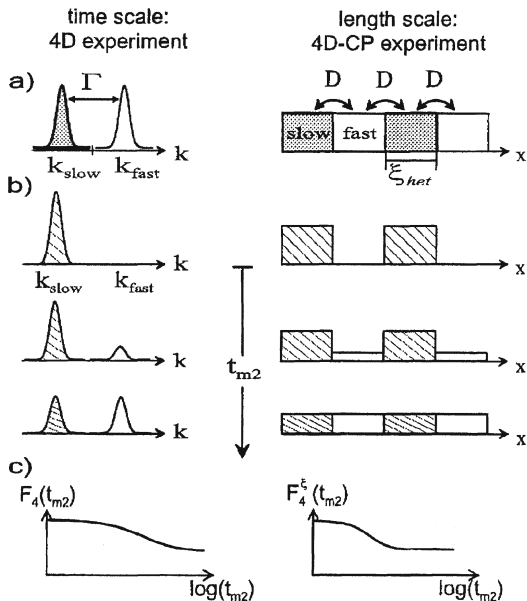
tional to $g_2(t)$, and a third one is not directly dependent on molecular orientations but on dynamic exchange processes. It was shown [85] that in the absence of an effective slow $\leftrightarrow$ fast exchange $L_4(t_{m2})$ does not decay to below $\frac{7}{15}$, even in the limit of long t_{m2} for which $g_4(t_{m2}) = g_2(t_{m2}) = 0$ [86]. However, in the presence of exchange processes $L_4(t_{m2})$ can drop below this plateau value of $\frac{7}{15}$. By considering simple rate exchange models it was demonstrated that the time scale on which such a decay takes place directly yields the exchange rate [85]. Thus, with respect to dynamic exchange $L_4(t_{m2})$ contains the same information as $F_4(t_{m2})$, however, without the requirement to make sure that the random-jump assumption, as implicit in the application of the low-pass filter, is appropriate. This advantage of $L_4(t_{m2})$ is obtained at the expense of the need to approach closely the limit $t_p \rightarrow 0$. Due to finite pulse lengths this conditions will be hard to meet in practice, unless similar 'tricks' to those in 2D exchange NMR are employed [74].

Let us recall that the technique described in this present section, so far, only addresses the issue of dynamic (sometimes called spectral) heterogeneity. In order to find out whether dynamic heterogeneity and spatial heterogeneity are related, ^{13}C-NMR experiments on organic glass formers have been performed [87, 88]. In this approach one augments the $F_4(t_{m2})$ technique with cross polarization (CP) steps [89] (i) from the carbons to the protons at the beginning of t_{m2} and (ii) back to the carbons near the end of t_{m2} ($\ll \tau_\alpha$). The analysis of the associated echo amplitude, $F_4^{CP}(t_{m2})$, is based on the following considerations. If the carbons selected by the first filter are spatially clustered, so will be the proton magnetization right after the first CP step, cf. Fig. 17.10b. However, during t_{m2} spin diffusion (which is very effective among the protons, but not among the carbons) will lead to a successive redistribution of the magnetization first to the protons in the vicinity of

the carbons in the selected spatial regions and then to all protons throughout the sample. Thus, the amount of proton magnetization which is transferred back (only those carbons in the initially selected regions are relevant) depends t_{m2}, i.e., it will be smaller the longer t_{m2} is; see Fig. 17.10b for a schematic illustration.

The main result of this combined dynamic and spatial selection procedure is that, as compared to $F_4(t_{m2})$, the echo amplitude $F_4^{CP}(t_{m2})$ exhibits an additional decay. The smaller the selected spatial regions are the shorter is the time scale on which this decay takes place. Thus, from measurements of $F_4^{CP}(t_{m2})$ one can learn whether the low-pass filtered spins are spatially clustered and then how large typical cluster sizes are. For further details see [87, 88].

17.3
Combined Dielectric and NMR Studies: Recent Experimental Examples

17.3.1
Dynamics in 'Simple' Glass Formers: Glycerol vs Toluene

There are several ways to compare results of NMR with those from dielectric spectroscopy. In the literature (and also in this chapter) this is most often done by compiling the characteristic relaxation (or correlation) times from both approaches. A more detailed view on the dynamics is, however, possible by comparing the shapes of the spectral densities or alternatively the (associated) spin-lattice relaxation times, via Eqs. (17.2) and (17.3). This is exemplified for the typical glass forming liquid glycerol in Fig. 17.11 [90] for a frequency of 55 MHz.
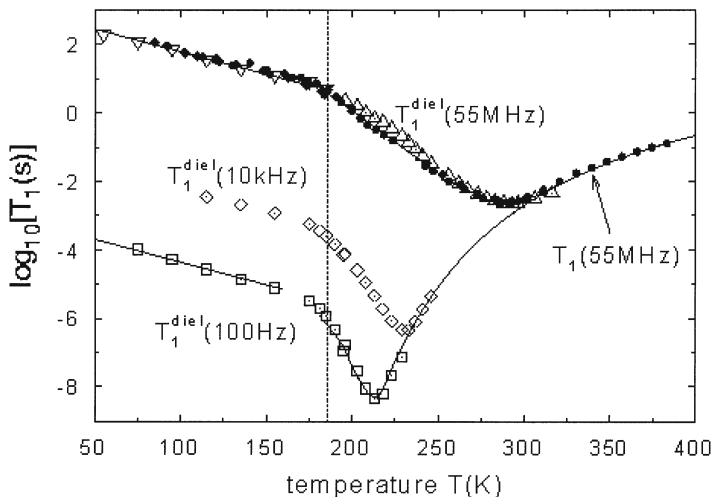
Fig. 17.11. Spin-relaxation times, T_1, of glycerol-d_3 as a function of temperature. The *solid symbols* are from NMR the *open symbols* from dielectric loss measurements. For comparable frequencies the data from both approaches agree. T_g is marked by the vertical line. Reproduced from [90] with permission

The agreement between the results of the two experimental techniques is seen to be very good. Most prominent is the minimum showing up in T_1 or in T_1^{diel} (roughly proportional to $1/\varepsilon''(T)$] which is associated with the structural relaxation, usually termed α-process. On a *qualitative* level T_1 data of other supercooled organic liquids look quite similar to those shown in Fig. 17.11; see, e.g., [91] for a recent compilation. However, when quantitatively comparing T_1 of different glass formers (even those recorded at similar Larmor frequencies) a number of differences show up: (i) if the widths of structural correlation times vary so do the depths of the T_1 curves (cf. Fig. 17.1); (ii) if the kinetic fragilities [92] of glassformers are larger than that of glycerol then the temperature corresponding to the T_1 minimum is closer to the glass transition on a T_g-normalized temperature scale; (iii) below T_g one finds that T_1 is dominated by processes which are fast with respect to the structural relaxation like, e.g., those giving rise to the so-called dielectric high-frequency wing or other secondary relaxations. In comparison to glycerol these are much more pronounced in, e.g., toluene. Consequently, below T_g the spin-lattice relaxation rate of toluene [93] is considerably shorter than that of glycerol. Let us mention that a comparison of $l = 1$ and $l = 2$ CFs was previously performed for this glass former by simultaneous dielectric and Kerr-effect measurements [94].

By analyzing T_1 data quantitatively and/or by carrying out frequency dependent dielectric measurements as a function of temperature, characteristic relaxation times can be gathered over wide ranges [93, 95–98]. In Fig. 17.12 time scale data for glycerol and toluene were collected from various experimental techniques covering a large dynamic window. In this Arrhenius plot the trace of the structural relaxation time data of toluene appears somewhat more curved than
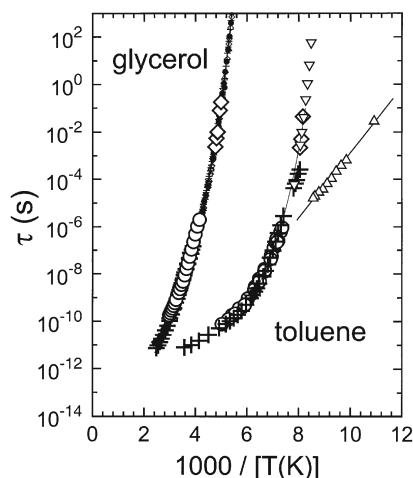
Fig. 17.12. Activation plot for toluene and glycerol as determined by NMR-techniques and broadband dielectric spectroscopy. For toluene: ^{2}H spin alignment (toluene-d$_3$, $\diamondsuit$), ^{2}H-T_1 (toluene-d$_5$, +) ^{1}H static gradient technique (toluene-d$_3$,$\bigcirc$) [93], and dielectric relaxation (*triangles*) [196]. For glycerol: ^{2}H spin alignment (glycerol-d$_5$, $\diamondsuit$ [105]; glycerol-d$_3$, $\diamondsuit$ [197]), ^{2}H-T_1 (glycerol-d$_5$, +) [197], ^{1}H static gradient technique ($\bigcirc$) [45], and dielectric relaxation (*small symbols*) [97, 98]

that of glycerol. This effect is even more pronounced in a T_g scaled plot (usually called Angell plot), demonstrating that the van der Waals glass former toluene is considerably more kinetically fragile than the hydrogen bonded network liquid glycerol [99]. Whenever a direct comparison is possible the results from the two techniques agree well within experimental uncertainty. It is also seen directly that apart from the primary response toluene exhibits a secondary, dielectrically active slow β-relaxation. This process is usually called Johari-Goldstein relaxation and it shows up in the dielectric spectrum as a well separated slow relaxation [100]. Johari-Goldstein processes are found for the majority of supercooled organic liquids and they are sometimes ascribed to slow *intra*molecular degrees of freedom. In view of the fact that in the (rigid) toluene molecule no dielectrically active side-group fluctuations can be imagined it may be conjectured that this relaxation is *inter*molecular in nature. Glycerol, on the other hand, has no well separated secondary relaxation, but only a pronounced high frequency wing. In recent experiments it could be shown that the signature of this process becomes more pronounced after aging for a period of five weeks [101]; see also Chap. 5. This indicates that the high frequency wing has to be viewed as a secondary relaxation, too. This secondary process, which has a different temperature dependence as the conventional Johari-Goldstein process [102], is usually masked by the dominating α-relaxation.

Another striking difference between glycerol and toluene is obvious when comparing the ^{2}H NMR solid-echo spectra in the correlation time window between about 1 and 100 μs, cf. Fig. 17.13 [97]. For glycerol the NMR line shape undergoes a transition from a motionally narrowed peak at high temperatures to a Pake spectrum at low temperatures. Keeping in mind that the deuteron NMR frequency is determined by the orientation of the C-^{2}H bond with respect to the external magnetic field, it is obvious that this observation corresponds to a transition from a fast to a slow *isotropic* reorientation on the scale of the inverse anisotropy parameter, δ^{-1}, of about 1 μs.

In contrast to glycerol, the ^{2}H NMR solid-echo spectra for toluene change only little with temperature in the range shown in Fig. 17.13. The absence of major spectral changes for toluene at $T < 125$ K indicates that the angular excursion of the molecular reorientations is too small to lead to significant modulations of the NMR frequency and/or that the distribution of associated correlation times is essentially out of the NMR time window (which for solid-echo spectroscopy ranges roughly from about 3 μs to 0.3 ms). A glance at the Arrhenius plot (Fig. 17.12) reveals that for $T < 125$ K the α-relaxation time of toluene is indeed much longer than δ^{-1}, but that the β-relaxation times are in the mentioned time window. Thus one may conclude that a geometrically highly restricted (i.e., anisotropic local) molecular motion is responsible for the β-process. We just mention here that these spectral changes can be well described by numerical random walk simulations [56]. In these computations it was assumed that *all* molecules perform small-angle rotational jumps, i.e., the orientation of each C-^{2}H bond is restricted to a cone with an opening angle of a few degrees. (Of course the orientations of these cones are isotropically distributed.) The important point is that it is not necessary to invoke the notion that only a subgroup of all molecules is involved in this process [97]. Thus, studies of one-dimensional

Fig. 17.13. ^{2}H NMR solid-echo spectra with inter-pulse delays of $t_p = 20$ μs for glycerol-d$_5$ and toluene-d$_5$. The correlation time window covers the range from 2 μs to 100 s. Taken from [97] with permission

glycerol-d$_5$ toluene-d$_5$

241 K   2 μs   125 K

236 K   123 K

234 K   121 K

233 K   10 μs   119 K

229 K   116 K

222 K   100 μs   77 μs   110 K

189 K   >>1/δ   71 K

-200 -100   0   100 200   -200 -100   0   100 200
ν [kHz]   ν [kHz]
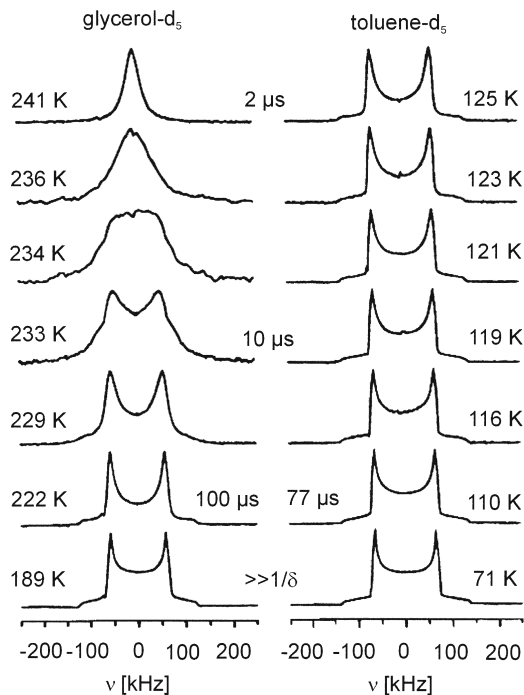
solid-echo spectra can give valuable insights into the geometry of the molecular motion which is associated with the β-process. Another option that we will only mention in this context is to record solid-echo spectra for variable inter-pulse delays. Then small-angle and large-angle motions each lead to characteristic line-shape changes. This technique, which is well known in the field of polymers [103, 104], has recently been revived also for supercooled liquids [97].

In order to unravel the motional mechanism governing the α-process, in the vicinity of the calorimetric glass transition, one may resort to techniques which operate on still longer time scales. Thus, one may apply two-dimensional spectroscopy in the frequency or time domains, which can cover the correlation time scale of about 0.1 ms to that of T_1 (usually in the range of seconds). In Fig. 17.14 we show stimulated-echo data, $F_2(t_p, t_m)$, of glycerol for wide ranges of evolution and mixing times. A model-free analysis of these data reveals that each C-^{2}H bond performs an overall isotropic reorientation [105]. This set of data was analyzed further by fitting the data using a stretched exponential function for each t_p. It turned out that the stretching of $F_2(t_m)$ depends only weakly on t_p. But the effective time scale $\tau(t_p)$ was found to be the smaller the larger the evolution time was. The resulting $\langle \tau(t_p) \rangle$ patterns for glycerol and for toluene are shown in Fig. 17.15 [106]. When comparing these experimental data with the simulation results presented in Fig. 17.4, it becomes clear that the average jump angle associated with the α-relaxation might be around 10°. An excellent quantitative de-

Fig. 17.14. Two-dimensional surface wire representation of experimental cosine correlation functions, $E^{\cos}(t_p,t)$ $= F_2^{\cos}(t_p,t)/F_2^{\cos}(t_p,t\to 0)$, for glycerol-d$_5$ measured at $T = 204$ K. Taken from [105]
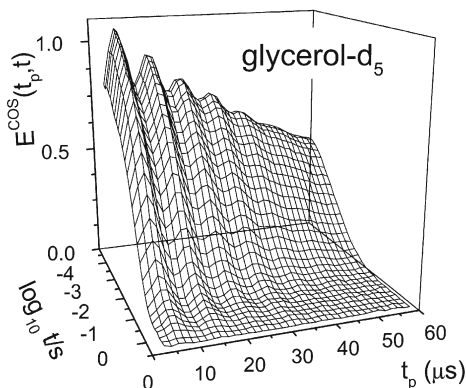
scription of the data shown in Fig. 17.15 is only possible (cf. the solid lines drawn there) by assuming suitable, strongly asymmetric, jump angle distributions [107]. Among the simplest choices are bimodal distributions involving a large fraction of small-angle jumps ($\leq 2 - 3°$) and a smaller fraction of large jump angles ($>25°$). The large-angle jumps typically contribute at least half of the root mean square angular displacement in these glass formers, but the relative contributions of small and large angle jumps were reported to differ somewhat for glycerol and toluene [106]. Overall the molecular motion in the α-relaxation regime of these substances is quite similar. It should also be mentioned that this type of composite reorientation process (see the sketch presented as inset to Fig. 17.15) is found in the primary response also of various other polymeric (see Sect. 17.3.4, below) and non-polymeric supercooled liquids near the glass transition [55, 105, 108–111]. Furthermore, there are indications that the mean jump angle increases with temperature [112].

Next let us address the question regarding the origin of the stretching of the two-time correlation functions, $F_2(t_m)$, or of the associated broadening of the dielectric loss spectra in glycerol and toluene. Evidence for dynamic heterogeneity in these materials was obtained from nonresonant hole burning [55, 64] (see also Chap. 14) and multiple-time stimulated-echo investigations. The heterogeneity lifetime was measured for these and other substances using four-time correlation functions. As an example in Fig. 17.16 we show an $L_4(t_{m2})$ correlation function for glycerol recorded at about $T_g + 20$ K [85]. It is clearly seen that $L_4(t_{m2})$, for long t_{m2}, drops below the threshold of 7/15. According to the considerations in Sect. 17.2.3.2, this signals the presence of dynamic exchange which furthermore takes place on the same time scale as the molecular reorientation. Similar results were obtained for a range of temperatures. Since the dynamic heterogeneity is thus short-lived (or highly transient) in character, it may be asked whether under these conditions it is possible to acquire direct experimental evidence for spatial heterogeneity. This issue was recently addressed in a 4D-CP NMR study of supercooled glycerol which demonstrated the existence of a finite heterogeneity length scale [88]. This finding reveals a close correspondence of dynamic and spatial aspects of heterogeneity. Similar
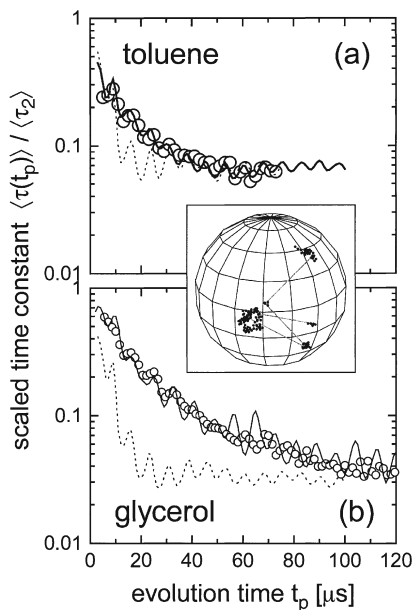
Fig. 17.15. Comparison of the $\langle \tau(t_p) \rangle$ patterns for: **a** toluene-d_5; **b** glycerol-d_5. The *lines* are from random walk simulations described in Sect. 17.2.2.2. In a, for toluene the *dotted line* reflects a single jump angle of $\varphi = 10°$ and the *solid line* represents simulations using a bimodal jump angle distribution with 80% 4° jumps and 20% 25° jumps. In b, for glycerol the *dotted line* reflects a single jump angle of $\varphi = 8°$, the *solid line* a bimodal distribution with 98% 2° jumps and 2% 20° jumps. The inset gives a schematic representation of an orientational trajectory projected onto a unit sphere that serves to illustrate the complex rotational motion near the glass transition. Adapted from [106]
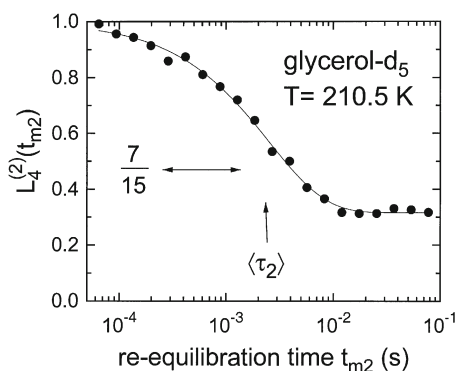
Fig. 17.16. A four-time rotational correlation function, $L_4(t_{m2})$, of glycerol-d_5 measured for $t_{m1} = t_{m3} = 6.4$ ms. The plateau value, i.e., $L_4(t_{m2} \to \infty)$, becomes much smaller than 7/15 (marked by the *double arrow*), indicating that dynamic exchange takes place on the same time scale as the molecular reorientation. The rotational correlation time $\langle \tau_2 \rangle$ is also indicated. Adapted from [85]

observations were also made for polymers, as discussed in more detail in Sect. 17.3.4, below.

17.3.2
Motional Processes of a Triphenylene-Based Discotic Liquid Crystal

Liquid crystals are used in many technological applications since they allow one to combine various favorable properties. However, these materials are also interesting to study from a scientific point of view because they are usually characterized by a complex molecular dynamics. Hence, dielectric spectroscopy and particularly NMR are useful for unraveling many of their static and kinetic properties [11, 113–115]. Here we will focus on triphenylene-based discotic liquid crystals which can be functionalized by a large number of different side groups [116]. In particular we will treat in some detail the liquid crystal of the type depicted in Fig. 17.17. This substance exhibits a broad temperature range in which the columnar mesophase is stable. Also it is a member of the group of those liquid crystals that show a calorimetric glass transition [117–121].

In order to characterize the dynamics of this system, broadband dielectric measurements were carried out. As demonstrated in Fig. 17.18 evidence for two relaxation processes was obtained. These can be ascribed to a secondary β-relaxation, with a well defined activation energy, and a primary relaxation associated with the dynamic glass transition. The α-relaxation times exhibit pronounced deviations from the Arrhenius law, see Fig. 17.19. At the calorimetric glass transition temperature, $T_g = 227$ K, the relaxation time is $\tau_\alpha(T_g) \approx 10$ s. Interestingly, X-ray investigations showed, however, no indication of a step in the thermal expansion coefficient, usually accompanying calorimetric glass transitions [121]. Rather the thermal expansion measured along the discotic columns exhibited such a feature at $T_g + 30$ K. Here the dielectric α-relaxation time is about 8 ms. This suggested that the glass transition in this system is strongly anisotropic and that the primary dielectric relaxation stems from a lo-
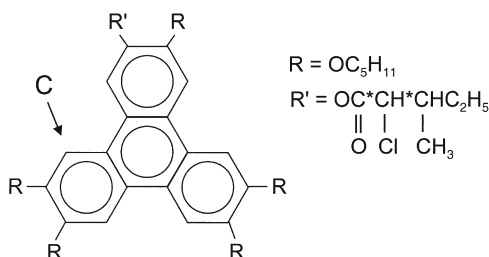
Fig. 17.17. Structure and chemical composition of the discotic liquid crystal (2S,3S)-2-chloro-3-methyl-penta-nonyloxy-pentakis(pentyloxy)-triphenylene. Here the substitution of one of the ether side chains by a chiral ester side group gives rise to an electric dipole moment. This substance has a clearing temperature as high, as 455 K and a hexagonally ordered D$_{h0}$ phase. No crystallization but a glass transition at $T_g = 227$ K is observed. The six C positions (one is marked) were selectively deuterated for the NMR investigations
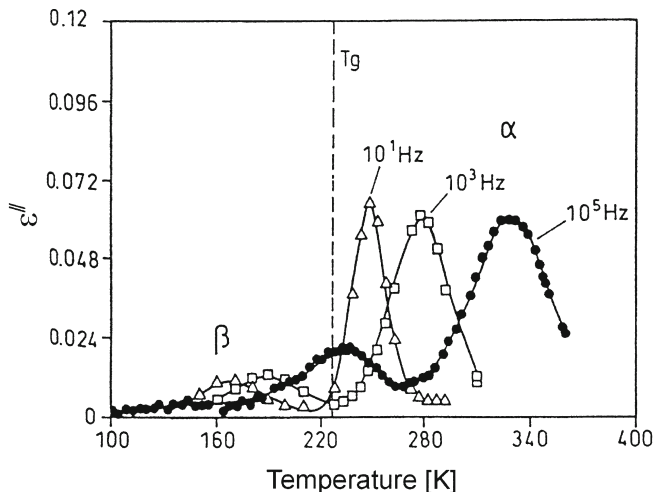
Fig. 17.18. Dielectric loss ε'' vs temperature of the substance shown in Fig. 17.17 at the frequencies indicated. The calorimetrically determined glass transition temperature T_g is indicated (*dashed line*)
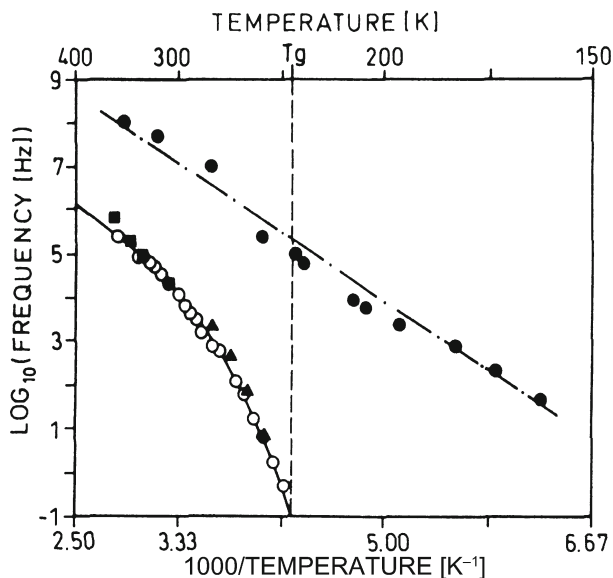
Fig. 17.19. The *circles* in this activation plot represent the two dielectric relaxation processes shown in Fig. 17.17. The NMR data from 1D line shape analysis (■) and 2D ^{2}H exchange spectroscopy (▲) nicely agree with those from the dielectrically active α-process. The β-process can be ascribed to librational fluctuations of the side chains. The *solid line* indicates a fit according to a Vogel-Fulcher equation and the *dashed-dotted line* is an Arrhenius law. The calorimetrically determined glass transition temperature T_g is indicated (*dashed line*). Reproduced from [126] with permission

Fig. 17.20. Solid state
^{2}H NMR spectra of an over-
all isotropic ("unoriented")
sample at the specified tem-
peratures. Additional *verti-
cal lines* near the singulari-
ties of the low temperature
spectra and the outer edges
of the high temperature
spectrum are drawn to
guide the eye. Reproduced
from [118] with permission

100 kHz

200 K

270 K

400 K
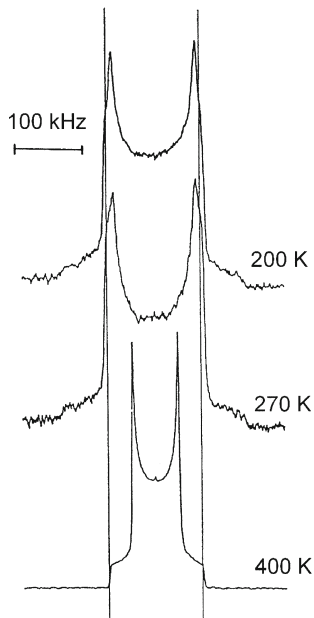
cal rotational motion. The inter-columnar and the intra-columnar motions are likely to be associated with different degrees of cooperativity [122].

In order to test the molecular motion via NMR, the system shown in Fig. 17.17 was selectively deuterated at the aromatic core. Thus one is sensitive to the overall rotational dynamics (rather than to side group motions). Temperature dependent ^{2}H NMR spectra for samples with an isotropic distribution of liquid crystalline domains are shown in Fig. 17.20 for three temperatures [118]. In this context it is important to note that the magnetic fields typically used for NMR do not realign the directors, unless the clearing point is very closely approached. At 200 K, well below T_g, a powder spectrum characteristic for rigid triphenylene rings is found. The spectrum remains unchanged up to 270 K, thus excluding ring motions at rates higher than approximately 10 kHz. In the temperature range between 280 K and 380 K the line shape changes due to the onset of ring motion with rates between 10 kHz and 10 MHz [123–125]. In the fast exchange limit (see the 400 K spectrum in Fig. 17.20) this motion leads to a Pake type spectrum which (with respect to that at low temperature) is reduced in width by about a factor of two. This is characteristic of an axial motion of the discs around their column axis. The motional correlation times as deduced from a detailed line shape analysis [126] of one-dimensional spectra are included in Fig. 17.19 and are seen to agree very well with the dielectric data.

In order to unravel the motional mechanism related to the dielectrically active α-process in more detail 2D ^{2}H NMR spectroscopy was employed [126]. Prior to the experiments which we describe in the following, the sample was cooled slowly through the isotropic to discotic transition at 455 K. In this case planar order is established, i.e., the directors of the discotic domains are all

Fig. 17.21. (*Top*) 2D ^{2}H NMR spectrum of the discotic liquid crystal shown in Fig. 17.17. It was measured at 270 K with a mixing time of 10 ms. The directors were randomly distributed in planes perpendicular to the external magnetic field (see sketch). (*Bottom*) Simulation based on the model of "jump-diffusion in a threefold potential". Reproduced from [126] with permission
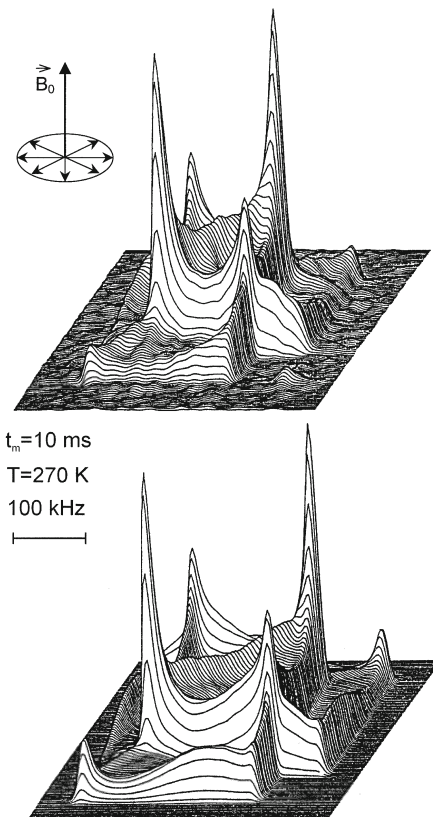
arranged perpendicular to the external magnetic field; see the inset of Fig. 17.21. A typical spectrum that was recorded with the mixing time t_m set longer than the α-relaxation time, τ_α, is shown in Fig. 17.21 (top). For the description of these spectra three scenarios were considered: (i) jumps of 120° perpendicular to the columnar axis, reflecting the approximate threefold molecular symmetry, (ii) one-dimensional small-step rotational diffusion, and (iii) a combination of the two cases which was termed "jump diffusion in a threefold potential", cf. Fig. 17.22 [126]. Only the simulation based on the latter scenario was found to give an excellent agreement with the experiment; see Fig. 17.21 (bottom). The distribution of reorientation angles on which this simulation rests was peaked at 0° and ±120°. Each peak exhibited a Gaussian shape which was about ±15° wide. The time constants that were derived from 2D-NMR measurements compare excellently with those from dielectric spectroscopy; see Fig. 17.19. Thus, the quasi-one-dimensional (intra-columnar) rotational dynamics can be regarded as well understood.

Furthermore, *static inter*-columnar properties are readily accessible using diffraction techniques. Dynamical aspects, on the other hand, can be mapped out by investigating the molecular transport [127]. In this context let us discuss results
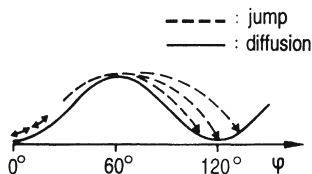
Fig. 17.22. Schematic visualization of the potential associated with the "jump-diffusion" model. Rotational diffusion can occur close to the potential minima. The barriers are crossed by approximate 120° jumps. Reproduced from [126] with permission

from a static field gradient proton NMR study [128] of the compound shown in Fig. 17.17 [129]. Some intermediate scattering functions, as acquired using the stimulated-echo technique for several (fixed) evolution times, are shown in Fig. 17.23 in a semi-logarithmic representation. This renders deviations from an exponential decay in $S_2(t_p,t_m)$ obvious. It is also recognized that the data for all t_p superimpose when they are plotted vs the scaling variable $t_p^2 t_m$ ($\sim q^2 t_m$). For comparison the limiting behaviors of $S_2(t_p,t_m)$ as calculated from Eq. (17.6) for 2D and 3D diffusion are included in this plot. The non-exponentiality of the experimental $S_2(t_p,t_m)$ nicely confirms the anisotropic nature of the inter-columnar motion in this liquid crystal. Thus, the expectation that diffusion along the director axis is much slower than perpendicular to it is borne out by experiment.

Temperature dependent diffusion coefficients as derived from the initial slope of $S_2(t_p,t_m)$ echo decays are shown in Fig. 17.24. For this plot a representation was chosen for which an Arrhenius law yields a straight line. Just below the clearing point ($T = 455$ K) deviations from thermally activated behavior show up. For all temperatures above about 400 K the q^{-2} dependence of the echo decays is nicely obeyed (see inset of Fig. 17.24). At lower temperatures deviations from this simple behavior show up, as also documented in Fig. 17.24.
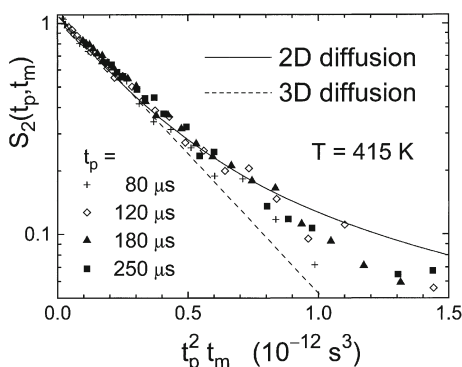
Fig. 17.23. Scaled intermediate scattering functions of the compound shown in Fig. 17.17. They were determined in a static magnetic field gradient of $g = 46.1$ T m^{-1}. The experimental data indicate that the behavior is neither pure 2D and nor isotropic (3D) in character. The lines are calculated using Eq. (17.6). The master plot is based on t_m dependent stimulated echoes acquired for the indicated evolution times [128]
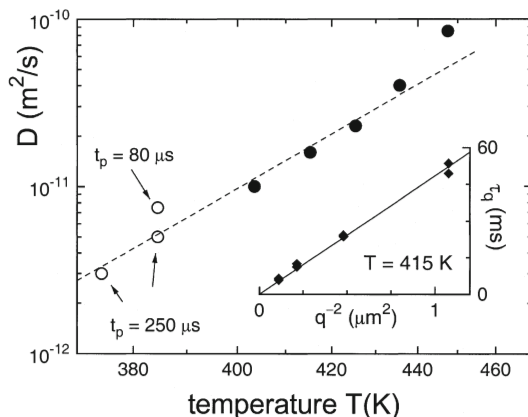
Fig. 17.24. Temperature dependence of effective self diffusion coefficients determined from the initial slope of $S_2(t_p, t_m)$. The inset demonstrates the q^{-2} behavior of the diffusion times, τ_q, for $T = 415$ K. Below about 400 K mechanisms other than translational diffusion commence to contribute to the echo decay. These obviously give rise to apparently t_p dependent diffusion coefficients. The *dashed line* corresponds to an Arrhenius law with an activation energy of 52 kJ mol^{-1} [128]

In this context it should be pointed out that stimulated proton echo decays can occur even in the absence of magnetic field gradients, e.g., when the internuclear vectors of dipolarly coupled spins reorient or change their length in the time regime set by t_m. Corresponding dipolar decorrelation effects are frequently employed in studies of liquid crystals since they allow one to monitor order parameter fluctuations [130]. When aiming at determining self-diffusion coefficients the modulation of dipolar interactions is of course unwanted, because it can lead to a speed-up of the stimulated echo decay (resulting in an *apparent* increase of diffusion, cf. Fig. 17.24). There are various options if one needs to circumvent these difficulties. One could increase the strength of the magnetic field gradient so that the diffusion decay is complete before the dipolar decorrelation sets in. Alternatively, one could suppress the dipolar correlation by means of multiple pulse techniques. These have proven valuable not only in homogeneous magnetic fields [9] but also in the presence of strong field gradients [131]. However, even without these measures the temperature range covered in Fig. 17.24 is wider than for many other liquid crystals, simply because the large width of the temperature range in which the mesophase of the compound shown in Fig. 17.17 is stable.

17.3.3
α- and β-Relaxations in Poly(methyl methacrylate)

In amorphous polymers, the dynamic glass transition (α-relaxation) is often attributed to the cooperative dynamics of main chain segments. At the calorimetric glass transition temperature the backbone fluctuations are characterized by

Fig. 17.25. Arrhenius plot of correlation times of the relaxation dynamics in PMMA. For the β-relaxation, time constants as estimated from NMR spectroscopy (▲) are compared to those evaluated from dielectric loss maxima (□) [137] and from dynamic-mechanical studies (○) [138]. The *straight line* corresponds to an activation energy of 65 kJ mol^{-1}. Reproduced from [132]
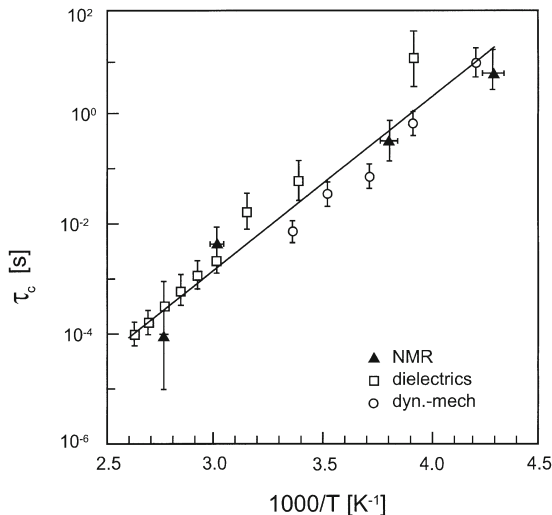
a relaxation time of about 100 s. Additionally secondary relaxations, often involving fluctuations of side groups, can be observed. These processes have been studied by a variety of experimental techniques and in keeping with the spirit of this review we will focus here on a single example, poly(methyl methacrylate) (PMMA) [132–136], which was particularly well studied using multidimensional NMR. Again we will emphasize the unique capabilities of multidimensional solid-state NMR to unravel the geometry of molecular motion for rotational correlation times ranging from milliseconds to seconds.

However, first let us give a brief overview of the dynamics in PMMA. To this end in Fig. 17.25 we present the characteristic relaxation times for PMMA as obtained from dielectric [137] and mechanical [138] relaxation studies in the regime of the β-process. Also included are data from 1D and 2D ^{13}C exchange NMR which were extracted from typical line shape changes (on the scale of the inverse anisotropy parameter, $\delta^{-1} \approx 5$ ms) and from the mixing-time dependence of the exchange intensity, respectively. The averaged correlation times obtained with the different methods all follow an Arrhenius law and agree well with one another (Fig. 17.25). This allows for an unambiguous assignment of the processes seen via NMR spectroscopy.

As for supercooled liquids (Sect. 17.3.1), the motional mechanism governing the α-process was studied using stimulated-echo and related NMR techniques for PMMA [132, 139] as well as for other polymers [140, 141]. It was generally found that a dominant fraction of small jump angles (< 5°) is present, but that a significant portion of the root mean square angular displacement is performed by large-angle reorientations (> 30°).

Rather than discussing the α-process again, let us here focus on the secondary relaxation which for PMMA often was ascribed to reorientational motions of the COOCH$_3$ side group. It is plausible to associate the strong (dielectrically active) β-process of this polymer with fluctuations of the large dipole mo-
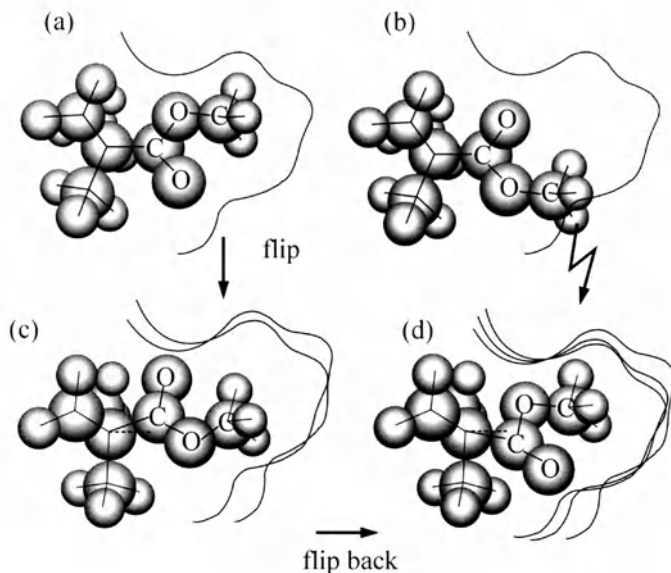
Fig. 17.26. Schematic sketches of the asymmetric side group of PMMA in its local environment: **a** initial side-group orientation; **b** after an exact 180° flip of the side group it does no longer fit into its local environment unless the latter undergoes major rearrangements; **c** only slight environmental deformations are required if the 180° flip is accompanied by an additional twist around the local chain axis; **d** the side group jumps back close to its original orientation in a. It should be noted that the unique principal axis of the CSA tensor at the carboxyl ^{13}C site (i.e., the ω_{33} axis) is perpendicular to the OCO plane (here: essentially the paper plane). Taken from [132] with permission

ment exhibited by the carboxyl group. Exactly how this motion proceeds has remained unclear for a long time. Often it was assumed that the entire side group performs a large-angle motion around the bond linking it to the main chain. Notably 180° flips have been favored in this context [3]. The local conformation of the ester methoxy group is depicted before and after such a flip in panels a and b of Fig. 17.26, respectively. However, as suggested in this figure a simple 180° flip may be impeded by sterical constraints imposed by the immediate environment of the strongly asymmetric side group. It has also been envisioned that significant main-chain motions could be involved in the β-relaxation [137]. For example, one could imagine that Fig. 17.26a and b represent two snapshots of a rocking motion involving side and main chains. Finally, it was discussed whether below T_g other (dielectrically inactive) motions, such as the rotation of the methoxy group around the C-OCH$_3$ bond, could take place in PMMA [138]. In a comprehensive multidimensional ^{2}H and ^{13}C NMR study, upon which we will focus next, the motional mechanism of the sub-T_g relaxation could unambiguously be clarified [132].

In Fig. 17.27a we reproduce a ^{13}C 2D-NMR spectrum of PMMA recorded with a mixing time of $t_m = 50$ ms at 333 K, here $\tau_\beta \approx 10$ ms. The sample with a molec-
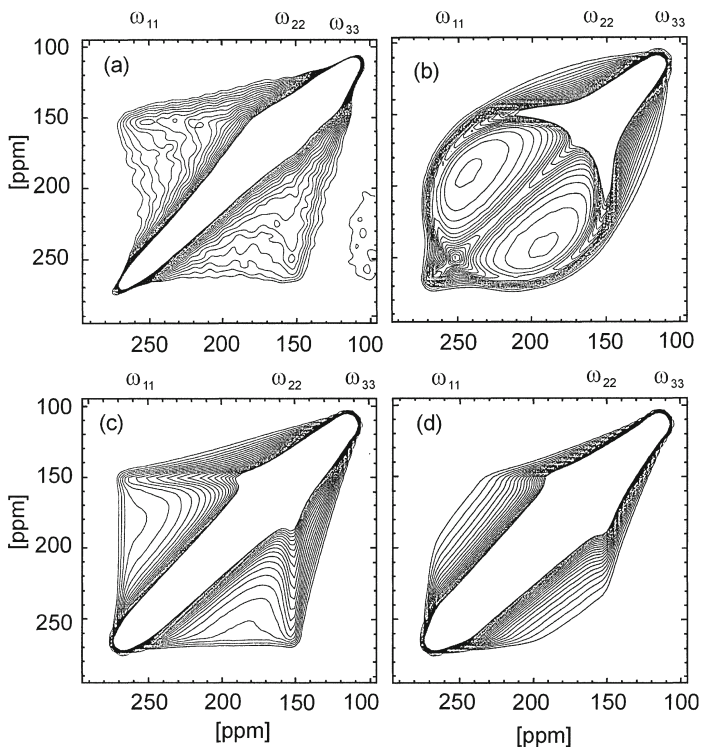
Fig. 17.27. a The 2D exchange ^{13}C NMR spectrum of PMMA recorded for $T = 333$ K and $t_m = 50$ ms with 20% of the ^{13}COO side groups labeled. **b** Simulation using a broad distribution of flip angles centered at 180°. **c** Simulation based on the assumption of a 180 ± 10° flip *and* a concomitant ~20° rotation around the ω_{33} direction (local chain axis). **d** Simulation based on the assumption of a rocking motion around the ω_{33} direction but without 180° flips. Only the simulation shown in c yields a satisfactory description of the experimental spectrum. Taken from [132] with permission

ular weight of $M_w = 112,000$ g mol^{-1} was 20% ^{13}C-labeled at the carboxyl carbon. Most of the spectral intensity is located at or close to the diagonal and only 25 ± 10% appears as exchange intensity. The latter is spread across almost the entire spectral plane. At first glance this spectrum looks as if about one quarter of the segments perform a quasi-diffusive isotropic motion. This is because the existence of well defined jump angles usually manifests itself by the occurrence of elliptical exchange ridges [9]. Of course, an exact 180° flip leaves the CSA tensor invariant, i.e., it produces no change in the NMR frequency and thus no exchange intensity. In this context it may be interesting to mention that, typical for carboxyl group ^{13}C shift tensors, the largest ("unique") principal axis (corresponding to a frequency ω_{33}) is perpendicular to the OCO plane and almost parallel to the local chain axis [132, 142]. Since in the experimental spectrum, Fig. 17.27a, practically all of the exchange intensity occurs between the frequencies ω_{11} and ω_{22}, corresponding to the other two principal axes, it may be anticipated that the mo-

tion leaves the ω_{33} axis essentially invariant. This implies that the ω_{33} axis either acts as a rotation axis, or that it is inverted during the process, or both.

Any motional model for the β-process of PMMA has to take this constraint into account. However, it also has to be ascertained that the quasi-diffusive exchange intensity does not reflect spin-diffusion. Any such suspicion was shown to be insubstantial because: (i) a natural abundance (i.e., 1.1 % ^{13}C) spectrum exhibited an exchange pattern similar to Fig. 17.27a, albeit with reduced signal to noise ratio – due to the great dilution of the ^{13}C spins in the natural abundance sample, the dipole-dipole interactions among the ^{13}C nuclei which gives rise to spin-diffusion, are practically irrelevant in this context; (ii) in spectra recorded for the isotopically enriched sample no exchange intensity occurs at low temperatures (233 K). This finding can only be understood if molecular motion is responsible for the off-diagonal intensity, because spin-diffusion is essentially temperature independent.

In order to describe the exchange pattern more quantitatively simulations based on various motional models were carried out in [132]. Figure 17.27b presents a spectrum computed for a π flip (cf. Fig. 17.26b) smeared out via a Gaussian distribution of jump angles with the center at 180° and a full width at half maximum of 60°. This scenario leads to almost circular ridges [143] which are, however, not observed experimentally. The assumption of a rocking motion alone also cannot explain the experimental spectrum. A calculated exchange pattern corresponding to an anisotropic motion around the ω_{33} axis with a root mean square amplitude of 25° is shown in Fig. 17.27d. Also this spectrum clearly does not describe the data. A similar conclusion can be drawn even if much smaller or larger angular excursions are considered [132]. As already suggested by Fig. 17.26c a combination of a 180° flip *and* a concomitant rocking motion may satisfy the local sterical constraints. Indeed a simulation based on a $180 \pm 10°$ flip and a simultaneous rotation around the ω_{33} axis (root mean square excursion $\pm 20°$) gives a good agreement with the experimental spectrum, cf. Fig. 17.27a,c. For a pictorial representation of this scenario see Fig. 17.26a,c. Obviously the $\sim 20°$ readjustment of the local main chain axis enables the entire side group to execute 180° flips without the necessity of major rearrangements in its environment. These findings are further corroborated by 3D exchange NMR experiments which revealed that the reorientation of each segment involves only two sites with relatively well defined potential energy minima [132]. By studying selectively methoxy deuterated PMMA it could also be demonstrated that, apart from tunneling excitations [136], the rotational motion around the O-CH$_3$ bond is essentially frozen below T_g [132]. Taken together the NMR results show that the β-relaxation in PMMA is not just a simple side group reorientation, but a complex process which involves coupled small and large angle processes of the side and local main chain axes.

In related experiments the molecular dynamics in poly(ethyl methacrylate) was also analyzed and compared with that of PMMA [133]. In the β-relaxation regime the two polymers behave similarly. Additionally in poly(ethyl methacrylate) strongly anisotropic motions were found to characterize its α-process which is quite untypical. When comparing the characteristic time scales of poly(ethyl methacrylate) good agreement between the results of NMR [133–135] and dielectric spectroscopy [144, 145] was found.

17.3.4
Dynamic and Spatial Heterogeneity in Poly(vinyl acetate)

Polymers, like practically all other glass formers, exhibit a broadening of the dielectric loss and of many other, e.g., dynamic-mechanical, susceptibility spectra. The first work which directly resolved the question whether or not a distribution of relaxation (or correlation) times is causing this broadening was carried out for poly(vinyl acetate) (PVAc) at T_g + 20 K [77]. In Fig. 17.28 we reproduce some ^{13}C spectra of the COO group from that NMR work. Figure 17.28a exhibits a 2D exchange spectrum recorded for a mixing time of t_m = 10 ms. The appearance of exchange intensity reveals the presence of reorientational motions on this time scale. The reduced 4D spectrum shown in Fig. 17.28b demonstrates that it is possible to select essentially only the "rigid" segments (on a scale of 30 ms); thus slow and fast motions can be distinguished. This observation is unequivocal evidence for a dynamically heterogeneous scenario. If however the re-equilibration time is chosen much longer (t_{m2} = 1 s, see Fig. 17.28c), considerable off-diagonal intensity is obtained in the reduced 4D spectrum. By comparison with the primary relaxation it was concluded the heterogeneities do not persist much longer than the mean structural relaxation time [146].

These important results gave the first answer to a list of questions relating to the heterogeneity of the α-response. Among them are the following. Is this heterogeneity based on a superposition of exponentials or does it involve intrinsic broadening? How long (in quantitative terms) does the selection persist? And most importantly: is dynamic heterogeneity also associated with the existence of spatial non-uniformities and, if so, what is their characteristic length? All these questions could be resolved by multidimensional NMR as we will review in the following. Furthermore, it is an issue whether the answers to these questions depend on the temperature at which the dynamics is probed. Here, it will be helpful to compare the NMR results with those from dielectric spectroscopy.

In Fig. 17.29 we show the rotational correlation functions, measured for ^{13}C enriched PVAc, with and without previous low pass filtering [95]. These functions were previously denoted as $G_4(t_{m3})$ and $F_2(t_m)$, respectively, and, on the one hand, nicely confirm the evidence for dynamic heterogeneity directly in the time domain. On the other hand, they allow one to map out the degree of intrinsic

Fig. 17.28. Contour plots of multidimensional ^{13}C spectra of PVAc recorded at 320 K (*upper row*) and corresponding simulations (*lower row*): **a** reference 2D spectrum with t_m = 10 ms; **b,c** reduced 4D spectra with the re-equilibration times set to t_{m2} = 10 ms and 1 s, respectively. Reproduced from [77] with permission
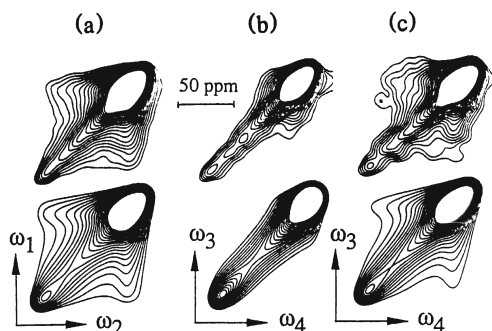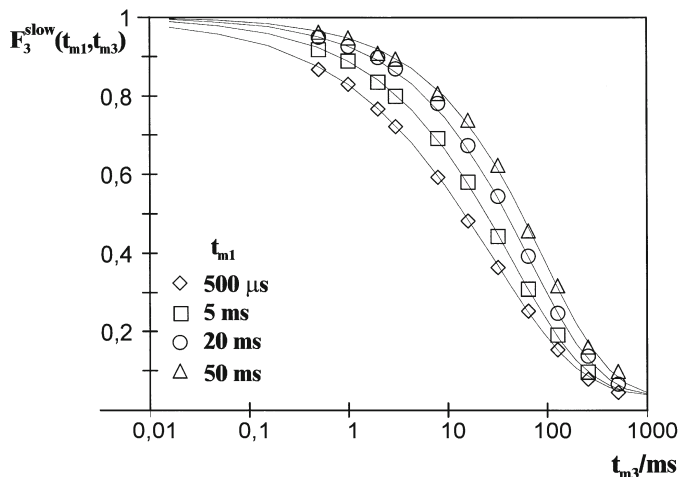
Fig. 17.29. Loss of orientational correlation in selected slow subensembles for PVAc at 315 K. The sample was 40 % ^{13}C enriched at the carbonyl site. It is seen that the larger the filter efficiency is (hence the longer t_{m1} is), the slower does $G_4(t_{m3})$ decay. The behavior of $F_2(t_m)$ is approached for $t_{m1} \rightarrow 0$. Adapted from [95] with permission

stretching. As we have emphasized in Sect. 17.2.3.2 the time constants, τ_4, characterizing the $G_4(t_{m3})$ functions, should get larger the more the efficiency of the low-pass filter is increased. If the loss of orientational correlation of PVAc can be decomposed into a distribution of exponentials, then this increase should follow the prediction of Eq. (17.11). In Fig. 17.30 we demonstrate that the experimental data excellently agree with what is expected from this equation. This demonstrates that exponential relaxation modes are responsible for the nonexponential loss of orientational correlation in PVAc. It should be noted that a similar behavior was also reported for a low-molecular weight liquid [84]. However, for the glassy crystal ortho-carborane indications for an intrinsic nonexponentiality were found [147].

The heterogeneity lifetime of PVAc was measured using the $F_4(t_{m2})$ experiment, cf. Fig. 17.31a and was found to be on the same scale as the loss of orientational correlation. This is occasionally expressed via the so-called rate memory parameter as $Q \approx 1$ [81]. Comparable results were reported for several other glass-formers; for recent reviews see [83, 91]. In order to resolve the length scale issue, the ^{13}C-NMR $F_4(t_{m2})$ experiment was enhanced by a module which renders it sensitive to proton spin-diffusion experiment as sketched in Sect. 17.2.3.2 [87]. In Fig. 17.31b we show the results of the corresponding so-called "one-filter" and "two-filter" experiments performed at $T_g + 10$ K.

The length scale information is contained in the "two-filter" experiment. Before being able to extract this information from these data it has to be taken into account that there is an inevitable loss of echo intensity in the course of these experiments even if there would be no finite heterogeneity length scale. This is due to the fact that at the end of the mixing time, even in the absence of

Fig. 17.30. Ratio of correlation times, τ_4/τ_2, as reported for PVAc at 315 K [95] (and partly reproduced in Fig. 17.29). The *solid line* is calculated from Eq. (17.29) using $\tau_2 = 17.5$ ms and $\beta_2 = 0.46$ [95]. These parameters characterize $F_2(t_m)$ as recorded for $t_p = 120 \,\mu$s. The *dashed line* would be expected in the completely homogeneous limit
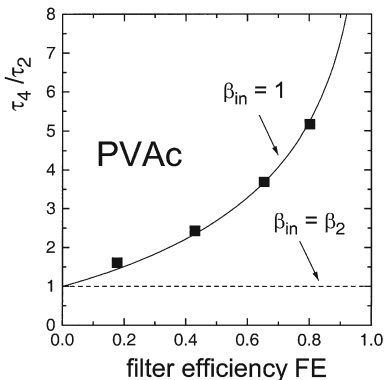
a dynamic selection, not all proton magnetization can be re-transferred to the carbon sites, since cross-polarization is efficient only in the vicinity of the ^{13}C nuclei (in a sphere of diameter d, say). Under the conditions of isotopic dilution, employed for the experiments we describe here, the average distance between the ^{13}C probes is larger than d. Thus from the so-called "one-filter" experiment (cf. Fig. 17.31b) the microscopic spin diffusion coefficient can be obtained, i.e., the ruler of this experiment is calibrated. With an additional dynamic filtering now being performed, cf. the "two-filter" curves, an additional decay arises if the dynamically selected spins are "clustered" on a spatial scale of ξ_{het}. This decay is faster the smaller the length scale ξ_{het} of the immobile regions is. From fits to the experimental data ξ_{het} was estimated to be 3 ± 1 nm [87]; see Fig. 17.31b. Reassuringly, this value is compatible with several previous, much more indirect, experimental estimates. It is important to keep in mind that these 4D-CP results, and those performed recently on the small molecule liquid glycerol (cf. Sect. 17.3.1), demonstrate that the aspects of dynamic and spatial heterogeneity are intimately linked to one another.

It may now be asked whether the heterogeneity length scale and/or the heterogeneity lifetime will increase upon approaching the calorimetric glass transition temperature more closely. A tremendous increase of the lifetime, with respect to that characterizing the structural relaxation, was indeed concluded from an optical deep-bleach experiment performed on a dye probe embedded in polystyrene [148]. However, it was pointed out that these findings are not necessarily incompatible with corresponding results from NMR [148]: the optical measurements were conducted closer to T_g than the NMR experiments. A similar situation is encountered for the supercooled liquid ortho-terphenyl [78, 149].

Several dielectric techniques were developed in the past few years to address the heterogeneity issue in a range of temperatures close to T_g. Among them are nonresonant dielectric hole burning [64] and a local dielectric approach based on solvation spectroscopy [79]. Both of these methods yielded evidence for dynamic heterogeneities in low molecular weight liquids. Recently, another powerful approach was devised. It is based on detecting local electrostatic forces using an atomic force microscope (AFM) operating in non-contact mode [150].
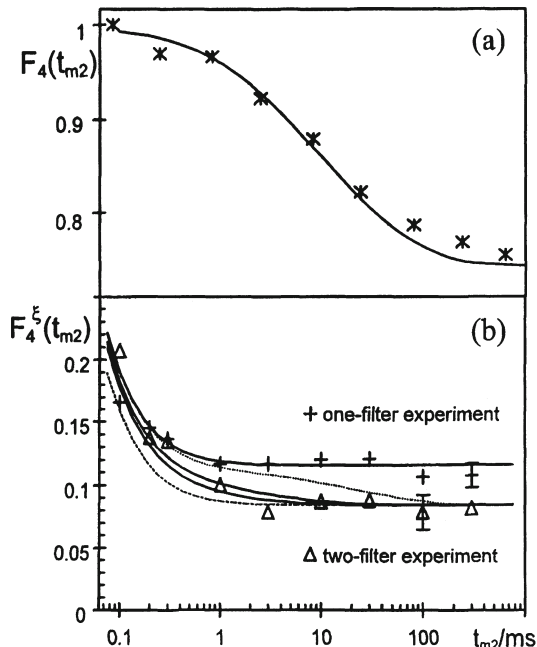
Extended time series of the electric polarization in (mesoscopic) probe volumes
of about 50 nm³ could be detected using this method.

This latter feature can be exploited to implement an interesting idea: if the
temporal resolution of the experiment is much faster than the structural re-
sponse time, then one should be sensitive to polarization contributions giving
rise to the high-frequency wing in the dielectric loss, $\varepsilon''(\omega)$. In view of the low
dielectric loss encountered in this regime (as compared to the loss at its maxi-
mum), it is suggestive to suppose that only relatively few relaxation modes con-
tribute to the polarization as measured on these short time scales. This trick of
going to the 'edge' of a loss (or absorption) curve, known from conventional hole
burning and from single molecule spectroscopy [151], provides spectral selec-
tivity in addition to the mesoscopic spatial selectivity inherent to the AFM
approach.

In Fig. 17.32 we reproduce polarization time series, recorded for PVAc just
above the glass transition [150]. We point out that not only two-time but also
multiple-time correlation functions could be evaluated from such time series
which would render the comparison with the NMR experiments even more di-
rect. It was reported that these traces frequently show switching among a finite
number of levels [150]. By evaluating the mesoscopic spectral density, $j(\omega)$, from
experimental time series recorded in one-hour periods, the results shown in
Fig. 17.33 were obtained. It was emphasized that the dynamics in these experi-
ments is probed at sample depths (of about 40 nm) below which surface-related
effects dominate [150]. In all cases shown in Fig. 17.33 $j(\omega)$ deviates from the
Lorentzian shape which would correspond to single exponential behavior. More
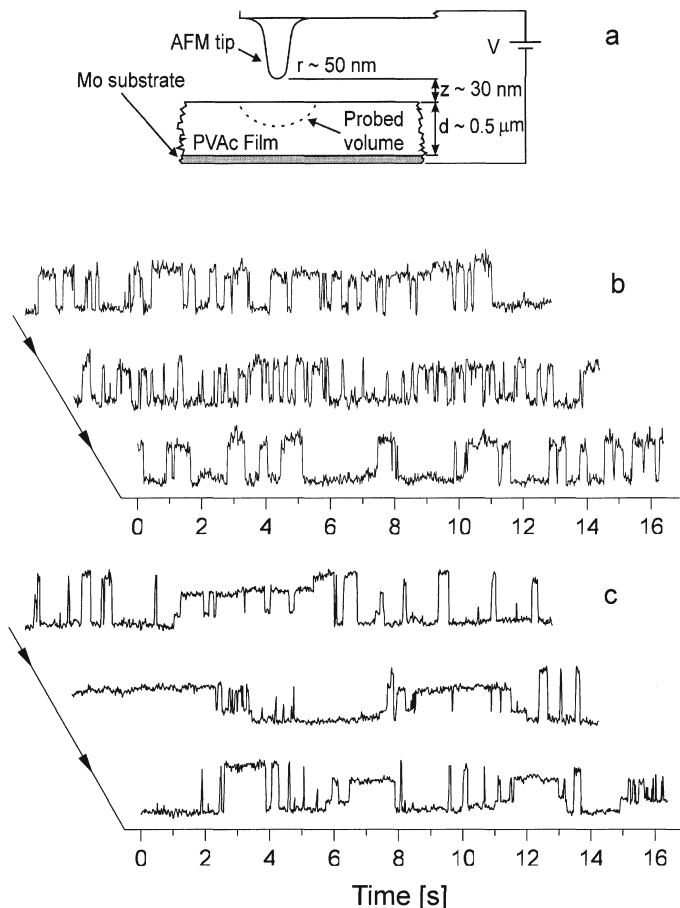
Fig. 17.32. The AFM technique sketched in **a** has been used to monitor the time series of polarization "noise" for PVAc at: **b** $T = 299$ K; **c** $T = 300$ K in a mesoscopic probe volume. Switching among a discrete set of levels is observed. Adapted from [150] and reproduced with permission

importantly, the shape and intensity of these spectral densities was found to change in time. It was reported that the shape of the macroscopic spectral density is reproduced only if the time series are averaged over periods of about one day. These observations are clear evidence for dynamic heterogeneity. The heterogeneity lifetime of PVAc has also been estimated from these data and, as we show in Fig. 17.34, turned out to be similar to the average primary relaxation time [150].

The evidence from the dielectric and the NMR measurements referred to in this section can be summarized as follows. (i) There is evidence for heterogeneity which is short-lived in a temperature range of more than 20 K, near and above T_g. (ii) Heterogeneity length scales of about 3 nm were inferred from both
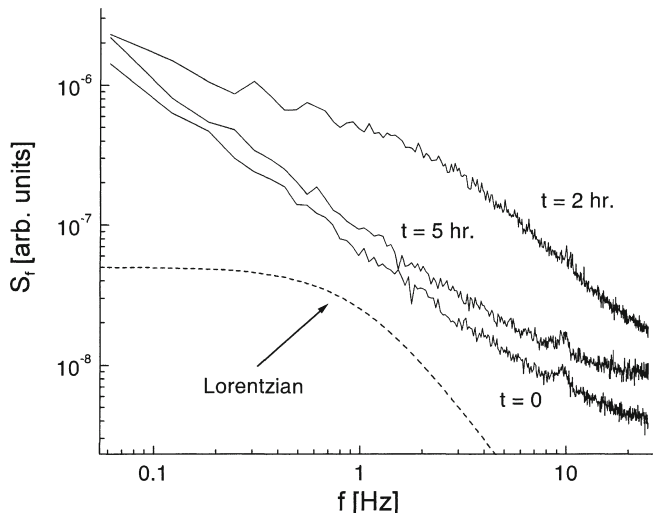
Fig. 17.33. Temporary mesoscopic spectral densities of PVAc as measured at 299 K using the AFM technique sketched in Fig. 17.32a. Adapted from [150] and reproduced with permission
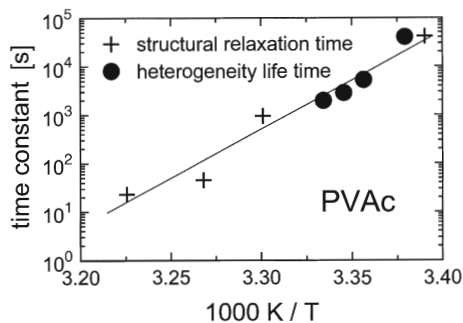
Fig. 17.34. Arrhenius plot showing that the heterogeneity lifetime agrees well with the structural relaxation time of PVAc as deduced from dielectric measurements. The time constants are given in seconds. Digitized from the data shown in [150]. The *solid line* is drawn as a guide to the eye

experimental approaches. (iii) The intrinsic relaxation process is compatible with a simple exponential (as also implied by the AFM experiments [150]).

The latter statement (iii) also holds for a low molecular weight liquid ([84], cf. Sect. 17.3.1), so that a questions immediately arises: does the absence of significant intrinsic non-exponentiality [152] now imply that each spatially selected region relaxes exponentially, i.e., that the local stretching parameter, β_{in}, is close to unity? The answer to this question cannot be affirmative if the dynamic heterogeneity is sufficiently short-lived [153] since then, on the average, a dynamical exchange takes place before rotational decorrelation is fully complete. Under

these circumstances one has to conclude that the auto-correlation function of the 'molecules' (or, more likely, nanoscale clusters) is non-exponential when viewed on the time scale of the primary relaxation. This implies that β_{in} should not be taken as a measure of the local stretching (or non-exponentiality) and merely suggests that a 'normal-mode' picture is more appropriate [76]. These spectrally distinguishable 'normal-modes' obviously exhibit an exponential (or close to exponential) response.

17.3.5
$2Ca(NO_3)_2 \cdot 3MNO_3$ as an Example for an Ion Conductor

There are intense scientific activities in the field of ionic conductors and consequently there are several NMR reviews on this subject [154–156]. In the spirit of the current presentation we will focus on just one particular example, namely the molten and glassy nitrates of the type $2Ca(NO_3)_2 \cdot 3MNO_3$ with $M = \{K, Rb\}$. These binary mixtures were intensively studied in the past using numerous experimental techniques including impedance spectroscopy [157–162] and NMR [163–165]. Furthermore, the nitrate systems were among the first for which the mode coupling theory [166] of the glass transition was tested [167] and also the first for which the predicted high-frequency susceptibility minimum could be demonstrated [160].

In Fig. 17.35 we compare the spectral density of $2Ca(NO_3)_2 \cdot 3RbNO_3$ as measured using NMR and impedance spectroscopy at similar frequencies. The calorimetric glass transition temperature of 333 K is marked by an arrow. The NMR experiments were carried at a Larmor frequency of $\omega_L = 86$ MHz with ^{87}Rb as the spin probe. This quadrupolar nucleus is most sensitive to the fluctuations of the electrical field gradient at the probe site, i.e., to the motions of the electric charges in its vicinity. Above T_g the ionic motions give rise to a large spin-lattice relaxation rate $1/T_1$ ($\sim \chi''$, with χ'' denoting the imaginary part of a generalized susceptibility). Then, for $T \leq T_g$ the spectral density near ω_L changes little in a wide temperature range, except for a slight maximum near 145 K. This maximum can be ascribed to the slow-down of the rotational motion of the planar nitrate group. Obviously this highly anisotropic motion modulates the electrical

Fig. 17.35. Comparison of the ^{87}Rb spin-lattice relaxation rate, $1/T_1$ [165], and the imaginary part of the electrical modulus, M'' [98], of $2Ca(NO_3)_2 \cdot 3RbNO_3$ as measured near 90 MHz. The *solid line* indicates that $1/T_1$ obeys a power law at low temperatures
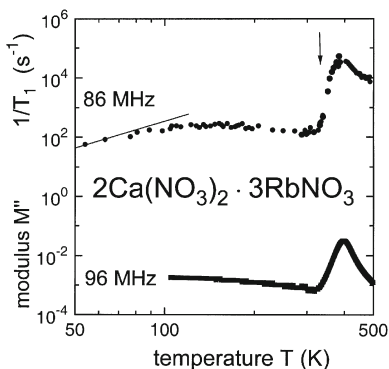
field gradient at the nuclear probe only relatively weakly and hence the local $1/T_1$ maximum is much smaller than the global one. For comparison, in Fig. 17.35 we also show the imaginary part of the electrical modulus, $M''(T)$, measured at a comparable frequency [98]. The overall shape of M'' is very similar to that of $1/T_1$. This indicates that the same dynamical process is probed by the two methods [168]. Even the localized NO_3 motion seems to show up in the modulus data. It has to be noted that at lower temperatures a dielectric loss peak of unknown origin was detected for $2Ca(NO_3)_2 \cdot 3KNO_3$ (near 50 K in the audio frequency range [158, 160]). Corresponding effects are not visible in the NMR data of $2Ca(NO_3)_2 \cdot 3RbNO_3$. Rather a power law behavior is found. In this context it should be noted that power laws are often observed for glasses at low temperatures. This behavior may be rationalized if the spin-lattice relaxation is dominated by excitations taking place in broad distributions of asymmetric double well potentials [169].

In Fig. 17.36 we have compiled the time scales as emerging from conductivity measurements, NMR, and several other techniques. It is seen that the conductivity relaxation times (from the d.c. conductivity and from the maxima in M'') exhibit a pronounced temperature dependence. However, near T_g they decouple from the structural response times and turn over to a thermally activated behavior. In $2Ca(NO_3)_2 \cdot 3MNO_3$ there exist a number of additional decoupled motions such as the Johari-Goldstein process [170] and the NO_3 reorientation [171, 172]. Figure 17.36 demonstrates that this seemingly simple molten and glassy salt, involving spherical and planar ions, only, exhibits a relatively complex activation map.

The question of dynamic heterogeneity has also been addressed for $2Ca(NO_3)_2 \cdot 3RbNO_3$ using NMR as well as dielectric methods. Direct evidence for dynamic heterogeneity in the molten state of this inorganic material was obtained by nitrogen NMR [163]. Here the planar NO_3^- group (with ^{15}N enrichment) was used as a probe. On increasing the temperature from 340 K ($\approx T_g +$
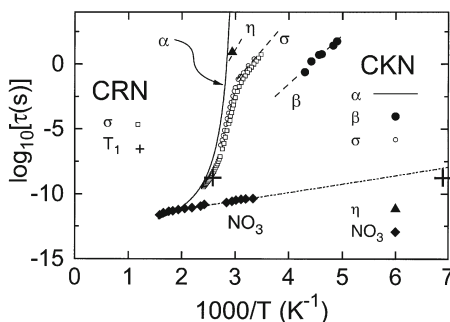
Fig. 17.36. Relaxation map of molten and glassy $2Ca(NO_3)_2 \cdot 3KNO_3$ and $2Ca(NO_3)_2 \cdot 3RbNO_3$. The T_1 minima are marked by the *crosses*. The data for the conductivity, σ, are from [157, 160]. Primary relaxation times, τ_α, are from [198]. Data for some decoupled processes [secondary process (β) [170], nitrate rotation (NO_3) [171], and local ion exchange (η) [199] are also included. The *dashed and dash-dotted lines* represent Arrhenius laws. Reproduced from [165] with permission
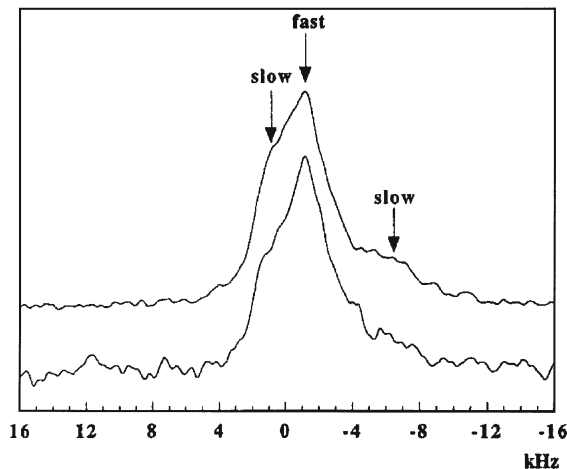
Fig. 17.37. Experimental ^{15}N NMR spectra of $2Ca(NO_3)_2 \cdot 3KNO_3$ obtained at $T = 361$ K for waiting times, t_w, of 500 s (*upper spectrum*) and 10 s (*lower spectrum*) after saturation of the magnetization. After a short waiting time only those components which relax fast (and which show a relatively narrow spectrum) have recovered. After sufficiently long t_w the slowly relaxing components, which exhibit a broader spectrum, are more pronounced. These results show that slow and fast motions coexist. Reproduced from [163] with permission

7 K) to above 370 K the static ^{15}N line shape evolves from a broadened pattern to a motionally narrowed one. At intermediate temperatures the spectra contain both broad (slower) and narrow (faster) contributions [173]. Rather than using a stimulated echo as a filter (cf. Sect. 17.2.3.1) the non-exponential ^{15}N T_1 relaxation was employed to select slow and fast components. Corresponding experimental spectra recorded 500 s and 10 s after saturation are shown in Fig. 17.37. It is seen that with the shorter waiting time the spectral contributions corresponding to slower motions (hence broader spectrum) are at least partially suppressed. The ability to perform a dynamic filtering demonstrates the existence of dynamic heterogeneity in molten $2Ca(NO_3)_2 \cdot 3KNO_3$.

In order to probe the heterogeneity in the glassy state which is directly associated with the translational ionic motion a dielectric technique, non-resonant spectral hole burning, was applied [174]. The results obtained there at 300 K (see also Chap. 14) show that the dynamic heterogeneity established by NMR in the supercooled liquid, freezes in upon cooling through T_g, thus giving rise to a heterogeneous ionic relaxation. These findings are in accord with previous theoretical predictions [175].

It has to be pointed out that the generally relatively long ^{15}N relaxation times will make it difficult to apply multidimensional NMR techniques (cf. Sect. 17.3.4) to this system. As an alternative one could also investigate suitably doped hydrate glasses (e.g., ^2H or ^{15}N enriched $Ca(NO_3) \cdot nH_2O$). This would not only facilitate the study of dynamic heterogeneities but also of spatial heterogeneities via the F_4^{CP} experiment (cf. Sect. 17.3.4) which in its current form requires a rare as well as an abundant spin 1/2 nucleus (here: ^{15}N and ^1H, respectively).

17.3.6
Self-Diffusion in Polymeric Systems

Magnetic field gradient NMR has been widely used to study self-diffusion in oligomeric and entangled polymer melts and diblock copolymers [176–180]. In Sect. 17.2.2.1 we already pointed out the far reaching analogy of spin echo attenuation, $S_2(q,t_m) \sim \exp(- q^2 D_T t_m)$, cf. Eq. (17.5) and the incoherent intermediate scattering function, $S_{inc}(q,t)$, known from scattering experiments such as neutron scattering [32]. This analogy in fact allows one to identify $S_2(q,t)$ with $S_{inc}(q,t)$.

In Fig. 17.38 we show $S_{inc}(q,t)$ vs $q^2 t$ for an asymmetric poly(ethylene propylene)-poly(dimethyl siloxane) diblock copolymer. In a semi-logarithmic representation $S_{inc}(q,t)$ should yield a straight line according to Eq. (17.5). The observed deviations are caused by the anisotropy of the diffusion processes, cf. Eq. (17.6).

For polymers exhibiting a dipole component locally parallel to the main chain these components generally add up to an end-to-end dipole vector (type A polymers [181, 182]; see also Chap. 7). Then the global chain dynamics can conveniently be studied by dielectric spectroscopy. For the dielectric relaxation of the end-to-end vector ("normal mode") the usual Fourier relationship

$$\frac{\varepsilon^*(\omega) - \varepsilon_\infty}{\Delta\varepsilon_{\text{Chain}}} = \frac{1}{\langle r_{ee}^2 \rangle} \int_0^\infty \left[-\frac{\partial \langle r_{ee}(0) r_{ee}(t) \rangle}{\partial t} \right] \exp(-i\omega t)\, \mathrm{d}t \qquad (17.13)$$

holds. Here $\Delta\varepsilon_{\text{Chain}}$ denotes the dispersion step associated with the chain motion, $\langle r_{ee}^2 \rangle$ is the mean squared (ensemble averaged) end-to-end vector, and $\langle r_{ee}(0)\, r_{ee}(t) \rangle$ the corresponding dipole correlation function which may be measured as the dielectric step response. It should be noted that at least two reasons for variations of the end-to-end vector of a given polymer chain exist which are relevant in the context of dielectric measurements. (i) If the end-to-end vector changes its direction with respect to the external electrical field, then this alters the orientational polarization in the usual way. (ii) Additionally the end-to-end vector can change its length. The consequent change in the electric dipole moment then gives rise to dielectric relaxation as well. In any case for dense polymeric systems $\langle r_{ee}(0)\, r_{ee}(t) \rangle$ can be expressed by [182, 183]

$$\langle r_{ee}(0) r_{ee}(t) \rangle / \langle r_{ee}^2 \rangle = (8/\pi^2) \sum_p p^{-2} \exp(-t/\tau_p) \qquad (17.14)$$

with τ_p being the relaxation time of the mode p. For undiluted oligomeric melts of flexible chains, τ_p can be calculated. Below the critical molecular weight for the formation of entanglements, M_C (typically $M_C \approx 10^4$ g mol^{-1}), one finds in the framework of the Rouse theory [184, 185]

$$\tau_p = \frac{\zeta N^2 b^2}{3\pi^2 k_B T p^2} \quad \text{with} \quad p = 1, 3, \ldots \qquad (17.15)$$

Here ζ is the segmental friction coefficient, b the segment length, and N the number of segments in the chain. From the p^{-2} dependence in Eq. (17.14) it follows that mainly the modes with $p = 1$ and 3 contribute to the dielectric loss
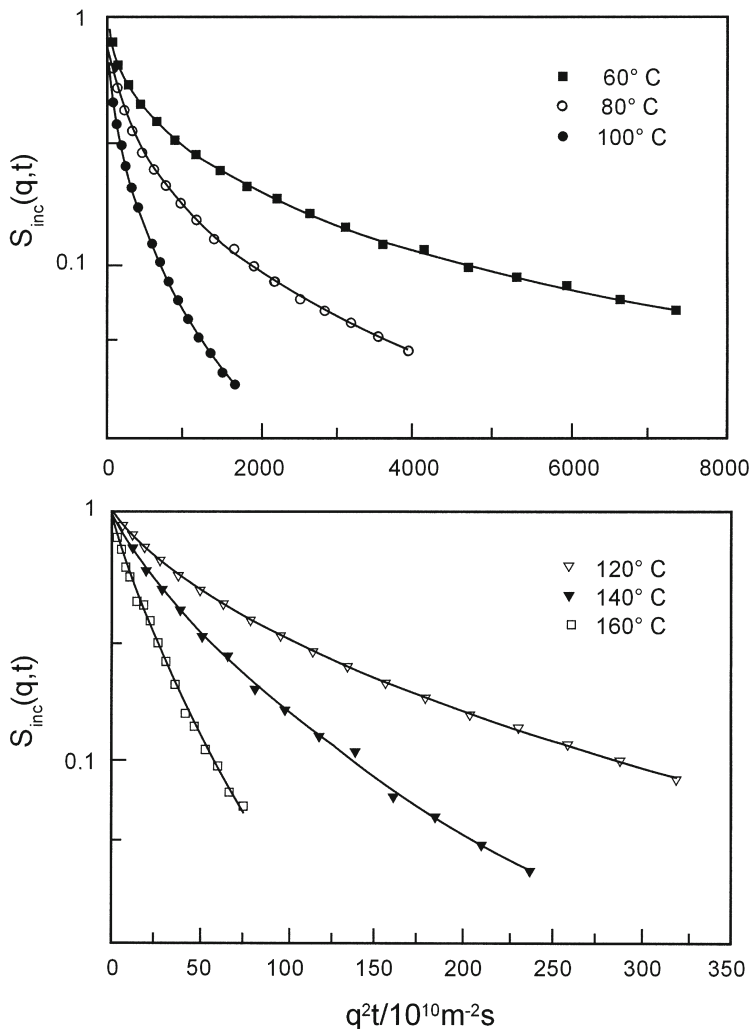
Fig. 17.38. Echo attenuation $S_2(q,t)$ vs q^2t in a semi-logarithmic representation at the temperatures indicated. The *lines* are fits of a log-normal distribution of self diffusion coefficients. The sample is an asymmetric poly(ethylene propylene)-poly(dimethyl siloxane) diblock copolymer. Reproduced from [178] with permission

[186]. Hence an effective normal mode relaxation time $\tau_N = 1/(2\pi f_{pN})$ can be defined with f_{pN} denoting the frequency of the corresponding dielectric loss maximum. For $M > M_C$ the polymeric chains are entangled. In that case the functional shape of Eq. (17.14) is maintained but the expression for the relaxation times has to be calculated in the framework of the reptation model [184]. If a denotes the diameter of a tube built up by the neighbors of a test chain then the relaxation time of mode p is $\tau_{p,\mathrm{Rept}} = \dfrac{\zeta N^3 b^4}{k_B T \pi^2 a^2 p^2}$. The inset of Fig. 17.39 shows

the dielectric loss for poly(propylene glycol) which is a typical type A polymer. The relaxation process at higher frequencies is the segmental relaxation (α-relaxation) and the process at lower frequencies corresponds to the fluctuations of the end-to-end vector. From the maximum position of the dielectric loss of the latter the normal mode relaxation frequency, f_{pN}, can be deduced. It has been shown for many polymers that the experimental results are in good agreement with the theoretical predictions implied by Eq. (17.15), at least for $M < M_C$ [187, 188].

In the framework of the Rouse theory the self-diffusion coefficient, D_0, corresponding to the center of mass motion of the polymer chains (sometimes referred to as the zero-th Rouse mode with the relaxation time τ_N) is given by $D_0 = k_B T/(N\zeta)$. With Eq. (17.15) and $\langle r_{ee}^2 \rangle = b^2 N$ one finds for $p = 1$

$$\tau_N D_0 = \langle r_{ee}^2 \rangle/(3\pi) \tag{17.16}$$

If $\langle r_{ee}^2 \rangle$ is known, D_0 can be calculated from dielectric data and then compared with results obtained by field gradient NMR. A relationship similar to that in Eq. (17.16) can also be obtained for the entangled state.

Figure 17.39 gives $S_{inc}(q,t)$ vs $q^2 t$ in a semi-logarithmic plot for poly(propylene glycol) with a molecular weight of $M_w = 2000$ g mol^{-1} which enables one to evaluate the translational self-diffusion coefficient, D_T, via Eq. (17.5). In Fig. 17.40 self-diffusion coefficients from pulsed and from static field gradient NMR studies are compared with those calculated from dielectric experiments via Eq. (17.16). Good agreement of the absolute values as well as of the temperature dependences is noted (Fig. 17.40). This agreement is particularly nice since there is no adjustable parameter in Eq. (17.16). The small difference in the tem-
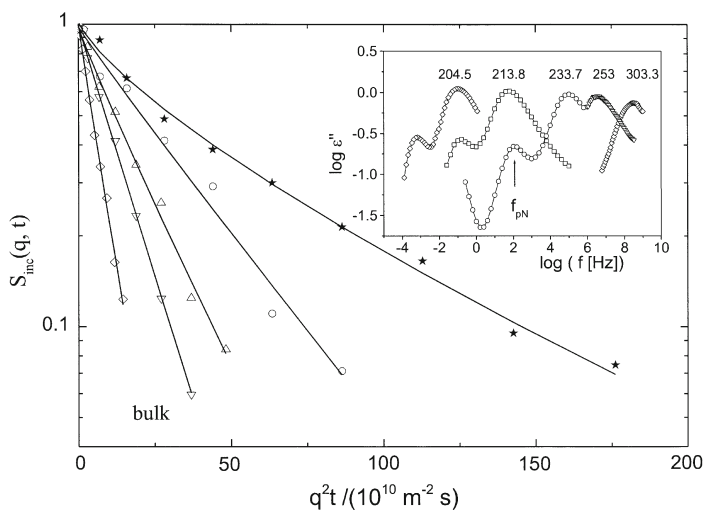
Fig. 17.39. $S_{inc}(q,t)$ vs $q^2 t$ in a semi-logarithmic plot for poly(propylene glycol) with a molecular weight of 2000 g mol^{-1}: *(open diamonds)* 333.15 K, *(open down triangles)* 323.15 K, *(open up triangles)* 313.15 K, *(open circles)* 305.15 K, *(stars)* 296.15 K. The *inset* shows the dielectric loss vs frequency at the indicated temperatures
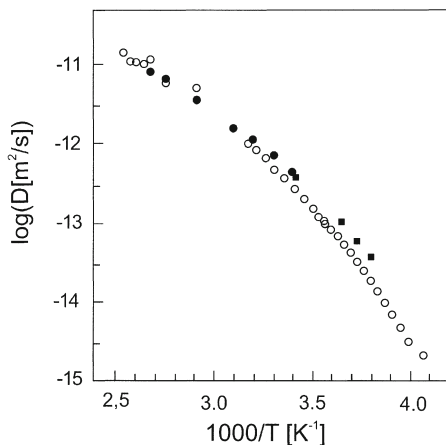
Fig. 17.40. Activation plot of the self-diffusion coefficients as measured with pulsed (●) and static (■) field gradient NMR (D_T) and and as calculated from dielectric relaxation measurements (D_0, ○). Sample: poly(propylene glycol) PPG $M_w = 4000$ g mol^{-1}. Reproduced from [200] with permission

perature dependence of the dielectric and of the NMR results can be explained by the temperature dependence of $\langle r_{ee}^2 \rangle$. Furthermore, the influence of chain interactions will vary with temperature. Similar results were also found for *cis*-1,4-polyisoprene [189] (see Chap. 7).

The chain dynamics of poly(propylene glycol) when immersed in nanoporous host matrices was recently addressed by a comparative field gradient NMR and dielectric study ([190], see also Chap. 6). One of the main results of that work was that the product of the dielectrically determined normal mode relaxation time τ_N and the translational diffusion coefficient D_T obtained with pulsed field gradient NMR was almost constant, as expected from Eq. (17.16) if $\langle r_{ee}^2 \rangle$ is not strongly temperature dependent.

17.4
Concluding Remarks

Dielectric and NMR spectroscopy are experimental tools which are often considered to start from rather different physical foundations. Dielectric spectroscopy can be understood in terms of classical physics. It essentially relies on measuring the fluctuations (of the orientation) of polar molecular moieties, on their interactions with one another and with external *electrical* fields. NMR, on the other hand, involves quantum mechanical transitions: it requires that one considers interactions of spins with one another and with external *magnetic* fields. Nevertheless the different strengths of both experimental methods combine favorably. Broadband dielectric spectroscopy is extraordinary in covering an enormous spectral range. Time and/or frequency ranges of ten decades and more can nowadays be covered with only a few experimental set-ups at a very good sensitivity and dynamic res-

olution. The relative ease of sample preparation, of performing the measurements, and of analyzing the dielectric data renders this method an ideal tool to gain a quick overall view on the dynamics of the material under study. The familiar data evaluation in terms of relaxation strengths, mean relaxation times, spectral widths, etc. is straightforward. However, in many cases this analysis can profitably be enhanced by additional input from molecular models or other experimental techniques, e.g., in order to strengthen the microscopic assignment of relaxation processes. As compared to NMR only relatively few variations to the conventional dielectric technique, such as electrical quadrupole relaxation, noise spectroscopy, or nonresonant hole burning, are in use to probe the fluctuations of (multi-)polar groups in condensed matter.

In NMR spectroscopy, on the other hand, the nuclear spin interactions which dominate the experimental observables are often highly specific thus facilitating efforts to obtain detailed information on local symmetries and dynamical properties, although sometimes at the expense of isotopic labeling. Furthermore, the effective spin interactions (or better the corresponding Hamilton operators) can be manipulated in so many different ways by the experimental conditions. This flexibility forms the basis for the tremendous number of different, and sometime quite sophisticated and time consuming, NMR techniques. Therefore knowledge from dielectric spectroscopy is often quite helpful when adjusting the experimental parameters, e.g., for a multidimensional NMR investigation. In this respect BDS and NMR are of course complementary. Although these techniques monitor the molecular and the segmental dynamics from different angles it is reassuring that the two methods combine often so excellently as we have exemplified in this chapter for several disordered and partially ordered materials including one-component small-molecule and polymeric liquids, liquid crystals, but also mixed ionic systems and diblock copolymers.

Appendix 17.1

Dynamic low-pass filters are based on the angular jump function, $F_2^{AJ}(t_m)$, and can be used to select slow subensembles. However, for their proper applications it should be ascertained that several conditions are met or closely approximated. (i) The most important one is that molecules which have jumped should not return to their original (or another frequency equivalent) orientation. Otherwise some 'fast' molecules survive the low-pass filter. In more technical terms this implies the assumption of so-called random-jump motions among an infinite number of orientations. It is clear that jumps among a discrete set of orientations, particularly

acute for the reorientations in crystals, requires special consideration [147]. (ii) In a real experiment the limit of very large t_p may not be attainable. This problem is particularly evident if the mechanism of rotational diffusion is active, since it is associated with infinitesimally small angular displacements [191]. In order to estimate how long t_p should be for small (but finite) angle jumps let us consider the following variant of Eq. (17.8) which has been employed in several NMR studies: $\frac{1}{2}[F_2^{\mathrm{SIN}}(t_p,t_m)+F_2^{\mathrm{COS}}(t_p,t_m)]=\langle\cos[(\omega_1-\omega_2)t_p]\rangle$. For this function to decay significantly at least the condition $|\omega_1-\omega_2|t_p>\pi/2$ has to be obeyed. If θ_0 denotes the initial angle, then for axially symmetric tensors this means that $t_p\delta\,|\,P_2(\cos\theta_0)-P_2(\cos[\theta_0\pm\Delta\theta])|>\pi/2$ or $t_p\delta>\frac{2\pi}{3}|\cos(2\theta_0)-\cos(2\theta_0\pm2\Delta\theta)|^{-1}$ should be fulfilled. Here it should be observed that the change in polar angle is $\Delta\theta\le\varphi$. However jumps inevitably occur, albeit with a small weight, which only change the azimuthal but not the polar angle, i.e., the NMR frequency.

Appendix 17.2

In Sect. 17.2.3.2 we defined the t_{m2} dependent four-time CF $L_4(t_{m2})\sim\langle P_2(\cos\theta_1)P_2(\cos\theta_2)P_2(\cos\theta_3)P_2(\cos\theta_4)\rangle$. Apart from its applicability to the issue of transient heterogeneity (cf. Sect. 17.3.1) it can be used to measure the rank $l=4$ rotational correlation function $g_4(t_{m2})$, cf. Eq. (17.1), in the following way. Consider the case $t_{m1}=0$ and $t_{m3}=0$ (cf. Fig. 17.7) so that the molecular orientation, specified by θ, cannot change during these mixing times. Then $\theta_1=\theta_2\equiv\theta_a$ and $\theta_3=\theta_4\equiv\theta_b$ and the 2t-CF $\langle[P_2(\cos\theta_a)]^2[P_2(\cos\theta_b)]^2\rangle$ results.

Like in the main text expressions such as

$$[P_2(\cos\theta)]^2=\tfrac{1}{35}[7+10P_2(\cos\theta)+18P_4(\cos\theta)]\tag{17.17}$$

can be derived in a straightforward way from the elementary definition of the Legendre polynomials. More elegantly one can apply the Clebsch-Gordan series $D_{\mu_1 m_1}^{(l_1)}\,D_{\mu_2 m_2}^{(l_2)}=\sum_l C(l_1 l_2 l;\mu_1\mu_2)C(l_1 l_2 l;m_1 m_2)\,D_{\mu_1+\mu_2,m_1+m_2}^{(l)}$ [192], in conjunction with $P_l(\cos\theta)=D_{00}^{(l)}$. Here the dependence of the Wigner rotation matrices, $D_{m_1 m_2}^{(l)}$, on the Euler angles, $\{\alpha,\beta,\gamma\}$, has not been written out, for brevity. For the same reason in the Clebsch-Gordan coefficients, $C(l_1 l_2 l;m_1 m_2)\equiv C(l_1 l_2 l;m_1 m_2 m)$, the third argument, $m=m_1+m_2$, has been dropped. In the present application the Clebsch-Gordan series thus reduces to

$$[P_{l'}(\cos\theta)]^2=\sum_{l=0}^{2l'}[C(l'l'l;00)]^2\,P_l(\cos\theta)\tag{17.18}$$

with $C(l'l'l;0\,0)$ vanishing for odd l. Since these coefficients are well tabulated, or even implemented in symbolic computer algebra programs, it is a simple matter to evaluate them numerically.

From the decomposition of, e.g., $[P_2(\cos\theta)]^2$ one recognizes how (even for $t_p\to0$) higher l CFs can become accessible. Carrying out the powder average for $t_{m3}\to\infty$ shows that

$$\langle[P_2(\cos\theta)]^2\rangle^2=\left(\tfrac{1}{35}\right)[7^2\langle P_0(\cos\theta)\rangle^2+10^2\langle P_2(\cos\theta)\rangle^2+18^2\langle P_4(\cos\theta)\rangle^2].\tag{17.19}$$

cf. Eq. (17.17. In Eq. (17.19) we have used $P_0 = 1$ to make the expression look more systematic and exploited the fact that due to the orthogonality of the Legendre polynomials terms with mixed l vanish. Using $\langle P_2(\cos\theta)\rangle^2 = \frac{1}{5}$ and $\langle P_4(\cos\theta)\rangle^2 = \frac{1}{9}$ the relative weights of the terms stemmin from $l = 0, 2,$ and 4 are $49, \frac{10^2}{5} = 20,$ and $\frac{18^2}{9} = 36$, respectively. In order to ensure that $L_4(t_{m2})$ is normalized to unity for $t_{m3} = 0$ (here is even $\theta_a = \theta_b$) one has to divide the above expressions by $\langle [P_2(\cos\theta)]^4 \rangle = \frac{3}{35}$. This shows that in the expression $\langle [P_2(\cos\theta)]^2\rangle^2/\langle [P_2(\cos\theta)]^4\rangle$ the CFs $g_l(t)$ of rank $l = 0, 2,$ and 4 appear with fractions of $\left(\frac{49}{35^2} / \frac{3}{35} =\right) \frac{7}{15}, \left(\frac{20}{35^2} / \frac{3}{35}\right) = \frac{4}{21}$, and $\left(\frac{36}{35^2} / \frac{3}{35} =\right) \frac{36}{105}$, respectively. In the present case with $(t_{m1} = t_{m3} \to 0)$ g_0 is just a constant. Thus, if $g_2(t)$ is known from independent measurements (cf. Sect. 17.2.2.2), then $g_4(t)$ can be determined from the time dependent part of $L_4(t_{m2})$. Obviously by properly decomposing $\langle [P_2(\cos\theta)]^k\rangle^2/\langle [P_2(\cos\theta)]^{2k}\rangle$ (for even $k > 2$) this scheme can be extended to determine $g_{2k}(t)$, i.e., 2t-CFs with successively higher l.

More general 4t-CFs, denoted as $L_4^{(l)}(t_{m2})$, can be defined [85] by correlating four Legendre polynomials via $\langle P_l(\cos\theta_1) P_l(\cos\theta_2) P_l(\cos\theta_3) P_l(\cos\theta_4)\rangle$. Again the normalization should be chosen such that $L_4^{(l)}(t_{m2} \to 0) = 1$. Above we have thus discussed $L_4^{(2)}(t_{m2})$. The evaluation of the corresponding expressions becomes particularly straightforward in the absence of dynamic exchange (and/or $t_{m1} = t_{m3} \to 0$). Then one has $L_4^{(l)}(t_{m2}) = \langle P_l(\cos\theta_1) P_l(\cos\theta_2) P_l(\cos\theta_3) P_l(\cos\theta_4)\rangle/\langle [P_l(\cos\theta)]^4\rangle$. As an example consider the rank $l = 1$ correlation function $\langle [P_1(\cos\theta)]^2\rangle^2/\langle [P_1(\cos\theta)]^4\rangle$. With $[P_1(\cos\theta)]^2 = \frac{1}{3}[2P_2(\cos\theta) + P_0]$ and $\langle [P_1(\cos\theta)]^2\rangle^2 = \frac{1}{9}[4\langle P_2(\cos\theta)\rangle^2 + P_0]$ and $\langle [P_1(\cos\theta)]^k\rangle = (k+1)^{-1}$ for $k = 4$ one obtains $\frac{1}{9} \times 4 \times \frac{1}{5}/\frac{1}{5} = \frac{4}{9}$ and $\frac{1}{9} \times 1/\frac{1}{5} = \frac{5}{9}$ for the terms with $l = 2$ and 0, respectively [193]. This means that in the absence of dynamic exchange (and/or $t_{m1} = t_{m3} \to 0$) one has $L_4^{(1)}(t_{m2}) = g_2(t_m) + \frac{5}{9}$.

List of Abbreviations and Symbols

a	Hopping distance
$A(q)$	Coupling coefficient
B_{loc}	Local magnetic field
B_0	Static magnetic field
C_λ	Coupling constant
d	Characteristic pore dimension
D	Diffusion coefficient
f_{pN}	Normal mode relaxation rate
FT	Fourier transformation
F_2	Two-time stimulated echo
F_4	Four-time stimulated echo
g	Magnetic field gradient
g_l	Rotational CF of rank l, Eq. (17.1)
$g(\tau)$	Relaxation time distribution function
G_4	Low-pass filtered CF

H_R	Haven ratio
$J(\omega)$	Spectral density
$j(\omega)$	Mesoscopic spectral density
L_4	Four-time rotational CF
n	Charge carrier density
P_l	Legendre polynomial of rank l
q	(Generalized) scattering vector
Q	Nuclear quadrupole
Q	Rate memory parameter
r	Space vector
r_{ee}	End-to-end vector
r_H	Hydrodynamic radius
$S(q,\omega)$	Dynamic structure factor
$S_{inc}(q,t)$	Intermediate incoherent scattering function
S_2	Translational two-time CF
t	(Probe) time
t_p	Preparation or evolution time
t_m	Mixing time
T_1	Spin-lattice relaxation time
T_g	Glass transition temperature
α_{CC}	Cole-Cole parameter
β_{CD}	Cole-Davidson parameter
β	Kohlrausch stretching exponent
β_2	Stretching of $F_2(t_m)$
γ	Gyromagnetic ratio
δ	Anisotropy parameter
ε	Dielectric function
$\Delta\varepsilon$	Dispersion step
η	Viscosity
η_λ	Asymmetric parameter
θ	Polar angle
ζ	Segmental friction coefficient
λ	$\in \{CSA, DD, Q\}$
Λ	Obstruction factor
μ	Mobility
ν_0	Attempt frequency
σ	Direct current (d.c.) conductivity
τ	Relaxation time
τ_{hop}	Hopping time
$\tau_{C,l}$	Rotational correlation time (from g_l)
τ_2	Decay time of $F_2(t_m)$
τ_4	Decay time of $G_4(t_{m3})$
τ_{AJ}	Angle jump correlation time
τ_N	Normal mode relaxation time
ϕ	Phase in the rotating frame
φ	Jump angle
Φ	Azimuthal angle

χ	Susceptibility
ω	Angular frequency
$\omega_{\alpha\alpha}$	Frequency associated with principal axis α
ω_L	Larmor frequency

AFM	Atomic force microscope
BDS	Broadband dielectric spectroscopy
BPP	Bloembergen, Purcell, and Pound
CF	Correlation function
CP	Cross polarization
CSA	Chemical shift anisotropy
DD	Nuclear dipole-dipole
EFG	Electric field gradient
FE	Filter efficiency
FID	Free induction decay
NMR	Nuclear magnetic resonance
NHB	Nonresonant spectral hole burning
PFG-NMR	Pulsed field gradient NMR
PMMA	Poly(methyl methacrylate)
PVAc	Poly(vinyl acetate)
RF	Radio frequency
RMTD	Reorientation mediated by translational displacement

References

1. Debye P (1929) Polare Molekeln. Hirzel S, Leipzig
2. Fröhlich H (1958) Theory of dielectrics. Oxford University Press, New York
3. McCrum NG, Read BE, Williams G (1967) Anelastic and dielectric effects in polymeric solids. Wiley
4. Hill N, Vaughan WE, Price AH, Davies M (1969) Dielectric properties and molecular behaviour. Van Nostrand Reinhold, New York
5. Böttcher CJF, Bordewijk P (1973) Theory of electric polarization, vol 2. Elsevier, Amsterdam
6. Scaife BKP (1998) Principles of dielectrics. Clarendon Press, Oxford
7. Abragam A (1961) The principles of nuclear magnetism. Clarendon, Oxford
8. Slichter CP (1990) Principles of magnetic resonance, 3rd edn. Springer, Berlin Heidelberg New York
9. Ernst RR, Bodenhausen G, Wokaun A (1987) Principles of nuclear magnetic resonance in one and two dimensions. Clarendon Press, Oxford
10. Schmidt-Rohr K, Spiess HW (1994) Multidimensional solid-state NMR and polymers. Academic, London
11. Kimmich R (1997) NMR: tomography, diffusometry, relaxometry. Springer, Berlin
12. It should be noted that recent optical techniques allow to achieve tremendous population differences ($>10^{-1}$) with many exciting applications
13. See, e.g., the contributions by Slichter WP and Connor TM in (1971) NMR of polymers, vol 4. Springer, Berlin Heidelberg New York
14. To keep the treatment simple, and since we mainly consider overall isotropic systems, we will not explicitly give the more general formulation in terms of spherical harmonics or Wigner rotation matrices
15. Beevers M, Elliott DA, Williams G (1980) Polymer 21:13 and references cited therein

16. Cole RH (1982) J Phys Chem 86:4700
17. Israeloff NE, Wang XZ (1997) Rev Sci Instrum 68:1543; Grigera TS, Israeloff NE (1999) Phys Rev Lett 83:5038
18. Musevic I, Kityk A, Skarabot M, Blinc R (1997) Phys Rev Lett 79:1062
19. O'Brien KP, Weissman MB, Sheehy D, Viehland DD (1997) Phys Rev B 56:11365
20. Bellon L, Ciliberto S, Laroche C (2001) Europhys Lett 53:511
21. Müller KA, Thomas H (1991) Structural phase transitions I. Topics in Current Physics, vol 23. Springer, Berlin Heidelberg New York
22. Bloembergen N, Purcell EM, Pound RV (1948) Phys Rev 73:679
23. Diezemann G, Sillescu H, Hinze G, Böhmer R (1998) Phys Rev E 57:4398
24. Cole KS, Cole RH (1941) J Chem Phys 9:341; Davidson DW, Cole RH (1951) J Chem Phys 19:1484
25. Chamberlin RV (1999) Phys Rev Lett 82:2520
26. Tarjus G, Kivelson D, Kivelson S (1997) ACS Sym Ser 676:67
27. Noack F (1971) In: NMR – basic principles and progress, vol 3. Springer, Berlin Heidelberg New York, pp 83–144
28. Beckman P (1988) Phys Rep 171:85
29. Angell CA, Böhmer R (2002) Mechanical relaxations of glassy systems. In: Magalas LB (ed) Mechanical spectroscopy and its applications in material science. Kluwer, Dordrecht, see also chap 16
30. Böhmer R, Giebenhain U, Loidl A (1994) Mol Phys 82:531
31. In fact, for Eq. (17.4) the assumption was made that $t_p \ll t_m$ or that no exchange takes place during t_p
32. Fleischer G, Fujara F (1994) In: NMR – basic principles and progress, vol 30. Springer, Berlin Heidelberg New York, pp 159–207
33. Callaghan PT (1991) Principles of NMR microscopy. Clarendon, Oxford
34. Blümich B (2000) NMR imaging of materials. Oxford University Press
35. McCall DW, Douglass DC, Anderson EW (1963) Ber Bunsenges Phys Chem 67:336; Stejskal EO, Tanner JE (1965) J Chem Phys 42:288
36. If pulsed field gradients are used q/γ is the product of width and strength of the gradient pulse and $S_2(q,t_m)$ can be obtained from the ratio of the spin echo amplitudes with and without field gradients applied
37. Hertz HG (1974) In: Lascombe J (ed) Molecular motion in liquids. Reindel, Dordrecht, p 337
38. Kärger J, Ruthven DM (1992) Diffusion in zeolites and other microporous solids. Wiley, New York
39. Feiweier T, Geil B, Pospiech EM, Fujara F, Winter R (2000) Phys Rev E 62:8182
40. Xu Z, Stebbins JF (1995) Science 270:1332
41. Larsen RG, Shore J, Schmidt-Rohr K, Emsley L, Long H, Pines A, Janicke M, Chmelka B (1993) Chem Phys Lett 214:220
42. e.g., Gullion T, Conradi MS (1985) Phys Rev B 32:7076
43. Blinc R, Dolinsek J, Zalar B (1995) Solid State Ionics 77:97
44. Haibel A, Nimtz G, Pelster R, Jaggi R (1998) Phys Rev E 57:4838
45. Chang I, Sillescu H (1997) J Phys Chem B 101:8794
46. Initially η rather than τ was used to monitor rotational correlation times
47. For a recent review of the dynamic conductivity, see Dyre JC, Schrøder TB (2000) Rev Mod Phys 72:873 and references cited therein
48. Here for simplicity a single diffusing ion species with charge e and concentration n are assumed
49. Isard JO (1999) J Non-Cryst Solids 246:16
50. Greaves GN, Ngai KL (1995) Phys Rev B 52:6358 and references cited therein
51. See, e.g., Elliot SR (1990) Physics of amorphous materials, 2nd edn. Longman, London
52. It may be anticipated that in well ordered crystals adjacent sites along the conduction pathway are characterized by considerable differences in the associated (EFG) tensors and thus NMR frequencies. This may be expressed by saying that viewed from the hopping ion the relevant tensor performs large-angle jumps

53. For an estimate for the mean rotation angle $\langle\theta_l\rangle$ which leads to a decay of $g_l(t_m)$ to $g_l(0)/e$ it may suffice here to consider $\theta(0) = 90°$ as the initial orientation. Then $P_l[\cos\theta(0)]$ $P_l[\cos\theta(t_m)] = P_l[\cos\theta(t_m)] = e^{-1}$ gives $\langle\theta_1\rangle = 68.4°$, $\langle\theta_2\rangle \approx 40.5°$, etc. Slightly different values are obtained (Sillescu H, private communication) if an average over all initial positions is carried out

54. Anderson JE (1972) Faraday Symp Chem Soc 6:82

55. Hinze G (1998) Phys Rev E 57:2010

56. Vogel M, Rössler E (2000) J Magn Reson 147:43

57. Fujara F, Wefing S, Spiess HW (1986) J Chem Phys 84:4579

58. Gallenkamp U, Jungnickel BJ (1989) Ber Bunsenges Phys Chem 93:585

59. Dejardin JL, Kalmykov YP (2000) J Chem Phys 112:2916 and references cited therein

60. Bellini T, Mantegazza F, Degiorgio V, Avallone R, Saville DA (1999) Phys Rev Lett 82:5160

61. Inoue T, Mizukami Y, Okamoto H, Matsui H, Watanabe H, Kanaya T, Osaki K (1996) Macromolecules 29:6240

62. Böhmer R (1991) J Phys D Appl Phys 24:1391

63. Ernst RM (1992) Phys Rev B 46:13,697

64. Schiener B, Böhmer R, Loidl A, Chamberlin RV (1996) Science 274:752; Böhmer R, Diezemann G (2002) Principles and applications of pulsed dielectric spectroscopy and nonresonant dielectric hole burning. In: Kremer F, Schönhals A (eds) Broadband dielectric spectroscopy. Springer, Berlin Heidelberg New York, chap 14

65. Böhmer R (1998) Phase Trans 65:211

66. This usually presents no problem for the probes, ^{1}H, ^{2}H, and ^{13}C, mainly discussed in the present article

67. Winterhalter J, Maier D, Grabowski DA, Honerkamp J, Müller S, Schmidt C (1999) J Chem Phys 110:4035 and references cited therein

68. Spiess HW, Sillescu H (1981) J Magn Reson 42:381

69. Kuhns PL, Conradi MS (1982) J Chem Phys 77:1771

70. Here, like in several other places, we leave out details, see [9]

71. Jeener J, Meier BH, Bachmann P, Ernst RR (1979) J Chem Phys 71:4546

72. Hagemeyer A, Schmidt-Rohr K, Spiess HW (1989) Adv Magn Reson 13:85

73. Schmidt C, Wefing S, Blümich B, Spiess HW (1986) Chem Phys Lett 130.184; Schmidt C, Blümich B, Spiess HW (1988) J Magn Reson 79:269

74. Schaefer D, Leisen J, Spiess HW (1995) J Magn Reson A 115:60

75. Glarum S (1960) J Chem Phys 33:1371

76. Anderson JE, Ullman R (1967) J Chem Phys 47:2178

77. Schmidt-Rohr K, Spiess HW (1991) Phys Rev Lett 66:3020

78. Cicerone MT, Ediger MD (1995) J Chem Phys 103:5684; Ediger MD (2000) Annu Rev Phys Chem 51:99

79. Richert R (1993) Chem Phys Lett 216:223; Richert R (2000) J Chem Phys 113:8404

80. Sillescu H (1996) J Chem Phys 104:4877

81. Heuer A (1997) Phys Rev E 56:730

82. Diezemann G (1997) J Chem Phys 107:10,112

83. Sillescu H (1999) J Non-Cryst Solids 243:81

84. Böhmer R, Chamberlin RV, Diezemann G, Geil B, Heuer A, Hinze G, Kuebler SC, Richert R, Schiener B, Sillescu H, Spiess HW, Tracht U, Wilhelm M (1998) J Non-Cryst Solids 235/237:1

85. Hinze G, Diezemann G, Sillescu H (1998) Europhys Lett 44:565

86. It should be noted that in the limit $t_{m1} = t_{m3} \to 0$ the term with $l = 0$ does not decay to below 7/15 even in the presence of exchange

87. Tracht U, Wilhelm M, Heuer A, Feng H, Schmidt-Rohr K, Spiess HW (1998) Phys Rev Lett 81:2727; Tracht U, Wilhelm M, Heuer A, Spiess HW (1999) J Magn Reson 140:460

88. Reinsberg SA, Qiu XH, Wilhelm M, Spiess HW, Ediger MD (2001) J Chem Phys 114:7299

89. Also for the 'normal' $F_4(t_{m2})$ experiments CP is used, but only to enhance the signal intensity and to reduce the recycle delay. These measures are also taken for the $F_4^{CP}(t_{m2})$ experiments, but they are not crucial to understand the clue of the approach

90. Blochowicz T, Kudlik A, Benkhof S, Senker J, Rössler E, Hinze G (1999) J Chem Phys 110:12011
91. Böhmer R, Diezemann G, Hinze G, Rössler E (2001) Prog NMR Spectrosc 39:191
92. Böhmer R, Angell CA (1994) In: Richert R, Blumen A (eds) Disorder effects on relaxational processes. Springer, Berlin Heidelberg New York, p 11 and references cited therein
93. Hinze G, Sillescu H (1996) J Chem Phys 104:314. Here we refer to toluene-d$_5$, deuterated at the aromatic ring, so that one is sensitive to the structural relaxation rather than to the methyl group dynamics
94. Beevers M, Elliott DA, Williams G (1980) Fararday Trans II 76:112
95. Tracht U, Heuer A, Spiess HW (1998) J Non-Cryst Solids 235/237:27
96. Schnauss W, Fujara F, Sillescu H (1992) J Chem Phys 97:1378
97. Vogel M, Rössler E (2001) J Chem Phys B 114:5802
98. Lunkenheimer P (1999) Dielectric spectroscopy of glassy dynamics. Shaker, Aachen; Lunkenheimer P (private communication)
99. Böhmer R, Ngai KL, Angell CA, Plazek DL (1993) J Chem Phys 99:4201
100. Johari GP, Goldstein M (1970) J Chem Phys 53:2372
101. Schneider U, Brand R, Lunkenheimer P, Loidl A (2000) Phys Rev Lett 84:5560
102. Ngai KL, Lunkenheimer P, Léon C, Brand R, Schneider U, Loidl A (2001) J Chem Phys 115:1405
103. Spiess HW (1985) Adv Polym Sci 66:23
104. Blum FD (1997) Macromolecules 30:5331
105. Böhmer R, Hinze G (1998) J Chem Phys 109:241
106. Diezemann G, Böhmer R, Hinze G, Sillescu H (1998) J Non-Cryst Solids 235/237:121
107. Strongly asymmetric jump angle distributions are also predicted on the basis of an elastic model, Dyre JC (1999) Phys Rev E 59:2458; Dyre JC (1999) Phys Rev E 59:7243
108. Diehl RM, Fujara F, Sillescu H (1990) Europhys Lett 13:257
109. Geil B, Fujara F, Sillescu H (1998) J Magn Reson 130:18
110. van Dusschoten D, Tracht U, Heuer A, Spiess HW (1999) J Phys Chem A 103:8359
111. Wachner AM, Jeffrey KR (1999) J Chem Phys 111:10,611
112. Jörg T, Böhmer R, Sillescu H, Zimmermann H (2000) Europhys Lett 49:748
113. Simon GP (1997) In: Runt J, Fitzgerald J (eds) Dielectric spectroscopy of polymeric materials: fundamentals and applications. Washington, ACS, chap 12
114. Dong RY (1994) Nuclear magnetic resonance of liquid crystals. Springer, Berlin Heidelberg New York
115. Schmidt C, Spiess HW (1998) In: Demus D, Goodby J, Gray GW, Spiess HW, Vill V (eds) Handbook of liquid crystals, vol 1. Wiley-VCH, Weinheim, p 595–618
116. Glüsen B, Kettner A, Kopitzke J, Wendorff JH (1998) J Non-Cryst Solids 241:113; Kettner A, Wendorff JH (1999) Liquid Cryst 26:483
117. Vallerien SU, Kremer F, Hüser B, Spiess HW (1994) Colloid Polym Sci 267:583
118. Vallerien SU, Werth M, Kremer F, Spiess HW (1990) Liquid Cryst 8:889
119. Werth M, Vallerien SU, Spiess HW (1991) Liquid Cryst 10:759
120. Schwiegk S, Werth M, Leisen J, Wegner G, Spiess HW (1993) Acta Polymer 44:31
121. Möller M, Wendorff JH, Werth M, Spiess HW (1994) J Non-Cryst Solids 170:295
122. Ngai KL (1996) J Non-Cryst Solids 197:1
123. Spiess HW (1985) Polym Sci 66:23
124. Goldfarb D, Luz Z, Zimmermann H (1981) J Phys 42:1303
125. Poupko R, Luz Z, Spielberg N, Zimmermann H (1989) J Am Chem Soc 111:6094
126. Leisen J, Werth M, Boeffel C, Spiess HW (1992) J Chem Phys 97:3749
127. Of course also dye diffusion is a useful tool, see, e.g., Daoud M, Louis G, Quélin X, Gharbia M, Gharbi A, Perett P (1995) Liquid Cryst 19:833
128. Böhmer R (unpublished)
129. Spiess HW is thanked for providing the sample
130. Grinberg F, Kimmich R (1995) J Chem Phys 103:365
131. Chang I, Diezemann G, Hinze G, Böhmer R, Sillescu H (1997) J Magn Reson 124:165

132. Schmidt-Rohr K, Kulik AS, Beckham HW, Ohlemacher A, Pawelzik U, Boeffel C, Spiess HW (1994) Macromolecules 27:4733

133. Kulik AS, Beckham HW, Schmidt-Rohr K, Radloff D, Pawelzik U, Boeffel C, Spiess HW (1994) Macromolecules 27:4746

134. Kuebler SC, Heuer A, Spiess HW (1996) Macromolecules 29:7089

135. Kuebler SC, Schaefer DJ, Boeffel C, Pawelzik U, Spiess HW (1997) Macromolecules 30:6597

136. Pfändler S (1995) Dissertation ETH No. 10924, Zürich; Cereghetti PM (2000) Dissertation ETH No. 13806, Zürich

137. Gomez-Ribelles JL, Diaz-Calleja R (1985) J Polym Sci Polym Phys Ed 23:1297

138. Muzeau E, Perez J, Johari GP (1991) Macromolecules 24:4713

139. Barrall GA, Schmidt-Rohr K, Lee YK, Landfester K, Zimmermann H, Chingas GC, Pines A (1996) J Chem Phys 104:509 studied PMMA dispersed in colloidal suspension

140. Tracht U, Heuer A, Spiess HW (1999) J Chem Phys 111:3720

141. Heuer A, Leisen J, Kuebler SC, Spiess HW (1996) J Chem Phys 105:7088

142. Kulik A, Spiess HW (1994) Makromol Chem 195:1755

143. If a single jump angle prevails circular ridges correspond to flip angles of $\pm 45°$ or $180 \pm 45°$, cf. [9]

144. Garwe F, Schönhals A, Lockwenz H, Beiner M, Schröter K, Donth E (1996) Macromolecules 29:247

145. Ishida Y, Yamafuji K (1961) Kolloid Z 177:97

146. Heuer A, Wilhelm M, Zimmermann H, Spiess HW (1995) Phys Rev Lett 75:2851

147. Winterlich M et al. (in preparation)

148. Wang CY, Ediger MD (1999) J Phys Chem B 103:4177

149. Böhmer R, Hinze G, Diezemann G, Geil B, Sillescu H (1996) Europhys Lett 36:55

150. Vidal Russell E, Israeloff NE (2000) Nature 408:695

151. Basché T, Moerner WE, Orrit M, Wild UP (1997) Single-molecule optical detection, imaging and spectroscopy. VCH, Weinheim

152. Sillescu H, Böhmer R, Diezemann G, Hinze G (2002) J Non-Cryst Solids (in press)

153. It has to be pointed out that from photobleaching studies it was concluded on a long lived heterogeneity, with a time scale separation from the primary response which depends strongly on temperature [78]

154. Farnan I (1998) Curr Opinion Solid State Mater Sci 3:371

155. Fitzgerald JJ (ed) (1999) Solid state NMR spectroscopy of inorganic materials. ACS, Washington DC

156. Brinkmann D (1992) Prog NMR Spectrosc 24:527

157. Howell FS, Bose RA, Macedo PB, Moynihan CT (1974) J Phys Chem 78:631; Hasz WC, Moynihan CT, Tick PA (1994) J Non-Cryst Solids 172/174:1363

158. Hayler L, Goldstein M (1977) J Chem Phys 66:4736

159. Funke K, Hermeling J, Kümpers J (1988) Z Naturforsch A 43:1094; Cramer C, Funke K, Buscher M, Happe A, Saatkamp T, Wilmer D (1995) Phil Mag B 71:713; Ngai KL, Cramer C, Saatkamp T, Funke K (1996) In: Giordano M, Leporini D, Tosi MP (eds) Non-equilibrium phenomena in supercooled fluids, glasses and amorphous materials. World Scientific, Pisa, pp 3–21

160. Pimenov A, Lunkenheimer P, Rall H, Kohlhaas R, Loidl A, Böhmer R (1996) Phys Rev E 54:676; Pimenov A, Lunkenheimer P, Nicklas M, Böhmer R, Loidl A, Angell CA (1997) J Non-Cryst Solids 220:83; Lunkenheimer P, Pimenov A, Loidl A (1997) Phys Rev Lett 78:2995

161. Wagner H, Richert R (1999) J Appl Phys 85:1750

162. Pimenov A, Loidl A, Böhmer R (1997) J Non-Cryst Solids 212:89

163. Sen S, Stebbins JF (1997) Phys Rev Lett 78:3495

164. Sen S, Stebbins JF (1998) Phys Rev B 58:8379

165. Zürn C, Titze A, Diezemann G, Böhmer R (1999) J Phys Chem B 103:4109

166. Götze W, Sjögren L (1992) Rep Prog Phys 55:241

167. Mezei F, Knaak W, Farago B (1987) Phys Rev Lett 58:571

168. It is clear that in detail many differences may exist between the spectral densities as derived from NMR and from impedance spectroscopy, see, e.g., Tatsumisago M, Angell CA,

Martin SW (1992) J Chem Phys 97:6968; Angell CA, Ngai KL, McKenna GB, McMillan PF, Martin SW (2000) J Appl Phys 88:3113

169. Lu X, Jain H, Kanert O, Küchler R, Dieckhöfer J (1994) Phil Mag B 70:1045
170. Mai C, Etienne S, Perez J, Johari GP (1985) Phil Mag B 50:657
171. Jacobsson P, Börjesson L, Hassan AK, Torell LM (1994) J Non-Cryst Solids 172/174:161
172. Kamiyama T, Shibata K, Suzuki K, Nakamura Y (1995) Physica B 213:483
173. Vogel M, Rössler E (1998) J Phys Chem A 102:2102 find a related superposition in a binary low molecular weight glass former. Using a 2D experiment they were able to map out the time scale on which dynamic exchange takes place
174. Richert R, Böhmer R (1999) Phys Rev Lett 83:4337
175. Moynihan CT (1998) J Non-Cryst Solids 235/237:781
176. Fleischer G, Rittig F, Štěpánek R, Almdal K, Papadakis CM (1999) Macomolecules 32:1956
177. Rittig F, Kärger J, Papadakis CM, Fleischer G, Štěpánek R, Almdal K (1999) Phys Chem Chem Phys 1:3923
178. Fleischer G, Rittig F, Kärger J, Papadakis CM, Mortensen K, Almdal K, Štěpánek R (1999) J Chem Phys 111:2789
179. Papadakis CM, Almdal K, Mortensen K, Rittig F, Fleischer G, Štěpánek R (2000) Eur Phys J E 1:275
180. Rittig F, Fleischer G, Kärger J, Papadakis CM, Almdal K, Štěpánek R (1999) Macromolecules 32:5872
181. Baur ME, Stockmayer WH (1965) J Chem Phys 43:4319
182. Adachi K, Kotaka T (1993) Progr Polym Sci 18:58
183. Strobl G (1996) The physics of polymers. Springer, Berlin Heidelberg New York
184. de Gennes PG (1979) Scaling concepts in polymer physics. Cornell University, Ithaca, NY
185. Doi M, Edwards SF (1986) The theory of polymer dynamics. Clarendon Press, Oxford, UK
186. It should be noted that the mode with $p = 2$ leaves the end-to-end vector invariant
187. Adachi K, Kotaka T (1985) Macromolecules 16:466
188. Boese D, Kremer F (1990) Macromolecules 23:829
189. Fleischer G, Appel M (1995) Macromolecules 28:7281
190. Rittig F, Fleischer G, Papadakis C, Schönhals A (2002) Macromolecules. To be published
191. Hinze G, Böhmer R, Diezemann G, Sillescu H (1998) J Magn Reson 131:218
192. e.g., Rose ME (1957) Theory of angular momentum. Wiley, London, p 57
193. Note that the factors $\frac{25}{29}$ and $\frac{4}{29}$ given in Eq. (3) of [85] (rather than $\frac{5}{9}$ and $\frac{4}{9}$, cf. Appendix 17.2) are obviously due to a misprint
194. Moynihan CT, Boesch LP, Laberge NL (1973) Phys Chem Glasses 14:122
195. Callaghan PT, Coy A, MacGowan D, Packer KJ, Zelaya FO (1991) Nature 351:467
196. Kudlik A, Tschirwitz C, Benkhof S, Blochowicz T, Rössler E (1997) Europhys Lett 40:649
197. Döß A, Paluch M, Sillescu H, Hinze G (2002) Phys Rev Lett 88:095701
198. Pavlatou EA, Rizos AK, Papatheodorou GN, Fytas G (1991) J Chem Phys 94:224
199. Böhmer R, Sanchez E, Angell CA (1992) J Phys Chem 96:9089
200. Appel M, Fleischer G, Kärger J, Chang I, Fujara F, Schönhals A (1997) Colloid Polym Sci 275:187

18 Polymer Dynamics by Dielectric Spectroscopy and Neutron Scattering – a Comparison

A. Arbe · J. Colmenero · D. Richter

18.1
Introduction

Polymeric systems show a very rich variety of dynamical processes which manifest themselves in different frequency ranges at a given temperature. Between vibrations taking place at time scales faster than the picosecond range and reptation at very long times, a number of dynamical processes can been detected in such systems. Some of them can be specific for the particular microstructure of the polymer, like, for instance, rotations of methyl groups. However, it is well established that two relaxation processes are present in all glass-forming polymers (see, e.g., [1, 2]): the primary or structural α-relaxation and the secondary or β-relaxation, also known as the Johari-Goldstein process [3]. The two relaxations coalesce in what we will call $\alpha\beta$-process in a temperature range 10%–20% above the glass transition temperature T_g. The α-relaxation is commonly believed to be related to segmental relaxations of the main chain. The temperature dependence of its relaxation time shows a dramatic increase around T_g, leading to the glassy state at lower temperatures. The β-relaxation is active above as well as below T_g, and occurs independently of the existence of side groups in the polymer. This relaxation has traditionally been attributed to local relaxation of flexible parts, e.g., side groups, and, in main chain polymers, to twisting or crankshaft motion in the main chain [1]. On the other hand, the α-relaxation relates to the structural relaxation of the material and is necessarily of intermolecular nature [4]. However, the molecular nature of the secondary relaxation and its relationship with the primary relaxation are still poorly understood.

The dynamics of glass-forming systems have mainly been investigated by means of relaxation techniques like dynamical mechanical measurements or broadband dielectric spectroscopy (BDS). With these techniques it has also been well established that, apart from the characteristics mentioned above, these two processes show another universal feature: their relaxation functions cannot be described by simple Debye processes. A stretched exponential or Kohlrausch-Williams-Watts (KWW) [5] functional form characterizes the α-process relaxation function in the time domain

$$\varphi_\alpha(t) \sim \exp\left[-\left(\frac{t}{\tau_w}\right)^\beta\right], \qquad 0 < \beta \leq 1 \tag{18.1}$$

and a broad and usually symmetric relaxation function is found in the case of the β-process [1]. These broad features can, at least from a purely mathematical point of view, be related to distributions of elemental exponential (Debye) relaxation processes. However, though phenomenological descriptions of the results by the relaxation techniques are possible, a deeper understanding of the nature of these relaxations and the way they coalesce requires a microscopic insight.

In order to access the relaxational processes on a molecular level, it is necessary to get spatial information of the relaxations. This information can be provided by quasielastic neutron scattering (QENS) techniques through the momentum transfer (Q) dependence of the dynamic structure factor $S(Q,t)$. A combination of QENS and broadband dielectric techniques is thus a powerful tool for this task. While the last facilitates precise information about the temperature dependence of the characteristic times and the spectral shape of the relaxations, QENS provides space-time information about the processes involved in the mesoscopic dynamics of the system. However, compared to BDS, the dynamic range of QENS is rather limited. Therefore, the combined use of both methods is necessary to achieve further progress in the understanding of the mechanisms behind the dynamics of the α-, β-, and $\alpha\beta$-relaxations in glass-forming systems.

The combination of different techniques is usually not straightforward and requires unified analysis methods. In the case of BDS and QENS, first of all, the correlators observed are rather different. QENS techniques allow one access to either to the density-density correlation function when coherent scattering is measured, or the selfcorrelation function of the atoms in the incoherent case. These observables provide direct space-time information about the actual microscopic relaxation processes. On the other hand, BDS observes the frequency dependent complex dielectric permittivity $\varepsilon^*(\omega)$, which reflects the orientational dynamics of the molecular dipoles in the sample. Therefore, we should, in principle, expect different results when a given relaxation process is observed either directly by QENS or indirectly by BDS. However, finally both sets of measurements should mirror, perhaps in a different way, the same physics.

In this work we first introduce the main concepts related to neutron scattering (NS) techniques, and the way they can be connected to the BDS. Thereafter we present some theoretical results about incoherent and coherent structure factors for different types of motions, localized and diffusive, and for the merging of two processes. Finally experimental examples on 1,4-polybutadiene as a showcase are presented.

18.2
Quasielastic Neutron Scattering

18.2.1
Neutron Cross Sections and Correlation Functions

An inelastic scattering event of a neutron is characterized by the transfer of momentum; $\hbar\boldsymbol{Q} = \hbar(\boldsymbol{k}_f - \boldsymbol{k}_i)$ and energy $\hbar\omega = \hbar^2(\boldsymbol{k}_f^2 - \boldsymbol{k}_i^2)/2m$ during scattering.

Thereby, $\hbar$ is the Planck constant $h/2\pi$; $\mathbf{k}_f$ and $\mathbf{k}_i$ are the final and initial wave vectors of the neutron, and m is the neutron mass. For a quasielastic scattering process $|\mathbf{k}_f| \cong |\mathbf{k}_i| = 2\pi/\lambda_o$ (λ_o: wavelength of the incoming neutrons) is valid. Accordingly, the magnitude of the scattering vector $\mathbf{Q}$ is given by

$$Q = |\mathbf{Q}| = \frac{4\pi}{\lambda_o} \sin\theta \qquad (18.2)$$

where 2θ is the scattering angle.

The intensity of the scattered neutrons is described by the double differential cross section $\partial^2\sigma/\partial\Omega\,\partial\hbar\omega$ being the probability that neutrons are scattered into a solid angle $\partial\Omega$ with an energy change $\partial\hbar\omega$.

For a system containing N atoms the double differential cross section in classical approximation is given by [6]

$$\frac{\partial^2\sigma}{\partial\Omega\,\partial\hbar\omega} = \frac{1}{2\pi\hbar}\frac{k_f}{k_i} \int_{-\infty}^{+\infty} dt \exp(-i\omega t)\left\langle \sum_{j,k}^{N} b_j b_k \exp\{i\mathbf{Q}\,[\mathbf{r}_j(t) - \mathbf{r}_k(0)]\}\right\rangle \qquad (18.3)$$

where $\mathbf{r}_j(t)$ and $\mathbf{r}_k(0)$ are position vectors of the atoms j and k at time t and time zero, respectively; b_j and b_k are the respective scattering lengths, and $\langle \ldots \rangle$ denotes the thermal average. Since neutron scattering occurs at the nuclei, the scattering lengths may depend both on the particular isotope and on the relative spin orientations of neutron and nuclei. This mechanism has two consequences:

1. In general the spin orientations of the atoms and neutrons are not correlated giving rise to 'disorder' or incoherent scattering. This also holds for isotope distributions. Hydrogen in particular possesses very different scattering length for different spin orientations. This leads to very strong incoherent scattering which in hydrogen-containing materials often dominates the total scattering.
2. The fact that different isotopes of the same nucleus may have different scattering length can be used to label on an atomic level. In particular, the scattering lengths of hydrogen and deuterium are significantly different ($b_H = -0.374 \times 10^{-12}$ cm; $b_D = 0.667 \times 10^{-12}$ cm) allowing an easy labeling of hydrogen-containing organic matter. For instance, the conformation of a polymer in a melt can only be experimentally accessed by such a labeling technique using small angle neutron scattering.

Thus, the scattering cross section (Eq. 18.3) generally contains a coherent and an incoherent part. For simplicity considering only one type of atoms the double differential cross section can be written as

$$\frac{\partial^2\sigma}{\partial\Omega\,\partial\hbar\omega} = \frac{k_f}{\hbar k_i}N\{[\langle b^2\rangle - \langle b\rangle^2]\,S_{\mathrm{inc}}(\mathbf{Q},\omega) + \langle b\rangle^2 S(\mathbf{Q},\omega)\} \qquad (18.4)$$

with

$$S_{\mathrm{inc}}(\mathbf{Q},\omega) = \frac{1}{2\pi N}\int_{-\infty}^{+\infty} dt\, e^{i\omega t} \sum_{j}^{N} \langle e^{-i\mathbf{Q}\mathbf{r}_j(0)}e^{i\mathbf{Q}\mathbf{r}_j(t)}\rangle \qquad (18.5)$$

and

$$S(\boldsymbol{Q},\omega) \equiv S_{\mathrm{coh}}(\boldsymbol{Q},\omega) = \frac{1}{2\pi N} \int\limits_{-\infty}^{+\infty} \mathrm{d}t e^{i\omega t} \sum_{j,k}^{N} \langle e^{-iQr_j(t)} e^{iQr_k(0)} \rangle \tag{18.6}$$

Thereby, $S(\boldsymbol{Q},\omega)$ and $S_{\mathrm{inc}}(\boldsymbol{Q},\omega)$ are the coherent and incoherent dynamic structure factors, respectively. $S(\boldsymbol{Q},t)$ and $S_{\mathrm{inc}}(\boldsymbol{Q},t)$ denote the same quantities in Fourier t-domain. The dynamic structure factors are the space-time Fourier transform of the pair and self correlation functions of the moving atoms (van Hove correlation functions). Classically, the pair correlation function can be understood as the conditional probability of finding an atom j at location $\boldsymbol{r}$ and time t, if another atom k was at location $\boldsymbol{r} = 0$ at time $t = 0$. For $k = j$ the self-correlation function is obtained. In Gaussian approximation, i.e., assuming Gaussian distribution for the position vectors $\boldsymbol{r}_j(t)$ and $\boldsymbol{r}_k(0)$, the intermediate dynamic structure factors can be written as

$$S(\boldsymbol{Q},t) = \frac{1}{N} \sum_{j}^{N} \sum_{k}^{N} \exp\left\{ -\frac{Q^2}{6} \langle [\boldsymbol{r}_j(t) - \boldsymbol{r}_k(0)]^2 \rangle \right\} \tag{18.7}$$

$$S_{\mathrm{inc}}(\boldsymbol{Q},t) = \frac{1}{N} \sum_{j}^{N} \exp\left\{ -\frac{Q^2}{6} \langle [\boldsymbol{r}_j(t) - \boldsymbol{r}_j(0)]^2 \rangle \right\} \tag{18.8}$$

Note that in this approximation the incoherent scattering measures the time dependent thermally averaged mean square displacement $\langle [\boldsymbol{r}_j(t) - \boldsymbol{r}_j(0)]^2 \rangle$.

18.2.2
Neutron Instrumentation

It is the task of inelastic neutron scattering to measure simultaneously the energy transfer $\hbar\omega$ and the momentum transfer $\hbar\boldsymbol{Q}$ of the scattered neutrons. In the following we will discuss three different techniques important for the investigation of the glass transition; namely, time of flight neutron spectroscopy, backscattering, and neutron spin echo (see [7, 8] as general references).

18.2.2.1
Time of Flight Spectrometer

Figure 18.1 displays schematically the setup of a neutron time of flight instrument. The role of the monochromator, thereby, is taken by a number of choppers preparing short neutron pulses from the incoming beam. A short pulse getting through chopper 1 contains the spectrum of all wavelengths present in the beam. Chopper 2 turns in a fixed phase relation to chopper 1. Since neutrons with different velocities arrive at different times at this second chopper it selects corresponding to the phase shift a certain neutron velocity v_i. These neutrons
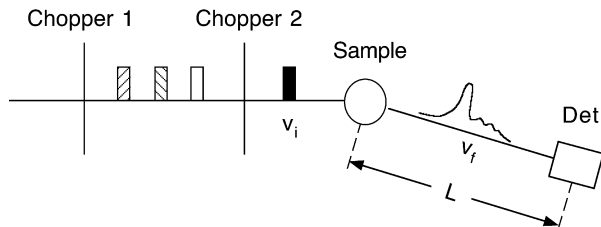
Fig. 18.1. Schematic sketch of a time of flight instrument; the choppers 1 and 2 prepare a monochromatic pulse of velocity v_i; the scattered neutrons are analyzed with respect to arrival time revealing the final velocity v_f. The differently shaded pulses symbolize different neutron velocities

are scattered at the sample and at a distance L after the sample the neutrons are recorded according to their arrival time. Neutrons which have gained energy at the sample will arrive earlier, those which have lost energy will arrive later. Thus, in determining the time of flight of the different neutrons, the final neutron velocity v_f can be obtained and by calculating the velocity difference $\Delta v = v_i - v_f$ the energy difference – and considering the scattering angle, also the momentum change – can be computed. Typically the precision of such velocity determinations is in the order of 1%.

18.2.2.2
Backscattering Instrument

In order to achieve higher energy resolution, one has to consider carefully the very weak neutron flux of a neutron source. While a typical laser provides 10^{22} monochromatic photons per second in a well collimated beam, the total neutron flux of the most powerful research reactor at the Institute Laue-Langevin (ILL) in Grenoble is in the order of 10^{15} neutrons s^{-1} cm^{-2}. Thus, a finer energy selection immediately reduces the available neutron flux to a point, where experiments are not possible any more. Therefore, high resolution techniques try to decouple intensity and resolution determining elements. Neutron backscattering exploits the fact that at a scattering angle of $2\theta = 180°$ the selected wavelength in a reflection from a crystal depends only to second order on the divergence of the incoming beam. Choosing backreflection from a perfect crystal in combination with relaxed collimation of the neutron beam leads to acceptable intensities and energy resolutions in the order of 10^{-4}.

Figure 18.2 displays the general layout of the backscattering spectrometer IN10 at the ILL in Grenoble. The neutrons are monochromatized by a perfect silicon crystal mounted on a Doppler drive which, as in Moessbauer experiments, varies the incident energy of the neutron by Doppler shifting. These monochromatized neutrons are deflected by a graphite crystal and directed towards the sample. The analyzer crystals are mounted on spherical hollowed plates with a radius of curvature such that they focus the reflected neutrons into detectors which are set up behind the sample. In this way a large solid angle is covered on
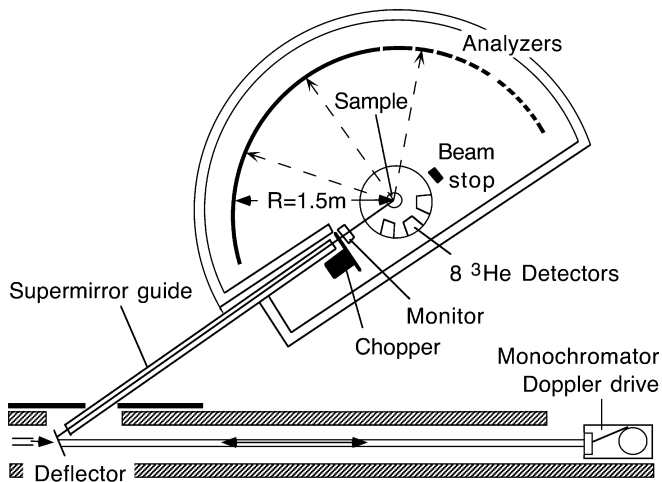
Fig. 18.2. Sketch of the backscattering spectrometer IN10 at the ILL reactor

the analyzer side. The typical resolution achieved with this instrument is in the order of 1 μeV.

18.2.2.3
Spin Echo Spectrometer

While in the two methods above the energy transfer at the sample is determined by first measuring the energy of the incident neutron and thereafter that of the scattered neutron taking the difference, the unique feature of neutron spin echo (NSE) is its ability to determine energy changes of neutrons during scattering in a direct way. Unlike the conventional time of flight technique NSE measures the neutron velocities of the incoming and scattered neutrons utilizing the Larmor precession of the neutron spin in an external guide field. Since the neutron spin vector acts like the hand of an internal clock attached to each neutron which stores the result of the velocity measurement on the neutron itself, this measurement is performed for each neutron individually. Therefore, the incoming and outgoing velocities of one and the same neutron can be compared directly and a velocity difference measurement becomes possible. Thus, energy resolution and monochromatization of the primary beam or the proportional neutron intensity are decoupled and an energy resolution of the order of 10^{-5} can be achieved with an incident neutron spectrum of 20% band width.

The basic experimental setup of a neutron spin echo spectrometer is shown in Fig. 18.3. A velocity selector in the primary neutron beam selects a wave length interval of about $\Delta\lambda/\lambda = 20\%$. The spectrometer offers primary and secondary neutron flight paths, where guide fields H and H' can be applied. At the beginning of the first flight path a super mirror polarizes the neutrons in the direction of propagation. A first $\pi/2$-coil turns the neutron polarization into a di-
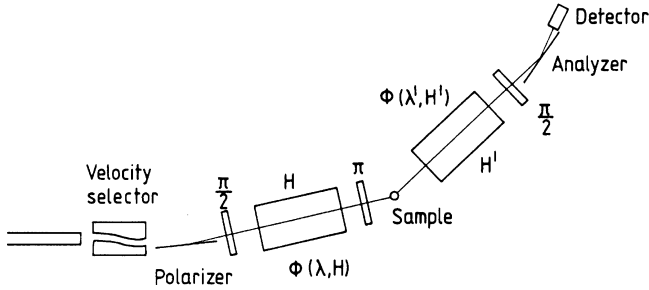
Fig. 18.3. Schematic setup of a spin echo spectrometer

rection perpendicular to the neutron momentum. From this well defined initial condition the neutrons commence to precess in the applied guide field. Without the action of the π-coil which turns the neutron spin by 180° around a perpendicular axis, each neutron performs a phase angle $\phi \propto \lambda \int H ds$. Since the wavelengths are distributed over a wide range, in front of the second $\pi/2$-coil the phase angle will be different for each neutron and the beam will be depolarized. A π-coil positioned at half the value of the total field integral avoids this effect. On its way to the π-coil the neutron may pass an angle $\phi_1 = 2\pi N + \Delta\phi_1$. The action of the π-coil transforms the angle $\Delta\phi_1$ to $-\Delta\phi_1$. In a symmetric setup where both field integrals before and after the π-coil are identical, the neutron spin turns by another phase angle $\phi_2 = \phi_1 = 2\pi N + \Delta\phi_1$. The spin transformation at the π-coil compensates the residual angles $\Delta\phi_1$ and in front of the second $\pi/2$-coil the neutron spin points again into its original perpendicular direction, independent of its velocity. The second $\pi/2$-coil projects this perpendicular component of the polarization into the forward direction and at the supermirror analyzer the total polarization is recovered. The experimental setup is spin focusing. As with NMR spin echo methods, the phase is focused to its initial value in front of the second $\pi/2$-coil for each spin separately.

In a spin echo spectrometer the sample is positioned close to the π-coil. If the neutron energy is changed due to inelastic scattering at the sample, the neutron wavelength is modified from λ to $\lambda = \lambda + \delta\lambda$. Then the phase angles ϕ_1 and ϕ_2 do not compensate each other and the second $\pi/2$-coil projects only the component of the polarization pointing in the original perpendicular direction into the forward direction which passes afterwards through the analyzer. Apart from resolution corrections, the final polarization P_f is related to the initial polarization P_i by

$$P_f = P_i \int_{-\infty}^{+\infty} S(\mathbf{Q}, \omega) \, \cos(\omega t) \, d\omega \tag{18.9}$$

The scattering function $S(\mathbf{Q}, \omega)$ thereby is the probability that during scattering at a certain momentum transfer $\hbar \mathbf{Q}$ an energy change $\hbar\omega$ occurs. We have introduced the time variable $t \sim \lambda^3 H$. From Eq. (18.9) it is realized that NSE is a Fourier method and essentially measures the real part of the intermediate scat-

tering function $S(\mathbf{Q},t)$. The time variation in a spin echo scan is performed by changing the magnetic field H. Additionally, changing the wavelength increases via $t \sim \lambda^3 H$ the dynamic range of the instrument. At present times up to 200 ns and a dynamic range of about 10^5 may be reached.

18.2.3
Relation to Dielectric Spectroscopy

The theoretical basis of the broadband dielectric spectroscopy, as well as the experimental details of these techniques, are widely described in other chapters of this book. Here we would only like to summarize briefly the dynamic variables obtained by means of these methods and how they are usually related to the quantities measured by neutron scattering.

Dielectric relaxation measurements of the orientational depolarization processes in glass forming systems are usually carried out in the frequency domain, though in some cases time domain techniques are also employed [9, 10]. The magnitude measured is the frequency-dependent complex dielectric permittivity $\varepsilon^*(\omega) = \varepsilon'(\omega) - i\varepsilon''(\omega)$, which can also be expressed as Laplace transformation of a time domain relaxation function $\varphi(t)$ as

$$\Phi^*(\omega) = \frac{\varepsilon^*(\omega) - \varepsilon_\infty}{\Delta\varepsilon} = \int\limits_0^\infty \left[-\frac{d\varphi(t)}{dt} \exp(-i\omega t) \right] dt \tag{18.10}$$

where ε_∞ is the high frequency limit value of the permittivity, $\Delta\varepsilon$ is the relaxation strength ($\Delta\varepsilon = \varepsilon_S - \varepsilon_\infty$, where ε_s is the static value of the permittivity) and, thereby, $\Phi^*(\omega)$ a normalized relaxation function. In this expression, $\varphi(t)$ represents the decay of the polarization of a fully polarized sample after removing the electric poling field, i.e., the response to a step-like excitation, which would correspond to the autocorrelation function of the total dielectric polarization.

Taking into account the well known property of the Laplace transformation: $[i\omega L_{i\omega}\{f(t)\} = L_{i\omega}\{\dot{f}(t)\} + f(0)]$ the expression at Eq. (18.10) can also be written in terms of $\varphi(t)$ itself as

$$\Phi^*(\omega) = 1 - i\omega \int\limits_0^\infty [-\varphi(t) \exp(-i\omega t)] dt \tag{18.11}$$

Under certain conditions $\left(\text{e.g., } \Delta\varepsilon \ll \varepsilon_\infty \text{ or } \dfrac{\varepsilon_S}{\varepsilon_\infty} \gg 1 \right)$ the step response function $\varphi(t)$ can also represent to a good approximation a microscopic like correlation function (see [11], vol II, p 159). In these cases $\varphi(t)$ can be written as

$$\varphi(t) = \frac{\langle \boldsymbol{\mu}_i(0)\boldsymbol{M}_1(t)\rangle}{\langle \boldsymbol{\mu}_i(0)\boldsymbol{M}_1(0)\rangle} = \frac{1}{g\mu^2} \langle \boldsymbol{\mu}_i(0)\boldsymbol{M}_1(t)\rangle \tag{18.12}$$

The moment $M_1(t)$ represents the sum of the permanent moments of the molecules in a sphere of macroscopic dimensions around molecule i but small with respect to the total dielectric, and g is the Kirkwood correlation factor which

measures the strength of molecular interactions between the i-th molecule and its neighbors [11]. However, an actual molecular interpretation in terms of the molecular dipole moments is extremely difficult in condensed systems as polymers, where cross-correlation terms $\langle \boldsymbol{\mu}_i(0)\boldsymbol{\mu}_j(t)\rangle$ contained in $\langle \boldsymbol{\mu}_i(0)M_1(t)\rangle$ in Eq. (18.12) cannot be neglected or easily evaluated. Only for those systems, where $g \approx 1$ due to the absence of specific interactions between molecules, $\varphi(t)$ could be interpreted as the autocorrelation function for the permanent dipole moment of a single molecule. In these cases $\varphi(t) = \langle \boldsymbol{\mu}(0)\boldsymbol{\mu}(t)\rangle/\mu^2$, which is called the dipole correlation function, is thereby equal to the step-response function of the orientational polarization.

Taking into account the above raised arguments and those described in the previous section of this chapter, we can conclude that the correlators observed by NS techniques and BDS techniques are rather different. Moreover, while a microscopic interpretation of neutron scattering results can be straightforwardly achieved through the van Hove correlation functions, this is not the usual case for BDS results. Therefore, one could expect different results when a given relaxation process is monitored either directly by NS or indirectly by BDS.

However, in some cases both methods can reflect – perhaps in a different way – the same physics. This is particularly relevant in the case of the so-called α-relaxation of glasses where some universal properties are expected. The generally accepted idea is that the α-relaxation is a structural relaxation which can directly be observed in the density-density correlation function, i.e., the dynamic structure factor directly measured, for instance, by neutron spin echo (NSE) [2, 4]. The observation of this process by means of other techniques, as for example dielectric relaxation, depends on how the structural relaxation is coupled to the magnitude measured by these techniques. In the case of the dielectric relaxation the important – and difficult – question is how the dynamics of molecular dipoles is driven by the structural relaxation.

In spite of these difficulties, there are several investigations of the α-relaxation in different glass-forming polymers by QENS and BDS which show compatible results within the experimental uncertainties [12–16]. The quantities which are usually compared are the dielectric relaxation function $\varphi(t)$ and the normalized intermediate scattering function $S(\boldsymbol{Q},t)$ either incoherent or coherent. In some cases, the comparison was also directly carried out in the frequency domain by constructing an incoherent neutron dynamic structure factor $S(\boldsymbol{Q},\omega)$ as $S(\boldsymbol{Q},\omega) \sim -\,\mathrm{Im}[\Phi^*(\omega)]/\omega$ where $\Phi^*(\omega)$ is the dielectric relaxation function introduced above [12]. It is worth emphasizing once again that while $\varphi(t)$ or $\Phi^*(\omega)$ only contain information about time or frequency dependence, $S(\boldsymbol{Q},t)$ or $S(\boldsymbol{Q},\omega)$ give, in addition, spatial information through the momentum transfer $\boldsymbol{Q}$-dependence. Therefore, in order to compare NS and BDS results we have to take into account this $\boldsymbol{Q}$-dependence in some way. This means that we have to compare for instance $\varphi(t)$ with $S(\boldsymbol{Q},t)$ at different values of $\boldsymbol{Q}$. NS results of many different systems show that the α-relaxation – as it is measured by NS – is a non-localized process ("diffusive-like"). As a consequence, the $\boldsymbol{Q}$-dependence of $S(\boldsymbol{Q},t)$ or $S(\boldsymbol{Q},\omega)$ mainly enters via the characteristic relaxation times, τ, which now are not only temperature dependent, but also $\boldsymbol{Q}$-dependent. Taking into account the reported cases where the α-relaxation has been investigated by NS and BDS, it

seems that the dielectric relaxation function and the scattering function measured by QENS show a similar non-exponential (non-Debye) (Eq. 18.1) shape, at least in the high frequency/temperature range where both techniques overlap. A careful investigation of dielectric results [9] shows that, in fact, the shape of the relaxation function (the β-value of Eq. 18.1 for instance) measured by dielectric techniques is changing from T_g until about 1.2 T_g from where the shape remains more or less constant and similar to what is estimated by NS. Moreover, the temperature dependence of the characteristic times of the relaxation function is also compatible in the high temperature/frequency range with the temperature dependence of the time scale of $S(Q,t)$ or $S(Q,\omega)$. Concerning the absolute values of these relaxation times, we have to take into account the Q-dependence of the time scale of the α-process measured by neutron scattering. Therefore, in principle, it is always possible to find a Q-value at which the time scale of the α-process measured by NS and BDS become similar. In particular when NS incoherent results and dielectric results of different polymers are compared, the value of this particular Q is always in the region of 1 Å^{-1} [15]. Whether or not this Q-value has a particular physical meaning is still an unsolved question.

Concerning dynamic processes other than the α-relaxation, which take place in glassy polymers such as, for instance, the so-called β-relaxation, the current situation is less clear. These processes have been investigated by relaxation spectroscopies including dielectric techniques from the early times of polymer science (see, e.g., [1]). Nowadays it seems to be well accepted that such relaxations are related to local molecular motions. However, almost nothing is known about the molecular mechanisms involved in the different cases. It is clear that experimental methods, such as NS, giving spatial information are needed to progress in this field. However, there are not many investigations of the β-relaxation by NS apart from those reported in this chapter [16–20]. Thereby, a comparison between NS and BDS results of the β-relaxation has only been carried out in a few cases. The generally accepted idea is that the β-relaxation is the consequence of spatially localized molecular motions, which are thermally activated. Due to the structural disorder which is inherent to the glassy state, a distribution of potential energy barriers is usually invoked to give account for the broad relaxation functions commonly observed by dielectric spectroscopy. The comparison between NS and BDS results is based on the idea that the relaxation times involved in the β-process do not depend on Q because the molecular motions involved are localized. Only the elastic part of the scattering functions $S(Q,t)$ or $S(Q,\omega)$ will depend on Q according to the geometry of the motions (see below). Moreover, it is also assumed that the distribution of potential barriers for molecular motions is just the same as the distribution obtained from BDS measurements. This in fact implies that the energy landscape explored by the molecular dipoles is the same as that explored by any molecule or molecular group contributing to the neutron scattering. Although this approach seems to work in the cases investigated, it is evident that in the low temperature range below the glass transition it can be in some cases a very rough approximation.

18.3
Dynamic Structure Factors for the α- and β-Process

18.3.1
Local Processes

The dielectric β-relaxation is considered to be a result of a partial reorientation of the molecular dipoles in the substance. It is interpreted as a local activated process, where the dipole fluctuates between two positions separated by an activation energy E. The relaxation time follows an Arrhenius behaviour

$$\tau_\beta(E) = \tau_o^\beta \exp\left(\frac{E}{k_B T}\right) \tag{18.13}$$

and due to the disorder in the material the activation energies E are distributed around an average value E_o. For the distribution function in general a Gaussian is usually assumed

$$g(E) = \frac{1}{\sqrt{\pi}\sigma} \exp\left[-\left(\frac{E - E_o}{\sigma}\right)^2\right] \tag{18.14}$$

Empirically it is found that the width $\sigma(T)$ decreases with increasing temperature. Although such processes have been investigated for a long time by spectroscopic techniques, their molecular origin is still unclear, as it has already been mentioned. Here QENS with its ability to provide space time resolution on the proper scales contributes to a further exploration of the molecular mechanisms behind these relaxations.

We now derive the dynamic structure factor for the β-process which we will consider as a hopping process between two adjacent sites. For such a process the self correlation function is given by a sum of two contributions

$$S_{\text{inc}}(Q,t) = \underbrace{\frac{1}{2}\left[1 + \frac{\sin(Qd)}{Qd}\right]}_{S^{\text{el}}} + \underbrace{\frac{1}{2}\left[1 - \frac{\sin(Qd)}{Qd}\right]}_{S^{\text{inel}}} \exp\left[-\frac{2t}{\tau(E)}\right] \tag{18.15}$$

Here d is the distance between the two sites and $\tau(E)$ is the jump time corresponding to an activation energy E. The complete scattering function is obtained in averaging Eq. (18.15) with the barrier distribution function $g(E)$ obtained, e.g., by dielectric spectroscopy [17, 18]. The Q-dependence of the two contributions to Eq. (18.15) is displayed in Fig. 18.4 as a function of $Q(d = 1.5$ Å$)$. From the oscillation of both contributions with Q the jump distance is obtained. The associated time scale is found from the time decay of the quasielastic part.

The corresponding pair correlation function is more difficult to obtain, since it is determined by a change of configurations of atoms rather than by single atom jumps. The conceptual difference between the pair and the self correlation function for jump processes may be visualized most easily considering rota-

Fig. 18.4. *Q*-dependence of the inelastic (*solid line*) and elastic (*dashed line*) contributions to the incoherent scattering function for a jump over a distance of 1.5 Å
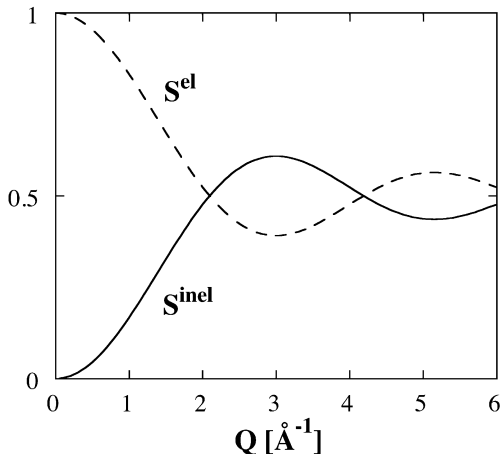
tional jumps. Let us regard, e.g., the 120° rotational jumps of a methyl group around its symmetric axis. An incoherent study would reveal the atomic jumps of the associated hydrogens. The pair correlation function reflects the change of atomic configurations before and after the jump. Since a 120° jump does not change the configuration, a coherent scattering experiment would not reveal anything.

Back to the pair correlation function for the β-process, where we will introduce a simple approximation [17, 18]. We know that for $t = 0$ the pair correlation function is reflected by the static structure factor $S(Q)$. Therefore for $t = 0$ the corresponding pair correlation function for the β-process must reveal $S(Q)$. We now assume that the inelastic scattering is related to uncorrelated jumps of the different atoms. Then all interferences for the inelastic process are destructive and the inelastic form factor should be identical to that of the self correlation function. For the normalized dynamic structure factor for the β-process we arrive at

$$\frac{S(Q,t)_{\beta}}{S(Q)} = \left\langle \frac{S(Q) - S^{\text{inel}}(Q)}{S(Q)} + \frac{S^{\text{inel}}(Q)}{S(Q)} \exp\left[-\frac{2t}{\tau(E)}\right] \right\rangle_{g(E)} \tag{18.16}$$

This incoherent approximation does not reveal, e.g., symmetry related cancellations, but displays a major feature of the corresponding dynamic structure factor, namely the relative suppression of the inelastic contributions from local jump processes at the maximum of the structure factor. Figure 18.5 displays the situation for polybutadiene (PB). There a β-process corresponding to a jump length of $d = 1.5$ Å has been found [17]. The corresponding inelastic dynamic structure factor is strongly reduced at the position of the first peak, while it contributes strongly at higher Q. This figure suggests a Q selectivity for the different relaxation processes: at the maximum of the structure factor local jump processes should not contribute and the relaxation due to structural relaxations should dominate. On the other hand at larger Q, in particular in the minimum of the structure factor, the secondary relaxation should reveal itself.

Fig. 18.5. Q-dependence of the amplitude of the relative quasielastic contribution of the β-process to the coherent scattering function obtained in the incoherent approximation for the inelastic part (*dashed line*). The static structure factor $S(Q)$ of PB at 160 K is shown for comparison (*solid line*)
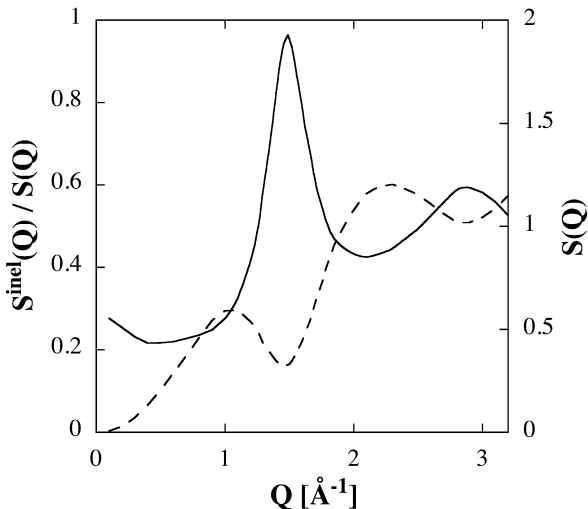
18.3.2
Diffusive (*Q* Dispersive) Processes

Regular diffusion like, e.g., that observed in a Brownian liquid, is characterized by the diffusion constant D and an exponential decay of the incoherent scattering function (see, e.g., [21])

$$S_{\text{inc}}(Q,t) = \exp(-Q^2 Dt) = \exp\left[-\left(\frac{t}{\tau_D^{\text{inc}}}\right)\right] \tag{18.17}$$

The characteristic time is then Q-dependent and given by

$$\tau_D^{\text{inc}} = D^{-1} Q^{-2} \tag{18.18}$$

In this simple case, the Gaussian approximation

$$S_{\text{inc}}(Q,t) = \exp\left[-Q^2 \frac{\langle r^2(t)\rangle}{6}\right] \tag{18.19}$$

is fulfilled and the mean squared displacement $\langle r^2(t)\rangle$ follows a linear time dependence, $\langle r^2(t)\rangle/6 = Dt$. This holds at large scales – small Q values – and long times, where the details of the mechanism (elemental jump) involved in the diffusion cannot be distinguished. On the other hand, the coherent scattering function in simple monoatomic liquids can be expressed as

$$S(Q,t) = S(Q) \exp\left[-\left(\frac{t}{\tau_D^{\text{coh}}}\right)\right] \tag{18.20}$$

where the characteristic time is given by $\tau_D^{coh} = S(Q)\,\tau_D^{inc} = S(Q)\,D^{-1}Q^{-2}$, showing the so-called de Gennes narrowing [22]. In this way Eq. (18.20) can be rewritten as

$$S(Q,t) = S(Q)\exp\left[-\left(\frac{Q^2}{S(Q)}Dt\right)\right] \tag{18.21}$$

This relationship has been experimentally verified in the very simple case of liquid argon [21]. For more complicated systems containing more than one atomic species it is not possible to formulate a similarly simple relation between coherent and incoherent functions. Other approximations have been proposed like, e.g., that by Vineyard [23]

$$S(Q,t) = S(Q)\,S_{inc}(Q,t) \tag{18.22}$$

or by Sköld [24], $S(Q,t) = S(Q)\,S_{inc}\left(\dfrac{Q}{\sqrt{S(Q)}}, t\right)$

Let us assume now anomalous diffusion characterized by a sublinear increase of the mean squared displacement, $\langle r^2(t)\rangle/6 = At^\beta$. If the Gaussian approximation holds, Eq. (18.19) leads to

$$S_{inc}(Q,t) = \exp(-Q^2 A t^\beta) = \exp\left[-\left(\frac{t}{A^{-1/\beta}Q^{-2/\beta}}\right)^\beta\right] = \exp\left[-\left(\frac{t}{\tau_w^{inc}}\right)^\beta\right] \tag{18.23}$$

which evidently has a KWW-like form (Eq. 18.1) with a KWW time τ_w given by [25]

$$\tau_w = \tau_w^{inc} = A^{-1/\beta}Q^{-2/\beta} \tag{18.24}$$

This implies stronger Q-dependencies than in the regular diffusion ($\beta < 1$). In the coherent case the equivalent expression to Eq. (18.21) would be

$$S(Q,t) = S(Q)\exp\left[-\frac{Q^2}{S(Q)}At^\beta\right] = S(Q)\exp\left[-\left(\frac{t}{A^{-1/\beta}S(Q)^{1/\beta}Q^{-2/\beta}}\right)^\beta\right] \tag{18.25}$$

leading to a $S(Q)^{1/\beta}Q^{-2/\beta}$ dependence of the characteristic time that produces a sharper modulation with $S(Q)$ than that expected in the Debye case. As pointed out before, however, this is an oversimplification of the problem for systems containing more than one kind of atom.

In the same way as the relaxation function, the coherent and incoherent intermediate scattering functions corresponding to the main (α-)relaxation in glass forming systems in general, and in polymers in particular, do not follow a single exponential decay, but can be well characterized by a KWW function. Thus the spatial information offered by neutron scattering is accessible through the Q-dependent characteristic times $\tau_w(Q,T)$. If the underlying mechanism of the α-relaxation consists of a sublinear diffusion of the scattering centers and

the Gaussian approximation is fulfilled, strong Q-dependences should be observed for the characteristic time of the main relaxation as studied by QENS [25–27].

18.3.3
Merging of the α- and β-Processes

The simplest way to approach the combination of two processes as the α and β processes is to assume that they are statistically independent. The van Hove self correlation function corresponding to an atom undergoing two different statistically independent processes, α and β, can be written as a convolution product of the corresponding self correlation functions

$$G_s^{\alpha\beta}(r,t) = \int G_s^{\beta}(r',t)\, G_s^{\alpha}(r-r',t)\, dr' \tag{18.26}$$

This implies that the self (incoherent) structure factor, which is given by the Fourier transformation of $G_S^{\alpha\beta}(r,t)$, reads as the direct product of the structure factors corresponding to the two processes

$$S_{\text{inc}}^{\alpha\beta}(Q,t) = S_{\text{inc}}^{\beta}(Q,t)\, S_{\text{inc}}^{\alpha}(Q,t) \tag{18.27}$$

However, in the coherent case the derivation of a similar expression is not straightforward, because the correlations between all the pairs of scatters (j, i) have to be taken into account. One possibility is to follow the procedure described in [18] which is based on a generalization of the Vineyard approximation [23] mentioned above. In this framework, the dynamic structure factor of the combined process can be written as

$$S^{\alpha\beta}(Q,t) = S^{\beta}(Q,t)\, S_{\text{inc}}^{\alpha}(Q,t) \tag{18.28}$$

where $S^{\beta}(Q,t)$ is the coherent structure factor of the β-process. In this scenario we obtain an expression for $S^{\alpha\beta}(Q,t)$ connecting the coherent structure factor of the β-relaxation with the relaxation function of the α-process, where in the language of the Vineyard approximation $S^{\beta}(Q,t)$ takes the role of $S(Q)$.

18.4
Experimental Examples

18.4.1
Polybutadiene as a Showcase

1,4-Polybutadiene (PB) is a main chain polymer built by a random sequence of mainly *trans*- and *cis*-groups (see Fig. 18.6). The main features described in the introduction are clearly found for the relaxations of this polymer when observed by means of broadband BDS. At temperatures below T_g ($T_g = 178$ K) only one relaxation process, the β-relaxation, is active in the dielectric frequency
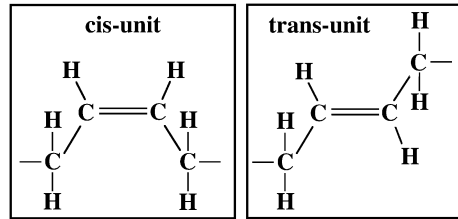
window, whereas above T_g the contribution of the α-relaxation is also measured. Figure 18.7 shows how the two loss processes approach each other with increasing temperature in a narrow temperature range above T_g. These correspond to the α-relaxation, that takes place at lower frequencies, and the β-relaxation. At high temperatures ($\approx T_g + 30$ K) the α- and β-relaxations merge and only one peak can be resolved in the experimental dielectric window.

As was mentioned and can be directly shown in Fig. 18.7, these processes are very broad. Therefore, the concept of a characteristic time is somehow ill defined for these relaxations. Phenomenologically a possible definition could be the inverse of the frequency at which the dielectric loss presents a maximum. Figure 18.8 shows the temperature dependence of the so determined characteristic times of the α- and β-relaxations in PB. In the region well below the merging these time scales can be univocally determined, but further away from T_g only a change in the slope of the high frequency tail of the dielectric loss indicates the presence of the β-relaxation (see Fig. 18.7). Therefore, in this temperature range only the evolution of one maximum, which would be in principle assigned to the main (α-)relaxation, can be followed. It is apparent in Fig. 18.8, that the time scale of the β-relaxation shows an Arrhenius-like temperature dependence, like many other glass-forming polymeric systems [1]. For the main process a temperature dependence of the characteristic time scale clearly different from an Arrhenius law is found, a feature which is also universal for polymers (see, e.g., [2]). It is noteworthy that the temperature behavior of this time is also different from that observed for the time scale associated to the viscosity (see Fig. 18.8). The temperature at which the time scales of the α- and β-relaxation coincide, around 210 K, will be referred to as the merging temperature T_M.

Let us now concentrate on the QENS results related to the α- and β-relaxations of this polymer, which in essence are displayed by Fig. 18.9. In the upper part this figure shows the static structure factor $S(Q)$ at different temperatures. The first peak shifts strongly with temperature, qualifying it as due to interchain correlations, while the second peak hardly changes with temperature. Here covalently connected intrachain correlations dominate. Figure 18.9b presents the coherent intermediate scattering functions measured by spin echo at Q_{max}, the Q-value of the first structure factor peak. They are scaled according to the temperature dependence $\tau_\eta(T)$ set by the viscosity relaxation. Applying this scaling relation all data collapse to a common master curve. Obviously the interchain correlations between adjacent chains decay with the same temperature law as the macroscopic flow. Trying the same scaling with data taken at the second, the

intrachain peak, a strikingly different result (Fig. 18.9c) is found. At that high Q-value the spectra do not assemble to a master curve but keep their identity. Obviously at the first two peaks of $S(Q)$ different dynamics are observed.

Now we consider the temperature dependencies of the characteristic relaxation times found with these experiments. Again we concentrate on the results corresponding to the first and second peak (Fig. 18.10). At the first peak, the characteristic times follow the dashed-dotted line representing the temperature law of the viscosity relaxation – this could already be inferred from the scaling with $\tau_\eta(T)$ – while at the second peak we observe an Arrhenius-like behavior coinciding exactly with that of the dielectric β-relaxation shown in Fig. 18.8.

Qualitatively the experimental results follow the expectation from our considerations on the dynamic structure factor. As a consequence of the $1/S(Q)$

Fig. 18.9. **a** Static structure factor for deuterated PB at different temperatures. **b** Scaling representation of the NSE data at 1.48 Å^{-1} ($\bigcirc$, 280 K; $\bullet$, 260 K; $\square$, 240 K; $\blacksquare$, 230 K; $\diamondsuit$, 220 K). (**c**) The same kind of representation for 2.71 Å^{-1} ($\bigcirc$, 300 K; $\bullet$, 260 K; $\square$, 220 K; $\blacksquare$, 205 K; $\diamondsuit$, 190 K; $\blacklozenge$, 180 K; $\triangle$, 170 K). *Solid lines* correspond to KWW functions (see text). Error bars are shown for all temperatures in b, and only at 170 K and 300 K in c for clarity. From [18]. Copyright (1996) by the American Physical Society)
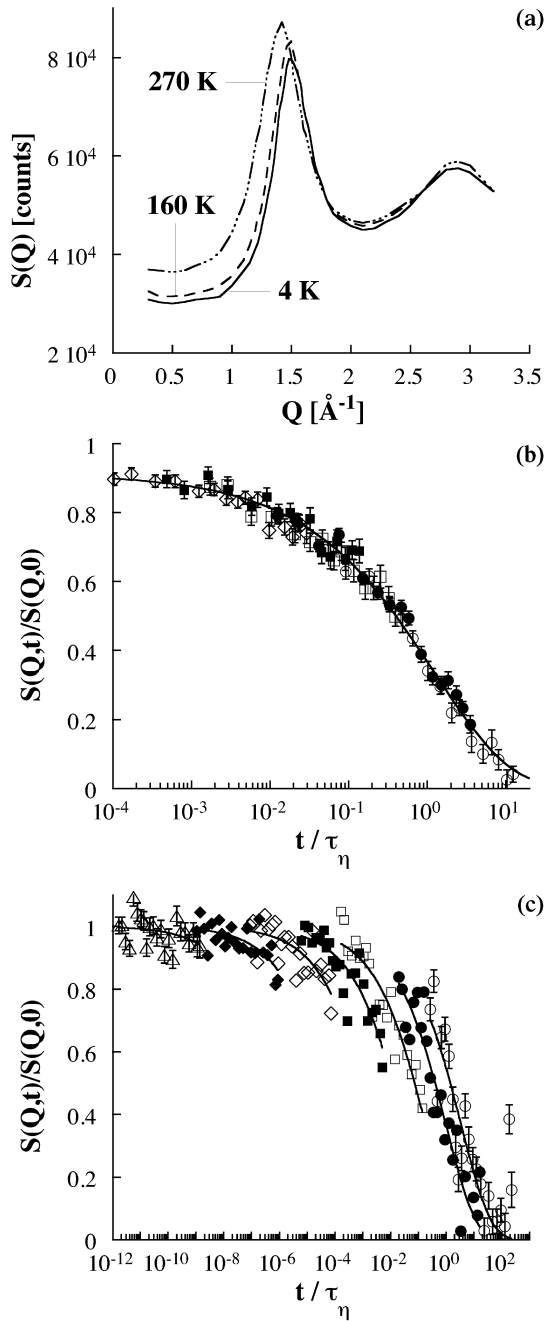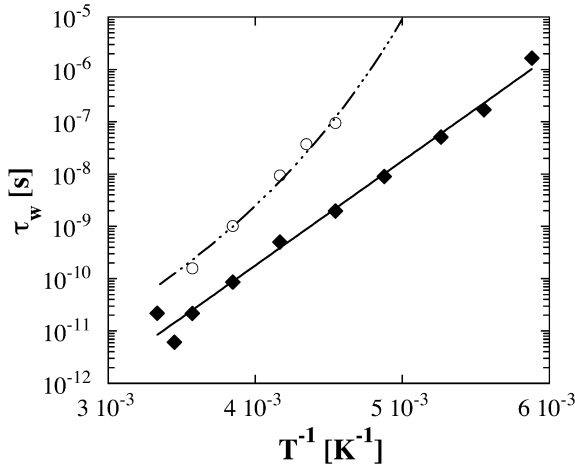
Fig. 18.10. Temperature dependence of the characteristic times τ_w obtained from the fits of $S(Q,t)$ to stretched exponentials with $\beta = 0.41$ at $Q = 1.48$ Å^{-1} (○) and 2.71 Å^{-1} (◆). *Dashed dotted line* corresponds to the Vogel Fulcher-like temperature dependence of the viscosity for $Q = 1.48$ Å^{-1} and the solid line to the Arrhenius-like temperature dependence of the dielectric β-relaxation for $Q = 2.71$ Å^{-1}. From [18]. Copyright (1996) by the American Physical Society)

renormalization following Eq. (18.16) the contributions of the secondary process are strongly suppressed at the position of the first structure factor peak Q_{max}. Therefore at Q_{max} the dynamic structure factor is selective for the diffusive α-relaxation. At higher Q's, (i) S^{inel} becomes stronger ({$1 - [\sin (Qd)]/Qd$} increases!) and (ii) the effect of the renormalization becomes weaker. Here $S(Q,t)/S(Q)$ becomes increasingly sensitive to local jump processes.

18.4.2
Combined Dielectric and Neutron Investigations of the β-Process

The wide frequency range accessible by BDS allows one to characterize the temperature dependence of both the time scale and the spectral shape of the β-relaxation in a very wide temperature interval below T_g, where this relaxation contributes to the dielectric signal well separated from other processes. The dielectric β-relaxation spectra of PB can be well described by assuming a Gaussian distribution of energy barriers $g(E)$ (Eq. 18.14) that translates in the following expressions for the relaxation function in the time domain $\varphi_\beta(t)$ and the response function in the frequency domain $\Phi_\beta^*(\omega)$:

$$\varphi_\beta(t) = \int_0^\infty g(E) \exp\left[- \frac{t}{\tau_o^\beta \exp\left(\dfrac{E}{k_BT}\right)} \right] dE \qquad (18.29)$$

$$\Phi_\beta^*(\omega) = \int\limits_0^\infty g(E)\, \frac{1}{1 + i\omega\tau_o^\beta \exp\left(\dfrac{E}{k_B T}\right)}\, \mathrm{d}E \tag{18.30}$$

For PB we find that the width σ decreases linearly with temperature (σ[eV] = 0.145 − 2.55 × 10^{-4} T [K]). The values of τ_o^β and E_o are determined from the temperature dependence of the position of the maximum of the relaxation, $\tau_{max} = \tau_o^\beta$ exp($E_o/k_B T$) (see Fig. 18.8) and they are τ_o^β = 3.5 × 10^{-17} s and E_o = 0.41 eV.

These results can be used as an input for interpreting the NSE data on PB and to extract further information on the microscopic mechanism beyond the β-process. Below T_M ($\approx$ 210 K) the α-relaxation slows down very rapidly with decreasing temperature and cannot be observed anymore within the window of NSE. Therefore, the analysis of the structure factor in this temperature range applies only to the contribution of the β-process.

The NSE data were fitted to the expression given by Eq. (18.16). The best fit was obtained for a most probable distance d = 1.5 Å, giving rise to the relative quasielastic contribution depicted in Fig. 18.5, and $\tau_o^{NSE} = \tau_o^\beta/205$. With this approach a very good description of all the NSE data at all the temperatures below T_M and at all Q-values investigated is obtained. Figure 18.11 shows an example. The astonishing result that the time scale observed for the relaxation of density fluctuations by NSE is shifted by approximately two orders of magnitude to shorter times with respect to the time scale observed for dipole relaxation is not yet understood. At this point it is worth referring to studies on the pair [16] and self [19] correlation functions of the β-relaxation carried out on polyisobutylene (PIB), also combining QENS and BDS. In that polymer a similar time scale was found for the secondary relaxation as observed by both techniques.

A more realistic modeling of the microscopic mechanism involved in the β-relaxation can be performed by considering the coherent scattering functions corresponding to rotations of the *cis*- and *trans*-units [18]. The conclusions are that the NSE data are compatible with rotational processes of the rigid building blocks of PB around an axis passing through their center of mass. However, the experi-

Fig. 18.11. NSE spectra at 205 K for the Q-values indicated. *Solid lines* are the fitting curves obtained in the incoherent approximation for the inelastic part of the β-process. From [18]. Copyright (1996) by the American Physical Society)
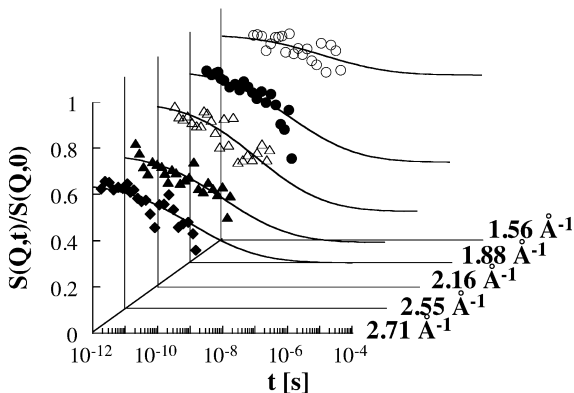
mentally observed Q-dependences lead to more pronounced sharper structures around $Q \approx 3$ Å^{-1} indicating that the scattering in this Q-region may contain interference terms from several building blocks along the chain. Thus reorientational motions involving cooperatively more than one building block are likely.

In summary, the results of this NSE and dielectric study of the β-relaxation suggest that its origin would be the rotational motion of the chain building blocks like *cis*- and *trans*-units within one chain, stressing the intramolecular nature of this process. It is worth noting that in order to facilitate the analysis it was of crucial importance to use the distribution function of the elementary relaxation processes provided by the dielectric results.

18.4.3
α-Process on Polybutadiene

18.4.3.1
Temperature Dependence

The characterization of the β-relaxation contribution to the spectra allows one to find the optimal experimental conditions for isolating the α-process contribution. As already seen, for coherent scattering the β-contribution is almost suppressed in the first maximum of $S(Q)$, and there information on such important features as the shape of the relaxation function or the temperature dependence of the characteristic time scale can be obtained for the pure α-process. The usual procedure for determining the shape of the dynamic structure factor consists of constructing a master curve like that shown in Fig. 18.9b. In this case the shift factors used were fixed by the temperature dependence set by the viscosity relaxation (monomeric friction coefficient), and a nice superposition of the curves corresponding to the different temperatures was obtained. As can be appreciated in Fig. 18.9b, the resulting master curve can be reasonably described by a KWW function with $\beta = 0.41$, which is the value deduced from the fit of the dielectric spectra at temperatures close to T_g, where it can be well determined. A free fit of the NSE data would give a somewhat higher β-value (≈ 0.45) [29]. Thus, it may follow that (i) the shape parameters obtained from both techniques are very close, and (ii) the time-temperature superposition principle holds to a good approximation for PB in a very wide temperature range. However, we note that the temperature dependence of the α-relaxation NSE data coincides with that obtained from viscosity measurements (Figs. 18.9b and 18.10), which differs from the observed behavior for the dielectric loss maxima in the same temperature range, as pointed out before (see Fig. 18.8). This could imply that the dielectric response would be very much influenced by the presence of the secondary relaxation – BDS observes the so called $\alpha\beta$-process.

18.4.3.2
Q-Dependence

The incoherent scattering function, on the other hand, is expected to correspond to a large amount to the α-relaxation at low enough Q-values where the inelastic contribution of the β-relaxation is negligible, i.e., approximately for $Q < 1$ Å^{-1} (see Fig. 18.4). Figure 18.12 shows incoherent spectra corresponding to a protonated PB sample at 280 K. A broadening with respect to the instrumental resolution is visible that increases with increasing Q. This kind of behavior is expected for diffusive processes, because the broadening of the quasielastic peak is directly related to the time scale of the dynamics taking place: the faster the dynamics the broader the spectrum becomes. Taking advantage of previous knowledge about the functional form of the α-relaxation, the spectra were fitted to the Fourier transforms of KWW functions with $\beta = 0.41$ and free time scale. The resulting fitting curves are shown in Fig. 18.12 as solid lines. The Q-dependence of the relaxation times obtained is much stronger than that expected for regular diffusion, as evidenced in Fig. 18.13, and can be well described by the law predicted in the case of anomalous diffusion in the Gaussian approximation (Eq. 18.24). This behavior has been found in a large series of polymers [25–27]. It seems then that, at least in the mesoscopic time scale covered by neutron scattering techniques, the apparent stretching of the α-relaxation function in glass forming polymers relates dominantly to sublinear diffusion and is not a result of a superposition of single exponential processes – this scenario would lead to a dependence on Q^{-2} of the time scale [27] which is not observed at least in the Q-range covered by the experiments carried out up to now.
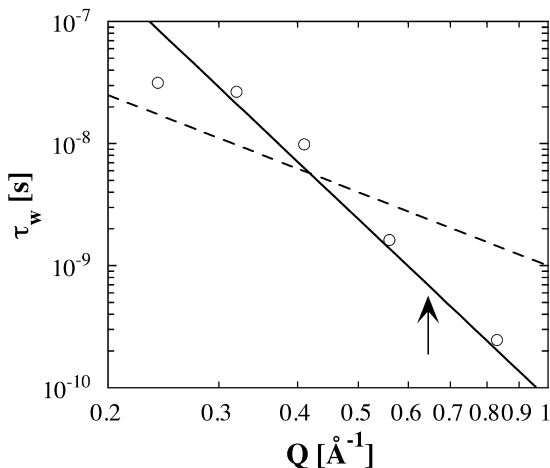
Fig. 18.13. Q-dependence of the KWW characteristic time of the α-relaxation obtained from the incoherent scattering function measured at 280 K by the BSS in Jülich. The *solid line* represents the Q-dependence expected in the Gaussian approximation (Eq. 18.24). *Dashed line* shows a Q^{-2} law. The *arrow* indicates the Q-value at which the characteristic time observed for the α-relaxation by dielectric spectroscopy matches the time scale obtained by QENS

18.4.3.3
Merging of α- and β-Processes

At temperatures close to the merging temperature T_M, the characteristic relaxation times of the primary α-relaxation reach similar orders of magnitude as that of the local β-relaxation. Therefore the description of the dynamic structure factor at any Q has to be generalized including both processes. The β-process has been successfully described as a local intrachain relaxation process that takes place within the fixed environment set by the other chains. When the segmental diffusion reaches the time scale of the local relaxation, given atoms and molecular groups will noticeably participate simultaneously in both motional mechanisms. Under the hypothesis that to first order both mechanisms are statistically independent from each other, the coherent dynamic structure factor $S^{\alpha\beta}(Q,t)$ can be expressed by Eq. (18.28). In this equation, $S^{\beta}(Q,t)$ is known from the study performed on the NSE data below T_M, and the values of the parameters involved can be extrapolated to higher temperatures. For the other function, $S^{\alpha}_{inc}(Q,t)$, also the spectral shape (KWW with $\beta = 0.41$) and the temperature dependence of the characteristic times ($\approx \tau_\eta(T)$) are known. The Q-dependence of this time scale would in principle be given by that shown by the incoherent times, but taking into account that the scenario used involves a number of assumptions, this dependence was obtained from the fitting of the NSE curves to the theoretical function. It is worth noting that the only free parameters in the fitting procedure are this Q-dependence and amplitude factors which give account for faster processes like phonons, which are not visible in the NSE window but contribute

Fig. 18.14. NSE spectra for the Q-values indicated at 220 K (▲), 240 K (△), 260 K (◆), and 280 K (◇). *Solid lines* are fitting curves (see text). From [18]. Copyright (1996) by the American Physical Society)
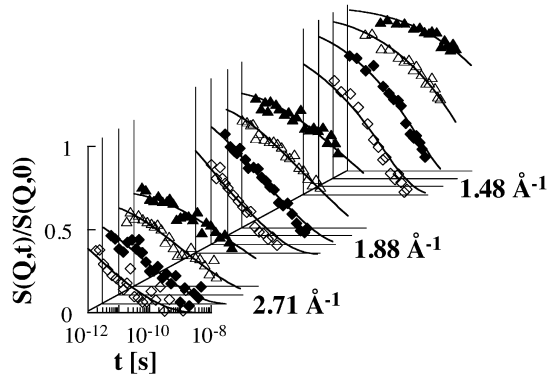
to the total amplitude. Figure 18.14 shows resulting fit curves for several temperatures at the first maximum, minimum, and second maximum of $S(Q)$. The excellent agreement between the model scattering function and the experiment strongly supports the hypothesis that the α- and β-relaxations behave independently of each other. The small deviations of the curves at 280 K for 1.48 Å^{-1} and 1.88 Å^{-1} could be related to a possible small increase of the shape parameter β of the α-relaxation at high temperatures.

The Q-dependence of τ_w is shown in Fig. 18.15. As commented before, a modulation of the characteristic time with $S(Q)$ could be expected in the coherent case. This modulation is not found in the obtained time scale, but it follows a power law in Q, as in the incoherent case. This result supports in some way the consistency of the used Vineyard approximation for the α-process which is based on the incoherent dynamic structure factor. As compared to the incoherent times – or to their extrapolation to the Q-range where the NSE have been obtained, however, a slightly weaker Q-dependence and lower absolute values are found. It is also worth pointing out that the absence of modulation could be due to the poor Q-resolution of these NSE measurements. Recent investigations carried out on PIB, which exhibits a sharper structure factor, with better Q-resolution [30] show a clear feature on the characteristic times that reminds $S(Q)$.

Within the experimental accuracy the coherent Q-dependent dynamic structure factor in the $\alpha\beta$-relaxation regime of PB can be consistently described under the assumption that both processes are statistically independent. This observation based on the Q- and temperature dependence of $S^{\alpha\beta}(Q,t)$ opens also a new approach for a better understanding of results from BDS on polymers.

18.4.3.3.1
Application to Dielectric Results

Dielectric data on glass-forming polymers are usually analyzed under the assumption that the total dielectric response can be obtained from the addition of the contributions of α- and β-relaxations. This seems to give a good description of the experimental data when both processes are well separated, i.e., well below
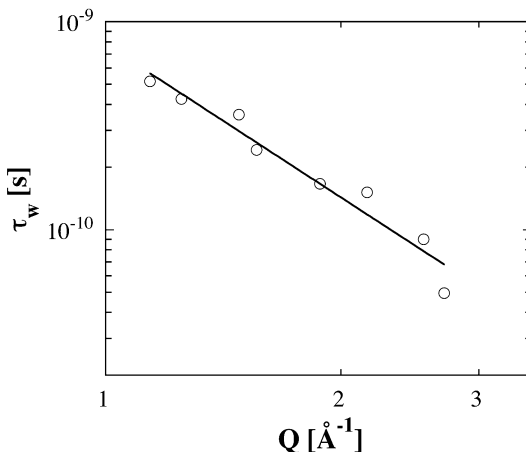
the merging. However, close or above this range it is not possible to describe consistently the total process as the addition of the two relaxations as extrapolated from the low temperature region, but some change in the mechanisms has to be invoked [31–33]. On the other hand, if a neutron experiment addressing the dynamics on a molecular level in space and time is very well compatible with a statistical independence of these processes, then this observation must imply that such an independence must be at the basis of an interpretation of results from other experimental techniques as well. This kind of approach was in fact proposed by G. Williams a long time ago [34] for the dielectric response and only recently has been quantitatively tested [18, 31–33, 35]. As for the density fluctuations which are seen by the neutrons, it is assumed that the polarization is partially relaxed via local motions, which conform the β-relaxation. While the dipoles are participating in these motions, they are surrounded by temporary local environments. The brake of these local environments is what we call α-process, and causes the subsequently total relaxation of the polarization. Note that as the atoms in the density fluctuations all dipoles participate at the same time in both relaxation processes. Similar to the dynamic structure factor $S^{\alpha\beta}(Q, t)$ (Eq. 18.28) the relaxation function $\varphi(t)$ corresponding to these two independent processes α, β, can be expressed as

$$\varphi(t) = f_\alpha \, \varphi_\alpha(t) + (1 - f_\alpha) \, \varphi_\alpha(t) \, \varphi_\beta(t) \qquad (18.31)$$

where f_α is the relative strength factor for the α-process, and $\varphi_\alpha(t)$, $\varphi_\beta(t)$ are the relaxation functions corresponding to the α- and β-processes. These are normalized functions, i.e., $\varphi_{\alpha(\beta)}(t = 0) = 1$, $\varphi_{\alpha(\beta)}(t = \infty) = 0$. It is noteworthy that Eq. (18.31) has the same form as $S^{\alpha\beta}(Q, t)$. However, while the neutron experiment occurs on the length scale of the α-relaxation leading to a dispersive *Q*-dependent characteristic time, BDS observes the effect of the different relaxation modes on a local probe – the dipole. Therefore the prefactors in Eq. (18.31), which in the case of neutrons relate to particular Fourier transformed density-density correlations observed on

their natural scale, also have a different meaning, f_α being the relative fraction of the polarization relaxed only by the α-relaxation.

In order to apply the approach described above to the experimental data, first the functional forms of $\varphi_\alpha(t)$ and $\varphi_\beta(t)$ have to be determined. Note that, if the time scales of the relaxation processes are well separated, $\varphi_\alpha(t)$ does not begin to decay until $\varphi_\beta(t)$ has completely vanished; $\varphi(t)$ decays in two stages and Eq. (18.31) can be approximated by

$$\varphi(t) \approx f_\alpha \varphi_\alpha(t) + (1 - f_\alpha) \varphi_\beta(t) \tag{18.32}$$

$$\frac{\varepsilon^*(\omega) - \varepsilon_\infty}{\varepsilon_s - \varepsilon_\infty} = \Phi^*(\omega) = f_\alpha \Phi_\alpha^*(\omega) + (1 - f_\alpha) \Phi_\beta^*(\omega) \tag{18.33}$$

i.e., under this condition we recover the usual description in terms of the addition of both contributions. Therefore, the functional forms of $\varphi_\alpha(t)$ and $\varphi_\beta(t)$ can be obtained from the usual analysis of the low temperature region spectra, where the time scale of the α-process is much slower than that of the β-process.

The characterization of the relaxation function of the β-relaxation has already been described in Sect. 18.4.2 (Eqs. 18.29 and 18.30). For the α-process we have mentioned in advance that $\varphi_\alpha(t)$ corresponds to a KWW function with $\beta \approx$ 0.41 in this temperature range. As the KWW function does not have an analytical Laplace transform, in practice, the procedure followed was based on the results presented in [36, 37]. In those works it was shown that the Laplace transform of KWW functions can be well described by Havriliak-Negami (HN) [38] functions

$$\Phi_\alpha^*(\omega) = \frac{1}{[1 + (i\omega \tau_{HN})^\alpha]^\gamma} \tag{18.34}$$

if their shape parameters α and γ fulfill certain relationships. In this expression τ_{HN} is the characteristic time. One should then restrict oneself to the HN-family functions which describe well the Laplace transform of KWW functions. In these cases, the relationships between HN- and KWW-shape parameters and their characteristic times are [36]

$$\alpha\gamma = \beta^{1.23} \tag{18.35}$$

$$\log_{10}\left(\frac{\tau_{HN}}{\tau_w}\right) = 2.6(1 - \beta)^{0.5} \exp(-3\beta) \tag{18.36}$$

The PB spectra were thus analyzed using Eq. (18.33) with the above described functions in the temperature range between T_g and $T_g + 22$ K, where it can be considered that the time scales of α- and β-relaxations are sufficiently separated (see Fig. 18.7). The values of the shape parameter β obtained lie around a mean value of $\beta = 0.41$ (corresponding HN shape parameters: $\alpha = 0.72$, $\gamma = 0.50$). If

the data were analyzed at higher temperatures also with this „addition ansatz" (Eq. 18.33), the following behavior would have been observed for the response function of the "secondary relaxation": (i) a strong asymmetrization of the spectral shape and (ii) a shift of the characteristic time scale towards faster times with respect to the values extrapolated from the low temperature range. This shift would increase with increasing temperature.

In order to analyze the experimental data at higher temperatures in the frame of the "Williams ansatz", it is useful to rewrite Eq. (18.31) as

$$\varphi(t) = f_\alpha \varphi_\alpha(t) + (1 - f_\alpha) \varphi_{\beta\,\mathrm{eff}}(t) \tag{18.37}$$

Here, we are introducing the concept of the relaxation function of the "effective β-relaxation", $\varphi_{\beta\,\mathrm{eff}}(t)$, given by the product $\varphi_\alpha(t)\varphi_\beta(t)$. The approach shown in Eq. (18.37) has the advantage that the total relaxation function is still given by the addition of two contributions, one corresponding to the α-relaxation, and the other by this "effective β-relaxation". The latter includes the modifications of the β-relaxation by the presence of the α-relaxation. In the following we will show how the response function corresponding to this relaxation can be constructed. The starting point is to know the distribution of relaxation times $g_\alpha(\ln \tau)$ and $g_\beta(\ln \tau)$ in terms of which the α- and β-processes can – at least formally – be decomposed:

$$\varphi_{\alpha(\beta)}(t) = \int\limits_{-\infty}^{+\infty} g_{\alpha(\beta)}(\ln\tau) \exp\left(-\frac{t}{\tau}\right) d(\ln\tau) \tag{18.38}$$

It is straightforward to deduce $g_\beta(\ln \tau)$ from the distribution of energy barrier heights $g(E)$ given in Eq. (18.14):

$$g_\beta(\ln\tau) = \frac{k_B T}{\sqrt{\pi}\sigma} \exp\left\{ -\left[\frac{k_B T \ln\left(\dfrac{\tau}{\tau_o^\beta}\right) - E_o}{\sigma} \right]^2 \right\} \tag{18.39}$$

In the case of the α-relaxation, the distribution function can be obtained in different ways, such as using the algorithm proposed by Imanishi, Adachi and Kotaka [39], or the distribution function reproducing the corresponding HN-function [40], or an approximated expression like that used in [33].

Once $g_\alpha(\ln \tau)$ and $g_\beta(\ln \tau)$ are determined, the relaxation function $\varphi_{\beta\,\mathrm{eff}}(t)$ can be calculated as

$$\varphi_{\beta\,\mathrm{eff}}(t) = \varphi_\alpha(t)\varphi_\beta(t) = \int\limits_{-\infty}^{+\infty} g_\alpha(\ln\tau)\exp\left(-\frac{t}{\tau}\right)d(\ln\tau) \int\limits_{-\infty}^{+\infty} g_\beta(\ln\tau')\exp\left(-\frac{t}{\tau'}\right)d(\ln\tau')$$

$$= \int\limits_{-\infty}^{+\infty} g_\alpha(\ln\tau)\left\{ \int\limits_{-\infty}^{+\infty} g_\beta(\ln\tau')\exp\left[-t\left(\frac{1}{\tau'}+\frac{1}{\tau}\right)\right]d(\ln\tau') \right\} d(\ln\tau) \tag{18.40}$$

and, taking into account the properties of the Laplace transformation, $\Phi^*_{\beta\,\text{eff}}(\omega)$ is given by

$$\Phi^*_{\beta\,\text{eff}}(\omega) = \int\limits_{-\infty}^{+\infty} g_\alpha(\ln\tau)\left\{\int\limits_{-\infty}^{+\infty} g_\beta(\ln\tau')\,\frac{1}{1+i\omega\left(\dfrac{1}{\tau'}+\dfrac{1}{\tau}\right)^{-1}}\,\mathrm{d}(\ln\tau')\right\}\mathrm{d}(\ln\tau) \quad (18.41)$$

Then, the function $\Phi^*_{\beta\,\text{eff}}(\omega)$ can be calculated by integration, avoiding any kind of Laplace transformation. PB data were fitted within this framework. Note that except for the values of the characteristic time of the α-relaxation, τ_w, and the relaxed fraction in the α-relaxation, f_α, which were left as free parameters in the fitting procedure, all the parameters were extrapolated from the low to the high temperature regime. We found a very good description of the data by this procedure, as can be seen in Fig. 18.7, for the whole range of temperatures investigated. Moreover, a very interesting result concerning the time scale of the α-relaxation, τ_w, arises from this analysis: its temperature behavior at high temperatures follows very nicely the temperature behavior of the time scale associated to the viscosity (see the behavior of τ_{HN}, which is proportional to τ_w (β is a constant) in Fig. 18.16). This is a non-trivial result which emerges naturally from the description made and supports the consistency of the analysis of the data, if we take into account that the same temperature dependence has been found for the characteristic time scale of the α-relaxation as observed by NSE.

The meaning of the effective β-relaxation introduced can be understood if we follow its development with temperature. Close to T_g, $\Phi^*_{\beta\,\text{eff}}$ and Φ^*_β are almost indistinguishable. However, as the temperature increases and the time scales of the primary and secondary relaxations become closer, significant differences appear concerning both the shape and the frequency of the maximum of these functions. $\Phi''_{\beta\,\text{eff}}$ becomes asymmetric and its characteristic time scale shifts towards higher frequencies with the proximity of the α-relaxation. Thus the β-like processes with characteristic times slower than the average relaxation time of the α-relaxation do not contribute any more to the relaxation of the polarization. This means that the dipoles whose local environment relaxes before the local dynamics takes place, relax through the α-relaxation. The higher the temperature, the more similar becomes the shape of the relaxation function of the effective β-relaxation to that of the α-relaxation, though it is shifted towards higher frequencies. The behavior found in this framework proposed by Williams for $\Phi''_{\beta\,\text{eff}}$ coincides with that observed for the contribution that is added to the α-relaxation in the frame of the addition ansatz. Therefore, the deviations observed with the addition ansatz for the behavior of the secondary relaxation with respect to that extrapolated from low temperatures find a natural explanation in the scenario here proposed.

Concerning the relative contributions of the α- and effective β-relaxations, the insert in Fig. 18.16 shows the results obtained for the relative fraction relaxed only by the α-relaxation, f_α. Close to T_g, the α-relaxation alone plays the most important role. f_α decreases then with increasing temperature, being small at tem-
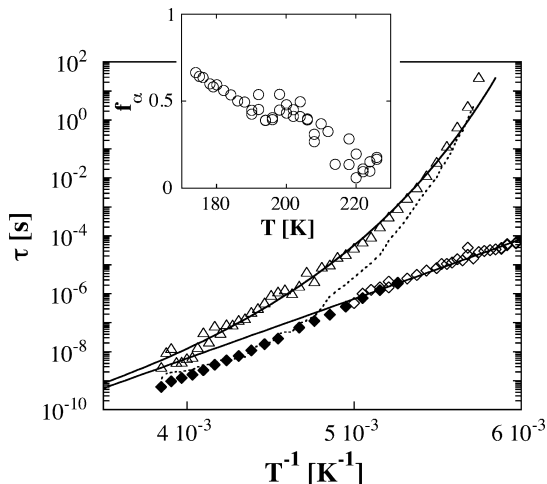
Fig. 18.16. Temperature dependence of the dielectric characteristic times obtained by the fitting procedure explained in the text: τ_{HN} ($\triangle$), τ_{max}^{β} ($\diamond$), and $\tau_{max}^{\beta\,eff}$ ($\blacklozenge$). The Arrhenius law shows the extrapolation of the temperature behavior of the β-relaxation. The solid line through τ_{HN} points shows the temperature behavior of the time scale associated to the viscosity. The dotted line corresponds to the temperature dependence of the characteristic time scales for the main relaxation process. Insert: Temperature dependence of the dipole component relaxed by the α-relaxation (A. Arbe, D. Richter, J. Colmenero and B. Farago, Phys. Rev. E 54 (1996) 3853–3869. Copyright (1996) by the American Physical Society)

peratures close to the merging, and in the merging region almost all the relaxation of the polarization is due to the other mechanism (local processes together with the α-relaxation). Therefore, in this range the temperature dependence of the total process follows the temperature dependence of the effective β-relaxation, as is shown in Fig. 18.16. There we have plotted the inverse of the frequencies of the maxima of $\Phi''_{\beta\,eff}$ for several temperatures. It is evident that when f_α reaches small values, the maxima of the total process coincide with that of $\Phi''_{\beta\,eff}$. In this way, we have found a simple explanation for the apparently different temperature dependencies observed for the relaxation of the dipoles and the viscosity (see Fig. 18.8).

It is finally noteworthy that the description found for the elementary process beyond the secondary relaxation from the NSE evaluation is compatible with the dielectric results. Rotations of the *cis*-unit of about 60–120°, as deduced from those results, would allow the polarization to relax to a large extent, leaving a small fraction to be relaxed only via the pure α-(segmental) process. In connection with this result, we would like to mention that from a theoretical point of view, the convolution ansatz proposed is supported by the results obtained in the framework of a free-energy landscape model for the dynamics of glass-forming systems, when a slow secondary relaxation is considered [41]. In this model the β-relaxation is attributed to restricted angular fluctuations, modeled by a superposition of simple two-site angular jumps within a cone, whereas the α-re-

laxation occurs via isotropic tumbling of the jump axis. Hence Eq. (18.31) allows a rather good description of the relaxation behavior in the merging region in the general case, and gives the exact solution for the particular case in which the two mechanisms are totally uncorrelated. The results obtained on PB would thus support this free-energy landscape approach.

In this example of PB we have shown the potential of the combination of BDS and QENS techniques in order to investigate the dynamical processes in glass-forming polymers. PB is perhaps one of the polymers better investigated in this way. However, cases like poly(vinyl methylether) PVME [12], polyisoprene PI [13, 20], poly(vinyl chloride) PVC [15], polyisobutylene PIB [16, 19], and poly(vinyl ethylene) PVE [20] can also be referred to as subjects of combined investigations of these two techniques (or even more, like PVME in [12], where also NMR, light scattering, and mechanical data are brought together). It is important to point out however that the study on PB here summarized opened a new way for understanding dielectric results on polymer systems at high temperatures because it provided a microscopic interpretation of the merging process of the α- and β-relaxations as statistically independent processes. Dielectric results of a series of polymers and glass forming systems have been successfully interpreted over the last years in the framework of this scenario. Moreover, the combination of QENS and BDS methods is currently being extended to investigate dynamics in polymer blends [20, 42, 43].

18.5
Conclusions

The complexity richness of the dynamical behavior of glass-forming polymers demands the combination of several experimental techniques in order to achieve a full characterization of the different dynamical processes and their possible interconnections. Broadband dielectric spectroscopy and quasielastic neutron scattering turn out to be very useful complementary techniques for such an investigation. While BDS can cover a huge dynamic range over more than 15 decades in time or frequency, QENS is the only technique giving spatial/time resolution, though in a rather narrow dynamic range. An unavoidable consequence of combining techniques assessing different correlators is that difficulties may arise when both kinds of results are analyzed and interpreted. While BDS observes the dielectric permittivity, which reflects the orientational dynamics of the molecular dipoles in the sample, QENS techniques have access either to the density-density correlation function (coherent scattering) or to the self correlation of the atoms (incoherent scattering), providing spatial information on the dynamical processes under study. Therefore, in principle, different results should be expected when a given relaxation process is observed either indirectly by BDS of directly by QENS. However, both sets of measurements should mirror the same physics. Using the combination of these techniques a huge frequency-temperature range can be covered, allowing one to study, e.g., the main dynamical processes in polymer systems – the primary and secondary relaxations – in the macro- and mesoscopic time scales. Precise information on the temperature dependence of the characteristic times and the spectral shape of

the relaxations can be obtained from BDS. This knowledge may allow one to perform an accurate analysis of the QENS results, which contain valuable spatial information necessary for a molecular understanding of the dynamical processes taking place in the system. The potential of the combination of these techniques has been exemplified in this chapter with the study of 1,4-polybutadiene dynamics.

List of Abbreviations and Symbols

A	T-dependent contribution to the relaxation time
b_j	Scattering length of the isotope j
d	Jump distance
D	Diffusion constant
E	Activation energy
E_o	Average value of the activation energy
f_α	Relative strength factor for the α-process
g	Kirkwood correlation factor
$g(E)$	Energy barriers distribution function
$g(\ln\tau)$	Relaxation time distribution function
$Gs(\boldsymbol{r},t)$	Self part of the van Hove correlation function
H,H'	Guide magnetic fields
k_B	Boltzmann constant
$\boldsymbol{k}_i(\boldsymbol{k}_f)$	Initial (final) wave vectors of the neutron
L	Distance between the sample and the detector
m	Neutron mass
$\boldsymbol{M}_1(t)$	Sum of the permanent moments of the molecules in a sphere of macroscopic dimensions around a molecule
N	Number of atoms in the system
$P_i(P_f)$	Initial (final) polarization of the neutron beam
Q_{max}	Position of the first static structure factor peak
$\boldsymbol{r}_j(t)$	Position vector of the atom j at time t
$S(Q)$	Static structure factor
$S(\boldsymbol{Q},t)$	Dynamic structure factor
$S_{\mathrm{inc}}(\boldsymbol{Q},t)$	Incoherent dynamic structure factor
$S(\boldsymbol{Q},\omega)$	Coherent dynamic structure factor
$S_{\mathrm{inc}}(\boldsymbol{Q},\omega)$	Incoherent scattering function
S^{inel}	Inelastic contribution to the dynamic structure factor
t	Time
T	Temperature
T_g	Glass transition temperature
T_M	Merging temperature
$v_i(v_f)$	Initial (final) neutron velocity
$\langle[\boldsymbol{r}_j(t)-\boldsymbol{r}_j(0)]^2\rangle$	Thermally averaged mean square displacement of atom i with respect to atom j
$\langle r^2(t)\rangle$	Average mean squared displacement of a single atom

$\hbar$	Planck constant h/2π
$\hbar \boldsymbol{Q}$	Momentum transfer
$\hbar \omega$	Energy change
α, β, or $\alpha\beta$ (subscripts/ superscripts)	Corresponding to the α-, β-, $\alpha\beta$-process
α, γ	HN shape parameters
β	KWW stretching exponent
$\partial^2 \sigma / \partial \Omega \, \partial \hbar \omega$	Double differential cross section
$\varepsilon^*(\omega) = \varepsilon'(\omega) - i\varepsilon''(\omega)$	Complex dielectric permittivity
ε_s	Static value of the permittivity
ε_∞	High frequency limit value of the permittivity
$\Delta\varepsilon = \varepsilon_s - \varepsilon_\infty$	Relaxation strength
ϕ	Phase angle
$\varphi(t)$	Relaxation function
$\lambda(\lambda_o)$	Wavelength of the (incoming) neutrons
$\boldsymbol{\mu}_i(t)$	Dipole moment of the molecule i
2θ	Scattering angle
$\sigma(T)$	Width of a distribution function
$\tau(E)$	Jump time corresponding to an activation energy E
$\tau_\eta(T)$	Characteristic time for viscosity relaxation
τ_o^β	Prefactor in the Arrhenius law for the characteristic time
τ_D^{inc} (τ_D^{coh})	Characteristic time for incoherent (coherent) scattering in a diffusive process
τ_{max}	Inverse of the frequency corresponding to the maximum of the relaxation
τ_w^{inc}	Characteristic time for incoherent scattering in an anomalous diffusive process
τ_w	KWW relaxation time
$\Phi^*(\omega) = \Phi'(\omega) - i\Phi''(\omega)$	Response function
BDS	Broadband dielectric spectroscopy
HN	Havriliak-Negami
ILL	Institute Laue-Langevin
KWW	Kohlrausch-Williams-Watts
NS	Neutron scattering
NSE	Neutron spin echo
PB	Polybutadiene
PI	Polyisoprene
PIB	Polyisobutylene
PVE	Poly(vinyl ethylene)
PVC	Poly(vinyl chloride)
PVME	Poly(vinyl methylether)
QENS	Quasielastic neutron scattering

References

1. McCrum NG, Read BE, Williams G (1967) Anelastic and dielectric effects in polymer solids. Wiley, London
2. Dianoux AJ, Petry W, Richter D (eds) (1993) Dynamics on disordered materials II. North-Holland, Amsterdam
3. Johari GP, Goldstein M (1970) J Chem Phys 53:2372
4. Götze W (1991) In: Hansen JP, Levesque D, Zinn-Justin J (eds) Liquids, freezing and the glass transition. North-Holland, Amsterdam
5. Kohlrausch F (1863) Pogg Ann Phys 119:352; Williams G, Watts DC (1970) Trans Faraday Soc 66:80
6. Lovesey SW (1987) Adair RK, Marshall W, Rees M, Elliott RJ, Wilkinson DH, Ehrenreich H (eds) Theory of neutron scattering from condensed matter. Clarendon Press, Oxford
7. Bée M (1988) Quasielastic neutron scattering. Adam Hilger, Bristol
8. Mezei F (ed) (1980) Neutron spin echo lecture notes in physics, vol. 128. Springer, Berlin Heidelberg New York
9. Alegría A, Colmenero J, Mari PO, Campbell IA (1999) Phys Rev E 59:6888
10. Alegría A, Goitiandía L, Tellería I, Colmenero J (1998) Recent Res Dev Macromol Res 3:49
11. Bötcher CJF, Bordewijk P (1980) Theory of electric polarization. Elsevier, Amsterdam
12. Colmenero J, Alegría A, Alberdi JM, Alvarez F, Frick B (1991) Phys Rev B 44:7321
13. Zorn R, Richter D, Farago B, Frick B, Kremer F, Kirst U, Fetters LJ (1992) Physica B 180–181:534
14. Colmenero J (1993) Physica A 201:38
15. Colmenero J, Arbe A, Alegría A (1994) J Non-Crystalline Solids 172–174:126
16. Richter D, Arbe A, Colmenero J, Monkenbusch M, Farago B, Faust R (1998) Macromolecules 31:1133
17. Arbe A, Buchenau U, Willner L, Richter D, Farago B, Colmenero J (1996) Phys Rev Lett 76:1872
18. Arbe A, Richter D, Colmenero J, Farago B (1996) Phys Rev E 54:3853
19. Arbe A, Colmenero J, Frick B, Monkenbusch M, Richter D (1998) Macromolecules 31:4926
20. Arbe A, Alegría A, Colmenero J, Hoffmann S, Willner L, Richter D (1999) Macromolecules 32:7572
21. Springer T (1972) In: Höhler G (ed) Quasielastic neutron scattering for the investigation of diffusive motions in solids and liquids. Springer, Berlin Heidelberg New York
22. de Gennes PG (1959) Physica 25:825
23. Vineyard G (1959) Phys Rev 110:999
24. Sköld K (1967) Phys Rev Lett 19:1023
25. Colmenero J, Alegría A, Arbe A, Frick B (1992) Phys Rev Lett 69:478
26. Colmenero J, Arbe A, Alegría A, Ngai KL (1994) J Non-Cryst Solids 172–174:229
27. Arbe A, Colmenero J, Monkenbusch M, Richter D (1998) Phys Rev Lett 81:590
28. Frick B, Richter D, Ritter Cl (1989) Europhys Lett 9:557
29. Richter D, Frick B, Farago B (1988) Phys Rev Lett 61:2465
30. Richter D, Monkenbusch M, Allgeier J, Arbe A, Colmenero J, Farago B, Cheol Bae Y, Faust R (1999) J Chem Phys 111:6107
31. Bergman R, Alvarez F, Alegría A, Colmenero J (1998) J Chem Phys 109:7546
32. Arbe A, Colmenero J, Gómez D, Richter D, Farago B (1999) Phys Rev E 60:1103
33. Gómez D, Alegría A, Arbe A, Colmenero J (2001) Macromolecules 34:503
34. Williams G (1979) Adv Polym Sci 33:60
35. Alvarez F, Hofmann A, Alegría A, Colmenero J (1996) J Chem Phys 105:432
36. Alvarez F, Alegría A, Colmenero J (1991) Phys Rev B 44:7306
37. Alvarez F, Alegría A, Colmenero J (1993) Phys Rev B 47:125
38. Havriliak S, Negami S (1967) Polymer 8:161

39. Imanishi Y, Adachi K, Kotaka T (1988) J Chem Phys 89:7593
40. Zorn R (1999) J Polym Sci B 37:1043
41. Diezemann G, Mohanty U, Oppenheim I (1999) Phys Rev E 59:2067
42. Cendoya I, Alegría A, Alberdi JM, Colmenero J, Grimm H, Richter D, Frick B (1999) Macromolecules 32:4065
43. Hoffmann S, Willner L, Richter D, Arbe A, Colmenero J, Farago B (2000) Phys Rev Lett 85:772

For Further Reading

Debye P (1925) In: Handbuch der Radiologie. Theorie der Elektrischen und Magnetischen Molekulareigenschaften. Akademische Verlagsgesellschaft mbH, Leipzig, p 597–781

Debye P (1929) Polare Molekeln. Verlag S. Hirzel, Leipzig

Debye P (1929) Polar molecules. Chemical Catalog Company, Inc, New York

Smyth CP (1931) Dielectric constant and molecular structure. Chemical Catalog Company, Inc, New York

Fröhlich H (1949) Theory of dielectrics. Clarendon Press, Oxford

Böttcher CJF (1952) Theory of electric polarisation. Elsevier Publishing Company, Amsterdam

von Hippel AR (1954) Dielectric and waves. John Wiley & Sons, New York, Chapman & Hall, London

von Hippel AR (ed) (1954) Dielectric materials and applications. John Wiley & Sons, New York, Chapman & Hall, London

Cable JW (1954) Induction and dielectric heating. Reinhold Publishing Corporation, New York

Smith JW (1955) Electric dipole moments, Butterworths, London

Smyth CP (1955) Dielectric behaviour and structure. McGraw-Hill Book Company, Inc, New York, Toronto, London

Fröhlich H (1958) Theory of dielectrics. Clarendon Press, Oxford, 2nd edition

Birks JB (1960) Modern dielectric materials. Heywood and Company, London

McCrum NG, Read BE, Williams G (1967) Anelastic and dielectric effects in polymeric solids. Wiley & Sons, New York, reprinted 1991 by Dover Publ, New York

Fyraud L (1967) Diélectriques solides anisotropes et ferroélectricité. Gauthier-Villars, Paris

Hill NE, Vaughan WE, Price AH, Davies M (1969) Dielectric properties and molecular behaviour. Van Nostrand Reinhold Company, London, New York, Toronto, Melbourne

Falkenhagen H (1971) Theorie der Elektrolyte. Hirzel Verlag, Leipzig

Karasz FE (ed) (1972) Dielectric properties of polymers. Plenum Press, NY

Böttcher CJF, van Belle OC, Bordewijk P, Rip A (1973) Theory of electric polarization. Vol I: Dielectric in static fields. Elsevier Scientific Publishing Company, Amsterdam, London, New York

Chamberlain J, Chantry GW (eds) (1989) High frequency dielectric measurement. IPC Science and Technology Press Ltd, 1973

van Turnhout J (1975) Thermally stimulated discharge of polymer electrets. Elsevier Scientific Publishing Company, Amsterdam, Oxford, New York

Hedvig P (1977) Dielectric spectroscopy of polymers. Adam Hilger, Bristol

Böttcher CJF, Bordewijk P (1978) Theory of electric polarization. Vol II: Dielectrics in time-dependent fields. Elsevier Scientific Publishing Company, Amsterdam, Oxford, New York

Grant EH, Sheppard RJ, South GP (1978) Dielectric behaviour of biological molecules in solution. Clarendon Press, Oxford

Blythe AR (1979) Electrical properties of polymers, Cambridge University, Cambridge

Pethig R (1979) Dielectric and electronic properties of biological materials. John Wiley & Sons, Chichester, New York, Brisbane, Toronto

Blythe AR (1980) Electrical properties of polymers. Cambridge University Press, Cambridge

Jonscher AK (1983) Dielectric relaxation in solids. Chelsea Dielectric Press, London

Agranovich VM, Maradudin AA (eds) (1989) The dielectric function of condensed systems. Elsevier Science Publishers, Amsterdam

Böttger H, Bryskin VV (1985) Hopping conduction in solids, VCH, Weinheim

Macdonald JR (1987) Impedance spectroscopy. John Wiley & Sons, New York, Chichester, Brisbane, Toronto, Singapure

Myers DF (1988) Dielectric spectroscopy of colloidal suspensions. Princeton University, Ann Arbor, MI

Takashima S (1989) Electrical properties of biopolymers and membranes. Adam Hilger, Bristol, Philadelphia

Riande E, Saiz E (1992) Dipole moments and birefringence of polymers. Prentice Hall, Englewood Cliffs, New Jersey

Böttcher CJF (1993) Theory of electric polarization. Elsevier, Amsterdam, Vol 1, Dielectrics in static fields (2nd revised edition)

Böttcher CJF (1996) Theory of electric polarization. Elsevier, Amsterdam, Vol 2, Dielectrics in time-dependent fields (2nd revised edition)

Craig DQM (1995) Dielectric analysis of pharmaceutical systems. Taylor & Francis, London

Jonscher AK (1996) Universal relaxation law. Chelsea Dielectric Press, London

Grigas J (1996) Microwave dielectric spectroscopy of ferroelectrics and related materials. Gordon and Breach Publishers, Australia, China, France, Germany, India, Japan, etc.

Runt JP, Fitzgerald JJ (eds) (1997) Dielectric spectroscopy of polymeric materials. American Chemical Society, Washington

Havriliak S, Havriliak SJ (1997) Dielectric and mechanical relaxation in materials, Hanser Verlag, München

Sessler GM (ed) (1998) Electrets, Caplacian Press, Morgan Hill, California, Vol 1 (3rd edition)

Gerhard-Multhaupt R (ed) (1999) Electrets, Caplacian Press, Morgan Hill, California, Vol 2 (3rd edition)

Gaiduk VI (2002) Dielectric relaxation and dynamics of polar molecules, World Scientific, Singapore

Subject Index